

Wanmer, Sapphire Rose (2018) *Characterisation of eruption and depositional processes of volcanic ash*. PhD thesis.

<https://theses.gla.ac.uk/30743/>

Copyright and moral rights for this work are retained by the author

A copy can be downloaded for personal non-commercial research or study, without prior permission or charge

This work cannot be reproduced or quoted extensively from without first obtaining permission in writing from the author

The content must not be changed in any way or sold commercially in any format or medium without the formal permission of the author

When referring to this work, full bibliographic details including the author, title, awarding institution and date of the thesis must be given

Characterisation of eruption and depositional processes of volcanic ash

Sapphire Rose Wanmer
Master of Geology, University of Leicester

Submitted in fulfilment of the requirements for the Degree of Doctor of
Philosophy

School of Geographical and Earth Sciences
College of Science and Engineering
University of Glasgow

April 2018

© Sapphire R. Wanmer 2018

Quotation

“...This is it!”

*David A. Johnston 8:32am May 18th 1980 as the eruption of
Mount St. Helens began*

Abstract

The morphologies of pyroclasts in basaltic and silicic ash deposits and tuffs in volcanic sequences have been used by previous authors to determine eruption processes in proximal settings commonly from modern eruption deposits. However, little research has been conducted on the finest tephra fraction, ash and fine-ash, in distal settings. The study of tephra in distal localities, >100 km from source, may provide important information regarding the dispersal of ash from highly explosive large-scale eruptions, for which proximal deposits are no longer present. The grain morphologies (blocky, bubble-wall, irregular and rod-like) and vesicularity of pyroclasts can be used to determine eruption processes and distinguish between ‘dry’ magmatic and ‘wet’ hydrovolcanic eruption-styles. This research is mainly concerned with the characteristics of pyroclasts in basaltic ash/tuff likely formed by highly explosive eruptions, and whether the explosivity of these eruptions was due to magma-water interactions and hydrovolcanism. This study includes a re-examination, and detailed petrographical analysis, of tuffs in the Early Eocene Balder Formation, North Sea Basin, and Harwich Formation, SE England, where the source of tephra produced by explosive volcanism and the extent of basaltic ash dispersal have been contested. Previously, these basaltic tuffs have been attributed to large-scale hydrovolcanic eruptions that occurred during initial sea-floor spreading in the NE Atlantic during the separation of Greenland from NW Europe. These tuffs are compared and contrasted with the basaltic Saksunarvatn Ash (10.3 ka BP) of Grímsvötn Volcano, Iceland, and various non-lava lithologies of the Miocene Columbia River Flood Basalt Province, USA.

The primary characteristics of pyroclasts may be modified by abrasion and alteration, particularly during additional transport and deposition. Therefore, the features created directly by the fragmentation and quenching of pyroclasts need to be distinguished from features created by the reworking of this material in the sedimentary environment. It is therefore essential to determine the characteristics of pyroclastic and volcanoclastic materials, which can be achieved by comparing data on the overall deposit characteristics, grain-types, grain-size distribution and grain-morphologies. For example, pyroclastic deposits of ash-grade are dominated by up to 100% igneous/volcanic grain-types, particularly

glassy pyroclasts; in thin-section the pyroclasts have smooth-edges and may have undergone limited alteration in modern deposits. In contrast, volcanoclastic deposits may contain a wide range of clast-types, including a greater number of non-volcanic grains, and sedimentary structures such as cross-stratification; in thin-section, reworked pyroclasts of ash-grade (volcanoclastic grains) often have jagged-edges, and varying levels of alteration. This study builds upon the observations and naming schemes of previous authors and proposes a scheme applicable to distal deposits of ash and fine-ash, of both basaltic and silicic composition, including highly altered material.

Table of contents

<i>Quotation</i>	2
<i>Abstract</i>	3
<i>List of figures</i>	11
<i>List of tables</i>	22
<i>Acknowledgement</i>	24
<i>Author's declaration</i>	26
<i>Abbreviations</i>	27
<i>Lithofacies</i>	28
Chapter 1: Introduction	29
1.1 Research Rational	30
1.1.1 Definition and terminology of pyroclastic and volcanoclastic deposits	30
1.1.2 Basaltic volcanism and hydrovolcanism and their ash	34
1.2 Research aims and objectives	39
1.3 Methods	40
1.3.1 Field work and core-store data collection	40
1.3.2 Petrography	41
1.3.3 Image analysis	42
1.4 Thesis outline	48
Chapter 2: The Saksunarvatn Ash, Iceland	52
2.1 Introduction	52
2.2 Geological history	54
2.3 Aims and objectives	60
2.4 Methods	60
2.5 Results	61
2.5.1 Field observations	61
2.5.1.1 Búrfellsstöð, Locality 1a-d	62
2.5.1.2 Hekla, Locality 2: 64°46'9.00"N 19°29'39.10"W	72
2.5.1.3 Kjaltell, Locality 3: 64°21'19.96"N 19°44'30.56"W	76
2.5.2 Optical microscopy	80
2.5.3 SEM	82
2.5.3.1 Búrfellsstöð, Locality 1a-d	83
2.5.3.2 Hekla, Locality 2	91
2.5.3.3 Kjaltell, Locality 3	96
2.5.3.4 Chemical composition of pyroclasts	100
2.5.4 Image analysis	102
2.5.4.1 Grain-size distribution	102
2.5.4.2 Sample characteristics, clast-types and features	106
2.5.4.3 Pyroclast characteristics	111
2.6 Discussion	116
2.6.1 Deposit characteristics and environments of deposition	116

2.6.1.1	Búrfellsstöð, Locality 1a-d	118
2.6.1.2	Hekla, Locality 2: 64°46'9.00"N 19°29'39.10"W	122
2.6.1.3	Kjaltell, Locality 3: 64°21'19.96"N 19°44'30.56"W	124
2.6.2	Eruption dynamics	125
2.6.2.1	Pyroclast morphology	125
2.6.2.2	Ash aggregates	133
2.6.3	Primary versus reworked volcanic material	134
2.6.3.1	Chemical composition of pyroclasts	137
2.6.3.2	Alteration of pyroclasts	138
2.7	Conclusions	139
Chapter 3: North Sea Basin Early Eocene stratigraphy		144
3.1	Introduction	144
3.2	Geological history and literature review	147
3.2.1	Late Palaeocene to Early Eocene stratigraphy of the North Sea Basin	152
3.2.2	The Balder Formation	156
3.3	Aims and objectives	162
3.4	Methods	162
3.5	Results	166
3.5.1	Observations of core	166
3.5.1.1	Well UKCS29/05a-7, 56°50'17.8"N 01°56'32.1"E	166
3.5.1.2	Well NOR25/7-5, 59°29'39.81"N 02°1'3.44"E	171
3.5.1.3	Well NOR25/11-17, 59°3'26.66"N 02°29'6.59"E	174
3.5.1.4	Well NOR30/2-1, 60°52'5.42"N 02°38'49.16"E	178
3.5.2	Optical microscopy and SEM	182
3.5.2.1	UKCS22/30a-1	182
3.5.2.2	UKCS29/05a-7	185
3.5.2.3	NOR25/7-5	190
3.5.2.4	NOR25/11-17	195
3.5.2.5	NOR Well 30/2-1	198
3.5.2.6	FSB 6104/25-1	199
3.5.3	Image analysis	201
3.5.4	Comparison of wire-line data to core analysis	214
3.5.4.1	UKCS22/30a-1	215
3.5.4.2	UKCS29/05a-7	216
3.5.4.3	NOR25/7-5	217
3.5.4.4	NOR25/11-17	218
3.5.4.5	NOR30/2-1	219
3.6	Discussion	221
3.6.1	Sedimentary features and the environment of deposition	221
3.6.1.1	Siliciclastic sandstone of NOR25/11-17	222
3.6.1.2	The origin of pyrite and pyrite framboids in the BF	223
3.6.1.3	Depositional processes indicated for tuffs in the BF	226
3.6.2	Eruption history and the location of source vents	227
3.6.2.1	Surtseyan and submarine eruptions	230
3.6.2.2	Fissure eruptions and sea-floor spreading	234
3.6.2.3	Transport and deposition of ash by water currents	236
3.6.2.4	Reworking of pyroclastic deposits in a terrestrial environment; re-deposition in the marine realm	238

3.6.2.5 Subaerial, central complex explosive volcanism	240
3.6.3 Volcanic activity elsewhere in NW Europe	241
3.7 Conclusions	242
Chapter 4: The Balder Formation of the Faroe-Shetland Basin, UKCS Quad 204 case study	248
4.1 Introduction	248
4.2 Geological history of the Faroe-Shetland Basin	251
4.3 Aims and objectives	256
4.4 Methods	256
4.4.1 Wire-line	257
4.4.2 Seismic	260
4.4.3 Spectral decomposition	262
4.4.4 Biostratigraphy	262
4.4.5 Additional data	263
4.4.6 Data limitations	263
4.5 Results	265
4.5.1 Wire-line	265
4.5.2 Seismic	267
4.5.3 Spectral decomposition	277
4.5.4 Biostratigraphy	278
4.6 Discussion	279
4.6.1 Wire-line characteristics of the Balder Formation	279
4.6.1.1 Cambo	279
4.6.1.2 Tornado-Suilven	284
4.6.2 2D seismic and 3D seismic data	289
4.6.2.1 Cambo	289
4.6.2.2 Tornado-Suilven	295
4.6.2.3 Other note-worthy features	298
4.6.3 Spectral decomposition	299
4.6.4 Biostratigraphy	302
4.6.4.1 Cambo	302
4.6.4.2 Tornado-Suilven	304
4.6.5 Comparison of all data	305
4.6.5.1 Wire-line	305
4.6.5.2 Seismic	308
4.6.5.3 Biostratigraphy	310
4.6.5.4 Comparison with composite logs	311
4.7 Conclusion	311
Chapter 5: The Harwich Formation, East Anglia	315
5.1 Introduction	315
5.2 Geological history	317
5.3 Aims and objectives	330
5.4 Methods	331
5.5 Results	333
5.5.1 Field observations	333
5.5.1.1 Wrabness	335

5.5.1.2	Harkstead	336
5.5.1.3	Levington/Nacton	339
5.5.1.4	Stutton	342
5.5.1.5	Walton-on-the-Naze	343
5.5.1.6	Shotley B borehole	344
5.6	Microscopy	348
5.6.1	Reflected and optical light microscopy	348
5.6.1.1	Wrabness Blue Band: WRAB_02	349
5.6.1.2	Harwich Stone Band (HSB): HARK_01, HARK_HB, LEVNAC_01A, LEVNAC_02A	350
5.6.1.3	Pale grey and dark grey bands: LEVNAC_01-02, LEVNAC_03A-LEVNAC_15	353
5.6.1.4	Shotley Borehole B	355
5.6.2	SEM features	357
5.6.2.1	Wrabness Blue Band: WRAB_02	357
5.6.2.2	Harwich Stone Band (HSB): HARK_01, HARK_HB, LEVNAC_01A, LEVNAC_02A	360
5.6.2.3	Pale and dark grey beds: LEVNAC_03A-LEVNAC_15A	364
5.6.2.4	Shotley Borehole B	368
5.7	Image analysis	369
5.8	Discussion	373
5.8.1	Characteristics and environment of deposition of the Wrabness Member sedimentary deposits	373
5.8.2	Characteristics of ash-rich deposits and inferred eruption dynamics	378
5.8.3	Location of source vent(s)	386
5.9	Conclusions	394
Chapter 6:	<i>Columbia River Flood Basalt Sedimentary Analogue</i>	402
6.1	Introduction	402
6.2	Aims and objectives	405
6.3	Geological history and literature review	406
6.3.1	Emplacement history of the Columbia River Flood Basalt Group	406
6.3.2	Characteristics of the Ellensburg Formation: source of material, resultant deposits and their depositional setting	407
6.3.2.1	The Ellensburg Formation of Washington	411
6.3.2.2	Pyroclastic and volcanoclastic deposits of the Ellensburg Formation	415
6.3.2.3	Lewiston Basin, Idaho	419
6.4	Methods	420
6.5	Results and interpretations	421
6.5.1	Horse Heaven Hills (L1)	422
6.5.1.1	Field observations	422
6.5.1.2	Interpretation of field observations	425
6.5.1.3	Optical microscopy and SEM analysis	426
6.5.1.4	Interpretation of optical microscopy and SEM analysis	427
6.5.2	Snipes Mountain (L2)	428
6.5.2.1	Field observations	428
6.5.2.2	Interpretation of field observations	431

6.5.3 Yakima Ridge (L3)	432
6.5.3.1 Field observations	432
6.5.3.2 Interpretation of field observations	433
6.5.3.3 Optical microscopy and SEM analysis	433
6.5.3.4 Interpretation of optical microscopy and SEM analysis	435
6.5.4 Beverly Quarry (L4)	436
6.5.4.1 Field observations	436
6.5.4.2 Interpretation of field observations	448
6.5.4.3 Optical microscopy and SEM analysis	449
6.5.4.4 Interpretation of optical microscopy and SEM analysis	465
6.5.5 Yellpit (L5)	467
6.5.5.1 Field observations	467
6.5.5.2 Interpretation of field observations	469
6.5.5.3 Optical microscopy and SEM analysis	470
6.5.5.4 Interpretation of optical microscopy and SEM analysis	472
6.5.6 Finley Quarry (L6)	473
6.5.6.1 Field observations	473
6.5.6.2 Interpretation of field observations	474
6.5.6.3 Optical microscopy and SEM analysis	474
6.5.6.4 Interpretation of optical microscopy and SEM analysis	476
6.5.7 Sellards Road (L7)	476
6.5.7.1 Field observations	476
6.5.7.2 Interpretation of field observations	479
6.5.7.3 Optical microscopy and SEM analysis	480
6.5.7.4 Interpretation of optical microscopy and SEM analysis	483
6.5.8 Mabton - Bickleton Road (Locality 8)	484
6.5.8.1 Field observations	484
6.5.8.2 Interpretation of field observations	487
6.5.8.3 Optical microscopy and SEM analysis	488
6.5.8.4 Interpretation of optical microscopy and SEM analysis	490
6.5.9 Whitebird, Idaho (L9)	491
6.5.9.1 Field observations	491
6.5.9.2 Interpretation of field observations	495
6.5.9.3 Optical microscopy	496
6.5.9.4 Interpretation of optical microscopy	497
6.5.10 Idaho, State Road 95 (L10)	497
6.5.10.1 Field observations	497
6.5.10.2 Interpretation of field observations	499
6.5.10.3 Optical microscopy and SEM analysis	500
6.5.10.4 Interpretation of optical microscopy and SEM analysis	503
6.5.11 Image analysis	504
6.6 Discussion	509
6.6.1 Depositional history of the central Washington Ellensburg Formation.	509
6.6.1.1 Horse Heaven Hills (L1)	509
6.6.1.2 Snipes Mountain (L2)	511
6.6.1.3 Yakima Ridge (L3)	512
6.6.1.4 Beverly Quarry, (L4)	513
6.6.1.5 Yellpit (L5)	515
6.6.1.6 Finley Quarry (L6)	516
6.6.1.7 Sellards Road (L7)	517
6.6.1.8 Mabton-Bickleton Road (L8)	519

6.6.2 Deposition of the Ellensburg Formation equivalent of western Idaho (Latah/Payette Member)	522
6.6.2.1 Whitebird (Locality 9)	522
6.6.2.2 Idaho, State Road 95 (L10)	523
6.7 Conclusions	525
6.7.1 Comparison of lithologies across the CRFBP	525
6.7.2 Lava-sediment interactions	526
6.7.3 Large-scale silicic volcanism recorded in the Ellensburg Formation, Washington	529
6.7.3.1 Diatoms in silicic pyroclastic deposits	531
6.7.3.2 Source areas for the silicic pyroclastic material of the Ellensburg Formation around Pomona Basalt time	537
Chapter 7: Discussion and conclusions	541
7.1 Summary	541
7.2 The use of distal ash in the interpretation of eruption processes	551
7.3 Pyroclastic versus volcanoclastic deposits	553
7.4 Revised nomenclature	558
7.5 Use of ash and fine-ash for the identification of eruption processes and the recognition of pyroclastic and volcanoclastic deposits in distal settings	563
7.6 Volcanism associated with flood basalt and large igneous provinces	565
7.7 Further work	565
List of references	567
Index of digital appendices	604
1. Vesicularity data	604
2. Image analysis grain data	605
3. Manual point-count data	605

List of figures

Figure 1-1 Suggested stages of explosive magma-water interaction within a layered medium.	36
Figure 1-2 Pyroclast morphologies used in this research and their interpreted modes of formation.	38
Figure 1-3 Methods adopted for the preparation of an AsB SEM image for the collection of grain data using ImageJ.	43
Figure 1-4 ImageJ methods used to separate grains of different composition.	45
Figure 1-5 Methods used for calculating the percentage porosity of a sandstone using ImageJ.	47
Figure 1-6 Published time-scales for volcanic activity in the area of the North Atlantic Igneous Province.....	49
Figure 2-1 Map of Iceland showing the location of field sites mentioned in this study	52
Figure 2-2 Distribution of the SA from Grímsvötn Volcano in Iceland.....	55
Figure 2-3 Comparison of the chemical composition of the SA	58
Figure 2-4 Seismic profiles from offshore Iceland showing the SA reflector	59
Figure 2-5 Locations of field sites at Búrfellsstöð (A-D)	62
Figure 2-6 Lithostratigraphy for Locality 1a at Búrfellsstöð	64
Figure 2-7 Types of ripple structure identified at Búrfellsstöð Locality 1a.	65
Figure 2-8 Sedimentary log from Búrfellsstöð Locality 1b	66
Figure 2-9 A sediment volcano, showing a high level of deformation	67
Figure 2-10 Sedimentary log from Búrfellsstöð Locality 1c.....	68
Figure 2-11 Types of ripple structures identified in the sedimentary deposits at Búrfellsstöð Locality 1c.....	69
Figure 2-12 . The lower section of sediment exposed at Búrfellsstöð Locality 1d	70
Figure 2-13 Sedimentary log showing the stratigraphy exposed at Búrfellsstöð Locality 1d	71
Figure 2-14 Normal-graded laminae (or varves), observed at the top of the logged section exposed at Hekla, Locality 2	73
Figure 2-15 Sedimentary log for the exposed section seen at Hekla, Locality 2	74
Figure 2-16 Soft sediment deformation at the base of an asymmetrical ripple composed of sand.	75
Figure 2-17 Localised extensional faulting, or slumping, of cohesive blocks of sand within the lower section of the lacustrine deposits exposed at Hekla, Locality 2.	76
Figure 2-18 Map showing the location of Locality 3, at the base of Kjaltell.	77
Figure 2-19 Parallel and ripple cross-laminated silts and clays observed at Kjaltell, Locality 3.	78
Figure 2-20 Sedimentary log representing the section exposed at Kjaltell, Locality 3	79
Figure 2-21 PPL optical microscopy images showing the range of different micro-structures observed in thin-section.....	81
Figure 2-22 PPL optical microscopy images showing a variety of granular features observed within the samples from Hekla, Locality 2.....	82
Figure 2-23 Main clast types identified in ICE_14 from Búrfellsstöð 1a.....	84
Figure 2-24 Examples of granular and crystalline igneous clast-types in samples from Búrfellsstöð 1a.	85
Figure 2-25 Examples of pyroclast types in sample ICE_14 from Búrfellsstöð 1a.....	86
Figure 2-26 Lava-like clasts and features of pyroclasts observed in ICE_16 and ICE_17 from Búrfellsstöð 1b.	87
Figure 2-27 Features of Type 2 pyroclasts (mid-grey colour) observed in ICE_18 and ICE_25 from Búrfellsstöð 1c.....	89

Figure 2-28 Irregular and fluidal-shaped pyroclasts in samples from Búrfellsstöð 1c.	90
Figure 2-29 The range of features associated with pyroclasts from Búrfellsstöð 1d.	91
Figure 2-30 SEM AsB images showing different bedding and lamination features in samples from Hekla, Locality 2.....	92
Figure 2-31 SEM AsB images showing the range of volcanic clast-types that can be identified within the Hekla, Locality 2 samples.	93
Figure 2-32 Various types of lithic clasts and an example of an ash aggregate observed in ICE_09A.	94
Figure 2-33 Possible hydration cracks within pyroclasts of the Hekla, Locality 2 samples.	95
Figure 2-34 Various types of crystalline igneous clasts (red arrows) within ICE_09A. .	96
Figure 2-35 Varying types of crystalline igneous clasts observed in samples from Kjaltell, Locality 3.	97
Figure 2-36 Lava and granular lithic clasts observed in samples from Kjaltell, Locality 3.....	98
Figure 2-37 Features of pyroclasts in samples from Kjaltell, Locality 3.	99
Figure 2-38 Features of a Type 2 pyroclast identified in sample K_20 from Kjaltell.	100
Figure 2-39 Comparison of the chemical spectra of the two types of pyroclast identified during SEM analysis of samples ICE_02A, ICE_04A and ICE_09A, from Hekla, Locality 2.....	101
Figure 2-40 Progressive alteration of pyroclasts observed in ICE_09A.	102
Figure 2-42 Grain-size distribution for Búrfellsstöð, Locality 1a-c.	104
Figure 2-43 Grain-size distribution for Búrfellsstöð, Locality 1d; Hekla, Locality 2; Kjaltell, Locality 3.	105
Figure 2-44 Comparison of the grain-size distribution (number frequency %) for Type 1 and Type 2 pyroclasts within ICE_02A, ICE_04A and ICE_09A.....	106
Figure 2-45 Graphs showing the percentage of each grain-type observed in all of the thin-sections and grain-mounts.....	108
Figure 2-46 Abundance of blocky, bubble-wall, irregular and rod-like pyroclast morphologies in each sample.	112
Figure 2-47 Example of the orientation data for elongate grains	116
Figure 2-48 Modern analogue for the formation and identification of clay drapes and fluvial deposits in Iceland	119
Figure 2-49 Diagram showing how coarse-grains can be transported by ice and deposited through an underlying water body	123
Figure 2-50 Results of the vesicularity of the SA samples (this study) compared with those given by Ross & White (2012) for a range of other eruption-types.	130
Figure 2-51 An example of a very fine-scale pyroclast feature preserved in a compacted sample from Hekla, Locality 2.....	132
Figure 2-52 Comparison of SEM chemical spectra data for glass and devitrified glass present in a partially altered pyroclast from sample ICE_09A.....	139
Figure 3-1 Divisions of the Late Palaeocene and Early Eocene stratigraphy of the North Sea and adjacent basins in which the BF was deposited	145
Figure 3-2 Palaeogeographic reconstruction of the NE Atlantic and NW Europe at 53 Ma.....	147
Figure 3-3 Distribution of ash corresponding to each volcanic phase and sub-phase identified by Knox & Morton (1983).	151
Figure 3-4 Lithostratigraphy of the UKCS central and northern NSB, as proposed by Knox & Holloway (1992).	154
Figure 3-5 Well correlation for lithostratigraphy, gamma-ray response and sonic log of the Moray Group in the northern NSB.	155

Figure 3-6 Trace element compositional discrimination diagrams for BF tuffs from NOR30/2-1.	161
Figure 3-7 Lithological and grain-size log for the Balder Formation of UKCS29/05a-7, 56°50'17.8"N 01°56'32.1"E.	167
Figure 3-8 Interbedded siltstone/claystone and sandstone in UKCS29/05a-7, core no. 1, 9621 ft depth.	168
Figure 3-9 Sedimentary features of core from UKCS29/05a-7, core no. 1.	169
Figure 3-10 Symmetrical ripple with an erosive interior where the original silt/clay has been eroded by a current and replaced by instantaneous deposition of sand ..	170
Figure 3-11 Deformed siltstone, claystone and sandstone observed in the upper section of UKCS29/05a-7, core no.1, 9582.6 ft depth.	171
Figure 3-12 Lithological and grain-size log of the Balder Formation of NOR25/7-5, 59°29'39.81"N 02°1'3.44"E.	172
Figure 3-13 Normal graded tuffs interbedded with claystone in NOR25/7-5, core 3, at 1991.7m depth.	173
Figure 3-14 Sedimentary structures observed within the core from NOR25/7-5, core 2, at 1979.8 m.....	173
Figure 3-15 Calcite and pyrite cement developed within a green normal graded tuff overlain by laminated claystone in NOR25/7-5, core 3, at 1995.2 m depth.	174
Figure 3-16 Units of fining upwards sandstone to siltstone/claystone with grain-loaded basal contacts and uncommon diffuse bedding or lamination seen in core from NOR25/11-17, core 1, at 1631.8 m.	175
Figure 3-17 Lithologic and grain-type log for Balder Formation core of NOR25/11-17, 59°3'26.66"N 02°29'6.59"E.	176
Figure 3-18 Sedimentary features observed in a small (<10 cm) section of core from NOR25/11-17, core 1, at 1630.8 m depth	177
Figure 3-19 Burrow-like features and soft-sediment deformation creating non-uniform bed boundaries within core from NOR25/11-17, core 1, at 1632.9 m depth. ...	178
Figure 3-20 Lithological and grain-size log for core of the Balder Formation of NOR30/2-1, 60°52'5.42"N 02°38'49.16"E.	179
Figure 3-21 Deformed interbedded sandstone and siltstone in NOR30/2-1, core 2, at 1956.25 m depth.....	180
Figure 3-22 Discontinuous lenses of tuff or soft-sediment deformation features that may be associated with reworking of green tuffs in NOR30/2-1, core 2, at 1960.5 m depth.	181
Figure 3-23 Poorly-developed calcite cement through several units of tuff, giving the appearance of mineral veins, in NOR30/2-1, core 2, at 1956.7 m depth.	182
Figure 3-24 AsB SEM images showing the various forms of pyrite in samples from UKCS22/30a-1.	183
Figure 3-25 AsB SEM images showing pyroclasts of various types and levels of alteration observed within SSK56012 of UKCS22/30a-1.....	184
Figure 3-26 AsB SEM images showing differing characteristics of pyrite observed in samples from UKCS29/05a-7.	185
Figure 3-27 AsB SEM images showing the various forms of pyroclasts and igneous crystalline clasts observed within SSK56374 from UKCS29/05a-7.	187
Figure 3-28 AsB SEM images showing the range of pyroclasts types and their differing levels of alteration in sample SSK56341 from UKCS29/05a-7.	188
Figure 3-29 Palagonitisation of originally glassy pyroclasts of sample SSK56341 from UKCS29/05a-7.	189
Figure 3-30 AsB SEM images of the main clast types in sample 033c from NOR25/7-5.	190

Figure 3-31 AsB SEM image of contact between clay and igneous clast-rich coarse sandstone with calcite cement in sample 033 from NOR25/7-5.	191
Figure 3-32 General nature of the fining-upwards sequence in sample 032 from NOR25/7-5.	192
Figure 3-33 Igneous clasts with a calcite (A) or pyrite (B, C) cement, in sample 043 from NOR25/7-5.	193
Figure 3-34 AsB SEM image of pyroclasts and crystalline igneous clasts in sample 036 from NOR25/7-5.	194
Figure 3-35 AsB SEM images of the varying degrees of alteration in pyroclasts of sample 039 from NOR25/7-5.	195
Figure 3-36 Plane-polarised light microscope images of vesicular pyroclasts (red arrows) surrounded by a calcite cement (white) in sample 002 from NOR25/11-17.	196
Figure 3-37 Plane-polarised light microscope images of a quartz-rich sandstone with abundant porosity and high permeability (blue), in sample 005 from NOR25/11-17.	197
Figure 3-38 AsB SEM image showing the components found in some parts of the sandstone in sample 005 of NOR25/11-17.	198
Figure 3-39 AsB SEM features of samples 018 and 023 from NOR30/2-1.	199
Figure 3-40 AsB SEM images of igneous clast-types in sample from FSB 6104/25-1 (Sula-Stelka).	200
Figure 3-41 Fluidal-shaped crystalline igneous clasts with irregular-shaped vesicles of various sizes.	201
Figure 3-42 Grain-size distribution for samples from UKCS29/05a-7, NOR25/11-17 and FSB 6104/25-1.	203
Figure 3-43 Grain-size distribution graphs for samples from NOR25/7-5 and NOR30/2-1.	204
Figure 3-44 Grain-size distribution comparison for tuffs of each of the wells.	205
Figure 3-45 Equations of settling velocity (variation of Stokes' Law 1851) used to calculate the duration of settling for grains of different sizes through water. .	205
Figure 3-46 Settling velocity calculated for non-vesicular and vesicular pyroclasts of the BF, linking grain-size to the likely time take to be deposited.	207
Figure 3-47 Folk (1968) equation for the calculation of the sorting coefficient for clastic materials.	208
Figure 3-48 Composition of NOR 005 from NOR25/11-17.	210
Figure 3-49 Percentage of different clast types within samples of siltstone and sandstone dominated by igneous clasts.	211
Figure 3-50 Percentage of blocky, bubble-wall, irregular and rod-like pyroclasts in samples from all wells.	212
Figure 3-51 Wire-line and completion log interpreted geology for the Balder and Sele Formations of UKCS29/05a-1	217
Figure 3-52 Wire-line data for the entire Rogaland Group available for NOR25/7-5 (NPD).	218
Figure 3-53 Wire-line data (gamma-ray and sonic-velocity responses) for NOR25/11-17 (Norsk Hydro 1993).	219
Figure 3-54 Wire-line data (gamma-ray and sonic response), and composite log interpreted lithology for NOR30/2-1	220
Figure 3-55 Summary of the percentage of different lithologies logged in core of the BF.	222
Figure 3-56 Formation processes of pyrite framboids.	224
Figure 3-57 Volcanic and sedimentary environments discussed in the text as possible origins of the BF tuffs.	229

Figure 3-58 The range of grain-size data collected for the NSB BF tuffs corresponds to the distal tephra deposits of Surtseyan eruptions	233
Figure 3-59 Transport and reworking in a fluid with a high or low particle concentration.	238
Figure 3-60 Summary of pyroclastic and volcanoclastic depositional settings.	240
Figure 3-61 Palaeo-reconstruction showing the sources of basaltic eruptions and the deposition of ash and fine-ash that has been interpreted for the Balder Formation tuffs in this chapter.	247
Figure 4-1 Location of UKCS Quad 204 and Faroes Quad 6004 in which the Tornado, Suilven and Cambo wells are located within the Faroe-Shetland Basin (FSB). ..	250
Figure 4-2 Structural map of the Faroe-Shetland Basin and the reported extent of Palaeocene and Eocene plays	253
Figure 4-3 Models of the palaeobathymetry proposed for the FSB and UK around 57 Ma	254
Figure 4-4 Diagram showing how to interpret various gamma-ray responses along with density and neutron porosity data.	259
Figure 4-5 Diagram explaining how Petrel uses input parameters to define the window in which it uses data above and below a picked horizon to create a 3D surface.	261
Figure 4-6 Gamma-ray wireline data encompassing the whole BF used for interpretation of the lithologies and characteristics of the BF in the Cambo prospect.	266
Figure 4-7 General wire-line data encompassing the whole BF, and sometimes also the Flett Formation, of undifferentiated composite log data used for interpretation of the lithologies and characteristics of the BF in the Tornado-Suilven prospect.	267
Figure 4-8 Examples of X-line and In-line seismic sections, orientated E-W and N-S respectively, intersected by Well 204/14-1.	268
Figure 4-9 Topography of the picked TCS surface generated from a grid of data points from the picked TCS.	269
Figure 4-10 RMS amplitude (24ms window with +12 ms offset) window covers +12 ms to -12 ms from the picked TCS horizon in the Tornado-Suilven region of Quad 204.	271
Figure 4-11 Maximum amplitude (30 ms window with +15 ms offset) covering the Tornado-Suilven area of Quad 204.	272
Figure 4-12 Minimum amplitude (24ms window with +12 ms offset), covering the Tornado-Suilven area of Quad 204.	273
Figure 4-13 Maximum amplitude (24ms window with -12 offset) surface representing the picked TCS Member of the Cambo area of UK Quad 204.	274
Figure 4-14 Minimum amplitude (12ms window with -6 offset) surface covering the Cambo area of Quad 204.	275
Figure 4-15 RMS (24ms window with +12 offset) for the Cambo area of Quad 204. .	276
Figure 4-16 Minimum amplitude (24ms window, -12ms offset) 3D surface of the Tornado-Suilven and Cambo areas.	277
Figure 4-17 RGB blended spectral decomposition surface of the Cambo prospect shown at a level representing a time interval around deposition of the BF.	278
Figure 4-18 Correlation of lithological units across wells within the Cambo prospect based on gamma-ray signatures.	281
Figure 4-19 More 'shaley' and more 'sandy' lithologies interpreted in the BF of the Cambo wells, based on gamma-ray, density and neutron-porosity wire-line data.	283

Figure 4-20 General lithologies interpreted in the BF of the Tornado-Suilven wells based on gamma-ray, density and neutron-porosity wire-line data.	286
Figure 4-21 Interpreted channel sandstone bodies within the wire-line responses of wells in the Tornado-Suilven prospect.	289
Figure 4-22 Example of a seismic section intersected by Well 204/18-1 in the Tornado-Suilven prospect.	290
Figure 4-23 Annotated in-line seismic section intersecting Wells 204/10-2 and 204/5A-1.....	291
Figure 4-24 Minimum amplitude (24 ms window thickness with a +12 offset) surface of part of the Cambo Prospect	293
Figure 4-25 Anomaly within 2D seismic section intersected by Cambo Well 204/10-1, compared with the gamma-ray response through the BF.....	294
Figure 4-26 Interpretation of the area affected by longshore drift in the Cambo prospect.	295
Figure 4-27 Bifurcating seismic response within the BF as highlighted on a 2D x-line seismic section through the Tornado-Suilven prospect.	296
Figure 4-28 In-line 2D seismic section showing on-lap of the Top Cambo horizon on top of a mound in the underlying topography.	297
Figure 4-29 Nature of the Brahmaputra River and delta in India (GoogleEarth Ltd 2015).	298
Figure 4-30 In-line (top) and x-line seismic (bottom) sections through an igneous region. Note that the Top Cambo horizon on-laps this topographic feature. ...	299
Figure 4-31 Movement of meander over time as shown by moving up through the surface of an RGB spectral decomposition surface in the west of the Cambo field.	300
Figure 4-32 Interpreted RGB blended spectral decomposition surface of the Cambo field showing the main features that can be identified at the level of the BF..	301
Figure 4-33 Correlation of deltaic facies northwards from the Tornado and Suilven prospect to the Cambo prospect.	307
Figure 4-34 Figure 4-10 annotated to highlight the main features that can be identified on the 3D seismic surface between the Tornado-Suilven and Cambo field areas.	309
Figure 4-35 Example of a possible analogue environment along the coast of San Salvador, Central America with similar characteristics to those of the Tornado-Suilven and Cambo areas labelled	310
Figure 4-36 Summary diagram showing the interpreted lithologies and environment of deposition during Balder Formation time (late Palaeocene-early Eocene) across the Tornado-Suilven and Cambo prospects in UK Quad 204, with all the main evidence for these	314
Figure 5-1 Location of the study area in the UK (inset map), the location of the study areas within E. Anglia and the distribution of Palaeogene sedimentary deposits	316
Figure 5-2 Diagram showing the variations in the stratigraphy of the Harwich Formation (HF) throughout E. Anglia	324
Figure 5-3 . Palaeo-environmental facies interpretations for 56.5 Ma and 55 Ma within the North Sea and Southern England	325
Figure 5-4 Summary log representing the stratigraphy at Wrabness, as described by Jolley (1996).	327
Figure 5-5 Map showing the estimated regions of deposition for ash deposits in the North Sea and NW Europe	328
Figure 5-6 Distribution of ash corresponding to each volcanic phase and sub-phase identified by Knox & Morton (1983).	329

Figure 5-7 Field views illustrating the general nature of the various localities.	333
Figure 5-8 Comparison of the nature of the WM between sites from Stutton in the west to Harkstead in the east.	334
Figure 5-9 Prominent blue band comprised of clay can be seen in a fresh exposure at the base of the estuarine cliffs at Wrabness.	336
Figure 5-10 Regional unconformity between the Eocene HF (Wrabness Member) and Pleistocene glacial deposits.....	337
Figure 5-11 Trace fossils identified within the HSB at Harkstead.	339
Figure 5-12 Field view and log of the site between Levington and Nacton with arrows indicating the positions of samples.	341
Figure 5-13 Normal fault with <i>ca.</i> 1 m apparent displacement within the WM exposed between Levington and Nacton.	342
Figure 5-14 Banded character of the WM exposed beneath trees in the cliffs at Stutton.	343
Figure 5-15 Summary log for Walton-on-the-Naze as described by Jolley (1996).	344
Figure 5-16 Location of the Shotley Borehole relative to the field localities between the River Stour and Orwell.	345
Figure 5-17 Lithological log and sample locations of Shotley Borehole B.	346
Figure 5-18 Annotated view of the Shotley Borehole B core, showing a lack of any distinct interbedding like that observed at exposures in the field.	348
Figure 5-19 Relative stratigraphical positions of each sample described in the text.	349
Figure 5-20 Nature of the Wrabness Blue Band (WRAB_02), as seen under RL.	350
Figure 5-21 Main features observed in the HSB.	351
Figure 5-22 Effects of bioturbation (burrowing) seen within the HSB in thin-section.	352
Figure 5-23 Fragments of micro-fossils observed in RL in LEVNAC_02.	353
Figure 5-24 Bioturbation is common throughout the thin-sections from beds above and below the HSB.	354
Figure 5-25 Abundant pyroclasts seen within a normal-graded bed within LEVNAC_14A	355
Figure 5-26 Main features observed in thin-sections from the Shotley Borehole B. ..	356
Figure 5-27 AsB SEM images showing the main features of the clastic units of WRAB_02.	357
Figure 5-28 AsB SEM images of the varying forms of pyrite along with circular (in 2D) grains of calcite.....	358
Figure 5-29 AsB SEM images showing some of the interpreted pyroclasts observed within WRAB_02.	359
Figure 5-30 AsB SEM nature of the calcite cement -dominated HSB with numerous igneous clast-types from Levington/Nacton (LEVNAC_01A).	360
Figure 5-31 AsB SEM images of non-vesicular and vesicular pyroclasts within the HSB of HARK_01.	361
Figure 5-32 AsB SEM images of esicular pyroclasts of varying morphology observed within the HSB of HARK_01.	362
Figure 5-34 Comparison of the representative spectral compositions of pyroclasts from all samples of the HSB (excluding HARK_01).	363
Figure 5-35 AsB SEM examples of organic clasts identified in the upper part of the HSB.	364
Figure 5-36 AsB SEM image showing the preservation of pyroclast shapes as voids within the sample.	366
Figure 5-37 AsB SEM images of variably altered vesicular and non-vesicular pyroclasts in LEVNAC_14A.....	367
Figure 5-39 Features of samples from the Shotley Borehole B.....	368

Figure 5-40 Percentage of blocky, bubble-wall (B-w) and rod-like pyroclast morphologies; percentage of vesicular and non-vesicular pyroclasts; and, the percentage of juvenile and accidental lithics in samples from the HSB and LEVNAC_14A.	372
Figure 5-41 Radiating gypsum crystals that grew within the pore-space of the sediment in the WM.	377
Figure 5-42 Parasequences of a transgressive systems tract interpreted within the Shotley Borehole B sedimentary log, correlated with episodes of sea-level rise.	378
Figure 5-43 Comparison of pyroclast sizes within the HSB (HARK_HB, LEVNAC_01A) and LEVNAC_14A.	380
Figure 5-44 Comparison of the vesicularity of pyroclasts from the WM and examples associated with a range of eruption types.	382
Figure 5-45 Characteristics of pyroclast edges indicating brittle fragmentation.	383
Figure 5-47 Possible distance from source based on grain-size from a plume with a height of at least 35 km.	388
Figure 5-48 Location of palaeogene igneous centres and basaltic lavas of the BPIP that were emplaced during the Early Palaeogene.	391
Figure 5-49 Areas where possible source vents could be located and distances from E. Anglia.	393
Figure 6-1 Location of the CRFBP and field localities referred to in this text.	403
Figure 6-2 The Ellensburg Formation and its members.	404
Figure 6-3 Distribution of the dykes (A) and lavas (B) of the CRFBP over time.	406
Figure 6-4 Relative ages and emplacement volumes of the major sub-divisions of the CRFBP.	407
Figure 6-5 Location of Washington sedimentary basins described in the text.	409
Figure 6-6 Interpretation of sedimentary deposits within the Ellensburg Formation from the ancestral Yakima River.	414
Figure 6-7 Palaeoenvironmental reconstruction of part of the CRFBP.	418
Figure 6-8 Sedimentary log that represents the Ellensburg Formation observed at Horse Heaven Hills (L1).	423
Figure 6-9 Main lithologies of the exposure at L1:	424
Figure 6-10 Cross-stratified sandstone.	425
Figure 6-11 AsB SEM clast-types of WASH_04 from L1.	427
Figure 6-12 Overview of the units exposed at Snipes Mountain (L2).	429
Figure 6-13 Sand injectites within cross-stratified sandstones and conglomerates.	430
Figure 6-14 Sand injectite within the lower section of L2.	431
Figure 6-15 Lahar deposits sourced from historical lahar-events at Mount Merapi, Indonesia.	432
Figure 6-16 Cross-stratified sandstones and siltstones.	433
Figure 6-17 AsB SEM clast-types and pyroclast morphologies exhibited by sample WASH_06 from L3.	434
Figure 6-18 AsB SEM various types of granular lithic clast in WASH_06 from L3.	435
Figure 6-19 Localities within Beverly Quarry discussed in the text.	437
Figure 6-20 Lithological log for the entire Ellensburg Formation exposed at Beverly Quarry (L4).	438
Figure 6-21 Ripple cross-laminated siltstone/fine-sandstone at L4.	439
Figure 6-22 Characteristics of ash aggregates within exposures at L4.	440
Figure 6-23 Variations in the nature of contacts over short (<1 m) distances in the quarry face of L4.	441
Figure 6-24 Varying nature of the deposits in L4 in which accretionary lapilli occur.	442

Figure 6-25 Parallel laminated siltstone comprised of silicic ash (tuff or volcaniclastic siltstone) at L4.	443
Figure 6-26 Stratified tuffs overlain by conglomerate in L4.	443
Figure 6-27 Quartzite-rich conglomerate and sandstone with lenses of clast-supported conglomerate rests upon parallel laminated silicic tuff at L4.	444
Figure 6-28 Lithologies of the mid-section of the L4 sedimentary sequence.	445
Figure 6-29 Detail of the cross-bedded sandstones and granule-conglomerate within L4.	446
Figure 6-30 The upper lava-sediment contact, where the Elephant Mountains Basalt lies above the Ellensburg Formation, exposed at L4.	447
Figure 6-31 Trace fossils.	448
Figure 6-32 Heterogeneous granular nature of sample WASH_20 from L4.	450
Figure 6-33 Optical microscope images showing the components of sample WASH_21 from L4.	451
Figure 6-34 AsB SEM calcite-cemented sandstone of WASH_21 from L4.	452
Figure 6-35 AsB SEM types of crystalline igneous clasts within WASH_21 from L4. ...	453
Figure 6-36 Abundant bubble-wall and rod-like pyroclasts in sample WASH_23 from L4 under RL.	454
Figure 6-37 Whole and fragmented ash aggregates surrounded by a matrix of pyroclasts in sample WASH_22 L4.	455
Figure 6-38 AsB SEM features of pyroclasts from WASH_22 of L4 that correspond to magmatic fragmentation processes.	456
Figure 6-39 AsB SEM examples of smooth and jagged pyroclasts as evidence for different transport and depositional origins of ash in WASH_22 from L4.	456
Figure 6-40 AsB SEM examples of concentrically-layered ash aggregates from WASH_22 at L4.	458
Figure 6-41 AsB SEM features of larger ash aggregates in WASH_22 from L4.	459
Figure 6-42 AsB SEM nature of ash aggregate fragments in WASH_22 from L4.	459
Figure 6-43 AsB SEM diatoms within the fine-ash rim of an ash aggregates in WASH_22 from L4.	460
Figure 6-44 AsB SEM diatoms and diatom fragments identified in the outer layers of ash aggregates from L4.	461
Figure 6-45 Nature of sample WASH_29 from the main silicic tuff unit of L4.	462
Figure 6-46 AsB SEM images of features of the silicic tuff (WASH_29), from L4.	463
Figure 6-47 An example of microscope features of a structureless volcaniclastic unit from the L4 silicic tuff (pumicite) viewed under Plane-polarised light.	464
Figure 6-48 AsB SEM images illustrating some of the features of WASH_30.	465
Figure 6-49 Lithological log displaying details of the exposure at Yellpit (L5).	468
Figure 6-50 Exposure at Yellpit (L5).	469
Figure 6-51 Nature of a glassy welded tuff (WASH_14) at the lava-sediment contact at Yellpit.	470
Figure 6-52 Fused tuff (WASH_13) with an internal fabric and rare, bubble-wall shard(?)	471
Figure 6-53 AsB SEM details of clast-types in WASH_13 from L5.	472
Figure 6-54 Overview of Finley Quarry (L6), showing multiple lavas of the Umatilla and Pomona Basalts.	474
Figure 6-55 Optical microscope images showing the nature of the material that comprises samples WASH_07 from Finley Quarry.	475
Figure 6-56 Lithological log showing the sedimentary sequence exposed at Sellards Road (L7).	477
Figure 6-57 Cross-ripple laminated sandstones and parallel laminated siltstone/fine sandstone.	478

Figure 6-58 Interbedded cross-stratified and parallel laminated siltstones at L7.....	479
Figure 6-59 Nature of a volcanoclastic sandstone (WASH_32) from L7.	480
Figure 6-60 Inclined and aligned grains indicate the presence of diffuse and erosional bed boundaries throughout sample WASH_33 from L7.....	481
Figure 6-61 Inclined, elongate clasts, including pyroclasts and mica, within sample WASH_33 from L7.....	482
Figure 6-62 AsB SEM features of reworked pyroclasts in WASH_34 from Sellards Road (L7).	483
Figure 6-63 Lithological log for the exposure at Mabton-Bickleton Road (L8).	485
Figure 6-64 Large-scale high-angle cross-stratification	486
Figure 6-65 Grain-types observed in sample WASH_37 from L8.....	488
Figure 6-66 Plain Polarised (A) and Cross Polarised Light (B) images showing the nature of sample WASH_40 from L8.	489
Figure 6-67 AsB SEM features of pyroclasts within WASH_44.....	490
Figure 6-68 Lithological logs for Whitebird (L9b and 9c).	492
Figure 6-69 Examples of deciduous tree leaf and seed pod moulds collected from the laminated claystones at the base of L9c.	493
Figure 6-70 Examples of <i>Taxodium</i> sp. leaf moulds from the laminated claystones at L9c.	493
Figure 6-71 Normal fault in sedimentary rocks of the Ellensburg Formation at L9c.	494
Figure 6-72 Tilted sequence of sedimentary rocks, with shear zone, exposed at L9c.	495
Figure 6-73 Abundant vesicular pyroclasts seen under RL in sample ID_05 from L9c.	496
Figure 6-74 Fine-grained, grey sandstone interbedded with siltstone at L10.	497
Figure 6-75 Reverse fault displacing grey sandstone marker unit at Idaho, State Road 95 (L10).	498
Figure 6-76 Invasive nature of the lava at the lava-sediment contact at Idaho, State Road 95 (L10).	499
Figure 6-77 Abundant vesicular pyroclasts in sample ID_13 from L10.	501
Figure 6-78 Clast-types identified in sample ID_16 from L10.	502
Figure 6-79 AsB SEM images showing the main features of sample ID_13.	503
Figure 6-80 Grain-size distribution graphs.	505
Figure 6-81 Grain-size distribution graphs.	506
Figure 6-82 Percentage of different grain-types in each sample that contains pyroclasts.	507
Figure 6-83 Percentages of blocky, bubble-wall, irregular and rod-like pyroclast morphologies.	509
Figure 6-84 Summary of the main events that led to deposition of the Ellensburg Formation exposed at Horse Heaven Hills (L1).....	511
Figure 6-85 Summary of the main events in the depositional history of Snipes Mountain (L2).	512
Figure 6-86 Interpretation of the depositional setting for the exposure at Yakima Ridge (L3).....	512
Figure 6-87 Summary of interpretations for the depositional history of the Ellensburg Formation exposed at Beverly Quarry (L4).	515
Figure 6-88 Depositional and volcanic history interpreted for the EF of L5.....	516
Figure 6-89 Depositional history interpreted for L6.	517
Figure 6-90 Interpretation of the depositional history of the EF of L7.	519
Figure 6-91 Summary of the depositional history of the Ellensburg Formation exposed at L8.	521
Figure 6-92 Interpretation of the depositional history of Whitebird (L9a-c).....	523
Figure 6-93 Interpreted depositional history for State Road 95 (L10).....	524

Figure 6-94 Temperature and duration of heating required for lava to weld an underlying tuff of X thickness.	528
Figure 6-95 Correlation of lavas and clastic deposits across the field localities	530
Figure 6-96 Various controls on the formation of accretionary lapilli and other ash aggregates.	533
Figure 6-97 Processes responsible for the incorporation of freshwater diatoms into eruption settings and ash aggregates.....	535
Figure 6-98 Interpreted scenario for the formation of diatom-bearing ash aggregates at Beverly Quarry (L4).	536
Figure 6-99 Location of various volcanic centres that were active 12-10 Ma around the CRFBP.	539
Figure 6-100 Isopach map showing the extent of silicic air-fall ash deposition from the eruption of Mount St Helens 1980.....	540
Figure 7-1 Comparison of the grain-size distribution of basaltic tuffs from the Balder and Harwich formations.	548
Figure 7-2 Flow diagrams showing the use of sedimentary structures and grain-scale features required to distinguish between deposits of pyroclastic, volcanoclastic and sedimentary material.	555
Figure 7-3 Environments of deposition for pyroclastic, volcanoclastic and sedimentary deposits.	557
Figure 7-4 Examples of the naming for primary (A) and secondary pyroclastic (B) and volcanoclastic (C) deposits using the terminology proposed in the current study.	560

List of tables

Table 1-1 Grain-size classification and nomenclature for sedimentary, pyroclastic and volcanoclastic deposits and rocks.	31
Table 2-1 Published ages of the Saksunarvatn Ash.	54
Table 2-2 Location name and grid reference for each of the field sites used in this study.	60
Table 2-3 Percentage of pyroclasts and non-pyroclasts in each sample.	109
Table 2-4 Maximum percentage of juvenile and accidental volcanic material in each sample.....	111
Table 2-5 Results of percentage vesicularity calculations for vesicular pyroclasts of all samples.	114
Table 2-6 Percentage of vesicular pyroclasts present in each sample.	115
Table 2-7 Pyroclast morphology can be used to interpret the fragmentation mechanism that led to their formation; this information can be used to interpret eruption dynamics.....	127
Table 2-8 Formation of bubble-wall shards within a vesiculating magma.	128
Table 2-9 Characteristic features of pyroclasts and deposits used to distinguish between primary pyroclastic and volcanoclastic material.	137
Table 3-1 List of samples from UKCS29/05a-7 and UKCS22/30a-1 accessed with permission from the British Geological Survey.	164
Table 3-2 List of samples from NOR25/11-17 and NOR30/2-1 accessed with permission from STATOIL, and NOR25/7-5 accessed with permission from Aker BP.	165
Table 3-3 Degree of sorting in BF tuffs.	209
Table 3-4 Percentage of pyroclasts versus non-pyroclasts (*), and, the percentage of pyroclasts that are vesicular versus non-vesicular for each sample.	213
Table 3-5 Average percentage vesicularity of vesicular pyroclasts.	214
Table 3-6 Thicknesses of the BF estimated for each of the wells.	215
Table 4-1 Stratigraphy of the Faroe-Shetland Basin (FSB) and North Sea Basin.	252
Table 4-2 Data that was available for the BF for each well used in this study..	257
Table 4-3 Data used in this study with a comparison of the resolution, and the pros and cons of each data type.	264
Table 4-4 List of information regarding the date and company responsible for compilation of each composite log for each well.	265
Table 4-5 List of observed biostratigraphy within the BF of the Cambo wells and the habitats that they inhabited.....	304
Table 5-1 Divisions of the Late Palaeocene to Early Eocene stratigraphy relevant to this study.....	315
Table 5-2 Stratigraphic divisions of London and E. Anglia (Aldiss 2014).	319
Table 5-3 Dinoflagellates, micro-fossils and macro-fossils identified at the Palaeocene-Eocene boundary in the WM of E. Anglia	321
Table 5-4 Significant events that have occurred throughout the Early Eocene which may have affected sedimentation in the NSB, including the region of E. Anglia. (from Steurbaut et al. 2009).	323
Table 5-5 Locations of sample sites for the WM.	331
Table 5-6 Mineral and clast-type components of each sample.	365
Table 5-7 Mineral and clast-types present in samples from Shotley Borehole B.	369
Table 5-8 Number Frequency (%) grain-size distribution for samples of Levington-Nacton calculated using image analysis.	371

Table 5-9 Vesicle percentages for samples of the HSB and LEVNAC_14A.	373
Table 5-10 Published time-scales for volcanic activity in the area of the North Atlantic Igneous Province (NAIP) that could have acted as a source for the volcanic material identified in the WM. Many of these dates have a large range of uncertainty, particularly regarding the methods used at the time these dates were acquired.	390
Table 5-11 Magmatic versus hydro volcanic deposit characteristics summarised for the primary ash fall deposits of the HSB and LEVNAC_14A (references in text).....	398
Table 6-1 Features of the various members of the Ellensburg Formation as interpreted by Smith (1988a, b).	412
Table 6-2 Silicic and andesitic pyroclastic and volcanoclastic deposits described within the CRFBP.	416
Table 6-3 List of locality names and locations, and samples that are described in the text.	421
Table 6-4 Number of vesicular pyroclasts.	508
Table 6-5 Percentage vesicularity results for all samples containing vesicular pyroclasts.	508
Table 6-6 Types of lava-sediment interaction identified in the CRFBP during the present investigation.	527
Table 7-1 Examples of pyroclast morphologies and their inferred mode of formation.....	552
Table 7-2 Comparison of the naming schemes used for pyroclastic and volcanoclastic deposits in the literature, and the naming schemes proposed by the current study.	558
Table 7-3 Summary of the revisions to the nomenclature of pyroclastic, volcanoclastic and sedimentary deposits/rocks proposed in the current study for ash-grade distal deposits and rocks.....	562
Table 7-4 The applicability of different sources of data used in the characterisation of distal deposits of ash and fine-ash.....	564

Acknowledgement

This research was sponsored by OMV, through the Volcanic Margins Research Consortium (VMRC).

Firstly thanks must go to my supervisors Dr Brian Bell and Dr David Brown, for giving me the opportunity to fulfil some of my wildest dreams. I will never forget the first 2 weeks of the PhD when the Vo@G team summited Mount Merapi at sunrise and camped on the shores of Anak Krakatau. Thank you for spending time with me in the field and for all your support and advice throughout the years.

Thanks to Giles Pickering who supported me during my internship at OMV (UK Ltd) and who provided feedback on my work. I had a great time working in the office alongside colleagues and friends from OMV and the VMRC. Particular thanks to Hugo Muchado and Liam Holt who have provided abundant support for many aspects of this research regarding the North Sea and Faroe-Shetland Basins, wire-line and seismic interpretation and training. And, Kirstie Wright for providing advice on spectral decomposition, and support throughout the PhD.

Fieldwork would not have been successful without the advice of local experts, including Steve Reidel (USA) and Thor Thordarson (Iceland) who provided assistance in the field, literature and resources. Thanks to David Jolley for initial advice regarding field localities for sampling of the Wrabness Member in E. Anglia (UK).

To the British Geological Survey, Norwegian Petroleum Directorate and Weatherford Laboratories for allowing me to access and sample core; particular thanks to Statoil for allowing sampling of NOR 25/11-17 and 30/2-1, and Aker BP for sampling of NOR 25/7-5. With thanks to John Gilleece and ALS Oil & Gas for producing high quality thin-sections of some very difficult samples, and to John for teaching me how to make my own grain-mounts. Thanks to Peter Chung for carbon coating my many samples and allowing me to use the SEM for data collection.

To Richard Brown, Nick Schofield, Richard Walker, Simon Passey, and all the members of the VMRC for allowing me to participate in fieldwork and workshops

that have given me an insight into many things that I wouldn't have otherwise ever considered, and helping to bridge the gap between industry and academia.

The undying support and encouragement of my family and friends has helped me to cope with the ups and downs of this PhD (Vo@G team: Jonny, Charlotte, Heather, Pamela (Bailey's and coke anyone?)). The original members of the corridor of doom, D&D companions, Pint of Science family, Ashwini, Annemarie, Jessica, Susan, Sarah, Katie and Mike). Very special thanks must go to my spudling sister Jade for putting up with my over-excitement when I felt I'd had a breakthrough, and for picking me up when I felt like it would never end. Finally, thanks to Jarek for making me smile and accompanying me on many unforgettable adventures.

Author's declaration

I declare that this thesis, except where acknowledged to others, represents my own work carried out in the School of Geographical and Earth Sciences, University of Glasgow. The research presented here has not been submitted for any other degree at the University of Glasgow, nor at any other institution. Any published or unpublished work by authors has been given full acknowledgement in the text.

Sapphire R. Wanmer

Abbreviations

BF - Balder Formation

BGS - British Geological Survey

BPIP - British Palaeogene Igneous Province

CRFBP - Columbia River Flood Basalt Province

EF - Ellensburg Formation

FSB - Faroe-Shetland Basin

GV - Grímsvötn Volcano

HF - Harwich Formation

HSB - Harwich Stone Band

NAIP - North Atlantic Igneous Province

NOR - Norwegian-Danish Basin

NP - Nannoplankton zone

NPD - Norwegian Petroleum Directorate

NSB - North Sea Basin

PDC - Pyroclastic Density Current

SA - Saksunarvatn Ash

UKCS - UK Continental Shelf

WM - Wrabness Member

Lithofacies

Ac - Accretionary lapilli

Clst - Claystone

Cong - Conglomerate

Ftuff - Fused tuff

Slt - Siltstone

Slt/Clst - Siltstone/Claystone

Sst - Sandstone

Sst/Slt - Fine sandstone/siltstone

Chapter 1: Introduction

Explosive volcanic eruptions can produce large volumes of ash that may be transported and deposited over large distances from source. The characteristics of the resultant deposits and the features of the ash can give an indication of eruption processes (Heiken 1972, 1974; Walker 1981; Wohletz 1983; Wohletz & Sheridan 1983; Carey & Sparks 1986; Cas & Wright 1988; Barberi et al. 1989; Houghton & Wilson 1989; Cioni et al. 1992; Blower et al. 2001; Riley et al. 2003; Gaonac'h et al. 2005; Houghton & Gonnermann 2008; Polacci et al. 2008; Clarke et al. 2009; Rose & Durant 2009; Mattsson 2010; Shea et al. 2010; Bonadonna et al. 2011; Brown et al. 2012; Ross & White 2012; Graettinger et al. 2013; Moitra et al. 2013; Cioni et al. 2014; D'Oriano et al. 2014; Heap et al. 2014), that can be important in assessing styles of ancient volcanic activity.

Characterisation of ash morphologies, including their shapes and vesicularity, as well as the overall nature of the deposit, is required to determine the type of eruption responsible for ash production, for example, whether eruptions involved purely magmatic fragmentation, via the expansion of volatiles, or hydrovolcanism, which involves magma-water interactions (e.g. Walker & Croasdale 1971; Heiken 1972, 1974; Wohletz 1983; Wohletz & Sheridan 1983; Cas & Wright 1988; Rose & Durant 2009; Brown et al. 2012; Graettinger et al. 2013). This is particularly relevant for the interpretation of the mechanisms responsible for highly explosive basaltic eruptions, the products of which are being more frequently recognised in the volcanic record, but are currently poorly understood (Walker et al. 1984; Hanson & Elliot 1996; Houghton et al. 2004; White et al. 2004; Gurenko et al. 2005; Carey et al. 2007; Kutterolf et al. 2007; Houghton & Gonnermann 2008; Costantini et al. 2009; Pérez et al. 2009; Costantini et al. 2010; Goepfert & Gardner 2010; Freda et al. 2011; Brand & Clarke 2012; Oddsson et al. 2012; Szramek 2016). In addition to identifying the eruption signatures preserved in ash deposits, now tuffs, it is essential to determine the differences between primary pyroclastic material, deposited directly by an eruption, and volcanoclastic material, that involves the additional transport (reworking) and re-deposition of pyroclastic material. Different definitions for volcanoclastic deposits exist in the literature (see section 1.1.1), but there remains problems in how to define the lithological and microscopic

features of ash and how to relate these to eruption and/or reworking processes (e.g. Frolova 2008; Lenhardt et al. 2011; D’Oriano et al. 2014).

1.1 Research Rational

1.1.1 Definition and terminology of pyroclastic and volcaniclastic deposits

Tephra is used here to describe all material produced during any volcanic eruption or explosion (e.g. Brendryen et al. 2010). The term pyroclastic can be applied to all material formed during an eruption involving the fragmentation of magma and its expulsion from a vent (e.g. Fisher 1961; Schmid 1981). Pyroclastic deposits include all material deposited on the Earth’s surface directly by eruption processes, for example air-fall ash or deposits of pyroclastic density currents (PDCs) (e.g. White & Houghton 2006). Once lithified these deposits are termed tuffs (e.g. Schmid 1981; Frolova 2008). Pyroclastic deposits and rocks may be classified based on their grain-size (e.g. Schmid 1981; Cas & Wright 1988; White & Houghton 2006; Waitt 2007; Table 1-1), similar to the classification of sediments and sedimentary rocks (e.g. Wentworth 1922; Table 1-1).

This research is focused on volcanic ash (unlithified), tuff (lithified) and their volcaniclastic equivalents (Table 1-1). Ash has a grain-size of <2 mm and can consist of glassy pyroclasts, crystalline igneous lithics and crystals (e.g. Schmid 1981; Cas & Wright 1988); further subdivisions of grain-size include fine-ash (up to 63 µm; Fisher 1961; Schmid 1981; White & Houghton 2006) and very fine-ash (up to 4 µm; White & Houghton 2006). The resultant tuff will be comprised of ash including glassy or devitrified pyroclasts, crystalline igneous lithics and crystals (e.g. Schmid 1981).

Phi (upper limit) (ϕ)	Metric (upper limit)		Wentworth (1922) grain-size classification (sediment)	Rock	Pyroclastic grain-size classification	Volcaniclastic grain-size classification (Cas & Wright 1988)
	(mm)	(μ m)				
<-8	>256		Boulder	Breccia/conglomerate	Block/bomb Rock: Breccia/ conglomerate	Volcaniclastic* (breccia/ conglomerate)
-8	256		Cobble			
-6	64		Pebble		Lapilli Rock: Lapilli-tuff	
-2	4		Granule			
-1	2		V. coarse sand	Sandstone (Sst)	Ash Rock: tuff	Volcaniclastic sand(stone)
0	1	1000	Coarse sand			
1	0.5	500	Medium sand			
2	0.25	250	Fine sand			
3		125	Fine sand/silt			
4		63	Silt	Slt	Fine-ash	Volcaniclastic silt(stone)
8		4	Clay	Clst	V. fine-ash	Volcaniclastic clay(stone)

Table 1-1 Grain-size classification and nomenclature for sedimentary, pyroclastic and volcaniclastic deposits and rocks. *Unconsolidated deposits would be termed volcaniclastic boulder, cobble, pebble, gravel deposit based on the Wentworth (1922) grain-size classification. The pyroclastic terminology of Cas & Wright (1988) has been modified to include subdivisions for fine-ash and very fine-ash.

If air-fall ash is transported (reworked) prior to lithification, then it will be re-deposited as volcaniclastic material (e.g. Cas & Busby-Spera 1991; Manville et al. 2009). The resultant rock-type should be defined based on its grain-size with the prefix 'volcaniclastic' (Table 1-1; Cas & Wright 1988).

Volcaniclastic deposits can be found in proximal and distal locations surrounding volcanoes, in all depositional environments (e.g. Frolova 2008). The supply of volcaniclastic sediments may be controlled by weathering and erosion and can be instantaneous, consisting of large volumes of material that can inundate sedimentary systems (Manville et al. 2009).

A volcaniclastic sediment or rock is one in which a significant proportion of the clasts are of volcanic origin. The British Geological Survey (BGS) define this as being 10% volcanic clasts, whereas Frolova (2008) defines volcaniclastic material as containing >50% volcanic clasts; others do not make a quantifiable distinction

(e.g. Fisher 1961; Ross et al. 2005; Manville et al. 2009). Therefore, even when identifying volcanoclastic material, there are discrepancies in how these are defined.

Volcanoclastic terminology was first introduced by Fisher (1961) who based definitions on the origin of grains (Fisher 1961; Manville et al. 2009). By Fisher's (1961) definitions, pyroclastic clasts originate from the explosive fragmentation of magma; hyaloclastic clasts are produced by water-lava interactions involving quench fragmentation; and, autoclastic clasts are produced by mechanical fragmentation during flow movement (mainly of lavas). Primary volcanoclastic material is defined as material directly formed and deposited during eruptions, whereas secondary volcanoclastic deposits involve reworking. In Fisher's (1961) definitions, epiclastic clasts are formed by the weathering and erosion of pre-existing rocks and do not include particles originating from unconsolidated loose material (Manville et al. 2009). McPhie et al. (1993) extended the use of epiclastic to include deposits originating from weathering and erosion of unconsolidated pre-existing volcanic material.

Cas & Wright (1987) suggested that the term pyroclastic should only be applied to material produced and transported by subaerial explosive eruptions, including deposits from ash-fall and PDCs. This does not include any pyroclastic material deposited through water. According to Cas & Wright (1987), pyroclastic material, irrespective of reworking, is a sediment once it touches water (Manville et al. 2009), and is therefore of volcanoclastic character.

White & Houghton (2006) defined volcanoclastic in terms of the initial depositional mechanism and they also redefined grain-sizes for different volcanoclastic grain terms. In their nomenclature, primary volcanoclastic rocks are described using volcanic clast names such as tuff (or ash) and lapilli tuff (or lapilli ash if non-lithified); clasts that are not deemed 'primary' and have been stored temporarily and therefore reworked are given sedimentary terms and are not referred to as being epiclastic. The term 'volcanoclastic' is not used to describe all volcanic material irrespective of origin, instead it is used to replace the term pyroclastic to describe particles deposited by volcanic eruptions (White & Houghton 2006; Manville et al. 2009). White & Houghton (2006) conclude that

the terms pyroclastic, autoclastic, hyaloclastic and peperitic are interpretations of deposits and should be used secondarily after a formal name has been given in terms of grain-size (supported by Manville et al. 2009). They also conclude that reworked 'volcaniclastic' rocks should be given sedimentary names without any reference to volcanic processes (supported by Manville et al. 2009).

Confusion clearly remains over the classification of pyroclastic and volcaniclastic deposits and rocks, with authors applying the classification best suited to them, rather than following any consensus and preferred naming convention. Regardless of this, direct observations of the features in exposures or samples that would allow classification of these rock-types has received little attention in the literature (e.g. Suthren 1985; Frolova 2008). These issues will be addressed in this thesis; definitions used are provided here for reference:

Pyroclastic - Any material produced and deposited directly from an eruption, this includes air-fall ash, deposits from PDCs and submarine eruptions.

Ash/Tuff - Any unconsolidated/lithified deposit composed of ash (pyroclastic grains of <2 mm), with no reference to the origin of the ash or depositional processes. This includes all subaerial and water-lain material. A noun may be applied to indicate the origin and nature of the deposit where known, for example, air-fall or water-lain ash/tuff.

Volcaniclastic - Any unconsolidated or lithified deposit containing >50% pyroclastic grain-types, where there is field or microscopic evidence of reworking and the re-deposition of grains.

In addition to naming issues, determining the differences between pyroclastic and volcaniclastic deposits is essential to our understanding of the processes of ash dispersal and therefore has implications for ash-related hazards at modern active volcanoes. Ashes will be analysed and compared from a range of environmental settings, including air-fall terrestrial, fluvial, lacustrine, shallow marine and deep marine.

1.1.2 Basaltic volcanism and hydrovolcanism and their ash

Basaltic magmas are commonly associated with eruptions of low explosivity, such as Strombolian- or Hawaiian-style eruptions, or the effusion of lavas (Thorarinsson et al. 1964; Walker 1973; Kokelaar & Durant 1983; White & Houghton 2000; Sorrentino et al. 2010; Vaughan & Webley 2010; Gjerløw et al. 2015). However, deposits of highly explosive basaltic eruptions, including Plinian-styles, are becoming more commonly recognised (Walker et al. 1984; Hanson & Elliot 1996; Houghton et al. 2004; White et al. 2004; Gurenko et al. 2005; Carey et al. 2007; Kutterolf et al. 2007; Houghton & Gonnermann 2008; Costantini et al. 2009; Pérez et al. 2009; Costantini et al. 2010; Goepfert & Gardner 2010; Freda et al. 2011; Brand & Clarke 2012; Oddsson et al. 2012; Szramek 2016). The conditions required to cause a basaltic magma to erupt explosively in this way are not fully understood, although, a growing quantity of research is being conducted (e.g. Wilson & Head 1981; Head & Wilson 1989; Zimanowski et al. 1997; Houghton et al. 1999; Houghton et al. 2004; Parfitt 2004; Gurenko et al. 2005; Houghton & Gonnermann 2008; Dellino et al. 2012; Graettinger et al. 2013; Pompilio et al. 2017). Explosive magma-water interactions may be one mechanism for the increased explosivity of these eruptions (Clarke et al. 2009; Dellino et al. 2012). Hydrovolcanic eruptions occur when a magmatic eruption, influenced by the expansion and release of volatiles, interacts with an external source of water (Sheridan & Wohletz 1983). These interactions can occur in any setting regardless of magma composition, and may involve magma interacting with groundwater, crater lake water, ice, infiltrating rainwater, or ocean water (e.g. Sohn et al. 2008). Hydrovolcanism may also occur where lava interacts with surface water, for example, in the formation of rootless cones (Hamilton et al. 2010; Reynolds et al. 2015). Hydrovolcanic eruptions involve the rapid transfer of heat from magma to water, which leads to further fragmentation of the magma (Walker 1981; Sheridan & Wohletz 1983; Németh & Cronin 2009; Houghton et al. 2011; Dellino et al. 2012). Therefore, hydrovolcanic eruptions are often more explosive than purely 'dry' magmatic eruptions, and therefore produce finer-grained deposits (Wohletz 1983; Dellino et al. 2012). Explosions during a hydrovolcanic eruption can produce shock waves that resonate in a vent and further enhance the fragmentation of the magma and clasts (Wohletz 1983).

Several authors regard hydrovolcanic eruptions as being like the fuel-coolant interactions observed in the metals industry, where the magma is the fuel and water is the coolant (Sheridan & Wohletz 1983; Wohletz 1983; White 1996; Trigila et al. 2007). These interactions are considered to involve: 1) Initial contact of water with magma that produces a vapour film which prevents the two phases from mixing (Figure 1-1a; Starostin et al. 2005). 2) Collapse of the vapour film between the water and magma allowing rapid mixing and fragmentation of the melt (Figure 1-1b-c; Sheridan & Wohletz 1983; Trigila et al. 2007). 3) Water flashes to steam during rapid heat transfer allowing rapid explosive expansion of the system (Figure 1-1d; Sheridan & Wohletz 1983; Trigila et al. 2007). This process can become self-sustaining until either the magma (fuel) or the water (coolant) runs out (Kokelaar 1983; Sheridan & Wohletz 1983; White 1996; Starostin et al. 2005; Trigila et al. 2007). Kokelaar (1983) suggests that explosive hydrovolcanic eruptions will only be sustained by active injections of magma into water and that expansion and explosion is therefore not self-sustaining. Some authors suggest that these fuel-coolant interactions are essential for hydrovolcanic eruptions (e.g. Starostin et al. 2005), whereas others suggest that this is important but not essential (e.g. Kokelaar 1983; White 1996).

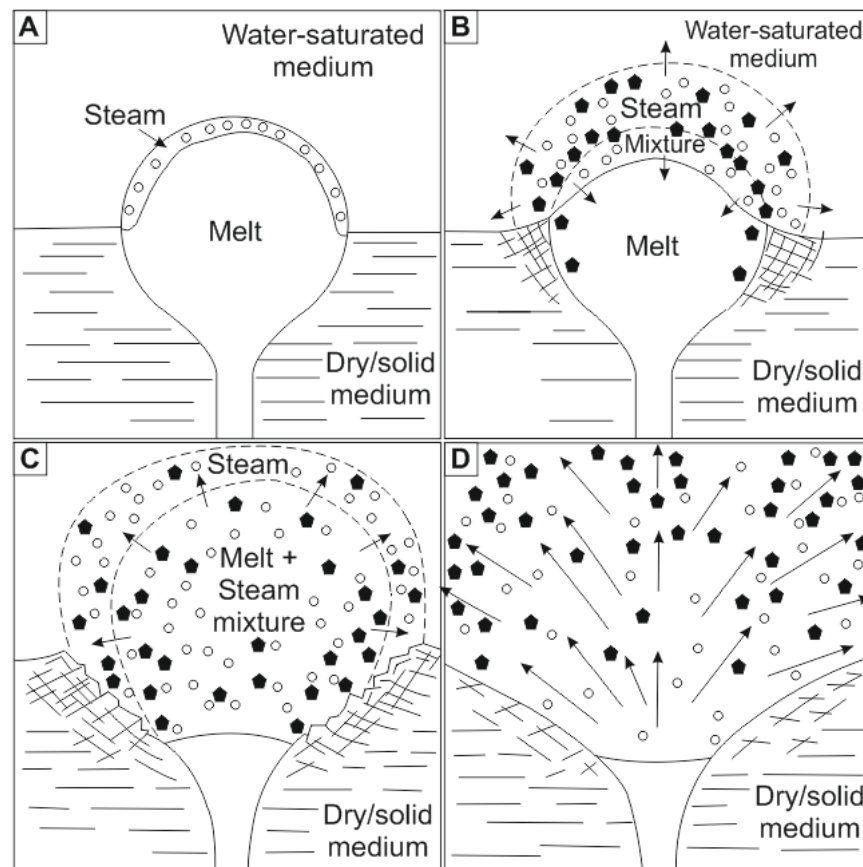


Figure 1-1 Suggested stages of explosive magma-water interaction within a layered medium. A) Formation of a vapour film at the magma-water contact. B) Increased pulsating produces a high-pressure steam. C) Large-scale magma-water interaction leads to explosion (D) (After Sheridan & Wohletz 1983).

There may be issues in applying the fuel-coolant interaction model to a real volcanic system (Kokelaar 1983; White 1996). For example, the model uses pure water, but in a volcanic setting an impure water or sediment-laden water is likely to be present therefore affecting the efficiency of the fuel-coolant interaction model (Kokelaar 1983; White 1996). This is because magma interaction with impure sediment-laden water can increase the efficiency of mixing, leading to greater interaction between the two phases (White 1996). The vent environment alone can affect fragmentation and explosiveness during these interactions (White 1996).

Observations of modern explosive hydrovolcanic eruptions show that explosions are periodic and pulsatory, with explosions occurring directly after magma-water contact or mixing (Shridan & Wohletz 1983). Observations show that the amount of water and apparent depth of explosions appear to affect the behaviour of the ejected pyroclasts the most (Sheridan & Wohletz 1983). Although, not all

magma-water interactions result in explosive activity, for example, too little water will have no effect, and too much water will inhibit explosive activity (Starostin et al. 2005). Experiments have shown that the optimum water:magma ratio for a basaltic magma is 1:3, resulting in the most explosive hydrovolcanic eruptions (Sheridan & Wohletz 1983). Additionally, the ejection of hydrovolcanic tephra above a vent would require explosive magma-water interactions to occur at shallow enough depths to eject material out of the vent (Valentine et al. 2014). It is not clear how a change in magma composition, volatile content or temperature of the magma and water would affect the explosivity of magma-water interactions.

Hydrovolcanic eruptions produce water, steam, brecciated country-rock (i.e. accidental lithics) and juvenile tephra (glassy pyroclasts, crystalline material and crystals). According to Wohletz (1983) hydrovolcanic eruptions produce five dominant pyroclast morphologies: 1) blocky equant clasts produced by brittle fragmentation and quenching, 2) vesicular irregular-shaped clasts with smooth surfaces formed by turbulent mixing with water before quenching, with smooth surfaces controlled by vesicle walls, 3) convoluted and moss-like clasts with highly irregular surfaces formed by agglutination of very fine clasts, 4) spherical or drop-like clasts which have more fluidal shapes that are commonly agglutinated together or attached to larger clasts, and 5) plate-like clasts which are typical of phreato-Plinian eruptions and consist of shattered vesicle walls which interacted with water. Blocky equant clasts are found in coarse-grained hydrovolcanic ash, and moss-like, convoluted, spherical, drop-like and plate-like clasts are all found in the fine-grained hydrovolcanic ash (Wohletz 1983). In contrast, purely magmatic tephra will contain more fluidal, spherical and drop-like shaped clasts that are less fragmented than clasts produced by hydrovolcanism (Clarke et al. 2009). All hydrovolcanic clasts may be coated in vesiculated glass or contain micro-fractures (Sheridan & Wohletz 1983), and are more likely to be coated in alteration minerals, secondary mineral overgrowths and have infilled vesicles than magmatic clasts due to the involvement of water (Sheridan & Wohletz 1983; Clarke et al. 2009). In the present research pyroclast shapes have been divided into four main types (Figure 1-2); blocky, bubble-wall, irregular and rod-like. Clasts produced by hydrovolcanic eruptions may undergo abrasion during transport, prior to or after their initial deposition, and evidence

of this will be recorded by the shape and features of the clasts (Sheridan & Wohletz 1983). For example, clasts may have edge modifications such as grooves, scratches and fractures, and may be adhered to other particles (Sheridan & Wohletz 1983).






	Blocky	Bubble-wall		Irregular	Rod-like
Examples					
Fragmentation mechanism	Brittle fragmentation, can be an indicator of rapid quenching of the erupted magma.	Bubble-walls with horizontal edges formed by brittle fragmentation (red) and magmatic fragmentation via the expansion of bubbles	Bubble-walls with edges that taper-off forming delicate sharp points, and circular segments of bubble films (blue), formed by magmatic fragmentation due to bubble growth	Fluidal shapes forming irregular pyroclast morphology, formed during slower cooling of the erupted magma which allows the pyroclasts to deform in a ductile-manner prior to solidifying	Elongate rod-like pyroclasts formed by stretching of silicic magma during rapid ascent, with brittle fragmentation of the magma caused by high strain. Or, water droplets interacting with an erupting basaltic magma creating Limu-o-Pele
Eruption type	Magmatic and/or Hydrovolcanic	Magmatic and/or Hydrovolcanic	Magmatic	Magmatic	Magmatic (silicic) or Hydrovolcanic (basaltic)

Figure 1-2 Pyroclast morphologies used in this research and their interpreted modes of formation. Blocky pyroclasts are considered to be formed by high levels of fragmentation and will be most common in very fine-ash deposits regardless of magmatic or hydrovolcanic processes. Bubble-wall pyroclasts are evidence of magmatic fragmentation of magma via the expansion of bubbles; these may fragment a magma forming bubble-wall pyroclasts with pointed edges, however, additional fragmentation of these clasts via quenching in a hydrovolcanic plume could allow brittle fragmentation of these. Irregular pyroclasts retain some fluidal morphology and may be evidence for magmatic fragmentation with slower cooling of the pyroclasts allowing them to fluidally deform within the ash plume prior to deposition. Rod-like pyroclasts may be formed in highly-explosive magmatic eruption in which bubbles within the magma are stretched into tubes and the surrounding magma fragments into rod-like glass fragments. Alternatively, rod-like pyroclasts may be evidence of the involvement of water within the vent at the time of eruption (Graettinger et al. 2013).

Hydrovolcanic deposits have commonly been interpreted based on their content of accidental lithics (e.g. Sheridan & Wohletz 1983; Ross et al. 2005; Clarke et al. 2009; Németh & Cronin 2009; Valentine et al. 2014). This clast-type is created when explosions occur within the vent and fragments of pre-existing rock (accidental lithics) become incorporated into an eruption plume and its deposits (e.g. Németh & Cronin 2009; Valentine et al. 2014). Hydrovolcanic deposits can contain a high proportion of accidental lithics, particularly if the

eruption involves interaction with groundwater (e.g. Valentine et al. 2014). However, accidental lithics are not always present in hydrovolcanic deposits, for example, they are less likely to be found in Surtseyan eruptions that occur where a volcanic island emerges from a body of water, with explosions that occur at a shallow level within the conduit that is not necessarily surrounded by country-rock (e.g. Kokelaar 1983; Sheridan & Wohletz 1983).

Hydrovolcanic ashes can have a wide dispersal, especially those produced by phreato-Plinian eruptions (Sheridan & Wohletz 1983) as the steam in hydrovolcanic plumes lofts particles to greater heights than in 'dry' purely magmatic eruption plumes (Dellino et al. 2012; Oddsson et al. 2012).

Literature on the deposits of hydrovolcanic eruptions is mostly concerned with proximal tephra deposits, with no analysis of truly distal fine-grained (ash) material. Analysis of basaltic ash in this thesis will provide additional evidence of highly explosive basaltic eruptions and an interpretation of the mechanisms of these based on the characterisation and interpretation of distal ash deposits.

1.2 Research aims and objectives

In order to gain a comprehensive understanding of the features of volcanic ash and the processes by which it forms, the following research objectives have been set:

- a) To assess the characteristics of ash produced by a range of eruption-types and styles, and deposited in a range of environments, by interpretation of deposit characteristics on a bed- to grain-scale.
- b) To determine the differences between pyroclastic and volcanoclastic features of fine-ash that could allow the discrimination of eruption versus reworking processes.
- c) To detail the features of distal ash deposits of highly-explosive basaltic eruptions, and relate these to potential mechanisms that led to the highly-explosive eruption of basaltic magma. Here, a particular focus is on

basaltic volcanism associated with the early sea-floor spreading events during formation of the Palaeogene North Atlantic Igneous Province.

- d) To assess the pyroclastic, volcanoclastic and siliciclastic deposition associated with the non-lava stratigraphy of flood basalt provinces, within and beyond the province. Here, a particular focus is on the non-lava stratigraphy of the Miocene Columbia River Flood Basalt Province, USA, and the Palaeogene North Atlantic Igneous Province.

1.3 Methods

1.3.1 Field work and core-store data collection

The Balder Formation of the North Sea and Faroe-Shetland Basin was initially the focus of this research, therefore the additional field areas were chosen based on their likely comparison to parts of the North Atlantic Igneous Province to allow a comprehensive interpretation of the Balder Formation and its tuffs.

- The Saksunarvatn Ash, Iceland, was chosen as a possible analogue for fine-ash produced in hydrovolcanic basaltic eruptions that are relatively fresh.
- The Harwich Formation of SE England was chosen as it represents an onshore exposure of the offshore Balder Formation, and extends the study area of the Balder Formation tuffs.
- The Ellensburg Formation, USA, was chosen for its well-exposed non-lava stratigraphy within a flood basalt province, allowing a greater understanding of sedimentary and volcanic processes.

Core of the Balder Formation was chosen based on references in the literature, and availability of core held by the British Geological Society and Norwegian Petroleum Directorate. Additional core was viewed but was too badly damaged to allow comprehensive study of the formation to be made (e.g. the type section in core of Norwegian well 25/11-1).

In the field, localities were chosen based on the ease of access and the quality of the exposure. Lithologic logging of exposures, and core, was carried out, in addition to sampling. Logging of the core was conducted on a mm-scale and a mm- to cm-scale in the field. Samples were taken systematically with an aim to characterise all the rock-types. Sampling of core typically involved a limit on the number and size of samples that could be retrieved; samples were therefore taken of each lithology and of tuffs that were most likely to remain intact during any subsequent sample preparation.

1.3.2 Petrography

Polished thin-sections were produced at the University of Glasgow, and ALS Petrography. Thin-section preparation of core samples involved kerosene as the rocks swelled when in contact with water. Many samples were impregnated with a blue-dyed resin, as is standard for samples used in the hydrocarbon industry, to assess porosity and permeability. Key samples from the Ellensburg Formation were thin-sectioned at the University of Durham but many were not labelled properly or sectioned to a high enough standard to allow analysis to be conducted.

Polished grain-mounts of unconsolidated samples were produced by myself at the University of Glasgow by gently mixing loose grains into a layer of epoxy resin on a glass slide. Once set, the surfaces of these samples were ground down until an even surface was formed and then polished with a 1200, 2500 and 4000 grit silicon carbide paper. Further polishing was carried out with 1 μm and 0.3 μm aluminium oxide on a Kemet polishing machine. Samples were cleaned with distilled water and placed in an ultrasonic bath between polishing stages. Finally, the polished samples were coated in colloidal silica to remove any subsurface damage and allow clearer imaging using a Scanning Electron Microscope (SEM).

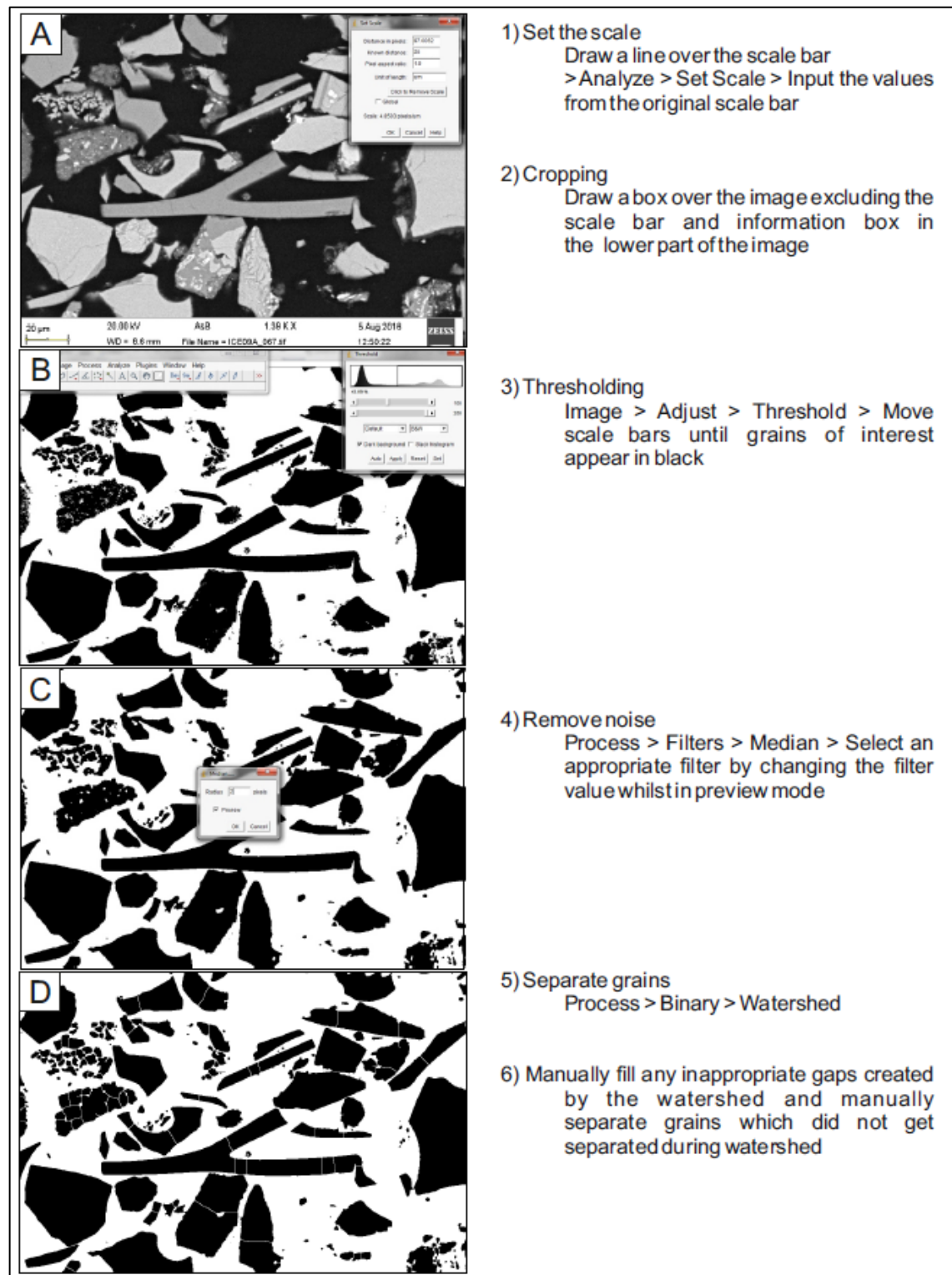
Optical microscopy was initially carried out on thin-sections using plane-polarised, cross-polarised and reflected light. Thin-sections and grain-mounts were analysed using a Zeiss Scanning Electron Microscope (SEM) at the University of Glasgow for more detailed analysis of clast shapes and the general

characteristics of the samples. All samples were carbon-coated in preparation for high-vacuum SEM analysis. Back-scatter (AsB) images were collected and Oxford software was used to provide basic chemical spectral analysis of the composition of minerals.

1.3.3 Image analysis

8-bit AsB SEM images were analysed using open source ImageJ software to obtain quantifiable data on various characteristics of the samples using image analysis based on the combined methods of Lewis et al. (2010), Ferriera & Rasband (2012), Jutzeler et al. (2012), and Heilbronner & Barrett (2014). This produced results regarding the grain-size distribution of the deposits, as well as more detailed characteristics of volcanic grains, including vesicle density and the abundance of pyroclasts of varying chemical composition. Data can be found in the digital appendices (Index of digital appendices p601).

When obtaining general grain data for the deposits, thresholding was applied to the 8-bit images to allow easier distinction of grains (Figure 1-3). Once thresholding was complete (Figure 1-3b), a median filter was used to reduce the noise of the image (Figure 1-3c). Following this, the application of a 'watershed' allowed for grains to be automatically separated where they were touching, to allow analysis of individual grains (Figure 1-3d). The process of applying the watershed to separate grains led to some errors that were then manually corrected by comparing the new image (Figure 1-3d) to the original SEM image (Figure 1-3a). Once grain data were calculated using ImageJ, they were copied into an excel spreadsheet in preparation for data analysis.



1) Set the scale
 Draw a line over the scale bar
 > Analyze > Set Scale > Input the values from the original scale bar

2) Cropping
 Draw a box over the image excluding the scale bar and information box in the lower part of the image

3) Thresholding
 Image > Adjust > Threshold > Move scale bars until grains of interest appear in black

4) Remove noise
 Process > Filters > Median > Select an appropriate filter by changing the filter value whilst in preview mode

5) Separate grains
 Process > Binary > Watershed

6) Manually fill any inappropriate gaps created by the watershed and manually separate grains which did not get separated during watershed

Figure 1-3 Methods adopted for the preparation of an AsB SEM image for the collection of grain data using ImageJ. A) Original AsB SEM image from sample ICE_09A: the first task in image pre-processing is to apply an appropriate scale so that data will remain true to the scale of the original image; the original scale bar is then cropped to eliminate errors in the data set when particle analysis is carried out. B) Thresholding. C) Application of a median filter to reduce noise and artefacts within the processed image. D) Watershed is then applied to separate touching grains; some errors are made by the programme but can then be corrected manually.

Look-up tables (LUTs) were used in ImageJ to modify the 8-bit AsB grey-scale images into pseudo-colour images (Figure 1-4b). The 'Jet' LUT was used, as this provided the best means of identifying and separating grains of different chemical composition (Figure 1-4b). The colours applied by the LUT are directly related to the original grey-scale values of the image (Heilbronner & Barrett 2014), and are therefore a direct representation of the original data. Application of an LUT allowed the original data within the images to be preserved. Grey-scale values could then be applied to separate grains of different types based on their chemical composition and the grouping of different grain-types based on the Jet LUT (Figure 1-4c-f). Grain separation was carried out using thresholding (described above).

Grain-size data (Appendix 2) were produced for individual grains separated in thresholded SEM AsB images. ImageJ was used to collect data on the feret diameter, which represents a value for the 'longest distance between any two points' along the grain-boundary (Ferreira & Rasband 2012). Grain-sizes were separated based on Wentworth (1922) grain-size values and nomenclature (Table 1-1). A percentage of each grain-size group was calculated and the results were used to create a grain-size distribution curve and grain-size charts.

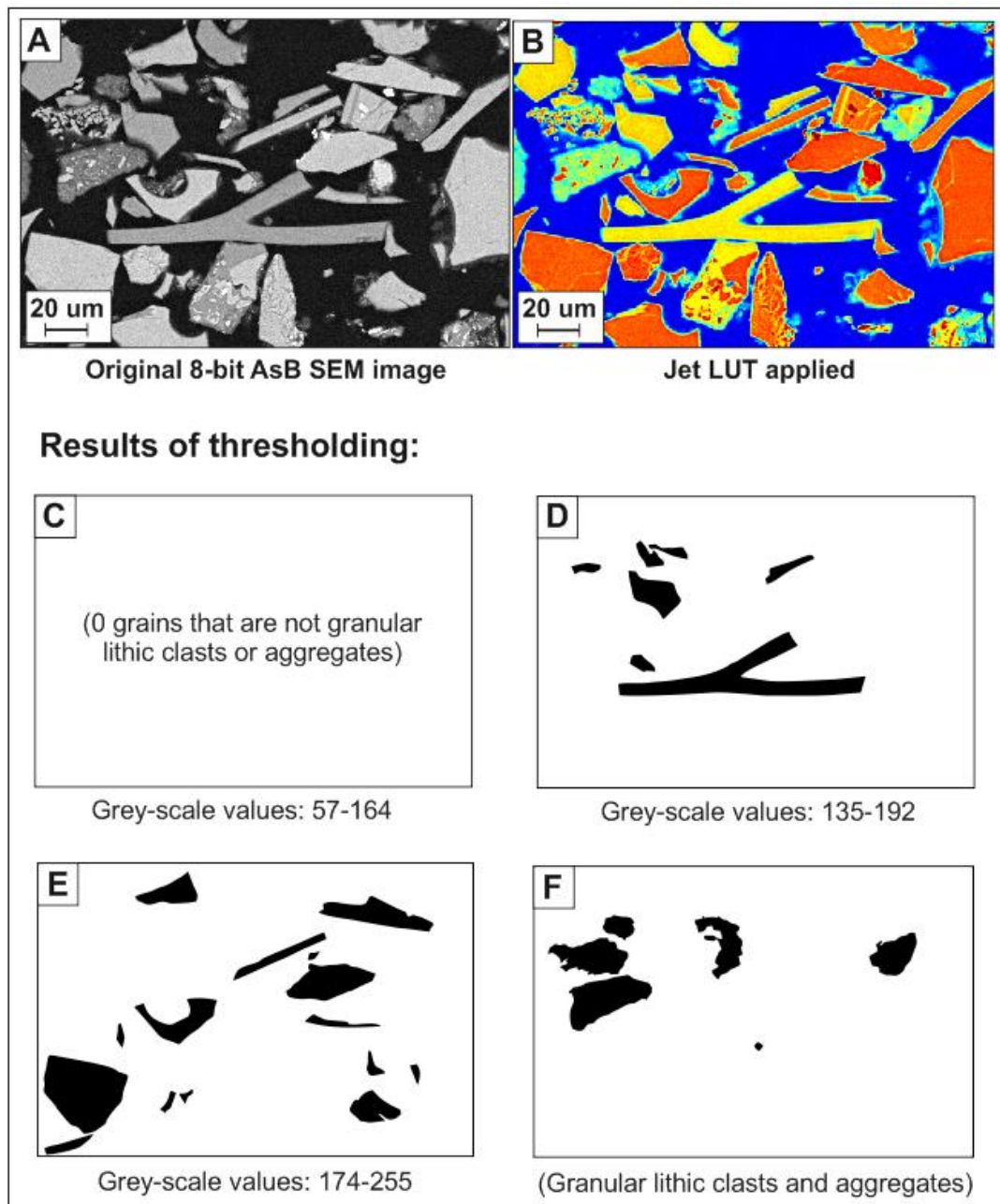


Figure 1-4 ImageJ methods used to separate grains of different composition. **A)** Original 8-bit AsB SEM image from sample ICE_09A, **B)** Application of the Jet LUT in ImageJ adds pseudo colour to the original 8-bit image; the colours are applied based on the original grey-scale values (0-255). In the original SEM image the grey-scale values (0-255) reflect differences in the composition of the grains, therefore the pseudo colours applied by the LUT reflect the same information but in a more visual format. **C-F)** Results of thresholding the Jet LUT image to separate grains of different composition within varying grey-scale value ranges 57-164, 135-192, 174-255 and clasts that have been identified as aggregates based on observations of the general characteristics of clasts.

Image analysis was applied to vesicular pyroclasts to calculate their vesicle densities. This was carried out by calculating the total area of the grain, with and without voids (vesicles). The results were copied from ImageJ into Excel and

used to determine the percentage of vesicles in each of the pyroclasts (Equation 1).

Equation 1

$$\left(\frac{\text{Total area of grain}}{\text{Area of grain excluding vesicles}} \right) \times 100 = \% \text{ vesicles}$$

Colour photo-micrograph images were used to calculate the porosity of thin-section samples that have a blue resin (Figure 1-5; Grove & Jerram 2011). Red-Green-Blue (RGB) colour images were collected from optical photo-microscopy then imported into ImageJ (Figure 1-5a). Firstly, the colour channels were split to create a grey-scale image representing the red, green and blue colour channels of the image (Figure 1-5b). The red channel separated the grains from the pore space with the most confidence; this channel was used for further analysis and the green and blue channels were ignored. Thresholding was applied to the red channel to separate the grains from the pore space (Figure 1-5c). The area occupied by the grains was calculated then subtracted from the total area of the image to give the area occupied by pore-space. This could then be converted to give the percentage of grains and the percentage of pore space in each image. This method was repeated for images of the same magnification then all data was averaged to provide the mean percentage porosity for the sample. Measurements could be made on a pixel area rather than a scaled image as this would not affect the result as a percentage.

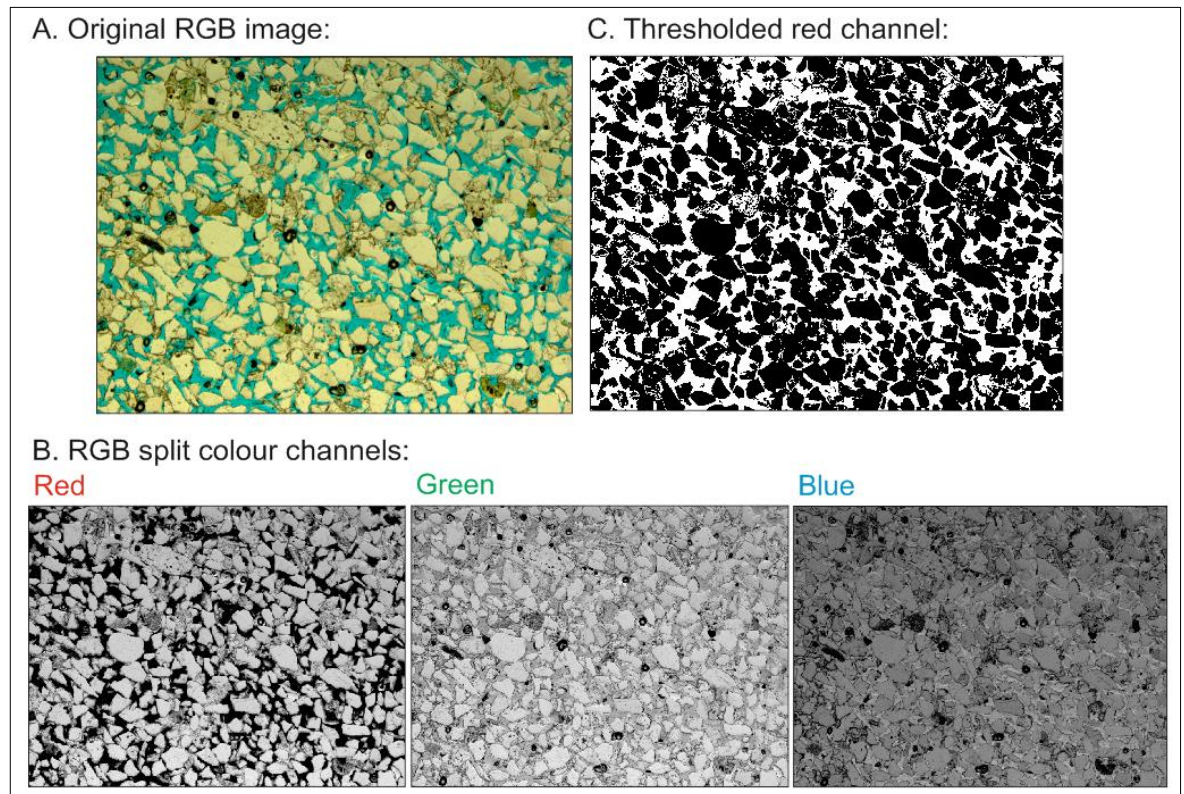


Figure 1-5 Methods used for calculating the percentage porosity of a sandstone using ImageJ. A) Original RGB full colour image, B) Original image split into separate red, green and blue colour channels which are portrayed as 8-bit grey-scale images, C) Grains are separated from the pore-space by thresholding the red channel, this image is then ready for analysis of the particles.

Manual point-count was carried out to obtain data on the number frequency of different grain-types. A 10 x 10 grid was applied to 8-bit SEM images and the grain-type manually recorded at each intersection of the grid; this method was repeated until at least 100 grains had been counted for each sample. Areas where the grid intersected empty space were not counted. The grain-count of each grain type (pyroclast, crystalline igneous, crystals, granular lithics, aggregates) was then input into excel to allow graphs to be made for the comparison of data. This method was also used to calculate the number frequency of different pyroclast shapes within pyroclast-bearing samples (blocky, bubble-wall, irregular and rod-like).

Additional methods are outlined with their results in the relevant chapters.

1.4 Thesis outline

The outline of this thesis will be detailed here for each chapter; supplementary material is provided in the appendix and referred to where relevant. Each of the case-studies (chapters 2 - 5) have been written to stand alone, and therefore each contain an introduction, geological history, results, discussion and conclusions.

Chapter 2: a field and petrological study of the Saksunarvatn Ash, a series of basaltic hydrovolcanic ashes deposited from Holocene eruptions of Grímsvötn Volcano, Iceland. This chapter introduces explosive basaltic volcanism associated with hydrovolcanic eruptions, and the characteristics of pyroclastic and volcaniclastic ash. This work provides the basis for the further development and characterisation of pyroclastic and volcaniclastic features and their relation to eruption processes and reworking, in the following chapters.

Chapters 3-5 all refer to deposits of Early Eocene volcanism associated with formation of the North Atlantic Igneous Province and the onset of sea-floor spreading. Figure 1-6 is relevant for all of these chapters and is provided here as a general reference for the ages of various tectonic and magmatic phases later referred to.

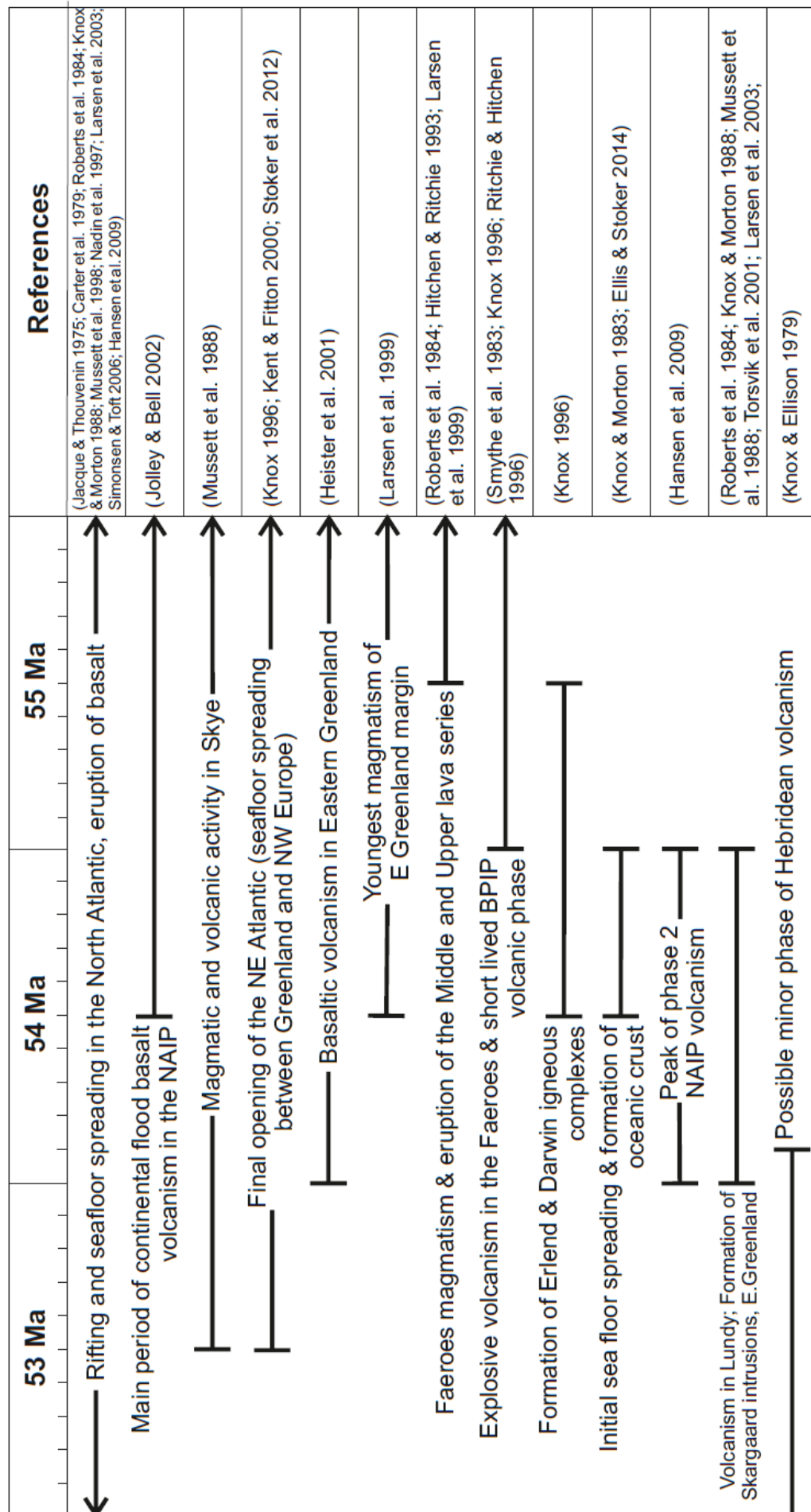


Figure 1-6 Published time-scales for volcanic activity in the area of the North Atlantic Igneous Province that could have acted as a source for the volcanic material deposited within the North Sea Basin (Chapter 3), Faroe-Shetland Basin (Chapter 4) and E. Anglia (Chapter 5) during the Early Eocene. Uncertainty remains on the suitability of these dates due to the uncertainties associated with dating of these material and the need for updated methods and dates.

Chapter 3: a core and petrological study of the Early Eocene Balder Formation of the North Sea Basin. This formation contains hundreds of basaltic tuffs that are associated with large-scale explosive volcanism during the formation of the North Atlantic Igneous Province. The tuffs provide details of the morphological features of pyroclastic and volcanoclastic ash deposited in a marine environment, and also shows how these deposits can be affected by alteration within the marine realm.

Chapter 4: a seismic and wire-line interpretation of the Balder Formation of UK Continental Shelf Quad 204 in the Faroe-Shetland Basin. No core of the Balder Formation is available in this part of the Faroe-Shetland Basin so all interpretations of the lithology of the Balder Formation and its pyroclastic and volcanoclastic content must be interpreted from offshore data. This chapter provides an additional case-study for improving our understanding of the nature of the Early Eocene Balder Formation.

Chapter 5: a field and petrographical study of the Wrabness Member of the Harwich Formation of SE England. These rocks were deposited in the North Sea Basin during the Early Eocene: they are a stratigraphic equivalent of the Balder Formation exposed on-land. This chapter extends the data-set for the Early Eocene ashes associated with opening of the NE Atlantic Ocean, and provides data on distal ash deposition within a shallow marine environment.

Chapter 6: a field and petrographical study of the Ellensburg Formation; the siliciclastic, pyroclastic and volcanoclastic rocks interbedded with the basaltic lavas of the Miocene Columbia River Flood Basalt Province, USA. This case-study investigates the controls on sedimentation during formation of a flood basalt province on land, with a particular focus on the distribution and preservation of distal ash deposits from explosive silicic eruptions. This chapter compliments the basaltic offshore data-set of the North Sea Basin (Chapter 3), Faore-Shetland Basin (Chapter 4) and E. Anglia (Chapter 5), by providing data of pyroclastic and volcanoclastic processes in a different environmental setting.

Chapter 6: a discussion of the main findings of the field, core and petrographical studies related to the interpretation of ash morphologies used to interpret

eruption processes, and to distinguish between pyroclastic and volcaniclastic ash deposited in distal locations. The main conclusions of the thesis will be given in this final chapter.

Chapter 2: The Saksunarvatn Ash, Iceland

2.1 Introduction

The Saksunarvatn Ash (SA), of tholeiitic basalt composition, was erupted from the Grímsvötn Volcano (GV) in Iceland (Figure 2-1), in the Early Holocene, ~10.3 ka BP (Andrews et al. 2002; Jennings et al. 2002; Gudmundsdóttir et al. 2011; Thornalley et al. 2011; Bramham-Law et al. 2013; Lind et al. 2013; Lohne et al. 2013; Jennings et al. 2014; Neave et al. 2015). The products of this eruption are found as primary pyroclastic and reworked volcanoclastic deposits, onshore and offshore Iceland. These deposits may represent a suitable analogue for the identification and understanding of the source and depositional history of Early Eocene basaltic pyroclasts found within the Balder Formation of the North Sea and Faroe Shetland Basins (NSB and FSB, respectively) (see Chapter 3).

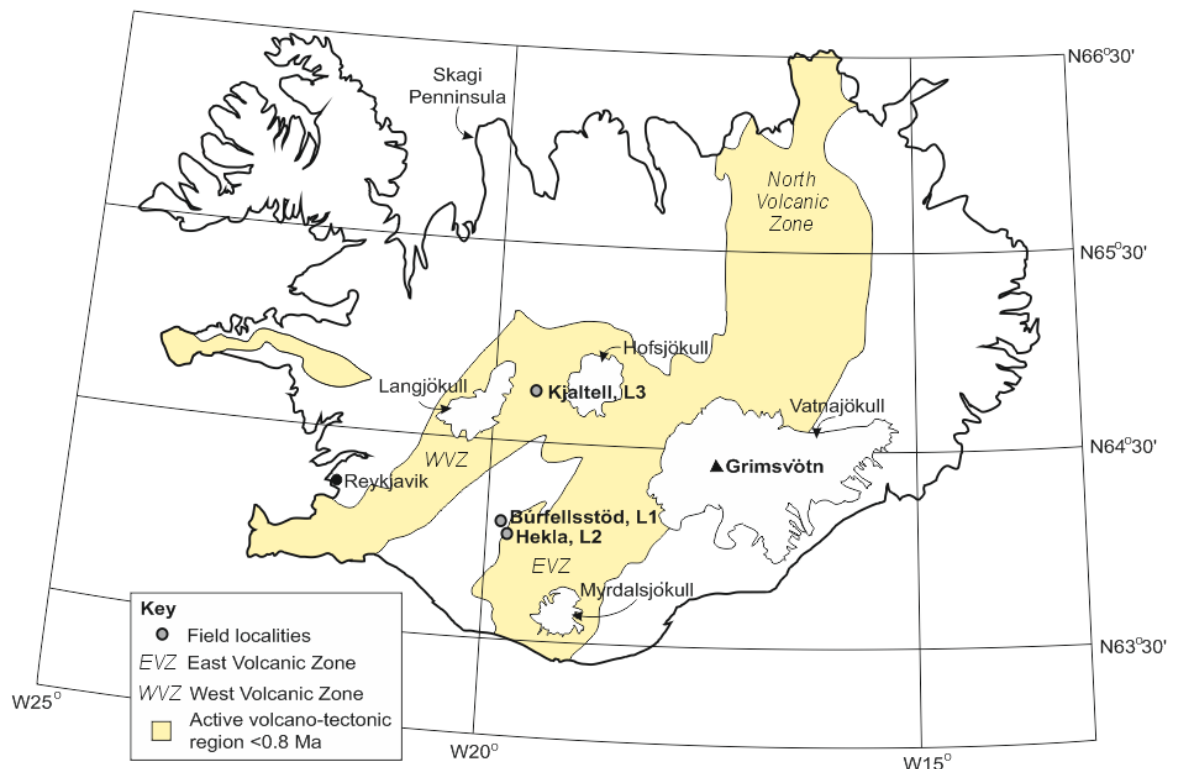


Figure 2-1 Map of Iceland showing the location of field sites mentioned in this study and the source volcano, Grímsvötn Volcano, beneath Vatnajökull (adapted from Google Earth 2016). The active volcano-tectonic regions of Iceland are also shown in yellow (Homuth et al. 2010).

The term ‘tephra’, used herein, includes all the material that is expelled during a volcanic eruption (e.g. Brendryen et al. 2010). Primary pyroclastic deposits are

produced from direct fall-out deposition (of tephra) from an eruption, and can form chronostratigraphical marker units across large areas and throughout a range of depositional environments (e.g. Boyle 2004; Brendryen et al. 2010; Gudmundsdóttir et al. 2011; Lind et al. 2013; Neave et al. 2015).

Tephra can easily become remobilised and re-deposited (e.g. Brendryen et al. 2010), for example by wind, water or ice, leading to the formation of reworked deposits which should be treated as sediments and explained in terms of sedimentary processes, and referred to as volcaniclastic deposits (e.g. Fisher 1961; Fisher 1984; Suthren 1985; Smith 1986; Waitt 2007; White & Houghton 2006, 2007; Frolova 2008; Manville et al. 2009; Doronzo & Dellino 2013; Schindlbeck et al. 2013). It is therefore important to study the volcanic deposits of one eruptive event, throughout a variety of environmental settings, to gain a better understanding of the characteristics of primary pyroclastic and volcaniclastic deposits (e.g. Gudmundsdóttir et al. 2011). Deposits of the SA can be found preserved in a range of environments including fluvial, lacustrine and marine (e.g. Mangerud et al. 1986; Sjøholm et al. 1991; Merkt et al. 1993; Andrews et al. 2002; Wallrabe-Adams & Lackschewitz 2003; Larsen & Eiríksson 2008; Gudmundsdóttir et al. 2011; Thornalley et al. 2011; Bramham-Law et al. 2013; Lind et al. 2013; Lohne et al. 2013, 2014; Thordarson 2014; Neave et al. 2015), as well as ice-core from the Greenland Ice Sheet (e.g. Grönvold et al. 1995; Jennings et al. 2002; Mortensen et al. 2005; Lind et al. 2013; Jennings et al. 2014). Onshore, these deposits are commonly easily accessible, so provide ample means for the study and comparison of this material between locations.

Volcanic deposits are most likely to be preserved in lacustrine or marine environments (Larsen & Eiríksson 2008), with a lack of preservation in terrestrial sequences. Therefore, deposits of the SA are characteristically incomplete or patchy (e.g. Bramham-Law et al. 2013; Lind et al. 2013).

In this chapter the geological history of the SA will be reviewed, followed by details of the aims of the current study undertaken. The methods of data collection, preparation and analysis will then be given, followed by the results of this investigation. Discussion and interpretation of the results will be presented followed by the conclusions of this study.

2.2 Geological history

The SA was deposited by multiple eruptive episodes of GV, around 10.3 ka BP (Table 2-1), which lies within the Eastern Volcanic Zone (EVZ) of Iceland, and forms an important stratigraphic marker in the North Atlantic (Andrews et al. 2002; Jennings et al. 2002; Larsen & Eiríksson 2008; Lind et al. 2013; Jennings et al. 2014; Neave et al. 2015). At least three eruptions that occurred over an interval of *ca.* 500 (Jennings et al. 2013; Lind et al. 2013) to 150 years (Larsen & Eiríksson 2008) were likely responsible for deposition of the SA.

Age	Dating method	Sample location	Reference
9,000 – 9,100 ¹⁴ C yr BP 10,200 cal yr BP	Radiocarbon	Saksunarvatn Lake, Faroe Islands	Grönvold et al. 1995; Birks et al. 1996; Wastl et al. 1999; Andrews et al. 2002; Jennings et al. 2014
10,210 ± 30 cal yr BP	Radiocarbon	Lake in Kråkenes, Western Norway	Bramham-Law et al. 2013; Lind et al. 2013; Lohne et al. 2013; Jennings et al. 2014
10,297 ± 45 cal yr BP	GICC05 (Greenland Ice Core age)	GRIP2 (Greenland Ice Core)	Rasmussen et al. 2006; Bramham-Law et al. 2013; Lind et al. 2013; Lohne et al. 2013; Jennings et al. 2014
10,380 cal yr BP	Calibrated radiocarbon	North Iceland Shelf	Jennings et al. 2014

Table 2-1 Published ages of the Saksunarvatn Ash.

Ash from these eruptions was deposited across Iceland, Eastern Greenland, the SE Greenland shelf, and southwards across NW Europe as far as northern Germany (Figure 2-2; Grönvold et al. 1995; Andrews et al. 2002; Jennings et al. 2002; Mortensen et al. 2005; Gudmundsdóttir et al. 2011; Thornalley et al. 2011; Bramham-Law et al. 2013; Lohne et al. 2013; Neave et al. 2015), and Central Norway (Lind et al. 2013). This ash has also been referred to as the Skagi tephra by some authors (e.g. Larsen & Eiríksson 2008; Fig 1), due to its identification in the Skagi Peninsula to the east of the Iceland Northwest Peninsula (NWP; Figure 2-1; Andrews et al. 2002).

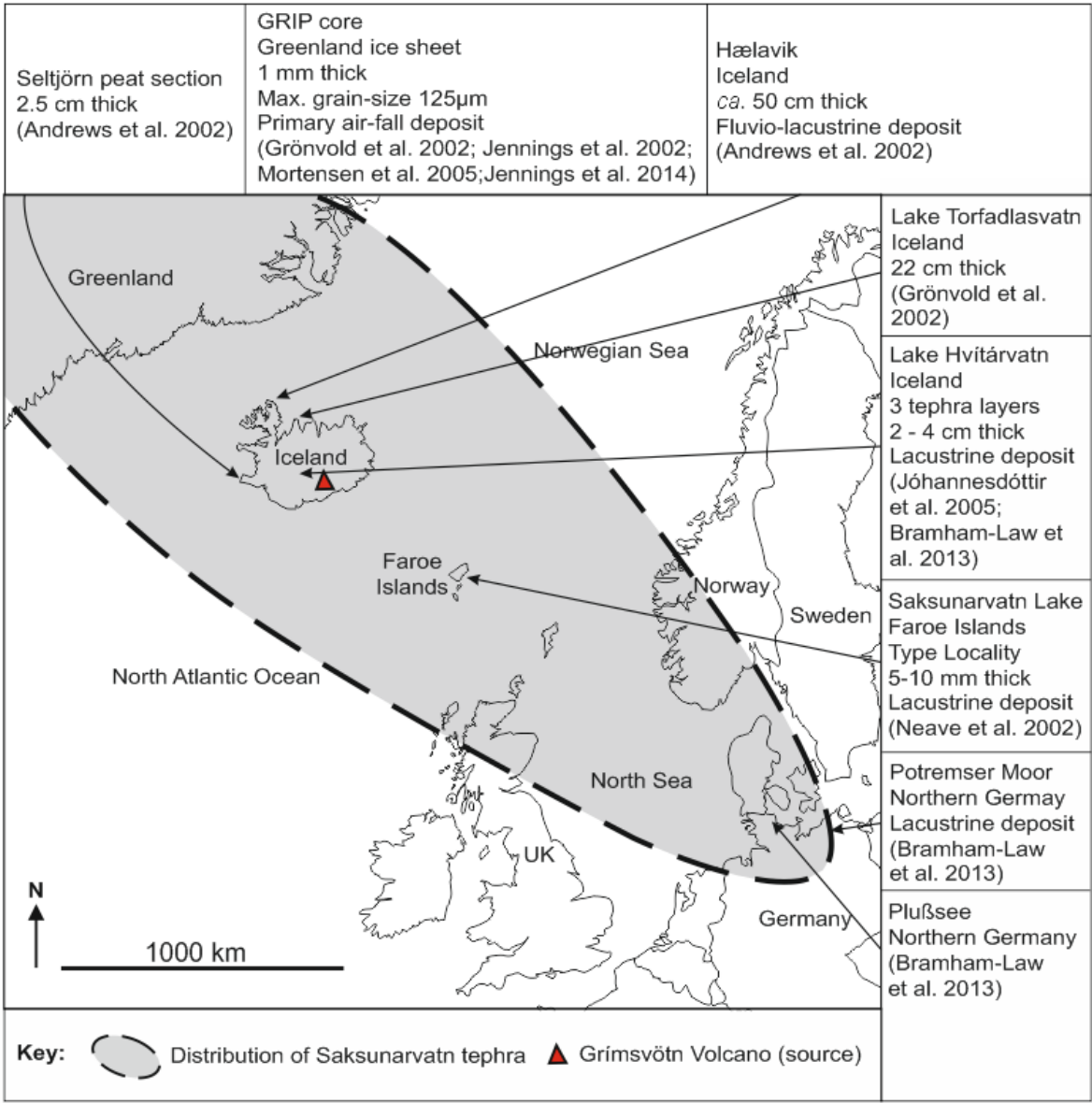


Figure 2-2 Distribution of the SA from Grímsvötn Volcano in Iceland with additional information for locations where the SA has been identified in the literature (Bramham-Law et al. 2013; Neave et al. 2015). The additional information shows the locality name, thickness of the SA unit, type of deposit, and the reference for the information. The thickest deposits (2-50 cm) are found in Iceland, with thinner deposits in the Greenland ice core (GRIP) (1 mm) and northern Germany.

The type locality of the SA lies in Lake Saksunarvatn in the Faroe Islands (Mangerud et al. 1986; Andrews et al. 2002; Neave et al. 2015). Compositional data show that the source of this tephra was the GV in Iceland (Figure 2-1; e.g. Mortensen et al. 2005; Jennings et al. 2014; Neave et al. 2015). At the type locality the deposit has a thickness of 5 - 10 mm (Figure 2-2; Neave et al. 2015). In a more proximal location in Lake Torfadlasvatn, Iceland, deposits reach a thickness of 22 cm (Figure 2-2; Grönvold et al. 1995). Corresponding deposits with an age of *ca.* 10.347 Ka have been identified within the NGRIP Greenland

ice cores (Table 2-1), where the deposits are 1 mm thick, with a maximum grain-size of 125 μm , silt/ash, (Figure 2-2; Grönvold et al. 2002; Jennings et al. 2002; Mortensen et al. 2005; Jennings et al. 2014). The shards identified within the NGRIP core are brown and have cusped, blocky and vesicular ash morphologies, and may have been deposited as primary air-fall ash (Mortensen et al. 2005). In general, all of the tephra deposits have a grain-size <250 μm , reaching a grain-size of medium-sand (ash) within the Seltjörn peat section to the west of Grímsvötn (Figure 2-2; Andrews et al. 2002). The coarser grain-size of the SA, distally, within the Greenland ice cores, suggests that this tephra was deposited from plumes that were blown to the west and north-west (Jennings et al. 2002; Jennings et al. 2014). This is in contrast with most atmospheric wind-direction models for this area during the Holocene, which imply that atmospheric wind directions would not have blown plumes to the west or north very often (e.g. Jennings et al. 2014). However, prevailing westerly winds could have transported tephra to the east and north at heights below 15 km (Jennings et al. 2002), which could suggest that the eruption plume responsible for dispersing this tephra reached at least 15 km in height. Multiple eruptions may have had varying dispersal axes; for example, it has been suggested that some eruptive episodes of GV dispersed ash to the north-west, reaching Greenland, and later eruptions dispersed ash to the south-east (Bramham-Law et al. 2013). Debate has occurred over the locations of the SA, Bramham-Law et al. (2013), suggest that only ash deposited in to the south-east should be referred to as the SA, and that ash deposited to the north-west should not. A greater abundance of coarser-grained ash deposited at distal locations can also be caused by the premature removal of fine-ash in proximal areas due to ash aggregation (Carey & Sigurdsson 1982; Durant et al. 2009; Taddeucci et al. 2011; Brown et al. 2012; Van Eaton et al. 2012; Mueller et al. 2016). Aggregation removes fine-ash from an eruption cloud by causing the fine-grains to coalesce and form a coarser, more-dense grain of aggregated finer-grained material (James et al. 2003; Scolamacchia et al. 2005; Taddeucci et al. 2011; Brown et al. 2012; Van Eaton et al. 2012; Mueller et al. 2016).

The eruptive activity of GV *ca.* 10.3 ka BP was explosive (e.g. Jennings et al. 2002; Johannsdottir et al. 2004; Larsen & Eiríksson 2008; Thordarson & Höskuldsson 2008; Bramham-Law et al. 2013; Jennings et al. 2014; Thordarson

2014), and likely involved phases of hydrovolcanic activity, including phases of phreato-Plinian style eruption, caused by the interaction of erupting magma and glacial water/ice (e.g. Johannsdottir et al. 2004; Larsen & Eiríksson 2008; Thordarson & Höskuldsson 2008; Neave et al. 2015). This interpretation can be supported by the 'presence of blocky and modestly vesiculated sideromelane glass' within the deposits (Mortensen et al. 2005; Neave et al. 2015).

A large volume of tephra was erupted during this event (Larsen & Eiríksson 2008; Neave et al. 2015), allowing widespread distribution of pyroclasts into many onshore and offshore environments, including lacustrine and marine environments (e.g. Grönvold et al. 1995; Andrews et al. 2002; Jennings et al. 2002; Larsen & Eiríksson 2008; Lind et al. 2013; Jennings et al. 2014; Neave et al. 2015). It is possible that the widespread distribution of the SA within the North Atlantic Ocean was enhanced by tephra deposition from ice rafting (Jennings et al. 2002).

Highly explosive hydrovolcanic eruptions are common in Iceland due to the presence of ice, glaciers and a high water table (Larsen & Eiríksson 2008). Large-scale eruptions of GV and formation of the SA during the early Holocene coincided with deglacial unloading of the Icelandic mainland (Thordarson 2014), which led to an increased abundance of volcanic activity in the region (Jennings et al. 2002; Thornalley et al. 2011).

The composition of the magma identified from the study of melt inclusions within plagioclase of the SA show that the original magma was very primitive (Thordarson 2014; Neave et al. 2015). Primitive melts like this are considered to be somewhat rare within the EVZ and have a high MgO content >7 wt % (Neave et al. 2015). In general, the composition of the tephra is homogenous, which allows for correlations to be made between sites (Andrews et al. 2002; Johannsdottir et al. 2004; Jennings et al. 2014; Thordarson 2014; Neave et al. 2015). This magma composition may be similar to that of the tephra preserved in the Early Eocene Balder Formation of the NSB and FSB (Pedersen et al. 1975; Knoc & Morton 1988; Roberts et al. 1984; Morton & Knox 1990; Waagstein & Heilmann-Clausen 1995; Haaland et al. 2000; Larsen et al. 2003; Brooks 2006; see Chapter 3:).

Originally, the SA was thought to have been deposited over a large area by a single eruption (Lind et al. 2013; Lohne et al. 2013; Jennings et al. 2014). However, dating and identification of corresponding deposits, based on geochemistry (Figure 2-3), in an increasing number of localities, suggests that the tephra were more likely deposited from multiple eruptive episodes (Larsen & Eiríksson 2008; Lind et al. 2013; Lohne et al. 2013; Jennings et al. 2014; Neave et al. 2015). These eruptive events occurred between 10.5 - 9.9 ka (Lind et al. 2013; Jennings et al. 2014; Neave et al. 2015). All of these deposits have the same chemical composition, suggesting that the ash came from one source, however, the SA was not deposited from an individual eruptive event but instead represents a series of eruptive and depositional phases (e.g. Jennings et al. 2014; Neave et al. 2015).

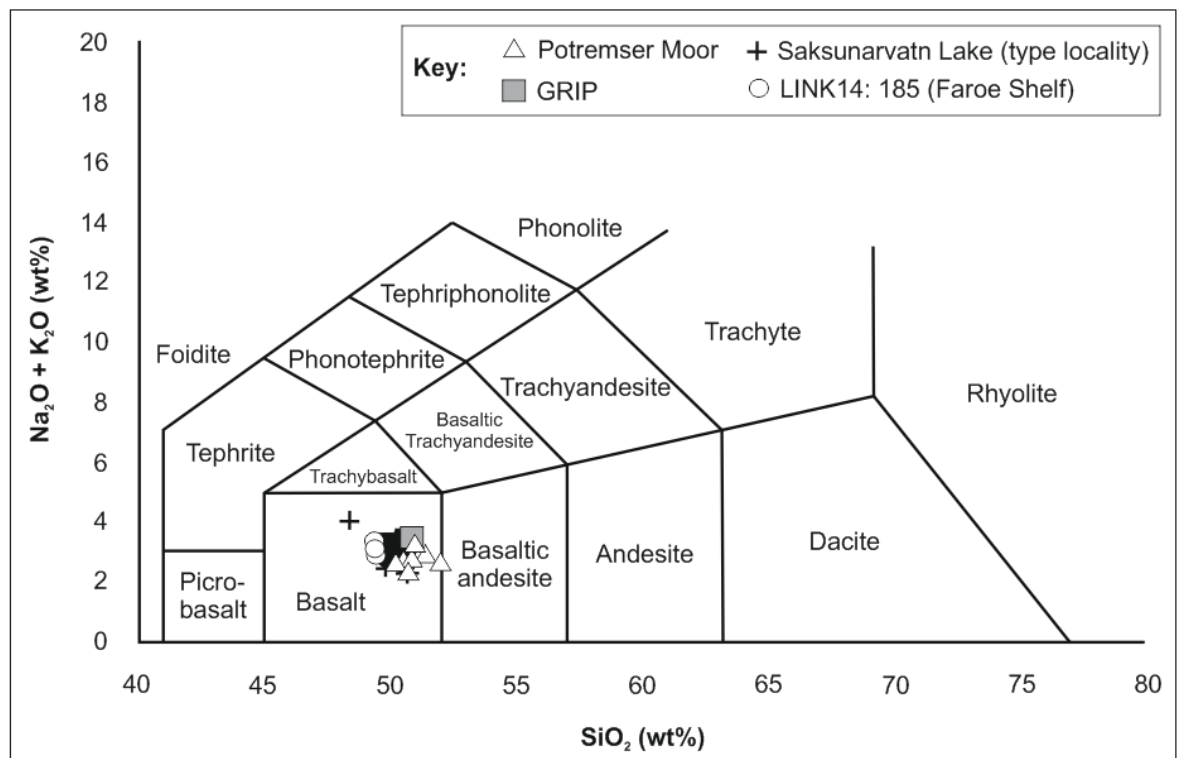


Figure 2-3 Comparison of the chemical composition of the SA from various localities (from Bramham-Law et al. 2013). GRIP data from the Greenland ice core (Grönvold et al. 1995), LINK 12: 185 data collected from core retrieved from the Faroe Shelf (Rasmussen et al. 2011). The data show that the Saksunarvatn Ash has a basaltic composition.

The SA can be identified within some North Atlantic Ocean marine cores drilled on the South Iceland Rise, where it is represented by an increase in the abundance of basaltic material (Andrews et al. 2002; Jennings et al. 2002; Thornalley et al. 2011). In these cores the rock comprises a black silty layer, 1-2

cm thick, with a sharp base (Thornalley et al. 2011). Within these marine deposits the individual grains of tephra are pale brown and contain abundant vesicles (Thornalley et al. 2011). The SA can also be identified where there is a reduction in the magnetic susceptibility of the material (Andrews et al. 2002), the tephra can also be identified regionally in seismic data, where it creates a strong sub-bottom reflector (Figure 2-4; Andrews et al. 2002).

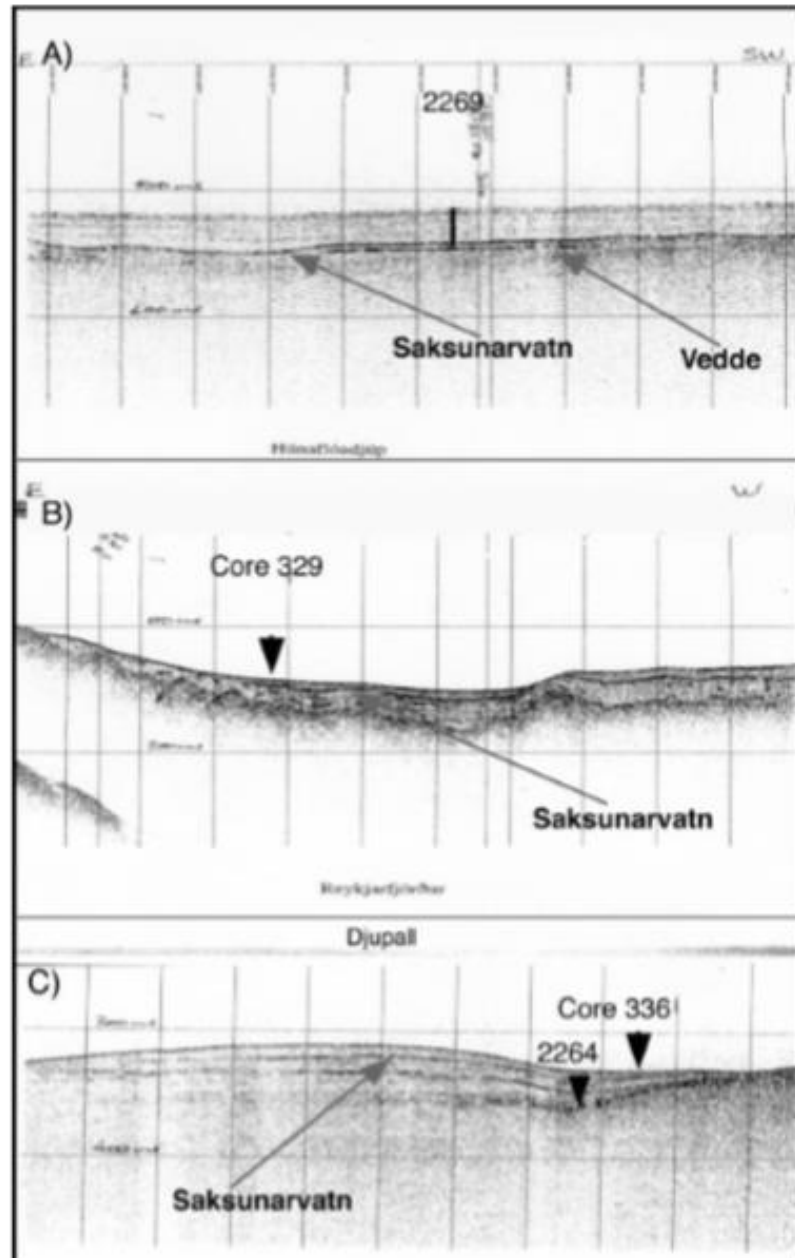


Figure 2-4 Seismic profiles from offshore Iceland showing the SA reflector which produces a recognisable hard kick in the seismic response (from Andrews et al. 2002).

2.3 Aims and objectives

The main aim of this investigation is to assess the SA deposits of the GV in terms of their eruption and depositional history. It is important to identify features of the basaltic pyroclasts of the SA to see whether there are characteristics that can be used to identify the nature of the eruption source, distance to source, together with other volcanic parameters and processes, including fragmentation/vesiculation history and eruption dynamics, as well as the depositional history and the discrimination between primary air-fall pyroclastic and reworked volcanoclastic deposits. This information can be gained from unaltered modern deposits exposed onshore in Iceland, and have the potential to allow a better understanding of the volcanic material identified within the Early Eocene deposits of the Balder Formation of the NSB and FSB (see Chapter 3:), by acting as an analogue.

2.4 Methods

Fieldwork was conducted for 2 weeks throughout August at several localities as found, recommended and shown by T. Thordarson (Table 2-2). The deposits visited are all characterised by unlithified material that has undergone a limited degree of compaction. The ash was deposited in various shallow sub-aqueous settings, including lacustrine and fluvial, which enabled preservation of the material.

Locality	Grid Reference
Búrfellsstöð, Locality 1a	64°5'57.78"N 19°49'4.69"W
Búrfellsstöð, Locality 1b	64°5'55.80"N 19°49'13.90"W
Búrfellsstöð, Locality 1c	64°5'58.02"N 19°49'0.57"W
Búrfellsstöð, Locality 1d	64°5'54.62"N 19°50'2.72"W
Hekla, Locality 2	64°46'9.00"N 19°29'39.10"W
Kjaltell, Locality 3	64°21'19.96"N 19°44'30.56"W

Table 2-2 Location name and grid reference for each of the field sites used in this study.

The morphology of various clasts, glass-shards and other material within each of the deposits can provide information about syn- and post-depositional processes (e.g. Brookfield 2004). The overall characteristics of a deposit can also provide this information, for example, the grain-size, roundness, sorting and the presence and nature of any depositional structures (e.g. Brookfield 2004). This can help when identifying pyroclastic and volcanoclastic material and understanding the depositional history of tephra after it was erupted and initially deposited.

Polished thin-sections impregnated with a blue resin were produced by ALS Petrophysics for optical microscopy and Scanning Electron Microscope (SEM) analysis (see 1.3 Methods). In addition to this, polished grain-mounts were produced, at the University of Glasgow, from loose grains that were collected as grab-samples (see 1.3 Methods). Petrographical and SEM analysis were conducted to provide information on the composition of the sediments, grain-size distributions and grain morphologies. SEM analysis also allowed chemical data to be collected for mineral identification and compositional classification of pyroclasts.

Image analysis was conducted on 8-bit backscatter (AsB) SEM images from polished thin sections to provide quantitative data regarding the grain-size distribution of the deposits, as well as more detailed characteristics of pyroclasts, including vesicle density and the abundance of pyroclasts of varying chemical composition (see 1.3 Methods).

2.5 Results

2.5.1 Field observations

Several sites to the west of GV were visited (Figure 2-1). At each locality full descriptions of the stratigraphy were prepared, along with lithological logs and sample collection. Presented below are the field observations for each locality.

2.5.1.1 *Búrfellsstöð, Locality 1a-d*

A partially dry river bed is present to the SE of the Búrfellsstöð hydropower plant, below the dammed Bjarnalón to the North of the Búrfell topographic high, and accessed off of the main 32 road (Figure 2-5; Figure 2-1). The deposits are exposed in metre-high cliffs, and waterfalls within the eroded river bank. To access some deposits it was necessary to dig through eroded loose sediment to reveal the features investigated in this current study (Figure 2-5, Locality 1a).

Deposits of the SA can be identified by an abundance of black, vitreous basaltic pyroclasts, with lesser amounts of rust-orange crystalline igneous clasts and transparent, vitreous fragments of plagioclase (Gudmundsdóttir et al. 2011; Thordarson pers. comms. 2015). These features are observed throughout the deposits at Búrfellsstöð within black sands and gravels.



Figure 2-5 Locations of field sites at Búrfellsstöð (A-D), located along, a mostly dry, river bed below a hydro-electric dam (Google Maps 2017).

The pale grey, pumice-rich deposits of Hekla 5 are visible above the sections logged in detail at the Búrfellsstöð (Thordarson pers. comms. 2015). The Hekla deposits are characteristically pale grey due to their more silicic composition and these can be easily identified in the field between layers of black (basalt-rich) volcaniclastic sediment.

Locality 1a: 64°5'57.78"N 19°49'4.69"W

The deposits at Locality 1a (Figure 2-5), are predominantly composed of fine- to medium-sand (125 - 25 μm) with abundant asymmetrical climbing ripples, clay drapes, lenses of coarser- or finer-grained sediment and less common beds of silt/clay (Figure 2-6). Diffuse parallel stratification may be present in some of the thicker units, which otherwise appear to be structureless.

The asymmetrical climbing ripples within the sequence all appear to climb in the same direction and show truncation of their upper surfaces; less commonly an additional set of climbing ripple cross-laminae is present above this or an interval of coarser-grained, more homogeneous, structureless sand (Figure 2-7). These are examples of subcritical climbing ripples which form when the accumulation rate of sediment is small in comparison to the rate at which the ripple is migrating (Collinson et al. 2006). The apparent orientation of the preserved foreset laminae of these ripple structures, as viewed in the field, suggest that water flowed towards the east, which is opposite to that seen at the present day at this location. Very fine laminations of paler grey clay drape the ripples and their foreset beds (Figure 2-7).

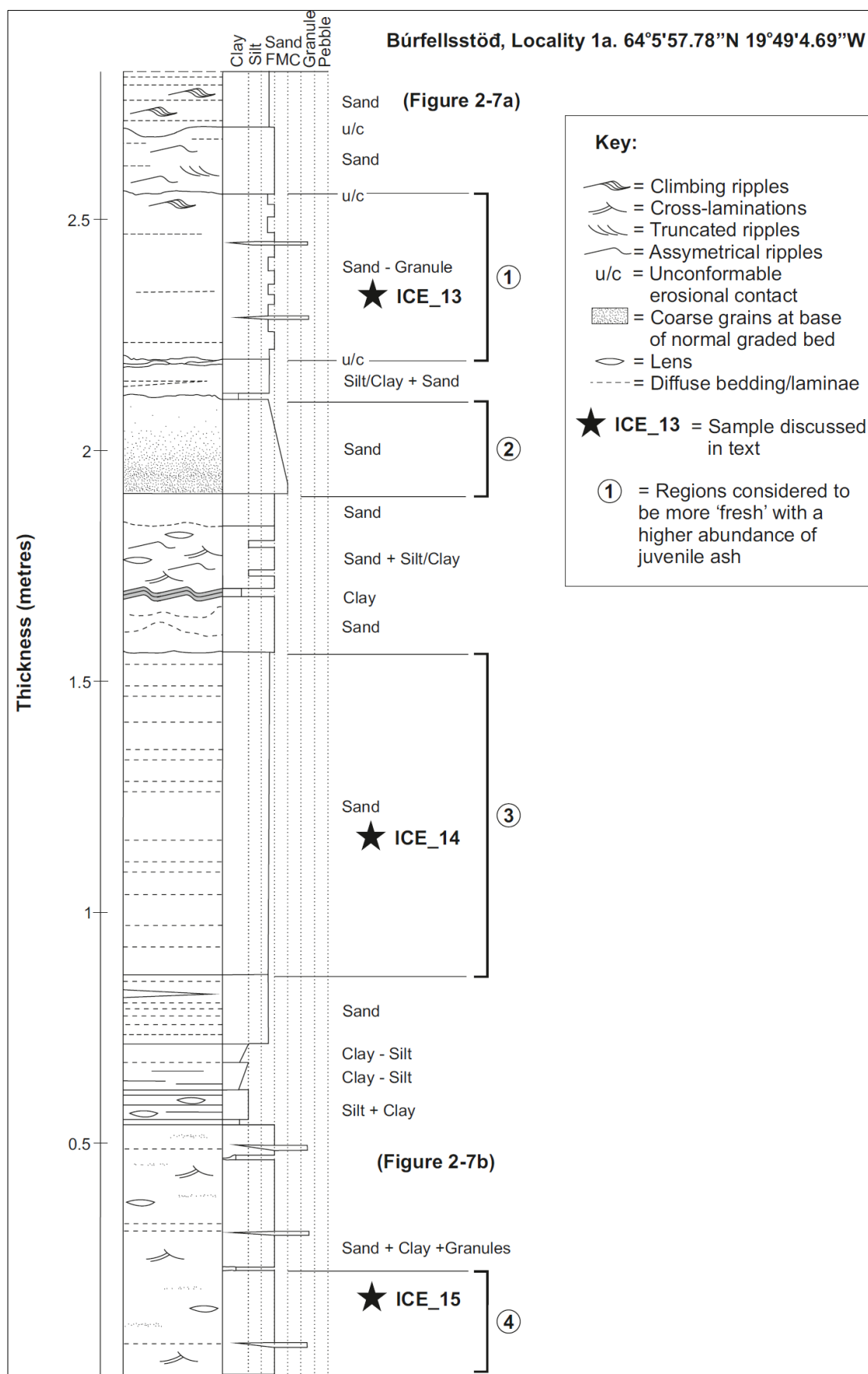


Figure 2-6 Lithostratigraphy for Locality 1a at Búrfellstöð (Figure 2-5). The sequence is dominated by fine to medium sand, with rare interbeds or drapes of clay and discontinuous

lenses of granules. Some areas appear a darker bluish black and are considered to be more fresh.

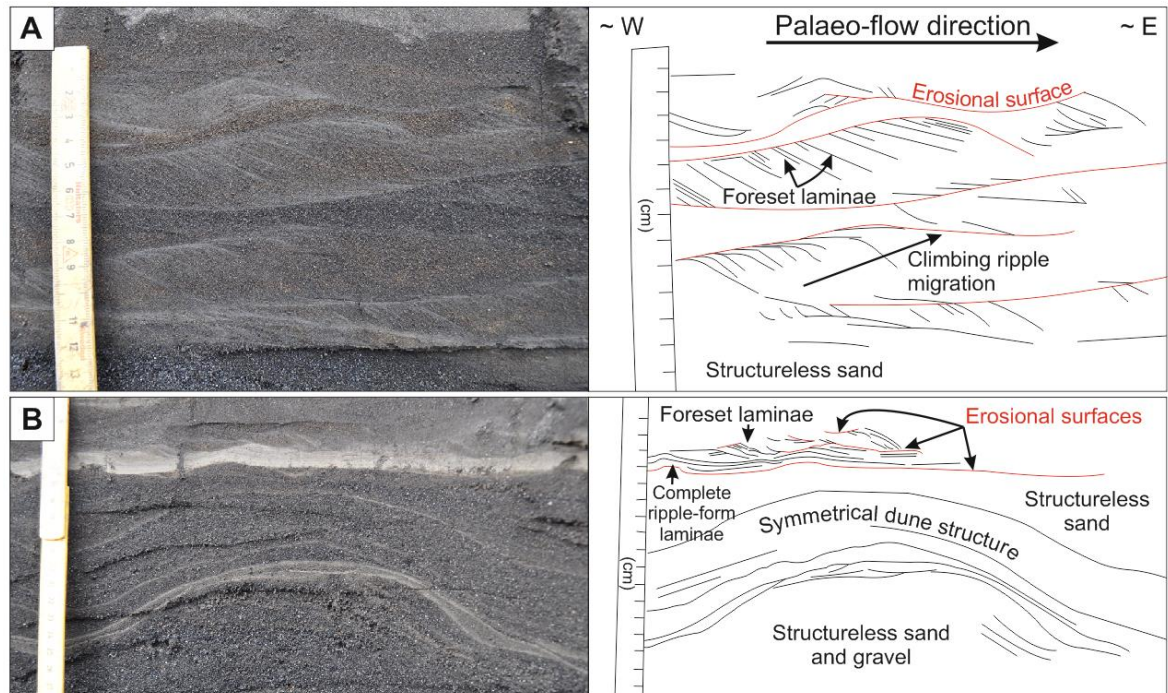


Figure 2-7 Types of ripple structure identified at Búrfellsstöð Locality 1a. **A)** Asymmetrical subcritical climbing ripples with fine, <1 mm, clay drapes and foreset laminations. All of the climbing ripples show the same apparent orientation, implying that the palaeo-flow direction was ca. west-to-east. **B)** Symmetrical dune structure with clay drape laminae. Above this lies an erosional surface with a greater abundance of clay (paler grey) with complete ripple-form laminae followed by asymmetrical truncated ripple cross-laminations shown by the presence of foreset laminae picked out by thin <1 mm drapes of clay.

Locality 1b: 64°5'55.80"N 19°49'13.90"W

Below a waterfall at Locality 1b (Figure 2-5), the SA deposit is predominantly composed of very coarse sand and gravel with some interbeds of peat and clay. Sub-rounded and well-rounded pebbles of black igneous rock are present towards the top of the section (Figure 2-8). The sand intervals are structureless, with possible diffuse bedding, although this is difficult to identify with certainty. Coarser grains are dominantly angular.

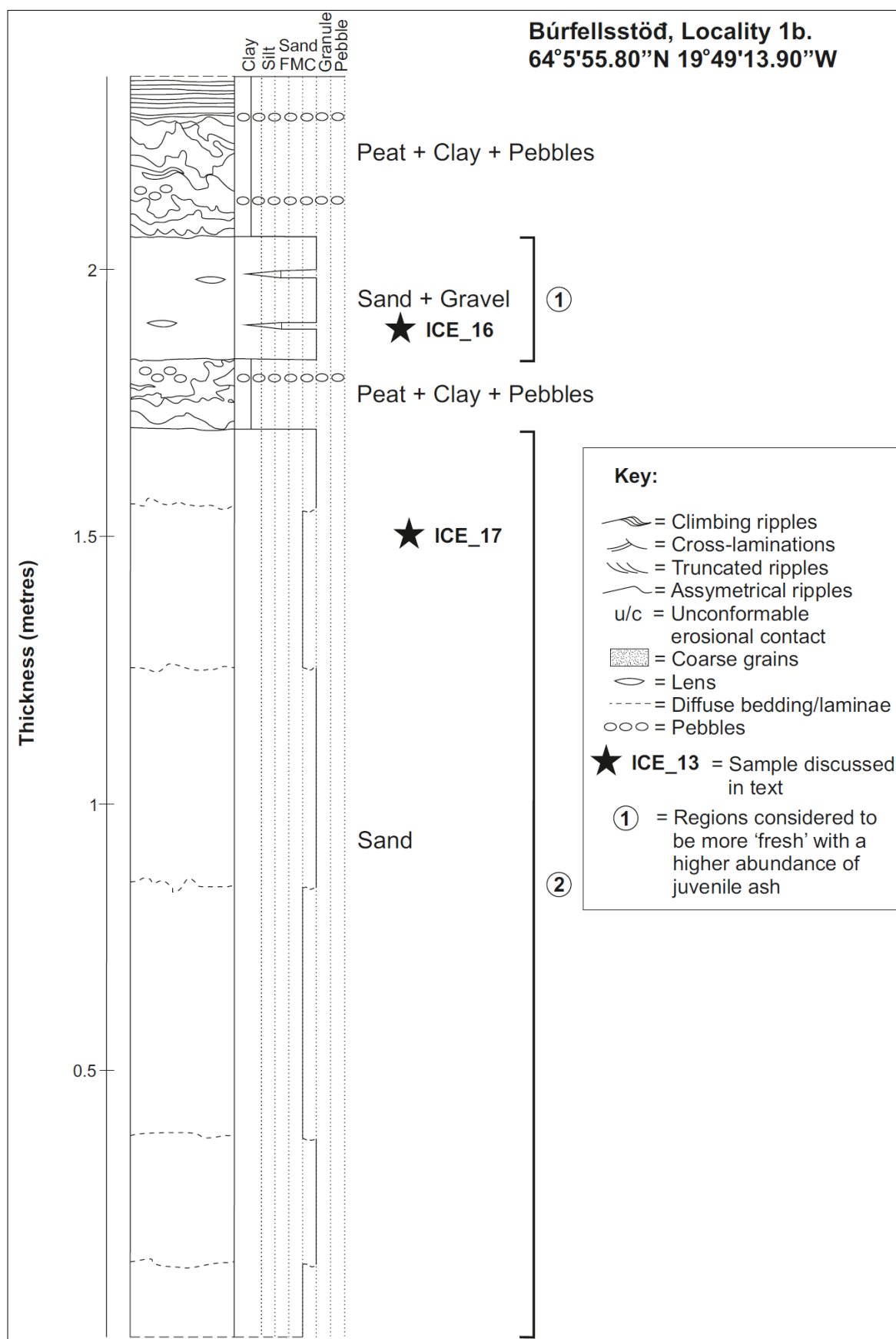


Figure 2-8 Sedimentary log from Búrfellsstöð Locality 1b (Figure 2-5). This section is dominantly composed of very coarse sand/gravel with interbeds of peat and pebbles towards the top of the exposed section. Some areas appear a darker bluish black and are considered to be more fresh.

Locality 1c: 64°5'58.02"N 19°49'0.57"W

The exposure at Búrfellsstöð Locality 1c (Figure 2-5) is composed of silt/fine sand, silt and clay (<125 µm) in a generally fining-upwards sequence. All of the contacts show loading features such as flames and ball-and-pillow structures (Figure 2-9; Figure 2-10), which may have been influenced by post-depositional seismic deformation (Figure 2-11). The deposits are moderately- to well-sorted with angular to sub-rounded grains observed within sand and gravel beds.

The upper part of this section is dominated by deformed beds of finer-grained sediments (silt and clay), that have irregular fluidal bed boundaries and show the mixing of sediment from different intervals. A cross-section of a sediment volcano cuts through these deformed sediments (Figure 2-9). The sediment volcano has formed by the expulsion of fine-grained sediments, which are no longer present within the structure. Any gaps left by the removal of these finer-grained sediments have been infilled by the upper levels of sediment, which have slumped into the structure (Figure 2-9). Deformation within the sediment volcano and the surrounding interbedded sediments has removed the original features of the sediments, such as the true nature of any bed boundaries.

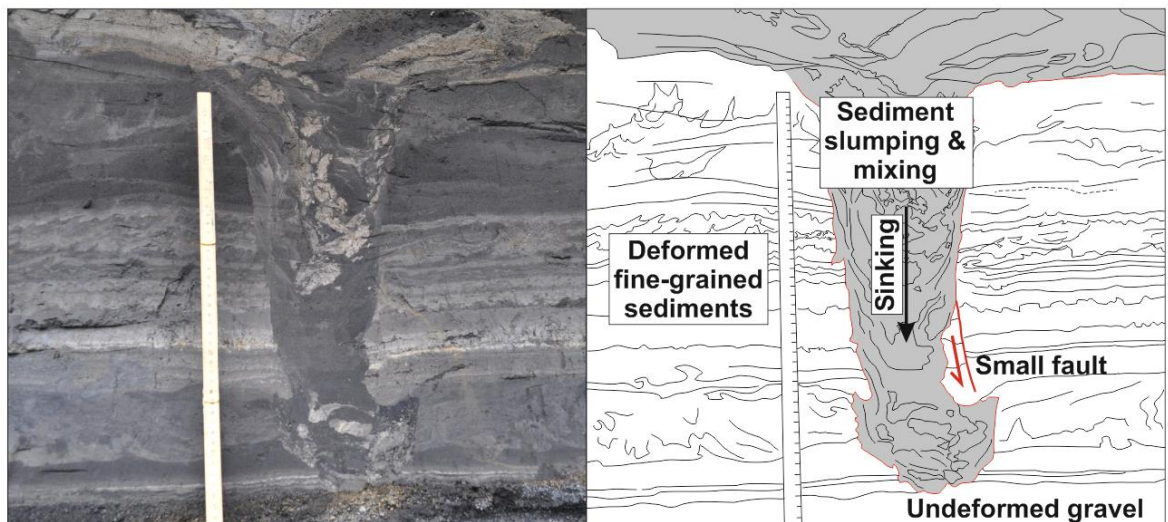


Figure 2-9 A sediment volcano, showing a high level of deformation, cuts through less deformed fine-grained sediments in the top section of the Búrfellsstöð Locality 1c exposure. The fine-grained sediment appears to have been expelled from the sediment volcano and the resultant void infilled by the slumping and mixing of sediment from above. Below the sediment volcano (shaded grey) lies an un-deformed gravel bed.

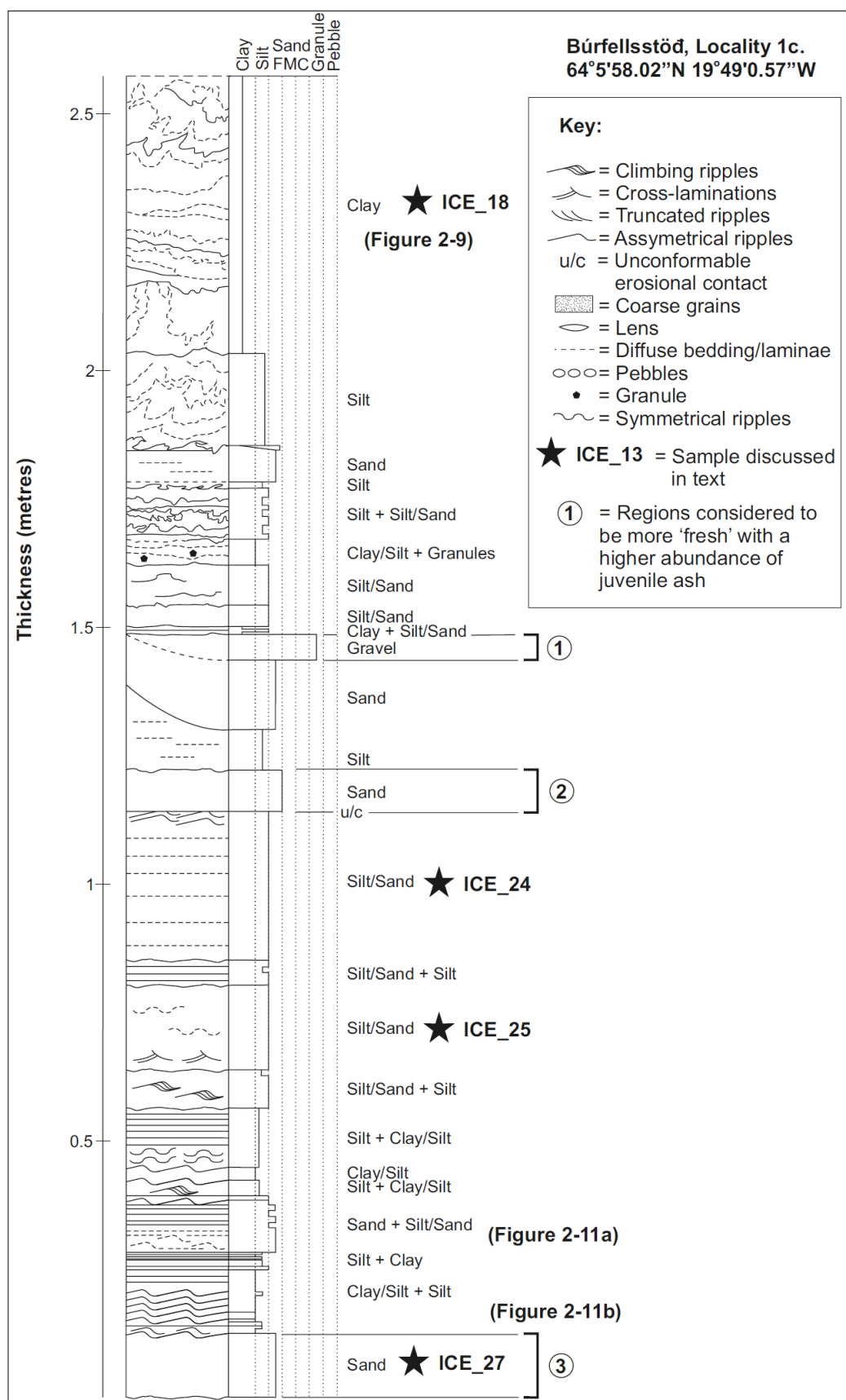


Figure 2-10 Sedimentary log from Búrfellsstöð Locality 1c (Figure 2-5). This section is composed of a generally fining-upwards sequence of silt/fine sand to silt then clay. All of the contacts between these beds and many of the internal structures of the beds are deformed, with fluidal flame features caused by post-depositional seismic deformation. Some areas appear a darker bluish black and are considered to be more fresh.

The lower parts of this exposure contain diffuse parallel bedding and laminations of silt and clay, as well as various types of ripple structures. Critical climbing ripples (Figure 2-11a) have formed due to the influence of a unidirectional current affecting sediment transport and deposition. Asymmetrical supercritical climbing ripples occur at several intervals (Figure 2-11b), indicating a period of deposition where a unidirectional current was present but where fine-grained sediments were not eroded after their initial deposition.

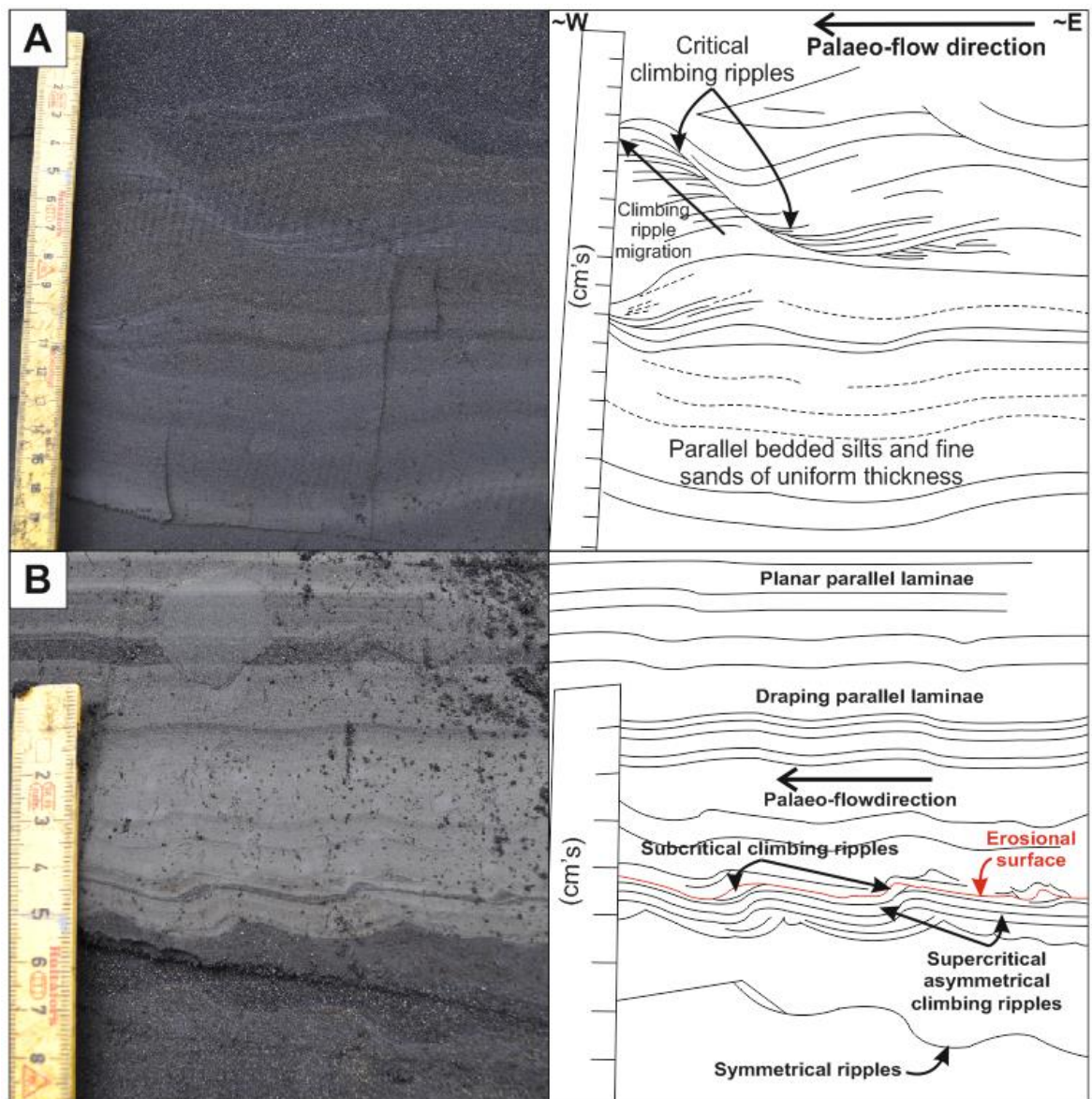


Figure 2-11 Types of ripple structures identified in the sedimentary deposits at Búrfellsstöð Locality 1c. A) Parallel, thinly bedded silts and fine sand followed by the deposition of asymmetrical critical climbing ripples are evidence of deposition in a fluvial environment (e.g. Collinson 1981; Prothero 1990; Stand 2005; Collinson et al. 2006), where the palaeo-flow direction was ca. east to west. B) Symmetrical ripples followed by asymmetrical supercritical climbing ripples with a thin interval of subcritical climbing ripple laminae. The palaeo-flow direction during deposition of this sequence is the same for that of A, i.e. east to west.

Differing ripple structures preserved throughout this sedimentary sequence show that the flow dynamics were constantly changing throughout deposition. The presence of asymmetrical climbing ripples shows that the flow was unidirectional, and indicative of a fluvial environment (e.g. Collinson 1981; Prothero 1990; Strand 2005; Collinson et al. 2006). Changes in the flow regime (strength and direction) are also reflected in the changing grain-size of the beds, from clays to gravels and vice versa with increasing and decreasing rates of water flow (e.g. Prothero 1990; Collinson et al. 2006).

Locality 1d 64°5'54.62"N 19°29'39.10"W

The section exposed at Búrfellsstöð Locality 1d (Figure 2-5) is predominantly composed of cross-stratified sands and gravels (Figure 2-12; Figure 2-13). This part of the fluvial stratigraphy lies below that investigated at Locality 1b, as inferred from the presence of black/grey/orange sands and gravels at the top of this section that have the same appearance as those observed at Locality 1b to the east of this locality (see above). This unit generally has the coarsest sediment, with more prominent depositional features, in comparison to the other sites at Búrfellsstöð; for example, it displays large-scale cross-bedding (Figure 2-13).

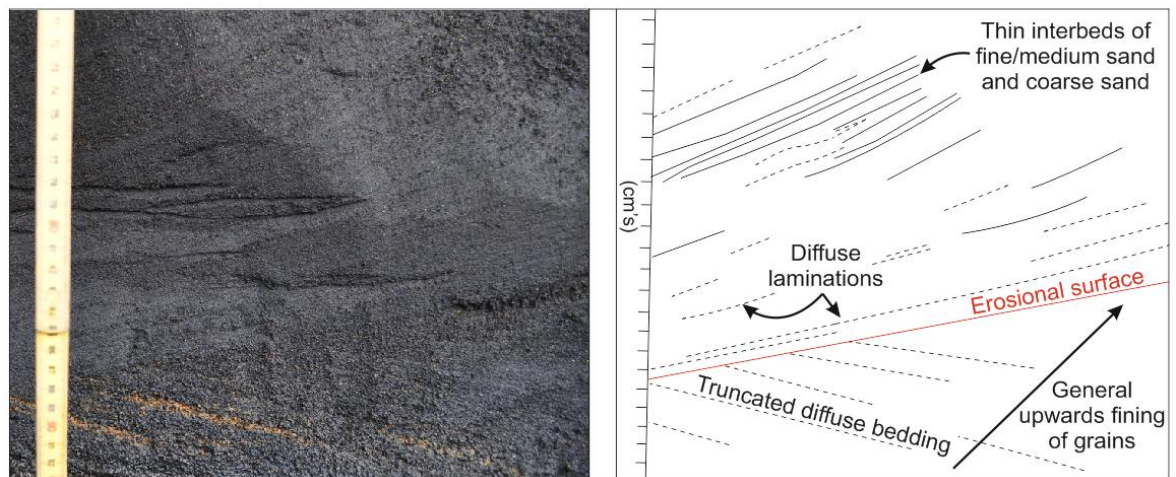


Figure 2-12 . The lower section of sediment exposed at Búrfellsstöð Locality 1d, with cross-stratified gravel and coarse sands truncated and overlain by cross-stratified fine/medium and medium sands. The gravel and coarse sand at the base display a general fining upwards in grain-size, whereas the dominantly finer-grained bed above shows an increasing abundance of medium sand upwards (coarsening upwards).

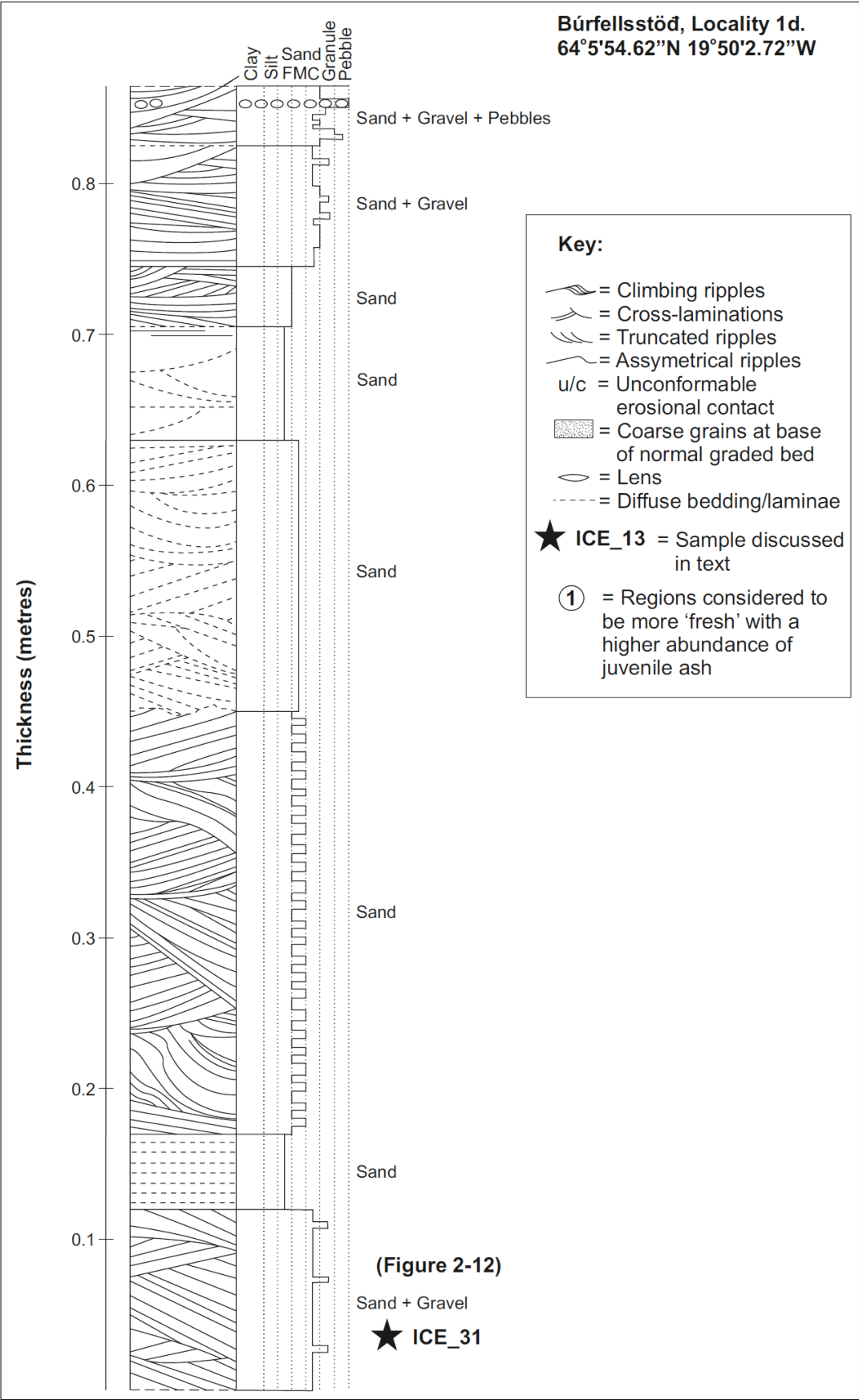


Figure 2-13 Sedimentary log showing the stratigraphy exposed at Búrfellsstöð Locality 1d (Figure 2-5). Features of the deposits are shown on the left and grain-size characteristics on the right. This section is dominated by cross-stratified coarse-grained sands and gravels, which are occasionally interbedded with diffusely-stratified or cross-stratified fine-grained

sands. Towards the top of the exposure are intervals of pebbles of igneous material. All of these deposits appear to be reworked and are not considered to be primary pyroclastic.

2.5.1.2 Hekla, Locality 2: 64°46'9.00"N 19°29'39.10"W

This exposure is found on the lower slopes of Hekla (Figure 2-1). The sequence is dominated by a lower section of sands with deformation structures (flame and load features) followed by parallel-laminated, finer-grained sands, and finally a repetitive sequence of laminae of fine-sand, silt and clay, which may represent varves (Figure 2-14; Figure 2-15; Collinson 1978; Prothero 1990; Glenn & Kelts 1991; Collinson et al. 2006). Each varve (normal-graded unit) represents one year of deposition in a low-energy, lacustrine environment; variations in thickness therefore reflect the abundance of material available for deposition present within the lake, which may mirror seasonal environmental or climatic conditions (Collinson 1978; Prothero 1990; Glenn & Kelts 1991; Collinson et al. 2006). For example, coarser-grained sediment is more likely to be deposited in the summer months due to an increase in melt water discharge into the lake, and finer-grained sediment is deposited during the winter when discharge into the lake is at a minimum due to the presence of ice on land.

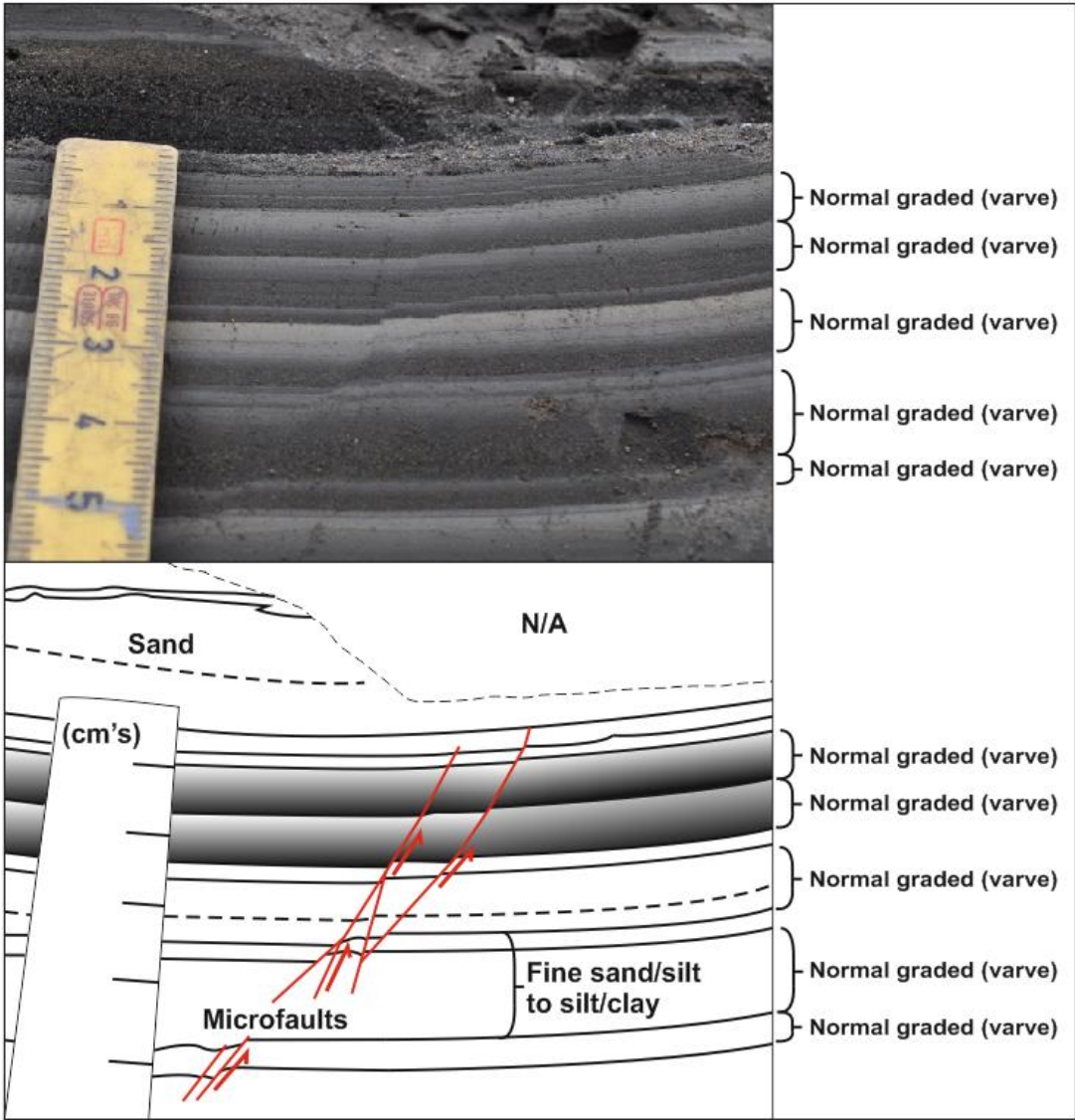


Figure 2-14 Normal-graded laminae (or varves), observed at the top of the logged section exposed at Hekla, Locality 2 (Figure 2-13). Each unit is normal-graded, with dark grey/black fine-sand/silt at the base, fining upwards into a pale grey silt or clay. Micro-faults can be seen displacing some of these units.

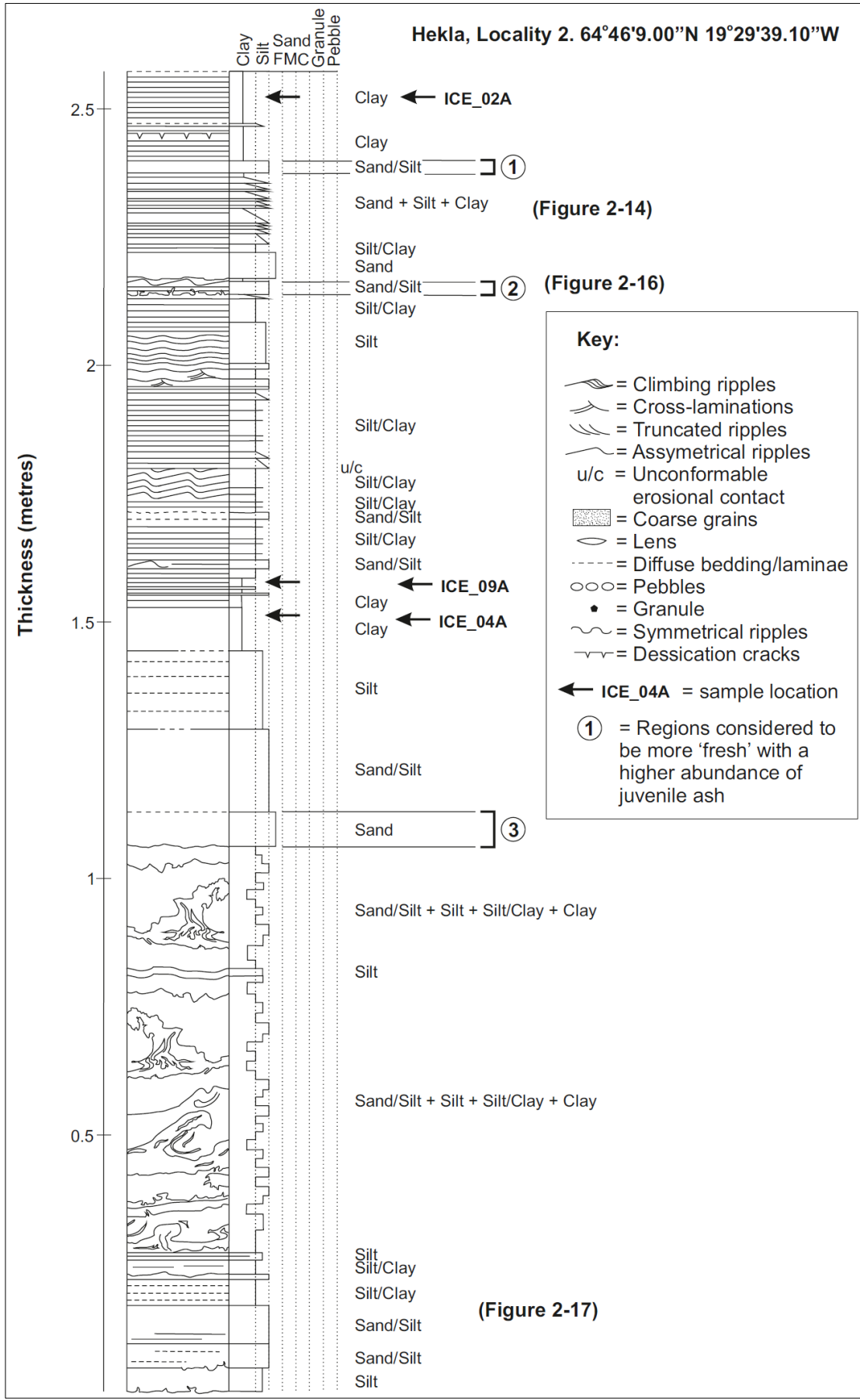


Figure 2-15 Sedimentary log for the exposed section seen at Hekla, Locality 2 (Figure 2-1). This sequence shows a general fining-upwards trend, with fine-sand and silt at the base and

thinly interbedded silts and clays at the top. Soft-sediment deformation features can be seen in the sand and silt unit at the base of the exposure. In contrast, the upper part of the sequence is dominated by parallel laminated or ripple-laminated sands, silts and clays. Some areas appear a darker bluish black and are considered to be more fresh.

The highly deformed material at the base of this sequence (Figure 2-15) may represent soft sediment deformation caused by seismic activity, similar to that identified at Búrfellsstöð Locality 1c (64°5'58.02"N 19°49'0.57"W).

Asymmetrical climbing ripples draped by finer-grained sediments and normal-graded varves can be identified locally throughout the section (Figure 2-15; Figure 2-16). These show that unidirectional currents rarely occurred within the lake to affect the nature of deposition.

Syn-depositional soft sediment deformation features are present at the base of some of beds of sand (Figure 2-15). These features are often associated with flame and ball-and-pillow structures at the base of a sand-rich unit which terminates in an asymmetrical ripple (Collinson et al. 2006). These loading features suggest that the sediments were water-saturated during deposition of the coarser-grained sands.

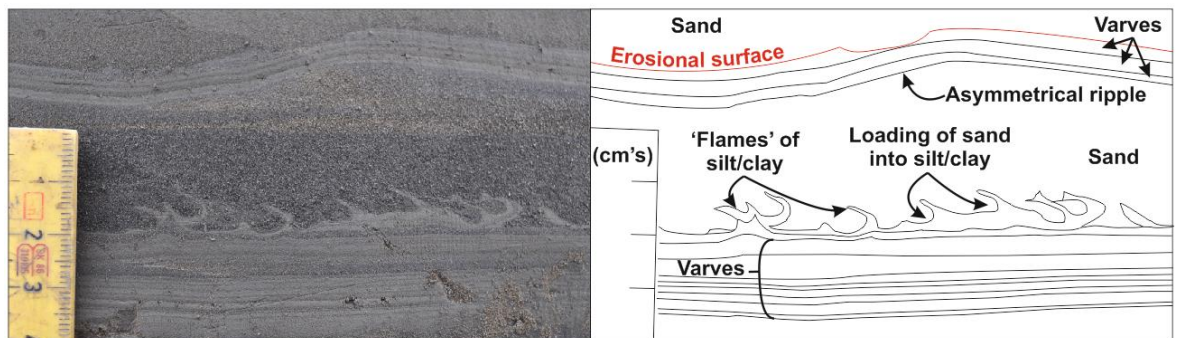


Figure 2-16 Soft sediment deformation at the base of an asymmetrical ripple composed of sand. Flames of finer-grained sediment (silt/clay) intrude into the lower section of the sand, above. The sand creates loading features into the upper part of the underlying silt/clay. The asymmetrical ripple is draped by finer grained sediments that form a series of varves. Another sand-rich unit occurs at the top of this image and has a slightly erosional contact with the underlying varves, instead of causing an interval of soft-sediment deformation.

Small-scale faults are present in the lowest section of this sequence (Figure 2-17). These faults are limited to a localised part of the succession and represent another type of post-depositional deformation, which takes the form

of slumping (Figure 2-17). Centimetre-scale displacement can be measured along these small faults.

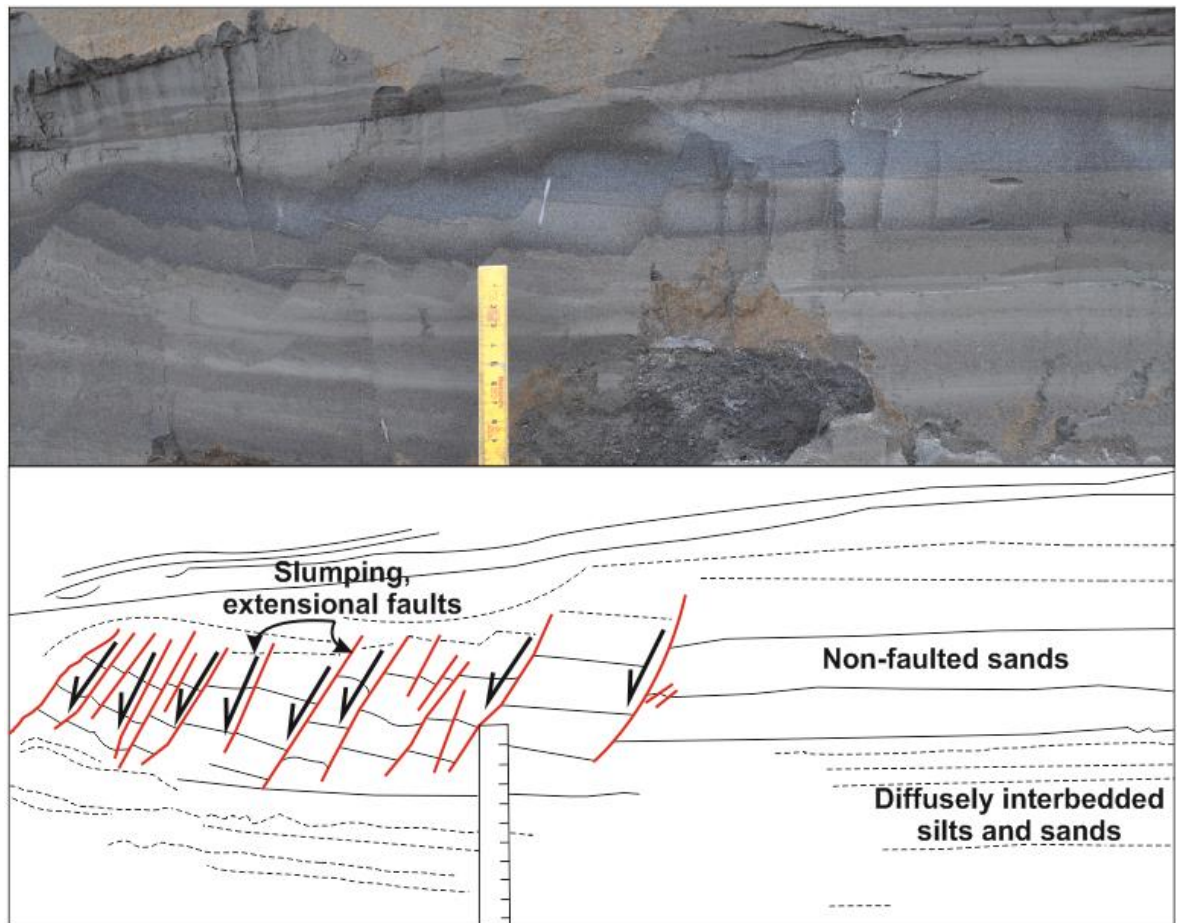


Figure 2-17 Localised extensional faulting, or slumping, of cohesive blocks of sand within the lower section of the lacustrine deposits exposed at Hekla, Locality 2.

2.5.1.3 Kjaltekk, Locality 3: 64°21'19.96"N 19°44'30.56"W

The exposure at Locality 3 is found at the base of Kjaltekk, a small Holocene volcanic edifice (Figure 2-18). The deposits lie below a pahoehoe lava-plain which was produced by later eruptions from Kjaltekk, following the deposition of the SA in this area.

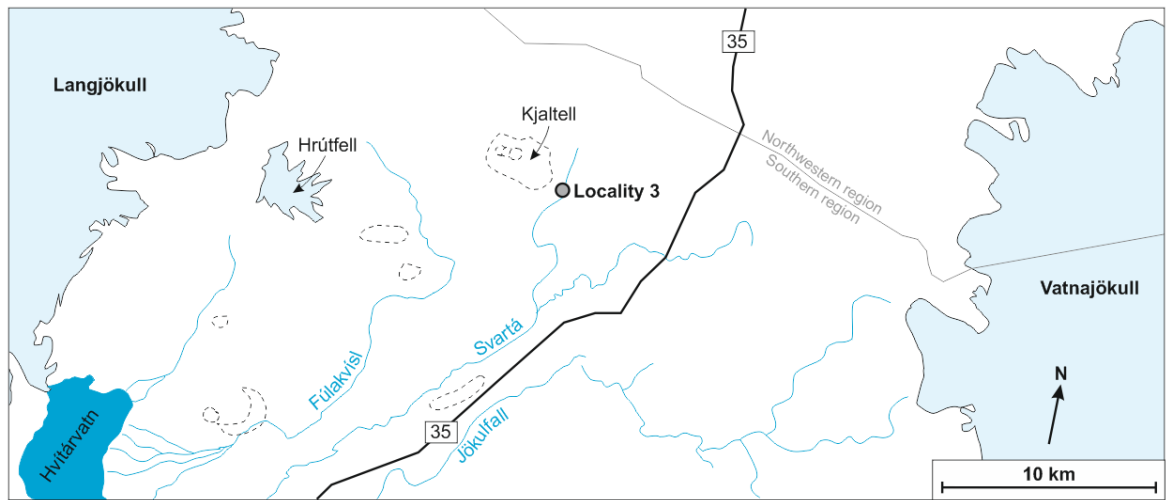


Figure 2-18 Map showing the location of Locality 3, at the base of Kjaltell. The position of this locality in regards to the other localities in Iceland can be seen in Figure 2-1. Locality 3 lies between Langjökull and Vatnajökull near to the boundary between the north-western and southern regions of Iceland.

Overall, the sequence is dominated by black, coarse- to fine-grained sand, that is composed of black vitreous pyroclasts and red and brown lithics mainly of basaltic composition (Figure 2-20). These units are interbedded with silts and clays, with some intervals displaying parallel or cross-ripple laminae (Figure 2-19). Many of the black sands contain abundant transparent fragments of plagioclase crystals, typical of deposits of the SA (Gudmundsdóttir et al. 2011; Thordarson pers. comms. 2015).

In general, the deposit exposed at Locality 3 appears to coarsen upwards, with thinly interbedded fine sands, silts and clays at the base and more structureless coarser-grained sands and gravels at the top (Figure 2-20).

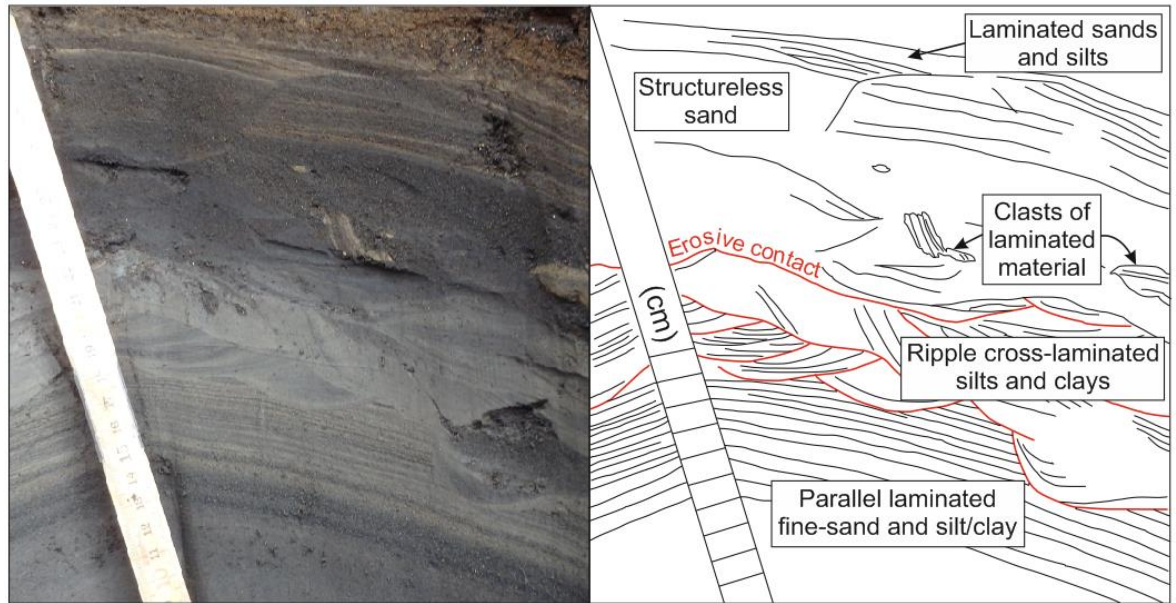


Figure 2-19 Parallel and ripple cross-laminated silts and clays observed at Kjaltell, Locality 3. In the lower part of this image, parallel laminated fine-sand and silt/clay are present. The top of this unit has been eroded, with ripple cross-laminae becoming the dominant sedimentary feature. The ripple cross-laminated silts and clays contain multiple erosional surfaces. Above this lies more structureless sand, which contains rare clasts of laminated clay. At the top of this image are parallel laminated sediments. (Photograph courtesy of T.Thordarson).

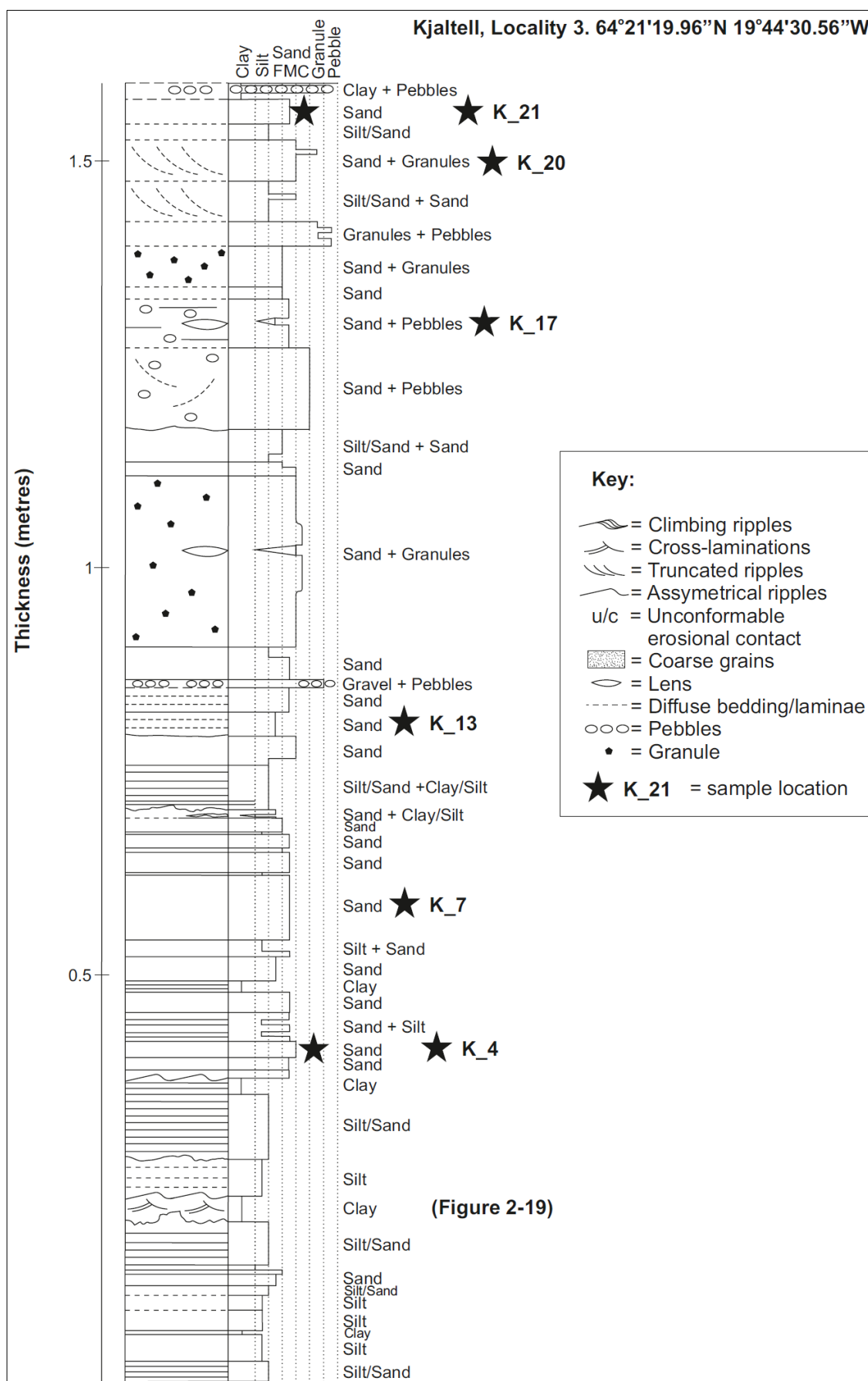


Figure 2-20 Sedimentary log representing the section exposed at Kjaltell, Locality 3 (Figure 2-1). The sequence is predominantly composed of interbedded sands, silts and clays, which

show parallel lamination and ripple cross-laminae. In general, the sequence coarsens upwards, with coarser, more structureless units of sand and pebbles, as well as diffusely cross-stratified sands and gravels towards the top. Samples were selected based on the apparent freshness of grab samples, black sand was considered more fresh than red sand. All parts of the deposit appear to have been reworked.

2.5.2 Optical microscopy

Polished thin-sections of consolidated samples from Hekla, Locality 2, were examined under plane- and cross-polarised light (PPL and XPL) to view the components of consolidated samples in more detail (Figure 2-15). Each of the thin-sections were impregnated with a blue resin to help to highlight the porosity of the samples: where the section is blue there is pore-space, or a fracture in the sample.

Thin-section/petrographic analysis has allowed minute features of the rocks to be identified that cannot be seen by eye in the field, for example, normal-graded laminations and fine-scale truncated cross-stratification (Figure 2-21). Some beds also have rare coarse sand to granule sized lithic clasts (Figure 2-21d; Figure 2-22b-d).

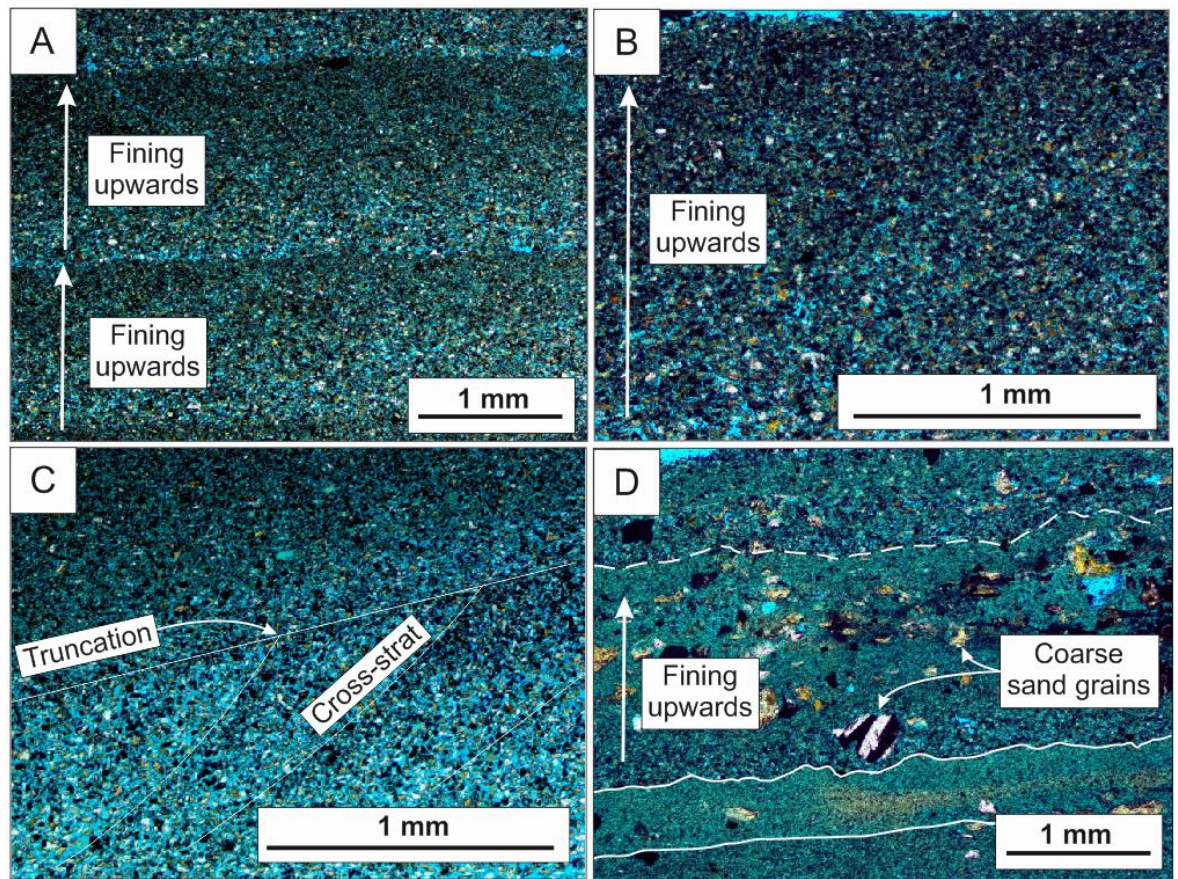


Figure 2-21 PPL optical microscopy images showing the range of different micro-structures observed in thin-section. A) Normal-graded laminations (ICE_09A). B) A normal-graded very fine bed/lamination (ICE_09A). C) Truncated cross-laminations and normal-graded laminations (ICE_09A). D) Laminations defined by varying grain-size, with abundant matrix-supported coarse sand grains of various compositions (ICE_04A).

In general, all of these sediments are composed of a range of mineral and lithic fragments ranging from angular to sub-rounded opaques, plagioclase, quartz(?), crystalline igneous lithics (Figure 2-22c-d), and vitreous pyroclasts (e.g. Figure 2-22b). The pyroclasts show a variety of different morphologies, including, vesicular and non-vesicular, blocky and bubble-wall shards; these types are shown in more detail in SEM images below (see section 2.5.3).

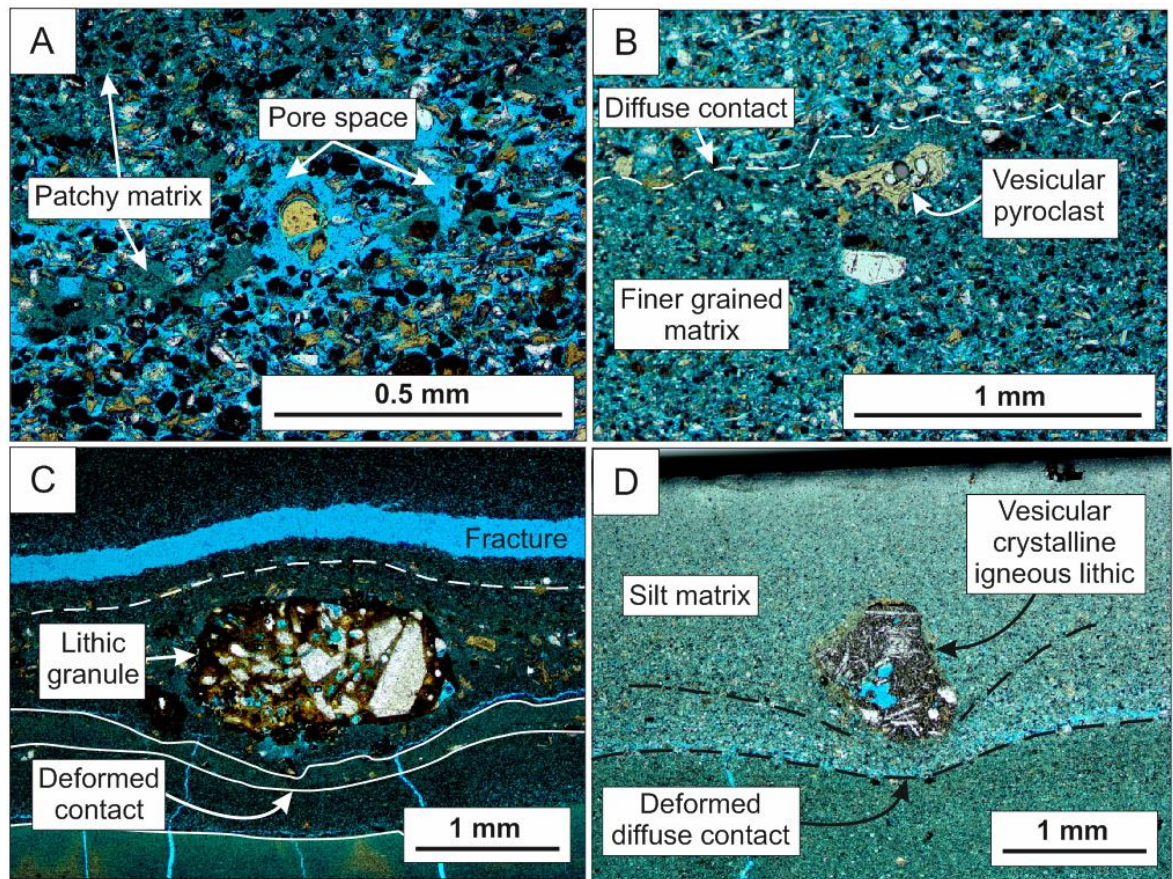


Figure 2-22 PPL optical microscopy images showing a variety of granular features observed within the samples from Hekla, Locality 2. A) High porosity and permeability of the sediment, as indicated by the large amount of blue resin between grains (ICE_04A). B) Diffuse bedding and coarser grains floating within a finer-grained matrix. These coarser grains include vesicular vitric pyroclasts and crystals (ICE_09A). C) Granule-sized lithic that has deformed/modified the fine-scale bedding below and is draped by sediment above (ICE_04A). A fracture is also present in this image (blue). D) A coarse vesicular crystalline igneous grain 'floating' within a finer-grained matrix, which deforms the diffuse bedding below it (ICE_04A).

The patchy matrix and greater amount of pore-space shown in Figure 2-22a may be an artefact of thin-sectioning, or an artefact created by 2D sectioning of a 3D material. It is possible that polishing of the thin-section has led to the removal of some of the finest material within these samples, thus, removing the matrix and making the porosity appear to be greater in the thin-section compared to that within the original deposit.

2.5.3 SEM

Polished thin-sections of the samples from Hekla, Locality 2, (Figure 2-1; Figure 2-15) were carbon coated for SEM analysis, alongside polished grain-mounts from Búrfellsstöð, Locality 1, and Kjaltell, Locality 3. SEM analysis provides a more

detailed view of the individual grains within these sediments, allowing a more in-depth investigation into the morphology of the igneous component, as well as the basic chemical composition of pyroclasts.

2.5.3.1 *Búrfellsstöð, Locality 1a-d*

Polished grain-mounts were produced from grab-samples from each of the localities of Búrfellsstöð (1.3 Methods); their characteristics are described here.

Búrfellsstöð Locality 1a: ICE_13 - 15

A range of clast types can be observed in samples from Búrfellsstöð 1a, with the same clast types being present in each. In general, all the clasts are angular to sub-rounded (Figure 2-23, Figure 2-24).

Granular clasts are present in varying amounts in all of the samples. One type of granular clast is comprised of a clay matrix with fragments of glassy pyroclasts (Figure 2-23b), another is comprised of fine-grains of all the clast-types that are otherwise present within the sample, for example, grains of crystalline igneous rock, fragments of plagioclase, granular lithic clasts, alongside less common grains of titanomagnetite (Ti-magnetite), supported by a clay matrix (Figure 2-24a-b).

Crystalline igneous clasts of varying compositions contain varying crystal sizes and types, for example, one type of crystalline igneous clast is comprised of pyroxene, plagioclase and ulvospinel, and can be more coarsely crystalline (Figure 2-23a) or more micro-crystalline (Figure 2-24c). Another type of igneous clast contains micro-crystals of euhedral plagioclase and pyroxene with localised accessory pyrite (Figure 2-23a). Rare crystalline igneous clasts comprised of euhedral olivine, and plagioclase can also be observed (Figure 2-24d).

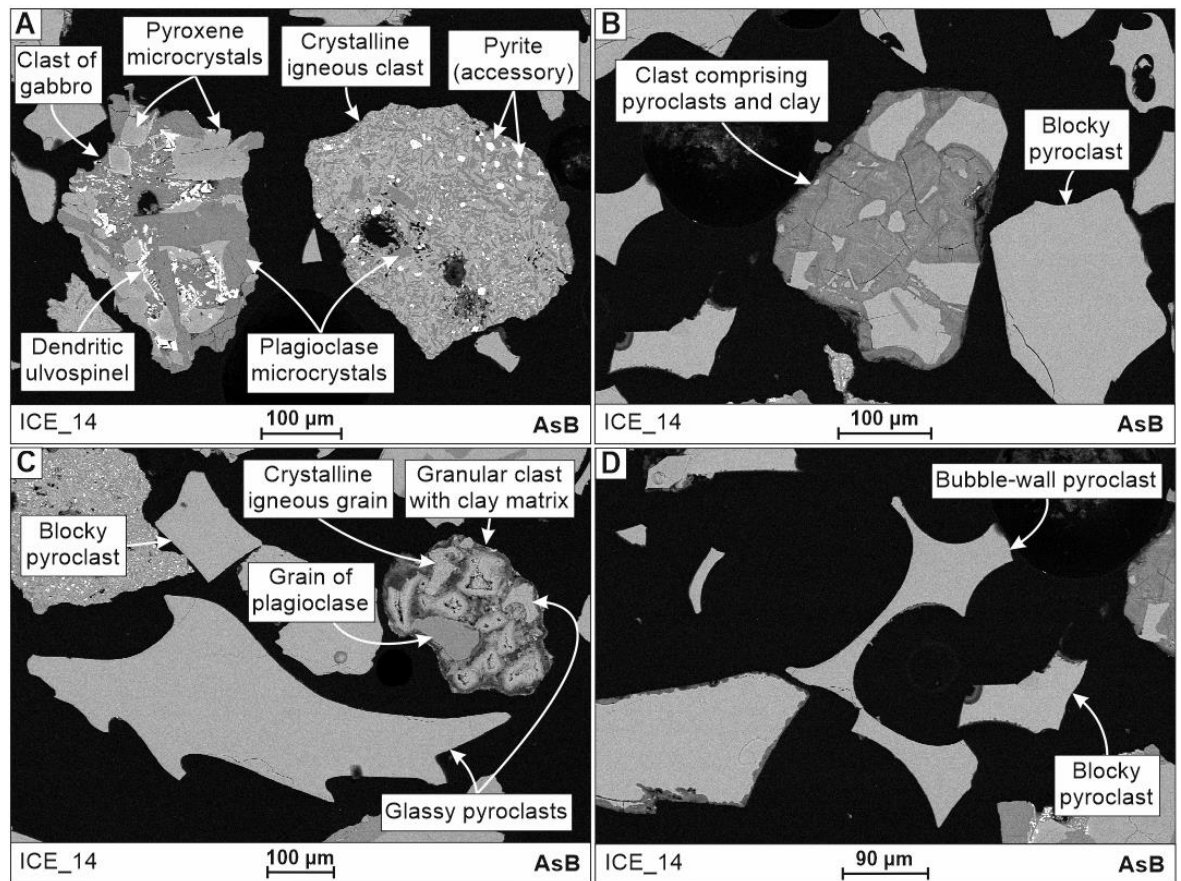


Figure 2-23 Main clast types identified in ICE_14 from Búrfellsstöð 1a. A) Two types of angular crystalline igneous clast; both are comprised of plagioclase with various other minerals, such as, pyroxene, ulvospinel and accessory pyrite. B) An angular clast comprised of fragments of pale grey (Type 1) pyroclast surrounded by a darker grey clay matrix. A blocky pyroclast can also be observed to the left of this clast. C) Sub-angular granular clast containing grains of crystalline igneous material, fragments of plagioclase and fine-grained glassy pyroclasts. Varying morphologies of blocky pyroclast can also be seen. D) Bubble-wall and blocky pyroclasts.

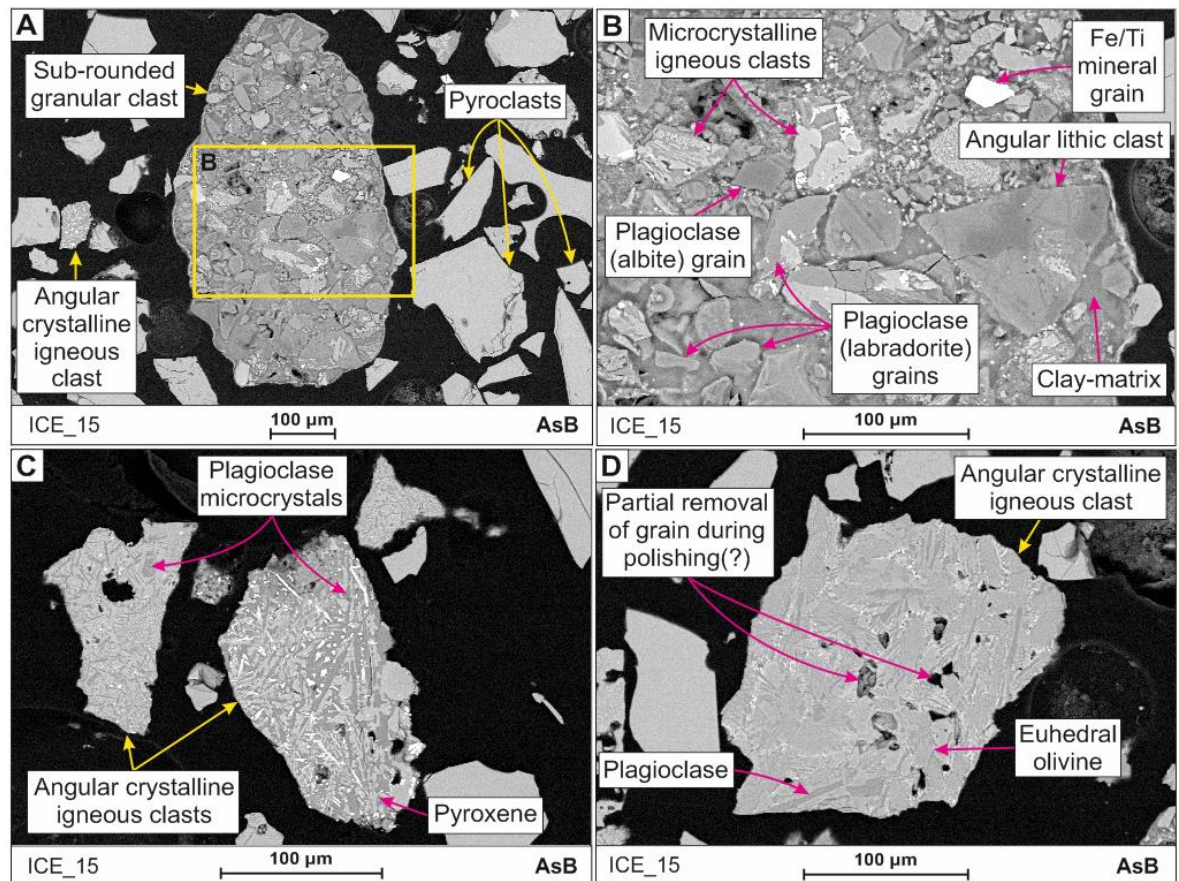


Figure 2-24 Examples of granular and crystalline igneous clast-types in samples from Búrfellsstöð 1a. A) Glassy pyroclasts, angular crystalline igneous clast and a coarser-grained sub-rounded granular clast. The yellow box shows the location of the B. B) Granular clast containing grains of microcrystalline igneous material, angular lithic clasts, plagioclase and Fe/Ti mineral grains, held together by a clay matrix. C) Angular crystalline igneous clasts containing varying proportions of plagioclase and pyroxene. D) Angular crystalline igneous clast, containing euhedral olivine and plagioclase, some of this grain may have been removed during sample preparation.

These samples contain a homogeneous composition of basaltic, glassy pyroclasts which appear pale grey under SEM AsB. Two sets of pyroclasts with different chemical compositions have been identified in some of the other samples (see descriptions below), thus, pale grey pyroclasts will now be referred to as Type 1 pyroclasts. The pyroclasts display a range morphologies, from blocky (Figure 2-23b-d), to bubble-wall (Figure 2-23d), and fluidal or irregular (Figure 2-25c). Rod-like pyroclasts can also be observed in ICE_15, but are absent from ICE_13 or ICE_14. The pyroclasts are non-vesicular to poorly vesicular with occasional highly-vesicular pumice (Figure 2-25).

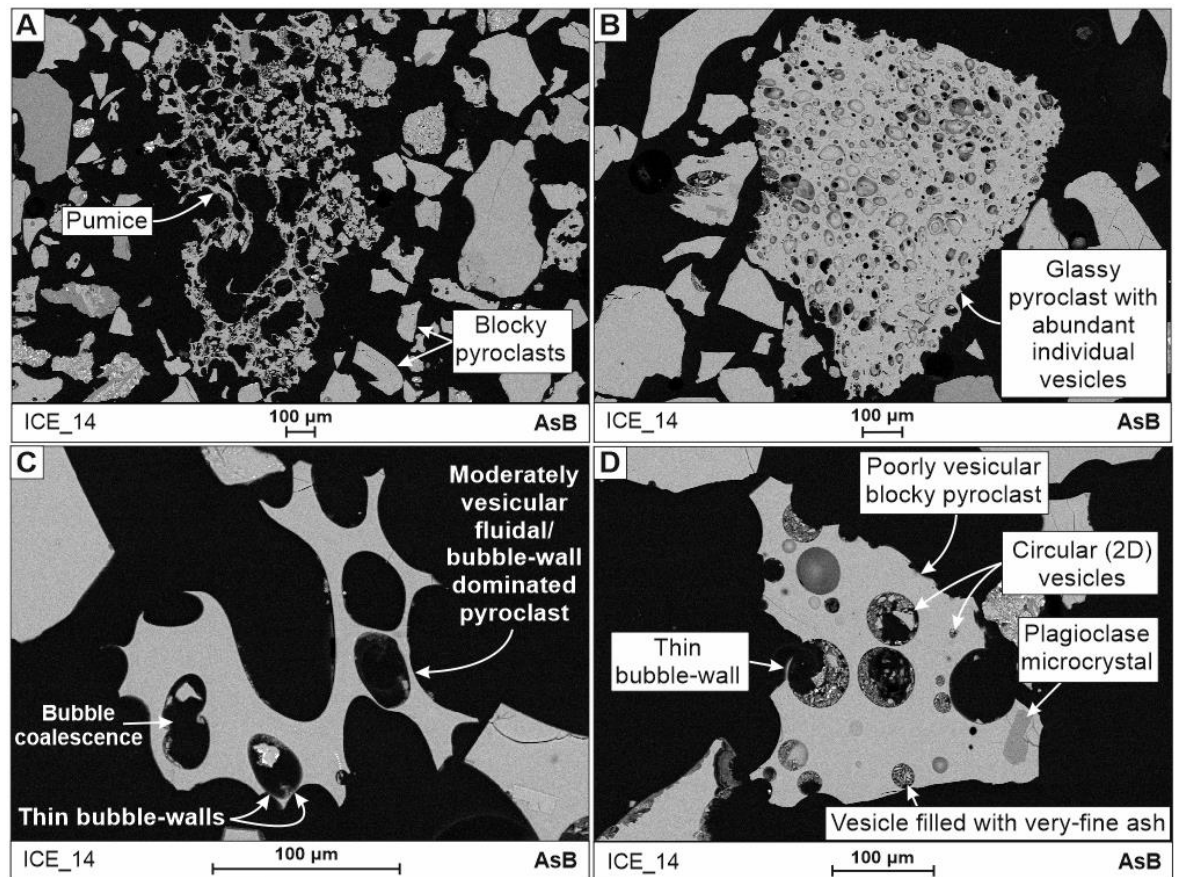


Figure 2-25 Examples of pyroclast types in sample ICE_14 from Búrfellsstöð 1a. A) Highly-vesicular pumice surrounded by generally blocky, Type 1 pyroclasts. B) Glassy pyroclast containing abundant rounded vesicles separated by bubble-walls, with only limited evidence of bubble-coalescence. Over-all this pyroclast has a blocky morphology. C) Glassy pyroclast with relatively large vesicles and thin bubble-walls between these. This pyroclasts shows evidence of bubble-coalescence where two vesicles intersect. The outer surface of the pyroclast is predominantly formed of bubble-walls giving the pyroclasts a fluidal or irregular overall morphology. D) Poorly vesicular pyroclast with rounded vesicles (in cross-section) of different sizes. Thin-bubble walls can still be noted within and on the outside of the pyroclast. This pyroclast also contains localised plagioclase phenocrysts (also referred to as microcrystals).

Búrfellsstöð Locality 1b: ICE_16 - 17

The composition of sediment in grain-mounts from Búrfellsstöð 1b are the same as that identified in samples from Búrfellsstöð 1a. However, clasts of vesicular, irregularly shaped, microcrystalline igneous rock can be observed in these samples; here, this clast-type is interpreted as lava-like clasts. Lava-like clasts are present in addition to, angular to sub-rounded crystalline igneous clasts, granular clasts, and pyroclasts. The nature of many of the pyroclasts also varies in samples ICE_16 and ICE_17. Many pyroclasts in these samples have clay-rich edges and/or vesicles filled with fine ash (Figure 2-26).

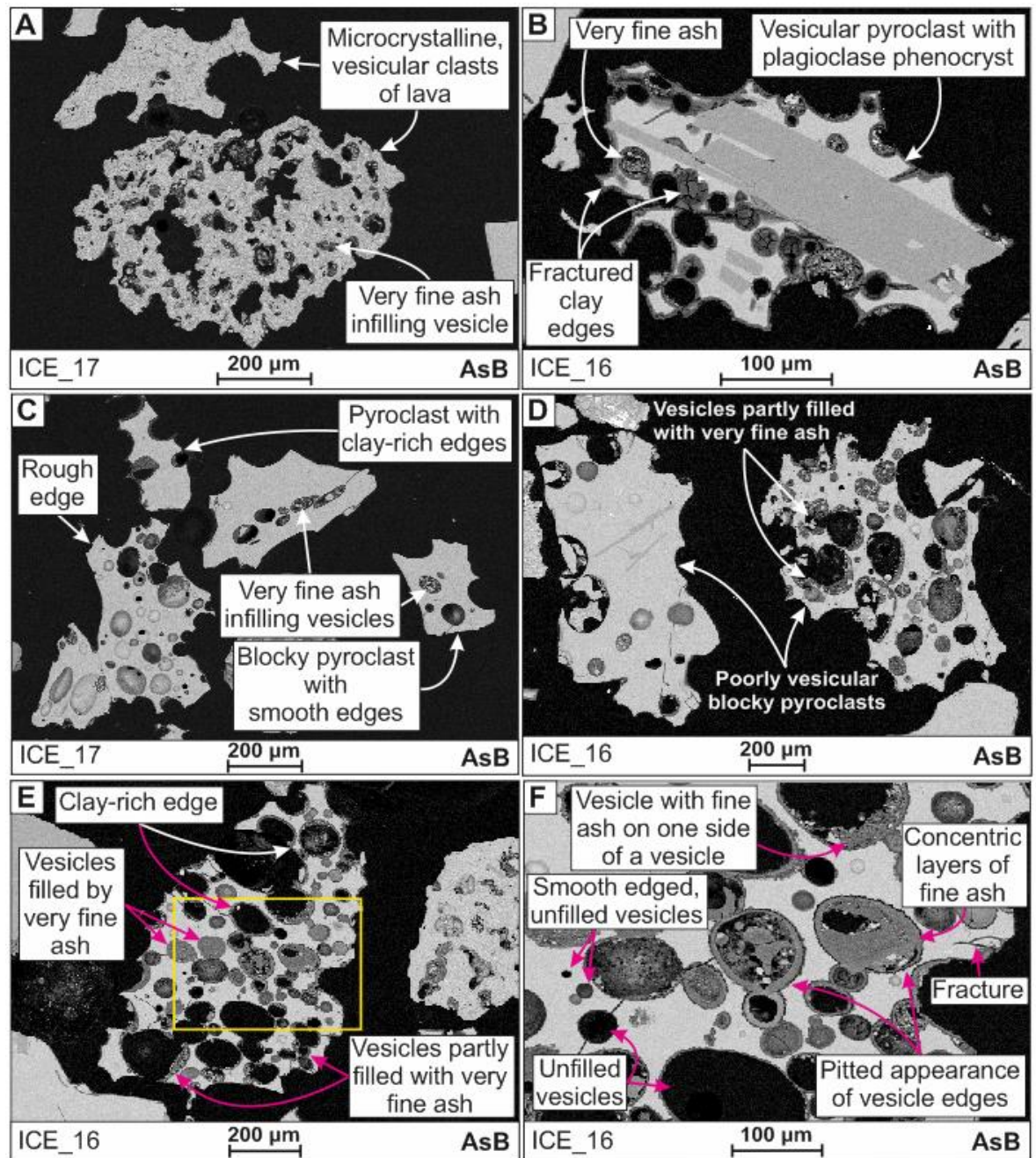


Figure 2-26 Lava-like clasts and features of pyroclasts observed in ICE_16 and ICE_17 from Búrfellsstöð 1b. **A)** Clasts of microcrystalline lava with irregular-shaped vesicles. **B)** Glassy vesicular pyroclast with euhedral phenocrysts of plagioclase. The edge of this pyroclast and its vesicles is comprised of fractured clay. Very fine ash infills some of the vesicles. **C)** Smooth-edged blocky pyroclasts with vesicles occasionally infilled with fine ash, and, a pyroclast with clay-rich edges. One of the blocky vesicular pyroclasts has a few sharp but rough/jagged edges. **D)** Two blocky pyroclasts with different appearances. Most of the vesicles in the pyroclast on the right are infilled either partially or completely by very fine ash. The pyroclast on the left contains less vesicles and vesicles that are generally smaller in size, some of which are infilled with very fine ash. **E)** A generally blocky vesicular pyroclast with abundant clay edges and spherical vesicles partly or completely infilled with very fine ash. The partly infilled vesicles all contain a layer of very fine ash on one side of the vesicle. The yellow box shows the location of **F)** Higher magnification shows that some vesicles are uninfilled and have smooth edges, others are uninfilled but have a pitted edge appearance (lower uninfilled vesicles). One vesicle is partly infilled with concentric layers of very fine ash. In general the partly or completely infilled vesicles have pitted edges and the uninfilled vesicles have smooth edges.

In general, the pyroclasts of ICE_16 and ICE_17 appear to be predominantly blocky and are more vesicular than those of the samples from Búrfellsstöð 1a, with much less bubble-wall and non-vesicular pyroclast types.

Búrfellsstöð Locality 1c: ICE_18, ICE_24 - 25, ICE_27

Samples from Búrfellsstöð 1c are similar to those of Búrfellsstöð 1a. All of the samples contain abundant Type 1 pyroclasts of vesicular and non-vesicular types, in addition to angular to sub-rounded crystalline igneous clasts, granular lithic clasts and fragments of plagioclase. However, in addition to this, samples ICE_18, ICE_24 and ICE_25 also contain a minor abundance of mid-grey pyroclasts (Type 2 herein). The Type 2 pyroclasts display similar characteristics to the Type 1 pyroclasts but are generally finer-grained. The Type 2 pyroclasts are vesicular and non-vesicular and display a range of pyroclast morphologies, from blocky to bubble-wall and rod-like (Figure 2-27). In some samples the Type 1 pyroclasts also exhibit an irregular morphology, that is often more fluidal in appearance (Figure 2-28).

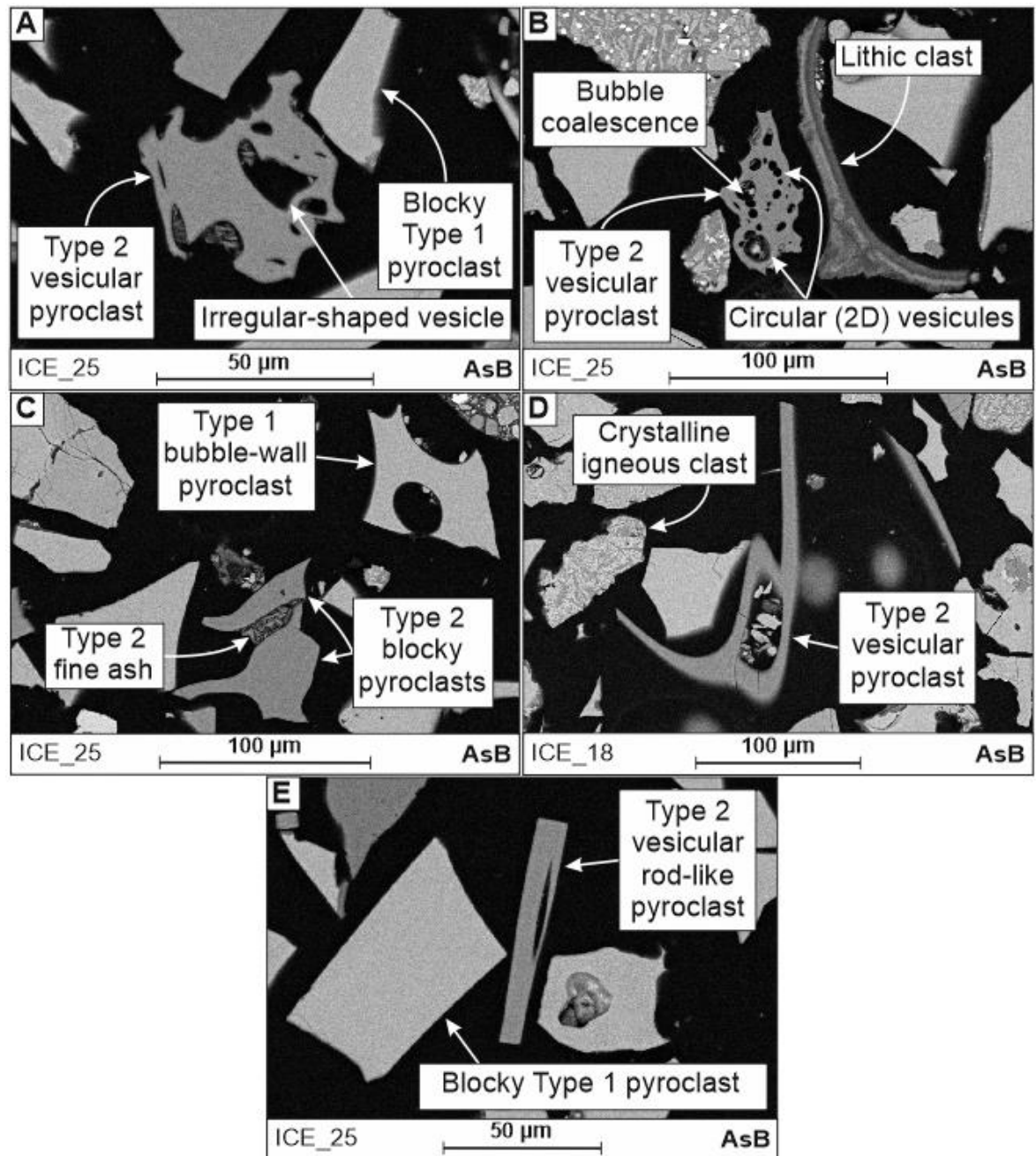


Figure 2-27 Features of Type 2 pyroclasts (mid-grey colour) observed in ICE_18 and ICE_25 from Búrfellsstöð 1c. A & B) Blocky, vesicular Type 2 pyroclasts. The vesicles in A are more irregular in shape than those in B, which are more circular. Image A also shows a blocky non-vesicular Type 1 pyroclast. C) Blocky non-vesicular Type 2 pyroclast associated with some very fine mid-grey ash. A Type 1 bubble-wall shard is also present in this image. D) Bubble -wall or rod-like Type 2 pyroclast with a lense-shaped vesicle. This image also shows the presence of angular crystalline igneous clasts and blocky Type 1 pyroclasts. E) A rod-like Type 2 pyroclast with an elongated vesicle, alongside a blocky Type 1 pyroclast.

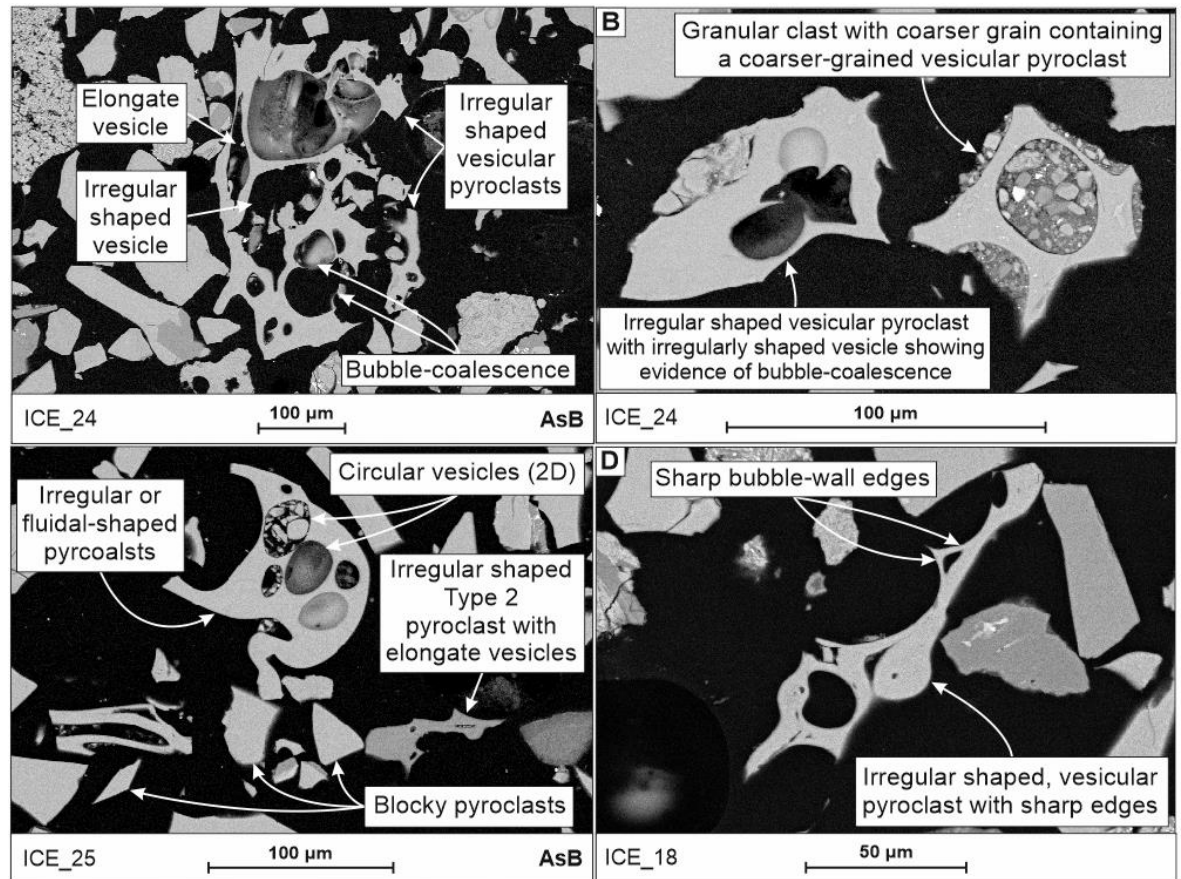


Figure 2-28 Irregular and fluidal-shaped pyroclasts in samples from Búrfellsstöð 1c. A) A coarser-grained example of an irregular shaped Type 1 pyroclast with multiple vesicles of varying morphology. Some vesicles in this example are elongate, irregular or more circular in cross-section. Some also show evidence of bubble-coalescence where bubble-walls have broken as the bubbles have begun to merge. B) A sharp-edged irregular-shaped pyroclast with irregular-shaped vesicles. The vesicles in this pyroclast also show evidence of bubble-coalescence. To the right of this pyroclast lies a granular clast which contains a coarser-grained vesicular pyroclast as one of its components. C) Fluidal shaped, vesicular pyroclasts with more circular vesicles in cross-section. An irregular-shaped Type 2 pyroclast with elongate vesicles is also present. D) An irregular shaped pyroclast with sharp edges, including the edges of bubble-walls.

Búrfellsstöð Locality 1d: ICE_31

One sample was selected from Búrfellsstöð 1d for comparison with the samples from the other Búrfellsstöð localities (Figure 2-5). The grains within sample ICE_31 are very similar in character to those described for Búrfellsstöð 1b, where there is evidence of alteration and/or reworked pyroclasts, in the form of clay-rich and fractured, jagged edges, and infilled vesicles (Figure 2-29 compared to Figure 2-26). The pyroclasts show a range of features, from smooth, sharp edges (Figure 2-29a-b) and partially infilled vesicles (Figure 2-29b), to completely filled vesicles (Figure 2-29c), rough surfaces and jagged

edges (Figure 2-29c) to clay-rich edges (Figure 2-29d). The infilled vesicles are predominantly filled with very fine-ash.

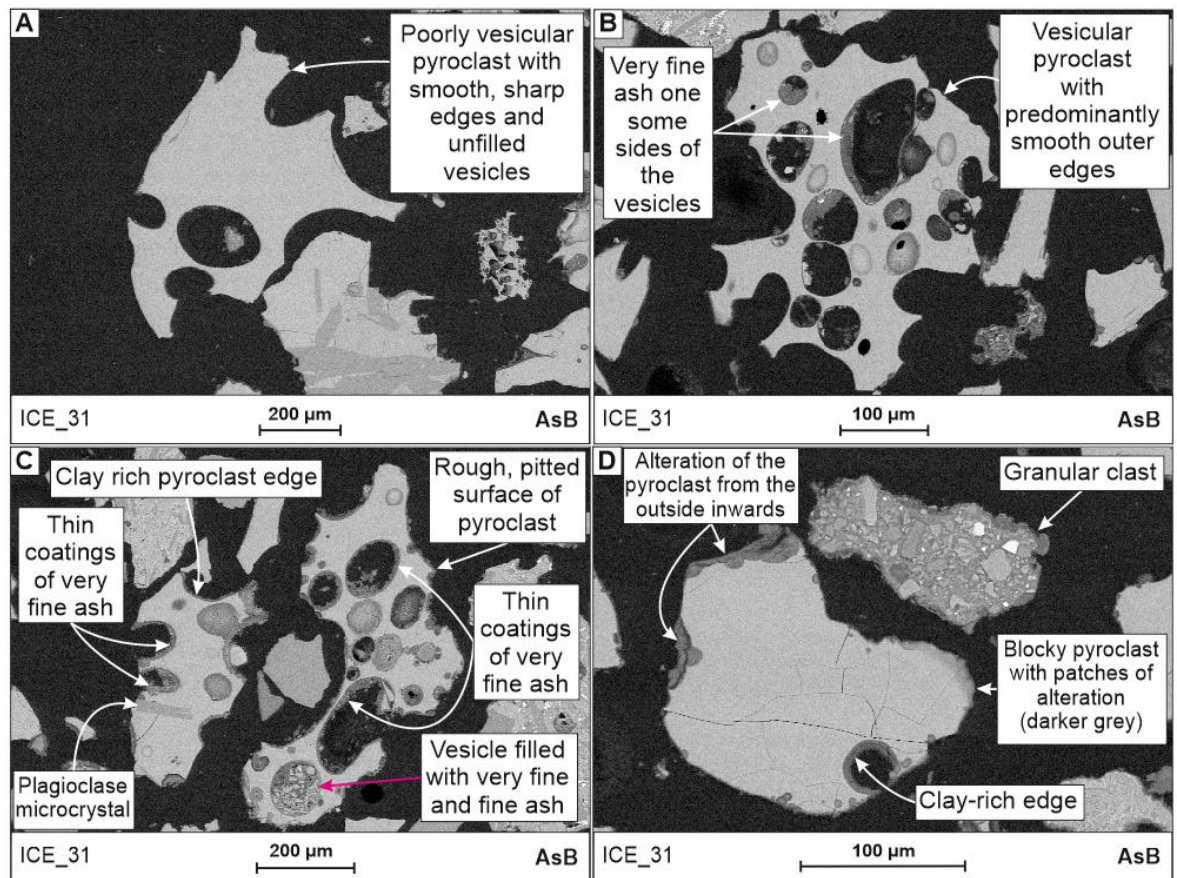


Figure 2-29 The range of features associated with pyroclasts from Búrfellsstöð 1d. A) A poorly vesicular pyroclast with smooth, sharp edges and empty vesicles. B) A poorly vesicular pyroclast with vesicles that are partially filled by a very fine ash. C) Two poorly vesicular pyroclasts with rough outer edges and partially to completely infilled vesicles. Some of the outside edges of these pyroclasts are comprised of bubble-walls, the edges of which are coated in a thin layer of very fine ash. D) A blocky pyroclast with rough outer edges caused by progressive alteration from the outside to the inside of the clast. The darker grey regions of the edge of this pyroclast are clay-rich. An angular granular clast can also be seen.

2.5.3.2 Hekla, Locality 2

Bedding characteristics identified by optical light microscopy (Figure 2-21) can also be identified with the SEM, along with features that were not initially identified in the Hekla, Locality 2 samples (Figure 2-30). Features that were not easily identified prior to SEM analysis include grain-scale laminations of coarser grains within finer-grained beds (Figure 2-30a).

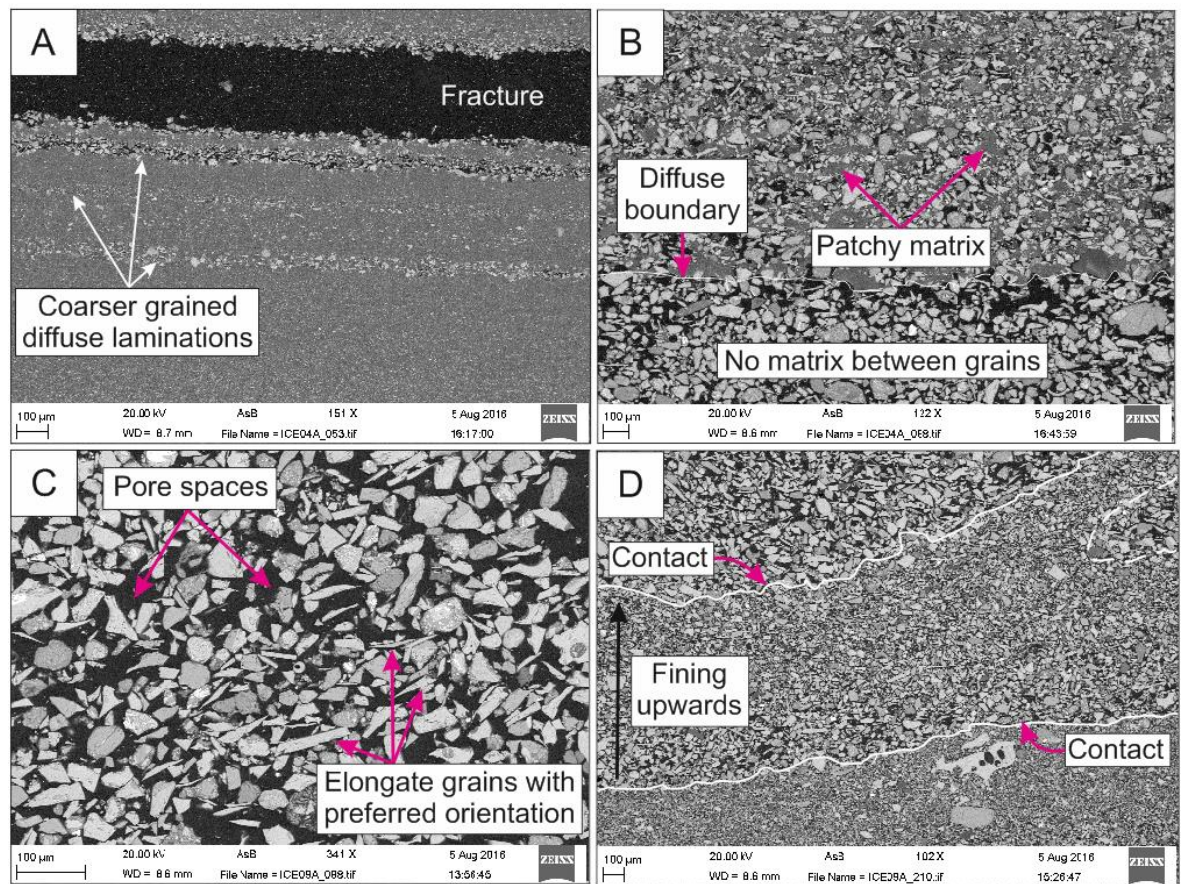


Figure 2-30 SEM AsB images showing different bedding and lamination features in samples from Hekla, Locality 2. A) Laminations caused by the presence of strings of coarser grains: the laminations are only a few grains thick, planar and generally continuous (ICE_04A). B) Some beds contain a patchy matrix of very fine ash grains, whereas others have no matrix at all and are grain-supported (ICE_04A). C) Many beds have abundant pore space with grains seeming to float (ICE_09A). D) An example of the normal-graded, fining-upwards unit (ICE_09A).

The pyroclastic material of these samples takes on several forms (Figure 2-31), from vesicular and non-vesicular pyroclasts of blocky and bubble-wall morphologies, to partially devitrified pyroclasts (Figure 2-31d). The finest grain-size fraction forms the interstitial matrix or forms clasts comprised of very fine-ash (Figure 2-31; Figure 2-32).

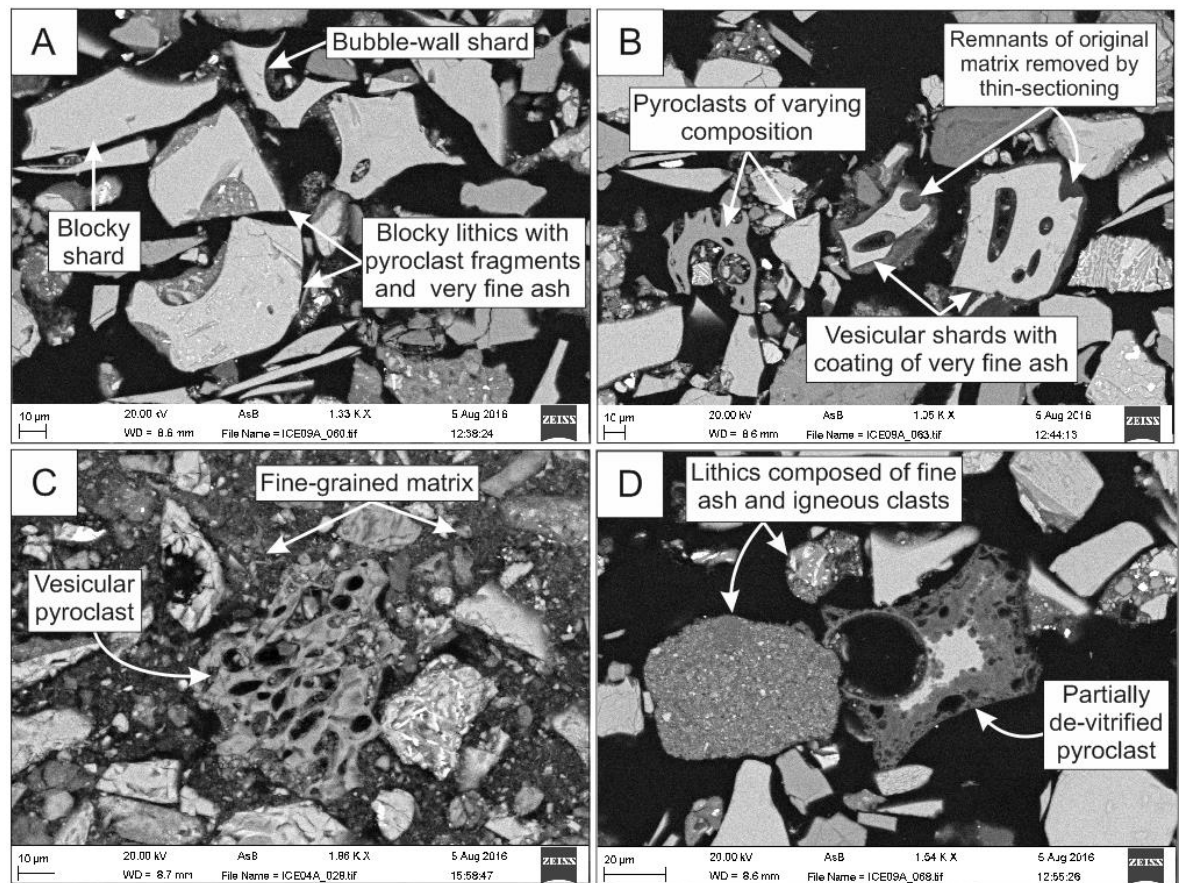


Figure 2-31 SEM AsB images showing the range of volcanic clast-types that can be identified within the Hekla, Locality 2 samples. A) Blocky shards and bubble-wall shards alongside blocky lithics containing pyroclasts and very fine-grained ash (ICE_09A). B) Pyroclasts with differing chemical compositions are identified by variations in the grey-scale of the SEM image; poorly vesicular pyroclasts are also present (ICE_09A). C) A vesicular Type 2 pyroclast within a fine-grained ash matrix (ICE_04A). D) A partially devitrified pyroclast and examples of granular lithics. One lithic is comprised of very fine ash, whereas others contain a greater variety of clast types (pyroclasts and grains of crystalline igneous material) and grain-sizes (ICE_09A).

Different types of fine-grained ash-rich lithics are present (Figure 2-32). Some are formed of poorly sorted material that includes pyroclast fragments and igneous clasts with a very fine-grained ash matrix (Figure 2-32a & c). Others are better sorted and composed of fine-ash only (Figure 2-32d). Some appear to be dominated by a single composition of volcanic glass, with little or no interstitial very fine-ash, giving them an unconsolidated appearance (Figure 2-32b), referred to as irregular aggregates (Scolamacchia et al. 2005). These are lithics in the sense that they are comprised of fine grains; however, ash aggregates can form by the aggregation of fine-ash during transport in an eruption plume. These unconsolidated-looking lithics could therefore be interpreted as ash aggregates (particle-cluster type) and should be considered as a primary pyroclastic clast-type, unless evidence of reworking can be found.

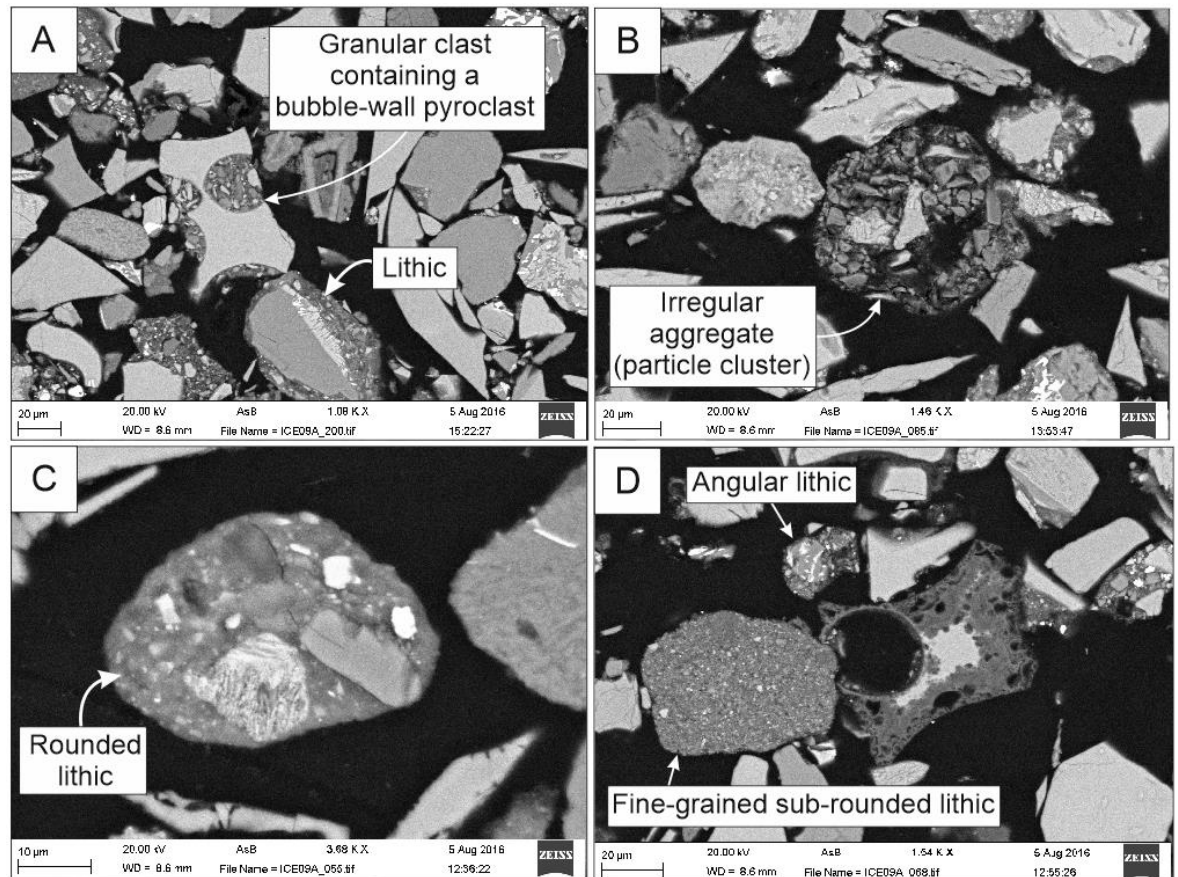


Figure 2-32 Various types of lithic clasts and an example of an ash aggregate observed in ICE_09A. A) Examples of lithic clasts that contain bubble-wall pyroclasts and other igneous material, fine ash forms the matrix of these lithic fragments. B) An irregular aggregate, or particle cluster, containing loosely compacted ash. C) Rounded lithic clast comprised of pyroclasts, feldspar, crystalline igneous rock fragments and other minerals. D) Examples of very fine-grained sub-rounded lithic and an more angular lithic comprised of grains with a wider range of compositions and grain-sizes, including coarser grains of crystalline igneous rock and finer grained ash.

Some pyroclasts show the presence of micro-fractures along their rims, which may be interpreted as hydration cracks (Figure 2-33; e.g. Scolamacchia et al. 2005; Mascarenhas-Pereira 2006).

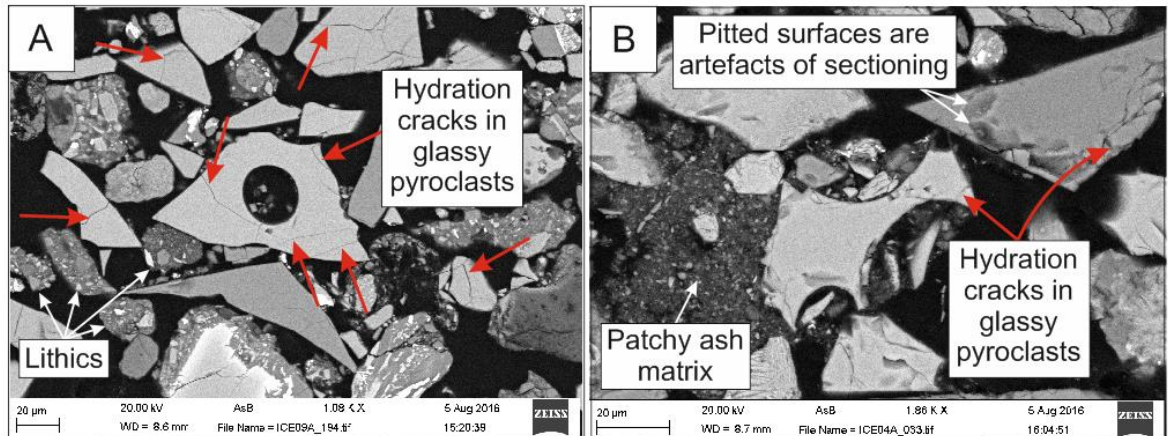


Figure 2-33 Possible hydration cracks within pyroclasts of the Hekla, Locality 2 samples. A & B) Very fine-scale cracks (red arrows) within pyroclasts of ICE_09A and ICE_04A may represent hydration cracks formed during rapid cooling of an erupted magma. B) Parts of the original fine-ash matrix which supported the grains in this deposit (ICE_04A).

In addition to pyroclasts, there are a variety of angular to sub-rounded crystalline igneous clasts (Figure 2-34). These clasts all appear to have the same general mineral composition, comprising hornblende, pyroxene and labradorite, although of varying abundance, shape and size (Figure 2-34).

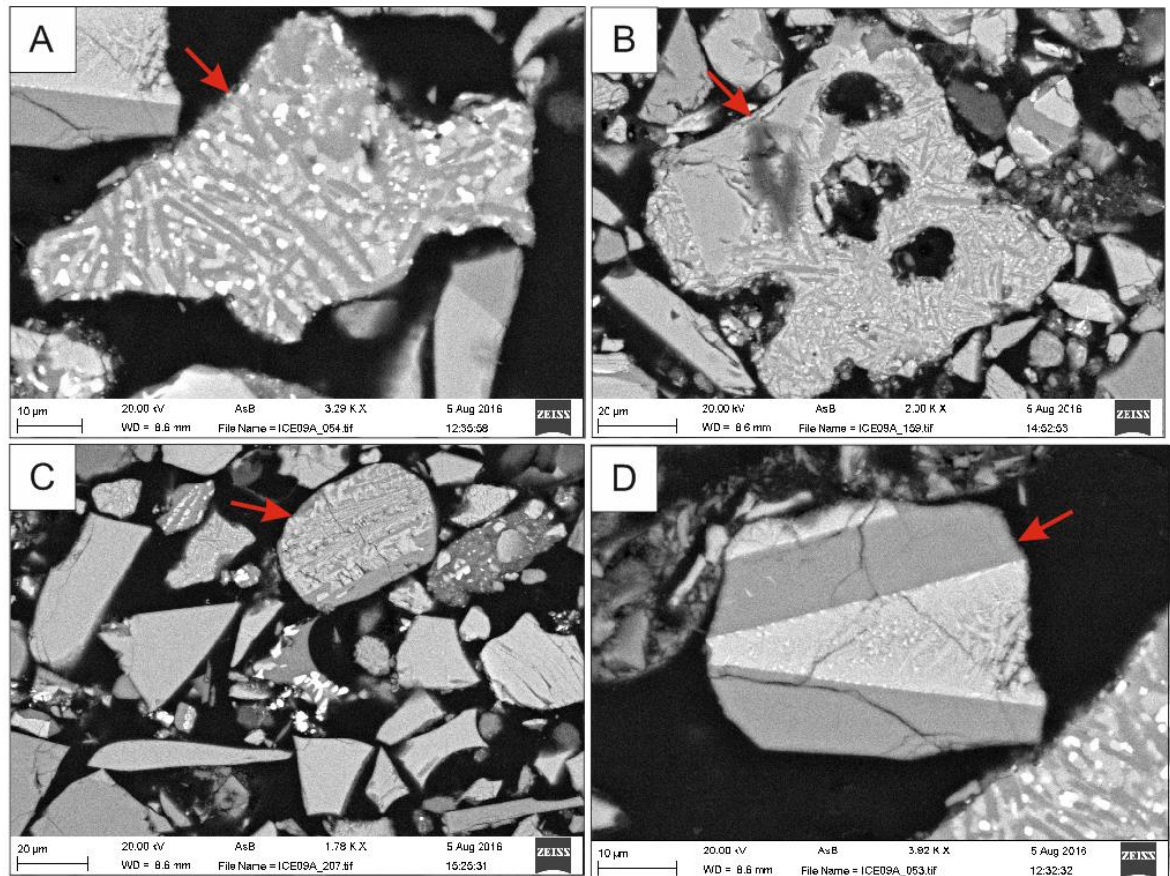


Figure 2-34 Various types of crystalline igneous clasts (red arrows) within ICE_09A. A) Sub-angular crystalline igneous clast with crystals of hornblende and pyroxene. B) Irregularly-shaped sub-angular clast with crystals of the same composition as in A, as well as irregularly-shaped vesicles. C) Rounded, clast dominated by labradorite (darker grey) with dendritic hornblende (paler grey). D) Striped angular crystalline clast containing larger-scaled crystals of hornblende and labradorite.

2.5.3.3 Kjalteill, Locality 3

Grain-mounts were produced for a selected number of samples from Kjalteill, Locality 3. Samples were chosen for analysis based on their apparent ‘freshness’. Samples that contain black vitreous sediment were considered as being ‘fresh’ and samples that appeared to be reddish-brown and more-dusty/dull in appearance were considered less-fresh. A range of samples were chosen, with the aim of identifying and comparing the difference between ‘fresh’ pyroclasts and more altered or potentially reworked pyroclasts.

All of the samples contain similar grain-types, including various crystalline igneous clasts (Figure 2-35), vesicular microcrystalline lava-like clasts (Figure 2-36a), granular lithic clasts (Figure 2-36b, c), fragments of plagioclase crystals, and pyroclasts (Figure 2-37).

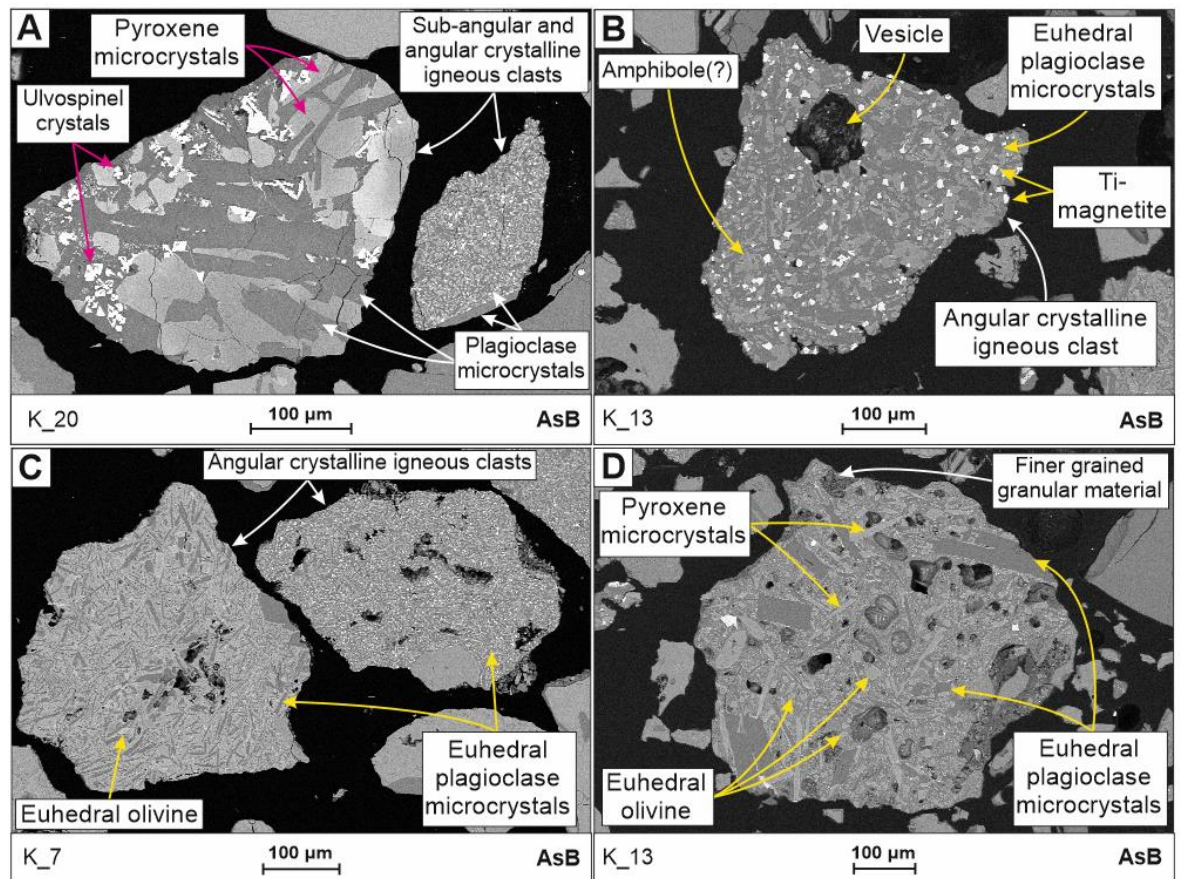


Figure 2-35 Varying types of crystalline igneous clasts observed in samples from Kjaltell, Locality 3. A) Sub-angular and angular crystalline igneous clasts containing euhedral laths of plagioclase as well as crystals of pyroxene and ulvospinel. B) An angular, vesicular crystalline clast comprised of euhedral plagioclase, amphibole(?), and Ti-magnetite. C) Angular crystalline igneous clasts with microcrystals of plagioclase. The clast on the left also contains crystals of euhedral olivine. D) A more coarsely crystalline sub-angular igneous clast with coatings of granular material. This igneous clast is comprised of euhedral plagioclase, pyroxene and olivine microcrystals.

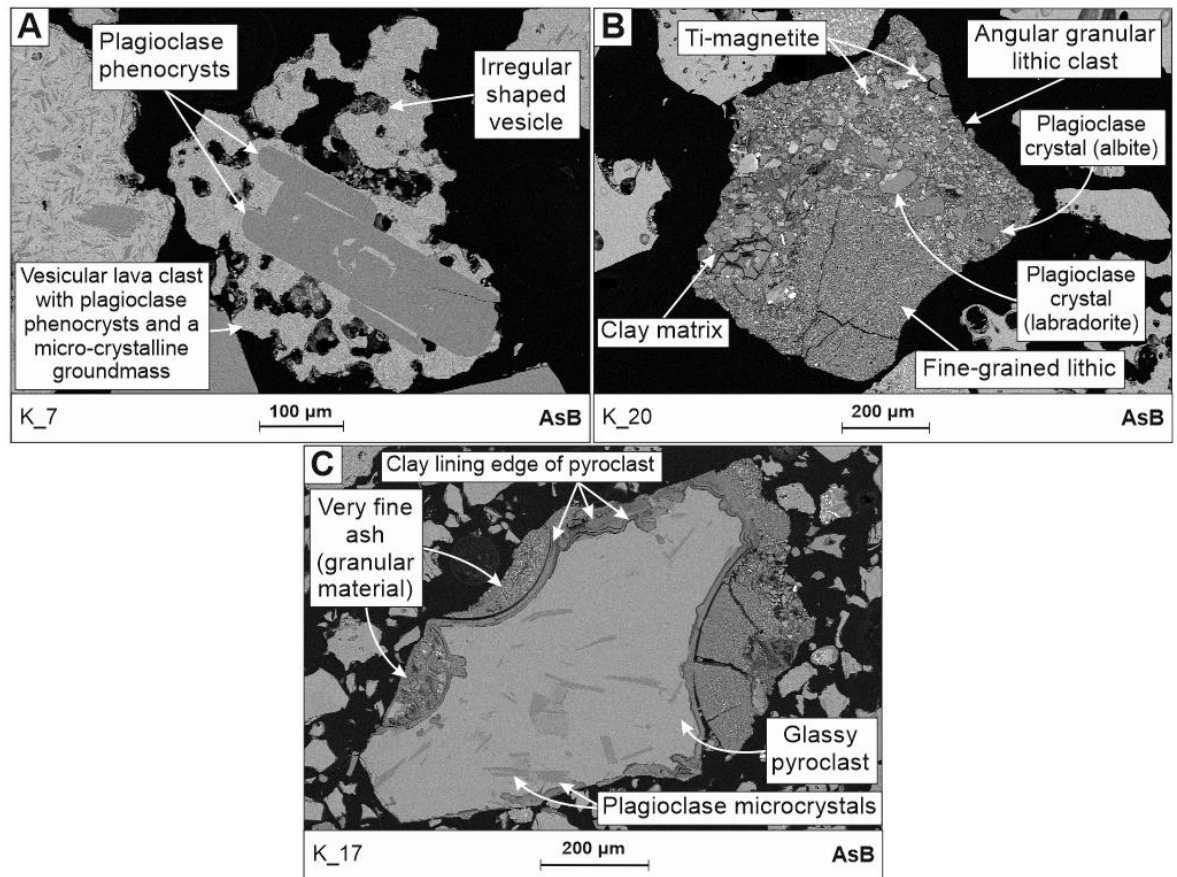


Figure 2-36 Lava and granular lithic clasts observed in samples from Kjaltef, Locality 3. **A)** Sub-angular/sub-rounded clast of vesicular lava with plagioclase phenocrysts and a micro-crystalline groundmass. **B)** Angular granular lithic clast comprising fine-grained fragments of plagioclase crystals (albite and labradorite), fine-grained lithic clasts, and Ti-magnetite, amongst a range of clast-types. A clay matrix can also be identified in some areas of this clast. **C)** An angular granular lithic clast dominated by one large glassy pyroclast. The glassy pyroclast contains euhedral plagioclase microcrystals and is lined by clay. Very fine ash makes up the rest of this granular clast.

The pyroclasts in these samples are of predominantly Type 1 pyroclasts (Figure 2-37) with very rare Type 2 pyroclasts (Figure 2-38). The Type 1 pyroclasts exhibit a range of features, from smooth edges (Figure 2-37a) and thin bubble-walls (Figure 2-37b), to jagged and fractured edges (Figure 2-37d, e) with evidence of replacement resulting in the pyroclasts being lined by clay (Figure 2-37e). Non-vesicular and poorly vesicular pyroclasts (Figure 2-37) are present in addition to uncommon highly vesicular pumice (Figure 2-37b). Vesicle shapes include circular (Figure 2-37a), irregular and elongate or tube (Figure 2-37d). The more highly vesicular pyroclasts show evidence of bubble-coalescence due to the preservation of broken bubble-walls and the irregular shape of some of the macro-vesicles, which indicates the coalescence of multiple bubbles (Figure 2-37b-c; Goanac'h et al. 2005; Polacci et al. 2008).

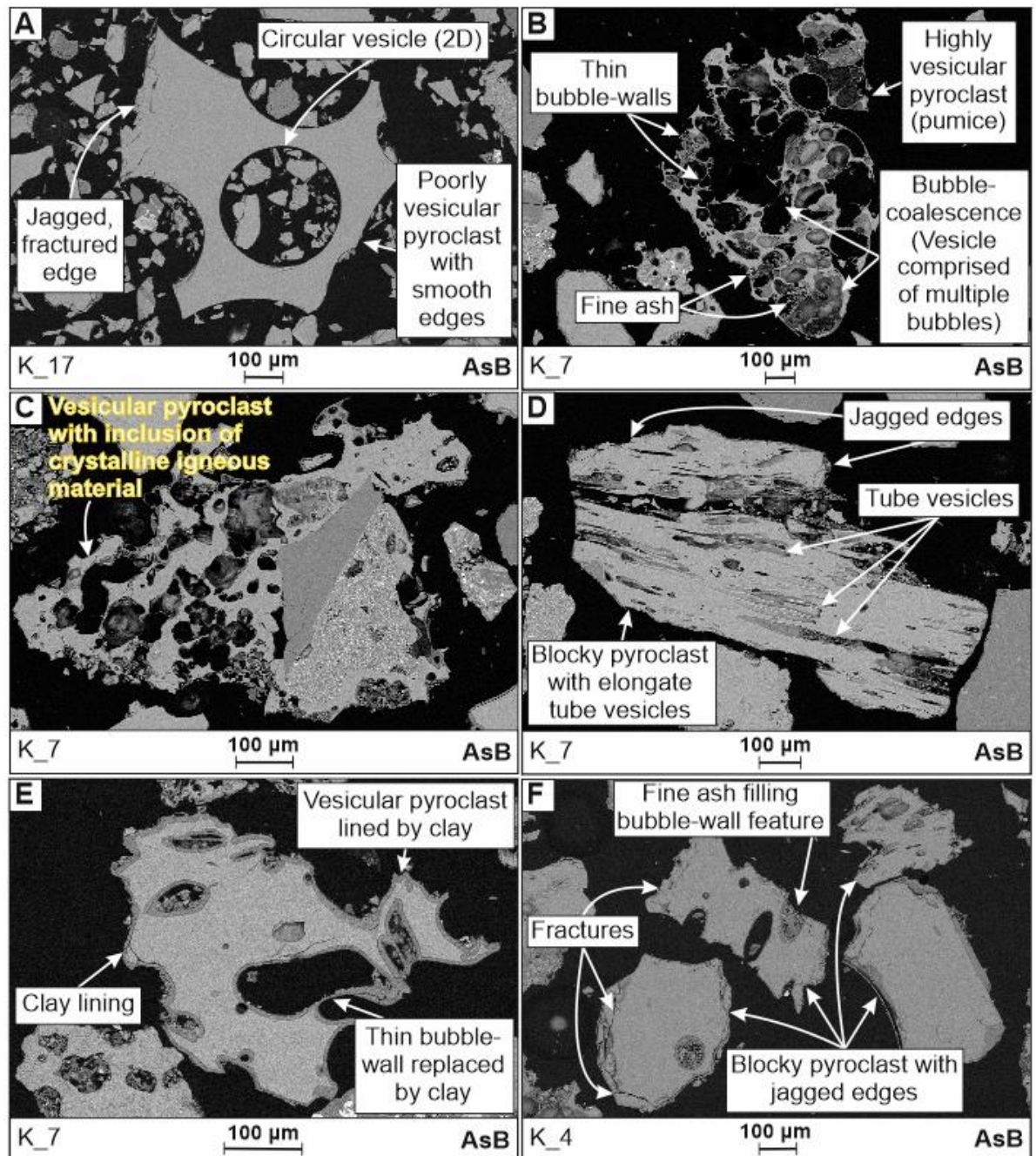


Figure 2-37 Features of pyroclasts in samples from Kjaltell, Locality 3. A) A smooth-edged poorly vesicular pyroclast with bubble-wall edges and jagged, fractured edges. The vesicle in the centre of the pyroclast is circular in this cross-section orientation. B) Pumice with very thin bubble-walls along with some localised very fine ash. Evidence for bubble-coalescence can be seen where bubble-walls have been breached and bubbles have merged, leading to the formation of a much larger, irregularly shaped vesicle. C) A vesicular pyroclast with an angular inclusion of crystalline igneous material. The crystalline igneous clast is comprised of a section of a plagioclase phenocryst and a more finely-crystalline groundmass that contains microcrystals of euhedral plagioclase. D) Blocky pyroclast with elongate tube vesicles. Some edges of this pyroclast are jagged and fractured. E) A more fluidal-shaped, poorly vesicular pyroclast lined by clay. The edges of vesicles and thin bubble-walls have also been replaced and lined by clay. The thickness of the clay lining is relatively consistent throughout. F) Various blocky vesicular and non-vesicular pyroclasts with abundant fractures and jagged edges. Some vesicles or bubble-walls are infilled with very fine ash. In general, these pyroclasts have a more jagged and fractured appearance compared to the smooth-edged pyroclast in image A.

Type 2 pyroclasts are rare or absent in the Kjaltell samples. Where present these pyroclasts have jagged corners and outer bubble-wall features are filled by very fine-ash (Figure 2-38).

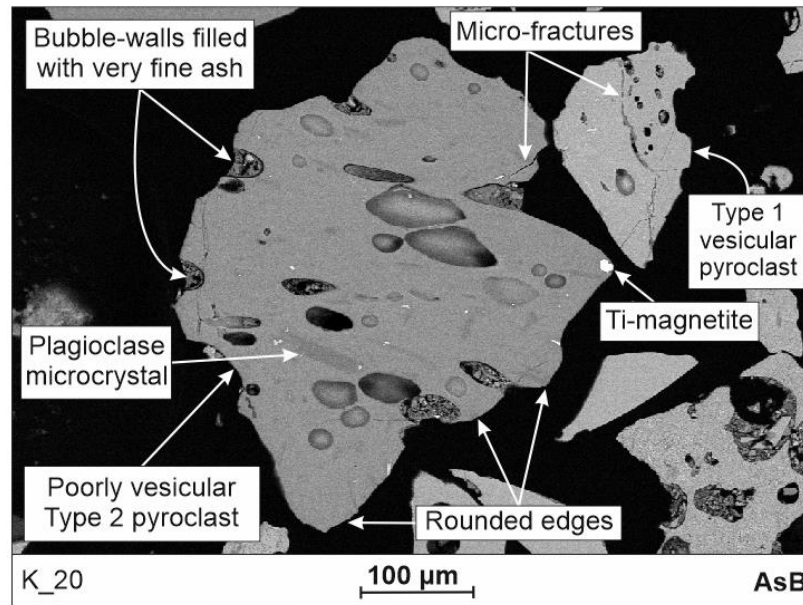


Figure 2-38 Features of a Type 2 pyroclast identified in sample K_20 from Kjaltell. This example of a vesicular Type 2 pyroclast from sample K_20 has rounded edges. Some of the external bubble-walls on the edges of the pyroclast are filled with very fine ash. Localised euhedral plagioclase phenocrysts are present within this glassy pyroclast. The vesicles are circular or elongate in cross-section. A blocky, vesicular Type 1 pyroclast is also present. Both the Type 2 and Type 1 pyroclasts have localised micro-fractures.

2.5.3.4 Chemical composition of pyroclasts

Individual eruptive events should produce glass shards that have a similar geochemistry, which can be used to correlate between deposits in separate locations and allow interpretation of the corresponding volcanic source based on compositional correlation (e.g. Brendryen et al. 2010). The SEM can be used to indicate the presence of pyroclasts of different compositions, for example, variations in the grey-scale of these reflect some variation in their chemical composition. In addition, the SEM can be used to provide non-quantitative information on the chemical composition of the different components by producing elemental spectra of the mineral or material (e.g. glass) that is selected for analysis. However, quantifiable chemical data should be obtained, for example from electron probe or laser ablation techniques (see Further Work 7.7), to allow proper comparison of the chemical variation of pyroclasts and allow comparison with data published in the literature.

Here, SEM images show that there are two compositions of pyroclast, as shown by variations in their grey-scale on backscatter SEM images. The spectra generated for these pyroclasts also suggests that there may be chemical differences in the composition of these. Two main compositions of pyroclast can be identified (Type 1 and Type 2; Figure 2-39). Type 2 pyroclasts have the highest abundance of Si and Type 1 pyroclasts contain the least Si (Figure 2-39). Type 1 appear pale grey under AsB, where-as Type 2 appear a mid-grey colour (e.g. Figure 2-38).

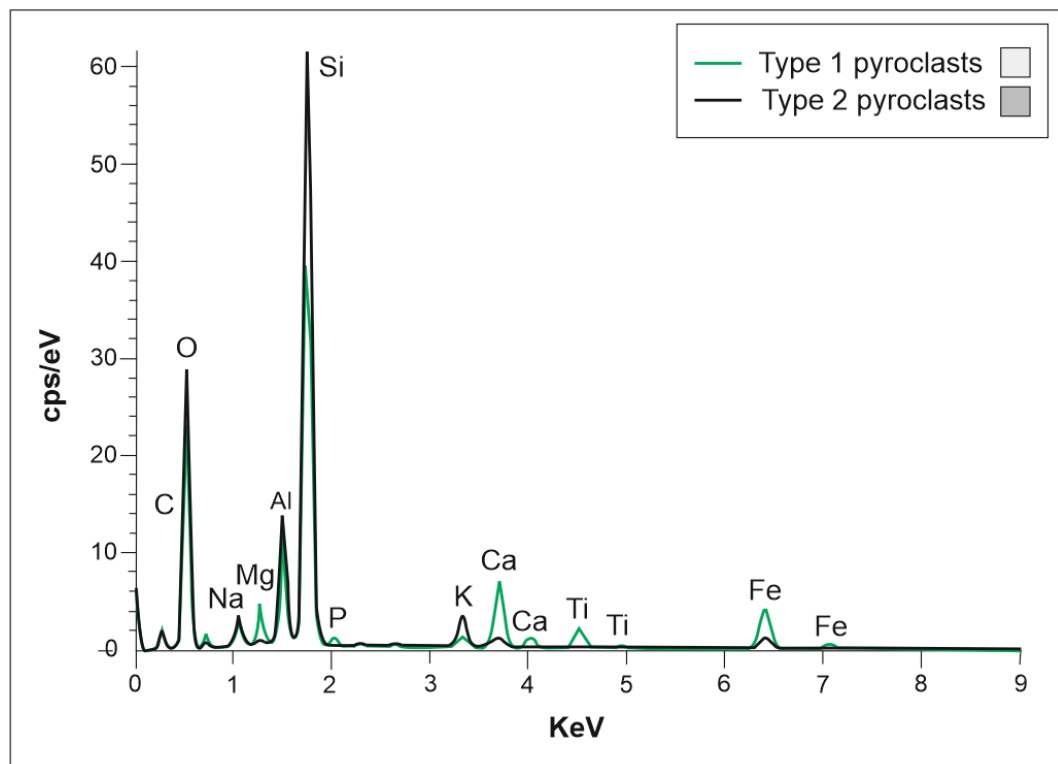


Figure 2-39 Comparison of the chemical spectra of the two types of pyroclast identified during SEM analysis of samples ICE_02A, ICE_04A and ICE_09A, from Hekla, Locality 2. Type 1 pyroclasts have slightly larger peaks for Mg, Ca, Ti and Fe compared to the other pyroclast types. The Type 2 pyroclasts have greater peaks in Si, Na and K.

Uncommon Type 1 pyroclasts appear to have darker grey embayments around their edges (Figure 2-40). In some cases, this feature has developed to almost replace the entire pyroclast (Figure 2-40b) This is evidence of the progressive nature of alteration of the originally glassy pyroclastics via palagonitisation.

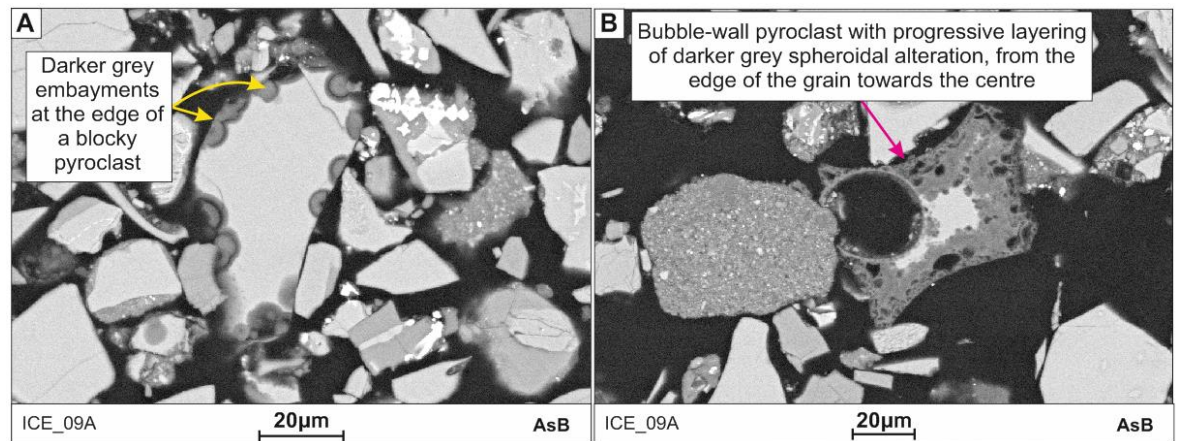


Figure 2-40 Progressive alteration of pyroclasts observed in ICE_09A. A) Small darker grey embayments around the edge of a blocky pyroclast. B) Continued alteration of the pyroclast leads to layering of these dark grey embayments, growing inwards from the edge of the pyroclast.

2.5.4 Image analysis

ImageJ software was used to gain quantitative data on: grain types and abundances, clast morphologies and vesicularity, as well as clast orientation. After basic pre-processing, the SEM AsB images (see 1.3 Methods) could be used for analysis of the grain characteristics in each of the samples.

2.5.4.1 Grain-size distribution

Quantifiable grain-size data (Figure 2-41, Figure 2-42) show that the samples have grain-sizes that range from clay (<125 µm) to very coarse sand (1-2 mm). These data do not include ash aggregate clasts or the size of their component grains.

Samples from Búrfellsstöð have a range of grain-sizes, from clay to very coarse sand. In general, samples from Búrfellsstöð 1c have the finest grain-sizes and those from Búrfellsstöð 1b and 1d are coarser-grained and display a larger grain-size distribution (Figure 2-41, Figure 2-42).

The grain-size distribution for Hekla, Locality 2, thin sections, range from clay (<125 µm) to fine sand (125-250 µm), and are predominantly comprised of silt-sized grains (Figure 2-42). The average grain-sizes of the Type 1 and Type 2 pyroclasts were also calculated separately to see how their grain-size distribution compares to the average grain-size distribution of the deposit as a

whole (Figure 2-43), and between the samples (Figure 2-41, Figure 2-42). In general, the grain-size distribution of both Type 1 and Type 2 pyroclasts mirrors that of the samples on a whole (Figure 2-42), being dominated by silt-sized grains (125 μm).

The samples from Kjaltell, Locality 3, often follow the same grain-size trend as those from Hekla, Locality 2 (Figure 2-42). However, samples K_4 and K_7 show a bi-modal grain-size distribution (Figure 2-42). These samples show peaks in silt and medium-sand sized grains. In general, the grain-size distribution for the selected Kjaltell samples is also larger than those from Hekla, Locality 2, and range from silt (3.9 - 62.5 μm) to coarse-sand (0.5 - 1 mm; Figure 2-42).

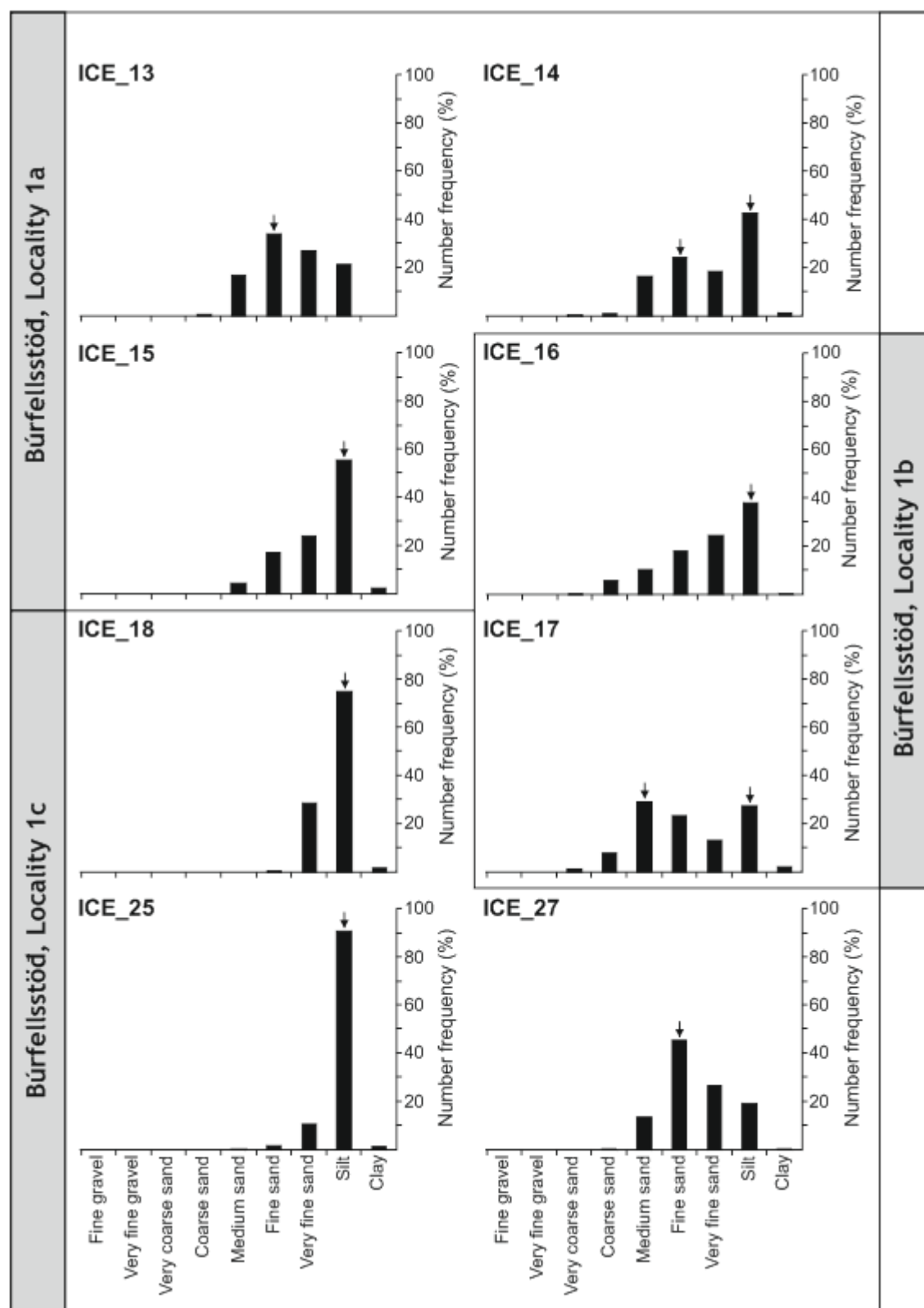


Figure 2-41 Grain-size distribution for Búrfellsstöð, Locality 1a-c. Samples ICE_13, ICE_14 and ICE_15 from Búrfellsstöð 1a have a grain-size distribution of clay up to very coarse sand, sample ICE_14 shows a bi-modal distribution with grain-size peaks (arrows) for silt and fine sand sized grains. Búrfellsstöð 1b samples have a grain-size distribution of clay to very coarse sand. ICE_16 shows a uni-modal distribution whereas ICE_14 shows a bi-modal grain-size distribution. Samples from Búrfellsstöð 1c have a grain-size distribution of clay to coarse sand. In general, ICE_18 and ICE_25 are finer-grained and are predominantly

comprised of silt-sized grains. However, ICE_27 is coarser-grained, with grains of predominantly fine-sand size.

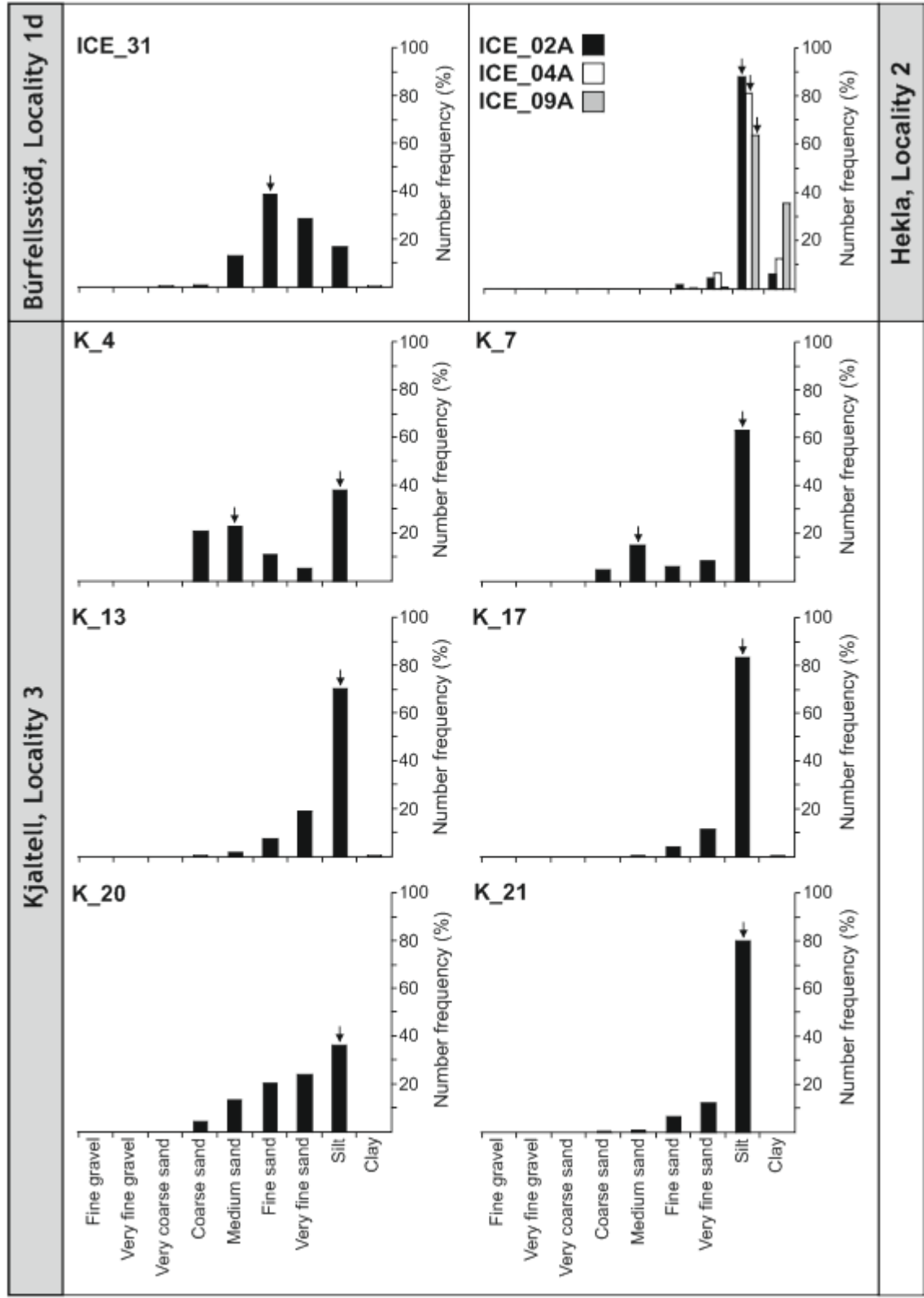


Figure 2-42 Grain-size distribution for Búrfellsstöð, Locality 1d; Hekla, Locality 2; Kjaltell, Locality 3. Sample ICE_31 from Búrfellsstöð 1d has a uni-modal grain-size distribution that ranges from clay to very coarse sand -sized grains with predominantly fine-sand -sized grains. All of the samples from Hekla, Locality 2, show the same grain-size distribution characteristics. ICE_02, ICE_04 and ICE_09 range from clay to fine sand, and are

predominantly comprised of silt-size grains. Samples from Kjaltell, Locality 3, are generally coarser-grained than those of Hekla, Locality 2. These samples have a general grain-size distribution of silt to coarse-sand. Most of these samples have a uni-modal grain-size distribution; however, K_4 and K_7 show a bi-modal distribution, with peaks for both silt-size and medium-sand sized grains.

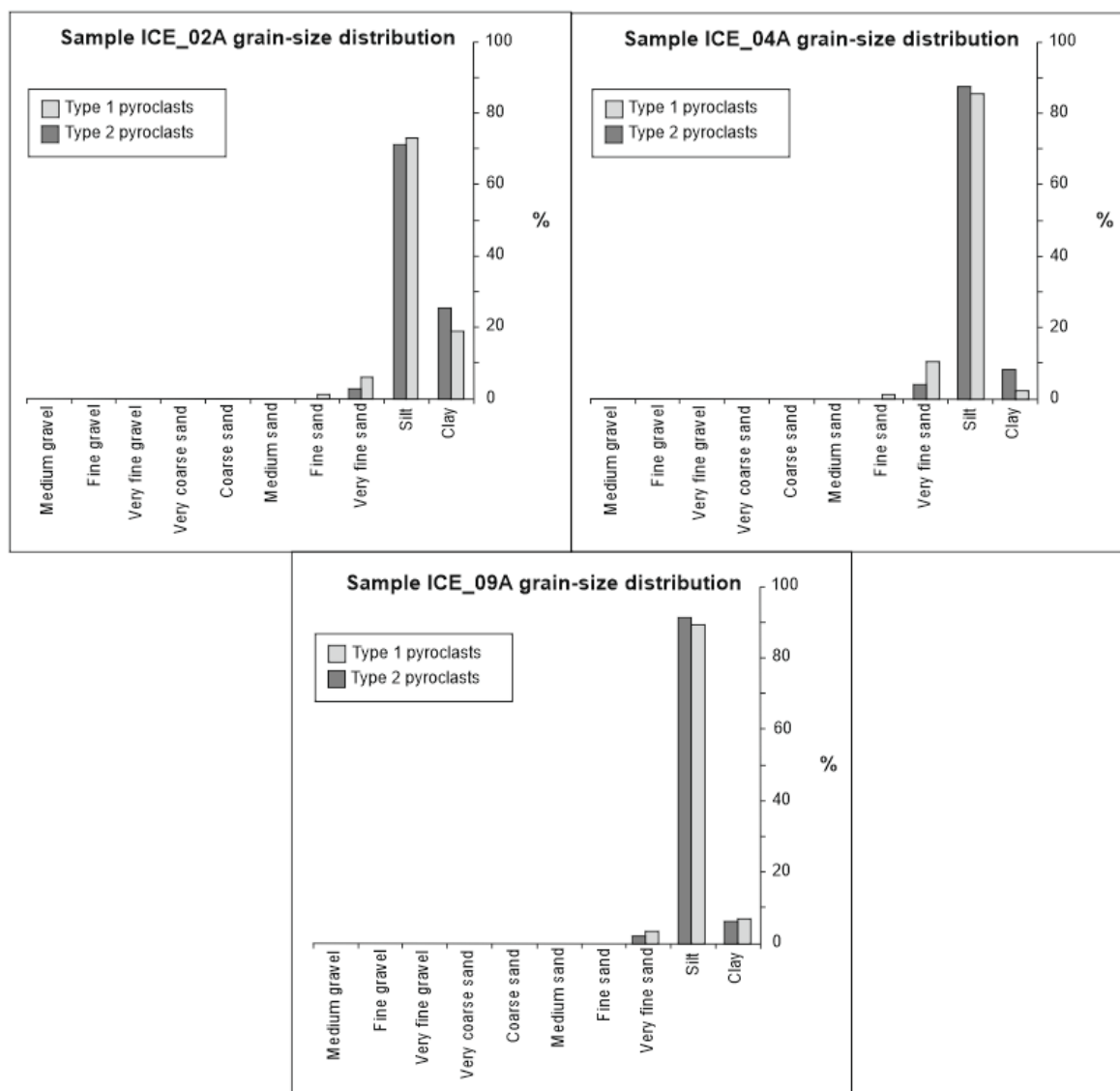


Figure 2-43 Comparison of the grain-size distribution (number frequency %) for Type 1 and Type 2 pyroclasts within ICE_02A, ICE_04A and ICE_09A. All of the grain-size distributions are similar for both pyroclast compositions with most pyroclasts being of silt-grade (125 μm).

2.5.4.2 Sample characteristics, clast-types and features

The results of the manual point count and image analysis point-count (see 1.3 Methods) of clast types for ICE_02A, ICE_04A and ICE_09A shows that Type 1 pyroclasts are the most abundant grain type in all of these samples, followed by granular lithic clasts or grains (Figure 2-44). Type 2 pyroclasts are the third most abundant grain type. Components of the ash matrix were not included in these

counts due to their fine grain-size and difficulty in determining individual shards and clasts from granular lithic clasts. In general, plagioclase crystals, lava-like clasts and aggregates are the least abundant clast-types in all of these samples (Figure 2-44).

Grain-mounts of Búrfellsstöð and Kjaltell samples do not contain any aggregate clasts. SEM analysis shows that some samples contain rare Type 2 pyroclasts; however, use of a ten-by-ten grid for manual point-counting did not intersect any of these pyroclasts, therefore, they do not appear in the graphs depicting the point-count data of grain-types in any of these samples (Figure 2-44). Irregular-shaped, vesicular, microcrystalline clasts, interpreted here as lava-like clasts, are observed in the Búrfellsstöð and Kjaltell samples, but were not counted in the Hekla, Locality 2, samples.

Results of the grain-type point-counts for all of the Búrfellsstöð samples shows that each of the samples contain similar abundances of the different clast-types; plagioclase crystals, pyroclasts, granular lithic clasts and grains, angular non-vesicular crystalline igneous clasts and irregular-shaped, vesicular, microcrystalline lava-like clasts (Figure 2-44). Pyroclasts are the most abundant grain-type in these samples, followed by crystalline igneous clasts. The abundance of lava-like and granular lithic clasts varies between the samples and plagioclase crystals are the least abundant grain-type.

The abundance of each grain-type observed in the Kjaltell samples vary considerably (Figure 2-44). These samples are also visually different to those of Búrfellsstöð, Locality 1, for example, the Kjaltell samples tend to have a greater abundance of crystalline igneous clasts and lava-like clasts. Sample K_4 has a composition of clast-types that is most similar to the Búrfellsstöð samples (Figure 2-44).

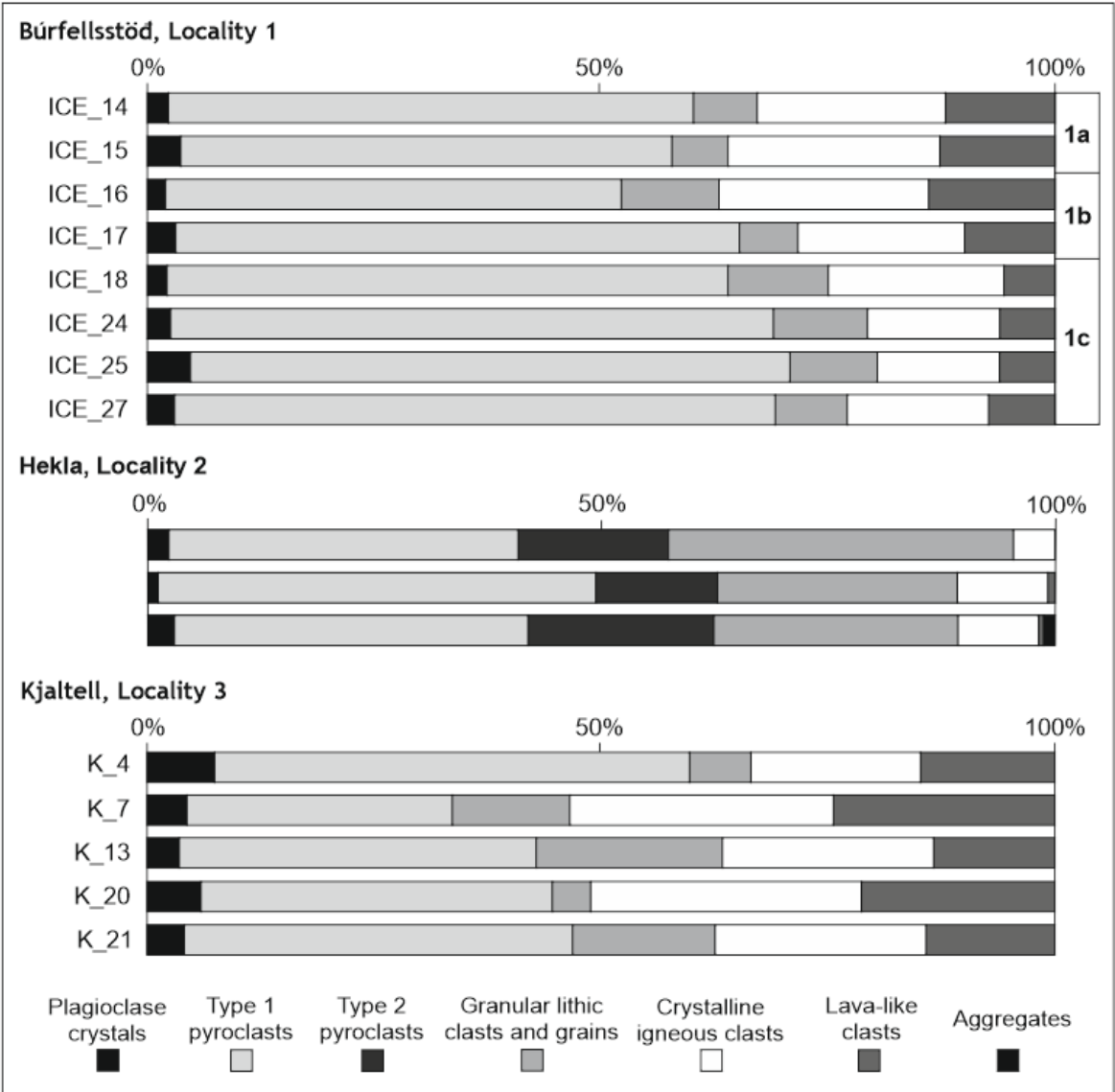


Figure 2-44 Graphs showing the percentage of each grain-type observed in all of the thin-sections and grain-mounts. These data were collected from manual point-count analysis of SEM AsB images. Only minimal lava-like clasts were observed in the Hekla, Locality 2 samples. However, these samples do contain a much greater abundance of Type 2 pyroclasts compared to their relative absence in the data for Búrfellsstöð and Kjaltell. The samples from Búrfellsstöð and Kjaltell do not contain any aggregate particles and only rare Type 2 pyroclasts which were not observed during the point-count. All of the samples are predominantly comprised of pale-grey pyroclasts. The samples from Kjaltell show the greatest differences in the percentage of each grain-type between the samples, where-as the abundances are similar throughout the samples from Búrfellsstöð. The order of the key reflects the order of the grain-types displayed in the graphs, for example, plagioclase crystals are represented by black bars on the left of the graph, Type 2 pyroclasts are represented by black bars in towards the centre of the graph and aggregates are represented by black bars on the far right.

This grain-type data can be considered in terms of pyroclasts versus non-pyroclasts, where pyroclasts include Type 1 and Type 2 pyroclasts and non-pyroclasts include all of the other grain-types; crystalline igneous clasts,

plagioclase crystals, granular lithic clasts and lava-like clasts (Table 2-3; Appendix 1).

	Sample ID	% Pyroclasts	% Non-pyroclast
Búrfellsstöð, Locality 1	ICE_13	69.47	30.53
	ICE_14	57.95	42.05
	ICE_15	54.15	45.85
	ICE_16	50.13	49.87
	ICE_17	62.01	37.99
	ICE_18	60.65	39.35
	ICE_24	62.56	37.44
	ICE_25	76.74	23.26
	ICE_27	61.76	38.24
	ICE_31	63.54	36.46
Hekla, L2	ICE_02A	54.89	45.11
	ICE_04A	61.54	38.46
	ICE_09A	60.69	39.31
Kjaltell, L3	K_4	52.35	47.65
	K_7	29.17	70.83
	K_13	37.77	62.23
	K_20	36.21	63.79
	K_21	42.75	57.25

Table 2-3 Percentage of pyroclasts and non-pyroclasts in each sample. The percentage of pyroclasts includes all Type 1 pyroclasts, Type 2 pyroclasts and aggregate clasts, all non-pyroclasts include: crystalline igneous, lava and granular clasts and plagioclase fragments. All of the Búrfellsstöð and Hekla samples contain >50% pyroclasts, whereas most of the Kjaltell samples contain <50% pyroclasts.

In general, the Búrfellsstöð and Hekla samples are comprised of more than 50% pyroclasts (Table 2-3). However, samples from Kjaltell contain 29 to 52% pyroclasts (Table 2-3); generally, fewer than samples from the other localities.

An additional way to sub-divide these data is to consider what are the juvenile and accidental, or accessory, volcanic products that may be found in these deposits (Table 2-4; Cas & Wright 1988). The juvenile and accidental clast-types are those which could have been produced and deposited directly from an eruption. Juvenile products include glassy pyroclasts and are generally the result of the direct fragmentation of erupting magma. Accidental clasts can be

considered as any other material that is caught-up in an eruption, for example, fragments of crystalline igneous rock that formed prior to the eruption and that became incorporated into the volcanic material that was subsequently erupted and deposited. In these samples juvenile versus accidental means: pyroclasts and ash aggregates versus crystalline igneous clasts and plagioclase crystals. It can be useful to consider the possible abundance of juvenile and accidental material as this can help to indicate eruption dynamics (Clarke et al. 2009; Németh & Cronin 2009; Valentine & White 2012; Graettinger et al. 2013; Valentine et al. 2014). For example, a greater number of accidental clasts are more-likely to form in hydrovolcanic eruptions, particularly if explosive magma-water interactions occur within a conduit and expel material outside of the vent (Graettinger et al. 2013). The maximum possible percentage of juvenile and accidental material has been calculated for each sample (Table 2-4); however, it is possible that the crystalline igneous material and/or plagioclase crystals were not formed during an eruption and are part of the background sediment being deposited in each environment. It is also possible that these samples are comprised of reworked pyroclasts and, therefore, these do not represent juvenile material. These aspects will be discussed further in section 2.6 Discussion. Ash aggregates are not included in the calculation of the percentage of juvenile versus accidental lithics as they may be formed from accumulations of fine grains of juvenile *and* accidental lithics.

The maximum percentage of juvenile material in samples from Búrfellsstöð and Hekla is >70% (Table 2-4). In contrast to this, samples from Kjaltell give a maximum percentage of juvenile material < 70% (Table 2-4).

	Sample ID	% Juvenile	% Accidental
Búrfellsstöð, Locality 1	ICE_14	71.70	28.30
	ICE_15	66.67	33.33
	ICE_16	66.78	33.22
	ICE_17	74.25	25.75
	ICE_18	74.87	25.13
	ICE_24	81.14	18.86
	ICE_25	81.61	18.39
	ICE_27	78.52	21.48
Hekla, L2	ICE_02A	88.78	11.22
	ICE_04A	84.58	15.42
	ICE_09A	83.41	16.59
Kjaltell, L3	K_4	66.40	33.60
	K_7	46.67	53.33
	K_13	61.78	38.22
	K_20	56.22	43.78
	K_21	61.08	38.92

Table 2-4 Maximum percentage of juvenile and accidental volcanic material in each sample. Calculation of the percentage of juvenile material includes the abundance of pyroclasts and aggregates, whereas the percentage of accidental material includes crystalline igneous clasts and plagioclase crystals. These results give the maximum percentages of juvenile and accidental volcanic material in each sample, as some of the included pyroclasts, crystalline igneous clasts or plagioclase crystals may have been reworked and should therefore be considered to be grains of sediment, which are not included in the percentage of juvenile to accidental material in a volcanic deposit. The Búrfellsstöð and Hekla samples contain >70% juvenile material; however, in contrast to this, the Kjaltell samples contain <70% juvenile material.

2.5.4.3 Pyroclast characteristics

The pyroclasts in all samples display a variety of morphologies, from blocky to bubble-wall and rod-like, and are either vesicular or non-vesicular. These morphologies can indicate the eruption dynamics and the nature of the source magma during initial magmatic or hydrovolcanic fragmentation (Carey & Sparks 1986; Cas & Wright 1988; Barberi et al. 1989; Cioni et al. 1992; Blower et al. 2001; Riley et al. 2003; Gaonac'h et al. 2005; Houghton & Gonnermann 2008; Polacci et al. 2008; Clarke et al. 2009; Mattsson 2010; Shea et al. 2010; Bonadonna et al. 2011; Ross & White 2012; Graettinger et al. 2013; Moitra et al. 2013; Cioni et al. 2014; Heap et al. 2014). Point-count analysis was carried out manually from SEM images, using a 10 by 10 grid, to gain information on the

abundance of different pyroclast morphologies (Figure 2-45). In addition, ImageJ software was used to calculate the percentage vesicularity of vesicular pyroclasts; these data were then analysed in Microsoft Excel to produce an average value for the percentage vesicularity of vesicular pyroclasts in each sample (Table 2-5).

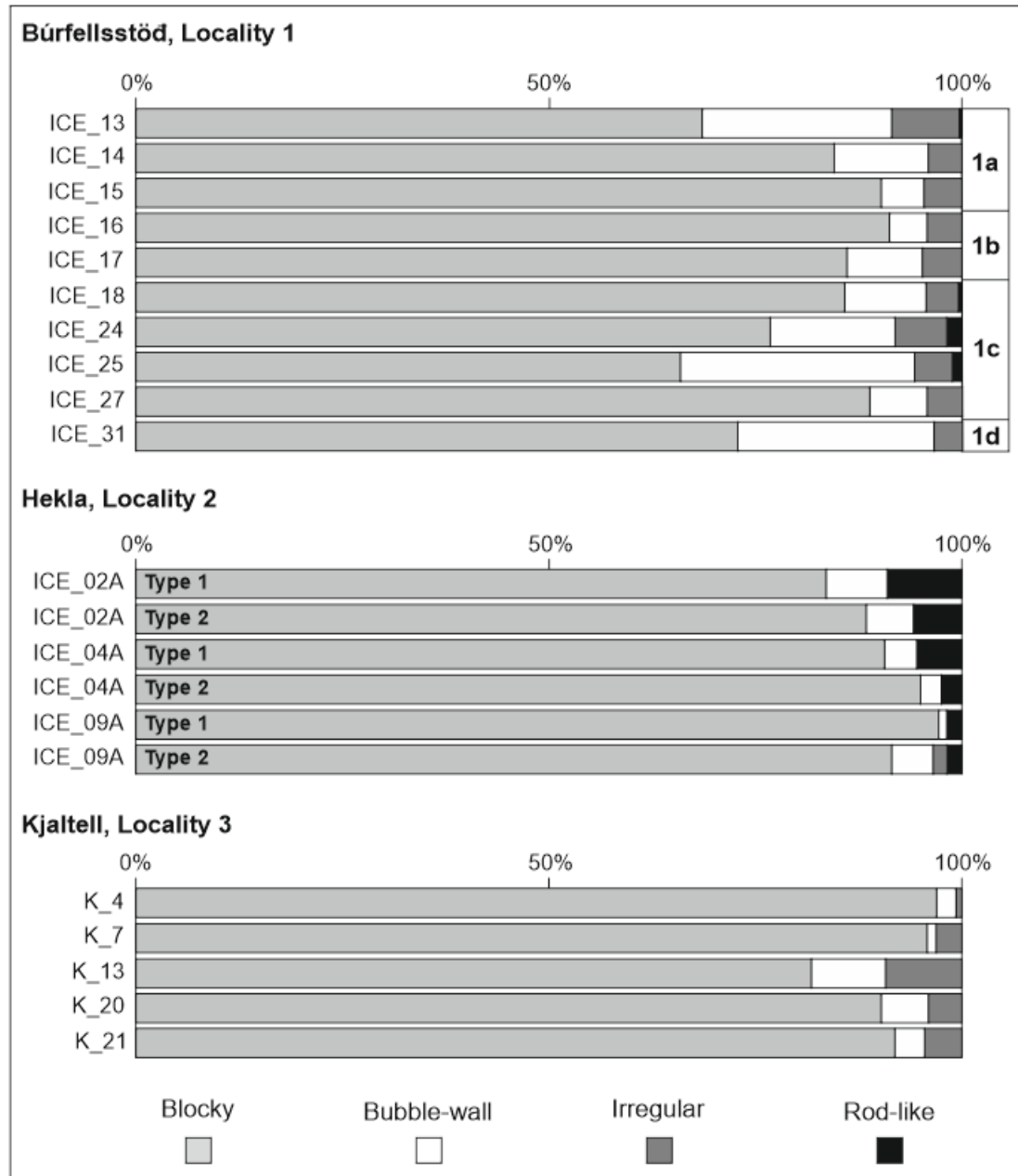


Figure 2-45 Abundance of blocky, bubble-wall, irregular and rod-like pyroclast morphologies in each sample. All of the samples are dominated by blocky pyroclasts. The pyroclast morphologies for Type 1 and Type 2 pyroclasts in samples from Hekla, Locality 2, are shown separately. In general, the Type 1 and Type 2 pyroclasts for each sample give very similar abundances of the different pyroclast morphologies, with the Type 2 fraction generally containing a higher percentage of blocky pyroclasts. However, this trend is absent in ICE_09A, where the Type 2 pyroclasts contain irregular morphologies and less blocky pyroclasts compared to the pale grey pyroclasts. Rod-like pyroclasts are only observed in

samples from Búrfellsstöð 1c and Hekla. Irregular morphologies are generally absent in samples from Hekla.

The results of this point-count analysis show that all of the samples are dominated by blocky shards, and that this character can be observed in both the Type 1 and Type 2 pyroclasts of ICE_02A, ICE_04A and ICE_09A (Figure 2-45). Bubble-wall shards are present within all of the samples, with the highest abundance being present in samples from Búrfellsstöð, particularly sample ICE_25. Rod-like pyroclasts are absent in half of the samples, but, are most abundant in samples from Hekla, Locality 2, where they can be found within the Type 1 and Type 2 compositional sub-divisions. Irregular-shaped pyroclasts have a more fluidal shape and are almost absent in all samples from Hekla, Locality 2, regardless of the chemical composition of the pyroclasts.

Type 1 and Type 2 pyroclasts show varying amounts of vesiculation, between samples, and also between localities (Table 2-5). The average vesicularity for all samples and both Type 1 and Type 2 pyroclasts from Búrfellsstöð and Hekla is less than 25% (Table 2-5). Three of the Kjaltell samples have a vesicularity that is greater than 25%, although, two have a vesicularity that is less than 20% (Table 2-5).

In general, the Kjaltell samples have a coarser grain-size compared to samples from the other localities (Figure 2-42). At finer grain-sizes the vesicular nature of pyroclasts at both Búrfellsstöð and Hekla may have been lost, either due to initial fragmentation of the magma during eruption or later due to reworking. Efficient fragmentation during eruption, and reworking, would both allow thin bubble-walls to fracture, and produce smaller grains. Pyroclasts with a high vesicularity are likely to be the most fragile grains during transport, leading to an increased concentration of non-vesicular or poorly vesicular pyroclasts in the resulting deposit. This can be seen when the abundance of vesicular and non-vesicular pyroclasts are compared for each sample (Table 2-6).

	Sample ID		Average %vesicularity	Range (%)
Búrfellsstöð, Locality 1	1a	ICE_13	19	2 - 42
		ICE_14	16	1 - 42
		ICE_15	13	2 - 26
	1b	ICE_16	25	4 - 36
		ICE_17	14	2 - 31
	1c	ICE_18	10	1 - 20
		ICE_24	16	4 - 38
		ICE_25	21	2 - 54
		ICE_27	9	<1 - 28
	1d	ICE_31	19	4 - 40
Hekla, L2	ICE_02A Type 1		20 (?)	More data needed
	ICE_02A Type 2		16	4 - 31
	ICE_04A Type 1		20	4 - 39
	ICE_04A Type 2		19	7 - 31
	ICE_09A Type 1		12	3 - 19
	ICE_09A Type 2		21	5 - 34
Kjaltell, L3	K_4		27	7 - 51
	K_7		32	8 - 56
	K_13		18	2 - 39
	K_20		24	4 - 37
	K_21		11	3 - 19

Table 2-5 Results of percentage vesicularity calculations for vesicular pyroclasts of all samples. In general, the vesicular pyroclasts from Búrfellsstöð have a percentage vesicularity (%vesicularity) of <25%. In general, these samples have a vesicularity within the range of <1 to 54%. Both the Type 1 and Type 2 pyroclasts of Hekla, Locality 2, samples are similar and all lie within the range of 3 to 39%. More data is required for ICE_02A Type 1 pyroclasts to give a reliable calculation; very few of these vesicular pyroclasts were observed in this sample. Samples from Kjaltell, Locality 3, generally have a higher percentage vesicularity compared to the other localities. However, their range shows a similar trend to that of all of the samples, with a range of 2 to 56%. K_4, K_7 and K_20 have a vesicularity of >20%, although, K_13 and K_21 have an average vesicularity <20%.

Samples from Hekla, Locality 2, contain the least amount of vesicular pyroclasts, <10% (Table 2-6), and generally have a low average vesicularity, < 21% (Table 2-5). In contrast to this, samples from Kjaltell have the greatest abundance of vesicular pyroclasts, some >50% (Table 2-6) and also have the highest average vesicularity, some >20% (Table 2-5). However, all samples have an average vesicularity of <40%, which shows that they are all poorly vesicular (Houghton et al. 2004; Ross & White 2012; Graettinger et al. 2013). The range given for the vesicularity of individual pyroclasts shows that some have a vesicularity of >40%;

these pyroclasts are considered to have a higher vesicularity and may also include fragments of pumice (Houghton et al. 2004; Graettinger et al. 2013).

	Sample ID	% of vesicular pyroclasts
Búrfellsstöð, Locality 1	1a	ICE_13
		ICE_14
		ICE_15
	1b	ICE_16
		ICE_17
	1c	ICE_18
		ICE_24
		ICE_25
		ICE_27
	1d	ICE_31
Hekla, L2	ICE_02A Type 1	
	ICE_02A Type 2	
	ICE_04A Type 1	
	ICE_04A Type 2	
	ICE_09A Type 1	
	ICE_09A Type 2	
Kjaltell, L3	K_4	
	K_7	
	K_13	
	K_20	
	K_21	

Table 2-6 Percentage of vesicular pyroclasts present in each sample. Samples that contain less than 10% vesicular pyroclasts are highlighted in red, those with more than 50% vesicular grains are highlighted in blue. From this it is clear that the Hekla samples contain the lowest occurrence of vesicular pyroclasts and samples from Kjaltell generally contain the greatest abundance of vesicular pyroclasts.

Finally, image analysis was also used to assess the orientation of grains from an orientated thin-section to determine if grains within ICE_09A have been affected by a significant current, or simply by deposition within a (low energy) lacustrine environment (Figure 2-46). Elongated grains, with a circularity between 0.0 - 0.5, were separated using ImageJ software and their orientations relative to the horizontal plane of the orientated sample were calculated. The results show that the majority of elongated grains lie relatively horizontal within the deposit. This result was also replicated throughout the data for ICE_02A and ICE_04A, for elongate grains with a circularity of 0.0 - 0.5.

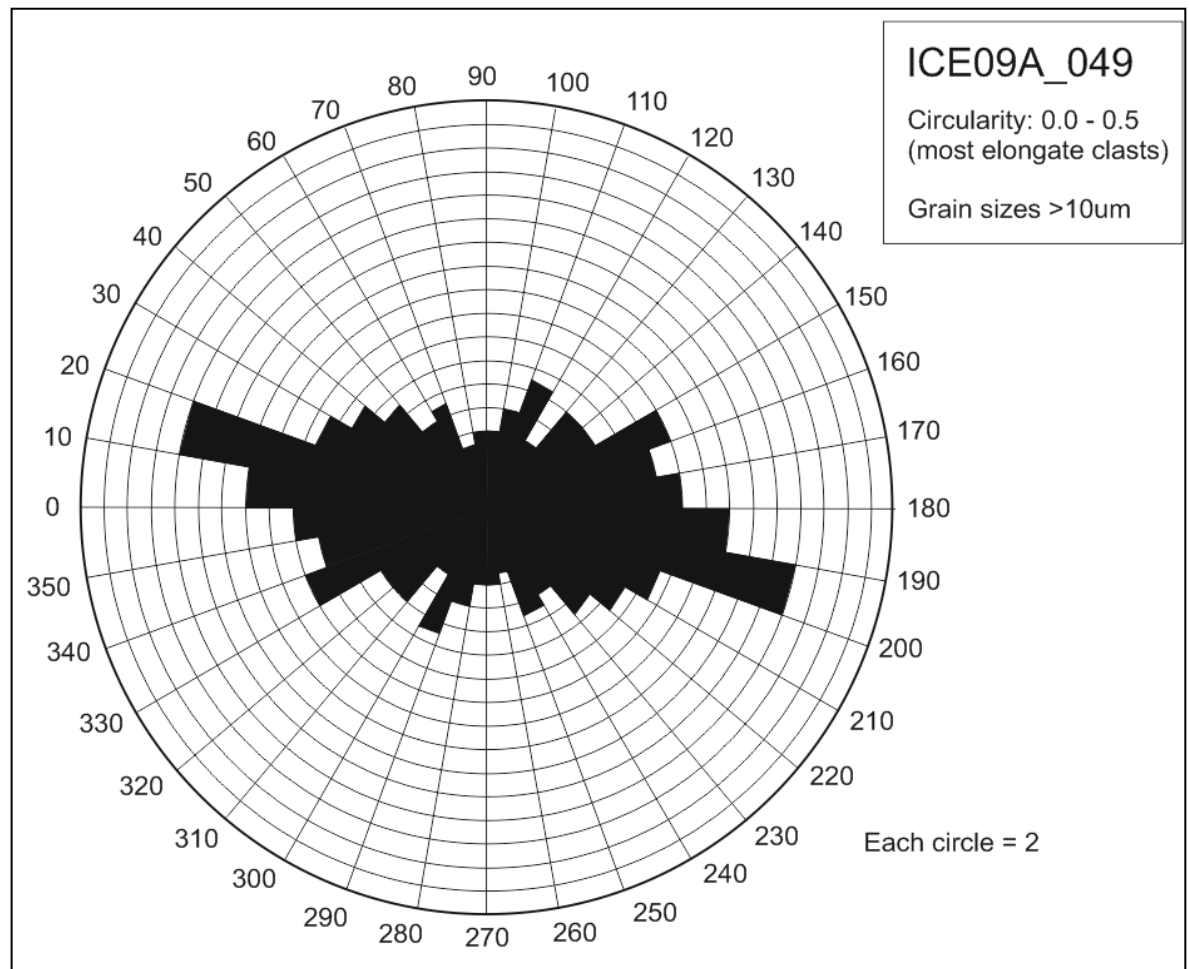


Figure 2-46 Example of the orientation data for elongate grains (circularity 0.0 - 0.5), as calculated by image analysis of an AsB SEM image for a layer within sample ICE09A. This data was produced from an orientated thin-section where the way-up was recorded in the field and on the section; this result shows that there is a preferred orientation of the grains in an almost horizontal plane.

2.6 Discussion

2.6.1 Deposit characteristics and environments of deposition

All of the deposits described have undergone very little burial and compaction. Where burial has occurred, for example at Hekla, Locality 2, and Kjaltell, Locality 3 (Figure 2-1), this has been very shallow, a few metres to tens of metres only. Burial has occurred due to the emplacement of further sediments (at Hekla), or lavas (at Kjaltell). The main diagenetic process has been grain compaction. No post-depositional lithification has occurred. Because of this, the coarser-grained sedimentary units of sand and gravel maintain a high porosity and permeability and are typically held together by grain-compaction.

The SA has been identified at each of the localities based on the observation of deposits that are predominantly composed of black/brown vitreous pyroclasts with minor amounts of rust-orange crystalline igneous clasts and fragments of plagioclase. However, the nature of the deposits in each locality differs due to the environmental conditions in which deposition took place. Reworking of primary volcanic material has also affected features of the clasts, for example, rounding of their edges, as well as the depositional features of the deposits, for example, reworking may have introduced cross-stratification upon re-deposition from a current.

All of the samples contain a varying amount of crystalline igneous clasts (Figure 2-44). These clasts generally contain hornblende (amphibole), pyroxene and plagioclase in various amounts typical of basalt. The crystalline clasts are therefore clasts of basalt, as they are too finely-crystalline to be gabbro, and may have come from within the vent or conduit of GV during eruption of the SA, and may be accidental clasts deposited as part of the 'primary' pyroclastic tephra. Many of the pyroclasts contain microphenocrysts of plagioclase, plagioclase is also present as crystal fragments within the deposits (Table 2-4). Therefore, it is highly likely that the plagioclase crystals in the deposit are also accidental clast-types and were also produced as a primary product in the eruption of the SA (Table 2-4).

A fluvial environment of deposition is interpreted for the deposits of Búrfellsstöð and Kjaltell based on field-observations of asymmetrical climbing ripples and cross-stratification. Hekla, Locality 2, can be interpreted as a lacustrine environment with deposition occasionally influenced by currents. This interpretation is based on the presence of sub-horizontal laminations and bedding planes along with repeated sequences of normal-graded cm-scale varves (e.g. Collinson 1978; Prothero 1990; Glenn & Kelts 1991; Collinson et al. 2006). Asymmetrical ripple structures suggest that deposition was occasionally influenced by unidirectional currents (e.g. Collinson 1978; Baas 1994; Mazumder 2000; Collinson et al. 2006; Miall 2014; Perillo et al. 2014; Bartholdy et al. 2015). At this locality, micro-faults and soft-sediment deformation suggest that the sediments were water-saturated (e.g. Collinson et al. 2006). The presence of post-depositional deformation, possibly caused by seismic activity, in the form

of soft-sediment deformation at Búrfellsstöð 1c and Hekla, and the presence of a sediment volcano at Búrfellsstöð 1c, may have been caused by liquefaction, suggesting that the deposits originally contained a high fluid content (e.g. Scott & Price 1988; Popescu 2002; Chen & Lee 2011).

Fluctuations in the concentration of sand- and gravel-sized grains predominantly composed of vitreous basaltic pyroclasts throughout the deposits may reflect seasonal changes in the catchment area of the sub-aqueous depositional systems. For example, spring and summer thaw of ice and snow on land would transport and deposit a greater abundance of coarser sediments into both fluvial and lacustrine environments (Collinson 1978; Prothero 1990; Glenn & Kelts 1991; Collinson et al. 2006). Alternatively, an increase in coarser-grained basaltic material could represent a greater availability of these clasts in the environment, for example, following an eruption (e.g. Riggs et al. 2001).

In this section, the characteristics of each deposit will be discussed, followed by comments regarding the pyroclastic components and what these indicate about the eruption dynamics which led to their formation. The characteristics of pyroclasts deposited as primary fall-out pyroclastic deposits and reworked volcanoclastic detritus will then be discussed.

2.6.1.1 Búrfellsstöð, Locality 1a-d

The stratigraphy of each locality at Búrfellsstöð, (Figure 2-1, Figure 2-5) represents part of a dynamic fluvial system, as shown by the presence of asymmetrical climbing ripples and small-scale to large-scale truncated cross-stratification, and the occurrence of gravel beds and pebbles (Collinson 1978; Prothero 1990; Collinson et al. 2006).

Clay drapes within dominantly fine- or medium-sand grade deposits and clay preservation of foreset laminations within ripples (e.g. Figure 2-7, Figure 2-11, Figure 2-19) may be associated with variations in the energy of currents within the fluvial system (Collinson 1978; Baas 1994; Mazumder 2000; Collinson et al. 2006; Miall 2014; Perillo et al. 2014; Bartholdy et al. 2015). Sand would be deposited during and shortly after high-energy periods, perhaps when the flow of water was greater during spring/summer, when ice and glaciers melt, or during

floods, whereas clay would be deposited during low energy conditions, perhaps in the winter when the flow of water was reduced, or in-between flooding events (e.g. Collinson 1978; Baas 1994; Mazumder 2000; Collinson et al. 2006). These features can be viewed in real-time at the Markfljót River in Iceland (Figure 2-47).

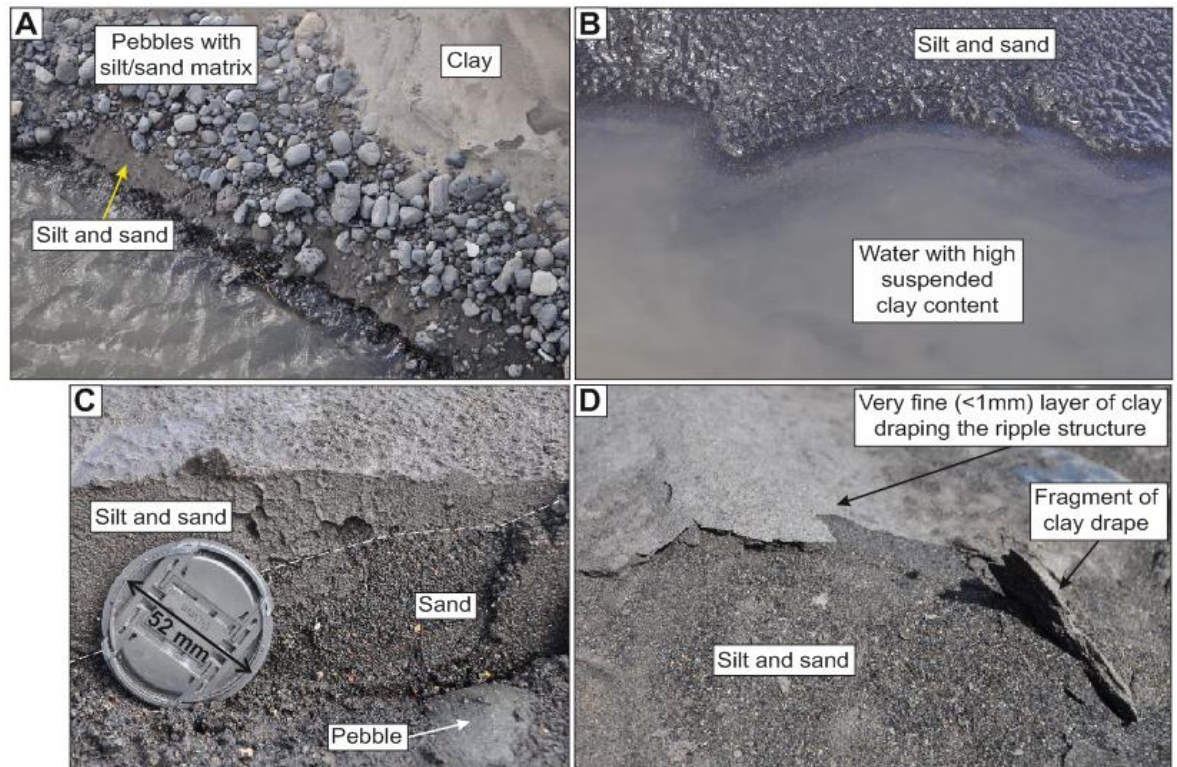


Figure 2-47 Modern analogue for the formation and identification of clay drapes and fluvial deposits in Iceland, from the Markfljót River used as a comparison for features of the Búrfellstóð localities. An example of the wide range of grain-sizes that can occur within a short distance (ca. 1m), including silt and sands to pebbles with a silt/sand matrix, overlain by clay. B) Clay may be deposited directly on-top of silts and sands from stream water that has a high suspended clay content. C) Small-scale cross section through fluvial deposits showing the range of grain-sizes experienced within <10 cm, from pebbles with a sand matrix to silt and sand. D) Very fine (<1 mm) layer of clay drapes a ripple structure comprised of silt and sand; silts and sands deposited above this will lead to clay draped ripples, like those identified in the deposits at Búrfellstóð (Figure 2-7, Figure 2-11).

Subcritical, critical and supercritical climbing ripples can all be identified within the deposits at Búrfellstóð 1a (Figure 2-7), b (Figure 2-8) and c (Figure 2-11). The presence of these different ripple types shows that there were variations in the flow regime of the fluvial system and/or changes in the sediment load available for deposition over time (e.g. Collinson 1978; Baas 1994; Mazumder 2000; Brookfield 2006; Collinson et al. 2006; Perillo et al. 2014; Bartholdy et al. 2015). Supercritical climbing ripples that can be traced without any changes to

the thickness of their laminations are found in some of the finer-grained sediments, mostly within clays. These suggest that the sediment was able to accumulate on both the lee- and stoss-slopes of the ripple at the same rate (Collinson 1978; Collinson et al. 2006), indicating that there was little influence from the flow of water at these locations during the formation of this feature. These ripple forms may have formed in the shallowest parts of the river channel, where the finest grains are deposited. In contrast, the presence of subcritical climbing ripples with truncated upper and lower surfaces are more indicative of more rapid water-flow (e.g. Collinson 1978; Collinson et al. 2006; Bartholdy et al. 2015). These might have formed during periods of flood or deepening of the river channel as it migrated over this area.

Large-scale dune cross-stratification is found at the top of the exposure at Locality 1d, (Figure 2-5). This suggests that this locality lay within the main river channel during deposition of these cross-stratified sands and gravels, and there was little or no deposition of fine-grained sediment at this time. A correlation of the upper unit of this sequence has been made, with a corresponding sand at the base of the section observed at Búrfellstóð 1b (Figure 2-5), to the east. If the sequence at Locality 1d does lie below that exposed at Locality 1b then it is possible that this whole sequence represents a fining upwards succession and a shallowing of the fluvial environment, eventually leading to the formation of a thin palaeosol (*ca.* 13 cm), composed of clay and peat. Above this palaeosol is more sand and gravel, suggesting that there was a flood event or a slight change in the position of the channel, allowing sediment to be deposited without the influence of vegetation. Above this, the environment of deposition becomes shallower again and the development of a thicker palaeosol composed of clay and peat developed.

At Búrfellstóð 1c, the presence of a preserved sediment volcano and deformation of the boundaries between interbeds of the adjacent clay and silt, in the form of liquefaction (Figure 2-9), suggest that a significant seismic event affected the sedimentary sequence after deposition. Scott & Price (1988) proposed a list of criteria that should be satisfied before seismic deformation of soft sediments should be considered; these criteria are satisfied at Búrfellstóð by: 1) the deformed sequence is located within a seismically active region, 2)

deformation is limited to a particular interval, with undeformed material above and below, 3) the original sediment was relatively flat-lying, so that deformation is not due to slope failure, 4) the original sediments had the potential to become liquefied, for example by being deposited in a fluvial or lacustrine environment.

The deformation of the interbedded silts and clays surrounding the sediment volcano, in addition to the expulsion of fine-grained sediment to form the sediment volcano, suggests that the sediments contained a high amount of water when the earthquake occurred (e.g. Popescu 2002; Chen & Lee 2011). These features also suggest that the sediments were relatively close to the surface (e.g. Scott & Price 1988). At the time of seismic deformation, the sediment had undergone little compaction, and had a higher porosity than is observed in the deposits today. This high porosity likely enabled grains to move about during the earthquake, allowing the beds to deform in a fluidal fashion, leading to changes in the bed boundaries and obscuring the original depositional characteristics of the deposits. This liquefaction induced soft-sediment deformation may correspond to the soft-sediment deformation observed in the lower part of the sequence exposed at Hekla, Locality 2 (Figure 2-15).

It has been suggested by several authors (e.g. Morgnester 1967; Kuribayashi & Tatsuoka 1975; Youd 1977; Scott & Price 1988) that liquefaction of shallow sub-surface sediments will only occur during earthquakes with a Richter magnitude of 5 and above, at a particular distance from the epicentre. For example, it has been predicted that liquefaction can occur during an earthquake with a Richter magnitude of 6 up to 4 km from the epicentre (Seed & Lee 1966; Scott & Price 1988). The duration of the seismic event has also been identified as an important factor in causing liquefaction, for example, shaking of more than 8 seconds (Seed & Lee 1966; Scott & Price 1988). Liquefaction and soft sediment deformation caused by ground movements can also be caused by volcanic explosion due to the shock waves that are produced (Scott & Price 1988). However, the extent of the deformation observed at Búrfellsstöð 1c and Hekla, Locality 2, and the presence of a sediment volcano, suggest that this was seismically induced deformation, caused by a nearby earthquake with a Richter magnitude of 5, or more.

2.6.1.2 Hekla, Locality 2: 64°46'9.00"N 19°29'39.10"W

The deposits exposed at Hekla, Locality 2, are representative of deposition in a lacustrine environment. The presence of mm-scale, normal-graded varves at intervals throughout the section (e.g. Figure 2-14), suggests that the body of water was present for a substantial amount of time, with little influence from volcanic activity during their formation. Thicker units of coarser-grained sediments commonly interrupt the sequence of varves and therefore indicate significant events that disturbed the low-energy depositional environment of the lake. The deposit is found on the lower slopes of the volcano, Hekla, therefore showing that during deposition of the varved sediments there was neither explosive activity at Hekla, nor from any neighbouring volcanoes, including GV.

In intervals where sand lies on top of varved silts and clays, the boundary displays loading structures such as flame and ball-and-pillow structures (Figure 2-16). The coarser-grained sediments above these boundaries therefore most likely represent events in which the coarser-grained material was rapidly introduced into the lake. These coarser-grained sediments are often overlain by a continuation of the varved, fine-grained sediment, and therefore likely represent a depositional event that disrupted this seasonal pattern of sedimentation (e.g. Collinson 1978; Prothero 1990; Glenn & Kelts 1991; Collinson et al. 2006). These coarser-grained beds could represent the sudden influx of volcanic material from an eruption, or an influx of grains following the reworking of erupted material that was originally deposited on the land surrounding the lake. Sequences like this occur in at least seven intervals throughout this exposure, possibly indicating that a minimum of seven eruption events influenced deposition in this region. The sands are all composed of basaltic pyroclasts with minor plagioclase fragments and crystalline igneous lithics, suggesting that these seven eruption events may represent at least this many eruptive episodes of GV, contributing to the formation and deposition of the SA.

Coarse-grains of crystalline igneous lithics, or vitreous pyroclasts surrounded by finer-grained sediment, with corresponding deformation of the bed boundaries below these (Figure 2-22c, d), may represent localised deposition of coarser-grains from ice (Figure 2-48; e.g. Collinson 1978; Bennett et al. 1996; Hass 2002;

Doublet & Garcia 2004; Bailey et al. 2013; Jonkers et al. 2015; St John et al. 2015). An alternative interpretation of these coarse-grains is that they could have been deposited as tephra fall-out during an eruption (e.g. Collinson 1978; Bennett et al. 1996). However, the rounding of some of these larger-grains and their isolation from any other coarse-grained material (Figure 2-22c, d) suggests that they may have been deposited from ice and were subsequently deposited into the lake (e.g. Hass 2002; Doublet & Garcia 2004; Bailey et al. 2013; Jonkers et al. 2015; St John et al. 2015).

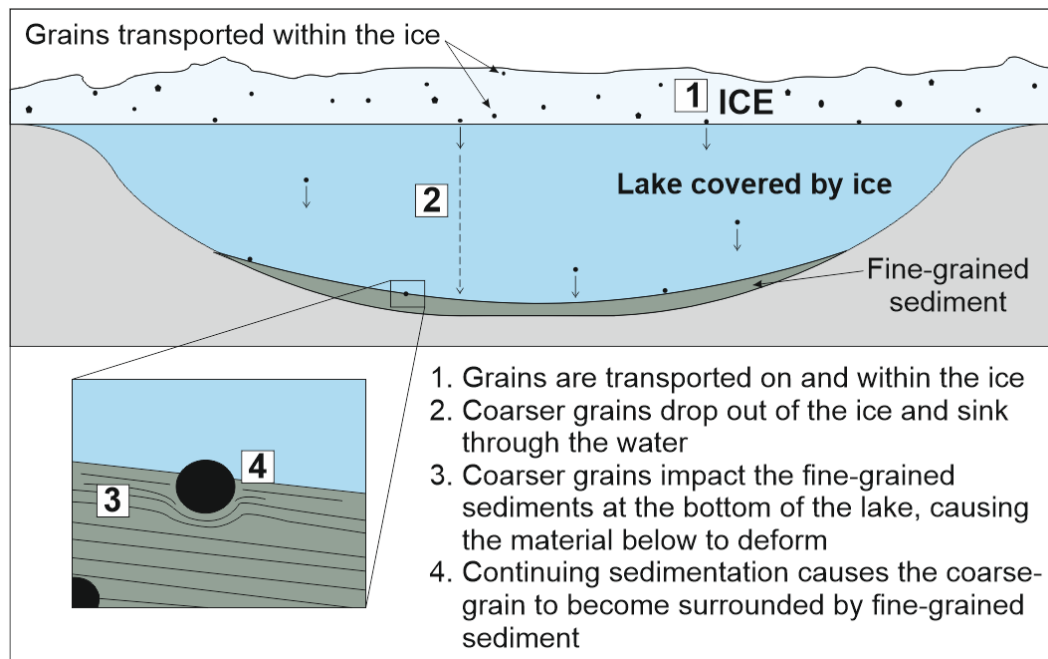


Figure 2-48 Diagram showing how coarse-grains can be transported by ice and deposited through an underlying water body to be deposited with fine-grained sediments.

Image analysis shows that in the sampled thin beds (ICE_02A, ICE_04A, ICE_09A), there is a preferred orientation of their elongate grains (Figure 2-46). This orientation is generally horizontal, suggesting that the grains were deposited in a low-energy sub-aqueous environment which was not influenced by any dominant currents. This observation could be expected of grains within the finer-grained units that were sampled, which are more likely to be deposited from suspension under very calm conditions (Collinson 1978; Baas 1994; Mazumder 2000; Collinson et al. 2006). The accumulation of thick sequences of fine-grained sediments that were likely deposited from suspension can be expected in lakes (Collinson 1978; Prothero 1990).

The deformed beds at the base of the exposed sequence at Hekla, may represent post-depositional soft-sediment deformation and liquifaction in response to a significant seismic event (greater than Richter magnitude 5; Morgnestern 1967; Kuribayahi & Tatsuoka 1975; Youd 1977; Scott & Price 1988). This may correspond to the seismically deformed beds and sediment volcano identified at Búrfellsstöð Locality 1c (64°5'58.02"N 19°49'0.57"W). The deformed sedimentary/volcaniclastic units at both of these localities might therefore act as a correlative sequence or marker unit linking the relative timing of sediment deposition and deposition of the SA in both of these areas. An alternative interpretation could be that the deformed units were formed in response to slumping of deposits within the lake related to earthquake (Elliott & Williams 1988; Perucca et al. 2014; Deev et al. 2015; Kale et al. 2016), or non-earthquake (Elliott & Williams 1988; Pisarska-Jamroży & Weckwerth 2012; Kale et al. 2016; Yang & van Loon 2016), related gravity driven processes. However, the entire sequence observed at Hekla is sub-horizontal and the deformed sequence can be traced laterally across the exposure, suggesting that something on a larger-scale than slumping in a relatively small lake was responsible for the deformation.

2.6.1.3 Kjaltekk, Locality 3: 64°21'19.96"N 19°44'30.56"W

The deposits of the SA described from Kjaltekk, Locality 3 (Figure 2-1), are similar to those of Búrfellsstöð, Locality 1a-c, having been deposited in a fluvial environment (see section 2.6.1.1). However, the sedimentary sequence at Kjaltekk, contains more sub-horizontal bedding, with less evidence of ripples and cross-stratification (Figure 2-20). This indicates that the fluvial system here behaved differently to that at Búrfellsstöð, and was, perhaps, more stable (Prothero 1990; Glenn & Kelts 1991; Collinson et al. 2006). Generally, the deposit appears to coarsen upwards, suggesting that the main channel of the fluvial system gradually migrated over to this locality, or that the river level fluctuated over time to allow deposition of only coarse-grained, more structureless units of sediment (Collinson 1978; Prothero 1990; Glenn & Kelts 1991; Collinson et al. 2006).

2.6.2 Eruption dynamics

Several features of the pyroclasts within the samples from each locality can be used to interpret the eruption dynamics which led to their formation. These features are discussed and interpreted below.

2.6.2.1 *Pyroclast morphology*

The morphology of pyroclasts can indicate the fragmentation mechanisms dominant during eruption of the magma at the GV source (e.g. Carey & Sparks 1986; Cas & Wright 1988; Barberi et al. 1989; Cioni et al. 1992; Blower et al. 2001; Riley et al. 2003; Gaonac'h et al. 2005; Houghton & Gonnermann 2008; Polacci et al. 2008; Clarke et al. 2009; Mattsson 2010; Shea et al. 2010; Bonadonna et al. 2011; Ross & White 2012; Graettinger et al. 2013; Moitra et al. 2013; Cioni et al. 2014; Heap et al. 2014). These can also indicate the type of eruption that occurred during the formation of the pyroclasts, and whether this was 'dry' magmatic or involved hydrovolcanic processes (e.g. Heiken 1972, 1974; Wohletz 1983; Wohletz & Sheridan 1983; Cas & Wright 1988; Rose & Durant 2009; Brown et al. 2012; Graettinger et al. 2013).

In general, all of the samples are dominated by non-vesicular blocky pyroclasts that are formed by brittle deformation of a magma and are a common pyroclast type identified in deposits from hydrovolcanic eruptions (Table 2-7; Heiken 1972, 1974; Wohletz 1983; Wohletz & Sheridan 1983; Cas & Wright 1988; Zimanowski et al. 1997; Mattsson 2010; Dellino et al. 2012; Ross & White 2012; Graettinger et al. 2013). The presence of highly vesicular pumice within some samples (Figure 2-25a, Figure 2-37b) is more indicative of fragmentation of a gas-rich magma formed during a 'dry' magmatic eruption and magmatic fragmentation (Cas & Wright 1988; Houghton et al. 2004; Mattsson 2010). Calculation of the percentage vesicularity of vesicular pyroclasts for each sample (Table 2-5), give values that are generally <40%, indicating that the pyroclasts are poorly vesicular (Houghton et al. 2004; Clarke et al. 2009; Mattsson 2010; Dellino et al. 2012; Ross & White 2012; Graettinger et al. 2013; Heap et al. 2014). A few pyroclasts have a vesicularity > 40%, reaching up to 56% (Table 2-5); these pyroclasts can be considered as moderately vesicular (Houghton & Wilson 1989; Ross & White 2012), but are not considered to be pumice, which

have the highest vesicle percentages (Cas & Wright 1988; Graettinger et al. 2013). For example, a reticulate can have a vesicularity of up to 98% (Heap & Chen 2014).

The presence of pyroclasts with an irregular/fluidal morphology (Figure 2-44) could suggest that quenching of the erupted magma did not occur instantaneously, and that the magma had time to deform during the eruption, before solidifying (Table 2-7; e.g. Ross & White 2012). These pyroclasts may indicate that hydrovolcanic processes were not operating throughout all of the eruptive phases that created the SA. The presence of water in hydrovolcanic eruptions would likely lead to more rapid quenching and therefore a lack of irregular/fluidal shaped pyroclast morphologies.

Bubble-wall pyroclasts are often more indicative of 'dry' magmatic eruptions, that are driven by the expansion of bubbles within the magma (Table 2-7; Wohletz 1983; Cas & Wright 1988; Hanson & Elliot 1996; Houghton et al. 2004; Mattsson 2010; Graettinger et al. 2013). However, it is possible to identify bubble-wall pyroclasts with sharp, horizontal edges that are unlikely to represent bubble-walls (Table 2-7). These edges are more likely to have formed by brittle fragmentation, either during the eruption or during transport and deposition. If brittle fragmentation of these pyroclasts occurred within an erupting vent then this may be an indicator of hydrovolcanic processes occurring simultaneously alongside a magmatic gas-expansion and magma fragmentation. Rapid quenching of the magma by interaction with water could cause magmatically formed bubble-wall pyroclasts to experience brittle fragmentation in this way. However, collisions of pyroclasts within an eruption cloud could also lead to brittle fragmentation of the delicate edges of bubble-walls during a 'dry' magmatic eruption. Impact of the pyroclasts with the Earth's surface may also lead to the edges of bubble-wall pyroclasts being broken off (e.g. Cas & Wright 1988). The second type of bubble-wall pyroclast shows no evidence of brittle fragmentation, with all of the bubble-walls remaining intact and edges tapering off into sharp points. These may be evidence of 'dry' magmatic fragmentation, where the expansion of bubbles within the magma has caused the magma to fragment without magma-water interactions (Table 2-8).


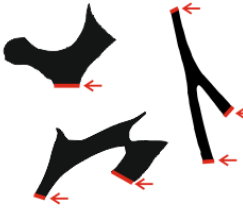


	Blocky	Bubble-wall		Irregular
Examples				
Fragmentation mechanism	Brittle fragmentation, can be an indicator of rapid quenching of the erupted magma.	Bubble-walls with horizontal edges formed by brittle fragmentation (red) and magmatic fragmentation via the expansion of bubbles	Bubble-walls with edges that taper-off forming delicate sharp points, and circular segments of bubble films (blue), formed by magmatic fragmentation due to bubble growth	Fluidal shapes forming irregular pyroclast morphology, formed during slower cooling of the erupted magma which allows the pyroclasts to deform in a ductile-manner prior to solidifying
Eruption type	Magmatic and/or Hydrovolcanic	Magmatic and/or Hydrovolcanic	Magmatic	Magmatic

Table 2-7 Pyroclast morphology can be used to interpret the fragmentation mechanism that led to their formation; this information can be used to interpret eruption dynamics. Blocky pyroclasts are formed by brittle fragmentation and are a common pyroclast-type in magmatic and hydrovolcanic eruption deposits (e.g. Wohletz & Sheridan 1983; Cas & Wright 1988; Ross & White 2012). Two main types of bubble-wall pyroclast can be identified in the samples from all localities, and imply slightly different stages of fragmentation. Bubble-wall shards with abrupt horizontal edges may be formed by the magmatic expansion of bubbles and brittle fragmentation of the bubble-wall edges. These features can form during rapid quenching and brittle fragmentation of the magma alongside magmatic fragmentation by the expansion of bubbles, however, brittle fragmentation may also occur due to abrasion of colliding particles within an ash-cloud, or upon impact of the pyroclast with the Earth's surface (e.g. Cas & Wright 1988). Bubble-wall shards that have edges that taper-off into a delicate, sharp point, are likely evidence of purely magmatic fragmentation by the expansion of bubbles. Irregular pyroclasts get their fluidal morphology from a slower-rate of cooling, which allows the magma to remain ductile and deform during transport from the erupting volcanic vent. The fluidal morphology is retained when the magma completely solidifies. This is evidence of a magmatic eruption-type where pyroclasts are expected to cool more slowly compared to rapid, or instantaneous, quenching if the eruption involved water.

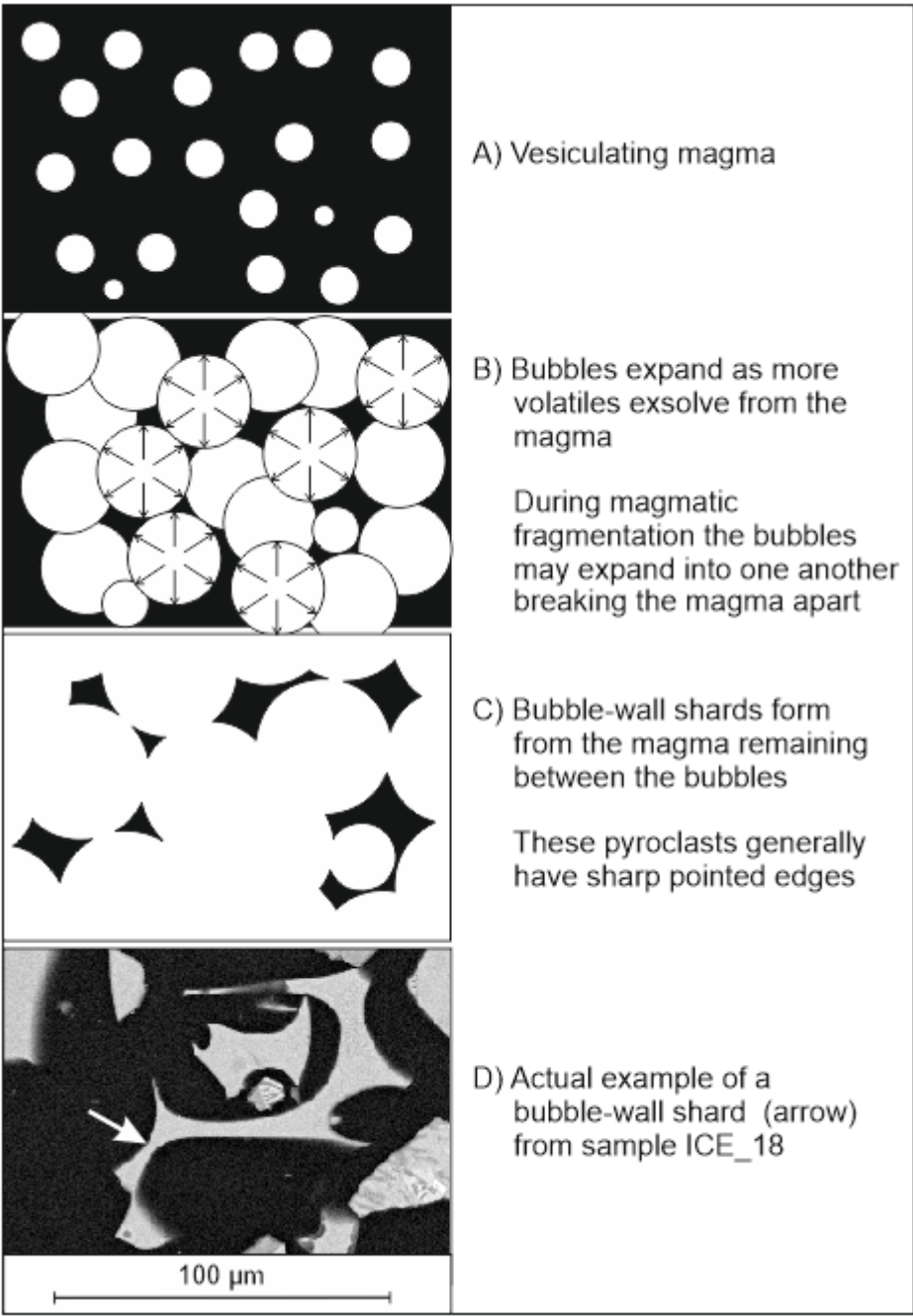


Table 2-8 Formation of bubble-wall shards within a vesiculating magma. Volatiles within the magma exsolve and begin to form bubbles (A). As volatiles continue to exsolve, the bubbles expand and eventually fragment the magma (B). Bubble-wall shards form from the magma that remains between the bubbles and have sharp pointed edges (C). An example of a bubble-wall shard from sample ICE_18 is given in D.

Rod-like pyroclasts may represent Limu-o-Pele (Graettinger et al. 2013). This pyroclast morphology is regarded as evidence for hydrovolcanic eruption dynamics, as Limu-o-Pele are suggested to form from the entrapment of water at the site of an eruption (Graettinger et al. 2013).

The percentage vesicularity of pyroclasts, the shapes of vesicles and relative sizes of vesicles can provide additional information on the conditions of the magma, magma ascent and the eruption dynamics (Gaonach et al. 2005; Mascarenhas-Pereira et al. 2006; Polacci et al. 2008; Shea et al. 2010; Ross & White 2012; Moitra et al. 2013; Heap & Chen 2014). The vesicularity of samples from each location range from poorly to more moderately vesicular (2 to 54%; Table 2-5; Ross & White 2012). This general low-level of vesicularity may represent the volatile component of the magma, showing that the magma may have had a low volatile content at the time of eruption (Moitra et al. 2013). It is also possible that the poor vesicularity is a result of rapid magma ascent, as this can inhibit volatile exsolution and therefore reduce vesicle formation and growth (Moitra et al. 2013). A low vesicularity may also indicate that the magma underwent degassing prior to the eruption of these pyroclasts (Ross & White 2012). It should also be noted that most of the samples are predominantly comprised of non-vesicular pyroclasts (Table 2-6), with the percentage of vesicular pyroclasts reaching >50% in samples from Kjaltell where the grain-sizes are larger (Figure 2-42), and the material has, most likely, been reworked, due to deposition in a fluvial or lacustrine setting. A lower degree of magma fragmentation may allow larger pyroclasts to preserve a greater number of vesicles, whereas higher degrees of fragmentation are more likely to form fine-ash from the breaking apart bubble-walls, thus, removing evidence of vesicularity from the resulting pyroclastic deposit.

The low vesicularity of pyroclasts (Table 2-5) within samples of the SA are indicative of deposits produced by hydrovolcanic eruptions (Houghton et al. 1999; Ross & White 2012; Graettinger et al. 2013). Comparison of the SA data with published data for the vesicularity of hydrovolcanic and 'dry' magmatic deposits show that the SA deposits match most closely with hydrovolcanic deposits (Figure 2-49). However, further pyroclast and deposit characteristics are needed to support this, and determination of hydrovolcanic versus 'dry' magmatic deposits cannot be based on vesicularity alone.

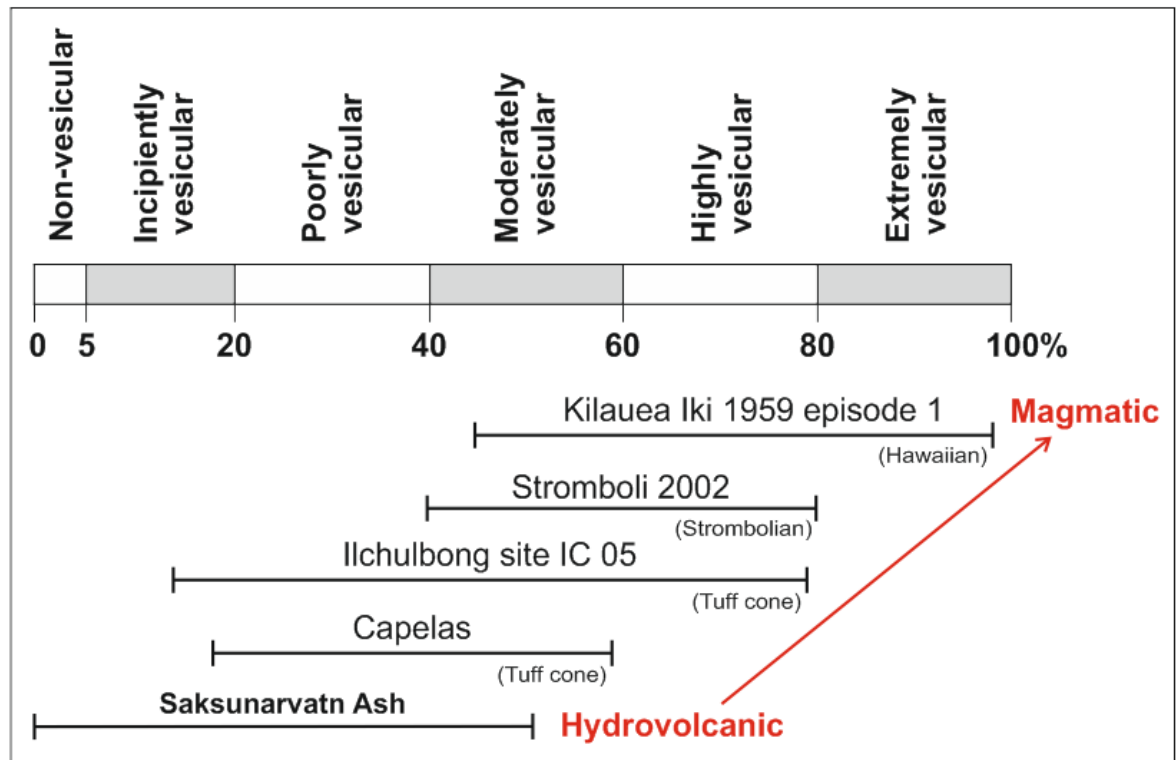


Figure 2-49 Results of the vesicularity of the SA samples (this study) compared with those given by Ross & White (2012) for a range of other eruption-types. Hawaiian fire fountaining and Strombolian eruptions are purely magmatic and have high vesicle abundance, these are represented by data for Kilauea Iki 1959 and Stromboli 2002 (Lautze & Houghton 2007; Stoval et al. 2011; Ross & White 2012). Vesicularities are also compared with results from two tuff cones: Ilchulbong and Capelas (Mattsson 2010; Murtagh et al. 2011; Ross & White 2012). The subdivisions of vesicle percentage and the corresponding non-vesicular to extremely vesicular range is the vesicularity index as proposed by Houghton & Wilson (1989).

Vesicles of a range of sizes are present in the pyroclasts; their sizes potentially representing different phases of volatile exsolution within the magma prior to or during magma ascent (e.g. Gaonach et al. 2005). The size of vesicles is also influenced by magma viscosity, crystal content, and volatile content (Heap & Chen 2014).

The shapes of vesicles can provide information of magma ascent and eruption dynamics, in addition to the rapidity of quenching after fragmentation of the magma has occurred. However, the published results of research into this aspect of pyroclasts, particularly for explosive basaltic eruptions, is limited (Ross & White 2012; Moitra et al. 2013). Four types of vesicle shapes have been identified throughout this study: circular (in 2D) (Figure 2-25d, Figure 2-28c, Figure 2-37a), tube or elongate (Figure 2-37f), irregular (Figure 2-28a), and those exhibiting bubble-coalescence (Figure 2-25c). Tube or elongate vesicles

likely represent shearing of the magma, possibly during rapid ascent in a conduit (e.g. Gaonach et al. 2005; Moitra et al. 2013). The fact that the bubbles have not had time to relax back to a more spherical shape suggests that the magma quenched rapidly, allowing this vesicle texture to be preserved. Circular vesicles in cross-section may represent the presence of spherical vesicles in 3D, this vesicle shape may represent relaxed bubbles within the magma, or suggest that the vesicles were able to relax during a slower-rate of cooling (e.g. Moitra et al. 2013). There is ample evidence for the early stages of bubble-coalescence, where bubbles have coalesced shortly before the magma erupted and quenched (Figure 2-28a-b). Here, the newly merged bubbles form a larger vesicle that still contains pointed bubble-walls that have not had time to relax prior to being quenched (Figure 2-28a-b). Irregular-shaped vesicles may be evidence of the later stages of bubble-coalescence, where the pointed bubble-walls between coalesced bubbles have had time to relax, but the larger newly formed bubble still retains the irregular shape of multiple vesicles (Figure 2-28a; Gaonach et al. 2005; Moitra et al. 2013).

The preservation of very fine-scale, delicate pyroclast features (Figure 2-50), may be evidence that few grain interactions occurred within the eruption column prior to their deposition. This could suggest that the eruption columns had a relatively low particle density, leading to only minimal grain interactions prior to and during deposition. The preservation of these very thin bubble-walls is also evidence for primary pyroclastic deposition with little or no reworking, as subsequent transport and deposition which would likely lead to fracturing and removal of these delicate features.

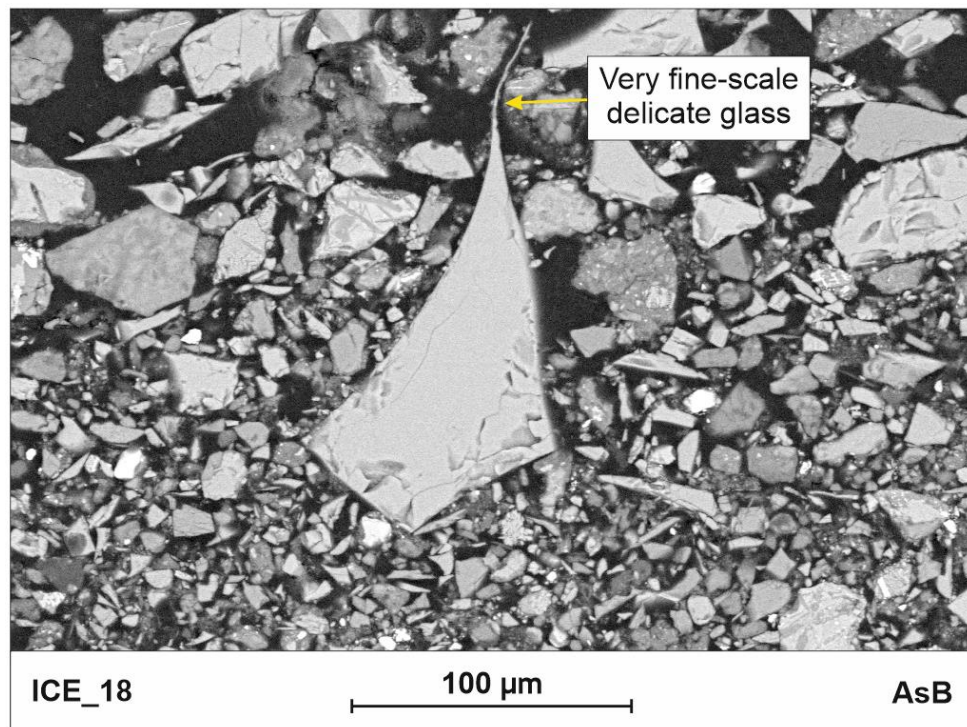


Figure 2-50 An example of a very fine-scale pyroclast feature preserved in a compacted sample from Hekla, Locality 2. The very fine nature of one tip of this shard suggests that it was transported in an area of the eruption column that had a low particle density. A shard of this thickness would be very fragile and would not likely survive if there was a high density of particles within the transport medium, where particle collisions would easily fracture such a fragile feature.

Micro-fractures are a common feature observed in pyroclasts from samples from Hekla, Kjaltell, and Búrfellstóð 1b. These fractures do not appear to be an artefact of sample preparation, but instead appear to be an original feature of these pyroclasts (Figure 2-33). The micro-fractures are more commonly associated with pyroclasts that show a degree of alteration and reworking, and they may therefore be associated with post-eruption processes such as weathering and erosion of primary volcanic deposits. However, it is also possible that some of these micro-fractures may have formed during eruption of the pyroclasts, and therefore, represent hydration cracks (e.g. Mascarenhas-Pereira et al. 2006).

Hydration cracks are commonly found in deposits from hydrovolcanic eruptions as they form due to contraction during rapid cooling of hot particles (Scolamachia et al. 2005; Mascarenhas-Pereira et al. 2006), for example when an already fragmented hot pyroclast comes into contact with cooler fluids.

A minor amount of euhedral microcrystals of olivine can be found in some pyroclasts, along with microcrystals of plagioclase. The presence of these crystals suggests that crystallisation of the magma had begun prior to eruption. It is possible for crystallisation to enhance the viscosity of the melt and therefore increase its explosivity (Moitra et al. 2013; Heap & Chen 2014). However, the minor amount of crystal fragments or microcrystalline pyroclasts compared to crystal-free pyroclasts suggests that the amount of crystals that were present in the melt was minimal, and was not sufficient to be a cause of the highly explosive eruptions that produced the Saksunarvatn Ash.

2.6.2.2 Ash aggregates

Samples from Hekla, Locality 2, appear to contain occasional clasts that could be considered as irregular ash aggregates or ash particle clusters (Figure 2-32b). These clasts are comprised of loosely compacted angular grains of fine-ash, that are generally homogenous with the same composition as the Type 2 pyroclasts that are also abundant in the samples from Hekla.

Ash aggregates are common products of ‘wet’ eruptions, such as those involving hydrovolcanic processes, although they can form in many types of eruption (Scolamacchia et al. 2005; Brown et al. 2012; Van Eaton et al. 2012). Irregular ash aggregates, or ash particle clusters, have an irregular shape and an interior character that is generally structureless (Figure 2-32b; e.g. Scolamacchia et al. 2005). In general, all of the component particles that make up these aggregates are $<10\mu\text{m}$, and composed of the very fine-ash.

Ash aggregates form in various ways, for example by electrostatic and/or capillary forces (Scolamacchia et al. 2005; Brown et al. 2012; Van Eaton et al. 2012; Mueller et al. 2016). The geometry of the aggregates depends on the conditions in the eruption plume; a major constraint on the nature of the aggregate is the original particle size distribution of the ash within the eruption column, as well as the abundance of fluids (Scolamacchia et al. 2005; Van Eaton et al. 2012). The way in which particles adhere to one another will affect the behaviour of the resultant ash aggregate and, therefore, influence the eruption dynamics of a plume. This can also affect fallout deposition and the resultant nature of the deposited material (Brown et al. 2012; Van Eaton et al. 2012;

Mueller et al. 2016). Ash aggregates are generally composed of particles of very fine- or fine-ash that aggregate together to form a larger clast. Therefore, aggregation of fine-ash within an eruption plume can lead to the premature fall-out of large quantities of fine-ash in proximal settings (e.g. Brown et al. 2012). Consequently, less fine ash will then be available for deposition in more distal settings.

Aggregate clasts are only observed in thin-sections from Hekla, Locality 2 samples, and are not observed in any of the grain-mounts from the samples of Búrfellstöð or Kjaltell. It is possible that the deposits of the SA are not chronologically synchronous between all of the localities and that the samples from Hekla represent an eruptive phase that is not observed, or was not sampled, at the other localities. Alternatively, it may be possible that these relatively uncompacted, unconsolidated aggregates broke apart during transportation to the slightly more distal localities of Búrfellstöð and Kjaltell and did not survive transport and deposition. The fluvial environments that have been interpreted for Búrfellstöð and Kjaltell, during deposition of the SA, may not have permitted the preservation of aggregates, even if they were deposited in these areas, as the higher-energy of rivers could easily break apart these fragile particle clusters. Preservation of aggregates within the varved sections of Hekla, Locality 2, may have been permitted due to their deposition in a very calm lacustrine environment.

2.6.3 Primary versus reworked volcanic material

During reworking, all clast-types are likely to fragment due to abrasion caused when grains come into contact with other particles or surfaces (e.g. Brookfield 2004). It is likely, therefore, that pyroclasts may fracture or fragment further during reworking than they originally did in the eruption column prior to their initial deposition. This should be considered when assessing the grain-size and grain characteristics when relating these to eruption processes, as the original eruption characteristics may be overwritten by later reworking (Brookfield 2004).

Pyroclasts in samples from Búrfellstöð 1b, 1d, Hekla and Kjaltell have jagged or rounded edges and commonly have a rim of clay-rich material (Figure 2-26; Figure 2-29; Figure 2-37). Vesicular pyroclasts within these samples are commonly associated with a partial or complete infill of very fine-ash (Figure 2-26; Figure 2-29c; Figure 2-31a; Figure 2-38). These pyroclast features may represent the effects of reworking (e.g. Mascarenhas-Pereira et al. 2006). When this is considered alongside the clast-types for each of these samples it can be noted that these features coincide with an increase in the abundance of granular lithic and lava-like clasts. These samples (ICE_16, ICE_17, all samples from Hekla and Kjaltell) generally contain the lowest abundance of pyroclasts that can be considered as ‘fresh’ glassy material (Figure 2-44). This suggests that these samples represent reworked volcanic sediments and are therefore volcanoclastic sedimentary deposits and not primary air-fall pyroclastic deposits of the SA.

The m-scale thickness of some of the volcanoclastic deposits of the SA within fluvial deposits from the Búrfellstöð, Locality 1, and Kjaltell, Locality 3 (Figure 2-1), do not give any indication of the thickness of the primary pyroclastic deposits or the total volume of tephra erupted or deposited during any eruptive episode of GV. The thickness of these deposits is more likely to be an exaggeration of the quantity of tephra deposited across this region. The presence of ripple structures and erosional bed boundaries are further evidence that the tephra observed at these localities has been reworked.

The upper part of the lacustrine deposit exposed at Hekla, Locality 2, is dominated by varved clays, silts and fine-grained sands, which likely formed seasonally in a low energy, sub-aqueous lacustrine environment (Figure 2-15; Collinson 1978; Prothero 1990; Glenn & Kelts 1991; Collinson et al. 2006). Deposition of this varved succession was intermittently interrupted by deposition of coarser-grained sands at least seven times. These coarser-grained sands may represent at least seven depositional events related to eruptions of GV and form an important part of the SA tephrostratigraphy. These sand-grade deposits are most likely composed of a combination of primary fall-out pyroclasts and volcanoclastic material washed into the lake, syn-eruption, or shortly thereafter. Thin-sections of samples from the uppermost portion of this deposit are dominated by vitreous pyroclasts, which have sharp rims and show no evidence

of transport during prolonged periods of reworking. It is possible that this material has been transported short distances, with little abrasion prior to final deposition and preservation within this lacustrine succession. Interbedded with these deposits containing more 'primary' volcanic material are beds where the features of the pyroclasts are more similar to those from Kjaltell. The pyroclasts in these sections have jagged edges, abundant micro-fractures and are associated with a higher abundance of sedimentary clasts (granular lithic and microcrystalline lava-like clasts; Figure 2-44). Due to the high number of non-pyroclast clast-types and evidence of abrasion (micro-fractures and jagged edges) these intervals could be interpreted as volcaniclastic deposits (Table 2-9).

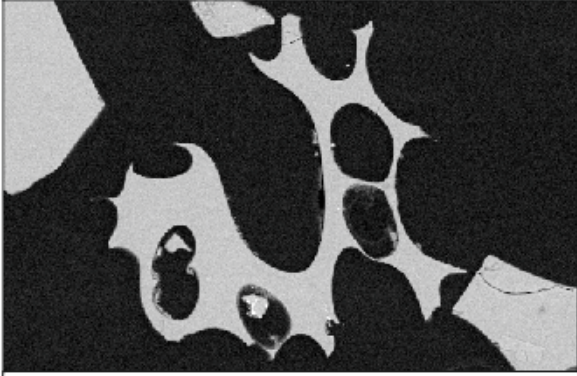
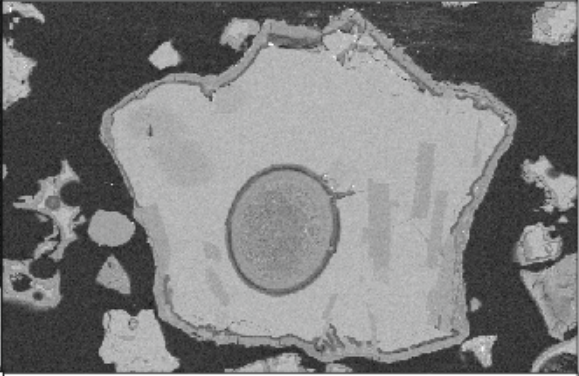
Primary volcanic	Reworked volcanoclastic
Pyroclasts have smooth, sharp edges	Pyroclast edges are jagged, and rounded with abundant micro-fractures that are present throughout the grain
Little or no alteration, deposits are predominantly comprised of glassy pyroclasts	Minimal to high-levels of alteration of pyroclasts, including clay-rich rims and altered embayments around the edges of pyroclasts
Vesicles are generally empty	Vesicles are often partially or completely filled with fine ash or fine-grains of sediment
Deposits are comprised of a high abundance of volcanic clasts with little or no sedimentary clasts	Deposits are comprised of a high abundance of clasts of sedimentary origin
	
ICE_14 100 μm AsB	K_13 200 μm AsB

Table 2-9 Characteristic features of pyroclasts and deposits used to distinguish between primary pyroclastic and volcanoclastic material. These criteria have been used for the samples investigated in this study and may or may not be applicable to deposits from other volcanoes. In these samples primary volcanic deposits are those that are comprised almost entirely of volcanic clasts, and pyroclasts that have smooth, sharp edges, empty vesicles and little or no alteration of the glassy pyroclast. In contrast to this, reworked volcanoclastic deposits are predominantly comprised of sedimentary clasts, and pyroclasts that have jagged, edges with abundant micro-fractures, higher levels of alteration and vesicles that are partly or completely filled with fine ash or fine-grained sediment.

2.6.3.1 Chemical composition of pyroclasts

Two types of pyroclast (Type 1 and Type 2) are abundant in the samples from Hekla, Locality 2. The two types can be identified in SEM AsB images as they produce two varying shades of grey, which are indicative of differences in the chemical composition of the two types. Type 1 pyroclasts are pale grey under

AsB SEM and Type 2 pyroclasts are a darker mid-grey. When comparing the chemical spectra of these two types of pyroclast (Figure 2-39), the Type 2 pyroclasts give a higher wt% of silica (Si). This could suggest that the Type 2 pyroclasts were produced by the eruption of a more evolved, silicic, parent-magma than those of Type 1 composition (Figure 2-39). This interpretation is also supported by the observation of lower wt% of Fe and Ca (Figure 2-39). Fe and Ca can be removed from a magma by the fractional crystallisation of magnetite and ilmenite, and plagioclase, respectively, and is evidence of the evolution of a magma to higher one with a higher silica content (Winchester & Floyd 1977; Hastie et al. 2007).

Deposits of the SA are said to be comprised of a homogenous composition of pyroclasts of tholeiitic basalt (Andrews et al. 2002; Jennings et al. 2002; Gudmundsdóttir et al. 2011; Thornalley et al. 2011; Bramham-Law et al. 2013; Lind et al. 2013; Lohne et al. 2013; Jennings et al. 2014; Neave et al. 2015). The presence of the more evolved pyroclasts (Type 2) in the samples from Hekla, Locality 2 (Figure 2-44), suggests that another eruption took place from an separate source, with deposition coinciding with at least one eruptive phase of GV, during deposition of the SA. It is unlikely that both compositions of pyroclast were erupted simultaneously from one vent because the Type 2 pyroclasts are not found in the deposits at every location. Where they are present in samples from Búrfellsstöð and Kjaltell, they are only a very minor component of the deposit and generally exhibit features identified as being indicative of reworking, i.e. jagged edges, abundant micro-fractures and infilled vesicles (Figure 2-38). This suggests that multiple eruptions were occurring in Iceland around ca. 10.3 ka BP and that ash from more than one vent can be incorporated into the same ash-fall deposits.

2.6.3.2 Alteration of pyroclasts

During devitrification and the general alteration of glassy pyroclasts, elements, such as Na, Mg, Ca and Fe can become mobile and be lost from the pyroclast; while immobile trace elements often remain unchanged (Hastie et al. 2007; Ross & Bédard 2009). The loss of mobile elements can be observed in the SA samples when comparing the chemical spectra of the original glass and devitrified glass

of partially devitrified pyroclasts (Error! Reference source not found.). Devitrification in these deposits shows a decrease in Na, Mg, Ca and Fe, with a concomitant minor decrease in Ti also observed within the spectral and weight percentage data (Error! Reference source not found.). In other examples of partially devitrified pyroclasts, there is a decrease in the abundance of K with little loss of Ti (Figure 2-51).

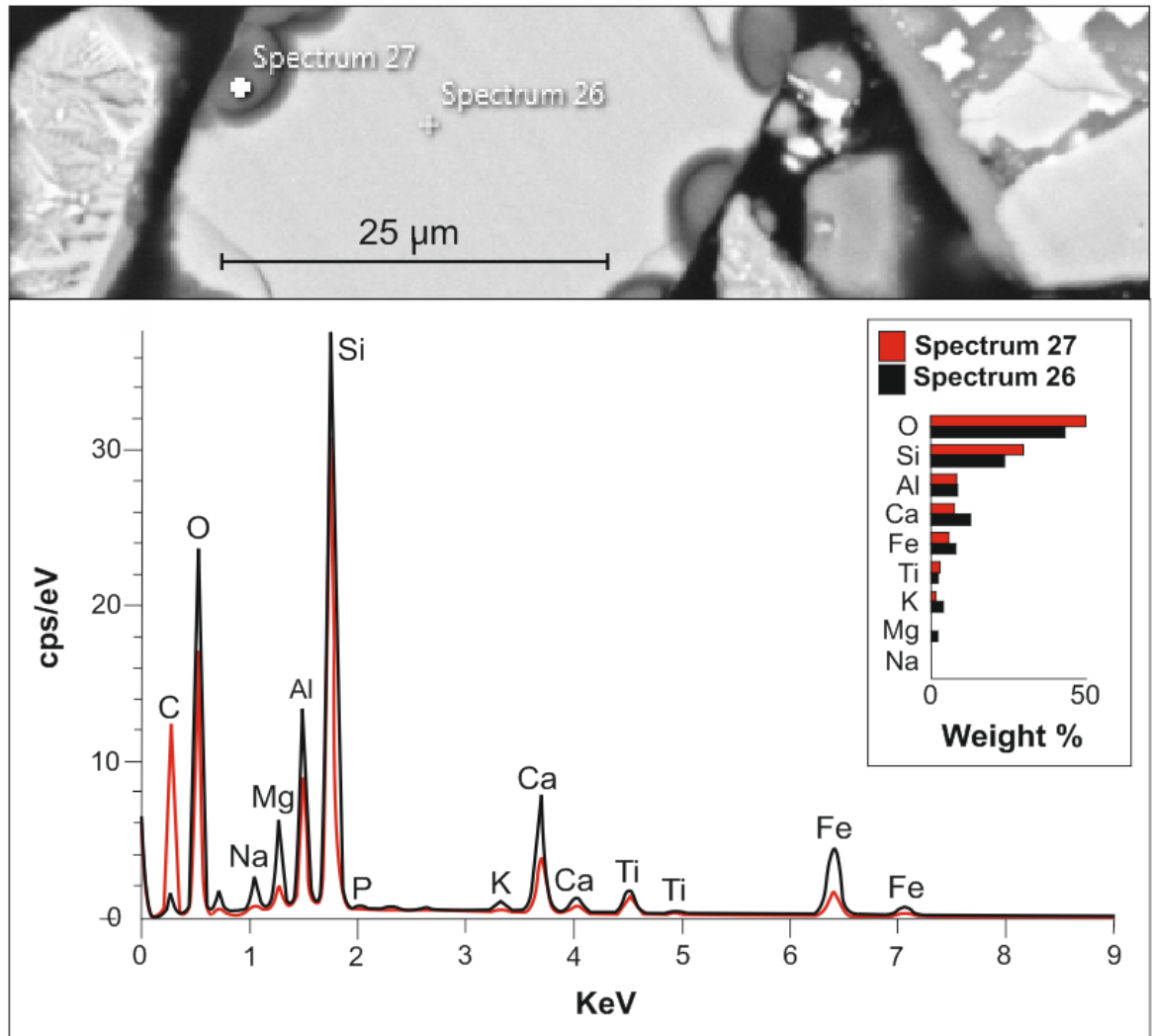


Figure 2-51 Comparison of SEM chemical spectra data for glass and devitrified glass present in a partially altered pyroclast from sample ICE_09A. In this example, the devitrified glass contains less Na, Mg, Al, K, Ca and Fe with little change in the abundance of Ti.

2.7 Conclusions

Volcaniclastic sediments composed of material deposited from multiple eruptive episodes of Gímsvötn Volcano, Iceland, and representative of the ~10.3 ka BP Saksunarvatn Ash are found at Búrfellsstöð, Locality 1, Hekla, Locality 2 and

Kjaltell, Locality 3 (Figure 2-1). The presence of asymmetrical climbing ripples (e.g. Figure 2-7), and interbeds of coarse sand, gravel and pebbles (e.g. Figure 2-20) are indicative of deposition and preservation of tephra in a fluvial environment for the Saksunarvatn Ash at both Búrfellsstöð and Kjaltell. Sub-horizontal stratified sediments and mm-scale normal-graded varves at Hekla (Figure 2-14, Figure 2-15), imply that this locality was dominated by a lacustrine environment during deposition of the Saksunarvatn Ash. At least seven separate eruptive deposits may be identified in the uppermost deposits at Hekla, suggesting that multiple eruptive episodes of Grímsvötn Volcano occurred relatively frequently to form the Saksunarvatn Ash. Burial of up to a few tens of metres is suggested for the deposits at Hekla and Kjaltell with little or no burial at Búrfellsstöð. The limited burial of the deposits has resulted in the formation of loose sediments, with a high porosity and permeability that are predominantly held together by grain compaction.

Some post-depositional deformation is recognised within the deposits. Micro-faults are present in the lacustrine deposits at Hekla (Figure 2-14, Figure 2-17), mm- to cm-scale displacement shows that slumping of these sediments occurred after deposition. Another type of soft sediment deformation can be observed at Búrfellsstöð 1c (Figure 2-10), and Hekla (Figure 2-15), where *ca.* 80 cm of deformation has occurred at both localities. This soft sediment deformation includes the presence of a sediment volcano at Búrfellsstöð 1c (Figure 2-9), and may have been caused by a significant seismic event of Richter magnitude 5 or greater (Seed & Lee 1966; Morgnestern 1967; Kuribayashi & Tatsuoka 1975; Youd 1977; Scott & Price 1988), or by ground motions with a duration of more than 8 seconds (Seed & Lee 1966; Scott & Price 1988). The deformation of the sediments shows that the material was water-logged and able to be mobilised during the seismic event. It is possible that the soft-sediment deformation observed at both of these localities can be correlated by; the deformation-type (seismically induced), thickness of the deformed unit (*ca.* 80cm in both localities) and the relatively small distance between these two localities (*ca.* 7.5 km). Therefore, this deformation may provide a relative chronostratigraphic marker for the region.

Pyroclasts of basaltic composition are the dominant clast-type in all of the samples (Figure 2-44, Table 2-3); however, the nature of the pyroclasts differ between each sample and locality. Pyroclast morphologies include: blocky, bubble wall, irregular, and rod-like (Figure 2-45). Blocky pyroclasts dominate all of the samples (Figure 2-45); these can form in all types of eruption but are the most common in deposits of hydrovolcanic eruptions (Table 2-7; Heiken 1972, 1974; Wohletz & Sheridan 1983; Cas & Wright 1988; Ross & White 2012; Graettinger et al. 2013). Samples from Búrfellsstöð contain the greatest abundance of bubble-wall pyroclasts (Figure 2-45), which are more indicative of magmatic fragmentation caused by the bursting of bubble-walls in a vesiculating magma (Table 2-8; Cas & Wright 1988). Bubble-wall, irregular and rod-like pyroclasts are present in a very minor abundance in the Hekla and Kjaltell samples (Figure 2-45). Hekla samples contain the greatest amount of rod-like pyroclasts (Figure 2-45), these may be Limu-o-Pele, which form via entrapment of water and may indicate hydrovolcanic eruptive processes (Graettinger et al. 2013). The low abundance of vesicular pyroclasts in most of the samples (Table 2-6), along with their low vesicularity (<40%; Table 2-5), indicates that the magma was poorly vesicular (Houghton & Wilson 1989). All samples are predominantly comprised of ash (<2mm) and fine-ash (<63 μm) with a very fine-ash matrix (<4 μm) confirming that a large amount of fine-grained tephra was deposited during each eruption (Figure 2-41, Figure 2-42). The low vesicularity and, therefore, low volatile content of the source magma, does not lend itself to highly-explosive eruptions and the production of large amounts of fine-grained tephra, if only 'dry' magmatic fragmentation is considered (e.g. Graettinger et al. 2013). Therefore, magma-water interactions, in the form of highly explosive hydrovolcanic processes, are the most likely source of the Saksunarvatn Ash. Fractures around the edges of some pyroclasts may represent hydration cracks, which are further evidence for the interaction of water during eruption of the magma (Scolamachia et al. 2005; Mascarenhas-Pereira et al. 2006).

Eruption of the Saksunarvatn Ash also involved the incorporation of accidental clasts, including crystalline igneous clasts of basalt and fragments of plagioclase crystals (Table 2-4). Plagioclase is present as individual crystals, and as microcrystals or phenocrysts within the crystalline igneous and lava-like clasts; euhedral olivine microcrystals are also present in some of these igneous clasts

alongside plagioclase. The presence of these crystals shows that crystallisation of the magma had begun prior to eruption of the Saksunarvatn Ash. A high crystal content in magma can act to enhance the viscosity and therefore increase the explosivity of a magma (Moitra et al. 2013; Heap & Chen 2014) and crystallisation may have enhanced the viscosity of the magma leading to more explosive eruptions of the Saksunarvatn Ash. However, all of the samples contain <50% crystalline igneous and microcrystalline lava-like clast-types, suggesting that the crystal content might not have been sufficient enough to significantly enhance the viscosity of the magma or the explosivity of the subsequent eruptions. Therefore, it is more likely that external magma-water interactions were responsible for the highly explosive nature of the eruptions that produced the Saksunarvatn Ash.

Samples from Hekla, Locality 2, contain two types of pyroclast, interpreted based on differences in their chemical composition (Figure 2-39). Type 1 pyroclasts have a lower Si, Fe and Ca content compared to Type 2 pyroclasts. The Type 2 pyroclasts are less common in samples from the other localities, where they occur as rare grains (Figure 2-44). The Type 2 pyroclasts likely represent ash from more silicic eruptions, as they have a higher Si content, suggesting that these pyroclasts originated in eruptions that occurred elsewhere in Iceland. Therefore, suggesting that multiple eruptions were occurring at different sources simultaneously with the ~10.3 ka BP eruptions of Grímsvötn Volcano that were responsible for the deposition of the Saksunarvatn Ash. Clasts resembling irregular aggregates or particle clusters comprised of fine-ash of this more evolved (Type 2) composition are found in the samples from Hekla (Figure 2-32b). The formation of ash aggregates is often associated with hydrovolcanic eruption processes and may therefore be evidence that the more evolved pyroclasts also formed during hydrovolcanic eruptions, possibly associated with eruptions through glaciers outside of the glacier covered Grímsvötn Volcano

The samples from Kjaltell, are predominantly comprised of pyroclasts that exhibit features of reworking (Table 2-9). These pyroclasts have fractured, jagged or rounded edges that were likely caused by abrasion, and are often associated with rims of clay and alteration (Figure 2-37e-f). Alteration via the process of devitrification of the glassy pyroclasts can be observed where there

has been a decrease in the weight percentage of sodium, magnesium, calcium and iron, possibly also with a concomitant minor decrease in titanium (**Error! Reference source not found.**, Figure 2-51). The vesicles of these pyroclasts are often partially or completely infilled with fine-grained granular sediment (Figure 2-36c, Figure 2-37f), showing that they represent lithic clasts and not 'primary' pyroclastic material. Interbeds of the deposits at Hekla, display 'primary' pyroclast features interbedded with material that is characterised by reworked features similar to those described for Kjaltell (Figure 2-31). Therefore, the Hekla deposits are likely comprised of both primary pyroclastic and volcanoclastic material deposited following reworking and re-deposition of the original pyroclastic deposits.

This chapter shows how pyroclast and deposit characteristics could be used to distinguish the differences between primary pyroclastic and volcanoclastic deposits, in addition to interpreting eruption and depositional processes. These topics will be addressed further in the following chapters.

Chapter 3: North Sea Basin Early Eocene stratigraphy

3.1 Introduction

The Early Eocene Balder Formation (BF) was deposited *ca.* 54.5 million years ago (Ma), and forms a prominent lithological and chronostratigraphical marker unit that can be identified throughout the North Sea and Faroe-Shetland basins (NSB & FSB; Figure 3-1; Jacqu   & Thouvenin 1975; Deegan & Scull 1977; Knox & Harland 1979; Knox & Morton 1983; Lott et al. 1983; Mudge & Bliss 1983; Malm et al. 1984; Roberts et al. 1984; Knox & Morton 1988; Vierick et al. 1988; Morton & Knox 1990; Jolley & Morton 1992; Knox & Holloway 1992; Mudge & Copestake 1992a; Hitchen & Ritchie 1993; Ebdon et al. 1995; Waagstein & Heilmann-Clausen 1995; Ali & Jolley 1996; Knox 1996; Mudge & Bujak 1994, 1996; Ritchie & Hitchen 1996; Nadin et al. 1997; Haaland et al. 2000; Smallwood & Gill 2002; Jolley & Bell 2002; Mudge & Jones 2004; Jolley & Widdowson 2005; Ross et al. 2005; Dmitrieva et al. 2012; Aldiss 2014; King 2016). This marker unit can be identified as a prominent reflector in seismic data in many parts of the NSB, and occasionally produces a characteristic bell-shaped response in wire-line data, where a decrease in gamma-ray and sonic velocity occur (see section 3.5.4; Mudge & Bliss 1983; Mudge & Bujak 1994; Watson et al. 2017; NPD Fact pages well completion reports). The cause of this characteristic behaviour may be due to an abundance of (>200) basaltic tuffs found throughout the BF (Mudge & Bujak 1994), that represent the preservation of a unique period of highly explosive basaltic volcanism not preserved anywhere else in the world. These tuffs have been associated with large-scale explosive volcanism that occurred during formation of the North Atlantic Igneous Province (NAIP) and may be associated with the possible Early Eocene initiation of sea-floor spreading in the NE Atlantic (Hallam 1972; Knox & Harland 1979; Knox & Morton 1983; Knox 1996; Ritchie & Hitchen 1996; Nadin et al. 1997; Haaland et al. 2000; Torsvik et al. 2001; Larsen et al. 2003; Jolley & Widdowson 2005; Ross et al. 2005; Breivik et al. 2006; Brooks 2006; Storey et al. 2007; Brunstad et al. 2008; Breivik et al. 2009; Gernigon et al. 2012). They may also be associated with impact of the proto-Icelandic mantle plume at the base of the East Greenland lithosphere, and movement of this to the opening rift between Greenland and NW Europe

The NSB is divided by two main territories referred to as the UK Continental Shelf (UKCS) to the west and the Norwegian-Danish Basin (NOR) to the east. Analysis was conducted on core-material from wells in both the UKCS (22/30a-1 and 29/05a-7; Figure 3-2) and NOR (25/7-5, 25/11-17 and 30/2-1; Figure 3-2), held by the British Geological Survey (BGS) and the Norwegian Petroleum Directorate (NPD), respectively. One sample from FSB Well 6104/25-1 (Figure 3-2) was provided by Brian Bell for analysis of a tuff interval within the BF of the FSB based purely on thin-section analysis. This one sample was used to provide some information on the nature of the volcanism that affected the FSB and whether this may correlate with features of the NSB BF tuffs. A detailed investigation into the lithologies of the BF of the NSB and the one sample from FSB Well 6104/25-1 will be presented here, with a detailed investigation into the nature of its volcanic content.

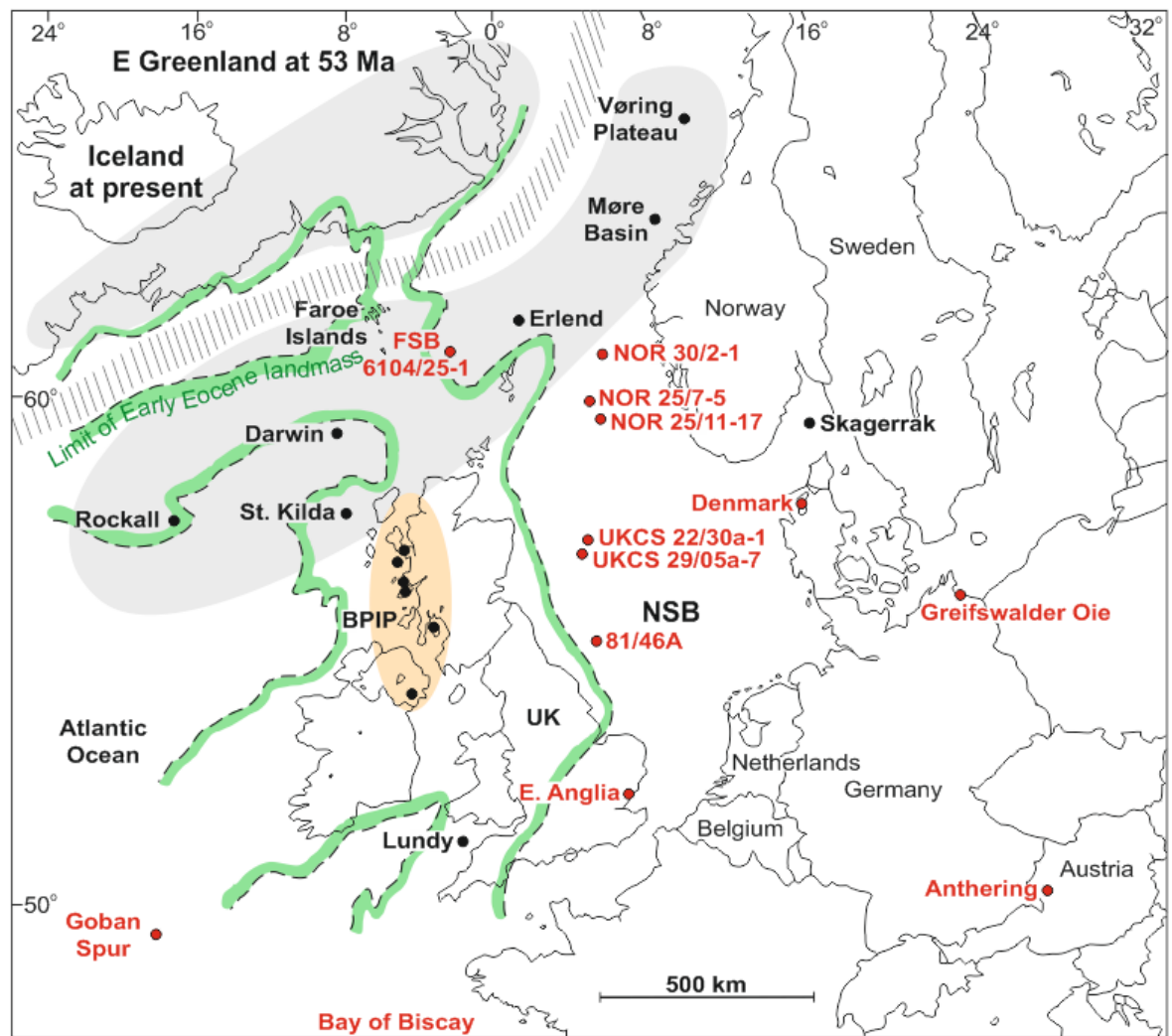


Figure 3-2 Palaeogeographic reconstruction of the NE Atlantic and NW Europe at 53 Ma. Green and dashed lines show the limit of the Early Eocene landmass proposed by Obst et al. (2015), superimposed on a plate reconstruction at 53 Ma proposed by Larsen et al. (2003). Red show where Early Eocene tuffs of the Balder Formation and its equivalents have been identified, including North Sea wells discussed in the text. Orange: the British Palaeogene Igneous Province (BPIP); Grey: North Atlantic Igneous Province (NAIP), either side of the developing spreading centre along the rift (dashed region) between E Greenland and NW Europe.

3.2 Geological history and literature review

Rifting between Greenland and NW Europe began in the Cretaceous (Jacqué & Thouvenin 1975; Carter et al. 1979; Mussett et al. 1988; Hitchen & Ritchie 1993; Knox 1996; Ritchie & Hitchen 1996; Nadin et al. 1997; Larsen et al. 1999, 1999a; Heister et al. 2001; Hansen et al. 2001; Torsvik et al. 2001; Ellis et al. 2002; Jolley & Bell 2002; Jerram & Widdowson 2005; Jolley & Widdowson 2005; Hansen et al. 2009), and resulted in sea-floor spreading and the formation of new oceanic crust *ca.* 56 - 52 Ma (Jacqué & Thouvenin 1975; Knox & Ellison 1979; Knox & Morton 1983, 1988; Kent & Fitton 2000; Torsvik et al. 2001; Simonsen &

Toft 2006; Storey et al. 2007; Stoker et al. 2012; Ellis & Stoker 2014). Large-scale magmatic activity was associated with rifting and led to the formation of the North Atlantic Igneous Province (NAIP), which includes the British Palaeogene Igneous Province (BPIP; Figure 3-2).

Two main phases of uplift have been correlated with an increased magma production and increased volcanic activity within the NAIP during rifting and the onset of sea-floor spreading. The first phase of uplift occurred *ca.* 61 - 59.5 Ma (Knox 1996; Kent & Fitton 2000), and may have been associated with initial impact of the proto-Icelandic mantle plume beneath the lithosphere of E Greenland (Knox 1996; Ritchie & Hitchen 1996; Nadin et al. 1997; Mudge & Jones 2004). This phase of uplift and magma generation was likely responsible for the main phase of magmatic activity in the BPIP, in addition to magmatism in E Greenland and the Faroe Islands (Knox & Morton 1983, 1988; Mussett et al. 1988; Hitchen & Ritchie 1993; Knox 1996; Ritchie & Hitchen 1996; Larsen et al. 1999a). This first major magmatic phase involved the intrusion and eruption of basaltic to felsic magmas and effusive eruption of basaltic lavas. This activity has been correlated to the 57 - 58 Ma tuffs of Knox & Morton (1983) Phase 1 volcanism, that includes tuffs of basaltic to rhyolitic and nephelinitic composition that can be found throughout the NSB (Sele Formation) and the Danish negative ash series (Figure 3-3; Pedersen et al. 1975; Knox & Morton 1983; Knox 1984; Knox & Morton 1988; Haaland et al. 2000; Larsen et al. 2003; Ross et al. 2005; Brooks 2006; Obst et al. 2015).

Another phase of uplift affected the NSB from *ca.* 56.5 Ma (Knox & Morton 1983; Knox 1996; Nadin et al. 1997; Kent & Fitton 2000) and might be associated with a marine regression (Knox & Harland 1979; Ali & Jolley 1996; Knox 1996), and a period of non-deposition in the southern NSB (see Chapter 5; Ali & Jolley 1996). Phase 2 volcanism of Knox & Morton (1983) followed this from *ca.* 56 Ma (Knox 1996) and included magmatism in E Greenland (Roberts et al. 1984; Larsen et al. 1999a), effusive eruptions of the Enni and Malinsstindur Formation lavas of the Faroe Islands (Roberts et al. 1984; Waagstein 1988; Hitchen & Ritchie 1993; Larsen et al. 1999a; Passey & Bell 2007; Passey & Jolley 2009), and explosive pyroclastic volcanism in the Faroe Islands (Smythe et al. 1983). In addition, some later-stage magmatic and volcanic activity may have occurred in the BPIP until

ca. 46 Ma (Jacqué & Thouvenin 1975; Knox & Ellison 1979; Knox & Morton 1983; Mussett et al. 1988; Hitchen & Ritchie 1993; Knox 1996; Ritchie & Hitchen 1996). This activity may have coincided with formation of new oceanic crust within the NE Atlantic rift (Jacqué & Thouvenin 1975; Knox & Ellison 1979; Knox & Morton 1983, 1988; Kent & Fitton 2000; Torsvik et al. 2001; Simonsen & Toft 2006; Storey et al. 2007; Stoker et al. 2012; Ellis & Stoker 2014).

Uplift and its associated marine regressions correspond to increased erosion of the landmasses surrounding the NSB, and the deposition of coarse clastic sediments into the NSB (Milton et al. 1990; Mudge & Bujak 1994). In contrast, marine transgressions led to a decrease in deposition of coarse clastic sediments and led to an increased deposition of clays and silts within the basin (Mudge & Bujak 1994; Knox 1996; Cattaneo & Steel 2003).

Phase 2 volcanism began *ca.* 56 - 55 Ma (Knox & Morton 1983; Knox 1996; Haaland et al. 2000; Ross et al. 2005) with a peak in volcanic activity *ca.* 54.5 Ma (Pedersen et al. 1975; Knox & Morton 1983; Larsen et al. 2003; Obst et al. 2015; Carriol et al. 2016; Watson et al. 2017). The Phase 2 volcanism has been separated into four sub-phases based on stratigraphy, deposit and grain characteristics, and the geochemical composition of the associated tuffs (Knox & Morton 1983; Knox 1984; Haaland et al. 2000). Many of these tuffs can be found within the Late Palaeocene - Early Eocene deposits of the NSB. A distinctive lack of micro-fauna and -flora inhibits precise age dating of these, however, corresponding deposits in the N Atlantic (e.g. in the Goban Spur) have allowed a correlation of the tuff sequence with age-appropriate nannoplankton (NP) zones; with the BF corresponding to NP10 (Figure 3-1; Knox & Morton 1988).

Sub-phase 2a occurred from mid NP9 to early NP10 times (Figure 3-1; Knox & Morton 1988) and consists of sporadic tuff layers that were deposited throughout the NSB, (Malm et al. 1984) and Denmark (Figure 3-3; Knox & Morton 1983). Tephra corresponding to sub-phase 2a may also be preserved in SE England, the Goban Spur and the Bay of Biscay (Knox & Morton 1983; Knox & Morton 1988).

Sub-phase 2b occurred between early to mid NP10 times (Figure 3-1; Knox & Morton 1988) and contains the largest amount of tuff, where over 200 layers

have been identified within cores from the NSB (Knox & Morton 1983; Knox & Morton 1988; Roberts et al. 1984). The tuffs are almost entirely of Fe-Ti tholeiitic basalt, except for two rhyolitic units (Norin 1940; Pedersen et al. 1975; Pedersen & Jørgensen 1981; Roberts et al. 1984; Knox & Morton 1988; Morton & Knox 1990; Elliott et al. 1992; Knox 1996; Larsen et al. 2003; Brooks 2006; Obst et al. 2015; Watson et al. 2017). These tuffs are also the most widespread and may be correlated throughout the NSB, Denmark (Norin 1940; Nielsen 1974; Pedersen et al. 1975; Knox & Harland 1979; Pedersen & Jørgensen 1981; Pedersen & Surlyk 1983; Knox 1984; Roberts et al. 1984; Knox & Morton 1988; Morton & Knox 1990; Elliott et al. 1992; Mudge & Copestake 1992a; Neal et al. 1996; Brooks 2006; Obst et al. 2015; Carriol et al. 2016), SE England (Pedersen et al. 1975; Knox & Ellison 1979; Knox & Harland 1979; Knox & Morton 1983; Mudge & Bliss 1983; Malm et al. 1984; Roberts et al. 1984; Knox & Morton 1988; Morton & Knox 1990; Ellison et al. 1994; Jolley 1996; Knox 1996; Neal et al. 1996; King 2016; Watson et al. 2017), the Netherlands (Pedersen et al. 1975; Knox & Harland 1979; Knox & Morton 1983; Roberts et al. 1984; Knox & Morton 1988; Morton & Knox 1990), N Germany (Nielsen 1974; Pedersen et al. 1975; Knox & Harland 1979; Pedersen & Jørgensen 1981; Knox & Morton 1983; Roberts et al. 1984; Knox & Morton 1988; Morton & Knox 1990; Neal et al. 1996), Belgium (Neal et al. 1996), Austria (Larsen et al. 2003; Brooks 2006; Egger & Brückl 2006), the Goban Spur (Knox 1984; Knox & Morton 1988; Morton & Knox 1990; Ali & Jolley 1996; Brooks 2006) and the Bay of Biscay (Knox 1984; Roberts et al. 1984; Knox & Morton 1988; Morton & Knox 1990), with a tentative compositional link made to bentonite in Anthering, in the Austrian Alps (Larsen et al. 2003; Brooks 2006; Egger & Brückl 2006; Carriol et al. 2016; Figure 3-2).

Above this lies sub-phase 2c, which occurs as sporadic tuff layers (Knox & Morton 1983) of mid NP10 to late NP10 or early NP11 times (Knox & Morton 1988). Sub-phase 2c is found in the northern NSB, Denmark and NW Germany (Figure 3-3; Knox & Morton 1983; Malm et al. 1984; Knox & Morton 1988).

Sub-phase 2d contains sporadic tuff layers that are observed in the central and northern NSB, SE England and may correlate to the sporadic tuffs of the Røsnaes Clay in Denmark (Figure 3-3; Malm et al. 1984; Knox & Morton 1988). The sub-phase 2d tuffs represent the final stage of major explosive volcanism in the NAIP

that occurred around early NP11 to late NP13 times (Knox & Morton 1983; Knox & Morton 1988).

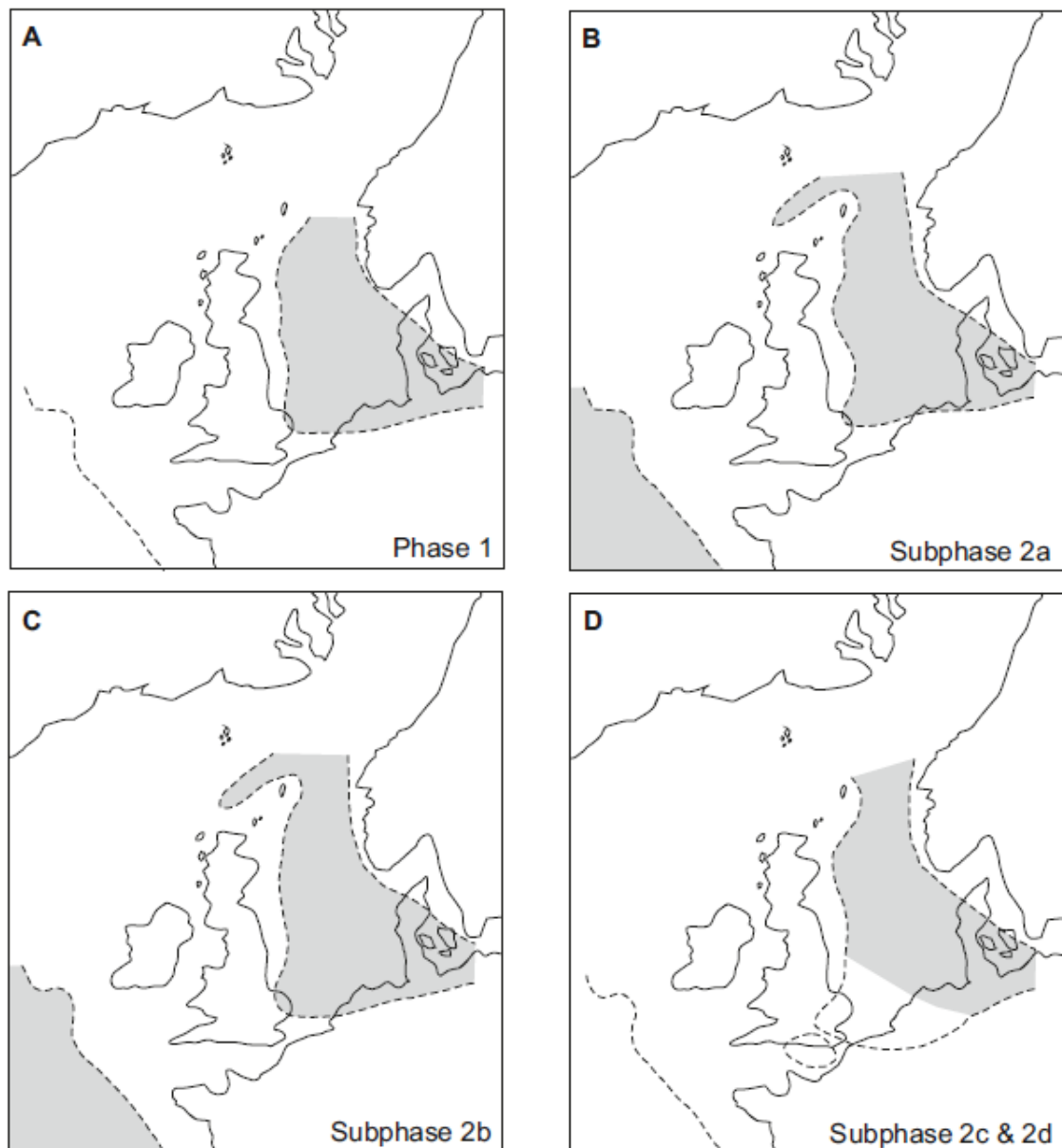


Figure 3-3 Distribution of ash corresponding to each volcanic phase and sub-phase identified by Knox & Morton (1983). Dashed lines show that extent of potential ash distribution during each phase with grey shaded regions indicating where ash has been preserved. (After Knox & Morton 1988).

The volcanism of Phase 2 is has been associated with separation of Greenland from NW Europe (Knox & Morton 1983), impact of the proto-Icelandic mantle plume (Ritchie & Hitchen 1996; Torsvik et al. 2001), and initiation of sea-floor spreading during development of the NE Atlantic Ocean (Knox & Morton 1983). The large volume of sub-phase 2b tuffs could correspond to a shift in crustal

tension from the rift margins to the centre of the rift as sea-floor spreading began between Greenland and Rockall around 54.5 - 54 Ma (Figure 3-2; Knox & Morton 1983; Larsen et al. 2003). This may have coincided with movement of a mantle plume from beneath E Greenland to within the opening rift of the NE Atlantic (Morton & Knox 1990).

Initial formation of oceanic crust may have been, at least partly, subaerial (Knox 1996; Breivik et al. 2009). With gradual subsidence and increasing sea level related to a regional marine transgression the volcanic vents may have become flooded, leading to highly explosive hydrovolcanic eruptions (Knox 1996) that dispersed basaltic ash large distances away from the spreading centre. A rapid decrease in the abundance of preserved ash-layers following the sub-phase 2b volcanism is observed throughout the BF of the NSB, and may correspond to a decrease in widespread explosive activity related to the establishment and stabilisation of sea-floor spreading and the proto-Icelandic mantle plume after 54.5 - 54 Ma (Knox & Morton 1983), which led to a decrease in magma production (Breivik et al. 2006, 2009; Gernigon et al. 2012). Alternatively, a greater submergence of the source volcano(es) caused by increasing sea level, could have submerged the vents below the water depth required for explosive magma-water interactions (Knox 1996). Marine transgression would improve the conditions for ash preservation within a marine basin, suggesting that the observed decrease in tephra is a true representation of a decrease in explosive volcanic events rather than a lack of preservation. After 49 Ma (sub-phase 2d) no ash associated with the opening of the NAIP is found preserved in the NSB, suggesting that this was the end of the large-scale explosive volcanic activity (Jacqué & Thouvenin 1975).

3.2.1 Late Palaeocene to Early Eocene stratigraphy of the North Sea Basin

The Late Palaeocene to Early Eocene stratigraphy of the UKCS NSB includes the Montrose, Moray, and Stronsay groups (Figure 3-4; Knox & Holloway 1992); which correspond to the Rogaland, Hordaland and Nordaland groups of the NOR NSB respectively (Deegan & Scull 1977). Here, special interest is given to the Moray

Group and its lateral equivalents as these include the Early Eocene tuffs of the BF that form the focus of this investigation.

The Moray Group comprises sediments that were deposited during the Late Palaeocene to Early Eocene in an anoxic marine environment during a time of progressing marine transgression (Deegan & Scull 1977; Mudge & Copestake 1992a). The Moray Group is 'dominated by dark grey to brownish grey, carbonaceous, often laminated and silty claystones, (which) contrasts with the non-laminated claystones of the underlying Montrose Group' (Mudge & Copestake 1992a). The Group includes the Dornoch, Sele and Balder formations, along with their equivalent members, for example, the Beaulieu Member of the BF (Figure 3-4; Knox & Holloway 1992). The Moray Group reaches 650 m thick in the Beryl Embayment where local sand bodies are present (Mudge & Copestake 1992a). In contrast the Group is only 50 - 150 m thick in the Viking Graben (Mudge & Copestake 1992a). A comparison of the wire-line response and interpreted lithologies present can be seen in Figure 3-5. The Group typically thickens where local sand bodies are present, for example the Odin and Beaulieu members of the BF present in UKCS wells 9/18a-4 and 8/27-1, respectively (Figure 3-5; Mudge & Copestake 1992a).

Deposition of Palaeogene sediments in the NSB was controlled by periods of marine regression and transgression (Deegan & Scull 1977). Episodes of uplift associated with magmatism in the NAIP and impact of the proto-Icelandic plume beneath E Greenland (Knox 1996) likely resulted in marine regression; for example, uplift occurred in the northern NSB in the Late Palaeocene (Mudge & Bliss 1983; Nadin et al. 1997; Breivik et al. 2006). Thus, the tectonic regime associated with plume impact, rifting, and sea-floor spreading during the separation of Greenland from NW Europe, influenced cycles of marine regression and transgression and therefore influenced sedimentation in the NSB.

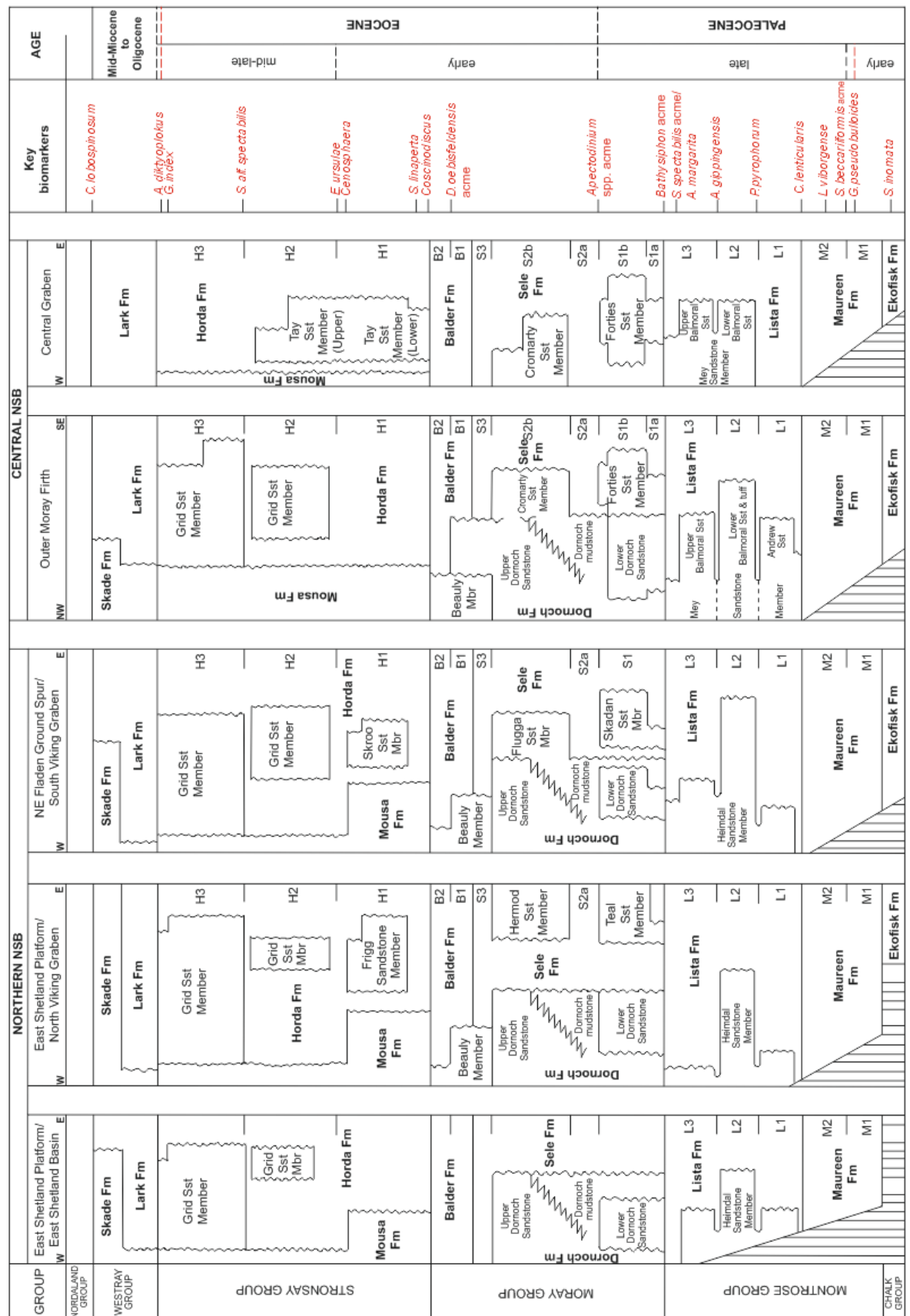


Figure 3-4 Lithostratigraphy of the UKCS central and northern NSB, as proposed by Knox & Holloway (1992).

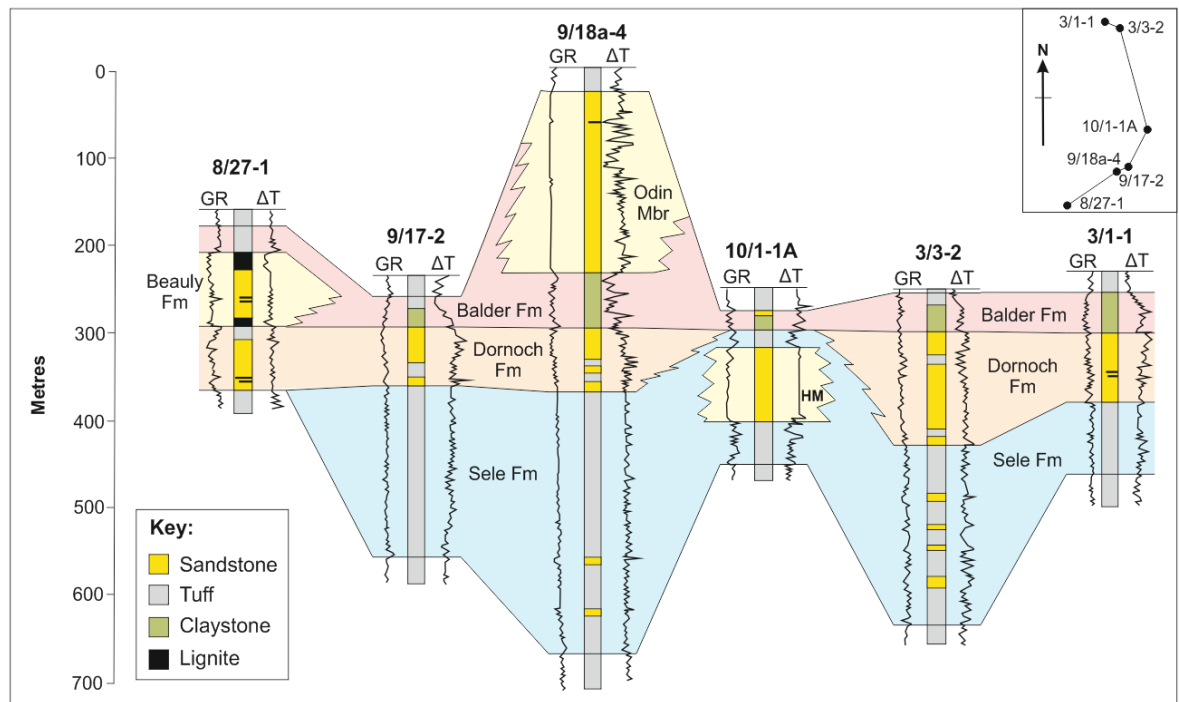


Figure 3-5 Well correlation for lithostratigraphy, gamma-ray response and sonic log of the Moray Group in the northern NSB. HM: Hermod Member (From Mudge & Copestake 1992a).

The NSB became partially or completely isolated from open marine circulation during the Late Paleocene uplift and marine regression (Knox & Harland 1979; Mudge & Bliss 1983; Mudge & Copestake 1992a), which restricted the sea to the central part of the basin (Knox & Harland 1979). This likely coincided with sub-phase 2a of volcanic activity in the NAIP (Knox & Morton 1983; Ali & Jolley 1996). Restricted ocean circulation in the NSB at this time likely led to the development of anoxic bottom waters, as shown by a low-diversity of dinocyst and macrofaunal assemblages within the corresponding strata (Knox & Harland 1979; Morton & Knox 1990; Mudge & Bujak 1994, 1996; Knox 1996). A marine transgression followed in the Early Eocene (NP10 - NP11), allowing the re-establishment of full marine circulation (Jacqué & Thouvenin 1975; Knox & Harland 1979; Mudge & Bliss 1983; Waagstein & Heilmann-Clausen 1995; Smallwood & Gill 2002; Jolley & Bell 2002), and the development of deep-marine conditions (Knox & Morton 1983; Mudge & Copestake 1992a). This transgression may be associated with subsidence of NW Europe following the initiation of sea-floor spreading and stabilisation of the proto-Icelandic mantle plume (Knox & Morton 1983; Knox 1996; Nadin et al. 1997; Breivik et al. 2006). This marine transgression occurred throughout BF-time and is associated with volcanic sub-phase 2b (Knox & Morton 1983).

3.2.2 The Balder Formation

The Sele and Dornoch formations, which are lateral equivalents, underlie the BF (Figure 3-4; Knox & Holloway 1992). The Dornoch Formation comprises deltaic sandstones and submarine fan sediments, and the Sele Formation is comprised of hemipelagic siltstones and claystones with minor amounts of tuff (Deegan & Scull 1977; Mudge & Bliss 1983; Knox & Morton 1988; Mudge & Copestake 1992a; Knox 1996). The tuffs of the Sele Formation are basaltic to rhyolitic in composition and have been correlated with the negative ash series of the Danish mo-clay Formation (Lott et al. 1983; Knox & Morton 1988; Morton & Knox 1990), and the products of the sub-phase 2a volcanism of Knox & Morton (1983).

The contact between the Sele Formation and the BF is shown on seismic profiles to represent an angular unconformity (Mudge & Bliss 1983; Smallwood & Gill 2002). At the contact there is a change to high sonic velocity and resistivity and low gamma-ray response in downhole logs, which corresponds to the abrupt increase in basaltic tuff content at the base of the BF (Malm et al. 1984; Mudge & Copestake 1992a). Elsewhere in the NSB, such as in the East Shetland Basin, East Shetland Platform and Beryl Embayment, the BF lies directly on top of sandstones of the Dornoch Formation (Mudge & Copestake 1992a).

Deposition of the BF in the Early Eocene was controlled by tectonic activity related to the opening of the NE Atlantic Ocean (Lott et al. 1983; Haaland et al. 2000). The BF is composed of hemipelagic claystone, tuff, sandstone, siltstone and localised thin beds of limestone (Mudge & Copestake 1992a; Dmitrieva et al. 2012). The Formation ranges in thickness, from 30 - 60 m in the Central and Viking grabens, to >270 m locally within the Moray Firth Basin and Beryl Embayment (Mudge & Bujak 1996). The Beaulieu Member (Figure 3-4) is present in the west and comprises deltaic sandstones and lignites (Deegan & Scull 1977; Mudge & Copestake 1992a). The Odin Member is another sandstone unit, and occurs in the Viking Basin and Beryl Embayment, and parts of the Moray Firth Basin (Knox & Morton 1983; Mudge & Bliss 1983; Mudge & Copestake 1992a; Mudge & Bujak 1996; Mudge & Jones 2004). Except for the Odin Member, the BF is considered to be absent from the stratigraphy of the Moray Firth Basin (Knox & Morton 1983; Mudge & Bliss 1983). The sandstones of the Odin Member have

been interpreted as deltaic deposits similar to those of the Beaulieu Member (Mudge & Copestake 1992a; Mudge & Bujak 1994; Mudge & Jones 2004). A deltaic depositional setting for these areas contrasts to the depositional setting interpreted for the rest of the NSB BF, which most likely involved hemipelagic deposition from turbidity currents in a deeper marine environment (Pedersen et al. 1975; Knox & Morton 1988; Neal et al. 1996; Mudge & Jones 2004; Obst et al. 2015; Carriol et al. 2016). In the rest of the NSB, the BF has a relatively uniform thickness, which has led some authors to suggest that it was mainly deposited during a period of decreased uplift of the sediment source rocks of the surrounding landmasses, including the Scottish Highlands, Orkney and Shetland Islands (Knox & Morton 1983; Mudge & Bliss 1983; Knox & Morton 1988). This cessation in uplift may have been caused by the transfer of crustal tension as sea-floor spreading began in the NE Atlantic (Knox & Morton 1983; Knox & Morton 1988; Breivik et al. 2009).

The rocks of the BF can be divided into two units based on the abundance of tuff; the lower part of the Formation contains abundant tuff beds whereas the upper part contains little or no tuff (Knox & Morton 1983; Roberts et al. 1984) and, instead, is dominated by high-gamma-ray response claystones (Mudge & Bujak 1996). The lower BF contains more than two hundred tuff beds (Knox & Morton 1988) and represents the main tephra-rich sequence of the NSB, which is related to the most violent period of volcanic activity (sub-phase 2b) during formation of the NAIP (Pedersen et al. 1975; Deegan & Scull 1977; Pedersen & Jørgensen 1981; Knox & Morton 1983; Roberts et al. 1984; Knox & Morton 1988; Morton & Knox 1990; Larsen et al. 2003; Brooks 2006; Obst et al. 2015; Carriol et al. 2016). These tuffs are almost entirely of tholeiitic basalt composition, except for two rhyolitic tuffs (Norin 1941; Pedersen et al. 1975; Pedersen & Jørgensen 1981; Roberts et al. 1984; Knox & Morton 1988; Morton & Knox 1990; Elliott et al. 1992; Knox 1996; Larsen et al. 2003; Brooks 2006; Gernigon et al. 2012; Obst et al. 2015; Watson et al. 2017). The tuffs of the BF are closely spaced and generally have a uniform thickness; ranging from 0.1 to 28 cm thick (Malm et al. 1984; Knox & Morton 1988). A thickness of 28 cm is thought to have been produced by reworking of pyroclastic deposits, as wind-transported water-lain tephra is unlikely to reach this thickness at such distal locations (Knox & Morton 1988). The tuffs are commonly normally graded, with a sharp lower boundary,

and are interbedded with claystone (Malm et al. 1984; Knox & Morton 1988). Cores from the NSB reveal that the BF commonly contains more than 100 tuff beds (Knox & Morton 1983; Malm et al. 1984; Morton & Knox 1990; Haaland et al. 2000), achieving more than 200 tuffs in Well 16/7a-2 (Morton & Knox 1990).

A yellow discolouration is present at the base of many of the tuffs that could be due to calcite cementation (Haaland et al. 2000). Some soft-sediment deformation features are also preserved (Malm et al. 1984), suggesting that reworking has influenced the deposition of some of the tuffs. However, most of the tuffs are undisturbed and of uniform thickness (Malm et al. 1984; Morton & Knox 1988). The generally undisturbed nature of these deposits suggests that deposition occurred in an anoxic environment that did not support the presence of burrowing organisms, or, that deposition of the tuffs was rapid enough to inhibit bioturbation (Pedersen & Jørgensen 1981; Mudge & Bliss 1983; Elliott et al. 1992; Mudge & Copestake 1992; Obst et al. 2015; Carriol et al. 2016). An anoxic marine environment is supported by the low diversity of dinocyst and microfaunal assemblages (Knox & Harland 1979; Mudge & Bujak 1996; Knox 1996) and the presence of restricted micro-flora (Knox & Harland 1979; Knox 1996). This is also evidence that the North Sea was relatively isolated from fully open marine circulation during the Early Eocene (Knox & Harland 1979; Mudge & Copestake 1992, 1992a; Knox 1996; Mudge & Bujak 1996; Carriol et al. 2016).

The BF tuffs are variably altered to smectite, chlorite and palagonite (Knox & Morton 1983; Malm et al. 1984; Knox & Morton 1988; Morton & Knox 1990; Jolley & Morton 1992) but are generally less altered compared to the tuffs of the underlying Sele Formation (Knox & Morton 1988). Some alteration of the tuffs within the BF may have resulted in the development of a secondary porosity; which led Malm et al. (1984) to suggest that the lower (tuff-rich) BF may be of reservoir potential.

The tuffs appear to thicken and become coarser-grained towards the north, which may suggest that their source lay towards the north and the Møre Basin (Figure 3-2; Malm et al. 1984; Knox & Morton 1988). Sixty-two, 2-12 cm thick altered tuffs have been identified in the BF of UKCS offshore borehole 81/46A (Lott et al. 1983), compared to the 200 tuffs preserved elsewhere in the basin.

This could be due to the closer proximity of Well 81/46A to land at the time of deposition, which allowed for erosion or non-deposition of the original ash. There is also evidence for bioturbation within these deposits, which may have led to the loss of thinner ash layers (Lott et al. 1983).

The presence of fewer tuff beds within the Eocene succession of the southern NSB, including offshore borehole 81/46A, is further supported by observations of core material studied by Rhys (1974), who observed that the BF below latitude 55° N contains only sporadic tuff units. A source of pyroclastic material to the north of the NSB is therefore implied (e.g. Malm et al. 1984; Knox & Morton 1988). However, Malm et al. (1984) compared the thickness of deposits in the equivalent Danish ash series to NSB Well 25/10-1 and concluded that the thickness trends did not match, suggesting that the tephra of the Danish ash-series came from a separate source. This was later disputed by Knox & Morton (1988) who suggested that slight thickness variations in the tuffs between the NSB and Denmark could have been caused by marine currents during deposition. They also argued that the deposits contain the same plagioclase and feldspar glass inclusion compositions, proving that the ashes originated from the same source (Knox & Morton 1988). Morton & Knox (1990) argued that the compositional and stratigraphical uniformity of the tuffs of the BF, and its lateral equivalents, 'argues against involvement of several intra-basinal volcanoes' being the source of the tephra.

Analysis of the grain characteristics of the BF tuffs by Knox & Morton (1983) show that well-defined glassy shards are not abundant within the NSB. However, some grain characteristics can still be determined, for example, Malm et al. (1984) identified grains of ash with irregular shapes, arcuate grain-boundaries and locally abundant vesicles. It has been suggested by several authors (Malm et al. 1984; Knox & Morton 1988; Haaland et al. 2000) that these characteristics are typical of the grains produced by hydrovolcanic processes. In support of this interpretation, Haaland et al. (2000) note that the BF tuffs contain two main pyroclastic clast types: 1. irregularly-shaped, microcrystalline, vesicular granules and, 2. vitric shards. The first clast type can form via shallow submarine eruptions, similar to Surtseyan hydrovolcanic eruptions (Pedersen & Jørgensen 1981; Haaland et al. 2000). Vitric shards can also form during hydrovolcanic

eruptions due to rapid quenching and granulation (Haaland et al. 2000). The presence of large amounts of fine-ash is indicative of explosive volcanism, but basaltic magmas rarely present such explosive behaviour, suggesting that another factor such as magma-water interactions likely occurred (e.g. Williams 1983; Morton & Knox 1990; Elliott et al. 1992; Houghton et al. 2004; Parfitt 2004; Carey et al. 2007; Constantini et al. 2009; Pérez et al. 2009; Constantini et al. 2010; Goepfert & Gardner 2010; Freda et al. 2011).

The composition of the BF tuffs has been affected by the varying degree of alteration that the deposits have undergone. Therefore, only immobile trace elements can be used for analysis and comparison of the chemical signatures of these deposits. Analysis of the immobile trace element composition of tuffs from NOR well 30/2-1 show that they have a tholeiitic basalt composition that is transitional between Within Plate Basalt (WPB) and Mid Ocean Ridge Basalt (MORB; Figure 3-6; Malm et al. 1984; Knox & Morton 1988; Haaland et al. 2000). This suggests that these ashes came from a source that was located within a transitional location between a continental and oceanic crustal setting (Malm et al. 1984); this may be evidence to support the theory that these ashes were produced in the last stage of explosive volcanism as the tectonic regime changed from continental rifting to the onset of sea-floor spreading (Hallam 1972; Knox & Harland 1979; Knox & Morton 1983; Knox 1996; Ritchie & Hitchen 1996; Nadin et al. 1997; Haaland et al. 2000; Torsvik et al. 2001; Larsen et al. 2003; Jolley & Widdowson 2005; Ross et al. 2005; Breivik et al. 2006; Brooks 2006; Storey et al. 2007; Brunstad et al. 2008; Breivik et al. 2009; Gernigon et al. 2012). Differences in composition between the WPB and MORB signatures (Figure 3-6) could also imply that multiple sources were responsible for producing the BF tuffs.

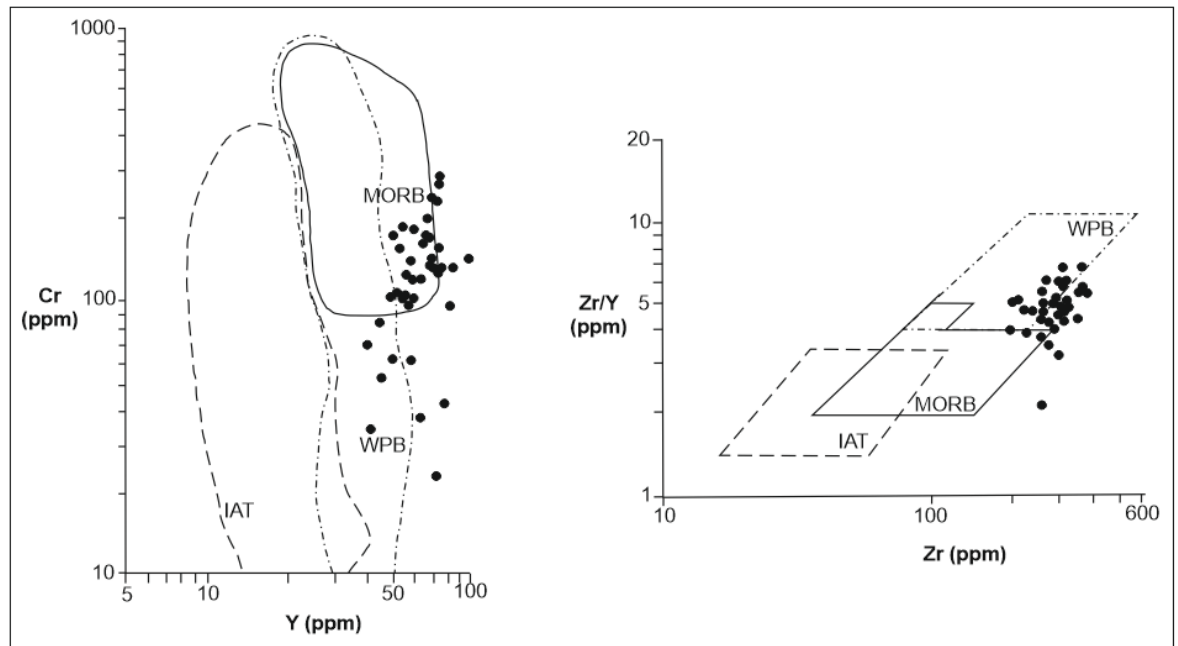


Figure 3-6 Trace element compositional discrimination diagrams for BF tuffs from NOR30/2-1. The Cr versus Y and Zr/Y versus Zr plots show that the BF tuffs have a chemical composition akin to Within Plate Basalt (WPB) and Mid-Ocean Ridge Basalt (MORB; from Malm et al. 1984).

Further geochemical analysis of the BF tuffs shows that they have low La/Ta ratios, which are more typical of Enriched Mid Ocean Ridge Basalt (EMORB) or Ocean Island Basalt (OIB) and which contrasts with the known composition of many of the volcanic centres of the NAIP (Morton & Knox 1990). However, this compositional distinction could link the tuffs to volcanism associated with the proto-Icelandic plume or an area of volcanism somewhere along the opening rift of the NE Atlantic, where the source vents have subsequently been destroyed (e.g. Larsen et al. 2003; Larsen, pers. coms. 2015).

An unconformity is present at the top of the BF that represents a period of erosion (Mudge & Bliss 1983). The top of the BF is also represented by a 'distinctive gamma-ray and sonic log marker (and a) strong, un-faulted seismic response' (Joy 1996). A decrease in gamma-ray response indicates where the high-gamma claystone of the upper BF is overlain by the low-gamma Hordaland Group (Haaland et al. 2000).

3.3 Aims and objectives

The nature of the BF can, in part, be determined from direct observations of core collected from drilling operations in the NSB. Therefore, the aims of this study are to assess the nature of the BF through logging of core and detailed study of thin-sections, and a comparison of core with wire-line data from the NSB. Analysis of this material can then be compared to additional data, such as, wire-line data, from other wells to extend our understanding of the nature of the BF into areas where core is not available, for example in the FSB (see Appendix I).

An important objective is to assess the presence of volcanic material within the BF, as reported in the literature. The presence of volcanic material was assessed from SEM data and image analysis, to try and identify differences between ‘primary’ pyroclastic and reworked volcanoclastic materials. Morphological features of original ash in the BF were analysed with SEM and image analysis techniques to provide data for the interpretation of the eruption processes that formed, transported and deposited the original pyroclastic ashes. Following interpretation of the results and the possible identification of eruption processes the final aim is to consider the possible location of source vents related to volcanism in the NAIP and NW Europe during the Early Eocene. These interpretations have implications for our understanding of the mechanisms responsible for highly explosive basaltic eruptions, which will also be discussed.

3.4 Methods

Core taken through the NSB BF was identified from previous literature, lists of core and well information on the BGS (British Geological Survey) and NPD (Norwegian Petroleum Directorate) websites and general government lists of well information for released wells in the UK sector. Available core could then be identified on the BGS and NPD websites and an initial study could be carried out using high quality online images of the cores, where available.

Lithologic logging of the core was conducted at the BGS core-store in Keyworth, Nottingham, and the NPD core-store and Weatherford Laboratories, Stavanger, Norway. Sampling of the UKCS core was carried out at the BGS core-store.

Sampling of the Norwegian core was carried out at Weatherford Laboratories with permission from STATOIL (wells 25/11-17, 30/2-1), and Aker BP (Well 25/7-5).

Logging was carried out on a mm-scale for each core. Photographs of the core and features of interest, such as bedding or sedimentary structures, were recorded alongside full rock descriptions. Samples were taken at selected intervals based on significant-looking units and the suspected presence of tuffs, with the aim to sample each rock-type and a representative suit of the tuffs. Sampling was not possible at the NPD either due to the poor condition of the core or due to the core being contained in blocks of resin.

Polished thin-sections of the BGS cores were produced from small samples at the University of Glasgow (Table 3-1), and Norwegian samples were impregnated with blue resin and thin-sectioned by ALS Petrography Ltd (Table 3-2). Thin-sections were studied under a petrographic microscope before being carbon coated and studied at a greater magnification under high-vacuum on a Zeiss SEM (Scanning Electron Microscope) at the University of Glasgow. Image analysis was carried out to gain quantitative data on grain-size and morphology, sorting and sediment composition using ImageJ software. More detail on thin-section preparation, SEM and image analysis processes can be found in section 1.3 Methods.

Well number	Depth (ft)	Sample number	Sectioned?
29/05a-7	9625'5	SSK56334	
	9605	SSK56335	Yes
	9577	SSK56336	Yes
	9588'10	SSK56337	Yes
	9597'2	SSK56338	
	9601'5	SSK56339	
	9627	SSK56340	
	9604'4	SSK56341	Yes
	9608'8	SSK56342	
	9621'2	SSK56374	Yes
	9610'1	SSK56375	Yes
	9596'1	SSK56376	
	9578	SSK56377	
	9578'3	SSK56378	
	9587'8	SSK56379	Yes
	9724'4	SSK56380	
	9721'7	SSK56381	Yes
	9717'7	SSK56382	
	9711'11	SSK56009	Yes
	9703'8	SSK56010	Yes
22/30a-1	9701'11	SSK56011	
	9704'6	SSK56012	Yes
	9697'5	SSK56013	
	9700	SSK56014	Yes
	9691'10	SSK56015	Yes

Table 3-1 List of samples from UKCS29/05a-7 and UKCS22/30a-1 accessed with permission from the British Geological Survey. Samples that were not sectioned did not survive transport or thin-section preparation.

Well number	Depth (m)	Sample number	Sectioned?
25/11-17	1630.5	001	Yes
	1630.85	002	Yes
	1632.05	003	
	1633.60	004	
	1634.85	005	Yes
	1640.35	006	
	1640.55	007	
30/2-1	1953.35	008	
	1953.45	009	
	1954.25	010	Yes
	1954.45	011	
	1954.70	012	
	1954.95	013	
	1956.33	014	Yes
	1957.68	015	
	1958.63	016A+B	Yes
	1959.40	017	
	1959.85	018A+B	Yes
	1961.62	019	
	1962.10	020	
	1963.35	021	
	1963.86	022A+B	Yes
	1964.35	023	Yes
	1964.63	024	Yes
	1964.62	025	Yes
	1966.05	027	Yes
	1967.78	028A-C	Yes
25/7-5	1978	029	Yes
	1981.28	030	Yes
	1981.48	031	Yes
	1982.40	032	Yes
	1982.85	033A-C	Yes
	1985.66	034	
	1985.82	035	Yes
	1986.36	036	Yes
	1988.48	037	
	1988.73	038	
	1989.28	039A+B	Yes
	1992.40	040	Yes
	1995.03	041	Yes
	1996.70	042	
	1998.92	043A+B	
	1999.57	044	

Table 3-2 List of samples from NOR25/11-17 and NOR30/2-1 accessed with permission from STATOIL, and NOR25/7-5 accessed with permission from Aker BP. Samples that were not sections did were not suitable for thin-sectioning, for example, due to being highly fractured.

3.5 Results

Three wells form the focus of direct observations of the BF from which core was logged and sampled for further analysis, UK Continental Shelf (UKCS): 29/05a-7, and Norwegian-Danish sector (NOR) of the NSB: 25/7-5, 25/11-17, 30/2-1 (Figure 3-2). Samples were analysed from two additional wells; UKCS22/30a-1 and FSB 6104/25-1 (Figure 3-2).

Here, sedimentary logs and rock descriptions for each of the wells will be presented, along with thin-section descriptions and the results of image analysis. Additional wire-line data from the completion well reports will be presented to augment this data set.

3.5.1 Observations of core

The BF is not commonly cored in full, therefore the core that was investigated here only represents a section of the BF and not the entire formation. Type core from other wells (e.g. NOR25/10-1) was also viewed but has not survived storage well enough to be examined in detail. The best-preserved cores are described here.

3.5.1.1 *Well UKCS29/05a-7, 56°50'17.8"N 01°56'32.1"E*

Core of UKCS29/05a-7 (Figure 3-2) is composed of highly interbedded, parallel laminated and massive claystone and siltstone with normal-graded green, yellow, blue and orange tuffs, and siliciclastic sandstones (Figure 3-7, Figure 3-8). Some of the tuffs and sandstones contain cross-stratification (Figure 3-9) and some bed boundaries show evidence of erosional surfaces (Figure 3-9), grain-loading (Figure 3-9), and symmetrical or asymmetrical ripple-structures (Figure 3-10). *Ca.* 3 m of the core contains mixed lithologies that show evidence of the deformation of partially soft sediments likely via slumping (Figure 3-7, Figure 3-11).

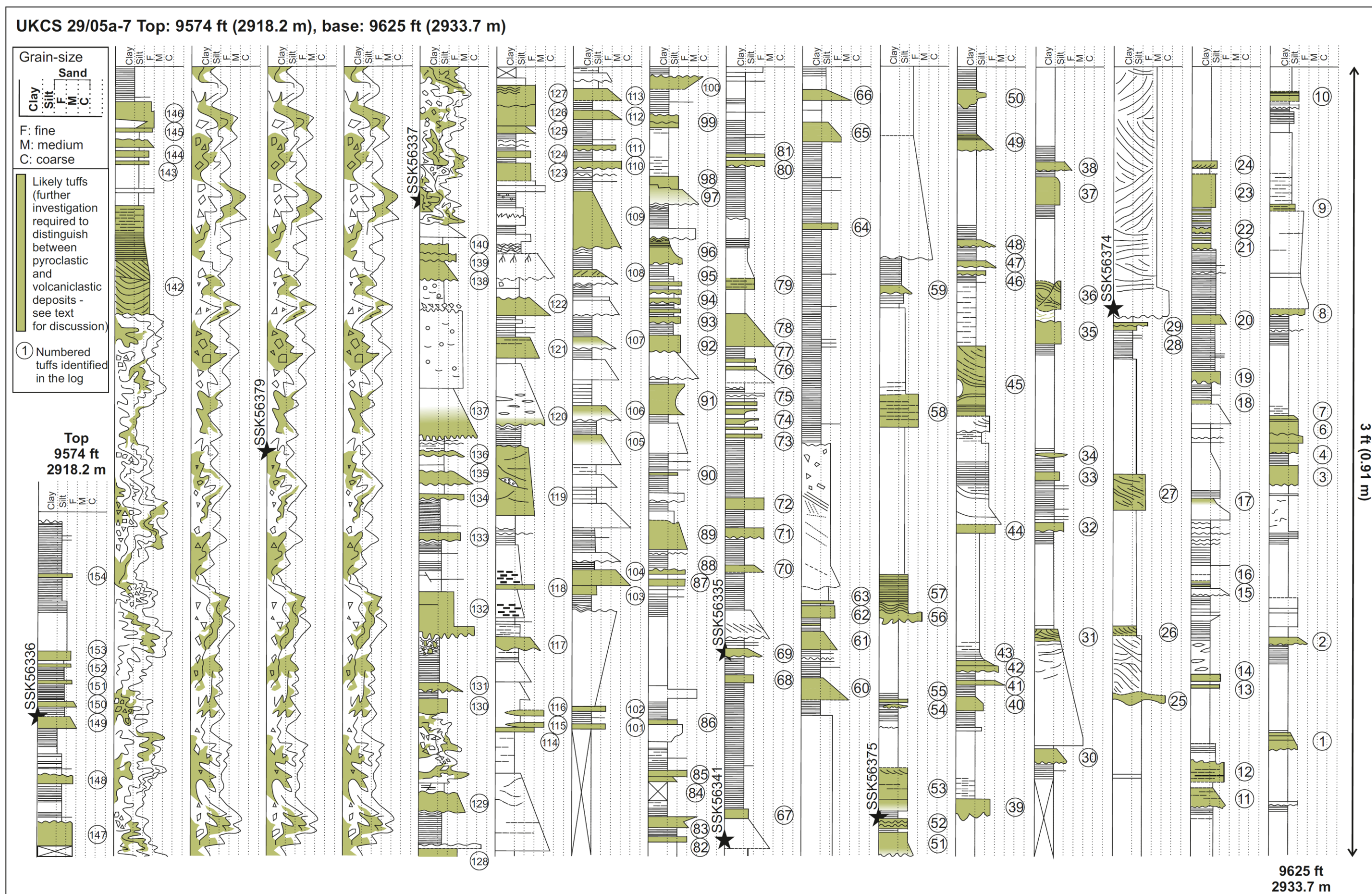


Figure 3-7 Lithological and grain-size log for the Balder Formation of UKCS29/05a-7, 56°50'17.8"N 01°56'32.1"E. Solid stars indicate the location of samples described in the text, white stars show where additional samples were collected that are not discussed further.

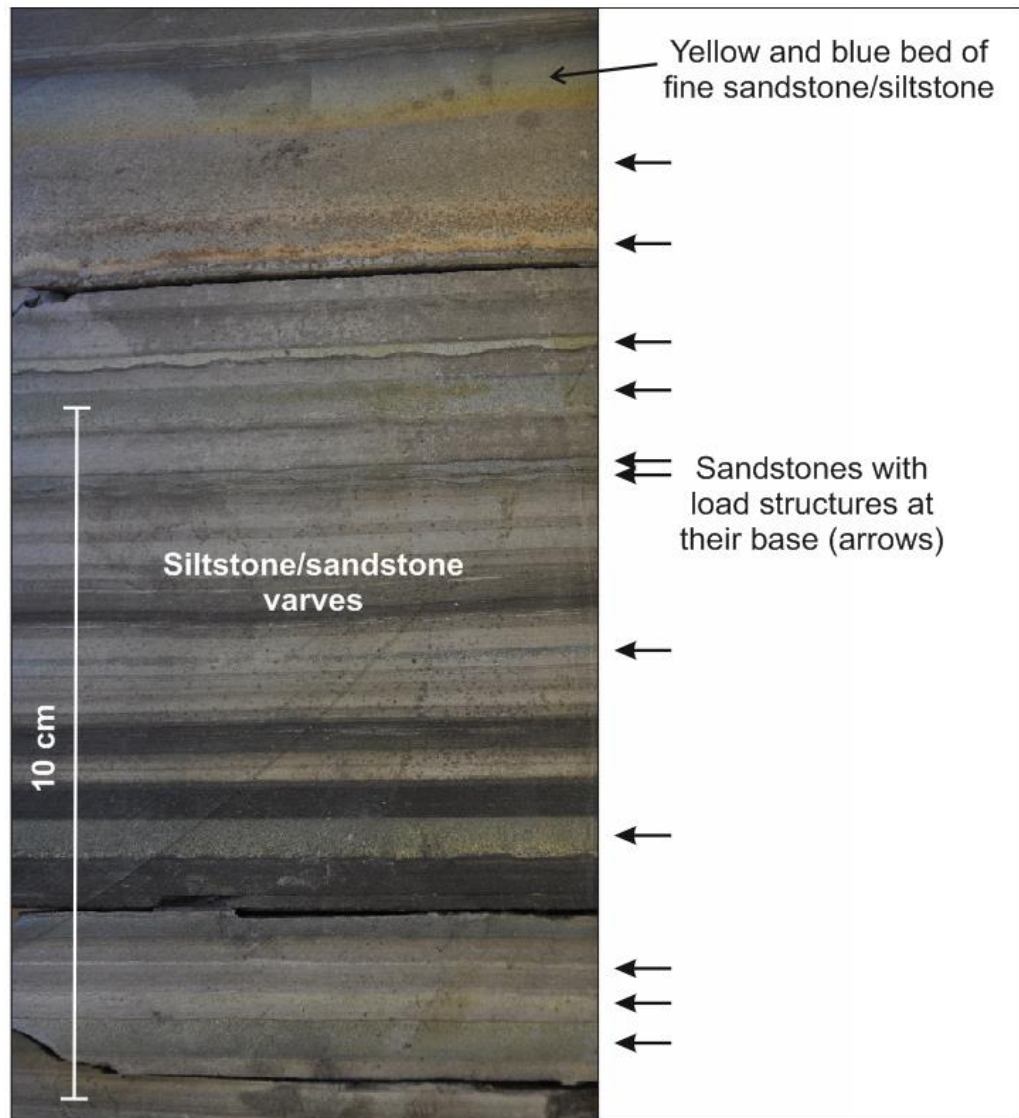


Figure 3-8 Interbedded siltstone/claystone and sandstone in UKCS29/05a-7, core no. 1, 9621 ft depth. The thin beds of sandstone (including volcaniclastic sandstones) vary from a few millimetres in thickness to a couple of centimetres and all have loaded basal contacts, where the coarser/larger grains have sunk into the underlying claystone or siltstone. The fine-grained sandstone/siltstone at the top of this section has a distinctive yellow and blue colouration and is most likely a tuff.

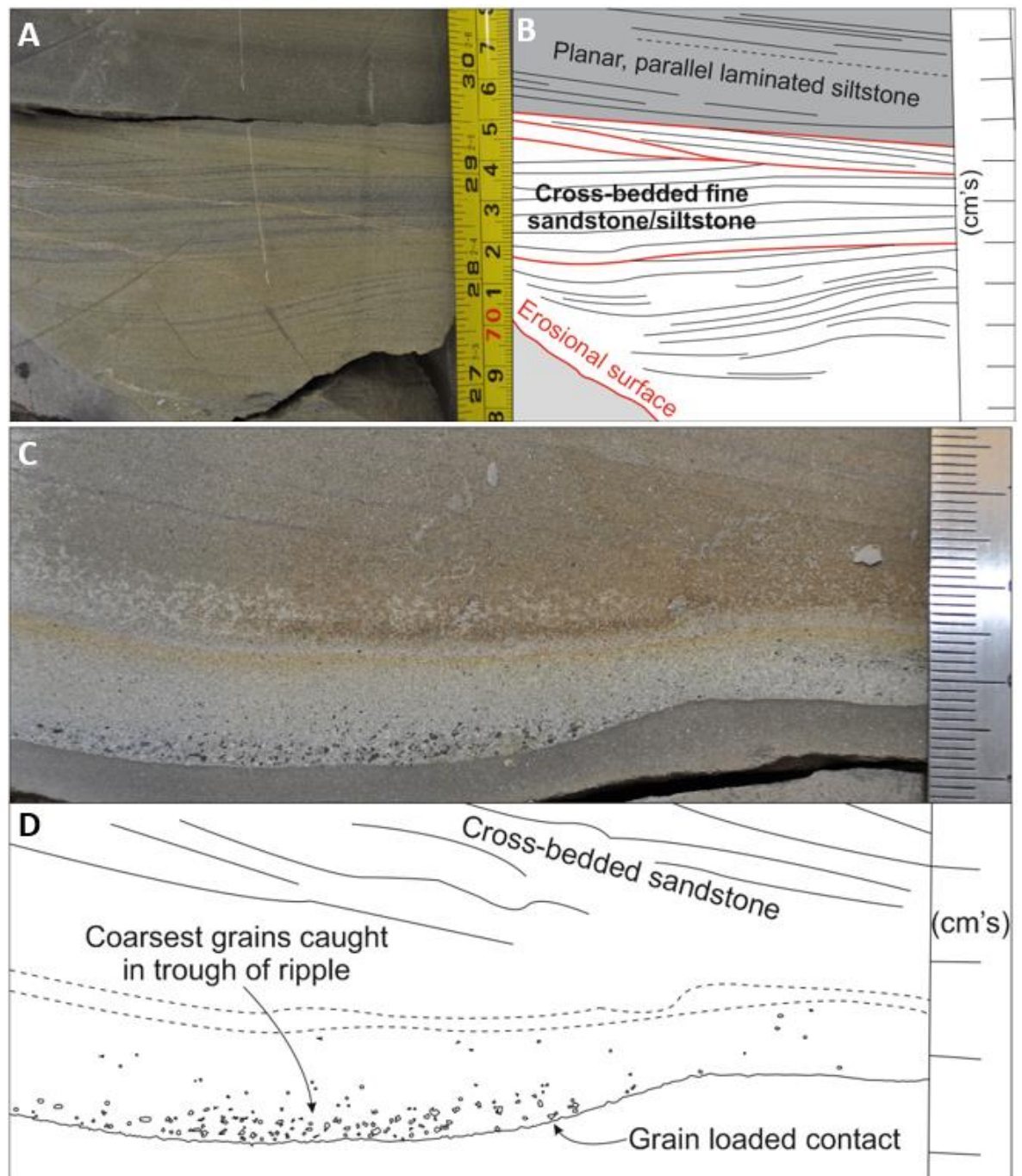


Figure 3-9 Sedimentary features of core from UKCS29/05a-7, core no. 1. A-B) Cross-bedded fine-sandstone/siltstone with erosional surfaces (red) that truncate the cross-beds. Above this unit lies a planar, parallel-laminated siltstone at 9577.7 ft depth. C-D) A ripple structure is preserved at the base of this image, its contact with the overlying sandstone shows evidence of grain-loading, where the coarser grains have sunken into the underlying siltstone/claystone. The coarsest grains of the sandstone are found in the trough of the ripple; at a depth of 9618.2 ft. The olive green units in these images likely represent tuffs, in this case the cross-stratification indicates that these tuffs have been reworked and are volcanoclastic deposits (discussed later).

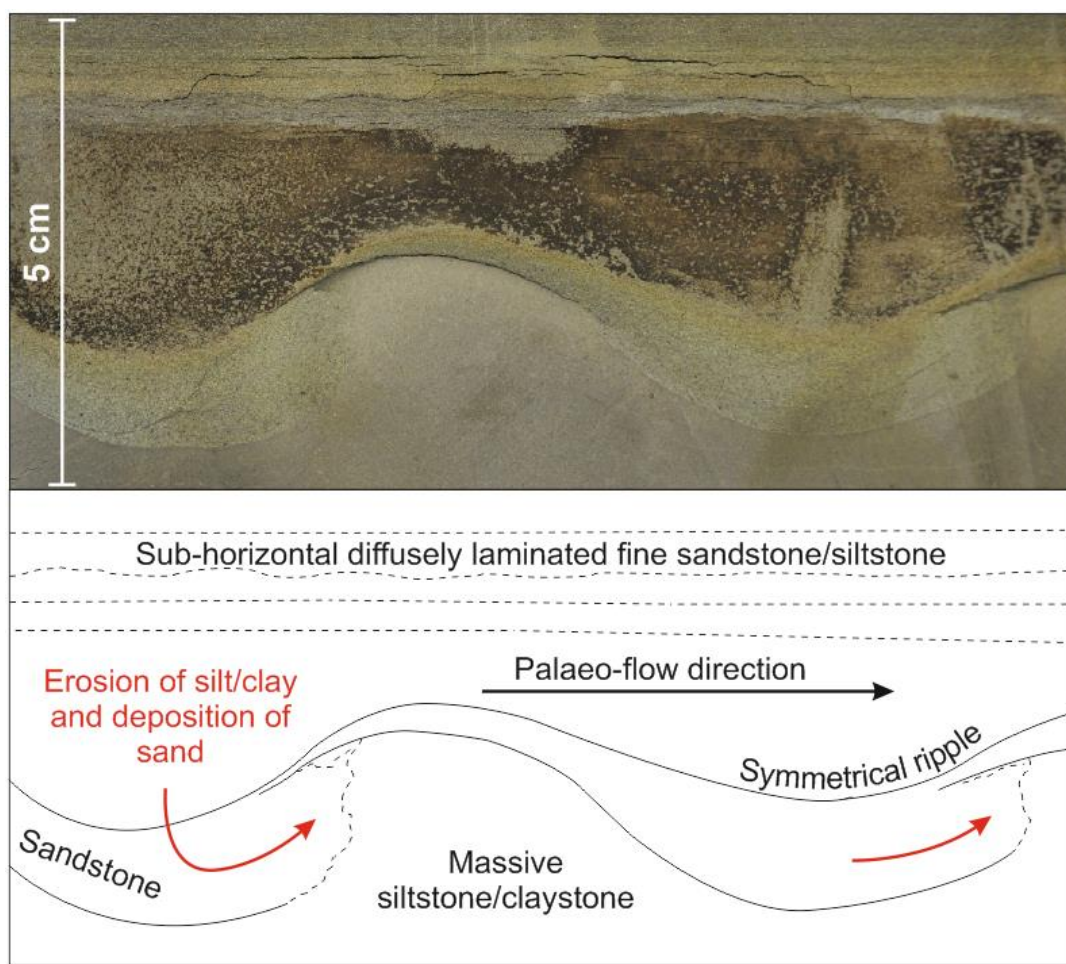


Figure 3-10 Symmetrical ripple with an erosive interior where the original silt/clay has been eroded by a current and replaced by instantaneous deposition of sand, indicating a palaeo-flow direction from left to right across the image; UKCS29/05a-7, core no. 1, 9608.9 ft depth. The olive green sandstones in this section are likely altered basaltic tuffs (discussed later).



Figure 3-11 Deformed siltstone, claystone and sandstone observed in the upper section of UKCS29/05a-7, core no.1, 9582.6 ft depth. The olive green colour of some units likely shows the presence of altered basaltic tuffs.

3.5.1.2 Well NOR25/7-5, 59°29'39.81"N 02°1'3.44"E

The BF of core from NOR25/7-5 (Figure 3-2) is similar to that of UKCS29/05a-7, and contains highly interbedded claystone, siltstone, sandstone and normal graded tuffs (Figure 3-12). The tuffs are characteristically green or blue and commonly grade from medium or fine sandstone to siltstone/claystone (Figure 3-13). Some of the tuffs show larger-scale soft sediment deformation at their base (Figure 3-14, Figure 3-15), and may also contain diffuse bedding and cross-stratification (Figure 3-14). Many of the tuffs have a calcite cement that effervesces with dilute hydrochloric acid. In addition, some tuffs contain patchy-developed interstitial pyrite (Figure 3-15). Most of the interbedded claystones and siltstones are finely parallel laminated and there is no evidence of slump features, or larger-scale deformation, as in UKCS29/05a-7 (Figure 3-11).

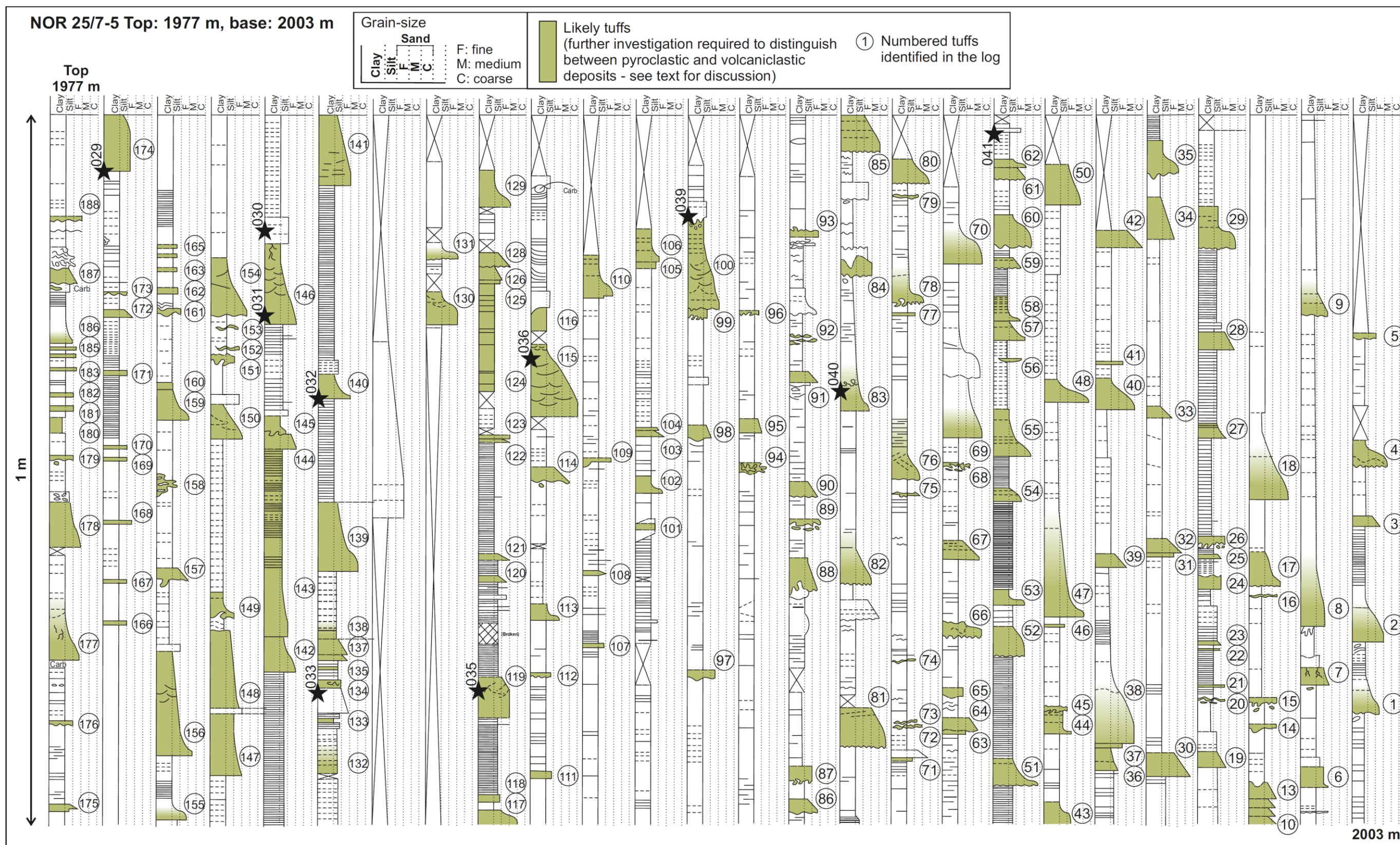


Figure 3-12 Lithological and grain-size log of the Balder Formation of NOR25/7-5, 59°29'39.81"N 02°1'3.44"E. Solid stars indicate the location of samples that are discussed in the text.

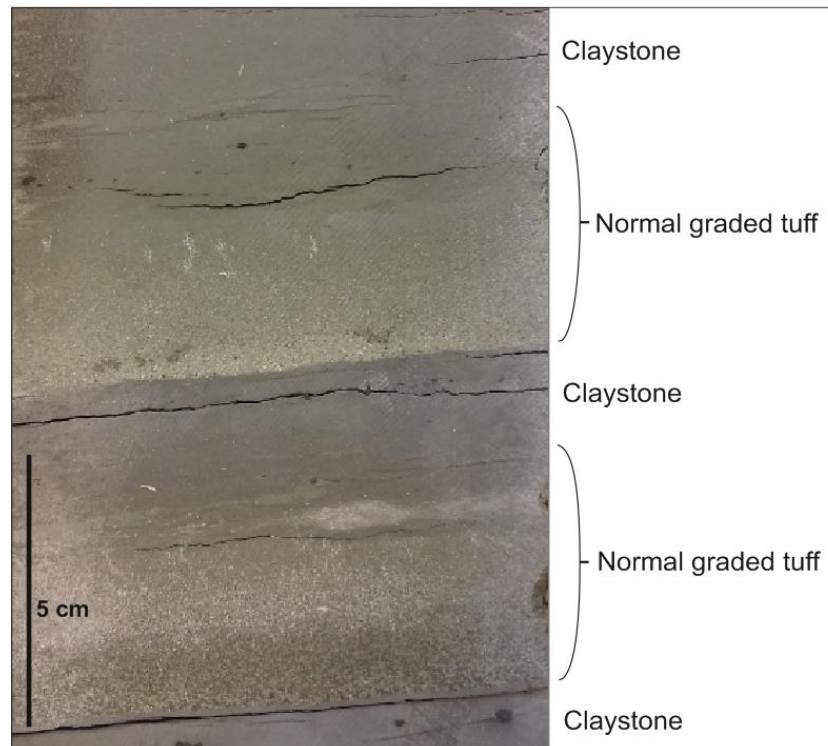


Figure 3-13 Normal graded tuffs interbedded with claystone in NOR25/7-5, core 3, at 1991.7m depth.

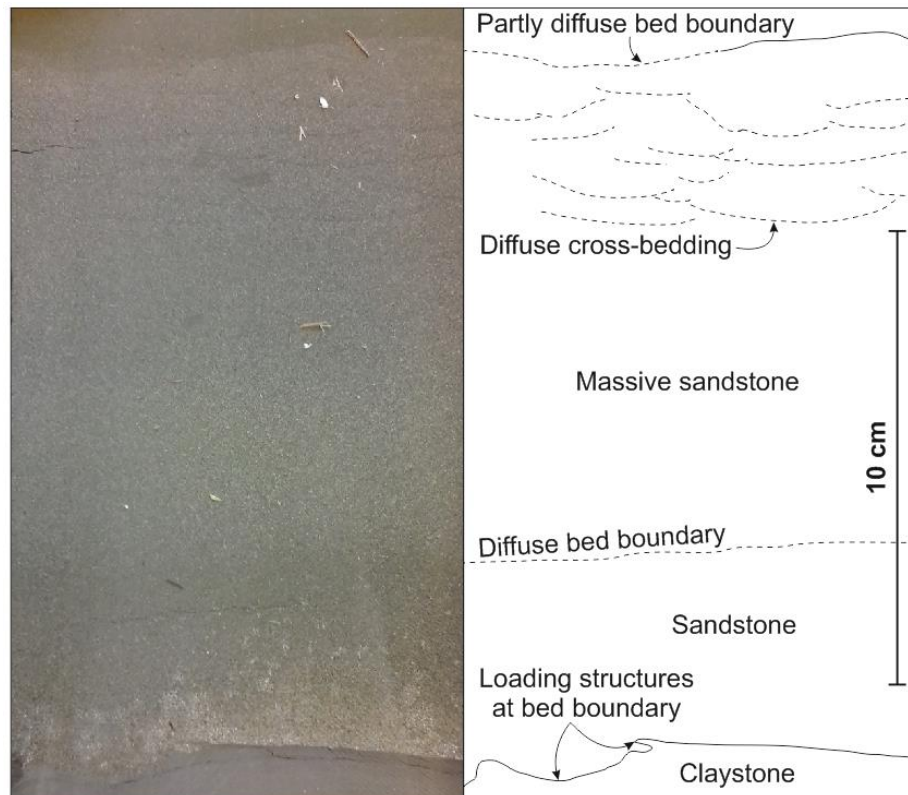


Figure 3-14 Sedimentary structures observed within the core from NOR25/7-5, core 2, at 1979.8 m, including diffuse cross-bedding and loading structures, as well as sharp and diffuse bed boundaries.

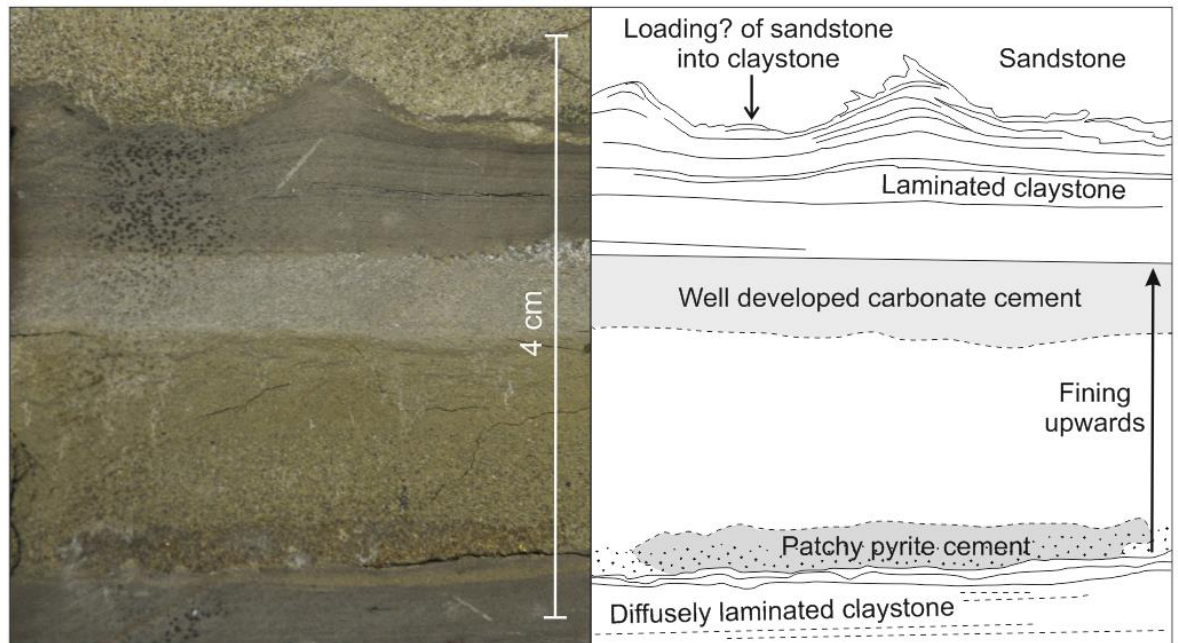


Figure 3-15 Calcite and pyrite cement developed within a green normal graded tuff overlain by laminated claystone in NOR25/7-5, core 3, at 1995.2 m depth. The overlying claystone has been deformed by deposition of the next normal graded tuff (olive-green coarse sandstone).

3.5.1.3 Well NOR25/11-17, 59°3'26.66"N 02°29'6.59"E

The BF of NOR25/11-17 (Figure 3-2) contains two *ca.* 5-6 m thick units of massive (structureless) white medium/coarse-sandstone (Figure 3-17) that appears to be predominantly comprised of quartz grains. Thinly interbedded claystone, siltstone and normal graded tuffs occur between the sandstones, and resemble the nature of the BF observed in all of the other wells. However, there is a greater concentration of normal-graded tuffs (Figure 3-16) between the sandstones of this core, and the base of these is often coarser-grained than the tuffs of the other wells (e.g. Figure 3-18).

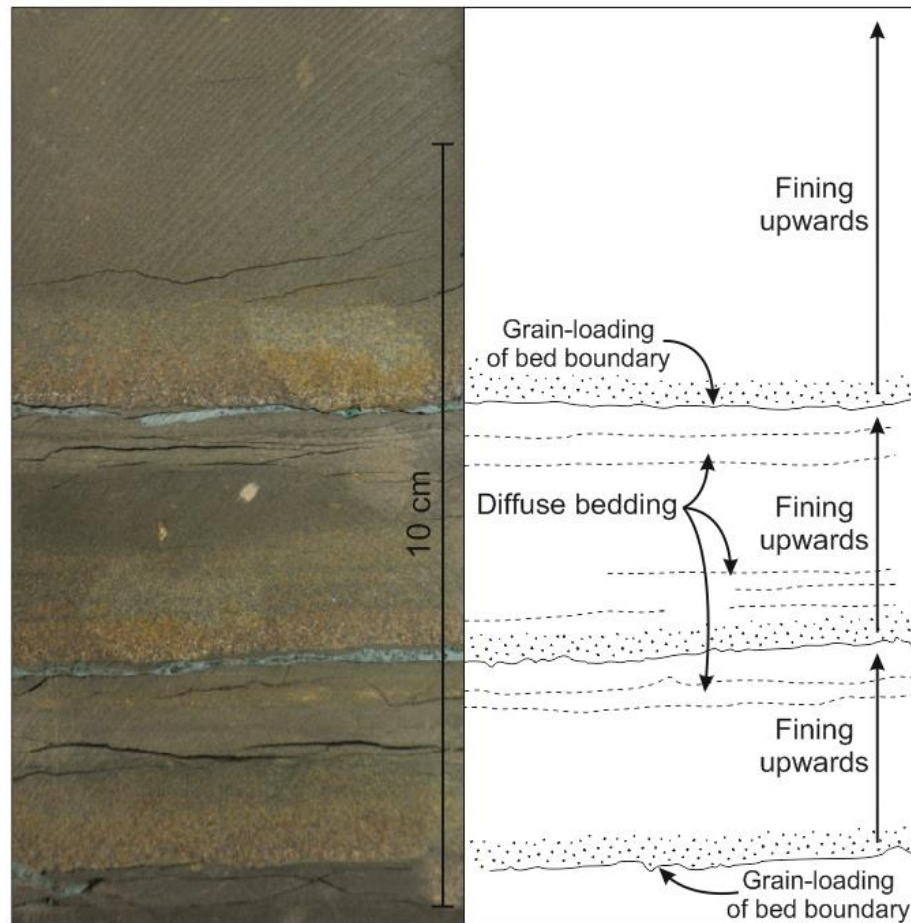


Figure 3-16 Units of fining upwards sandstone to siltstone/claystone with grain-loaded basal contacts and uncommon diffuse bedding or lamination seen in core from NOR25/11-17, core 1, at 1631.8 m. Each of these olive green coloured fining-upwards sequences likely represent normal-graded tuffs (confirmed by petrographic analysis in the following section).

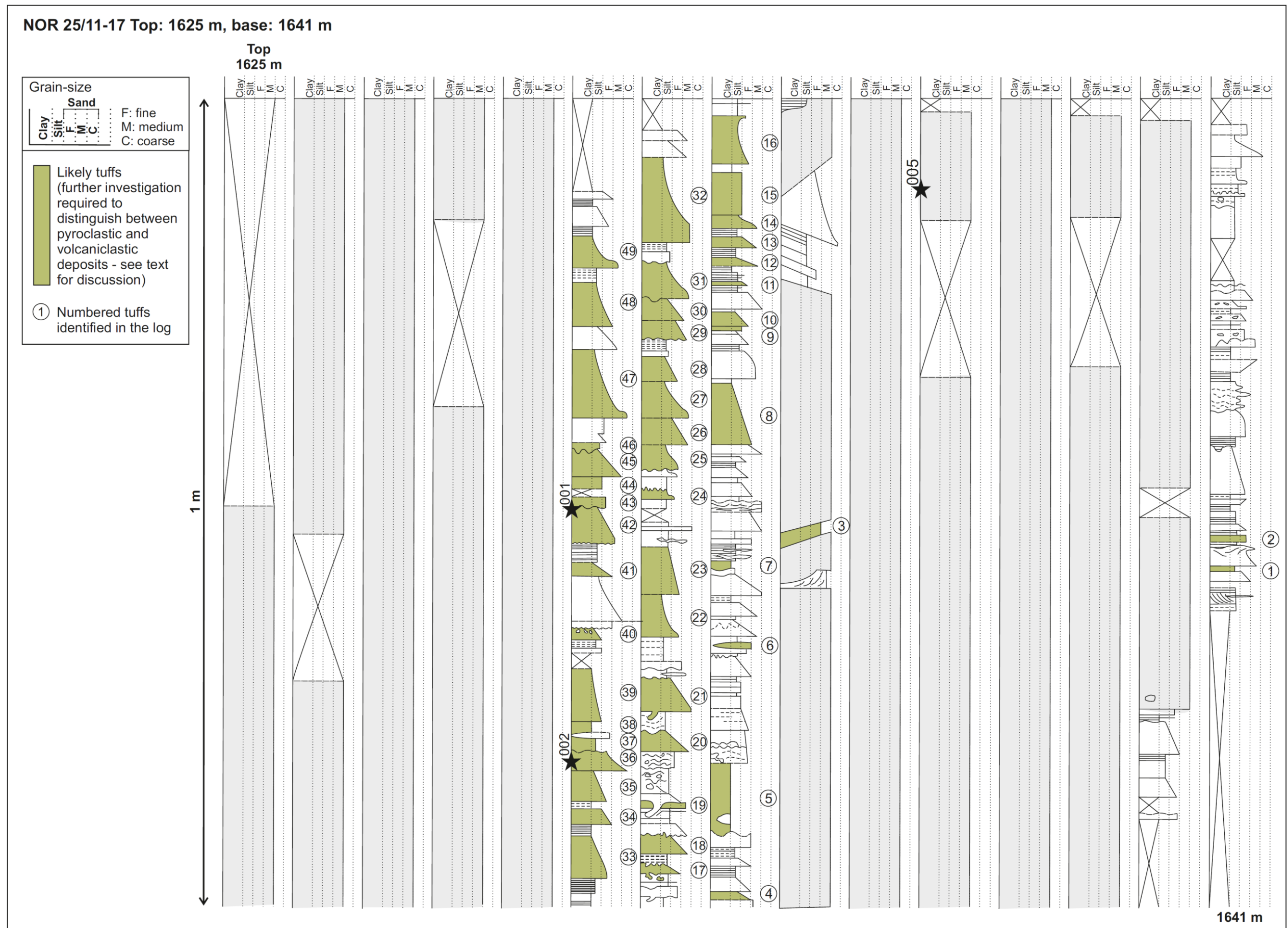


Figure 3-17 Lithologic and grain-type log for Balder Formation core of NOR25/11-17, 59°3'26.66"N 02°29'6.59"E. Solid stars indicate the location of samples that are described in the text

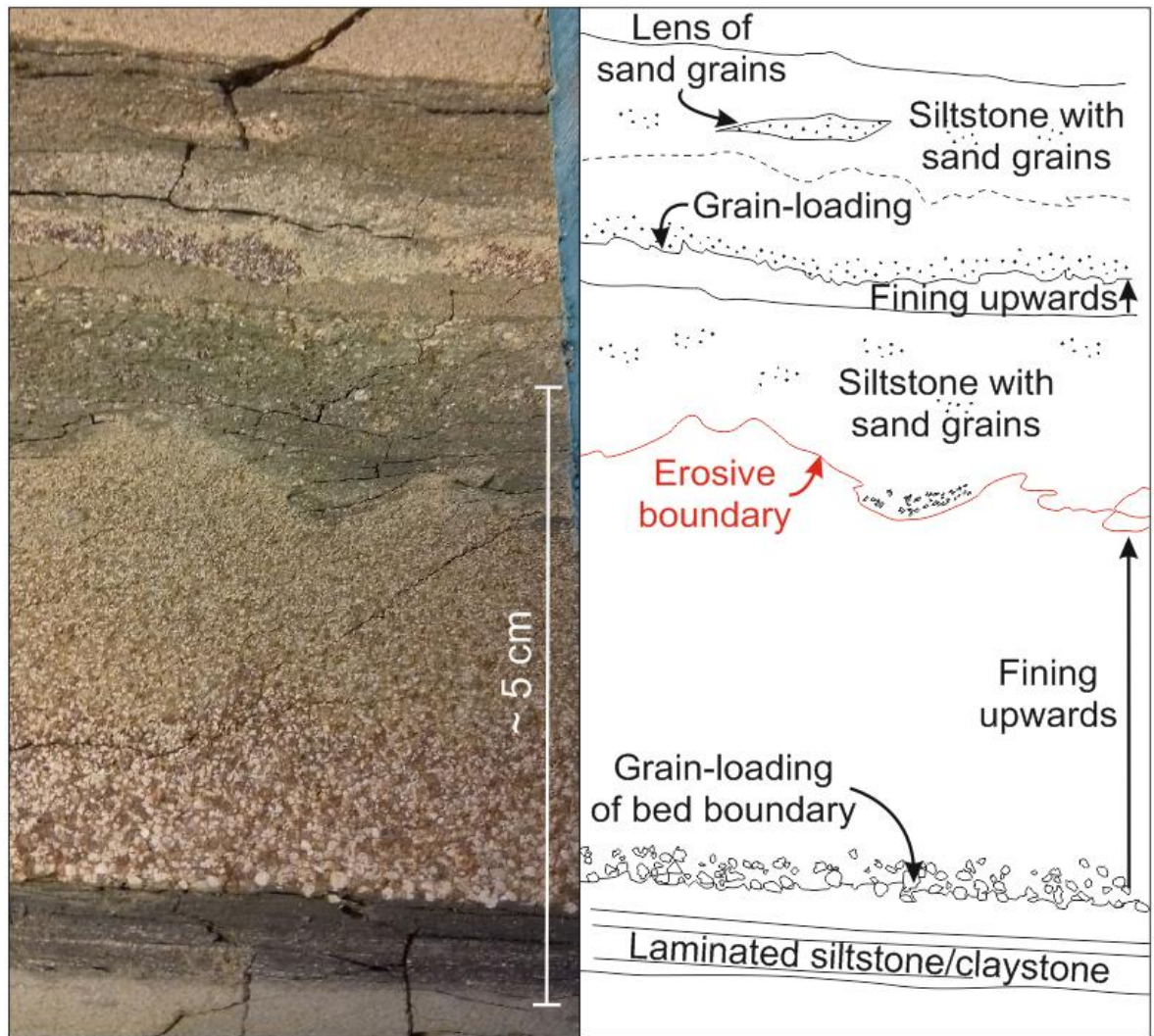


Figure 3-18 Sedimentary features observed in a small (<10 cm) section of core from NOR25/11-17, core 1, at 1630.8 m depth; including, parallel laminated siltstone/claystone to fining-upward sandstone with erosive contacts and grain-loaded bed boundaries. The olive green colouration of the rock likely indicates the presence of altered basaltic volcanic material (tuffs).

Abundant burrow-like features and evidence of soft-sediment deformation are present at some intervals (Figure 3-19), and represent reworking of the coarser-grained units (likely tuffs). These features are more prevalent in this core than the other cores.

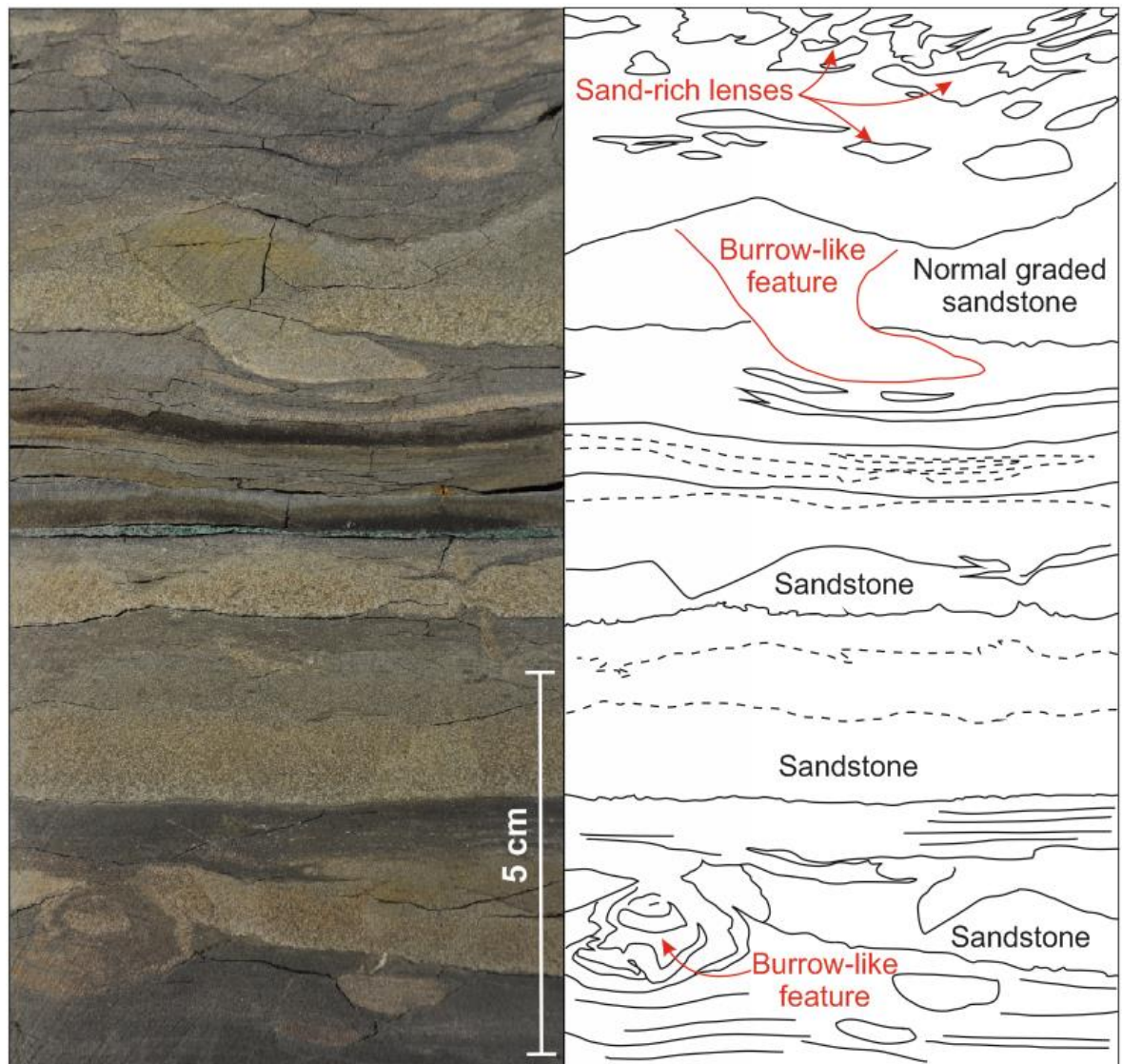


Figure 3-19 Burrow-like features and soft-sediment deformation creating non-uniform bed boundaries within core from NOR25/11-17, core 1, at 1632.9 m depth. The olive green units likely represent tuffs, the burrow-like features in these units show that the tuffs have been, at least partially, reworked.

Many units of this core were not recovered during drilling, with most of this material lost from within the sandstone units. Recovery of the highly interbedded units between the sandstones appears to be more complete.

3.5.1.4 Well NOR30/2-1, 60°52'5.42"N 02°38'49.16"E

Core of NOR30/2-1 (Figure 3-2) is very similar to the core of UKCS29/05a-7. It is characteristically highly interbedded and composed of parallel-laminated claystone and siltstone with normal-graded green tuffs (Figure 3-20). Like UKCS29/05a-7 (Figure 3-11) this core also contains sections of deformed beds that resemble slump structures (Figure 3-21).

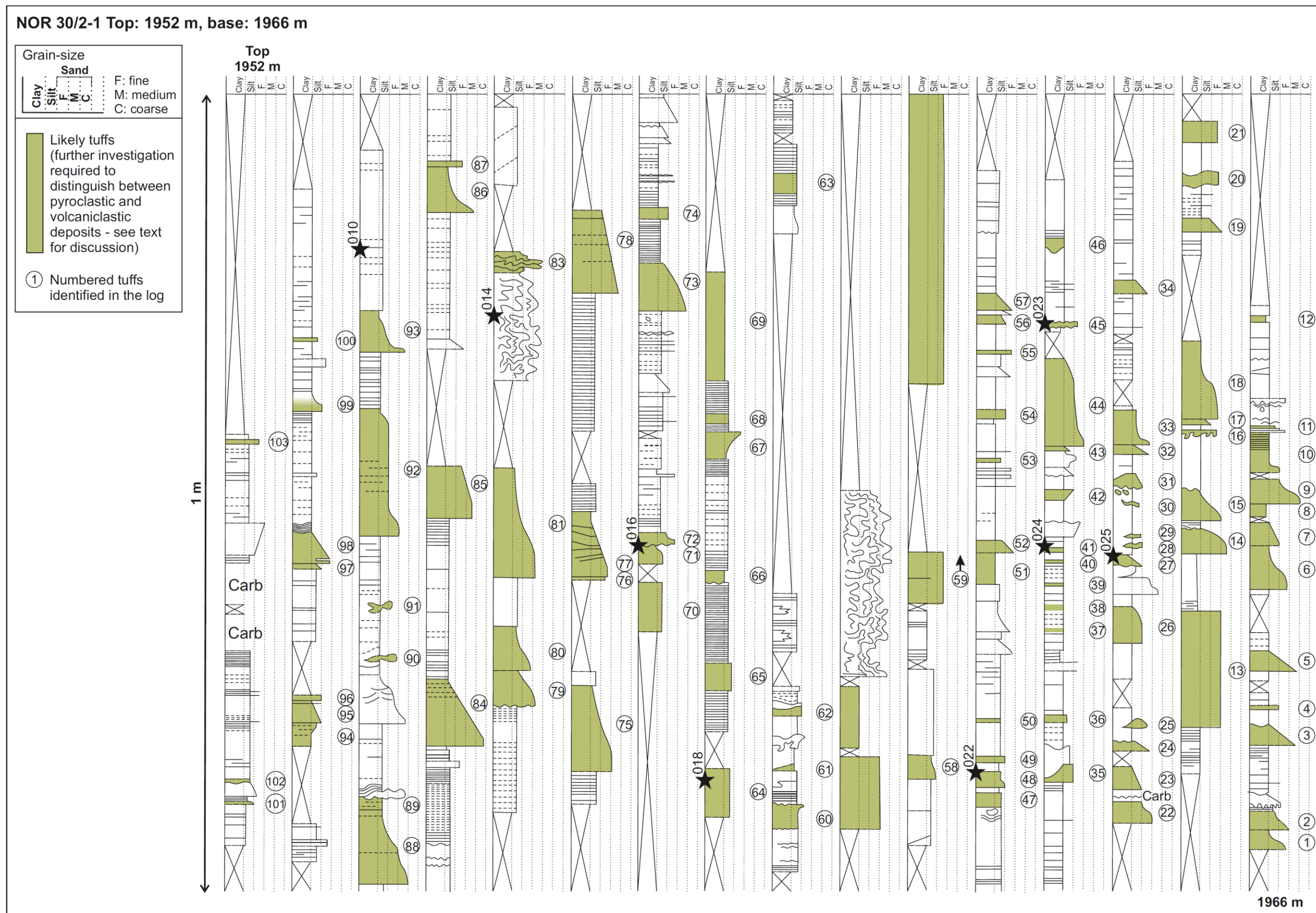


Figure 3-20 Lithological and grain-size log for core of the Balder Formation of NOR30/2-1, 60°52'5.42"N 02°38'49.16"E.

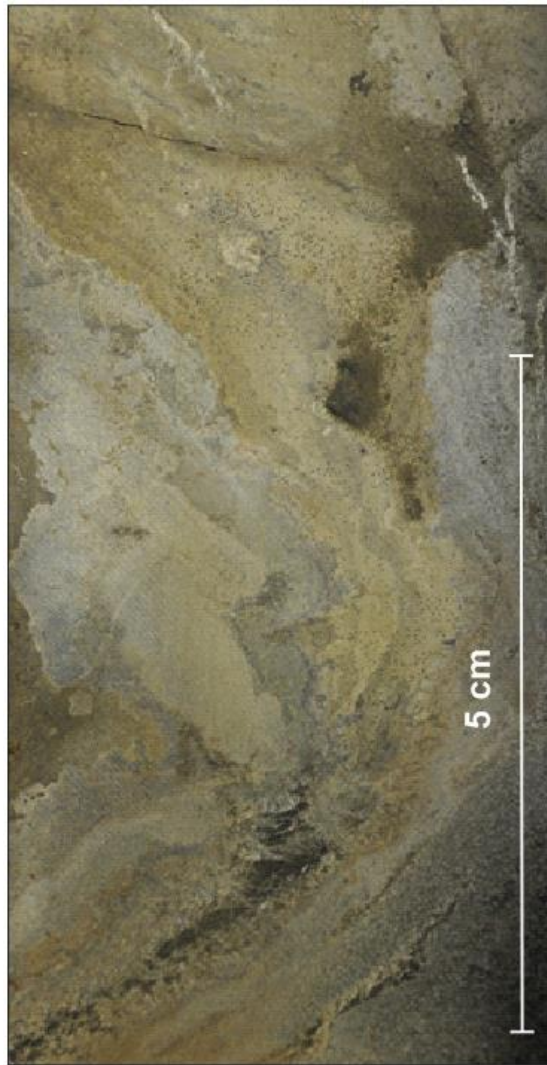


Figure 3-21 Deformed interbedded sandstone and siltstone in NOR30/2-1, core 2, at 1956.25 m depth. Similar to the feature identified in UKCS29/05a-7 (Figure 3-11).

Discontinuous lenses of olive-green tuff occur in some intervals (Figure 3-22), these have a burrow-like appearance or may represent soft-sediment deformation and be associated with a reworking of the original dis tuff-beds.

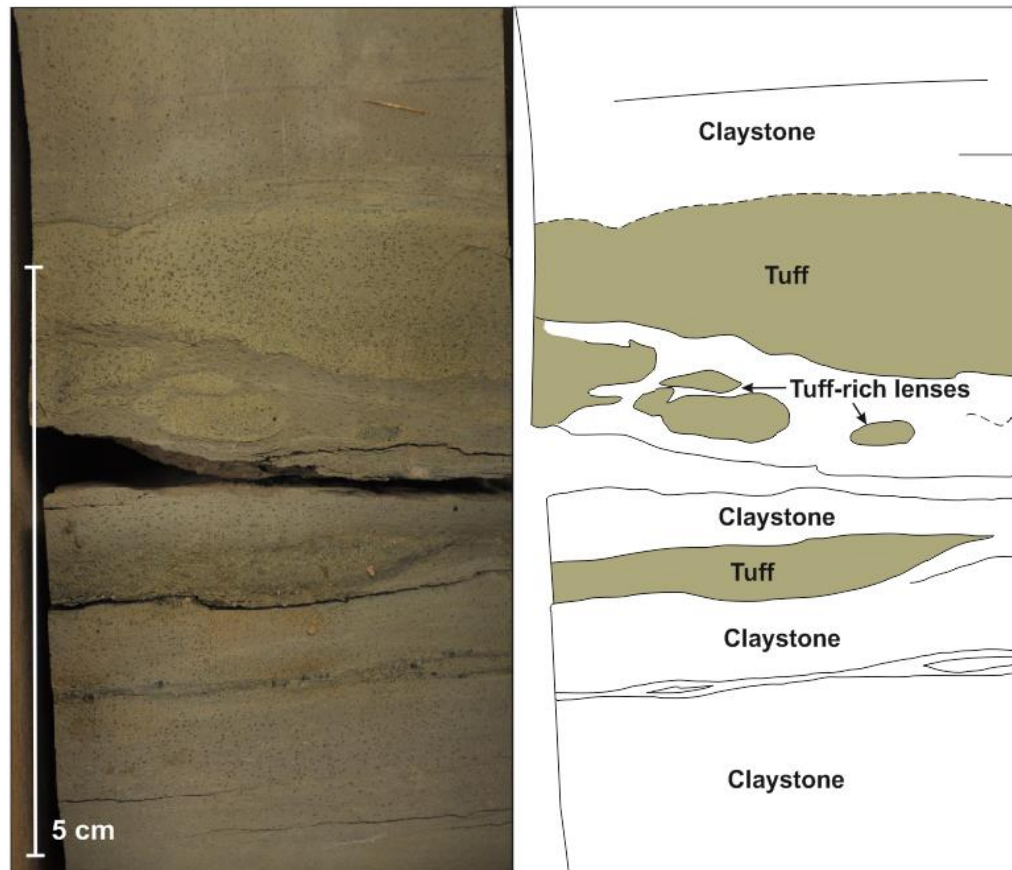


Figure 3-22 Discontinuous lenses of tuff or soft-sediment deformation features that may be associated with reworking of green tuffs in NOR30/2-1, core 2, at 1960.5 m depth. As indicated previously, olive green units are taken to represent the location of altered basaltic tuffs (this is confirmed by SEM analysis in the following section).

Some of the tuffs have a well-developed calcite cement, whereas others have a poorly-developed calcite cement that gives the appearance of mineral veins (Figure 3-23). Patches of pyrite cement are also present in some of the tuffs.

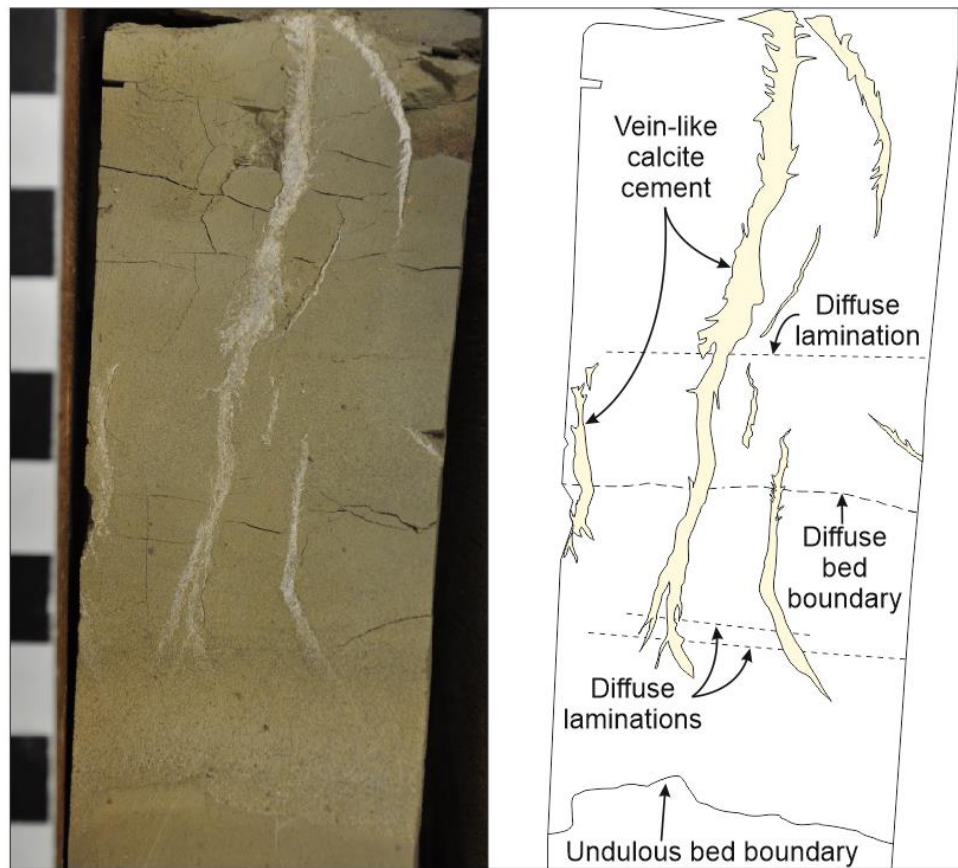


Figure 3-23 Poorly-developed calcite cement through several units of tuff, giving the appearance of mineral veins, in NOR30/2-1, core 2, at 1956.7 m depth.

3.5.2 Optical microscopy and SEM

Polished thin-sections of samples taken from core were studied first on a petrographic microscope; SEM analysis was then conducted on carbon-coated thin-sections. The SEM was used to collect detailed images of clasts and matrix material, and to obtain major-element chemical data to support identification of clast- and mineral-types. Here, the results of these investigations will be presented for each well.

3.5.2.1 UKCS22/30a-1

Samples from UKCS22/30a-1 are composed of claystone with interbedded siltstone and sandstone. The contact of the coarser-grained units with underlying claystones often preserves grain-loaded contacts, where coarser grains have sunken into the clay-rich laminae below (e.g. Figure 3-24d). The tuffs are of siltstone and sandstone grade and are commonly highly altered to various clays and contain a clay matrix and/or calcite cement. The samples appear to be

predominantly comprised of crystalline igneous clasts, although, alteration has blurred grain-boundaries, making individual clasts difficult to distinguish. However, these units do contain some of their original granular features, for example, where grains have been replaced or coated by secondary minerals, such as pyrite (Figure 3-24a, b).

Pyrite is present in many forms; grain-replacing secondary pyrite (Figure 3-24a), grain-coating pyrite (Figure 3-24b), framboidal pyrite (Figure 3-24c), and as a patchy pyrite cement (Figure 3-24d).

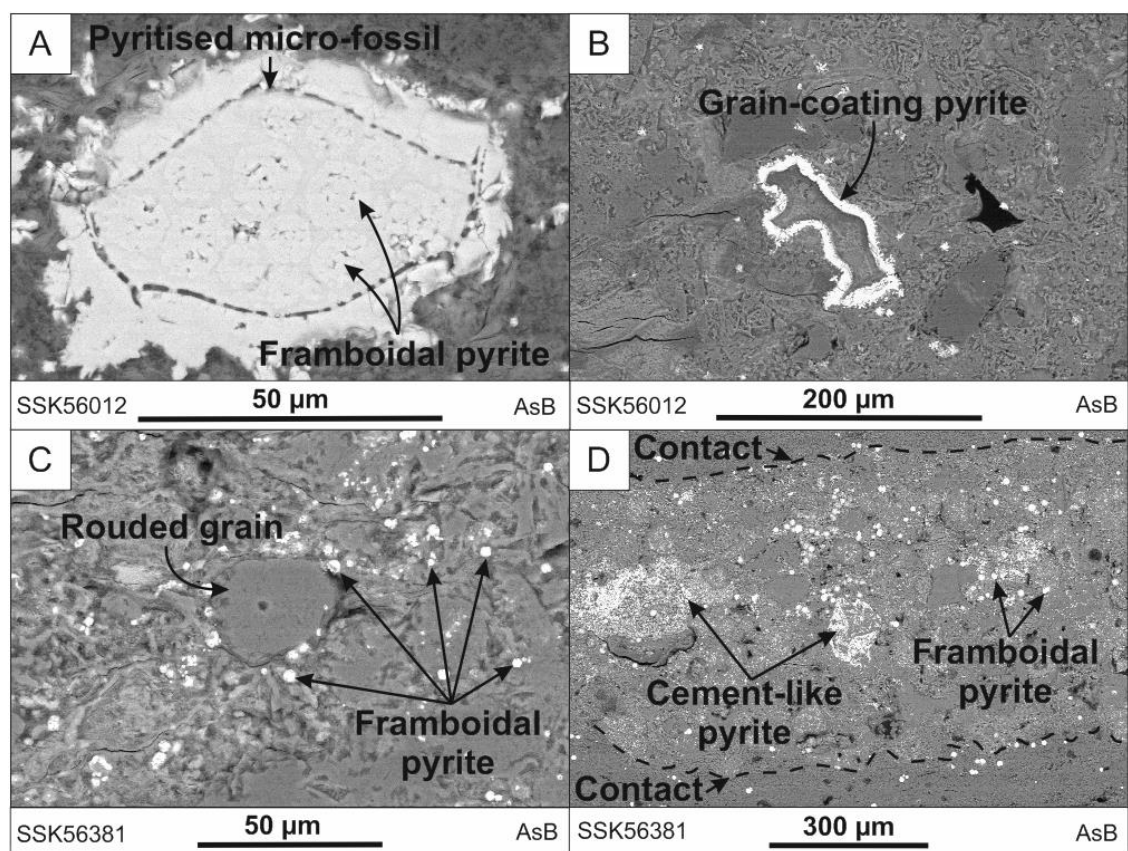


Figure 3-24 AsB SEM images showing the various forms of pyrite in samples from UKCS22/30a-1. A) Replacement of organic material by pyrite in SSK56012. B) Grain coated with pyrite in SSK56012. C) Micro-crystalline pyrite framboids in SSK56381. D) Cement-like pyrite filling spaces between grains in SSK56381.

Pyroclasts can be identified as non-crystalline clasts, commonly with vesicles or amygdaloides (Figure 3-25). The outer edges of these clasts are commonly concave in places and resembles bubble-wall rims (Figure 3-25). Vesicular (Figure 3-25a) and non-vesicular (Figure 3-25f) pyroclasts of blocky (Figure 3-25d, f), bubble-wall (Figure 3-25b, e), and irregular (Figure 3-25a) morphologies are present.

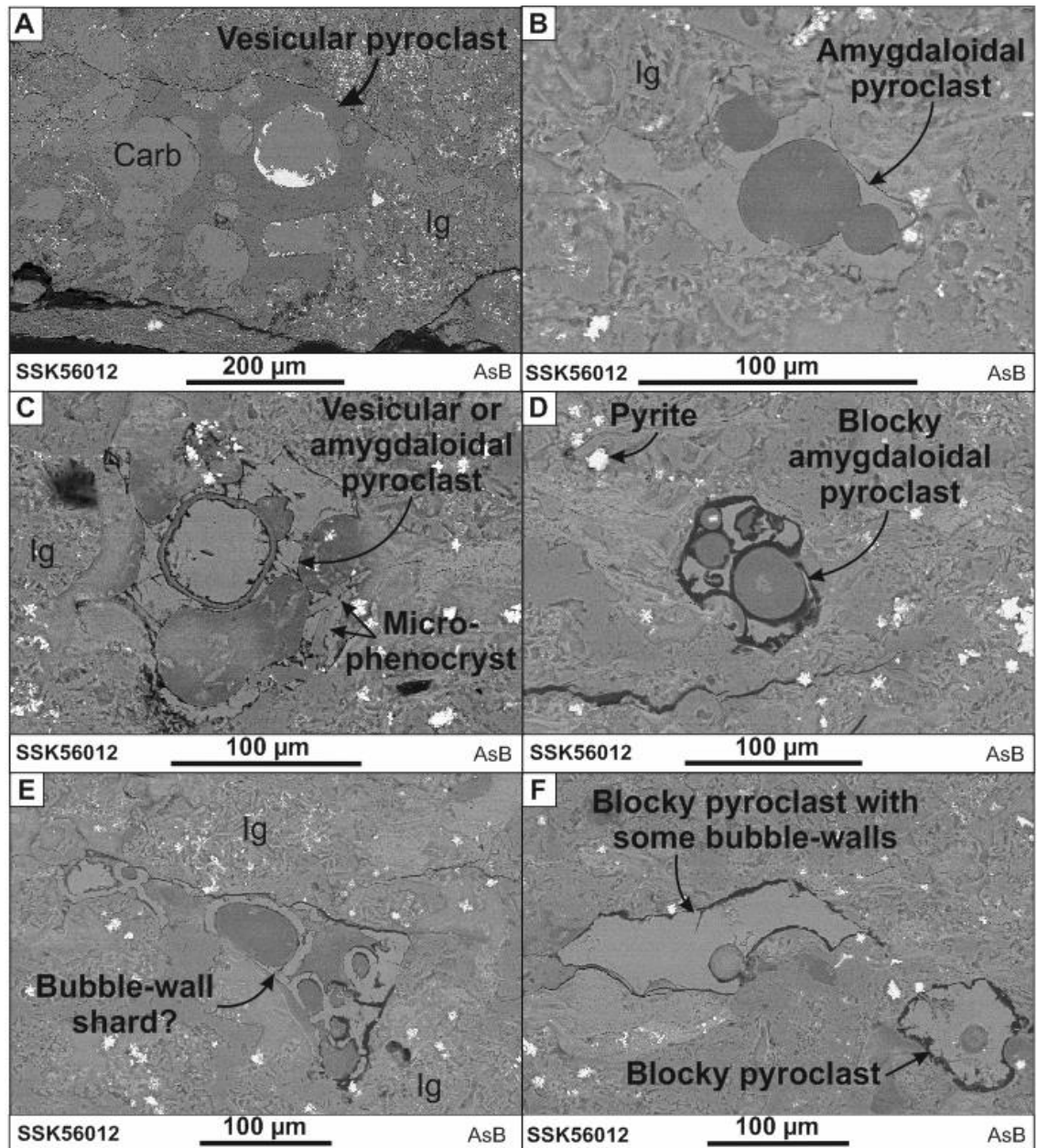


Figure 3-25 AsB SEM images showing pyroclasts of various types and levels of alteration observed within SSK56012 of UKCS22/30a-1. A) Vesicular, altered pyroclast. B) Amygdaloidal pyroclast. C) Altered, vesicular or amygdaloidal pyroclast with plagioclase micro-phenocrysts. D) Altered amygdaloidal pyroclast. E) Altered bubble-wall pyroclast, circular features that look like amygdaloides may be a result of alteration. F) Altered blocky pyroclasts with concave bubble-wall features.

3.5.2.2 UKCS29/05a-7

Samples from UK29/05a-7 share similar features to those of UK22/30a-1; being composed of claystone, siltstone and sandstone. Pyrite is a common feature of all of the samples, and is present as grain-coating pyrite surrounding pyroclasts (Figure 3-26a, b), spheroids of framboidal pyrite (Figure 3-26c, d), amorphous framboidal pyrite (Figure 3-26e), euhedral cubic pyrite crystals (Figure 3-26c) and, pyritised grains (Figure 3-26f).

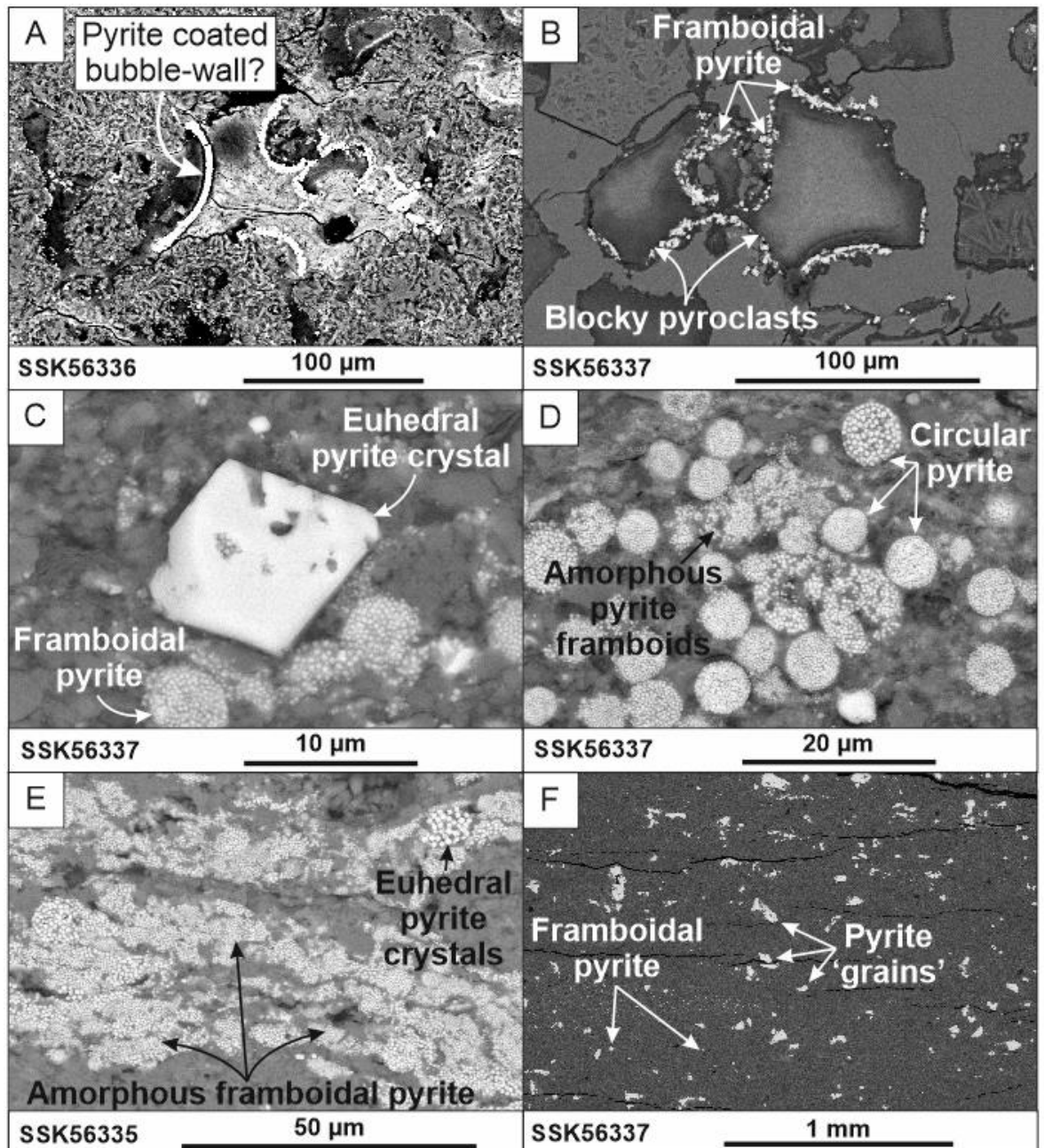


Figure 3-26 AsB SEM images showing differing characteristics of pyrite observed in samples from UKCS29/05a-7. A-B) Pyrite coating the edges of grains. C) Single euhedral pyrite. D) Cluster of variously sized circular and amorphous pyrite framboids. E)

Amorphous pyrite framboids and clustered euhedral pyrite crystals. F) Individual 'grains' of pyrite and circular pyrite framboids

The siltstones and sandstones commonly contain a significant amount of crystalline igneous clasts (Figure 3-27), and highly altered pyroclasts (Figure 3-28), and are therefore considered to be tuffs. The crystalline igneous clasts have fluidal morphologies and are commonly vesicular (Figure 3-27), these are interpreted as lava-like clasts. These clasts are generally micro-crystalline (Figure 3-27) and have a different morphology and texture compared to the altered pyroclasts that occur in the same deposits (Figure 3-28).

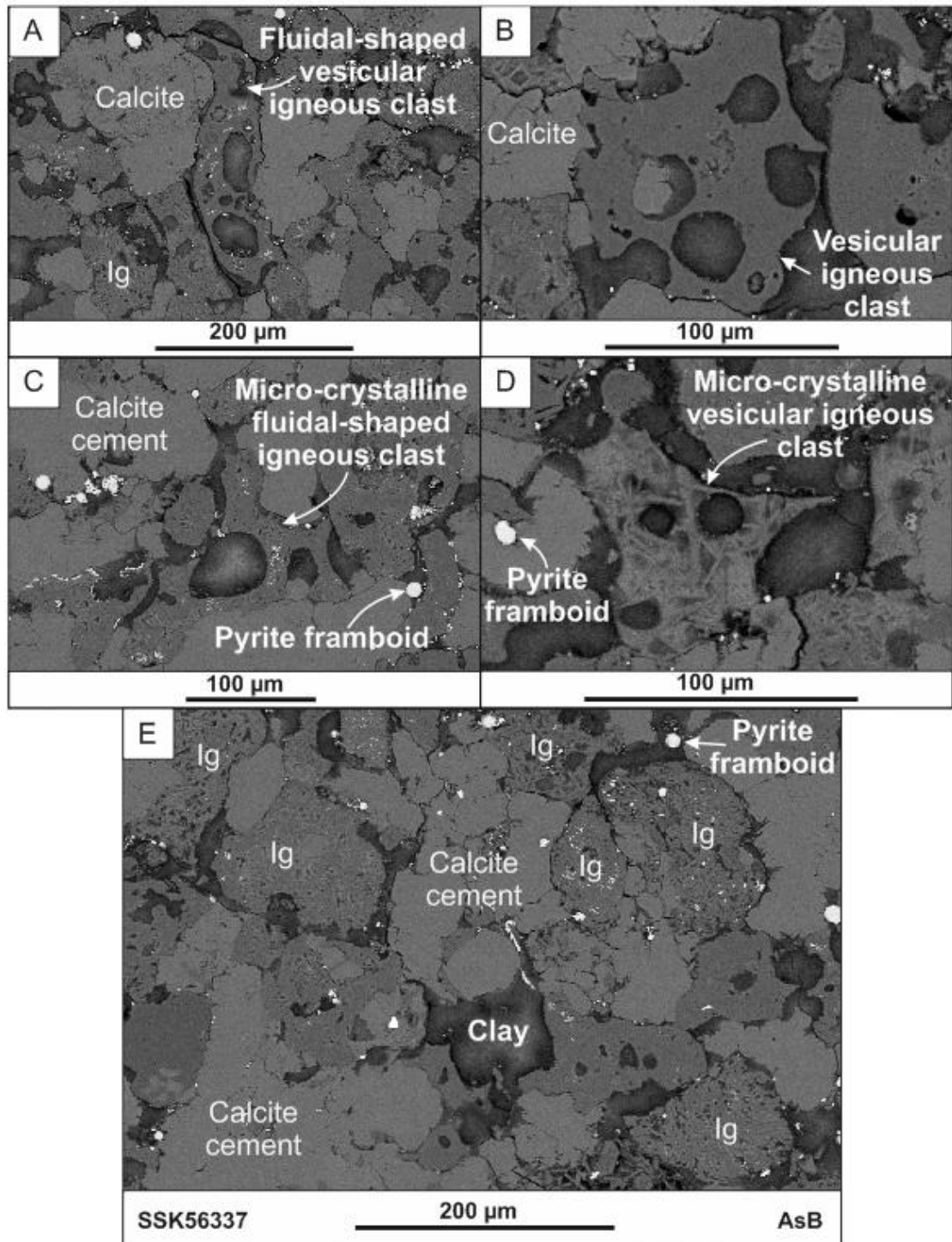


Figure 3-27 AsB SEM images showing the various forms of pyroclasts and igneous crystalline clasts observed within SSK56374 from UKCS29/05a-7. An abundant calcite cement occurs. A) Elongate, vesicular pyroclast with a fluidal morphology. B) Vesicular, blocky pyroclast. C) Fluidal-shaped pyroclast with micro-crystalline texture, possibly caused by alteration. D) Vesicular crystalline igneous clast with micro-crystalline texture. E) Abundant crystalline igneous clasts (lg) and pyroclasts within a calcite cement.

The pyroclasts display a range of morphologies; vesicular (Figure 3-28a, b) and non-vesicular (Figure 3-28c-f), blocky (Figure 3-28f), bubble-wall (Figure 3-28c-f), and irregular (Figure 3-28b).

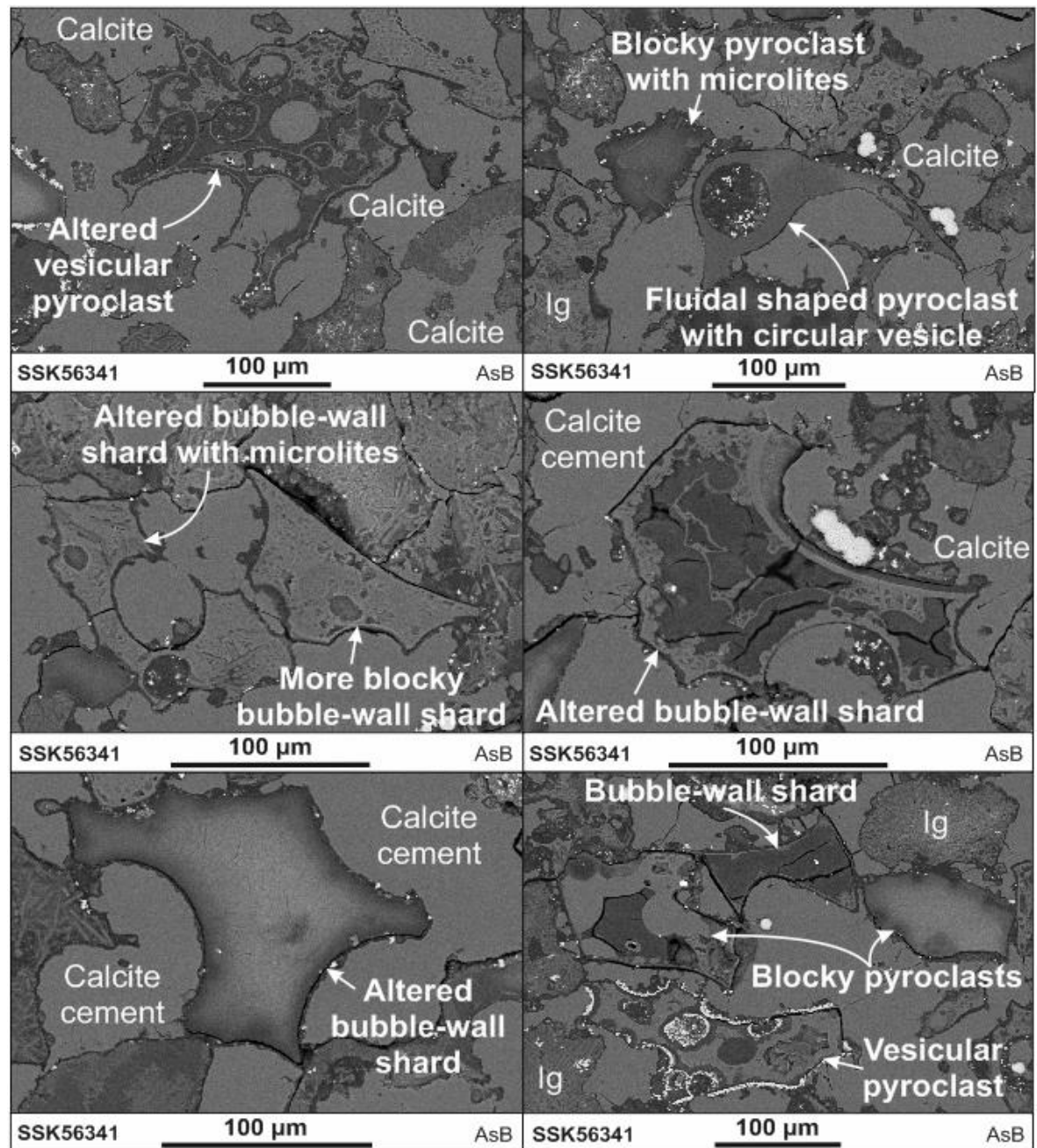


Figure 3-28 AsB SEM images showing the range of pyroclasts types and their differing levels of alteration in sample SSK56341 from UKCS29/05a-7. All of the pyroclasts are surrounded by a calcite cement and occur alongside crystalline igneous grains (Ig). A) Vesicular pyroclast surrounded by fractured bubble-wall structures, mottling of the surface of the pyroclast shows differing levels of alteration within this pyroclast. B) Fluidal vesicular pyroclast, and a blocky pyroclast with minor micro-crystals. C-E) Bubble-wall shards with varying levels and textures of alteration as shown by their varying surface features and mottling. F) Range of different pyroclasts showing the full range of alteration types and a range of pyroclast morphologies, including blocky, bubble-wall and vesicular

The pyroclasts are all altered, although to varying degrees. Some appear to have undergone palagonitisation (Figure 3-28e) and are characterised by clay with a gradual decrease in Fe and Ti from the centre of the pyroclast outwards, correlating with an increase in K (Figure 3-29). These pyroclasts appear to be

concentrically zoned under plane-polarised-light (Figure 3-29), showing the progressive replacement of the original glassy pyroclast by palagonitisation; from the formation of a fibrous palagonite, to gel-palagonite and eventually to smectite (clay).

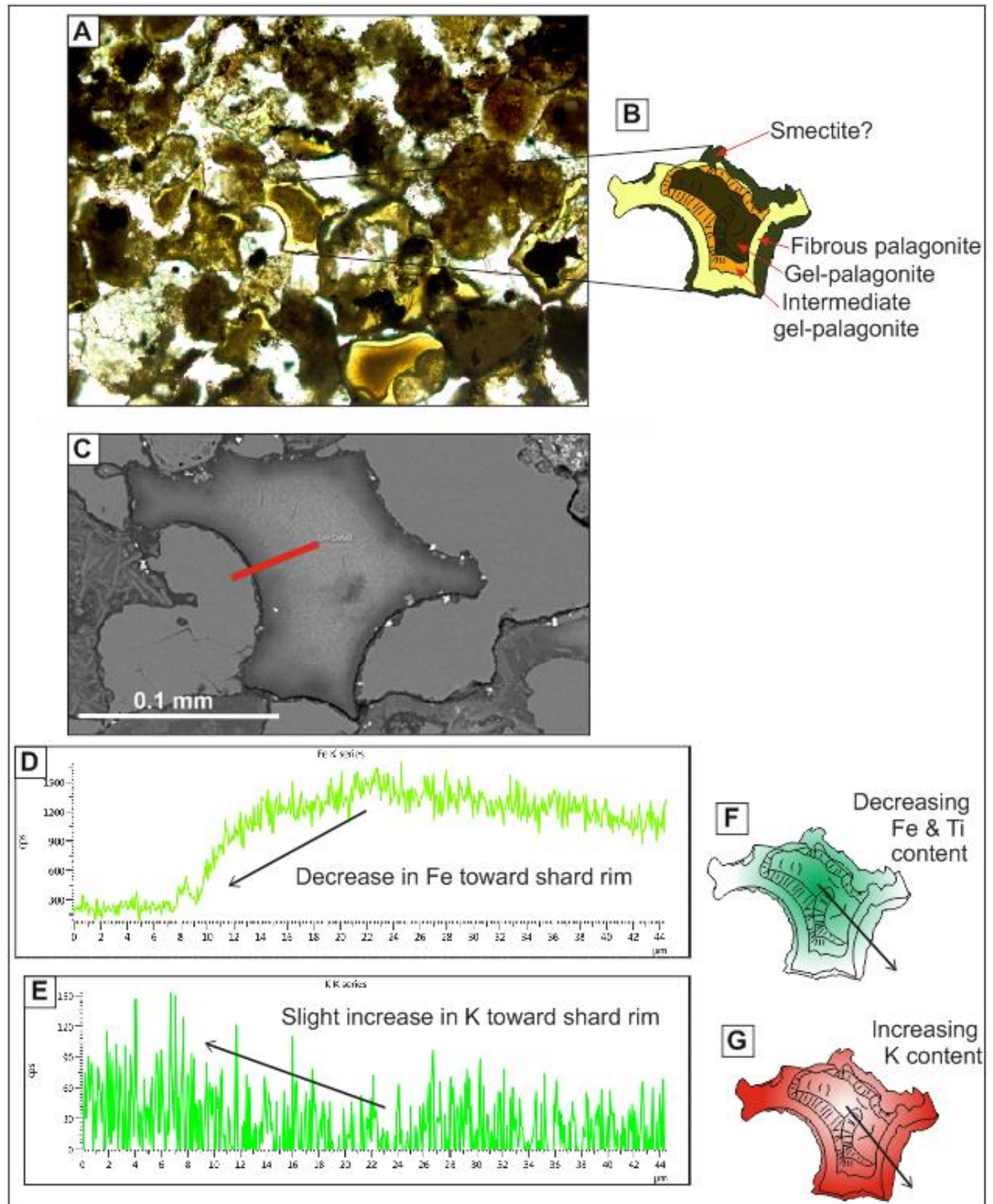


Figure 3-29 Palagonitisation of originally glassy pyroclasts of sample SSK56341 from UKCS29/05a-7. A – B) Palagonitisation identified in thin-section under plane-polarised-light; including fibrous palagonite, gel-palagonite and smectite, indicating increasing levels of alteration towards the rims of the pyroclast. C) Backscatter SEM image of the same pyroclast as B. Red line shows the location that spectra D and E were taken. D) The

concentration of iron (Fe) decreases from core to rim (F). This corresponds to a slight increase in the concentration of potassium (K) from core to rim (E and G).

Other pyroclasts appear to have surpassed the stages of palagonitisation and have completely altered to smectite (Figure 3-28a, d). Following this, some smectite-pyroclasts have been completely or partly replaced by calcite (Figure 3-28c, d, f).

3.5.2.3 NOR25/7-5

Similar to the UKCS samples, samples from NOR25/7-5 are predominantly of claystone, siltstone and sandstone. The main clast-types found in these deposits include: woody organic fragments (Figure 3-30a), variably altered pyroclasts (Figure 3-30b), and crystalline igneous clasts (Figure 3-30c). Framboidal pyrite occurs throughout.

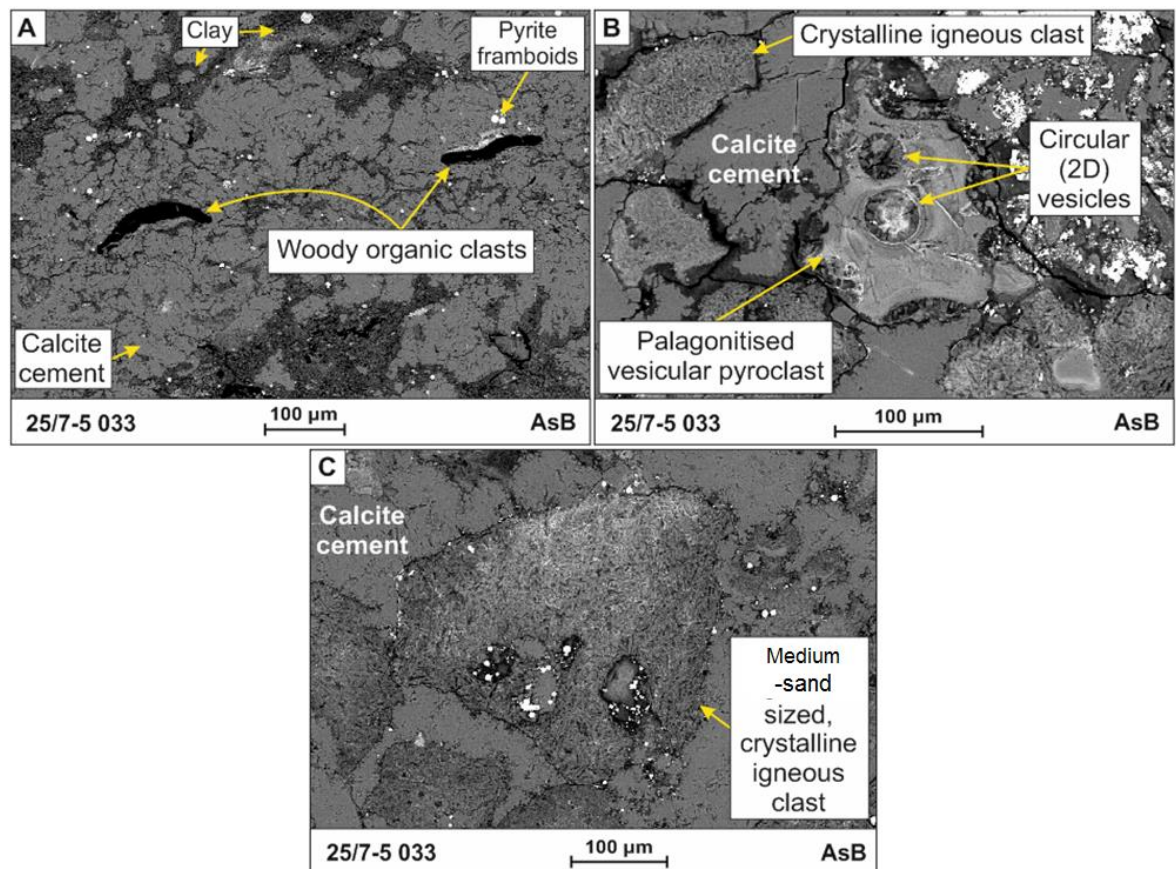


Figure 3-30 AsB SEM images of the main clast types in sample 033c from NOR25/7-5. A) Amorphous woody organic clasts within clay that has been partially replaced by calcite. B) A palagonitised vesicular pyroclast with circular vesicles in thin-section (2D) occurs with crystalline igneous clasts surrounded by a calcite cement. C) The crystalline igneous clasts medium-sand grade.

Below, focus is given to the siltstone and sandstone units that contain >50 % igneous or pyroclastic clast-types representative of tuffs (e.g. Frolova 2008). The lower contact of the tuffs commonly displays grain-loading where the clasts have partially sunken into the underlying finer-grained claystones (Figure 3-31). A calcite cement has replaced some of the original clay within these deposits (e.g. Figure 3-31).

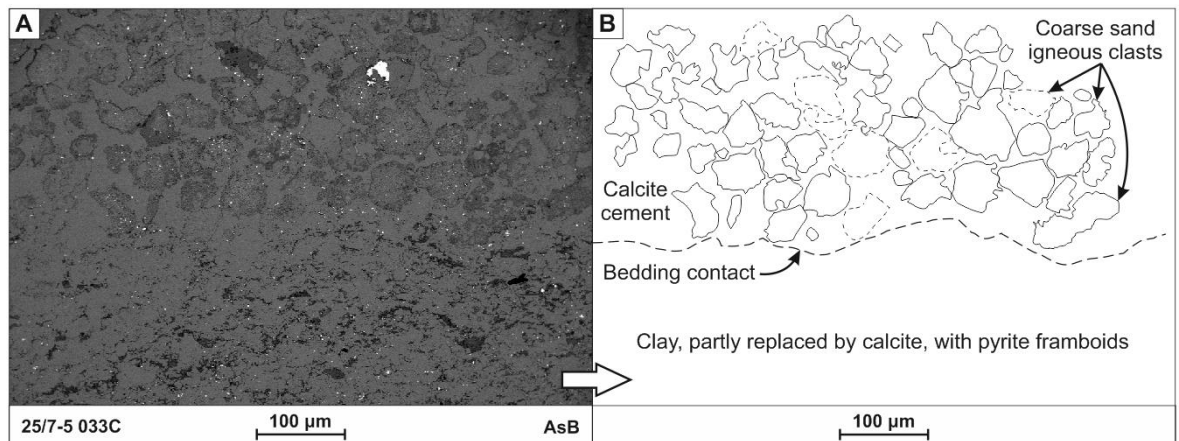


Figure 3-31 AsB SEM image of contact between clay and igneous clast-rich coarse sandstone with calcite cement in sample 033 from NOR25/7-5.

Crystalline igneous clasts within the tuffs contain micro-crystals of plagioclase and amphibole (Figure 3-30c, Figure 3-34c). Minor occurrences of rounded, more coarsely crystalline lithic clasts, comprising euhedral laths of labradorite and acicular spheres of gedrite are also present (Figure 3-34d).

Palagonitised pyroclasts are abundant in some of the tuffs (032, 043; Figure 3-32, Figure 3-33a), in addition to crystalline igneous clasts. The tuffs often contain a calcite cement (Figure 3-33a), although in some tuffs localised patches of pyrite cement are also present (Figure 3-33b, c).

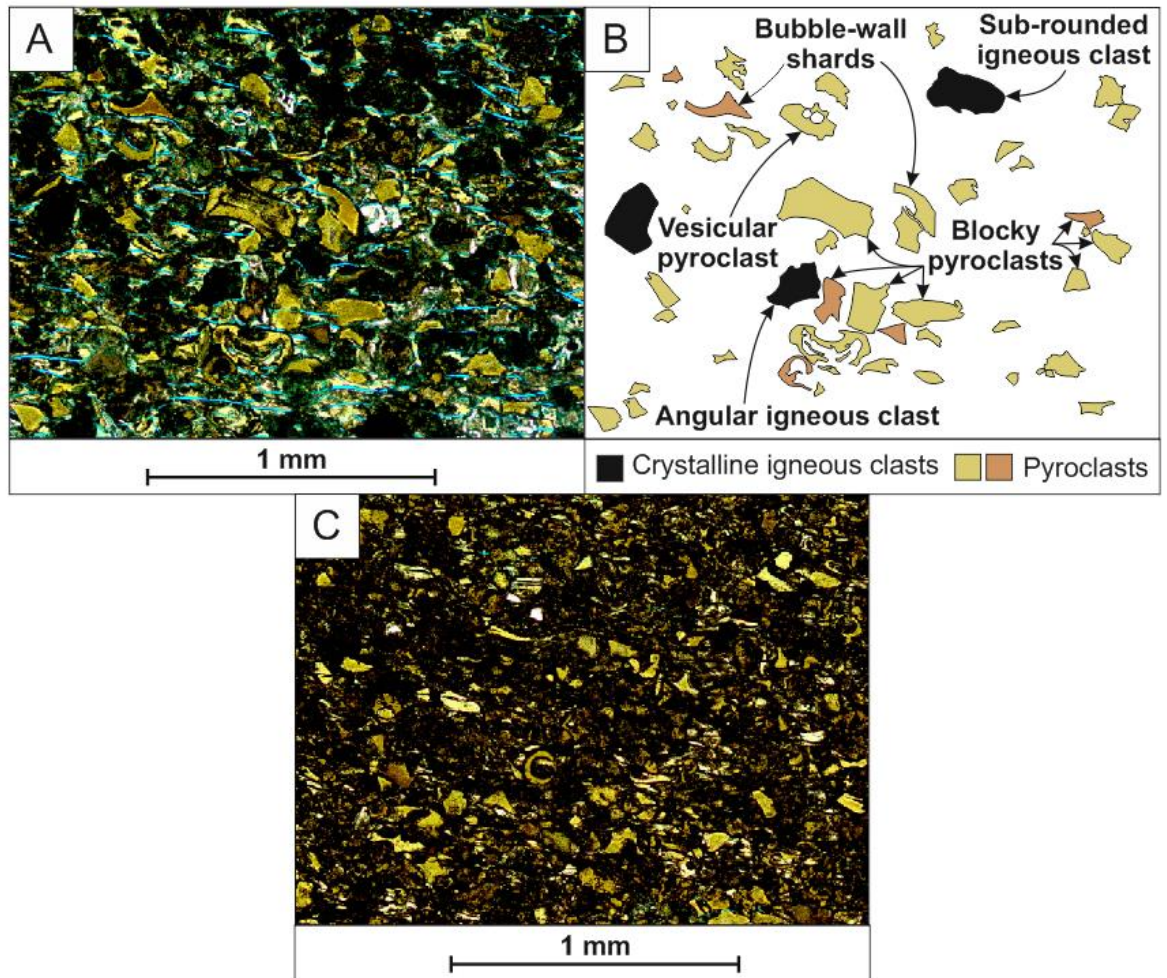


Figure 3-32 General nature of the fining-upwards sequence in sample 032 from NOR25/7-5. The bed contains pyroclasts and crystalline igneous clasts (A-C). B) Some crystalline igneous clasts and pyroclasts picked out of image A and labelled to show the varying pyroclast morphologies that can be identified in this deposit, including blocky and vesicular pyroclasts and bubble-wall shards, alongside angular to sub-rounded crystalline igneous clasts. C) Finer grain-size material, with abundant yellow/brown pyroclasts within a very fine-grained clay matrix (dark brown).

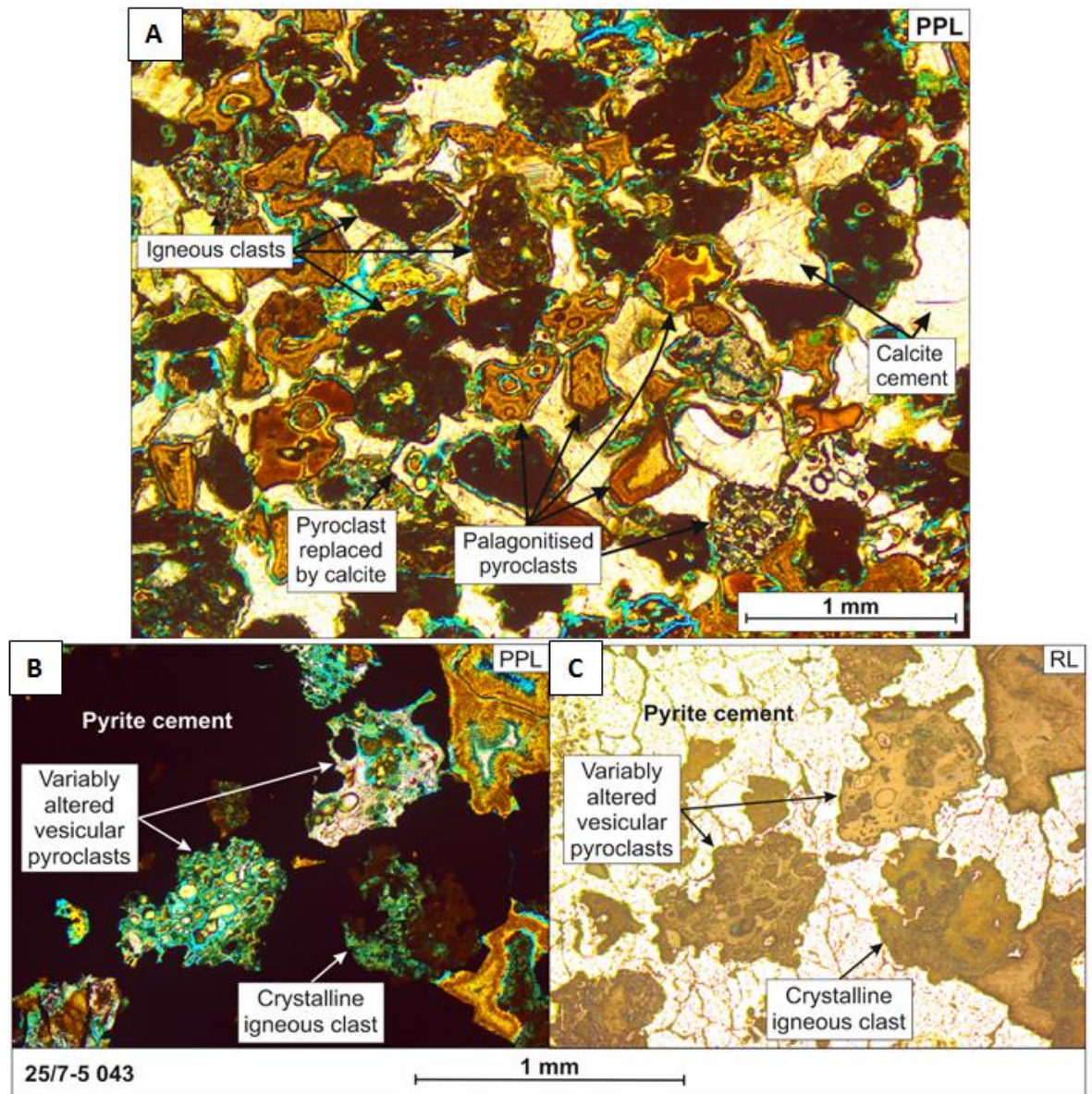


Figure 3-33 Igneous clasts with a calcite (A) or pyrite (B, C) cement, in sample 043 from NOR25/7-5.

Pyroclasts show a variety of morphologies and levels of alteration under the SEM, including; palagonitised vesicular and non-vesicular bubble-wall (Figure 3-34a) and blocky pyroclasts (Figure 3-35a), and pyroclasts altered and replaced by clay (Figure 3-35b), with partial replacement by calcite (Figure 3-34c, Figure 3-35d). Some pyroclasts have been completely replaced by calcite, but retain some of their original compositional signature, allowing them to be seen under the SEM (Figure 3-34b). Other pyroclasts may have been replaced by concentric layers of gedrite, giving the clast a layered appearance (Figure 3-35c).

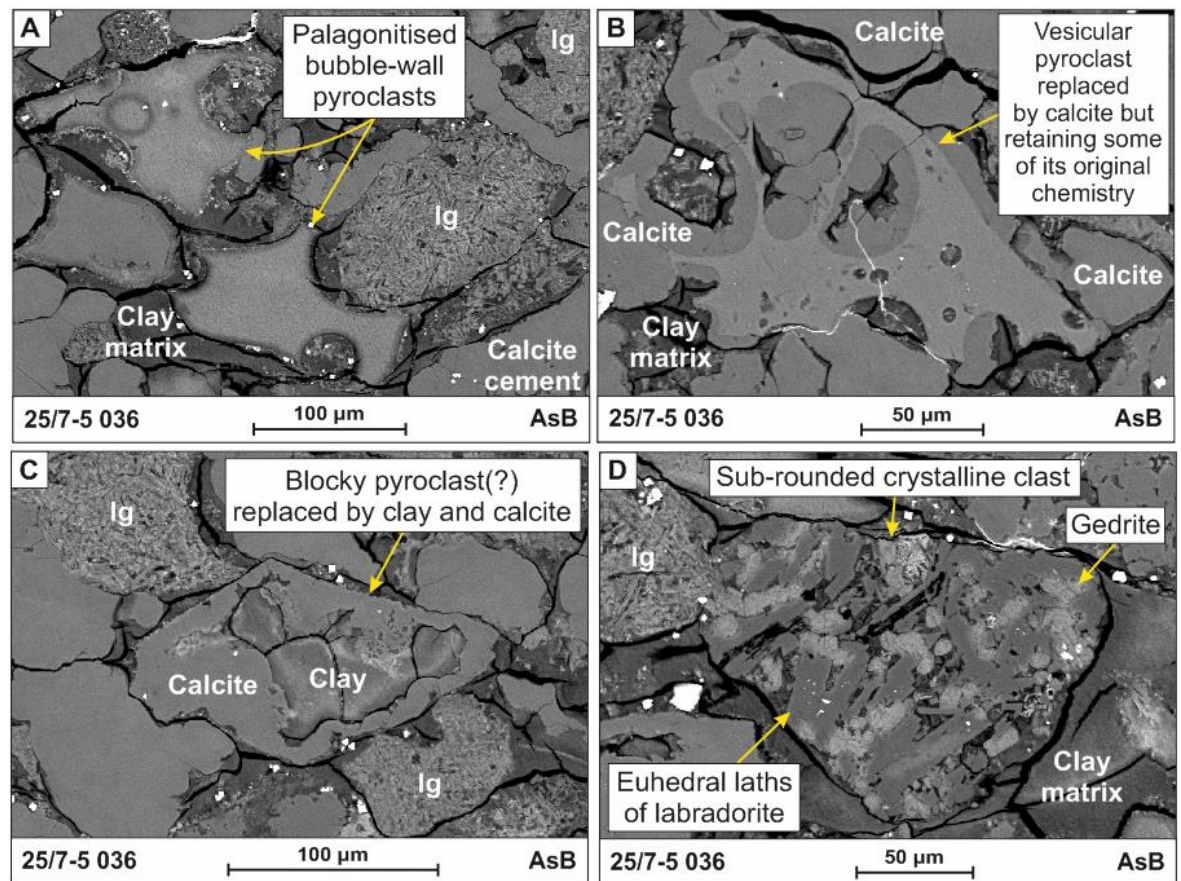


Figure 3-34 AsB SEM image of pyroclasts and crystalline igneous clasts in sample 036 from NOR25/7-5. A) Palagonitised bubble-wall pyroclasts surrounded by clay matrix that has been partially replaced by calcite. Sub-angular crystalline igneous clasts also present (Ig). B) A vesicular pyroclast completely replaced by calcite but retaining some of its original chemistry, making it visible within a calcite cement. The vesicles of this pyroclast are non-circular (in 2D). A clay matrix is present, but has been partially replaced by calcite. C) A heavily altered blocky pyroclast (?) replaced by clay that has been subsequently partially replaced by calcite. D) A sub-rounded crystalline igneous clast with euhedral laths of labradorite and acicular spheres of amphibole. Surrounded by a clay matrix.

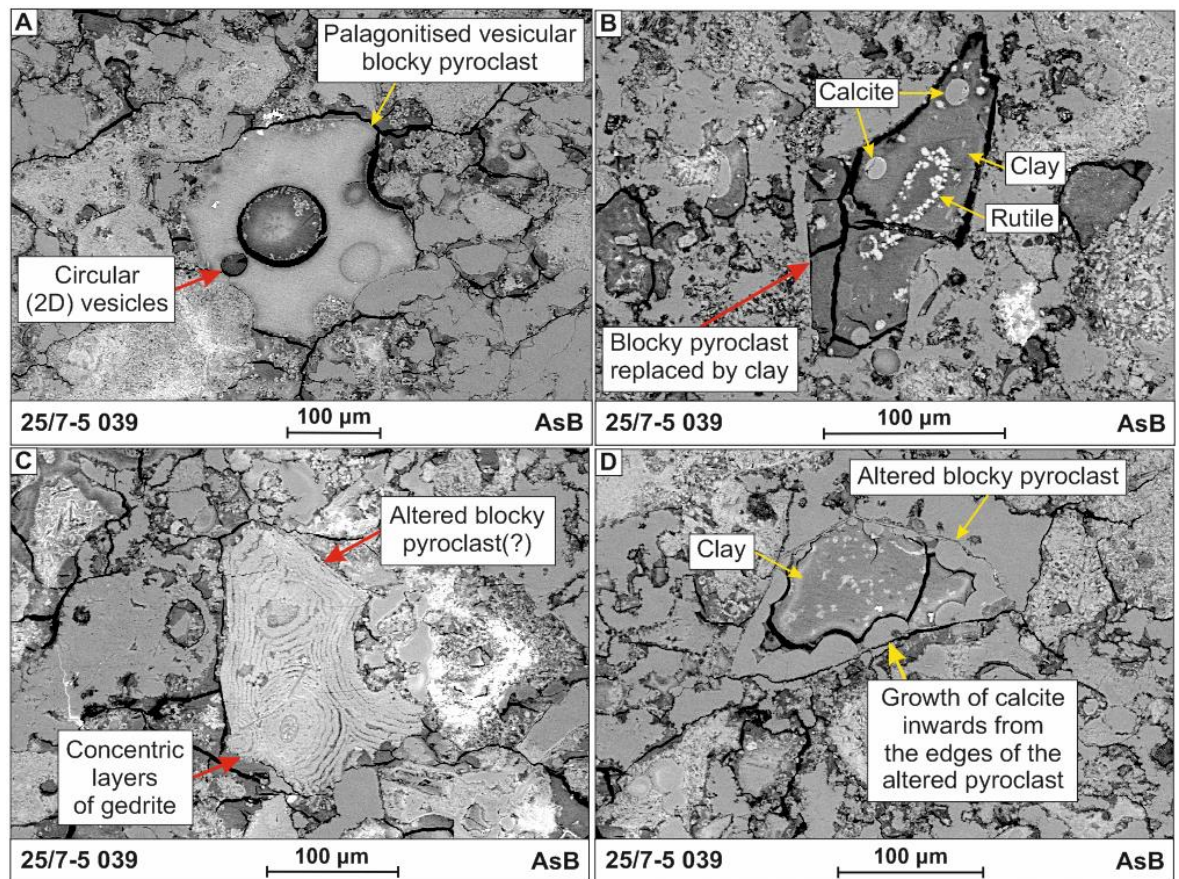


Figure 3-35 AsB SEM images of the varying degrees of alteration in pyroclasts of sample 039 from NOR25/7-5. Palagonitised vesicular blocky pyroclast with uniform alteration across the pyroclast. This pyroclast has circular vesicles in cross-section. B) A blocky pyroclast that has undergone palagonitisation and been replaced by clay. The original shape of the pyroclast is preserved within a calcite cement. C) A blocky pyroclast that has undergone stages of alteration that have led to the formation of concentric layering of gedrite (a type of amphibole). D) Palagonitised blocky pyroclast that has been replaced by clay. Additional partial replacement by calcite, indicated by concentric growths of calcite originating from the edge of the clast.

3.5.2.4 NOR25/11-17

Crystalline igneous clasts are a prominent feature of sample 001 and 002 from NOR25/11-17, and represent two tuffs. Vesicular and non-vesicular, blocky pyroclasts also occur and commonly appear to have been replaced by calcite and are surrounded by a calcite cement (Figure 3-36).

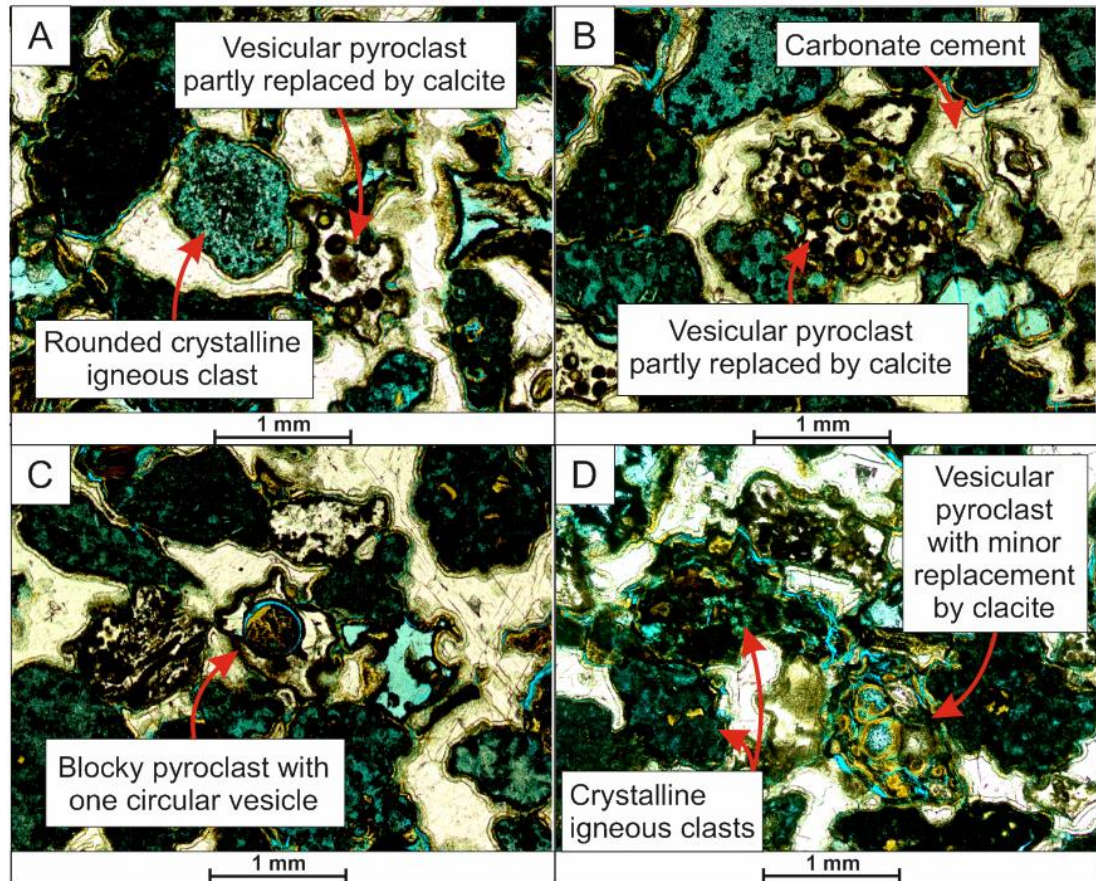


Figure 3-36 Plane-polarised light microscope images of vesicular pyroclasts (red arrows) surrounded by a calcite cement (white) in sample 002 from NOR25/11-17. A-C) Variably vesicular pyroclasts replaced by calcite with original features preserved, D) Orange/brown vesicular pyroclast that has not been replaced by calcite. The same features are also observed in sample 001.

In contrast, thick units of quartz-rich sandstone (quartz arenite) occur between the tuffs. Under plane-polarised-light, the sandstone is highly porous (blue dye) and predominantly composed of angular quartz grains (Figure 3-37). The sandstone of sample 005 is generally moderately sorted, however, localised sections of poorly-sorted sandstone also occur (Figure 3-37c, d).

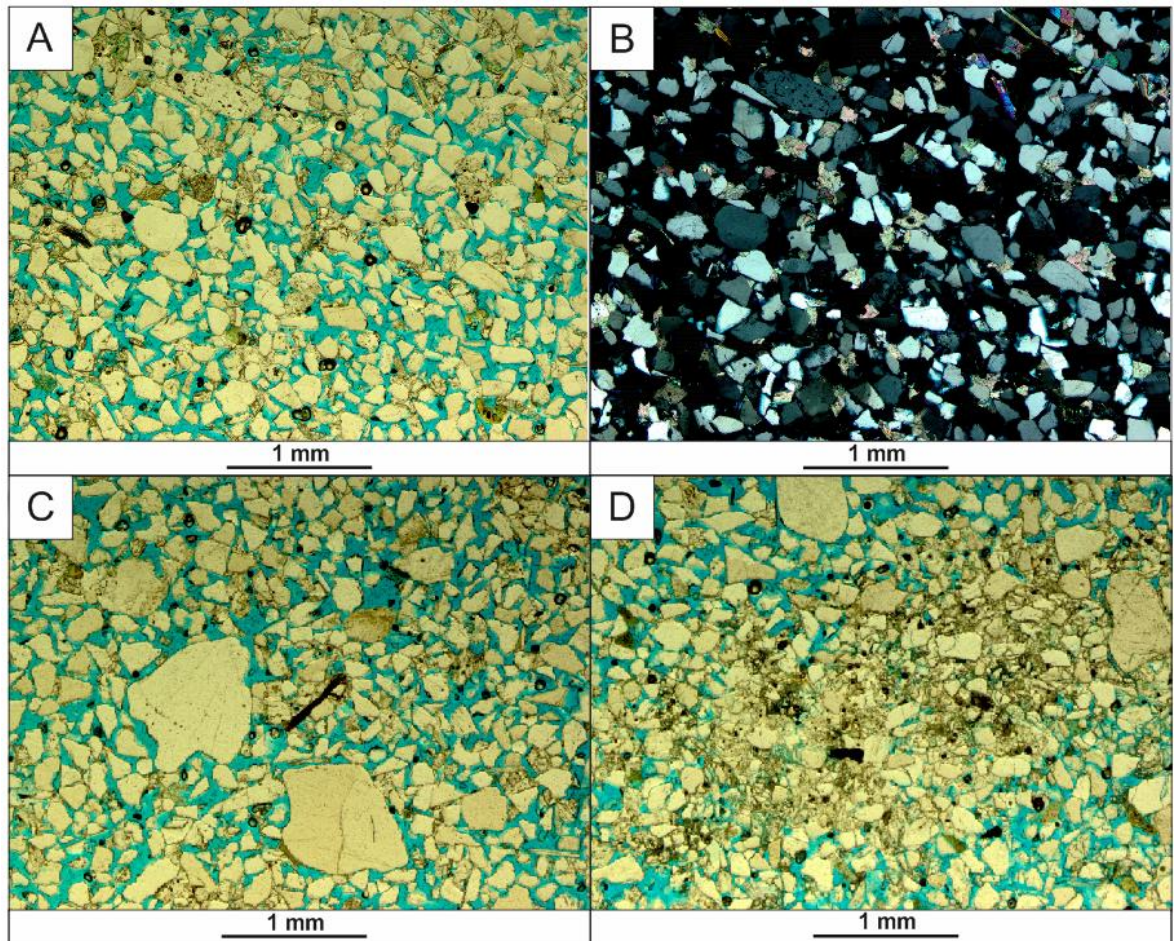


Figure 3-37 Plane-polarised light microscope images of a quartz-rich sandstone with abundant porosity and high permeability (blue), in sample 005 from NOR25/11-17. A-B) Plane-polarised light and corresponding cross-polarised light images showing the general nature of the sandstone which is dominated by angular quartz grains with minor amounts of feldspar, pyroxene, mica, calcite and chlorite. C) A range of grain sizes can be observed, with uncommon coarse sand grains. D) Some areas have a larger amount of fine calcite grains between the predominantly fine sand grade quartz grains.

The sandstone (sample 005) is dominated by angular quartz grains, together with minor amounts of feldspar (orthoclase and plagioclase), amphibole, stilpnomelane and pyrite, and localised pore-filling evaporate minerals: crystalline gypsum, amorphous halite and very minor amounts of K-salts. Ankerite occurs in some areas as pore-filling euhedral growths around quartz grains (Figure 3-38), surrounded by amorphous halite (Figure 3-38).

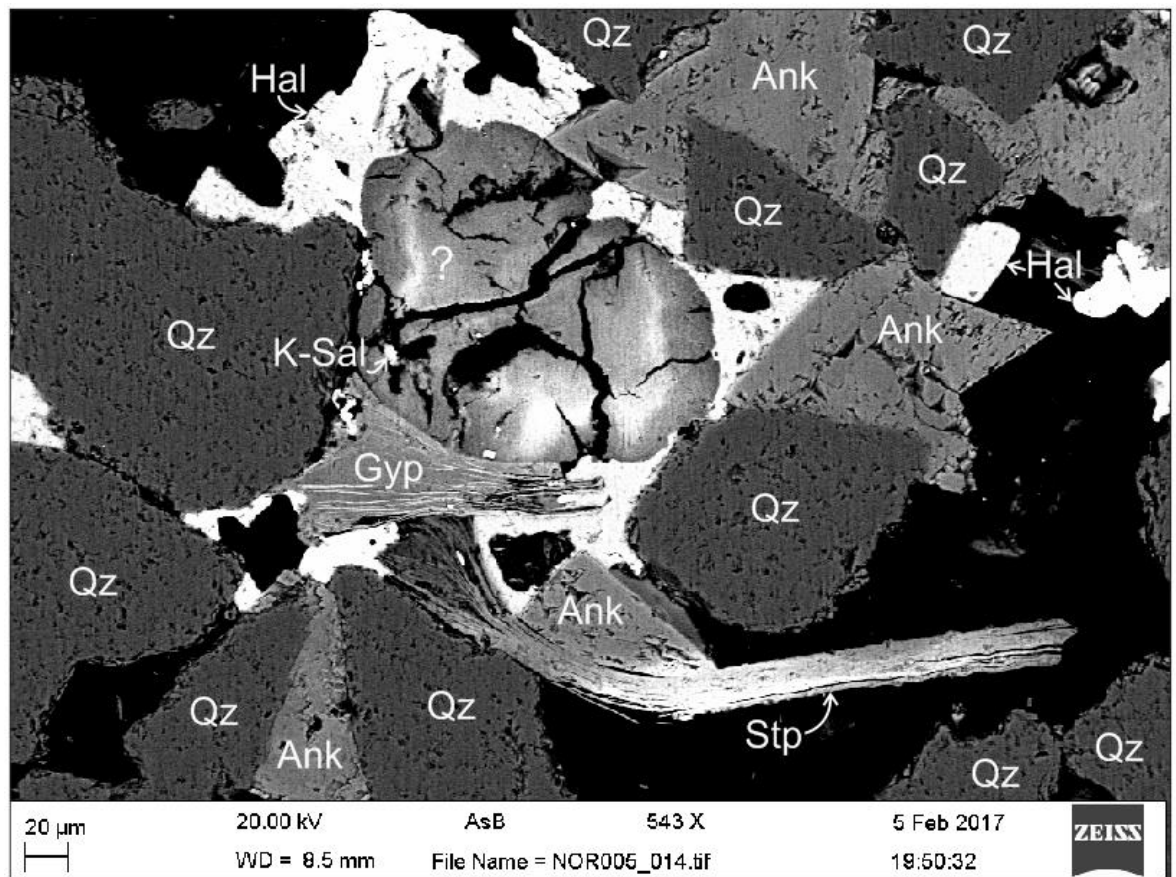


Figure 3-38 AsB SEM image showing the components found in some parts of the sandstone in sample 005 of NOR25/11-17. Ank: Ankerite (carbonate), Gyp: Gypsum, Hal: Halite, K-sal: K-salt, Qz: Quartz, Stp: Stilpnomelane, ?: Unknown unstable lithic clast. Black in this image represents pore spaces within the sample.

3.5.2.5 NOR Well 30/2-1

Samples of tuff from NOR30/2-1, are predominantly composed of sub-angular to well-rounded crystalline igneous clasts comprised of micro-crystals of plagioclase and amphibole (Figure 3-39). Altered pyroclasts display a similar crystalline-like appearance as the crystalline igneous clasts (Figure 3-39b). Other features resemble pyroclasts that have been replaced by clay and calcite but retain their original pyroclast morphology (Figure 3-39f). Pyrite is present as secondary mineral growths surrounding some grains and as a partial pyrite cement (Figure 3-39a), as well as pyrite framboids (Figure 3-39e). Generally, these samples contain a clay matrix (Figure 3-39).

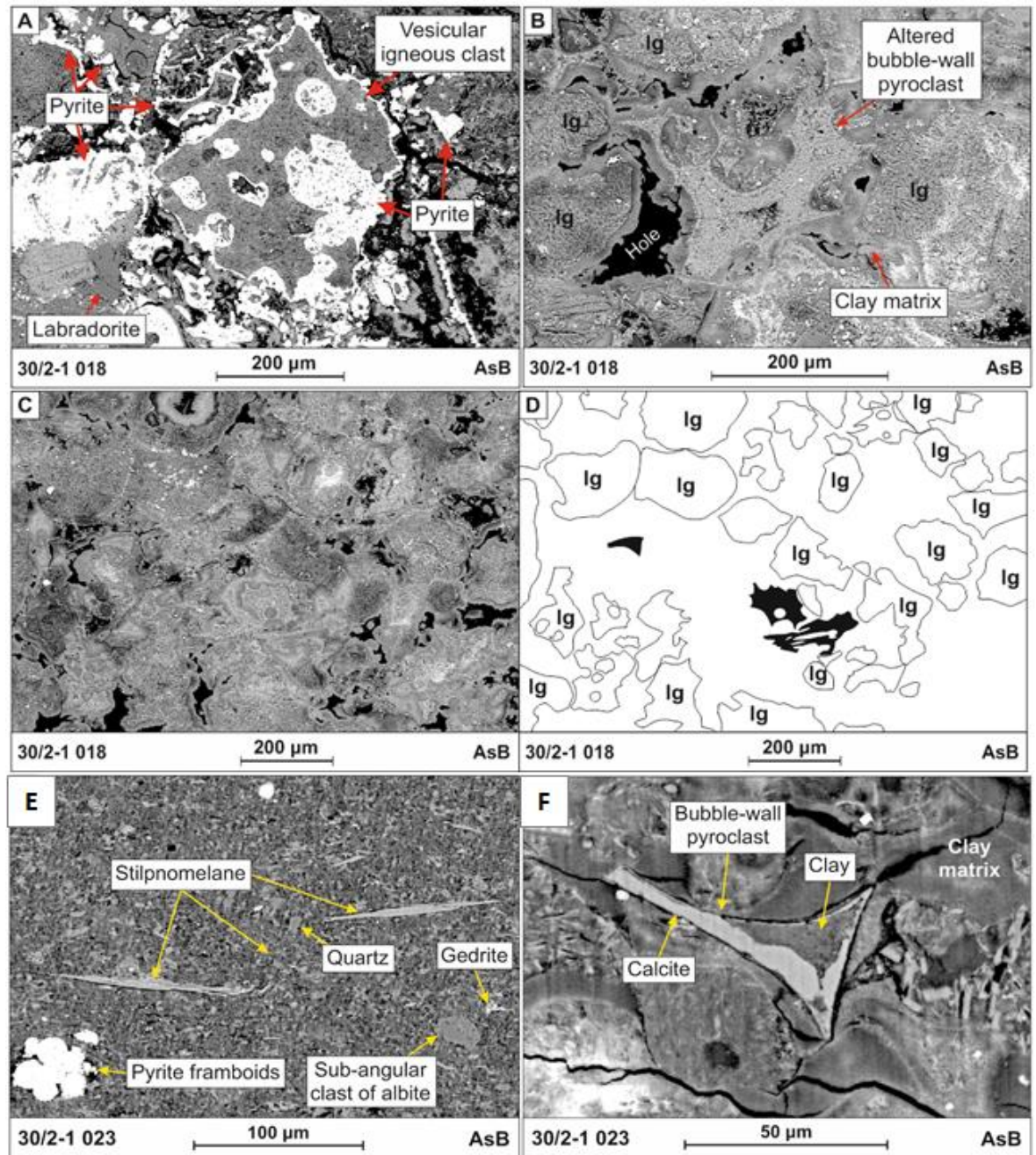


Figure 3-39 AsB SEM features of samples 018 and 023 from NOR30/2-1. A) Vesicular igneous clast surrounded by pyrite. B) Highly altered bubble-wall pyroclast and sub-angular crystalline igneous clasts held in a clay matrix. C-D) Granular nature of the deposit with sub-angular to sub-rounded vesicular and non-vesicular crystalline igneous clasts (Ig), and altered pyroclasts (black in D). E) Siltstone with grains of quartz, albite, gedrite, elongate stilpnomelane and, pyrite framboids, F) A bubble-wall pyroclast replaced by clay and calcite, in a clay matrix.

3.5.2.6 FSB 6104/25-1

One sample from the BF was analysed from Well 6104/25-1 (Sula-Stelka) from the Faroe-Shetland Basin (FSB). This sample contains a range of igneous clast types,

including variably altered, originally glassy, pyroclasts of non- to poorly-vesicular, blocky and irregular morphologies (Figure 3-40a, b).

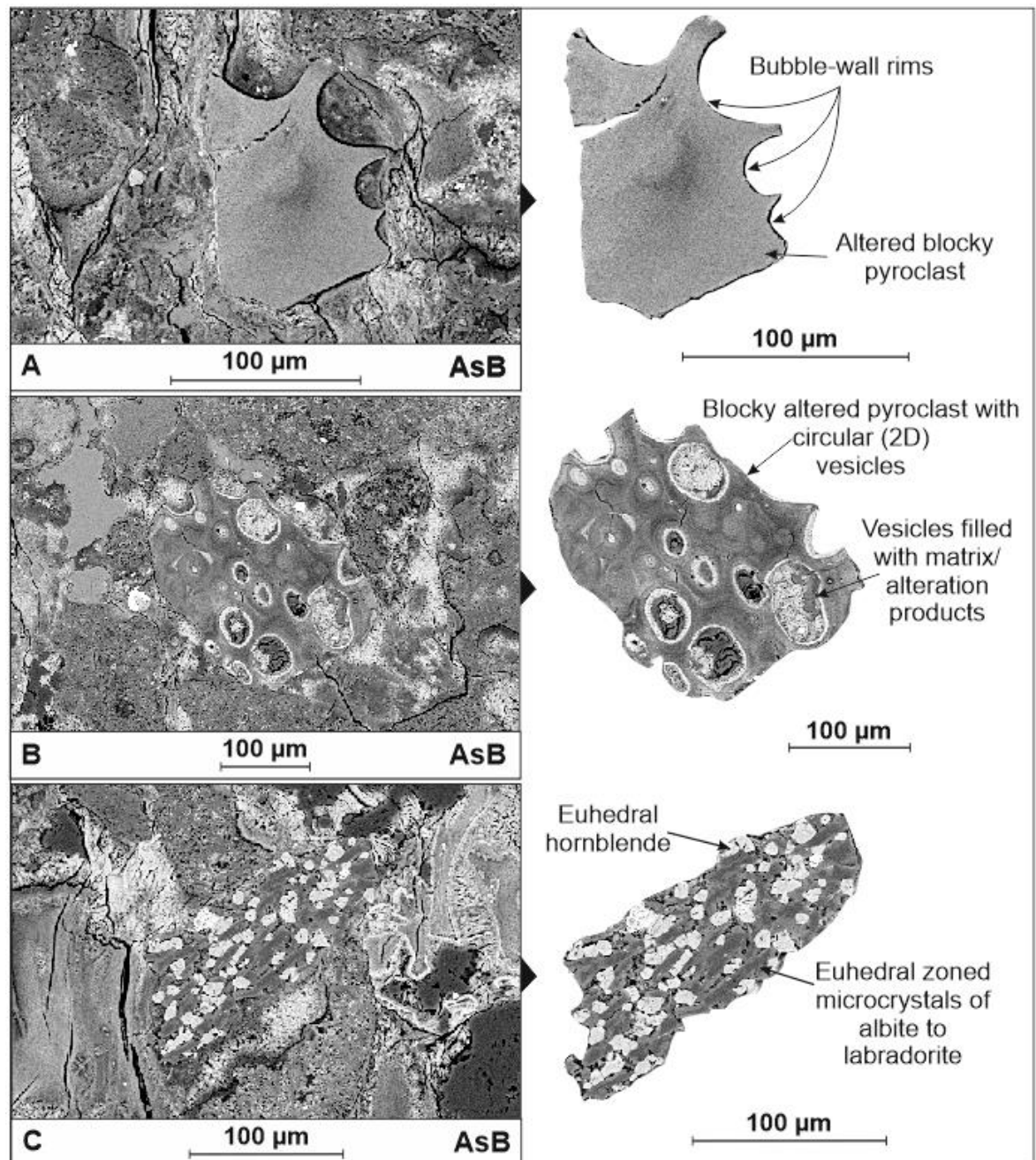


Figure 3-40 AsB SEM images of igneous clast-types in sample from FSB 6104/25-1 (Sula-Stelka). **A)** Blocky pyroclast with several bubble-wall rims. **B)** Highly palagonitised blocky pyroclast with circular (in cross-section) vesicles. The vesicles are filled with clay, or secondary minerals that formed during alteration. **C)** Angular crystalline igneous clast composed of euhedral hornblende (a type of amphibole) and feldspar microcrystals. The feldspar crystals are zoned and have a core of albite surrounded by labradorite.

Fluidal-shaped, or rounded, crystalline igneous clasts are the most abundant clast-type in this sample; many of these clasts are vesicular, with vesicles of varying size and shape (Figure 3-41).

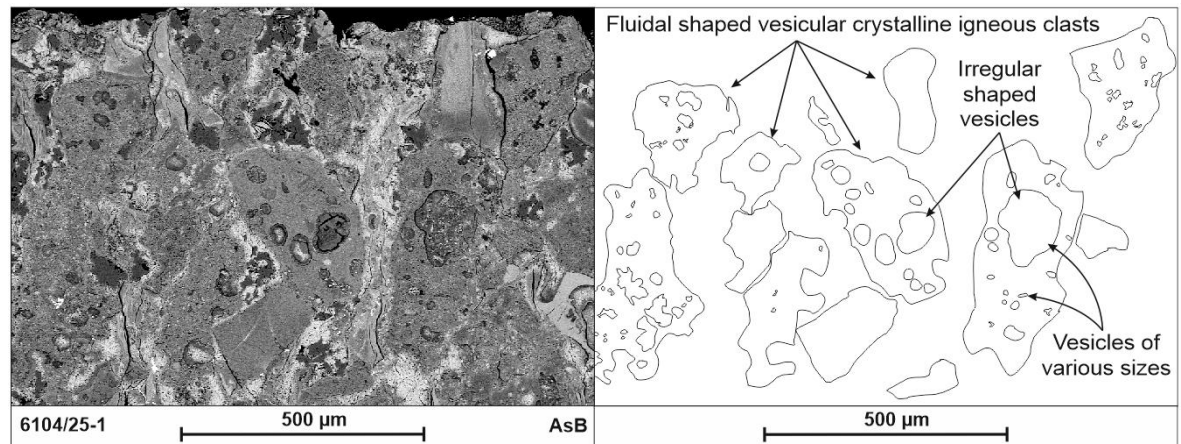


Figure 3-41 Fluidal-shaped crystalline igneous clasts with irregular-shaped vesicles of various sizes. These are the dominant clast-type in the sample from FSB 6104/25-1 (Sula-Stelka).

Additional types of crystalline igneous clast are also present, including angular lithics with euhedral amphibole and feldspar microcrystals. The feldspar in these clasts are zoned euhedral crystals with an albite core surrounded by a rim of labradorite (Figure 3-40c). The exact composition of the outer rim is uncertain due to uncertainty in the level of alteration and the accuracy of major element data on the SEM. The zoning could be the effect of alteration, or it could be related to changes in the magmatic system in which the feldspar crystallised. This clast-type has not been identified in any of the NSB samples.

3.5.3 Image analysis

Image analysis performed on backscatter (AsB) SEM images was used to obtain data on grain characteristics such as the abundance of each grain-type, grain-size distribution and pyroclast vesicularity. Image analysis was also used to calculate the porosity of sandstone within NOR25/11-17 (sample 005).

The grain-size distribution was calculated for samples that contain individual clasts that could be easily distinguished from the surrounding matrix or cement. This ruled out many of the samples from the UKCS wells, as high-levels of alteration have blurred clast-matrix boundaries. The results show that none of the samples contain clasts greater than very coarse sand grade (1-2 mm; Figure 3-42, Figure 3-43). Many of the samples have a unimodal grain-size peak between silt (3.9 - 62.5 µm) and medium sand (250 - 500 µm), although sample

018 does not have a peak at one specific grain-size range, but instead has an almost equal abundance of silt to fine-sand grade clasts (Figure 3-43). Other samples have a bimodal grain-size distribution with two grain-size peaks; SSK56375, 005, 033, 036 and 039 (Figure 3-42, Figure 3-43). If the grain-sizes of these deposits are described using pyroclastic terminology, then all of the samples are comprised of ash (<2 mm; Cas & Wright 1988). The sandstone of sample 005 is comprised of finer-grains than the tuffs, with a greater amount of fine-sand to silt-grade clasts (samples 001 and 002; Figure 3-42).

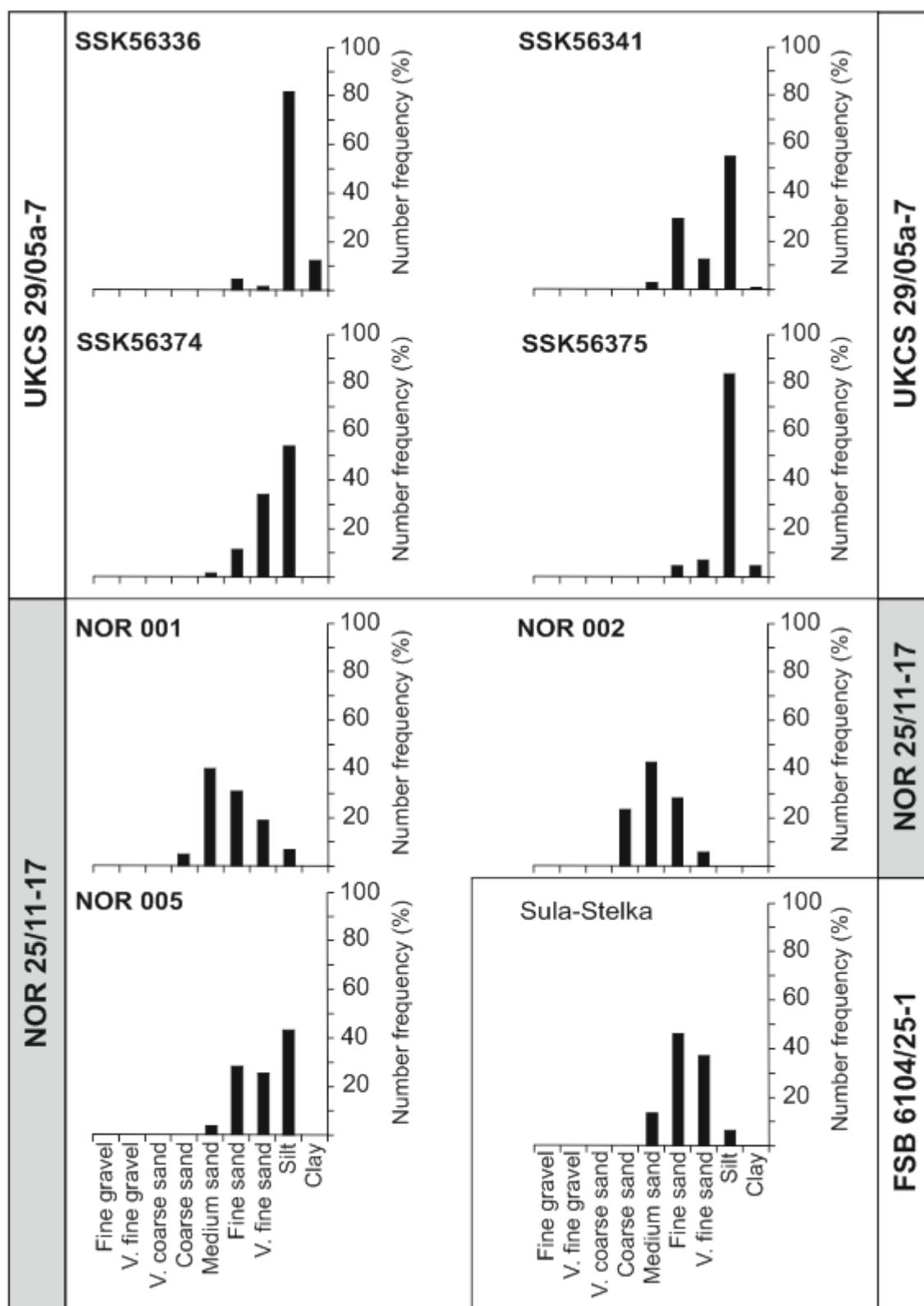


Figure 3-42 Grain-size distribution for samples from UKCS29/05a-7, NOR25/11-17 and FSB 6104/25-1. All of these samples are representative of tuffs, except NOR 005 which represents a quartz-rich siliciclastic sandstone (quartz arenite). Descriptions are given in the text.

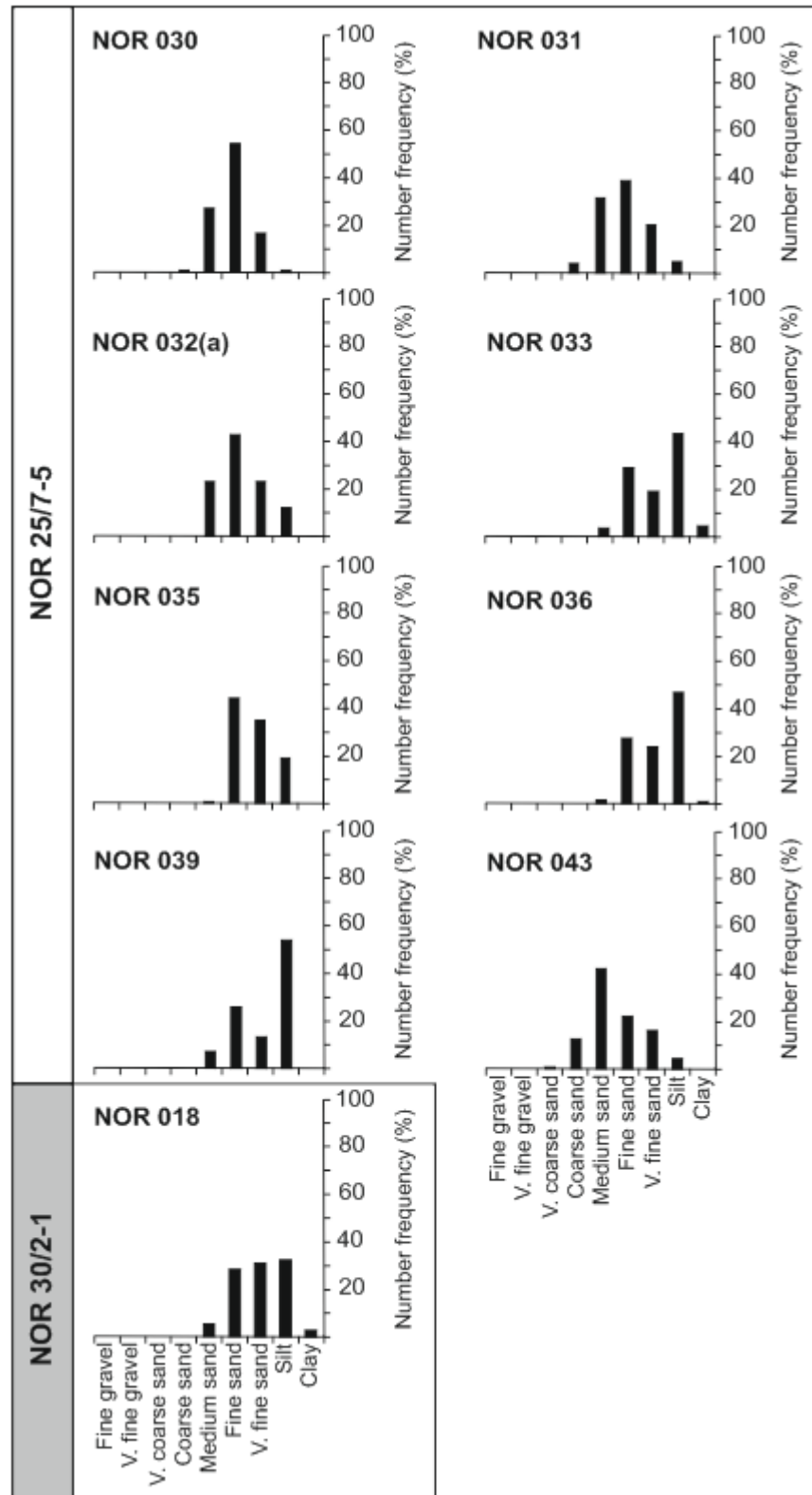


Figure 3-43 Grain-size distribution graphs for samples from NOR25/7-5 and NOR30/2-1. Sample 032(a) is representative of the grain-size distribution at the base of a normal-graded tuff from N25/7-5. Descriptions are given in the text.

A comparison of the grain-size distribution of samples between each well shows that the range of grain-sizes are generally coarser-grained in samples from NOR25/11-17 and are finer-grained in UKCS29/05a-7 (Figure 3-44).

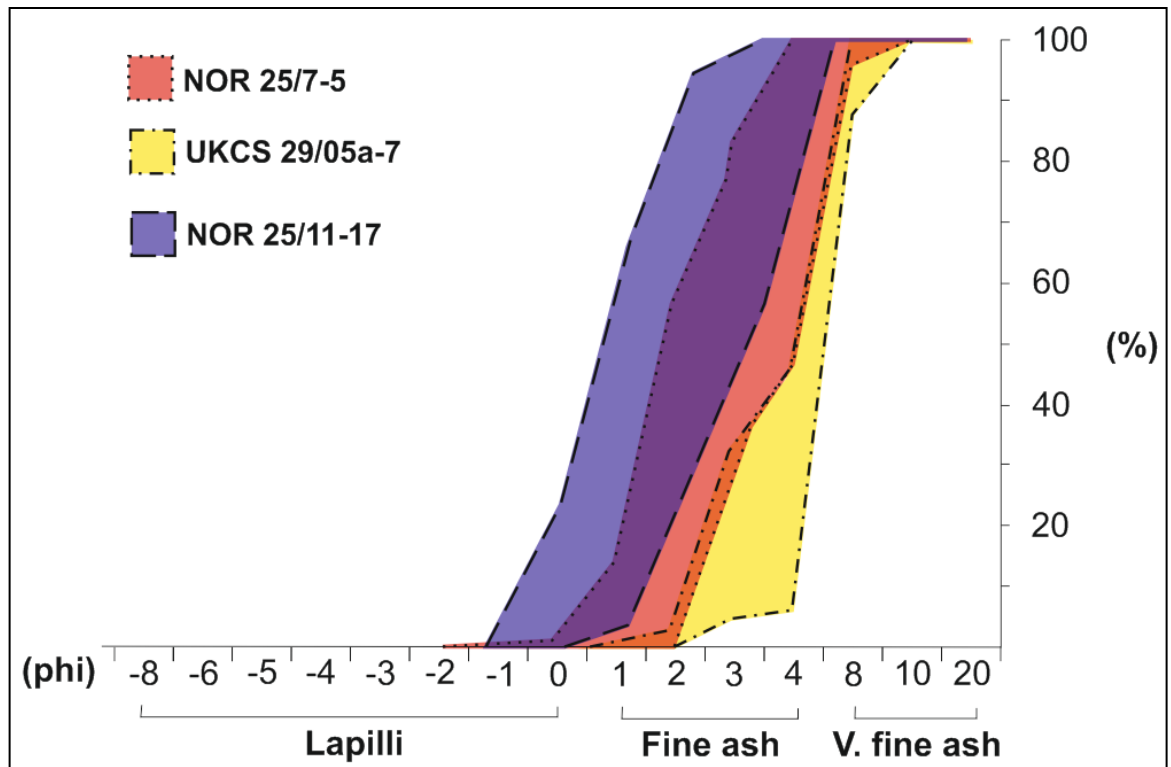


Figure 3-44 Grain-size distribution comparison for tuffs of each of the wells. The tuffs are generally coarser-grained in samples from NOR25/11-17 and finer-grained in samples from UKCS29/05a-7.

Stokes' Law can be applied to the grain-size data to calculate the settling velocity of different sized grains and predict the time it could take for these grains to settle through different depths of water (Figure 3-45).

A. Settling velocity =
$$\frac{(g \times d^2) \times (\rho_{\text{Particle}} - \rho_{\text{Medium}})}{(18 \times \text{Viscosity}_{\text{Medium}})}$$

B. Settling velocity =
$$\frac{(9.8 \text{ m/s}^2 \times \text{Feret}^2) \times (2.74 \times 10^{-6} \text{ kg/m}^3 - 9.98 \text{ kg/m}^3)}{(18 \times 0.001 \text{ kg/m}^{-5})}$$

Figure 3-45 Equations of settling velocity (variation of Stokes' Law 1851) used to calculate the duration of settling for grains of different sizes through water. Gravity (g): 9.8 m/s²; particle diameter (d), the maximum and minimum feret diameter for grains measured by image analysis were used as values for (d) and converted from μm to metres; the density of basalt (2.74 x 10⁻⁶ kg/m³) was used for the particle density (ρ_{Particle}) (Wohletz & Heiken 1992);

a medium density (ρ_{Medium}) of 9.98 kg/m³ was used to represent the density of water at 1 bar pressure and a temperature of 20°C; the viscosity of water ($\text{Viscosity}_{\text{Medium}}$) at 1 bar pressure and 20°C is 0.001 kg/m^{-s}.

Stokes' Law is based on several assumptions that could affect the settling velocity of grains deposited through a water column. For example, this calculation does not consider: grain roughness (all grains are considered as spheres), water salinity (only pure water was assumed in this calculation), currents and variations in their strength. This calculation does not account for the vesicularity of clasts, but instead, considers all grains to be non-vesicular; however, vesicularity could decrease the density of grains, therefore causing coarser grains to have a decreased settling velocity than predicted by these calculations. To predict the settling velocity of a vesicular grain the vesicles need to be removed from the original non-vesicular feret value (measured). To do this the percentage vesicularity of the grains was converted to a percentage of the length of the original feret value; this was then deducted from the original value to give a result for the feret minus vesicles. This new value was then used to calculate the settling velocity. Grain-size, and therefore the original feret value, remains the same, it is only the density that changes due to the presence of vesicles (voids) within a grain, therefore the new settling velocity was plotted against the original feret value. This shows that vesicular grains likely settle at a slower rate through water compared to dense, non-vesicular grains of the same grain-size. However, these calculations do not consider the influence that 'air-bubbles' trapped as vesicles will have on the buoyancy of the grains, as this could decrease the settling velocity further. Although the abundance and size of vesicles is low for most pyroclasts in these samples, the density of the pyroclast would likely be high enough to prevent any effect of buoyancy; also, the rapid break-down of volcanic glass would likely allow water to enter the vesicles and replace the air within them (Vaughan & Webley 2010).

Generally, the settling velocity of the basaltic pyroclasts suggests that all grains of fine-sand grade (ash), and greater, will settle through 100 m of pure, still water within 1.5 days. Very fine ash, of less than fine-sand grade will settle within 1.5 to ca. 200 days (Figure 3-46).

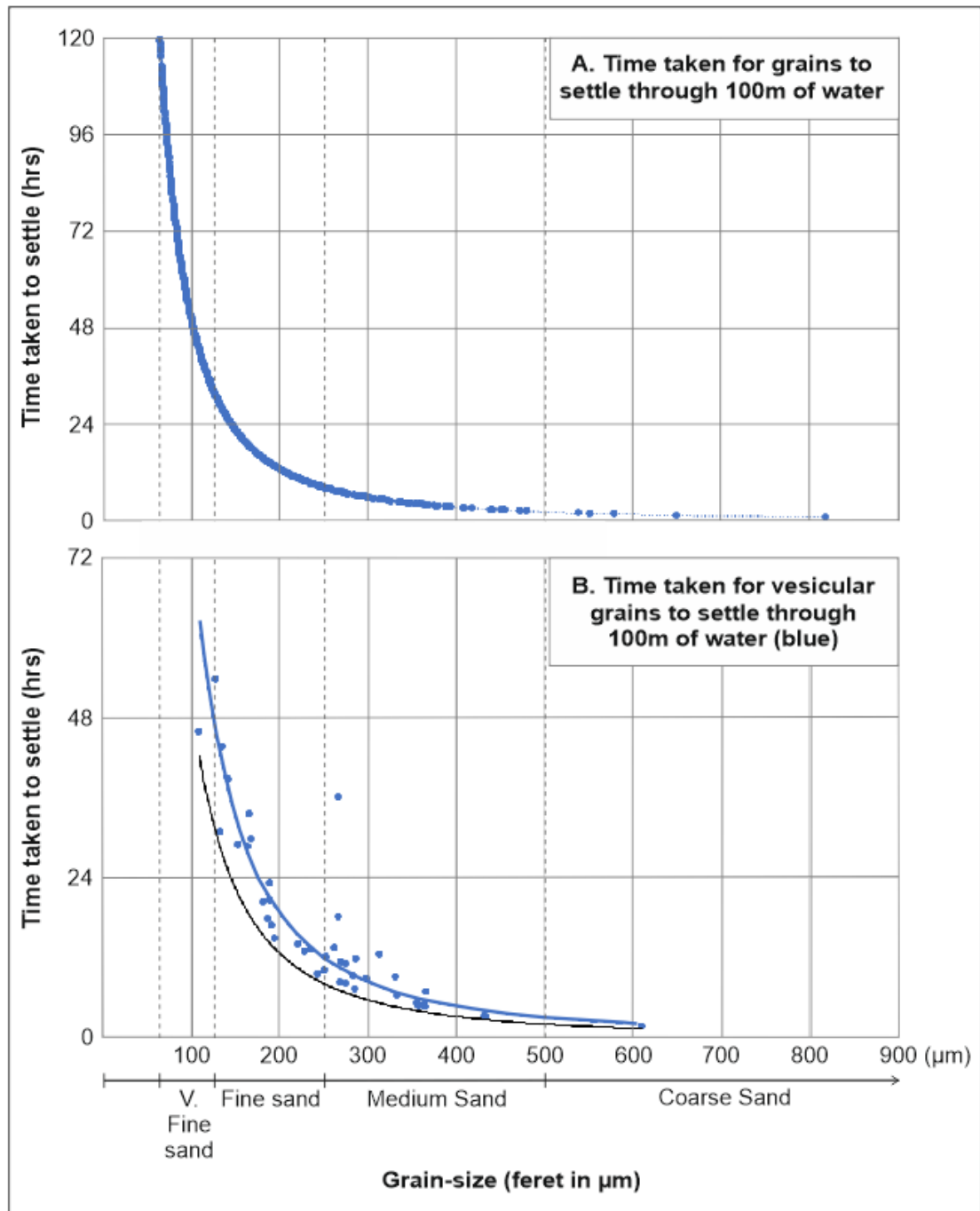


Figure 3-46 Settling velocity calculated for non-vesicular and vesicular pyroclasts of the BF, linking grain-size to the likely time take to be deposited.

The degree of sorting for each of the samples was calculated using the methods of Folk (1968), where the sorting coefficient (σ_1) is found using the 5th (ϕ_5), 16th (ϕ_{16}), 84th (ϕ_{84}) and 95th (ϕ_{95}) percentile values of grain-size (in Phi), given on a grain-size distribution curve (Figure 3-47).

$$\sigma_1 = \frac{(\phi_{84} - \phi_{16})}{4} + \frac{(\phi_{95} - \phi_5)}{6.6}$$

Figure 3-47 Folk (1968) equation for the calculation of the sorting coefficient for clastic materials.

A value of <0.35 is considered very well sorted, 0.35 - 0.5 well sorted, 0.5 - 0.71 moderately sorted, 0.71 - 1 moderately sorted, 1 - 2 poorly sorted, 2 - 4 very poorly sorted and >4 is extremely poorly sorted (Folk 1968).

The results (Table 3-3), show that the tuffs range from very poorly sorted to moderately sorted, and that the sandstone of sample 005, from NOR25/11-17 is poorly sorted.

Well	Sample ID	σ_1	Sorting
UKCS 29/05a-7	SSK56336	1.9	Poorly sorted
UKCS 29/05a-7	SSK56341	1.8	Poorly sorted
UKCS 29/05a-7	SSK56374	1.55	Poorly sorted
UKCS 29/05a-7	SSK56375	1	Moderately sorted
NOR 25/7-5	NOR 030	1.31	Poorly sorted
NOR 25/7-5	NOR 031	0.95	Moderately sorted
NOR 25/7-5	NOR 032a	1.56	Poorly sorted
NOR 25/7-5	NOR 033	2.4	Very poorly sorted
NOR 25/7-5	NOR 035	0.8	Moderately sorted
NOR 25/7-5	NOR 036	1.35	Poorly sorted
NOR 25/7-5	NOR 039	2.4	Very poorly sorted
NOR 25/7-5	NOR 043	1.7	Poorly sorted
NOR 25/11-17	NOR 001	0.95	Moderately sorted
NOR 25/11-17	NOR 002	0.7	Moderately well sorted
NOR 25/11-17	NOR 005	1.4	Poorly sorted
NOR 30/2-1	NOR 018	2.4	Very poorly sorted
FSB 6104/25-1	Sula-Stelka	0.95	Moderately sorted

Table 3-3 Degree of sorting in BF tuffs. These results were calculated using the methods of Folk (1968).

Point-count analysis of SEM images shows that the sandstone of sample 005 is predominantly composed of angular quartz grains (70%) with lesser amounts of orthoclase (8%) and stilpnomelane (<1%), with secondary growth of ankerite (12%) and halite (10%) around these (Figure 3-48).

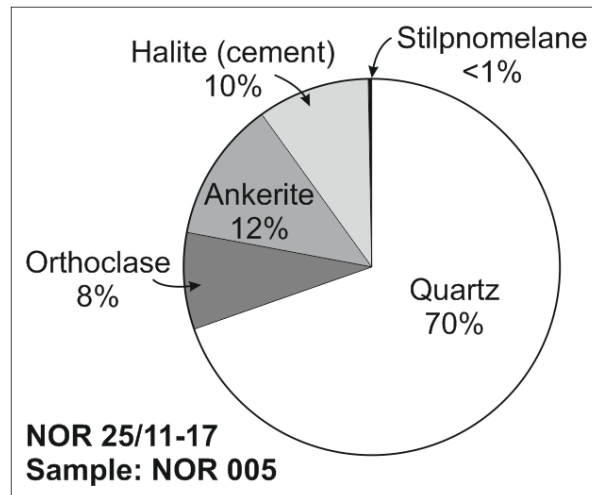


Figure 3-48 Composition of NOR 005 from NOR25/11-17. This sandstone is dominated by quartz grains (70%), with a lesser abundance of orthoclase, stilpnomelane, ankerite and halite.

The total porosity of the siliciclastic sandstone of sample 005 was calculated by removing the total area occupied by grains from the area of an AsB SEM image using a similar approach to Manger (1963) (see 1.3 Methods). The results for a suite of images were converted into percentages and averaged; the sandstone has a total porosity of *ca.* 40%.

The other siltstone and sandstone samples are all dominated by crystalline igneous clasts, including crystalline lithics and lava-like clasts (Figure 3-49), comprising <50 % of the unit, and are therefore considered to be tuffs (see Chapter 1). All samples from NOR25/7-5 and NOR25/11-17 appear to be predominantly comprised of fluidal-shaped, vesicular, micro-crystalline lava-like clasts (Figure 3-49). Altered pyroclasts are commonly the second most abundant clast-type within these deposits (Figure 3-49). Minor amounts of siliciclastic grains, including granular lithic clasts, and pyrite also occur (Figure 3-49).

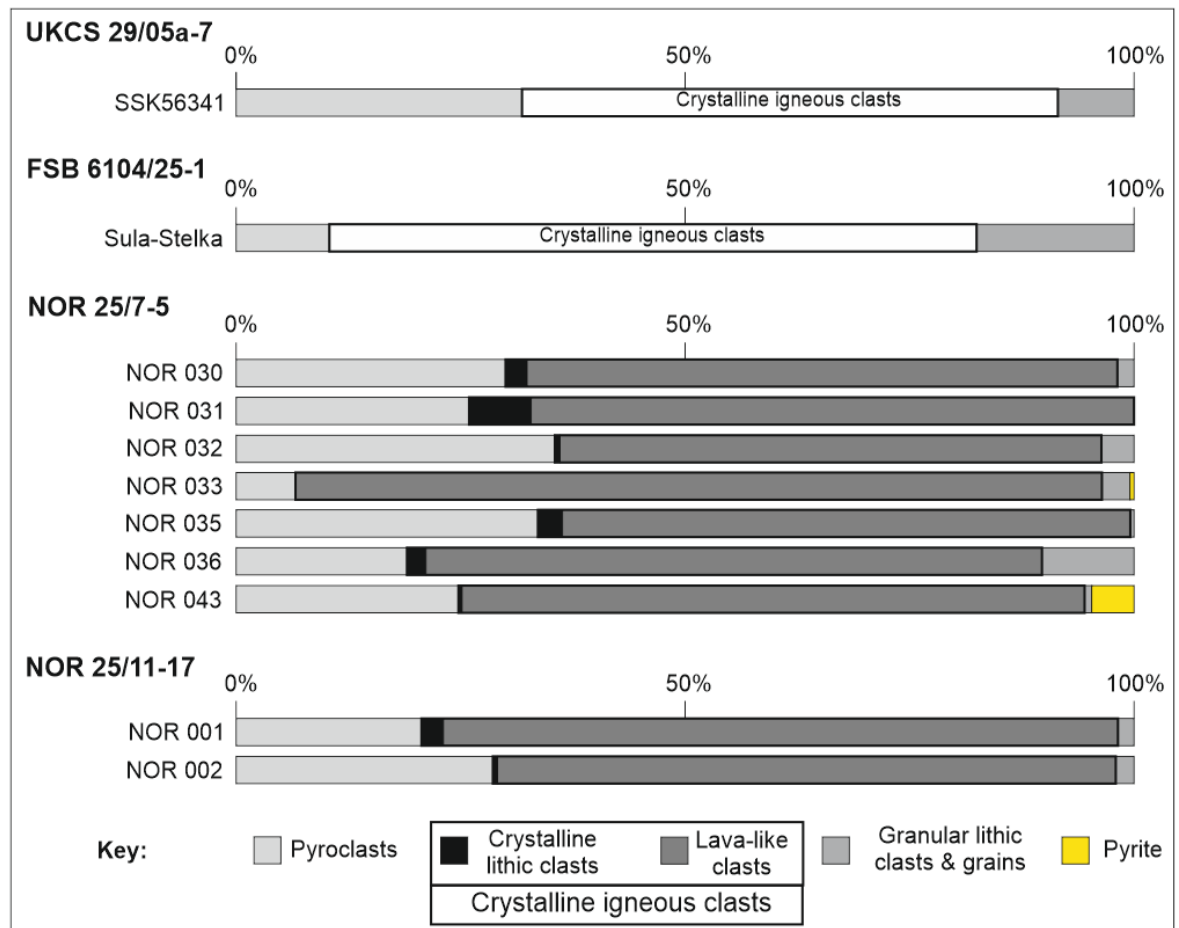


Figure 3-49 Percentage of different clast types within samples of siltstone and sandstone dominated by igneous clasts. Crystalline igneous clasts, including crystalline lithic clasts and lava-like clasts, are the most common clast-type in all of the samples. Pyroclasts are often the second most abundant clast-type.

The original features of pyroclasts have commonly been preserved, regardless of the level of alteration that has occurred. This preservation permits the pyroclasts to be divided into groups based on their overall morphology: blocky, bubble-wall, irregular and rod-like. Point-count data were collected from backscatter SEM images and converted to a percentage. The results show that blocky morphologies are the most common pyroclast-type across all the samples (Figure 3-50). Rod-like morphologies are absent from all samples, and bubble-wall and irregular morphologies occur in varying amounts throughout (Figure 3-50). Irregular pyroclast morphologies in these samples are generally quite angular and not fluidal, unlike those identified in Iceland (see Chapter 2) or the USA (see Chapter 6).

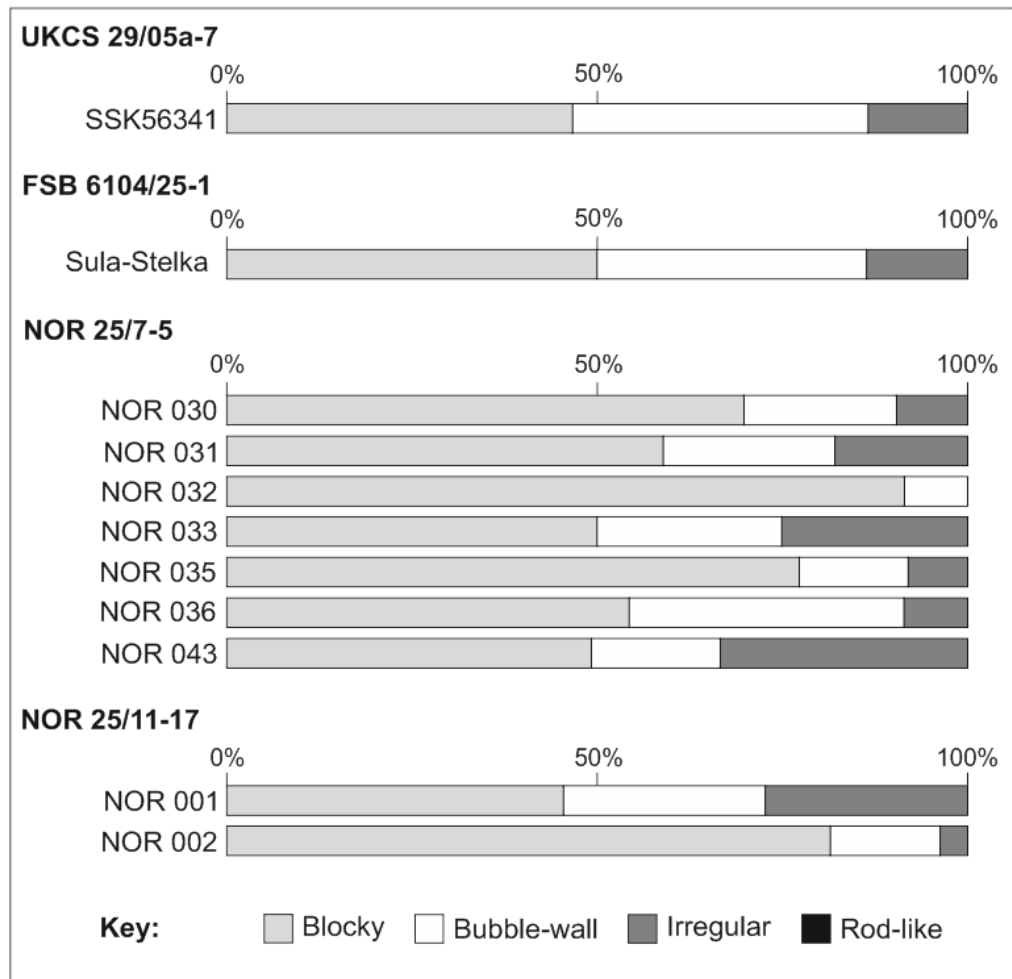


Figure 3-50 Percentage of blocky, bubble-wall, irregular and rod-like pyroclasts in samples from all wells.

Pyroclasts are a minor component of the samples (Figure 3-49, Table 3-4), and are predominantly non-vesicular (Table 3-4). However, over 50% of pyroclasts in samples 001, 002 and 043 are vesicular (Table 3-4). The average vesicularity of the vesicular pyroclasts is less than 45% in all of the samples, indicating that the pyroclasts are poorly vesicular (Table 3-5; Houghton et al. 2004; Graettinger et al. 2013). The vesicularity ranges from 2%, i.e. very poorly vesicular, up to 60%, i.e. moderately vesicular (Table 3-5; Houghton et al. 2004; Graettinger et al. 2013).

Well	Sample	Pyroclasts (%)	Non-pyroclasts* (%)	Vesicular pyroclasts (%)	Non-vesicular pyroclasts (%)
NOR 25/7-5	NOR 030	29	71	22	78
NOR 25/7-5	NOR 031	25	75	21	79
NOR 25/7-5	NOR 032	35	65	27	73
NOR 25/7-5	NOR 033	6	94	38	63
NOR 25/7-5	NOR 035	33	67	28	72
NOR 25/7-5	NOR 036	19	81	34	66
NOR 25/7-5	NOR 043	25	75	51	49
NOR 25/11-17	NOR 001	20	80	58	42
NOR 25/11-17	NOR 002	28	72	63	37
UKCS 29/05a-7	SSK56341	31	69	37	63
FSB 6104/25-1	Sula-Stelka	10	90	32	68

* crystalline igneous clasts, lava-like clasts, crystals, granular lithic clasts, grains

Table 3-4 Percentage of pyroclasts versus non-pyroclasts (*), and, the percentage of pyroclasts that are vesicular versus non-vesicular for each sample. Non-pyroclasts (*) includes: crystalline igneous lithic clasts (Figure 3-30c), lava-like clasts (Figure 3-27), crystals, and siliciclastic clast-types, including granular lithic clasts (see Chapter 2) and grains, such as quartz (Figure 3-38). All of the samples are dominated by non-pyroclasts. Pyroclasts form a minor component of the deposits, of which, most are non-vesicular. Of the pyroclasts >50% are vesicular in samples 001, 002 and 043 (red).

Well	Sample ID	Average vesicularity (%)	Range (%)	Number of pyroclasts counted
UKCS 22/30a-1	SSK56012	20.78	2 - 42	14
UKCS 29/05a-7	SSK56341	22.82	3 - 60	20
UKCS 29/05a-7	SSK56374	21.29	4 - 37	4
FSB 6104/25-1	Sula-Stelka	26.09	10 - 46	8
NOR 25/11-17	NOR 001	15.22	5 - 35	19
NOR 25/11-17	NOR 002	11.03	2 - 23	14
NOR 30/2-1	NOR 016	11.73	10 - 13	2
NOR 25/7-5	NOR 030	17.66	4 - 55	20
NOR 25/7-5	NOR 031	15.53	4 - 30	15
NOR 25/7-5	NOR 032	15.92	3 - 29	10
NOR 25/7-5	NOR 035	14.07	4 - 28	7
NOR 25/7-5	NOR 036	12.68	2 - 35	7
NOR 25/7-5	NOR 039	22.81	5 - 31	9
NOR 25/7-5	NOR 043	16.2	7 - 27	5

Table 3-5 Average percentage vesicularity of vesicular pyroclasts. The average vesicularity is <45% for all samples, indicating that the pyroclasts are poorly vesicular. The vesicularities range from 2%, very poorly vesicular, to 60%, moderately vesicular. Some samples do not contain many vesicular pyroclasts that could be used in these calculations, e.g. NOR 016, therefore, the results for these samples are less reliable, but are shown here as a rough estimate of the vesicularity for comparison.

3.5.4 Comparison of wire-line data to core analysis

Well data are freely available for the NOR wells on the NPD website, and information from the UKCS can be accessed via the Oil and Gas Authority. Here, final well reports and completion logs with wire-line data and rock descriptions are critically evaluated, to allow a comparison of the wire-line data with observations of core in this study. It is important to compare the wire-line and core as the core gives the highest resolution of the formation, compared to wire-line, which can give a maximum resolution of around 15 cm (Watson et al. 2017; see Appendix I). If the core and wire-line data can be correlated, then it may be possible to extend interpretations of the BF to other wells in the NSB where core is not available.

The composite logs and well reports, compiled after drilling of the wells, give a good guide to the depth of the upper and lower boundaries of the BF in the NSB. These depths can be used to estimate the thickness of the BF (Table 3-6).

Well	Depth of Top BF	Depth of base BF	Thickness of BF	Reference
UKCS 22/30a-1	9683 (ft)	9724 (ft)	41 ft (ca. 12 m)	Shell/ESSO
UKCS 29/05a-7	9454 (ft)	9628 (ft)	83 ft (ca. 25 m)	Shell/ESSO
NOR 25/7-5	1915 (m)	2017 (m)	102 m	NPD
NOR 25/11-17	1587 (m)	1647 (m)	60 m	NPD
NOR 30/2-1	1967 (m)	2041 (m)	74 m	NPD

Table 3-6 Thicknesses of the BF estimated for each of the wells.

It is possible that the upper and lower boundaries of the BF have been relocated following further analysis of the well data since the final well reports were compiled. However, these initial sources of information provide a fair guide as to the location of the formation boundaries and the nature of the lithologies of the BF.

3.5.4.1 UKCS22/30a-1

The final well report for UKCS22/30a-1 states that the BF is composed of thinly interbedded claystones and fine-grained tuff, along with structureless organic matter (UEE/33 1985). The presence of claystones with organic material has been interpreted as an indicator of a deep basinal setting (UEE/33 1985). According to the report, the tuff units are thicker at the base of the BF and have been interpreted as an indicator that these were deposited nearer to land (UEE/33 1985). These interpretations imply that this locality was submerged to greater water depths over time, possibly due to basin subsidence, and/or marine transgression, both of which likely did occur during deposition of the BF throughout the NE Atlantic and NW Europe (Nielsen 1974; Knox & Harland 1979; Mudge & Copestake 1992; Mudge & Bujak 1994; Knox 1996; Neal et al. 1996; Mudge & Jones 2004; Thomas & Bralower 2005; Carriol et al. 2016).

Only a small part of the BF of this well was cored, but the core shows that the BF is comprised of highly interbedded claystone and volcanoclastic sandstone and

siltstone, with some sections being more claystone-rich and others containing thicker units of coarser-grained units of siliciclastic sandstone (see section 3.5.2.1). These observations match the interpretations of wire-line data in the final well report. SEM analysis of a limited number of samples suggests that pyritised micro-fossils can be found (Figure 3-24a), however no other ‘organic’ features have been observed.

3.5.4.2 UKCS29/05a-7

Wire-line data provided in the completion log for UKCS29/05a-7 show that the BF is composed of a range of rock types that produce varying wire-line responses (Figure 3-51). For example, fluctuations in the gamma-ray response show that there are sand-rich and clay-rich lithologies (sandstone and claystone, respectively). Additionally, limestone can be interpreted where there is an increase in the density response and corresponding decrease in neutron porosity.

The composite log data suggest that the cored section should be comprised of sandstone to claystone and tuff (Figure 3-51), which is confirmed by analysis of the core (see section 3.5.1.1). The lower portion of the BF is also composed of claystone, as seen in the core (Figure 3-8), and indicated by the higher gamma-ray response in the wire-line data (Figure 3-51). The upper boundary of the BF is given by a characteristic increase in the gamma-ray response, which has been recorded in many wells that intersect the BF across the NSB (Mudge & Bliss 1983; Mudge & Bujak 1994; Joy 1996; Watson et al. 2017).

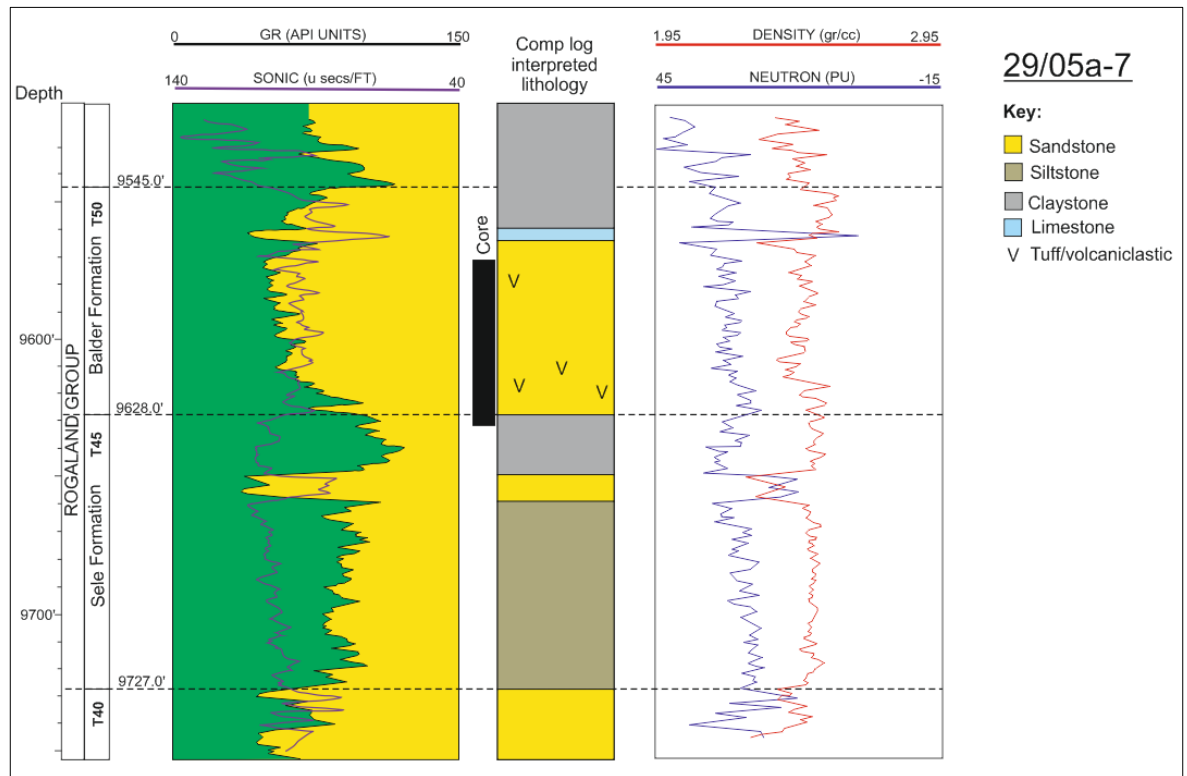


Figure 3-51 Wire-line and completion log interpreted geology for the Balder and Sele Formations of UKCS29/05a-1 (Shell/ESSO Completion Log 1990). Depth in feet.

3.5.4.3 NOR25/7-5

Wire-line data, including gamma-ray response, density, neutron porosity and sonic, are available for NOR25/7-5 (Figure 3-52). The responses show that the BF can be subdivided into a lower section where sand-rich lithologies are more abundant (low gamma-ray response), and an upper section comprised of more clay-rich lithologies (higher gamma-ray response; Figure 3-52). The upper boundary of the BF suggested in the well report does not coincide with an increased gamma-ray response as in UKCS29/05a-7, but does coincide with a characteristic increase in sonic velocity (Figure 3-51; Joy 1996), suggesting that the nature of the upper boundary of the BF in these wells is slightly different. This could be evidence of an erosional unconformity that overlies the BF and separates it from the overlying Hordaland Group (Mudge & Bliss 1983).

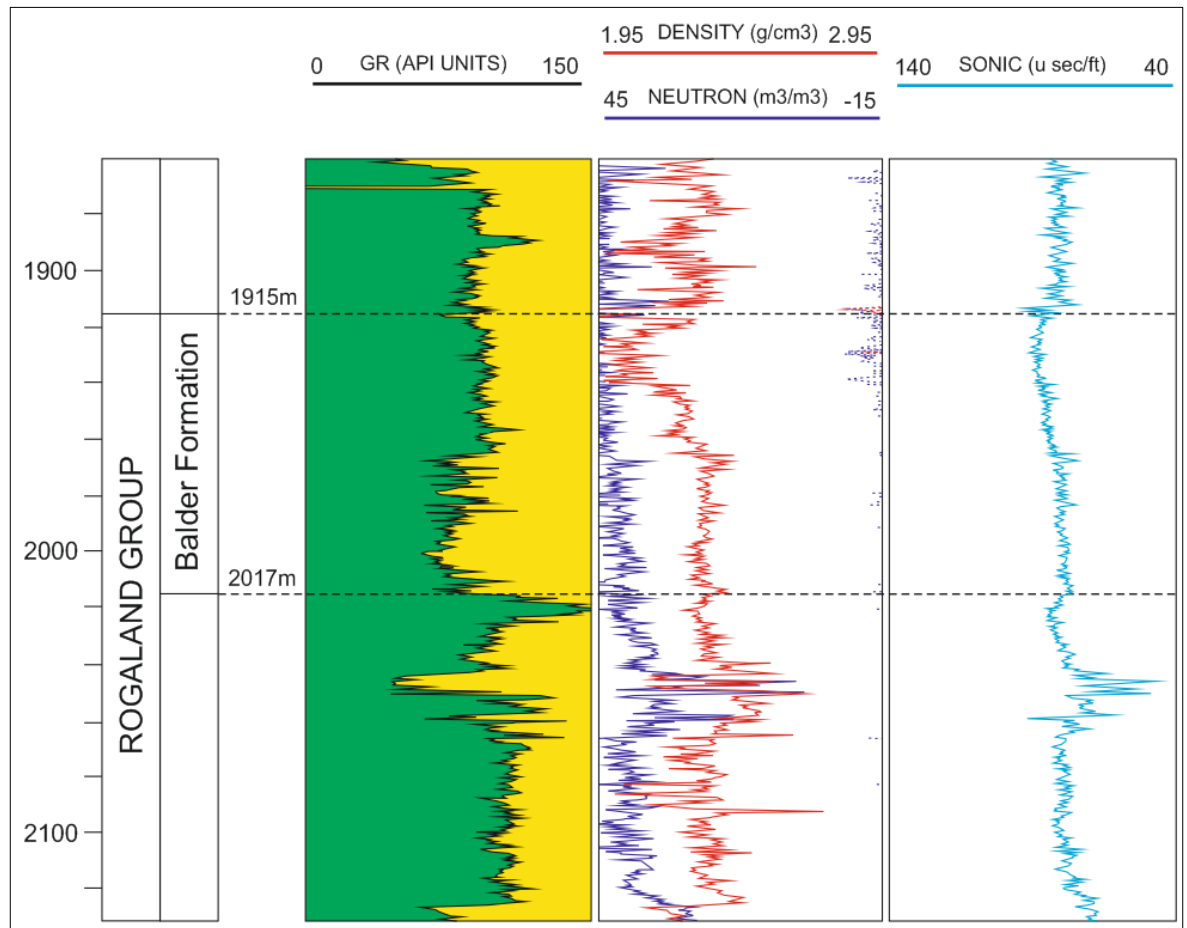


Figure 3-52 Wire-line data for the entire Rogaland Group available for NOR25/7-5 (NPD). Depth in metres.

3.5.4.4 NOR25/11-17

The gamma-ray response is low for most of the BF in the wire-line data for NOR25/11-17 (Figure 3-53), suggesting that the lithology of the BF in this well is more homogeneous compared to the other wells (Figure 3-51, Figure 3-52). The gamma-ray response fluctuates more at the base of the BF and a little towards the top, suggesting that more clay-rich lithologies, such as claystone and siltstone, are interbedded with sandstones at these depths. The sonic velocity and gamma-ray responses both reflect similar changes in the stratigraphy (Figure 3-53). A marked increase in the gamma-ray response marks the upper boundary of the BF in this well (Figure 3-53), similar to that of UKCS29/05a-7 (Figure 3-51). The completion report states that the BF ‘consists predominantly of sandstone with minor tuff and claystone’ (Norsk Hydro 1993), as shown by the stratigraphic log of the core (Figure 3-18), and the generally low-gamma response of the wire-line.

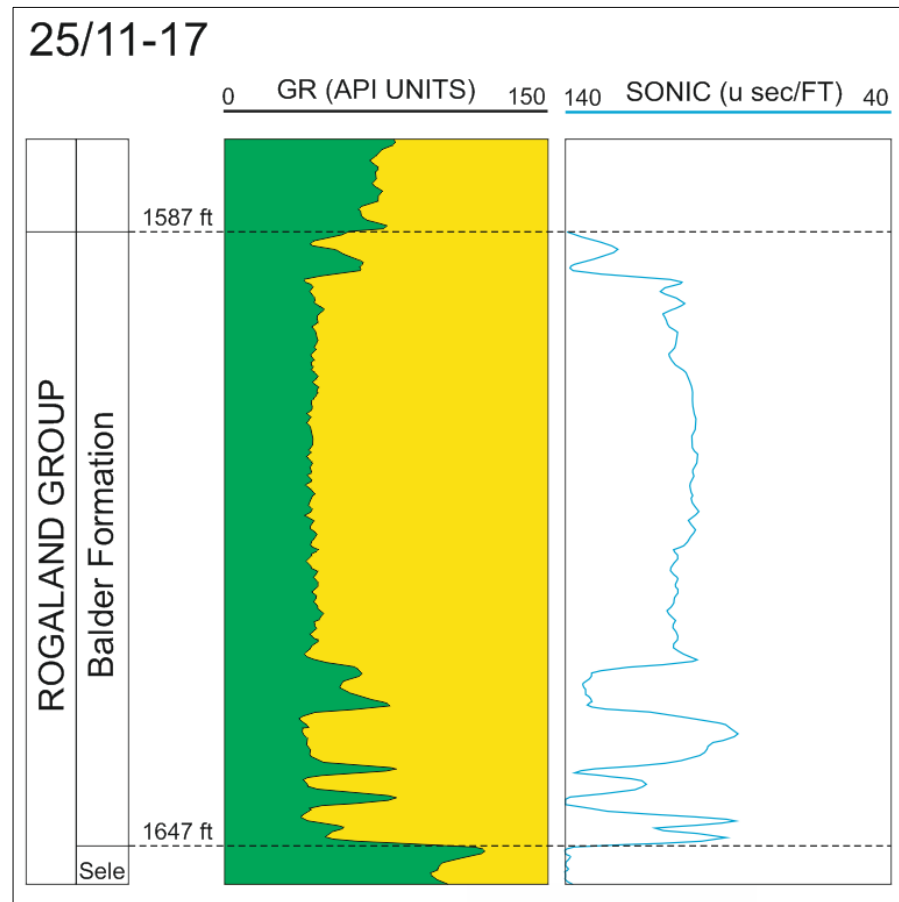


Figure 3-53 Wire-line data (gamma-ray and sonic-velocity responses) for NOR25/11-17 (Norsk Hydro 1993).

3.5.4.5 NOR30/2-1

The gamma-ray response of NOR30/2-1 is low at the base of the BF, however, towards the top the gamma-ray response fluctuates. The sonic velocity response is generally high throughout (Figure 3-54). This suggests that most of the BF here is composed of sand-rich lithologies, with more interbedded sandstone to claystone towards the top of the formation (Figure 3-54). An increase in gamma-ray response marks the upper boundary of the BF in the wire-line data (Figure 3-54). However, a marked increase in gamma-ray response coinciding with an increase in sonic velocity is present below this and may therefore be more characteristic of the top of the BF as seen in other wells (e.g. Figure 3-51), suggesting that the upper boundary of the BF in this final well report could be reinterpreted. The gamma-ray and sonic responses mirror each other throughout; however, there is no real change in the sonic response between the upper part of the BF and the overlying Hordaland Group as depicted in the composite log (Figure 3-54).

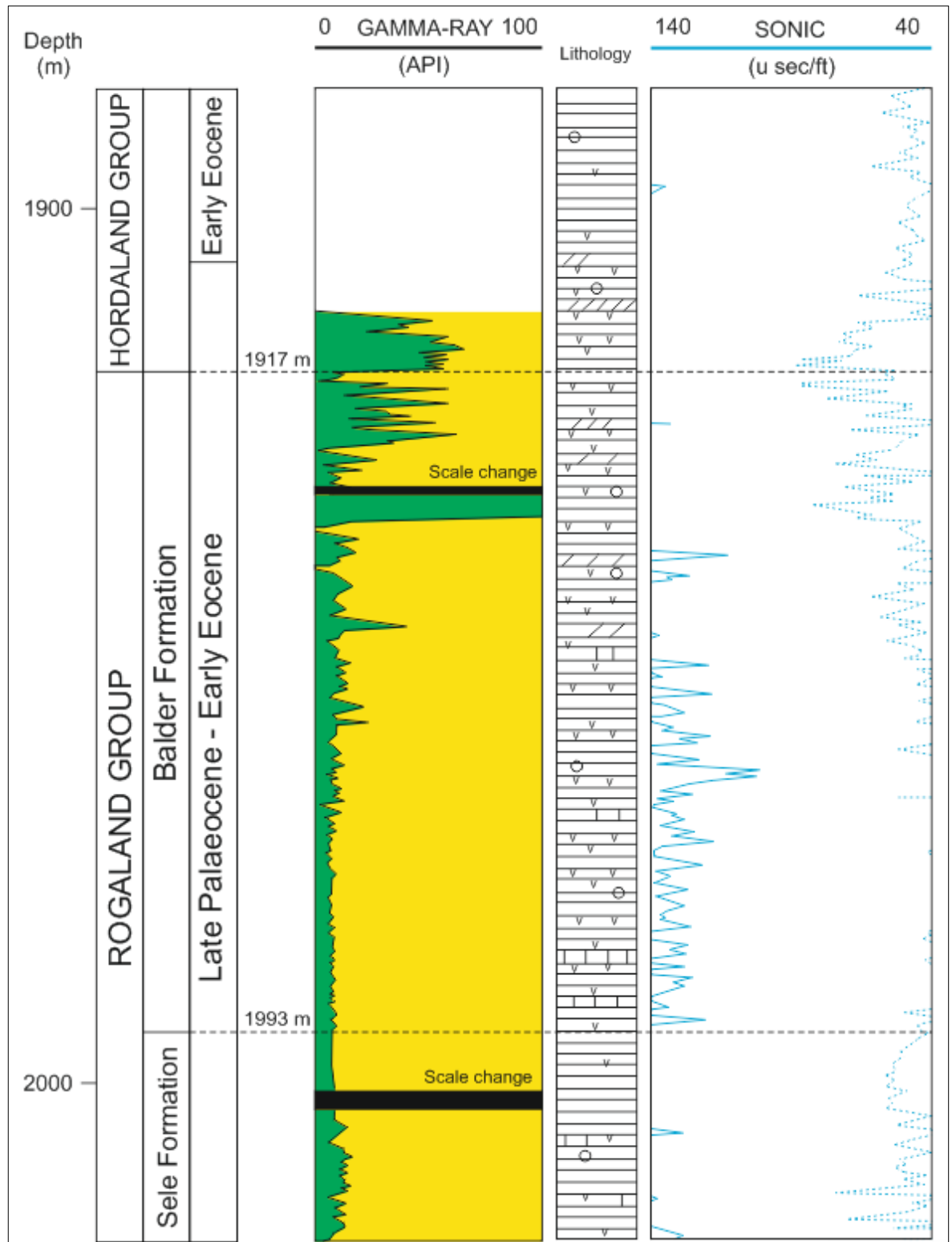


Figure 3-54 Wire-line data (gamma-ray and sonic response), and composite log interpreted lithology for NOR30/2-1 (NPD; Statoil/Union/Tenneco 1984).

3.6 Discussion

3.6.1 Sedimentary features and the environment of deposition

Logging of core and comparison of core with wire-line data show that the BF is composed of a wide range of lithologies, typically changing in character between wells. Generally, the BF contains interbedded siliciclastic claystone, siltstone and sandstone, in addition to tuffs, including volcanoclastic siltstones and sandstones, that were deposited in a restricted lake-like marine basin (Knox & Harland 1979; Mudge & Copestake 1992, 1992a; Knox 1996; Carriol et al. 2016). All of the cores have a similar appearance of highly interbedded lithologies, except core of NOR25/11-17, which contains 5-6 m thick units of poorly-sorted sandstone (quartz arenite; Figure 3-55).

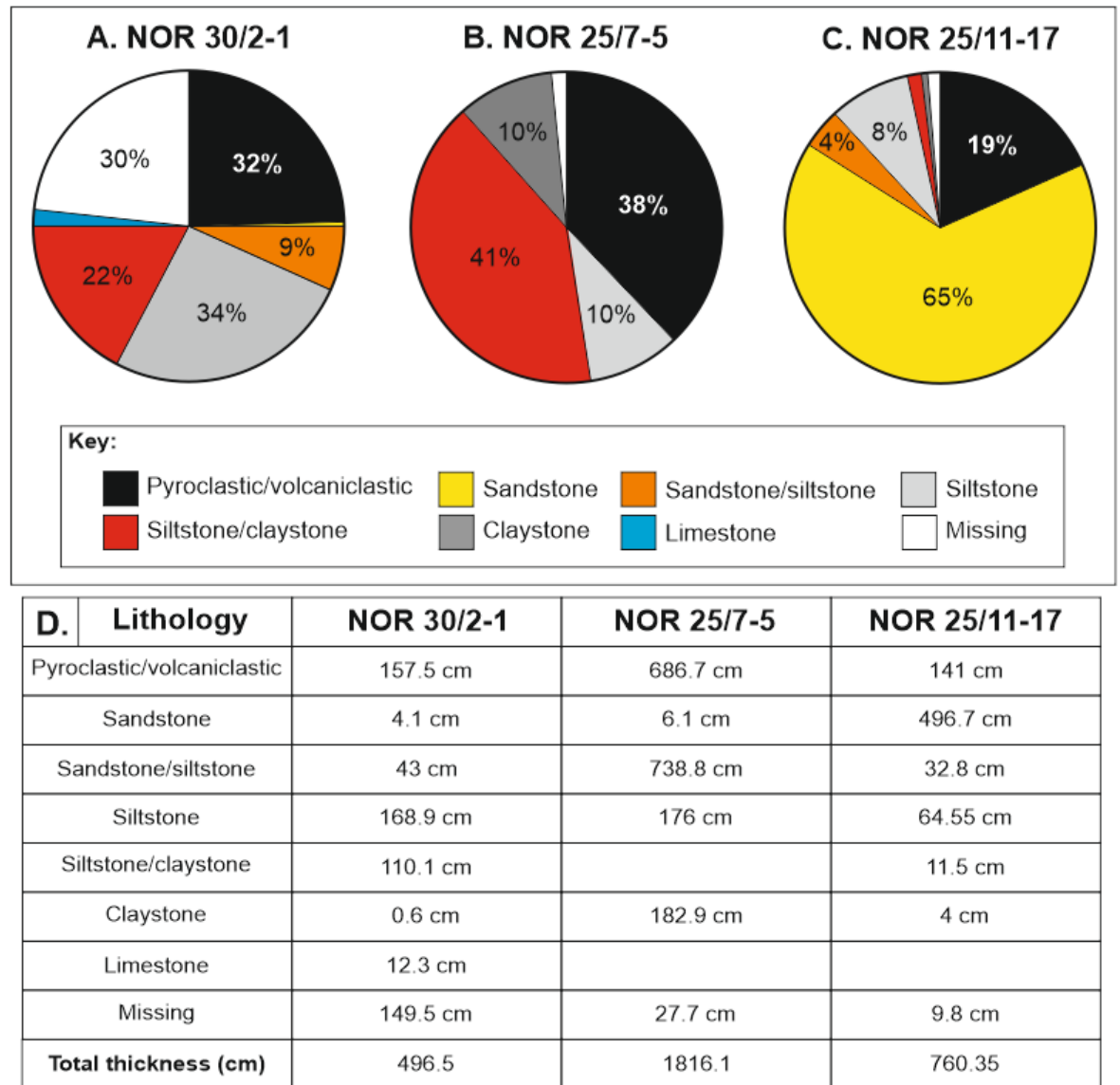


Figure 3-55 Summary of the percentage of different lithologies logged in core of the BF. NOR30/2-1 (A) is the most northern well of the present study, and NOR25/11-17 (C) is the most southern Norwegian well. The lithologies of each well vary as shown by the abundance of different lithologies and their relative combined thicknesses for each of the Norwegian cores. NOR25/11-17 contains 65% sandstone, contrasting to the sand-poor lithologies of the other two cores.

3.6.1.1 Siliciclastic sandstone of NOR25/11-17

Sandstones occur in various parts of the NSB, mostly within prograding delta facies that developed basinward from the Scottish landmass (Milton et al. 1990; Mudge & Copestake 1992a; Mudge & Bujak 1994; Knox 1996; Neal et al. 1996; Mudge & Jones 2004). The quartz-rich sandstones (sample 005) of NOR25/11-17 are predominantly composed of angular quartz grains with a moderate porosity (*ca.* 40%; Figure 3-37, Figure 3-48). Localised occurrences of ankerite, gypsum, halite and K-salts are present throughout the sample (Figure 3-38). Similarly

ankerite has been identified as concretions and cements within sandstones in the southern NSB, where they are common in continental sandstone facies (Hendry et al. 2000). Ankerite has also been identified in Jurassic shelf sandstones in UKCS Block 22 and 29, where it has been associated with the sandstones proximity to underlying Permian evaporites (Hendry et al. 2000). In these examples the ankerite is also found in quartz-rich sandstones that also contain orthoclase, and the ankerite likely crystallised during deep burial of the sandstones and associated fluid flow, with fluids containing organic carbon from the alteration of bioclastic material (Hendry et al. 2000). NOR25/11-17 most likely intersects an area of sand-body development that extended out into the NSB from the Scottish landmass during the Early Eocene (i.e. Milton et al. 1990; Mudge & Bujak 1994; Knox 1996). The sands are associated with thinly interbedded tuffs, although these are fewer, and more concentrated in comparison to the other cores (Figure 3-18). There is significantly less siliciclastic siltstone and claystone in this core, compared to the other cores analysed. It is possible that the ankerite and evaporite minerals crystallised during deep burial of these sandstones (e.g. Hendry et al. 2000). The lack of bioturbation and presence of interbedded claystones and tuffs, suggest that these materials were originally deposited as a submarine fan in an anoxic environment (e.g. Hendry et al. 2000; Pszonka & Wendorff 2017). Therefore, the BF of NOR25/11-17 may have been deposited by turbidity currents, with subsequent reworking of material into submarine fans deposited in anoxic conditions in the deeper-marine part of the NSB during the Early Eocene.

3.6.1.2 The origin of pyrite and pyrite framboids in the BF

The interbedded claystones, siltstones and some tuffs contain abundant pyrite framboids. Pyrite has also been found as a localised cement, or where it has replaced microfossils (Figure 3-24a). Pyrite framboids are found in modern and ancient sediments that were deposited in a range of sub-aqueous environments (Rickard 1970; Wilkin et al. 1996; Butler & Rickard 2000). The sizes and shapes of pyrite framboids can give information on the environment of deposition (Figure 3-56; Rickard 1970), for example, whether the environment was oxic or anoxic during deposition (Wilkin et al. 1996). However, there has only been limited comparison of pyrite framboid formation across different environmental

settings at present, and limited correlations between these and the mechanisms of framboid formation (e.g. Ohfuji & Rickard 2005). Comparison of these ancient pyrite textures with those observed in more modern sediments, for example, can aid in the identification of the environmental conditions present during deposition of the BF (e.g. Wilkin et al. 1996). Pyrite is most commonly found in anoxic sediments and forms early during anoxic diagenesis, commonly within the top few centimetres of the sediment (Wilkin et al. 1996).

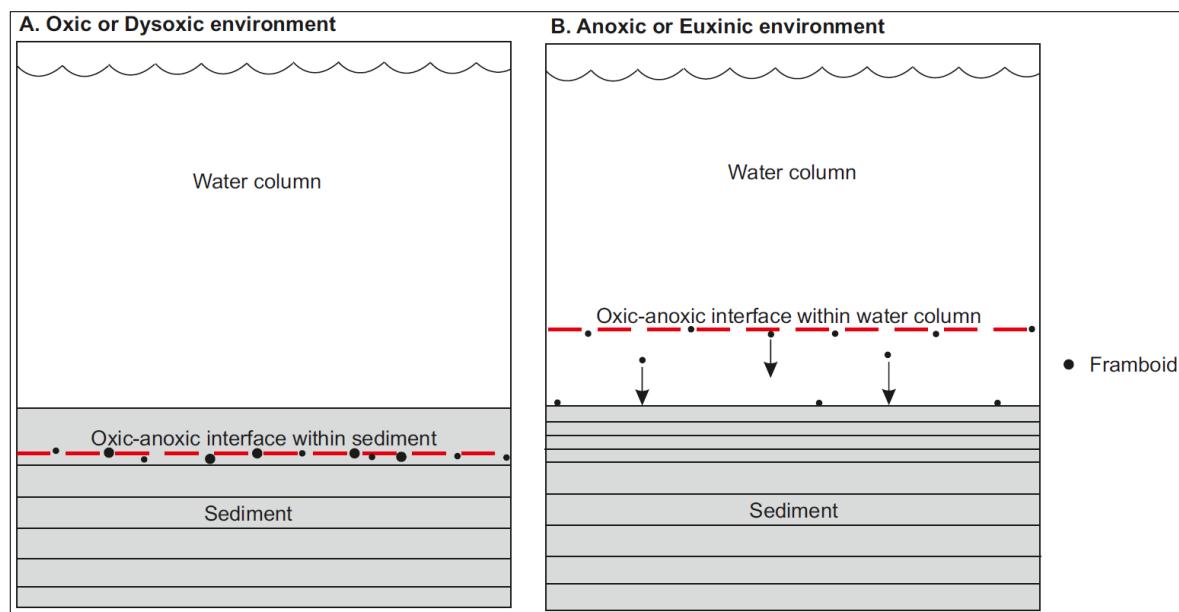


Figure 3-56 Formation processes of pyrite framboids. When the water column is fully oxygenated (oxic, also referred to as dysoxic) then the oxic-anoxic boundary will lie within the sediment (A). In this scenario pyrite framboids will form within the sediment. However, if the water column is anoxic (also referred to as euxinic) then the oxic-anoxic boundary will lie above the surface of the sediment, and therefore pyrite framboids will form within the water column and sink onto the surface of the basin-floor sediments (B).

It is stated in the literature that framboids generally have a diameter of 1-10 μm with constituent micro-crystals of 0.2-2 μm (Rickard 1970; Butler & Rickard 2000; Ohfuji & Rickard 2005). In this study the framboids have an average diameter of <10 μm , although individual framboids are *ca.* 2-20 μm in diameter. In these samples, micro-crystals within the framboids tend to be <2 μm , are equant and equidimensional octahedral, cubo-octahedra, and rarely pyritohedra (Ohfuji & Rickard 2005). The micro-crystals are typically arranged in a disordered array within the framboidal structure (e.g. Ohfuji & Rickard 2005). All of these features of the BF pyrite framboids are comparable with the

observations of other pyrite framboid-containing sediments around the world (Rickard 1970; Wilkin et al. 1996; Butler & Rickard 2000; Ohfuji & Rickard 2005).

A review of the literature by Ohfuji & Rickard (2005), regarding the formation of framboidal pyrite, suggests that these features are most likely to form in environments/sediments that have pyrite supersaturated allowing pyrite to nucleate at a greater rate than the crystals can grow. The conditions for framboid growth in this way can be achieved in a sub-aqueous environment by increasing the temperature or Eh (oxidation/reduction), or by an increase of free-sulphur (S) in the environment (Butler & Rickard 2000; Ohfuji & Rickard 2005).

Some framboids appear to be associated with the replacement of micro-organisms (Figure 3-24a), although the majority do not appear to be associated with any form of organic material. The inherent lack of microfossils throughout the BF in these wells supports a hypothesis that these pyrite textures did not form due to the presence of organic material (e.g. Ohfuji & Rickard 2005). They are therefore associated with inorganic processes.

Individual micro-crystals are not obvious in all spherical pyrite forms, which could be due to later growth of pyrite that infilled voids between the micro-crystals within framboids (Ohfuji & Rickard 2005). This 'infilling' may be due to continued growth of the micro-crystals over time (Ohfuji & Rickard 2005).

In some beds, particularly claystones, there are amorphous accumulations of fine micro-crystallites of pyrite that are similar to those observed within pyrite framboids (Figure 3-26d, e). These are not considered as framboids (Rickard 1970; Ohfuji & Rickard 2005), although they may have formed in a similar setting.

The lack of bioturbation and micro-fauna and -flora within the NSB BF has been interpreted previously as evidence for anoxic bottom waters in the basin during the Early Eocene (Deegan & Scull 1977; Knox & Harland 1979; Pedersen & Jørgensen 1981; Mudge & Bliss 1983; Morton & Knox 1990; Elliott et al. 1992; Mude & Copestake 1992, 1992a; Mudge & Bujak 1994; Knox 1996; Obst et al.

2015; Carriol et al. 2016). The presence of pyrite framboids indicates that anoxic conditions prevailed either within the top few centimetres of the sediment, or a few centimetres above the sediment-water interface (e.g. Rickard 1970; Wilkin et al. 1996; Ohfuji & Rickard 2005). The anoxic environment allowed the growth of pyrite framboids throughout BF time (e.g. Nielsen et al. 1974; Pedersen et al. 1975; Obst et al. 2015).

3.6.1.3 Depositional processes indicated for tuffs in the BF

Units of tuff, consisting of originally glassy pyroclasts and crystalline igneous lithics (Figure 3-49) are common within the core of the NSB BF (e.g. Figure 3-7; Figure 3-55). Several of the tuffs contain a well-developed calcite cement; the cement is often well-developed in the coarser-grained parts, but less well developed within finer-grained material. Localised poorly-developed pyrite cement is sometimes associated with the calcite cement of the coarser-grained units (Figure 3-33). The ash component within the cemented tuffs is commonly better preserved (Figure 3-26b) than in the non-cemented tuffs (Figure 3-26a), suggesting that cementation occurred early during diagenesis and prevented fluids from causing significant alteration of the ash (Pedersen & Jørgensen 1981; Larsen et al. 2003; Brooks 2006). The uncemented tuffs are likely to be more compacted (Nielsen et al. 1974; Morton & Knox 1988; Larsen et al. 2003; Brooks 2006), but all the tuffs have a low porosity and permeability, due to the abundance of clay minerals and clay-grade matrix material (see section 3.5.2).

The (original) ash, of the tuffs, was deposited through a marine water column, as suggested by interbedded rock-types, including laminated claystone (see section 3.6.1), the presence of pyrite framboids (e.g. Figure 3-26d), and occasional micro-fossils (e.g. Figure 3-24a). These deposits are therefore volcanoclastic, following the definitions of Cas & Wright (1987), as they have been re-deposited after being initially deposited as air-fall ash onto the sea, and therefore, the Earth's, surface (Cas & Wright 1987; Manville et al. 2009). The definition of 'volcanoclastic' includes all tephra that is deposited through water, as the term 'primary' pyroclastic deposit refers to tephra deposited by air-fall only (Cas & Wright 1987). Therefore, for example, pyroclastic material primarily deposited within water from a submarine eruption, would not be included as

‘primary’ pyroclastic deposits (Cas & Wright 1987; Manville et al. 2009). These definitions do not consider primary air-fall tuff that lands on a surface of water and is directly deposited through the water column, therefore not obtaining any *real* reworking characteristics, such as mixing with additional sedimentary grains/clasts, or moving laterally by currents. Settling through water could impart different settling characteristics on the ash, for example, by deposition of aggregated clumps of ash rather than individual pyroclasts (Winterwerp 2002; Manville & Wilson 2004; Manville et al. 2009; Yamamoto et al. 2015), but the overall characteristics may be similar to those of air-fall ashes deposited on land (e.g. Roberts et al. 1984; Morton & Knox 1990; Obst et al. 2015). However, some truly reworked ashes, transported by wind or water into a basin could subsequently settle through the water column and obtain characteristics similar to those of non-reworked air-fall, water-lain ash deposits. Therefore, there remains ambiguity in the appropriateness and application of ‘primary’ and ‘volcaniclastic’ terms, particularly regarding water-lain tephra (see chapter Chapter 7).

Following the considerations in the other chapters of this thesis, the pyroclastic and crystalline igneous clast-rich units of the BF are referred to as tuffs without reference to the origin of the deposit: whether deposition occurred directly from fall-out of ash or from reworking and re-deposition. This removes the need to define water-lain ash as volcaniclastic, where the processes of transportation and re-deposition cannot be determined. These issues will be discussed further in Chapter 7. The remaining discussion is focused on the use of grain-scale characteristics of the tuffs for the interpretation of eruption processes and the likely source of these basaltic ashes associated with the NAIP and Early Eocene volcanism in NW Europe.

3.6.2 Eruption history and the location of source vents

Initial opening of the NE Atlantic Ocean and subsequent sea-floor spreading involved significant magmatism that resulted in development of the NAIP (see section 3.2). This large-scale magmatic episode was likely due to the presence of the proto-Icelandic mantle plume (Pedersen et al. 1975; Knox & Morton 1988, 1990; Knox 1996; Ritchie & Hitchen 1996; Nadin et al. 1997; Kent & Fitton 2000;

Thomas & Bralower 2005; Breivik et al. 2006, 2009; Obst et al. 2015). The plume may have intersected with the rift and helped to initiate sea-floor spreading and the formation of new oceanic crust via active mantle upwelling and decompression melting (Breivik et al. 2009) in the Early Eocene (Hallam 1972; Knox & Harland 1979; Knox & Morton 1983; Knox 1996; Ritchie & Hitchen 1996; Nadin et al. 1997; Haaland et al. 2000; Torsvik et al. 2001; Larsen et al. 2003; Jolley & Widdowson 2005; Ross et al. 2005; Breivik et al. 2006; Brooks 2006; Storey et al. 2007; Brunstad et al. 2008; Breivik et al. 2009; Gernigon et al. 2012). Magmatism and its associated volcanism occurred in a large area from E Greenland to the Faroes, Scotland and the BPIP and into the Norwegian continental shelf (Figure 3-2; Pedersen et al. 1975; Pedersen & Jørgensen 1981; Knox & Morton 1983; Roberts et al. 1984; Knox & Morton 1988; Morton & Knox 1990; Kanaris-Sotiriou et al. 1993; Mudge & Bujak 1994; Knox 1996; Nadin et al. 1997; Saunders et al. 1997; Larsen et al. 1999, 1999a; Kent & Fitton 2000; Skogseid et al. 2000; Jolley & Bell 2002; Larsen et al. 2003; Thomas & Bralower 2005; Brooks 2006; Passey & Jolley 2009; Stoker et al. 2012; Obst et al. 2015; Watson et al. 2017). The basaltic tuffs of the BF were likely deposited following a period of intense explosive volcanism, the type and source of which has been debated throughout the literature (e.g. see section 3.2). Below is a discussion of the different scenarios in which these ashes could have formed (Figure 3-57), and been deposited, using interpretations from the literature, and the results of the analysis of the UKCS and NOR core material presented here (see section 3.5).

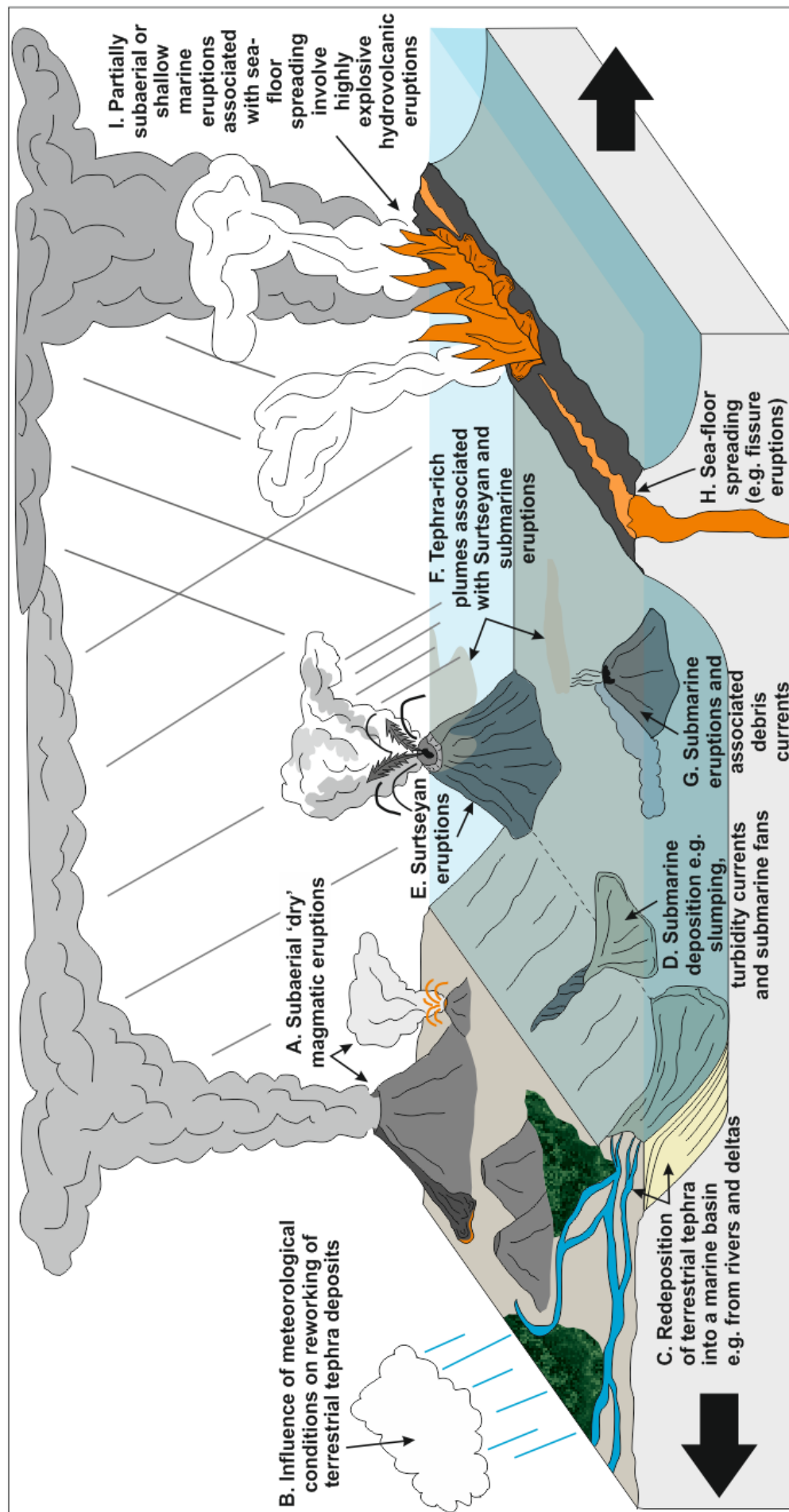


Figure 3-57 Volcanic and sedimentary environments discussed in the text as possible origins of the BF tuffs.

Previous interpretation of trends in the total thickness of tuffs in the NSB, Denmark, SE England, northern Germany and the Netherlands imply that there is a general thickening of the deposits northwards (Norin 1940; Pedersen et al. 1975; Pedersen & Jørgensen 1981; Knox 1984; Knox & Morton 1988; Morton & Knox 1990; Brooks 2006; Egger & Brückl 2006; Carriol et al. 2016), suggesting that the source of the ashes lay towards the north or NW, towards the NE Atlantic rift (Rhys 1974; Pedersen & Jørgensen 1981; Knox & Morton 1983; Malm et al. 1984; Knox & Morton 1988; Larsen et al. 2003; Brooks 2006). Textural analysis of the ash component of the tuffs shows that they are dominated by blocky pyroclast morphologies (Figure 3-50) with variable vesicularities (Table 3-4, Table 3-5), and a high abundance of fine-ash (Figure 3-44): these features are typically produced by hydrovolcanic eruptions whereby fragmentation of an erupting magma is enhanced by brittle fragmentation due to interaction with water (Heiken 1972, 1974; Wohletz 1983; Wohletz & Sheridan 1983; Cas & Wright 1988; Zimanowski et al. 1997; Mattsson 2010; Dellino et al. 2012; Ross & White 2012; Graettinger et al. 2013). Hydrovolcanic eruptions are a likely explanation for the unusually high levels of explosivity that the original basaltic magmas must have experienced to produce such a large quantity of basaltic ash, and to distribute it over large areas (Figure 3-2, Figure 3-3; e.g. Knox & Morton 1983, 1988; Morton & Knox 1990; Jolley 1996; Jolley & Bell 2002).

3.6.2.1 Surtseyan and submarine eruptions

Surtseyan eruptions occur when a volcanic edifice builds up from the ocean floor and becomes shallow enough for explosive magma-water interactions to take place (Figure 3-57e; Kokelaar & Durant 1983; Sorrentino et al. 2010; Vaughan & Webley 2010; Moorehouse et al. 2015). Sometimes these eruptions can build a subaerial tuff cone (Machado et al. 1962; Kokelaar & Durant 1983; Wohletz & Sheridan 1983; Solgevik et al. 2007; Corcoran & Moore 2008; Mattsson 2010; Vaughan & Webley 2010; Mantas et al. 2011; Gjerløw et al. 2015). This type of eruption is hydrovolcanic with magma-water interactions affecting the explosivity and the volume of ash produced (Machado et al. 1962; Cole et al. 2001; Solgevik et al. 2007; Vaughan & Webley 2010; Mantas et al. 2011; Augustín-Flores et al. 2015; Gjerløw et al. 2015). Without any interaction with water the magma would erupt in a Hawaiian or Strombolian style (Thorarinsson

et al. 1964; Walker 1973; Kokelaar & Durant 1983; White & Houghton 2000; Sorrentino et al. 2010; Vaughan & Webley 2010; Gjerløw et al. 2015), as seen when growth of a subaerial tuff ring eventually becomes isolated from sea-water and the style of eruption becomes Strombolian or less explosive (e.g. Kokelaar & Durant 1983; Mattsson 2010; Vaughan & Webley 2010; Mantas et al. 2011). Therefore, these eruptions commonly involve magma with low viscosity that would not normally produce significant amounts of ash (Machado et al. 1962; Walker 1973; Mattsson 2010), particularly when basaltic magma is involved (Vaughan & Webley 2010). Surtseyan eruptions are typically associated with monogenetic volcanism (Corcoran & Moore 2008; Gjerløw et al. 2015; Moorehouse et al. 2015), where eruptions are short-lived (typically up to two years) and only occur over one eruptive phase (Corcoran & Moore 2008; Sorrentino et al. 2010; Gjerløw et al. 2015). In New Zealand, aggregations of Surtseyan edifices can be found, where monogenetic volcanoes erupted in the same region millions of years apart (Corcoran & Moore 2008; Moorehouse et al. 2015). Therefore, it is possible for Surtseyan cones to overlap one another to form a larger volcanic edifice over time. Multiple vents can be active during the same eruptive phase and form submarine volcanoes and/or multiple Surtseyan islands, for example Surtsey and Surtla, Iceland (Kokelaar & Durant 1983), and Home Reef, Tonga (Mantas et al. 2011).

The explosive hydrovolcanic phase of Surtseyan eruptions typically involves pulsed explosions and eruption of ash in characteristic black 'tephra jets' accompanied by plumes of steam (e.g. Machado et al. 1962; Thorarinsson et al. 1964; Kokelaar & Durant 1983; Cole et al. 2001; Mattsson et al. 2010; Sorrentino et al. 2010; Vaughan & Webley 2010; Gjerløw et al. 2015; Moorehouse et al. 2015). These may be accompanied by pyroclastic density currents (PDCs), also referred to as base surges, that occur above and below water (Mueller et al. 2000; White 2000; Cole et al. 2001; Mattsson 2010; Vaughan & Webley 2010; Sorrentino et al. 2013; Agustín-Flores et al. 2015; Gjerløw et al. 2015). Generally, eruption plumes, comprised of steam and tephra, only reach a few kilometres above sea level (Machado et al. 1962; Cole et al. 2001; Sorrentino et al. 2010; Vaughan & Webley 2010) with steam plumes extending a little higher (Machado et al. 1962). Tephra, including fine-ash, from fall-out, has a limited dispersal (Machado et al. 1962; Kokelaar & Durant 1983; Cole et al. 2001;

Mattsson 2010; Gjerløw et al. 2015), reaching *ca.* 20 km (Surtsey and Capelinhos, Volcanic Explosivity Index (VEI) 2 sized eruptions; Gjerløw et al. 2015), however, for more explosive phases (up to VEI 4) tephra may be deposited *ca.* 110 km from source (Eggøya; Gjerløw et al. 2015). Deposition of tephra from PDCs occurs up to 2 km from the vent (Gjerløw et al. 2015).

Ash produced by Surtseyan eruptions contains features that are indicative of hydrovolcanic processes, for example, a high proportion of fine-ash (Walker 1973; Cas & Wright 1987; Pyle 1989; Gjerløw et al. 2015) and the morphologies of the constituent pyroclasts are predominantly blocky (>50 %; Gjerløw et al. 2015).

Textural analysis of tuffs in the Danish positive ash-series (BF equivalent) led Pedersen & Jørgensen (1981) to interpret that the ashes were formed by Surtseyan eruptions. Initial interpretation of the ash from the current analysis also supported Surtseyan-type eruptions as an origin for the tuffs in the Norwegian wells, as the BF tuffs are fine-grained (Figure 3-42; Figure 3-43; Figure 3-44), and comprised of blocky (Figure 3-50), low-vesicular to non-vesicular ash (Table 3-4; Table 3-5), which are typically produced in Surtseyan eruptions (Kokelaar & Durant 1983; Dellino et al. 2001; Mattsson et al. 2010; Gjerløw et al. 2015), and the grain-size of the BF tuffs is similar to that of the distal deposits of these eruptions (Figure 3-58; Cole et al. 2001). However, the areal distribution of the BF tuffs, exceeding 400,000 km² (Figure 3-2; Figure 3-3; Bøggild 1918; Knox 1984; Knox & Morton 1988), appears to be too large to have been produced by this type of eruption, as Surtseyan eruptions disperse ash over a relatively small area, with ash of negligible thickness (a few cm), similar to the thicknesses observed in the BF (e.g. Figure 3-7), are deposited <50 km from the vent (Machado et al. 1962; Corcoran & Moore 2008; Mattsson 2010; Vaughan & Webley 2010; Gjerløw et al. 2015). As Surtseyan eruptions are commonly an expression of monogenetic volcanism (Kokelaar & Durant 1983; Walker 1993; Solgevik et al. 2007; Corcoran & Moore 2008; Gjerløw et al. 2015; Moorehouse et al. 2015), one implication is that the 200 ash layers of the BF could be interpreted as the products of up to 200 separate eruptions (e.g. Pedersen & Jørgensen 1981), although not taking into account that some tuffs may have been deposited exclusively from reworking. The limited dispersal of the ash from

these Surtseyan eruptions would require the source vents to be located within the NSB (e.g. Pedersen & Jørgensen 1981); however, extensive seismic surveys of the NSB do not indicate the presence of any magmatic or volcanic vents of BF age (Morton & Knox 1990; Schofield pers comms 2017). Therefore, it is more likely that the features of the ash are indicative of hydrovolcanic eruptions that are not related to Surtseyan volcanism in this manner.

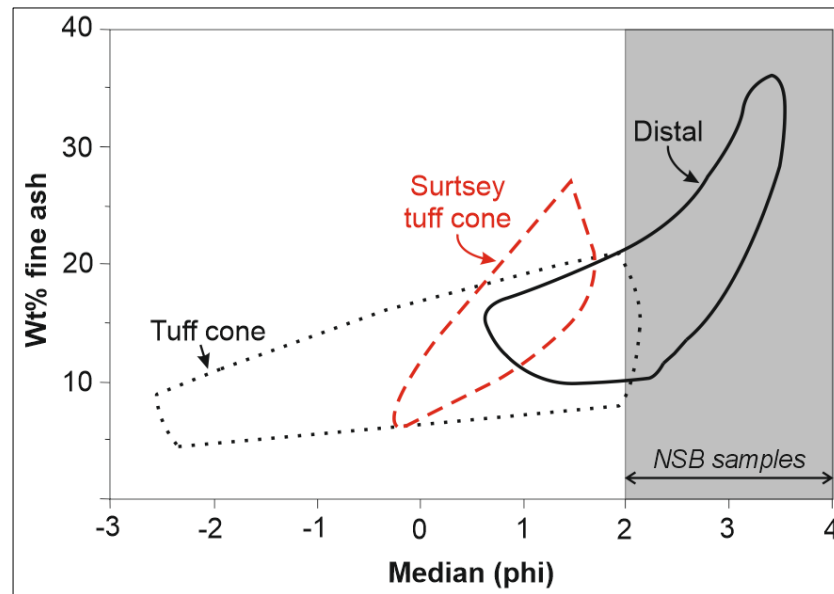


Figure 3-58 The range of grain-size data collected for the NSB BF tuffs corresponds to the distal tephra deposits of Surtseyan eruptions by Cole et al. (2001).

A limited volume of magma is erupted in a similar way during submarine eruptions (Figure 3-57g; Kokelaar & Durant 1983; Urai & Machida 2005; Manville et al. 2009; Mantas et al. 2011; Sorrentino et al. 2013), and these eruptions may precede Surtseyan activity (Figure 3-57e; Machado et al. 1962; Kokelaar & Durant 1983; Mantas et al. 2011). Submarine eruptions can still be explosive and may deposit relatively large amounts of fine-grained tephra within a marine basin (Mandeville et al. 1996; Bryan et al. 2004; Manville et al. 2009; Mantas et al. 2011; Sorrentino et al. 2013). These eruptions may even produce subaqueous pyroclastic density currents, or, slumping of the material on the slopes of volcanic edifices may produce volcanoclastic deposits (Figure 3-57g; White 2000; Manville et al. 2009; Mattsson 2010; Mantas et al. 2011; Sorrentino et al. 2013; Moorehouse et al. 2015). However, these eruptive episodes are typically short-lived, similar to Surtseyan eruptions (Corcoran & Moore 2008; Sorrentino et al. 2010; Vaughan & Webley 2010; Mantas et al. 2011; Moorehouse et al. 2015), and

disperse pyroclastic material over very small distances from the vent when compared to more explosive volcanism on land. Therefore, these eruptions would likely be too small to explain the distribution of the BF tuffs, and represent the same issues as Surtseyan eruptions, in that no vents or intrusions can be identified within the proximal NSB.

3.6.2.2 Fissure eruptions and sea-floor spreading

Deposition of the BF may have been contemporaneous with the initiation of sea-floor spreading within the NE Atlantic (Figure 3-57h; Jacqué & Thouvenin 1975; Carter et al. 1979; Knox & Ellison 1979; Knox & Morton 1983, 1988; Jolley & Morton 1992; Larsen et al. 1999a; Kent & Fitton 2000; Torsvik et al. 2001; Larsen et al. 2003; Simonsen & Toft 2006; Storey et al. 2007; Stoker et al. 2012; Ellis & Stoker 2014; Jerram et al. 2009). At times, this sea-floor spreading was likely subaerial or occurred within relatively shallow water (Figure 3-57i; Pedersen & Jørgensen 1981; Knox 1996; Thomas & Bralower 2005; Breivik et al. 2009), therefore it is likely that explosive magma-water interactions took place. Continued eruptions, or eruptive episodes along this new plate boundary could have provided magma of a relatively homogeneous composition over a long period of time (hundreds of thousands of years; Morton & Knox 1990; Larsen et al. 2003), and be responsible for the homogeneous tholeiitic basalt composition of the majority of the BF tuffs (e.g. Larsen et al. 2003). It has been suggested previously that the homogeneous nature of the BF tuffs could be linked to eruptions associated with the sea-floor spreading centre (Pedersen et al. 1975; Morton & Knox 1990; Larsen et al. 2003). It is reasonable to assume that large volumes of basaltic magma generally erupt with low explosivity, for example, as fissure eruptions involving Hawaiian or Strombolian eruption-styles, and will involve effusive eruptions of large volumes of lava (e.g. Williams 1983; Morton & Knox 1990; Houghton et al. 2004; Parfitt 2004; Carey et al. 2007; Constantini et al. 2009; Pérez et al. 2009; Constantini et al. 2010; Goepfert & Gardner 2010; Freda et al. 2011). We know that these typically low-explosivity and effusive eruptions did occur in some regions of the NAIP during the Late Palaeocene into the Early Eocene, as shown by the thick piles of lava of the Faroe Islands, parts of Scotland and Northern Ireland (e.g. Pedersen & Jørgensen 1981; Smythe et al. 1983; Roberts et al. 1984; Mussett et al. 1988; Morton & Knox 1990; Hitchen &

Ritchie 1993; Kanaris-Sotiriou et al. 1993; Knox 1996; Ritchie & Hitchen 1996; Larsen et al. 1999, 1999a; Heister et al. 2001; Torsvik et al. 2001; Ellis et al. 2002; Larsen et al. 2003; Brooks 2006; Simonsen & Toft 2006; Hansen et al. 2009; Jerram et al. 2009; Passey & Jolley 2009; Carriol et al. 2016).

Eruptions of basaltic lava and the formation of new oceanic crust in shallow water could lead to magma-water interactions and be a mechanism for highly-explosive basaltic eruptions (Figure 3-57i; Hanson & Elliot 1996; Larsen et al. 2003; White et al. 2004). The low percentage of vesicular pyroclasts (Table 3-4), and the low vesicularity of these (Table 3-5) suggest that the original magma did not have a high volatile content at the time of eruption (e.g. Moitra et al. 2013). These characteristics suggest that the magma was of low viscosity and low volatile content and would not have erupted explosively without the addition of an external factor (e.g. Carey et al. 2007; Moitra et al. 2013). This interpretation appears to be valid for the originally glassy pyroclasts within the tuffs (e.g. Figure 3-28) of the UKCS and NOR NSB (i.e. Pedersen & Jørgensen 1981; Morton & Knox 1988; Morton & Knox 1990). However, the most abundant clast-type in these tuffs is crystalline igneous or lava-like clasts (Figure 3-49) that contain a high proportion of micro-crystals (e.g. Figure 3-27). It is possible that these crystals formed within the magma prior to eruption, therefore increasing the viscosity of the melt (e.g. Morton & Knox 1990; Houghton et al. 2004). A higher viscosity magma would lead to more-explosive eruptive behaviour. Interactions of these more-explosive magmas with water may have allowed these eruptions to become Plinian in size, leading to Plinian-scale distribution of basaltic ash over hundreds of kilometres from the vent (e.g. Houghton et al. 2004; Parfitt 2004). The explosivity of basaltic magmas can also be increased by rapid magma ascent rates and varying conduit dimensions (Houghton et al. 2007), though evidence for these factors is absent as sea-floor spreading would have subsequently destroyed it.

Initial sea-floor spreading may have been associated with anomalously high rates of spreading (*ca.* 30 mm.a⁻¹; Breivik et al. 2006, 2009), which lasted for a few million years (Breivik et al. 2006, 2009). This could explain the time-frame for which the BF tuffs were likely produced (possibly <1 million years; Pedersen et al. 1975; Roberts et al. 1984; Elliott et al. 1992; Brooks 2006). As the proto-

Icelandic plume became established and sea-floor spreading slowed, the volume of magma involved and associated resultant volcanism rapidly decreased (Knox & Morton 1983; Knox 1996; Nadin et al. 1997; Larsen et al. 2003). In addition, a regional marine transgression and subsidence of many of the surrounding basins may have submerged the active sections of the rift over time, therefore inhibiting explosive magma-water interactions (e.g. Knox 1996; Obst et al. 2015). Alternatively, violent hydrovolcanic eruptions could have occurred during emergence of a proto-Iceland, with hydrovolcanism ceasing once the island developed above sea-level and the magma system isolated itself from further magma-water interactions (Larsen et al. 2003). These ideas could explain the abrupt cessation of basaltic ash deposition recorded throughout the NSB, marking the end of the BF tuffs and explosive volcanism in the NAIP (e.g. Pedersen et al. 1975; Knox & Morton 1983; Knox 1984; Roberts et al. 1984; Morton & Knox 1990; Nadin et al. 1997; Obst et al. 2015).

3.6.2.3 Transport and deposition of ash by water currents

The grain-sizes of many of the tuffs from the NSB are coarser than would be expected for distal deposits that have accumulated as ‘primary’ air-fall water-lain tuffs hundreds of kilometres from a source in the NE Atlantic (Pedersen & Jørgensen 1981; Jolley & Bell 2002; Larsen et al. 2003; Jolley & Widdowson 2005). It is accepted that the BF tuffs were deposited through water and that this waterbody likely had some sort of current (Carriol et al. 2016). For example, upwelling currents most likely existed along the eastern areas of the NSB during the Early Eocene, as suggested by the presence of a thick sequence of marine diatomites interbedded with tuffs of the Danish positive ash-series (Nielsen 1974; Pedersen et al. 1975; Pedersen & Jørgensen 1981; Pedersen & Surlyk 1983; Elliott et al. 1992; Brooks 2006; Obst et al. 2015; Carriol et al. 2016). Could the ashes have been deposited as fall-out in a more proximal area to the vents and then been transported to more distal locations by such currents? Little research has been conducted on the transport of tephra within the ocean, however, submarine and Surtseyan eruptions can produce turbid plumes of tephra and other constituents (Figure 3-57f) that have been observed to travel up to 120 km from the vent (Mantas et al. 2011). Pumice rafts that form during larger-scale hydrovolcanic eruptions can travel many thousands of kilometres, for example,

pumice from the 1883 eruption of Krakatau travelled >6000 km (Bryan et al. 2004; Sorrentino et al. 2013). The settling velocity of ash within the BF through 100 m of completely still, non-saline water would take up to 3 days (Figure 3-46). A greater depth of water, increased salinity or the presence of currents, or non-spherical and vesicular grains would increase the amount of time taken for all of the ash to be deposited within the NSB (Figure 3-46; Furguson & Church 2004; Manville & Wilson 2004; Wu & Wang 2006; Manville et al. 2009; Cuttler et al. 2017). Flocculation of fine ash on the water's surface may lead to more rapid deposition due to the greater density of the particles when aggregated (Winterwerp 2002; Manville & Wilson 2004; Manville et al. 2009; Yamamoto et al. 2015). The coarsest ash particles would be deposited first, and finer grains might be winnowed away and deposited elsewhere (Figure 3-46; e.g. Manville & Wilson 2004). Therefore, the grain-size distribution of the tuffs might not be a true representation of the original fall-out. However, it is unlikely that the ash was transported very far by currents before being deposited, as inferred from a general lack of depositional features such as cross-stratification or ripple structures, in many of the tuffs.

However, some of the tuffs do display cross-stratification, ripple structures and evidence of soft sediment deformation (Figure 3-10, Figure 3-15), suggesting that density currents, including turbidity currents (Figure 3-57d), may have been responsible for the transport and deposition of some of the BF tuffs. Deformed bedding, in the form of slump structures in core of UKCS29/05a-1 (Figure 3-11) and NOR30/2-1 (Figure 3-21), indicate that deposition occurred in a dynamic environment, where post-depositional, gravity-driven, mass movement occurred in some areas. The presence of a submarine fan, interpreted for the BF of NOR25/11-17 (see section 3.6.1), supports this interpretation. The slumping may be related to the triggering of turbidity currents, and therefore the redistribution of volcanic material throughout the basin. However, transport commonly leads to the abrasion of particles, which is negated by the delicate features of the original BF ashes that have commonly been preserved (Figure 3-28, Figure 3-34). These features are more likely to be preserved if they are not reworked, although, reworking via a medium in which particle concentration is low, could inhibit abrasion of the grains, potentially allowing the preservation of these delicate features (Figure 3-59). It is also possible that glassy material is

more resistant to the effects of abrasion during transportation than is currently considered in the literature (e.g. Merrison 2012; Buckland et al. 2018).

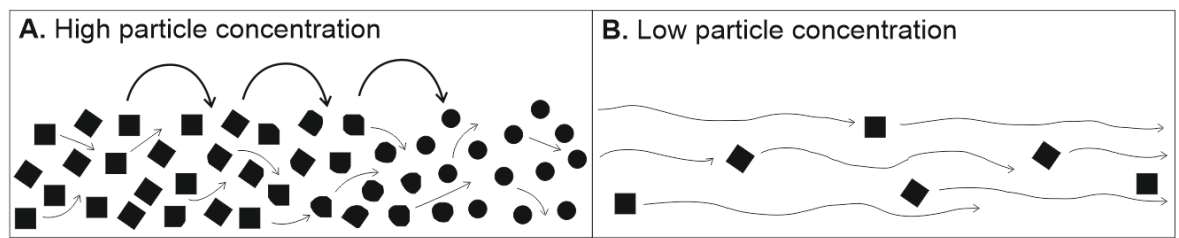


Figure 3-59 Transport and reworking in a fluid with a high or low particle concentration. Clasts/grains transported within a fluid that contains a high concentration of other clasts (A) are likely to undergo frequent collisions and abrasion with other clasts and the Earth's surface. This will lead to rounding of the clasts and a loss of primary delicate pyroclast features. In contrast, transport within a medium containing a low concentration of particles (B) may allow such delicate pyroclast features to be preserved, as abrasion by clast-clast contact and contact with the Earth's Surface will be minimised.

3.6.2.4 Reworking of pyroclastic deposits in a terrestrial environment; re-deposition in the marine realm

The deposits of the Early Eocene NSB, including Denmark, contain the largest number of tuffs (>200) compared to regions outside of the basin (Pedersen & Jørgensen 1981; Roberts et al. 1984; Knox & Morton 1988; Morton & Knox 1990; Larsen et al. 2003; Obst et al. 2015; Carriol et al. 2016), for example, the Goban Spur and Bay of Biscay contain *ca.* 40 ash layers (Knox 1984; Roberts et al. 1984; Knox & Morton 1988; Morton & Knox 1990). The NSB was almost completely land-locked during deposition of the BF tuffs (Knox & Harland 1979; Mudge & Copestake 1992a; Knox 1996; Kender et al. 2012; Carriol et al. 2016), with river systems supplying clastic material into the basin from Scotland and Norway (Knox & Morton 1983; Knox 1996; Larsen et al. 1999; Kender et al. 2012). This is known by the presence of the Beaulieu and Odin sandstone members which were deposited in prograding deltas (Figure 3-57c; Knox & Morton 1983; Mudge & Copestake 1992a; Mudge & Bujak 1994; Neal et al. 1996; Larsen et al. 1999; Mudge & Jones 2004). Other rivers with lower sediment loads may have supplied material to the basin, but these did not build substantial deltas (e.g. Newell 2014). Large-scale explosive volcanism would likely have deposited ash over the NSB *and* its surrounding landmasses. Weathering and erosion of these air-fall deposits, on-land, may have led to the secondary deposition of ash within the NSB (Figure 3-60; e.g. Manville et al. 2009). This may have occurred seasonally,

as the climate at the time was subtropical, wet and humid (Figure 3-57b; Newell 2014; Suan et al. 2017), whereby periods of increased precipitation may have allowed more material to be eroded and washed into the basin, with little or no input of ash during drier periods. Initial reworking could deposit substantial amounts of material into the basin, with later/subsequent input decreasing due to the establishment of vegetation and the decreasing availability of unconsolidated ash (Manville et al. 2009). The evidence of slumping (Figure 3-11; Figure 3-21) and inferred role of turbidity currents for the BF deposits (e.g. Kender et al. 2012) implies that reworking and re-deposition of ash did occur, and that resultant deposits may look like their air-fall water-lain less volcanoclastic equivalents (Figure 3-60; e.g. Pedersen & Surlyk 1983; Mudge & Copestake 1992; Morton & Knox 1990; Obst et al. 2015). Reworking of the ashes from land is also supported by the absence of ashes in the equivalent terrestrial deposits, for example in S England (see Chapter 5). However, during reworking, particularly from land, it is more likely that other grain-types and organic material will also be incorporated into the deposits (Fisher 1961, 1984; White & Houghton 2006; Manville et al. 2009). The tuffs analysed in this study do not contain a significant siliciclastic component and are almost entirely comprised of igneous material (Figure 3-49). This may suggest that ash was deposited on-land in such large quantities that it inundated the normal sedimentary transport systems (e.g. Manville et al. 2009), or, that the tuffs are representative of air-fall water-lain deposition that has not involved significant periods of reworking.

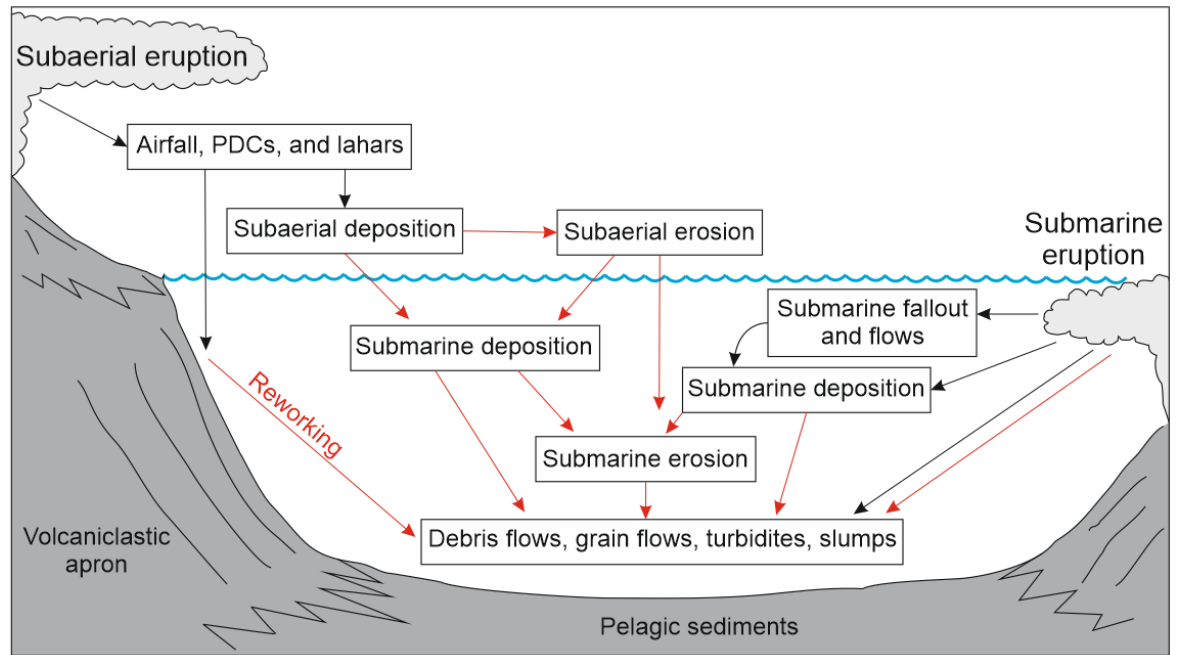


Figure 3-60 Summary of pyroclastic and volcanoclastic depositional settings. Primary pyroclastic deposits (black arrows) are formed by direct deposition of tephra from subaerial or submarine eruptions. These deposits may be reworked (red arrows) and become volcanoclastic deposits in a marine basin (from Manville et al. 2009).

The greater number of tuffs within the NSB may be due to the axis of the eruption plume most frequently travelling over the NSB. Although the dominant wind direction was likely from the N/NW during the Early Eocene (Kender et al. 2012; Carriol et al. 2016) it is possible that the axis of tephra dispersal did not always extend in the same direction. As shown by the multiple eruption dispersal axes exhibited by ash deposited by the 10.3 ka eruption of Grímsvötn, Iceland (see Chapter 2; Bramham-Law et al. 2013; Jennings et al. 2014), showing that ash can be dispersed in more than one direction for each phase of eruption, even from a single vent. Varying directions of tephra dispersal could be misinterpreted as depositing one single, large deposit (e.g. Lind et al. 2013; Lohne et al. 2013; Jennings et al. 2014), whereas, in reality, multiple eruptive episodes may produce correlative deposits, of similar composition and age over smaller areas (e.g. see Chapter 2).

3.6.2.5 Subaerial, central complex explosive volcanism

Silicic volcanism accompanied basaltic eruptions during the formation of the NAIP and these were particularly frequent prior to eruption of the BF tuffs, as indicated by the tuffs of varying composition in the Danish negative ash-series,

and the NSB Sele Formation (Knox 1984; Morton & Knox 1990; Obst et al. 2015). Volcanism in BF time was almost exclusively basaltic, although, at least two silicic tuffs have been identified (including +19 of the Danish positive ash series; Pedersen & Jørgensen 1981; Knox 1984; Obst et al. 2015). This suggests that explosive silicic volcanism (Figure 3-57a) was still occurring in the NAIP during the Early Eocene, although basaltic explosive eruptions were more frequent. Silicic volcanic centres are known to have been present in E Greenland and the BPIP (Roberts et al. 1984; Mussett et al. 1988; Hitchen & Ritchie 1993; Knox 1996; Ritchie & Hitchen 1996; Larsen et al. 2003), and may have continued to be active sporadically during the Early Eocene (e.g. Larsen et al. 2003). It is highly likely that the ash produced in these areas, adjacent to the spreading centre, could have involved magmas of different compositions. The high level of alteration of some of the BF tuffs has prevented comparison of the compositions of tuffs at different stratigraphic intervals (Larsen et al. 2003), but the general consensus is that all of the tuffs are of a relatively homogeneous composition, with little variation (Bøggild 1918; Pedersen et al. 1975; Pedersen & Jørgensen 1981; Roberts et al. 1984; Knox & Morton 1988; Morton & Knox 1990; Larsen et al. 1999a, 2003; Brooks 2006; Obst et al. 2015). Variations in the style of alteration of originally glassy ash within and between different tuffs (Figure 3-35), could imply that their ashes are of different chemical compositions. Alternatively, varying styles of alteration could be caused by alteration in different environments, and the mixing of these clasts in one tuff layer could imply that the tuff is volcanoclastic and comprised of variably reworked ash or ash from different sources.

3.6.3 Volcanic activity elsewhere in NW Europe

The Skagerrak region to the south of Norway (Figure 3-2) has been interpreted as a potential source of the Danish positive ash series (Pedersen et al. 1975; Pedersen & Jørgensen 1981). However, there is little evidence that this volcanic centre was active during BF times (Larsen et al. 2003). Other volcanic centres have been identified surrounding the NSB, for example in southern Sweden, although this had ceased to be active by the Early Eocene (Tappe 2004). Other areas that were considered as potential sources did not become active until long after deposition of the BF tuffs, for example, ca. 48 Ma in the German Rhine

Graben (Central European Volcanic Province; Jung et al. 2006), and *ca.* 34 Ma in the Alps region (Bergomi et al. 2015). Therefore, no other reasonably likely volcanic source regions were active during deposition of the BF tuffs, except for those directly associated with formation of the NAIP.

3.7 Conclusions

The Early Eocene Balder Formation of the North Sea Basin is composed of a wide range of lithologies: siliciclastic and volcanoclastic claystone, siltstone, sandstone, and tuffs (e.g. Figure 3-8), that were predominantly deposited through water in a restricted lake-like sea surrounded by land (Figure 3-61). A period of uplift, associated with magmatism in the North Atlantic Igneous Province provided coarse clastic sediments into the west of the basin, as evidenced by sandstone units sourced from the Scottish Highlands into the More Basin in the west of the North Sea Basin (Beaulieu Member; Mudge & Copestake 1992a; Mudge & Bujak 1994; Neal et al. 1996). Additional sand deposition occurred in submarine fans (Milton et al. 1990; Mudge & Copestake 1992a; Mudge & Bujak 1994) that extended at least as far as NOR25/11-17 (Figure 3-2), where 5-6 m intervals of high-porosity, high-permeability quartz-rich sandstone (quartz arenite) are interbedded with claystones and tuffs in the Balder Formation (Figure 3-18). Elsewhere, deposition occurred in a marine setting, and was dominated by pelagic settling and deposition of parallel-laminated clays and normal-graded, water-lain ashes. Deposition also occurred from turbidity currents, which may have been triggered by slumping (e.g. Figure 3-11, Figure 3-21) and mass-movement within the basin. Pyrite framboids are common within the claystones, siltstones and tuffs (e.g. Figure 3-26) and support the interpretation that the North Sea had a stratified water column, where the bottom waters were anoxic (Figure 3-56; e.g. Nielsen et al. 1974; Pedersen et al. 1975; Obst et al. 2015; Carriol et al. 2016). This is also supported by the significant lack of micro-fossils within the Balder Formation (Morton & Knox 1990), with rare pyritised forms found in only two samples during this study (e.g. Figure 3-24). Some intervals of the formation show possible evidence of bioturbation, with burrow-like features (Figure 3-19), suggesting that, at times, these areas may have been shallow enough and oxygenated enough for

burrowing organisms to exist (e.g. Nielsen 1974; Pedersen & Surlyk 1983; Brooks 2006).

The Balder Formation was deposited during the development of the North Atlantic Igneous Province (including the British Palaeogene Igneous Province), which involved large-scale magmatism and volcanism associated with rifting and sea-floor spreading that led to the separation of Greenland from NW Europe and development of the NE Atlantic Ocean (Hallam 1972; Pedersen et al. 1975; Knox & Harland 1979; Knox & Morton 1983, 1988, 1990; Knox 1996; Ritchie & Hitchen 1996; Nadin et al. 1997; Haaland et al. 2000; Kent & Fitton 2000; Torsvik et al. 2001; Larsen et al. 2003; Jolley & Widdowson 2005; Ross et al. 2005; Thomas & Bralower 2005; Breivik et al. 2006; Brooks 2006; Storey et al. 2007; Brunstad et al. 2008; Breivik et al. 2009; Gernigon et al. 2012; Obst et al. 2015). Initial sea-floor spreading began at *ca.* 54 - 56 Ma, and likely coincided with large-scale magmatic and volcanic activity that led to the deposition of more than 200 basaltic ash-layers in the North Sea (Figure 3-61), including Denmark, SE England, N Germany and the Netherlands (Knox & Morton 1983; Larsen et al. 1999a; Larsen et al. 2003). Additional ash-layers were deposited in the Faroe-Shetland Basin to the north, the Goban Spur, the Bay of Biscay, and possibly as far south as Austria (Figure 3-2; Brooks 2006; Egger & Brückl 2006; Carriol et al. 2016; Watson et al. 2017). Over time, the ash-layers have undergone burial and high levels of alteration and are now present as altered tuffs within the lower Balder Formation (e.g. Morton & Knox 1990; Brooks 2006). These tuffs are typically and characteristically olive-green, yellow or blue, normal-graded ash to fine-ash units with a calcite and/or patchy pyrite cement (see section 3.5.1).

Regardless of secondary alteration, the morphologies of the originally glassy ash are commonly preserved; these are typically non- to poorly-vesicular, with blocky pyroclast shapes (Figure 3-50, Table 3-5). These features are characteristic of the brittle fragmentation of magma caused by hydrovolcanic eruptions involving magma-water interactions (Wohletz & Sheridan 1983; Cas & Wright 1988; Mattsson 2010; Dellino et al. 2012; Ross & White 2012; Graettinger et al. 2013). The wide area over which these basaltic ashes were distributed (Figure 3-2, Figure 3-3), the frequency of tuff layers within the North Sea stratigraphy and their generally homogeneous chemical compositions imply that

large volumes of basaltic magma were able to erupt explosively during the Early Eocene (Figure 3-61). The non-vesicular to poorly-vesicular nature of the original glassy pyroclasts suggest that the parent basalt magma would not have erupted explosively without some additional factor. Magma-water interactions could enable basalt magma to erupt more explosively, however, this alone may not account for the areal extent of these deposits. Most of the tuffs analysed in this study are predominantly comprised of micro-crystalline igneous clasts or lava-like clasts (Figure 3-49), and not originally glassy pyroclasts. If the micro-crystals of these clasts formed within the magma prior to its eruption, then this could have increased the viscosity of the basaltic magma enough to allow more highly explosive eruptions to occur, regardless of magma-water interactions. However, it is likely that magma-water interactions did occur and that the ashes of the Balder Formation are hydrovolcanic, based on the blocky non-vesicular morphologies of glassy pyroclasts (Table 3-4, Table 3-5), and the exclusive occurrence of ash to fine-ash sized grains within the deposits (Figure 3-44; Wohletz & Sheridan 1983; Cas & Wright 1988; Mattsson 2010; Dellino et al. 2012; Ross & White 2012; Graettinger et al. 2013). This suggests that an increased viscosity of the magma due to a higher crystal content, and the interaction of this higher viscosity magma with water, may have enhanced the explosivity of the erupting basaltic magma, possibly allowing these eruptions to become Plinian or phreato-Plinian. This could have enabled the basaltic ash to be distributed on a Plinian-scale, up to several hundreds of kilometres from source (e.g. Carey & Sigurdsson 1982; Kutterolf et al. 2008; Lerbekmo 2008; Nash & Perkins 2012; Janebo et al. 2016), from somewhere along the opening NE Atlantic rift to the Bay of Biscay and Austria (Figure 3-2).

It is unlikely that the >200 tuff beds of the North Sea Balder Formation were deposited by the equivalent number of individual eruptions. Instead, it is equally or more likely that fewer eruptions of Plinian-scale took place, and that reworking, either within the basin itself, or by reworking of air-fall ash on-land, subsequently re-deposited this material into the basin (Figure 3-61). Tuffs in the Goban Spur and Bay of Biscay have been correlated with those of the North Sea Basin, based on geochemistry and relative age dating via nannoplankton zonation in the N Atlantic (Knox 1984; Roberts et al. 1984; Knox & Morton 1988; Larsen et al. 2003). The tuffs of the NE Atlantic are fewer than those of the North Sea

Basin, which may be due to an enhanced number of reworked tuffs within the North Sea due to the basin being land-locked during the Early Eocene (e.g. Knox & Harland 1979; Milton et al. 1990; Mudge & Copestale 1992a; Mudge & Bujak 1994; Knox 1996; Kender et al. 2012; Carriol et al. 2016). In addition, these differences could represent variations in the dispersal axis of ash from the eruption plumes, which could have resulted in deposition of ash over a narrower region (see section 3.6.2; Figure 3-61). Therefore, ashes of the same composition could be deposited over different areas during the same eruptive phase, leading to an overestimation of the area over which ash was deposited for each individual phase of an eruption. It is proposed here that the ashes of the Goban Spur and Bay of Biscay may have been deposited from different eruptions to those that deposited ash into the North Sea Basin, even though these eruptions most likely came from the same source region, for example, along the NE Atlantic spreading centre, during the same phase of eruptions (see section 3.6.2.4). It is possible that the initial opening phase of the NE Atlantic involved rapid magma extrusion and a fast spreading-rate (Larsen et al. 2003; Breivik et al. 2006, 2009), therefore supplying large volumes of compositionally similar magma along sections of the rift over time. Flooding of the actively erupting parts of the rift may have led to multiple large-scale basaltic Plinian-style hydrovolcanic eruptions that were the source of ash preserved in the North Sea Basin Balder Formation (e.g. Larsen et al. 2003).

A marine transgression throughout the Early Eocene may have eventually led to the submergence of sea-floor spreading to greater depths that eventually inhibited explosive magma-water interactions (Knox 1996; Obst et al. 2015). Alternatively, the emergence of proto-Iceland and isolation of its magma from sea-water may have also inhibited magma-water interactions over time (Larsen et al. 2003). These processes may explain the rapid reduction in tuffs preserved in the upper Balder Formation (Knox & Morton 1983; Knox 1984), and indicate a general reduction in explosive volcanism within the North Atlantic Igneous Province.

At least two rhyolitic tuffs are present in the Balder Formation (e.g. +19 and +13 of the Danish positive ash series; Knox 1984; Larsen et al. 2003). These likely represent the final expression of explosive silicic volcanism from elsewhere in

the North Atlantic Igneous Province, unrelated to the basaltic tuffs (Figure 3-61). These may be related to a late phase of volcanism in the British Palaeogene Igneous Province or E Greenland, and are the final expression of explosive silicic volcanism in the Early Eocene North Atlantic Igneous Province.

Therefore, the tuffs of the Balder Formation record a period of explosive volcanism with a range of sources, from hydrovolcanic eruptions that may have been associated with opening and flooding of the NE Atlantic Ocean, and volcanism associated with volcanic centres elsewhere in the North Atlantic Igneous Province (Figure 3-61). The tuffs likely record <200 large-scale (up to Plinian-scale) ash-fall water-lain ash deposits as well as multiple volcaniclastic deposits that represent re-deposition of ash from subaerial and submarine reworking (see section 3.6). The large areal distribution of the ashes from the Faroe-Shetland Basin, to the Bay of Biscay and Austria (Figure 3-2), can be explained by Plinian-scale eruptions. However, a varying axis of tephra dispersal may have led to an overestimation of the areal extent of deposits from individual eruptions, with multiple deposits of the same chemical composition being deposited over narrower regions from individual eruptions.

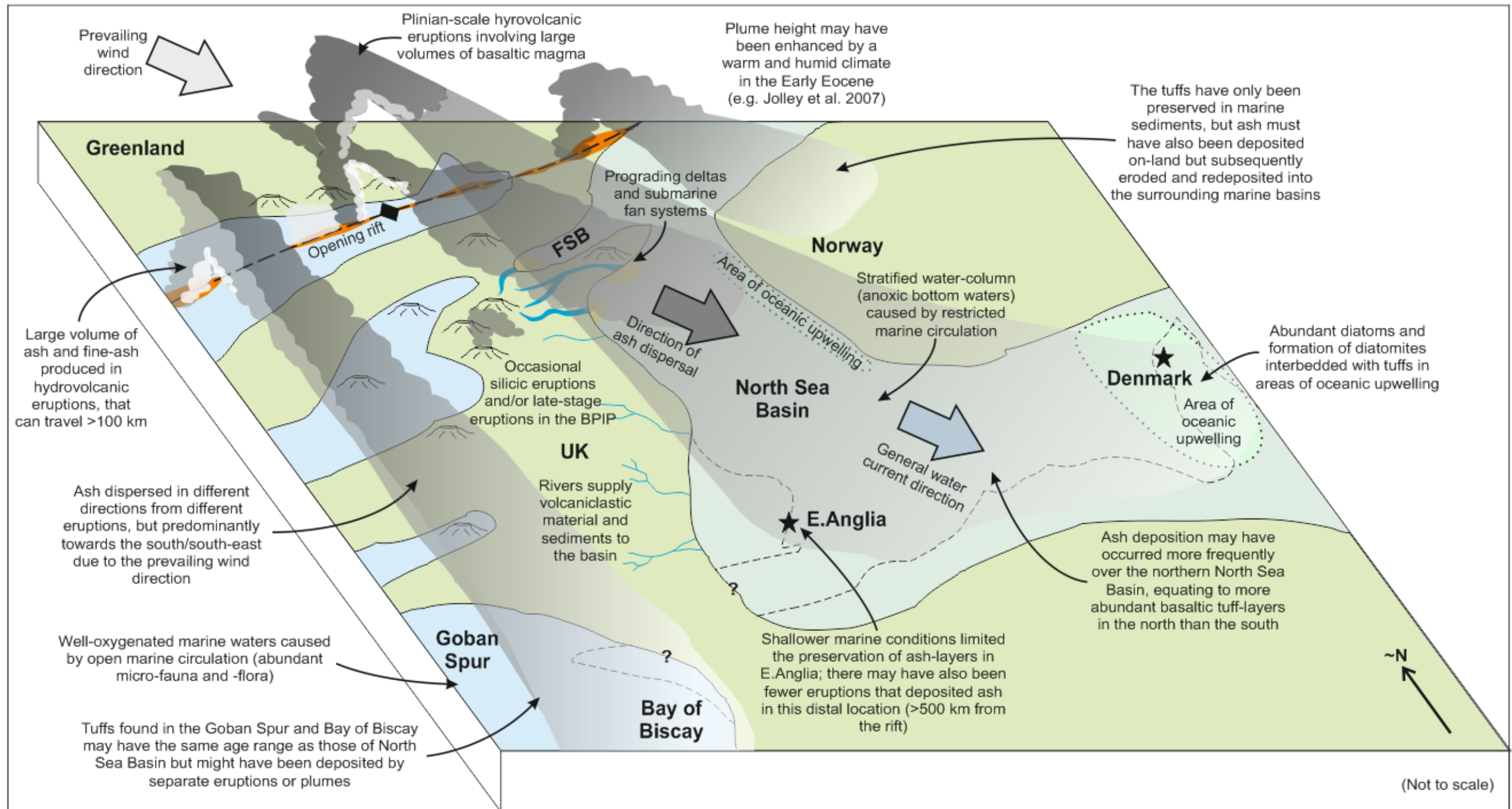


Figure 3-61 Palaeo-reconstruction showing the sources of basaltic eruptions and the deposition of ash and fine-ash that has been interpreted for the Balder Formation tuffs in this chapter. FSB: Faroe-Shetland Basin

Chapter 4: The Balder Formation of the Faroe-Shetland Basin, UKCS Quad 204 case study

4.1 Introduction

The Early Eocene Balder Formation (BF) is a sequence of predominantly sedimentary rocks that was deposited *ca.* 54.5 Ma (Knox & Morton 1983; Roberts et al. 1984; Knox & Morton 1988; Vierick et al. 1988; Hitchen & Ritchie 1993; Mudge & Bujak 1995; Mudge & Bujak 1996; Ritchie & Hitchen 1996; Haaland et al. 2000; Smallwood & Gill 2002; Mudge & Jones 2004; Ross et al. 2005; Jolley & Widdowson 2005; Dmitrieva et al. 2012; Aldiss 2014). The BF is intersected by a series of wells from the northern part of UK Continental Shelf (UKCS) Quad 204 within the Faroe Shetland Basin (FSB; Figure 4-1). These include wells from the Cambo, Tornado and Suilven oil and gas fields, and additional exploration wells. Biostratigraphic reports available for wells of the Cambo field state that deposition of the BF occurred in the Early Eocene (Table 4-1; Mahdi 2004; Jolley 2011; Costa 2012; Dawson et al. 2013), but a more precise age is not given. This Formation has not been studied in great detail within the FSB but is an important stratigraphic unit that deserves to be the focus of further research (e.g. Ebdon et al. 1995) due to its problematic nature during the drilling of wells (OMV (U.K.) Limited pers. coms. 2014, 2015, 2016) as well as its unknown potential as a hydrocarbon target. The characteristics of the BF are better known from core samples recovered from the North Sea Basin (NSB.; Jacqué & Thouvenin 1975; Deegan & Scull 1977; Knox & Harland 1979; Knox & Morton 1983; Lott et al. 1983; Mudge & Bliss 1983; Malm et al. 1984; Roberts et al. 1984; Knox & Morton 1988; Morton & Knox 1990; Jolley & Morton 1992; Knox & Holloway 1992; Mudge & Copestake 1992a; Waagstein & Heilmann-Clausen 1995; Ali & Jolley 1996; Knox 1996; Mudge & Bujak 1996; Nadin et al. 1997; Haaland et al. 2000; Smallwood & Gill 2002; Jolley & Bell 2002; Mudge & Jones 2004; Dmitrieva et al. 2012; Aldiss 2014), and surrounding onshore-exposed deposits in E. Anglia, UK (Knox & Ellison 1979; Knox & Morton 1983; Knox 1984; Roberts et al. 1984; Knox & Morton 1988; Ali & Jolley 1996; Knox 1996; Aldiss 2014), and Fur, Denmark (Böggild 1918; Norin 1940; Nielsen 1974; Pedersen et al. 1975; Jacqué & Thouvenin 1975; Knox & Morton 1983; Mudge & Bliss 1983; Malm et al.

1984; Knox 1984; Roberts et al. 1984; Knox & Morton 1988; Morton & Knox 1990; Neal 1996; Larsen et al. 2003; Brooks 2006).

The aim of the study in this chapter is to assess the characteristics of the BF in the FSB from the interpretation of wire-line data, including gamma-ray, density and, neutron-porosity data, and seismic data from the FSB11/12 3D broadband survey. Information from biostratigraphical reports and the original composite logs for each of the wells provide additional information to test and support interpretations made from the wire-line and seismic data. Access to this information was provided by OMV (U.K.) Limited during a month-long internship in November 2015. Data was provided for Cambo wells: 204/10-1, 204/10-2, 204/10a-4, 204/10a-3, 204/5A-1, Tornado wells: 204/13-1, 204/13-1z, Suilven wells 204/14-2, 204/19-8z, and exploration wells 204/14-1, 204/15-1, 204/19-5, 204/19-1, 204/18-1 (Figure 4-1).

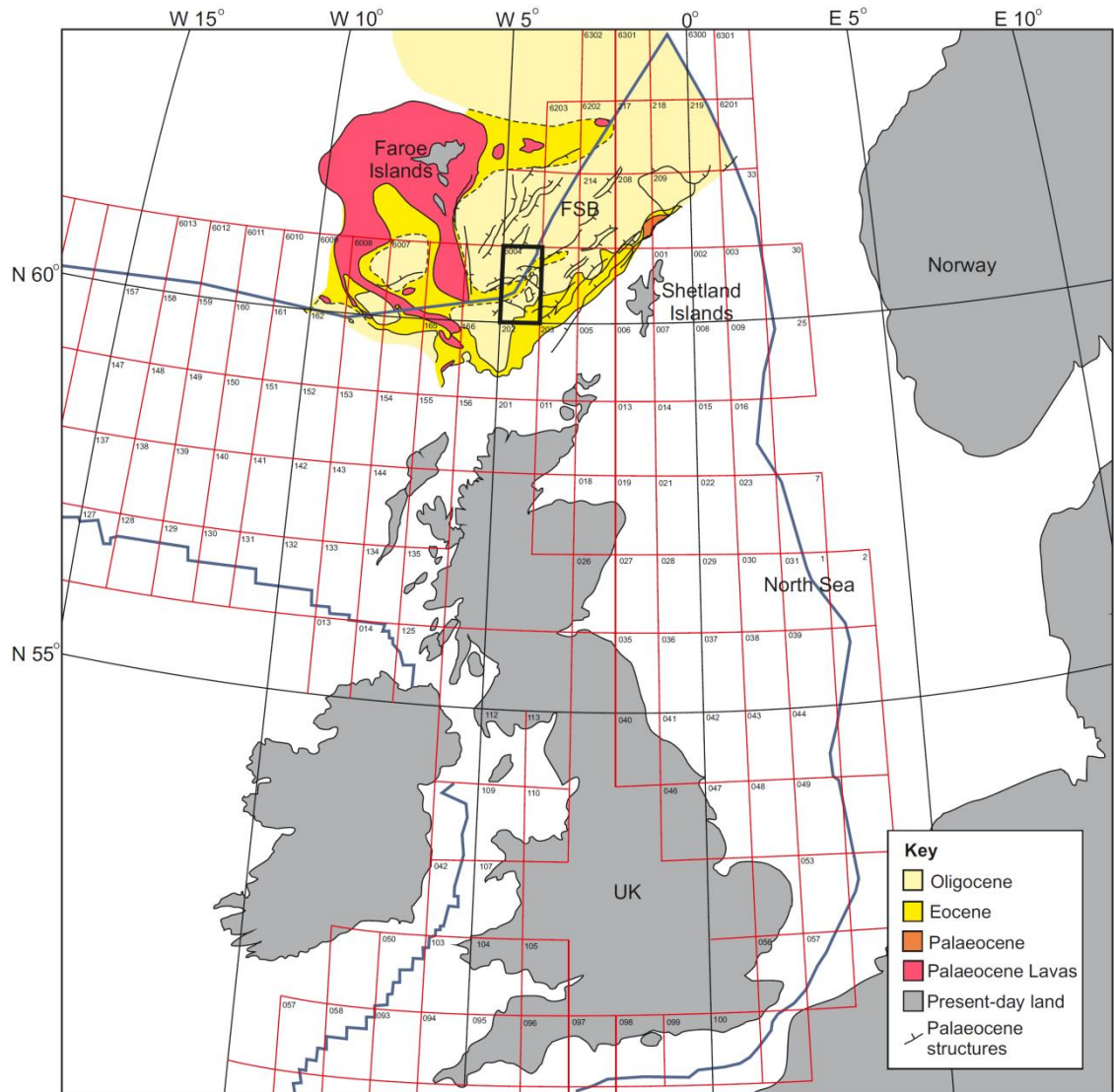


Figure 4-1 Location of UKCS Quad 204 and Faroes Quad 6004 in which the Tornado, Suilven and Cambo wells are located within the Faroe-Shetland Basin (FSB). Some of the general subsurface Palaeogene geology of the FSB is also shown (Ebdon et al. 1995).

The tectonic and stratigraphic history of the FSB is presented first, followed by a brief discussion of the methods of data interpretation. The results of the present study are then presented and a discussion of the inferred characteristics of the BF present in the Cambo, Tornado and Suilven field areas are given. This is followed by concluding remarks regarding the interpreted stratigraphy of the BF and the likely environment of its deposition.

4.2 Geological history of the Faroe-Shetland Basin

The FSB is an elongate, NE-SW trending, fault-bounded marine basin that was formed during at least five stages of rifting that occurred in an area between the Shetland Islands and the Faroe Islands on the NW European Atlantic margin (Figure 4-2; Haszeldine et al. 1987; Dean et al. 1999). Between 62 - 50 Ma, large-scale igneous activity occurred in the NE Atlantic, and the surrounding margins, leading to formation of the North Atlantic Igneous Province (NAIP; Jacqué & Thouvenin 1975; Carter et al. 1979; Knox & Morton 1983; Roberts et al. 1984; Knox & Morton 1988; Mussett et al. 1988; Hitchen & Ritchie 1993; Knox 1996; Ritchie & Hitchen 1996; Nadin et al. 1997; Larsen et al. 1999a; Naylor et al. 1999; Kent & Fitton 2000; Torsvik et al. 2001; Jerram & Widdowson 2005; Storey et al. 2007; Hansen et al. 2009). A major period of volcanism occurred in NW Scotland during the Palaeocene (Selandian to Early Thanetian; Table 4-1), which was accompanied by uplift of Scotland (Knox & Morton 1983; Knox & Morton 1988; Mussett et al. 1988; Knox 1996; Lamers & Carmichael 1999; Naylor et al. 1999; Kent & Fitton 2000; Morton et al. 2002; Jolley et al. 2005; Freeman et al. 2008; Mansurbeg et al. 2008; Sluijs et al. 2008; Smallwood 2008; Mudge 2014). This led to deposition of abundant coarse-grained clastic sediments into the FSB (Naylor et al. 1999; Morton et al. 2002; Freeman et al. 2008; Smallwood 2008). The basin itself experienced uplift during the Palaeocene (Ebdon et al. 1995; Jordt et al. 1995; Mudge 2014), possibly due to the intrusion of sills (Naylor et al. 1999) and establishment of the Iceland hotspot or plume (Ebdon et al. 1995; Lamers & Carmichael 1999; Naylor et al. 1999; Morton et al. 2002; Mansurbeg et al. 2008; Mudge 2014), or a 'major underplating event' (Sørensen 2003; Mansurbeg et al. 2008; Smallwood 2008). At this time the basin also became increasingly restricted due to the emplacement of lava flows from the Faroe Islands area, which filled parts of the basin and contributed volcanoclastic material to the basin sediments (Naylor et al. 1999; Jolley & Morton 2007). From the Late Thanetian, into the Eocene, there was a rise in relative sea-level (Ebdon et al. 1995; Naylor et al. 1999; Morton et al. 2002), that allowed sedimentation to become progradational, meaning that deposition of coarse-grained clastic sediments became restricted to areas where deltas prograded into the basin, for example west of the Westray Ridge (Naylor et al. 1999; Morton et al. 2002). During the Palaeogene the majority of sediment was

supplied to the FSB from the SE with some sediment also supplied from the west, the Faroes Platform and East Greenland (Morton et al. 2002; Jolley & Morton 2007; Smallwood 2008).

AGE	Magnetostratigraphy	Biostratigraphy			Sequence Stratigraphy			Lithostratigraphy								
		Nano-zones	Paly		Micro	North Sea	FSB		Seismic Horizon	North Sea		FSB		E. Anglia (UK)		
55 Ma	C24r	Np10	Pt11		Mt7	T50	T50		BALDER	Moray Group	Balder Formation	Moray Group	Balder Formation	Thames Group	Harwich Formation	
			Pt9-10				T45									Base T45 /T50
		Np9	Pt8			T45	T45	Base T45 /T50	Sele Formation		Flett Formation					
	C25n	Np8	Pt8		Mt6	T38	T38		Base T38	Montrose Group	Lista/ Forties/ Andrew Formation	Faeroe Group	Lamba Formation	Lambeth Group	Upnor Formation	
																Base T38
		Np8	Pt7	C B		Mt5	T30	T30	T36		Top Kintail Top Cullin		Maureen Formation			Vaila Formation

Table 4-1 Stratigraphy of the Faroe-Shetland Basin (FSB) and North Sea Basin (e.g. Knox & Holloway 1992; Knox & Morton 1988; Ebdon et al. 1995; King 2016; BGS 2016).

The Moray Group of the FSB includes the Flett Formation (T45) which is overlain by the BF (T50; Table 4-1). The Moray Group extends throughout the FSB and the NSB (Table 4-1) and is capped by the Stronsay Group with its basal Glauconite marker horizon (Ebdon et al. 1995). In the south of the FSB, the Flett Formation is dominated by ‘delta top and coastal plain sediments capped by coals’ (Naylor et al. 1999; Ebdon et al. 1995). In the Early Eocene the region around the Schiehallion and Foinaven fields of UKCS Quad 204 (Figure 4-2), was occupied by a non-marine paralic environment (Morton et al. 2002), suggesting that uplift affected this region into the Eocene and may have had an effect on deposition of the BF in the Tornado, Suiilven and Cambo field areas.

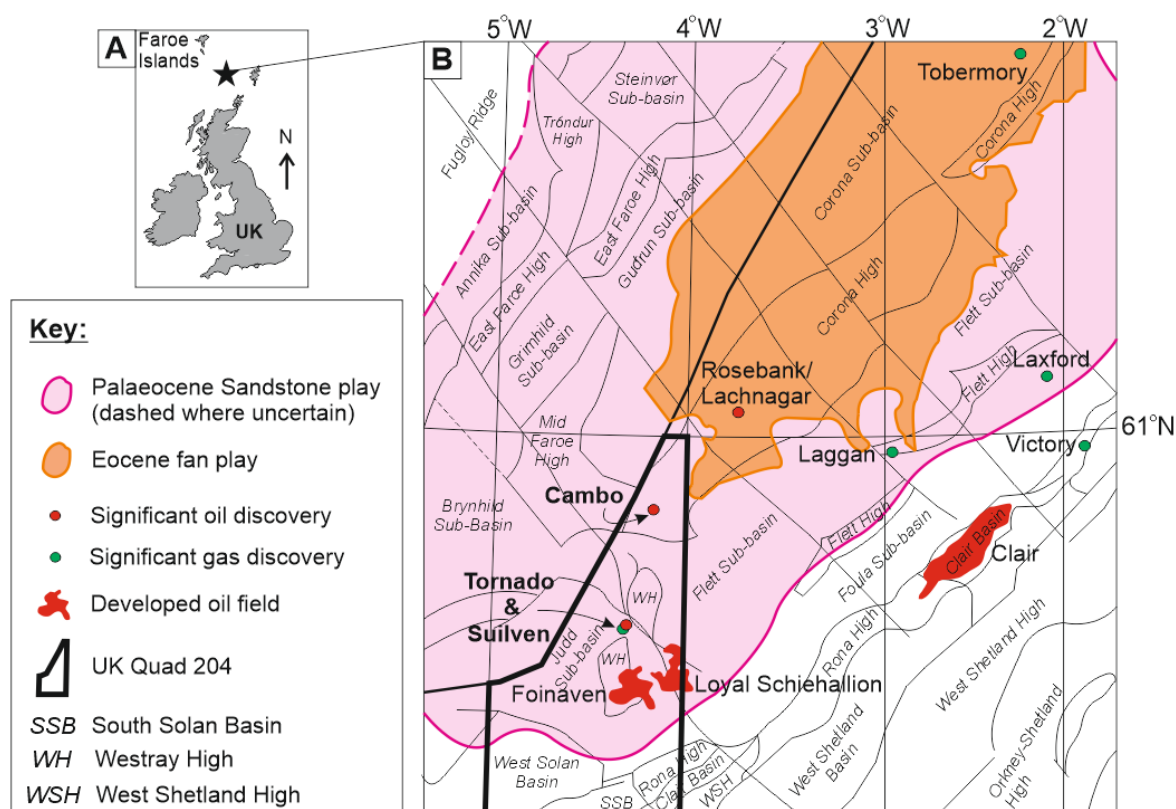


Figure 4-2 Structural map of the Faroe-Shetland Basin and the reported extent of Palaeocene and Eocene plays (Quinn et al, 2011; Ritchie et al. 2011). UK Quad 204 is highlighted.

Major oil and gas discoveries have been made within the Palaeogene strata of the FSB, for example, in the Schiehallion Field (UKCS Quad 204), therefore research of the Palaeogene strata is very important for exploration (Deegan & Scull 1977; Naylor et al. 1999; Morton et al. 2002; Smallwood & Kirk 2005; Harding et al. 2011). Oil and gas discoveries have also been made within the Paleocene strata of the Flett Sub-basin (Morton et al. 2002; Quinn et al. 2011).

3D seismic mapping and interpretation of Paleocene and Eocene strata within the FSB was undertaken by Smallwood & Gill (2002), who suggested that uplift of the southern region of the FSB occurred during the Paleocene and that this was followed by rapid subsidence during the Early Eocene (Smallwood & Gill 2002). A marine transgression occurred throughout the Eocene so that deeper marine conditions took hold in the basin from the Early Eocene onwards (Ebdon et al. 1995; Harding et al. 2011). The effects of this marine transgression are also observed in the stratigraphy of adjacent areas in the NSB, most notably in the London Basin.

Continental break-up and sea-floor spreading between NW Europe and Greenland began in the Paleocene around 60 - 55 Ma (Jolley et al. 2007; Smallwood 2008). It has been suggested that the main stages of rifting within the FSB had ceased by the time that the BF was deposited, based on the absence of any evidence for significant extensional faulting within Eocene strata of the FSB (Moy & Imber 2009; Stoker & Varming 2011). Therefore, deposition of the Eocene sediments was predominantly controlled by the pre-existing Palaeocene topography (Figure 4-3; Moy & Imber 2009; Stoker & Varming 2011).

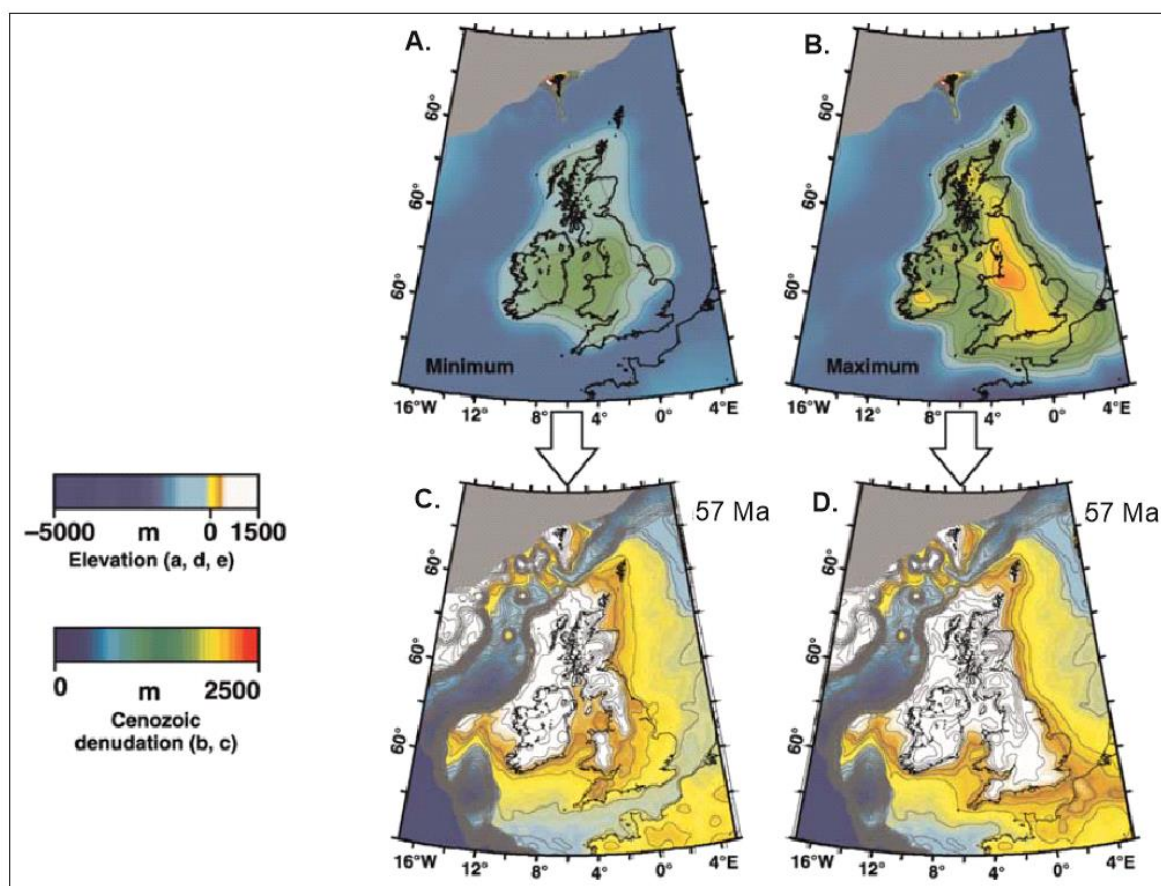


Figure 4-3 Models of the palaeobathymetry proposed for the FSB and UK around 57 Ma with corresponding maps of the present-day topography and bathymetry (From Smallwood 2008).

At the base of the BF there is commonly an unconformity where the underlying Flett Formation has been completely eroded and the BF lies disconformably on top of the Lamba Formation (Table 4-1). Erosion of the Flett Formation prior to deposition of the BF may have occurred due to a period of uplift caused by magmatism during continental break-up and the initiation of sea-floor spreading between Greenland and NW Europe (Mittlehner 1996; Jolley & Bell 2002; Morton et al. 2002; Smallwood & Gill 2002; Smallwood 2008; Moy & Imber 2009; Stoker

& Varming 2011). During the Paleocene and Early Eocene 'restricted circulation marine conditions with considerable fluvial input' were dominant in the NE Atlantic (Jolley et al. 2005). The major marine transgression that followed caused the BF to onlap the basalt lavas in the NW of the FSB (Smallwood 2008).

During deposition of the Flett and Balder formations the climate was warm and humid (Jolley et al. 2007). Increased rainfall on the uplifted land areas surrounding the FSB would have allowed large amounts of clastic sediment to have been eroded and transported into the FSB during deposition of the Flett and Balder formations. For example deposition in the late Thanetian - Ypresian (Table 4-1), was controlled by the presence of prograding deltas in the south, which deposited coarse-grained clastic sediments (Naylor et al. 1999; Morton et al. 2002; Anell et al. 2010). At this time deposition of deeper marine sediments was restricted to the north of the basin (Naylor et al. 1999). Lava flows prograded into the basin from the Faroe Islands allowing deposition of basin floor fans (Naylor et al. 1999), that would likely have been dominated by volcanic material supplied by advancing lava flows. Hemipelagic claystones are also present and form potential stratigraphic seals over these basin floor fan deposits (Naylor et al. 1999).

During deposition of the BF, tephra was deposited within the FSB, forming tuffs (Knox & Morton 1983, 1988; Naylor et al. 1999; Moy & Imber 2009). In older literature the term 'tuff' or 'tuffaceous' has been used to describe volcanic material of various origins; it is not often clear what is meant by the term 'tuff' in previous literature, therefore, in many cases it is taken to indicate the presence of rocks containing a significant proportion of volcanic material of unknown primary or secondary origin. In this study a sedimentary rock containing abundant volcanic clasts of secondary nature is termed a volcanoclastic sediment or rock.

In the FSB the BF contains a package of coarser-grained material known informally as the Cambo Sandstone Member (CSM). In previous literature this Member has been referred to as a Formation and is sometimes shown to represent the entire BF (Machado. pers. comm. 2015). In reality the CSM

includes multiple units of sandstone and is not *sensu strictu* a member. This will be discussed further elsewhere in this chapter.

4.3 Aims and objectives

This study was conducted to interpret the nature of the BF with regards to its lithologies and their environment of deposition. The BF, including its informally defined CSM, forms the focus of this study (Figure 4-1, Table 4-1). A discussion on the suitability of the use of the informal definition of the CSM is also included. The wells of interest in the Tornado, Suilven and Cambo field areas were originally drilled to investigate the Palaeocene sandstone reservoirs that lie below the BF.

4.4 Methods

Petrel E&P Software Platform 2014 developed by Schlumberger (referred to as Petrel hereafter) was used to interpret wire-line and seismic data provided by OMV U.K. Limited.

Gamma-ray, density and neutron-porosity wire-line data (courtesy of OMV (U.K.) Limited) and, 3D seismic data (courtesy of TGS-NOPEC) were provided for analysis. The wire-line and seismic data were used alongside biostratigraphy reports and composite logs, where available, for each well to gain a more complete understanding of the characteristics of the BF (Table 4-2). The data was studied separately for each well then compared between the wells of the Cambo, Tornado and Suilven field areas. All data across the study was then correlated to reach a wider-scale conclusion regarding the interpreted stratigraphy and the environment(s) of deposition. Multi-component analysis via comparison of different data sets is particularly important in this case because not all of the data types were available for all of the wells (Table 4-2).

‘The combination of horizontal and vertical seismic sections and gamma-ray logs provides a powerful tool for the interpretation of depositional systems which ... may enable exploration to focus directly on prospective units’ (Miall 2014).

Well	Gamma	Density	Neutron	Seismic	Biostratigraphy Report	Composite Log
204/10-2	✓	✓	✓	✓	✓	✓
204/10-1	✓	✓	✓	✓	✓	✓
204/10a-4	✓			✓	✓	✓
204/10a-3	✓			✓	✓	✓
204/5A-1	✓	✓	✓	✓	✓	✓
204/13-1 & 1z	✓	✓	✓	✓	✓	✓
204/14-2	✓			✓	✓	✓
204/19-8z	✓			✓	✓	✓
204/14-1	✓	✓	✓	✓	✓	✓
204/15-1	✓			✓		✓
204/19-5	✓	✓	✓	✓		✓
204/19-1	✓					
204/18-1	✓	✓	✓	✓		✓

Table 4-2 Data that was available for the BF for each well used in this study. Not all sources of data were available for every well.

4.4.1 Wire-line

An increase in the gamma-ray signature indicates that the rock contains more radioactive elements such as K, U and Th, which is typical of more fine-grained lithologies such as claystone or shale. A decrease in gamma indicates that the rock contains a low amount of radioactive elements, which is more typical of clean (quartz dominated) sandstones. During hydrocarbon exploration two of the most important lithologies are shale/claystone, which could be a hydrocarbon source or seal, and sand/sandstone which can act as a hydrocarbon reservoir. Therefore, the gamma-ray signature is described in terms of being more ‘shaley’ when there is a higher gamma and more ‘sandy’ when there is a lower gamma-ray response. Coarsening-upwards or fining-upwards packages can be identified where there is a gradual decrease or increase in the gamma-ray response respectively (Figure 4-4).

Density tools measure the electron density of the rock, which can be converted to give an indication of the porosity and bulk density of the material (Gluyas & Swarbrick 2004). This method can be useful for the identification of water and hydrocarbons within strata (Gluyas & Swarbrick 2004). The higher the density the less pore-space there is in the rock and therefore the less space for fluids. Neutron-porosity is measured in a similar way by recording the concentration of hydrogen-atoms within the rock (Gluyas & Swarbrick 2004; Railsback 2011). Hydrogen-atoms are most abundant in oil and water within pore-spaces, although they are also present within claystones (Railsback 2011), therefore giving a higher neutron-porosity value. When interpreted together the density and neutron-porosity responses can indicate the presence of claystone, porous sandstone, coal and limestone (Figure 4-4).

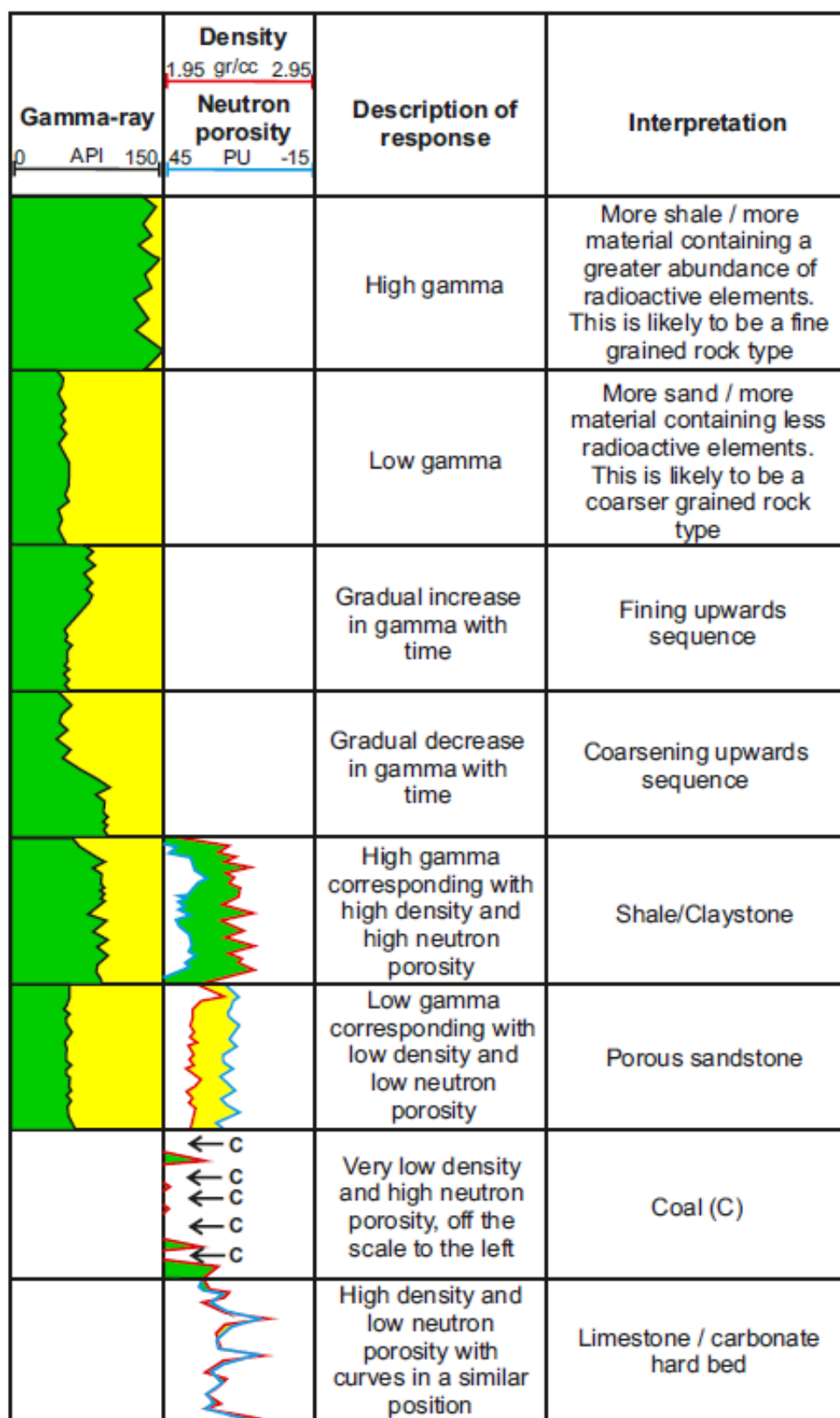


Figure 4-4 Diagram showing how to interpret various gamma-ray responses along with density and neutron porosity data. These observations and interpretations were used when analysing the wire-line data of the BF provided by OMV.

Initially the Top Balder and Base Balder horizons were picked in wire-line sections for each of the wells, using information given in the composite logs to

allow identification of the possible boundaries between formations. The position of these horizons was critically evaluated by assessing the position of the horizons relative to characteristics observed in the gamma-ray, density and neutron-porosity signatures. Subsequently, the depths of the picked horizons were compared to the positions of the Top and Base Balder boundaries stated in the biostratigraphy reports. Based on this information the position of some of these horizons was corrected to better fit the data.

The horizon boundaries and lithologies for all of the wells have been analysed previously by OMV. For some wells only gamma-ray data are available (Table 4-2), therefore, only a basic interpretation of the rocks present, in terms of whether they are more or less ‘sandy’ or ‘shaley’, can be made when these data are looked at independently from other data sources.

4.4.2 Seismic

3D seismic data is acquired from the use of controlled seismic sources, and an array of seismic receivers. A large quantity of seismic waveforms are collected during the acquisition using air guns and hydrophones. The data include the X, Y position of the data (known as traces) and the reflected signal caused by variations in the properties of rock in the sub-surface (reflectors). Each value within the seismic trace represents the signal at a given two-way time (TWT), the time taken for the seismic wave to travel from the source to the reflector and back to the receiver. These traces are formed into a 3D cube, allowing the mapping of these reflectors, across the area of the survey. The vertical resolution of the reflectors varies with the method of acquisition and the depth within the sub-surface of the reflector. The depth variation is caused by the reduction of the original higher frequency content of the data by adsorption as the signal travels through the sub-surface and back to the receiver. For this study, at the target the seismic data has a vertical resolution of 20 - 30 m. The original seismic data from the FSB11/12 3D broadband survey was cleaned up to improve the quality of the data, by OMV (U.K.) Limited, prior to this investigation. The seismic data was not flattened to any surface prior to or during this investigation.

A marker reflector within the sections in the seismic data set was taken to represent the Top Cambo Sandstone (TCS), of the CSM, an informally named member within the BF. This reflector was traced on in-line (orientated N-S) and x-line (orientated E-W) seismic sections across the entire Cambo, Tornado and Suilven area at 50 m intervals. This created a net of data representing the location of the traced TCS surface. This information was then used to create several different 3D surface models, known as seiscrops (Miall 2014), from the TWT of this picked surface, using Petrel, for seismic attribute analysis. Seismic attributes can be the original signal amplitude from the seismic, or various properties derived from the signal, such as average amplitude within a TWT window or a measure of the signal frequency within the window. These seiscrops represent a horizontal plane within the seismic data, which is created from the selected reflector and referred to as a stratal slice (Miall 2014). The various seiscrops were produced by selecting different parameters for Petrel to use to create the surface, such as, changing the width or position of the window of data being analysed (Figure 4-5). Seiscrop models were created of the study area to allow identification of features that can be used to interpret the environment of deposition of the BF. The identification of features in this way are known as seismic-geomorphic interpretations (Miall 2014). Interpretation of these 3D surfaces is limited by the resolution of the original seismic data, and also by the size of the interval between the data points that was used to construct the seiscrop. The creation of seiscrops is essential when trying to identify the nature of an ancient surface from 3D seismic data (Miall 2014).

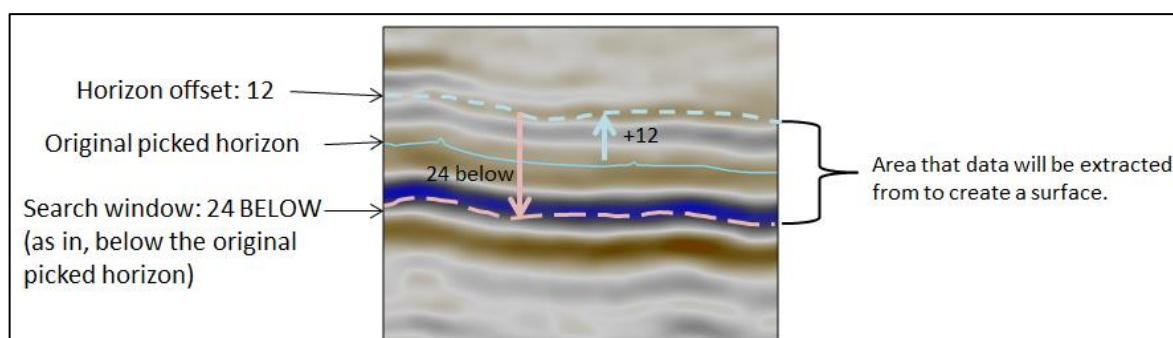


Figure 4-5 Diagram explaining how Petrel uses input parameters to define the window in which it uses data above and below a picked horizon to create a 3D surface. In this example a window thickness of 24ms is used with an initial offset of +12 above the original TCS picked horizon. This means that the window where data were analysed to create the corresponding seiscrop comes from +12ms above and -12ms below the TCS horizon giving an overall window thickness of 24ms.

4.4.3 Spectral decomposition

A spectral decomposition model, using RGB spectral decomposition blending, was created by, and provided for study by OMV (U.K.) Limited. This analysis was created from acquired seismic data over the Cambo field and does not cover the Tornado and Suilven fields to the south.

RGB spectral decomposition blending divides the original seismic data into narrower frequency components, with each colour representing a different frequency (Partyka et al. 2011). The surface that is created by carrying out spectral decomposition 'reveals interference occurring across the available bandwidth of signal' (Partyka et al. 2011) and creates a surface similar to that produced by remote sensing, which can be used to identify subtle geological features that might not be observed in other forms of seismic data (Partyka et al. 2011; Ackers & Bryn 2015). The RGB blended surface provided for this study allows the user to alter the depth and thickness of the data window that is being analysed so that it is possible to move through the data over TWT, between different stratigraphic intervals. The colours of the RGB blend of the spectral decomposition can be used as an estimate of the general thickness of the sediment packages. For example, deeper red tones indicate where the rocks are thicker, whereas blue tones indicate where the rocks are thinner.

Volcanic rocks are likely to appear white on an RGB blended spectral decomposition image as these rocks create a strong response within all of the frequencies (Wright, pers. coms. 2016). In contrast faults will appear black (Cooke et al. 2014).

4.4.4 Biostratigraphy

All of the cuttings and biostratigraphy data - which were obtained from cuttings material - have been described on a First Downhole Occurrence (FDO) in the reports and additional data sources used in this study. Descriptions are carried out in this way in an attempt to limit the amount of error caused by the mixing of cuttings within the well before they are received at the surface.

Biostratigraphy reports, provided by OMV (U.K.) Limited, were available for some of the wells (Table 4-2), and provide information on the interpreted positions of formation Tops based on the palaeobiology identified in cuttings material. An interpretation of the palaeoenvironment is often also provided in these reports, based on the types of fossil micro-organisms, spores, pollen and dinoflagellates identified in the cuttings or cored material from different depth intervals.

4.4.5 Additional data

Additional data was provided in the form of composite logs and final well reports, which were available for most of the wells (Table 4-2). These sources of information were used for initial study of the lithology and the upper and lower boundaries of the BF to give guidance on the position of the sections to be studied in each well.

4.4.6 Data limitations

Each of the data sets used has its own benefits and limitations. For example, each of the data sets has a different resolution and can give information on a varying scale (Table 4-3). This can be beneficial for looking at features at different scales but means that no one data set can be used to give reliable information on the lithology or environment of deposition on its own. Therefore, the more data sets that are available for each well the more reliable any interpretation of the BF characteristics will be. For wells where only one data source is available the information is not reliable, and these wells have largely been ignored (Table 4-2).

Data	Seismic	Wire-line	Core	Cuttings
Resolution	20-30m	15cm	Any	Any
Pros	Lots of data can be acquired over a large area relatively quickly	Some averaging effects applied so data does not directly correlate to stratigraphy. Fine features not recorded	Direct, fine-scale observation of the stratigraphy	Fine-scale observation of the components of the stratigraphy where core is not available
Cons	Large scale of resolution Finer detail not shown	Collection of data quickly on a range of different rock properties	Larger scale features could be missed or mis-interpreted due to restricted width of core	Mixing of cuttings from different levels causes errors in interpretation of the depth to certain lithologies/biostrat

Table 4-3 Data used in this study with a comparison of the resolution, and the pros and cons of each data type.

The seismic data used in this study was only flattened to the level of the sea bed, as this level could be easily identified without error from the seismic data. This means that any tectonic activity that has affected the BF post-deposition has not been eliminated. This means that some topographic features within the BF may have formed due to later tectonic activity and not reflect the true nature of the topography during deposition of the BF. This adds a large error to the larger scale topographic interpretations of the entire study area.

The composite logs and final well reports used in this study were produced by a range of different companies over a range of different drilling years (Table 4-4), and therefore some interpretations of the lithologies present in each well are different based on varying levels of training and importance of the stratigraphic units according to each company. The composite logs can therefore only be used for initial study of the stratigraphy of each well and should not be used for reliable interpretations of the nature of the BF.

Well	Composite log produced by	Date of drilling & composite log construction
Cambo		
204/10-2	HESS	2004
204/10-1	HESS	2002
204/10a-4	CHEVRON	2011
204/10a-3	CHEVRON	2009
204/5A-1	CHEVRON	2013
Tornado-Suilven		
204/13-1 & 1z	OMV	2010
204/14-2	BP, CONOCO	1998
204/19-8z	BP	1996
204/14-1	BP, CONOCO	1998
204/15-1	CONOCO	1999
204/19-5	BP	1995
204/19-1	BP	1986
204/18-1	BP	2001

Table 4-4 List of information regarding the date and company responsible for compilation of each composite log for each well.

4.5 Results

4.5.1 Wire-line

Fluctuating gamma-ray response is given in all wells and often corresponds to variations in the density and neutron-porosity values, where available, given by the wire-line tools through the BF (Figure 4-6, Figure 4-7). The wire-line data was investigated for the entire BF as well as the signature above and below this to check the proposed position of the BF.

In all of the Cambo wells the gamma-ray response is generally intermediate and fluctuates. In wells 204/10-2 and 204/10-1 peaks in the gamma-ray response become abundant towards the top of the BF (Figure 4-6).

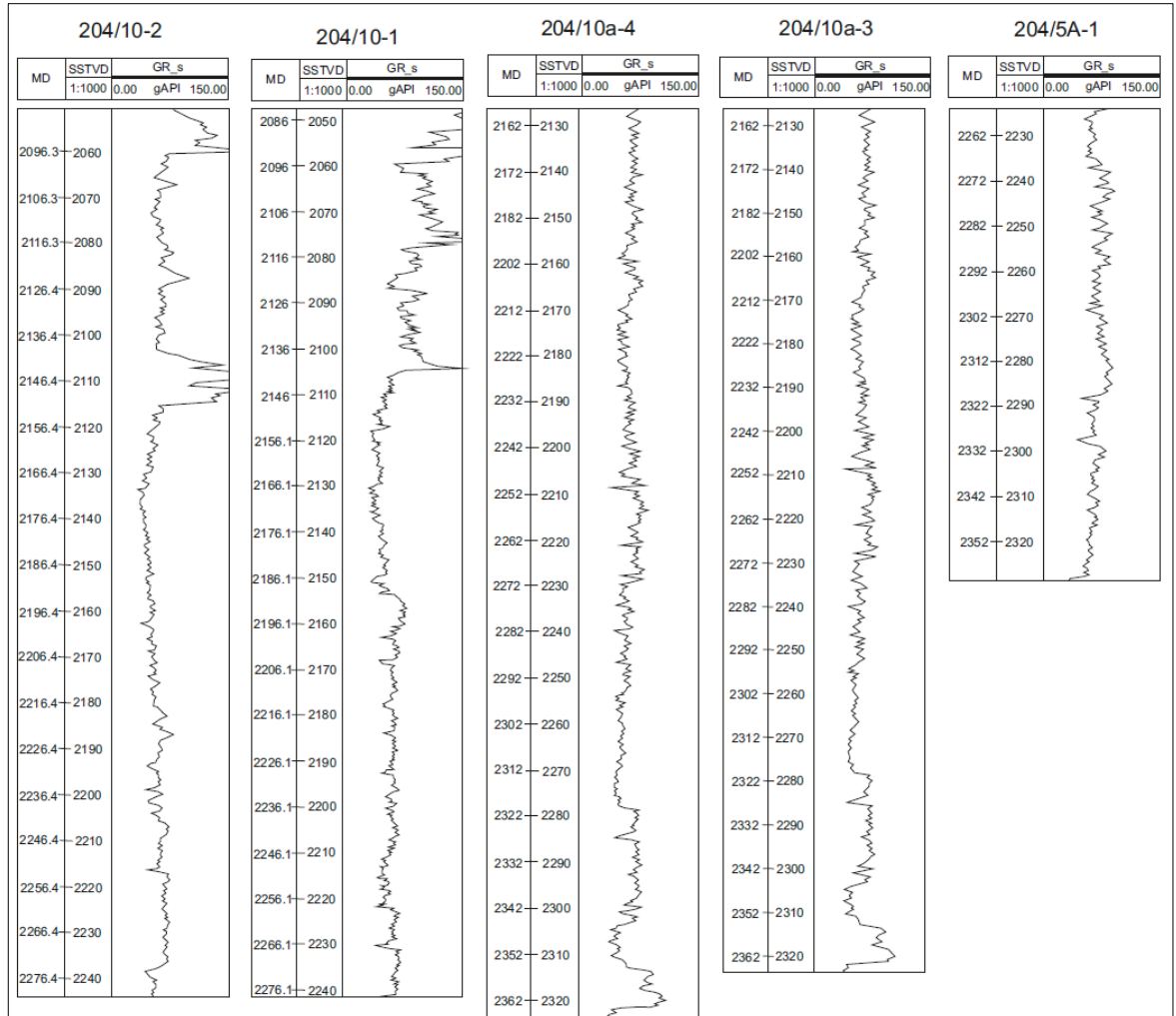


Figure 4-6 Gamma-ray wireline data encompassing the whole BF used for interpretation of the lithologies and characteristics of the BF in the Cambo prospect. This data has been flattened to the top BF horizon.

The wire-line data throughout the Tornado and Suilven wells (Figure 4-7) gives a more varied response compared to the signature observed through the BF of the Cambo wells (Figure 4-6). In these wells the gamma-ray response is predominantly moderate to low with abundant variations in the signature. Alongside this the density and neutron-porosity values are highly variable. In general, when the gamma-ray response is low, density is also low and the neutron porosity is high.

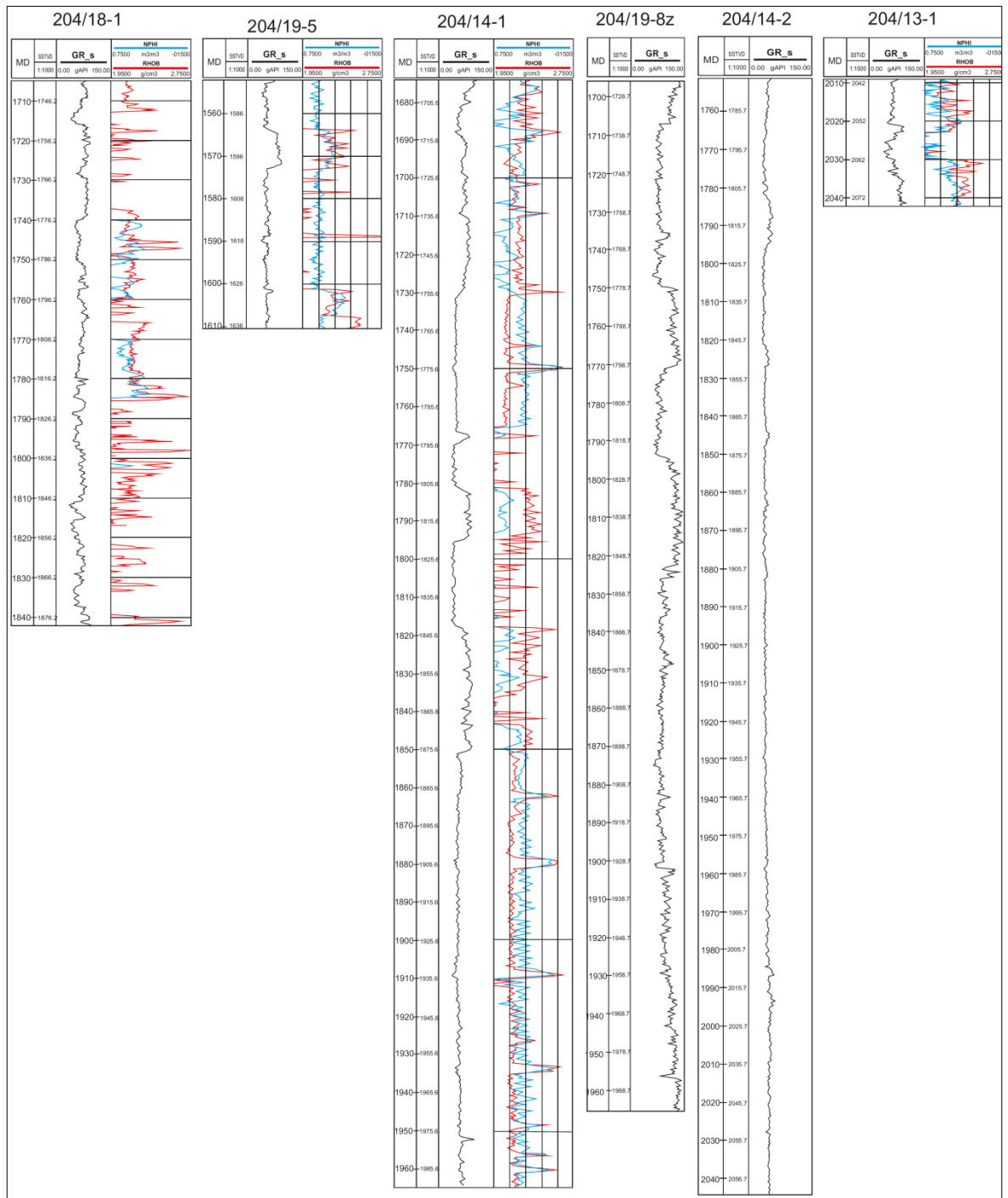


Figure 4-7 General wire-line data encompassing the whole BF, and sometimes also the Flett Formation, of undifferentiated composite log data used for interpretation of the lithologies and characteristics of the BF in the Tornado-Suilven prospect. Including gamma-ray response (black), density (red) and neutron porosity (blue) data. As shown this data is flattened to the top BF horizon.

4.5.2 Seismic

Examples of in-line and x-line seismic sections (courtesy of TGS-NOPEC) are given in Figure 4-8. At the level of the BF the seismic response generally appears as a bright reflection, which produces a marker horizon that can be picked in 2D

seismic sections (Figure 4-8). In some areas this marker horizon is less clear and the seismic response fluctuates in brightness and continuity. In these regions it is more challenging to pick the BF, leading to a possible error in positioning of the BF and TCS for the creation of 3D seiscrops.

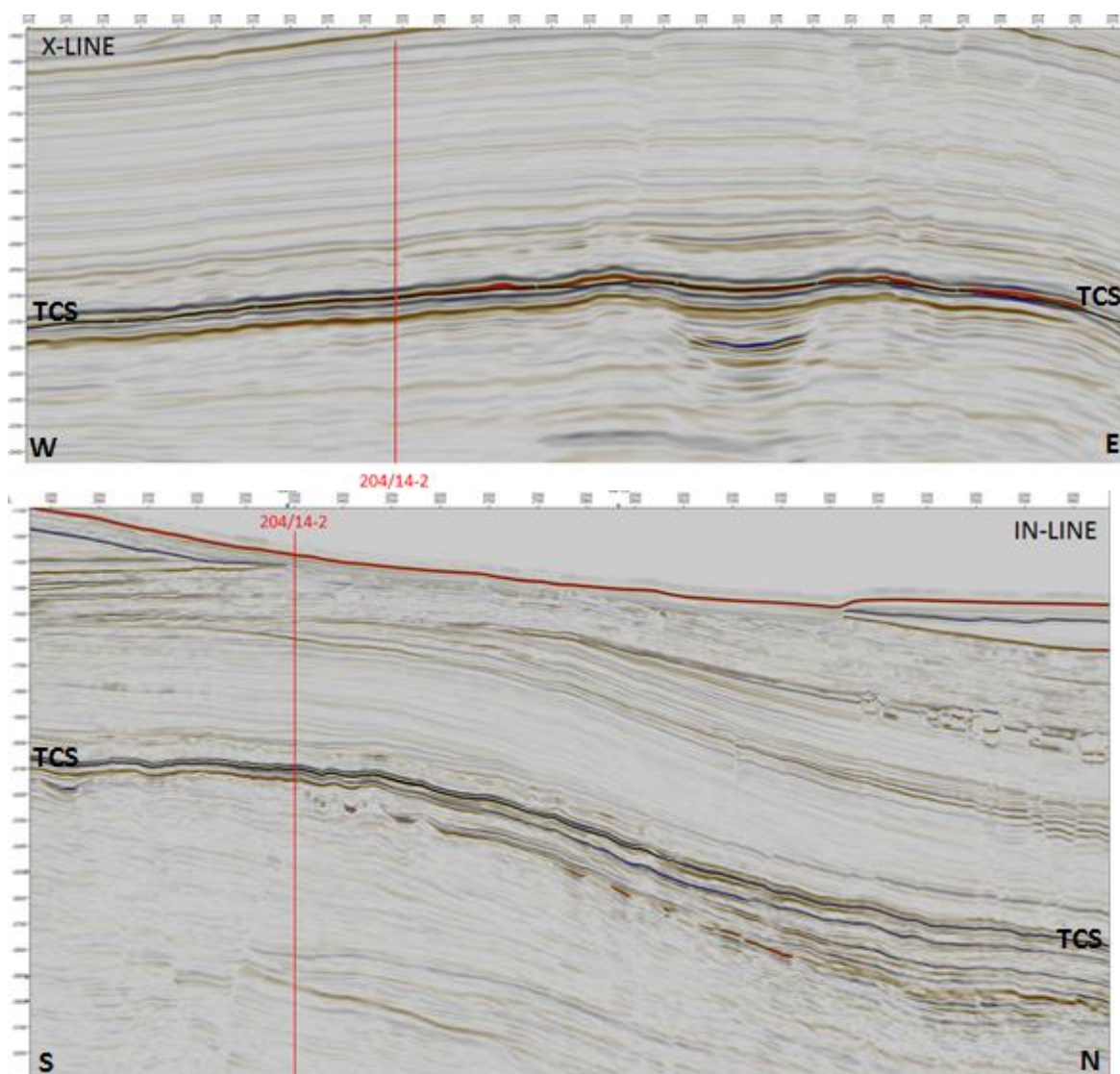


Figure 4-8 Examples of X-line and In-line seismic sections, orientated E-W and N-S respectively, intersected by Well 204/14-1. Features seen within these two sections can be identified elsewhere within the BF throughout the study area. The thicker black line represents the position of the TCS member of the BF. These seismic sections have not been flattened, therefore any structures may be tectonic and not related to the original deposition of sediments. These sections are also vertically exaggerated meaning that the dips of the responses are not as steep in reality.

A topographic model (seiscrop) of the TCS was produced following amalgamation of the data points within the TCS picked surface of the seismic data set (Figure 4-9). The seiscrop shows areas of apparent higher and lower relief with higher relief represented by reds and warmer colours and deeper regions indicated by

blues and cooler colours (Figure 4-9). This surface shows the present-day topography of the TCS horizon within the BF.

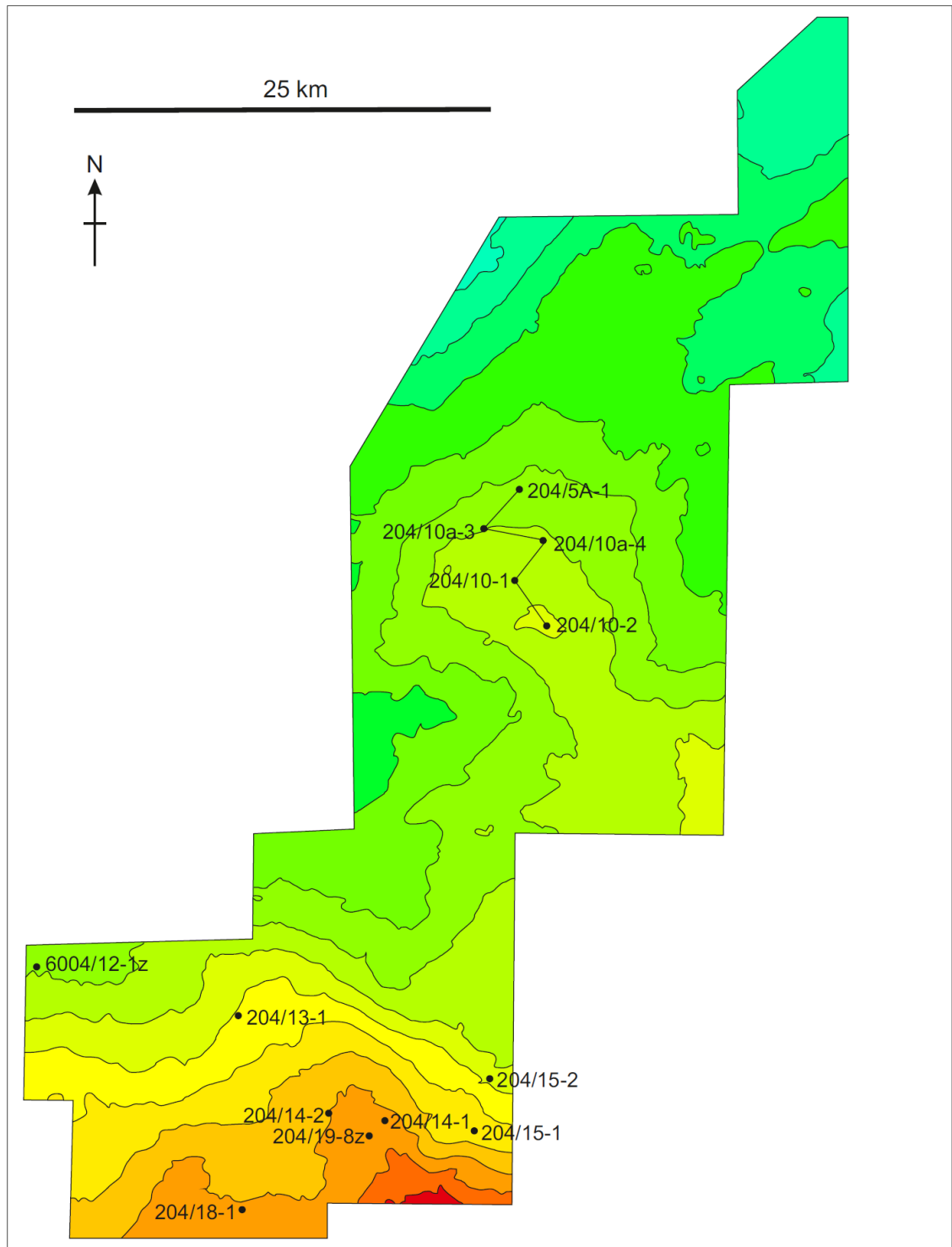


Figure 4-9 Topography of the picked TCS surface generated from a grid of data points from the picked TCS. Red shades indicate the presence of higher relief whereas blue shades indicate the presence of lower relief. This topography was created using non-flattened seismic data, and therefore represents the current topography of the BF rather than a true representation of the surface during deposition of the BF. It is known that tectonic activity and erosion have affected the area post-BF deposition.

The Tornado and Suilven fields lie to the south of the study area in a region dominated by the highest relief (Figure 4-8). The Cambo field lies further to the north within a ridge-like feature surrounded by deeper topography (Figure 4-8). This area forms part of the Corona Ridge (Figure 4-2).

Various other surfaces were created from the seismic data to produce 3D seiscrop models of the TCS surface across the Tornado, Suilven and Cambo field areas (Figure 4-10 - Figure 4-16). Different features can be observed on each of these surfaces in a varying amount of detail. For example, in general, the Tornado and Suilven areas are composed of chaotic shades of black, grey and white, whereas further to the north there are linear features striking NW-SE across the area (Figure 4-10 - Figure 4-15). These linear features continue into the Cambo field area to the north where the general appearance on all of the 3D surfaces is smooth and is less chaotic compared to the Tornado-Suilven area (Figure 4-16 - Figure 4-18).

Some regions of the seiscrops have an unclear, 'watery' appearance. This occurs where the data window used to extract the data for creation of the surface was either too small or too large compared to the thickness of the BF analysed (Figure 4-10). In these regions no interpretation of the surface features or nature of the BF can be made.

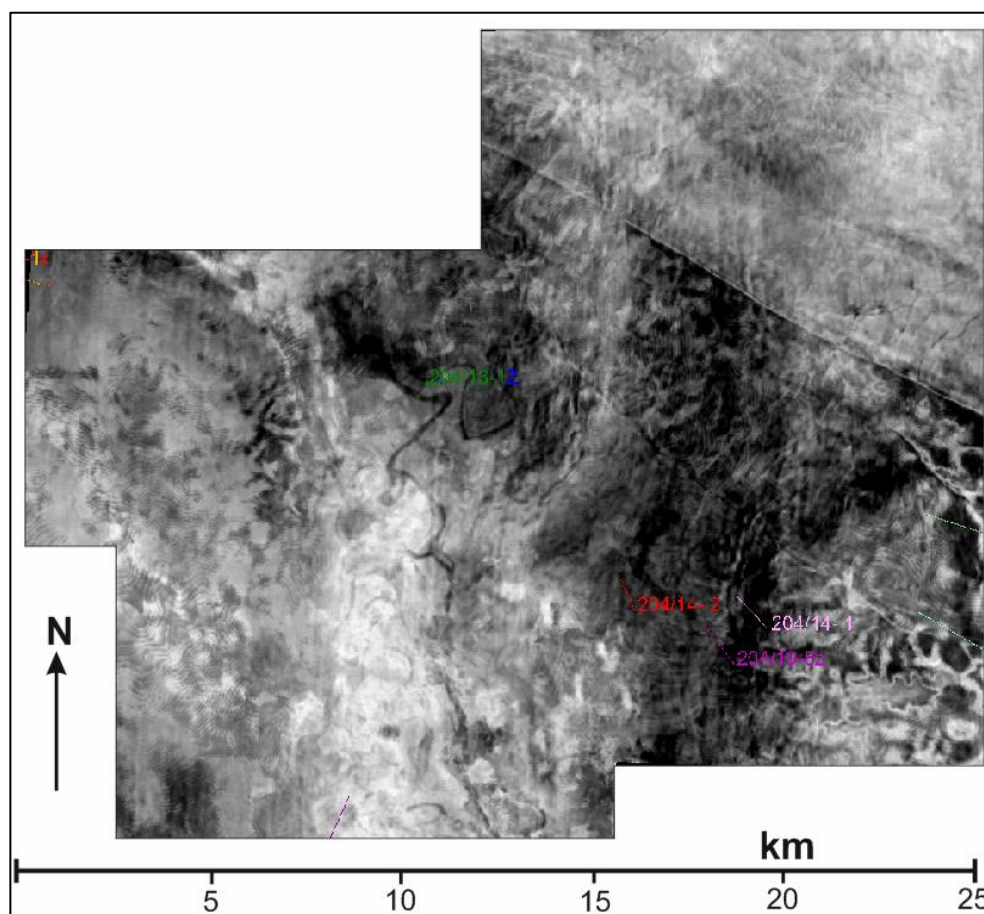


Figure 4-10 RMS amplitude (24ms window with +12 ms offset) window covers +12 ms to -12 ms from the picked TCS horizon in the Tornado-Suilven region of Quad 204. Variations in grey show the presence of different features within the surface, for example, the presence of darker sinuous features in the centre of the image and paler linear SE-NW orientated features to the north. The unclear, 'watery' appearance of the surface in the lower right corner is caused by the data window being too thick compared to the thickness of the BF at this location, therefore additional data is analysed leading to distortion in the surface produced.

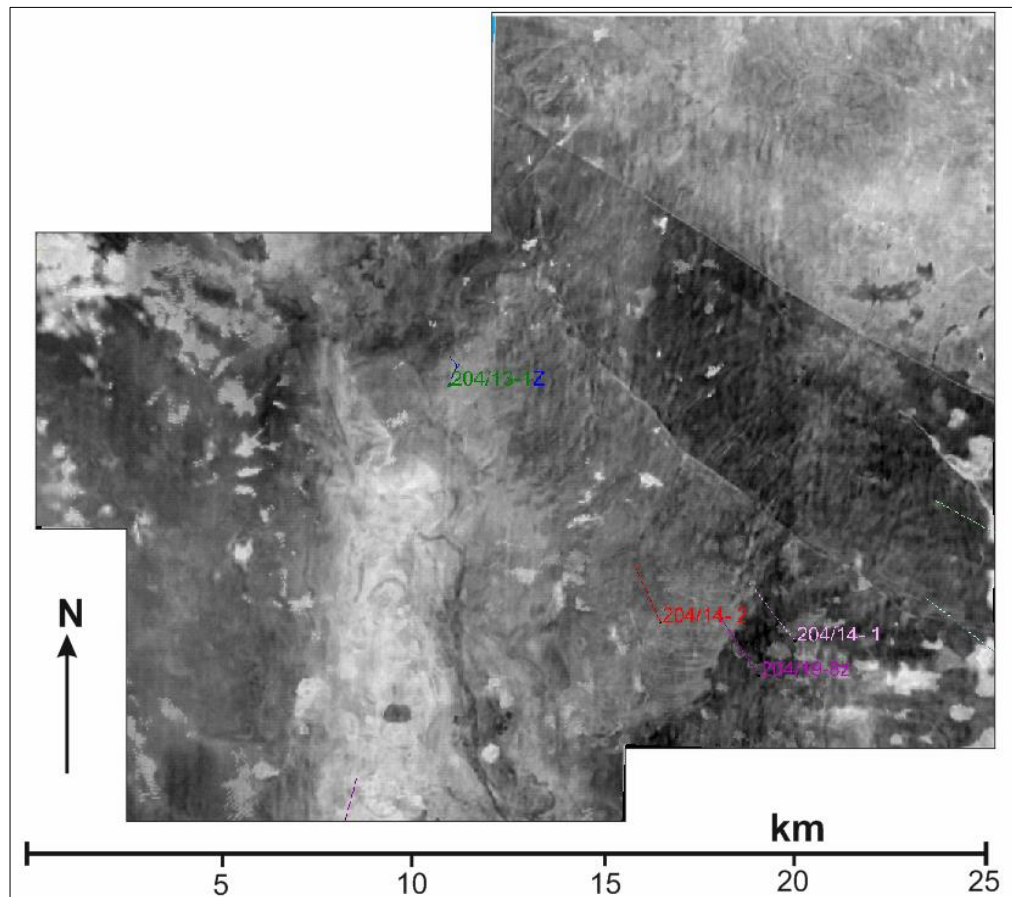


Figure 4-11 Maximum amplitude (30 ms window with +15 ms offset) covering the Tornado-Suilven area of Quad 204. This image shows features in different detail compared to Fig. 12, for example the sinuous features in the middle are more subtle.

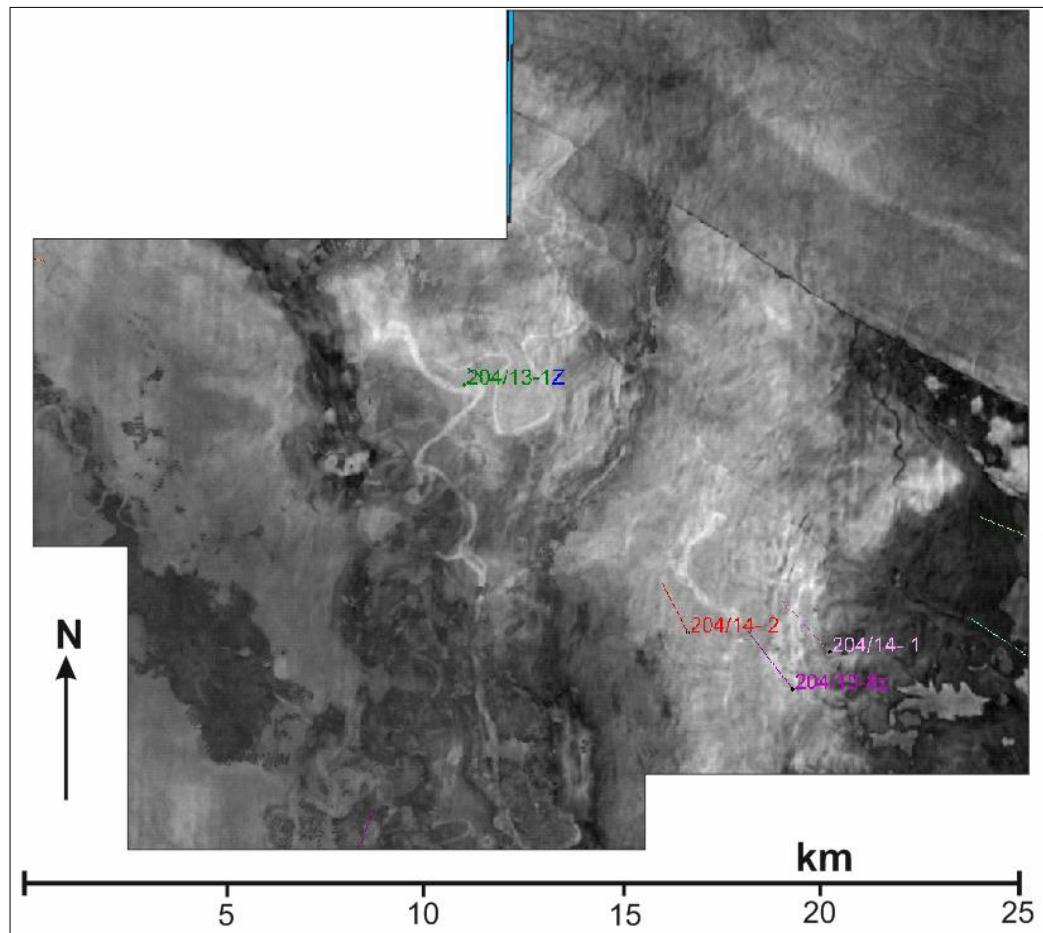


Figure 4-12 Minimum amplitude (24ms window with +12 ms offset), covering the Tornado-Suilven area of Quad 204. This surface gives a much clearer overview of the Tornado-Suilven area, for example, sinuous features are more abundant and highlighted by a paler grey shade of data response, and a darker grey result to the mid-right of the image.

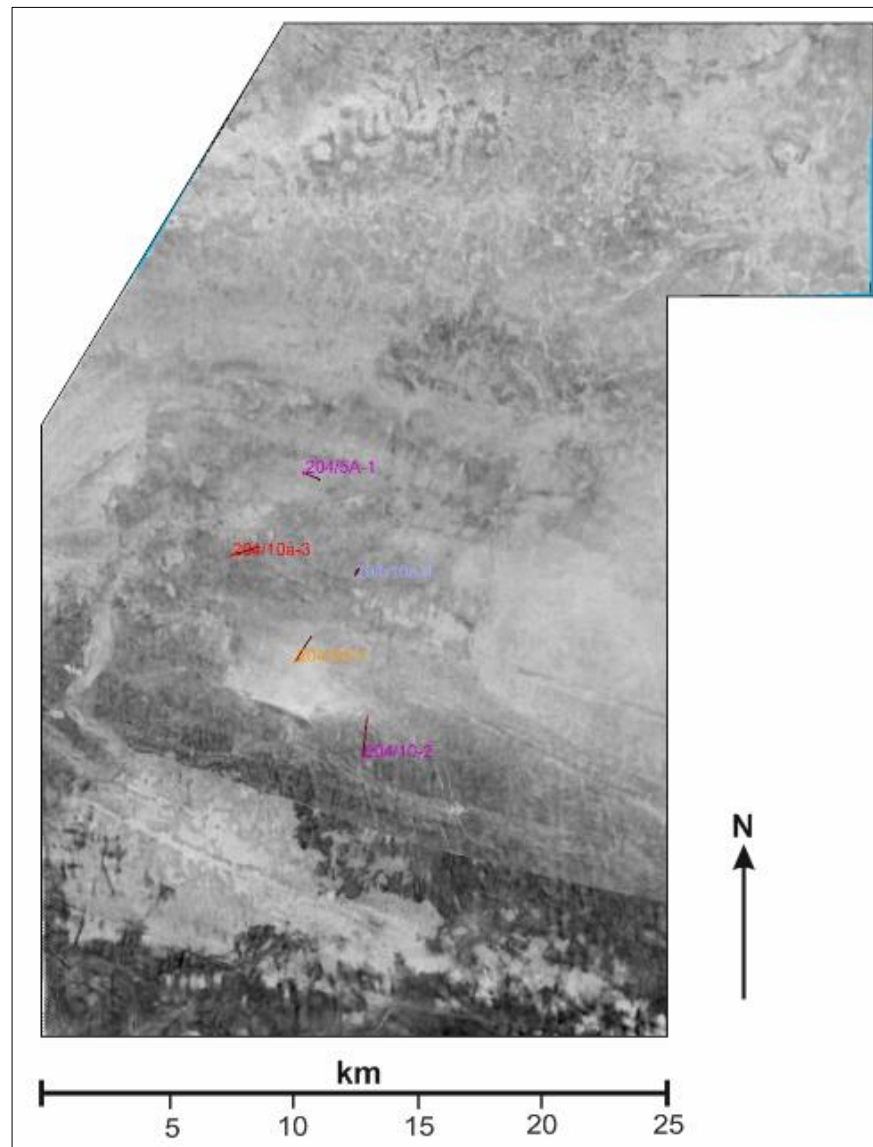


Figure 4-13 Maximum amplitude (24ms window with -12 offset) surface representing the picked TCS Member of the Cambo area of UK Quad 204. Variations in the grey shading of the surface help in identification of surface characteristics such as linear SE-NW orientated features across the entire area, and a paler grey sinuous feature to the mid-left.

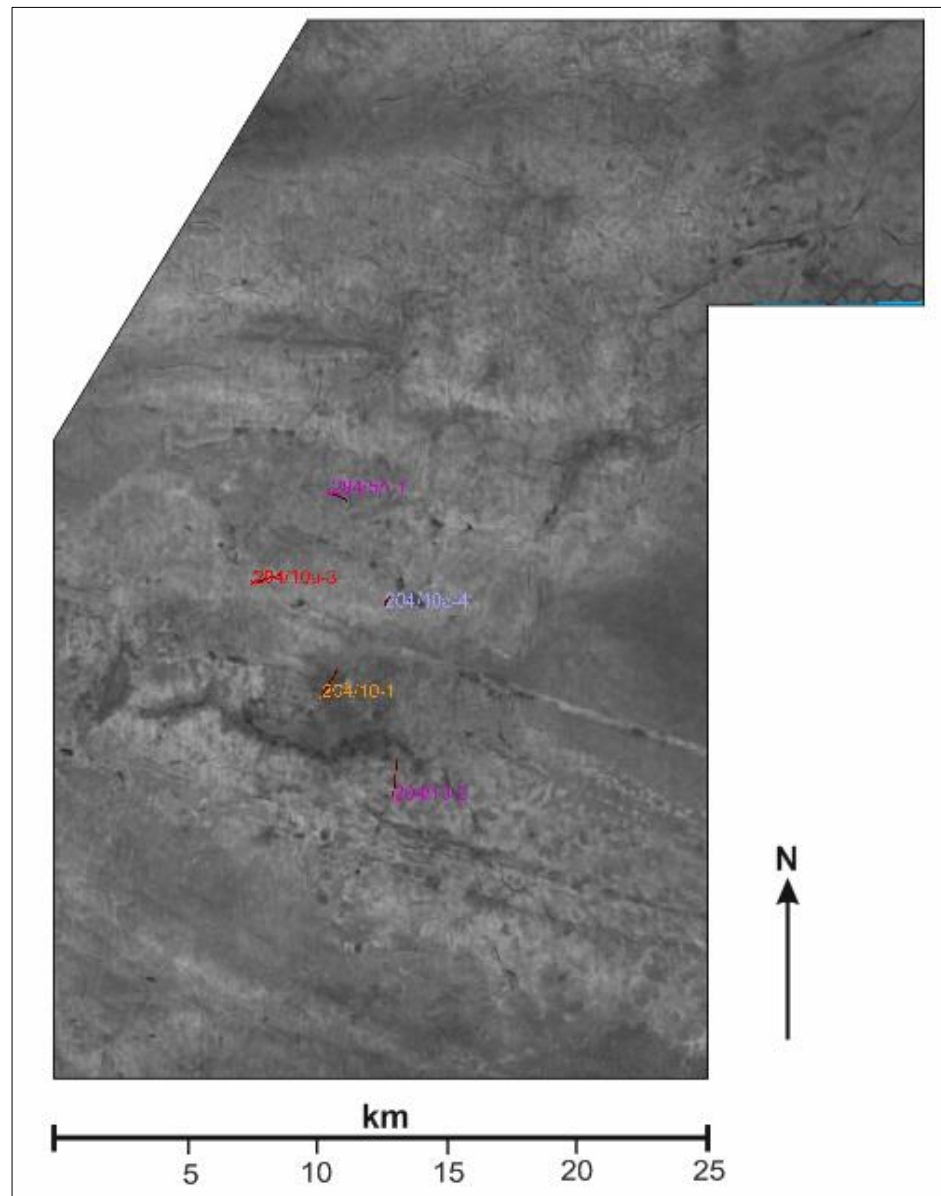


Figure 4-14 Minimum amplitude (12ms window with -6 offset) surface covering the Cambo area of Quad 204. This surface shows additional features to those in figure 13, for example, an area of darker grey towards the centre of the image and more detailed results for the lower left region of the image that is absent in figure 13.

An anomalous darker shaded region appears within the Cambo area in most of the seicrops (Figure 4-15). This darker region is elongated in a roughly E-W orientation with patches of lighter response observed within it.

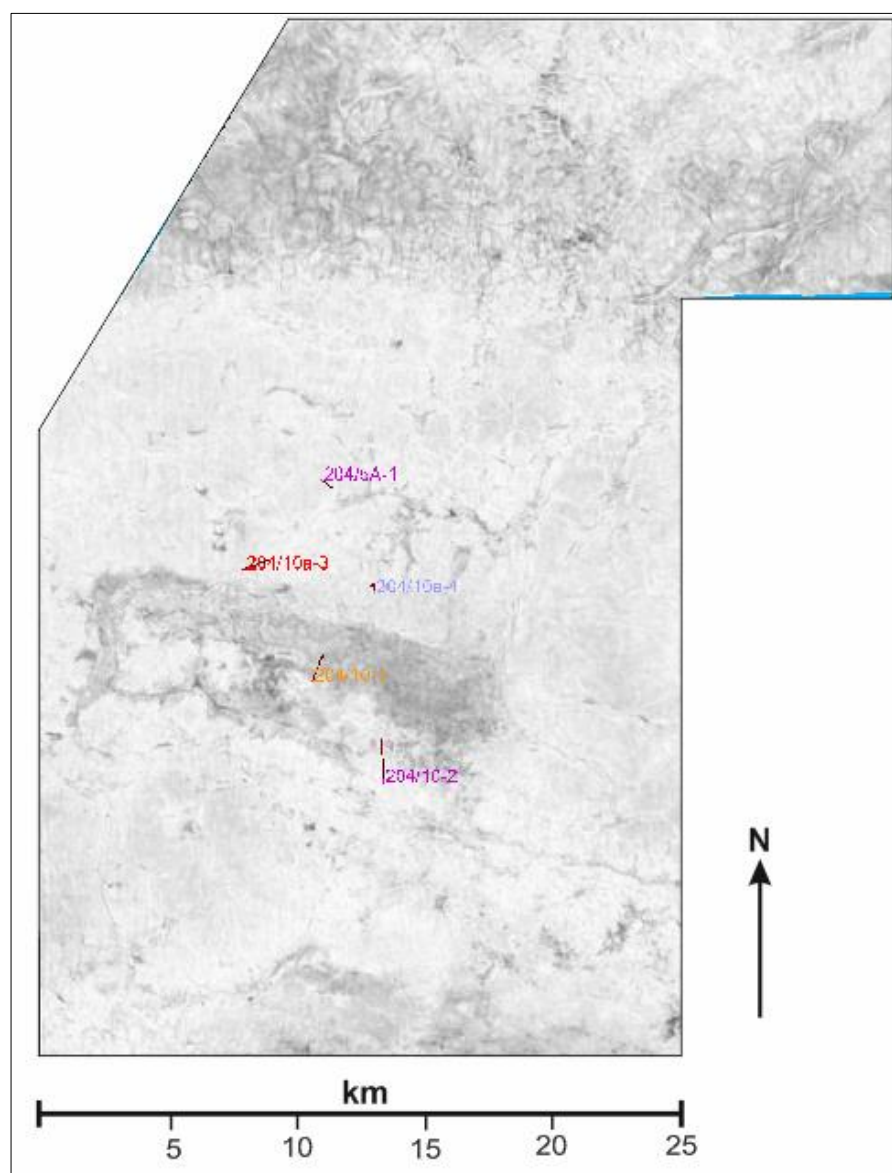


Figure 4-15 RMS (24ms window with +12 offset) for the Cambo area of Quad 204. This surface gives a very different response compared to those shown in Fig. 17-18. This surface gives a very different response compared to those shown in Fig. 17-18. Here the majority of the surface gives a bright white response. An elongated darker grey region can be seen in the centre of the image intersecting Wells 204/10-2 and 204/10-1.

The Tornado, Suilven and Cambo surfaces have contrasting appearances in all of the seiscrops (Figure 4-16). These varying surface characteristics are directly related to the nature of the BF across this study area and are unlikely to have been produced or influenced by post-depositional tectonic activity.

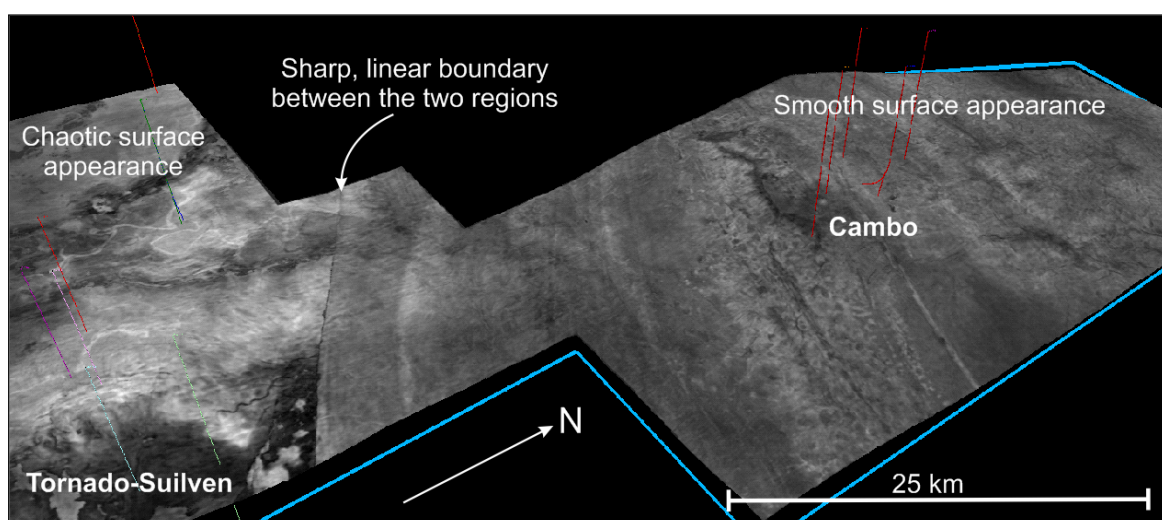


Figure 4-16 Minimum amplitude (24ms window, -12ms offset) 3D surface of the Tornado-Suilven and Cambo areas. Clear differences can be observed between the nature of the Top Cambo surface between these two areas.

4.5.3 Spectral decomposition

The RGB blended spectral decomposition surface could be adapted to show data from different depths and thicknesses. At the level of the TCS (Figure 4-17), there is an area of deeper red colours to the south and duller blues to the north, corresponding to thicker and thinner deposits respectively. Black low amplitude linear features trending N-S are present to the east of the Cambo wells (Figure 4-17). Brighter white areas are present corresponding to areas of high amplitude. Linear features striking roughly E-W can also be observed towards the centre of the Cambo field area (Figure 4-17).

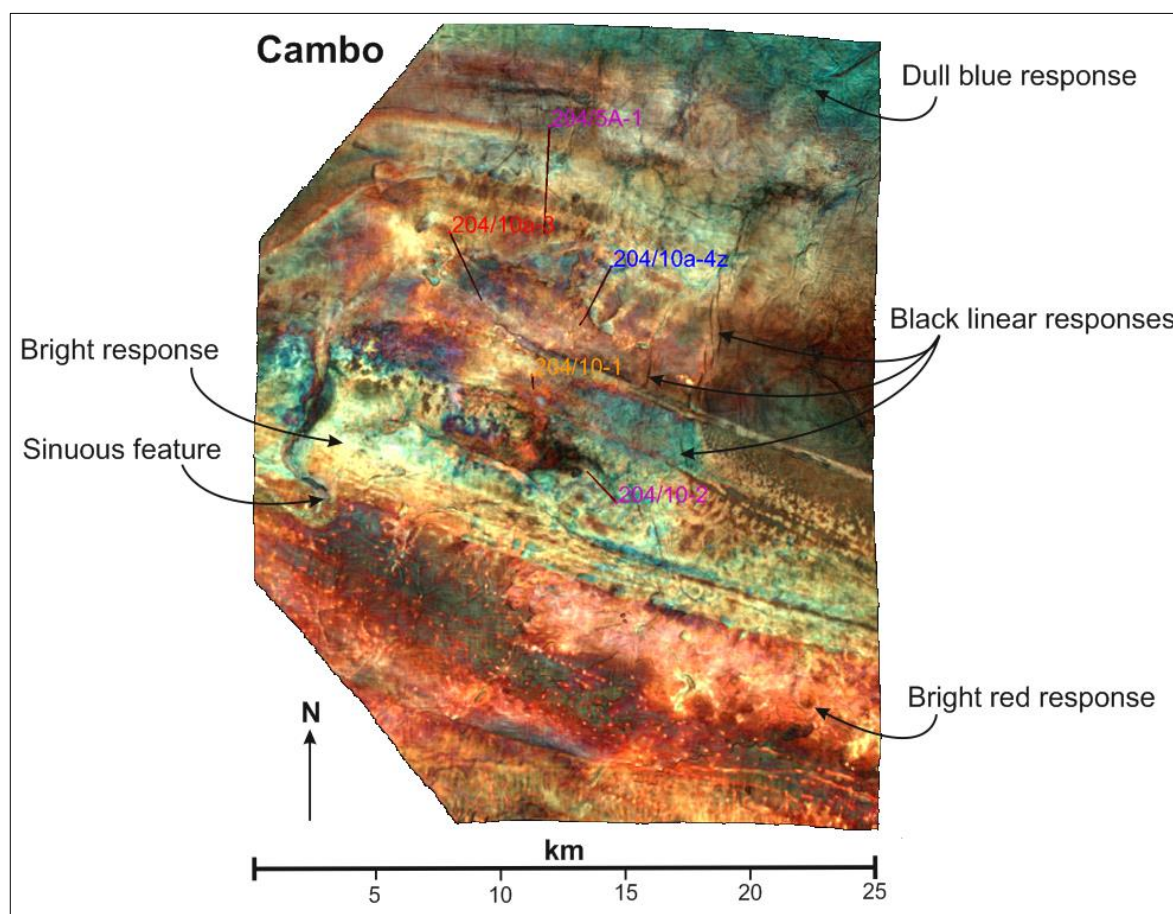


Figure 4-17 RGB blended spectral decomposition surface of the Cambo prospect shown at a level representing a time interval around deposition of the BF. Annotated to show the main results that can be identified in this image. Image/data provided by OMV U.K. Limited.

4.5.4 Biostratigraphy

All biostratigraphy data came from the biostratigraphy reports provided by OMV. These were cross-referenced with information given in the literature regarding the palaeobiology and palaeoenvironmental indicators that are discussed in these reports. No results can be given as an original contribution, but the biostratigraphy will aid interpretations of the environment of deposition made later in the discussion.

4.6 Discussion

4.6.1 Wire-line characteristics of the Balder Formation

4.6.1.1 *Cambo*

In all of the Cambo wells the BF appears to be a general continuation of the underlying Flett Formation, as shown by the similar nature of the wire-line signature throughout the Flett Formation and their continuation into the BF. This continuation of similar wire-line responses suggests that there was little or no change in the environment of deposition, and therefore no change in the sedimentary units that were deposited in this area, between Flett and Balder times. At the top of the BF there is an unclear distinction between the upper boundary of the BF with the overlying Stronsay Group, with its lower Glauconite Member (e.g. Ebdon et al. 1995). Again, the wire-line signature is similar between these two sequences so, identification of this upper boundary depends on information provided by other data, for example the biostratigraphy and cuttings descriptions.

The BF in all of the Cambo wells gives a similar moderate gamma-ray response, with some areas of higher or lower gamma indicating the presence of more shale-rich and sand-rich lithologies respectively. The upper part of the BF in wells 204/10-2 and 204/10-1 has a very high gamma-ray response, which is not observed in any of the other Cambo wells. This gamma peak suggests that these two wells contain a significant unit of claystone at the top of the BF. This claystone could indicate the presence of volcanic material which is suggested to be present in the top of these two wells, as stated in the composite logs and in the cuttings descriptions. The gamma-ray response itself does not necessarily indicate the presence of volcanic material at this interval. Further evidence, for example, from additional descriptions of cuttings material, would be needed to confirm the presence of volcanic material. Therefore, from the wire-line results it can only be concluded that a unit of claystone or material containing abundant K, U and Th, able to produce a peak in gamma-ray response, is present at this level.

The Cambo Sandstone Member (CSM) can be identified where there is a decrease in the gamma-ray signature, which indicates the presence of more 'sandy' material. This can be identified in all of the Cambo wells, except 204/5A-1. The location of this feature within the gamma-ray signature matches the depth ranges given for the CSM in the composite logs, which have been positioned based on cuttings, biostratigraphy and well correlations conducted soon after the drilling of each well. In Well 204/5A-1 the depths given for the CSM do not correspond to a general region of decreased gamma-ray response. Instead, the gamma-ray signature fluctuates, indicating the presence of other lithologies such as claystone and siltstone, rather than a dominance of sandstone as seen in the other wells. The CSM has also been identified at a greater depth in this well compared to all of the other wells; therefore, this indicates that this well is located in a deeper marine more distal depositional environment. Less sand would be deposited in this distal environment, which is supported by the lack of a dominant low-gamma response in the wire-line data. The CSM is typically encountered at greater depths towards the north, but also appears to decrease in thickness towards the north; however, post-depositional compaction and erosion may have removed some of the original thickness of the BF.

A basic stratigraphic column based on interpretation of the gamma-ray, density and neutron-porosity wire-line responses can be constructed for each well based on whether the signature denotes a more 'shaley' or more 'sandy' package. The inferred lithologies present within Well 204/5A-1 show that this well contains a greater amount of fine-grained material than any of the other wells, as shown by its generally higher gamma-ray values. The apparent abundance of fine-grained material in the wells appears to increase from the south to the north.

The BF is thickest (~193m) and coarsest in the south in Wells 204/10-2 and 204/10-1 and is thinnest (~103m) and contains the most fine-grained material in the north at Well 204/5A-1. Therefore, there appears to be a general thinning and fining of the Formation northwards, which can be highlighted by carrying out a correlation between all of the wells (Figure 4-18). These observations likely correspond to a general deepening of the subaqueous environment of deposition and/or deepening of the basin. Correlations between the wells also show that some sequences can be correlated between all of the wells, but others are

interpreted as pinching out towards the north. The pattern created by the correlations gives a general sigmoidal geometry to the BF. This is a commonly observed geometry in modern day deltas (Somoza et al. 1998). The lithology types and the thinning and fining character of the BF between the Cambo wells along with the geometry of the deposits is evidence to suggest that this area was occupied by a delta during deposition of the BF.

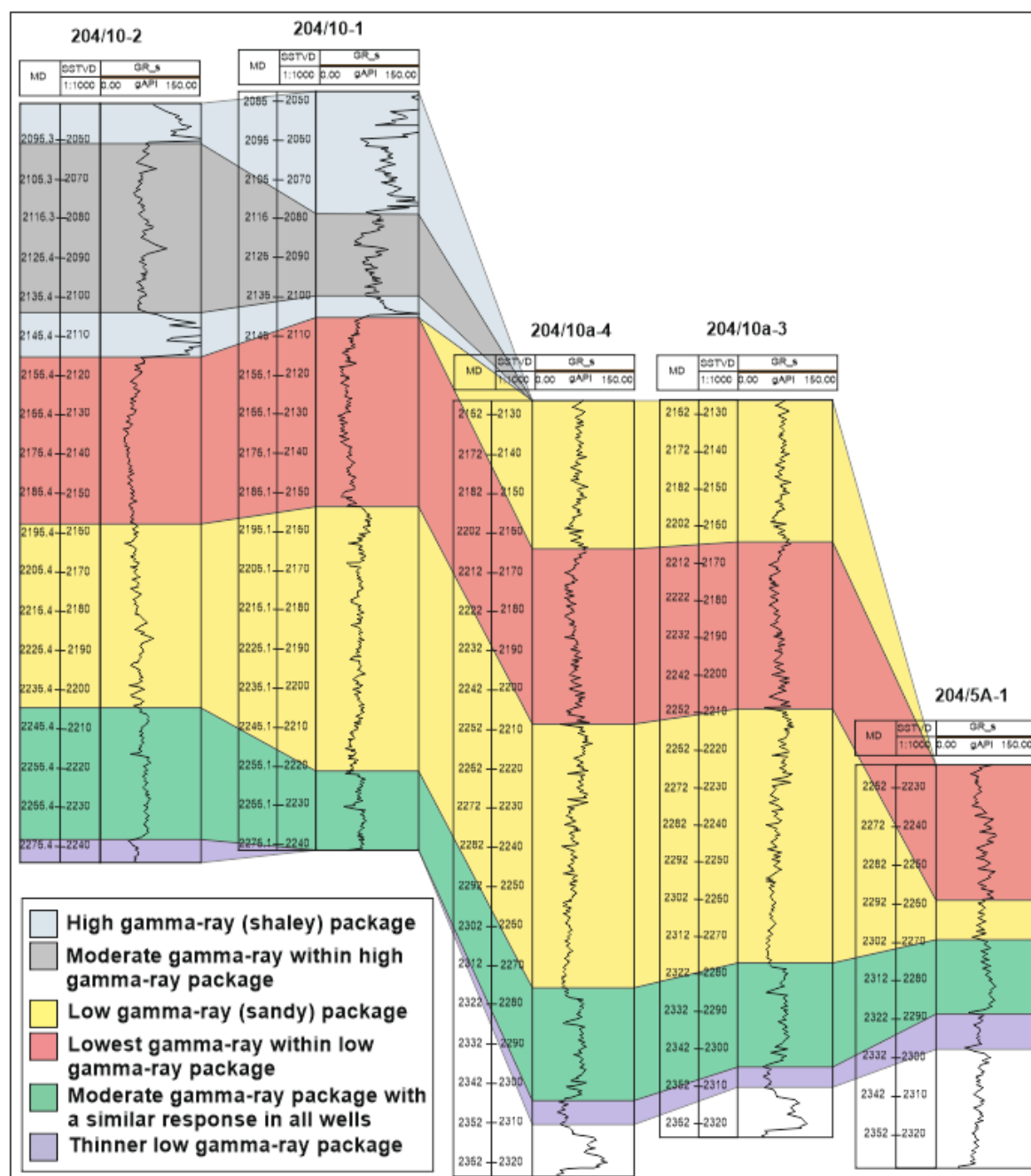


Figure 4-18 Correlation of lithological units across wells within the Cambo prospect based on gamma-ray signatures.

Deltaic sandstones can often be ideal reservoir rocks. The Cambo wells were originally drilled to target the deltaic Hildasay Formation sandstones and deeper units which lie below the Moray Group (Table 4-1; Ritchie et al. 2011). In this case the BF was not a target in this region. The low-gamma response at the top of two of the 204/10-2 and 204/10-1 wells shows that a suitable claystone seal may be present above potentially reservoir quality sandstones within the BF. The sigmoidal geometry of these sequences could provide a suitable trap for hydrocarbons, particularly if they form a 4-way-dip-closure like the hydrocarbon target below. No oil or gas within the BF is indicated in any of the composite logs for these wells. This suggests that migration may not have occurred due to sufficient seal above the oil bearing Hildasay Formation below (Pickering pers comms. 2016).

It is possible that these deposits were deposited as part of a northwards prograding delta within the pro-delta region. These ideas will be tested in later sections with seismic, spectral decomposition and biostratigraphy.

No neutron-porosity data is available for the BF in any of the Cambo wells. Density data is available and fluctuates, indicating the presence of different rock types. There is no indication of the presence of coals as the density signature is persistently too high. This suggests that the Cambo prospect was further from the shore and/or was more oxic, allowing the decomposition of organic material and no coal formation.

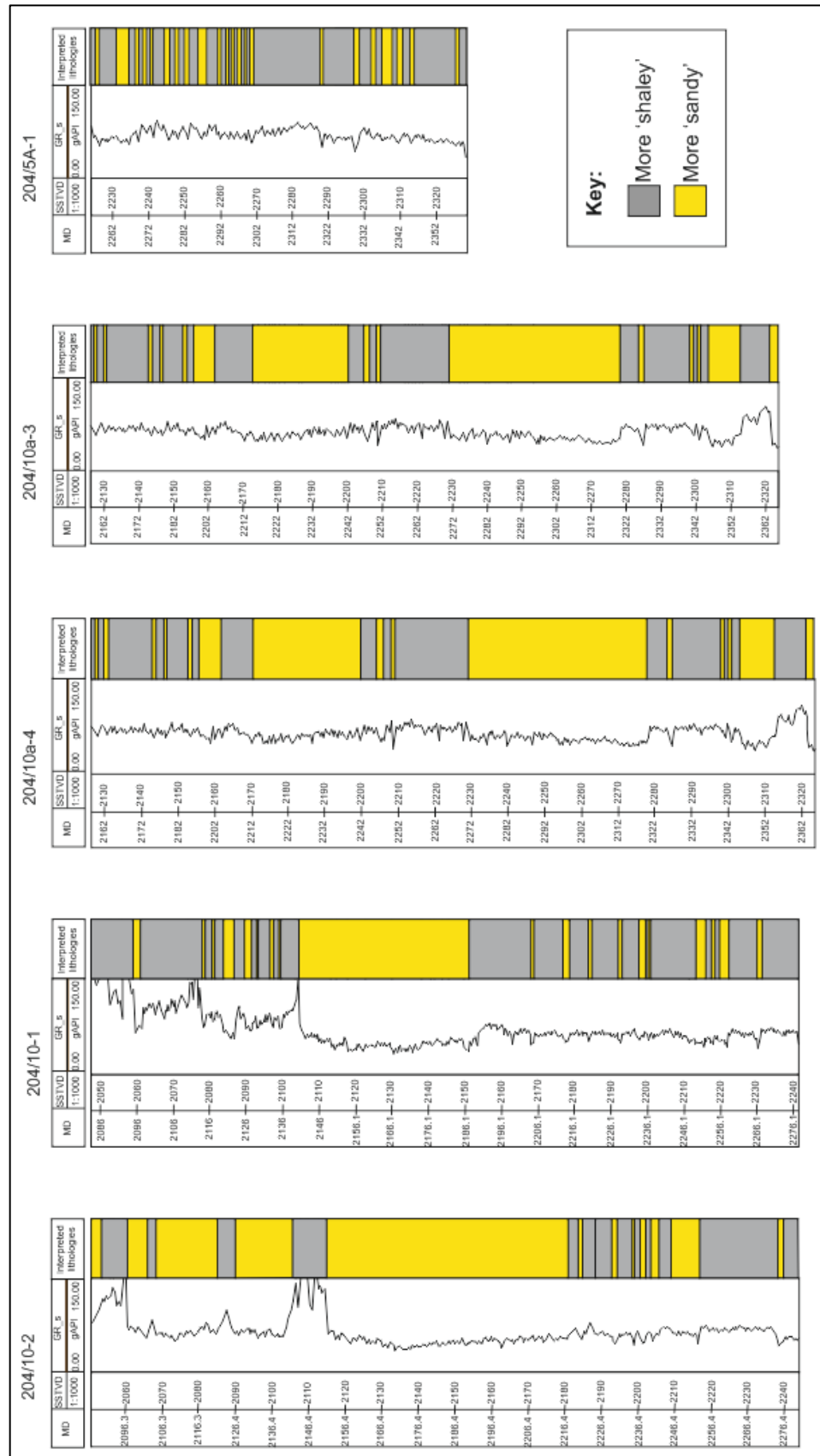


Figure 4-19 More 'shaley' and more 'sandy' lithologies interpreted in the BF of the Cambo wells, based on gamma-ray, density and neutron-porosity wire-line data. The data has been flattened on the Top Balder surface to allow a simpler comparison of the interpretations.

4.6.1.2 Tornado-Suilven

The thickness of the BF within the Tornado and Suilven wells is interpreted to range from *ca.* 22.6 m to *ca.* 292.6 m, with varying gamma-ray density and neutron-porosity signatures between each of the wells (Figure 4-20). In wells 204/13-1&1z, 204/19-8z, 204/19-5, 204/19-1 and 204/18-1 the BF overlies the Flett Formation and appears to be a continuation of this Formation, as shown by the similar nature of their gamma-ray, density and neutron-porosity signatures. In wells 204/14-2, 204/14-1 and 204/15-1 the Flett Formation is absent and the BF lies directly on top of the Lamba Formation due to an unconformity at the base of the BF in these wells. The upper boundary with the overlying Stronsay Group is not clearly identifiable in the wire-line data, and the stratigraphy appears to continue upwards from the BF instead. The upper and lower boundaries can be identified with reference to other data as discussed later.

The gamma-ray response for most of the Tornado and Suilven wells fluctuates, corresponding to more clay-rich and sand-rich lithologies (Figure 4-20). A gradual increase and decrease in the gamma-ray signature implies the presence of fining-upwards and coarsening-upwards sequences between these two end members. Within the sand-rich intervals and fining-upwards successions the low density and high neutron-porosity values indicate the presence of coals. These characteristics in the wire-line data can be identified throughout the Moray Group (Table 4-1) in the Tornado and Suilven areas.

The gamma-ray response in wells 204/14-2 and 204/15-1 looks significantly different with markedly lower gamma-ray values throughout. No density or neutron-porosity data are available for these wells but the gamma-ray values suggest that the BF here is predominantly composed of sandstone, with much less claystone and siltstone compared to the other wells of the Tornado and Suilven areas (Figure 4-20).

The BF is thickest in wells 204/14-2, 204/19-8z and 204/14-1 where it reaches a maximum thickness of 292.6 m. The gamma-ray response varies drastically between these three wells (Figure 4-20). Well 204/14-2 is interpreted to be dominantly composed of a thick sequence of sandstone, as shown by its abundantly low-gamma-ray signature (Figure 4-20). Well 204/19-8z shows a

highly variable gamma-ray response, with repeating units of clay-rich and sand-rich lithologies with some slight coarsening-upwards and fining-upwards sequences in-between (Figure 4-20). No density or neutron-porosity data were available for this Well so it is not known whether there is any coal present in the Formation at this locality. It could be assumed, based on the characteristics of other wells with a comparable gamma-ray response (e.g. 204/13-1&1z and 204/19-5) and available corresponding density and neutron-porosity data, that coal would be present within the sand-rich (low-gamma) and fining-upwards sequences that are intersected by this well. This contrasts to the more stable or persistent environment of deposition implied by the consistently sand-rich nature of Well 204/14-2 which lies ~2500m to the NW.

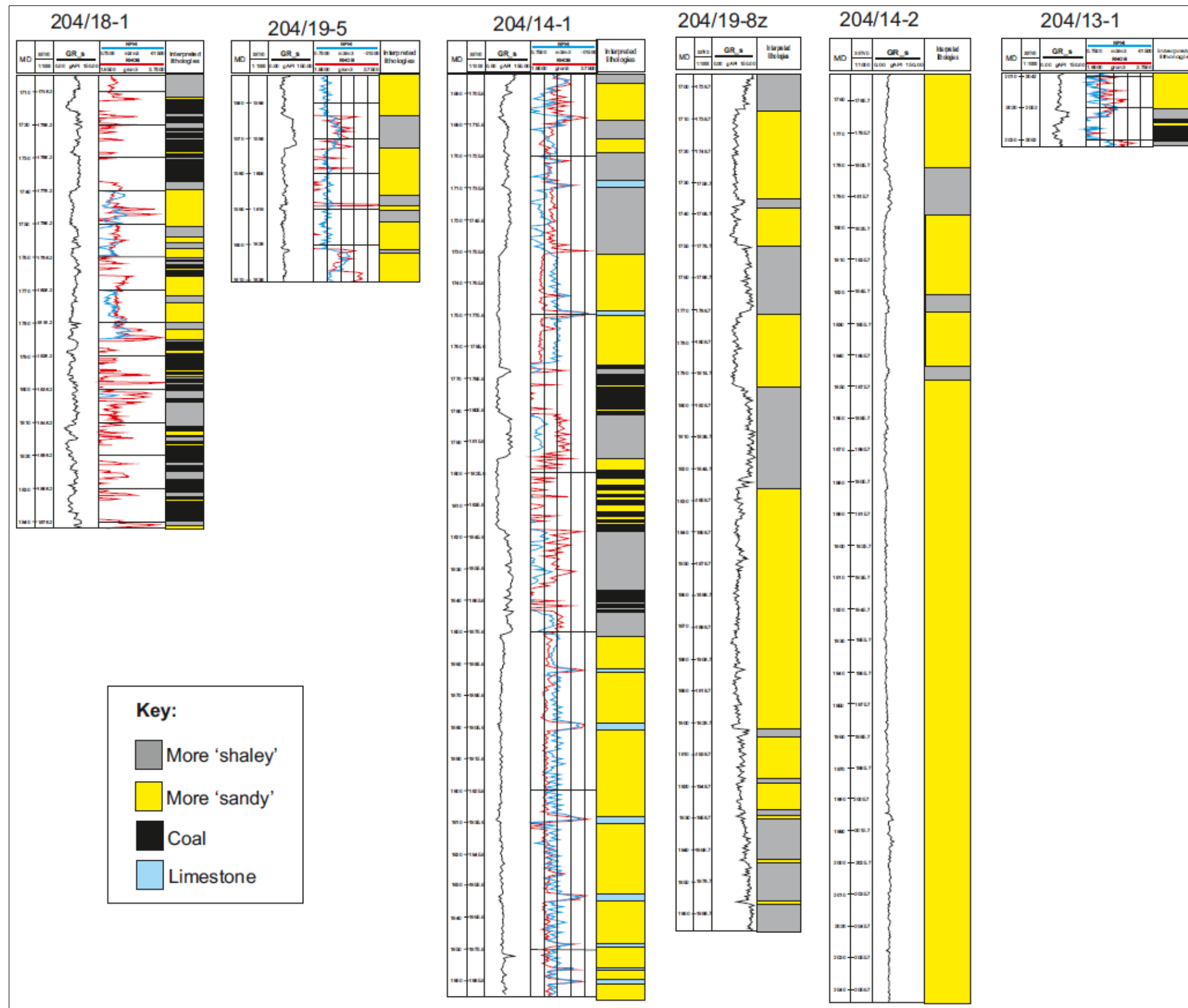


Figure 4-20 General lithologies interpreted in the BF of the Tornado-Suilven wells based on gamma-ray, density and neutron-porosity wire-line data.

Well 204/14-1 has a similar gamma-ray response to Well 204/19-8z but the units of sand-rich material are generally interpreted to be thicker (Figure 4-20). Density and neutron-porosity data for Well 204/14-1 shows that coal is abundant within the thinner sand-rich units in the middle of the BF, as shown by areas of very low density and high neutron-porosity values (Figure 4-20). This may be indirect evidence that can be used to predict the presence of coal within the sandstone units of Well 204/19-8z, where density and neutron porosity data is not available. High density and low neutron-porosity responses in the wire-line data of Well 204/14-1 likely indicates the presence of limestone stringers or carbonate cemented horizons (Figure 4-20).

In Well 204/15-1 the BF is dominantly sand-rich, with only minor amounts of more clay-rich rock types, as shown by the dominantly low gamma-ray signature with only occasional increases (Figure 4-20). The BF is much thinner in Well 204/19-5 but it has the same general gamma-ray signature and therefore the same inferred rock types as wells 204/19-1 and 204/18-1 (Figure 4-20). These three wells all have variable gamma-ray signatures, indicating the presence of interstratified units of claystone, siltstone and sandstone, with some coarsening-upwards and fining-upwards sequences indicated by gradual decreases or increases in the gamma values, respectively. The density and neutron-porosity data for Well 204/18-1 suggests that there are also abundant units of coal within the BF (Figure 4-20). As for all of the other wells in the Tornado and Suilven areas, all of this suggests that the sediments of the BF in these wells were deposited in a deltaic environment.

The common presence of coal within all of the Tornado and Suilven wells (Figure 4-20) suggests that the BF of this region was deposited in a terrestrial environment, likely within the sub-intertidal flats region of a delta. This environment would have been dominantly terrestrial and influenced by the shifting of fluvial systems over time, but there may have also been an occasional marine or estuarine influence in this near-shore environment. This is possible due to fluctuations in relative sea level that occurred throughout the Palaeogene (Riegel et al. 2015).

A peak in the gamma-ray signature towards the top of Well 204/19-1 (Figure 4-20), could be caused by the presence of basaltic volcanic material within the strata either as primary volcanic tuff or volcanoclastic sedimentary rocks. Knowing that the environment was likely very dynamic with discontinuous areas of erosion and deposition in terrestrial fluvial environments, with the potential for occasional marine or estuarine influences, it is most likely that any pyroclastic material would be present as volcanoclastic sedimentary rocks rather than lithified primary pyroclastic fallout (primary air-fall tuff). Once pyroclastic material has been remobilised it should be treated as any other sediment (e.g. Cas & Wright 1988). As with the high gamma-ray peaks observed in the Cambo field (Figure 4-19) this wire-line signature is not direct evidence for the presence of volcanic material, but instead the presence of a claystone of higher K, U and Th abundance.

In conjunction with the biostratigraphy data, the Cambo Sandstone Member (CSM) is interpreted as being present in all of the Tornado and Suilven wells. However, this unit is not solely composed of sandstone as shown by the varying wireline responses throughout each well. The Tornado and Suilven areas is proposed to represent a terrestrial fluvial environment during deposition of the BF, and it is therefore unlikely that significant thicknesses of sandstone would be correlatable across the entire area (e.g. Miall 2014). It is more likely that the CSM is composed of several sand bodies which may or may not interlink (Figure 4-21). Therefore, the sandstones identified informally as the CSM should not be regarded as a continuous sandstone body and should not be considered as a member.

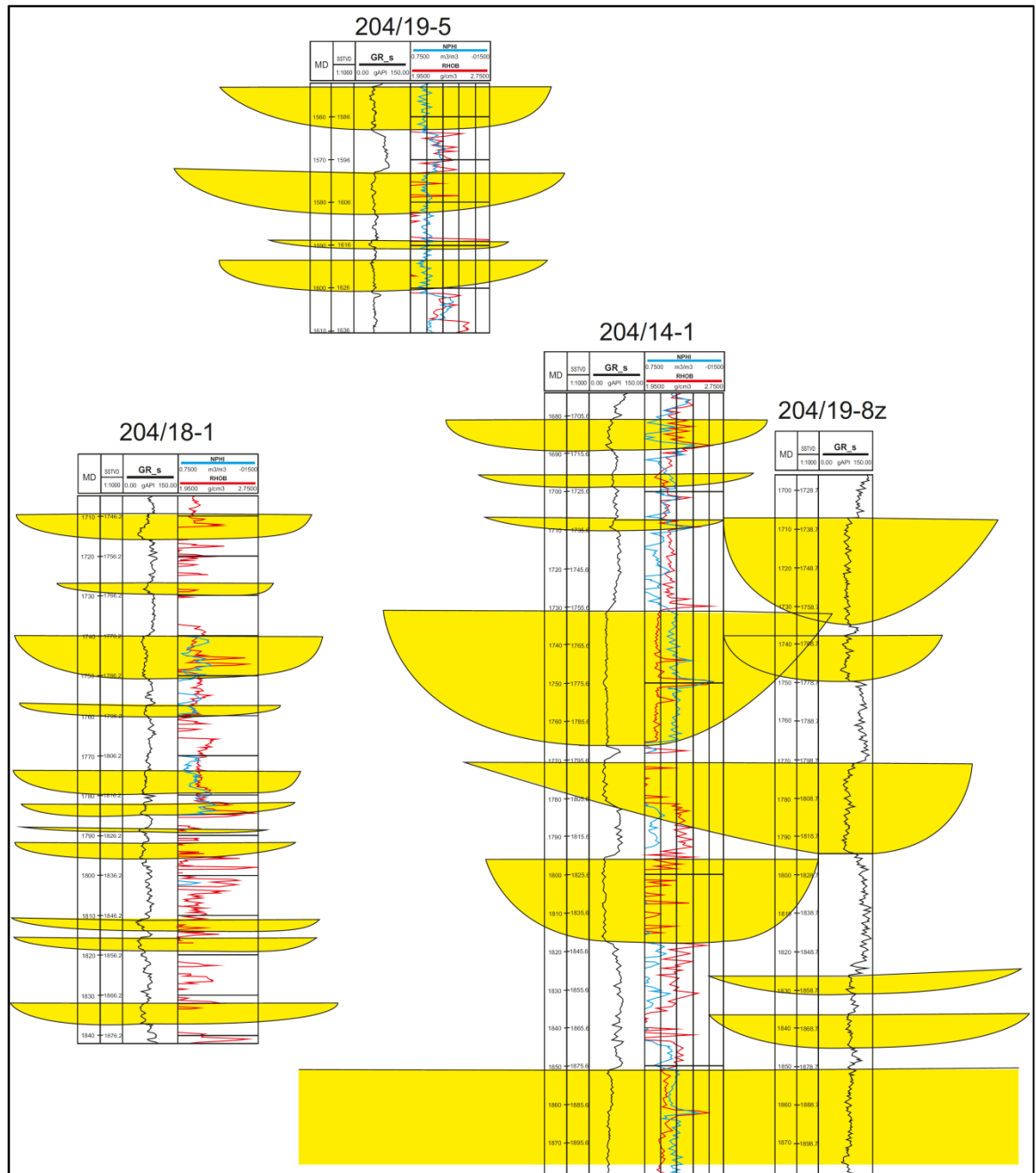


Figure 4-21 Interpreted channel sandstone bodies within the wire-line responses of wells in the Tornado-Suilven prospect. The informally identified Cambo Sandstone Member is likely not composed of a single continuous sandstone but of several sandstone bodies which may or may not be interlinked.

4.6.2 2D seismic and 3D seismic data

4.6.2.1 Cambo

In wells 204/10-2, 204/10-1 and 204/5A-1 the in-line seismic responses are disturbed and show bifurcating features (Figure 4-22). These are taken to imply the presence of discontinuous lithologies produced by more erratic erosional and

depositional cycles that shifted their position regularly over time, which is common in a fluvial setting (Miall 2014). More continuous parallel responses, such as those seen on the in-line and x-line sections surrounding Well 204/10a-4, could indicate a low-energy environment of deposition, which allowed less erratic and more continuous sequences of finer-grained sediment to accumulate. A more quiescent environment that could allow this kind of sediment deposition could include an isolated marine setting such as a bay or lagoon.

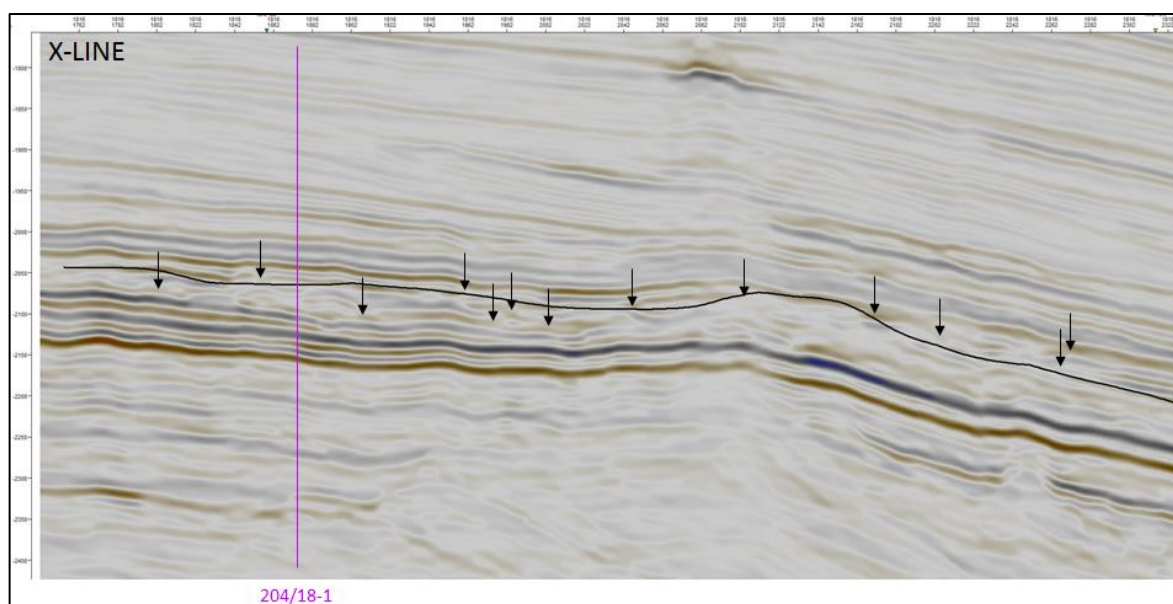


Figure 4-22 Example of a seismic section intersected by Well 204/18-1 in the Tornado-Suilven prospect. The black line shown by the position of the TCS within the BF does not follow any seismic response in particular as the BF in this section is highly bifurcated (arrows) and irregular. This disappearance and reappearance of the seismic response shows the location of meandering channels.

In some of the seismic sections the reflectors dip northwards, for example on the in-line seismic section intersected by wells 204/10-1 and 204/5A-1 (Figure 4-23). This shallow dip could be caused by post-depositional processes such as faulting and/or folding, although other evidence such as the truncation and prograding nature of the shallowly dipping seismic lines around the TCS suggests that the shallow dip is caused by the stratigraphy. It should also be noted that the dip of the seismic response is exaggerated in this view due to an exaggeration of the vertical scale. However, there is still a very shallow northwards dip to the seismic responses (Figure 4-23), which may imply that this area represents an apparent northwards prograding delta succession. This is only

an apparent direction of dip and progradation due to the 2D nature of the cross-section that the seismic data portrays.

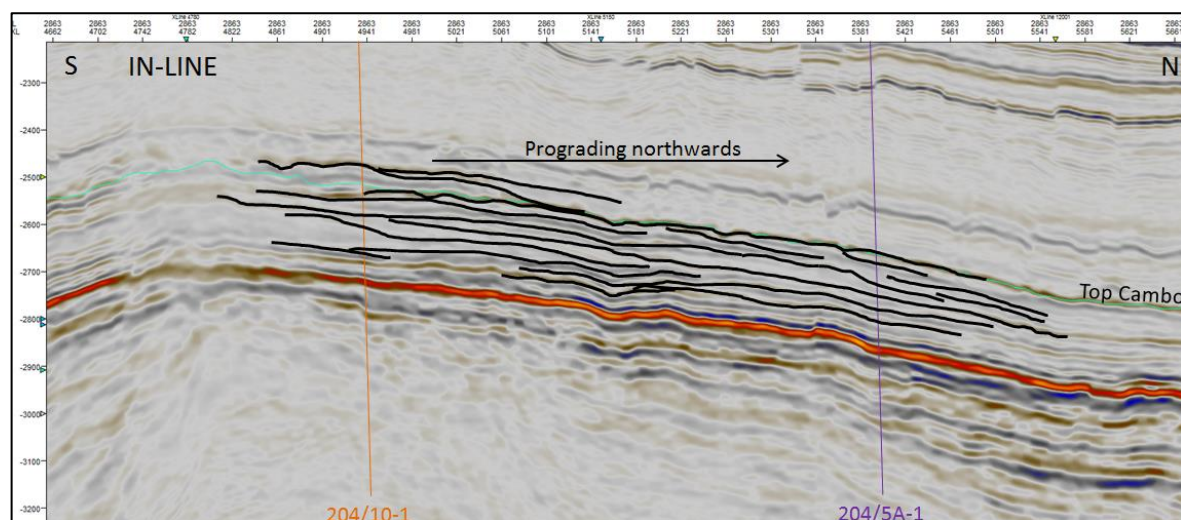


Figure 4-23 Annotated in-line seismic section intersecting Wells 204/10-2 and 204/5A-1. The seismic lines dip northwards showing the northward progradation of a delta at this location.

The 3D surfaces created from the seismic data show many SE-NW striking linear features throughout the Cambo area (e.g. Figure 4-13, Figure 4-14). These could represent coastline features, indicating the position of the shore-line over time. It is generally accepted that an increase in relative sea-level (e.g. Ebdon et al. 1995; Ali & Jolley 1996; Joy 1996; Jolley & Bell 2002; Dore & Lundin 2005; Stoker & Varming 2011; Dmitrieva et al. 2012), for example, caused by a marine transgression (e.g. Knox & Harland 1979; Mudge & Bliss 1983; Milton et al. 1990; Waagstein & Heilmann-Clausen 1995; Knox 1996; Smallwood & Gill 2002; Costa 2012; Schofield & Jolley 2013; Aldiss 2014; Mudge 2014), occurred in the late Palaeocene and Eocene, during the time that the BF was being deposited. Therefore, these linear features could document the rise of sea-level and subsequent landwards migration of the coastline. Alternatively, and more likely, these linear features represent the prograding nature of a delta and therefore the seaward movement of the coastline (with time), and the formation of linear strand-plains (Fraser et al. 2005; Kinsela et al. 2016). It has been suggested that this area was experiencing uplift during the late Palaeocene-early Eocene due to establishment of the mantle plume within the NE Atlantic (Knox & Morton 1983; Knox & Morton 1988; Mussett et al. 1988; Knox 1996; Lamers & Carmichael 1999; Naylor et al. 1999; Kent & Fitton 2000; Morton et al. 2002; Jolley et al. 2005;

Freeman et al. 2008; Mansurbeg et al. 2008; Sluijs et al. 2008; Smallwood 2008; Mudge 2014), and therefore, these linear features could also represent an apparent decrease in relative sea-level .

On some of the 3D seismic surfaces a channel feature can be identified along with a fan shaped feature at its northern end (Figure 4-24). This could be interpreted as a fluvial channel with a sedimentary fan deposit at its mouth. The linear feature which runs to either side of the river mouth and the landward edge of the sedimentary fan (Figure 4-24) could be interpreted as a palaeo-coastline or shelf. These interpretations can be confirmed with the analysis of spectral decomposition data (discussed later). An alternative explanation, for this image, is that the channel feature represents a deeper water channel with an associated debris fan (e.g. Morton et al. 2002). This explanation is not plausible in this region for Balder time however, as the water depth required for deep marine channel and fan formation is >500m (Normandeau et al. 2013). As the depth thickness of the BF in this region reaches a maximum of ~194m, even taking into account subsequent compaction since deposition, it is unlikely that these sediments accumulated in water depths as great as this. The stratigraphic evidence indicating the presence of a deltaic environment and shallow marine processes at this time also eliminates a deep marine interpretation for the channel and fan within the 3D surfaces of the Cambo prospect.

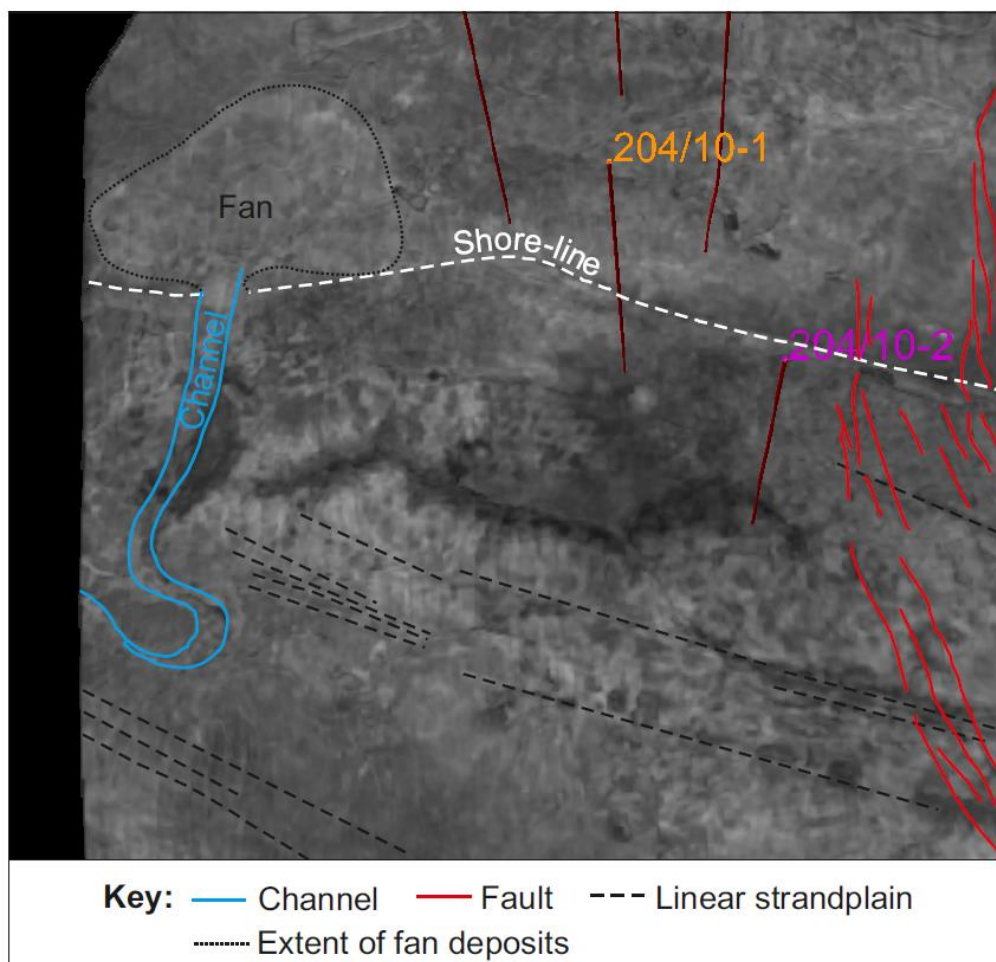


Figure 4-24 Minimum amplitude (24 ms window thickness with a +12 offset) surface of part of the Cambo Prospect with interpretations of the geomorphological features that can be interpreted on this surface, for example a large channel feature with a sedimentary fan shaped area of paler data at its mouth, which is interpreted as being a depositional fan where the fluvial channel meets the shoreline of an ancient BF (T50) aged coastline.

In most of the 3D surfaces a paler grey or darker grey anomaly can be seen in the centre of the Cambo Prospect (e.g. Figure 4-15), or a discontinuous anomaly in TWT data (Figure 4-25), and is intersected by Wells 204/10-2 and 204/10-1. When picked on TWT seismic sections this anomalous response forms the same shape as that created by the grey anomaly in the 3D surfaces. It can be assumed that this feature corresponds to the high-gamma-ray response that is observed in these two wells (Figure 4-18), and that the seismic anomaly may represent the outline of a calmer environment of deposition, such as a bay or lagoon.

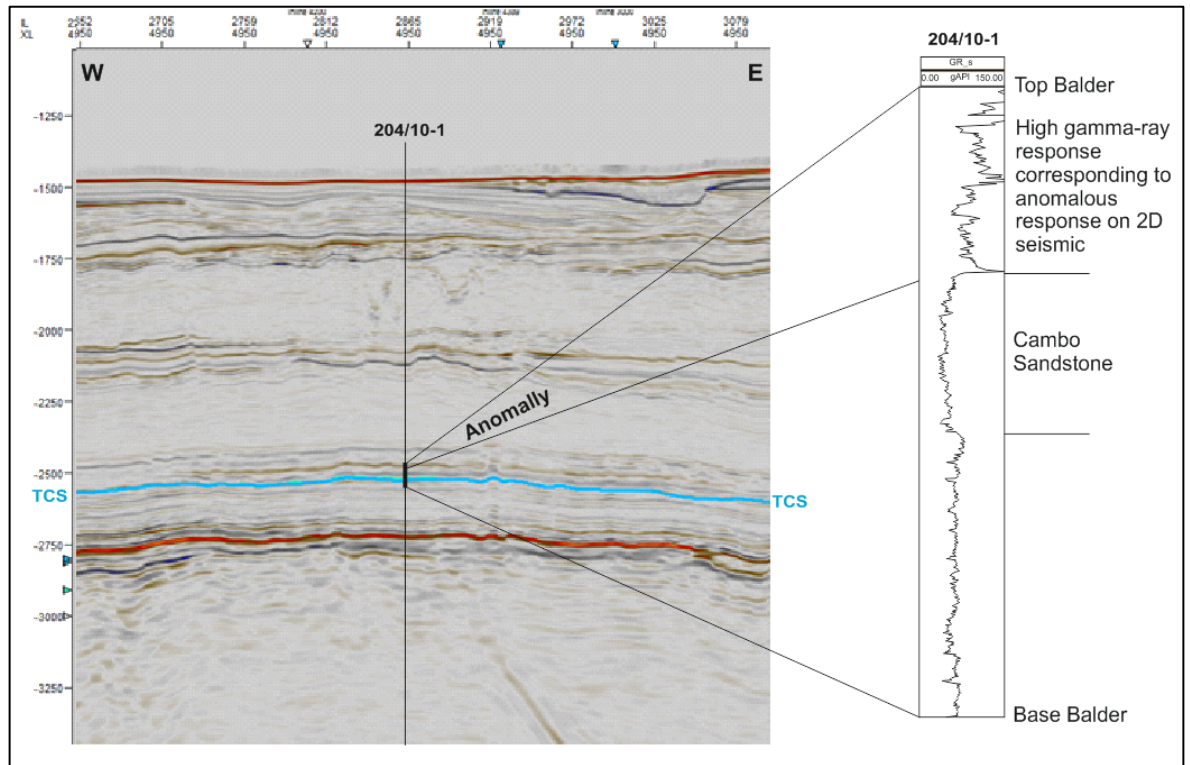


Figure 4-25 Anomaly within 2D seismic section intersected by Cambo Well 204/10-1, compared with the gamma-ray response through the BF. The high gamma-ray response at the top of the BF in this well corresponds to the anomaly within the 2D seismic data.

The elongated nature of this anomaly away from a fluvial channel suggests that sediment may have been deposited to the ~SE by longshore drift (Figure 4-26). A dominant current direction flowing towards the SE would have caused fine-grained material to be deposited away from the source of sediment supply (e.g. Ta et al. 2002). The fan deposit identified at the mouth of the fluvial system is fairly symmetrical suggesting that the current was not strong enough to affect the deposition of coarser grains. It is possible that this fan was deposited later, after a period of deposition in which longshore drift took place. This led to a relatively symmetrical accumulation of sediment within a fan, with no dispersal of grains due to a dominant current. No wells intersect the fan deposit, so the lithology of these features is not known and can only be assumed based on the understanding of sedimentological processes (Figure 4-26).

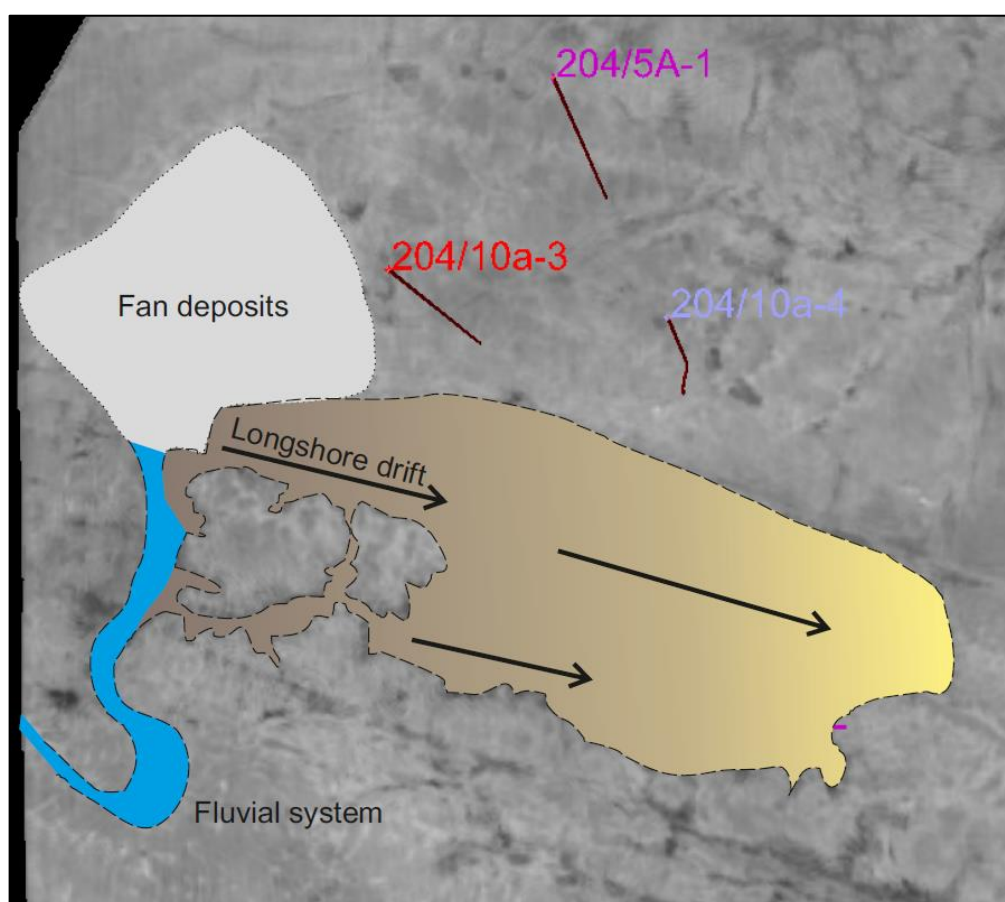


Figure 4-26 Interpretation of the area affected by longshore drift in the Cambo prospect.

4.6.2.2 Tornado-Suilven

Within the Top Cambo Sandstone (TCS) picked horizon of TWT sections in the Tornado and Suilven areas the seismic response is disturbed with discontinuous and bifurcating responses (Figure 4-27). However, the seismic lines at and below the picked TCS in the vicinity of Well 204/14-2 are uniform, continuous and parallel, although above this the seismic response is disturbed (Figure 4-21). This suggests that the BF in the Tornado and Suilven areas was deposited in a dynamic, fluvial environment where channels could form and lenses of sedimentary packages could be deposited (Miall 2014). This implies that the area was terrestrial during Balder times.

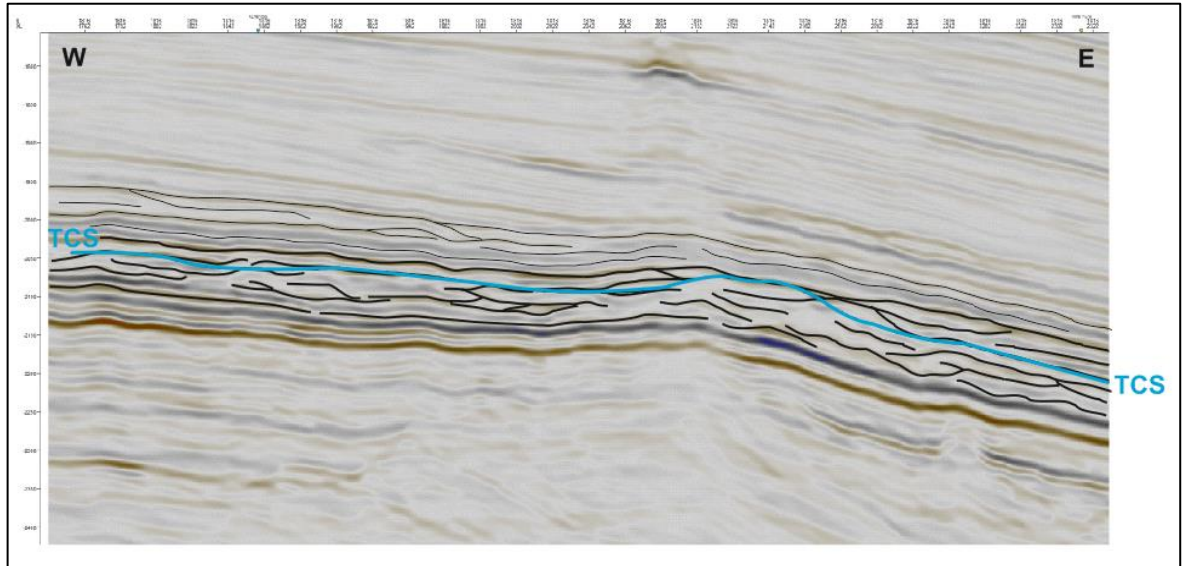


Figure 4-27 Bifurcating seismic response within the BF as highlighted on a 2D x-line seismic section through the Tornado-Suilven prospect. TCS: Top Cambo Sandstone, a picked horizon within the BF. In this section the TCS follows a path that corresponded with the surrounding data but does not seem to follow any response in particular.

Some topographic features of the underlying stratigraphy have influenced the area where the BF sediments were deposited. For example, to the south of Well 204/15-1 there is an area of apparent higher relief in the underlying stratigraphy and the TCS horizon onlaps this at either side, but does not drape the topography (Figure 4-28). This underlying mound- or ridge-like feature may have acted as a barrier, trapping and/or shedding sediment to either side of it. Another possible interpretation for the nature of this feature is that the BF originally draped this mound or ridge but was later eroded from this region of higher relief.

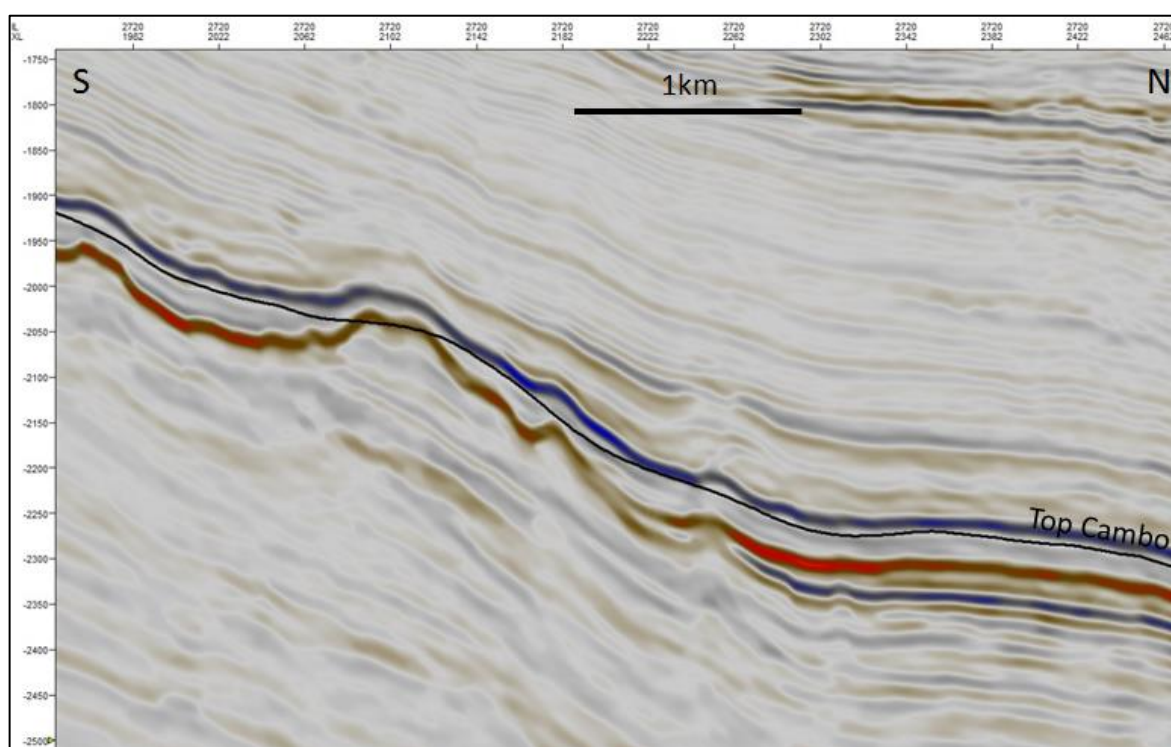


Figure 4-28 In-line 2D seismic section showing on-lap of the Top Cambo horizon on top of a mound in the underlying topography.

The 3D seis crops created of the Tornado and Suilven areas show many features akin to a fluvial system (Figure 4-12). Meandering features are common and can be compared with modern day analogues (Figure 4-12 versus Figure 4-29). The large-scale area of meandering fluvial channels that has been identified could be compared to modern day braided river systems (e.g. Figure 4-29). Many features of the fluvial system in the Tornado and Suilven areas can be identified in GoogleEarth Ltd (2015) images of the Brahmaputra River and delta in India (Figure 4-29). An issue with this correlation is the small scale of the Tornado-Suilven area (25 km wide) that has been investigated compared to the much larger scale of the Brahmaputra River and delta system (500 km wide), although it is possible that the area of data analysed around the Tornado and Suilven wells is only a small part of a much larger system. Other similarities can be seen with other modern deltas around the world as observed on satellite images and those of Google Earth (discussed later).

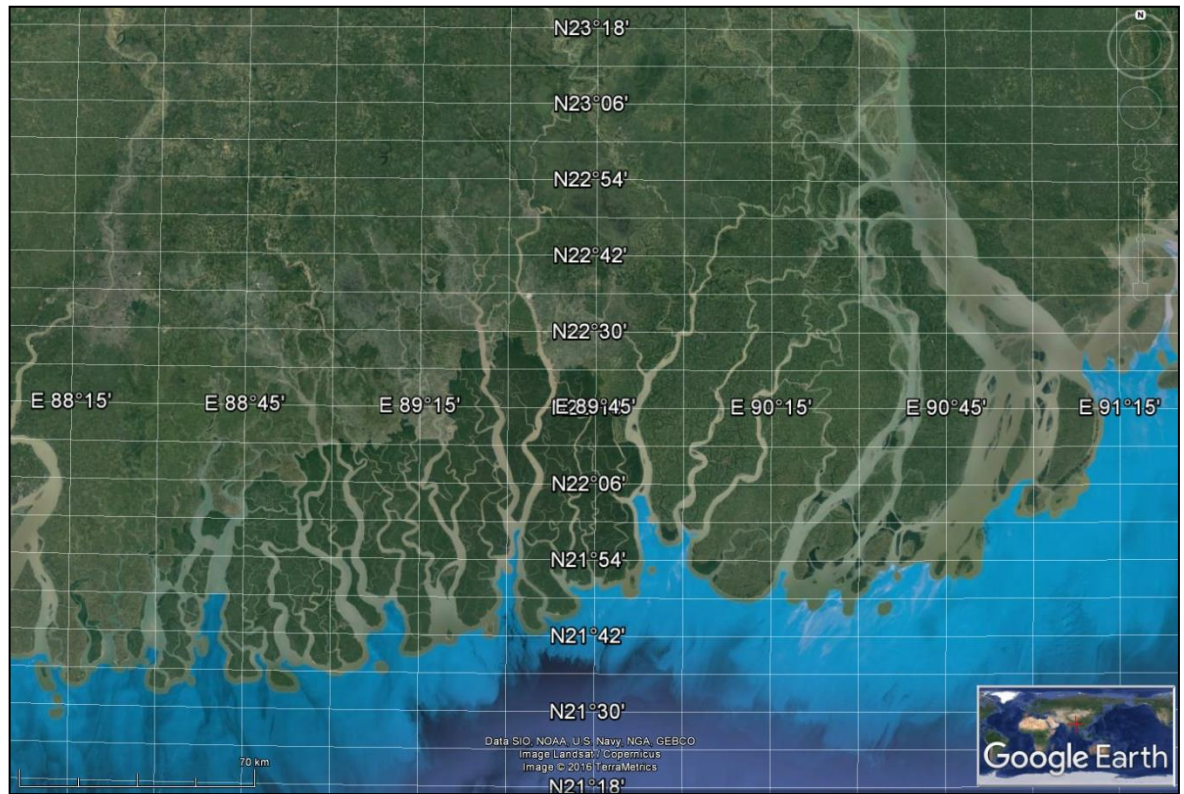


Figure 4-29 Nature of the Brahmaputra River and delta in India (GoogleEarth Ltd 2015). These features are comparable to those observed in the Tornado-Suilven field area but on a larger scale.

4.6.2.3 Other note-worthy features

Towards the north east of the Cambo area lies an anomalous topographic feature of roughly BF age, that may represent the presence of a volcanic vent and its edifice (Figure 4-30). This is shown by the on-lapping nature of the seismic reflectors in this region (Figure 4-30). There is also a strong red reflector visible in the seismic sections within this anomalous region which could indicate the presence of an igneous intrusion, such as a sill, or volcanic material such as a lava flow (Figure 4-30). Additionally, these features could indicate the presence of a volcanic edifice.

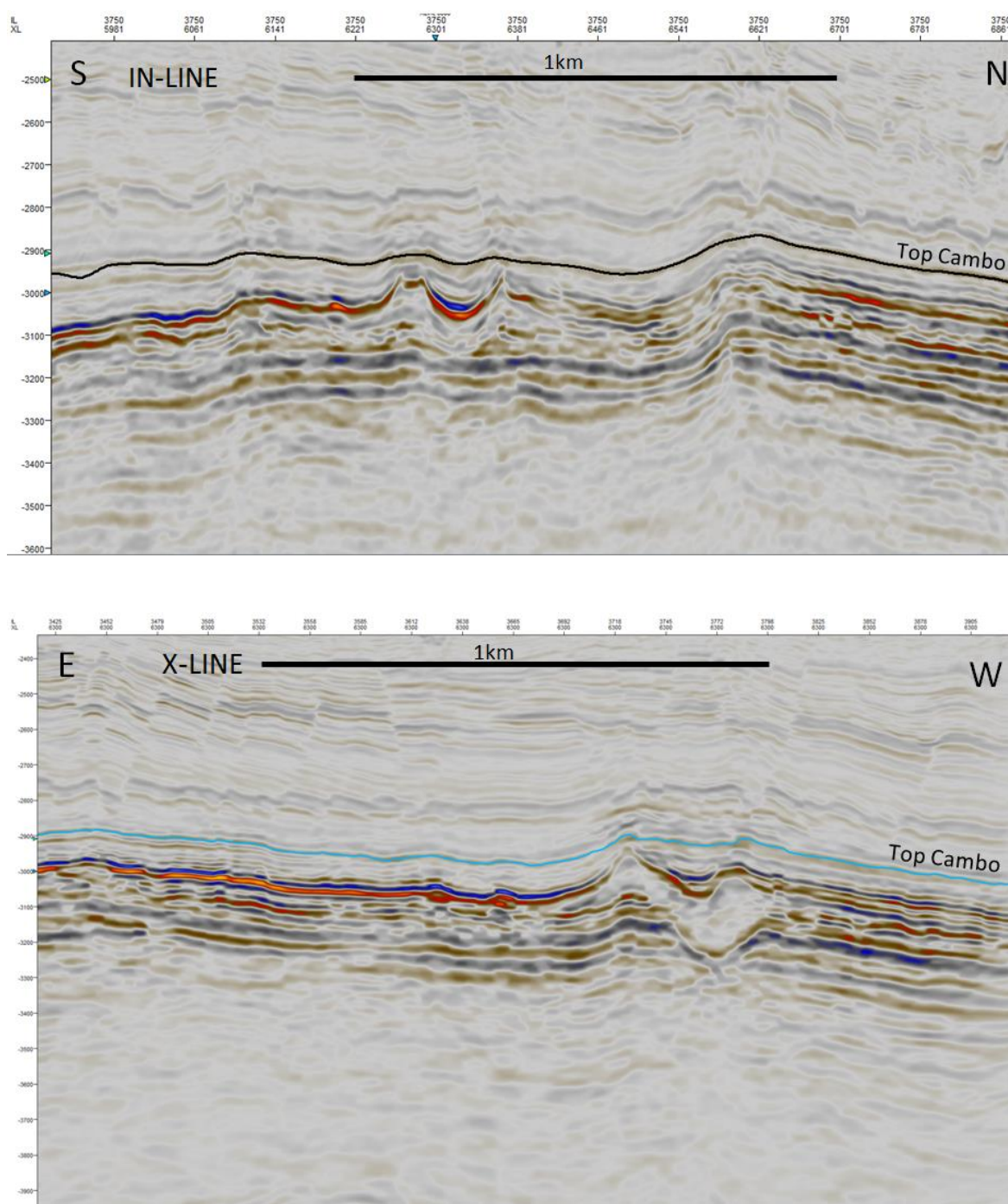


Figure 4-30 In-line (top) and x-line seismic (bottom) sections through an igneous region. Note that the Top Cambo horizon on-laps this topographic feature. Note that the Top Cambo horizon on-laps this topographic feature. The red reflector could represent the presence of an intrusive igneous body such as a sill or could represent volcanic material such as a package of lavas.

4.6.3 Spectral decomposition

RGB blended spectral decomposition has been used previously in some areas of the North Sea and has been used to identify channels, splays, avulsions and

remobilised units of sediment within the BF, for example in the Frøy Field of Quad 25 (Ackers & Bryn 2015).

A spectral decomposition model covering the Cambo field was produced by OMV based on 3D seismic data. By moving the depth of the data window in this model it is possible to observe the movement and meandering of a large fluvial channel to the west of the Cambo wells over time (Figure 4-31).

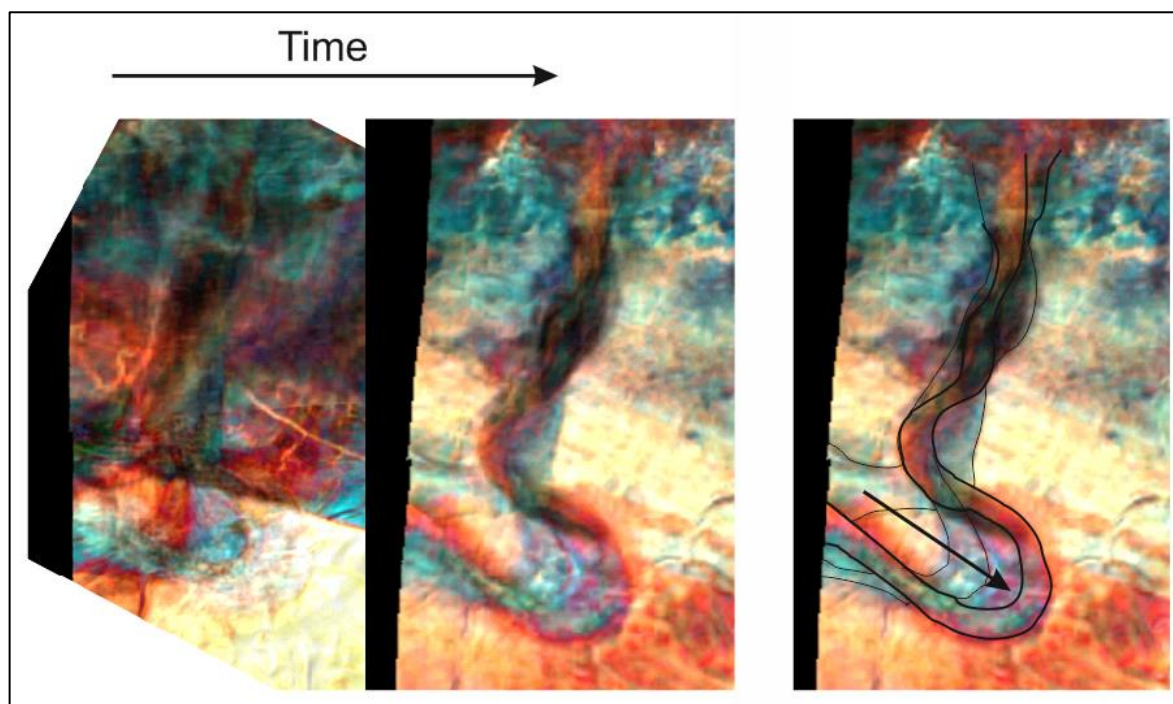


Figure 4-31 Movement of meander over time as shown by moving up through the surface of an RGB spectral decomposition surface in the west of the Cambo field.

In general, red areas indicating the presence of thicker sedimentary packages within the Cambo area are present in the south and blue coloured thinner packages of strata are present in the north (Figure 4-32). This suggests that there is a general thinning of the BF towards the north.

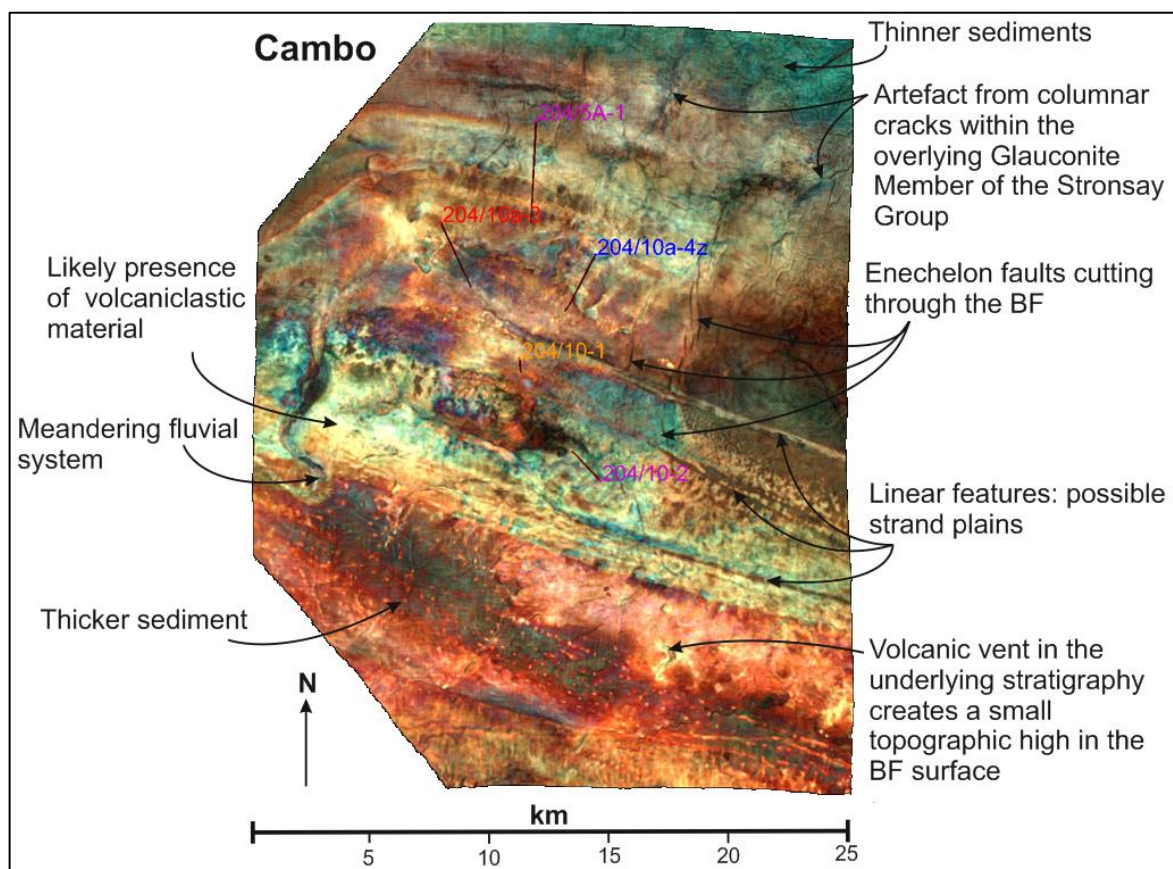


Figure 4-32 Interpreted RGB blended spectral decomposition surface of the Cambo field showing the main features that can be identified at the level of the BF.

A bright anomaly in the spectral decomposition model is present in the centre of the Cambo field and is intersected by wells 204/10-2 and 204/10-1 (Figure 4-32). This feature corresponds to the anomalous region identified in the 3D seismic surfaces (e.g. Figure 4-15) and the TWT seismic sections (Figure 4-25). This bright area appears to originate at the fluvial channel in the west (Figure 4-32). By moving through the spectral decomposition surface it can be seen that lavas originating from a remnant volcanic source in the south of the surface are present across the south of the Cambo field. Therefore, the fluvial channel intersects these lavas and likely eroded them entraining sediment of volcanic material. This reworked volcanic material was likely redeposited by the fluvial system and subsequent longshore drift and marine processes deeper within the basin to the north. The extent of the bright area (suggested to be representative of volcanoclastic material deposited by longshore drift to the -SE) may be fault bounded by a major N-S trending fault system (Figure 4-32).

4.6.4 Biostratigraphy

4.6.4.1 Cambo

Biostratigraphic reports are available for all of the Cambo wells and all state that deposition of the BF (T50) occurred in the early Eocene (Mahdi 2004; Jolley 2011; Costa 2012; Dawson et al. 2013). However, a more precise age is not given.

In these reports the upper and lower boundaries of the BF are given based on micro-plankton and pollen types and abundance. For the majority of the Moray Group, including the BF, microfossils are sparse (Costa 2012). This could be due to 'highly restricted benthonic conditions' (Costa 2012) and/or an increase in coarser clastic sediment input into the basin at this time (Dawson et al. 2013). Reworked palynoflora are found within the BF and generally originate from Middle Jurassic strata (Costa 2012), indicating that Jurassic material has been incorporated into the younger sedimentary sequence.

In Wells 204/10a-3, 204/10a-3 and 204/10-1, the base of the BF can be placed where there is an influx of *Areoligera* spp. (Costa 2012). There is also a change in the type and abundance of palynofloras between the top of the underlying Flett Formation and the BF, which can be used to give a depth location for this boundary (Costa 2012). The presence of the BF can also be defined by the recognition of *Hystriosphæridium tubiferum* and *Inaperturopollenites* spp. (Costa 2012). *Hystriosphæridium tubiferum* is a type of marine palynomorph (Table 4-5; Bowan et al. 2012; Smith et al. 2014) that corresponds to nannoplankton zone NP10 (Aleksandrova et al. 2012), which is defined in the North Sea and correlates to the early Eocene and the BF (e.g. Knox & Morton 1988; Bujak & Mudge 1994). The Cambo Sandstone Member can be picked out by an increase of *Paralecaniella indentata* microplankton, which are indicative of marginal marine and shallow-marine environments (Table 4-5; Costa 2012). These microplankton are euryhaline and are therefore able to survive in waters with a variable salinity, although they prefer shallow-water low-salinity conditions (Zaporozhets et al. 2006). *Paralecaniella indentata* were also present during the Palaeocene to early Eocene (Elsik 1977), confirming that the BF is of this age. A shallow-marine environment is also suggested by the presence of

marine dinocysts, including *Eocladopyxis* spp. and *Areoligera* spp., which are stress-tolerant taxa (Costa 2012). *Eocladopyxis* spp. occurs in sedimentary rocks of Late Paleocene to Early Eocene age (McLean 1976) and is a type of dinoflagellate that prefers to inhabit 'marine-brackish, near-shore' environments such as those found in 'semi-enclosed, shallow-water bays with restricted circulation with the open ocean' (Table 4-5; McLean 1976). *Areoligera* spp. occur throughout Paleogene sediments; these dinocysts are 'dominant in inner-neritic and coastal environments' (Table 4-5; Guasti et al. 2005; Soliman 2012).

The most detailed explanation of the biostratigraphy and palaeo-environmental conditions are given in the report for Well 204/10a-4, which also refers to Well 204/10a-3. This report concludes that the BF in these wells was deposited in a marginal marine setting with most of the Formation having a palynoflora that indicates a 'paralic setting with persistent shallow-marine influences and high freshwater input' (Costa 2012). The palynology of the Cambo Sandstone Member corresponds to a marginal marine environment and 'deposition in a very shallow neritic to estuarine setting' (Costa 2012).

Observation of miospores such as the pollen *Inaperturopollenites* spp. suggest that the region was near-shore, as these are associated with the proximal occurrence of mangrove swamps (Figure 4-32; Costa 2012) in a terrestrial environment (Cors et al. 2014). Further evidence for the occurrence of nearby swamps or mires (Jolley 2011) is given by the presence of coals, which may have formed in a shallow water environment from the accumulation of drift wood and other organic material (Jolley 2011). The occurrence of coal suggests that localised anoxic conditions were present, which is also suggested by the biostratigraphy report for Well 204/10-1 (Mahdi 2003).

The presence of mangrove swamps supports the interpretation that this region would have had a warm and humid climate (e.g. Riegel et al. 2015), as these habitats are common to tropical and sub-tropical environments.

Biostratigraphy	Palaeo-environment
<i>Hystriosphæridium tubiferum</i>	Marine
<i>Paralecaniella indentata</i>	Marginal marine; Shallow-marine; Euryhaline; Prefers low-salinity, shallow-marine
<i>Eocladopyxis</i> spp.	Shallow-marine; Marine-brakish; Near-shore; Restricted ocean circulation; Shallow-marine bay
<i>Areoligera</i> spp.	Shallow-marine; Inner-neritic; Coastal
<i>Inaperturopollenites</i> spp.	Mangrove swamp; Mire

Table 4-5 List of observed biostratigraphy within the BF of the Cambo wells and the habitats that they inhabited.

A marginal marine location, including deltaic, shallow-marine/inner-neritic and paralic depositional palaeo-environments are suggested by the biostratigraphy for the Cambo field. The reports also suggest that there is a gradual deepening in the aqueous environment northwards, from wells 204/10-2 and 204/10-1, which were deposited in a shallow water embayment (Mahdi 2003), to Well 204/5A-1, which was deposited in a deeper marine, possibly middle-neritic marine environment (Jolley 2014).

4.6.4.2 Tornado-Suilven

A biostratigraphic report covering the BF is only available for Wells 204/13-1 & 1z, 204/14-2 and 204/14-2. The level of detail given in these reports is less than that provided in the reports for the Cambo wells.

The biostratigraphy reports conclude that the sediments of the BF were deposited in a marginal marine environment where there were localised areas of low salinity caused by the presence of rivers and their estuaries entering a deltaic setting (Holmes et al. 1999a; 1999b; Viera & Ayress 2010). No specific information regarding the microfossils that these interpretations are based on are given.

It is suggested that the underlying Flett Formation was mainly deposited in a non-marine environment (Viera & Ayress 2010). This implies that there was increased subsidence or a general increase in relative sea-level between deposition of the Flett Formation and the sediments of the BF.

4.6.5 Comparison of all data

4.6.5.1 Wire-line

All of the wire-line data for the Tornado, Suilven and Cambo wells shows that the BF is composed of interstratified units of claystone, siltstone and sandstone with minor amounts of coal and limestone stringers or carbonate cemented hard beds (Figure 4-19, Figure 4-20). The gamma-ray signature generally fluctuates more frequently and with a more pronounced magnitude within the Tornado and Suilven wells (Figure 4-20) compared to the Cambo wells (Figure 4-19), indicating that there is more variability in the lithologies intersected by these wells. There are also more units of coal and a greater amount of clearly defined upward-fining and upward-coarsening sequences identifiable within the wire-line responses of the Tornado and Suilven wells. This implies that the environment of deposition in the Tornado and Suilven areas was more dynamic and therefore terrestrial or near-shore. The Cambo wells lack coals and are instead dominated by greater thicknesses of high density and high neutron-porosity strata, indicating the presence of more 'shaley' material (Figure 4-19). This may imply that the Cambo area was occupied by a shallow-marine to marginal marine environment. The Cambo prospect can be described as being off-shore in comparison to the Tornado and Suilven prospects during BF time.

No direct correlations can be made by matching the lithologies between the Tornado, Suilven and Cambo wells due to the significant differences in the depositional environment of these two adjacent areas during Balder times. A general correlation between the two areas can be made, however, when considering the stratigraphic succession of deltaic sequences (sub-intertidal flats, delta front and pro-delta facies) (Figure 4-33, Figure 4-34).

The thinning and deepening of the BF towards the north supports a northward dipping deltaic succession in this area (Figure 4-33, Figure 4-34). This trend can

also be observed in the seismic data supporting this conclusion. This general morphology of the facies interpreted within the BF is typical of a delta (e.g. Somoza et al. 1998).

The delta-front facies depicted in the interpretation of all of the wire-line data from south to north across the study area (Figure 4-33) have a coarsening-upwards nature. Coarsening-upwards sequences are characteristic of delta-front facies (Ta et al. 2002).

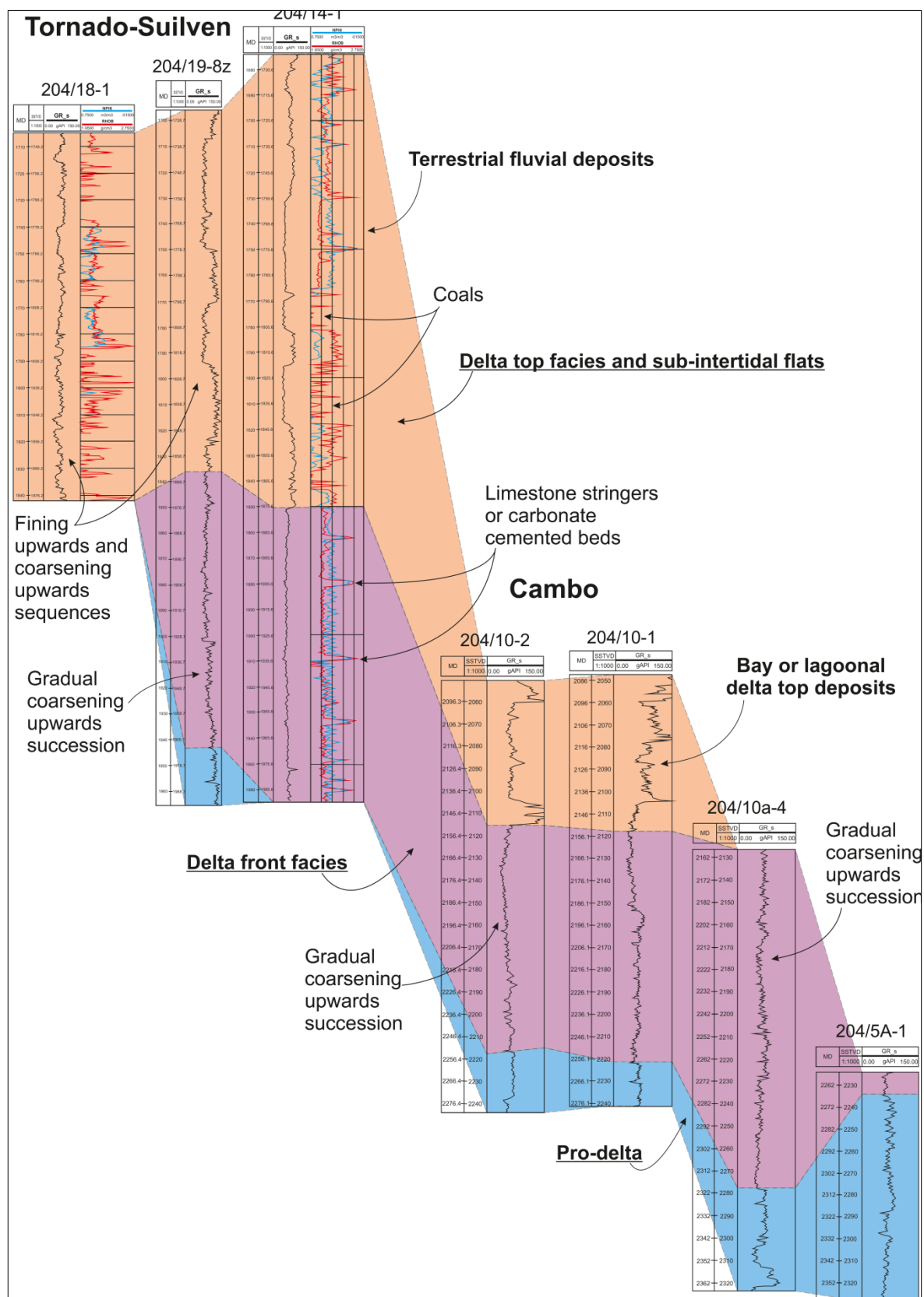


Figure 4-33 Correlation of deltaic facies northwards from the Tornado and Suilven prospect to the Cambo prospect. Some of the main lithological observations are also labelled.

4.6.5.2 Seismic

In-line and x-line seismic sections through the Tornado and Suilven areas are generally more disturbed and show a greater degree of bifurcation than those in the Cambo area. This supports the above interpretations from the wire-line data that the Tornado and Suilven region is dominated by delta-top facies and the Cambo prospect is dominated by deeper marine delta front and pro-delta facies.

A 3D seiscrop that encompasses the two field areas also shows that there are clearly observable differences in the environment of deposition between these two regions (Figure 4-35). The Tornado and Suilven fields are covered in braided, meandering fluvial systems and is therefore terrestrial, whereas to the NE of the Tornado and Suilven areas the seismic surface becomes smoother with linear strand-plains becoming the dominant characteristic of the Cambo TCS surface (Figure 4-34). This shows that there is a change in the environment of deposition from terrestrial/fluvial to a marginal marine deltaic environment with deepening occurring towards the north.

Submergence and deepening of the environment of deposition towards the north is also supported by the fact that the BF gradually gets deeper within the wells from Tornado-Suilven to Cambo (e.g. Figure 4-33). The BF is generally shallower in the south in Tornado-Suilven wells than it is to the north in the Cambo wells. This is highlighted by the seiscrop topographic image created of the surface of the TCS Member, which has a northward dip (Figure 4-9). A limitation to this interpretation is the unknown effect of post-depositional tectonic activity on the topography of the BF. The presence of en-echelon faults within the Cambo prospect (Figure 4-34) suggests that some faulting has occurred since deposition of the BF, but the wider implications of this are unknown.

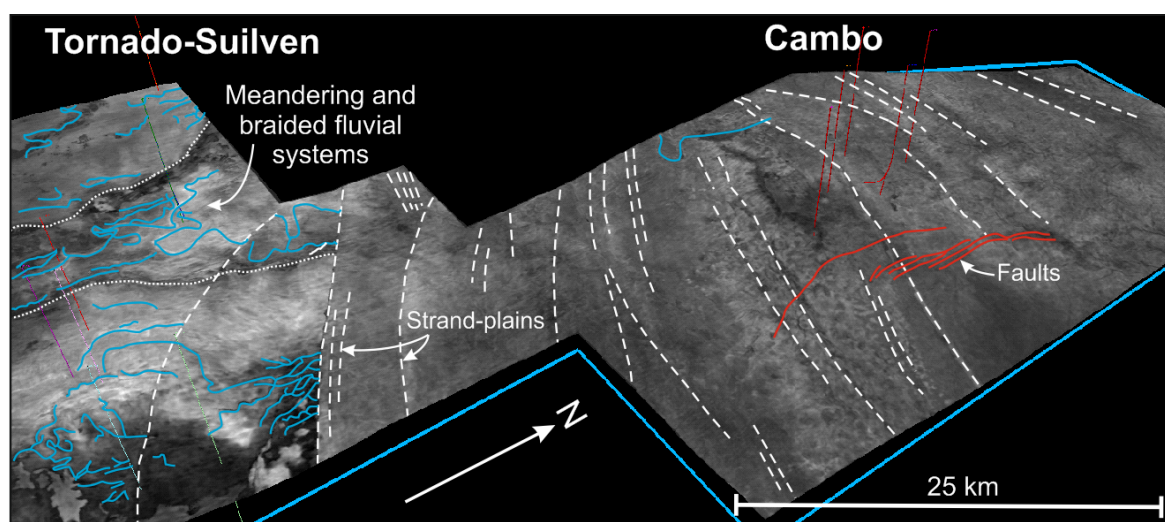


Figure 4-34 Figure 4-10 annotated to highlight the main features that can be identified on the 3D seismic surface between the Tornado-Suilven and Cambo field areas. The Tornado-Suilven field is dominated by meandering and braided fluvial systems whereas the Cambo region is dominated by linear strand-plain like features. Solid red lines striking N-S show the location of major faults that intersect the BF.

The sharp change between the chaotic terrestrial environment of the Tornado and Suilven field areas and the smooth strand-plain dominated north indicates the limit of the ancient shoreline during deposition of the BF (e.g. Figure 4-34). With time the presence of the strand-plains suggests that the shoreline moved northwards. The linear nature of the strand-plains suggests that this delta was wave-dominated rather than tide-dominated (Reading 1996; Brookfield 2004). The strand-plains themselves may have formed during a period of relative sea-level fall (Somoza et al. 1998; Fraser et al. 2005; Kinsela et al. 2016), although strand-plains can also form due to varying sand supply and periods of stable sea level (Kinsela et al. 2016). It is generally accepted that a marine transgression occurred from the late Palaeocene onwards throughout BF time (e.g. Ebdon et al. 1995; Naylor et al. 1999; Morton et al. 2002), however, the conclusion here is that the history of relative sea-level during this time is more complicated with periods of either stable sea level or regression.

Suitable modern analogues may be found in tropical regions particularly along the west coast of Central America. These fluvial systems have well developed strand-plains and wave-dominated deltas along with large scale and small scale meandering river channels akin to all of the features identified in the 3D seismic surfaces across the study area of UK Quad 204 for BF time (Figure 4-35). These

modern systems are also on a comparable scale to the Tornado-Suilven and Cambo areas (Figure 4-36).

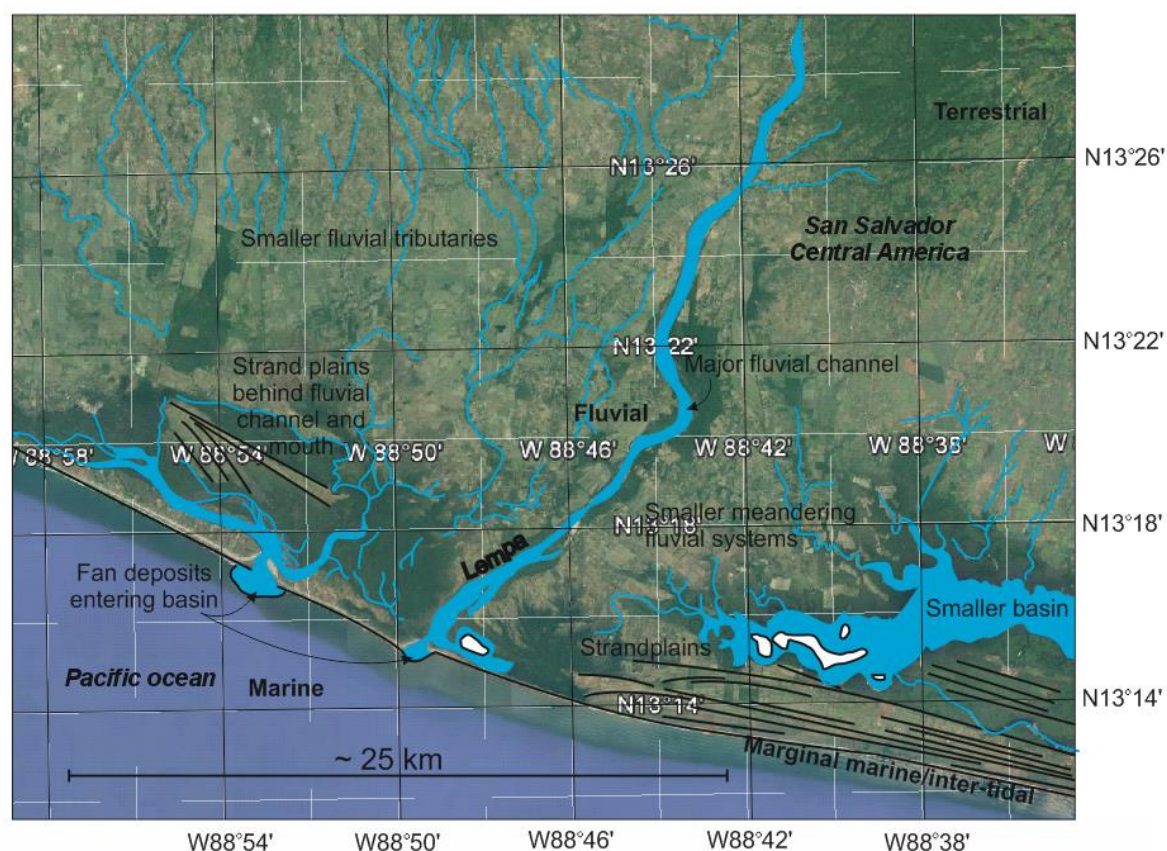


Figure 4-35 Example of a possible analogue environment along the coast of San Salvador, Central America with similar characteristics to those of the Tornado-Suilven and Cambo areas labelled (GoogleEarth 2015).

4.6.5.3 Biostratigraphy

Limited data or interpretation is given for the Tornado and Suilven wells, although it is stated that the underlying Flett Formation was most likely deposited in a non-marine environment. The BF generally appears to be a continuation of the Flett Formation, so it might therefore be assumed that this was also a terrestrial or shallow-marine environment during deposition of the BF. It is also suggested that this area was influenced by fluvial or estuarine processes, indicating that a fresh-water and saline marine water influence may have been present.

Micro-fossils observed within the cuttings from the Cambo wells suggest that there is a northwards deepening in the environment of deposition within the

Cambo field area. It is also stated that the BF interval within the Cambo wells contains an abundance of miospores related to the presence of nearby swamps. Therefore, the Cambo area was near to a terrestrial environment with swamps, which could correspond to the Tornado and Suilven region to the south.

4.6.5.4 Comparison with composite logs

Study of the composite logs for each of the wells allows a comparison of the interpretations made in this study with the basic information that is provided from initial interpretations of the wire-line, biostratigraphy, and mud logs based on cuttings descriptions, made at the well site. Much of the information of the composite logs and well site reports is based on raw data. The composite logs support my interpretations for the stratigraphy of the wells, although some discrepancies do exist. For example, the interpretation of abundance volcanic material within some of the wells (e.g. 204/10a-4) cannot be justified without further analysis of cuttings material. In this case only a sedimentary origin can be interpreted thus far from the data used in this study. This does not mean that interpretations of the volcanic content of the wells, given in the composite logs, is incorrect but it also does not confirm the interpretation. Identification of volcanic material within the BF for this area does not affect interpretations of the environment of deposition but could affect the quality of hydrocarbon seals or reservoirs in these areas.

4.7 Conclusion

The Balder Formation is dominantly composed of inter-stratified claystone, siltstone and sandstone with varying amounts of coal and limestone (Figure 4-19, Figure 4-20). The presence of igneous or pyroclastic material within the deposits cannot be proved nor disproved with the current data set. The study of cuttings material in greater detail than given in the composite logs and final well reports would be required to make this distinction.

During deposition of the Balder Formation sediments the Tornado and Suilven field was dominated by a braided, meandering fluvial system in a swampy terrestrial near-shore environment with mangrove swamps (Figure 4-36). Northwards towards the Cambo field the sedimentary unit of the Balder

Formation generally thickens and then thins and becomes more claystone rich with fewer units of coal (Figure 4-19). The BF was deposited in a deeper marine environment but with abundant fresh-water input into the Cambo area (Figure 4-36). Other evidence for this includes features such as linear strand-plains (Figure 4-34) and alluvial fans with only one large fluvial channel present within the Cambo field, in contrast to the more irregular and disturbed area of smaller scale meandering fluvial systems in the south (Figure 4-34).

The linear strand-plain features and the meandering river channel within the Cambo field area (e.g. Figure 4-31, Figure 4-32) may have been caused by increasing sea-level due to a marine transgression throughout the early Eocene, which would have led to the movement of the coastline landwards towards the south/SW.

The wire-line and seismic data, biostratigraphy reports and composite logs all suggest that the environment of deposition (basin) gets deeper with a greater marine influence towards the north from the Tornado and Suilven region. The deltas forming at this time also prograded in this general direction as shown by the northwards fining of strata and the decrease in terrestrial organics towards the north, as well as the orientation of the strand-plain like lineations (Figure 4-34, Figure 4-36).

In the Cambo field area the presence of an anomalous feature within the seismic data and seiscrops (Figure 4-15, Figure 4-25) coincides with the presence of more claystone rich rocks within the upper section of the BF in Wells 204/10-2 and 204/10-1 (Figure 4-18). The biostratigraphy reports suggest that the BF sediments in these two wells were deposited in a bay (Figure 4-36). This would have allowed the presence of calmer, shallower aqueous conditions enabling the deposition of fine-grained material. From the observation of a large estuary-like feature to the west of the Cambo wells (Figure 4-31, Figure 4-32) and the presence of dinocysts that are found within environments of a variable salinity, it is possible that this fine-clay was transported into the bay from the northwards flowing river system due to longshore drift to the ~SE (Figure 4-26). The significant amount of claystone in this area (wells 204/10-1 and 204/10-2; Figure 4-18) is restricted due to the bay being the only place where the calm

conditions required for deposition and preservation of fine clay-sized grains were prevalent. It is suggested in the composite logs that this anomaly indicates the presence of tuff, but this would need to be confirmed by the detailed study of the cuttings material at the appropriate depths to confirm the presence of volcanic material at this interval. The presence of lavas beneath the BF in the south of the Cambo field suggests that any volcanic material within these wells would be of volcanoclastic nature and would have originated from erosion of the underlying lavas.

Faulting is likely to have been active following deposition of the BF as shown by the presence of en-echelon faults intersecting the eastern region of the Cambo field area (Figure 4-34). However, it is not known what effect this faulting may have had on the overall topography of the BF surface.

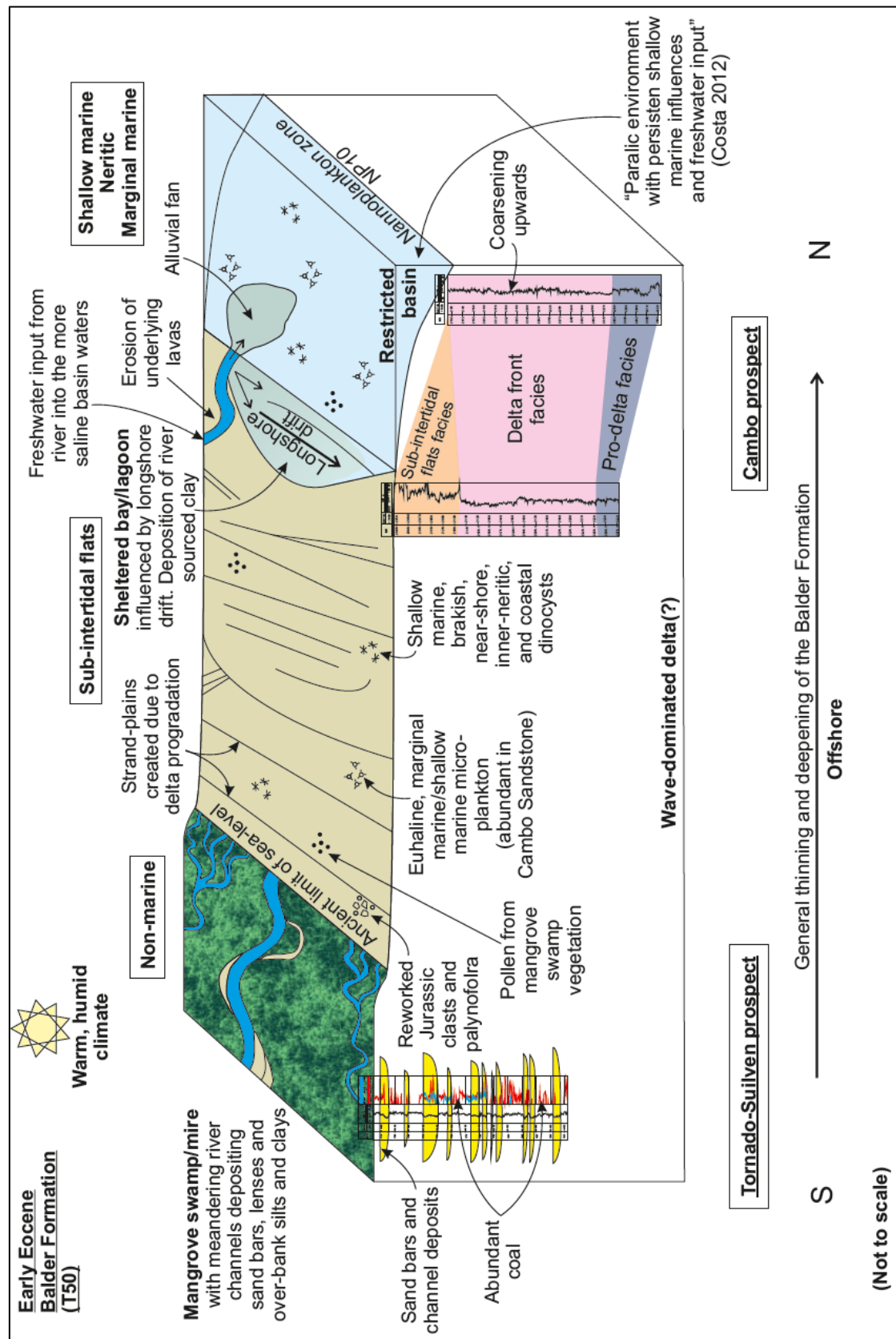


Figure 4-36 Summary diagram showing the interpreted lithologies and environment of deposition during Balder Formation time (late Palaeocene-early Eocene) across the Tornado-Suilven and Cambo prospects in UK Quad 204, with all the main evidence for these interpretations also labelled.

Chapter 5: The Harwich Formation, East Anglia

5.1 Introduction

East Anglia (E. Anglia, herein) and parts of the London Basin are exposed areas of the present-day landmass of the UK (Figure 5-1). Throughout the geological literature the Early Eocene Wrabness Member (WM) of the Harwich Formation (HF) has been cited as being equivalent to the ‘*upper tuff-rich* section’ of the North Sea Balder Formation (BF; Table 5-1; Knox & Ellison 1979; Knox & Morton 1983; Mudge & Bliss 1983; Malm et al. 1984; Roberts et al. 1984; Knox & Morton 1988; Morton & Knox 1990; Ellison et al. 1994; Jolley 1996; Knox 1996; King 2016). Only a limited amount of research has been published regarding the nature of the WM (Knox & Ellison 1979; Ellison et al. 1994; Hooker 1996; Jolley 1996), with microscopic and X-ray diffraction chemical studies only being carried out by Elliott (1971) and Knox & Ellison (1979). Advances in technology, such as the use of a Scanning Electron Microscope (SEM) to view material in microscopic detail, allows for a more in-depth investigation into the nature of the sediments that comprise these deposits, following on from the initial investigations of Elliott (1971) and Knox & Ellison (1979). The Paleocene and Eocene successions in E. Anglia have been summarised recently by King (2016), in the form of a literature review with limited additional original data, and no petrological observations.

55 Ma	AGE	Magnetostратigraphy	Biostratigraphy			Sequence Stratigraphy			Lithostratigraphy				
			Nano-zones	Paly	Micro	North Sea	FSB	Seismic Horizon	North Sea	FSB	E. Anglia (UK)		
55 Ma	Early Eocene (Ypresian)	C24r	Np10	Pt11	Mt7	T50	T50	BALDER	Moray Group	Balder Formation	Balder Formation	Thames Group	Harwich Formation
				Pt9-10									
			Np9	Pt8		T45	T45			Sele Formation	Flett Formation		Woolwich/Reading Formation
		C25n	Np8	C	Mt6	T40	T40	Base T45 /T50	Montrose Group	Lista/ Forties/ Andrew Formation	Lamba Formation	Lambeth Group	Upnor Formation
							T36			Maureen Formation	Vaila Formation		

Table 5-1 Divisions of the Late Palaeocene to Early Eocene stratigraphy relevant to this study (Knox & Holloway 1992; Knox & Morton 1988; Ebdon et al. 1995; BGS 2016; King

2016). Paly: Palynological zone. Micro: Microfossil zone. The HF of the Thames Group is an Early Eocene formation that coincides with magnetochron C24r. The Formation is the stratigraphic equivalent of the Balder Formation of the North Sea and Faroe Shetland basins (NSB and FSB, respectively).

The Shotley Borehole was drilled in 1977, from which core through Early Eocene deposits was recovered, including tuff-rich intervals (Figure 5-1). The core was described in detail by Ellison & Knox (BGS Shotley borehole records, 1977; Knox & Ellison 1979); however, since this description was made our understanding of the Early Eocene stratigraphy has advanced, including multiple revisions of formation and member names and boundaries (Ellison et al. 1994; Ali & Jolley 1996; Jolley 1996; Knox 1996; Aldiss 2014). Yet, the literature on these deposits has barely changed since initial observations were made in the 1970s.

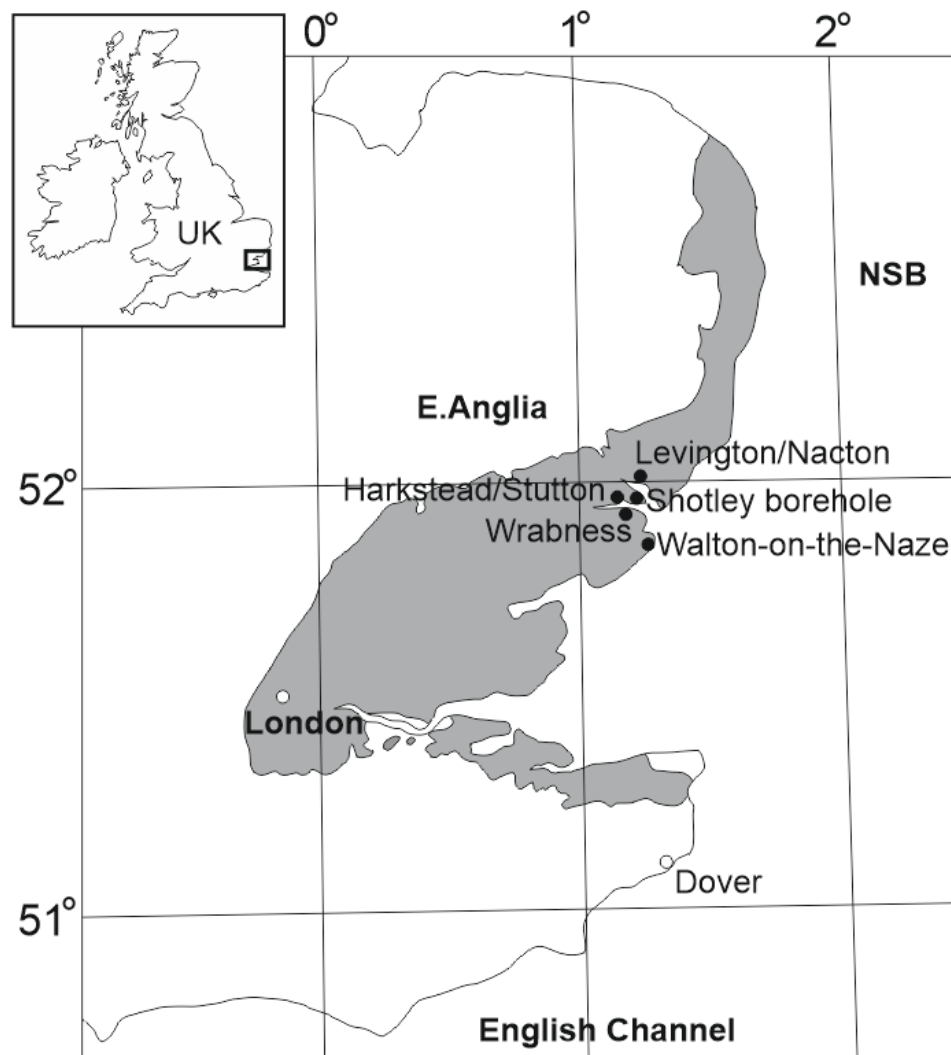


Figure 5-1 Location of the study area in the UK (inset map), the location of the study areas within E. Anglia and the distribution of Palaeogene sedimentary deposits (shaded). NSB: North Sea Basin (from Knox 1996). The field localities can be seen in more detail in Figure 5-7 and Figure 5-16.

The Harwich Formation (HF) was introduced as a Formation of the Thames Group by Ellison et al. (1994), and was described as:

‘Bioturbated silty clays and sandy, clayey silts with subordinate, partly glauconitic, sandy silts and silty sands. Volcanic ash beds are common in the top part and sporadic in the lower part.’

Subsequent sub-divisions of the HF were proposed by Jolley (1996), based on palynological association sequences. Observations of palynoflora (Table 5-1) within the HF led Jolley (1996) to propose the presence of the Wrabness Member (WM), and to suggest that deposition of this unit began 54.27 million years ago (Ma); no margin of error is stated for this.

The Harwich Stone Band (HSB) is a calcite-cemented hard band that can be used as a marker unit within the WM. This unit was first recorded by Elliott (1971), in a study that provided the first account of volcanic ash within the sequence in E. Anglia:

‘Sectioning reveals that the band contains variable amounts of volcanic ash, and is sometimes largely composed of it...It contains angular brown glass pyroclasts, some of which are streaky and resemble pumice, crystal fragments (often plagioclase), and lithic fragments full of opaque granules and containing minute elongate feldspar crystals.’

What follows in this chapter will build upon the work carried out by Elliott (1971), and Knox & Ellison (1977, 1979), to investigate the strata of the WM and comment on its volcanic content. Firstly the relevant geological history (Section 5.2) will be provided, followed by the results (Section 5.5) of the present study. The results will then be discussed (Section 5.8), and the conclusions of this given (Section 5.9).

5.2 Geological history

The HF is part of the Thames Group, which is present across SE England (Figure 5-1; Table 5-1, Table 5-2; Ellison et al. 1994; Ali & Jolley 1996; Knox 1996; Royse et al. 2012; Aldiss 2014; King 2016). The Formation was deposited in the Early Eocene during C24r and corresponds to nannoplankton zone NP10 (Table 5-1; Brooks 1980; Knox & Morton 1988; Ellison et al. 1994; Ali & Jolley 1996; King

2016); it has also been correlated with the early Eocene *Apectodinium hyperacanthum* dinoflagellate zone (Ellison et al. 1994; Ali & Jolley 1996). The HF includes the WM following sequence associations of palynoflora, Jolley (1996) places the basal sediments of the WM at 54.27 Ma, with the main period of deposition of the HF occurring between 54.0 and 54.5 Ma (Ali & Jolley 1996; Jolley 1996).

The HF correlates with the Early Eocene sedimentary rocks of the adjacent North Sea Basin (NSB), including the BF, (e.g. Elliot 1971; Knox & Ellison 1979; Knox & Morton 1983; Mudge & Bliss 1983; Malm et al. 1984; Roberts et al. 1984; Knox & Morton 1988; Morton & Knox 1990; Ellison et al. 1994; Jolley 1996; Knox 1996; Aldiss 2014; King 2016) and is therefore considered to be an extension of the same stratigraphical sequence. The base of the HF is defined by an unconformity that cuts through the underlying Lambeth Group (Table 5-2; Ellison et al. 1994; Ali & Jolley 1996; Knox 1996; Royse et al. 2012; King 2016), which represents a period of non-deposition that may have lasted around 0.4 million years (Ali & Jolley 1996). The London Clay Formation disconformably overlies the HF (Ellison et al. 1994; Royse et al. 2012). Within the study area, the HF was deeply eroded by Pleistocene glacial activity and its upper contact with the London Clay Formation cannot be seen (Table 5-2; e.g. Aldiss 2014). Therefore, the Early Eocene stratigraphy of E. Anglia is incomplete (e.g. Knox & Ellison 1979; Ellison et al. 1994; Knox 1996). The exposed sections are also much thinner than the corresponding succession observed within the NSB (see Chapter 3).

Group	Formation	Member	Bed
Thames	London Clay	Claygate	
		Sheppey	
		Aveley	
		Ockendon	
		Walton	
	Harwich	Swanscombe	Lessness Shell Harwich Stone Band Suffolk Pebble
		Oldhaven	
		Blackheath	
		Wrabness	
		Orwell	
Lambeth	Woolwich	<i>Woolwich Sands</i>	Cobham Lignite
		<i>Upper Shelly Clay</i>	
		<i>Striped Loams</i>	
		<i>Laminated Beds</i>	
		<i>Lower Shelly Clay</i>	
		Shorne	
	Reading	<i>Upper Mottled Clay</i>	
		<i>Lower Mottled Clay</i>	
	Upnor		

Table 5-2 Stratigraphic divisions of London and E. Anglia (Aldiss 2014). The Harwich Formation (HF) is part of the Thames Group; this formation overlies the Lambeth Group and is overlain by the London Clay Formation. The HF is sub-divided into the Orwell, Wrabness (WM), Blackheath, Oldhaven and Swanscombe members. The WM contains a marker bed known as the Harwich Stone Band (HSB).

During deposition of the HF, E. Anglia was occupied by a shallow, marginal marine (marine/inner- to mid-neritic) environment that was an extension of the southern NSB (Elliot 1971; Ali & Jolley 1996; Knox 1996; Kender et al. 2012; Royse et al. 2012; Aldiss 2014; King 2016). This marine environment was likely to have been restricted, as the North Sea was isolated from oceanic circulation with the North Atlantic at this time (Knox & Harland 1979; Mudge & Bliss 1983; Mudge & Copestake 1992a; Knox 1996; Steurbaut et al. 2009; Kender et al. 2012; Aldiss 2014). This restriction resulted in a low diversity of fauna and flora in the E. Anglian deposits (Ellison et al. 1994; Jolley 1996; Knox 1996; Mudge & Bujak 1996;), throughout the NSB (Mudge & Bujak 1996; Knox 1996; Steurbaut et al. 2009), and elsewhere across NW Europe, particularly in the Paris and Belgian basins (Steurbaut et al. 2009).

A limited number of biostratigraphical observations have been made within the HF or the WM (Table 5-3; Elliot 1971; Knox & Ellison 1979; King 1981; Ellison et al. 1994; Hooker 1996; Jolley 1996; Knox 1996; Mudge & Bujak 1996; King 2016). The dinoflagellate *Deflandrea oebisfeldensis* is found within the WM, and has been applied as a biozone within the Early Eocene HF (Jolley 1996; King 2016). Various microfossil gastropods have been noted from the HSB, for example, *Heliconoides (Spiratella, Valvatina) mercinensis* (Table 5-3; King 1981; King 2016). Macrofossils have also been identified, for example, the horse-like mammal *Pliolophus vulpiceps* has been found within the HSB (Hooker 1996). The HSB also forms a reference unit for the occurrence of macrofossils defined as part of the PE III *Platychoerops daubrei-Cantius eppsi* Concurrent Range Zone (Table 5-3), which can be used to locate the position of the Palaeocene-Eocene boundary and correlate the stratigraphy of the London, Paris and Belgian basins (Hooker 1996).

The limited presence of micro-fossils within the Early Eocene deposits of SE England may be due to deposition within a shallow marginal marine environment with a low salinity (Knox 1996; Royse et al. 2012; Aldiss 2014; King 2016), with the presence of very restricted types of micro-flora (Knox 1996), which support this interpretation. Glauconite has been observed within the sediments of the HF, the occurrence of which is generally limited to a marine environment, and particularly marine lowstands or the early stages of sea-level rise, which also supports this interpretation (Jeans et al. 2000).

Dinoflagellates	Micro-fossils	Macro-fossils in the PE III <i>Platychoerops daubrei</i>- <i>Cantius eppsi</i> Concurrent Range Zone
<i>Deflandrea oebisfeldensis</i>	<i>Heliconoides</i> (<i>Spiratella</i> , <i>Valvatina</i>) <i>mercinensis</i> (gastropod)	<i>Palaeonictis</i> cf. <i>occidentalis</i>
<i>Glaphyrocysta ordinata</i>		<i>Pliolophus vulciceps</i>
<i>Cometodinium comatum</i>		<i>Arcius fuscus</i>
<i>Impletosphaeridium</i> <i>ligospinosum</i>		<i>Phenacodus lemoinei</i>
<i>Caryapollenites circulus</i>		<i>Microparamys russelli</i>
<i>Intratroporopollenites</i> <i>microreticulatus</i>		<i>M. chandoni</i>
<i>Apectodinium</i> <i>hyperacanthum</i>		Esthonychidae
		<i>Bunophorus cappettai</i>
		<i>Diacodexis varleti</i>
		<i>Placentidens lotus</i>
		<i>Platychoerops daubrei</i>
		<i>Apatemys mutiniacus</i>
		<i>Plesiadapis remensis</i>
		<i>Cantius eppsi</i>
		<i>Coryphodon</i>
		<i>Paschatherium dolloi</i>
		<i>Microhyus musculus</i>
		<i>Landenodon woutersi</i>

Table 5-3 Dinoflagellates, micro-fossils and macro-fossils identified at the Palaeocene-Eocene boundary in the WM of E. Anglia (King 1981; Ellison et al. 1994; Ali & Jolley 1996; Hooker 1996; Jolley 1996; King 2016).

From the Late Palaeocene to the Early Eocene, sea-level fluctuated in response to regressive-transgressive cycles (Table 5-4; Jacqué & Thouvenin 1975; Deegan & Scull 1977; Knox & Harland 1979; Mudge & Bliss 1983; Mudge & Copestake 1992a; Waagstein & Heilmann-Clausen 1995; Ali & Jolley 1996; Jolley 1996; Knox 1996; Nadin et al. 1997; Smallwood & Gill 2002; Jolley & Bell 2002; Aldiss 2014), causing the position of the coastline of the surrounding landmasses to migrate

over time. Overall, there was a gradual marine transgression throughout the Early Eocene and onwards, which led to a gradual deepening of the marine environment (Table 5-4; Jacqu   & Thouvenin 1975; Knox & Harland 1979; Knox & Morton 1983; Mudge & Bliss 1983; Mudge & Copestake 1992a; Waagstein & Heilmann-Clausen 1995; Jolley 1996; Knox 1996; Smallwood & Gill 2002; Jolley & Bell 2002), as indicated by thick accumulations of clay within the London Clay Formation, (Knox & Harland 1979; Ellison et al. 1994; Ali & Jolley 1996; Royse et al. 2012; Aldiss 2014). Fluctuations in relative sea-level during the Late Palaeocene to Early Eocene may correspond to tectonic and igneous activity (Table 5-4). Rifting and the initiation of sea floor spreading within the NE Atlantic led to the separation of Greenland from NW Europe around 54.5 - 54 Ma (Halam 1972; Knox & Harland 1979; Knox & Morton 1983; Knox 1996; Nadin et al. 1997), corresponding with periods of fluctuating sea-level in the NSB. At this time the region was also beginning to be affected by compression related to the beginning of the Alpine Orogeny in the south (Aldiss 2014; Newell 2014).

	Nature	Cause	Consequences	Expression	Extent	Sequence Stratigraphy
EVENT 13 at 55.8 Ma mammalian faunal turnover + migrations	Maximum uplift	Global pale-tectonic convergence	Major erosion, paleovalleys (100m deep, 0.5-10km wide)	Major unconformity (Surface A)	Global Europe N. Africa	Lower boundary Seq. Y-A1
EVENT 14 at 55.8 Ma burial of Dormaal biota (e.g. mammals)	Onset of relative sea-level rise	Tectonic dilation	Infill of paleovalleys and lowlands	Land: Fluvio-lacustrine Basin rim: Lagoonal strata	Global	Base lowstand systems tract of Y-A1
EVENT 15a at 55.5 Ma	Relative sea-level fall	Decrease in accommodation space; North Atlantic uplift pulses	Emergence	Formation of paleosols (Surface B)	Regional	Top lowstand systems tract of Y-A1
EVENT 15b at 55.5 Ma carbon isotope event (CIE)	Rise in water table	Relative sea-level rise due to climatic warming	Development of marshes and swamps	Lignite (L1)	Global	Transgressive surface Y-A1
EVENT 16	Relative sea-level fall	Final phase of North Atlantic uplift	Minor erosion, channelling	Unconformity (Surface C)	Regional	Lower boundary Seq. Y-A2
EVENT 17 at 54.8 Ma	Substantial sea-level rise	Plate-tectonic dilatation	Major flooding landwards facies shift	(Surface D), start ash-rich deposits	Regional?	Transgressive surface Y-A2
EVENT 18 at 54.6 Ma Base Ypresian Stage s.s.	Major flooding	Thermal subsidence of NE Atlantic region	Marine depositional system throughout NW Europe	Major unconformity (Surface E)	Global	Lower boundary Seq. Y-B

Table 5-4 Significant events that have occurred throughout the Early Eocene which may have affected sedimentation in the NSB, including the region of E. Anglia. (from Steurbaut et al. 2009).

In E. Anglia, the HF has a typical thickness of 15 - 20 m (Ellison et al. 1994; Ali & Jolley 1996), reaching a maximum thickness of 40 m (Ali & Jolley 1996; Knox 1996). The HF contains abundant glauconitic sands and sandy clays, along with tuffs that individually reach a maximum thickness of 4 cm within the upper levels of the Formation (Figure 5-2; Ellison et al. 1994; Ali & Jolley 1996). These sediments were likely deposited in a shallow/shelf marine environment (Ali & Jolley 1996; Royse et al. 2012; Aldiss 2014). Mudstone/distal facies are dominant in the northern deposits, around Norfolk, and sandstone/proximal facies are dominant in the south, around Ipswich (Figure 5-3; Ellison et al. 1994; Knox 1996). In the field, correlation of deposits within this Formation is hampered due to rapid facies changes and discontinuous beds towards the north (Knox 1996); there is an 'absence of regionally distinctive lithostratigraphical markers' within the HF, making local and regional correlations difficult (Knox 1996). These laterally distinct facies changes are suggested to correspond to a deepening of the marine environment towards the north (Figure 5-3; Ellison et al. 1994; Knox 1996).

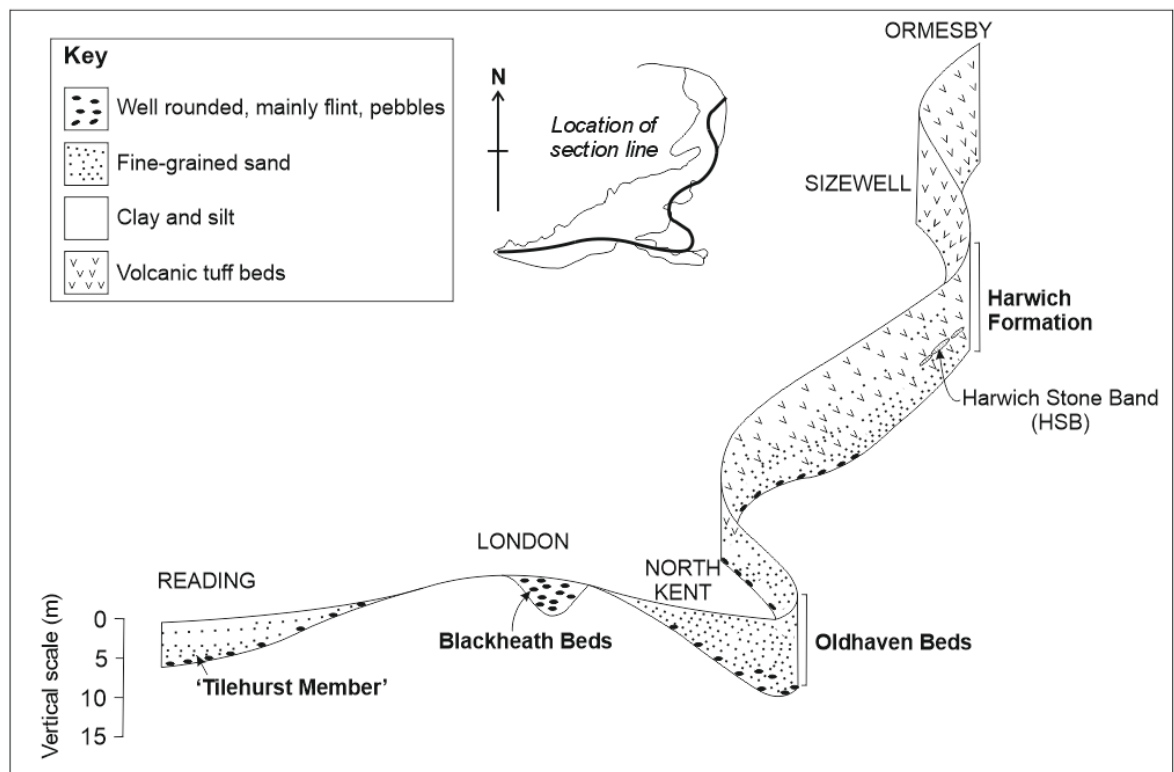


Figure 5-2 Diagram showing the variations in the stratigraphy of the Harwich Formation (HF) throughout E. Anglia (from Ellison et al. 1994).

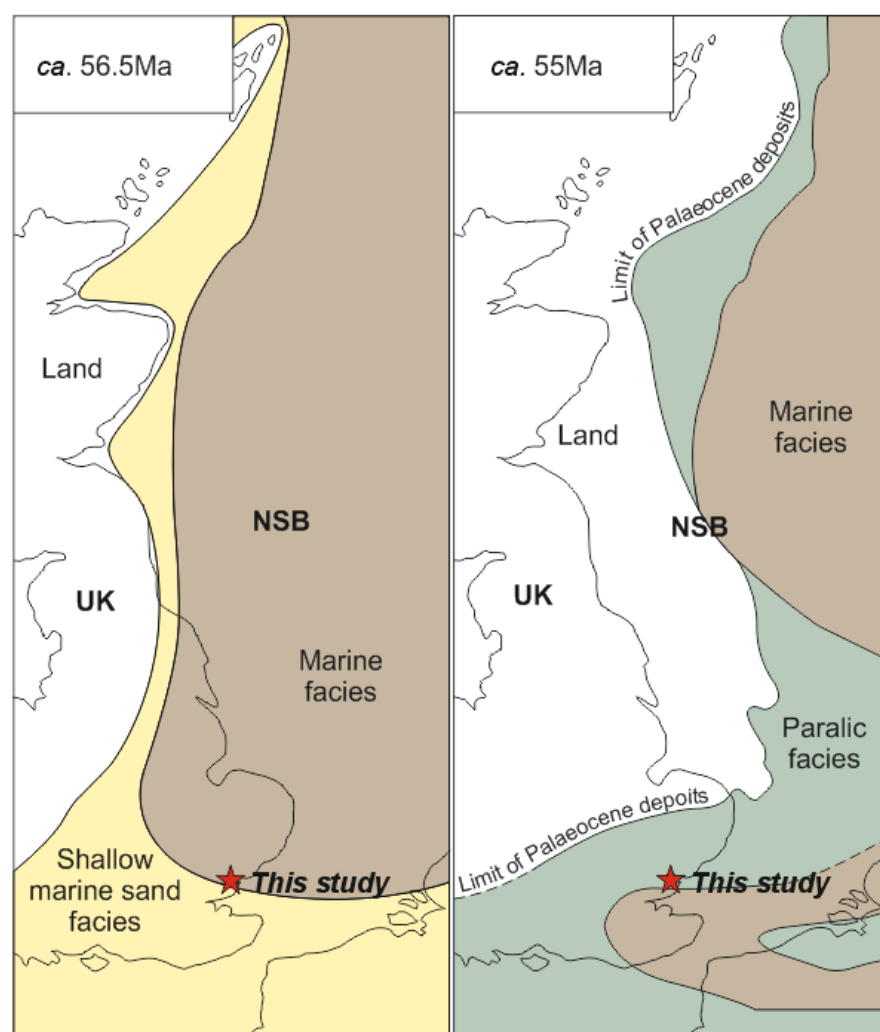


Figure 5-3 . Palaeo-environmental facies interpretations for 56.5 Ma and 55 Ma within the North Sea and Southern England (Knox 1996). At ca. 56.5 Ma, the study area (red star) lay between a true deep marine environment and a shallow marine environment of deposition. At ca. 55 Ma, the study area was most likely dominated by a paralic environment of deposition.

The WM is a member of the HF (Table 5-2; Jolley 1996), that contains a lower tuffaceous siltstone (Unit A of Jolley 1996), with an upper unit of ash-free siltstones and structureless sandstones (Unit B of Jolley 1996). An offshore muddy depositional environment has been suggested for the WM (Knox 1996), although the water depth or energy levels of the environment implied by this ‘offshore’ setting are not stated.

Subsidence of NW Europe during the Early Eocene may have led to an increase in relative sea-level preceding deposition of the WM (Knox 1996). Subsequent to this, uplift may have occurred due to the magmatic activity and the initial impact of the Iceland Plume within the rifting NE Atlantic and formation of the

North Atlantic Igneous Province (NAIP) (Table 5-4; e.g. Jacqué & Thouvenin 1975; Knox & Morton 1983; Knox 1984; Knox & Morton 1988; Morton & Knox 1990; Ali & Jolley 1996; Knox 1996; Ritchie & Hitchen 1996; Harland et al. 2000; Torsvik et al. 2001; Larsen et al. 2003; Gutjahr et al. 2017). Uplift and eastward tilting of the UK during the Early Eocene may have been associated with initiation of sea-floor spreading and formation of the NE Atlantic Ocean (Hallam 1972; Knox 1996); this uplift would likely have created a period of relative sea-level fall, followed by a relative increase in sea-level and a marine transgression (Table 5-4; e.g. Knox 1996; Jolley 1996; Nadin et al. 1997). This sequence of fluctuating sea-levels can explain the occurrence of periodic regressive progradational sequences observed in the WM (e.g. Ali & Jolley 1996; Jolley 1996). At least seven parasequences, representing periods of relative sea-level rise have been proposed within the WM, based on palynological associations (Jolley 1996). A phase of subsidence is also associated with the major marine transgression interpreted for the London Clay Formation above the HF (Table 5-2; Figure 5-5), possibly caused by thermal subsidence following the onset of sea-floor spreading within the NE Atlantic (King 1981; Knox 1996; Nadin et al. 1997; Aldiss 2014).

The WM includes the Harwich Stone Band (HSB), which is a 15 cm thick calcite-cemented layer that contains a well preserved tuff bed (Elliott 1971; Knox & Ellison 1979; Ali & Jolley 1996; King 2016). Other cemented discontinuous concretions are also present within this Member (Elliott 1971; Ellison et al. 1994; Ali & Jolley 1996) and most likely formed early during diagenesis, allowing preservation of ash as tuffs, at least, within the HSB (Elliott 1971).

Elliott (1971) first identified one ash layer within the HSB in E. Anglia; since then 44 ash-layers have been reported within the HF of the Shotley Borehole by Knox & Ellison (1979), with at least 32-34 identified within the WM (Figure 5-4; Knox & Ellison 1979; Ali & Jolley 1996; Jolley 1996). These volcanic deposits are considered to be relatively continuous, with varying thicknesses along section due to reworking (Elliott 1971; Knox & Harland 1979); no further details of this reworking is given. If the volcanic material has been reworked, then these deposits should be considered like any other sediment and defined as being volcanoclastic, rather than being referred to as ash, which implies primary

deposition, for example as direct fall-out from an eruption cloud (see Chapter 1). Primary deposition of ash or any other tephra would likely involve different depositional processes and have different grain-scale characteristics to those deposited as a result of reworking.

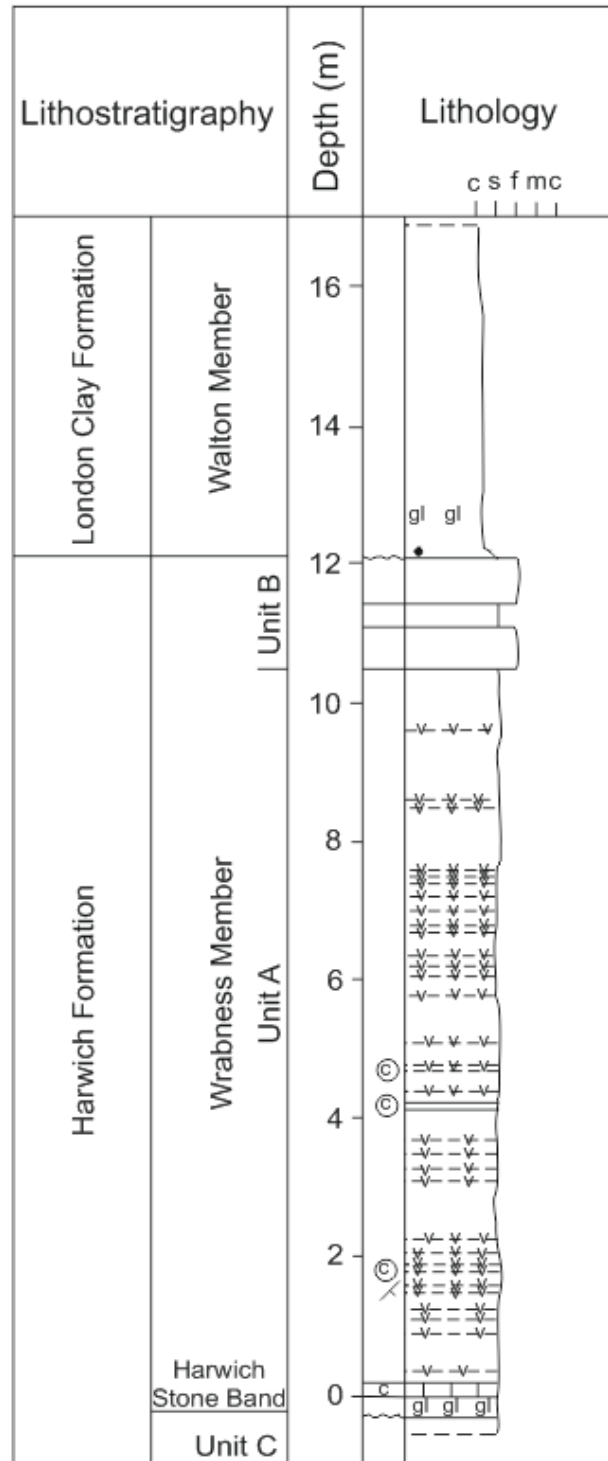


Figure 5-4 Summary log representing the stratigraphy at Wrabness, as described by Jolley (1996). This section suggests that at least 32 tuff layers have been identified in the WM. gl: glauconite; v: ash-layer; c: calcite concretions. Unit A contains the greatest abundance of volcanic material, whereas tuffs are not present in unit B, at the top of the WM. At

Wrabness, the WM is directly overlain by the Walton Member of the London Clay Formation (Table 5-2). The research detailed in this chapter investigates this same section at Wrabness with new data that contradicts this (see results, discussion and conclusions of this chapter).

The ash of the tuffs within the WM and adjacent NSB BF (Figure 5-5), was erupted toward the end of the Phase 2 volcanism of Knox & Morton (1983) (Figure 5-6), associated with formation of the NAIP (Knox & Morton 1983; Knox 1996; Haaland et al. 2000; Ross et al. 2005; Brooks 2006; see Chapter 3). Phase 2 volcanism has been divided into sub-phases, according to the stratigraphy, grain characteristics and the geochemical composition of the deposits (Knox & Morton 1983; Knox 1984; Haaland et al. 2000). The tephra deposited within the WM corresponds to sub-phase 2b (Figure 5-6; Knox & Morton 1983; Mudge & Bliss 1983; Knox 1984; Roberts et al. 1984; Knox & Morton 1988; Morton & Knox 1990; King 2016; see Chapter 3).

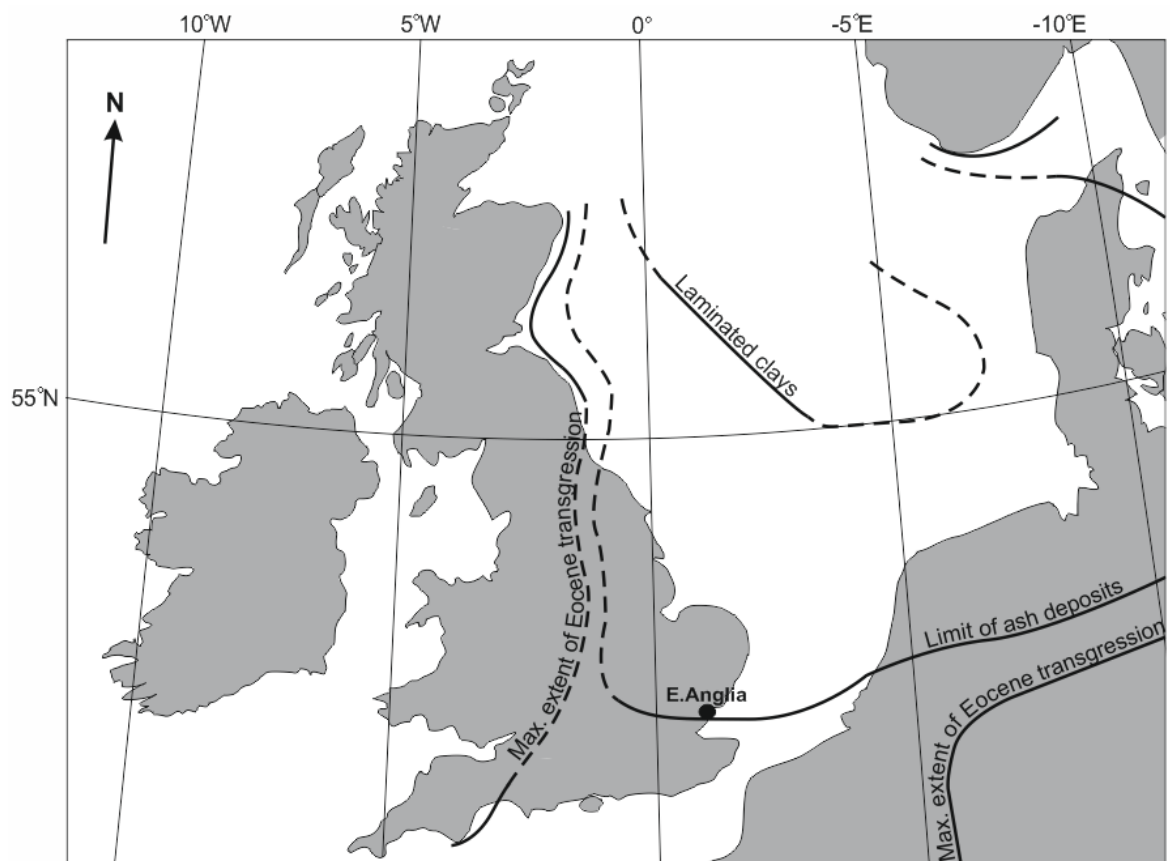


Figure 5-5 Map showing the estimated regions of deposition for ash deposits in the North Sea and NW Europe (from Knox & Harland 1979). The maximum extent of the Eocene transgression is also shown.

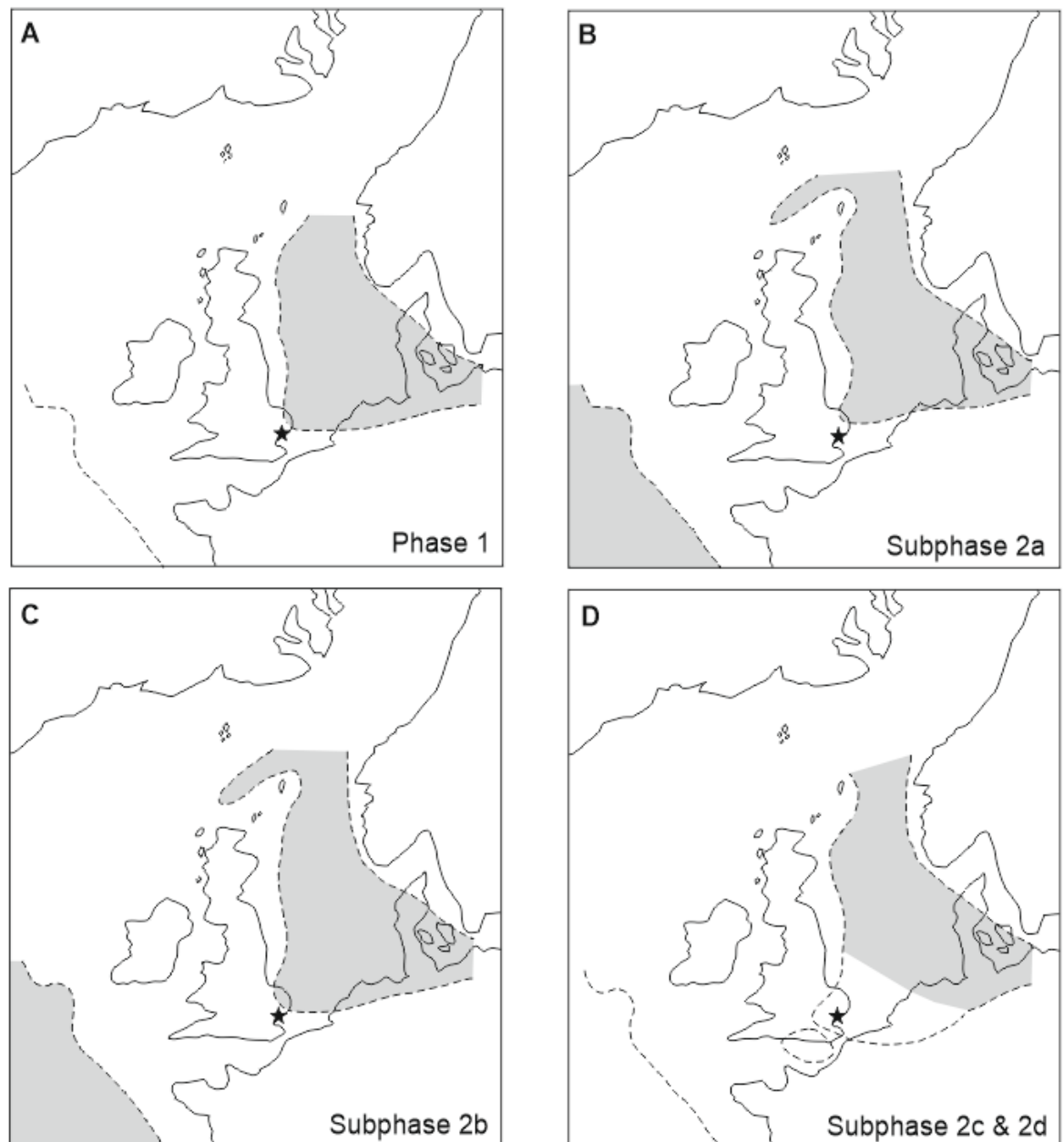


Figure 5-6 Distribution of ash corresponding to each volcanic phase and sub-phase identified by Knox & Morton (1983). Dashed lines show the estimated extent of ash distribution during each phase. Grey shaded areas show where ash has been preserved (from Knox & Morton 1988). Stars show the position of the field localities in E. Anglia.

It has been proposed that the ashes of sub-phase 2b tuffs was erupted during the initiation of sea-floor spreading and development of the NE Atlantic Ocean, alongside impact of the proto-Icelandic plume and the changes in crustal tension associated with these events (Knox & Harland 1979; Knox & Morton 1983; Ritchie & Hitchen 1996; Torsvik et al. 2001; Larsen et al. 2003). Previous studies have shown the igneous component of these sediments to be of basaltic composition (Pedersen et al. 1975; Malm et al. 1984; Knox & Morton 1988; Morton & Knox 1990; Haaland et al. 2000; Larsen et al. 2003; Brooks et al. 2006).

Large volumes of ash can be produced from basaltic magma during hydrovolcanic eruptions, where highly explosive magma-water/fuel-coolant interactions take place (Sheridan & Wohletz 1983; Elliot et al. 1992; White 1996; Trigila et al. 2007). These interactions enhance the level or degree of fragmentation, producing large quantities of fine-grained tephra (e.g. Graettinger et al. 2013). The basaltic composition of the volcanic material and its reported abundance in the Early Eocene deposits of E. Anglia suggest that highly explosive hydrovolcanic eruptions were needed to disperse this tephra to locations 1000-2000 km away (Jacqué & Thouvenin 1975; Knox 1984; Knox 1996; Jolley & Bell 2002) from their interpreted source within the NE Atlantic Ocean (Larsen et al. 2003; Egger & Brückl 2006; Larsen. pers. coms. 2015; Carriol et al. 2016).

5.3 Aims and objectives

The WM of the HF is an important onshore sequence where a directly corresponding stratigraphic sequence to the North Sea BF can be observed (King 2016). It is therefore appropriate to analyse these easily accessible exposures to gain a better understanding of the depositional environment(s) of the BF. Analysis of the WM can also help with identifying the source of the sediments, the nature of the depositional environment(s), and post-depositional processes. In addition to this, petrological analysis allows the identification and quantification of igneous components. One of the key aims of the present investigation is to determine the distribution, depositional environment and conditions of preservation of the pyroclastic component, and what this informs about the eruption dynamics and possible source of the volcanism.

It is assumed in the published literature that there is an abundant volcanic component to the Early Eocene stratigraphy of E. Anglia, but very little detailed analysis of the nature of this material has been published (see section 5.2 Geological History). Thus, a more in-depth analysis of the stratigraphy and samples from these locations is vital for our wider understanding of the volcanism that affected NW Europe during the Early Eocene, and our knowledge of the characteristics of the NSB BF with its significant volcanic component. This research investigates the volcanic content of the same units previously studied by those previously (i.e. Elliott 1971; Knox & Ellison 1979; Jolley 1996).

Additional aims that support these objectives are to collect and produce quantifiable data representative of the clastic and pyroclastic components of deposits using image analysis methodology.

5.4 Methods

Fieldwork was conducted over a total of three days along the River Stour and Orwell estuaries in E. Anglia, UK (Figure 5-1). Five sites were chosen for a detailed study of the WM: Wrabness (type locality), Harkstead, Levington to Nacton, Stutton and Walton-on-the-Naze (Table 5-5). With additional data produced via study of the Shotley Borehole B core (Table 5-5) housed at the British Geological Survey (BGS) core-store in Nottingham.

Location	Grid Reference
Wrabness	From TM 17289 51°56'49.49"N 1°9'42.51"E to 51°56'46.31"N 1°9'19.76"E
Harkstead	TM 18783 33780 +/- 11m 51°57'34.72"N 1°10'57.93"E
Levington/Nacton	TM 22543 38672 +/- 8m 52°0'5.97"N 1°14'28.07"E
Stutton	TM 14259 33214 +/- 6m 51°57'21.87"N 1°6'59.96"E
Walton-on-the-Naze	51°52'49.47"N 1°17'21.94"E to 51°52'1.28"N 1°17'25.63"E
Shotley Borehole B	TM 2439 3460 51°57'52.86"N 1°15'53.69"E

Table 5-5 Locations of sample sites for the WM. Shotley Borehole B was accessed at the BGS core-store (Nottingham); all other localities are field-locations where direct observations of exposures were made.

Samples were taken from each of the localities for petrological analysis. Sampling was problematic due to the highly weathered and altered nature of the exposed rocks; many of the samples are very fragile and easily broken. Kubana tins were proposed as a solution to this problem, but given the solid nature of the rocks when completely dry their use was not possible. It may be possible to use Kubana tins for sample collection during long spells of wet weather,

although this could make sampling more dangerous and lead to contamination of surfaces by the movement of material from higher levels in the exposure to the surface below, or between cracks into the rocks. It should be noted that the rocks quickly swell in contact with water. The exposures can only be accessed at low tide in most cases. Borehole samples from the Shotley Borehole were studied in detail via lithological logging and sampling at the BGS core-store, Nottingham.

During sampling, in the field and at the core-store, the way-up of each sample was recorded. Notes, sketches and photographs were collected to document the locations of each of the samples and the general nature of the sequences that they were taken to represent.

Systematic sampling was attempted on a second sampling session at the exposure between Levington and Nacton. This involved the collection of samples from each identifiable sequence, upward from the HSB, and was carried out in this way in an attempt to sample each bed identified by a variation in the colour of the rock. Samples from higher levels in the sequence were sampled by traversing the exposure, while tracing picked units, to areas where access could be achieved. The highest levels of the exposures were out of reach and could not be sampled.

Samples were taken where possible from Shotley Borehole B, although the highly fragmented nature of the borehole core limited the amount of material that could be selected for further study. An aim of this sampling session was to sample areas that may correspond to material previously obtained from the field sites, such as the HSB.

Initial thick-sections of the samples were prepared at the University of Glasgow with great difficulty, using kerosene as a replacement for water to reduce any swelling of the rock. Further polished thin-sections impregnated with a blue resin were prepared using kerosene by *ALS Petrography*.

Petrographic analysis was conducted on polished thin-sections using plane-polarised light (PPL), cross-polarised light (XPL), and reflected light (RL)

microscopy. Where sections are thick or contain abundant clay-sized grains, RL was the only form of optical microscope analysis that could be used to gain any information about the nature of the samples. Subsequent analysis was conducted on a Zeiss Scanning Electron Microscope (SEM) to provide more detailed images of the samples and their components. SEM images were used for image analysis to provide quantitative data on grain characteristics. More information on the methods used can be found in section 1.3 Methods.

5.5 Results

5.5.1 Field observations

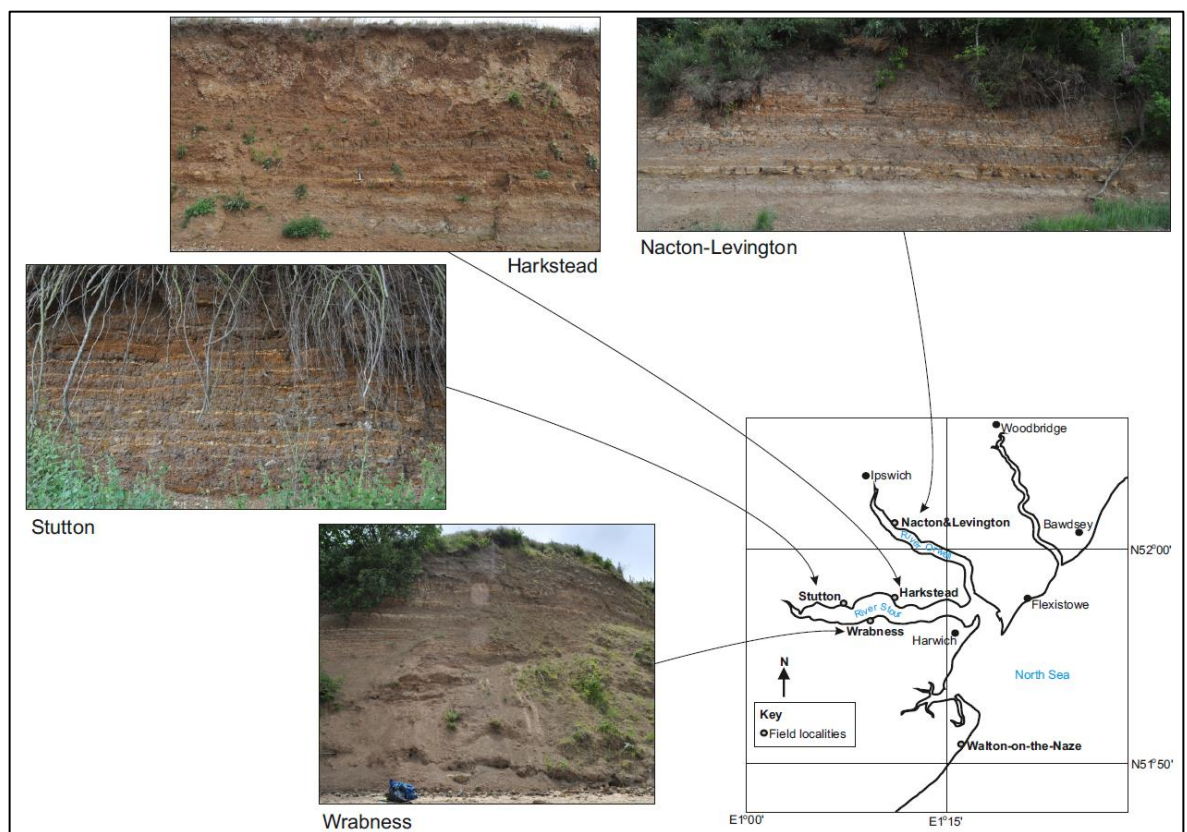


Figure 5-7 Field views illustrating the general nature of the various localities. All of the localities have the same general character, with sub-horizontal stratification shown by changes in the colour of the rock, and exposed in sub-vertical estuary cliffs. See Figure 5-16 for a more detailed view of the location map.

In general, all of the exposures studied in E. Anglia have a similar appearance (Figure 5-7). The bedded nature of the deposits of the WM make them easily identifiable, and the HSB forms a prominent marker-unit that is more resistant

to weathering and can be identified, where exposed, at each location (Figure 5-8; Knox & Ellison 1979).

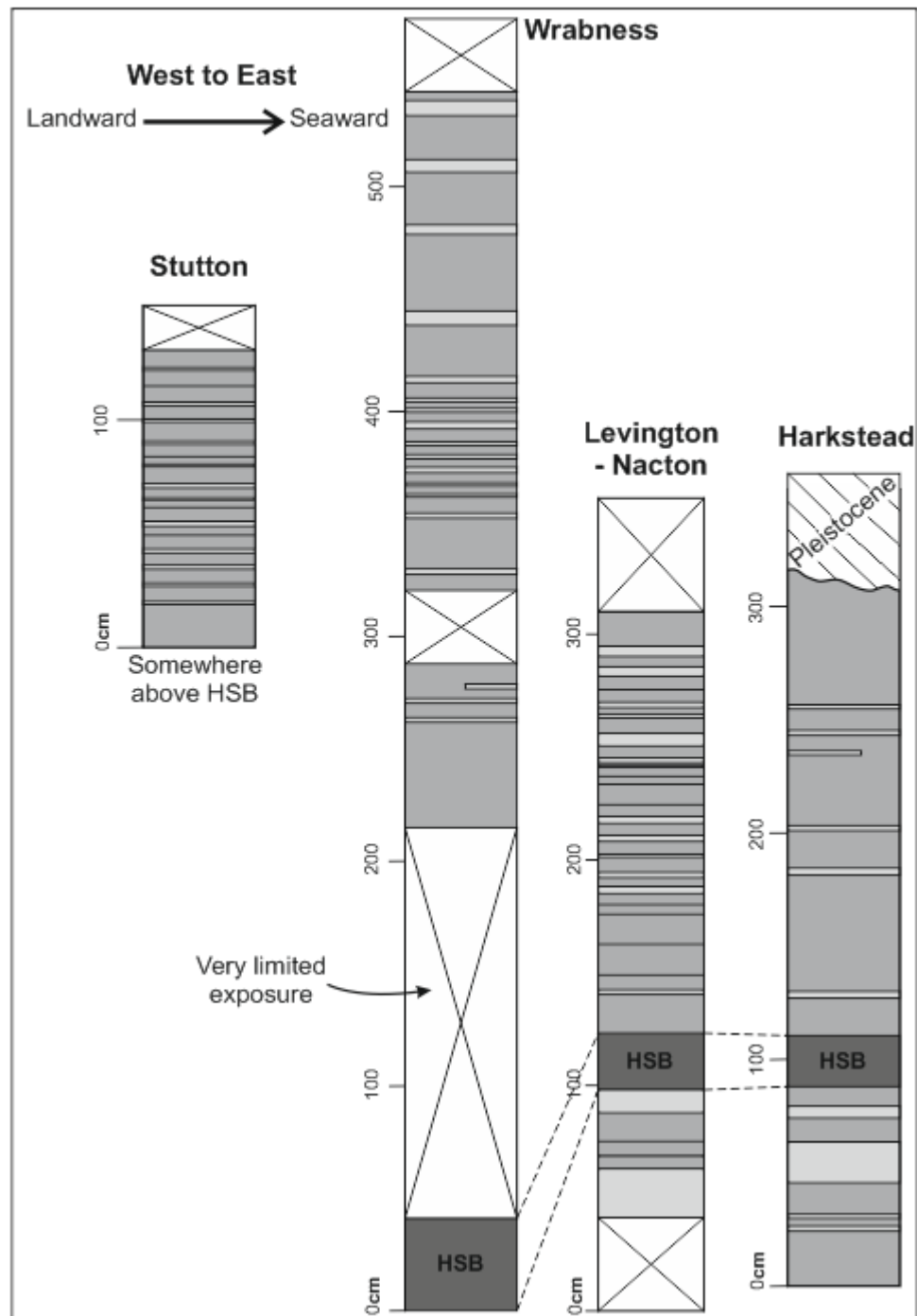


Figure 5-8 Comparison of the nature of the WM between sites from Stutton in the west to Harkstead in the east. HSB: Harwich Stone Band. Different grey-shades are used to reflect the position of pale and darker grey units witnessed in the exposures. In published literature the position and abundance of pale grey layers marks the position of tuff beds (Knox & Ellison 1979; interpreted from Jolley 1996 logs). The best preserved and easily accessible exposure of the WM can be found in the cliff section between Levington and Nacton, although, the most complete section occurs at Harkstead.

5.5.1.1 *Wrabness*

The WM is exposed in low cliffs to the south of the River Stour at Wrabness [51°56'49.49"N 1°9'42.51"E to 51°56'46.31"N 1°9'19.76"E]. This location is the type locality for the WM, as stated in the literature (Aldiss 2014; BGS Lexicon of named rocks). The fragile cliffs are composed of highly altered rock and loose scree of grey clays and silts with paler grey/white continuous centimetre-scale bands. Up to 18 pale grey/white units can be identified within a *ca.* 6 m high cliff section that provides the thickest and most laterally continuous exposure along this section of the estuary [51°56'49.49"N 1°9'42.51"E]. At the base of the exposure is a thicker (*ca.* 50 cm) calcite-cemented layer known as the Harwich Stone Band (HSB; Elliot 1971; Knox & Ellison 1979). Above the HSB is a claystone that is a significant blue colour when observed on a fresh surface (Figure 5-9). This clay band is more consolidated than the surrounding material and has a total thickness of *ca.* 55 mm, although the thickness appears to vary, as indicated by lateral colour variations caused by alteration. Diffuse laminations can also be identified within this bed in some places (Figure 5-9). This blue band is laterally continuous across local exposures, along an interval of <100 m. Blue claystone bands have been described in the literature as being tuff-rich intervals (Knox & Ellison 1979; Jolley 1996; Giresse & Wiewióra 1999; King 2016). Sample WRAB_02 was obtained from this bed for detailed component analysis; this unit is named the 'Wrabness Blue Band' herein.

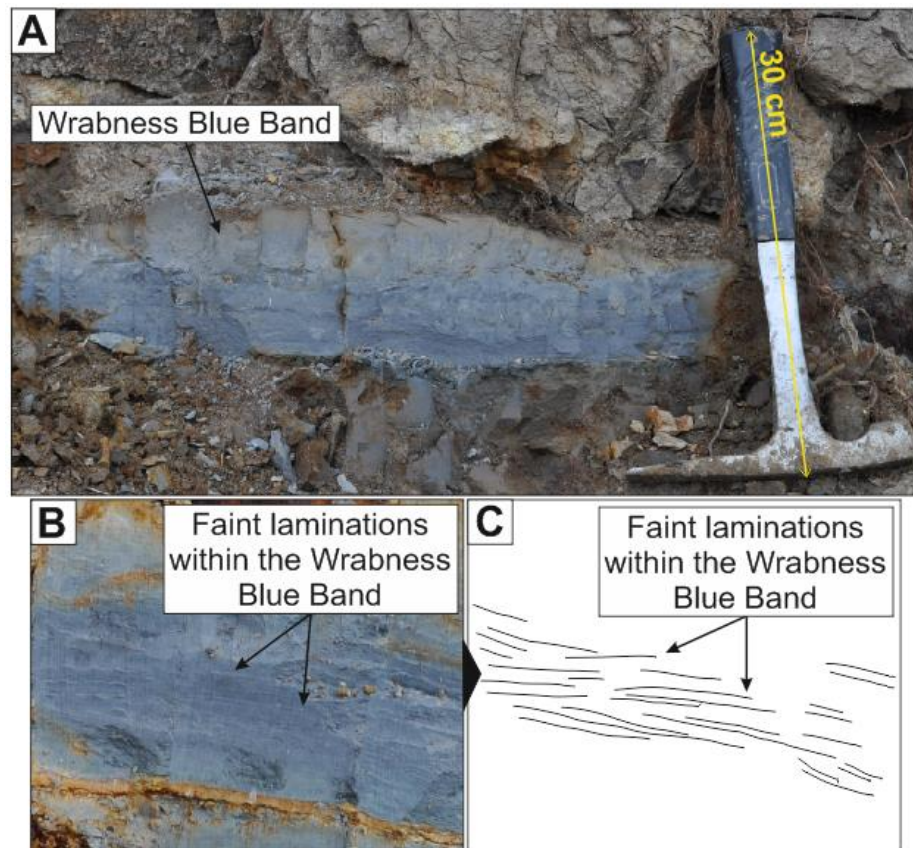


Figure 5-9 Prominent blue band comprised of clay can be seen in a fresh exposure at the base of the estuarine cliffs at Wrabness. This band is locally continuous and is found just above the HSB. Diffuse (faint) laminations can be seen within the blue band (B-C).

5.5.1.2 *Harkstead*

A river cliff section that exposes the WM, up to *ca.* 3.5 m high and several hundreds of metres long, is exposed on the north side of the River Stour at Harkstead [51°57'34.72"N 1°10'57.93"E]. The basal contact of the member is not exposed but an upper erosional contact is exposed where Pleistocene glacial deposits lie unconformably on top in channel-like erosional features (Figure 5-10). The surface of the exposure is highly weathered and fragmented. The cliff is composed of claystones and siltstones that are highly erodible and swell when wet, and fracture and crumble when dry. Continuous layers of pale grey and darker grey rock can be traced along the entire length of the exposure.

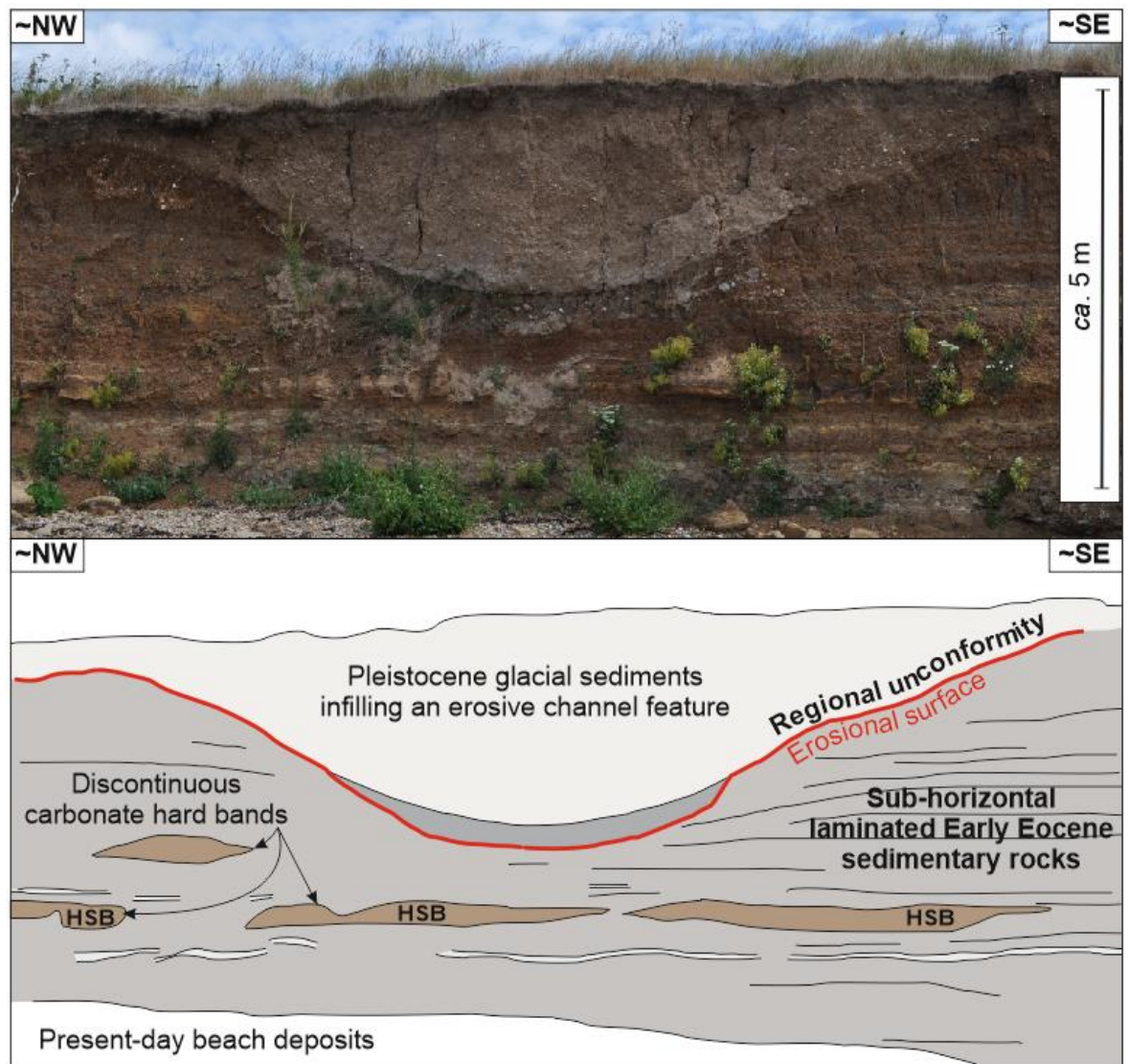


Figure 5-10 Regional unconformity between the Eocene HF (Wrabness Member) and Pleistocene glacial deposits shown by an infilled channel cutting through the Early Eocene sedimentary rocks exposed in a ca. 5 m high cliff at Harkstead. Multiple discontinuous carbonate-cemented hard bands can be seen at this locality. Ca. 1 m from the base of the cliff lies the HSB; here this band is discontinuous and sections pinch-out along section.

Calcite-cemented concretions of varying thickness, are present continuously and discontinuously along the exposure. At first glance, these concretions appear to follow particular bedding planes, but, on closer inspection, do not: they are random and often jump across bed boundaries (Figure 5-10). The concretions are more resistant to weathering and erosion, and form ledges that protrude from the cliff. The HSB is present ca. 1 m from the base of the cliff; here the HSB varies in thickness, commonly pinching out completely, and also appears to jump slightly across bed boundaries (Figure 5-10). On the upper surface of the HSB there is evidence of bioturbation that can be identified by the presence of abundant trace fossils (Figure 5-11; Ellison et al. 1994; Obst et al. 2015),

particularly on loose blocks lying on the beach below the cliffs. Cross-sections through cylindrical *endichnia* burrows (Rindsberg 2012), can be seen in vertical sections through the HSB (Figure 5-11c). Features that resemble root or burrow structures are preserved as trace fossils that lie both parallel and perpendicular to the bedding surface (Figure 5-11d-f). These fossil types may be representatives of the *Skolithos* and/or *Cruziana Inchofacies* typical of shoreface environments (Pemberton et al. 2012); alternatively they may be associated with a *Scoyenia Ichnofacies* typical of lacustrine environments (Scott et al. 2012), or assemblages that are formed by bioturbation in a hemipelagic/pelagic basin (Wetzel & Uchman 2012). Therefore, these trace-fossils are evidence of subaqueous deposition, most likely associated with a shoreface or shallow-marine setting.

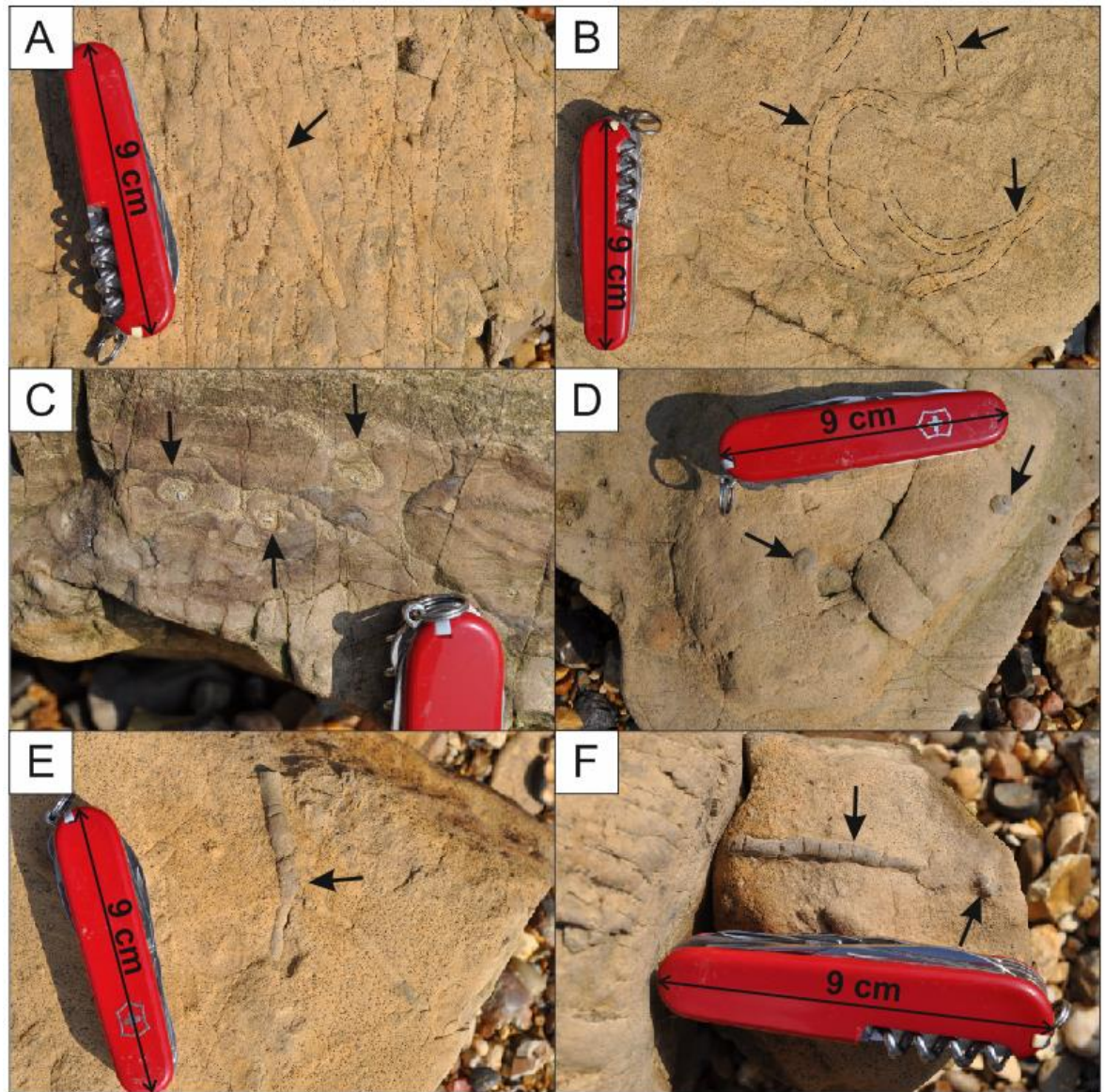


Figure 5-11 Trace fossils identified within the HSB at Harkstead. A) A straight burrow or track seen parallel to bedding. B) Curved sections through burrows, or the surface expression of curved tracks observed parallel to bedding. C) Cross-section through the HSB, with abundant bioturbation present as an inclined burrow (top-most arrow), and cross-sections through cylindrical *endichnia* burrows that lie parallel to bedding. D) Cross-section of two cylindrical sections through body fossils or burrows that intersect a sub-horizontal bedding plane. E-F) Possible body fossils, or root structures that lie parallel to bedding. The circular cross-section of a burrow or body fossil on the right of image F, has an orientation that is not parallel to bedding.

5.5.1.3 *Levington/Nacton*

The deposits exposed in the river cliffs adjacent to Levington, between Nacton and Levington [52°0'5.97"N 1°14'28.07"E], have been poorly documented in previous literature (Ali & Jolley 1996). The exposures of the WM include material from below the HSB, to near the eroded top of the Member (Figure 5-12; Ali & Jolley 1996), in cliffs up to *ca.* 10 m high. This is therefore the most complete

section of the WM that has been investigated during the present study; it is also the best preserved and therefore surpasses the type locality at Wrabness in terms of its suitability as a representative section through the WM.

The exposure here is composed of siltstones and fine sandstones, with an abundant clay content indicated by the general swelling nature of the deposits when in contact with water. Continuous bands of varying colour can be observed within the exposure, although in hand specimen these do not appear to correspond to any observable changes in grain-size or composition. It is possible the differences in microscopic minerals within the clay matrix, or changes in bulk composition are the cause of these colour variations.

The HSB effervesces slightly with 10% hydrochloric acid, confirming the presence of a calcite cement. As at other locations (e.g. Harkstead), the HSB does not always occupy the same stratigraphic interval and may actually jump between various beds showing that it is not an original feature of the stratigraphy and that it likely formed during diagenesis (e.g. Elliott 1971). In some areas the HSB is deformed and contains extensional fractures that have been filled with fibrous calcite. The presence of these features suggests that some form of post-depositional and syn- or post-diagenetic deformation has taken place. The HSB at this locality is less resistant to weathering compared to the HSB at Harkstead. This could be due to the presence of thick vegetation overhanging the cliff section at Levington-Nacton, with vegetation affecting the chemistry of water that runs down the cliff during periods of rainfall and enhancing weathering of the HSB at this locality. There does not appear to be any observable difference in the nature of the HSB between the localities; therefore, differences in composition of the HSB are not likely to be the cause of the differences observed in weathering of the HSB.

According to Ali & Jolley (1996) 'a number of degraded ash beds' can be observed within the exposure at Levington. However, a true identification of fine-grained volcanic clasts cannot be achieved in the field by eye. Additional interpretations of the volcanic content of the deposits at this location had to be conducted later via optical microscopy and SEM analysis of systematically collected samples (Figure 5-12; see below).

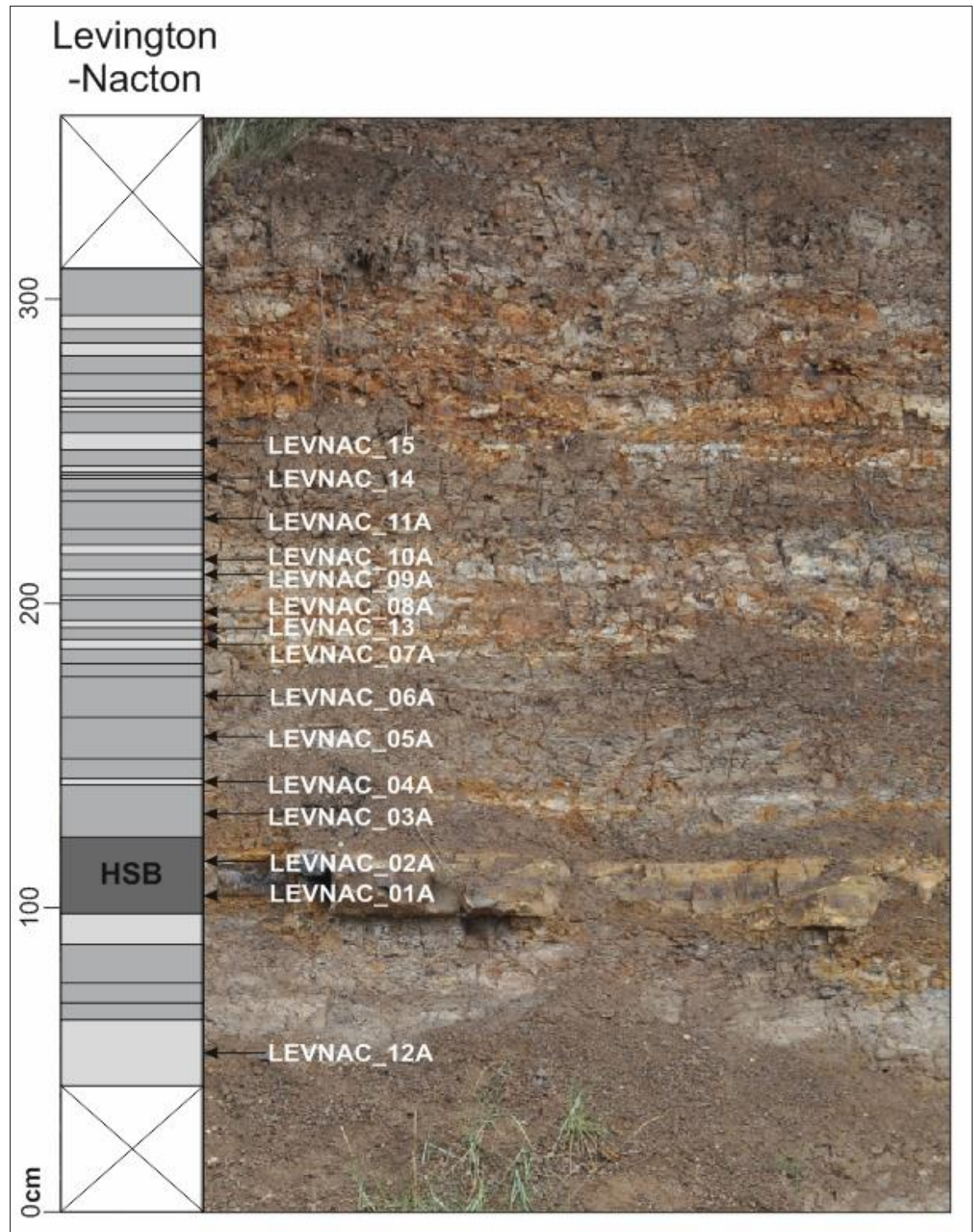


Figure 5-12 Field view and log of the site between Levington and Nacton with arrows indicating the positions of samples. The pale and dark grey colours within the log to the left reflect the position of pale and dark grey units observed in the field.

Two normal faults, with an apparent vertical displacement of *ca.* 1 m, can be seen within this cliff section (Figure 5-13). Further along the section, to the west, in a larger exposure, a third fault with a larger displacement can be seen. At [TM 22543 33672] the HSB appears to be plastically deformed but not faulted.

In the deformed regions of the HSB, extensional fractures are filled with fibrous calcite and calcite veins. The surrounding non-cemented material appears to have been faulted, with some smearing of finer grains along the fault boundary (R. Walker. pers. coms. 2017). The timing of this faulting is unknown and may be related to structural influences of the nearby Ipswich-Felixstowe high (J. Smith. pers. coms. 2017).



Figure 5-13 Normal fault with ca. 1 m apparent displacement within the WM exposed between Levington and Nacton. Two prominent pale grey/white bands have been highlighted to show the displacement of the strata. The HSB is not faulted but has undergone ductile deformation.

5.5.1.4 Stutton

Good field exposures of the WM are found within the roots of large trees perched on the cliff edge along the northern edge of the River Stour at Stutton [51°57'21.87"N 1°6'59.96"E]. Exposures are a little over a metre thick and are composed of heavily weathered and eroded material (Figure 5-14). Continuous pale grey and darker grey bands can be traced between the exposures (Figure 5-14). Some traceable fainter pale brown layers are also visible upon closer inspection. At least 13 bands of pale grey material, interbedded with grey/brown material, can be identified within the exposure. Here, the interbedded material appears to have a coarser grain-size in general, for example being composed of silt-sized material, rather than clay, as observed at the other localities. The continuous beds have sharp basal contacts, although the

nature of the upper contacts is less clear; it is possible that the upper contacts are more diffuse and may indicate that the beds are normally graded.



Figure 5-14 Banded character of the WM exposed beneath trees in the cliffs at Stutton. The sequence comprises interbedded dark grey and pale grey/white siltstones; the pale grey units occur with a relatively regular periodicity, upwards through the section.

5.5.1.5 Walton-on-the-Naze

Very little of the WM is exposed in the cliff sections of Walton-on-the-Naze [51°52'49.47"N 1°17'21.94"E to 51°52'1.28"N 1°17'25.63"E]. Here the top of the Wrabness Member is exposed at the base of the sea cliffs (e.g. Jolley 1996).

Two diffuse, green beds can be identified at the base of the sea cliffs where exposure is best. These beds are of clay/silt grade and slightly coarser-grained compared to the surrounding claystones. These two units may be the two ash layers identified at this locality by Jolley (1996) (Figure 5-19). No further information could be gained from these deposits during this study due to the altered nature of the rock, the lack of good exposure, and its position at sea-level.

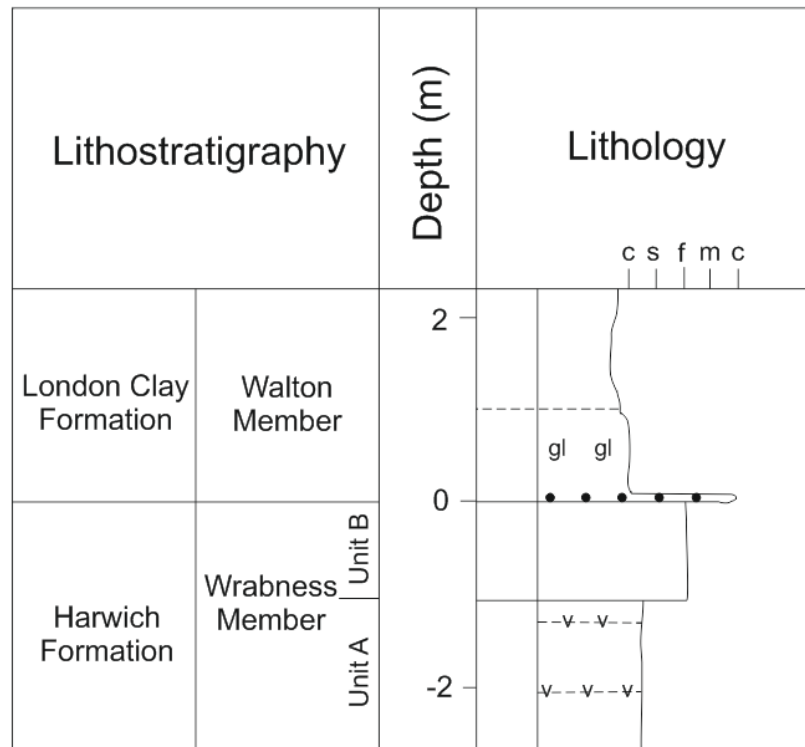


Figure 5-15 Summary log for Walton-on-the-Naze as described by Jolley (1996).

5.5.1.6 Shotley B borehole

Borehole material was obtained from Shotley Borehole B [51°57'52.86"N 1°15'53.69"E] and is stored at the BGS core-store in Nottingham. The core was initially described by Ellison & Knox in 1977. However, since these descriptions were made, the location of formation boundaries have changed and the WM has been introduced (Ellison et al. 1994; Ali & Jolley 1996; Jolley 1996). To avoid confusion it was necessary to fully describe and log the core afresh (Figure 5-17).

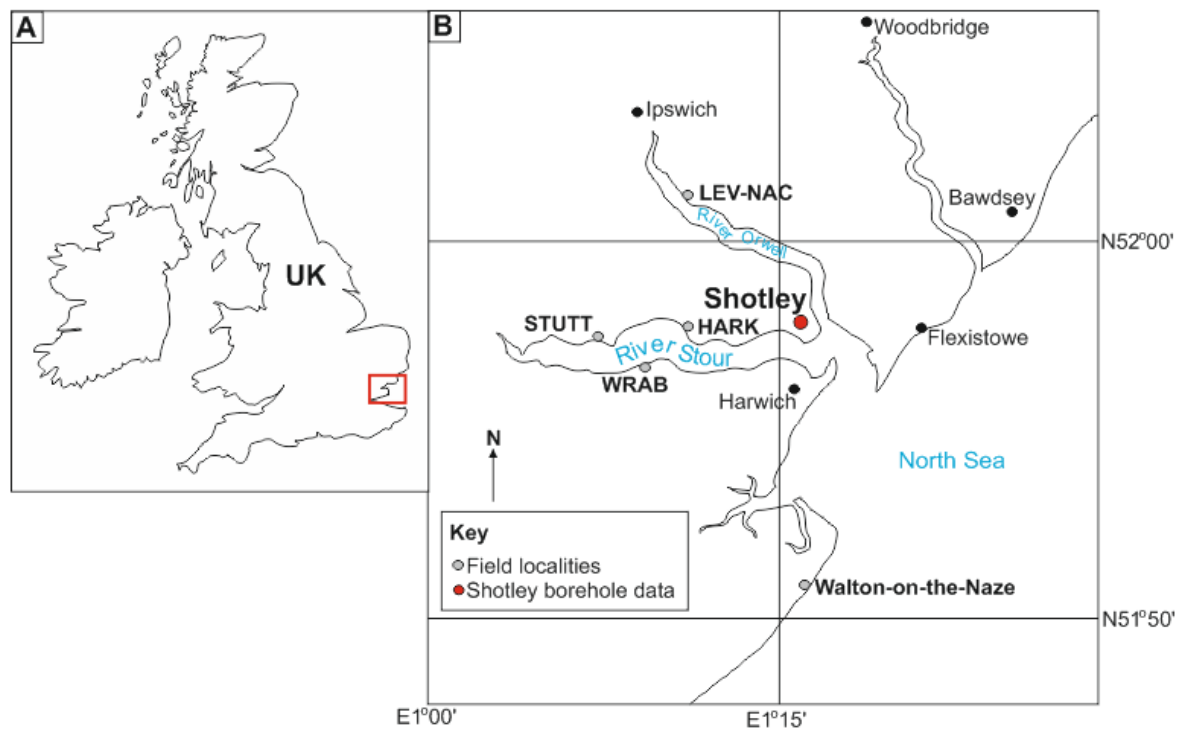


Figure 5-16 Location of the Shotley Borehole relative to the field localities between the River Stour and Orwell. The location of (B) is indicated by the red box on a map of the UK (A). B) Shotley Borehole (red circle) lies to the east of Harkstead (HARK), Levington-Nacton (LEV-NAC), Stutton (STUTT) and Wrabness (WRAB). Map A shows the location of B on a map of the British Isles.

The location of this borehole lies between Levington-Nacton and Harkstead (Figure 5-1). Two boreholes were drilled: Shotley A and Shotley B. Shotley A contains material from the Cretaceous-Paleogene boundary, the WM is minimal or not present within this core. Shotley B contains the higher levels of Early Eocene strata that are preserved below an erosional unconformity with the overlying Pleistocene drift deposits that are present at the top of this borehole. Shotley B, at a depth of ~10 - 24.5 m below ground surface, forms the focus of this borehole study.

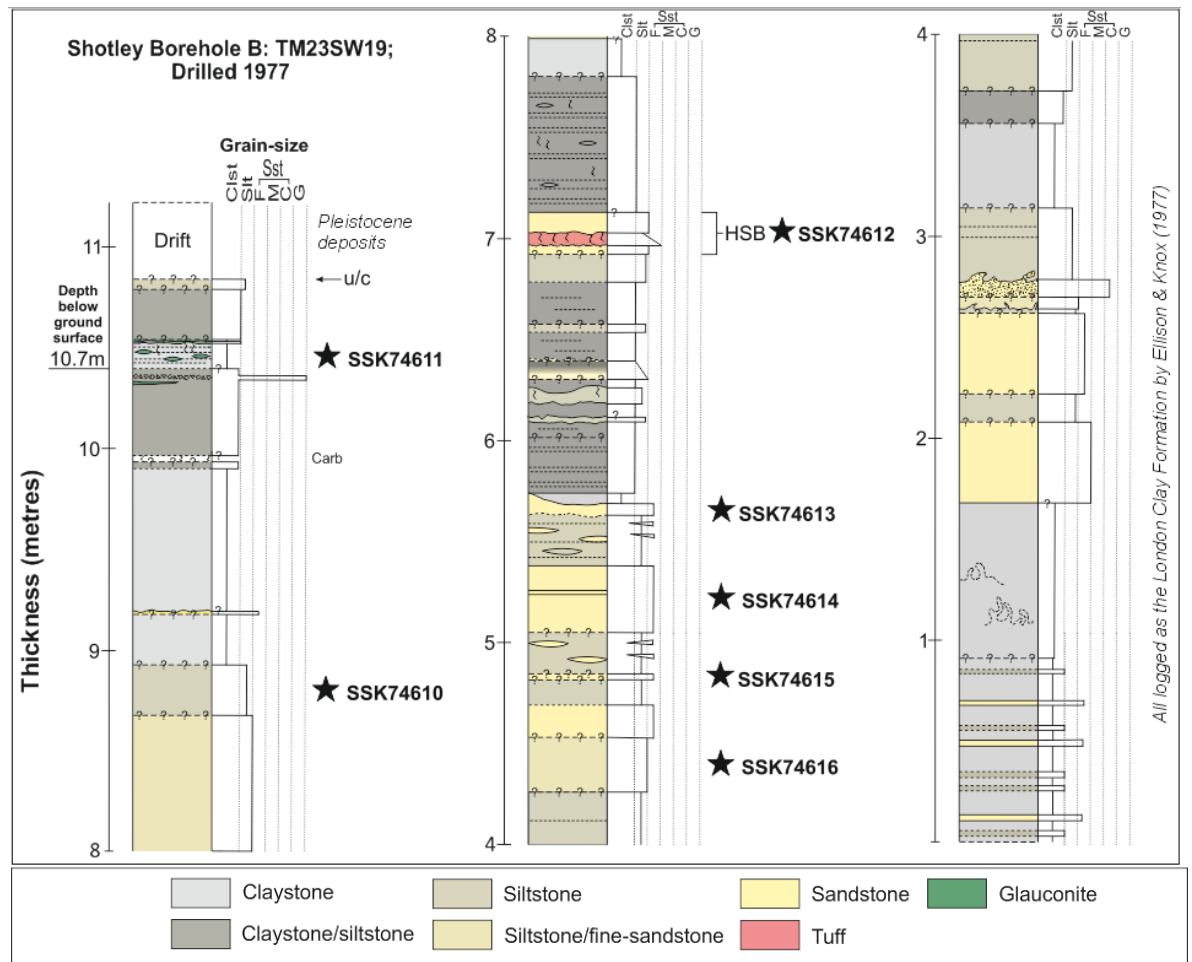


Figure 5-17 Lithological log and sample locations of Shotley Borehole B. 11 m of core were logged at the BGS core-store. The section contains interbedded siltstones and claystone with sandstones reaching medium-sand grade. This entire section was logged as the London Clay Formation by Ellison & Knox (1977); however, this nomenclature has since been superseded by subsequent subdivisions of the strata. Based on observation of the WM during the current study, a proposed position for the base of the WM is given (approximately around four metres from the base of the core). The WM may terminate as an erosional unconformity with an overlying unit of Pleistocene drift deposits. The HSB is identified where a bedded carbonate-cemented hard-band with characteristics identical to those observed in the field at Harkstead and Levington-Nacton.

In general, the material of the Shotley B borehole is composed of interbedded claystone, siltstone and sandstone, with rare limestone stringers and calcite-cemented concretions. The HSB is easily identified as being darker with a characteristic change in colour to a paler brown/grey half way through, coinciding with a greater abundance of trace fossils (burrows). Here, the HSB is a calcite-cemented interval that displays all the same features as those observed in Harkstead, Levington-Nacton and Wrabness, including a normal-graded sandstone bed, containing igneous or pyroclastic clast-types, and heavy bioturbation towards the top of the unit.

Initial descriptions of this borehole by Ellison & Knox (1977) allocated the entire succession to the London Clay Formation. It was important to try to locate the WM within this material to allow comparison of the core with the field localities. The HSB can be used as a marker unit within the WM, as shown by its lateral continuity across all of the field-localities. The presence of the HSB was therefore taken to be a direct indication of the WM in the Shotley B borehole, and occurs *ca.* 7 m from the base of the core (Figure 5-17; Knox & Ellison 1979). Elliott (1971) stated that the HSB can be found 6-7 m above the base of the London Clay Formation (which is now the base of the HF), at Harwich. This is supported by the observations made by Ellison and Knox (1979) and the observations made in the present study (Figure 5-17). Ellison et al. (1994) describe the contact between the Harwich Formation and the overlying Walton Member of the London Clay Formation as:

‘A stratigraphic discontinuity...In proximal areas this is marked by a change from glauconitic arenaceous sediments to silty clays and clayey silts, generally with a thin basal glauconitic and pebbly bed. In distal areas there is usually a thin bed of silty sand of the HF, which is overlain by a sandy clay’

A relatively thin (*ca.* 13 cm) interval containing pebbles, associated with green discontinuous beds of glauconite, can be observed *ca.* 10.4 m above the base of the core, overlain by claystone. These beds may represent the upper boundary of the WM, where it is directly overlain by the Walton Member of the London Clay Formation. This would therefore represent an unconformity, as the remainder of the HF appears to be absent (Table 5-2).

It may therefore be assumed that Shotley Borehole B represents a section through the entire WM. An erosional contact exists at the top of the borehole where the fine-grained sedimentary rocks of the WM are overlain by the red coarse-sands of Pleistocene drift (Figure 5-17). This would also suggest that the Walton Member is only *ca.* 80 cm thick in the Shotley Borehole, where it is unconformably overlain by coarse red sands most likely of Pleistocene age (Figure 5-17).

More fine-scale details of the stratigraphy can be identified within this core, when compared with the highly weathered exposures observed in the field. This

provides a more informative assessment of the lithologies, that could not be achieved in the field, and confirms that there are multiple lithologies present in the WM. Pale grey and darker grey/brown interbeds, that are the main characteristic of the WM in the field, are not present in the borehole core (Figure 5-18). There does not appear to be any repetitive changes in the grain-size or grain-types observed throughout the core that could be used to explain the interbedded pale grey and dark grey/brown strata observed in the field (e.g. Figure 5-17). Petrographical analysis of field and borehole samples are needed to investigate whether the pale-grey bands observed in the field are truly representative of lithological changes, for example, representing tuffs (e.g. Knox & Ellison 1979; Jolley 1996); this data will be detailed in subsequent sections of this chapter.



Figure 5-18 Annotated view of the Shotley Borehole B core, showing a lack of any distinct interbedding like that observed at exposures in the field.

5.6 Microscopy

5.6.1 Reflected and optical light microscopy

All of the described localities are taken to be representative of sections through the WM. The HSB forms a marker that can be used for correlation between the sites to interpret the relative stratigraphic level at which the observations are made (Figure 5-8). The location of each of the field-samples relative to each other within the stratigraphy is given in Figure 5-19. The locations of samples from the Shotley Borehole B are given in Figure 5-17.

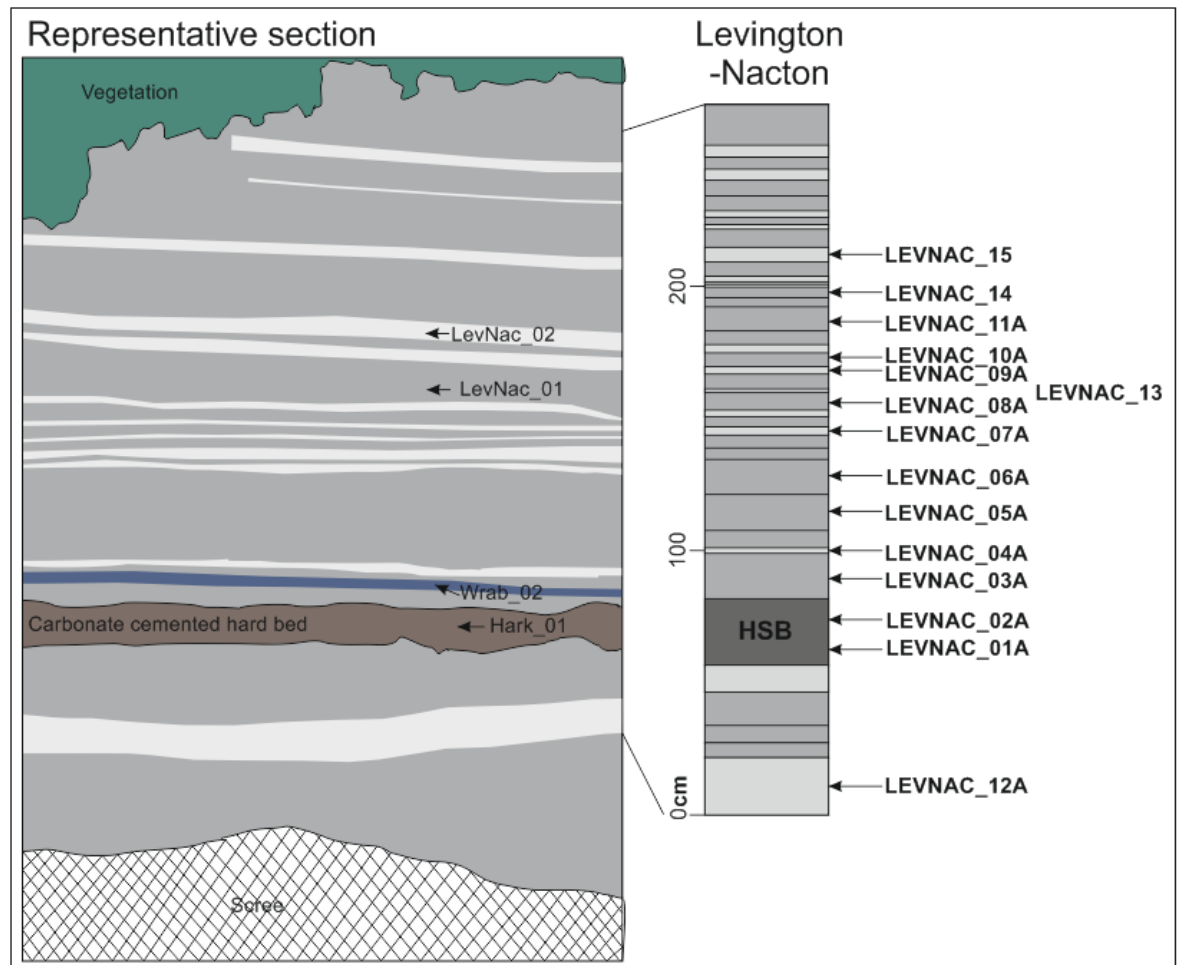


Figure 5-19 Relative stratigraphical positions of each sample described in the text. Sample HARK_01 and HARK_HB were collected from the same position as LEVNAC_01A but from the HSB in Harkstead. Colours are representative of the colour of the rock observed in the exposures, for example WRAB_02 is from the blue coloured claystone above the HSB.

Below, the general petrological characteristics of the lithologies are described. Quantitative data, regarding grain shapes, grain-size distribution and mineralogy, will be discussed subsequently (Section: 5.6 and 5.6.2), along with SEM-derived image analysis data (Section: 5.7).

5.6.1.1 Wrabness Blue Band: WRAB_02

WRAB_02 was collected from the blue band exposed above the HSB at the base of the cliffs at Wrabness (Figure 5-1). Under reflected light (RL), the sample has a fine-grained, granular appearance (Figure 5-20a), indicating that this unit is *not* solely composed of clay-sized material. Pyrite can be identified due to its high reflectivity and is present as circular and amorphous framboids (Figure 5-20b). In the field, this lithology appears to consist only of a blue claystone and, although a large amount of very fine-grained material is present, there is

also a significant abundance of coarser grains. Light is not transmitted through these thick-sections, therefore only reflected light microscopy could be used for study of this sample prior to SEM analysis (Figure 5-20).

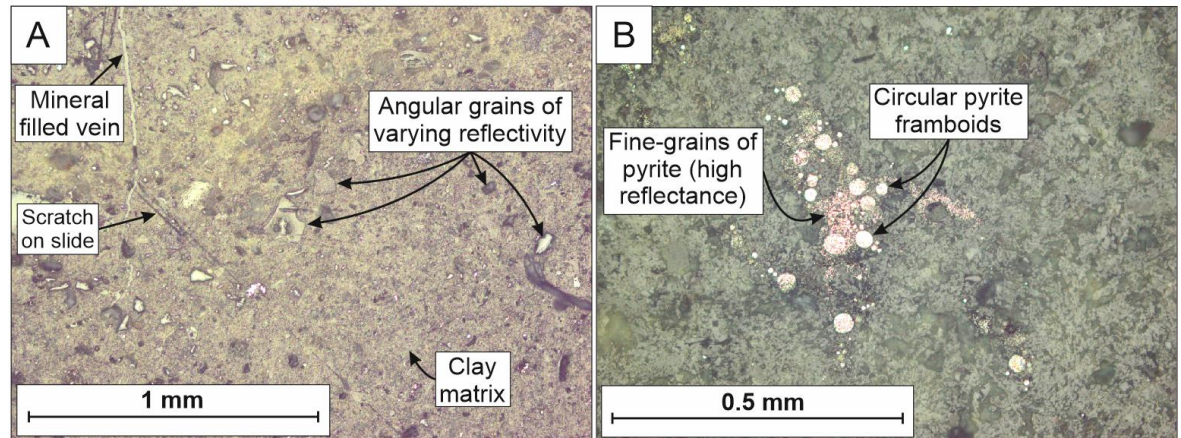


Figure 5-20 Nature of the Wrabness Blue Band (WRAB_02), as seen under RL. A) Clastic nature of thick-section, with angular grains of various types as shown by their different levels of reflectance. In general, the sample is predominantly comprised of clay, which forms a matrix around the coarser silt-size grains. B) Circular framboidal pyrite, associated with fine grains of pyrite, with a bright reflectivity, are common throughout the sample.

5.6.1.2 Harwich Stone Band (HSB): HARK_01, HARK_HB, LEVNAC_01A, LEVNAC_02A

All of the samples from the HSB contain fine-sand size grains of various shapes and compositions, including grains of quartz, plagioclase, and chlorite, in addition to crystalline igneous clasts and, glassy and altered pyroclasts (Figure 5-21). The HSB forms a characteristic hard-band due to the presence of a calcite cement, which can easily be identified in all of these samples (Figure 5-21a-b).

A sharp contact can be seen in some of the samples (HARK_HB & LEVNAC_01A), where a calcite-cemented siltstone is in contact with a coarse-grained calcite-cemented clastic bed that is predominantly composed of angular, vesicular igneous clasts. This volcanic-rich clastic unit is normal-graded and contains both angular vesicular and non-vesicular pyroclasts (Figure 5-21). These pyroclasts have different colours, orange to black (Figure 5-21a, d, e), which may reflect differences in their chemical composition, or variation in the levels of alteration that they have experienced.

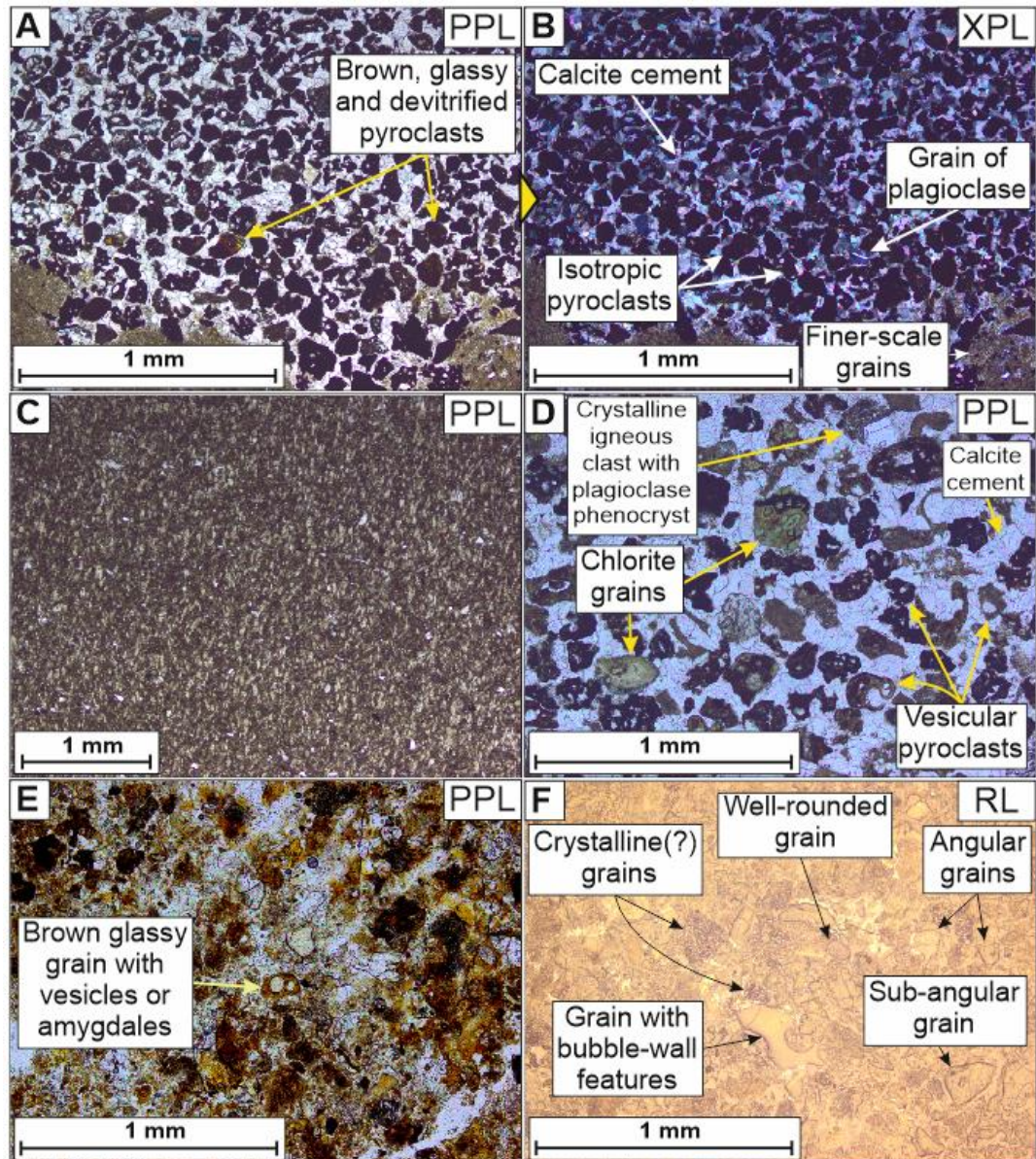


Figure 5-21 Main features observed in the HSB. A) PPL image of the base a calcite-cemented bed composed predominantly of black, opaque, vesicular and non-vesicular pyroclasts (HARK_HB). B) XPL view of image A, shows that the volcanic clasts are isotropic. Angular grains of plagioclase can also be identified under XPL. C) General character of a very fine-grained bed that lies below the volcanic-rich bed of the HSB. This fine-grained bed also has a calcite cement (HARK_HB). D) PPL image of coarser-grained clasts at the base of the volcanic-rich bed. In addition to volcanic clasts, this bed also contains a range of angular grains of green chlorite, and crystalline igneous clasts. Most of the clasts in this bed form floating clasts that are completely surrounded by calcite cement (LEV_NAC_01A). E) Brown/orange vesicular pyroclast with a glassy appearance under PPL (HARK_01). F) RL can be used to view grain-morphologies in more detail. A range of clast-morphologies can be identified, ranging from angular to well-rounded. Some clasts appear to have pyroclastic morphologies such as bubble-walls (HARK_01).

Some bioturbation, in the form of burrows, occurs throughout these samples (Figure 5-22). Bioturbation is particularly obvious in LEVNAC_02A, where it has caused mixing of different units, which has led to some homogenisation of the sediment (Figure 5-22a-b). Some coarser calcite grains, representing fragments

of body fossils or micro-fossils, can be identified in some areas of the HSB (Figure 5-22c-d); these form a very minor component of the sediment, and are rare in occurrence. It is not clear whether the fossil fragments are from pelagic or benthic organisms, or, whether these were micro-organisms or larger creatures. However, the presence of these fossil fragments alongside the presence of heavily bioturbated sediments shows that this area was inhabited by organisms during deposition of the WM (e.g. Obst et al. 2015).

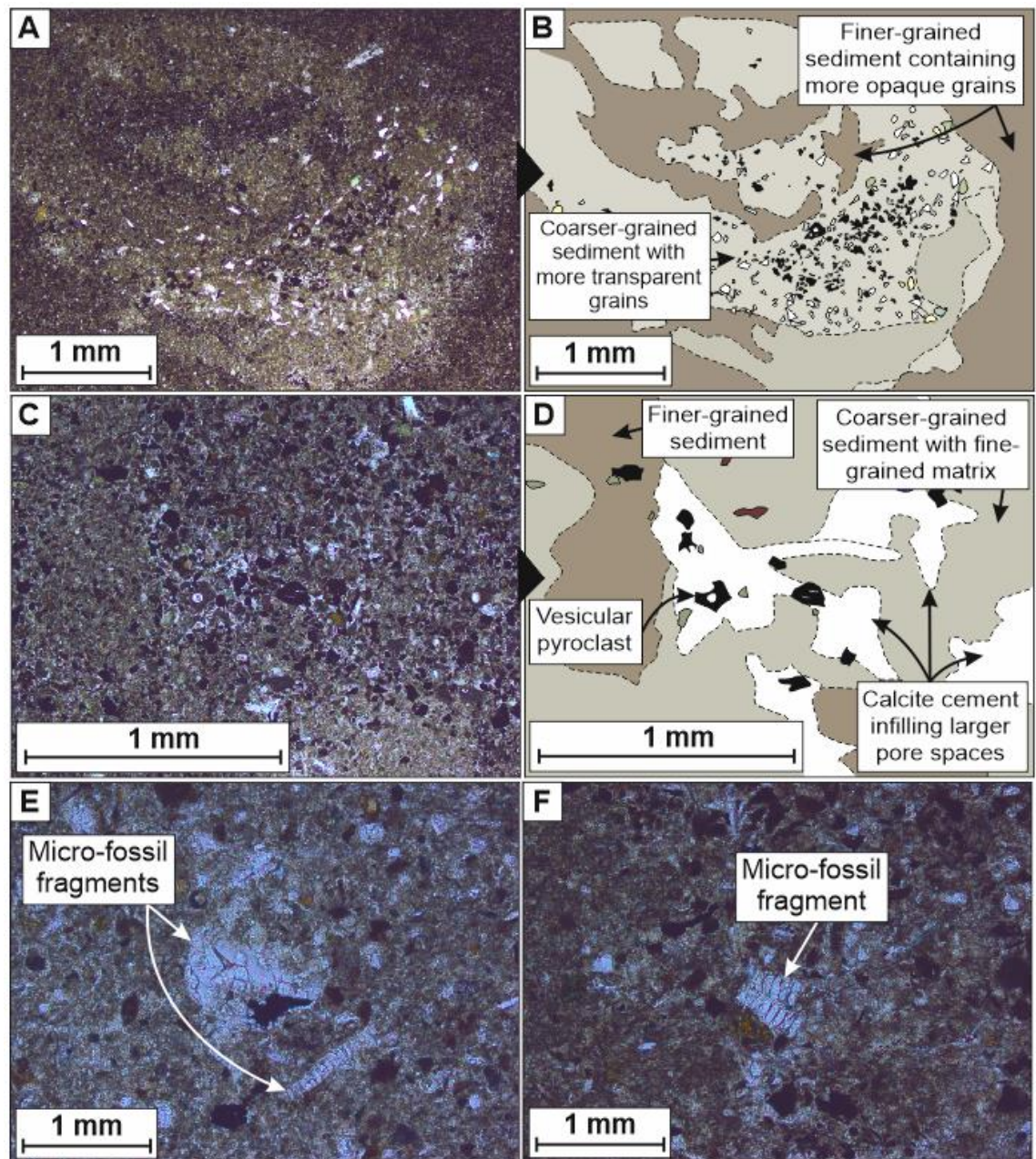


Figure 5-22 Effects of bioturbation (burrowing) seen within the HSB in thin-section. A-B) Bioturbation acts to mix different layers of sediment together when an organism burrows into relatively soft sediment (e.g. Rindsberg 2012; LEVNAC_02A). In this example, fine-grained sediment with dark minerals has been mixed with coarser-grained sediment

comprised of more transparent minerals, such as, quartz and calcite. C-D) Further evidence of bioturbation and the mixing of sediments in sample LEVNAC_02A. A vesicular pyroclast can also be identified in this image, along with a calcite cement. E-F) Calcite micro-fossil fragments observed in the finer-grained volcanic-poor sediment within the HSB that lies directly below the volcanic-rich unit (LEVNAC_02A).

5.6.1.3 Pale grey and dark grey bands: LEVNAC_01-02, LEVNAC_03A-LEVNAC_15

Optical microscopy shows that deposits above and below the HSB are composed of a range of grain sizes from fine silt to fine-sand; these grains are predominantly angular (Figure 5-23, Figure 5-25), and are predominantly of quartz. Fragments of unidentified micro-fossils form a minor component of the sediments (Figure 5-24).

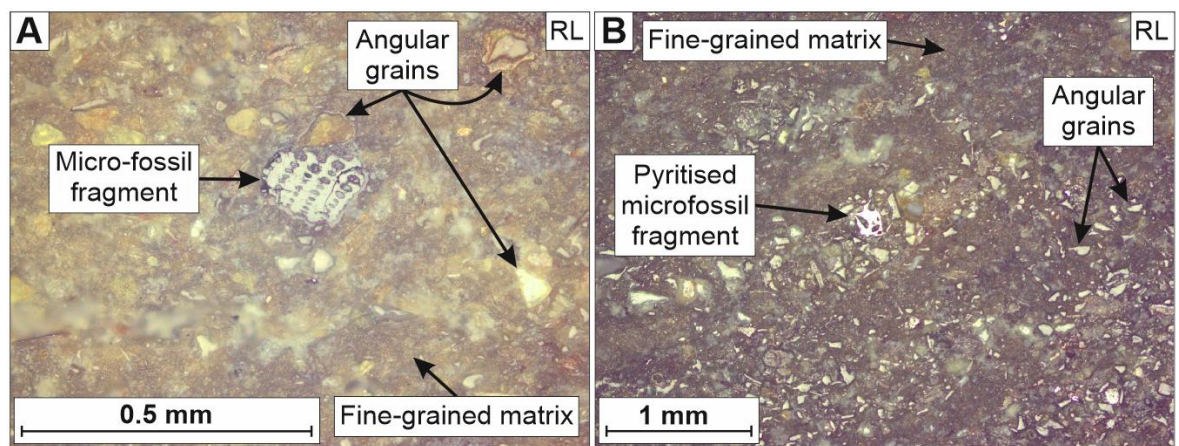


Figure 5-23 Fragments of micro-fossils observed in RL in LEVNAC_02. These fragments are less than 0.5 mm across, but may be fragments of a larger organism. It has not been possible to identify these specimens in any greater detail.

The relatively homogeneous character of all of the samples may be due to bioturbation (Figure 5-24; Obst et al. 2015), but may also be partially due to the original nature of the deposits. It is difficult to distinguish between the extent of bioturbation and the original character of the deposits as bioturbation can overwrite the original depositional features of the sediment (e.g. Knox & Ellison 1979; Obst et al. 2015).

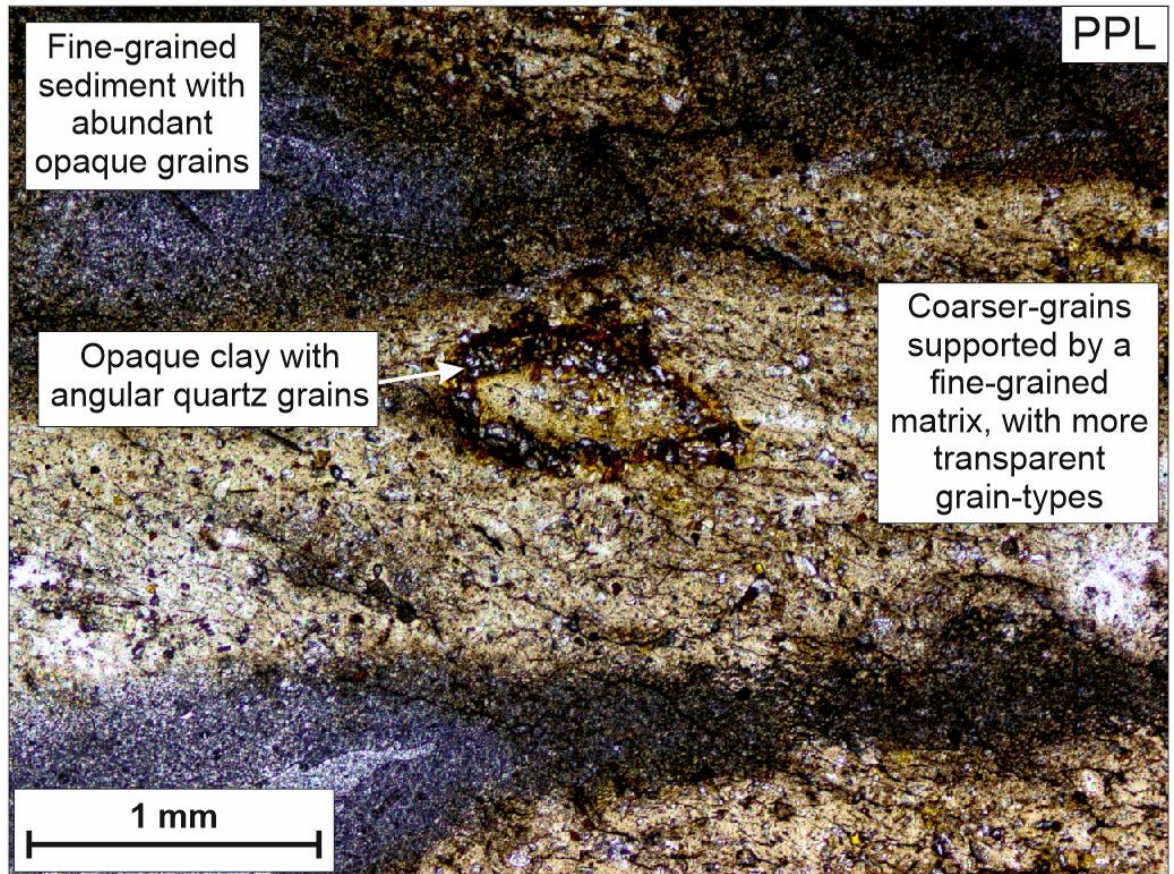


Figure 5-24 Bioturbation is common throughout the thin-sections from beds above and below the HSB. This image, from LEVNAC_01 shows the range of different grain sizes, from clay/silt to fine sand, with some areas containing more dark grains and some containing coarser grains of quartz. Mixing of these different sediment types is most likely due to bioturbation, during which burrowing organisms can mix/homogenise relatively soft sediments (e.g. Rindsberg 2012).

Abundant glass pyroclasts occur in a dark grey band (LEVNAC_14A) (Figure 5-25). This bed is predominantly composed of isotropic, mostly transparent, vesicular pyroclasts with abundant bubble wall pyroclasts (Figure 5-25), which contrasts to the black/opaque pyroclasts within the HSB at Harkstead and Levington (Figure 5-21).

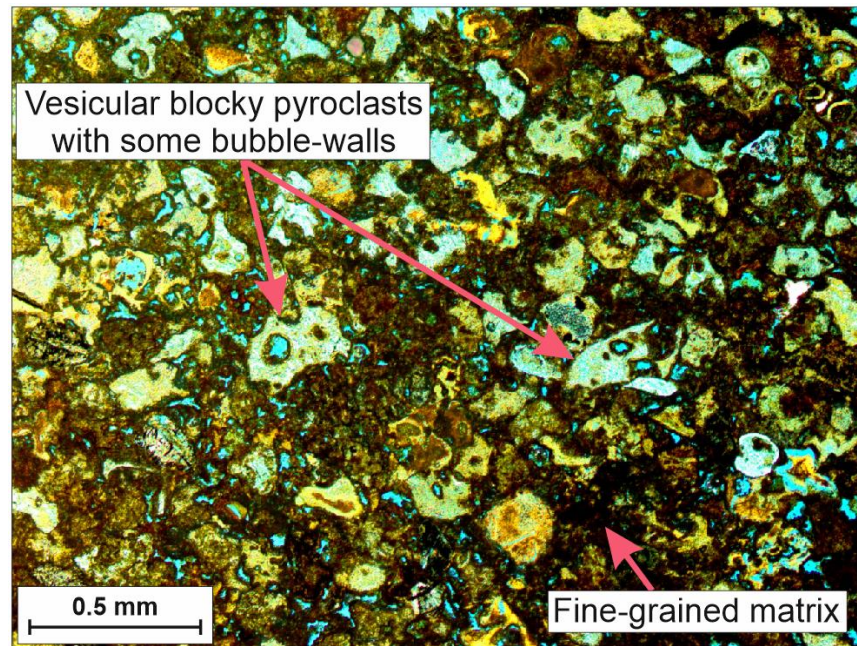


Figure 5-25 Abundant pyroclasts seen within a normal-graded bed within LEVNAC_14A. . This sample comes from a dark grey band from the WM exposed between Levington and Nacton. The pale, transparent nature of the pyroclasts in this sample suggests that they are of a different chemical composition to the dark brown/black pyroclasts identified in the HSB. Blue resin was used in the making of this thin section, therefore, blue areas represent poor space or holes in the slide.

5.6.1.4 Shotley Borehole B

Thin-sections from the Shotley Borehole B are composed predominantly of angular quartz grains of silt to fine sand grade, and clay (Figure 5-26). Laminations within the sediments can be identified where dark clay contrasts with the transparent quartz grains of adjacent coarser-grained units (Figure 5-26a-c). Some samples contain localised, seemingly hollow, rounded grains which may be micro-fossils (Figure 5-26e).

Sample SSK74612 was taken from the HSB and contains an abundance of opaque coarse- to fine-sand size grains of igneous origin, including pyroclasts and crystalline igneous clasts (Figure 5-26d). This bed also contains a well-developed calcite cement which is not seen in any of the other borehole samples (Figure 5-26). The nature of the HSB is directly comparable to the observations made of HSB samples from HARK_01, HARK_HB, LEVNAC_01A and LEVNAC_02A (Figure 5-21).

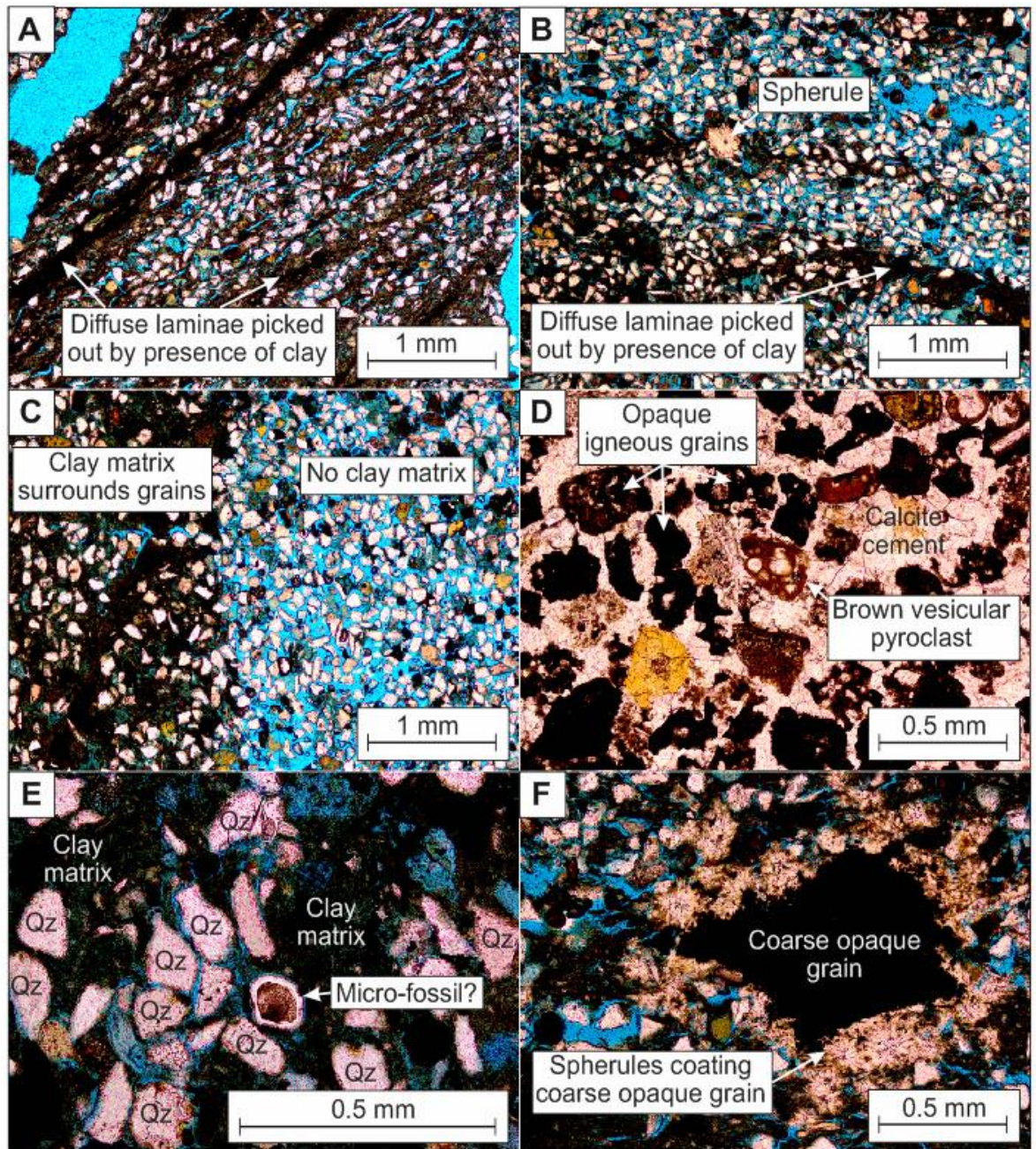


Figure 5-26 Main features observed in thin-sections from the Shotley Borehole B. A-B) Diffuse laminations can be picked out by thin layers of clay which are opaque compared to the rest of the sediment, SSK74615 and SSK74616 respectively. Image B also includes a spherule of gypsum. C) Contrasting thin beds within SSK74613, where some areas have a clay matrix which is absent in adjacent units. D) Brown vesicular and opaque igneous clasts observed at the base of the HSB volcanic-rich unit in SSK74612. E) All of the samples (except SSK74612) are comprised of angular to sub-rounded quartz (Qz), sometimes with a clay matrix and occasional micro-fossils (SSK74613). F) Coarse opaque grain surrounded or coated by spherules (SSK74616).

Samples SSK74613, SSK74615 and SSK74616 contain radiating spherules of gypsum that commonly surround coarser-grained opaque clasts (Figure 5-26f). The gypsum crystals have pointed edges where they have grown into the pore-space, and, locally, completely surrounds finer silt-sized grains, suggesting that

the gypsum grew within the sediment after deposition (e.g. Charola et al. 2007). It is not clear at this stage, whether the gypsum grew *in situ* shortly after deposition of the surrounding sediment, or whether it grew much later-on, for example, after the core was retrieved (Charola et al. 2007), and may therefore be unrelated to the Early Eocene deposition of the WM.

5.6.2 SEM features

SEM analysis allows a more detailed investigation of the mineralogy and textural characteristics of the samples, together with the acquisition of compositional data.

5.6.2.1 *Wrabness Blue Band: WRAB_02*

In general, the blue band at Wrabness is predominantly composed of clay minerals; in some areas diffuse and discontinuous beds of angular to well-rounded silt-grade material occurs within a clay matrix (Figure 5-27). Uncommon well-rounded fine-sand size grains are also present (Figure 5-27b), along with a patchy carbonate cement (Figure 5-27b). Pyrite is present as framboids associated with very fine grains of cubic pyrite (Figure 5-28a). Pyrite can also be seen replacing micro-fossils (Figure 5-28d).

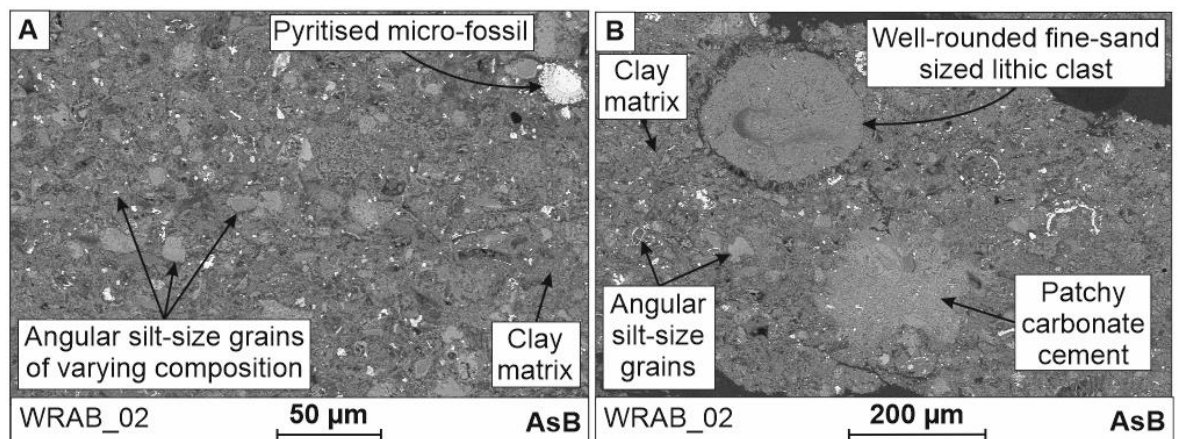


Figure 5-27 AsB SEM images showing the main features of the clastic units of WRAB_02. A) Angular silt-sized grains and pyritised micro-fossils are present within a clay matrix. B) A well-rounded fine sand sized lithic clast is present alongside angular silt-size grains, and surrounded by a clay matrix and carbonate cement.

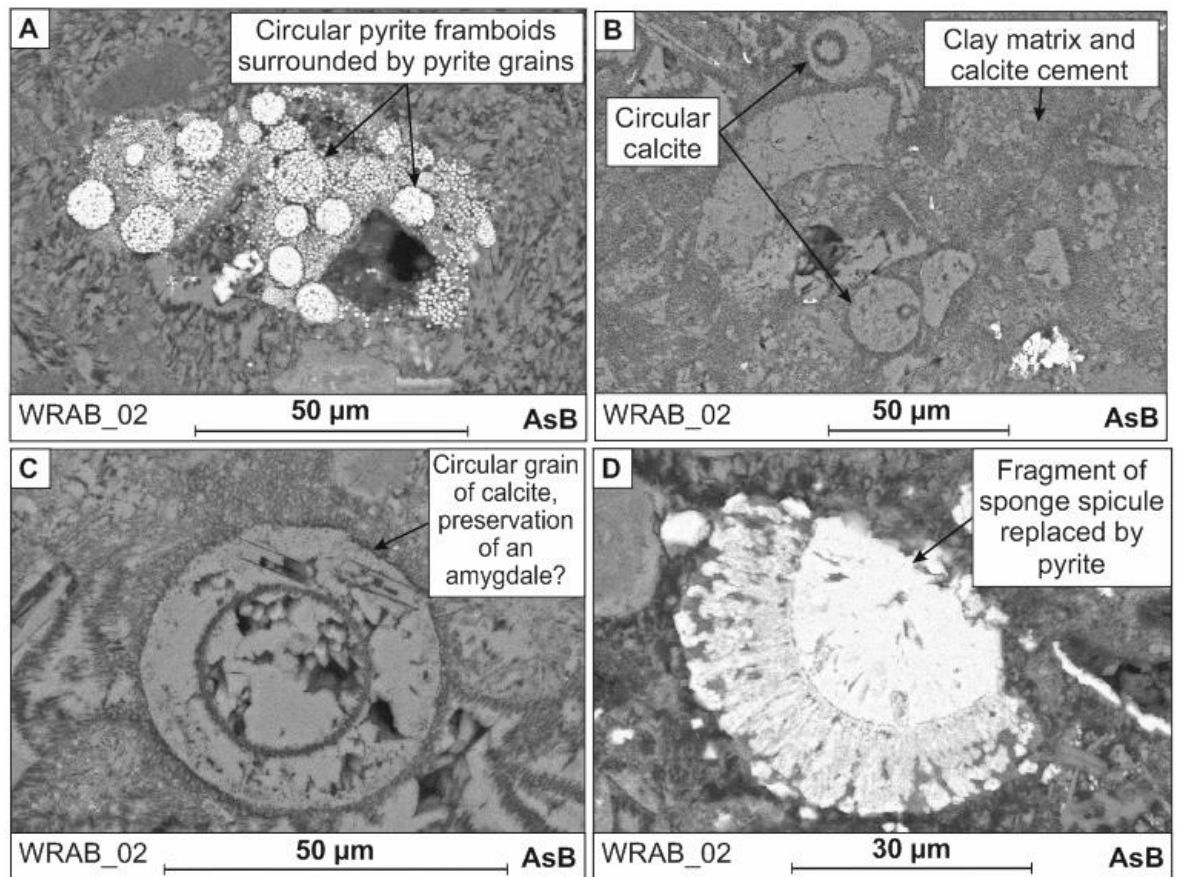


Figure 5-28 AsB SEM images of the varying forms of pyrite along with circular (in 2D) grains of calcite which may represent the preservation of amygdales. A) Pyrite framboids of various sizes, associated with fine grains of cubic pyrite. B) A range of different shaped calcite clasts within the deposit, including circular sections through clasts and sub-angular to amorphous clasts of the same composition C) Detail of near-perfectly circular section through a calcite clast. This may represent calcite replacement of a microbial cyst (Gradstein et al. 1992; Martín-González et al. 2009), or preservation of an amygdale from an igneous clast which is no longer present. D) Possible pyritised fragment of sponge spicule.

Features resembling pyroclasts are present locally within the sample (Figure 5-29). These have bubble-wall (Figure 5-29a, c), and blocky vesicular (Figure 5-29d) morphologies, and are surrounded by a clay matrix, in addition to a calcite cement. The composition of these clasts no longer represents the original volcanic material but has instead been replaced by calcite.

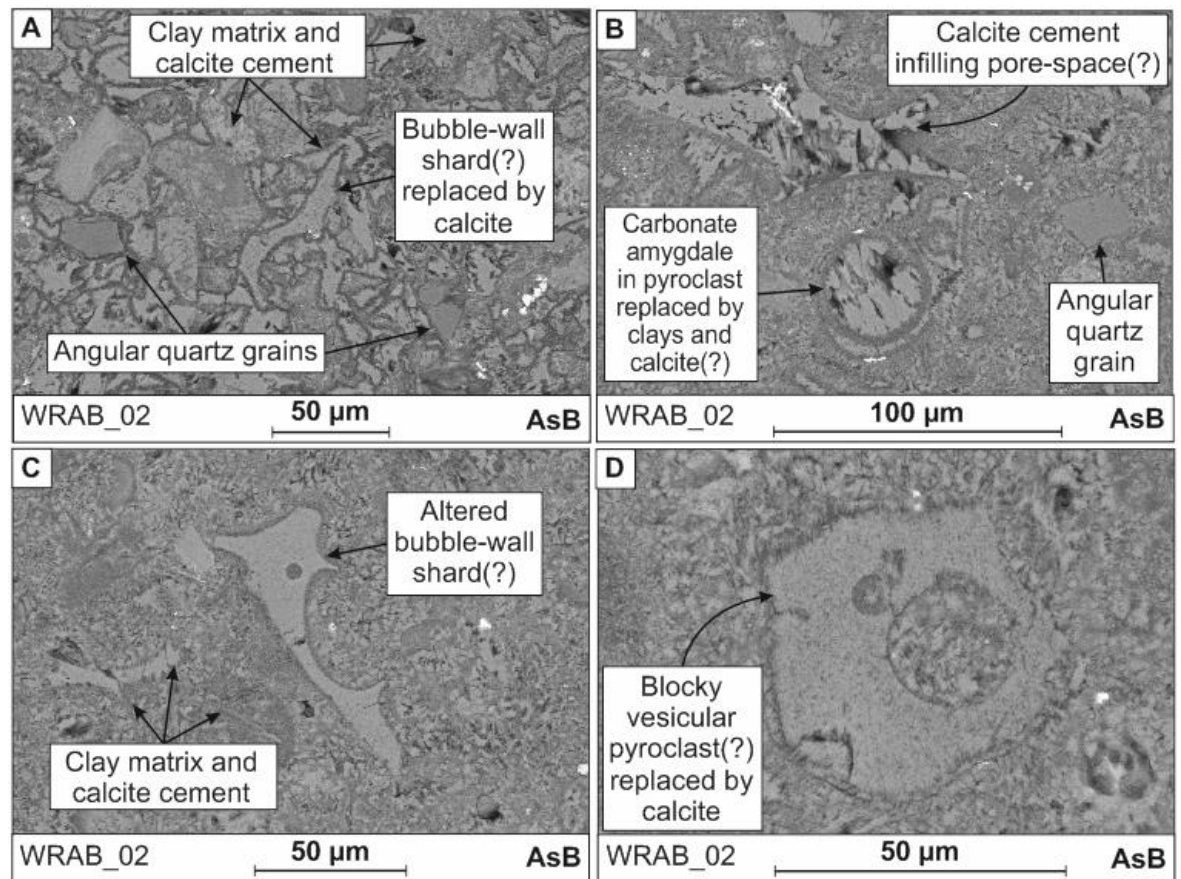


Figure 5-29 AsB SEM images showing some of the interpreted pyroclasts observed within WRAB_02. A) Granular appearance of the sample with a bubble-wall shard, in which the original volcanic glass has broken down and eventually been replaced by calcite. Angular quartz grains are also present, surrounded by a clay matrix and calcite cement. B) Calcite cement infilling an original pore-space, or an angular bubble-wall shard replaced by calcite. Circular calcite may represent preservation of an amygdale in which the surrounding pyroclast has been removed by alteration. C) Vesicular bubble-wall shard surrounded by amorphous clay matrix and a calcite cement. D) Vesicular blocky shard replaced by calcite.

The clay matrix with calcite cement and the interpreted pyroclasts have the same overall composition. In hand-specimen, the Wrabness Blue Band has the consistency of clay (Figure 5-9); however, SEM analysis shows that it contains a calcite cement associated with its clay matrix (Figure 5-29). The rock has a completely different character to that of the calcite-cemented HSB; this may be due to the high clay content that is observed in the WRAB_02 sample, which is not found within the HSB samples (see section 5.6.2.2). The presence of a high abundance of clay minerals may have inhibited the calcite from forming a strong interlocking network of crystals in the cement, which is likely responsible for the characteristic hardness of the HSB.

5.6.2.2 Harwich Stone Band (HSB): HARK_01, HARK_HB, LEVNAC_01A, LEVNAC_02A

The HSB contains a calcite cement that can be identified easily in most sections (HARK_HB, LEVNAC_01A, LEVNAC_02A; Figure 5-30), but appears to have been removed by dissolution in HARK_01 (Figure 5-31, Figure 5-32). It is possible that the calcite cement of this sample was removed during the thin-sectioning process. In the field the HSB is generally cemented throughout (see Section 5.5.1).

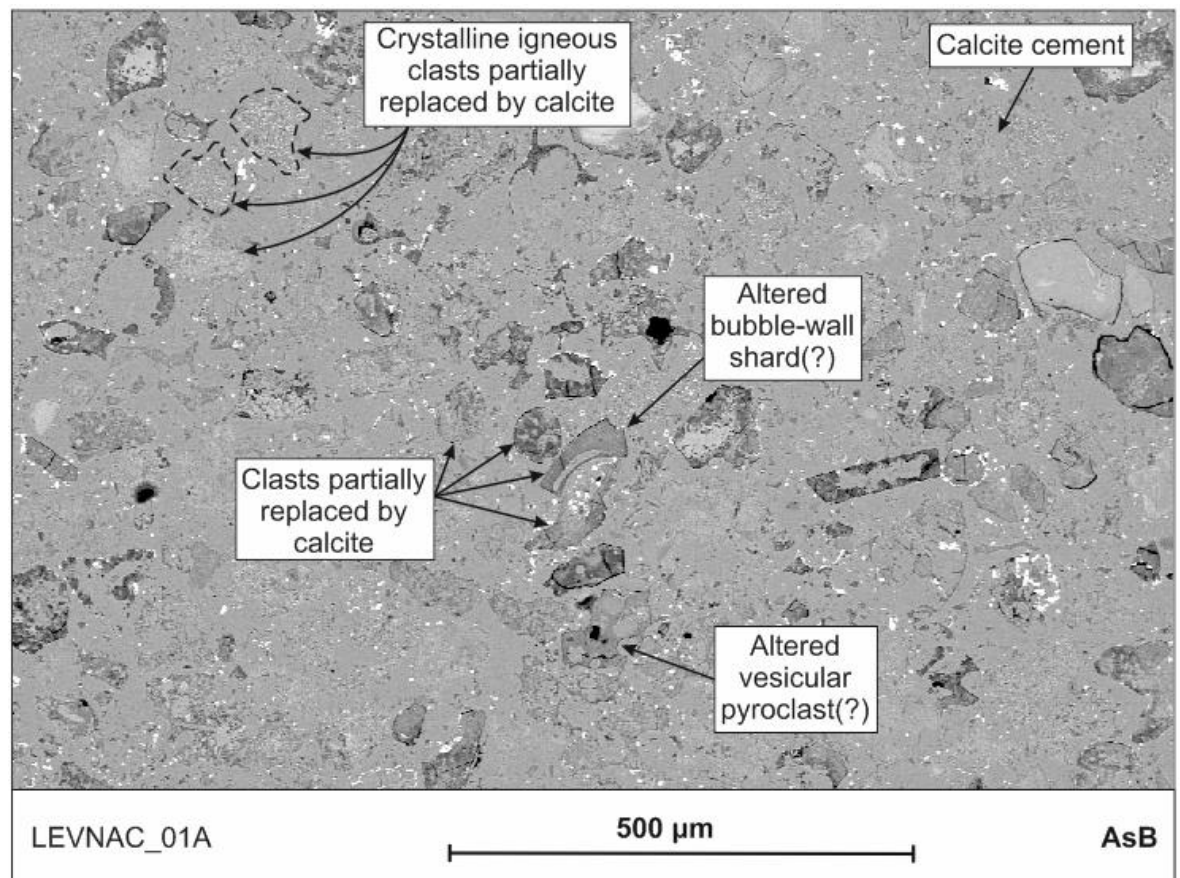


Figure 5-30 AsB SEM nature of the calcite cement -dominated HSB with numerous igneous clast-types from Levington/Nacton (LEVNAC_01A). Many of the primary features of the deposit have been partially or almost completely replaced.

The base of the HSB is composed of uncommon angular quartz grains, along with chlorite, feldspar, and small amounts of pyrite; in general, this unit is predominantly composed of calcite cement. Above this lies a normal-graded bed with abundant igneous clasts, including, pyroclasts and crystalline igneous clasts, in addition to minor amounts of angular quartz (Figure 5-30). The pyroclasts display a range of morphologies, including blocky (Figure 5-31c-d) and

bubble-wall pyroclasts (Figure 5-31a-b, Figure 5-32a), and are commonly vesicular (Figure 5-31c-d, Figure 5-32). Irregular-shaped vesicular pyroclasts have rounded edges, which may have been caused by abrasion of angular edges during reworking (Figure 5-32c-d). In contrast to this, most of the pyroclasts are angular (Figure 5-31, Figure 5-32a-b).

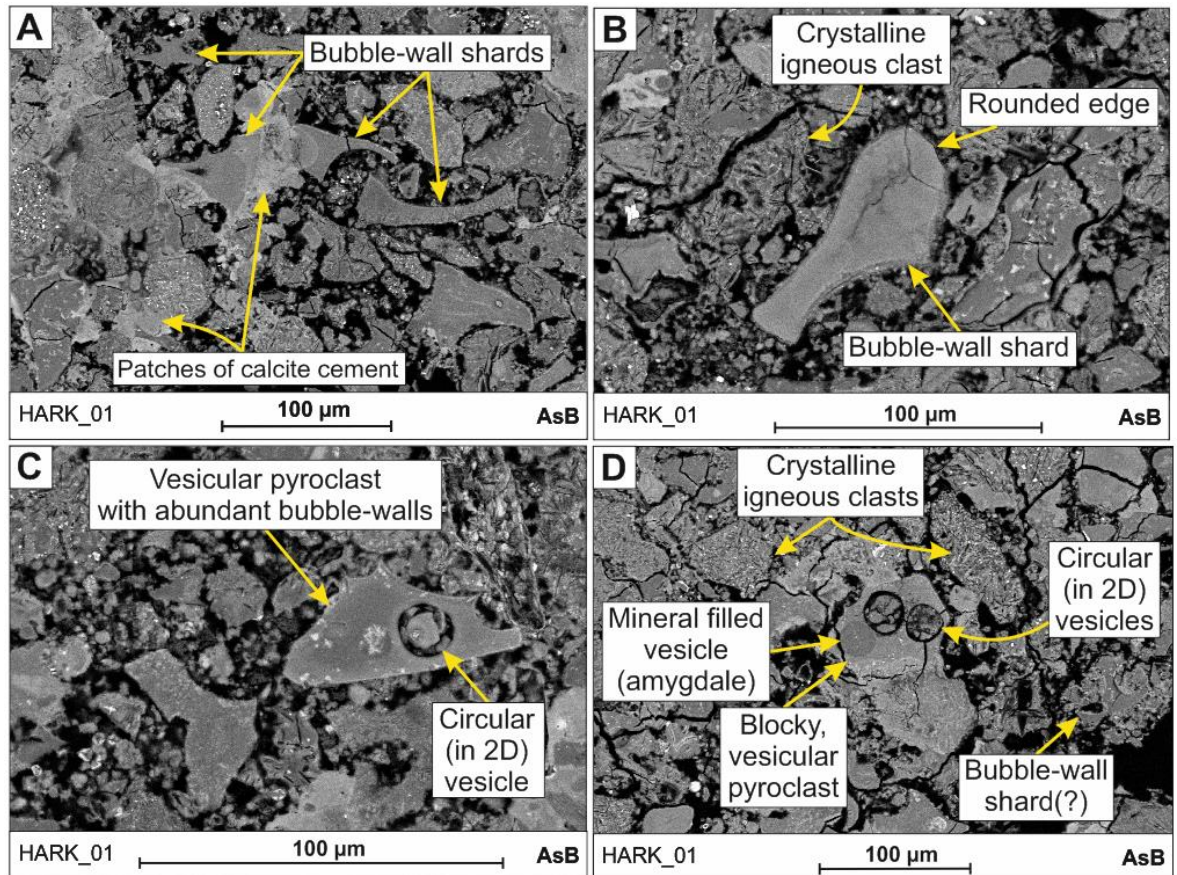


Figure 5-31 AsB SEM images of non-vesicular and vesicular pyroclasts within the HSB of HARK_01. A) Multiple bubble-wall pyroclasts can be observed within the sample; here they are associated with a patchy calcite cement. The calcite cement may have been partially removed during thin-sectioning, and was likely present throughout the sample. B) A bubble-wall shard with a rounded edge and a rounded crystalline igneous clast. C) A vesicular blocky pyroclast with abundant bubble-walls. The vesicle is circular in cross-section. D) Rounded crystalline igneous clasts are present alongside blocky vesicular pyroclasts and bubble-wall pyroclasts. The vesicles in this pyroclast are circular in cross-section, and one is filled by a chlorite(?) amygdale.

The shape of vesicles in the vesicular pyroclasts display a range of morphologies, including: circular (Figure 5-31c-d), and irregular (Figure 5-32d). Some also show evidence of bubble-coalescence, where multiple bubbles have merged shortly before the magma was erupted and the pyroclast quenched (Figure 5-32c).

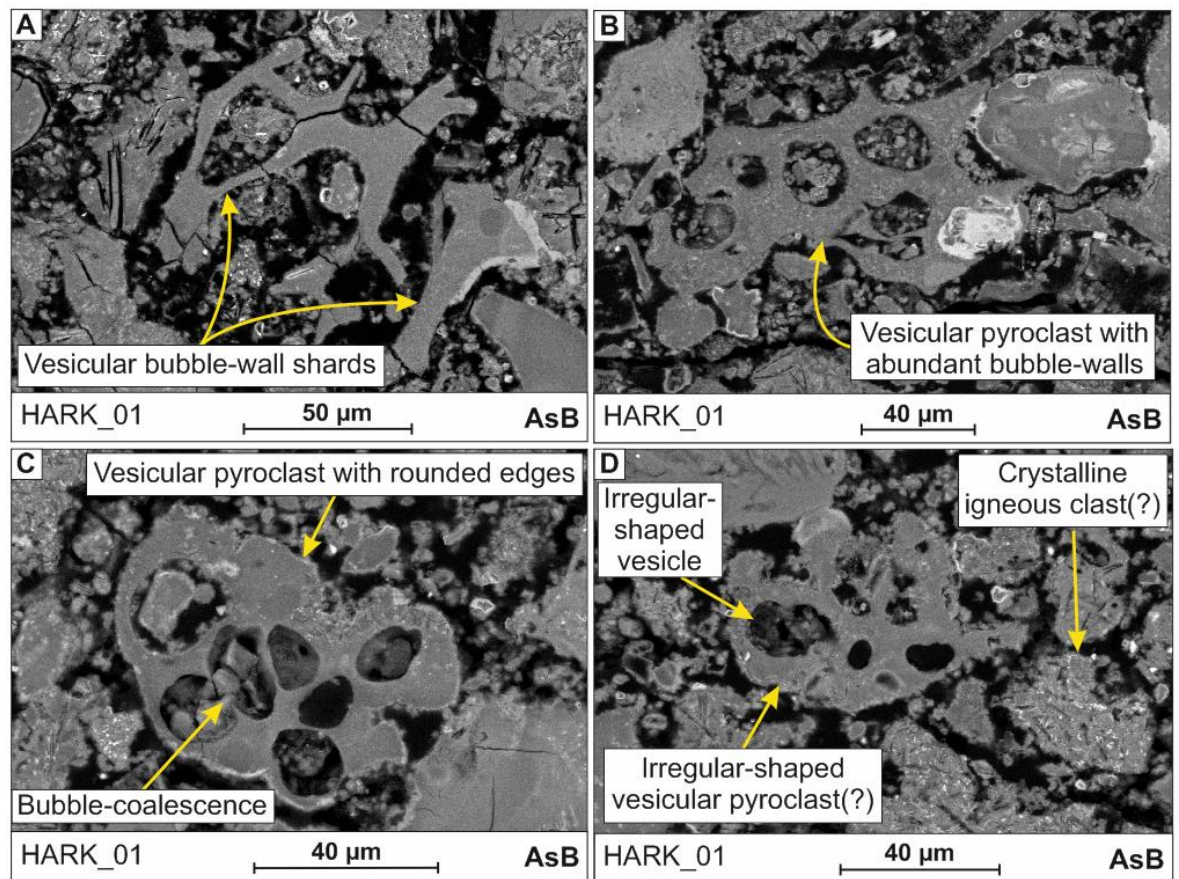


Figure 5-32 AsB SEM images of vesicular pyroclasts of varying morphology observed within the HSB of HARK_01. A) Pyroclast with a high bubble density and irregular-shaped vesicles. B) Angular, blocky pyroclast with individual vesicles and abundant bubble walls around its edge. C) A more rounded, irregularly-shaped pyroclast with some evidence of bubble coalescence. D) An irregularly-shaped pyroclast with irregular-shaped vesicles with evidence of bubble coalescence.

In some samples (HARK_HB, LEVNAC_01A, LEVNAC_02A), there are differences in the abundance of major elements in the pyroclasts can be identified from simple non-quantitative chemical spectra (Figure 5-33). The variation in the abundances of the major elements may be due to the increased mobility of these elements during alteration (Webster et al. 1995; Jeans et al. 2000; Hastie et al. 2007; Kipli et al. 2008), with alteration affecting pyroclasts differently within the same deposit (e.g. Samson et al. 1995). In general, all of the pyroclasts contain spectral peaks in the same major elements (Figure 5-33), and are basaltic in composition.

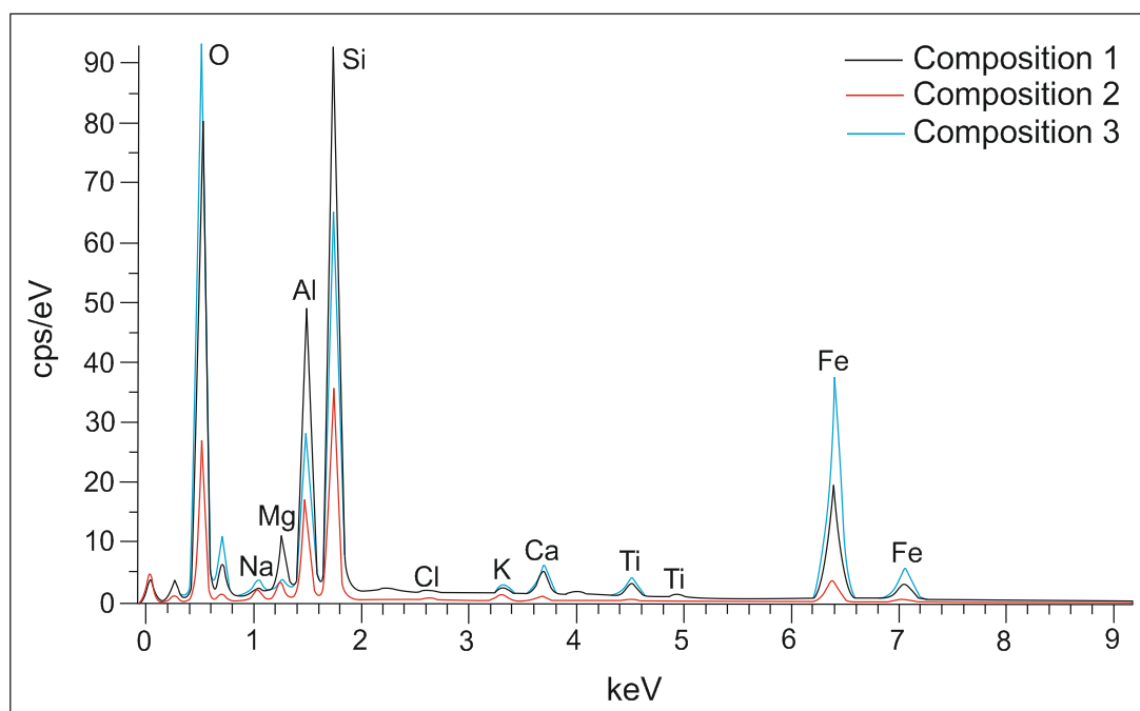


Figure 5-33 Comparison of the representative spectral compositions of pyroclasts from all samples of the HSB (excluding HARK_01). This shows that variations in the abundance of major elements, particularly, Al, Si and Fe, may occur between pyroclasts in these samples, which may indicate some variation in the composition of these. This would need to be investigated further by electron probe or laser ablation techniques which were beyond the scope of the current research (see suggestions for Further Work 7.7). The variations in the peaks of the major elements may also be an aspect of alteration (e.g. Hastie et al. 2007). In general, these spectra show that the pyroclasts are basaltic in composition.

Igneous clasts are less easily identifiable within samples of the HSB from Levington/Nacton; here a calcite cement dominates and many of the original clasts have been replaced (Figure 5-30). Regardless of this more dominant alteration, the same features as those identified within samples from Harkstead can still be observed, for example, vesicular pyroclasts, blocky and bubble-wall pyroclasts and crystalline igneous clasts (Figure 5-30).

Organic material in the form of micro-fossils and woody fragments can be found in the upper section of the HSB (Figure 5-34). Microfossils are not abundant in the samples, but are sometimes found where they have been replaced by amorphous pyrite and pyrite framboids (Figure 5-34). Small burrow-like trace-fossils can be seen in thin-section under an optical microscope (Figure 5-22); however, on the SEM they are too large to be imaged or identified.

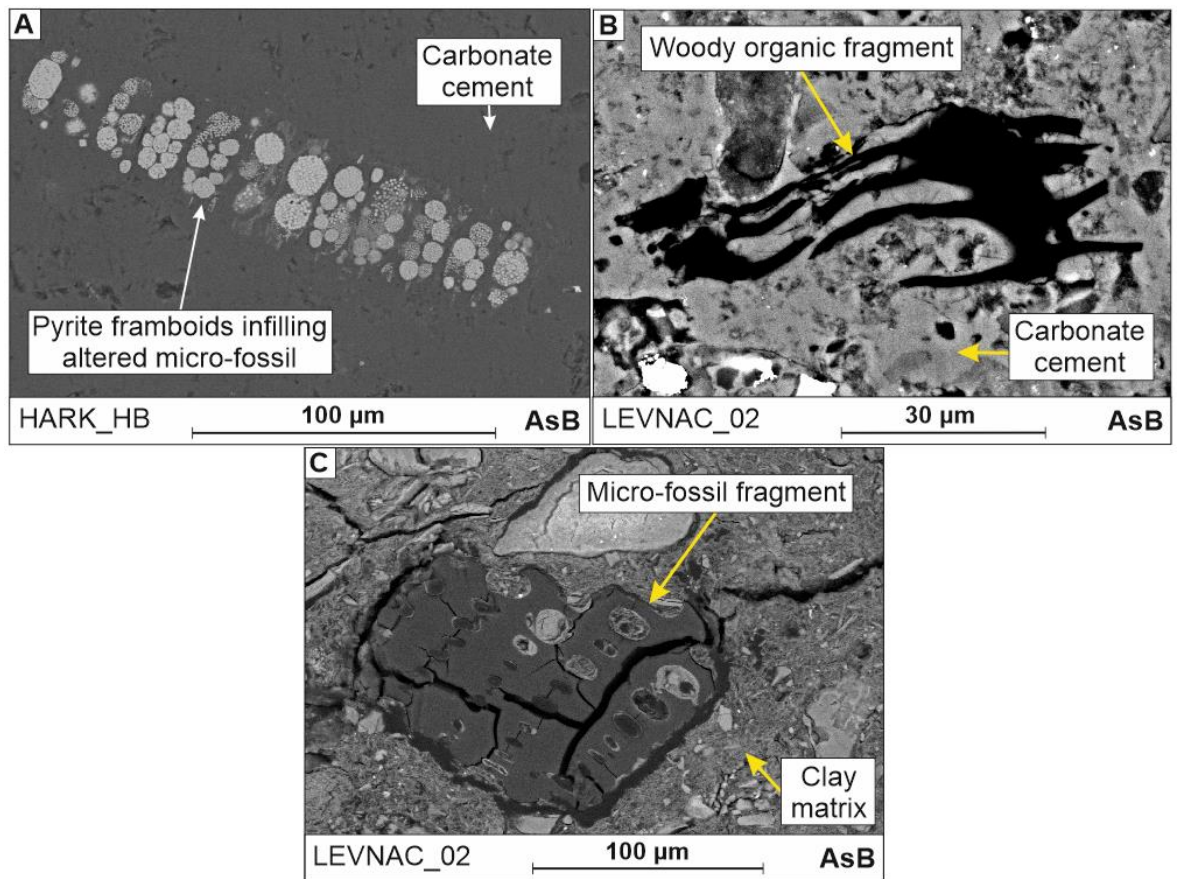


Figure 5-34 AsB SEM examples of organic clasts identified in the upper part of the HSB. A) Micro-fossil (diatom-like), replaced by calcite and filled with pyrite framboids. B) Fragment of woody organic material. C) Micro-fossil fragment surrounded by a clay matrix (same as RL image in Figure 5-23).

5.6.2.3 Pale and dark grey beds: LEVNAC_03A-LEV_NAC_15A

In contrast to the HSB, most of the other samples representative of the pale and darker grey bands within the WM contain only siliciclastic sedimentary (non-igneous) clasts. Most of the samples are dominated by clay minerals, which form a matrix surrounding coarser angular grains of quartz, mica and feldspar, with minor amounts of pyrite, ilmenite, zeolites, chlorite, ulvöspinel, and rutile (Table 5-6). Gypsum can be found as coarse angular crystals within LEVNAC_12A (Table 5-6).

Sample ID	Type	Minerals and clast-types present in sample (x)																							
		Amphibole	Barite	Calcite (mirco-fossils; cement)	Chlorite	Crystalline igneous clasts	Dolomite	Feldspar (Albite)	Feldspar (Labradorite)	Feldspar (Orthoclase)	Fluroapatite	Garnet	Gypsum	Illite	Ilmenite	Kaolinite	Magnetite	Mica (Muscovite)	Pyrite	Pyroclasts	Quartz	Rutile	Stilpnomelane	Ulvospinel	Zeolite (Clinoptilite)
HARK_01	HSB		x	x					x						x		x			x		x			x
LEVNAC_01A	HSB	x		x					x						x				x	x					
LEVNAC_02A	HSB	x													x				x						
LEVNAC_01	Dark	x	x							x					x		x	x				x	x		x
LEVNAC_02	Dark			x															x						
LEVNAC_03A	Dark	x												x	x						x				
LEVNAC_14A	Dark	x	x							x					x		x			x			x		
LEVNAC_09B	Pale									x					x	x					x				
LEVNAC_10A	Pale				x					x							x				x				
LEVNAC_12A	Pale					x				x									x						
LEVNAC_15A	Pale	x								x									x		x				
WRAB_02	Blue Band	x	x	x			x		x		x				x				x	x	x				x

Table 5-6 Mineral and clast-type components of each sample. In general, all of the samples except for those of the HSB and Wrabness Blue Band contain orthoclase feldspar, quartz and muscovite mica. Calcite cement, pyroclasts and labradorite are only observed in the HSB and Wrabness Blue Band. Dark coloured minerals, such as: amphibole, ilmenite, magnetite, pyrite and rutile, appear to be more abundant in samples from the dark grey/brown beds than in pale grey beds.

Angular vesicular and blocky non-vesicular pyroclasts occur in LEVNAC_14A. Under the optical microscope, these pyroclasts appear to be transparent,

whereas under the SEM it is apparent that much of the original pyroclasts have been removed and, in many cases, a void is now present. This may have occurred due to progressive breakdown and replacement of the original volcanic glass. Fluid movement through the deposit may then have allowed secondary minerals to be removed by dissolution, resulting in a secondary porosity. Thus, the surrounding clay-rich matrix preserves the original shape of the pyroclasts (Figure 5-35). Alternatively, pyroclasts might have been picked out during polishing of the thin-section.

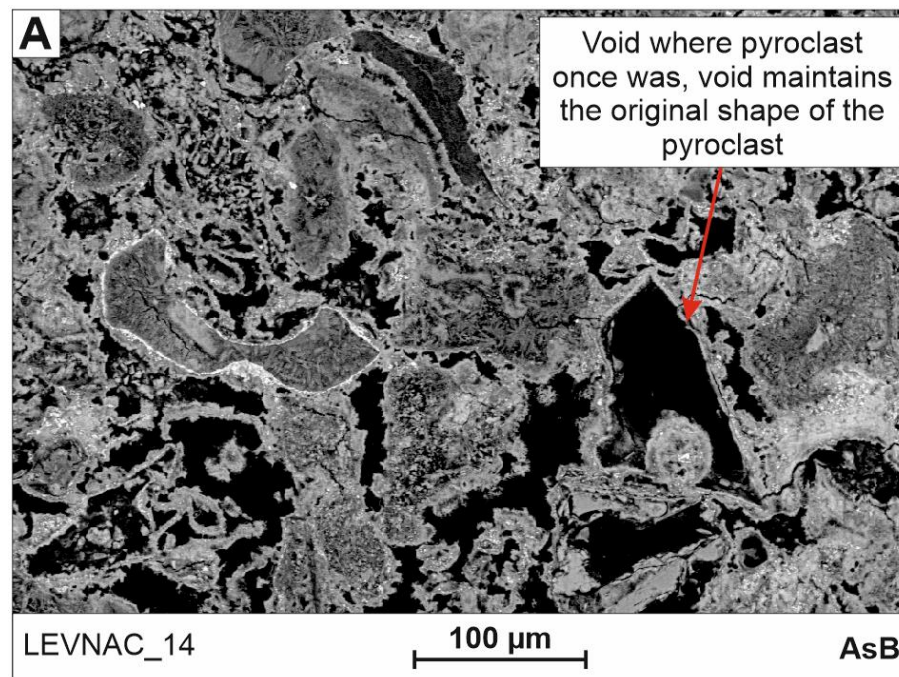


Figure 5-35 AsB SEM image showing the preservation of pyroclast shapes as voids within the sample. *In situ* dissolution of the pyroclast may have occurred prior to thin-sectioning, alternatively the pyroclast may have been removed during thin-sectioning.

In other examples the original pyroclasts have not been removed, but show varying levels of alteration (palagonitisation) and replacement e.g. by clays (Figure 5-36). The morphologies of the pyroclasts, where preserved, include vesicular (Figure 5-36a-b, e), and non-vesicular (Figure 5-36c), blocky (Figure 5-36b, e), and bubble-wall pyroclasts (Figure 5-36a, c), similar to those observed within the HSB (Figure 5-31, Figure 5-32). Some pyroclasts are heavily altered to clay and resemble crystalline igneous clasts; however, chemical analysis shows that the composition of these micro-crystalline textured clasts is the same as the surrounding clay (Figure 5-36d).

In addition to altered pyroclasts, LEVNAC_14A contains an abundance of crystalline igneous clasts. These clasts are also variably altered to clay, and are generally more well-rounded than the pyroclasts (Figure 5-36a).

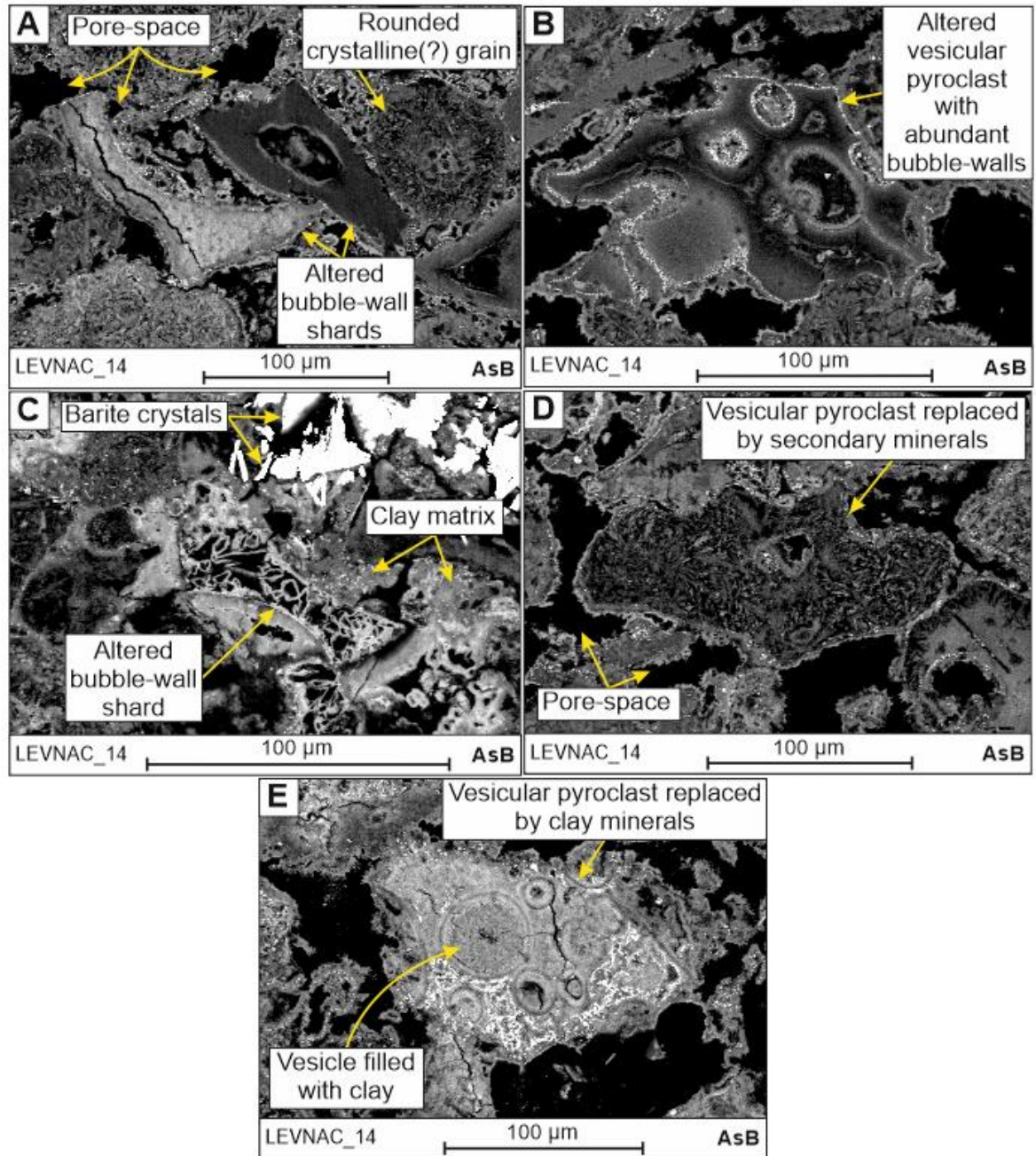


Figure 5-36 AsB SEM images of variably altered vesicular and non-vesicular pyroclasts in LEVNAC_14A. A) A pale grey bubble wall shard adjacent to a vesicular dark grey shard, both exhibiting a different stage or type of alteration. To the right of this clast is a rounded crystalline igneous clast B) Vesicular shard with heterogeneous alteration (showing a range of degrees of palagonitisation). C) Bubble-wall shard-shaped feature containing voids and solid minerals in an amorphous pattern through the shard. D) Crystalline vesicular pyroclast. The microcrystals within this clast may have been part of the original igneous material or may be the result of clay mineralisation during alteration of the pyroclast. E) Altered amygdaloidal blocky pyroclast, showing a different stage or type of alteration to the other pyroclasts (A-D).

5.6.2.4 Shotley Borehole B

The samples of the Shotley Borehole B are predominantly comprised of angular to sub-rounded quartz grains surrounded by a fine-grained clay-rich matrix (Figure 5-37). Various other grain-types are present in smaller amounts (Table 5-7). Rare-occurrences of micro-fossils can also be identified (Figure 5-37c-d), these have in some instances been replaced by pyrite (Figure 5-37d).

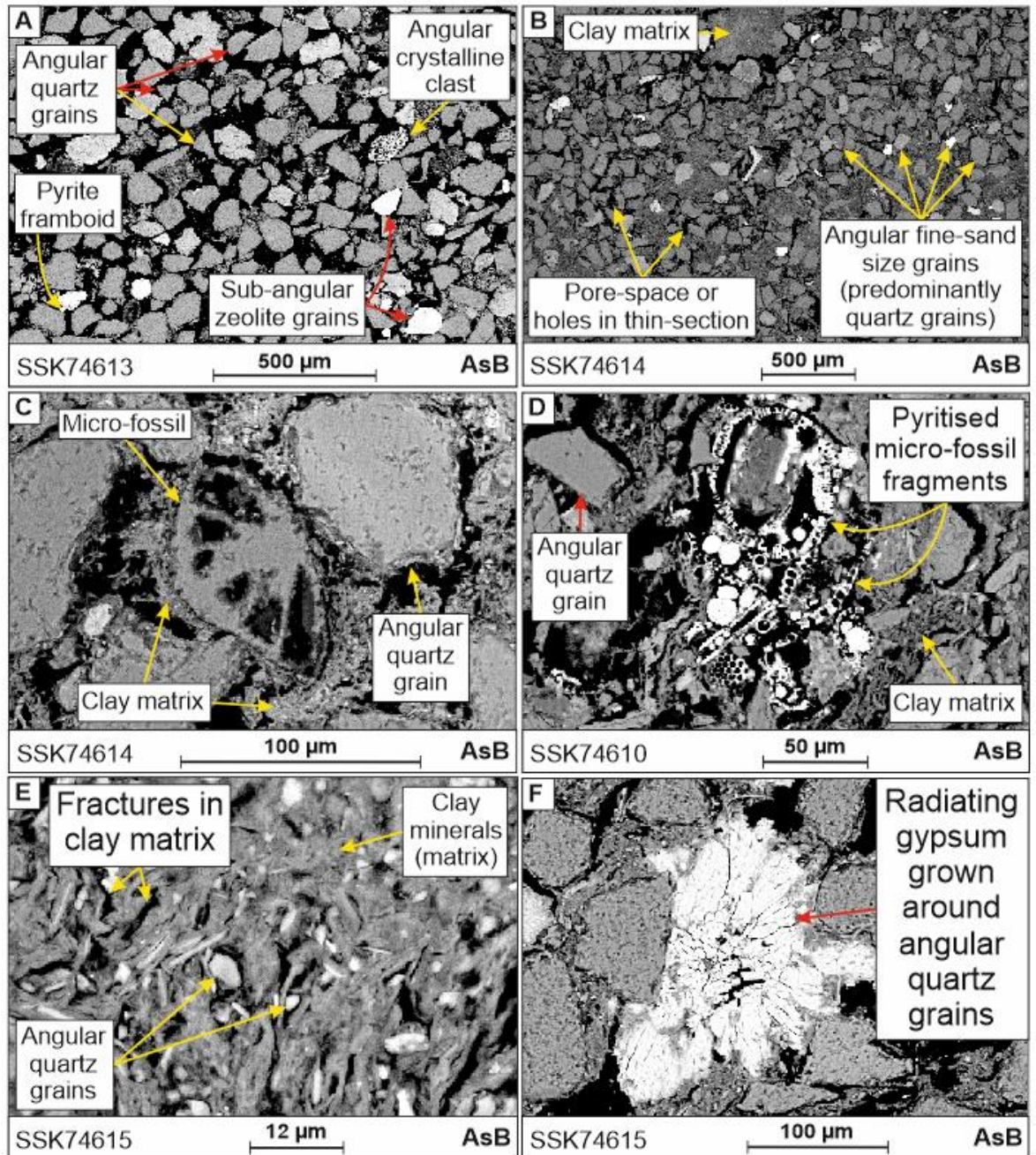


Figure 5-37 Features of samples from the Shotley Borehole B. Granular nature of samples with abundant angular quartz grains, in addition to framboidal pyrite, crystalline igneous clasts, zeolite grains and clay matrix. Grains are generally of fine sand grade. C) Calcite micro-fossil within a clay matrix. D) Pyritised micro-fossil fragments (diatom-like). E) Nature

of the clay matrix, comprised of very fine-grained clay minerals and fine grains of angular quartz. The clay contains abundant fractures. F) Radiating gypsum crystals that have grown between angular quartz grains.

		Minerals and clast-types present in sample (x)																							
Sample ID	Type	Amphibole	Barite	Calcite (micro-fossils; cement)	Chlorite	Crystalline igneous clasts	Dolomite	Feldspar (Albite)	Feldspar (Labradorite)	Feldspar (Orthoclase)	Fluorapatite	Garnet	Gypsum	Illite	Ilmenite	Kaolinite	Magnetite	Mica (Muscovite)	Pyrite	Pyroclasts	Quartz	Rutile	Stilpnomelane	Ulvospinel	Zeolite (Clinoptilite)
General		x		x					x	x	x		x		x	x	x	x	x	x	x	x	x	x	
SSK74612	HSB	x		x		x		x	x	x	x	x			x			x	x			x	x	x	

Table 5-7 Mineral and clast-types present in samples from Shotley Borehole B.

The matrix is composed of clay minerals and fine grains of angular quartz (Figure 5-37e). The clay contains abundant fractures, which may be the result of the swelling nature of these clays, as observed in the field.

Crystals of gypsum that radiate outwards from a central point can be found scattered through the samples. They are commonly found between angular grains of quartz (Figure 5-37f). The radiating nature of these crystals suggests that the gypsum grew within the sediment after deposition (e.g. Charola et al. 2007). Although the timing of the growth is not clear; for example, it may have formed shortly after the sediments were deposited or much later on in response to conditions that are not related to the original depositional conditions (Charola et al. 2007).

5.7 Image analysis

Image analysis was conducted using ImageJ Software to obtain quantitative data regarding the shapes, sizes, abundances and distributions of different clast populations within each of the samples. This analysis was conducted on pre-processed backscatter (AsB) SEM images for the collection of quantifiable data from image analysis (see 1.3 Methods). Image analysis was conducted on a selection of the field-samples from Harkstead and Levington-Nacton. Analysis was not conducted on samples from the Shotley Borehole B as it was considered that these samples can be better represented by those of Harkstead and

Levington-Nacton, based on their similar microscopic characteristics and chemical composition (see section 5.6). Analysis of the Shotley Borehole B would therefore only supplement the data set and was considered unnecessary.

A minimum of 90 grains were included for analysis of the grain-size distributions (number frequency), excluding any matrix material (fine clay grade) (Table 5-8). Samples that contain abundant igneous/pyroclastic clasts (LEVNAC_01A and LEVNAC_14A) appear to have the coarsest grain-size distribution, which ranges from silt (3.9-62.5 μm) to fine-sand grade (125-250 μm), with the grain-size peaking at very fine-sand grade (62.5-125 μm) for LEVNAC_14A (Table 5-8). All of the other samples have a predominant grain-size of silt-grade (Table 5-8).

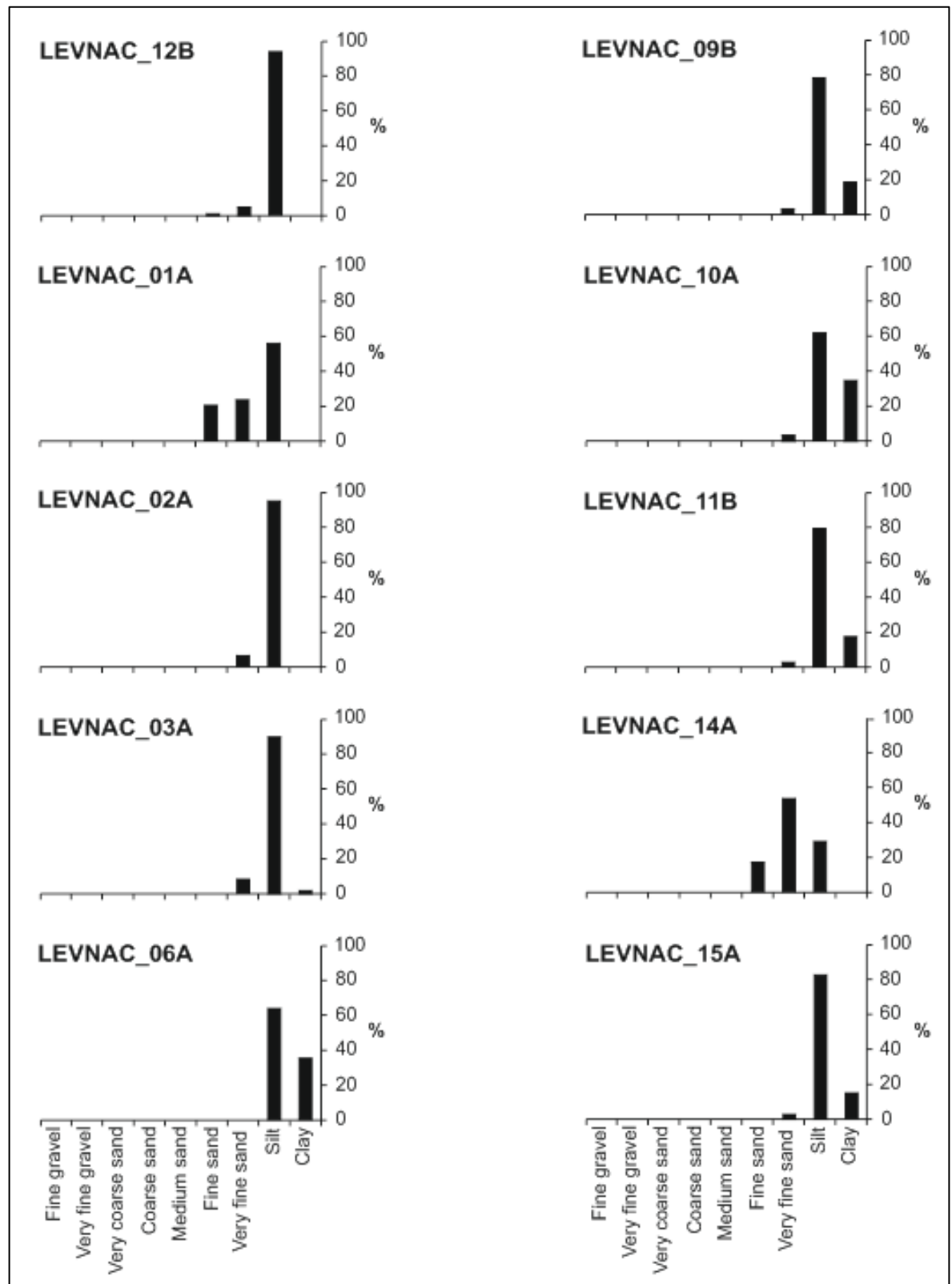


Table 5-8 Number Frequency (%) grain-size distribution for samples of Levington-Nacton calculated using image analysis. The data are shown for the lowermost sample of the WM (LEVNAC_12B) to the upper-most sample (LEVNAC_15A) and includes the HSB (LEVNAC_01A and LEVNAC_02A). This analysis does not take into account the components of clay matrix. In general, all of the samples, except LEVNAC_14A, are composed of silt-size grains (3.9-62.5 μm), with variable minor amounts of very fine-sand (62.5-125 μm) and clay size grains (>3.9 μm). Sample LEVNAC_01A shows that the volcanic unit of the HSB is composed of a larger amount of coarser grain sizes, reaching fine sand grade (125-250 μm).

This coarser grain-size distribution also occurs in the ash -rich LEVNAC_14A, which has a peak grain-size of very fine sand (62.5-125 μm), coarser than that of all of the other samples.

Manual point-count analysis of the igneous component of each sample of the volcanic units, HSB and LEVNAC_14A, show that the igneous fraction is predominantly composed of accidental clasts (crystalline igneous clasts) (Figure 5-38). Accidental clasts are those that are not formed directly from an erupted magma, but are pre-existing clasts or fragments of rock that get incorporated into an eruption, for example, crystalline igneous rocks in the conduit may become incorporated by an eruption and deposited with pyroclasts (e.g. Cas & Wright 1988; Graettinger et al. 2013). The pyroclasts can be considered as the juvenile component of an eruption deposit, as these formed directly from the cooling of erupted magma (e.g. Cas & Wright 1988). The pyroclasts of each of these samples are predominantly non-vesicular and of blocky morphology (Figure 5-38).

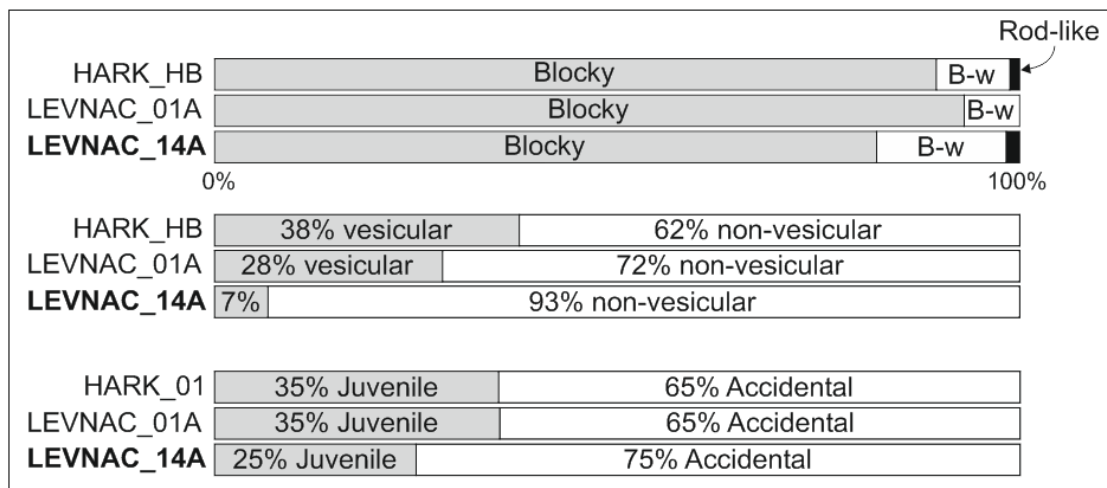


Figure 5-38 Percentage of blocky, bubble-wall (B-w) and rod-like pyroclast morphologies; percentage of vesicular and non-vesicular pyroclasts; and, the percentage of juvenile and accidental lithics in samples from the HSB and LEVNAC_14A. The dominant pyroclast-type in each of the samples is blocky. The majority of pyroclasts are non-vesicular. Each of the samples is composed predominantly of accidental lithics (crystalline igneous clasts), with a lesser percentage of juvenile clasts (pyroclasts).

Image analysis was used on vesicular pyroclasts to calculate their vesicle densities (see 1.3 Methods). The percentage vesicularity is less than 45% for all of the samples from the HSB and LEVNAC_14A (Table 5-9). These low percentages are representative of poorly vesicular pyroclasts (Gradstein et al. 2013).

Sample ID	HARK_01	HARK_HB	LEVNAC_01A	LEVNAC_14A
Average vesicle population (%)	22.30	35.45	22.39	19.71
Range (%)	1 - 46	10 - 70	11 - 38	15 - 28 (more data needed)

Table 5-9 Vesicle percentages for samples of the HSB and LEVNAC_14A. The average vesicularity of pyroclasts in all of the samples is below 45% and considered as being poorly vesicular (Graettinger et al. 2013). HARK_HB gives the greatest range of vesicularity (10-70%), with one pyroclast with a vesicularity greater than 60% and representative of pumice (Graettinger et al. 2013; Heap et al. 2014). More data is needed for the vesicularity of pyroclasts in the LEVNAC_14A interval; however, calculations from three vesicular pyroclasts gives a range of 15-28% and an average vesicularity of 19.71%.

5.8 Discussion

5.8.1 Characteristics and environment of deposition of the Wrabness Member sedimentary deposits

Detailed investigation into the characteristics of the Wrabness Member (WM) exposed at four localities (Figure 5-1), and a borehole (Table 5-5), in E. Anglia, has provided data for the interpretation of the siliciclastic and igneous/pyroclastic components of the main lithologies. Interpretation of these data (field observations, petrography, SEM imaging, chemical data and image analysis), for each locality will be discussed below.

Analysis of the grain-size distributions of all of the samples show that the sediments are well sorted and dominated by silt-sized grains held within a clay matrix (Table 5-8). LEVNAC_01A and LEVNAC_14A have a slightly coarser grain-size compared to the other samples, with grains of silt to fine-sand grade (Table 5-8). Therefore, these two beds represent depositional events that contrast with the pattern of background sedimentation. Both, LEVNAC_01A and LEVNAC_14A contain a high percentage of igneous clasts, including variably altered pyroclasts (Figure 5-38). In addition, LEVNAC_01A from the Harwich Stone Band (HSB) displays normal-grading and has a sharp lower contact with the underlying sedimentary unit, as seen in all samples from the HSB (e.g. Figure 5-17). These features show that there were at least two periods when igneous clasts were deposited. The pyroclasts retain their original angularity in most cases,

regardless of alteration (Figure 5-36), suggesting that little, or no, reworking of the pyroclasts took place prior to their deposition. Reworking would likely cause abrasion of the angular edges of pyroclasts and lead to more rounded surface characteristics (e.g. Cas & Wright 1988), as observed in unaltered modern volcanic deposits in Iceland (see Chapter 2). Very few clasts of non-volcanic origin are observed within the HSB and LEVNAC_14A samples, suggesting that the environment became overwhelmed with pyroclastic material at this time. Deposition of siliciclastic material was inhibited by the the influx of pyroclastic material, directly from fall-out and settling of particles through the water column, or as wash-in detritus from the land. Following these two pyroclastic-depositional 'events' the process of siliciclastic deposition recommenced. All of this suggests that both tuffs of the HSB and LEVNAC_14A likely represent primary pyroclastic deposits and are representative of the direct fall-out of basaltic ash, from two separate eruptive phases, over E. Anglia, around 54.5 Ma.

Igneous clasts are not observed in any other samples from the field localities or the Shotley Borehole B (Table 5-6, Table 5-7), except as rare, calcite-replaced grains in WRAB_02 (discussed below, section 5.8.2). This suggests that igneous material was not always available for deposition in this region, and was only supplied periodically when volcanic eruptions delivered ash. Knox & Ellison (1979) concluded that at least 44 ash-layers can be found in the WM, this was later revised to a minimum of 32 ash-layers by field observations in later studies (Jolley 1996; Ali & Jolley 1996; King 2016). The estimation of 32 ash-layers was based on the observation of pale grey bands within the WM, without detailed petrological investigation (Jolley 1996; Ali & Jolley 1996). The present study shows that 'primary' ash-layers can only be observed in two units (the HSB and LEVNAC_14A), and that pyroclasts are not observed within any of the other units of the WM (Table 5-6). It is also unlikely that substantial alteration of the pale grey units has removed all evidence of pyroclasts due to the presence of well-preserved pyroclasts within a non-cemented interval represented by LEVNAC_14A. If pyroclasts were present in the pale grey bands above and below LEVNAC_14A then you could assume that some visible trace of them would be preserved, or that no evidence of pyroclasts should be present in LEVNAC_14A. The coloration of the bands is therefore not considered to be indicative of the presence of ash. Comparison of clast-types, grain-size distribution and the

chemical composition of the clay matrix indicates that the lithology is generally similar across all of the pale grey and dark grey samples. However, it does appear that darker grey samples contain a greater amount of dark-coloured mineral types (Table 5-6), including amphibole(?), ilmenite, magnetite, pyrite and rutile, which are less common in the pale grey samples. This may account for the colour differences observed in the field; however, observations of the Shotley Borehole B, show that the core lacks any interbedded pale grey or dark grey/brown layers (Figure 5-18). The lack of any layering at all, suggests that the colour variations observed in the field are the result of differences in weathering, and may suggest that subtle differences in modal mineralogy (and hence bulk rock composition) may yield observable (field) differences to the sequence.

The HSB forms a prominent feature that can be identified and traced at every locality, where exposed. However, the HSB is not a 'bed' but is instead a lithological band with a well-developed calcite cement. This band can be seen to range in thickness laterally and, rarely appears to cross bed boundaries (Figure 5-10). The extensive nature of this cemented hard band may correspond to the presence of a basaltic tuff/bentonite which is present within this same stratigraphic interval (see section 5.6.1.2), with calcite cementation occurring due to the presence of the volcanic clasts (Elliott 1971; Knox & Ellison 1979; Obst et al. 2015; Shifa et al. 2016). Elsewhere, ash does not form a significant component of the sedimentary rocks, except for, perhaps, two intervals above the HSB. These two intervals are represented in samples WRAB_02, from what is referred to here as the Wrabness Blue Band, and LEVNAC_14A. The Wrabness Blue Band lies within a few centimetres of the HSB and contains a calcite cement that is more poorly developed due to the presence of a greater abundance of clay grade matrix (Figure 5-27), which is not observed within the HSB (Figure 5-30). LEVNAC_14A is not associated with a calcite cement; the limited thickness of this unit compared to the tuff unit of the HSB may be insufficient for the development of an extensive calcite cement. Alternatively, the environmental conditions may have inhibited the formation of a calcite cement following deposition of the LEVNAC_14A material, for example, a reduction in calcium within the water column or sediment and pore/marine waters, or rapid sedimentation and burial could inhibit development of calcite

cement (Flügel 2010). The calcite cement of the HSB is most likely a type of abiotic carbonate (e.g. Flügel 2010), which formed due to the precipitation of calcite, with no influence from micro-organisms. In thin-section the clasts of the HSB do not appear to have undergone any compaction prior to the growth of the calcite cement, suggesting that the cement formed early during diagenesis (Obst et al. 2015).

In the published literature, the restricted nature of the NSB marine environment during deposition of the WM is suggested to have caused anoxic conditions that limited the occurrence of life throughout the basin (Knox & Harland 1979; Mudge & Bliss 1983; Mudge & Copestake 1992a; Knox 1996; Mudge & Bujak 1996; Steurbaut et al. 2009; Kender et al. 2012; Aldiss 2014). During the Early Eocene, the E. Anglia region is suggested to have been inundated by shallow water, therefore it is possible that this region was 'less stagnant due to wave turbulence' (Knox & Harland 1979), which did allow life to persist. Abundant trace-fossils and evidence of bioturbation throughout the WM is readily noted (Figure 5-11, Figure 5-22). This region must therefore have been well oxygenated, and is evidence to support the suggestion of a shallow marine or lacustrine environment (Pemberton et al. 2012; Scott et al. 2012; Wetzel & Uchman 2012; Obst et al. 2015). No complete body fossils of micro-organisms are preserved; the few that are present are fragmented and replaced with secondary minerals, such as pyrite (Figure 5-23), and calcite (Figure 5-34). Therefore, in this study, micro-fossils could not be used to indicate the conditions persisting in the environment at the time of deposition. A greater knowledge and understanding of micro-fossil and trace-fossil types and their identification goes beyond the scope of the present study, but may support environmental interpretations of these sedimentary rocks in the future. Previous studies of dinoflagellates imply a shallow marine/inner neritic environment of deposition (King 1981; Ellison et al. 1994; Ali & Jolley 1996; Hooker 1996; Jolley 1996; King 2016). The general lack of micro-fossils within these deposits has been interpreted to imply a shallow marine setting at the time of deposition for the WM (Knox 1996; Royse et al. 2012; Aldiss 2014; King 2016).

Gypsum is commonly associated with the evaporation of sea-water (Ortí et al. 2002; Charola et al. 2007). It is present within the samples as radiating crystals

(Figure 5-26f, Figure 5-37f), or as angular grains (LEVNAC_12A; SSK74612). The radiating crystals were most likely formed *in situ* within the pore space of the sediment (Figure 5-39), either shortly after deposition of the sediment, or later-on, during subaerial exposure of the rocks (Charola et al. 2007). This form of gypsum has a relatively low abundance within the sediments and is therefore not likely associated with evaporation of the waters of the NSB during the Early Eocene. However, in addition, angular grains of gypsum observed in LEVNAC_12A and SSK74612 most likely represent grains that were eroded from a pre-Early Eocene gypsum deposit, that was eroded and re-deposited within the sediments of the WM, and is therefore detrital gypsum (e.g. Lawton & Buck 2006).

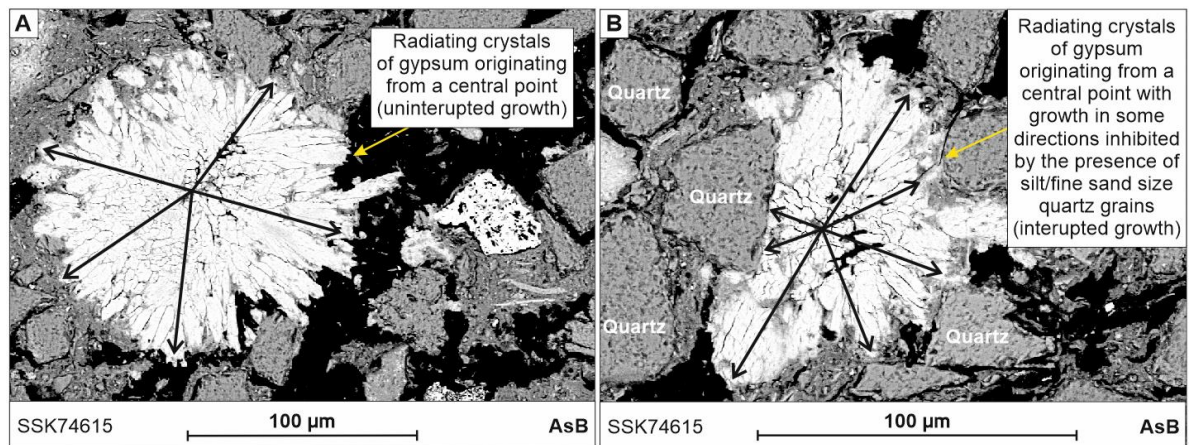


Figure 5-39 Radiating gypsum crystals that grew within the pore-space of the sediment in the WM. The gypsum in both of these examples grew outwards from a central point; in A the gypsum was able to grow within the sediment with no restrictions from surrounding grains, producing a radiating morphology, with crystals of equal length in all directions. In B, growth of the gypsum was inhibited by contact with surrounding quartz grains, leading to an irregular or elongate morphology with crystals of unequal lengths.

The lithological log of the Shotley Borehole B, illustrates repetitive sequences of fine-grained and coarse-grained sediments (Figure 5-17), in shallowing upwards sequences (Figure 5-40; e.g. Brookfield 2004). These sequences can be interpreted as parasequences within a transgressive systems tract, where the shoreline migrated landwards over time (Figure 5-40; e.g. Brookfield 2004). Each parasequence is separated by a flooding surface (FS), that can be identified where claystones/mudstones lie directly above coarser-grained siltstones and sandstones (Figure 5-40; Brookfield 2004). The parasequences may therefore be evidence of stages of the marine transgression which eventually led to the deposition of the marine sediments of the London Clay Formation (Table 5-2;

Jacqué & Thouvenin 1975; Knox & Harland 1979; Knox & Morton 1983; Mudge & Bliss 1983; Mudge & Copestake 1992a; Ellison et al. 1994; Waagstein & Heilmann-Clausen 1995; Ali & Jolley 1996; Jolley 1996; Knox 1996; Smallwood & Gill 2002; Jolley & Bell 2002; Royse et al. 2012; Aldiss 2014). Three parasequences can be identified, and correlate to the three parasequences interpreted by Jolley (1996) from the study of micro-fossils within the Harwich Formation (HF).

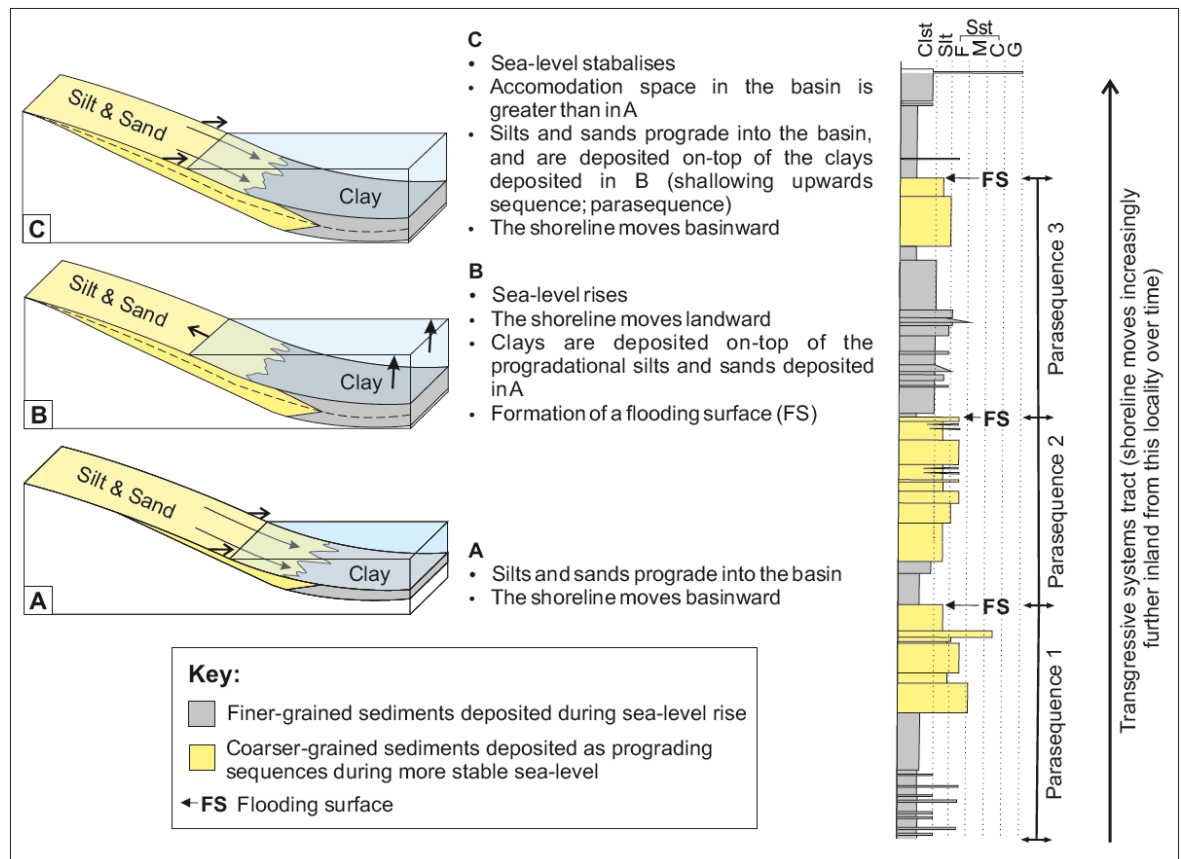


Figure 5-40 Parasequences of a transgressive systems tract interpreted within the Shotley Borehole B sedimentary log, correlated with episodes of sea-level rise. Each parasequence comprises a siltstone/sandstone abruptly overlain with claystone that represents a flooding surface, and a period of sea-level rise (A). A sea-level rise causes an increase in the accommodation space for sediments at the coastline and within the basin (B). Coarser-grained sediments are able to prograde into the basin leading to the deposition of silts and sands above the deeper marine clays that were deposited at an earlier stage of sea-level rise (C). Three parasequences can be identified in the Shotley Borehole B, these correlate with the three parasequences interpreted by Jolley (1996), and are related to an overall transgressive systems tract.

5.8.2 Characteristics of ash-rich deposits and inferred eruption dynamics

The presence of volcanic material within the Early Eocene deposits of E. Anglia suggests that volcanism was occurring at this time, leading to deposition of

primary ash-fall, together with possible reworking of ash and other pyroclastic material within the NSB, including that of the Balder Formation (BF; Knox & Ellison 1979; Knox & Morton 1983; Mudge & Bliss 1983; Malm et al. 1984; Roberts et al. 1984; Knox & Morton 1988; Morton & Knox 1990; Ellison et al. 1994; Jolley 1996; Knox 1996; Obst et al. 2015; King 2016). Understanding the characteristics of this material can provide information about the eruption dynamics and the source of the volcanic material (Carey & Sparks 1986; Cas & Wright 1988; Barberi et al. 1989; Cioni et al. 1992; Blower et al. 2001; Riley et al. 2003; Gaonac'h et al. 2005; Houghton & Gonnermann 2008; Polacci et al. 2008; Clarke et al. 2009; Mattsson 2010; Shea et al. 2010; Bonadonna et al. 2011; Ross & White 2012; Graettinger et al. 2013; Moitra et al. 2013; Cioni et al. 2014; Heap et al. 2014).

Fine-ash includes pyroclasts of $<63\ \mu\text{m}$; clast sizes that are greater than $250\ \mu\text{m}$ are referred to as lapilli (Wohletz 1983; Cas & Wright 1988; Rose & Durant 2009; Bonadonna et al. 2011; Brown et al. 2012; See Chapter 1). The pyroclasts of the HSB volcanic unit and LEVNAC_14 have a grain-size distribution of 17 to $180\ \mu\text{m}$ (Table 5-8, Figure 5-41), therefore including fine- and coarse-ash. The most abundant grain-size in LEVNAC_01A of the HSB is of fine ash ($<63\ \mu\text{m}$), whereas the peak grain-size for HARK_HB is of coarser-grained ash ($125\text{--}250\ \mu\text{m}$; Figure 5-41). The peak grain-size for LEVNAC_14 is of ash grade ($63\text{--}125\ \mu\text{m}$; Figure 5-41).

Highly explosive eruptions involve more efficient fragmentation of the erupting magma, and thus, produce a greater amount of fine-ash (e.g. Wohletz 1983; Rose & Durant 2009; Brown et al. 2012). The two ash-rich intervals contain a greater abundance of fine-ash, ash and coarse-ash (each equating to a thickness of several centimetres), which suggests that the source eruptions may have been highly explosive (e.g. Wohletz 1983; Brown et al. 2012; Graettinger et al. 2013), irrespective of pyroclast morphology. Basaltic eruptions are not commonly considered as being highly explosive due to the low viscosity of basaltic magma, with eruptions more likely to be of Hawaiian or Strombolian style (Walker & Croisdale 1971; Williams 1983; Walker et al. 1993; Houghton et al. 2004; Parfitt 2004; Gurenk et al. 2005; Carey et al. 2007; Constantini et al. 2009; Pérez et al. 2009; Constantini et al. 2010; Goepfert & Gardner 2010; Freda et al. 2011). However, explosive basaltic eruptions are becoming more well documented in

the literature (e.g. Williams 1983; Walker et al, 1984; Hanson & Elliot 1996; Coltelli et al. 2000; Houghton et al. 2004; Parfitt 2004; Vergnolle & Caplam-Auerbach 2004; White et al. 2004; Gurenko et al. 2005; Vergnolle & Caplam-Auerbach 2006; Mannen 2006; Carey et al. 2007; Höskuldsson et al. 2007; Kutterolf et al. 2007; Houghton & Gonnermann 2008; Rose et al. 2008; Clarke et al. 2009; Constantini et al. 2009; Pérez et al. 2009; Constantini et al. 2010; Goepfert & Gardner 2010; Brand & Clarke 2012; Oddsson et al. 2012; Ferguson et al. 2016) and may be responsible for the ash deposits of the WM; particularly if hydrovolcanic eruptions were responsible; evidence for the style of eruptions will be discussed when considering the microscopic characteristics of the ash below.

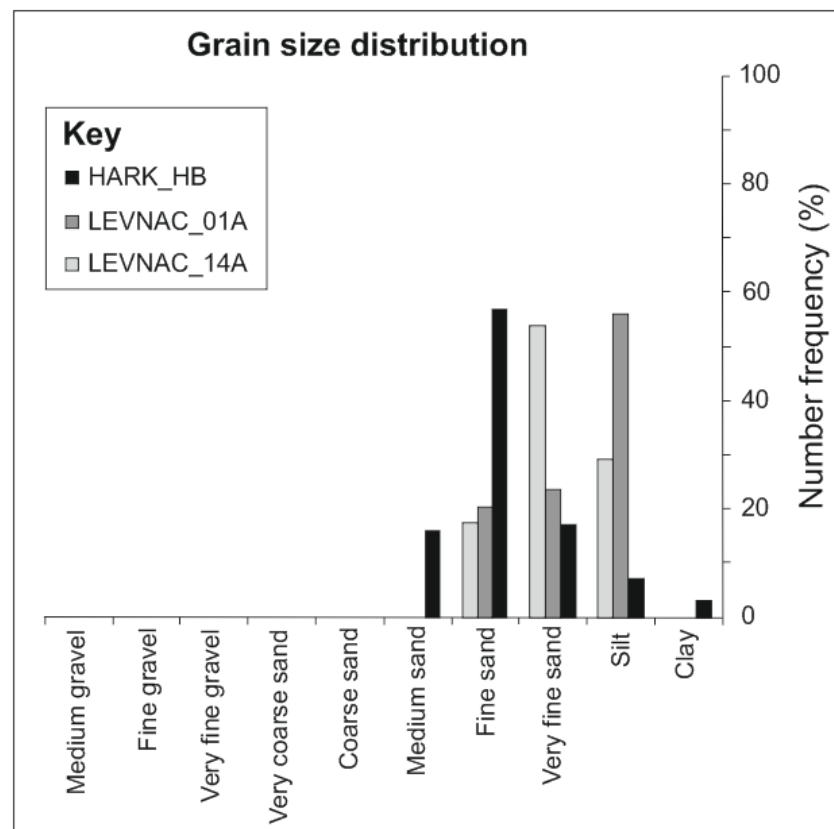


Figure 5-41 Comparison of pyroclast sizes within the HSB (HARK_HB, LEVNAC_01A) and LEVNAC_14A. In general these volcanic-rich samples have a grain size of silt (3.9-62.5 μm ; fine ash) to fine sand (125-250 μm ; lapilli). Samples from Levington-Nacton (LEVNAC_01A and LEVNAC_14A) are generally finer-grained than that of the HSB at Harkstead (HARK_HB). The HSB of LEVNAC_01A has a peak grain size of silt (fine ash), and, LEVNAC_14A has a peak grain-size of very fine sand (coarse ash). HARK_HB gives the largest grain-size distribution of clay (<3.9 μm ; very fine ash) to medium sand (250-500 μm ; lapilli).

Point-count analysis of the types of igneous clasts within the HSB and sample LEVNAC_14A (Figure 5-38) show that both are dominated by crystalline igneous

clasts (accidental lithics; >60%), with a much smaller percentage of juvenile pyroclasts (<40%). This higher percentage of accidental lithics is commonly regarded as an important characteristic of hydrovolcanic deposits, due to explosive magma-water interactions occurring within the vent or conduit, that excavate and incorporate more 'accidental' or pre-existing rock into the eruption products (Clarke et al. 2009; Németh & Cronin 2009; Valentine & White 2012; Graettinger et al. 2013; Valentine et al. 2014).

A range of pyroclast morphologies exist within the two tuffs identified in the WM (HSB and LEVNAC_14A), including non-vesicular and vesicular, blocky and bubble-wall pyroclasts (Figure 5-38). The presence of vesicles in some pyroclasts (Figure 5-38), suggests that the source eruption involved a magmatic component, associated with the expansion of volatiles from within the magma (e.g. Houghton et al. 2004; Mattsson 2010). In addition, the presence of pyroclasts that do not contain vesicles and have a blocky or bubble-wall morphology show a link between magmatic and hydrovolcanic eruption processes (e.g. Wohletz 1983; Hanson & Elliot 1996; Houghton et al. 2004; Mattsson 2010; Graettinger et al. 2013). Non-vesicular blocky pyroclast morphologies dominate these deposits (Figure 5-38), suggesting that they formed during hydrovolcanic processes; at least for pyroclasts with a grain-size of 100 µm or greater (Wohletz 1983; Zimanowski et al. 1997; Mattsson 2010; Dellino et al. 2012; Graettinger et al. 2013), as they are interpreted to form as the result of brittle fragmentation caused by rapid quenching and contraction of magma cooled by interactions with external water (e.g. Wohletz 1983). However, blocky pyroclast morphologies seem to dominate the fine-ash fraction of pyroclastic deposits from a wide range of eruptive types, not solely hydrovolcanic (see Chapter 7). This is likely because fine-ash represents material that was produced by high levels of fragmentation, regardless of eruption-type, and blocky pyroclasts form during highly efficient fragmentation, which is typical of hydrovolcanic eruptions, but also occurs in the fine-grained fraction of other explosive eruptions e.g. 'dry' silicic Plinian eruptions (Wohletz 1983). Thus, the presence of blocky fine-ash alone, is not indicative of eruption-type, and should be considered alongside all other observations of a volcanic deposit when considering eruption processes.

Image analysis shows that the average vesicularity of all samples is less than 40% (Table 5-9), and therefore represents poorly vesicular pyroclasts that are typically abundant in hydrovolcanic deposits (Figure 5-42; Houghton et al. 2004; Clarke et al. 2009; Mattsson 2010; Dellino et al. 2012; Ross & White 2012; Graettinger et al. 2013; Heap et al. 2014). A high density of vesicles within fine-grained pyroclasts suggests that the parent magma contained abundant volatiles that were actively exsolving at the point of eruption (e.g. Mattsson 2010; Ross & White 2012; Graettinger 2013). This would be evidence for magmatically-dominated eruption processes, with little or no interaction with water (e.g. Ross & White 2012).

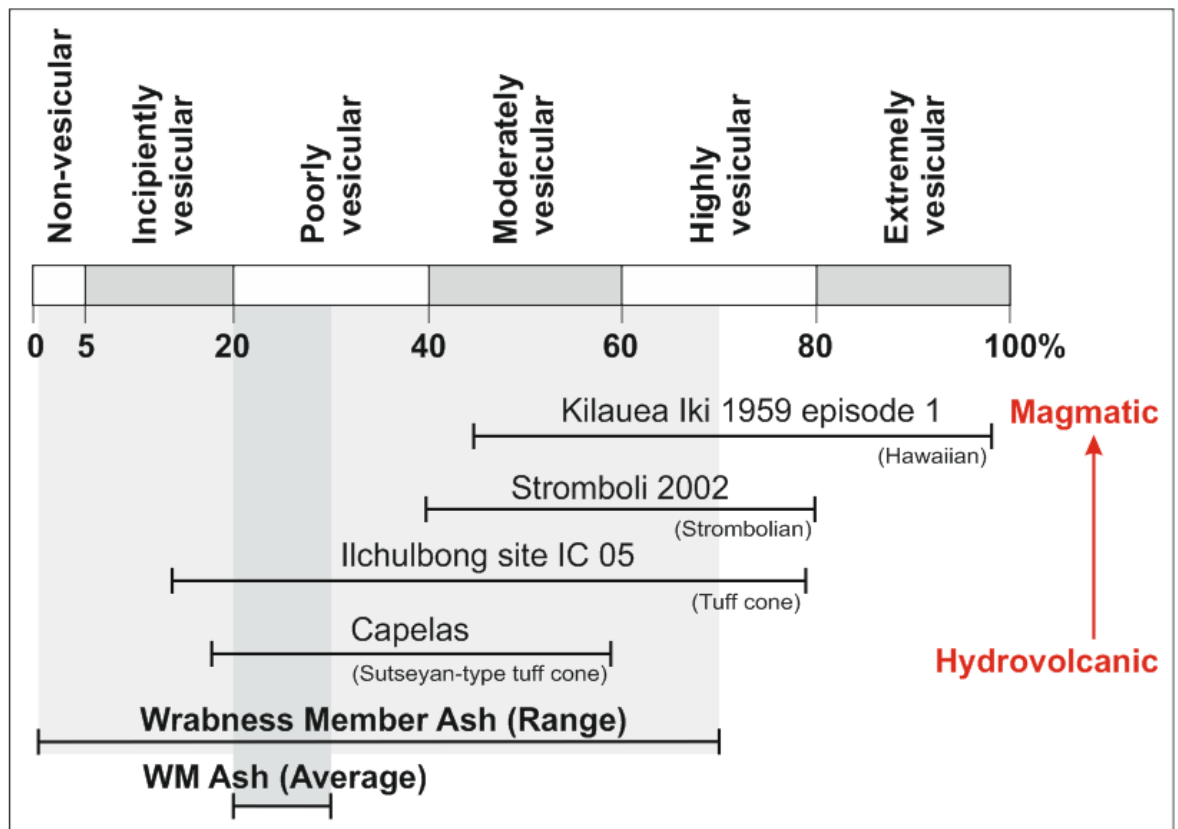


Figure 5-42 Comparison of the vesicularity of pyroclasts from the WM and examples associated with a range of eruption types (Ross & White 2012). Hawaiian fire fountaining and Strombolian eruptions are purely magmatic and have a high vesicle abundance, represented by data for Kilauea Iki 1959 and Stromboli 2002 (Lautze & Houghton 2007; Stoval et al. 2011; Ross & White 2012). Vesicularities are also compared with results from two tuff cones: Ilchulbong and Capelas (Mattsson 2010; Murtagh et al. 2011; Ross & White 2012). The subdivisions of vesicle percentage and the corresponding non-vesicular to extremely vesicular range is the vesicularity index as proposed by Houghton & Wilson (1989). Data for the full range of vesicularities of the WM pyroclasts is given, alongside the average vesicularities of the same samples. The full range of vesicularities spans 1 to 70%, which spans both hydrovolcanic and magmatic vesicularities (e.g. Ross & White 2012). The average vesicularities from the WM pyroclasts from each sample (HARK_HB, HARK_01, LEVNAC_01A and LEVNAC_14A), give values that correspond more closely with the low vesicularity of pyroclasts associated with hydrovolcanic eruption processes.

The lack of any highly vesicular pyroclasts (pumice; >75% vesicles; Table 5-9) suggests that the magma had a relatively low volatile content, or that the magma had a low viscosity that allowed degassing prior to quenching of the magma during an eruption, and that the eruption dynamics would not have been greatly explosive if water was not involved (e.g. Houghton et al. 2004; Mattsson 2010; Ross & White 2012; Graettinger et al. 2013; Moitra et al. 2013). The fractured edges of the pyroclasts (Figure 5-43) suggests that they have been subjected to brittle fragmentation, possibly during quenching and/or abrasion with other particles within the eruptive column (e.g. Sheridan & Wohletz 1983; Wohletz 1983; Mattsson 2010). The high angularity and fragile nature of these pyroclasts suggest that they have undergone little or no transport since deposition (e.g. Mattsson 2010).

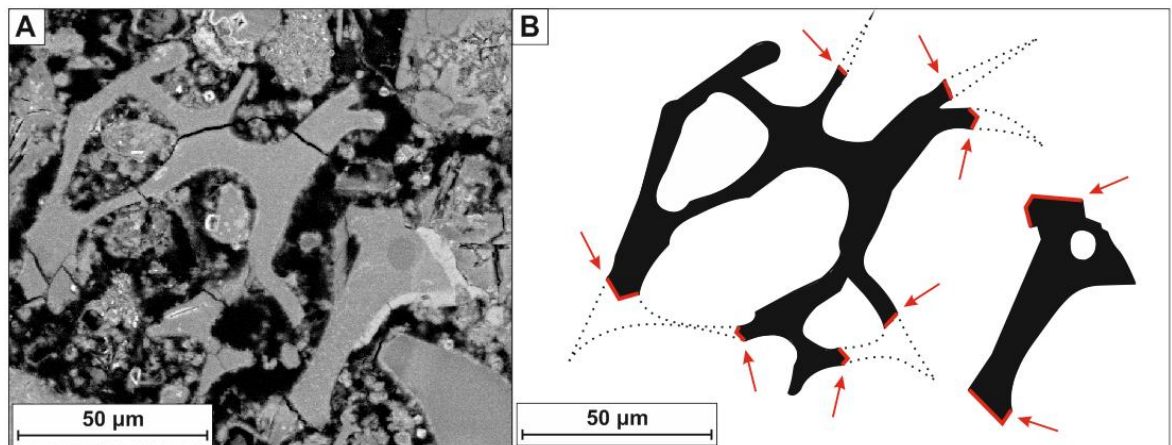


Figure 5-43 Characteristics of pyroclast edges indicating brittle fragmentation. A) Original AsB SEM image showing two pyroclasts that exhibit brittle fragmentation. B) Brittle fracturing can be interpreted by the abrupt terminations of the pyroclast edges (red arrows). If magmatic fragmentation, via the expansion of bubbles within the magma, were responsible for fragmentation it could be expected pyroclast edges to be dominated by more curvi-planar, bubble-wall, features (stippled lines).

In general, vesicles may be stretched into elongate shapes as they exit a vent; but, as the pyroclasts cool, the bubbles can elastically relax and eventually become spherical (Gaonac'h et al. 2005; Shea et al. 2010; Moitra et al. 2013). Rapid quenching of pyroclasts will inhibit bubble relaxation and preserve non-spherical vesicles (Gaonac'h et al. 2005; Shea et al. 2010; LaRue et al. 2013; Moitra et al. 2013). Rapid quenching can occur during hydrovolcanic eruptions where water vapour acts to rapidly cool fragments of erupting magma (Ross & White 2012; LaRue et al. 2013). The amorphous shape of some vesicles in the

HSB and LEVNAC_14A pyroclasts (Figure 5-32), along with those that show the coalescence of individual bubbles in which the bubble walls have not yet relaxed to form one continuous spherical bubble rim (Figure 5-32c), suggests that these pyroclasts were rapidly quenched (e.g. Gaonac'h et al. 2005; Mattsson 2010; Shea et al. 2010; Moitra et al. 2013). The presence of rod-like pyroclasts (Figure 5-38), could be evidence of Limu-o-Pele pyroclasts, which are believed to be evidence for the entrapment of water and therefore a hydrovolcanic influence on eruption parameters (Walker & Croisdale 1971; Graettinger et al. 2013).

The observed similarity between the relatively unaltered pyroclasts of the HSB (in appearance and SEM chemical spectra) suggests that all of the pyroclastic material came from the same parent magma and therefore the same source, this supports the view that all of these samples from the HSB volcanic unit can be correlated and are representative of a single (although possibly lengthy) volcanic interval. The pyroclasts of WRAB_02 cannot be compared in this way due to their high level of alteration and replacement by calcite. Minor differences in the compositions of pyroclasts in each of the representative samples (HSB, WRAB_02, LEVNAC_14A) may be due to alteration, with mobile elements being removed from the pyroclasts over time (Hastie et al. 2007). If these variations are not related to alteration then they could suggest that the source magma of the LEVNAC_14A ash may have been more evolved, and therefore, slightly more silicic in composition. It is possible that this ash had a different source than the ash of the HSB (e.g. Obst et al. 2015), although it is also possible that they had the same source, but the magma had time to evolve slightly between the eruptions of the HSB and LEVNAC_14A ashes; if elemental differences between the samples were a true representation of the original magma composition. Immobile trace-element compositions are required to determine the differences between these samples and the possible relation to a single or multiple volcanic source. The SEM analysis carried out here is not quantitative and should be investigated further by future research via electron probe and/or laser ablation techniques (see Further Work 7.7), this would allow the alteration or magmatic history of the clasts to be analysed and may also allow for correlation of the tuffs with those of the adjacent Balder Formation and the Danish Ash-series.

It is possible that more ash-fall deposits were formed, but that these were later reworked and removed from the stratigraphic record (Knox & Ellison 1979; Ellison et al. 1994; Ali & Jolley 1996; Knox 1996; Mattsson 2010; Royse et al. 2012; King 2016). Pyroclastic deposits are easily eroded after they have been deposited, except where high rates of sedimentation and burial occur; primary pyroclastic units are often not preserved (e.g. Collinson et al. 2006; Reading 2009). During the Early Eocene, the WM was deposited in a shallow marine environment which may, in part, have been present above wave-base (Elliot 1971; Knox & Harland 1979; Ali & Jolley 1996; Jolley 1996; Knox 1996; Kender et al. 2012; Royse et al. 2012; Aldiss 2014; King 2016); this is an environment that would likely inhibit the preservation of pyroclastic material due to its higher levels of turbulence, organic activity and erosion (e.g. Collinson et al. 2006; Reading 2009). A more complete record of volcanism during this time may be found in the adjacent NSB, where marine deposits of the Balder Formation (BF) that may contain more than 200 ash-layers, occur (Jaqué & Thouvenin 1975; Deegan & Scull 1977; Knox & Morton 1983; Mudge & Bliss 1983; Knox 1984; Malm et al. 1984; Knox & Morton 1988; Roberts et al. 1984; Morton & Knox 1990; Knox 1996; Harland et al. 2000; Obst et al. 2015; King 2016). A detailed discussion comparing the E. Anglia and NSB deposits and the source of volcanism is given in the final discussion and conclusion chapter of this thesis (Chapter 7). Prior to comparison with other regions, it is apparent that a *minimum* of two primary ash-fall deposits can be found within the Wrabness Member, based on the presence of igneous material in only two intervals of a systematically sampled section of the WM. Identification of non- to poorly-vesicular, predominantly blocky pyroclasts, indicate that the original ashes of both tuffs were likely produced by hydrovolcanic eruptions, corresponding to *at least* two separate eruptive events that supplied igneous clasts to this region.

Pyroclastic textures are also observed in the Wrabness Blue Band (Figure 5-29; Knox & Ellison 1979; Jolley 1996; Giresse & Wiewióra 1999; King 2016). However, these pyroclasts are only a minor component of the sediment, although, high-levels of alteration and replacement by calcite and clay minerals may have removed other pyroclastic features (Figure 5-29; Jeans et al. 2000). The band does not contain sufficient material to be regarded as a deposit of primary ash-fall origin. Instead, the minor abundance of these highly altered pyroclasts could

indicate the occurrence of epiclastic/reworked pyroclasts at this level. These pyroclasts may be associated with reworking of the volcanic material deposited during formation of the volcanic unit of the HSB, due to the stratigraphic proximity (tens of centimetres) of these two units. It is possible that the colour and nature of the blue clay is the result of the breakdown of volcanic material via palagonitisation and replacement by authigenic minerals, such as, smectite, chlorite, zeolites, calcite and albite (Petzing & Chester 1979; WoldeGabriel et al. 1996; Giresse & Wiewióra 1999; Jeans et al. 2000; Shifa et al. 2016); feldspar, and silica minerals can also form (Jeans et al. 2000), as suggested by the similar chemistry of the pyroclasts and surrounding clay. In general, pyroclasts are thermodynamically unstable and can easily alter when in contact with water (Jeans et al. 2000; Shifa et al. 2016). In a previous study of blue-green deposits, correlations were made between the presence of blue clays and volcanic deposits (Giresse & Wiewióra 1999). In a study by Giresse & Wiewióra (1999), blue clay was considered to represent the breakdown of fine-grained pyroclastic matrix material. The distinctive Wrabness Blue Band (Figure 5-9) has not been identified beyond the Wrabness locality, this could be due to erosion and removal of this unit, giving an incomplete record of the volcanic and siliciclastic deposits of this region (e.g. Knox & Ellison 1979; Ellison et al. 1994; Ali & Jolley 1996; Knox 1996; Royse et al. 2012; King 2016).

5.8.3 Location of source vent(s)

It is expected that, in general, the grain-size and thickness of pyroclastic deposits will diminish with distance from the source vent (e.g. Williams 1983; Carey & Sparks 1986; Pyle 1989; Wohletz et al. 1995; Bursik 1998; Riley et al. 2003; Mannen 2006; Kutterolf et al. 2007; Pérez et al. 2009; Goepfert & Gardner 2010; Houghton et al. 2011; Oddsson et al. 2012; Bonadonna & Costa 2013). Consideration needs to be given regarding the possible location of source vents for this volcanic material. Here, preliminary interpretations will be made for the source of the volcanic material in E. Anglia. Later comparison of these interpretations with detailed information for the equivalent NSB BF should provide a more detailed picture of the volcanic source from a more regional perspective (see Chapter 7).

Hydrovolcanic eruptions involve magma coming into contact with water (Kokelaar 1983; Sheridan & Wohletz 1983; Wohlets 1983; White 1996; Starostin et al. 2005; Trigila et al. 2007; Clarke et al. 2009). The water involved can be present in a variety of settings, including, groundwater, crater lakes, sea water and/or glaciers. Small amounts of water will not lead to highly explosive hydrovolcanic eruptions, and large amounts of water will act to inhibit the explosivity, for example in deep marine settings (e.g. Starostin et al. 2005). The source of water involved in these eruptions cannot be determined from the fine ash of the present study, as too much uncertainty exists, particularly due to alteration of the pyroclasts.

The fine-ash produced during hydrovolcanic eruptions can have a wider area of dispersal than many magmatic eruptions (Sheridan & Wohletz 1983; Oddsson et al. 2012). This is due to steam-rich hydrovolcanic plumes that loft fine particles to greater heights in the atmosphere compared to 'dry' magmatic eruptions (Kokelaar 1983; Woods 1993; Oddsson et al. 2012). However, deposition of fine tephra fractions can be enhanced nearer to the vent due to accretion of particles, which is likely caused by the presence of abundant water vapour (Walker 1981; Brown et al. 2012; Bonadonna & Costa 2013; Mueller et al. 2016). Therefore, it is possible that the ash deposited in E. Anglia fell as ash aggregates that broke apart upon deposition on the Earth's surface (e.g. Brown et al. 2012). Aggregation of fine tephra in this way can lead to secondary thickening of ash deposits at distal locations (Brown et al. 2012). This could explain the thickness (up to *ca.* 4 cm) of these accumulations at a distal location, away from the source vent. Alternatively, the thickness of the ash-rich intervals in E. Anglia may suggest that the source volcano was more proximal. A more proximal setting is also implied by the presence of coarse-ash and lapilli (62.5-250 μm), and not solely fine and very fine ash, which is typical of distal pyroclastic deposits (Figure 5-41; e.g. Williams 1983; Carey & Sparks 1986; Pyle 1989; Wohletz et al. 1995; Bursik 1998; Riley et al. 2003; Kutterolf et al. 2007; Pérez et al. 2009; Goepfert & Gardner 2010; Dellino et al. 2012; Oddsson et al. 2012). With greater distance from source, the deposition of fine-ash will not reflect the true nature of the eruption characteristics, because, for example, hydrovolcanic eruptions are often pulsatory over short time-scales (e.g. Brown et al. 2012). This will not be recorded in deposits, due to a greater duration of suspension of fine particles in

the atmosphere, allowing mixing of particles from different eruptive pulses, particularly at more distal localities (Bursik 1998; Mattsson 2010).

Several factors can affect the dispersal of tephra from an eruption column, including: style of eruption, height of eruption plume, particle characteristics such as size and shape, and atmospheric conditions such as wind-speed and direction (Carey & Sparks 1986; Bursik 1998; Bonadonna & Costa 2013). The distribution of fine-ash, even from relatively small eruptions, can also be enhanced by eruption into a moist atmosphere (Woods 1993). The climate of NW Europe during the Early Eocene may have been warm and humid (Thomas et al. 2003; Svensen et al. 2004; Lourens et al. 2005; Zachos et al. 2008; Gradstein et al. 2012; Kender et al. 2012; Newell 2014; Winnick et al. 2015), which may have allowed eruption columns to ascend to greater heights in the atmosphere, allowing a greater dispersal of fine pyroclasts (e.g. Sheridan & Wohletz 1983; Woods 1993; Oddsson et al. 2012).

Based on the grain-size distribution of the HSB and LEVNAC_14A samples, application of other models can be used to estimate the distance to the source vent. Calculations by Carey & Sparks (1986) suggest a plume height of *ca.* 35 km would allow deposition of fine-ash grains more than 50 km distant from the source vent, and coarse-ash and lapilli *ca.* 30-43 km away (Figure 5-44).

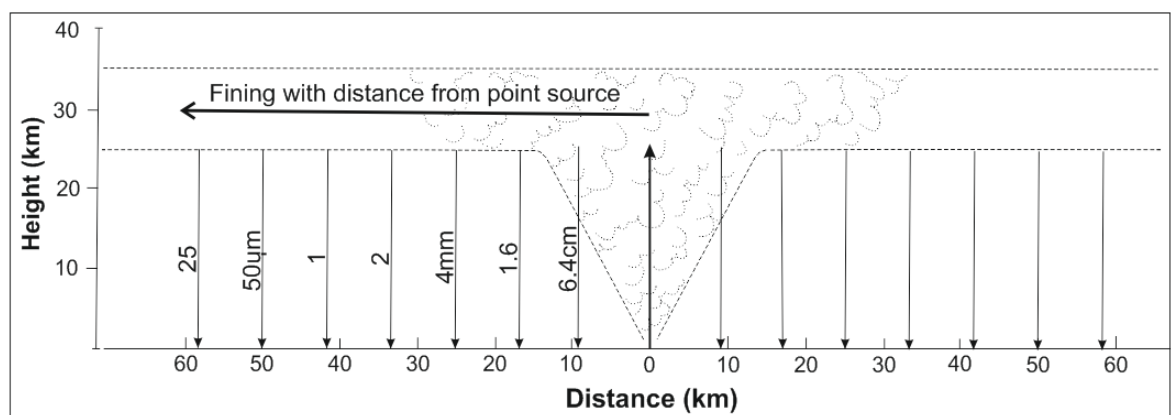


Figure 5-44 Possible distance from source based on grain-size from a plume with a height of at least 35 km, which does not take into account atmospheric winds (Carey & Sparks 1986).

Volcanic deposits have been identified from their alteration products within the Jurassic and Early Cretaceous stratigraphy of England and the adjacent NSB

(Jeans et al. 2000). The sources for this material were most likely volcanic centres related to rifting in the NSB (Jeans et al. 2000). It has been stated that these igneous centres ceased to be active after late Albian times, around 100 Ma (Jeans et al. 2000). Therefore, it is unlikely that any of these centres were the source of the volcanic material identified within the Early Eocene deposits of E. Anglia. The primary pyroclastic nature of the deposits in E. Anglia also shows that reworking of these Jurassic and Early Cretaceous volcanic deposits is not the source of this material (see section 5.8.2).

Seafloor spreading had begun in the NW Atlantic in the Early Eocene (Hallam 1972; Knox & Morton 1983; Ellis & Stoker 2014). This would have provided large quantities of relatively homogenous basaltic magma for eruption in shallow aqueous settings as much as 1000-2000 km away from E. Anglia (Jacqué & Thouvenin 1975; Knox 1984; Knox 1996; Jolley & Bell 2002; Larsen et al. 2003; Larsen. pers. coms. 2015). A possible source of fine-ash therefore may have been the active spreading centres in the NW Atlantic (Table 5-10). Alternatively, the central igneous complexes of the British Palaeogene Igneous Province (BPIP) may also be a suitable source of the ash (Figure 5-45), particularly as separate sources are envisaged for the HSB and LEVNAC_14A volcanic units.

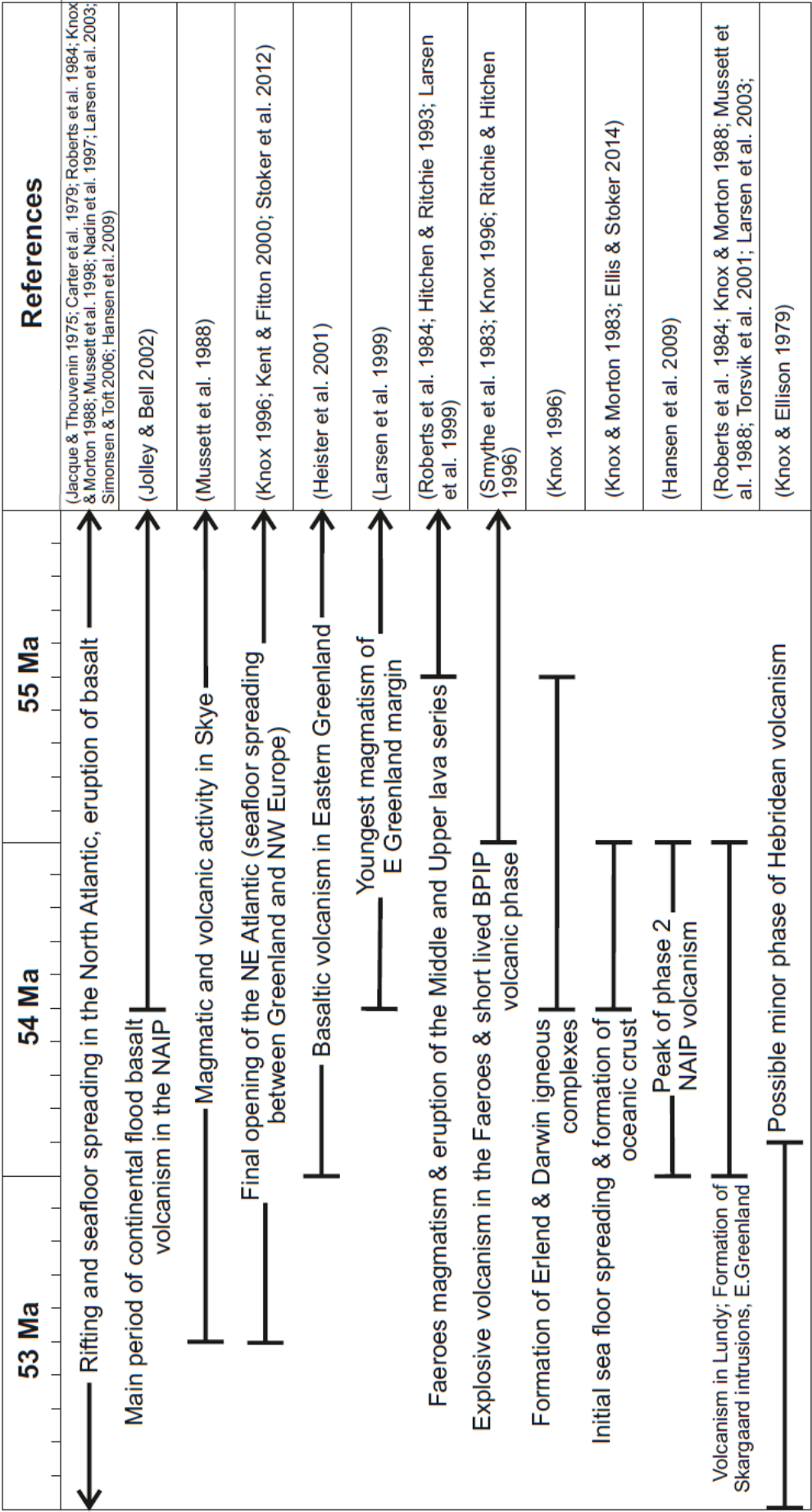


Table 5-10 Published time-scales for volcanic activity in the area of the North Atlantic Igneous Province (NAIP) that could have acted as a source for the volcanic material identified in the WM. Many of these dates have a large range of uncertainty, particularly regarding the methods used at the time these dates were acquired.

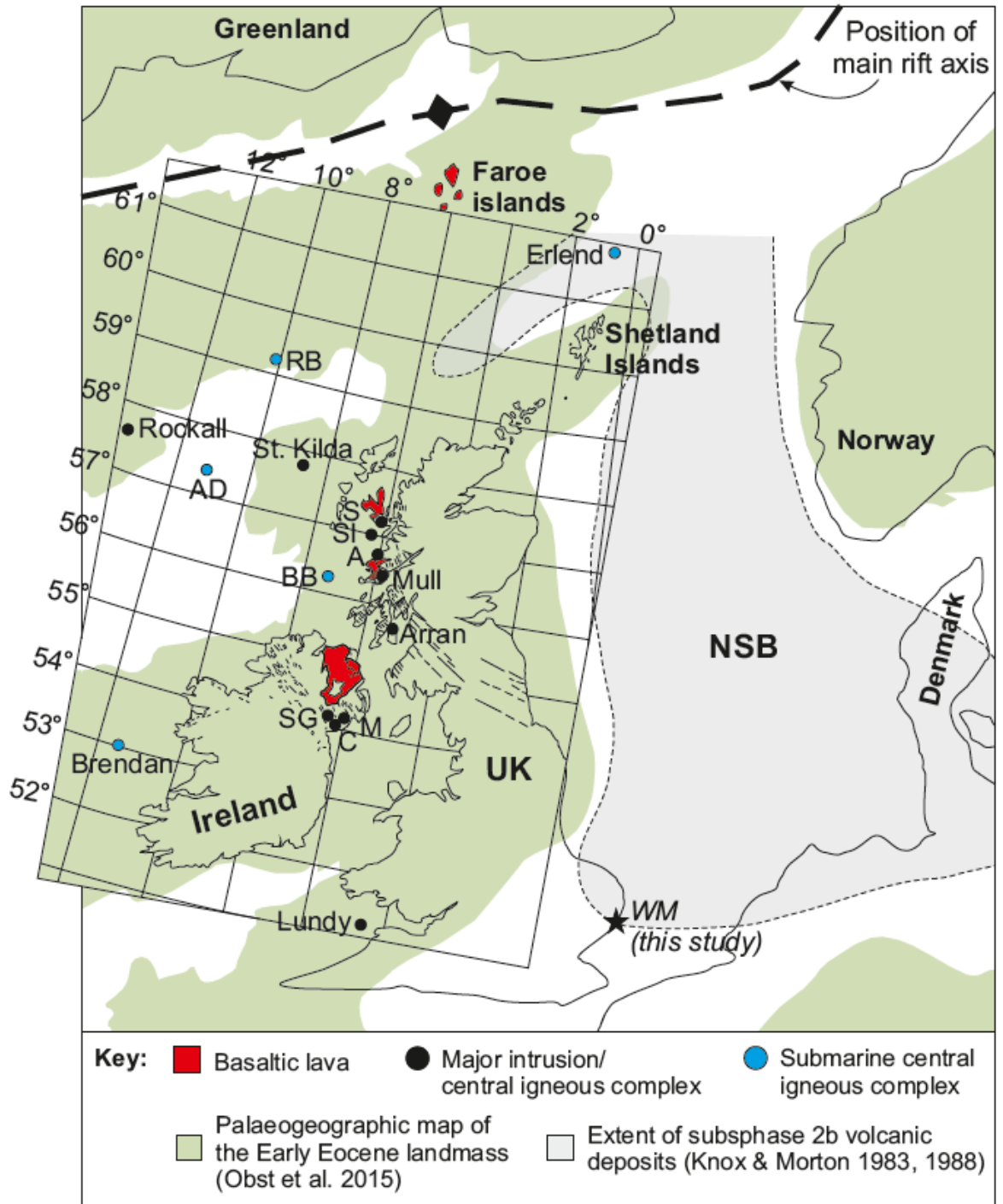


Figure 5-45 Location of palaeogene igneous centres and basaltic lavas of the BPIP that were emplaced during the Early Palaeogene. (Mussett et al. 1988), superimposed on the ash-distribution (grey) map for subphase 2b volcanism proposed by Knox & Morton (1983, 1988). An Early Eocene palaeogeography is shown in green, along with the approximate position of the main rift axis (from Obst et al. 2015). A: Ardnamurchan, AD: Anton Dohrn, BB: Blackstones Bank, C: Carlingford, S: Skye, SG: Slieve Gullion, SI: Small Isles, WM: Wrabness Member. Additional volcanic centres onshore and offshore may also be present, those shown are major centres that have been dated and studied in the most detail in the literature so far.

Understanding previously recorded characteristics and thicknesses of deposits from explosive basaltic eruptions can help in the identification of possible sources for the E. Anglia tuffs. For example, isopach maps representing deposit thickness with distance from the vent for the 122 BC Plinian eruption of Mount Etna show that deposits with a thickness of 2-4 cm occur at distances of more than 30 km from the vent (Houghton et al. 2004). Isopach data for deposits of the 1886 basaltic Plinian fissure eruption of Tarawera suggest that deposits of this thickness can be found *ca.* 50 km from the vent (Walker et al. 1984; Houghton et al. 2004). Calculations for variously-sized eruption columns and the distribution of tephra suggest that a deposit of 2-4 cm thick would occur at a distance >40 km from the vent (Walker et al. 1984; Houghton et al. 2004). Strong atmospheric winds (particularly in the troposphere) can help to enhance the distance to which fine-ash will be dispersed (Carey & Sparks 1986). None of these observations or calculations take into account the effect of enhanced eruption column height during eruption into a warm, moist atmosphere, or the effect of wind speed.

It is possible for the column of hydrovolcanic eruptions to reach greater heights than those of purely magmatic eruptions (Kokelaar 1983; Woods 1993; Oddsson et al. 2012). With strong tropospheric winds it would be possible to deposit tephra of greater thickness at an even greater distance from the vent (Carey & Sparks 1986). Therefore, tephra could be deposited at distances much larger than 50 km. Dominant wind directions at the time of deposition may have occurred from the north or northwest (NW) making a source towards the NW from E. Anglia likely (Malm et al. 1984; Knox 1997). It is therefore possible that the source of these deposits lies within the BPIP or more easterly sections of the NAIP that were active at this time (Figure 5-46, Table 5-10; Jacqu   & Thouvenin 1975; Carter et al. 1979; Knox & Ellison 1979; Brooks 1980; Morton 1983; Roberts et al. 1983; Smythe et al. 1983; Knox & Morton 1988; Mussett et al. 1988; Hitchen & Ritchie 1993; Knox 1996; Ritchie & Hitchen 1996; Knox 1997; Nadin et al. 1997; Larsen et al. 1999; Kent & Fitton 2000; Heister et al. 2001; Torsvik et al. 2001; Jolley & Bell 2002; Larsen et al. 2003; Simonsen & Toft 2006; Hansen et al. 2009; Stoker et al. 2012; Ellis & Stoker 2014; Carriol et al. 2016; King 2016).

Considerations based solely on the thickness of the primary ash-fall deposits of E. Anglia suggest that it is unlikely that the source lay beyond 1000 km away (Figure 5-46), as suggested by studies of the BF (Jacqué & Thouvenin 1975; Knox 1984; Knox 1996; Jolley & Bell 2002; Larsen et al. 2003; Egger & Brückl 2006; Carriol et al. 2016). This, therefore lends itself to the exclusion of volcanic sources as being any of the known volcanic centres in the NW Atlantic, that were active at this time, such as East Greenland (Brooks 1980; Knox & Morton 1983; Roberts et al. 1984; Larsen et al. 1999a), the Faroe Islands (Jacqué & Thouvenin 1975; Brooks 1980; Roberts et al. 1984; Hitchen & Ritchie 1993; Ritchie & Hitchen 1996; Nadin et al. 1997), or Rockall (Brooks 1980; Knox & Morton 1983; Mussett et al. 1988; Knox 1996; Ritchie & Hitchen 1996), making a source in the BPIP more likely (Figure 5-46; e.g. Richey et al. 1961; Carter et al. 1979; Knox & Morton 1983; Mussett et al. 1988; Hitchen & Ritchie 1993; Ritchie & Hitchen 1996; King 2016).

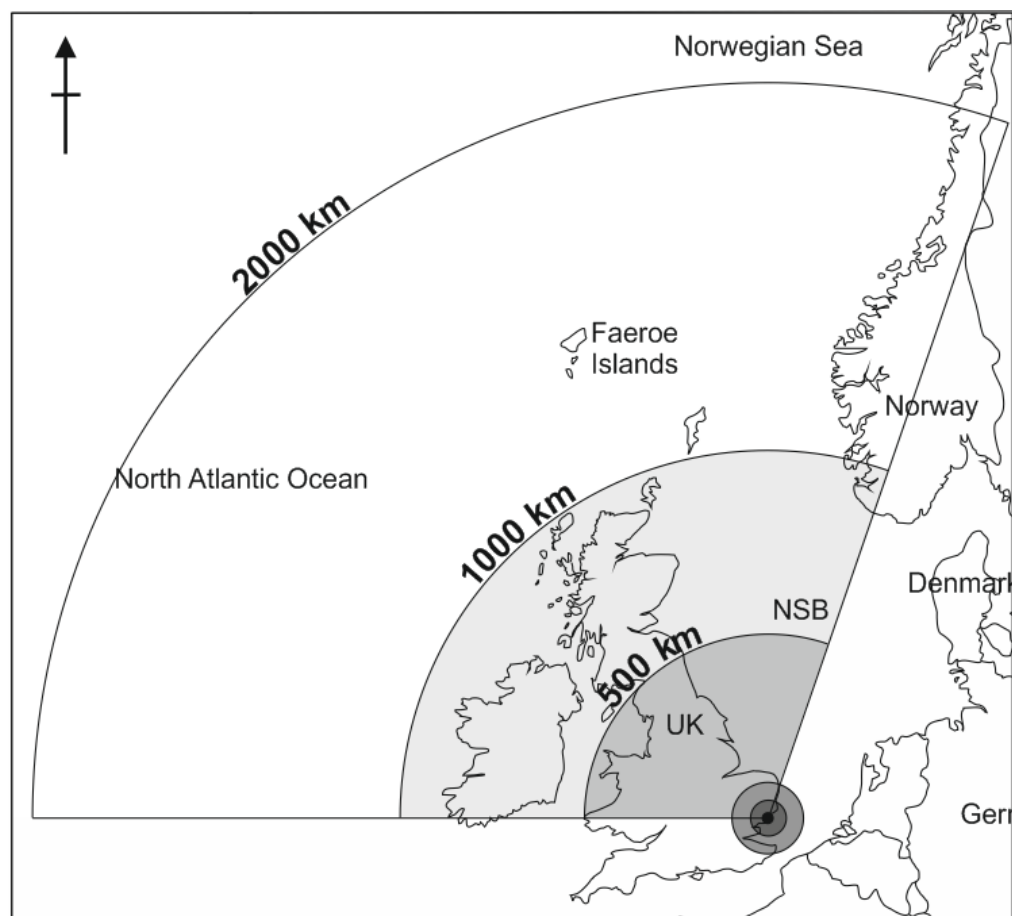


Figure 5-46 Areas where possible source vents could be located and distances from E. Anglia. The dominant wind direction at the time was most likely from the N-NW therefore more distal sources were more likely located towards the NW (Malm et al. 1984). Darkest grey circle represents areas of 50km from the E. Anglia study area (black circle).

A more detailed comparison of the ages of activity for volcanic centres in the BPIP will be considered when the ash of the WB is compared on a regional scale with the ash-rich deposits of the BF (see Chapter 3). For now, a source within the BPIP is interpreted for both ashes of the WM based on deposit thickness and grain-size distribution.

5.9 Conclusions

The Early Eocene Wrabness Member is an important unit within the Harwich Formation of E. Anglia that can be used to assess the nature of volcanism that affected the region at *ca.* 54-54.5 Ma. The Wrabness Member was investigated in estuarine cliff-sections along the Stour and Orwell Rivers at Harkstead, Levington to Nacton, Stutton and Wrabness (Table 5-5, Figure 5-7). Additional investigation into the characteristics of the Wrabness Member was provided by sedimentary logging and sample collection from the Shotley Borehole B (see section 5.5.1.6).

Field descriptions and petrological analysis show that the Wrabness Member is predominantly comprised of clay-rich siltstones, with angular quartz grains, along with minor amounts of other minerals, including barite, chlorite, feldspar (albite, labradorite and orthoclase), fluoroapatite, garnet, gypsum, ilmenite, magnetite, muscovite, pyrite, rutile, stilpnomelane, ulvospinel and zeolite (clinoptilite) (Table 5-6, Table 5-7). The sediments were deposited in an oxygenated, shallow marine environment, as suggested by abundant trace fossils and evidence of bioturbation, that have been identified throughout the section (Figure 5-11, Figure 5-22a-b, Figure 5-24), and palaeostratigraphical interpretations in the literature (King 1981; Ellison et al. 1994; Ali & Jolley 1996; Hooker 1996; Jolley 1996; King 2016).

The Harwich Stone Band is a prominent marker unit within the Wrabness Member, comprised of a well-developed, diagenetic (abiotic) layer dominated by calcite cement. This band is generally present throughout all of the exposures, and the Shotley Borehole B. It can easily be identified as it is generally more resistant to weathering than the surrounding soft, clay-rich siltstones, and is commonly present at, or just above, the present-day shoreline (Elliott 1971;

Knox & Ellison 1979). However, at Harkstead, the Harwich Stone Band appears to cross bed boundaries and pinch out, and is thus, absent across small (<1 m) distances (Figure 5-10). Isolated calcite-cemented concretions occur in other intervals of the Wrabness Member (Elliott 1971; Knox & Ellison 1979; this study), and can be seen at Harkstead (Figure 5-10). The calcite cement of the Harwich Stone Band likely formed early during diagenesis at a shallow depth of burial, as it comprises well preserved pyroclasts that have undergone low levels of alteration -which most likely can only be achieved if cementation was rapid in isolating the pyroclasts from circulating fluids within the deposit (e.g. Elliot 1971). Trace fossils, such as *endichnia*, are abundant within the upper part of the Harwich Stone Band (Figure 5-11) and provide evidence for a shallow marine environment of deposition and a near-surface depth of cementation.

In the field, the deposits have a characteristic stratified character, as shown by alternating layers of pale grey and dark grey/brown rock (Figure 5-7). In the literature, the pale grey units have been interpreted as volcanic units (Knox & Ellison 1979; Jolley 1996). The evidence for this conclusion was provided by petrographic investigations by Knox & Ellison (1979) from samples of the Shotley Borehole B, where the ash appears as 'dark blue-grey' units, although their evidence for these being volcanic is not provided in detail, and recent investigation of the Shotley Borehole B shows that it does not display any of the variations in colour that are observed in the field or by blue-grey intervals (Figure 5-18). The interpretation given by Jolley (1996) lacks any scientific evidence at all, and is based on assumptions rather than petrographic observations. Although Jolley (1996) does not specify exactly where the volcanic units are located within the Wrabness Member, and how they were identified in the field, his logs, depicting volcanic units, correlate with the positions and number of pale bands at each of the field-localities.

Systematic sampling of pale grey and dark grey/brown units at Levington-Nacton was carried out to investigate the volcanic component of the Wrabness Member. However, in general, all of the samples are similar in appearance and composition, and do not contain any volcanic material (Table 5-6; except for LEVNAC_14A from a dark grey/brown unit). The chemical composition of the clay matrix in all samples is similar. Therefore, the only difference identified in this

study, is that the dark grey/brown units seem to contain more types of dark coloured minerals; amphibole(?), ilmenite, magnetite, pyrite and rutile, compared to the pale grey units (Table 5-6). The repetitive layering of variable colour observed in the field is absent in the core of Shotley Borehole B (Figure 5-18), therefore the colours may be a result of weathering (e.g. Knox & Ellison 1979), and could correspond to subtle differences in the modal mineralogy and bulk composition between the pale grey and grey/brown layers.

Shotley Borehole B was drilled in 1979 at a location to the east of Harkstead, between the rivers Stour and Orwell (Figure 5-16). It was logged and described in detail as the London Clay Formation and Harwich Member by Knox & Ellison (BGS Borehole Report); however, since the 1970s the formation and member boundaries of the Shotley Borehole and the E. Anglia succession have changed (Ellison et al. 1994; Ali & Jolley 1996; Jolley 1996; Knox 1996; Aldiss 2014). To avoid confusion the borehole was logged again (this study; Figure 5-17). The borehole core is comprised of claystones and siltstones with lesser amounts of fine to coarse sandstone (Figure 5-17). A gravel and pebble-rich bed towards the top of the logged section may represent the contact between the Wrabness Member and the overlying Walton Member of the London Clay Formation (Ellison et al. 1994; Jolley 1996; Aldiss 2014). The core comprises repeating sequences of clay-rich rocks overlain by silt and sand-rich rocks; it is likely that these repetitive rock types represent at least three parasequences whereby relative sea-level increased in stages over time (Figure 5-40). A flooding surface (FS) is present where claystone is found directly overlying silt/sandstone (Figure 5-40). Therefore, it is interpreted that these parasequences represent a transgressive systems tract that eventually led to the establishment of deep marine conditions across SE England, which led to deposition of the London Clay Formation (Jolley 1996; Aldiss 2014). An interpretation of at least three parasequences of an overall transgressive systems tract within the Wrabness Member has also been proposed by Jolley (1996), based on analysis of palaeobiology of palynoflora/fauna.

Knox & Ellison (1979) concluded that more than 44 ash-layers can be identified in the Harwich Formation, based on their analysis of the Shotley Borehole. Jolley (1996) proposed that there are at least 32 ash-layers within the Wrabness

Member (Harwich Formation; Ali & Jolley 1996; Jolley 1996; King 2016). One easily identifiable ash-layer, *ca.* 4 cm thick, is present within the Harwich Stone Band, where it has been preserved within a well-developed calcite cement (Elliott 1971; Knox & Ellison 1979). This deposit is normal-graded and has a sharp contact with the underlying calcite-cemented siliciclastic siltstone. The deposit is predominantly composed of pyroclasts and crystalline igneous clasts, with very little background (siliciclastic) sediment e.g. quartz grains. The grain-size of the deposit is of coarse to fine ash (17 - 180 μm ; Table 5-8), with 35% juvenile pyroclasts and 65% accidental lithics (crystalline igneous clasts; Figure 5-38). In general, the igneous clasts are angular, with the pyroclasts retaining their original delicate, angular shapes. The pyroclasts have predominantly blocky morphologies with smaller amounts of bubble-wall pyroclasts and rod-like (Limu o Pele) morphologies (Figure 5-38). *Ca.* 28-38% of the pyroclasts within the Harwich Stone Band samples (HARK_HB, HARK_01, LEVNAC_01A) are vesicular (Figure 5-38), with an average vesicularity of 22-35% (Table 5-9). The volcanic unit of the Harwich Stone Band is interpreted as a primary air-fall ash that was produced during a hydrovolcanic eruption (Table 5-11), due to the low vesicularity (<45%) of pyroclasts, and the dominance of blocky, non-vesicular pyroclast morphologies (Wohletz 1983; Zimanowski et al. 1997; Mattsson 2010; Dellino et al. 2012; Graettinger et al. 2013), and the high percentage of accidental lithics compared to juvenile pyroclasts (Clarke et al. 2009; Németh & Cronin 2009; Valentine & White 2012; Graettinger et al. 2013; Valentine et al. 2014). The high angularity of the pyroclasts and their general ‘fresh’ morphologies suggest that this material has not undergone reworking prior to deposition, as this would likely lead to abrasion and rounding of the delicate pyroclasts, in addition to the inclusion of more siliciclastic sediment into the resulting deposit (see Chapter 7).

Parameter	Magmatic	Hydrovolcanic	HSB	LEVNAC_14A	Interpretation
Pyroclast morphology	Fluidal, accnelith, blocky	Dominantly blocky; accretionary aggregates	Dominantly blocky & poorly vesicular	Dominantly blocky & poorly vesicular	Rapid quenching, limited influence from magmatic degassing
% Accidental lithics	Low to none	Typically high	65% (high)	75% (high)	Weakly magmatic, dominantly hydrovolcanic
Deformation regime	More ductile	Brittle	Brittle Abundant brittle fractures	Brittle Abundant brittle fractures	Hydrovolcanic
% vesicles	>75%	<40%	Average 26.7%	19.7%	Hydrovolcanic
Vesicle morphology	Spherical, polylobate, tube (all sizes)	Small & spherical, other morphologies preserved from previously degassed magma	Dominantly spherical or near spherical with some coalescence	Dominantly spherical or near spherical with some coalescence	Weakly magmatic, dominantly hydrovolcanic
Abundance of fine ash produced	Low to moderate	Moderate to high	Fine ash dominant in deposit	Fine ash dominant in deposit	Highly explosive eruption

Table 5-11 Magmatic versus hydro volcanic deposit characteristics summarised for the primary ash fall deposits of the HSB and LEVNAC_14A (references in text).

The Wrabness Blue Band lies above the Harwich Stone Band at Wrabness (see section 5.5.1.1). Scanning Electron Microscopy (SEM) analysis shows that a minor component of this unit includes pyroclasts that have been replaced by calcite. The minor abundance of these pyroclasts within a predominantly siliciclastic siltstone suggests that this volcanic material has been reworked. The deposit is clay-rich and has a poorly developed calcite cement (Figure 5-27) that does not form a hard-band like that of the underlying Harwich Stone Band, most likely due to its high clay content. The close stratigraphic proximity of the Wrabness Blue Band to the volcanic unit of the Harwich Stone Band (within a few tens of centimetres), may suggest that the primary volcanic deposit of the Harwich Stone Band could be the source of reworked pyroclasts in the Wrabness Blue Band. No comparison of the chemistry of the pyroclasts in each unit could be achieved due to the complete calcite replacement of pyroclasts in the Wrabness Blue Band.

Another volcanic-rich unit can be observed within a dark grey/brown interval at Levington-Nacton, above the Harwich Stone Band. This unit is represented by sample LEVNAC_14A, and is predominantly composed of igneous clasts, including variably altered pyroclasts and crystalline igneous clasts (Figure 5-25, Figure 5-36), of fine ash to coarse ash (63-125 μm ; Table 5-8). Image analysis shows that there are *ca.* 25% juvenile pyroclasts and 75% accidental lithics (crystalline igneous clasts; Figure 5-38), and that the pyroclasts are predominantly non-vesicular (93%) with a blocky morphology (Figure 5-38). Lesser amounts of bubble-wall and rod-like (Limu-o-Pele) morphologies are present (Figure 5-38). The low occurrence of vesicular pyroclasts makes it difficult to accurately calculate the average vesicularity; however, an estimation of 15-28% vesicularity is given by the range of vesicularities calculated from a small sample set from LEVNAC_14A (Table 5-9). The original angularity and bubble-wall features of the pyroclasts remain, suggesting that this deposit represents a primary air-fall water-lain ash deposit, with similar features as the volcanic unit of the Harwich Stone Band. The poor vesicularity, low abundance of vesicular pyroclasts (7%) and high abundance of accidental lithics (75%) suggest that this deposit represents the product of hydrovolcanic activity.

The primary air-fall ashes of the Harwich Stone Band and LEVNAC_14A display a range of grain-sizes from fine-ash ($<63\ \mu\text{m}$) to lapilli ($250\ \mu\text{m}$; Table 5-8). Fine ash is likely to dominate distal pyroclastic deposits, furthest from the source vent (Williams 1983; Carey & Sparks 1986; Pyle 1989; Wohletz et al. 1995; Bursik 1998; Riley et al. 2003; Kutterolf et al. 2007; Pérez et al. 2009; Goepfert & Gardner 2010; Dellino et al. 2012; Oddsson et al. 2012); however, the presence of lapilli may suggest that the source was in a more proximal location. Comparison with deposit thicknesses and grain-sizes from previously studied volcanic vents, can help suggest a possible distance to the-source(s) of the two Wrabness Member tuffs. Carey & Sparks (1986) estimate that a plume height of 35 km can produce deposits of lapilli to fine-ash >30 or >50 km from the source (Figure 5-44). By comparison with deposit characteristics from the 122 BC Plinian basaltic eruption of Etna, a source for the Wrabness Member ash could lie >30 km distant, and deposits from the 1886 Plinian basaltic fissure eruption of Tarawera suggest a distance of >50 km (Walker et al. 1984; Houghton et al. 2004). However, these estimates do not take into account atmospheric conditions such as wind or humidity, or hydrovolcanic eruption dynamics, which can enhance the spread of ash and lapilli (Carey & Sparks 1986; Sheridan & Wohletz 1983; Woods 1993; Oddsson et al. 2012). Eruptions in the Early Eocene would have occurred into a warm, moist atmosphere (Thomas et al. 2003; Svensen et al. 2004; Lourens et al. 2005; Zachos et al. 2008; Gradstein et al. 2012; Kender et al. 2012; Newell 2014; Winnick et al. 2015), which may have enhanced plume height and allowed ash and lapilli to be distributed much further from the source vent. The predominant wind direction was from NW to SE (Carriol 2016), suggesting that the source vent(s) lie more than 50 km to the NW of E. Anglia.

Several volcanic centres were active during the Early Eocene within the British Palaeogene Igneous Province (BPIP; Figure 5-45); these lie to the NW within a range of <1000 km from the E. Anglia field localities (Figure 5-46). It is possible that two separate sources produced the two ashes of the Wrabness Member.

Correlation of the Wrabness Member ashes with those of the age equivalent North Sea Balder Formation should provide a more concise interpretation for the source of this volcanic material (see Chapter 3). Thus, for now, an interpretation

of basaltic hydrovolcanic eruptions >50 km to the NW can be inferred, and a potential source within the British Palaeogene Igneous Province implied. In contrast to the over-estimation of 32-44 ash-layers (Knox & Ellison 1979; Ali & Jolley 1996; Jolley 1996; King 2016), a minimum of two eruptive phases are indicated by the direct petrographic identification of two well-preserved primary air-fall ash units within the Wrabness Member. It is possible that additional volcanic eruptions influenced sedimentation in E. Anglia during the Early Eocene; however, the shallow marine environment interpreted for this locality has led to an incomplete stratigraphic succession in this region (Knox & Ellison 1979; Ellison et al. 1994; Ali & Jolley 1996; Knox 1996; Royse et al. 2012; King 2016).

Chapter 6: Columbia River Flood Basalt Sedimentary Analogue

6.1 Introduction

The Columbia River Flood Basalt Province (CRFBP) is a Large Igneous Province (LIP) that covers >208,000 km² of central and eastern Washington, Idaho and north-central Oregon, USA (Figure 6-1; Schmincke 1967a; Camp 1981; Hooper 1982; Smith 1988b; Camp 1995; Brueseke et al. 2007; Barry et al. 2013; Camp 2013; Wolff & Ramos 2013; Miller 2014; Reynolds et al. 2015). The CRFBP was emplaced between 17 and 6 million years ago (Ma) during the Miocene (Swanson et al. 1979; Camp 1981; Hooper 1982; Smith 1988b; Camp 1995; Brueseke et al. 2007; Nash & Perkins 2012; Barry et al. 2013; Wolff & Ramos 2013; Miller 2014; Reynolds et al. 2015). Abundant research has been carried out on the various lavas of this Flood Basalt Group, however, little attention has been paid to the interbedded siliciclastic and volcanoclastic units deposited during eruption hiatuses or on inactive parts of the province (e.g. Waters 1965; Camp 1981; Smith 1988b; Smith et al. 1988; Nash & Perkins 2012; Miller 2014). These sedimentary units are an important part of the geological history of this area and include ash from a poorly-documented source of silicic explosive volcanic activity in the region (Smith 1988b; Smith et al. 1988; Nash & Perkins 2012; Miller 2014; Reidel pers comms. 2015).

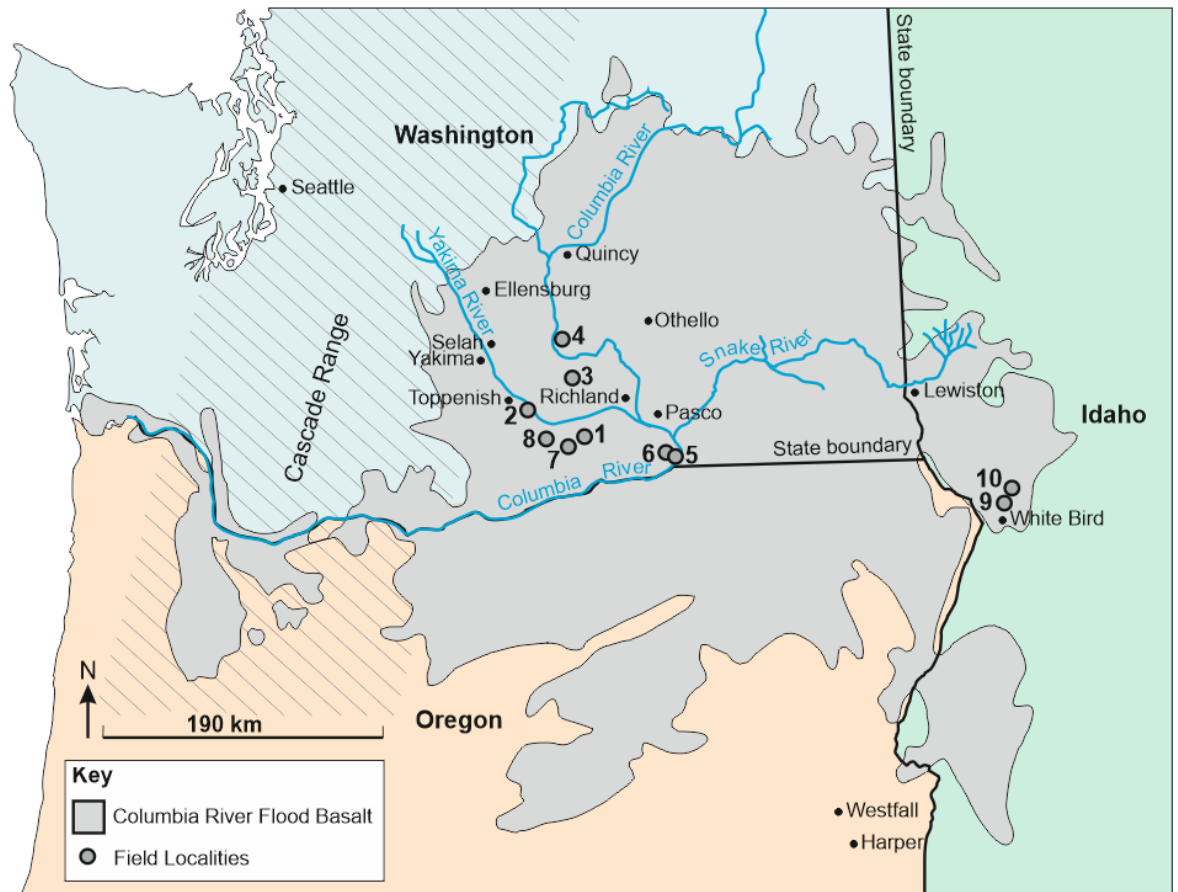


Figure 6-1 Location of the CRFBP and field localities referred to in this text. Dashes show the location of the Cascade Range (Schmincke 1967b; Google Earth 2015).

The sedimentary intervals within the CRFBP have been named as several different formations and members, although the correlation between packages in each location has not been identified or commented on in detail (Waters 1965; Camp 1981; Smith 1988a, 1988b; Smith et al. 1988; Nash & Perkins 2012; Miller 2014). Observations of the high variability in the sedimentary packages within the Lewiston Basin by Camp (1981) show the difficulty in correlating these deposits (e.g. Waters 1965; Camp 1981). The sediments studied in the current investigation have been identified as being part of the Ellensburg Formation (EF) (Figure 6-2; Waters 1965; Schmincke 1967b; Smith 1988b; Smith et al. 1988; Nash & Perkins 2012; Ebinghaus et al. 2014). This Formation is predominantly comprised of siliciclastic sediments (conglomerates, sandstones, siltstones and claystones) along with minor deposits from large silicic explosive eruptions (Waters 1965; Schmincke 1967a; Smith 1988a, 1988b) and straddles the interval between the *ca.* 17 Ma Grande Ronde Basalt and the Saddle Mountains Basalts at

ca. 4.7 Ma (Smith 1988b), essentially spanning the entire lava sequence of the CRFBP (Figure 6-2). Thus, it cannot be used as a marker interval for correlation.

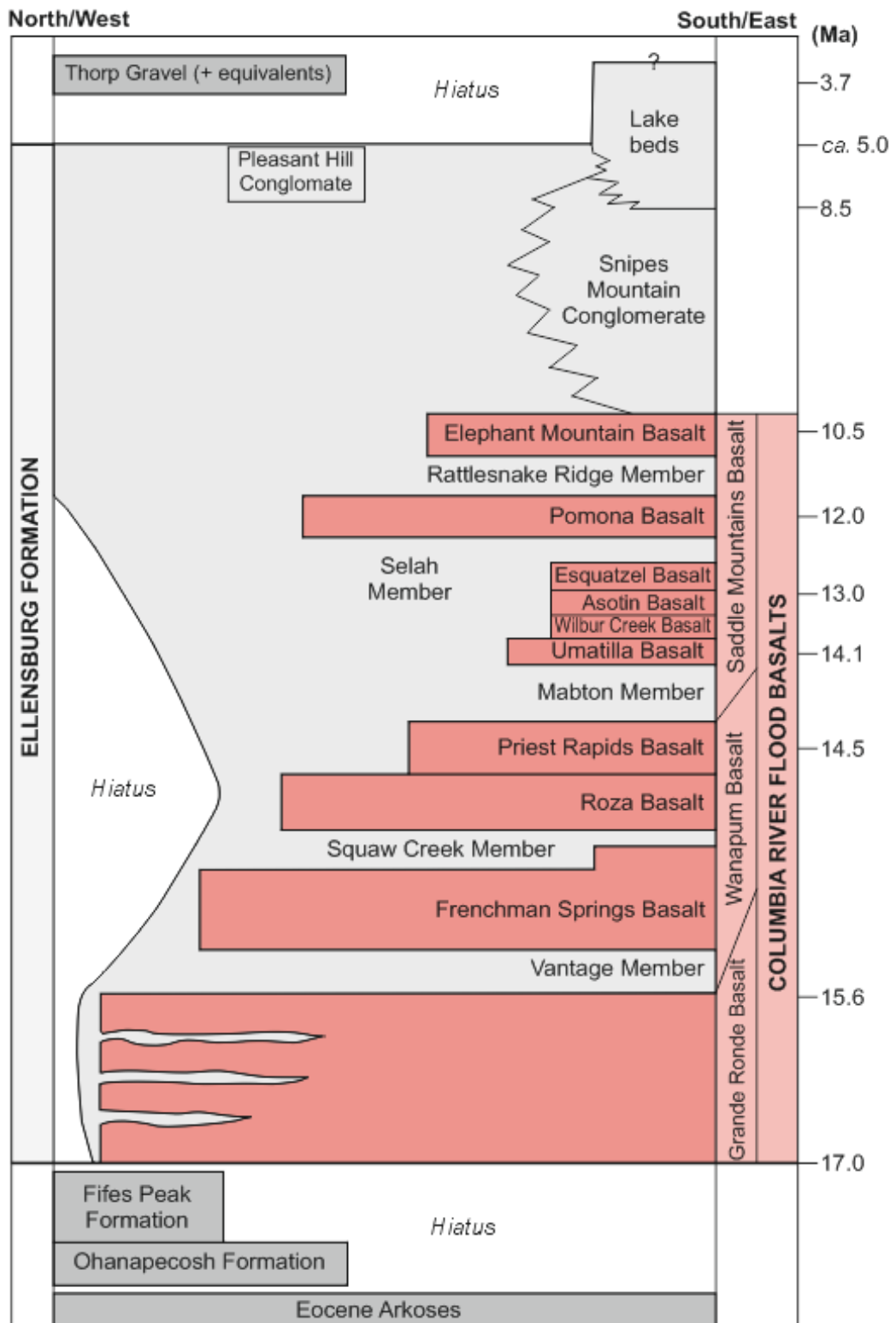


Figure 6-2 The Ellensburg Formation and its members (Vantage, Squaw Creek, Mabton, Selah and Rattlesnake which can be found between the main sub-divisions of the Columbia River Flood Basalts) (from Smith 1988b).

6.2 Aims and objectives

The aim of this study is to understand the nature and significance of the sedimentary units interbedded with the lavas of the CRFBP in Washington, particularly around the Tri-Cities area, and sites in western Idaho. The sedimentary, volcanoclastic and pyroclastic deposits of this region have not been studied in detail since initial observations were made by Mackin (1961), Schmincke (1967) and Smith (1988). Thus, a great deal of information on sedimentation and volcanism of this flood basalt province can be gained from detailed analysis of these deposits.

This chapter provides data and interpretations for the eruption, distribution and depositional processes of volcanic material within a terrestrial flood basalt province and compliments the work detailed in Chapters 3 - 5 of these processes within a marine environment. This chapter provides additional information on the distal deposition of ash from silicic eruptions that compliment the basaltic data set of the other chapters (Chapter 2 - 5).

6.3 Geological history and literature review

6.3.1 Emplacement history of the Columbia River Flood Basalt Group

The CRFBP lavas, are of predominantly tholeiitic basalt composition (Schmincke 1967b; Snavely et al. 1973; Camp 1995; Retallack et al. 2002; Brueseke et al. 2007; Camp 2013; Wolff & Ramos 2013). They cover an area of >208,000 km², and were erupted during multiple eruptive phases from *ca.* 17 - 6 Ma (Figure 6-3, Figure 6-4; Schmincke 1967a; Camp 1981; Hooper 1982; Smith 1988b; Camp 1995; Brueseke et al. 2007; Barry et al. 2013; Camp 2013; Wolff & Ramos 2013). The lavas generally flowed westward from fissures until they reached the growing Cascades mountain range (Figure 6-3; Smith 1988b), and are found within the back-arc basin of the Cascade Range (Ebinghaus et al. 2014).

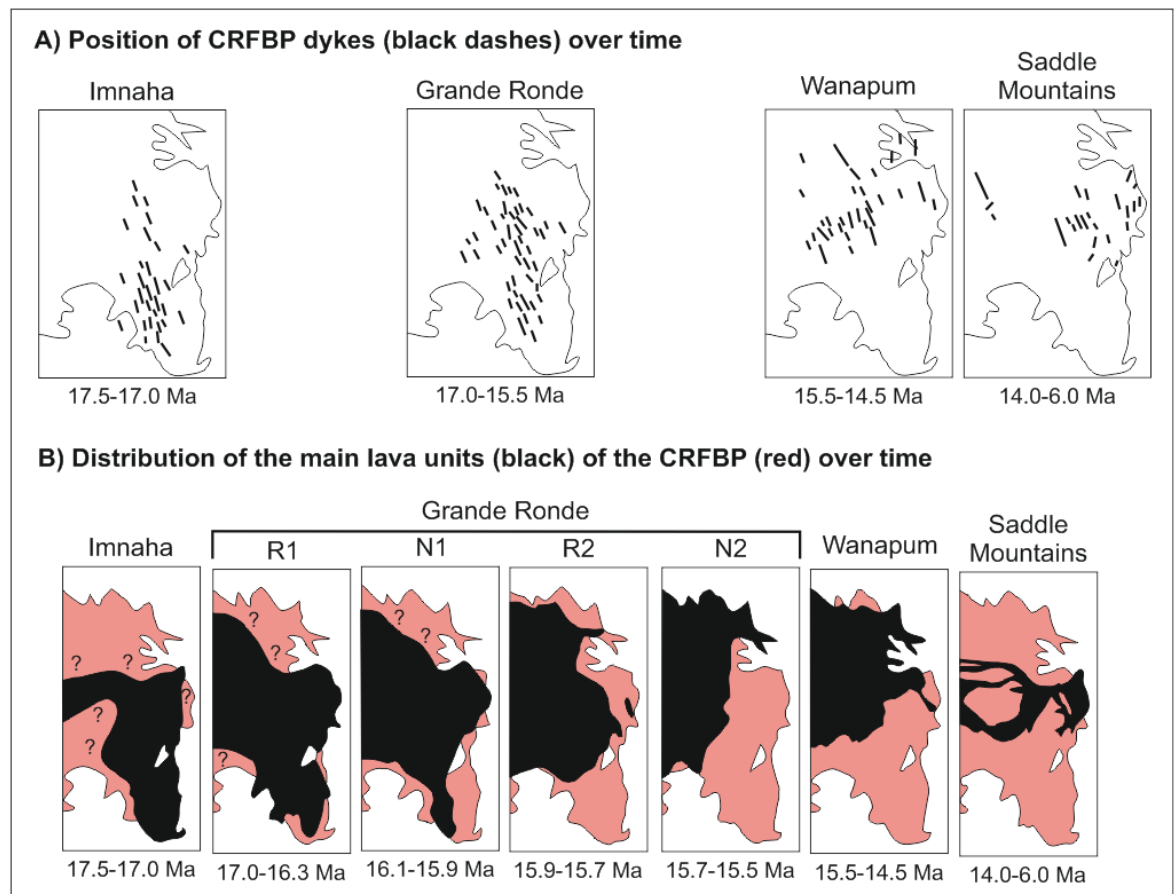


Figure 6-3 Distribution of the dykes (A) and lavas (B) of the CRFBP over time (from Camp 1995). The lavas generally flowed westward from fissures associated with the dykes located towards the east (Smith 1988b).

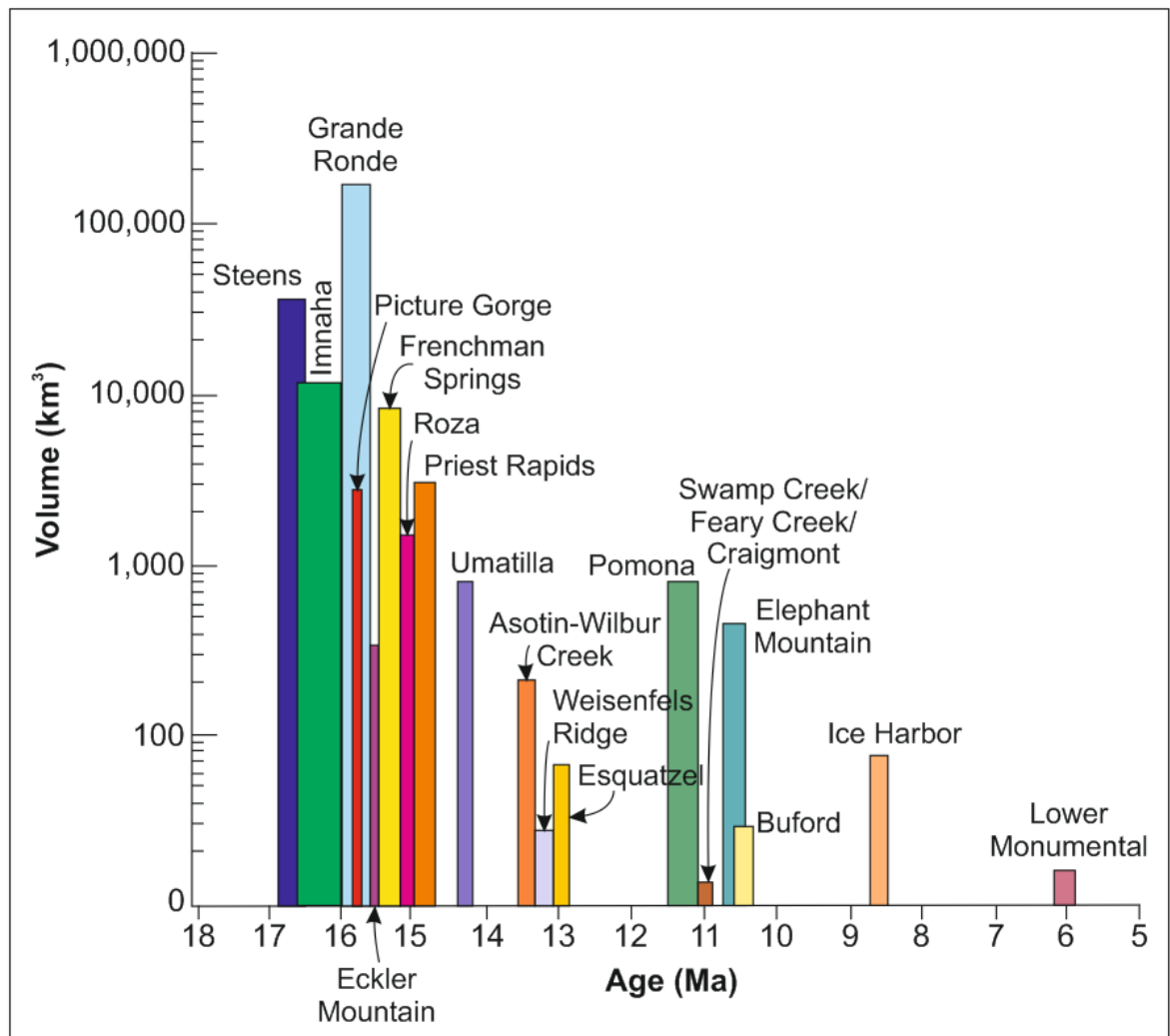


Figure 6-4 Relative ages and emplacement volumes of the major sub-divisions of the CRFBP. The sedimentary deposits of the Ellensburg Formation investigated during this research are generally found between the Pomona and Elephant Mountain members, which are units within the Saddle Mountains Group of the CRFBG (From Barry et al. 2013).

Around 90% of the total volume of the CRFBP was emplaced between 16.6 and 15 Ma (Nash & Perkins 2012), and the erupted volume of lava decreased over time (Figure 6-4; Hooper 1982; Barry et al. 2013). More lengthy hiatuses between eruptions of lava occurred following eruption of the Priest Rapids Member (Figure 6-4; Barry et al. 2013).

6.3.2 Characteristics of the Ellensburg Formation: source of material, resultant deposits and their depositional setting

The extent of the CRFBP was influenced by the contemporaneous (ancestral) Columbia, Snake and Yakima rivers in Washington (e.g. Camp 1981; Hooper 1982; Smith 1988b; Miller 2014), and the Clearwater River in Idaho (e.g. Camp

1981; Hooper 1982; Smith 1988b). Deposition of sediments during the Miocene was influenced by these rivers, with deposition, including that of the Ellensburg Formation (EF), mainly concentrated within the Nile, Selah, Kittitas, Yakima and Toppenish basins in Washington (Figure 6-5; Smith 1988a, 1988b; Smith et al. 1988), and the Lewiston Basin in Idaho (Schmincke 1967a; Camp 1981; Hooper 1982).

Many of the sedimentary units between packages of basaltic lava within the CRFBP of southern Washington may be associated with the disruption of drainage systems, such as the ancestral Columbia River, during the emplacement of lavas (Mackin 1961; Waters 1965; Schmincke 1967a; Smith 1988b; Nash & Perkins 2012; Reidel pers comms. 2015). The emplacement of subsequent lavas on top of these sediments has led to the removal of some deposits and the deformation and welding of others (e.g. Schmincke 1967b). For example, in some areas, the EF is overlain by the Pomona basalt which has caused welding of the underlying pyroclastic or siliciclastic deposits (Schmincke 1967b).

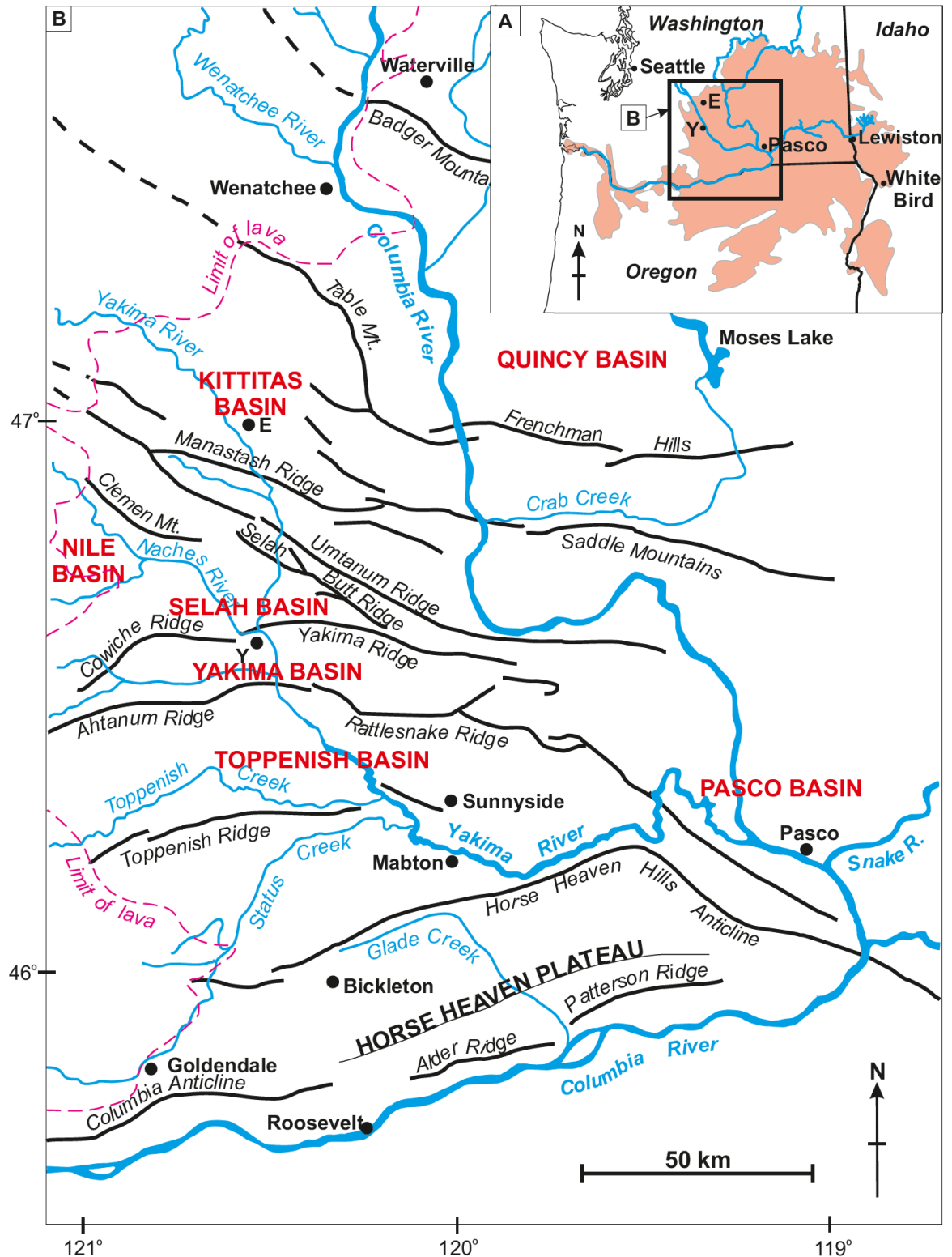


Figure 6-5 Location of Washington sedimentary basins described in the text. Insert (A) shows the location of the map (B) with reference to the rest of the CRFBP (Waters 1965; Swanson et al. 1979; Smith 1988b).

Both the ancestral Columbia and Clearwater rivers transported large sediment loads (e.g. Camp 1981; Smith 1988b), and their drainage systems were utilised by the CRFBP lavas (Camp 1981; Hooper 1982; Smith 1988b). For example,

arkosic and subarkosic sandstones found in the Lewiston Basin contain material that was originally transported from the granitic highlands by the ancestral Clearwater River (Schmincke 1967a). Sediments deposited by the ancestral Columbia River across areas of Washington include components of plutonic and metamorphic rocks sourced from northern Washington (Mackin 1961; Schmincke 1967a; Smith 1988b), as well as pyroclastic material sourced from the Cascade Range (Schmincke 1967a; Smith 1988b). Freshwater diatomites are also a feature of the sedimentary succession, alongside micaceous and quartz-rich siltstones and claystones with very fine-scale lamination (Berry 1934; Waters 1965; Smith 1988b). Multiple localities of diatomite have previously been attributed to the presence of a shallow but extensive lake (Makin 1947; Waters 1965; Smith 1988b). However, it is possible that smaller ephemeral lakes existed between the lavas, forming in different places over time (Waters 1965; Smith 1988b), as river courses were disrupted by the emplacement of lavas.

The main controls on siliciclastic, volcanoclastic and pyroclastic deposition within the CRFBP were: 1) ancestral river systems; 2) the effect of basaltic lava flows on the courses of rivers and the formation of ephemeral lakes; 3) volcanism in the Cascade Range Volcanic Arc and surrounding areas of the CRFBP; 4) sediment sourced from the tectonic uplift of highland regions; and, 5) general basin subsidence (e.g. Waters 1965; Smith 1988a; 1988b). This was summarised by Smith (1988b) as follows:

‘...Sedimentology of the Neogene section in central Washington reflects the complicated combined influences of synchronous flood-basalt volcanism, continental-margin arc volcanism, and fold-belt deformation superimposed on a broad subsiding basin’ (Smith 1988b).

The sedimentary units of the EF are generally poorly consolidated or unconsolidated (e.g. Waters 1965) and have undergone a limited amount of burial, particularly in the upper sections, where fewer lavas were emplaced and sediments have remained at or close to the surface (e.g. Waters 1965). Subsequent folding and the growth of anticlines and synclines, including the Horse Heaven Hills Anticline (Figure 6-5), occurred during the middle Miocene and Pliocene, associated with the growth of the Yakima Fold Belt, has affected the interstitial deposits, which have commonly acted as shear planes during

faulting and folding (Waters 1965; Smith 1988a, b; Blakely et al. 2011; Pratt 2012; Miller 2014).

6.3.2.1 *The Ellensburg Formation of Washington*

The Late Miocene Ellensburg Formation (EF) is composed of several members, including the Douglas Creek, Vantage, Squaw Creek, Quincy, Selah and Rattlesnake Ridge members, as well as interbeds that are unassigned to a particular member (Figure 6-2, Table 6-1; Smith 1964; Waters 1965; Smith 1988a, 1988b; Rettallack et al. 2002; Ebinghaus et al. 2014). These sedimentary units are predominantly found in areas along the margins of the CRFBP and where local structural basins allowed the accumulation of sediment (Camp 1981; Smith 1988b). These members were proposed based on their relationship to the intervening basaltic lavas by Schmincke (1964, 1967a).

Member Name	Underlying unit	Overlying unit	Lithology	Interpretation (Depositional environment)	Interpretation (Sediment source and palaeoflow direction)	Thickness (m)
Vantage Member	Grande Ronde Basalt	Wanapum Basalt	Siliciclastic, dacitic volcaniclastic, localised conglomerate and claystone	Deposition influenced by fluvial systems e.g. Columbia River	Palaeoflow towards SE for siliciclastic, SW for volcaniclastic deposits	ca. 35
Squaw Creek Member	Frenchman Springs flow (Wanapum Basalt)	Roza flow (Wanapum Basalt)	Diatomite, siltstone, cross-stratified sandstone	Lacustrine and fluvial	-	ca. 10
Selah Member	(Saddle Mountains Basalt)	Pomona flow (Saddle Mountains Basalt)	Dacite and basalt-rich conglomerate, pumice and basalt-rich sandstone, vitric tuff, siliciclastic siltstone and sandstone, quartzite-rich conglomerate	Sediments transported by rivers e.g. Columbia & Yakima Rivers	Palaeoflow towards the south Sediment sourced from the north and minor amounts from the west	ca. 6
Rattlesnake Ridge Member	Pomona flow (Saddle Mountains Basalt)	Elephant Mountains flow (Saddle Mountains Basalt)	Volcaniclastic, dacitic breccias, at least two rhyodacitic pumiceous air-fall tufts	Deposition from block-and-ash flow and a large Plinian eruption. Deposition from streams and rivers & large alluvial fans	Eruptive activity from the S and SE towards the Yellowstone/Snake River Plain. Sediments from nearby growing anticlines	-

Table 6-1 Features of the various members of the Ellensburg Formation as interpreted by Smith (1988a, b).

The EF reaches a thickness of at least 350 m within the Yakima and Toppenish basins, where it overlies the Pomona and Elephant Mountain lavas (Figure 6-5; Smith 1988a, 1988b), and more than 350 m within the Selah Basin (Figure 6-5; Smith et al. 1988). The Formation has a minimum thickness of 300 and 100 m in the Nile and Kittitas basins respectively, where it overlies lavas of the Grande Ronde Basalt Member (Figure 6-5; Smith 1988b).

The characteristics of the EF strata suggest that deposition was associated with shallow lakes, including lava-dammed fluvial-lacustrine environments, fluvial systems, sediment deltas and fans (Figure 6-6; Waters 1965; Schmincke 1967a; Camp 1981; Smith 1988b; Smith et al. 1988). Conglomerates are common throughout the Formation and likely represent deposition following episodes of uplift and increased erosion of the Cascade Range Volcanic Arc during the Late Miocene (Smith 1988a, 1988b; Smith et al. 1988).

A mixture of fluvial and lacustrine sedimentary deposits present between lavas should be expected in areas of flood basalt emplacement due to the damming of river channels and overflowing of rivers due to the emplacement of lava (Waters 1965; Camp 1981; Smith 1988b; Hamblin 1994).

‘Streams draining the highlands to the northwest were dammed by the advancing (lava) flows and spread out in shallow lakes along the periphery of the volcanic field’ (Waters 1965).

The ephemeral lakes formed across the province were frequently inundated by subsequent lava flows, leading to the formation of pillow lavas and palagonite sequences at the bases of lavas (Waters 1965; Smith 1988b; current study).

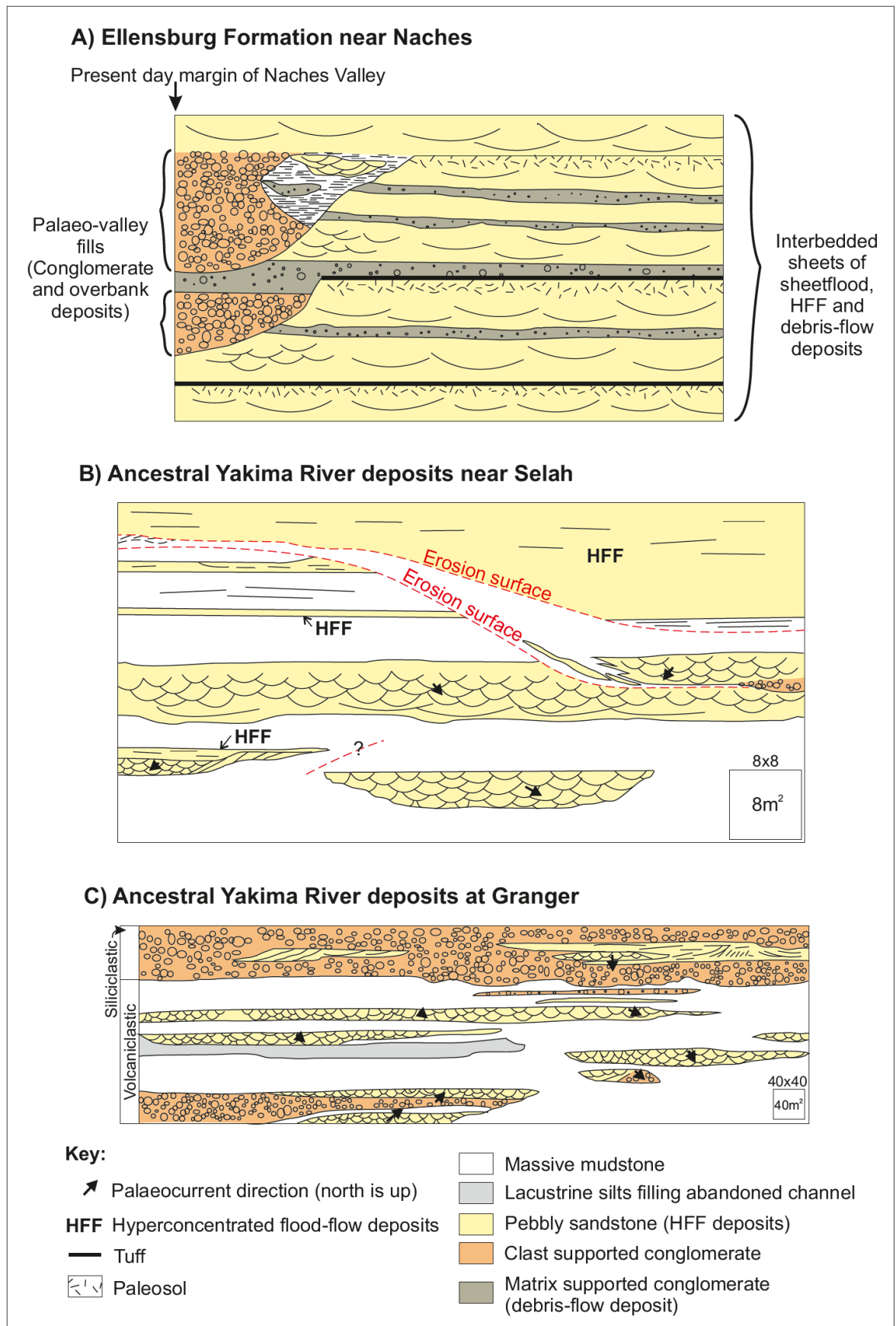


Figure 6-6 Interpretation of sedimentary deposits within the Ellensburg Formation from the ancestral Yakima River (from Smith 1988a). The regions of Naches, Selah and Granger all include fluviially-deposited sediments, including conglomerates and over-bank deposits and

hyperconcentrated flood-flow (HFF) deposits. Alongside these, there are also deposits from debris-flows, and tuffs (Smith 1988a).

6.3.2.2 Pyroclastic and volcanoclastic deposits of the Ellensburg Formation

In addition to siliciclastic strata, the EF contains primary pyroclastic and reworked volcanoclastic units (Table 6-2; Waters 1965; Schmincke 1967a, b; Smith 1988a, b; Smith et al. 1988; Retallack et al. 2002; Nash & Perkins 2012). These include silicic and andesitic deposits that are associated with volcanism in the Cascade Range Volcanic Arc (Waters 1965; Smith 1988a, b; Smith et al. 1988; Nash & Perkins 2012), the Yellowstone and Snake River Plain hotspot (Perkins et al. 1995, 1998; Cathey & Nash 2004; Branney et al. 2008; Ellis et al. 2012; Nash & Perkins 2012; Ellis et al. 2013; Kent-Corson et al. 2013; Knott et al. 2016), and within the High Lava Plain of the Harney Basin in Oregon (Smith et al. 1988; Perkins et al. 1998; Retallack et al. 2002; Streck & Grunder 2008). Lahars have also been identified (Waters 1965; Reidel pers. comms. 2015; this study).

Deposit description	Location of deposition	Age (Ma)	Interpretation	Source	Reference(s)
Volcaniclastic (silicic)	Kittitas Basin	17 - 12 Ma	Silicic volcanism and reworking of pyroclastic material	Cascade Range	Smith et al. 1988
Dacitic block-and-ash flow deposits and volcaniclastic sediments	Nile Basin	12 - 7.4 Ma	Dacitic volcanism	Source within 20 km of the Nile Basin (e.g. Bumping Lake, ca. 8.8 - 4.7 Ma)	Smith et al. 1988
Andesitic pyroclastic and volcaniclastic sediments; pumice lapilli, vitric tuffs & andesitic gravel	-	Above the Wenas Basalt	Pyroclastic and volcaniclastic deposits	Cascade Range	Waters 1965
Dacitic primary air-fall tuffs and pumiceous deposits; lahar deposits; reworked volcaniclastic sediments	Nile Basin	-	Air-fall ash and PDC deposits	Cascade Range	Waters 1965; Schmincke 1967b; Smith 1988a, b; Smith et al. 1988; Nash & Perkins 2012
1.5 - 8 m thick silicic vitric tuffs and ash aggregates	Throughout the basins of the CRFBP	-	Large Plinian eruptions	Yellowstone hotspot/ Snake River Plain Cascade Range	Nash & Perkins 2012 Schmincke 1967a, b; Smith et al. 1988
5 cm thick air-fall tuffs <50 cm thick pumice lapilli	Selah Basin Nile Basin	ca. 7 Ma	The Rattlesnake ash-flow tuff	Harney Basin, High Lava Plains of Oregon	Smith et al. 1988; Retallack et al. 2002

Table 6-2 Silicic and andesitic pyroclastic and volcaniclastic deposits described within the CRFBP.

The source of any pyroclastic material within the CRFBP cannot be identified with certainty due to the erosion of source volcanoes during the Neogene (Smith et al. 1988; Smith 1988b). Burial by younger sediments and volcanic material may also have acted to remove the visual record of volcanic centres that were active during the Miocene, and were a source for pyroclastic material in the EF (Smith et al. 1988). However, correlation of deposits via chemical fingerprinting and general descriptions of exposures may allow for the approximate region or direction to the original vent to be estimated (e.g. Shaw 2003; Lowe 2011).

Erosion of pyroclastic deposits and volcanic regions within the Cascade Range, most likely supplied volcanic sediment to the CRFBP, where it can now be identified as volcanoclastic deposits (Figure 6-7; Schmincke 1967a; Smith 1988a, b; this study).

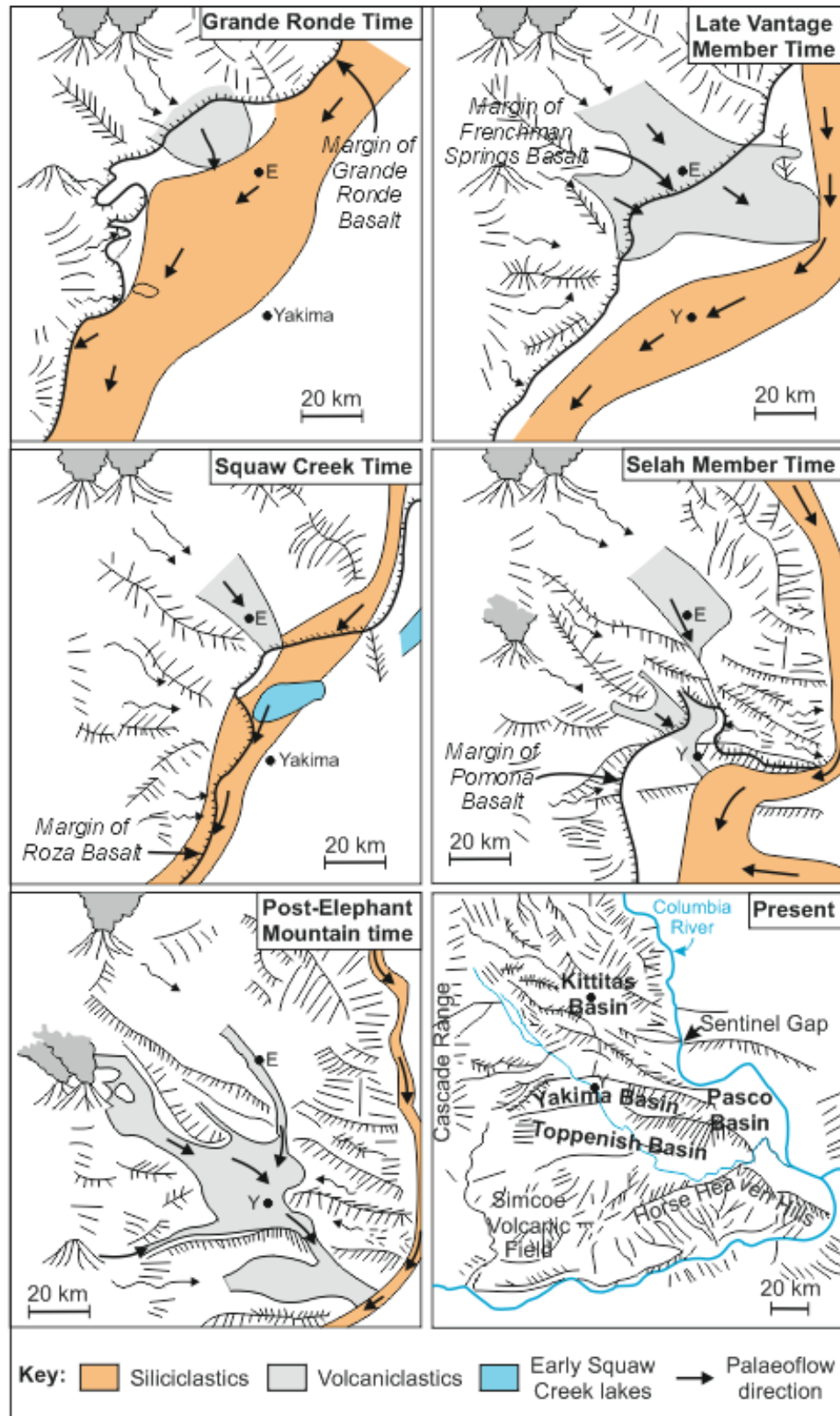


Figure 6-7 Palaeoenvironmental reconstruction of part of the CRFBP highlighting the sources of sediment deposition in the CRFBP within central Washington (from Smith 1998a, b). The Simcoe Volcanic Field (present) became active ca. 5 Ma (Ertan & Leeman 1999), and is therefore younger than the CRFBP.

6.3.2.3 Lewiston Basin, Idaho

The Lewiston Basin, Idaho, is comprised of a repetitive sequence of basaltic lavas with intercalated sedimentary deposits from the ancestral Clearwater River (Camp 1981). Arkosic and subarkosic fluvial-derived sandstones are commonly intercalated with the lavas; these sediments most likely originated from erosion of the granitic highlands to the north (Camp 1981). Stream-derived cobble-conglomerates are also present locally between the lavas (Camp 1981). Sedimentary units between lavas of the Saddle Mountains Basalt have been identified as more lacustrine-like deposits, that contain localised evidence of fluvial processes in the form of cross-stratification and erosional surfaces (Camp 1981).

To the east, within the Lewiston Basin, the stratigraphy is different, reflecting emplacement of the Wanapum and Saddle Mountains Basalts, which originated in the north, within the vicinity of the Clearwater River (Camp 1981; Hooper 1982). These lavas were emplaced intermittently from *ca.* 13.5 - 6 Ma (Camp 1981). Sediments are found between the lavas and are associated with movement of the ancestral Clearwater River; including, damming and migration of the river channel due to lava emplacement (Camp 1981; Hooper 1982). The Saddle Mountains Basalt lavas were emplaced towards the end of the CRFBP, when eruption intensity and duration was waning (Figure 6-4; Camp 1981; Hooper 1985; Smith 1988a), thus allowing ample time for the erosion and migration of stream channels and canyons (Camp 1981). Both the Pomona and Elephant Mountains lavas took advantage of the ancestral river drainage system within the Lewiston Basin (Camp 1981).

The Miocene sediments of western Idaho, within the Lewiston and Whitebird regions, are an important locality for fossilised leaves. These fossils are found within deposits from lakes that developed across Idaho, on top of lavas, and were subsequently buried beneath younger lavas (Berry 1934). These sedimentary units have been referred to as the Payette or Latah members and are a lateral equivalent of the Ellensburg Formation that can be found throughout the CRFBP of Washington (Berry 1934). The Latah Member was deposited *ca.* 21 to 12 Ma (Engel 2004). Some of the best localities for fossil

leaves occur around Whitebird, where a wide variety of flora can be identified (Berry 1934). The range of plant species that are preserved shows that there was an extensive flora present in Idaho during the Miocene. In addition to leaves, discoveries of fruits, seeds, insects, sponge spicules and small fish bones have also been made (Berry 1934).

6.4 Methods

Fieldwork was conducted within Washington and Idaho over two weeks in July and August 2014. Suitable localities were advised by S. Reidel from his previous experience of working on the CRFBP and from information provided in the literature.

Localities (Table 6-3) were chosen for more detailed logging and sample collection based on the quality of the exposure, ease of access, and the suitability of the rock types for assessing sedimentary and pyroclastic processes. Other localities were visited, logged and sampled in detail due to being of geological interest regarding inter-sedimentary units within a flood basalt province (Table 6-3). These regions could provide a comparison for areas of the North Atlantic Igneous Province and provide a wider understanding of the sedimentary units and tuffs found within Flood Basalt/Large Igneous Provinces, in general.

Thin-sections of consolidated samples were produced by ALS Petrophysics with a blue resin, and polished grain-mounts were produced at the University of Glasgow for petrographical and Scanning Electron Microscope (SEM) analysis (Table 6-3). Key samples were sent to the University of Durham for thin-sectioning, however, most of these sections could not be used in this study due to the lack of adequate labelling and the poor quality of the returned sections. Unfortunately, the remaining parts of the samples were not returned, and no replacement sections could be made.

More detailed information regarding sample preparation, data collection and interpretation can be found in the Methods section (see 1.3 Methods).

Locality	Longitude & Latitude	Samples referred to in text
Horse Heaven Hills (L1) Washington	46°12'14.70"N 119°42'33.40" W	WASH_04
Snipes Mountain (L2) Washington	46°20'3.30"N 120°10'50.20" W	-
Yakima Ridge (L3) Washington	46°32'47.70"N 119°50'5.70" W	WASH_05, WASH_06
Beverly Quarry (L4) Washington	46°46'42.80"N 119°54'47.20" W	WASH_20, WASH_21, WASH_22, WASH_23, WASH_29, WASH_30
Yellpit (L5) Washington	46°3'52.40"N 118°57'23.70" W	WASH_13, WASH_14
Finley Quarry (L6) Washington	46°7'7.37"N 119°2'34.99" W	WASH_07
Sellards Road (L7) Washington	46°7'38.80"N 119°50'41.50" W	WASH_32, WASH_33
Mabton-Bickleton Road (L8) Washington	46°8'26.70"N 120°1'32.30" W	WASH_37, WASH_40, WASH_44
White Bird (L9a) Idaho	45°46'24.80"N 116°17'24.60" W	-
White Bird Site (L9b) Idaho	45°46'52.8"N 116°16'30.2"W	-
White Bird Site (L9c) Idaho	45°47'4.30"N 116°16'17.10" W	ID_05
State Road 95 (L10) Idaho	45°49'58.00"N 116°14'28.80" W	ID_13, ID_16

Table 6-3 List of locality names and locations, and samples that are described in the text.

6.5 Results and interpretations

Lithological logs and samples were collected from localities within the CRFBP in both central Washington and western Idaho (Figure 6-1, Table 6-3). These localities will be described here, along with lithological logs, photographs and sample information. Several samples were chosen for thin-sections and grain-mounts for optical microscopy and SEM analysis; the results from these samples will be presented, followed by the results from the image analysis of backscatter (AsB) SEM images.

Unless conclusive evidence was available, fine-grained deposits in the field could not be separated into siliciclastic, volcanoclastic or pyroclastic types with

confidence. Samples were collected to allow for identification of the deposit types, based on petrography and the interpretation of depositional processes, and are discussed in detail in the following sections (see 6.6 Discussion). For simplicity in the field, all deposits were described as sedimentary, using the terms sandstone, siltstone and claystone. This terminology is used here solely as a guide to the grain-size (sand, silt, clay) of the deposit, with no indication to the processes which led to deposition of the constituent grains. It has already been established (see section 6.3), that the majority of the EF, and its Idaho equivalents, was deposited in a fluvial or lacustrine environment; therefore, the deposits are most likely to be comprised of siliciclastic and volcanoclastic material that should both be regarded as sedimentary. Where deposits were found, after more detailed investigation, to contain ‘primary air-fall’ pyroclastic material, then the terminology was converted to that appropriate for pyroclastic deposits, i.e. lapilli and ash (see Chapter 1 & Chapter 7).

6.5.1 Horse Heaven Hills (L1)

6.5.1.1 *Field observations*

Towards the top of the Horse Heaven Hills along State Highway 221 (Figure 6-1), the EF is exposed beneath a thin unit of basaltic lava, which forms the crest of the hills. All the sedimentary rocks here are poorly consolidated and highly friable.

The sediments at the base of the exposure include interbedded claystone, siltstone and sandstone, with some units showing normal grading (Figure 6-8). The normal-graded units generally grade from medium-sandstone to siltstone. Within this interval is a prominent layer of darker grey sandstone (Figure 6-9) that can be traced along the entire exposure and appears to be composed of vitreous pyroclasts of <1 mm. Above this layer, ripple cross-stratified siltstone is present, with discontinuous lenses of coarser-grained sandstone. The exposure is dominated by a *ca.* 5 m thick unit of cross-stratified sandstone present at the top of the exposure (Figure 6-8, Figure 6-10).

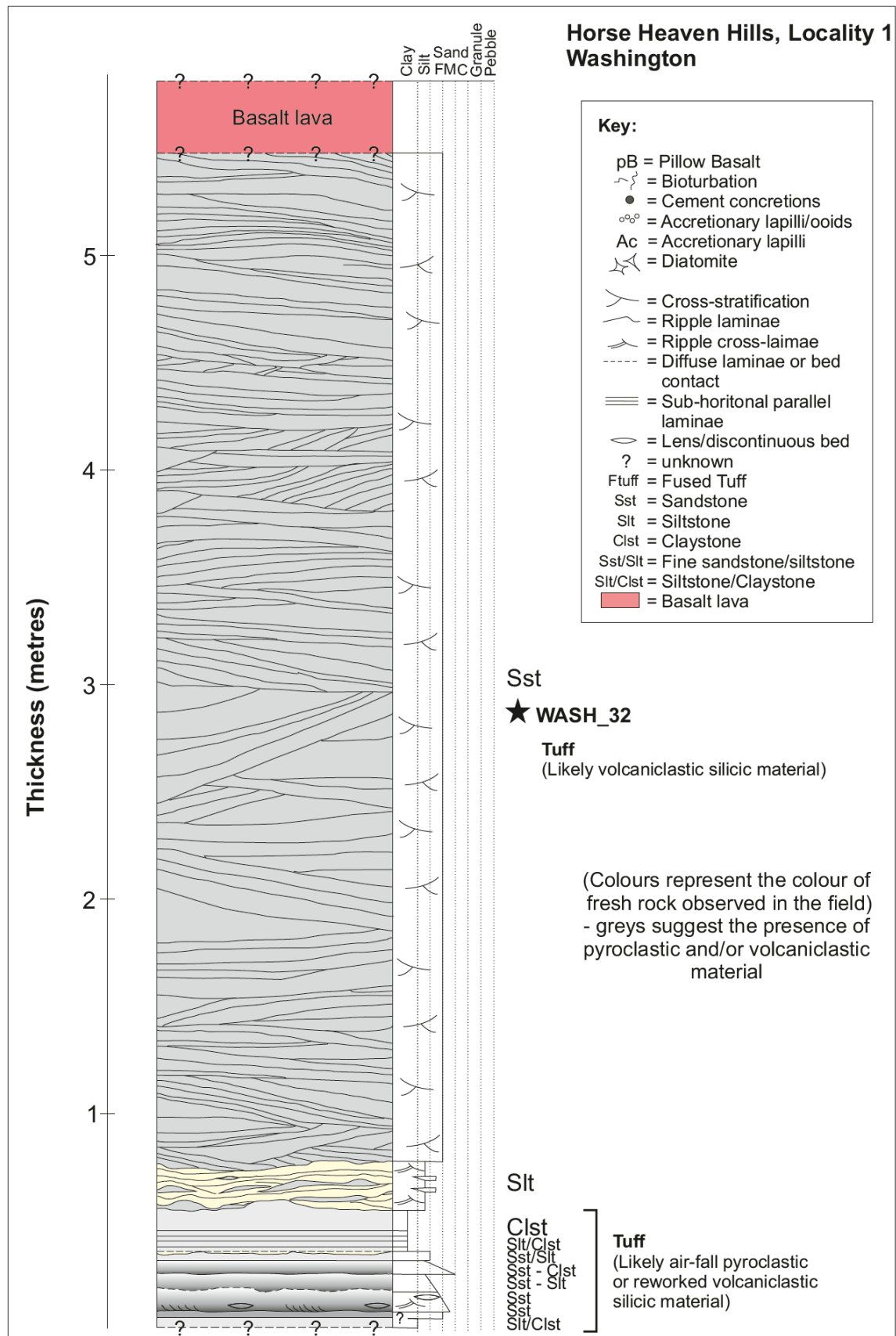


Figure 6-8 Sedimentary log that represents the Ellensburg Formation observed at Horse Heaven Hills (L1). At the base of the exposure are interbedded normal-graded sandstones, some showing ripple cross-laminae and discontinuous lenses of coarser-grained material. Claystone, with a lower section displaying sub-horizontal parallel laminations, is present above this. An erosional contact separated the claystone from the overlying cross-

laminated siltstones. The upper ca. 6 m of the exposure comprises cross-stratified coarse-medium sandstone, that is overlain by a basalt lava. Pink: basalt lava, other colours in the log represent the colour of the rock observed in the exposure; grey indicates the locality of pyroclastic or volcanoclastic silicic material.

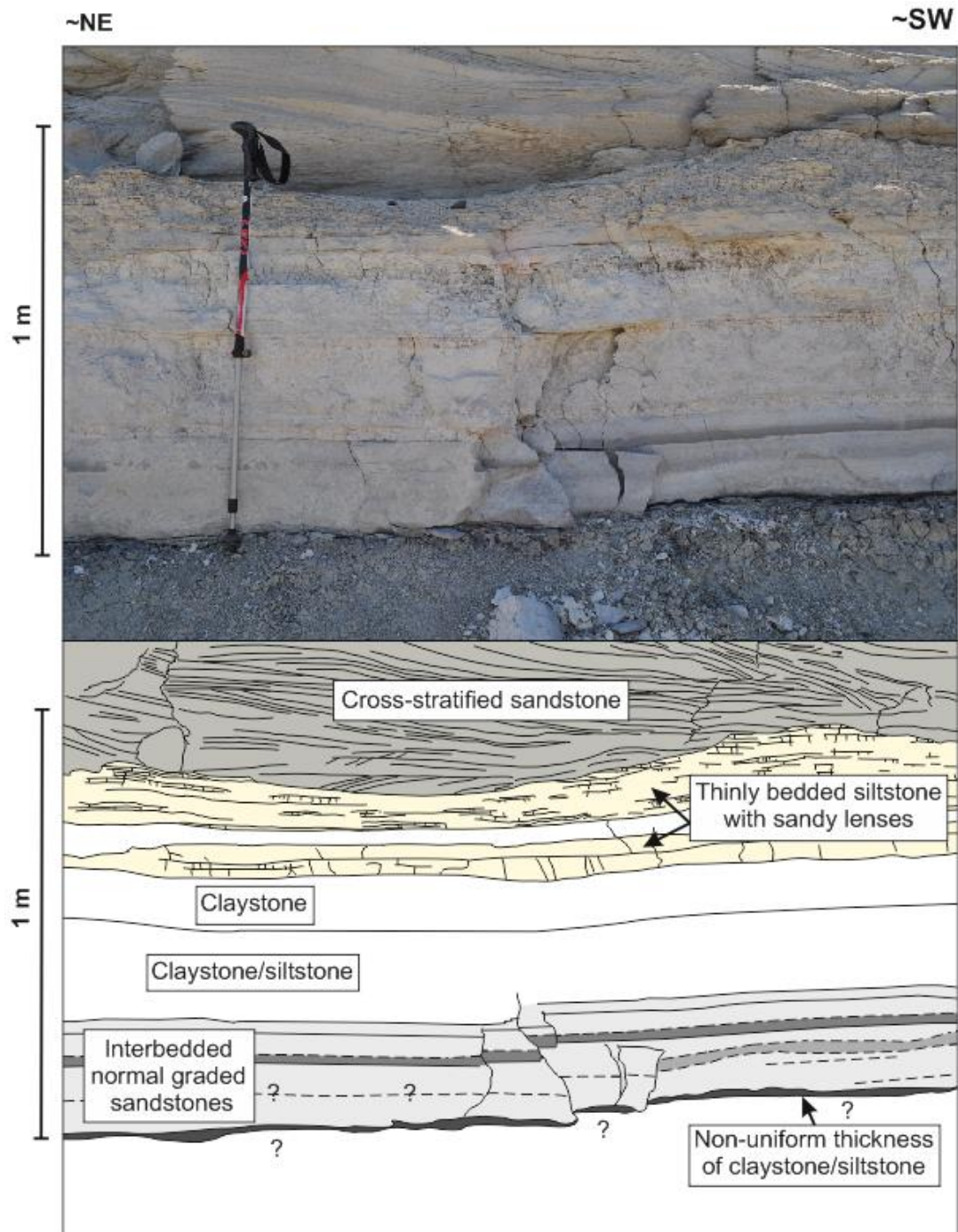


Figure 6-9 Main lithologies of the exposure at L1: thin diatomaceous(?) siltstones and normal-graded sandstones. Above this is a cross-stratified sandstone.

The cross-stratification within the upper sandstone unit shows a range of orientations and erosional surfaces where bedding has been truncated (Figure 6-10).

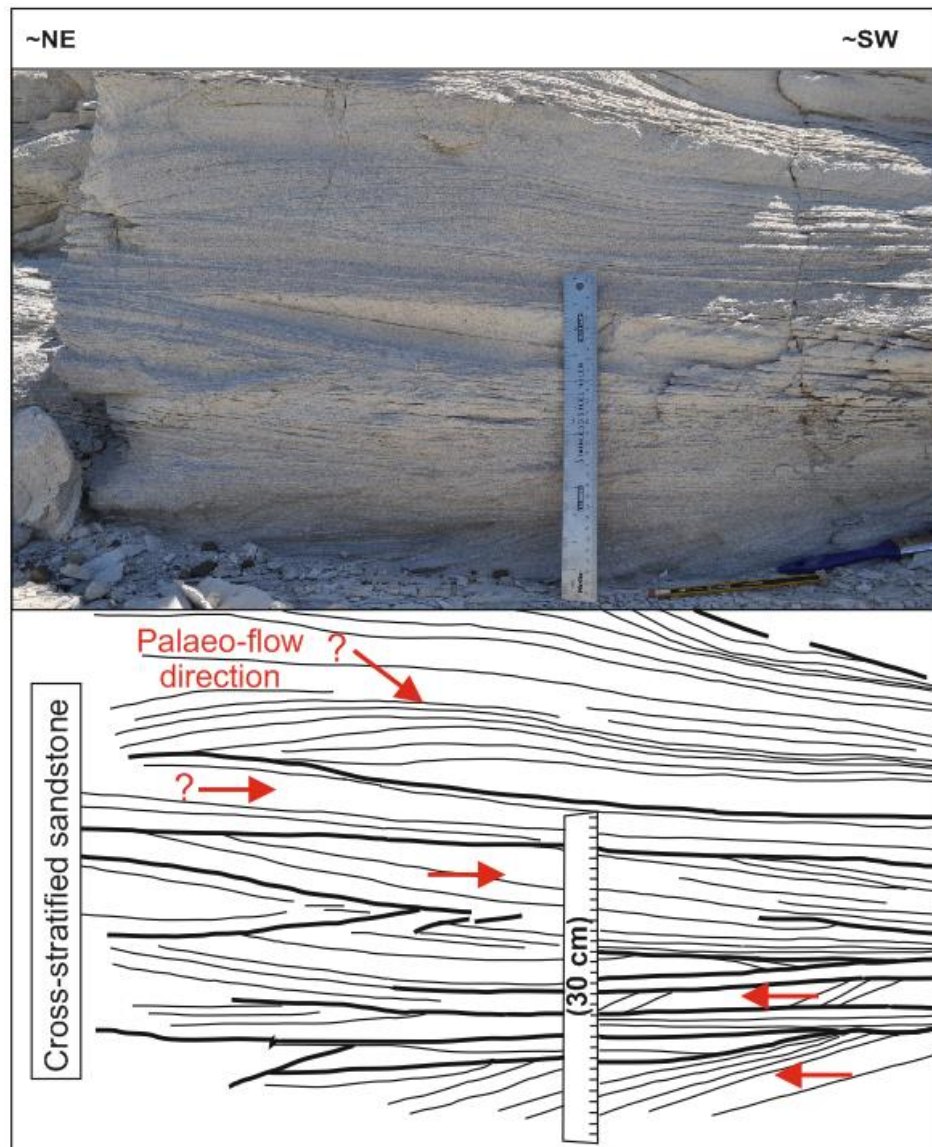


Figure 6-10 Cross-stratified sandstone in the upper part of the L1 exposure, which lies directly below a basaltic lava.

6.5.1.2 Interpretation of field observations

The L1 deposits are interpreted as a fluvial succession, with the lowermost parallel stratified claystones and siltstones deposited in an overbank setting. The normal-graded sandstones at the base of the exposure (Figure 6-8) are predominantly comprised of ash, with normal grading likely developed due to deposition in a water column. These units were followed by a change to the deposition of a more channel-like facies, as indicated by the cross-stratified siltstones and sandstones toward the top of the exposed sequence (Figure 6-8, Figure 6-10). The range of orientations present within the cross-stratified siltstones and sandstones shows that the river was dynamic, with currents that

changed course, resulting in the truncation of previously deposited cross-stratified sediments and the deposition of beds in a different orientation (Figure 6-10).

Many of the sediments in this sequence are dominated by igneous clasts (crystalline igneous rocks, crystals and pyroclasts), showing that volcanic eruptions likely supplied material to this depositional setting over time. For example, the normal-graded sandstones (Figure 6-9) at the base of the exposure appear to be comprised of vitreous ash.

Lastly, basalt lava was emplaced (Figure 6-8). The contact between the lava and the underlying sediments is not exposed.

6.5.1.3 Optical microscopy and SEM analysis

WASH_04 was collected from the uppermost cross-stratified sandstone of L1 (Figure 6-8). The sample is loosely consolidated and predominantly comprised of angular clasts (Figure 6-11a). The sediment includes crystalline igneous clasts (Figure 6-11b), granular lithic clasts (Figure 6-11c), and crystals of albite, apatite, gedrite, montmorillonite, muscovite, orthoclase, quartz, rutile and stilpnomelane. The granular lithic clasts are comprised of an aggregate of a range of minerals, including those found as individual crystals throughout the sample, plus clinoptilite(?), labradorite, magnetite, and altered bubble-wall and rod-like pyroclasts (Figure 6-11c, e). Crystalline igneous clasts include micro-crystals of ilmenite, labradorite, orthoclase, quartz and titanomagnetite (Figure 6-11b). Patches of a remnant clay matrix coat some grains and hold others together (Figure 6-11d).

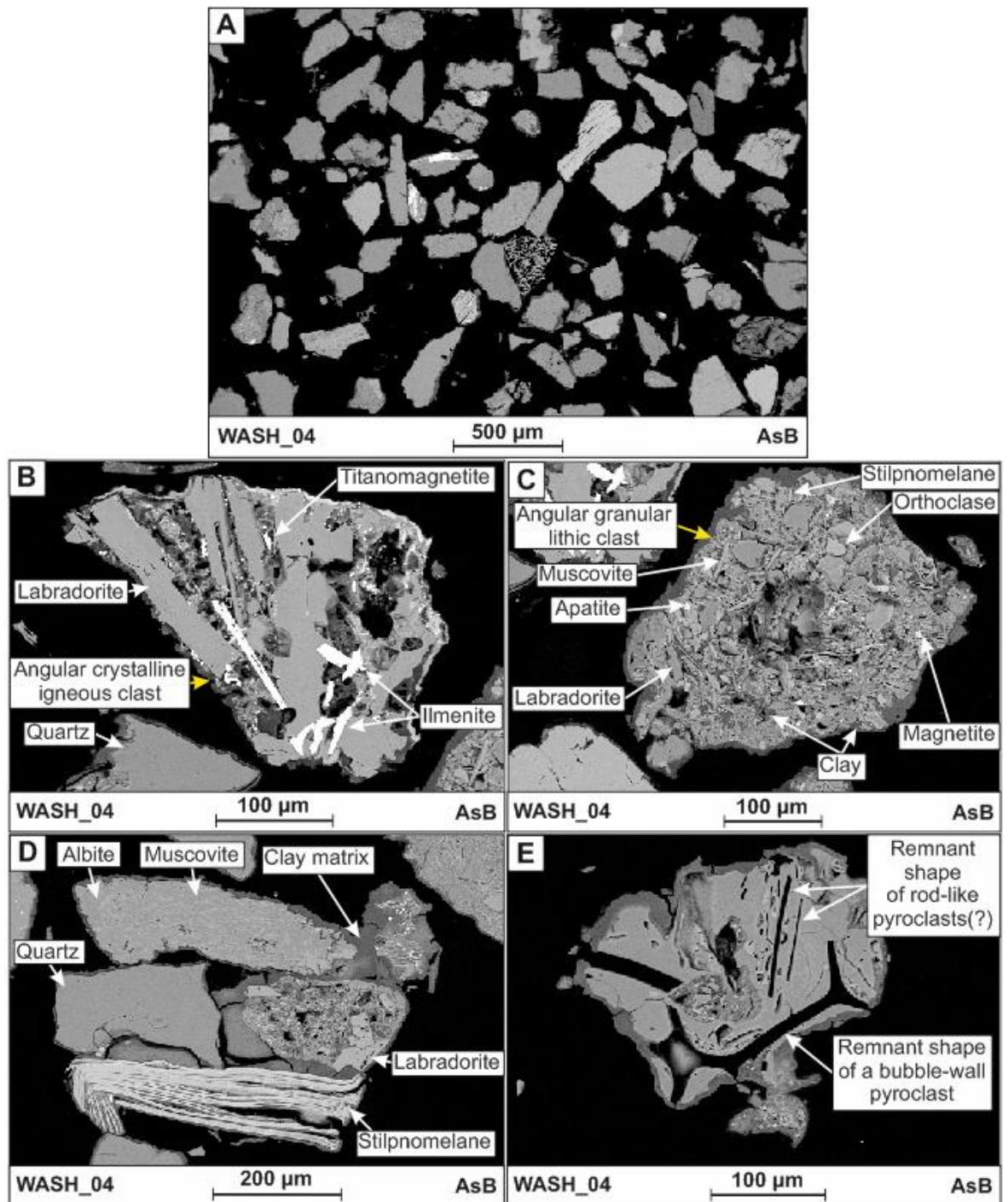


Figure 6-11 AsB SEM clast-types of WASH_04 from L1. A) The sediment is composed of angular siliciclastic material, including: B) angular crystalline igneous lithic clasts with microcrystals of ilmenite, labradorite, and titanomagnetite. C) Angular granular lithic clasts comprised of angular apatite, labradorite, magnetite, muscovite, orthoclase and stilpnomelane, in addition to a clay matrix. D) Clasts of albite, labradorite, muscovite, quartz and stilpnomelane held together by a clay matrix. E) Angular clast preserving the shapes of bubble-wall and rod-like pyroclasts that are no longer present.

6.5.1.4 Interpretation of optical microscopy and SEM analysis

The cross-stratified sandstone (WASH_04) at the top of the exposure at L1 is comprised of siliciclastic material (Figure 6-8). Granular lithic clasts containing

bubble-wall and rod-like pyroclasts are evidence of the reworking of pyroclastic or volcanoclastic rocks. All the clasts of this sample are angular to sub-angular suggesting that they may have originated from the erosion of relatively local sources.

6.5.2 Snipes Mountain (L2)

6.5.2.1 *Field observations*

This locality was not investigated in detail, but a brief note will be given here on the general overview of the stratigraphy, as a point of reference for future research (Figure 6-12).

Coarse-sandstones and gravels at the base of the exposure exhibit large-scale cross-stratification that contain abundant erosional surfaces, and common pebbles. Pebble-rich intervals occur throughout this unit. Amongst the deposits, blocks (Figure 6-13), and dykes/injections (Figure 6-14) of cream-coloured finer-grained sandstone can be found. These features cut through the darker-grey sandstone, gravel and pebble deposits, and are interpreted as sand injectites.

The cross-stratified deposits are overlain by sub-horizontal, stratified finer-grained sediments (Figure 6-12). The rest of the sequence above this consists of quartzite-rich conglomerates that appear to form lenses and lobes of conglomerate interbedded with finer-grained sediments. One of the thickest intervals of finer-grained sediment displays large-scale cross-stratification and has been (partially) eroded and overlain by another unit of conglomerate (Figure 6-12).

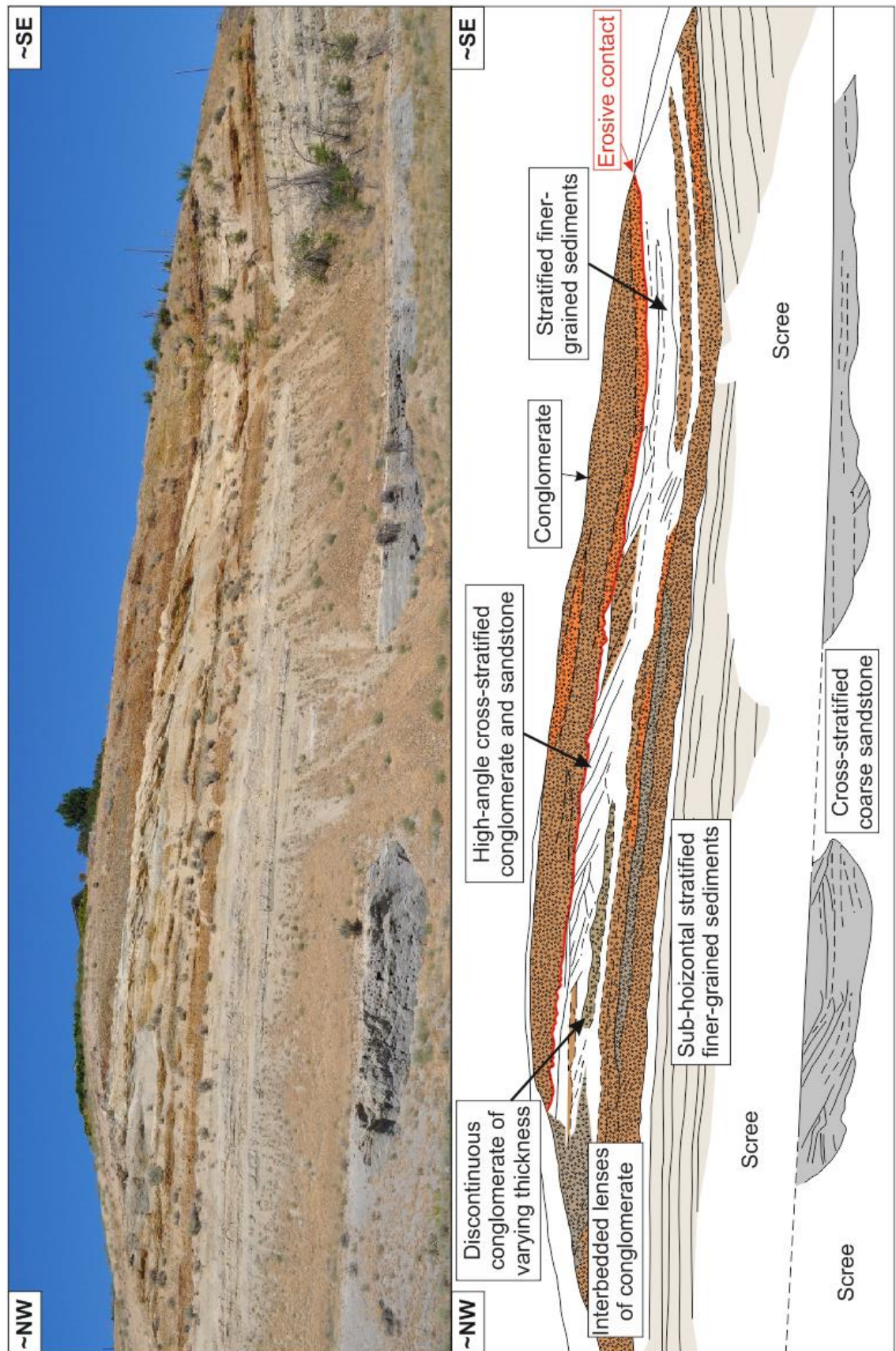


Figure 6-12 Overview of the units exposed at Snipes Mountain (L2). This sedimentary sequence is comprised of cross-stratified sandstone and gravel at the base, followed by limited exposure and sub-horizontal stratified finer-grained sediments (siltstone/sandstone?). The upper half of the exposure is dominated by channel-fill

conglomerates with lenses of cross-stratified sandstone which likely represent channel bars.

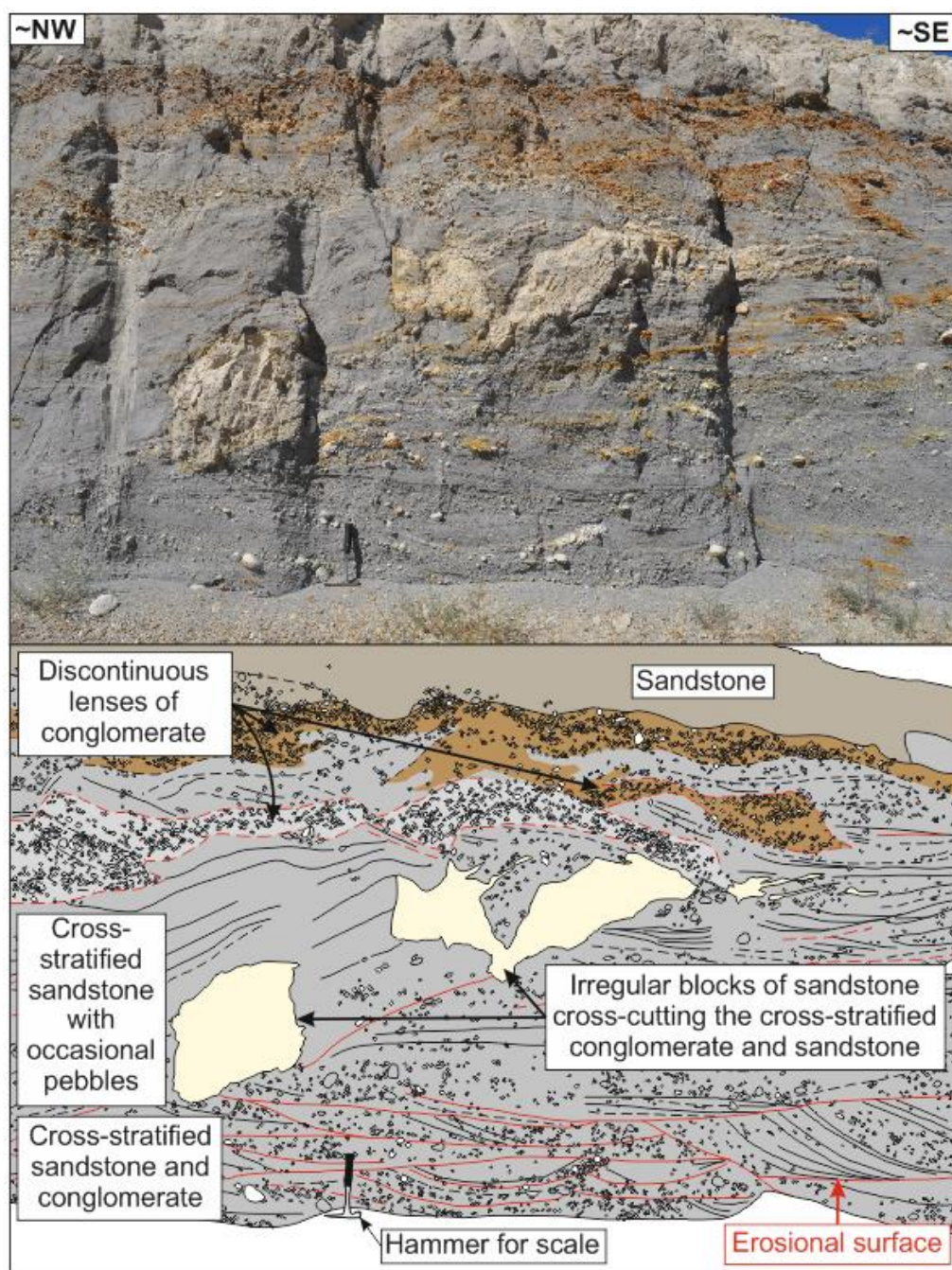


Figure 6-13 Sand injectites within cross-stratified sandstones and conglomerates in the lower section of the exposure at L2.

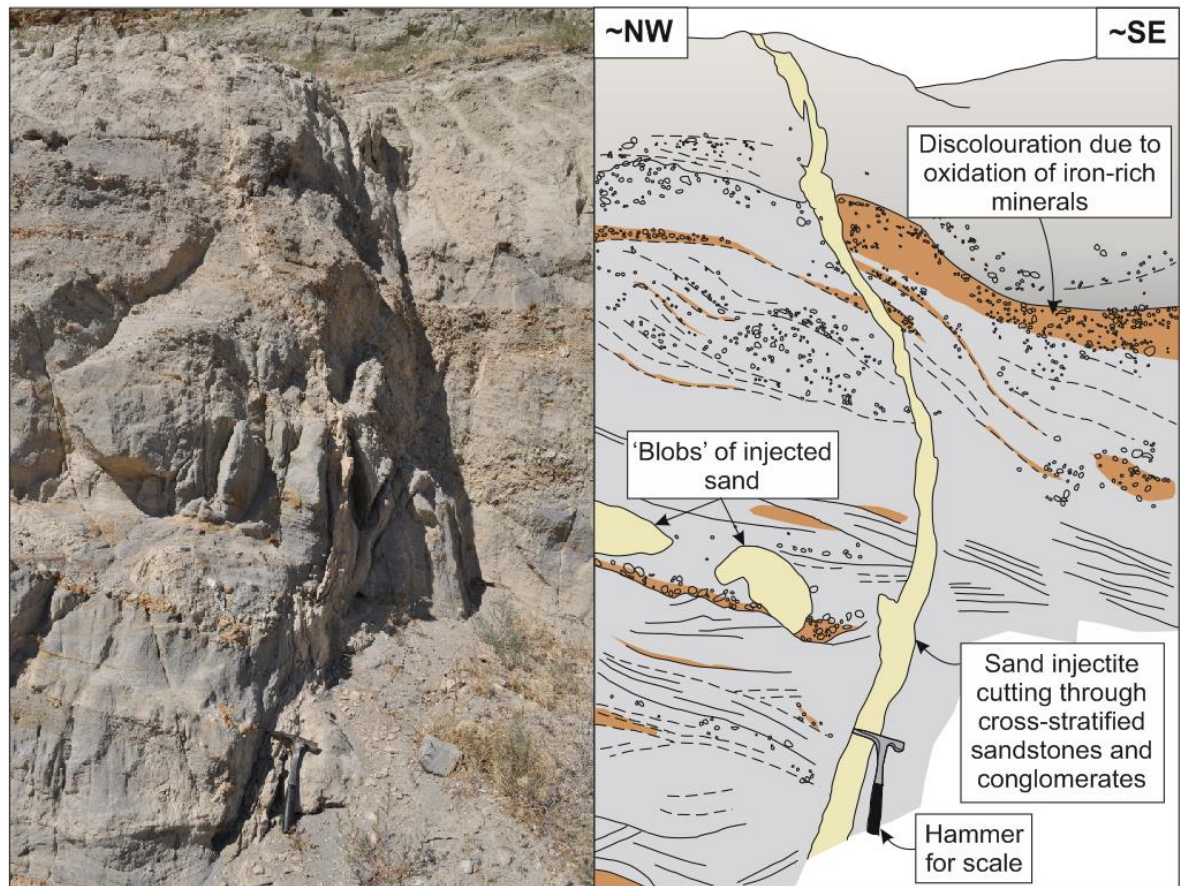


Figure 6-14 Sand injectite within the lower section of L2. 'Blobs' of sandstone are also present and represent oblique sections through sand injectites. Discolouration of intervals in the surrounding cross-stratified sediment may be due to oxidation of iron-rich minerals that are more abundant in these intervals.

6.5.2.2 Interpretation of field observations

Interbedded units of cross-stratified conglomerate and sandstone at L2 were most likely deposited by rivers and lahars (e.g. Schminke 1967a, and references herein). The quartzite-rich conglomerates are typical of deposits from the ancestral Columbia River (Warren 1941; Mackin 1961; Waters 1965; Schminke 1967a; Smith 1988a, 1988b). In contrast, the interbedded darker-grey, poorly-sorted sandstones and granule-conglomerates with pebbles and cross-stratification, at the base of the exposure, are more characteristic of deposition from lahars (Schminke 1967a; Reidel pers coms. 2015). These deposits (e.g. Figure 6-13, Figure 6-14) share similar features to those of modern-lahar deposits, such as those at Mount St. Helens, USA, and Mount Merapi, Indonesia (Figure 6-15); this may support the early conclusions of Schminke (1967a) who interpreted these units as lahar deposits.

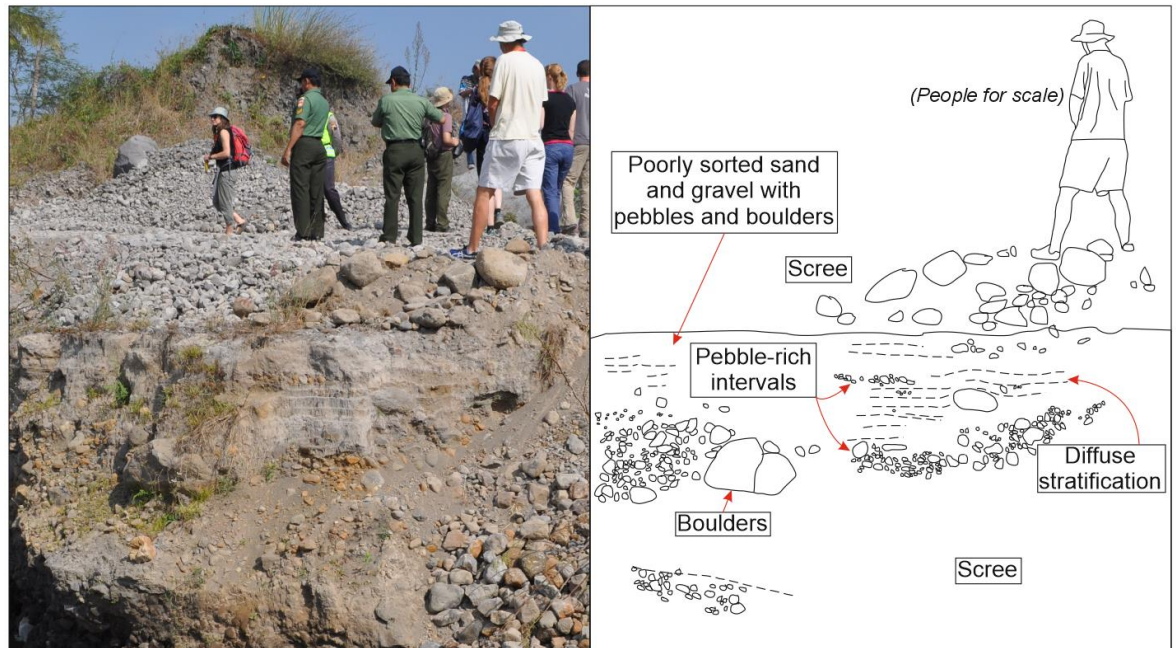


Figure 6-15 Lahar deposits sourced from historical lahar-events at Mount Merapi, Indonesia. Lahar deposits from Mount Merapi have similar features to those identified at Snipes Mountain (Figure 6-14), including: poorly sorted deposits of sand and gravel with pebble-rich intervals and boulders. Some areas of diffuse stratification can be seen within the finer-grain fraction of the deposit, like that at Snipes Mountain (Figure 6-14). The grey colour of the deposit and occasional orange/brown staining is also similar between these two deposits.

Sand injectites that cross-cut the lahar deposits at L2 (Figure 6-13, Figure 6-14), show that the material of the lahar deposits was most-likely laid-down rapidly on top of unconsolidated sands (Jonk 2010; Kane 2010; Hurst et al. 2011). The presence of the sand injectites suggests that sandstone may be found beneath the lahar deposits, or that sand was once present below the lahar material when the lahar deposit was emplaced (e.g. Kane 2010); if the underlying sand unit was thin, it might have been completely remobilised into sand injectites, and therefore, no longer be present as a separate unit.

6.5.3 Yakima Ridge (L3)

6.5.3.1 Field observations

The exposure at Yakima Ridge (L3) (Figure 6-1) is incomplete and patchy, with little good exposure. Sandstones and siltstones with a high abundance of vitric volcanic material can be observed. These deposits display cross-stratification with beds that are orientated in many directions, and separated by erosional surfaces (Figure 6-16).

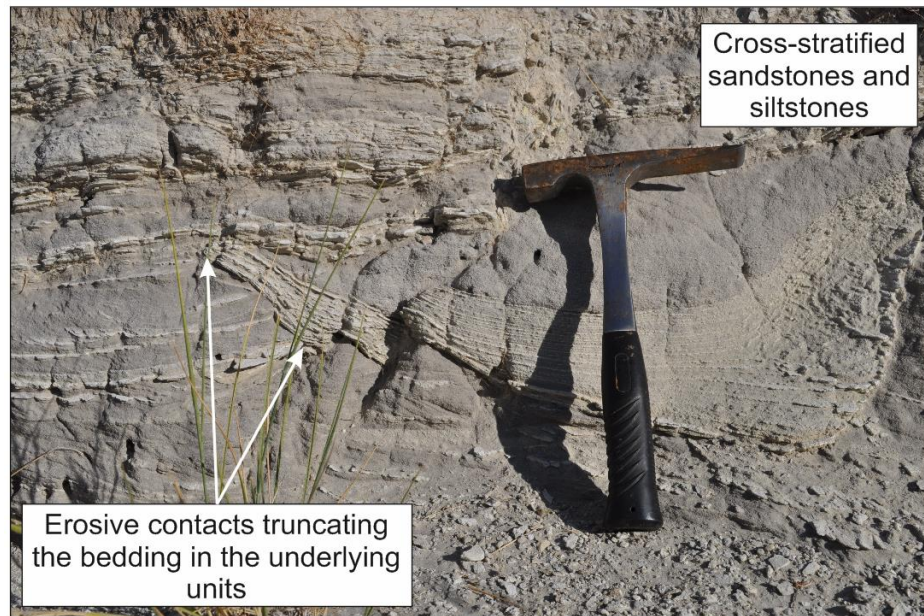


Figure 6-16 Cross-stratified sandstones and siltstones exposed within the gentle slope at L3.

6.5.3.2 Interpretation of field observations

The limited exposure at L3 inhibits an interpretation of the depositional environment at this locality. However, the presence of cross-stratification suggests that deposition occurred from a current. Erosional surfaces and truncation of foresets suggest that the palaeo-flow of the current changed direction, at least locally, multiple times. Therefore, these sandstones and siltstones were most likely deposited in a river or stream with flowing water that often changed its course.

6.5.3.3 Optical microscopy and SEM analysis

WASH_06 contains a range of clast-types, including vesicular and non-vesicular pyroclasts (Figure 6-17). Two types of granular lithic clast can be identified: one is comprised of mineral grains with a fine-ash or clay-grade matrix (Figure 6-18a), the other contains pyroclasts with a fine-ash matrix (Figure 6-17d, Figure 6-18b, c).

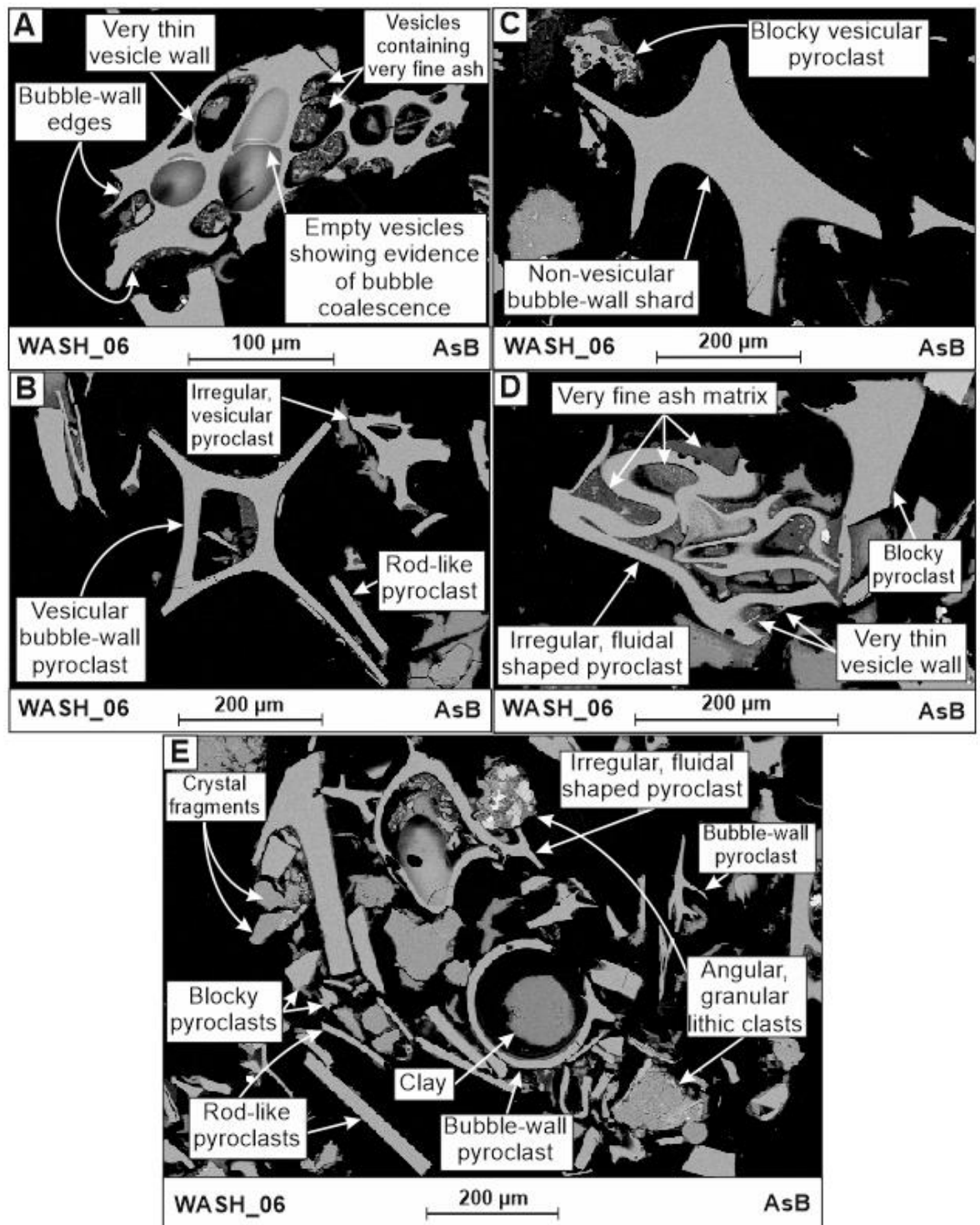


Figure 6-17 AsB SEM clast-types and pyroclast morphologies exhibited by sample WASH_06 from L3. A) Vesicular pyroclast with some bubble-wall edges. Some vesicles are infilled with very fine ash, others are empty. The vesicles show a range of shapes including vesicles with very thin bubble-walls and evidence for bubble-coalescence shortly prior to solidification of the glassy pyroclast. B) Non-vesicular bubble-wall shard and a very fine blocky, vesicular pyroclast. C) Vesicular bubble-wall pyroclast with a non-spherical vesicle along with rod-like and irregular, vesicular pyroclasts. D) A highly irregular, fluidal-shaped pyroclast with a very fine ash matrix and very thin bubble-walls, along with blocky non-vesicular pyroclasts. E) Range of pyroclast morphologies, granular lithic clasts and crystal fragments.

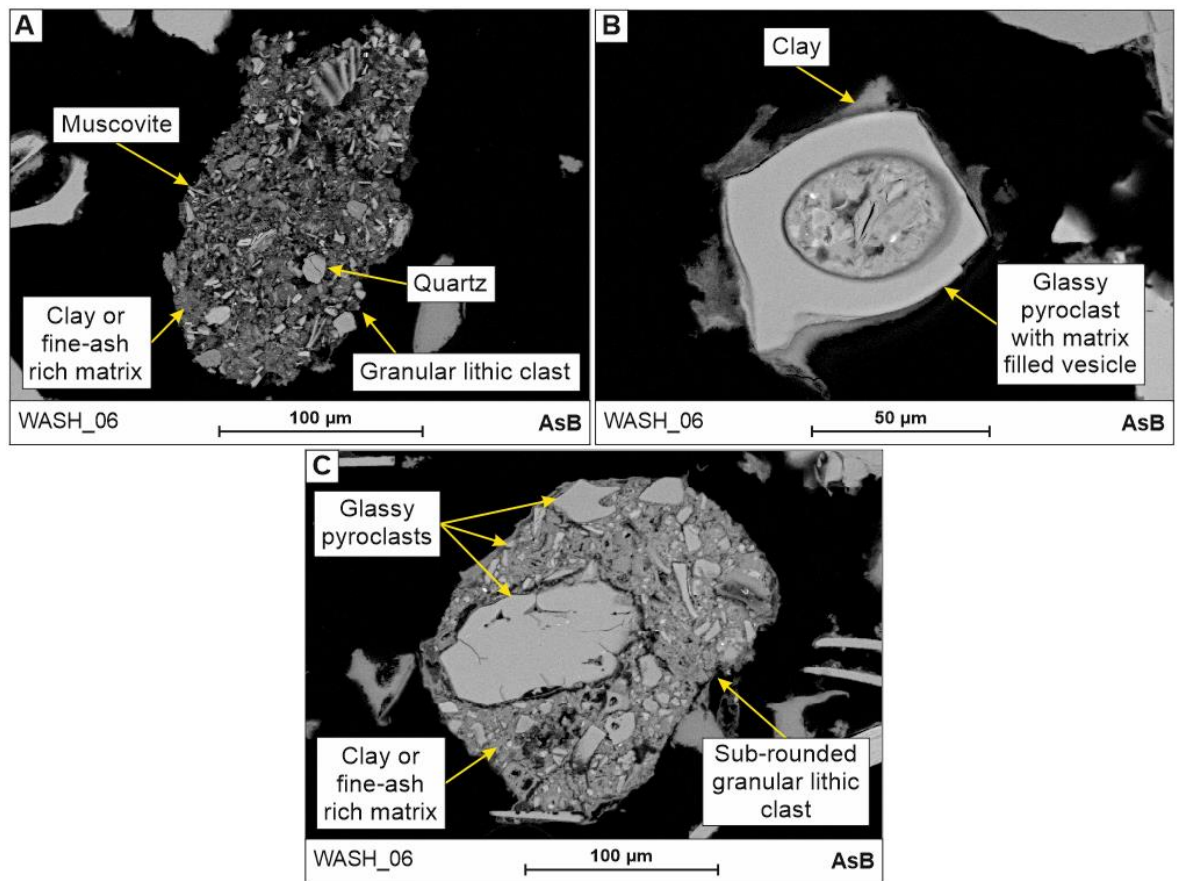


Figure 6-18 AsB SEM various types of granular lithic clast in WASH_06 from L3. A) Granular lithic clast comprising angular silt-sized clasts of quartz and muscovite with a clay or fine-ash matrix. **B)** Granular lithic clast containing a glassy pyroclast surrounded by and infilled with a clay-grade matrix. **C)** Granular lithic clast with reworked angular glassy pyroclasts and a well-consolidated clay or fine-ash matrix.

6.5.3.4 Interpretation of optical microscopy and SEM analysis

Sample WASH_06 contains a high proportion of glassy pyroclasts mixed with clay-grade matrix and siliciclastic clast-types, including granular lithic clasts. The clasts are angular to sub-rounded suggesting that they have undergone varying amounts of transport prior to deposition. The pyroclasts are often found as a component of granular lithic clasts; therefore the pyroclasts are considered to have been reworked and the sample therefore likely represents a volcanoclastic deposit.

6.5.4 Beverly Quarry (L4)

6.5.4.1 *Field observations*

Beverly Quarry (L4) reveals some of the inter-lava strata between the Priest Rapids Basalt and the Elephant Mountain Basalt and is ‘intruded’ by the Pomona Basalt (Figure 6-4; Makin 1961; Reidel pers. coms. 2015). When active, the quarry was used for the removal of thick units of ‘pumicite’, a silicic tuff, which dominates the exposure within the main quarry pit (e.g. Mackin 1961). The term ‘pumicite’ is used to describe fine-grained pyroclastic rocks that are comprised of highly vesicular ash; the term is applied without reference to depositional processes, and includes both pyroclastic and volcaniclastic material (e.g. Collins English Dictionary 2014), and is therefore an outdated term for ‘tuff’. The quarry gives the thickest exposure of the EF observed during fieldwork of the present study. Several sedimentary logs were made in separate locations (Figure 6-19) around the quarry, and were subsequently pieced together to document the complete inter-lava stratigraphy. (Figure 6-20).

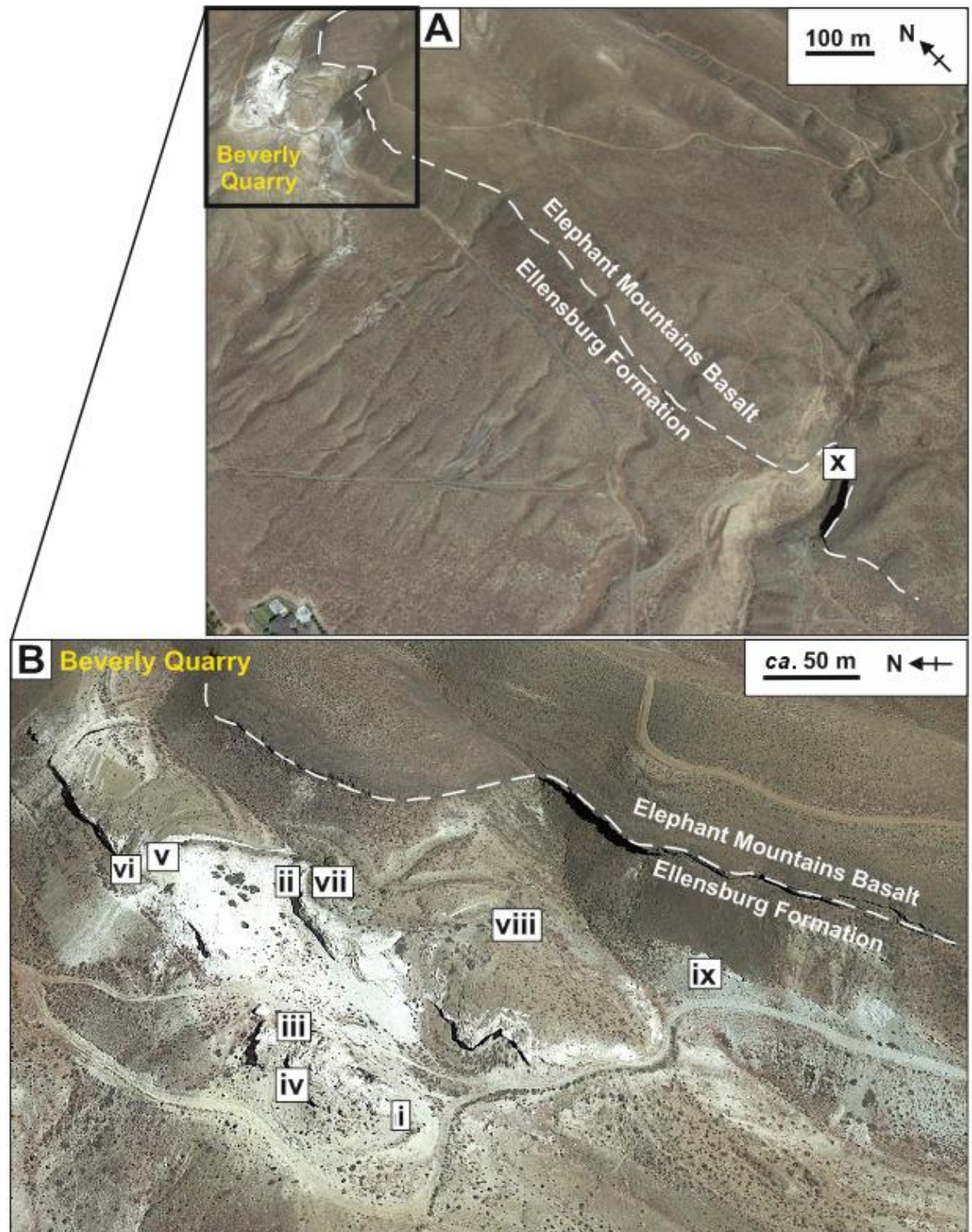


Figure 6-19 Localities within Beverly Quarry discussed in the text. (After Google Earth 2015).



volcaniclastic siltstone and siliciclastic sandstone and conglomerate. Pumicite is used to describe a tuff comprised of silt-grade silicic ash. The siltstone at the top of the sequence is heavily bioturbated and overlain by pillow lava of the Elephant Mountains Basalt.

The basal unit (i) of the exposure comprises cross-stratified ripple laminated (Figure 6-21), sub-horizontal planar laminated siltstones, and a massive siltstone with lenses of sandstone (Figure 6-20).

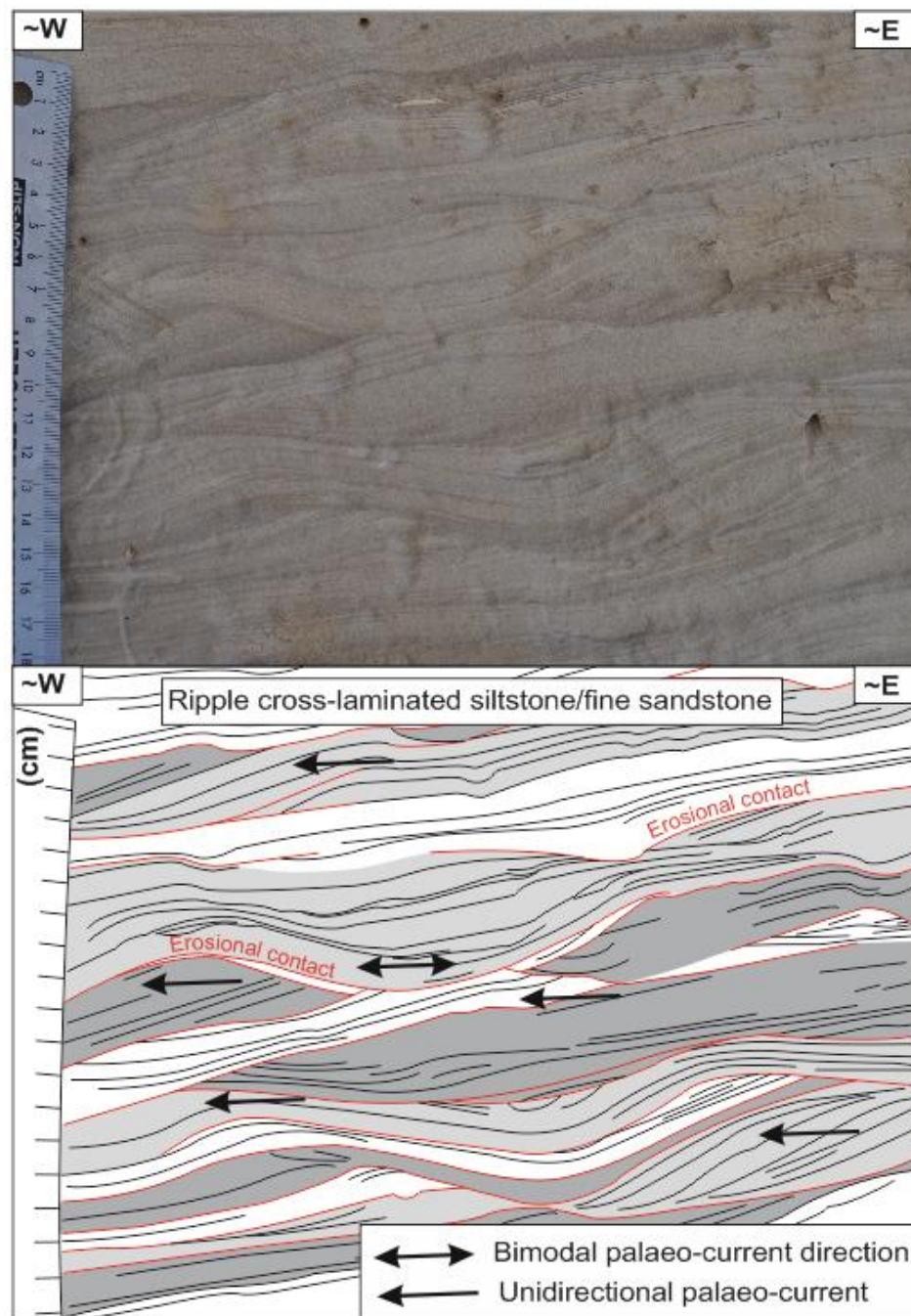


Figure 6-21 Ripple cross-laminated siltstone/fine-sandstone at L4 displaying climbing ripples and erosional contacts between ripple sets (Figure 6-19ii). The apparent palaeo-current direction appears to have been predominantly towards the west. Colour has been added to the sketch to make the identification of the different major ripple sets easier.

Above this lies a unit of pale-grey sandstone/tuff composed of coarse silicic ash and layers of whole and fragmented spherical ash aggregates (i.e. accretionary lapilli and coated ash pellets) up to 4 mm in diameter (Figure 6-22).

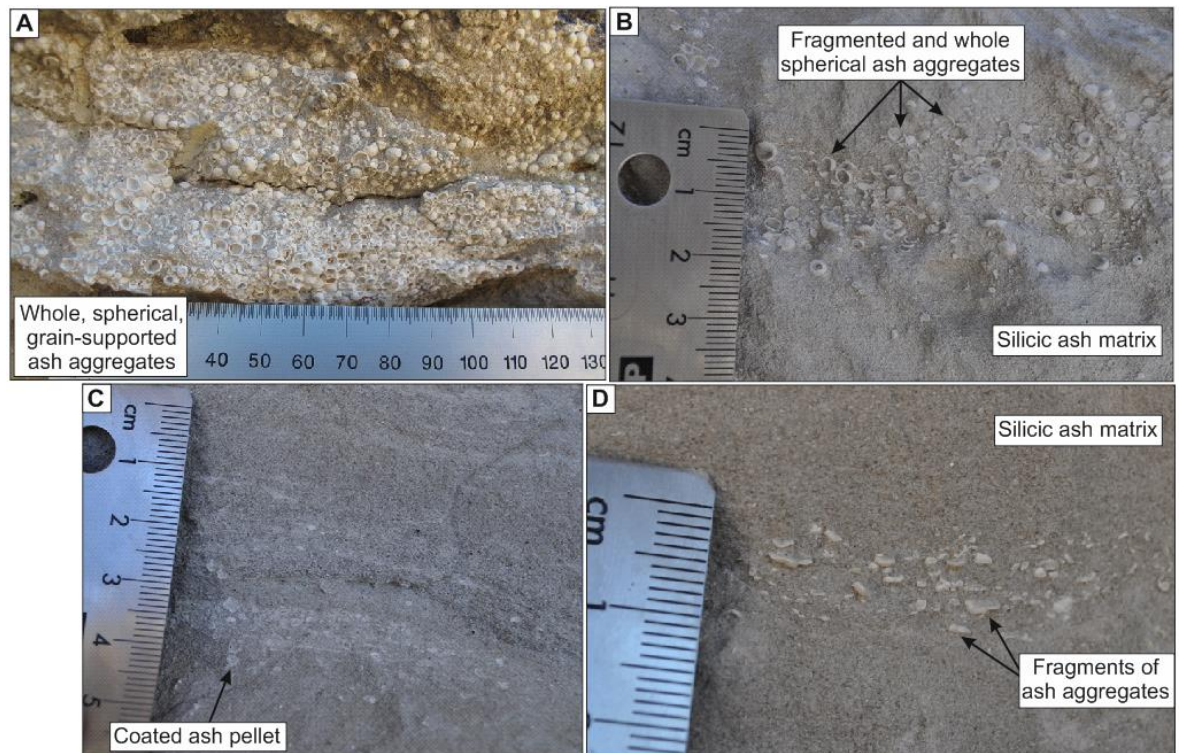


Figure 6-22 Characteristics of ash aggregates within exposures at L4. A) Grain-supported accretionary lapilli, with diameter up to 4 mm (Figure 6-19iii). Most are spherical and whole, however, on the weathered outer surface some of the outer rims have fractured and the core has been removed, leaving a shell. B) Matrix-supported accretionary lapilli up to 2 mm in diameter. Whole and fragmented accretionary lapilli are present, surrounded by a silicic tuff (Figure 6-19iv). C) Matrix-supported accretionary lapilli with less well-developed cement-rims. These are most likely ash pellets or coated ash pellets that have not developed cemented rims noted in A and B. This example is supported by a matrix of silicic tuff and occurs in the sequence below B and D (Figure 6-19iv). D) Remnant fragments of the outer rim of cemented accretionary lapilli (or ash pellets), no whole accretionary lapilli are seen in this interval which lies a few tens of centimetres below B (Figure 6-19iv). These fragments are generally aligned sub-horizontal to the bedded planes and occur in a matrix of silicic tuff.

The ash aggregates occur in a range of bedding-types, from continuous sub-horizontal planar bedded (Figure 6-23, Figure 6-24), to thin (1 cm) discontinuous lenses (Figure 6-24b), and deformed units that resemble macro-scale soft-sediment deformation with flame structures (Figure 6-24a). There is also evidence for very localised post-depositional deformation of the planar bedded units (Figure 6-23), where the white, fine-grained deposits have been removed and the overlying stratified sediments have slumped into the void, retaining some of their original stratification. This feature indicates that the deposits

were reasonably well consolidated when they slumped, resulting in limited internal deformation (Figure 6-23). Some silicic tephra from the main unit of silicic tuff above had likely already been deposited when fluid escape occurred, as shown by the mixed cream-coloured sediment at the top of this feature (Figure 6-23). Fluid-escape caused by overpressure could have been caused by rapid burial and rapid emplacement of overlying units (Owen et al. 2011), or by seismic shaking (earthquake trigger; Owen et al. 2011). There is no ‘zone’ of deformation in the quarry-face surrounding the fluid escape feature, which could suggest that a seismic trigger was not responsible for the fluid-escape. Undeformed bedding above this feature suggests that an unconformity, or break in sedimentation, is present (Figure 6-23).

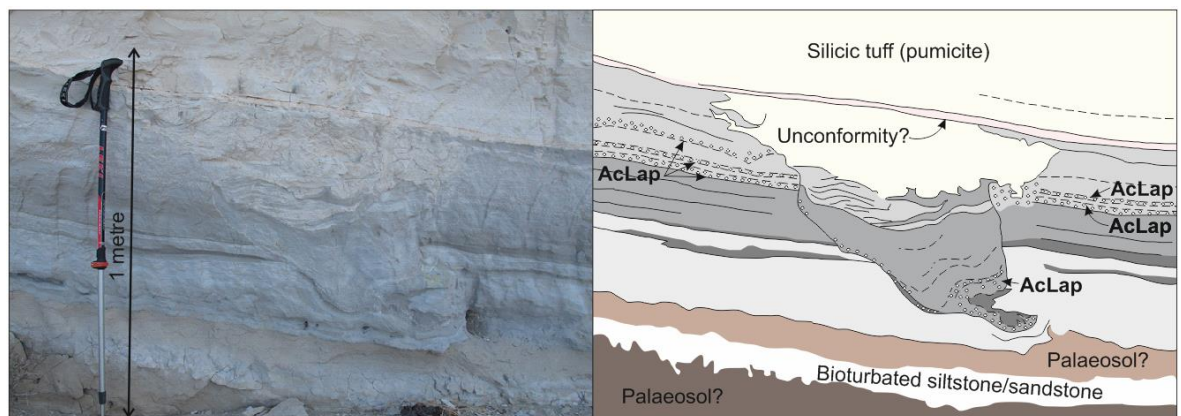


Figure 6-23 Variations in the nature of contacts over short (<1 m) distances in the quarry face of L4 (Figure 6-19v). Accretionary lapilli (AcLap) occur in continuous sub-horizontal beds, interbedded with silicic tuff. The uppermost layer is less uniform and contains fewer accretionary lapilli. Post-depositional deformation has created the unusual slumped feature in the centre of the image (which may be a sediment volcano, see discussion). Accretionary lapilli can be seen at the bottom of this feature, mixed with darker-grey, coarser-grained tuff. The sub-horizontal pinkish silicic tuff at the top of this feature continues throughout the exposure, and the base of this unit most likely represents an unconformity. Perpendicular to the quarry face, the sequence is more irregular (Figure 6-24).

Soft-sediment deformation structures, such as flame and ball-and-pillow, occur in some parts of the accretionary-lapilli bearing tuff (Figure 6-24). These structures may suggest that the main unit of silicic tuff was deposited rapidly on top of the accretionary lapilli-bearing pyroclastic units.

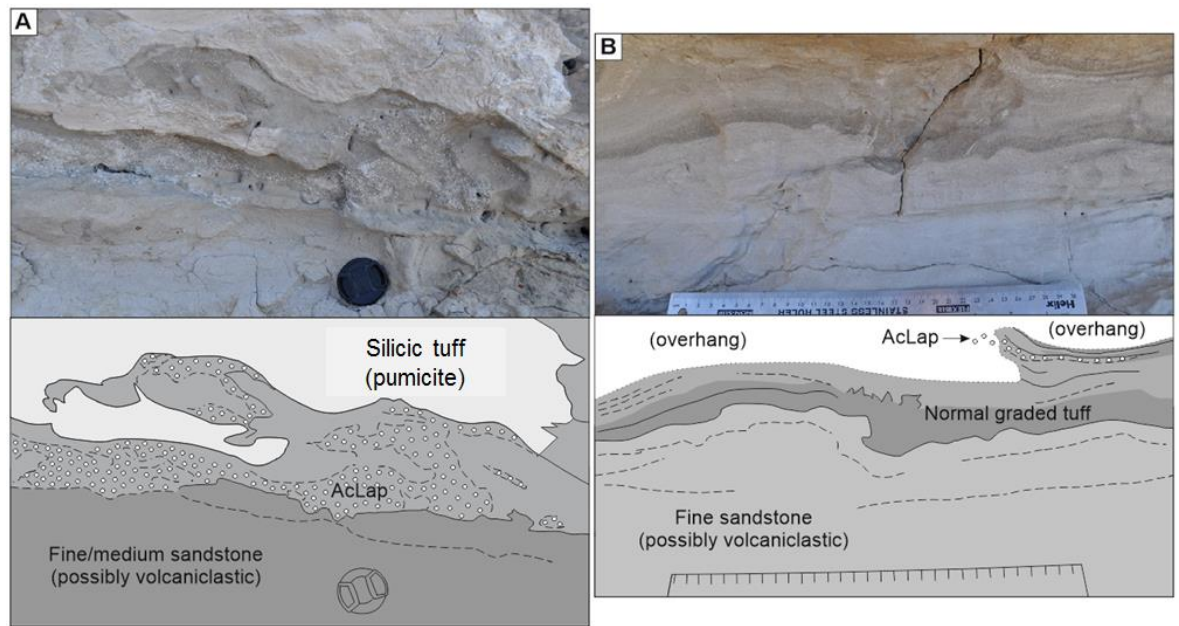


Figure 6-24 Varying nature of the deposits in L4 in which accretionary lapilli occur. A) Fluidal boundary between an accretionary lapillus-bearing tuff and the overlying silicic tuff (Figure 6-19vi). The nature of this boundary resembles soft sediment deformation. The tuff layer is deformed, with irregular, diffuse stratification. The contact of this unit with the fine/medium sandstone below is sharp in some places (centre), but diffuse in others (left). The lowermost unit may be volcaniclastic or pyroclastic, but is devoid of accretionary lapilli. **B)** A normal-graded tuff with diffuse stratification and a thin layer (<1 cm) of grain-supported accretionary lapilli (Figure 6-19iii). In the centre of the image the contacts between units have a fluidal appearance resembling soft-sediment deformation; however, adjacent to this on either side, the beds have a more uniform thickness.

Overlying the ash-aggregate bearing pyroclastic unit is a *ca.* 12 m section of very fine-grained, white and pale-grey silicic tuff or 'pumicite'. This unit is parallel laminated at the base where the tuff drapes some underlying ripple structures (Figure 6-25). The silicic tuff is bedded and contains a unit of coarser-grained tuff, up to siltstone-grade, comprised of glassy pyroclasts (Figure 6-26, Figure 6-20). The silicic tuff has subsequently been tilted and is unconformably overlain by a quartzite-rich conglomerate (Figure 6-26).

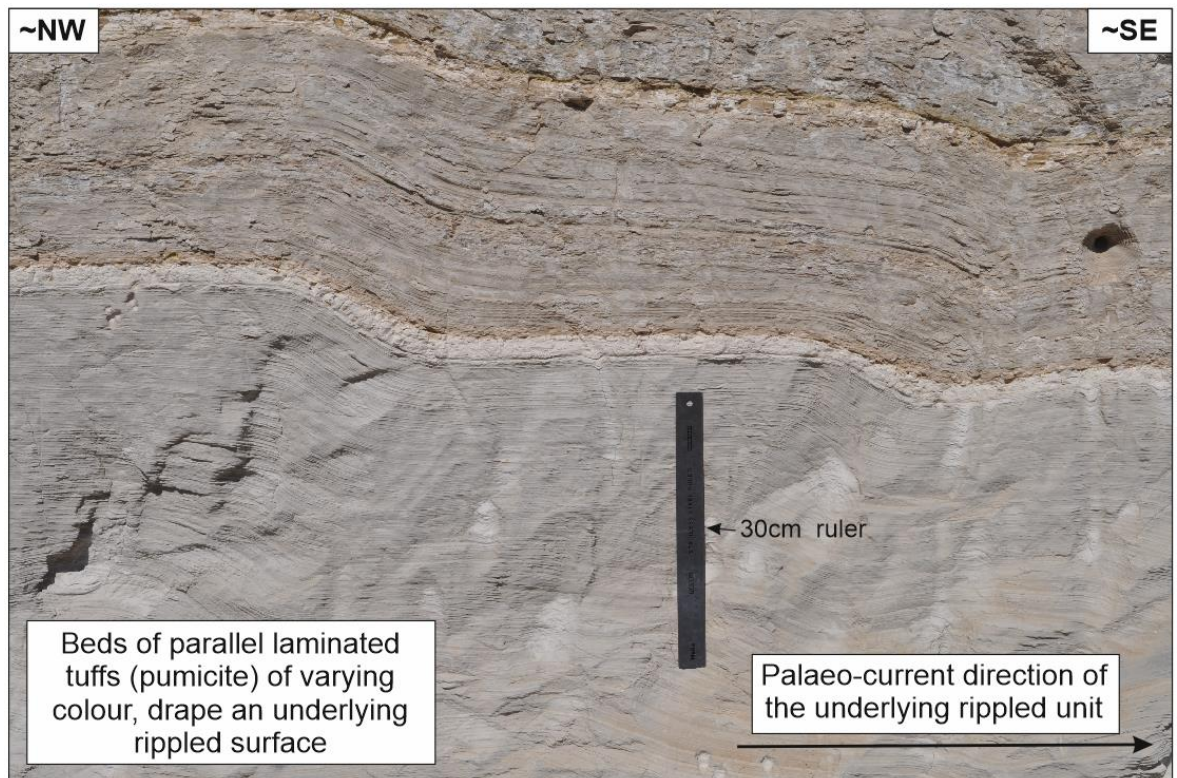


Figure 6-25 Parallel laminated siltstone comprised of silicic ash (tuff or volcaniclastic siltstone) at L4. The original ash was deposited on a pre-existing rippled surface of silicic tuff and therefore maintains these ripple features throughout the deposit (Figure 6-19v).

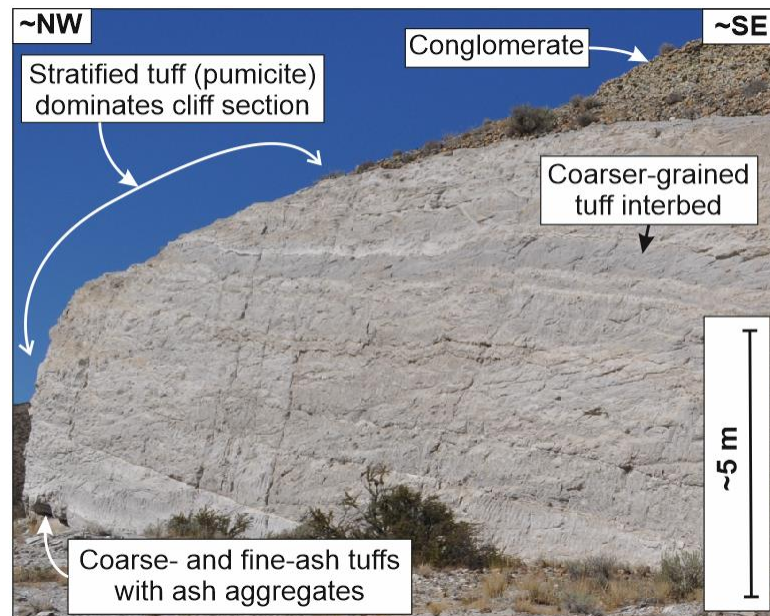


Figure 6-26 Stratified tuffs overlain by conglomerate in L4 (Figure 6-19v).

An erosional unconformity lies between the main sedimentary units of L4 and the overlying very coarse pebble and cobble quartzite-rich conglomerates. The conglomerate also includes well-rounded cobbles and pebbles of basalt (Figure

6-28). These conglomerates are disconformably overlain by a pillow basalt facies of the Elephant Mountains Basalt in the area of vii (Figure 6-19).

The base of the quartzite-rich conglomerate shows diffuse and discontinuous stratification, with units of pebble-poor, finer-grained sandstone (Figure 6-27).

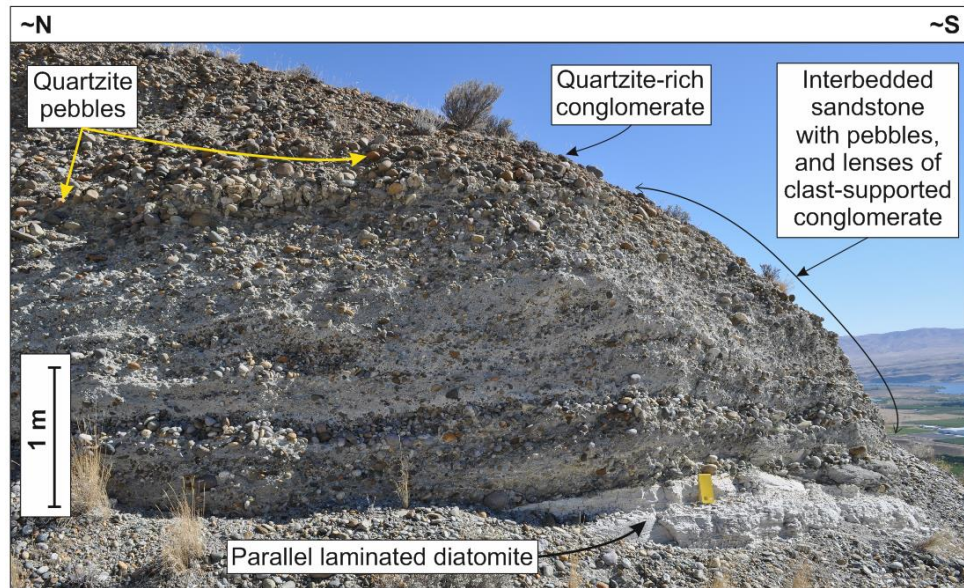


Figure 6-27 Quartzite-rich conglomerate and sandstone with lenses of clast-supported conglomerate rests upon parallel laminated silicic tuff at L4 (Figure 6-19vii).

Discontinuous metre-scale lenses of grey coarse-sandstone with granules and pebbles, and paler-grey cross-stratified sandstone are present within the quartzite-rich conglomerate (Figure 6-28).

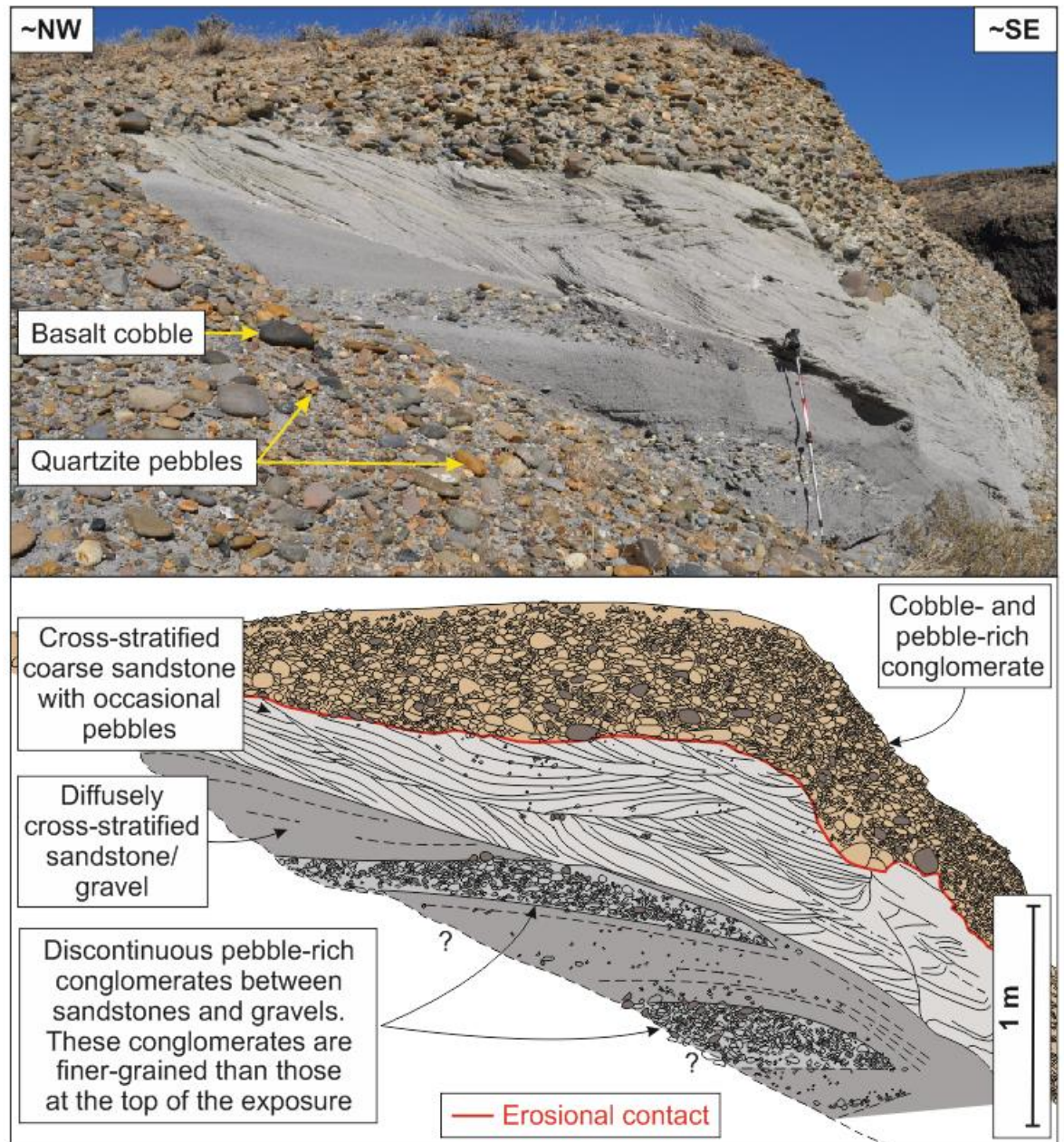


Figure 6-28 Lithologies of the mid-section of the L4 sedimentary sequence. Diffusely cross-stratified coarse-sandstones and gravels are interbedded with lenses of discontinuous pebble-rich conglomerate. An erosional contact separates the sandstone unit from the overlying cobble- and pebble-rich conglomerate, which contains well-rounded clasts of basalt and quartzite (Figure 6-19viii).

Cross-stratified, coarse-sandstone and granule-conglomerate with spherical concretions (Figure 6-29a) overlie the quartzite-rich conglomerate and are themselves unconformably overlain by the Elephant Mountains Basalt (Figure 6-29, Figure 6-20). A stratigraphic contact within this sandstone and conglomerate unit is identified where a colour change from grey to paler grey represents a change to slightly finer-grained sandstone (Figure 6-29). These

deposits are poorly consolidated and held together by grain compaction and localised cementation that forms golf-ball-sized concretions (Figure 6-29a).

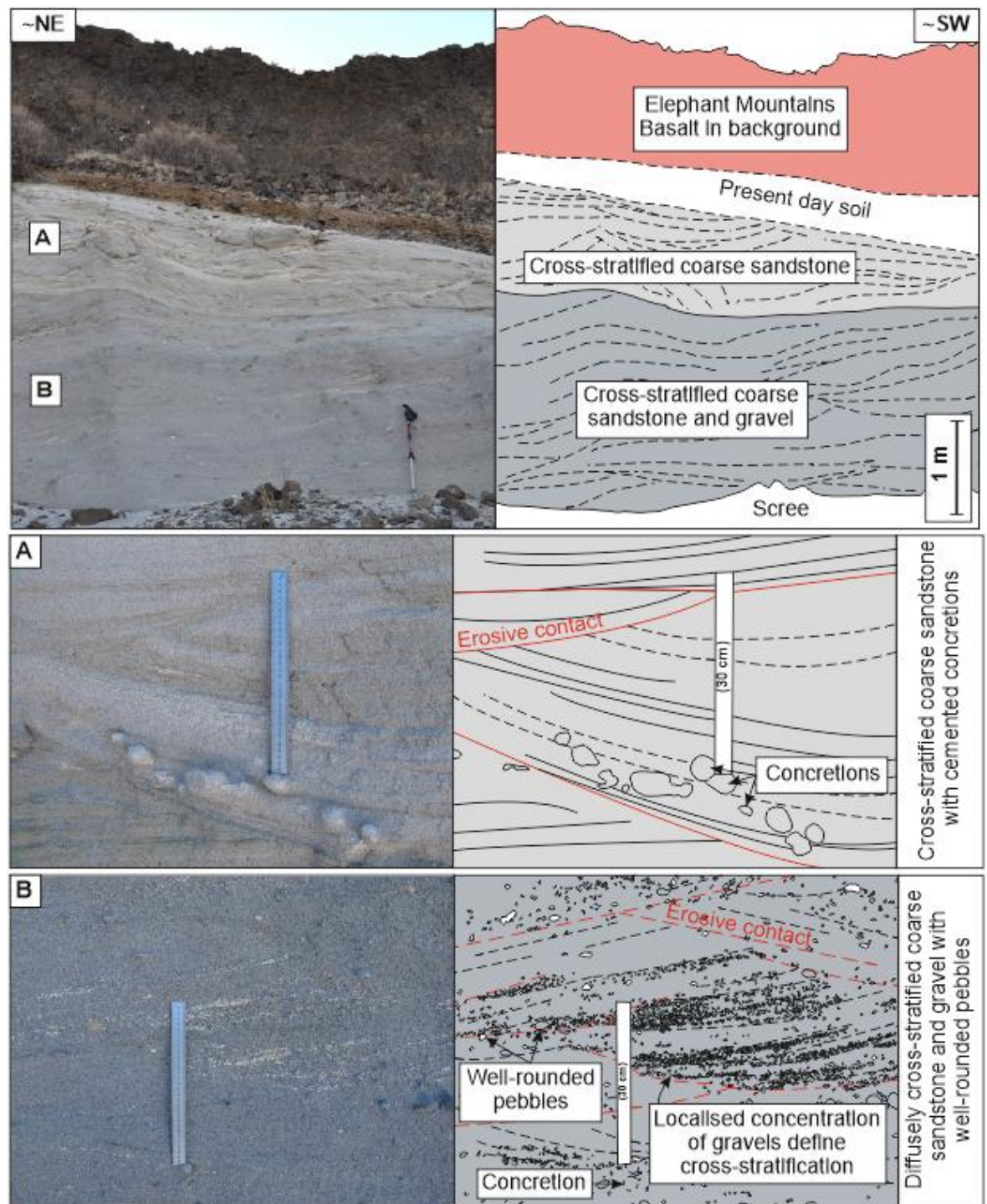


Figure 6-29 Detail of the cross-bedded sandstones and granule-conglomerate within L4 (Figure 6-19ix). Overall characteristics of the exposure, with the Elephant Mountains Basalt visible in the background with: A) details of the paler grey cross-stratified sandstone with localised sub-spherical concretions. B) Diffusely cross-stratified coarse sandstones and gravels (granule-conglomerates), with some cross-stratification defined by concentrations of gravel-sized clasts with more abundant white, rounded pumice clasts.

Down-dip, these sandstones are overlain by a cream-coloured siltstone that has diffuse stratification at its base, and is heavily bioturbated towards the top (Figure 6-20; Figure 6-30), with abundant trace fossils (Figure 6-31). A discontinuous bed of paler-coloured siltstone is present between the bioturbated siltstone and the overlying Elephant Mountain Basalt (Figure 6-30).

The upper contact of the sedimentary package and the overlying basaltic lava is sharp (Figure 6-30). Pillow basalts lie at the base of the lava, with no evidence of baking or fusing of the fine-grained siltstone directly below.

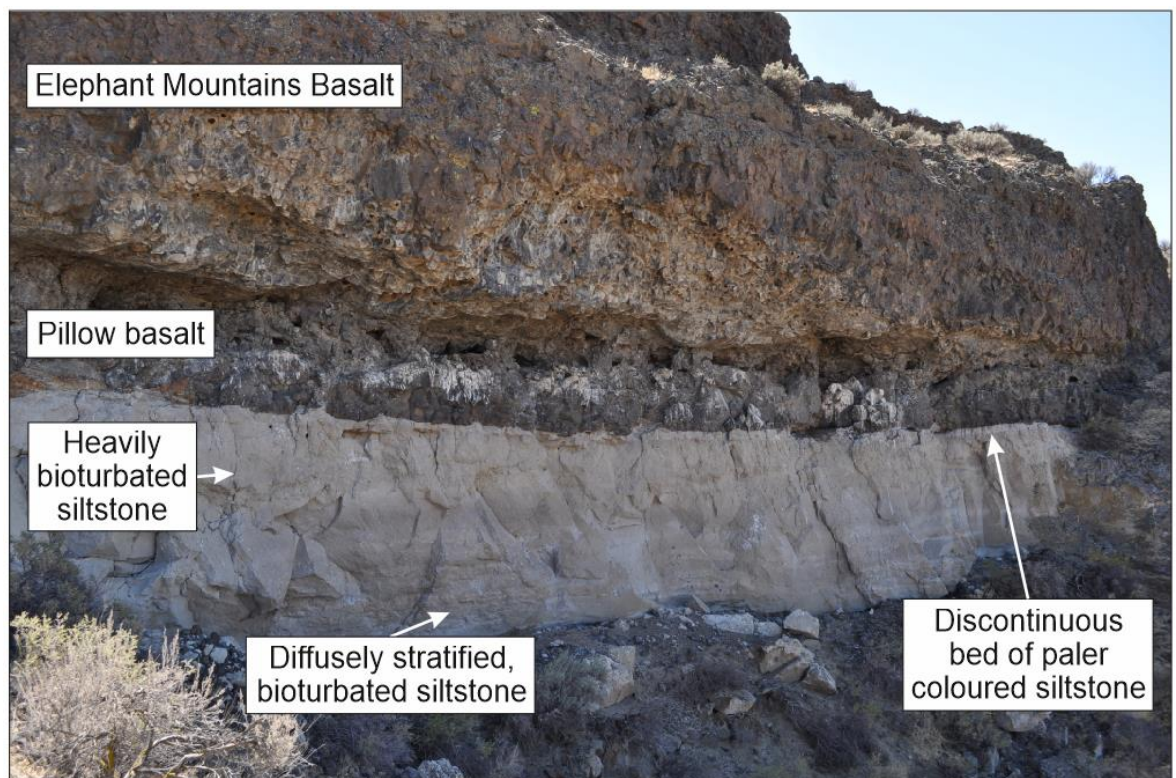


Figure 6-30 The upper lava-sediment contact, where the Elephant Mountains Basalt lies above the Ellensburg Formation, exposed at L4. The sedimentary unit here is heavily bioturbated, and pillow basalt occurs at the base of the lava (Figure 6-19x).

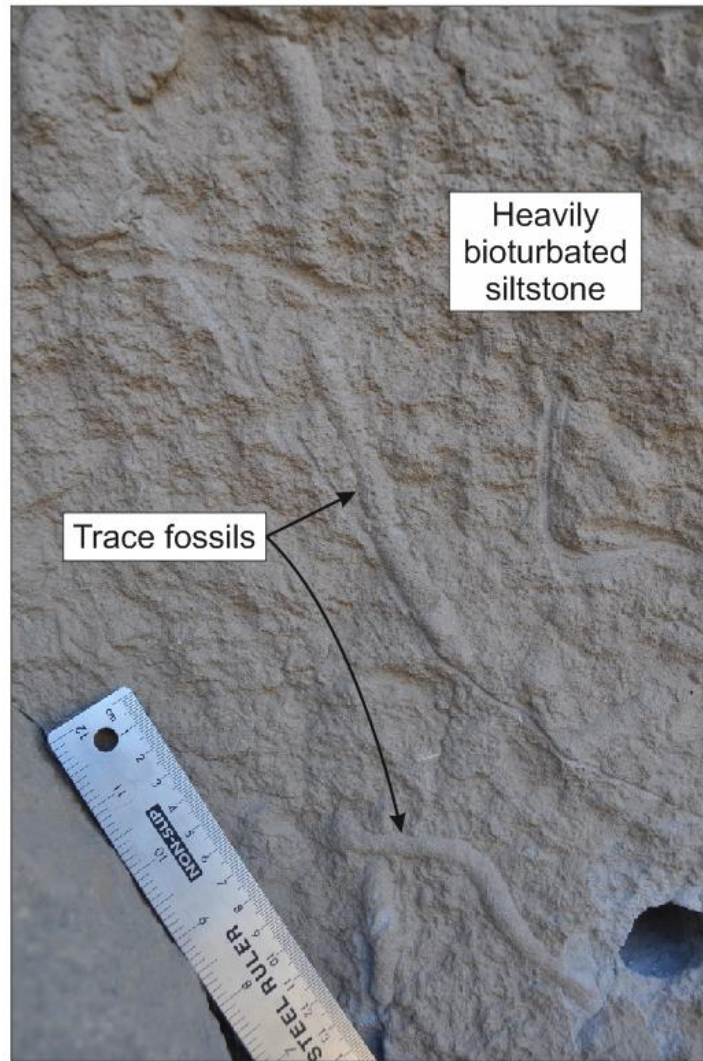


Figure 6-31 Trace fossils within a heavily bioturbated siltstone at the top of the sedimentary sequence exposed in L4. These trace fossils may include burrows and root moulds (Figure 6-19x).

6.5.4.2 Interpretation of field observations

At the base of the exposed sequence, the ripple-laminated, cross-stratified, and sub-horizontal laminated siltstones, along with the massive siltstone with lenses of sandstones, were most likely deposited in an overbank setting (e.g. Singh et al. 1999; Bayliss & Pickering 2015; Yamada et al. 2016). Where ripple and cross-stratified sediments were likely deposited from traction currents and sub-horizontal laminated sediments deposited from suspension as water levels or current velocity decreased (Selley 1976). The cross-ripple laminae are orientated and truncated in multiple directions, suggesting that the sediments were deposited from a current that often changed direction. These sedimentary rocks are interpreted as an overbank facies that involved deposition of siliciclastic and

volcaniclastic sediments under predominantly low-energy conditions, possibly interrupted by periodic deposition from currents associated with flood waters (e.g. Yamada et al. 2016).

Following this overbank facies, silicic pyroclastic material was deposited across the entire area of L4 and, most likely, much further afield, as represented by pale grey tuffs and ash aggregates. Subsequent input of silicic material from eruptions or reworking of primary pyroclastic deposits led to the deposition of parallel-laminated silicic tuffs (pumicite).

Subsequently, eruptions ceased and the main channel of the ancestral Columbia River established itself, eroding some of the pre-existing deposits and unconformably depositing thick units of quartzite-rich conglomerate and cross-bedded sandstones across the area. The discontinuous metre-scale lenses of cross-stratified sandstone were most likely deposited in sand bars within the main river channel.

Subsequent migration of the main river channel then led to the re-establishment of an overbank setting, in which siltstones were deposited and into which organisms were able to burrow. The sediments and the burrowing organisms were likely present below a body of water, as shown by the presence of pillow basalts at the base of the overlying Elephant Mountain Basalt (e.g. Schmincke 1967b). It is possible that emplacement of the Elephant Mountain Basalt dammed parts of the fluvial system, allowing fine-grained sediment to be deposited under lower energy conditions, which allowed burrowing organisms to establish themselves. The dominantly sub-aerial emplacement of lava then proceeded, sealing and preserving the EF at this location.

6.5.4.3 Optical microscopy and SEM analysis

Samples WASH_20 and _21 represent material from the overbank facies within the lowermost part of the exposure at L4. WASH_20 is dominated by angular quartz grains and sub-angular to sub-rounded crystalline igneous clasts (Figure 6-32). Crystals are also present, including: amphibole and biotite (Figure 6-32). In comparison, WASH_21 is predominantly composed of angular, crystalline igneous clasts containing groundmass of plagioclase microcrystals (Figure 6-33).

Fragments of plagioclase crystals are also present (Figure 6-33c, d). Some of the plagioclase display zoning under cross-polarised light (XPL; Figure 6-33d).

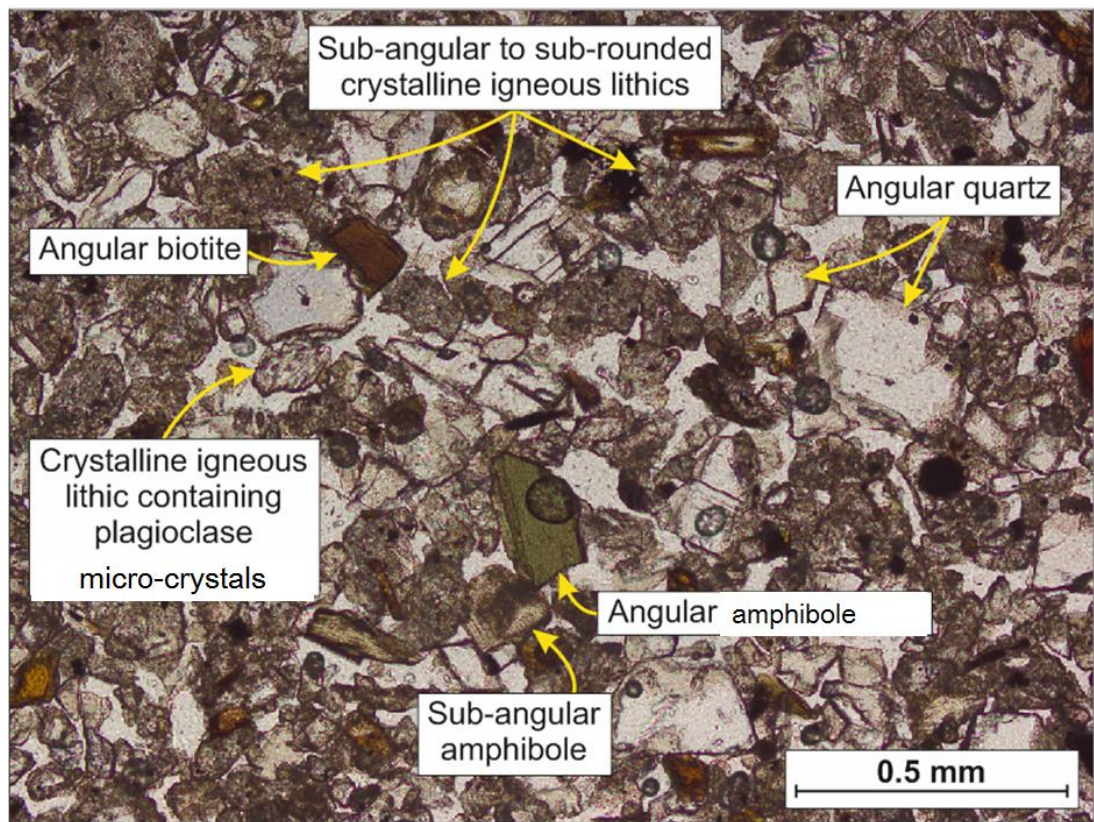


Figure 6-32 Heterogeneous granular nature of sample WASH_20 from L4. Angular amphibole, biotite, and quartz occurs along with sub-angular to sub-rounded crystalline igneous lithic clasts that contain plagioclase micro-phenocrysts and micro-crystals.

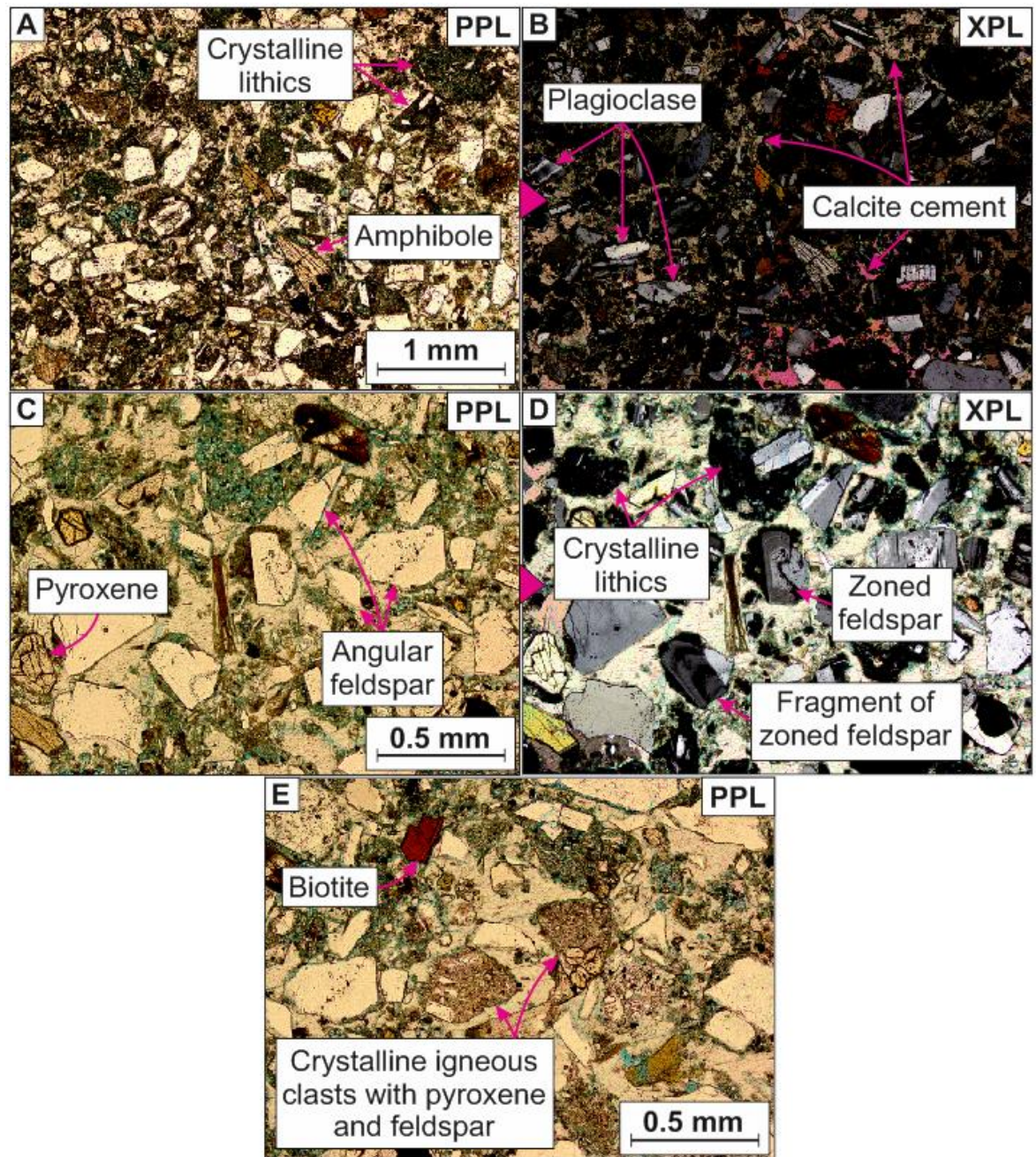


Figure 6-33 Optical microscope images showing the components of sample WASH_21 from L4. This sample is predominantly comprised of crystalline igneous lithics (A - E), with larger crystals of amphibole (A), biotite (E), plagioclase feldspar (B - E), and pyroxene (C - E), within a calcite cement. Some of the plagioclase displays zoning in XPL (D). Images B and D are the XPL views of images A and C, respectively.

SEM analysis of clasts within WASH_21 shows that most clasts are parts of crystalline igneous rock, including the larger crystal fragments, which commonly retain a small amount of the micro-crystalline groundmass (Figure 6-34). Some phenocrysts have mineral inclusions within them, for example, some amphibole crystals contain minor inclusions of magnetite, labradorite and apatite (Figure 6-34c).

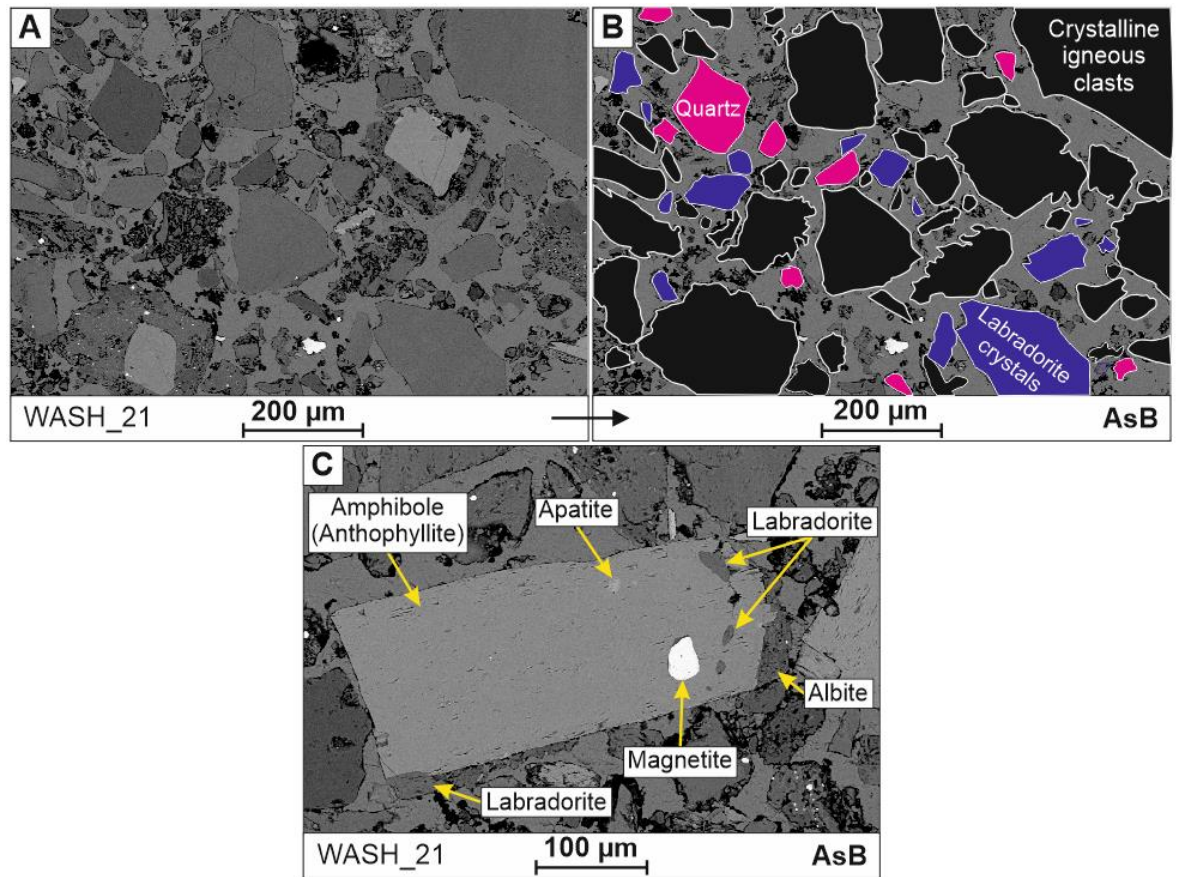


Figure 6-34 AsB SEM calcite-cemented sandstone of WASH_21 from L4. A) The sample comprises crystalline igneous clasts (black in B), and crystals of quartz (pink in B) and labradorite (blue in B). C) A crystalline igneous clast consists of a phenocryst of amphibole containing inclusions of apatite (pale grey), magnetite (white) and labradorite (darker grey). This crystal is present with minor remnants of labradorite and albite at its edges.

Several types of crystalline igneous clast can be identified in WASH_21 (Figure 6-35). These include: angular clasts with phenocrysts of plagioclase and pyroxene (Figure 6-35a), or, labradorite, pyroxene and ilmenite (Figure 6-35b). Another type contains micro-crystals of euhedral labradorite and titanomagnetite, with minor occurrences of apatite, quartz and amphibole (Figure 6-35c, d).

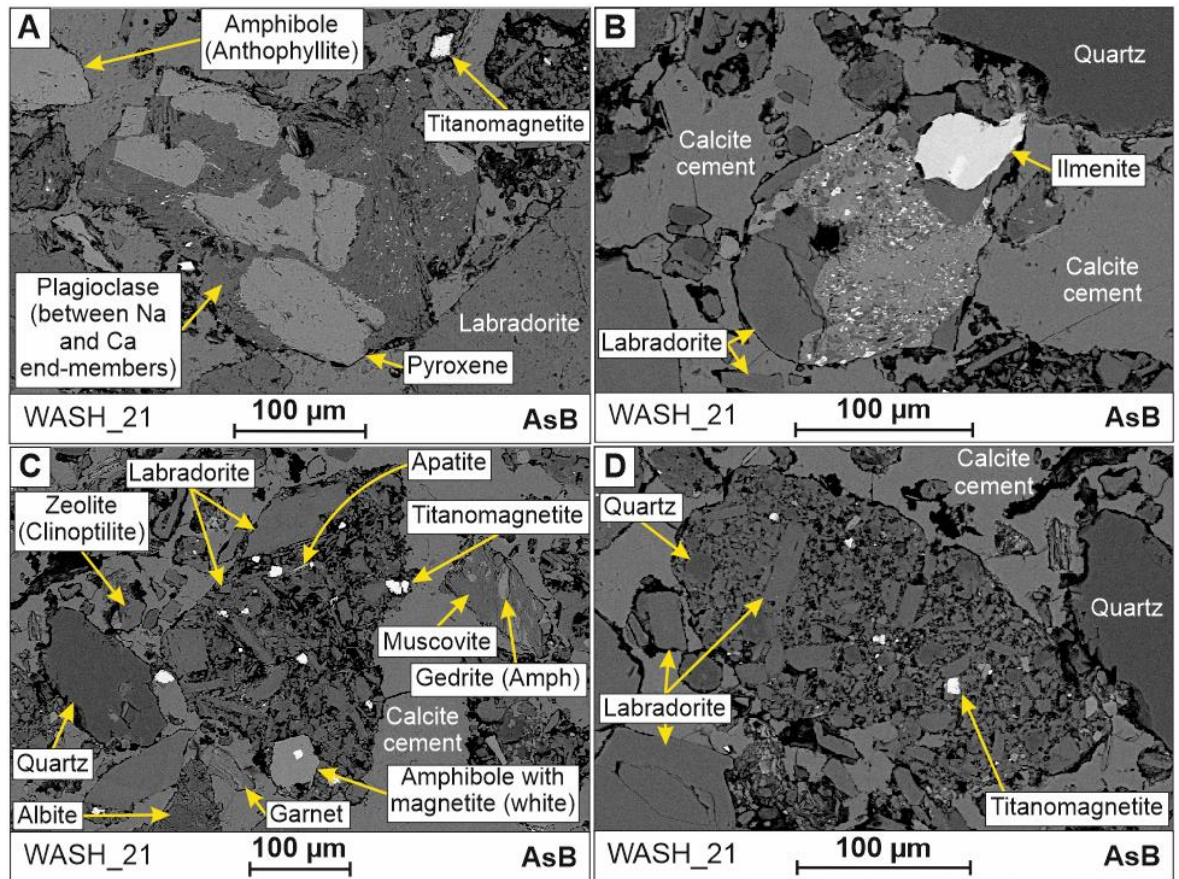


Figure 6-35 AsB SEM types of crystalline igneous clasts within WASH_21 from L4. A) A crystalline igneous clast composed of plagioclase and pyroxene. B) A sub-rounded crystalline igneous clast containing ilmenite and labradorite. Quartz crystals are also present, and these clasts occur within a calcite cement. C) Angular, microcrystalline igneous clast composed of euhehedral labradorite, apatite, titanomagnetite. An amphibole with a magnetite inclusion is also present. Quartz and garnet crystals are present as additional clast-types in this sample. D) Another example of a crystalline igneous clast comprised of euhehedral laths of labradorite and titanomagnetite, with the addition of quartz.

Sample WASH_23 represents material from the base of the pyroclastic facies (Figure 6-20). Reflected light microscopy (RL) shows that it is composed of coarse-ash that display bubble-wall and rod-like morphologies (Figure 6-36). Additional well-rounded to sub-rounded grains of other (unknown) clast-types are also present, as shown by variations in the colour of clasts observed beneath RL (Figure 6-36).

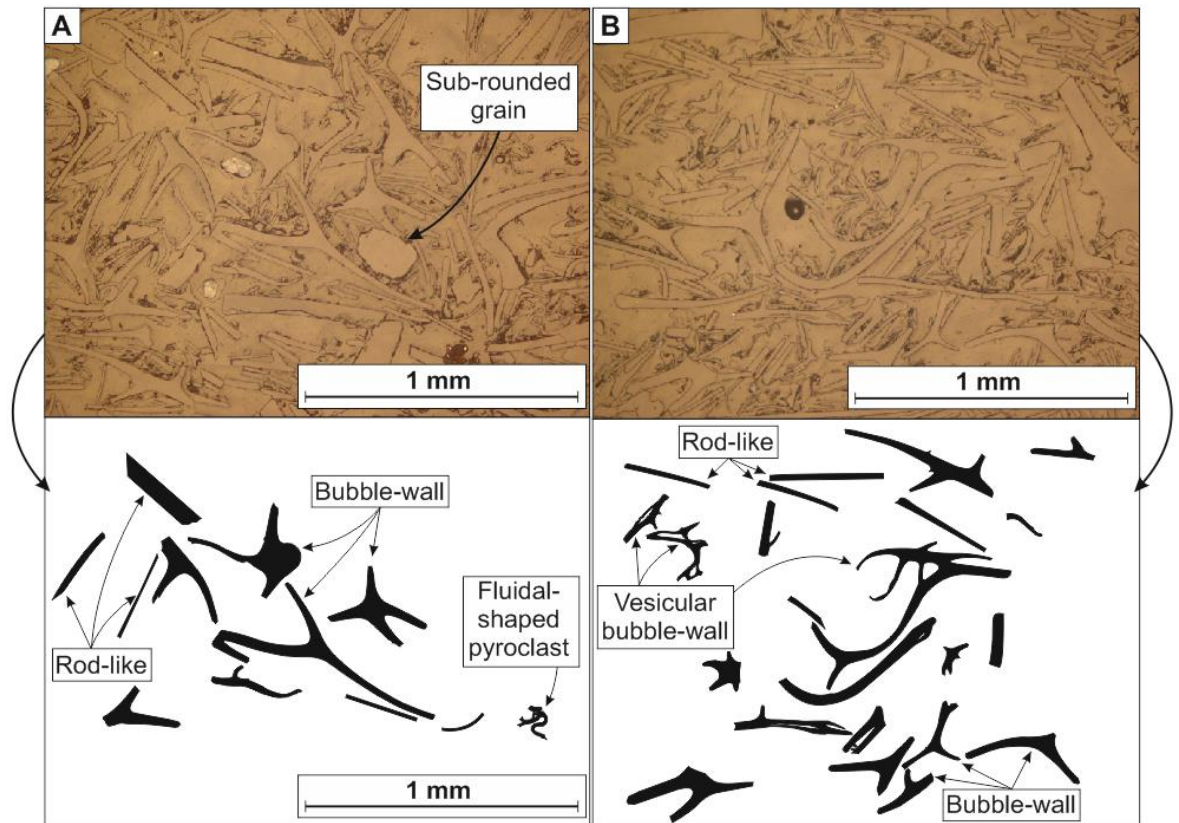


Figure 6-36 Abundant bubble-wall and rod-like pyroclasts in sample WASH_23 from L4 under RL. A & B illustrate areas dominated by pyroclasts with bubble-wall and rod-like morphologies, as is highlighted by a few sketched grains shown below the RL images. A) In addition to these pyroclast types, this image also shows a pyroclast with a more fluidal morphology. B) Alongside the main pyroclast types, this image illustrates some vesicular bubble-wall shards.

Sample WASH_22 contains whole and fragmented ash aggregates up to 4 mm in diameter (including: accretionary lapilli and coated ash pellets; e.g. Brown et al. 2010), and composed of coarse to very fine ash, surrounded by a matrix of coarse-ash (Figure 6-37).

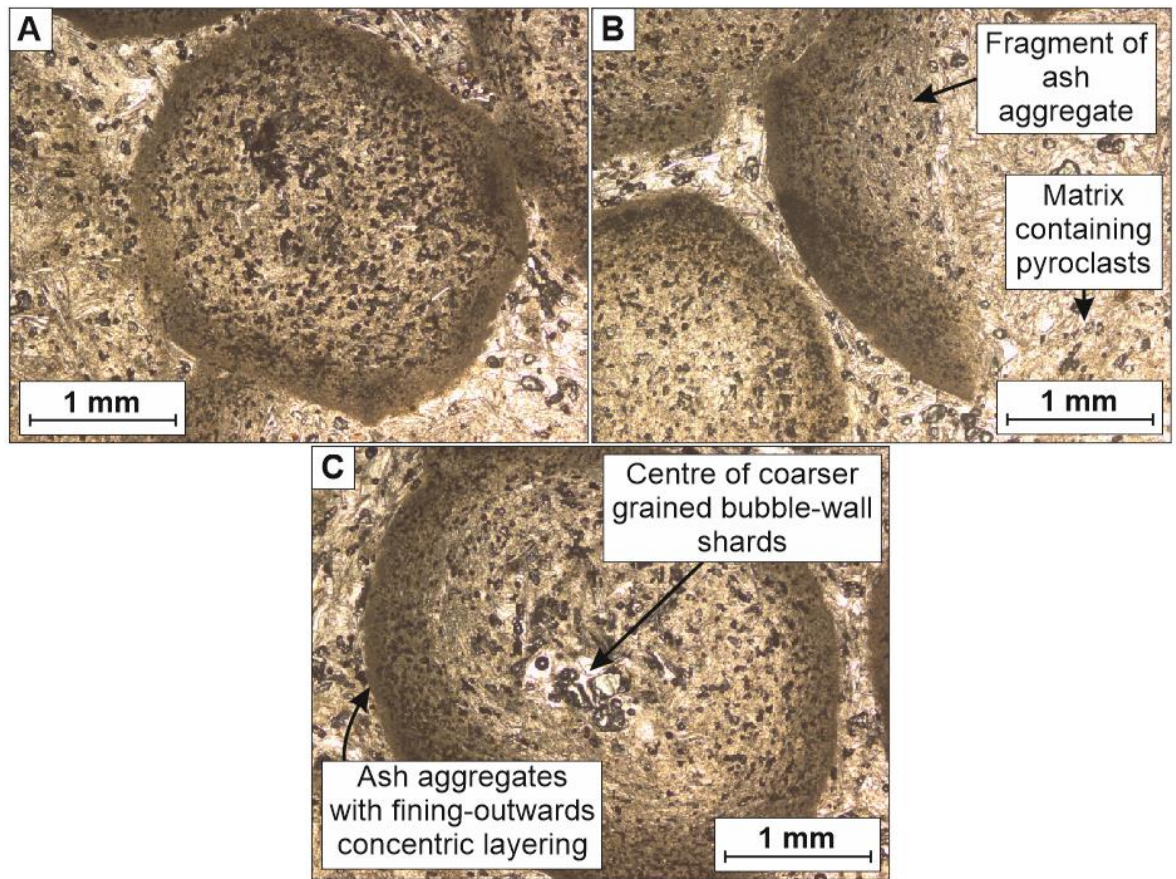


Figure 6-37 Whole and fragmented ash aggregates surrounded by a matrix of pyroclasts in sample WASH_22 L4. A) A whole accretionary lapillus of <4 mm in diameter showing concentric layering of finer and finer pyroclastic material. B) Fragment of an accretionary lapillus surrounded by a matrix of pyroclasts. C) Whole accretionary lapillus showing coarse-to-fine grading, from the core to the rim. This example has a core containing coarser-grained bubble-wall shards.

Pyroclasts of the matrix show a range of morphologies and features that can be used to predict the eruption conditions in which they formed (Carey & Sparks 1986; Cas & Wright 1988; Barberi et al. 1989; Cioni et al. 1992; Blower et al. 2001; Riley et al. 2003; Gaonac'h et al. 2005; Houghton & Gonnermann 2008; Polacci et al. 2008; Clarke et al. 2009; Mattsson 2010; Shea et al. 2010; Bonadonna et al. 2011; Ross & White 2012; Graettinger et al. 2013; Moitra et al. 2013; Cioni et al. 2014; Heap et al. 2014). Pyroclastic features include: fluidal pyroclast shapes (Figure 6-38), highly vesicular pumice clasts (Figure 6-38c), a significant amount of rod-like pyroclasts (Figure 6-38b), and pyroclasts with micro-fractures (Figure 6-38). The pyroclasts have smooth (Figure 6-39a), or jagged/rough edges (Figure 6-39b).

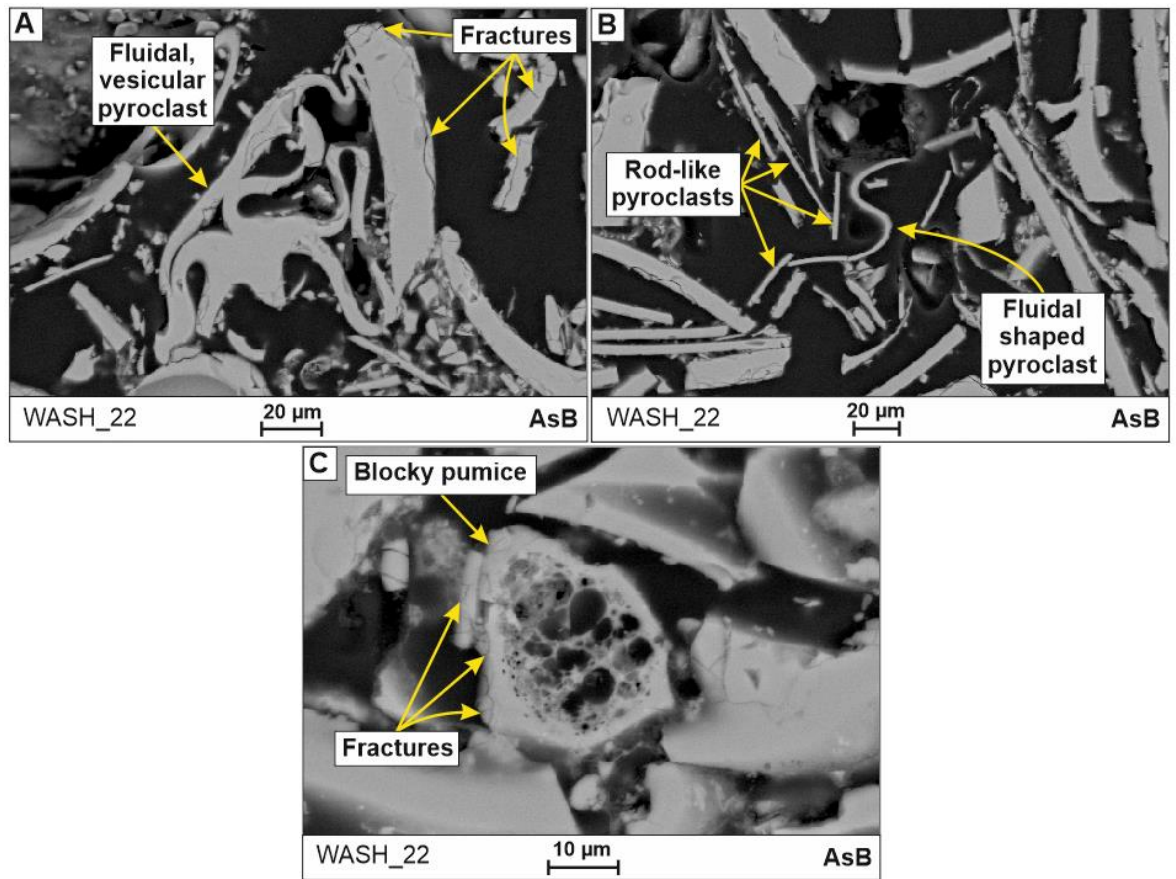


Figure 6-38 AsB SEM features of pyroclasts from WASH_22 of L4 that correspond to magmatic fragmentation processes. A) An irregular-shaped pyroclast with fluidal bubble-walls. Fracturing of the edge of the pyroclasts is indicated. B) Planar rod-like pyroclasts and a fluidal-shaped pyroclast indicative of ductile deformation of the pyroclast before quenching. C) Blocky, very fine ash with a highly vesicular pumiceous centre.

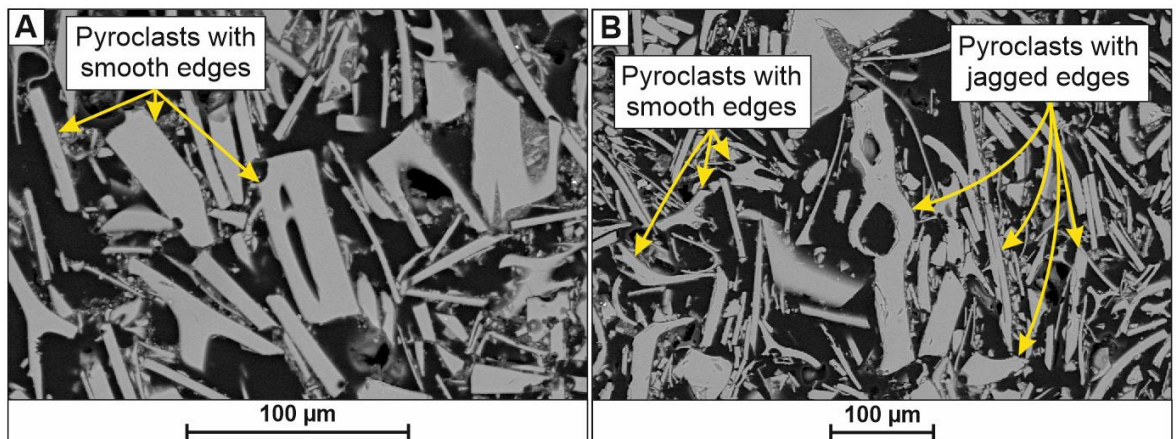


Figure 6-39 AsB SEM examples of smooth and jagged pyroclasts as evidence for different transport and depositional origins of ash in WASH_22 from L4. Pyroclasts with smooth edges show that they have not undergone abrasion. This could be evidence of primary air-fall, with no subsequent reworking or evidence of a clast-poor transportation and depositional fluid (air or water). B) Some pyroclasts with jagged edges are found with smooth-edged pyroclasts. The jagged edge of some pyroclasts suggests that they have experienced abrasion during transport.

Sample WASH_22 from L4 includes whole and fragmented ash aggregates (Figure 6-40, Figure 6-42). These aggregates have an unstructured core of ash with a fine-grained rim (Figure 6-40, Figure 6-41). Many show normal-grading from the coarser-grained core, outward to the rim (Figure 6-40, Figure 6-41), although, others appear to have a coarse-grained core that is surrounded by a finer-grained lamination that is not graded (Figure 6-40b, Figure 6-41). These features are identified in both the smallest aggregates (1-2 mm; Figure 6-40) and the larger aggregates (up to 4 mm; Figure 6-41). Aggregates that appear to only be composed of fine-grained ash, or those with a very thick fine-grained lamination, may not be truly representative of the aggregates, and instead represent an oblique (and incomplete) cross-section through the aggregate (Figure 6-40c, Figure 6-42a).

Fragments of ash aggregates are found between complete aggregates. These can be identified as patches of fine-ash, commonly with a partly circular edge (Figure 6-42), resembling sections of the outer edges of the complete aggregates (Figure 6-40, Figure 6-41). The core of these aggregates is less likely to be preserved if the aggregate fragmented, due to its unconsolidated nature (e.g. Figure 6-40), instead ash from the centre of these broken aggregates has, most likely, contributed to the ash in the surrounding matrix.

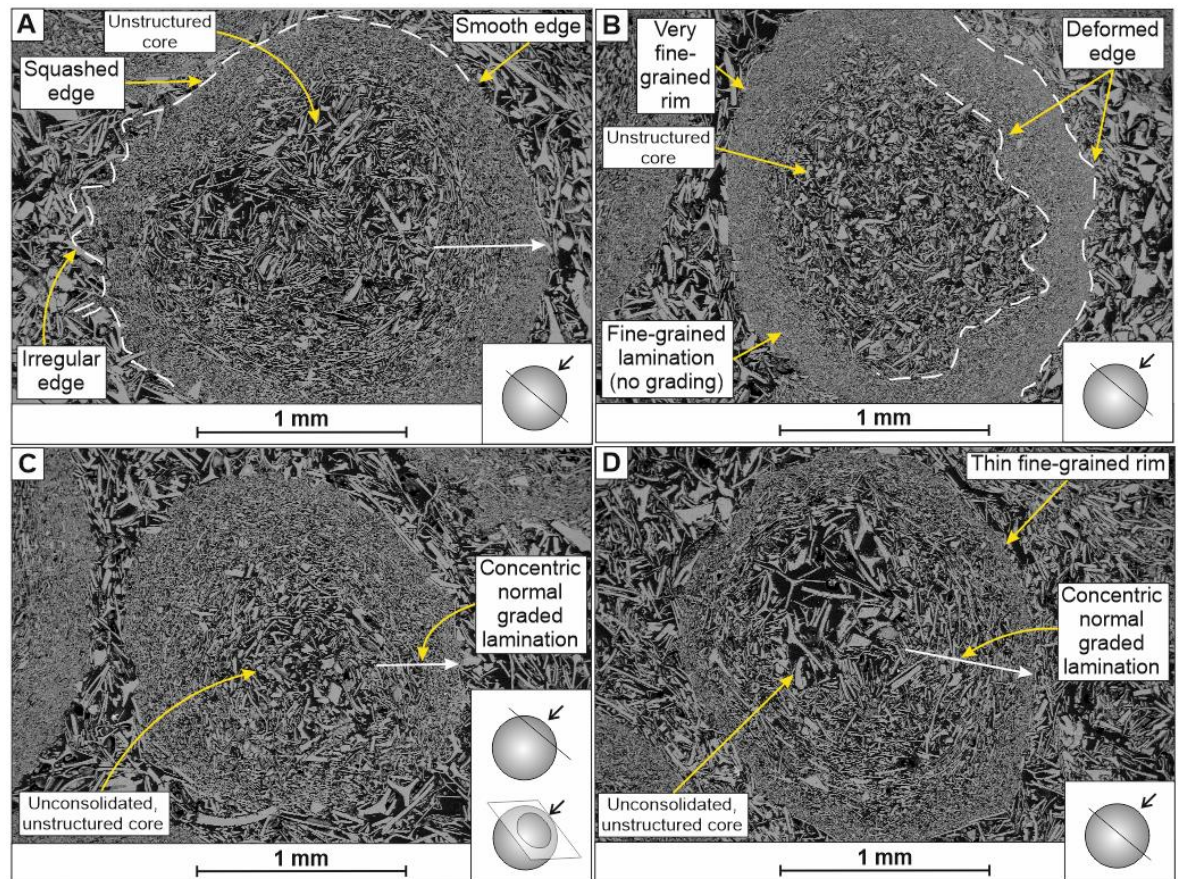


Figure 6-40 AsB SEM examples of concentrically-layered ash aggregates from WASH_22 at L4. A) An aggregate with a relatively large unstructured core surrounded by a normal-graded lamination that grades outward into a very fine-grained rim. The rim is mostly smooth, but shows some flattening where it is in close contact with another aggregate. The rim to the left is irregular and deformed. **B)** An ash aggregate with a thicker, very fine-grained rim composed of a greater abundance of fine grains in the outer lamination. This aggregate appears to have a coarser-grained core that does not grade outward to the rim - instead the core and rim appear to be separate entities. The outer edge to the right is partially deformed. **C)** A slightly smaller ash aggregate that is dominated by its fine-grained rim, which may be due to sectioning at an oblique angle through the spherical aggregate (insert). Normal-graded and an unconsolidated, off-centre, unstructured core. One normal-graded lamination occurs outward from the core and is surrounded by a second normal-graded lamination. This example is therefore an accretionary aggregate of lapilli-size (an accretionary lapillus; e.g. Brown et al. 2010).

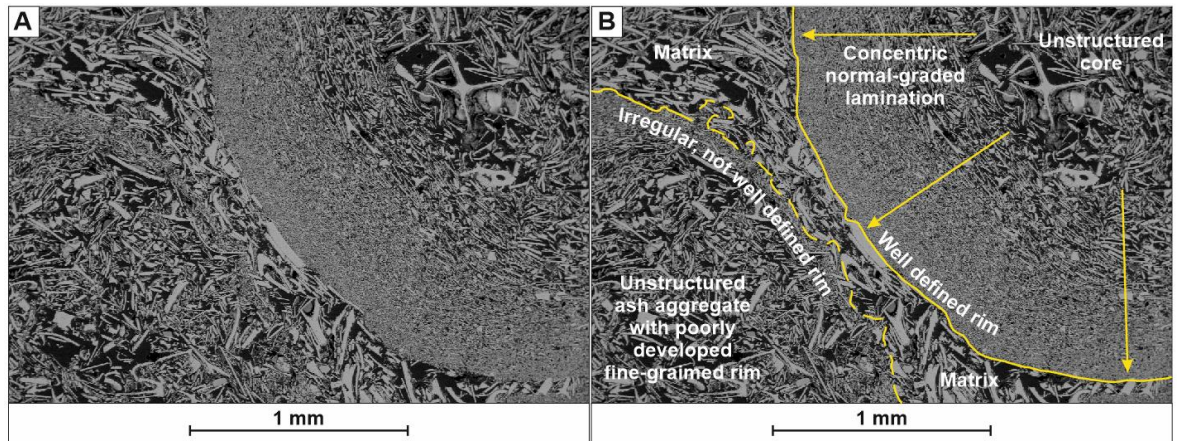


Figure 6-41 AsB SEM features of larger ash aggregates in WASH_22 from L4. Two different aggregates, one with an unstructured core and a concentric normal-graded lamination with a well-defined rim edge (right). This contrasts with the aggregate on the left, which is predominantly composed of unstructured ash with a thin, ill-defined fine-grained outer rim with an irregular, slightly diffuse edge. The aggregates are surrounded by an ash matrix with similar features to the cores of the aggregates. The matrix and aggregates are predominantly composed of non-vesicular rod-like, bubble-wall and blocky ash.

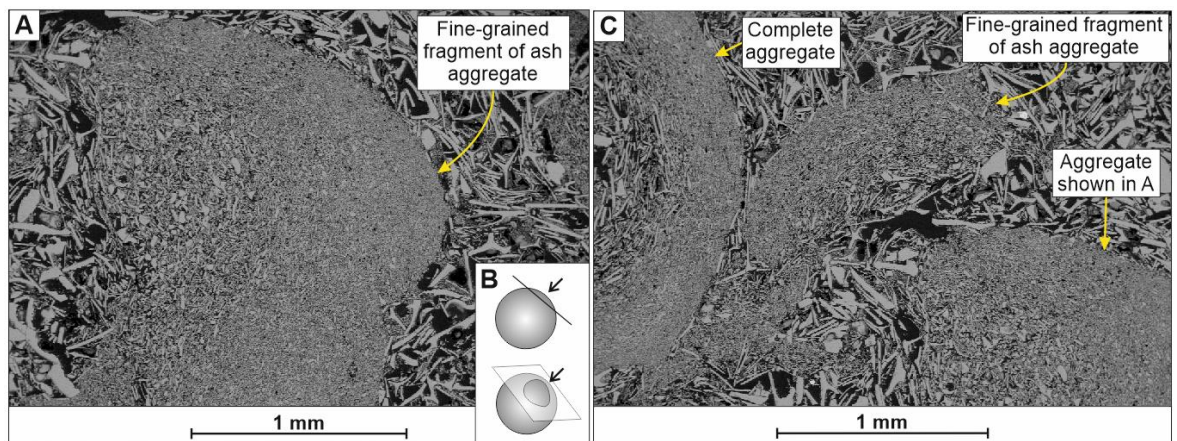


Figure 6-42 AsB SEM nature of ash aggregate fragments in WASH_22 from L4. A) Fragment of the fine-grained outer edge of an ash aggregate. This section of aggregate appears to contain a thicker unit of fine ash than any of the other aggregates, possibly because of the angle as which the thin-section was cut (B), which sampled just the outer part of a fragment of a spherical ash aggregate, where the finest grain-size fraction is found (B).

Close examination of the fine-grained rim of these aggregates shows that they are not exclusively comprised of pyroclasts, but also contain fragmented siliceous diatom frustules (Figure 6-43; Round et al. 1990).

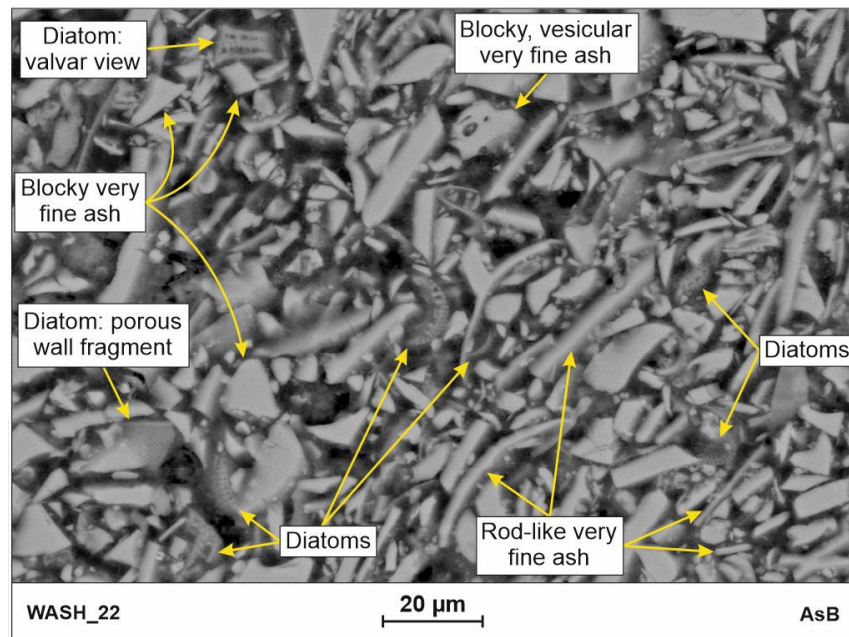


Figure 6-43 AsB SEM diatoms within the fine-ash rim of an ash aggregates in WASH_22 from L4.

The diatoms are all $<10\ \mu\text{m}$ (Figure 6-44), and have been incorporated into the fine-grained edge of the aggregates with pyroclasts of a similar size (Figure 6-43). The diatoms are predominantly representative of centric types and thus, represent non-motile (free-floating) species (Figure 6-44; Round et al. 1990). A few examples appear to be asymmetrical (Figure 6-44J) and represent freshwater non-motile diatoms that were likely free-floating in a lake when alive (Round et al. 1990).

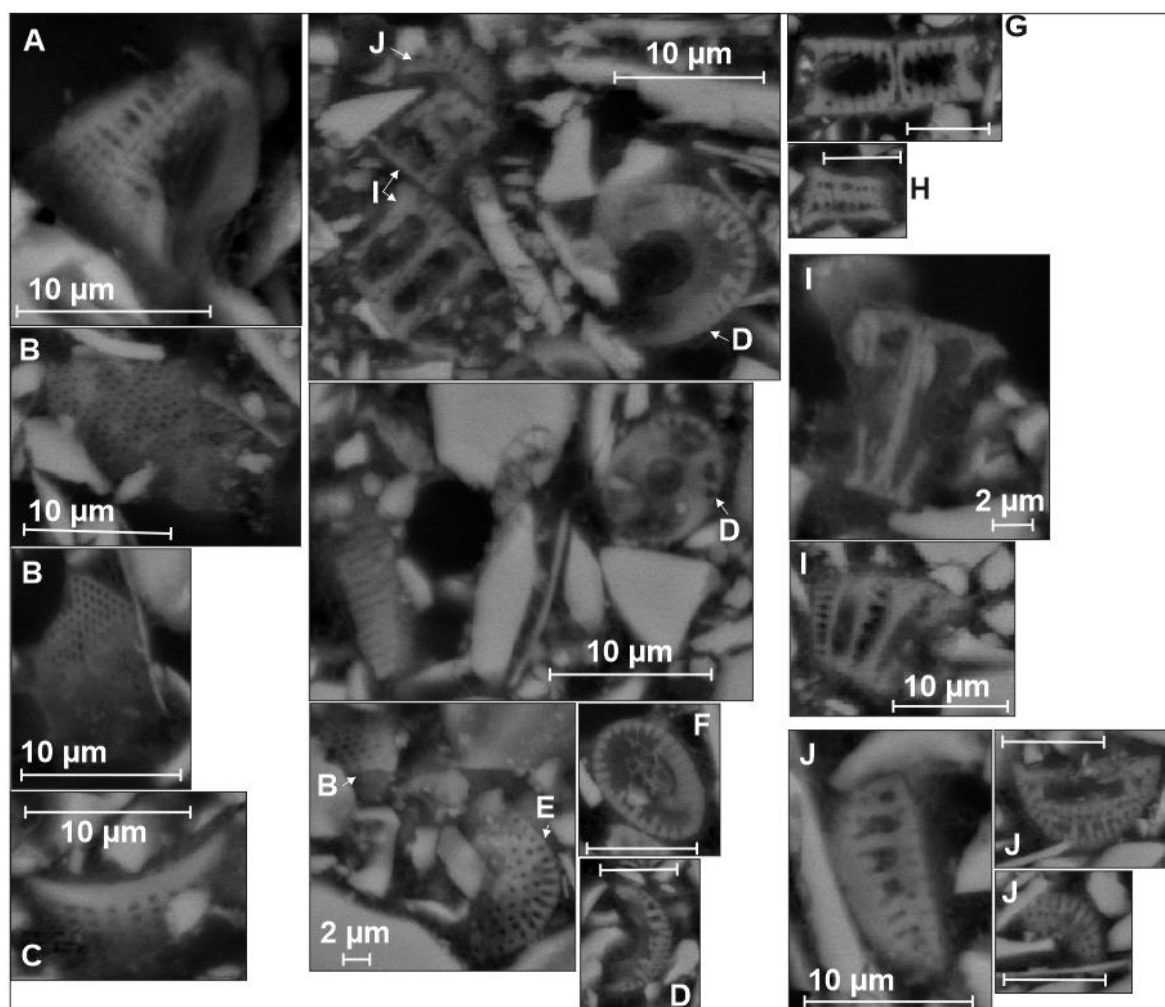


Figure 6-44 AsB SEM diatoms and diatom fragments identified in the outer layers of ash aggregates from L4 A) Centric diatom with a porous wall. B-C) Fragments of porous walls. D-F) Example of valves. G-H) Valvar (cross-section) view through different diatoms, some have a girdle in the centre joining the upper and lower valves (G). I) Fragments of diatom valves? J) Asymmetrical diatom valves and fragments.

Samples from the main quarry face (e.g. WASH_29; Figure 6-19v), represent fine-grained silicic tuff, predominantly comprised of glassy pyroclasts, with minor sub-angular to well-rounded granular lithic clasts (Figure 6-45, Figure 6-46).

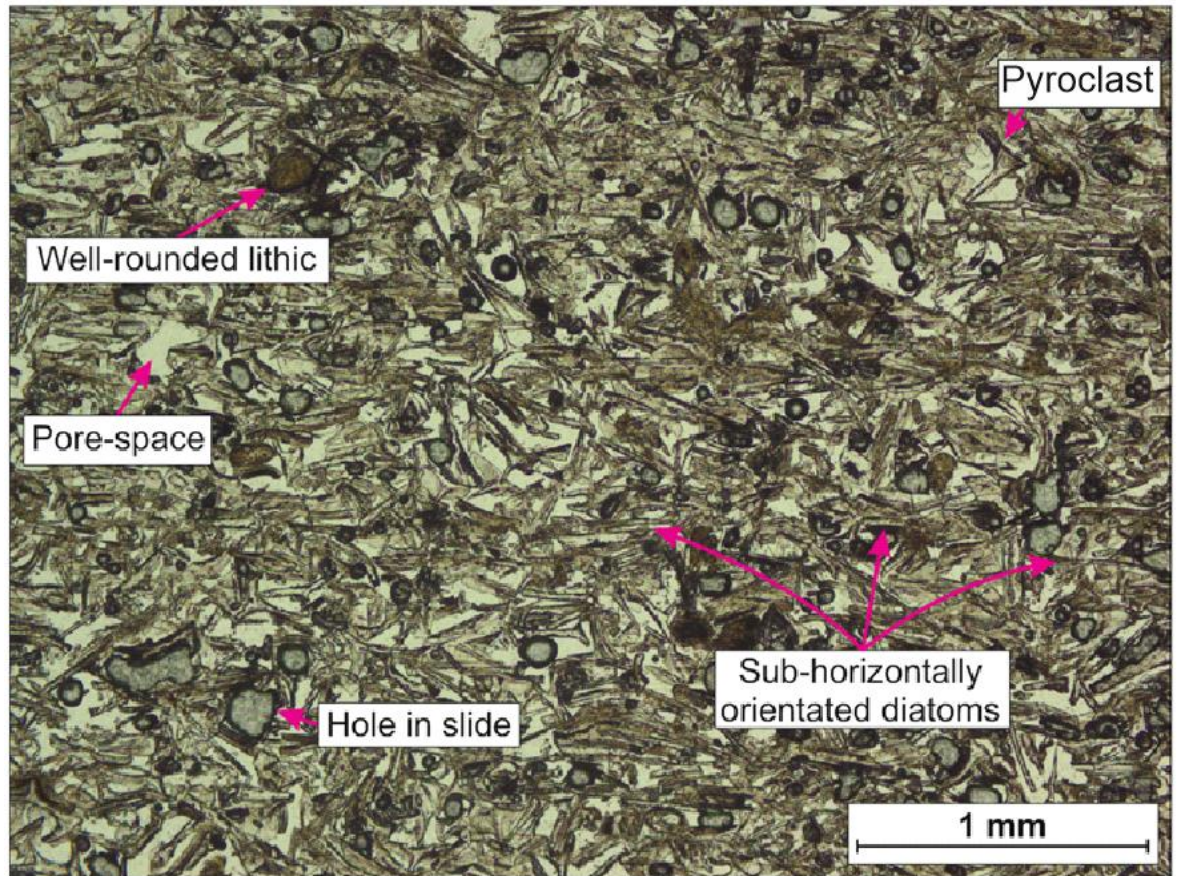


Figure 6-45 Nature of sample WASH_29 from the main silicic tuff unit of L4. This sample shows conspicuous preferred orientation of the glassy pyroclasts, which form the parallel laminations visible in the field (Figure 6-25). Well-rounded lithic clasts can also be identified. The deposit contains abundant pore space and the rock is held together by grain-grain contacts and compaction, with no cement or matrix material apparent in Plane Polarised Light.

Upon closer inspection the pyroclasts of WASH_29 have jagged edges and are in some instances associated with a fine-ash matrix that surrounds them or infills vesicles (Figure 6-46). The pyroclasts show a range of morphologies, including vesicular and non-vesicular, irregular/fluidal, bubble-wall and rod-like (Figure 6-46).

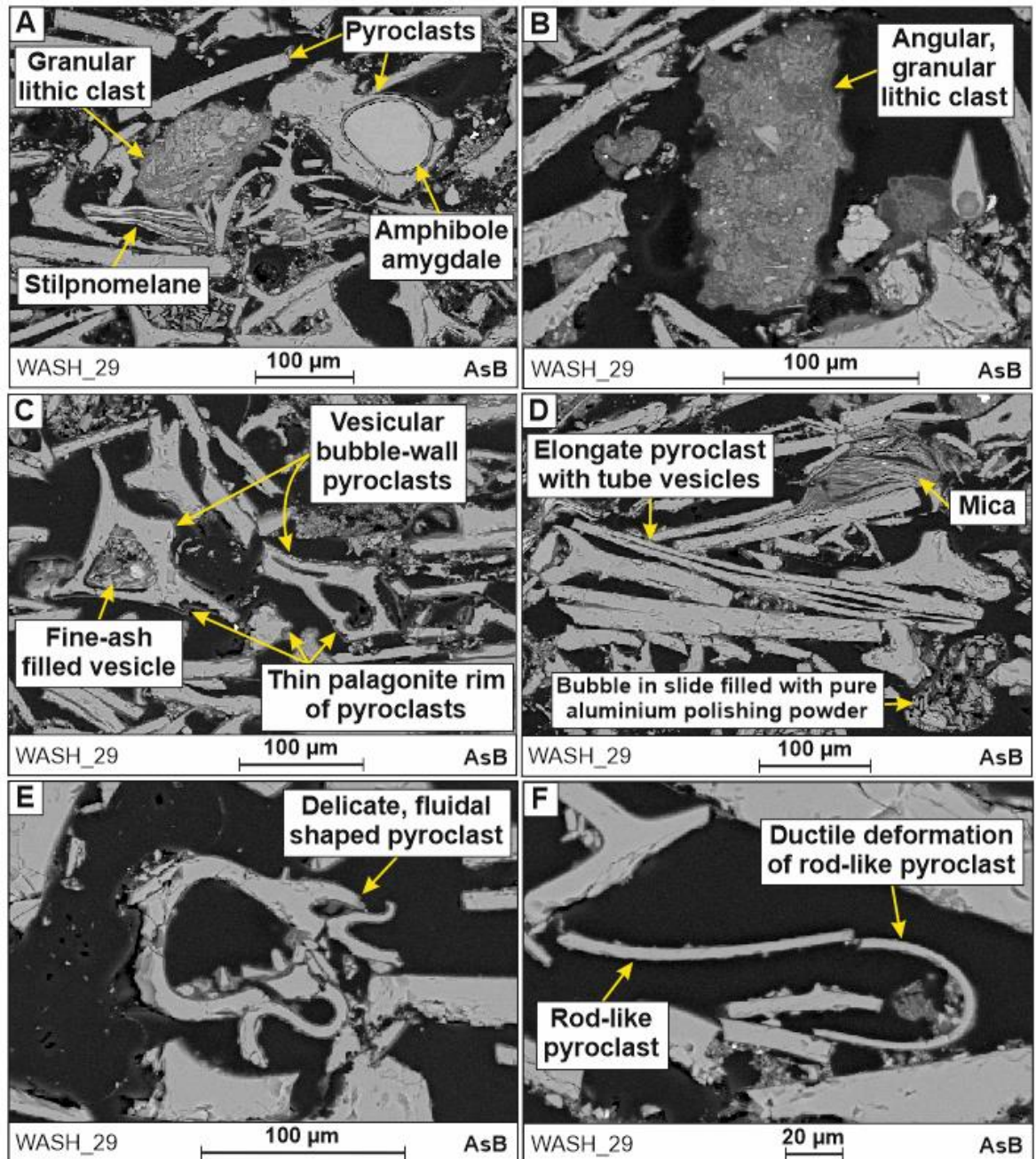


Figure 6-46 AsB SEM images of features of the silicic tuff (WASH_29), from L4. A) A range of volcaniclastic clast-types, including glassy pyroclasts with amphibole amygdalae and granular lithic clasts comprised of fine ash and glassy pyroclasts. Crystals of stilpnomelane are also present. B) Angular granular lithics predominantly comprised of fine ash. C) Vesicular pyroclasts with palagonite rims show that the pyroclasts have begun to undergo alteration to clay. Some vesicles are infilled with a fine-ash, but others remain empty. D) Elongate rod-like pyroclasts are common in this sample, some also include elongate tube vesicles. Bubbles in the slide, filled with fine grains pyroclasts produced during sample preparation should not be confused with natural features of the deposit. E) An irregular, fluidal-shaped pyroclast. F) Delicate rod-like pyroclasts, showing evidence of ductile deformation.

Similar clast-types and features can be identified in sample WASH_30, from a structureless unit of the silicic tuff (Figure 6-20; Figure 6-47; Figure 6-48).

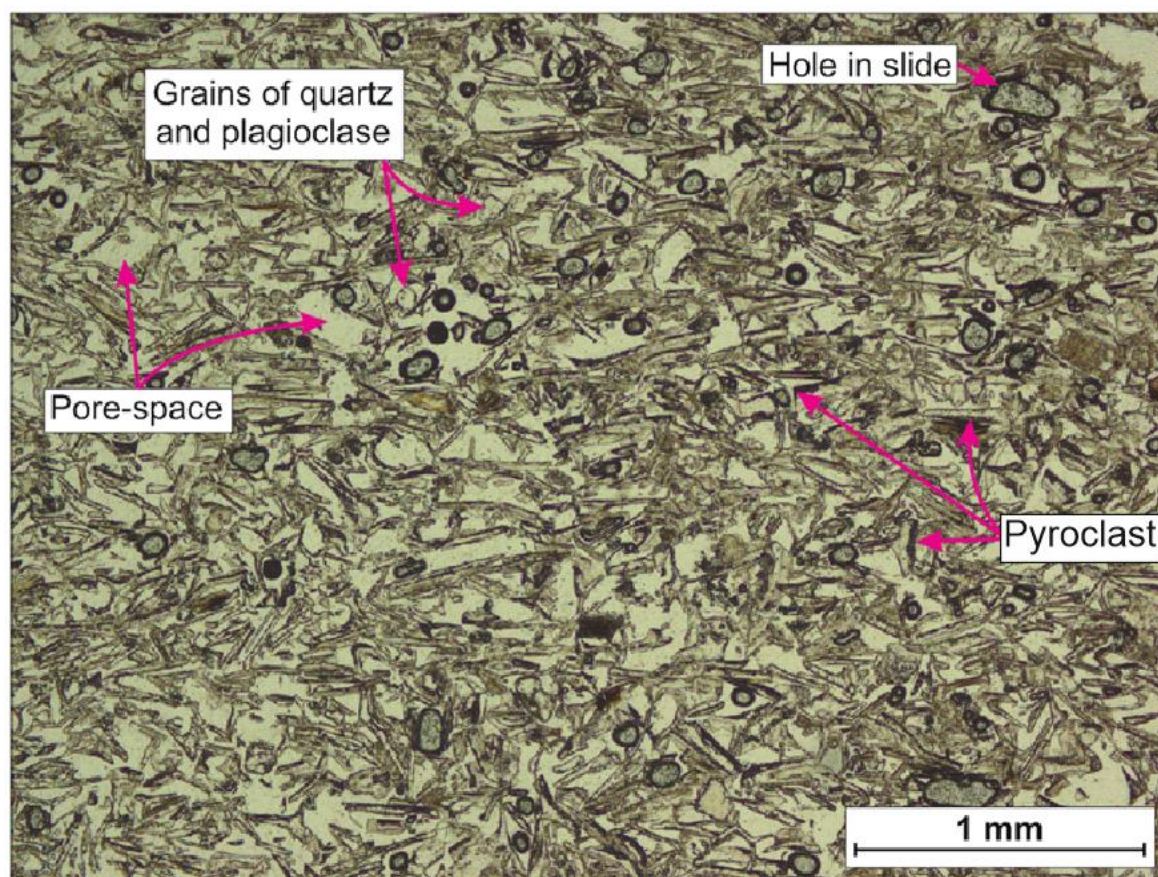


Figure 6-47 An example of microscope features of a structureless volcaniclastic unit from the L4 silicic tuff (pumicite) viewed under Plane-polarised light. This sample (WASH_30), has abundant pore-space between pyroclasts with uncommon sub-rounded to sub-angular crystals of quartz and/or plagioclase.

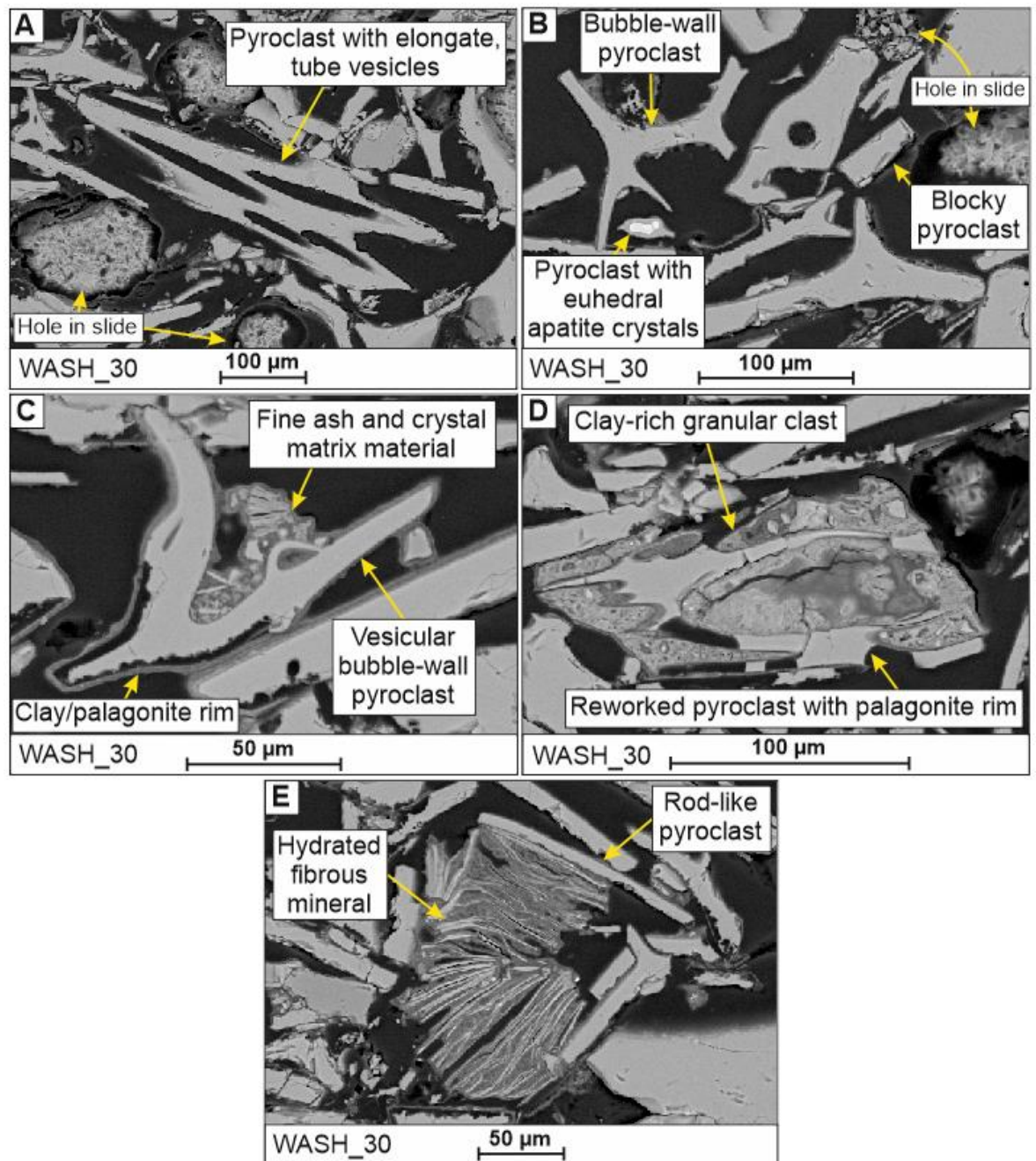


Figure 6-48 AsB SEM images illustrating some of the features of WASH_30. A) Pyroclast with elongate vesicles. B) Bubble-wall and blocky pyroclasts. Some pyroclasts include micro-crystals of euhedral apatite. C) Fluidal, bubble-wall pyroclast with non-sphericle vesicles and a palagonite rim. A fine ash and crystal matrix is associated with this pyroclast. D) A granular lithic clast containing a reworked bubble-wall pyroclast that has a palagonite rim and a fine clay-rich matrix. E) A hydrated fibrous mineral, possibly mica(?) and rod-like pyroclasts.

6.5.4.4 Interpretation of optical microscopy and SEM analysis

WASH_20 and _21 are comprised of siliciclastic grain-types and show that sedimentation in the proposed overbank facies at the base of the L4 exposure was not influenced by volcanism.

The fluidal (Figure 6-38a, b), rod-like (Figure 6-38b), and highly vesicular (Figure 6-38c) pyroclasts of WASH_22 are evidence of an eruption driven by ‘dry’ magmatic processes, for example, via the expansion of gas bubbles (Walker & Croasdale 1971; Heiken 1972, 1974; Wohletz 1983; Wohletz & Sheridan 1983; Cas & Wright 1988; Rose & Durant 2009; Brown et al. 2012; Graettinger et al. 2013). The rod-like pyroclasts might be Limu-o-Pele, considered to form in the presence of water and may be evidence for hydrovolcanic eruptions (at least in basaltic eruptions; Graettinger et al. 2013). Micro-fractures present in pyroclasts throughout the sample (Figure 6-38) may be hydration cracks formed by rapid quenching of the erupted ash (Scolamacchia et al. 2005; Mascarenhas-Pereira 2006), or due to later abrasion during transport (e.g. Selley 1976) or sample preparation.

The roughness of pyroclasts, indicated by the smooth or jagged appearance of their edges, varies between clasts within WASH_22, and implies that the pyroclasts have been subject to a range of different processes (Figure 6-39). Pyroclasts with a rough, or jagged, edge have most likely undergone abrasion, with other clasts within the eruption column or pyroclastic density current (PDC), and/or by contact with the Earth’s surface, during transport, for example, during reworking (Figure 6-39b). These clasts may have undergone recycling within the eruption column, close to the vent, where they were entrained within the eruption, multiple-times, and abrasion occurred in a similar way to grain contacts within a PDC or during reworking. Smooth-edged pyroclasts have not undergone significant abrasion and were more likely deposited from air-fall or within a clast-poor medium where grain-contact and interaction with the Earth’s surface were minimal or absent (Figure 6-39a).

A high abundance of granular lithic clasts and the rough surface of the pyroclasts in WASH_29 and _30 suggest that material of the main silicic tuff unit (pumicite) is volcanoclastic and is dominated by pyroclasts that were deposited from reworking of an original pyroclastic deposit.

6.5.5 Yellpit (L5)

6.5.5.1 *Field observations*

The exposure at Yellpit (L5) (Figure 6-1), is composed of sub-horizontal parallel laminated siltstone with discontinuous lenses of siltstone with accretionary lapilli. Above this lies a more structureless siltstone with occasional diffuse sub-horizontal lamination. Towards the top of this unit the siltstone contains ripple cross-laminations. The boundary between the sedimentary rocks and the overlying Pomona Basalt the sediments have been baked and grade from a fused tuff to a glassy fused tuff within *ca.* 10 cm of the lava contact (Figure 6-49, Figure 6-50). The glassy fused tuff contains mineral-filled fractures.

The exposure is dominated by by >2.5 m of basalt lava with a pillow facies at its base (Figure 6-49, Figure 6-50).

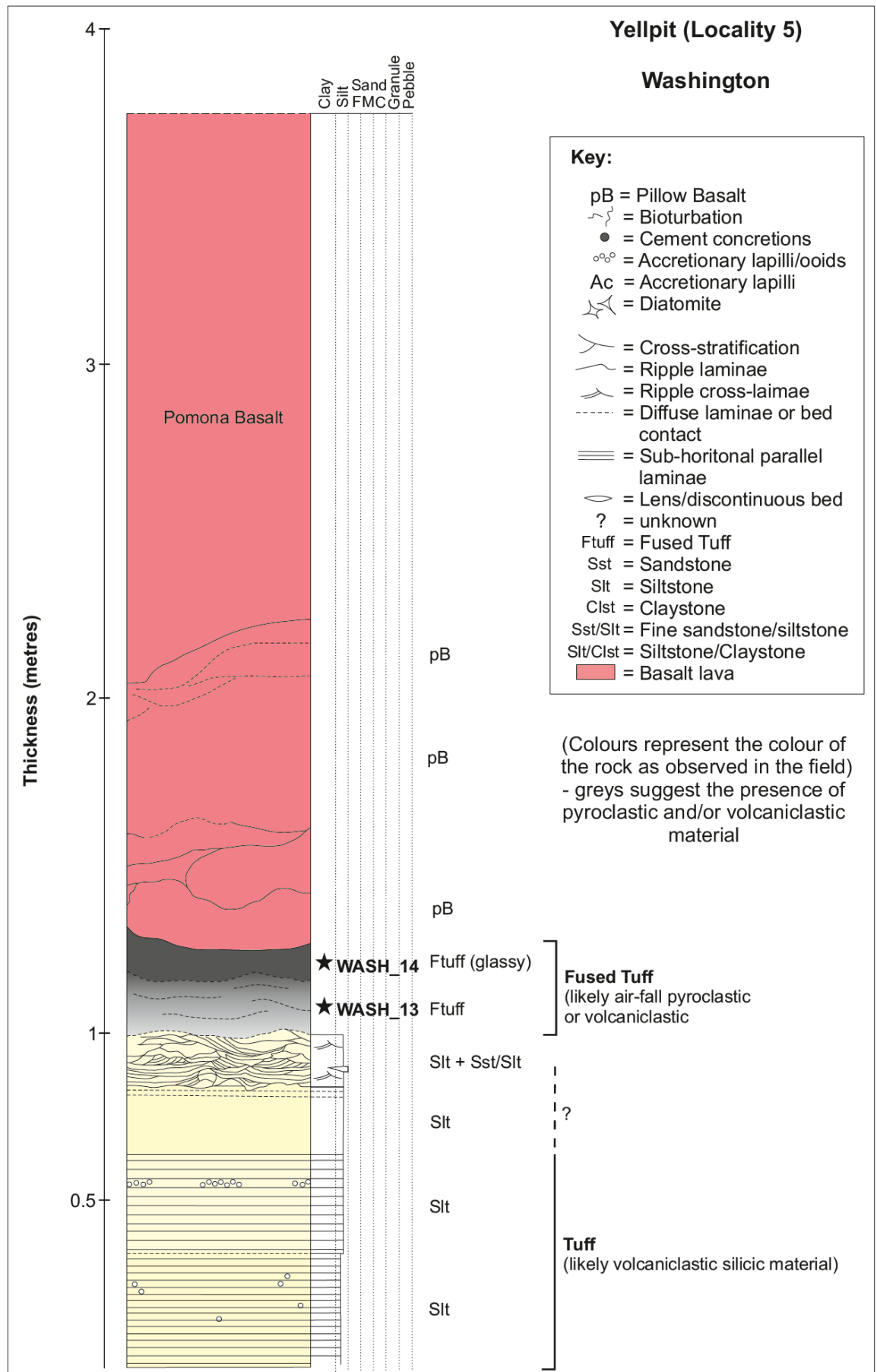


Figure 6-49 Lithological log displaying details of the exposure at Yellpit (L5). The sedimentary sequence at this locality is predominantly comprised of siltstone, which has

sub-horizontal parallel laminations at the base, along with uncommon fragments of accretionary lapilli of gravel grade. The siltstone also shows ripple cross-lamination in the upper part of the exposed sediments. The Pomona Basalt overlies the sediments, at the lava-sediment contact the sediment has undergone extreme thermal alteration ('baked') to a glassy fused tuff (assuming a high volcanic content within the original underlying sediment). At the base of the lava there is a development of pillow facies, implying eruption into standing water.

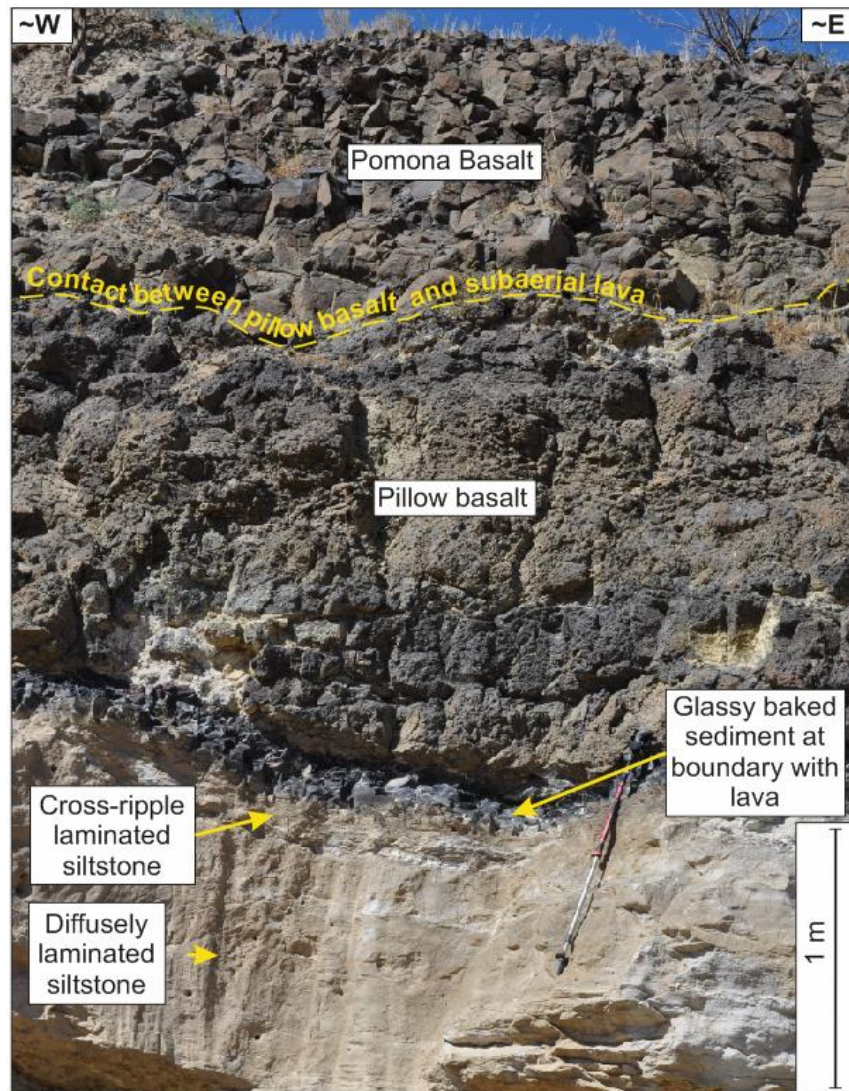


Figure 6-50 Exposure at Yellpit (L5). Here, diffusely laminated siltstones, overlain by ripple-cross laminated siltstones are overlain by the Pomona Basalt which displays pillow textures at its base. At the boundary between the lava the underlying siltstones have been thermally altered to a glassy (fused) material.

6.5.5.2 Interpretation of field observations

At L5 the EF is dominated by siltstones, the presence of lenses containing fragmented accretionary lapilli, within the lowermost siltstone, suggests that the siltstone contains reworked volcanoclastic material. The siltstones were likely deposited within a water body, as indicated by the presence of cross-ripple laminations and implied by the development of a pillow facies at the base

of the overlying Pomona Basalt (e.g. Schmincke 1967b). The mineral-filled fractures of the glassy fused tuff suggest that hot fluids circulated below the lavas, allowing minerals to precipitate in cracks that developed by (rapid) cooling of the underlying altered sediments.

6.5.5.3 *Optical microscopy and SEM analysis*

The siltstone at the lava-sediment boundary at Yellpit (L5), has been baked by the overlying lava (Figure 6-50), and comprises a glassy fused tuff (WASH_14; Figure 6-51) (e.g. Schmincke 1967b). The glassy fused tuff is solely comprised of glass, with spherical vesicles and conchoidal fracture when viewed under SEM (Figure 6-51b). However, remnant transparent blocky pyroclasts can be identified under plane polarised light (Figure 6-51a). Below this lies a fused tuff (WASH_13; Figure 6-52) that appears to have a wavy fabric, formed by the alignment of elongate pyroclasts (Figure 6-52).

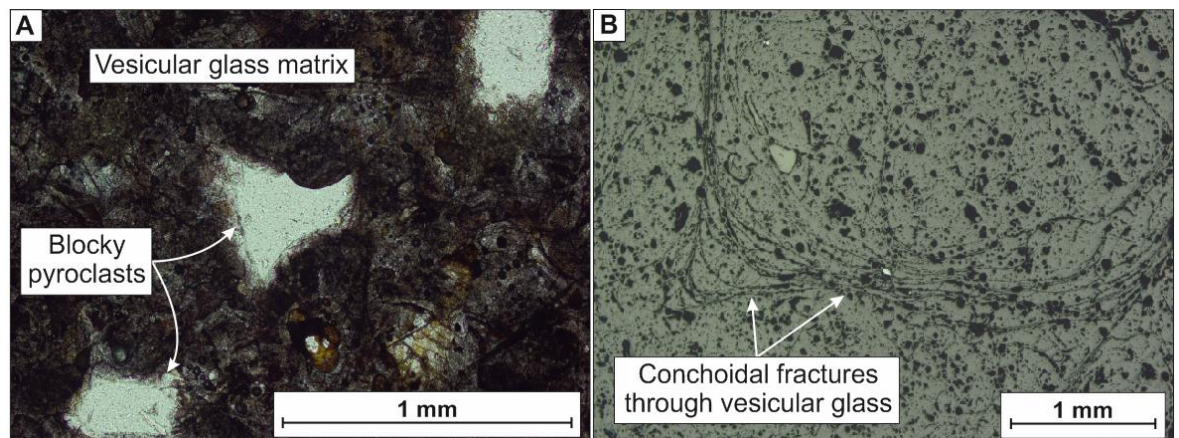


Figure 6-51 Nature of a glassy welded tuff (WASH_14) at the lava-sediment contact at Yellpit. This sample contains rare blocky pyroclasts surrounded by a glassy matrix (A), that contains conchoidal fractures (B).

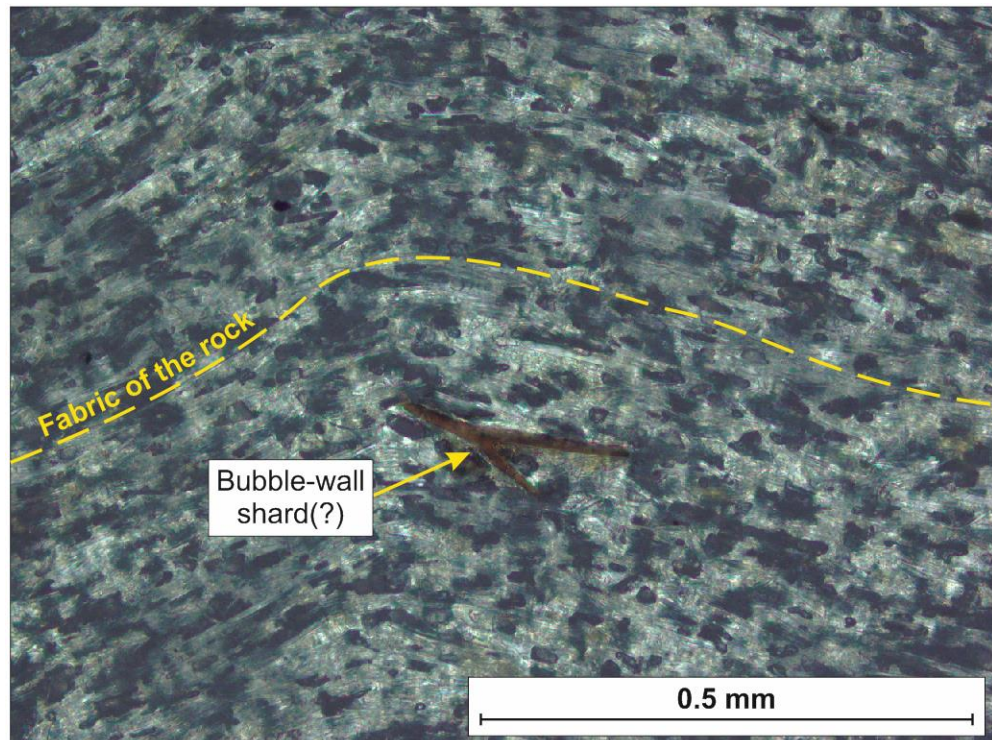


Figure 6-52 Fused tuff (WASH_13) with an internal fabric and rare, bubble-wall shard(?) from within 15 centimetres of the lava-sediment contact at Yellpit.

Samples of the non-fused siltstone are predominantly comprised of elongate, rod-like glassy pyroclasts that are aligned (Figure 6-53a), that creates the wavy fabric of the rock (Figure 6-52), and is therefore not a siltstone but a tuff. In addition, minor amounts of blocky and bubble-wall and vesicular pyroclasts can be identified (Figure 6-53c). The pyroclasts have smooth edges (Figure 6-53). Rare centric freshwater diatoms and clay-rich clasts are also present (Figure 6-53b).

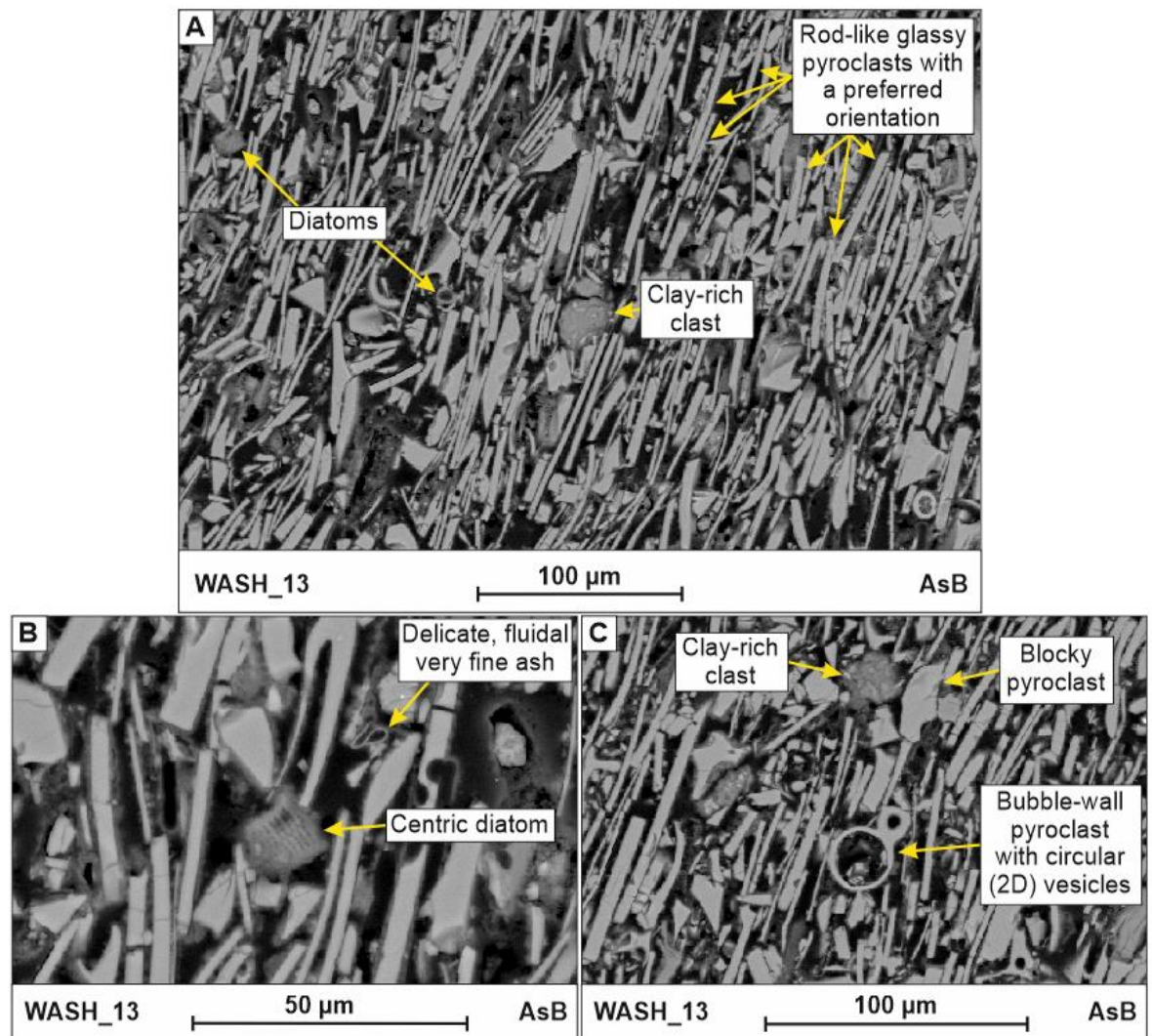


Figure 6-53 AsB SEM details of clast-types in WASH_13 from L5. Orientated elongate, rod-like glassy pyroclasts are the most abundant clast-type in this sample (A). Centric fresh-water diatoms (A, B), and clay-rich clasts (A, C) and vesicular or bubble-wall pyroclasts (C) are also present in lesser amounts.

6.5.5.4 Interpretation of optical microscopy and SEM analysis

The dominance of rod-like glassy pyroclasts in the non-fused tuff suggests that this pyroclastic material was produced by explosive silicic eruptions (Walker & Croasdale 1971; Heiken 1972, 1974; Wohletz 1983; Wohletz & Sheridan 1983; Cas & Wright 1988; Rose & Durant 2009; Brown et al. 2012; Graettinger et al. 2013). The smooth surfaces of the pyroclasts imply that little abrasion of the ash has taken place and therefore suggest that the ash was deposited as fall-out or has undergone reworking and re-deposition in a medium that contained relatively low concentrations of clasts (e.g. Selley 1976). The presence of clay-rich clasts and freshwater diatom frustules could imply that reworking has occurred, or that deposition of the ash occurred through a water column, such as into a lake,

where diatoms and clay were the background sediment. Deposition through relatively still water could minimise abrasion of the ash (e.g. Selley 1976), but allow deposition of pyroclasts alongside siliciclastic clasts, such as diatoms or clay-rich clasts, already present within this environment.

The alignment of the rod-like pyroclasts in WASH_13 might reflect their deposition through a water column. Alternatively, the alignment could be caused by deposition of ash from a pyroclastic density current (PDC), with the ash subsequently being fused and compacted, causing the alignment of elongate clasts.

6.5.6 Finley Quarry (L6)

6.5.6.1 *Field observations*

The Finley Quarry (L6) dissects several lavas: at the base of the quarry face are Umatilla Basalts, which are overlain by the Pomona Basalt (Reidel pers coms 2015). The relief on the boundary between the two units (Figure 6-54) suggests the development of a palaeo-valley in the Umatilla Basalts, later filled the Pomona Basalt (Figure 6-54). A thin (< 1 metre) white clastic unit of fine-grained material is present between these major basalt units.

The Umatilla Basalts are highly jointed with <1 m-scale jointing throughout the lowermost and uppermost basalts (Figure 6-54). In contrast the darker-brown/black basalt contains thicker m-scale columnar jointing (Figure 6-54). The Pomona Basalt is highly jointed and contains features resembling lava-filled channels and lava lobes with a layer of columnar jointing radiating outwards around these features (Figure 6-54).

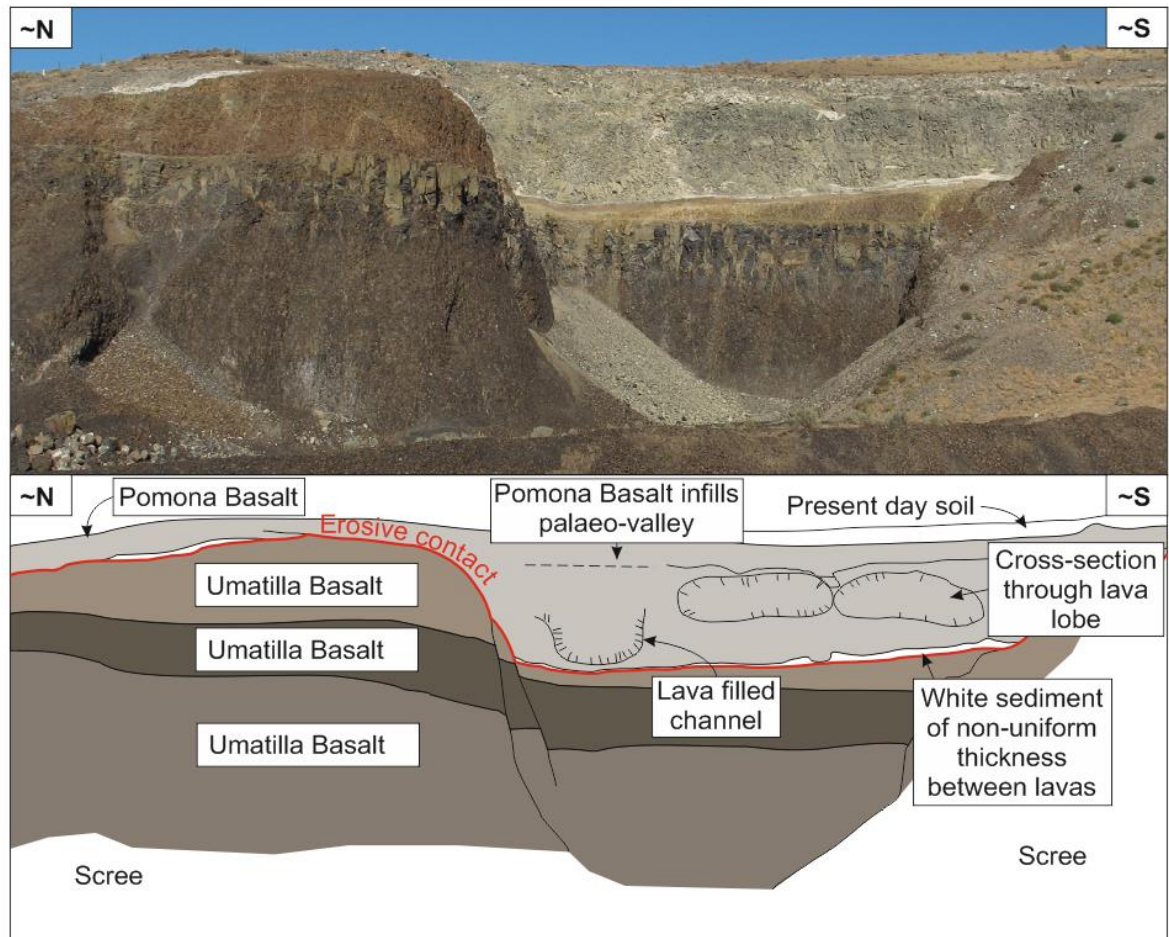


Figure 6-54 Overview of Finley Quarry (L6), showing multiple lavas of the Umatilla and Pomona Basalts. The uppermost Umatilla lava has a varying thickness. Following emplacement of the Umatilla Basalts, erosion formed a valley which was later filled by flows of the Pomona Basalt. Between the two units is a thin white clastic unit of varying thickness (sample WASH_07). The Pomona Basalt is comprised of several units, including those which infilled palaeo-channels and formed lava lobes.

6.5.6.2 Interpretation of field observations

Lava flows repeatedly exploited depressions in the underlying topography. These channels may have been produced by rivers, however, no sediments have been preserved between the lavas. The thin (<1 metre) unit of white clastic material may represent pyroclastic, volcanoclastic or siliciclastic material emplaced in this locality prior to emplacement of the Pomona Basalt.

6.5.6.3 Optical microscopy and SEM analysis

Sample WASH_07 was collected as a non-orientated grab sample from the poorly accessible thin (<1 m) grey/white sedimentary unit between the Umatilla and Pomona lavas exposed at L6 (Figure 6-54). The rock is predominantly composed

of transparent glassy white and brown bubble-wall pyroclasts along with minor amounts of sub-angular quartz grains (Figure 6-55). The pyroclasts show no evidence of alteration and have been well-preserved within a finer-grained ash matrix (Figure 6-55).

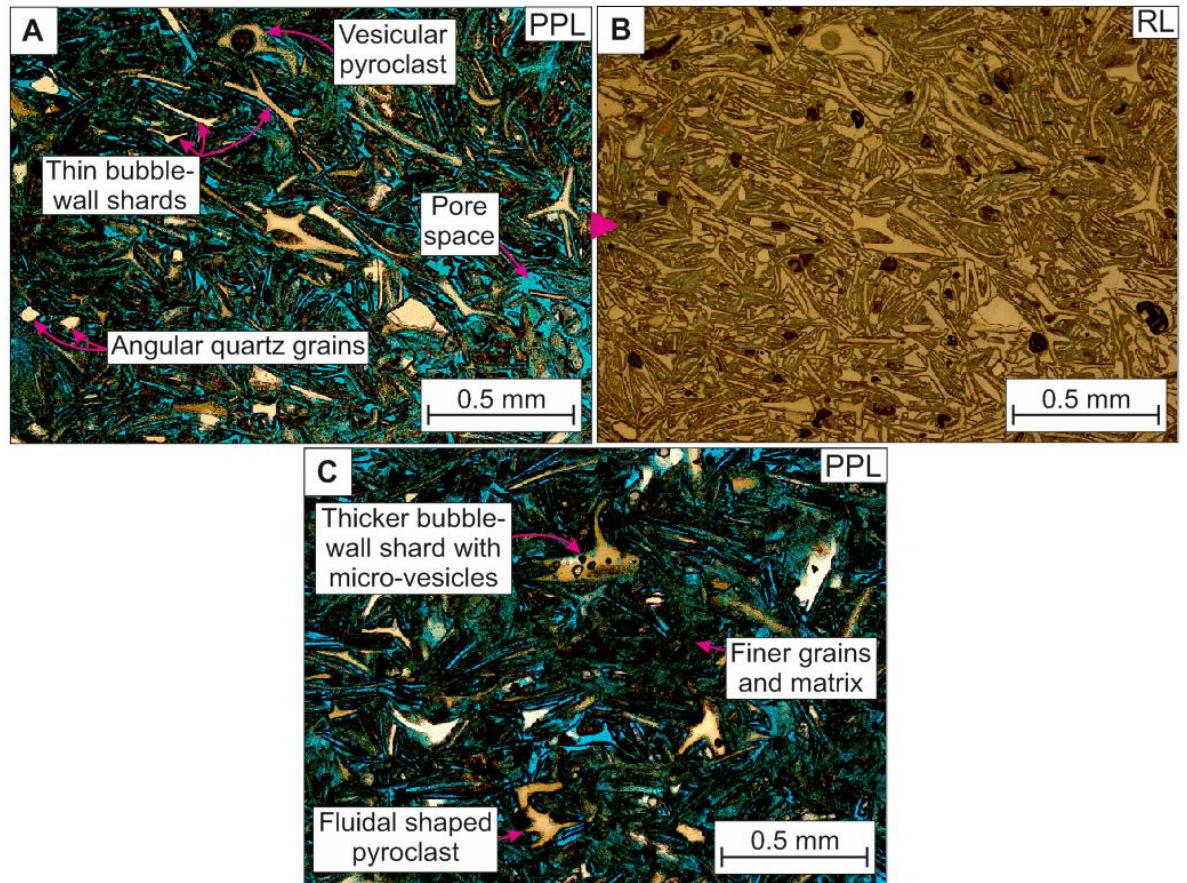


Figure 6-55 Optical microscope images showing the nature of the material that comprises samples WASH_07 from Finley Quarry. A & C) Thin bubbles-wall shards dominate the deposit, some containing micro-vesicles, and having fluidal shapes. Pore space can be seen where the image is blue, although, in some areas the pores have been filled by finer grains and an interstitial matrix of fine silt/clay. B) RL image showing the same field of view as that in A. RL shows the grain-boundaries more clearly, particularly where grains are finer in the darker patches of the PPL image.

SEM analysis was inhibited by charging effects across the sample due to the highly fractured nature of the material. However, SEM analysis does suggest that many of the pyroclasts of this sample are no longer present and instead create a secondary porosity, with pores that often retain the shape of the original pyroclasts. The remaining glassy pyroclasts are brown when observed under PPL, typical of basaltic pyroclasts; however, under the SEM their chemical composition resembles that of other silicic pyroclasts within the CRFBP. However, this unit does provide evidence for the occurrence of explosive silicic

eruptions supplying material across the CRFBP prior to emplacement of the Pomona Basalt.

6.5.6.4 Interpretation of optical microscopy and SEM analysis

WASH_07 is comprised of silicic pyroclasts and minor amounts of quartz grains. It is not clear as to whether this pyroclastic material is primary or has been reworked. However, no other clastic units are found in the exposure at L6, which could suggest that this white tuff represents a primary fall-out deposit. This interpretation cannot be made with confidence without further investigation and a better quality of thin-section.

6.5.7 Sellards Road (L7)

6.5.7.1 Field observations

Sellards Road (L7; Figure 6-1) is exposed on the northern side of the road, which has been graded to a gentle and accessible slope (Figure 6-56).

A limited amount of medium-sandstone with uncommon fragmented and intact accretionary lapilli can be observed at the base of the exposure (Figure 6-56). The contacts between most of the units are not exposed, however, the medium-sandstone is followed by diffusely parallel-laminated siltstone that becomes ripple-cross laminated before returning to diffuse sub-horizontal parallel laminations. Above this siltstone the grain-size increases to a medium-sandstone with sub-horizontal parallel laminae, which becomes ripple cross-laminated up-section (Figure 6-56, Figure 6-57). At the top of this unit the generally grey medium-sandstones become more brown/orange in colour. Above this, siltstones become more dominant, these are generally structureless and interbedded with ripple cross-laminated fine-sandstone and white claystone (Figure 6-56, Figure 6-58). Towards the top of this interbedded unit is an interval containing blocks of laminated material (Figure 6-56). The overlying unit is comprised of sub-horizontal parallel laminated siltstone with a more massive and diffusely laminated central interval of siltstone. The siltstone is fractured where it is in contact with the overlying basalt lava (Figure 6-56).

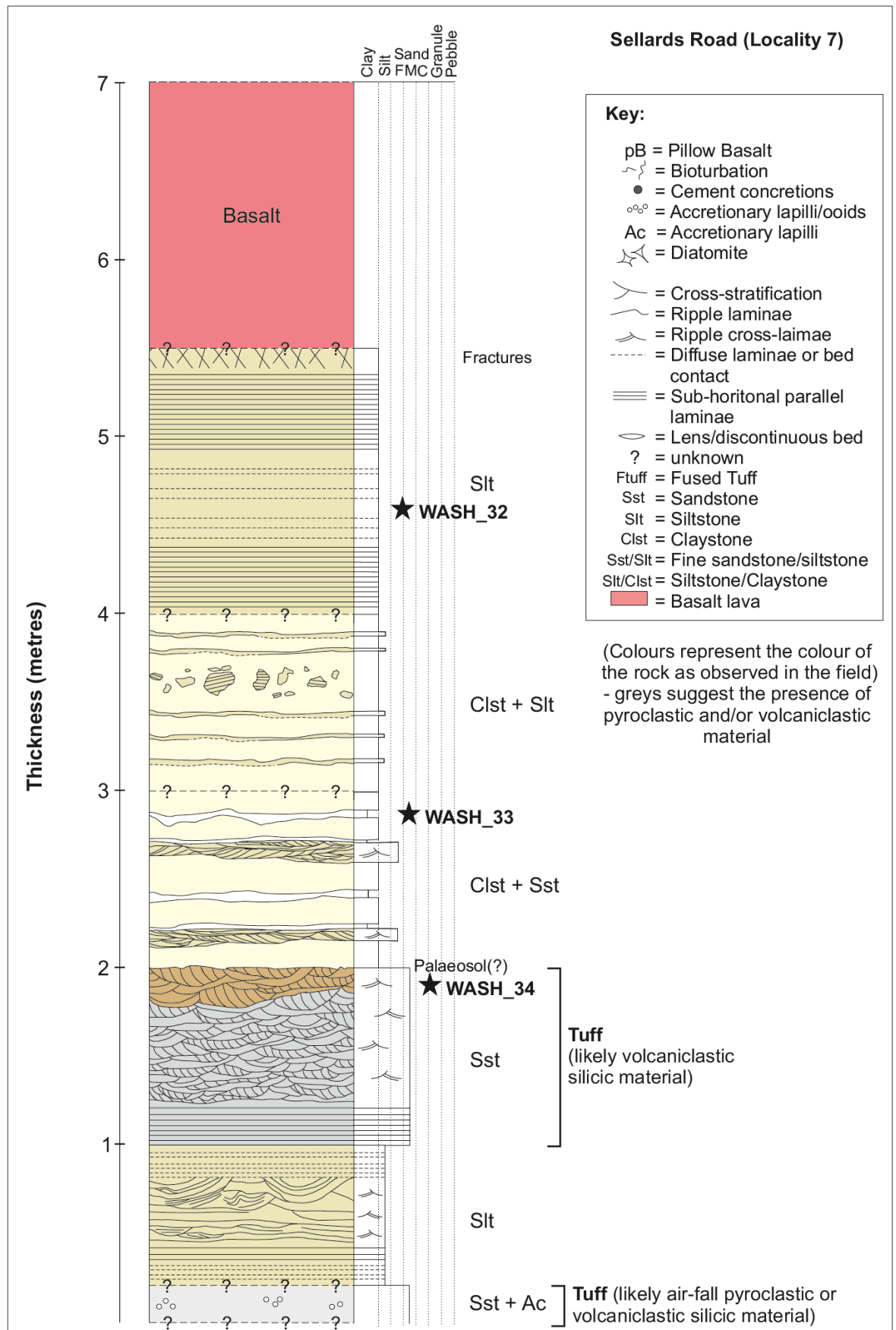


Figure 6-56 Lithological log showing the sedimentary sequence exposed at Sellards Road (L7). The sedimentary rocks here are predominantly comprised of siltstones that commonly display sub-horizontal parallel laminations or ripple cross-laminae. Interbedded with the

siltstones are beds of claystone and sandstone. The medium sandstone at the base of the exposure contains uncommon fragments of accretionary lapilli. The whole sequence is capped by a basaltic lava (likely the Pomona or Elephant Mountains Basalt).

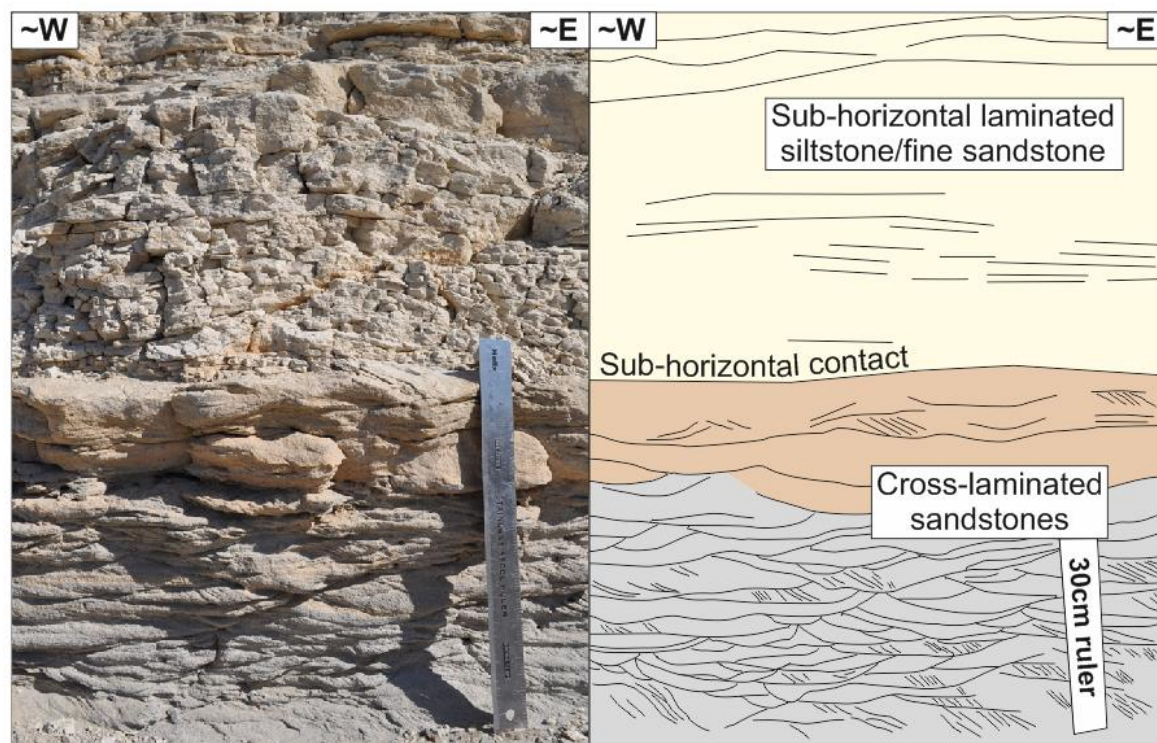


Figure 6-57 Cross-ripple laminated sandstones and parallel laminated siltstone/fine sandstone within the lower section of the L7 exposure. The components of the cross-laminated sandstones have been determined from sample WASH_34.

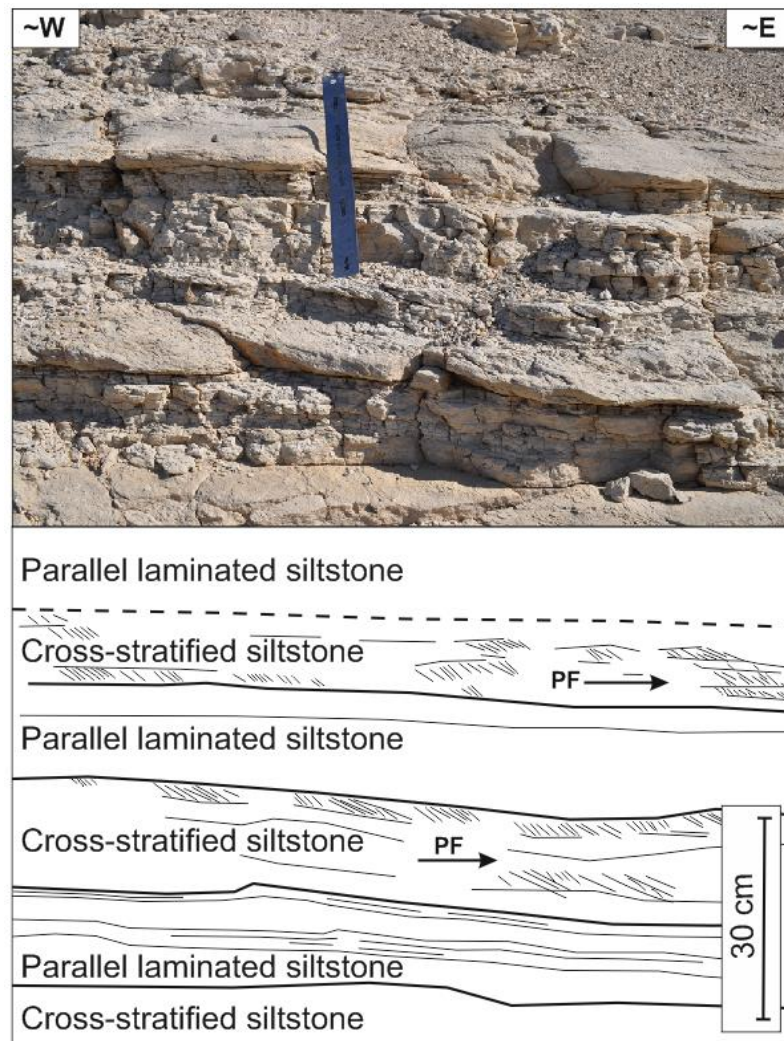


Figure 6-58 Interbedded cross-stratified and parallel laminated siltstones at L7. PF = Palaeo-flow direction, predominantly west-to-east as inferred from by the down-dip direction of the cross-stratification.

6.5.7.2 Interpretation of field observations

This sedimentary sequence likely represents material that was likely deposited in an overbank setting and associated a fluvial environment. This interpretation is suggested by the presence of fine-grade lithologies with sub-horizontal parallel laminations and occasional cross-lamination (e.g. Figure 6-58), which may be indicative of deposition from suspension in a low-energy environment occasionally influenced by traction currents, for example, during floods (Selley 1976; Singh et al. 1999; Bayliss & Pickering 2015; Yamada et al. 2016). The orange/brown coloration of the top of the cross-laminated sandstone (Figure 6-57), may represent a palaeosol. This may indicate a period of non-deposition, in which the sandstone was exposed subaerially before deposition resumed leading to development of the overlying overbank siltstones (Figure 6-56).

Fracturing of the sedimentary rock close to its contact with the overlying basalt lava, with no fluidal interaction of the sediment and lava, suggests that this area was dry (not water-saturated) at the time of lava emplacement (e.g. Schmincke 1967b).

6.5.7.3 *Optical microscopy and SEM analysis*

Samples from Sellards Road (L7) contain varying amounts of pyroclasts and crystalline igneous rocks. WASH_32, from the uppermost siltstone (Figure 6-56), is composed of angular rod-like and bubble-wall pyroclasts, in addition to well-rounded crystalline igneous clasts (Figure 6-59).

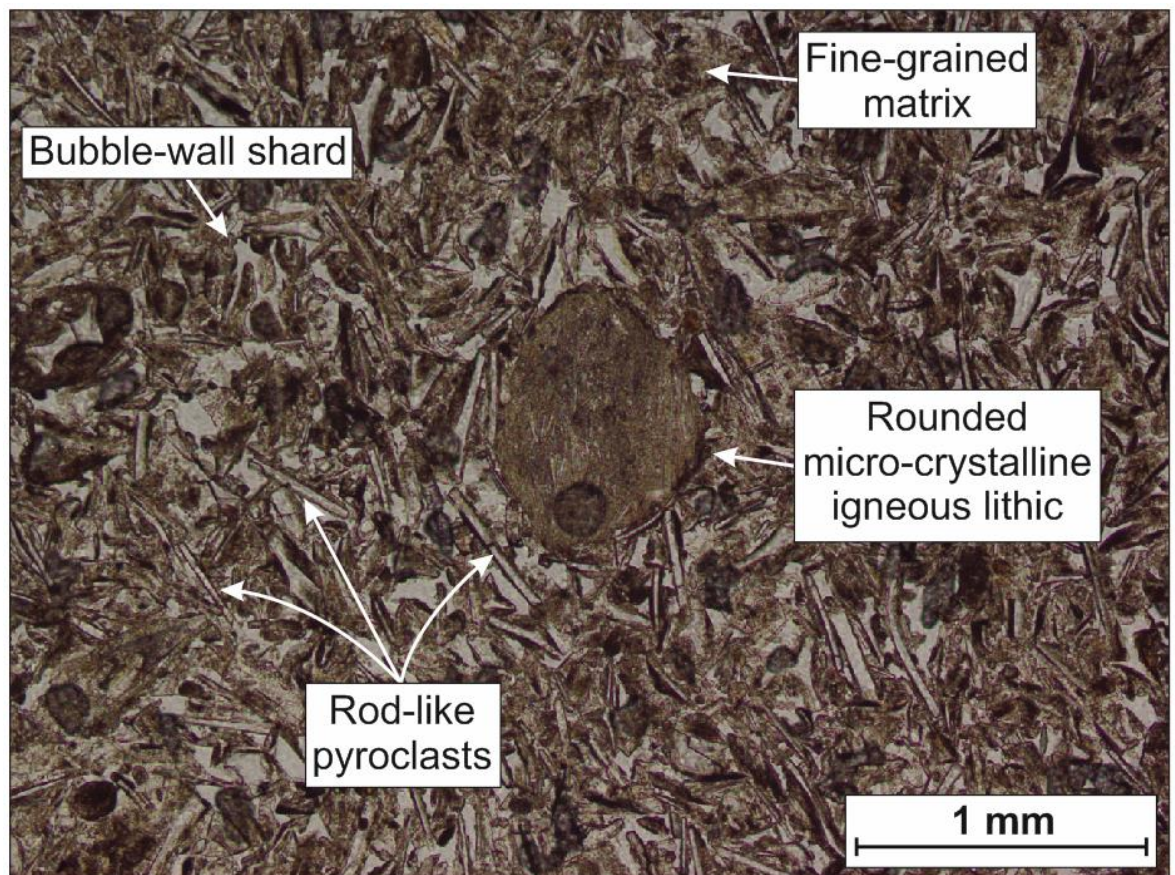


Figure 6-59 Nature of a volcaniclastic sandstone (WASH_32) from L7. A well-rounded micro-crystalline igneous lithic, surrounded by rod-like and bubble-wall shards with a fine-grained ash or clay-rich matrix.

WASH_33 from the upper section of the upper claystone and siltstone unit (Figure 6-56), is diffusely laminated and contains pyroclasts, granular lithic clasts and rounded quartz crystals (Figure 6-61). In this sample, laminations are defined by changes in grain-size (Figure 6-60). Elongate pyroclasts are orientated

parallel to the laminations, truncated contacts between the laminations can be identified where the orientation of these elongate pyroclasts changes (Figure 6-60a).

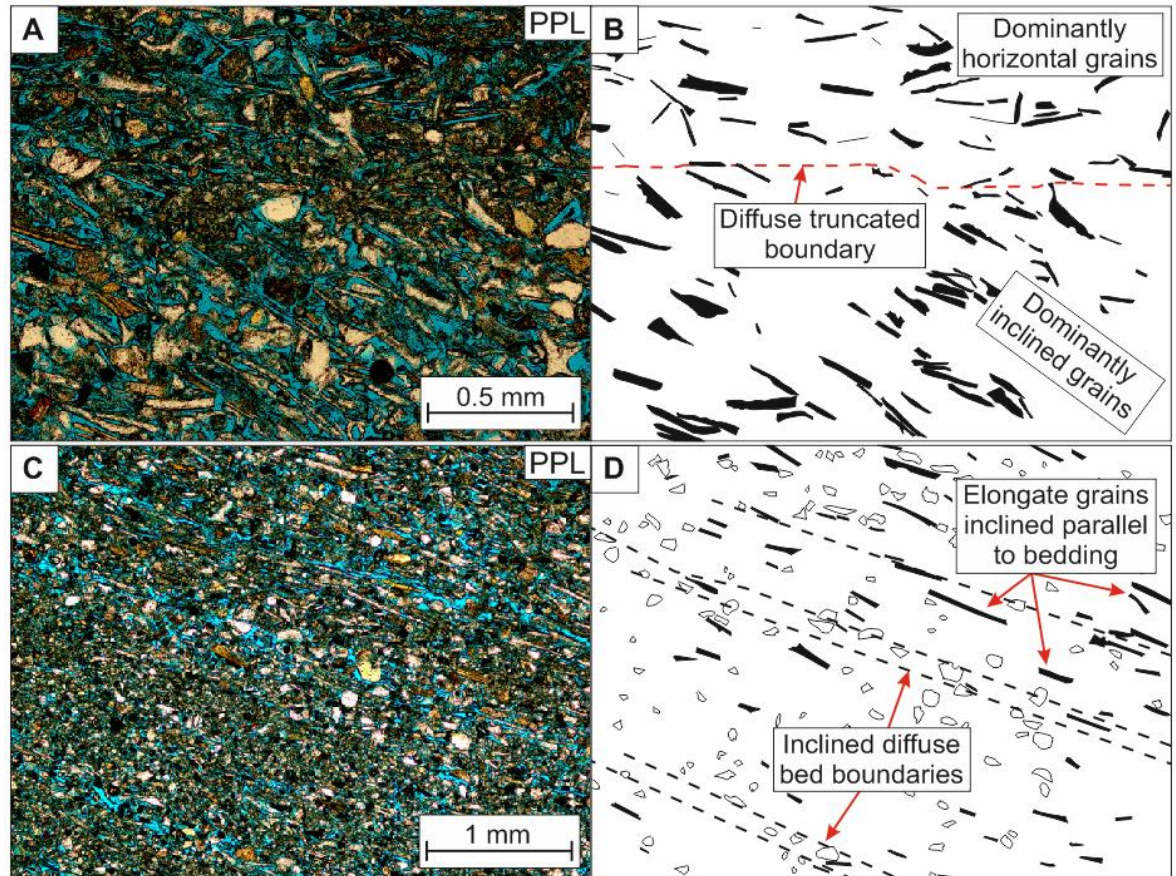


Figure 6-60 Inclined and aligned grains indicate the presence of diffuse and erosional bed boundaries throughout sample WASH_33 from L7. A & B) The varying direction of preferred orientation of elongate grains suggests that two beds are present. With the fabric created by the inclined grains of the lower bed being truncated by the sub-horizontal fabric created by the different orientation of elongate grains in the overlying bed. C & D) Inclined bedding with interbedded finer- and coarser-grained beds. Elongate grains are orientated parallel to the orientation of the bedding.

Under plane-polarised light (PPL) the pyroclasts range from transparent white to brown and display bubble-wall morphologies (Figure 6-60, Figure 6-61). SEM analysis shows that the glassy pyroclasts of this sample have a silicic composition, and therefore the colour of the pyroclasts under plane polarised light does not reflect their major element composition.

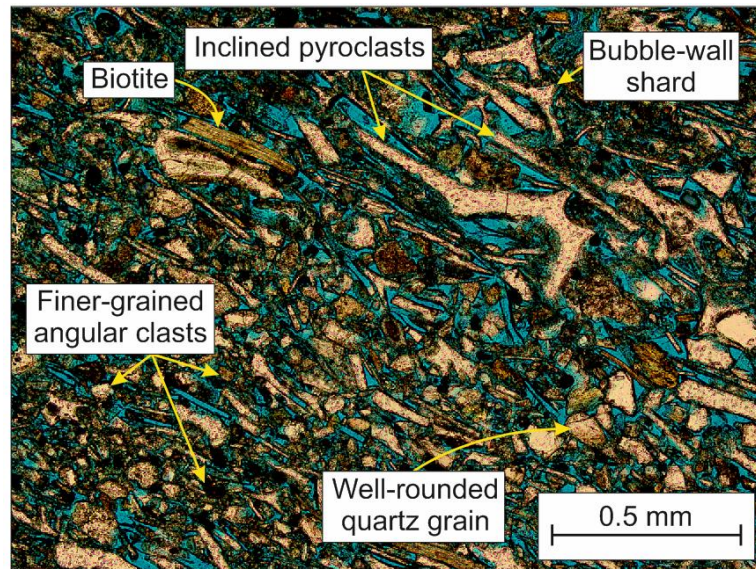


Figure 6-61 Inclined, elongate clasts, including pyroclasts and mica, within sample WASH_33 from L7. Angular to well-rounded clasts of finer-grained quartz are also present and have no preferred alignment.

SEM analysis of these sample shows that the pyroclasts and quartz crystals are supported by a clay matrix. This clay matrix and is highly fractured and leads to electron charging across the sample during SEM analysis, therefore inhibiting the collection of clear images.

A grain-mount of WASH_34 reveals silicic pyroclasts with rough, fractured edges and vesicles filled with a very fine-ash matrix (Figure 6-62a); in addition, there are crystal fragments of quartz and orthoclase and angular to well-rounded granular lithic clasts (Figure 6-62b). Euhedral zircon crystals can be found within some of the glassy pyroclasts (Figure 6-62c).

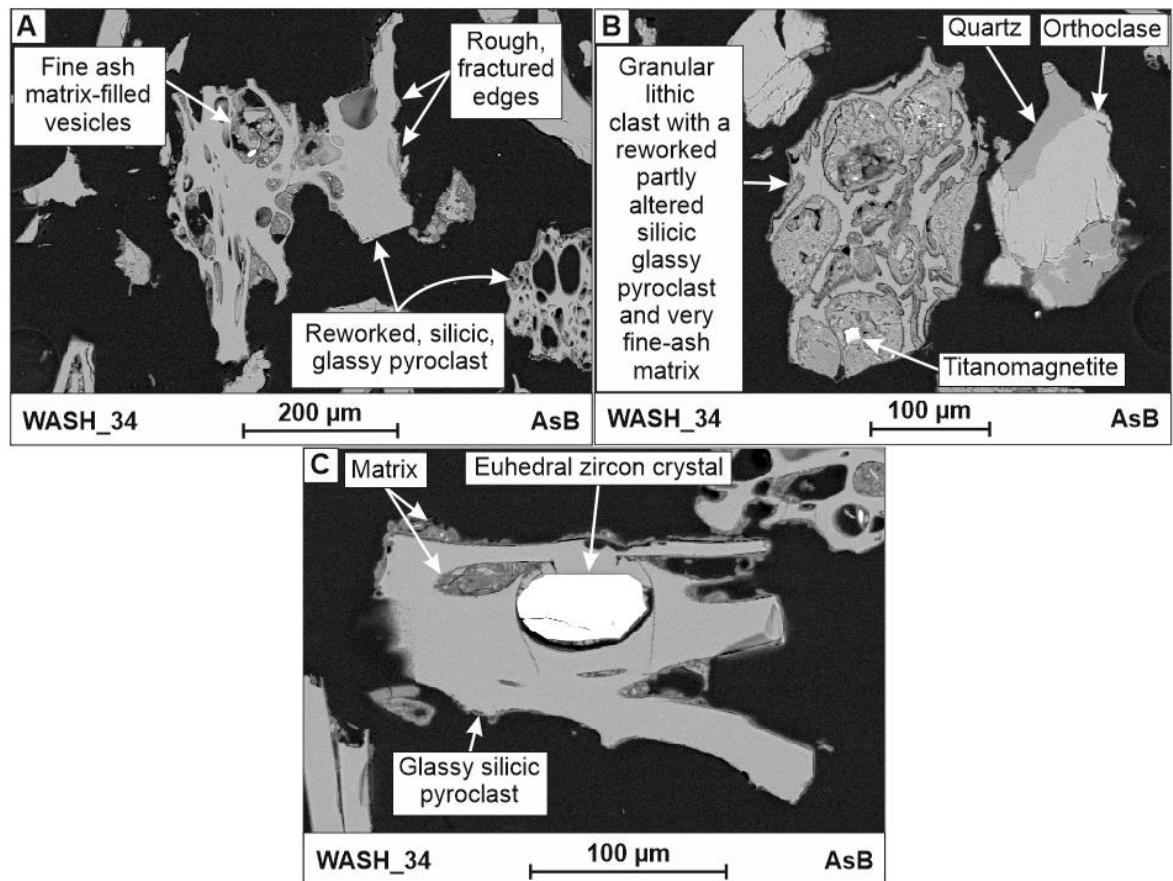


Figure 6-62 AsB SEM features of reworked pyroclasts in WASH_34 from Sellards Road (L7). A) Vesicular pyroclast with rough, fractured edges and vesicles infilled with very fine-ash matrix. B) A granular lithic clast that includes a reworked, partly altered glassy silicic pyroclast. C) A poorly vesicular silicic pyroclast with a euhedral zircon crystal.

6.5.7.4 Interpretation of optical microscopy and SEM analysis

Both WASH_32 and _33 are comprised of pyroclastic and siliciclastic clast-types. This range of clast-types and the presence of laminated and truncated cross-stratified intervals suggest that both samples represent siliciclastic or volcanoclastic deposits. This interpretation will be investigated further using image analysis (see section 6.5.11), although, it can be concluded here that these are sedimentary deposits, likely laid-down in an overbank setting due to their fine-grained nature and preferred orientation of elongate grains being indicative of occasional deposition from traction currents (Selley 1976).

WASH_34 contains reworked pyroclasts, as inferred from their rough, fractured edges and their association with a very fine-ash matrix and granular lithic clasts (Figure 6-62). The mixture of these clast-types as sand-sized grains suggests that this sample is representative of a volcanoclastic sandstone.

6.5.8 Mabton – Bickleton Road (Locality 8)

6.5.8.1 *Field observations*

This locality (L8), on the Mabton-Bickleton Road, lies within the Horse Heaven Hills, west of Locality 1 (Figure 6-1). The road intersects deposits of the EF which lie between two of the Saddle Mountains Basalts (Reidel pers comms 2015). The whole stratigraphy dips down the hill due to the occurrence of the Horse Heaven Hills anticline (Blakely et al. 2011; Pratt 2012). The lowest part of the sequence consists of interbedded siltstone/claystone and fine-sandstone/siltstone, above which there are at least eight normal-graded beds of medium-/coarse-sandstone to siltstone/claystone (Figure 6-63). Above this is a structureless siltstone overlain by a medium-/coarse-sandstone with large-scale cross-stratification (Figure 6-64). At the top of the sequence a *ca.* 21 m-thick medium-sandstone with localised development of ripple-cross laminae and sub-horizontal parallel laminae (Figure 6-63). The (exposed) top of the sedimentary sequence is a quartzite-rich conglomerate, below which is a thin (<0.5 m) (Saddle Mountains) basaltic lava (Figure 6-63).

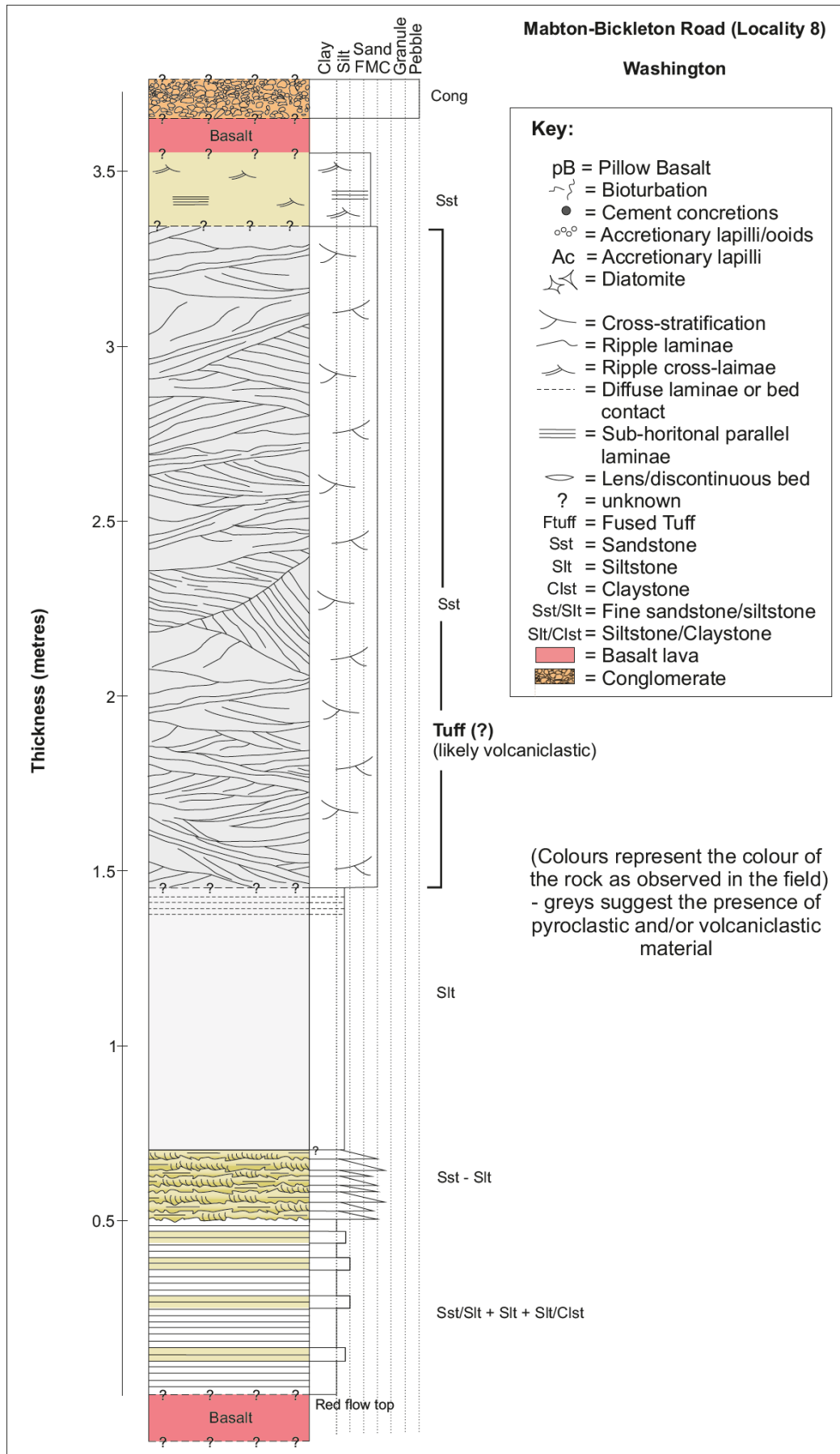


Figure 6-63 Lithological log for the exposure at Mabton-Bickleton Road (L8). The sedimentary sequence occurs between two Saddle Mountains basaltic lavas. Interbedded

siltstones and sandstones are present at the base of the sedimentary sequence, overlain by at least eight normal-graded sandstones / fine siltstones with ripple cross-laminations. The thickest unit of this sequence is the overlying cross-stratified medium/coarse sandstone, above which are medium sandstones with localised parallel laminae and ripple cross-laminations. A thin basaltic lava separates the top of the sandstone from the overlying quartzite-rich conglomerate.

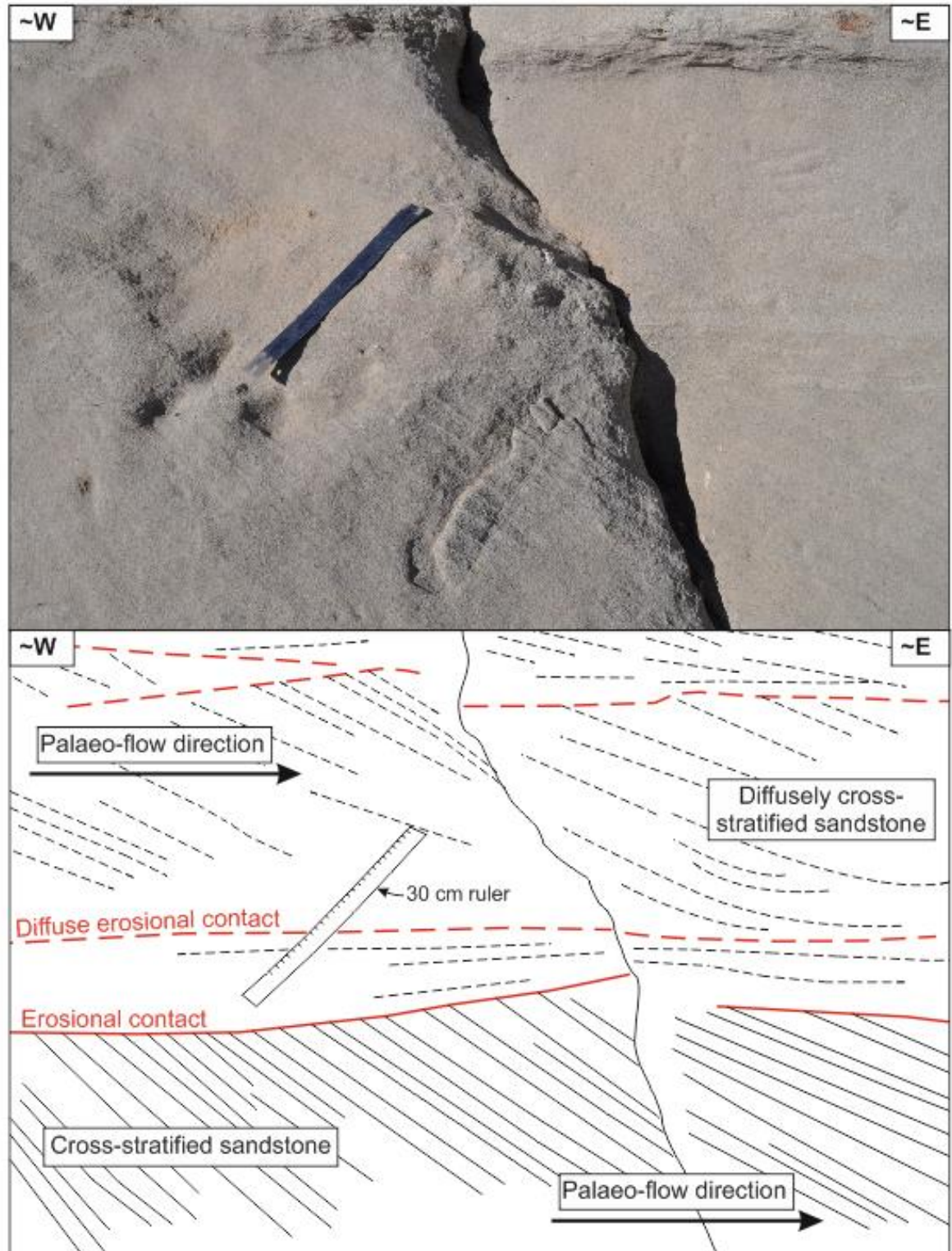


Figure 6-64 Large-scale high-angle cross-stratification within a sandstone within the L8 exposure. The rocks at this locality have been tilted and dip towards the north, however, the orientation of this image has corrected and shows the sequence as sub-horizontal.

6.5.8.2 Interpretation of field observations

The sedimentary material of this deposit was most likely deposited from traction currents within a fluvial environment and its associated overbank setting (e.g. Selley 1976). The base of the sequence likely represents deposition that occurred in an overbank setting where parallel laminated and ripple cross-laminated sands, silts and clays were deposited from suspension and traction currents respectively (e.g. Selley 1976; Singh et al. 1999; Bayliss & Pickering 2015; Yamada et al. 2016). The large-scale cross-stratified sandstones which are present above this, followed by conglomerate, suggest that the main channel of the river migrated over the area leading to deposition of channel lag conglomerates typical of the main Columbia River channel (Warren 1941; Mackin 1961; Waters 1965; Schmincke 1967a; Smith 1988a, 1988b). The presence of a thin lava between sediments at the top of this sequence suggests that the emplacement of lava may have been responsible for the changing location of the main river channel.

Following deposition, major tilting of the stratigraphy was caused by growth and formation of the Horse Heaven Hills Anticline within the Yakima Fold Belt (Blakely et al. 2011; Pratt 2012).

6.5.8.3 Optical microscopy and SEM analysis

Samples from L8 (Figure 6-63) are predominantly of siliciclastic sediments, with abundant angular to sub-rounded quartz grains with a silt-/clay-grade matrix (Figure 6-65, Figure 6-66). Clast-types include quartz and biotite mica, in addition to grains of microcrystalline basalt (e.g. WASH_37; Figure 6-66).

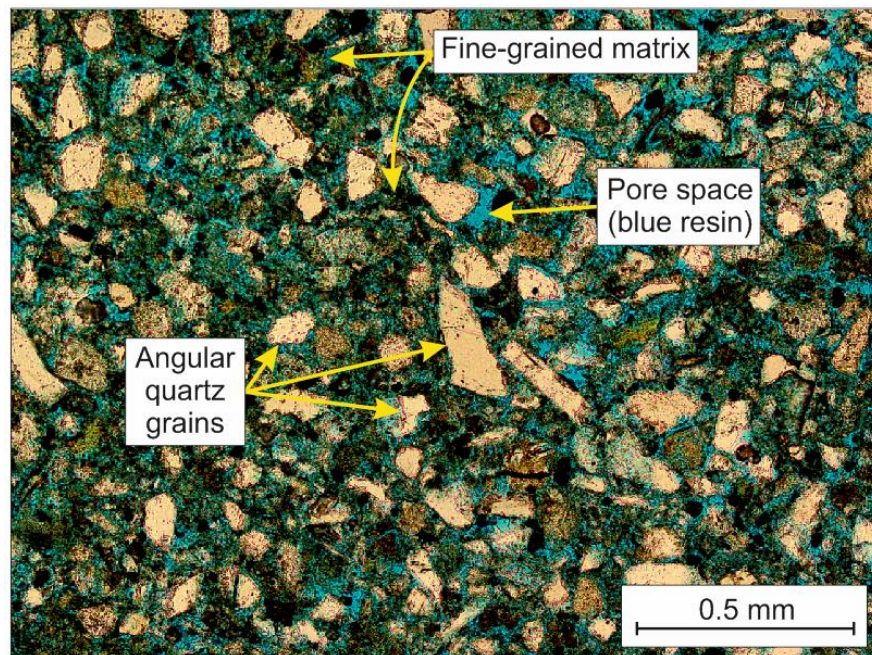


Figure 6-65 Grain-types observed in sample WASH_37 from L8. This sample is predominantly composed of angular quartz grains within a fine-grained matrix.

Additional samples from the normal-graded sandstone unit (e.g. WASH_40; Figure 6-63) contain siliciclastic clast-types including: sub-rounded, vesicular clasts of basalt lava/crystalline igneous clasts, in addition to sub-rounded to sub-angular quartz grains and elongate biotite mica (Figure 6-66).

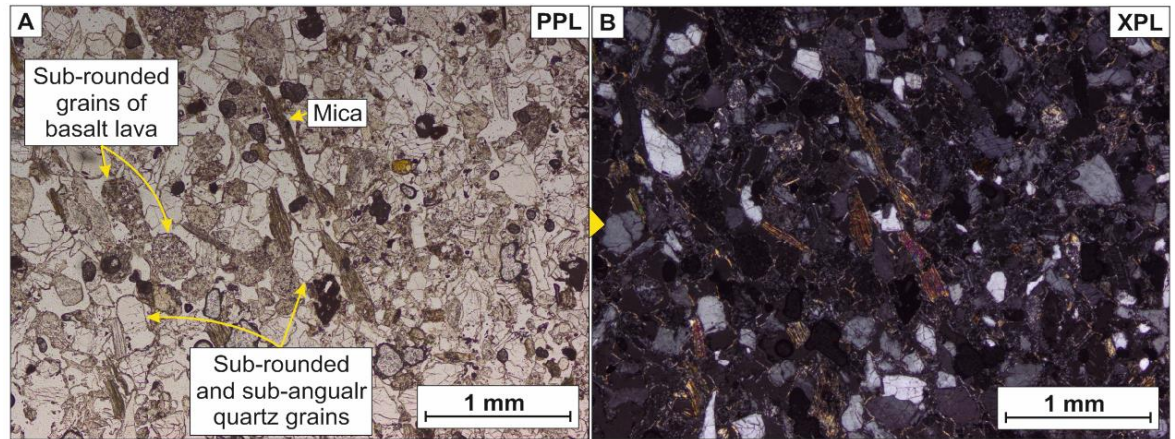


Figure 6-66 Plain Polarised (A) and Cross Polarised Light (B) images showing the nature of sample WASH_40 from L8. The main grain-types observed in this sample are biotite mica, sub-rounded basalt lava/crystalline igneous clasts and sub-rounded to sub-angular quartz.

In addition to siliciclastic clast-types, sample WASH_44 (grain-mount), from the upper unit of fawn-coloured sandstone (Figure 6-63), contains a component of glassy, non-vesicular and vesicular bubble-wall and blocky pyroclasts (Figure 6-67). All of the clasts within this grain-mount are surrounded by a veneer of clay or fine-ash, suggesting that a fine-grained matrix of clay or fine-ash was present in the rock.

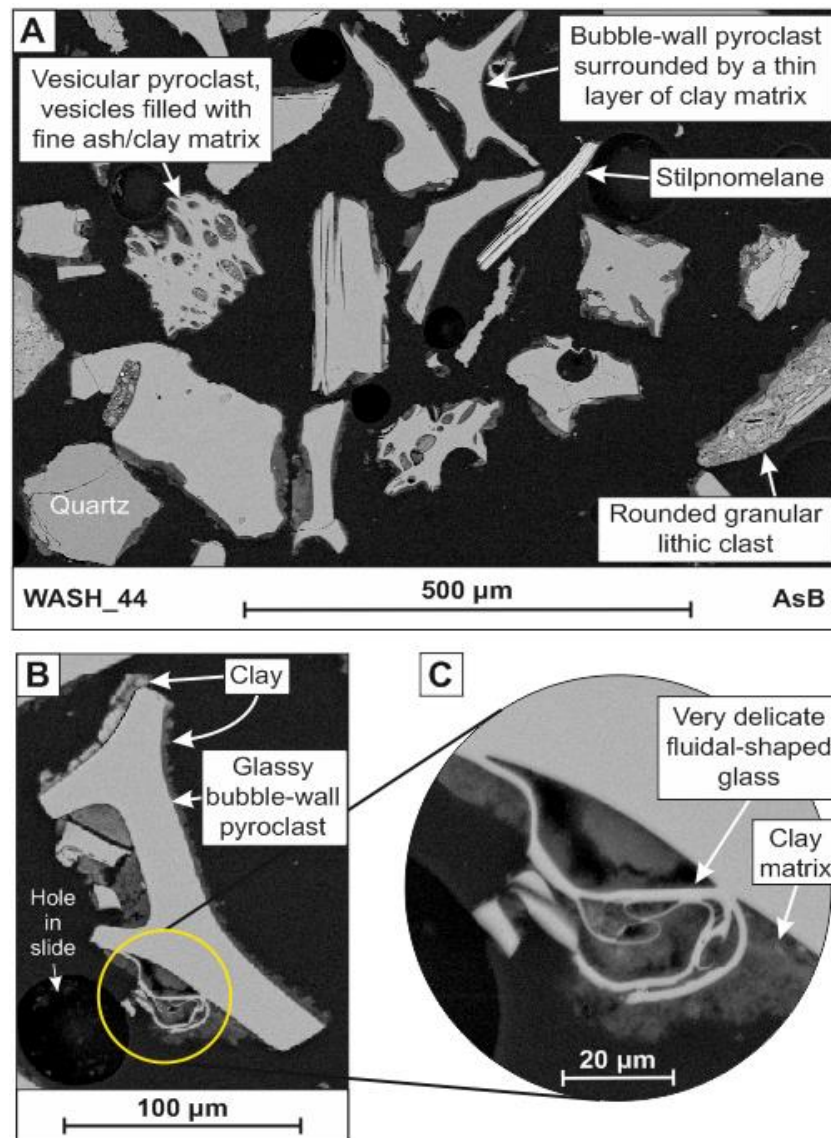


Figure 6-67 AsB SEM features of pyroclasts within WASH_44. A) The sample contains a range of clast-types including rounded granular lithic clasts and angular quartz crystals. This image is dominated by glassy pyroclasts surrounded by thin veneers of clay matrix, and vesicles filled by clay/fine ash matrix. B) A bubble-wall pyroclast surrounded by clay. The presence of a clay matrix has helped to preserve the fine, delicate fluidal features of this pyroclast (C).

6.5.8.4 Interpretation of optical microscopy and SEM analysis

Both WASH_37 and WASH_40 are of siliciclastic deposits that do not contain any pyroclastic clast-types, therefore suggesting that volcanism did not influence the fluvial system at the time that these sediments were deposited. However, later on, the clast-types include a significant amount of silicic pyroclasts, suggesting that silicic volcanism supplied material into the catchment of the streams and rivers that are interpreted to have deposited the material at L8.

WASH_44 contains a range of clast-types, including pyroclasts, granular lithic clasts and crystals of quartz and stilpnomelane (Figure 6-67). All of the clasts in this sample are associated with a fine-ash or clay matrix, implying that they are of volcanoclastic and siliciclastic origin. The clay matrix appears to have prevented delicate bubble-wall features of the pyroclasts from being lost due to abrasion during transport and re-deposition (Figure 6-67).

6.5.9 Whitebird, Idaho (L9)

6.5.9.1 Field observations

Three exposures along Old Highway 95 east from Whitebird (Localities 9a, b and c) were identified for logging and/or sampling of the Latah/Payette Member, the state equivalent of the Washington EF. Each exposure is dominated by thinly interbedded siltstone and claystone, with uncommon interbeds of sandstone (Figure 6-68). Between the cm-scale beds, lignite occurs as brown laminae or sub-horizontal laminated beds (Figure 6-68). The claystones and siltstones are white and appear to have a very low density, it is highly likely that these are clay-/silt-grade diatomite layers (e.g. Yang & Huang 2003).

Delicate leaf and seed pod moulds are revealed on broken surfaces of the laminated claystones and siltstones (or diatomites?) throughout the deposit at L9c. These fossilised flora represent a range of species (Figure 6-69), from intricately veined leaves of deciduous species, such as, *Fagus Pacifica* and *Cercis idahoensis* (Figure 6-69a & c), and their seed pods (Figure 6-69; Berry 1934), to leaves from conifers, such as *Taxodium* sp. (Figure 6-70; Berry 1934; Lockheart et al. 2000).

Faulting is evident in the exposure at L9c, where brittle deformation has resulted in normal faults (Figure 6-71). Some of this faulting has resulted in the development of shear planes (Figure 6-72). The entire sequence has been tilted and has an apparent dip toward the NW (Figure 6-72).

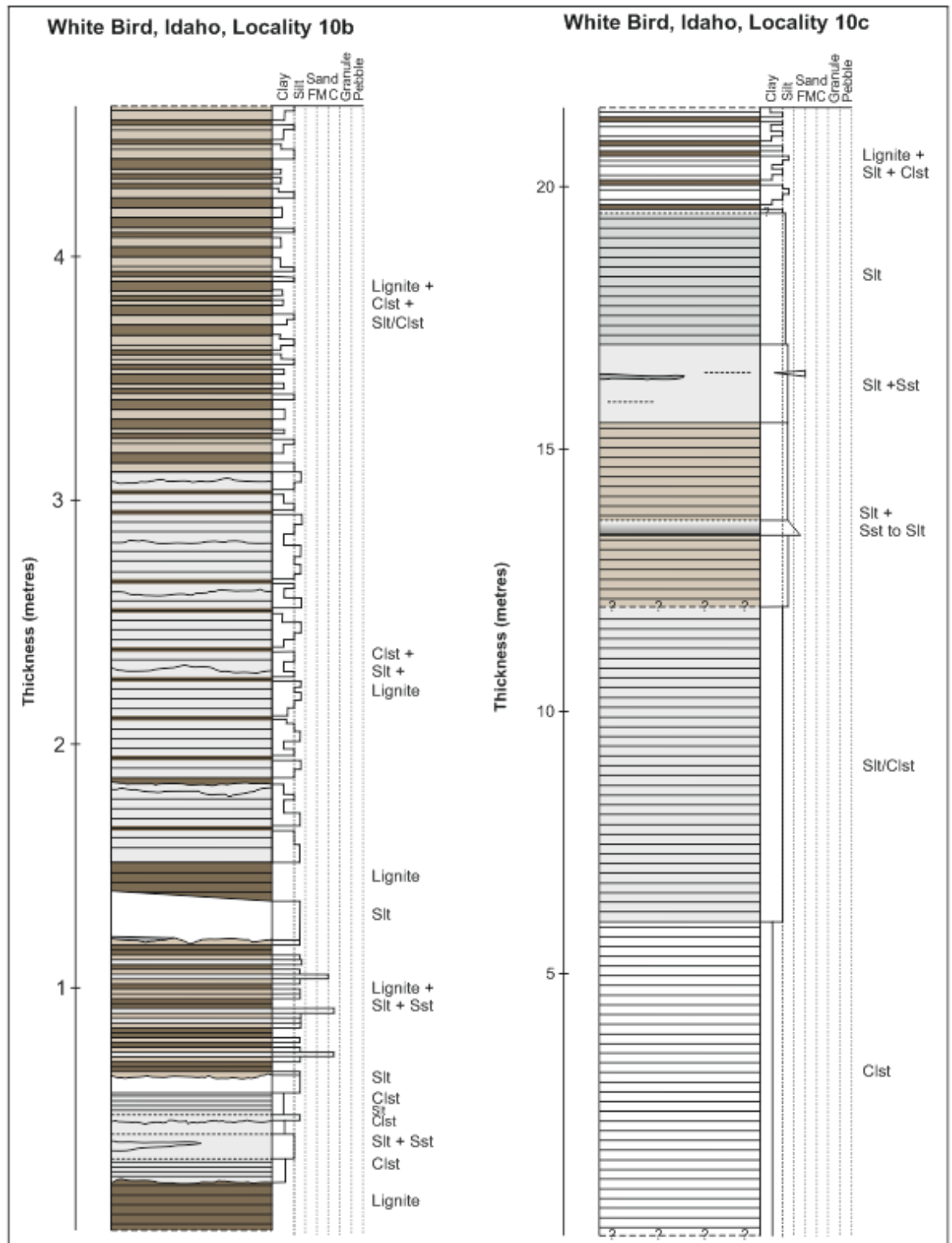


Figure 6-68 Lithological logs for Whitebird (L9b and 9c). The two sequences are dominated by fine-grained lithologies, including claystone and siltstone, together with lignite. L9b contains a higher abundance of lignite compared to the section at L9c, which contains more homogenous units of parallel-laminated claystone and siltstone. Colours on this log reflect the colour of the rocks observed in the exposure. Clst: Claystone, Slt: Siltstone, Sst: Sandstone.

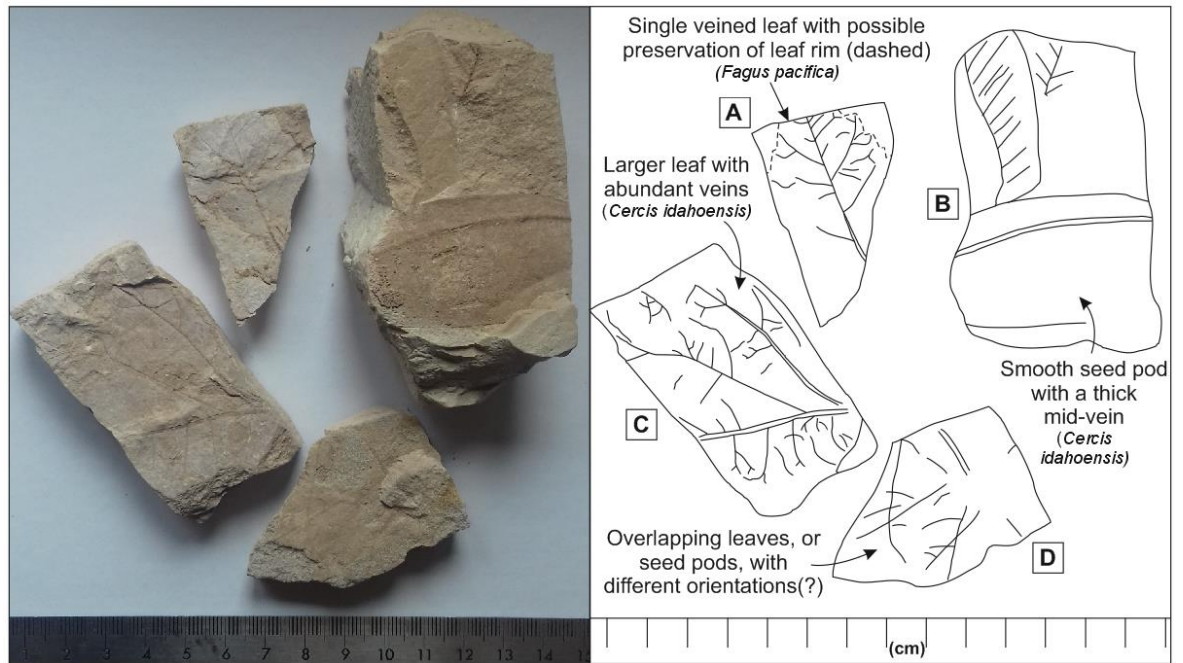


Figure 6-69 Examples of deciduous tree leaf and seed pod moulds collected from the laminated claystones at the base of L9c. A) A single leaf mould of *Fagus pacifica* with veins and possible preservation of the original leaf rim (dashed) (Berry 1934). B) Several leaf and seed pods. One is smooth with a thick mid-vein, and is characteristic of a seed pod of *Cercis idahoensis* (Berry 1934). C) Section of a larger leaf of *Cercis idahoensis* (Berry 1934). D) Multiple overlapping leaves, or seed pods, laid on top of each other in different orientations.

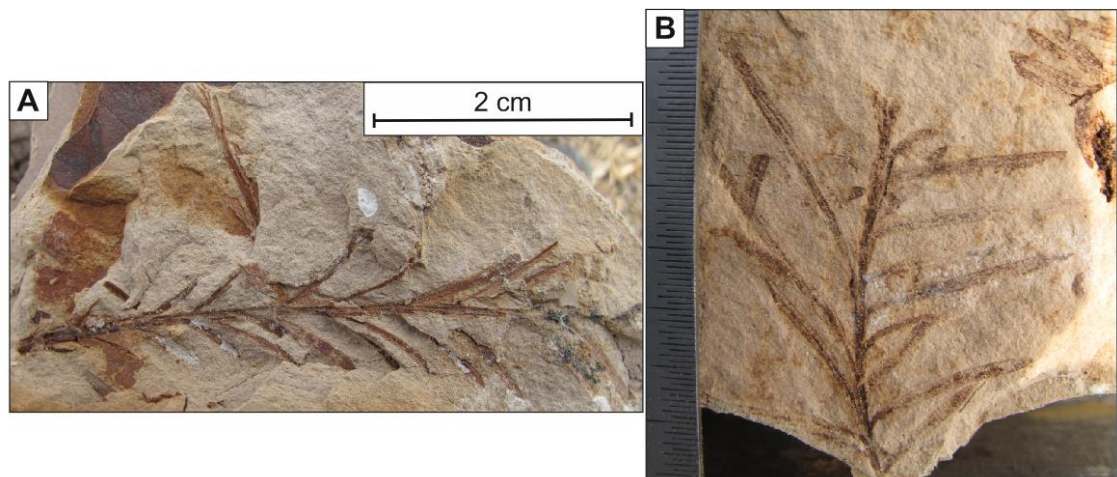


Figure 6-70 Examples of *Taxodium* sp. leaf moulds from the laminated claystones at L9c.

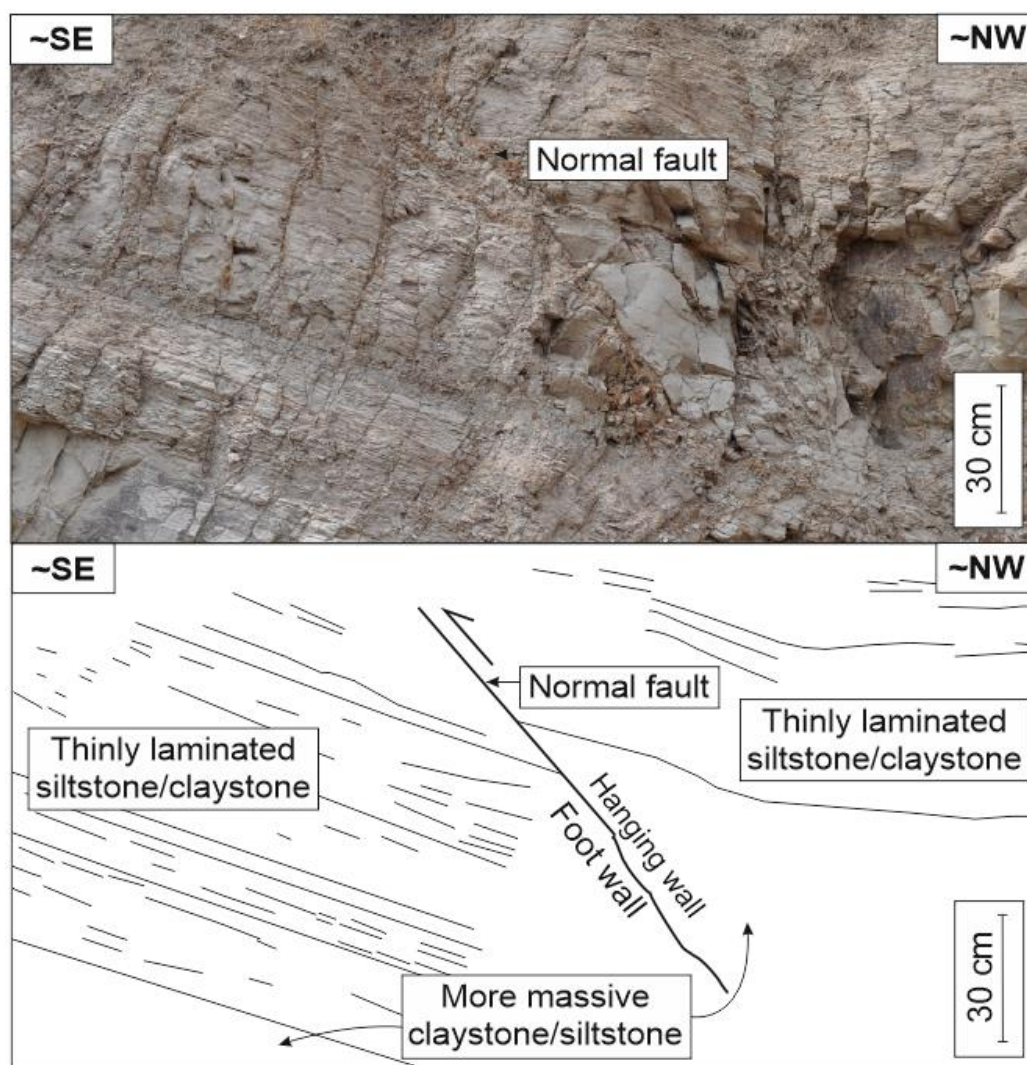


Figure 6-71 Normal fault in sedimentary rocks of the Ellensburg Formation at L9c. The fault has displaced the rocks within the hanging wall to the ~NW.

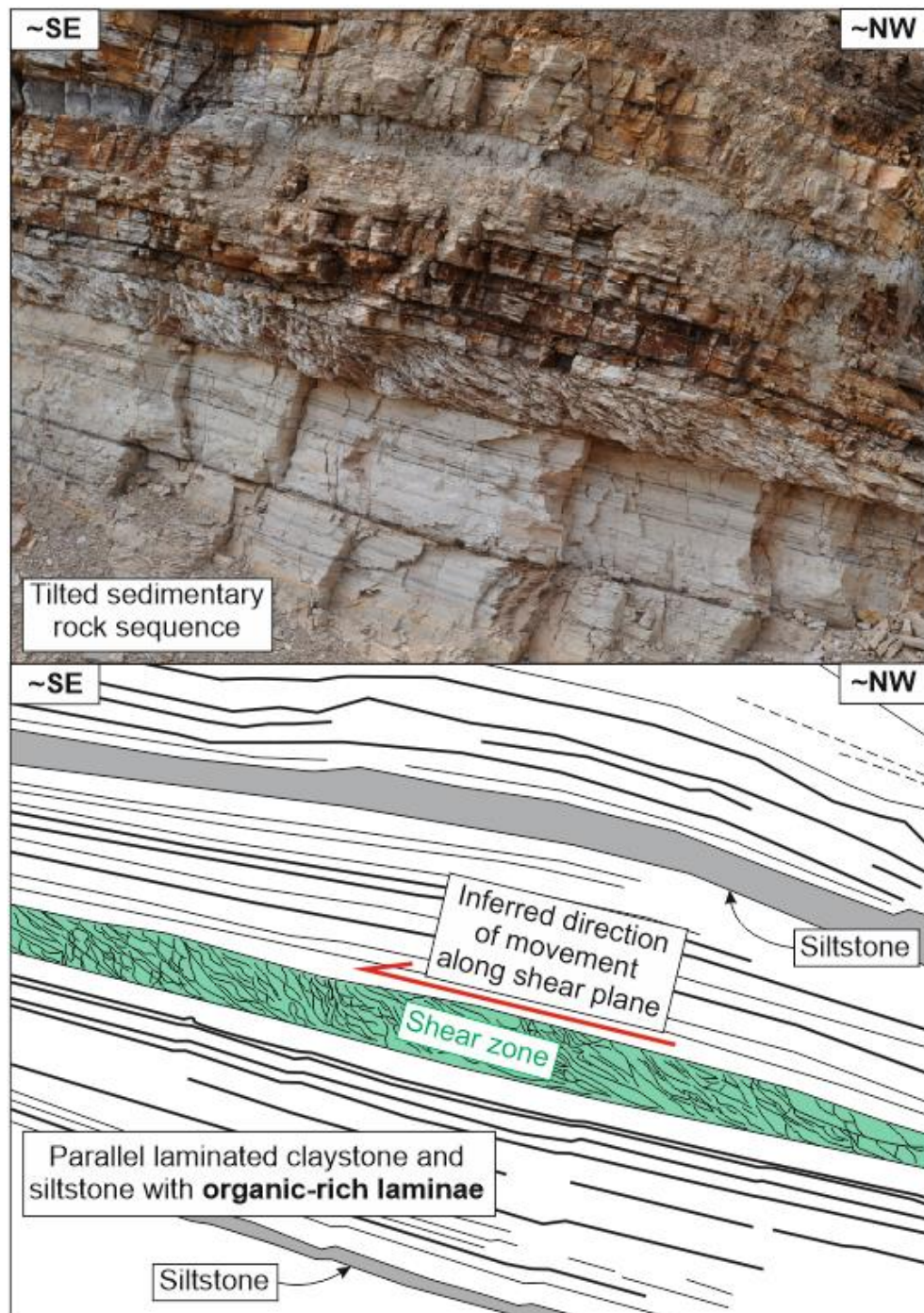


Figure 6-72 Tilted sequence of sedimentary rocks, with shear zone, exposed at L9c. Thin parallel-laminated claystone with thicker organic-rich layers (thick black lines), and uncommon interbeds of pale grey siltstone. A shear zone can be seen where the laminated material has been tilted relative to the surrounding rock, giving an inferred direction of movement from ~SE to ~NW.

6.5.9.2 Interpretation of field observations

The leaf and seed pod fossils identified at Whitebird (L9) show that this area was inhabited by a mixture of deciduous and conifer trees, indicative of a temperate climate with ample rainfall throughout the year (Berry 1934). Leaf fossils are

found throughout the Latah and Payette members (equivalents of the Washington EF) as far (from this site), toward the west, as Spokane (Smith 1988a). This reasonably suggests that this temperate climate occurred across Idaho to Washington during the Miocene (Berry 1934).

The sediments were likely deposited in a lacustrine setting under low-energy subaqueous conditions that allowed the deposition from suspension and preservation of delicate flora (e.g. Smith 1988a; Selley 1976). The lack of cross-stratified or coarser-grained units within the deposit and the frequency of laminations containing leaf fossils, implies that deposition did not occur in an overbank setting, and likely represents more seasonal influxes of diatoms and leaves into a relatively stagnant body of water (this is discussed further in section 6.6.2.1).

6.5.9.3 *Optical microscopy*

Sample ID_05 from L9c is composed of angular and sub-rounded clasts of unknown composition, but including sub-rounded vesicular pyroclasts (Figure 6-73).

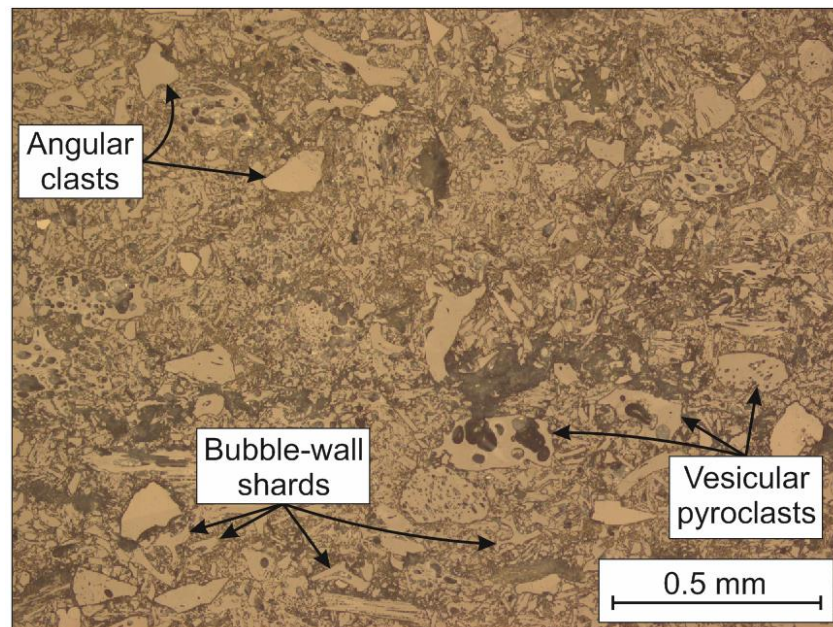


Figure 6-73 Abundant vesicular pyroclasts seen under RL in sample ID_05 from L9c. Bubble-wall shards and angular clasts can also be identified in this sample.

6.5.9.4 Interpretation of optical microscopy

ID_05 is a sample of a sedimentary rock that comprises siliciclastic clast-types with rare pyroclasts. The pyroclasts were likely incorporated into this deposit due to reworking. Unfortunately high levels of electron charging on this sample has prevented further analysis of this sample using SEM.

6.5.10 Idaho, State Road 95 (L10)

6.5.10.1 Field observations

Parallel-laminated siltstone (Figure 6-74b) and thin, discontinuous interbeds of fine-sandstone (Figure 6-74a) are exposed in a road-cut along State Road 95 at L10. This exposure represents part of the Latah/Payette Member, which is the state equivalent of the Washington EF.

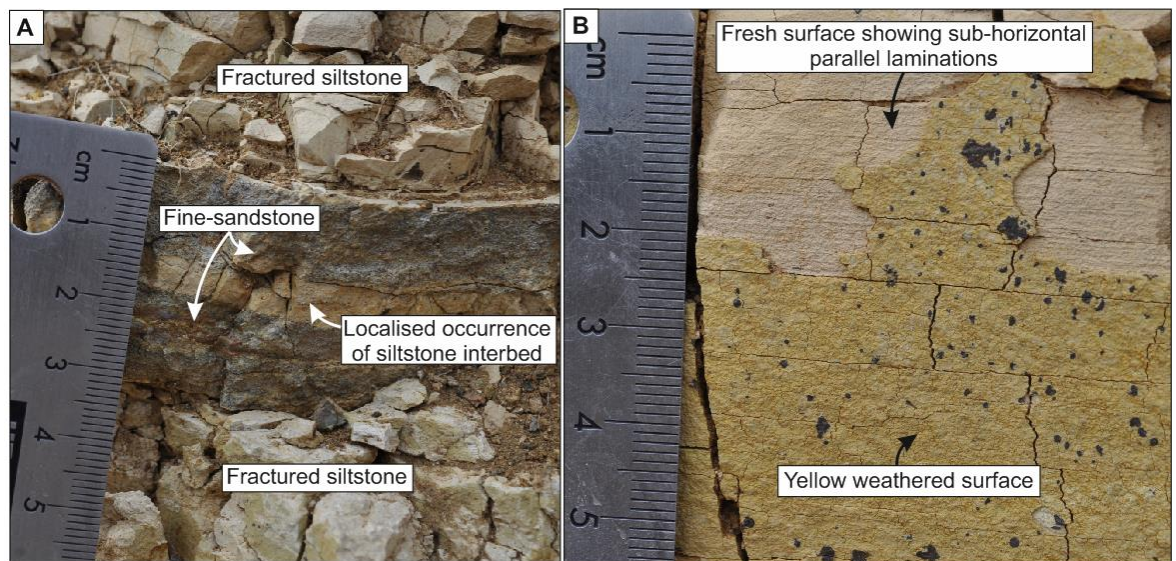


Figure 6-74 Fine-grained, grey sandstone interbedded with siltstone at L10. **A)** The fine-grained sandstone (sample ID_13) has a variable thickness and occurs with or without a siltstone interbed within it. Even though it varies in thickness, this sandstone acts as a good marker unit throughout this exposure. **B)** Sub-horizontal parallel laminated siltstone. Weathered surfaces are yellowish and do not show the thin laminations present on a fresher surface of the exposure.

Faults affect part of the exposure, for example, a reverse fault with a vertical displacement of *ca.*32 cm (Figure 6-75). This faulting has resulted in smaller amounts of displacement compared to the metres of displacement observed by the normal fault at L9c (Figure 6-71).

Lava directly overlay these strata and the contact between the two is sharp and shows some areas where the lava has invasively intruded into the underlying sequence (Figure 6-76).

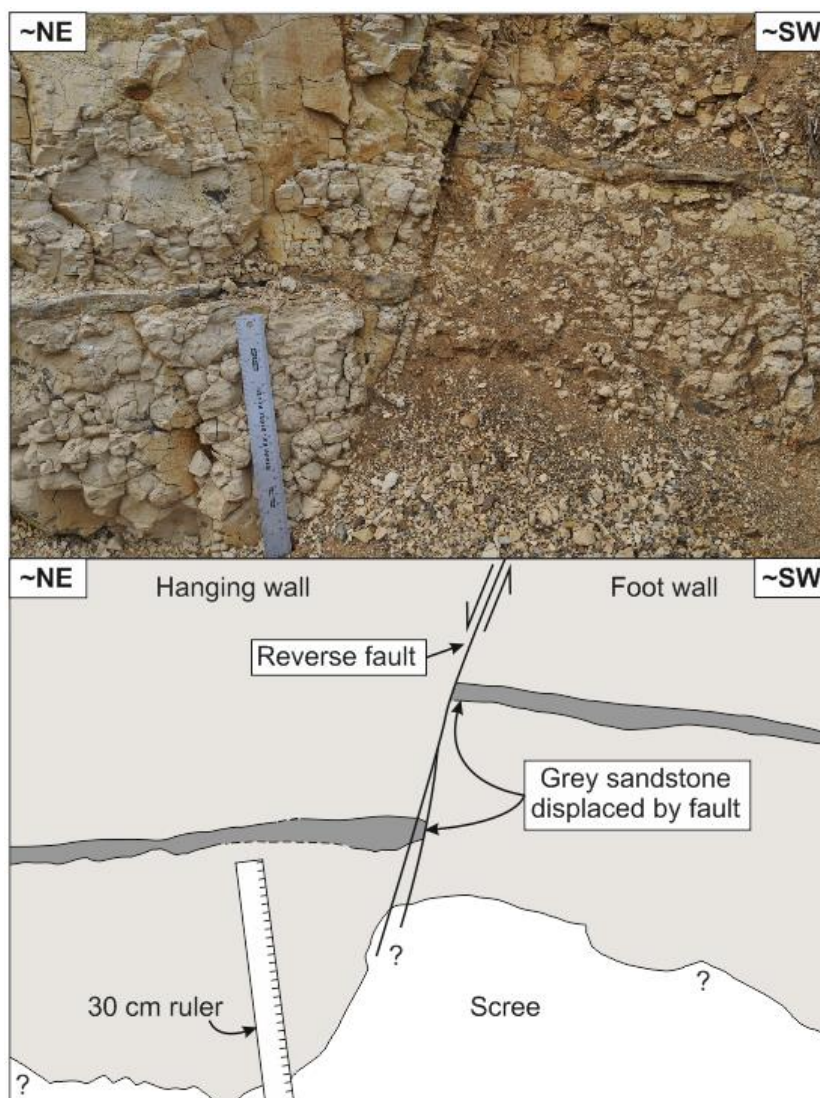


Figure 6-75 Reverse fault displacing grey sandstone marker unit at Idaho, State Road 95 (L10). Movement along the fault has caused ca. 32 cm of vertical displacement.

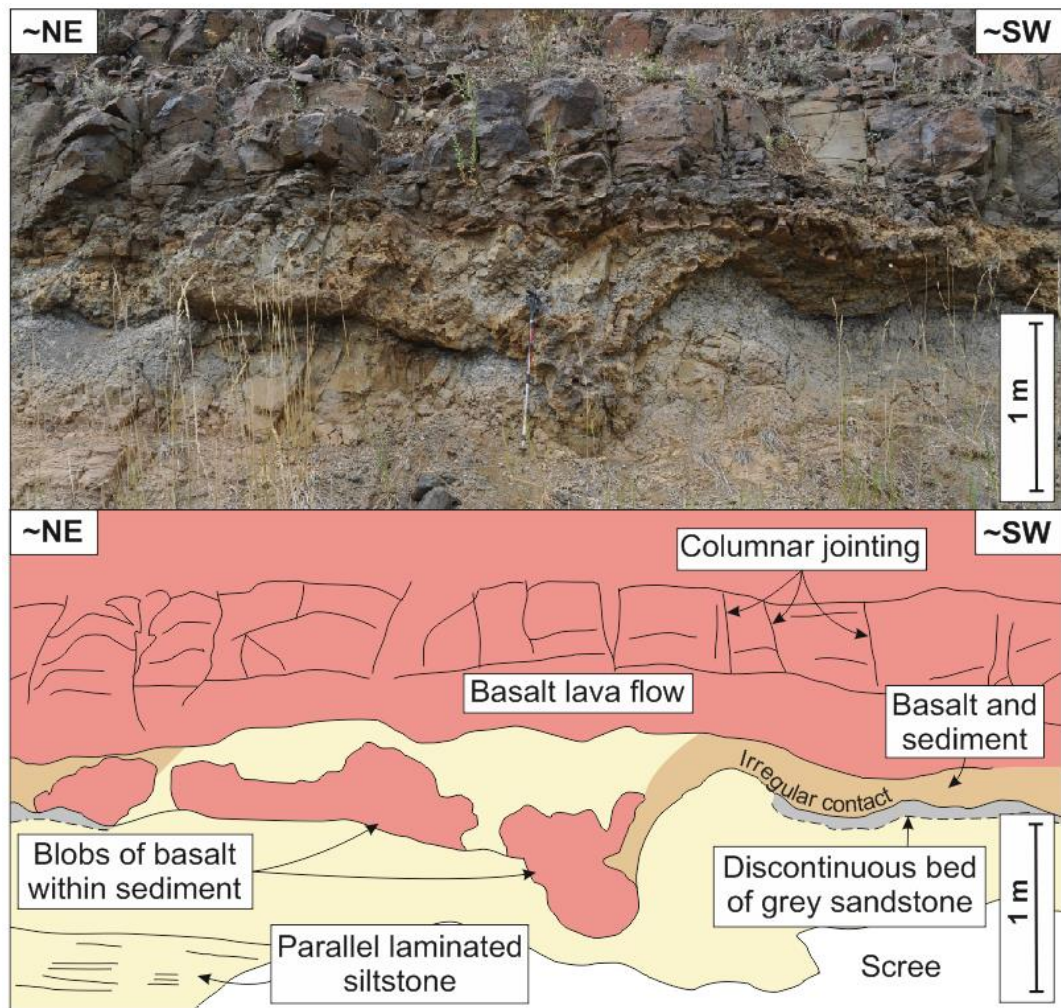


Figure 6-76 Invasive nature of the lava at the lava-sediment contact at Idaho, State Road 95 (L10). Blobs of lava that are surrounded by sediments can be identified below the main body of the overlying lava. Discontinuous units of grey sandstone were sampled for petrographic analysis (sample ID_16).

6.5.10.2 Interpretation of field observations

The sedimentary rocks at L10 were most likely deposited in an overbank setting adjacent to a fluvial system, due to the presence of fine-grained siliciclastic rock-types with parallel laminations and interbeds of coarser-grained fine-sandstone (e.g. Singh et al. 1999; Bayliss & Pickering 2015; Yamada et al. 2016). The discontinuous lenses of dark-grey fine-sandstone may contain a greater number of dark igneous clasts, although this cannot be reliably concluded in the field, instead samples are investigated further (SEM, see section below). However, the presence of coarser-grained sediments interbedded with siltstones in overbank deposits suggests occasional higher energy conditions, for example, during flooding, thus allowed coarser material to be deposited in this otherwise low-energy, silt-rich environment (Yamada et al. 2016).

The invasive nature of the lava at the lava-sediment contact indicates that the sediments had a limited yield strength and some ductility at the time of lava emplacement, which enabled the lava to intrude. The continuation of sedimentary structures (planar parallel bedding) within disrupted parts of the sediments also shows that the sediment was relatively coherent when the lava was emplaced. There are no pillow structures at the base of the lava, suggesting that the region was not significantly waterlogged at the time of lava emplacement. However, columnar joints, comprising a relatively thinly-jointed colonnade and thick entablature, is well developed in the lower part of the overlying lava, suggesting that water, was present at some point during lava emplacement (e.g. Hetényi et al. 2012; Phillips et al. 2013).

6.5.10.3 *Optical microscopy and SEM analysis*

Sample ID_13 from mid-way up in the exposure (Figure 6-74) is predominantly composed of glassy pyroclasts of vesicular and non-vesicular types, with a fine-ash matrix (Figure 6-77). In contrast ID_16, from just below the sediment-lava contact, is comprised of a mixture of pyroclasts and angular to sub-rounded sand-grade clasts of crystalline igneous rock (Figure 6-78).

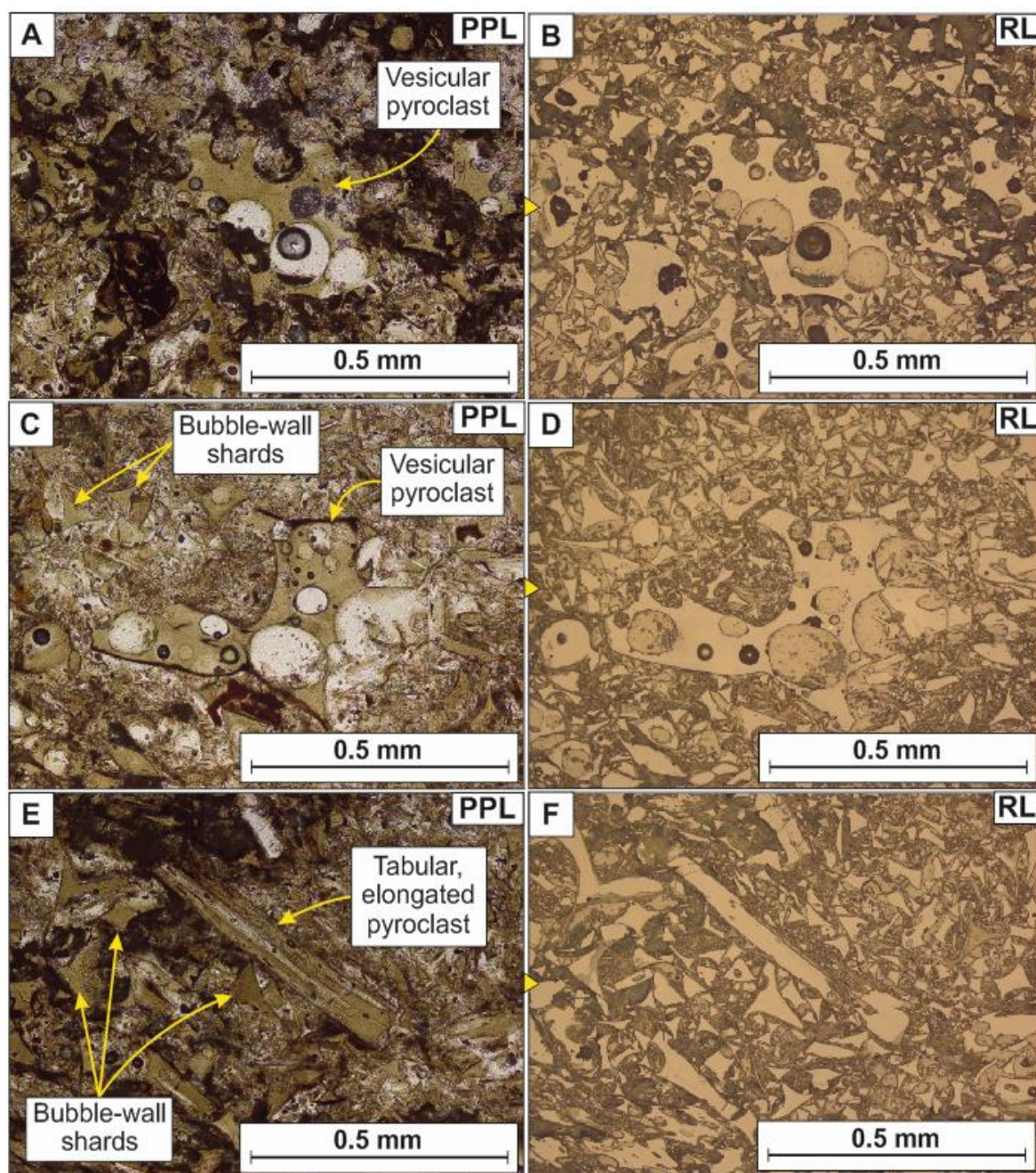


Figure 6-77 Abundant vesicular pyroclasts in sample ID_13 from L10. A & C) Vesicular pyroclasts appear brown in plain-polarised light (PPL), but their morphologies are more notable when viewed in reflected light (RL; B & D), where blocky-shapes with bubble-wall rims can be seen. E & F) Tabular or platy pyroclasts can also be found, along with bubble-wall shards.

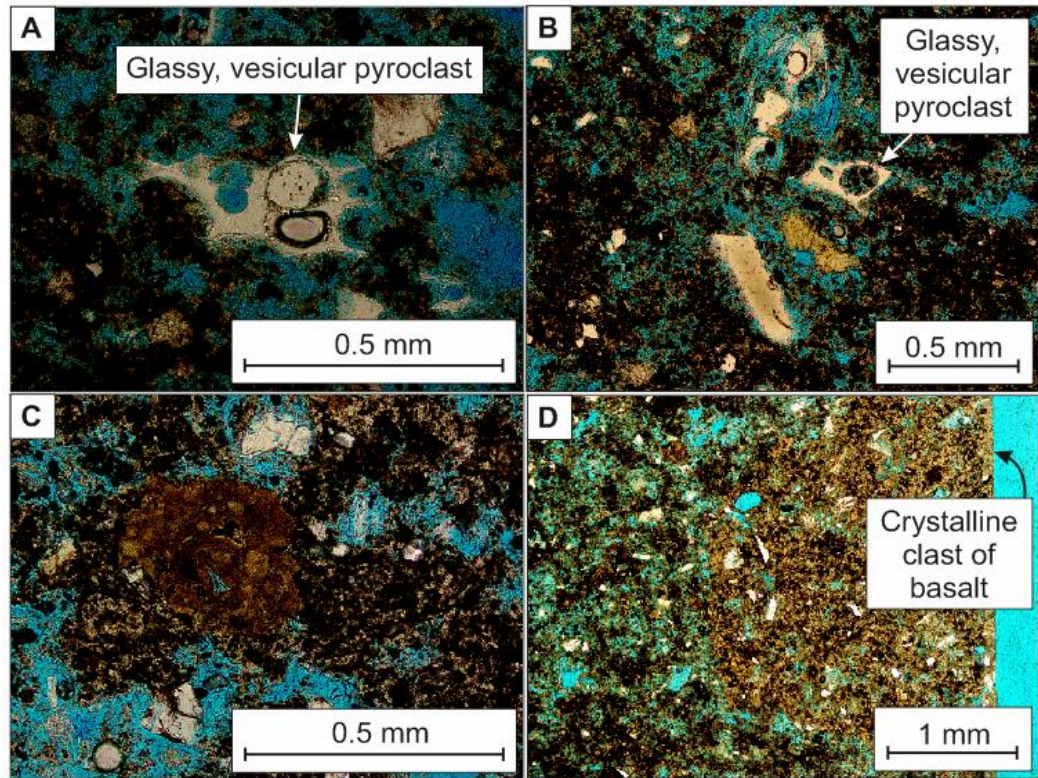


Figure 6-78 Clast-types identified in sample ID_16 from L10. A & B) Glassy vesicular pyroclasts surrounded by finer-grained material with rare coarser-grains of feldspar and amphibole. C) Sub-rounded, brown, vesicular micro-crystalline igneous clast within a finer-grained matrix. D) Part of a sub-angular granule of crystalline basalt. This clast contains micro-crystals of plagioclase.

SEM analysis shows that ID_13 contains fine-grained siltstone laminae interbedded with units of fine-grained sandstone and siltstone (Figure 6-79a). The matrix of the sandstone/siltstone is comprised of angular pyroclasts (fine to very-fine ash; Figure 6-79b). The sample is predominantly comprised of glassy, basaltic pyroclasts. The pyroclasts show a range of morphologies from vesicular to non-vesicular, bubble-wall and blocky morphologies (Figure 6-79c-e). Localised rounded pyroclasts occur in association with the finer-grained laminae (Figure 6-79f). Localised plagioclase microcrystals can be found with some of the pyroclasts (Figure 6-79d).

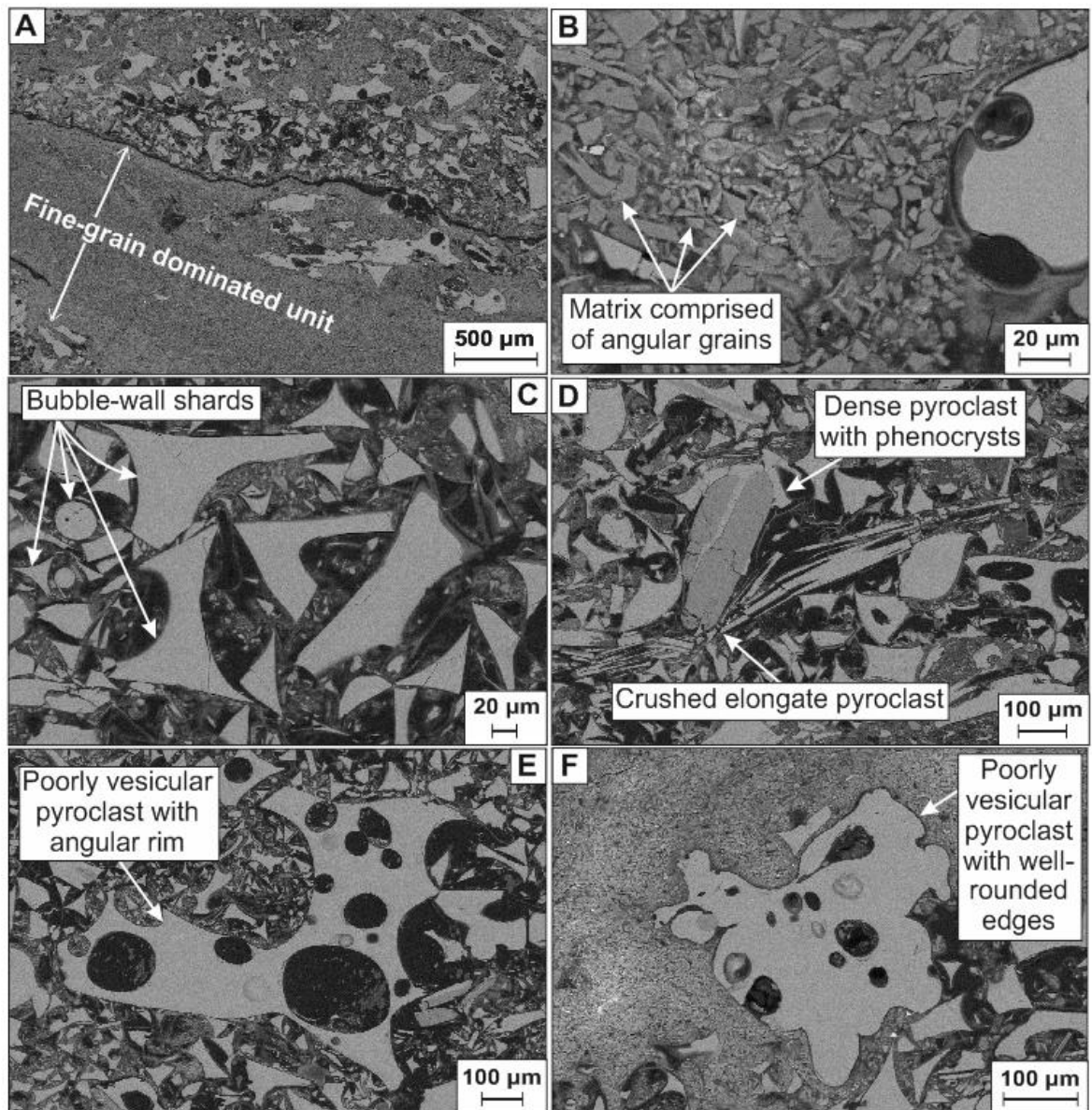


Figure 6-79 AsB SEM images showing the main features of sample ID_13. A) Unit of finer-grained clay-grade lamination within a coarser-grained matrix supported bed. The matrix is of clay-grade similar to that of the fine-grained lamination that is devoid of coarser-grained clasts. B) In some parts of the sample the matrix is composed of very fine-grained angular clasts. C) The coarser-sized grains within this sample are predominantly of bubble-wall shards. D) An elongated pyroclast has been crushed *in situ* and is intensely deformed around a dense pyroclast containing phenocrysts (darker grey). E) A poorly vesicular pyroclast with a sharp, angular outer rim, surrounded by other angular pyroclasts and a very fine-grained matrix. This is the same vesicular pyroclast illustrated in Figure 6-77C & D. F) A poorly-vesicular pyroclast with a well-rounded rim, surrounded by a very fine-ash matrix.

6.5.10.4 Interpretation of optical microscopy and SEM analysis

ID_13 is composed of basaltic ash with non-vesicular to poorly-vesicular, blocky and bubble-wall morphologies, most likely formed by hydrovolcanic eruptions (Heiken 1972, 1974; Wohletz & Sheridan 1983; Cas & Wright 1988; Ross & White 2012; Graettinger et al. 2013). The diatomite-rich lithologies exposed at L9

(section 6.5.9.2), suggest that lakes were present across areas of the CRFBP at times; suggesting that explosive interactions between lava and lakes or rivers could have allowed rootless explosions to occur, producing basaltic ash from these lava-water interactions (e.g. Branney et al. 2008; Hamilton et al. 2010; Reynolds et al. 2015; Fitch et al. 2017).

The smooth edges of the pyroclasts suggest that the ash has not undergone significant reworking; however, the laminated character of these fine-grained deposits, interbedded with coarser-grained, poorly sorted tuff, could imply that deposition after fluvial reworking has occurred.

6.5.11 Image analysis

Image analysis was carried out using ImageJ software on backscatter (AsB) SEM images of each sample. This analysis was carried out to collect quantitative data on the grain-size distribution of samples in addition to the percentage of different grain-types. Pyroclastic samples were also analysed to identify the abundances of different pyroclast types based on their morphology (vesicular or non-vesicular; blocky, bubble-wall, irregular or rod-like), in addition to the percentage vesicularity of vesicular pyroclasts.

Grain-size distribution graphs (Figure 6-80, Figure 6-81), show that most samples have a peak grain-size of silt (3.9 - 62.5 μm); in contrast WASH_04 and _44 have a peak grain-size of fine sand (125 - 250 μm). The coarsest grains in any of these samples are of coarse sand grade (0.5 - 1mm), and are observed in WASH_04, _34 and _44. WASH_22 contains accretionary lapilli and coated ash pellets up to 4 mm in diameter (for the analysis of grain-size distribution only the clasts in the matrix were used, as aggregates cause the premature fall-out of very fine ash, and their deposition involved processes that are considered here to be outside of the norm for the depositional history of the majority of this deposit).

A range of clast-types can be identified in each of the samples that contain pyroclasts (Figure 6-82). Pyroclasts are commonly the most abundant clast-type in these samples (Figure 6-82); however, granular lithic clasts and grains are also abundant in some samples (e.g. WASH_06 and _44).

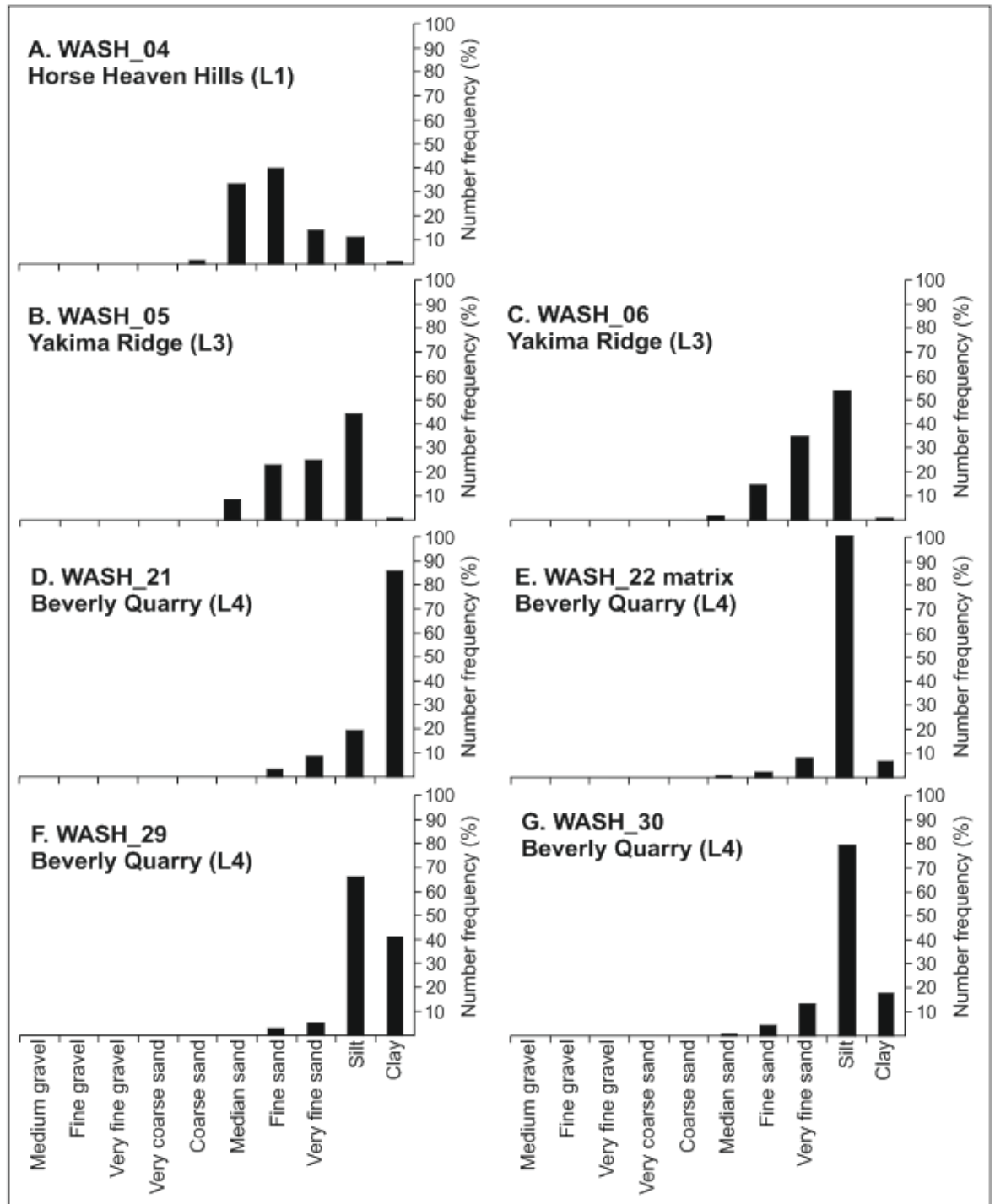


Figure 6-80 Grain-size distribution graphs. WASH_04 (A) has the widest grain-size distribution, with grains ranging from clay to coarse sand. The grain-size peak for this sample is fine sand. The peak grain-size for WASH_21 (D) is clay, making it the finest grain-size peak. All of the other samples have a peak grain-size of silt. Generally, all of the samples have a grain-size distribution of clay to median (B, C, E, F), or fine sand (D, E).

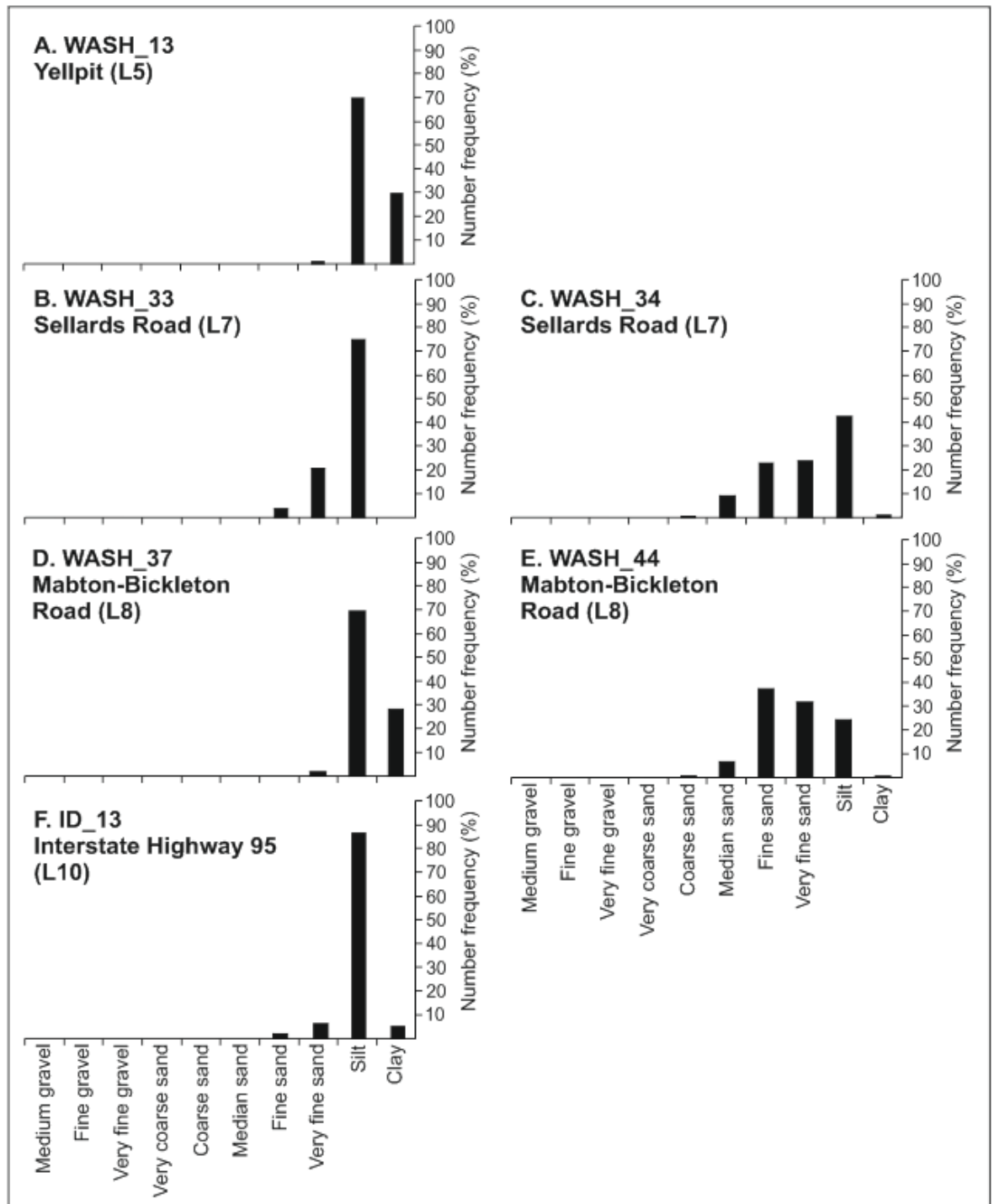


Figure 6-81 Grain-size distribution graphs. Most of these samples have a peak grain-size of silt, except for WASH_44 (E) which has a peak grain-size of fine sand. WASH_34 (C) and WASH_44 (E) have a grain-size distribution of clay to coarse sand. WASH_33 (B) and ID_13 (F) have a grain-size distribution of clay to fine sand. WASH_13 (A) and WASH_37 (D) have a grain-size of clay to very fine sand.

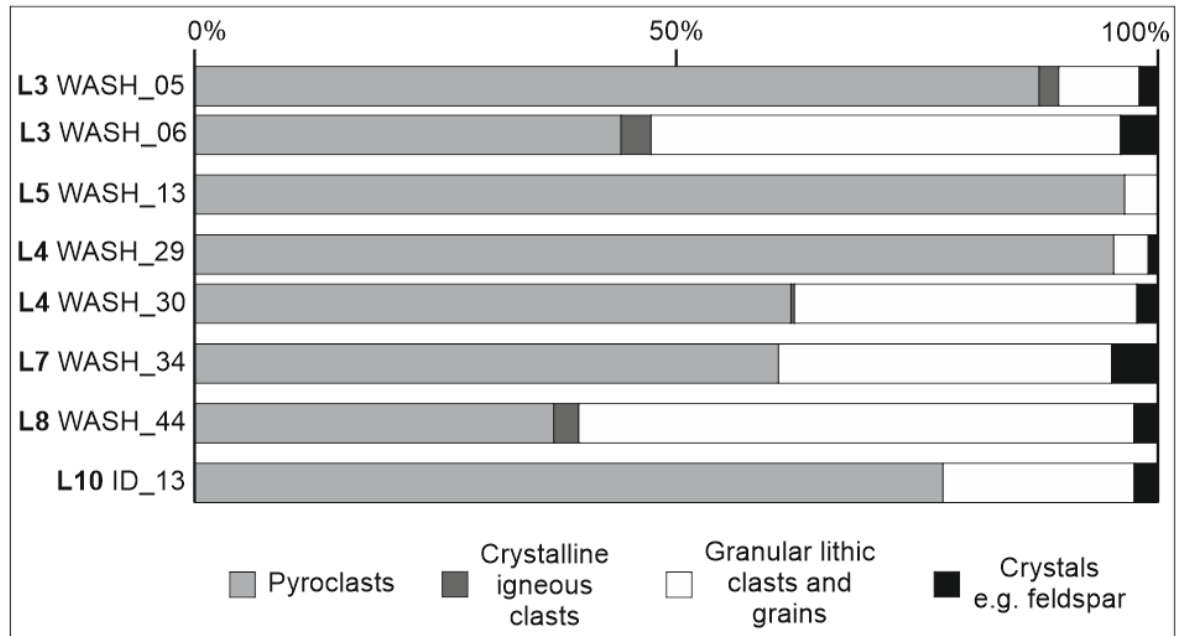


Figure 6-82 Percentage of different grain-types in each sample that contains pyroclasts. WASH_06 and _44 have the lowest percentage of pyroclasts and are dominated by granular lithic clasts and grains. Pyroclasts constitute the highest percentage in the other samples (WASH_05, _13, _29, _30, _44 and ID_13). Igneous crystalline clasts are generally present in very minor amounts or absent. Crystals also form a minor component of these samples.

Pyroclasts display a range of features and morphologies. The percentage of vesicular versus non-vesicular pyroclasts was calculated using imageJ, and shows that less than 25% of all pyroclasts within each sample are vesicular and, in most cases, this value is less than 10% (Table 6-4). The vesicular pyroclasts were used to calculate the average and range of vesicularities (Table 6-5). The average percentage vesicularity in all pyroclasts across all samples is less than 45%, showing that they are poorly vesicular (Graettinger et al. 2013). However, the range of vesicularities for individual vesicular pyroclasts shows that some pyroclasts reach moderate vesicularity (>45% but <75%; Houghton & Wilson 1989; Ross & White 2012).

Locality	Sample ID	Number of vesicular pyroclasts (%)
L3	WASH_05	12
L3	WASH_06	5
L5	WASH_13	2
L4	WASH_22*	2
L4	WASH_29	1
L4	WASH_30	4
L7	WASH_34	20
L8	WASH_44	9
L10	ID_13	9

Table 6-4 Number of vesicular pyroclasts. Less than 25% of pyroclasts are vesicular in all of the samples. Most of the samples contain less than 10% vesicular pyroclasts (red) and are dominated by non-vesicular pyroclasts. * matrix only, excludes ash aggregates.

Locality	Sample ID	Average vesicularity (%)	Range (%)
L3	WASH_05	26	5 - 64
L3	WASH_06	23	2 - 57
L5	WASH_13	33	4 - 63
L4	WASH_22	18	2 - 51
L4	WASH_29	20	5 - 45
L4	WASH_30	21	4 - 59
L7	WASH_33	27	8 - 67
L7	WASH_34	32	5 - 66
L8	WASH_44	25	1 - 56
L10	ID_13	14	1 - 38

Table 6-5 Percentage vesicularity results for all samples containing vesicular pyroclasts. All samples have an average percentage vesicularity of less than 45% and, thus, represent poorly vesicular pyroclasts (Graettinger et al. 2013). The range of vesicularities shows that a variety of poorly vesicular to moderately vesicular pyroclasts are present. Results for WASH_22 are representative of pyroclasts within the matrix and do not include pyroclasts within ash aggregates.

Image analysis shows that the pyroclasts of each sample display a range of morphologies and these have been divided into blocky, bubble-wall, irregular and rod-like (Figure 6-83). Rod-like or blocky morphologies dominate the silicic samples (except ID_13), with lesser amounts of bubble-wall and irregular types (Figure 6-83). ID_13 is of a basaltic tuff with pyroclasts that are predominantly of blocky and bubble-wall morphology (Figure 6-83).

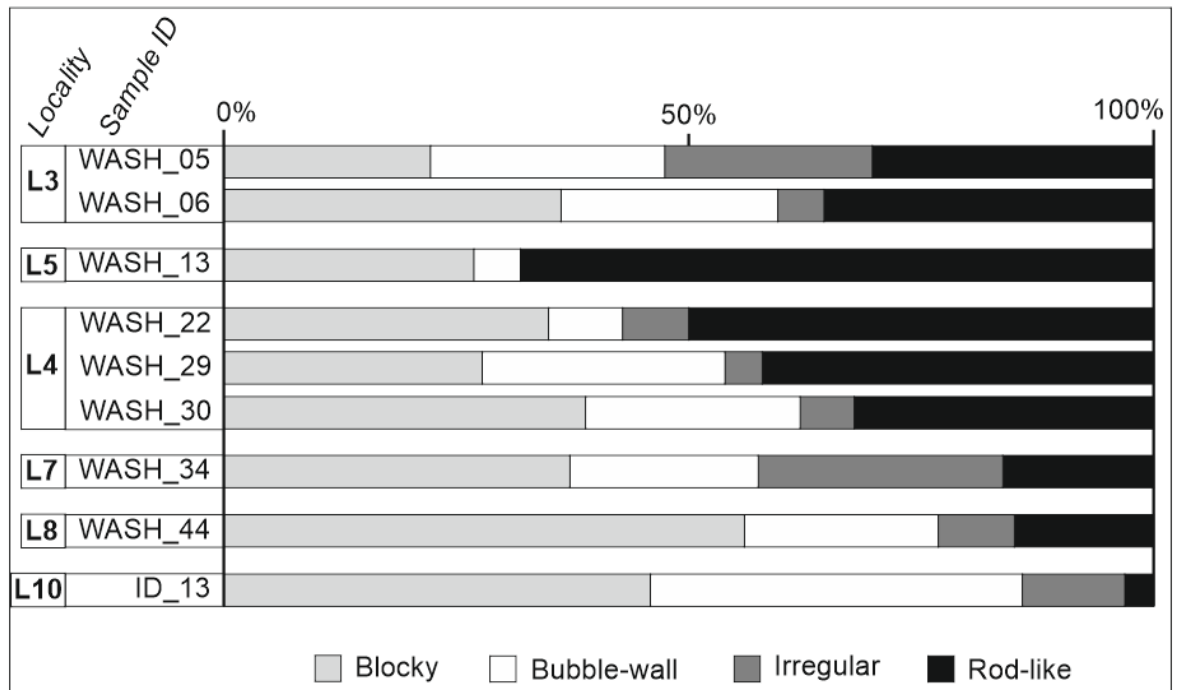


Figure 6-83 Percentages of blocky, bubble-wall, irregular and rod-like pyroclast morphologies. Rod-like morphologies are the most common type of pyroclast recorded in point-count analysis for WASH_05, _13, _22 matrix, and WASH_29. Blocky morphologies are most common in the remaining samples (WASH_06, _30, _34, _44, and ID_13). Irregular morphologies are generally present in minor amounts, or not at all (e.g. WASH_13).

6.6 Discussion

6.6.1 Depositional history of the central Washington Ellensburg Formation.

The palaeo-environment of deposition can be interpreted for each of the localities, from field evidence, including lithological logs, together with petrography, SEM analysis and image analysis. Here an interpretation of each locality will be presented separately.

6.6.1.1 Horse Heaven Hills (L1)

The first unit to be deposited at L1 was a ripple cross-laminated sandstone with lenses of coarser-grained sandstone/granule-conglomerate and normal-graded sandstones (Figure 6-8). This sequence most likely represents deposition of sediment from a fluctuating flow within a fluvial system (Figure 6-84a; e.g. Selley 1976; Reading 1978). The orientation of the cross-stratification in many directions, within the lower-most unit, suggests that deposition occurred from traction currents that periodically changed direction (e.g. Selley 1976; Reading

1978). The normal-graded sandstones appear to be composed of unaltered silicic ash, and may have entered the sedimentary system as primary fallout material, or by erosion of previously-deposited tuffs. Unfortunately, a more confident conclusion regarding the source of this material (primary pyroclastic versus reworked) could not be achieved with the current sample set in this study, due to the poor quality of returned thin-sections. Subsequently, there was a decrease in the energy of the transport system, with an apparent absence of currents, which led to the deposition of sub-horizontal, parallel-laminated clays (Figure 6-8), most likely within an overbank setting (Figure 6-84b; Reading 1978; Singh et al. 1999; Bayliss & Pickering 2015; Yamada et al. 2016). This was followed by a change to more energetic conditions and traction currents, with varying flow direction, that allowed the deposition of interbedded, ripple cross-laminated silt with discontinuous lenses of fine-sand (Figure 6-84b; Selley 1976). Next, a further increase in the energy of the environment occurred as shown by the presence of a coarser-grained homogenous sandstone unit with truncated cross-stratification (Figure 6-10; Reading 1978). Changing flow directions may have caused deposition of foreset-beds in different orientations and allowed for small erosional surfaces to form between these (Figure 6-10). This unit could be interpreted as having been deposited closer to the main river or stream channel (Figure 6-84b; e.g. Reading 1978), suggesting that the position of the water-body varied during the deposition of this entire sedimentary sequence. Finally, a basaltic lava was emplaced (Figure 6-84c).

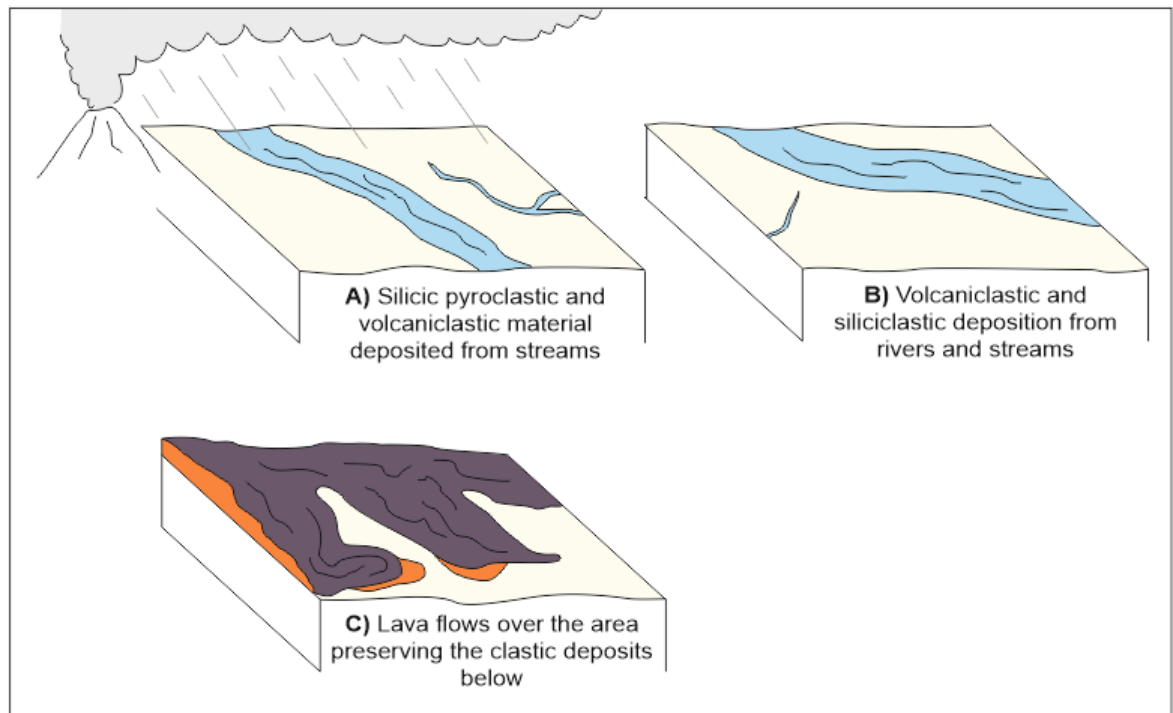


Figure 6-84 Summary of the main events that led to deposition of the Ellensburg Formation exposed at Horse Heaven Hills (L1). A) Silicic eruptions deposited air-fall ash; some/all of this was reworked and forms volcaniclastic material deposited by streams. B) Further reworking of pyroclastic and volcaniclastic material by rivers and streams deposited volcaniclastic material along with background siliciclastic siltstones and sandstones. Lavas are present at the top of the exposure and help preserve the underlying pyroclastic, volcaniclastic and siliciclastic siltstone and sandstone units.

6.6.1.2 Snipes Mountain (L2)

The exposure at L2 is dominated by coarse-grained siliciclastic sandstones and conglomerates, and volcaniclastic (lahar) deposits (Figure 6-12, Figure 6-85). However, the grey, very poorly sorted, pebble- and granule-rich sandstones at the base (see section 6.5.2.2), are likely comprised of igneous clast-types, suggests that occasionally lahars deposited large amounts of material rapidly across this area (Figure 6-85a). The rapid deposition of the lahar deposits can be inferred by the presence of sand injectities (Figure 6-13, Figure 6-14; Hurst et al. 2011). Above the lahar deposits deposition of finer-grained siliciclastic sediment most likely took place within a floodplain or overbank setting (Figure 6-85b; Reading 1978). Over time, a river flowed across the region, leading to deposition of channel lag conglomerates with interbedded sand-bars (Figure 6-85c). The characteristic quartzite-rich nature of the conglomerates suggests that the ancestral Columbia River was responsible for the deposition of these

channel-lag deposits (Warren 1941; Mackin 1961; Waters 1965; Schmincke 1967a; Smith 1988a, 1988b).

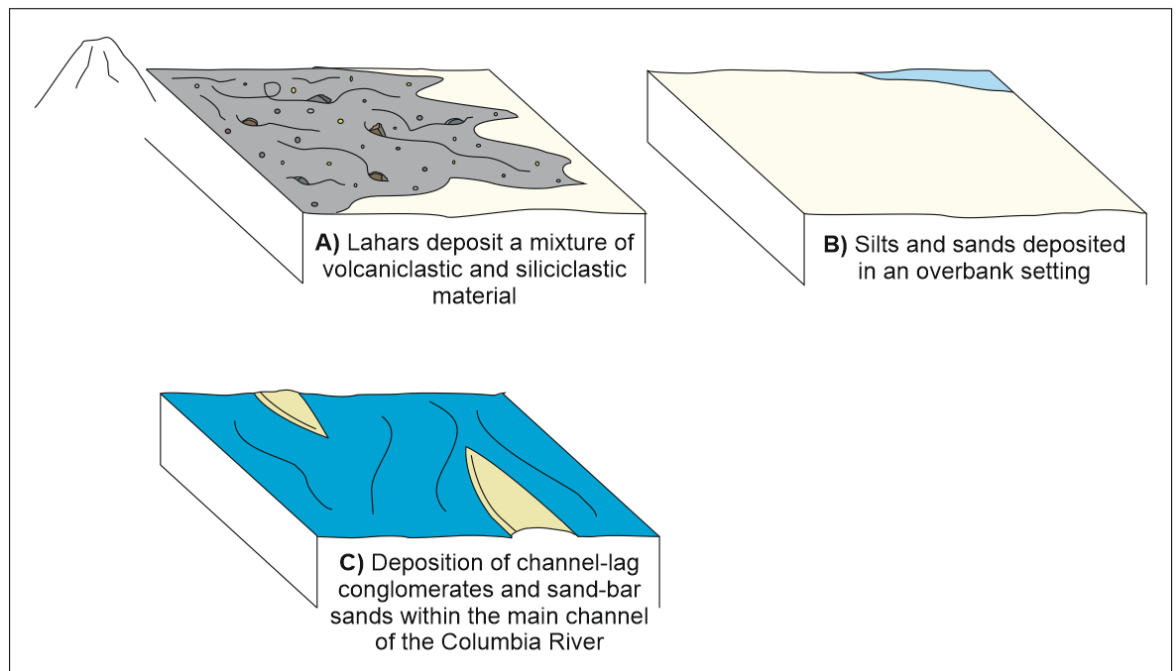


Figure 6-85 Summary of the main events in the depositional history of Snipes Mountain (L2). A) The base of the exposure is comprised of very poorly sorted sandstone and conglomerate, with gravel and pebbles deposited from lahars. Above this (B), silts and sands were deposited in an overbank setting, or from a transition to stream-flow, possibly found adjacent to a main river channel. C) Channel-lag conglomerates and lenses of cross-stratified sandstone represent deposition in a channel of the ancestral Columbia River.

6.6.1.3 Yakima Ridge (L3)

Only one unit is exposed in the road-side at L3 and comprises cross-stratified volcaniclastic siltstone and sandstone (Figure 6-16), most likely deposited from a stream or river (Figure 6-86).

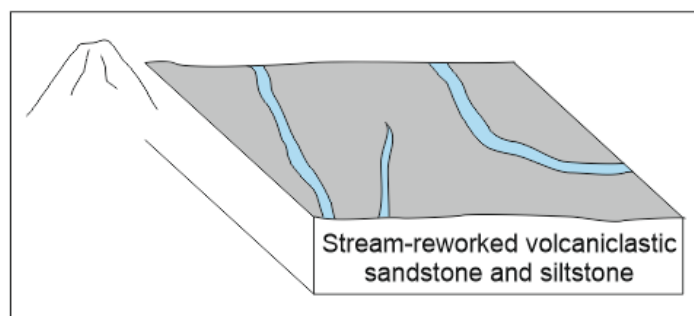


Figure 6-86 Interpretation of the depositional setting for the exposure at Yakima Ridge (L3). The volcaniclastic cross-stratified sandstones and siltstones of this locality were most likely deposited due to reworking and re-deposition of pyroclastic material by streams.

6.6.1.4 Beverly Quarry, (L4)

The EF exposed at L4 shows the diversity of the lithologies within the Formation within a small (*ca.* 1 km²) area. Here, the EF includes pyroclastic deposits, together with overbank and fluvial channel (sedimentary) facies, with significant erosional surfaces (see section 6.5.4). An interpretation of the sedimentary depositional environments is given here, with detail regarding the volcanic and volcanoclastic depositional story in subsequent sections.

Units at the base of the sequence include cross ripple-laminated siltstones (Figure 6-21) and massive siltstones with lenses of sandstone (Figure 6-20), most likely deposited in an overbank setting (Figure 6-87a; Reading 1978; Singh et al 1999; Bayliss & Pickering 2015; Yamada et al. 2016). A period of explosive silicic volcanism occurred next (Figure 6-87b), depositing pyroclastic material (see section 6.5.4.4). Reworking of these deposits led to the formation of a thick (*ca.* 12 m) sequence of interbedded, parallel-laminated volcanoclastic claystones and siltstones (Figure 6-45 - Figure 6-48), that form the main silicic tuff ‘pumicite’ unit of the main quarry face (Figure 6-20, Figure 6-26). This material may have been deposited in a lake (Figure 6-87c), as can be inferred from the parallel laminations throughout the deposit (Figure 6-25; e.g. Makin 1961, Schmincke 1967b). The damming of water may have been influenced by emplacement of the Pomona Basalt lava, which is interbedded with the strata close to L4 (see also Makin 1961). This lava is not found within the quarry itself and appears to have terminated here (e.g. Makin 1961; Reidel pers comms 2015). The presence of overbank deposits below, and river-channel deposits above, this lava suggests that a fluvial channel was operative when the Pomona Basalt was emplaced. Therefore, emplacement of the lava could have diverted water courses and dammed them, leading to the formation of a lake in the Beverly Quarry area (e.g. Makin 1961). Within this lake, the reworked volcanoclastic unit (i.e. the pumicite) would have been deposited under very low-energy conditions (Figure 6-87c; e.g. Selley 1976; Reading 1978).

This was followed by a period of erosion, possibly caused by a lake outburst flood that drained the lake (e.g. Hamblin 1994); or, by arrival of the main Columbia River. Cross-bedded sandstones (Figure 6-28, Figure 6-29),

representative of sand-bars, within a sequence of quartzite-rich channel-lag conglomerates (Figure 6-27, Figure 6-28), were deposited within the main river channel and overlie the lacustrine volcanoclastic claystones and siltstones (Figure 6-87d; Reading 1978). The cross-stratified sandstones containing layers of well-rounded pebbles (Figure 6-28), showing that the current from which these sediments were deposited frequently changed its course and energy over time, with the well-rounded pebbles indicating that the bedload has been transported over large distances (e.g. Reading 1978).

The Elephant Mountains Basalt lies unconformably above these river-channel deposits at some locations within the quarry (Figure 6-29). However, to the west, the lava lies on top of a bioturbated siltstone (Figure 6-30). This siltstone may have been deposited within a low-energy sub-aqueous environment, which may have been created due to displacement and ponding of water from the Columbia River that was present prior to lava emplacement (Figure 6-87e). The siltstones have been homogenised by burrowing organisms and or, plant roots (Figure 6-31). This high degree of bioturbation within the fine-grained sediments below the lava suggests that the sedimentary system here existed long enough for an ecosystem to become established (Figure 6-87e). A thin (<10 cm), discontinuous unit of white siltstone overlies this bioturbated siltstone, with a sharp, sub-horizontal contact (Figure 6-20). Above this unit, *ca.* 1 m of pillow basalts marks the beginning of the Elephant Mountains Basalt (Figure 6-30). The presence of the pillow basalt suggests that initial emplacement of the lava occurred within a shallow water-body (Figure 6-87f). No baking of the sediment has occurred, suggesting that the lava quickly lost heat due to the presence of water (e.g. Reidel et al. 2013). The pillow basalts are densely packed although it is possible that small amounts of sediment may exist between the pillows.

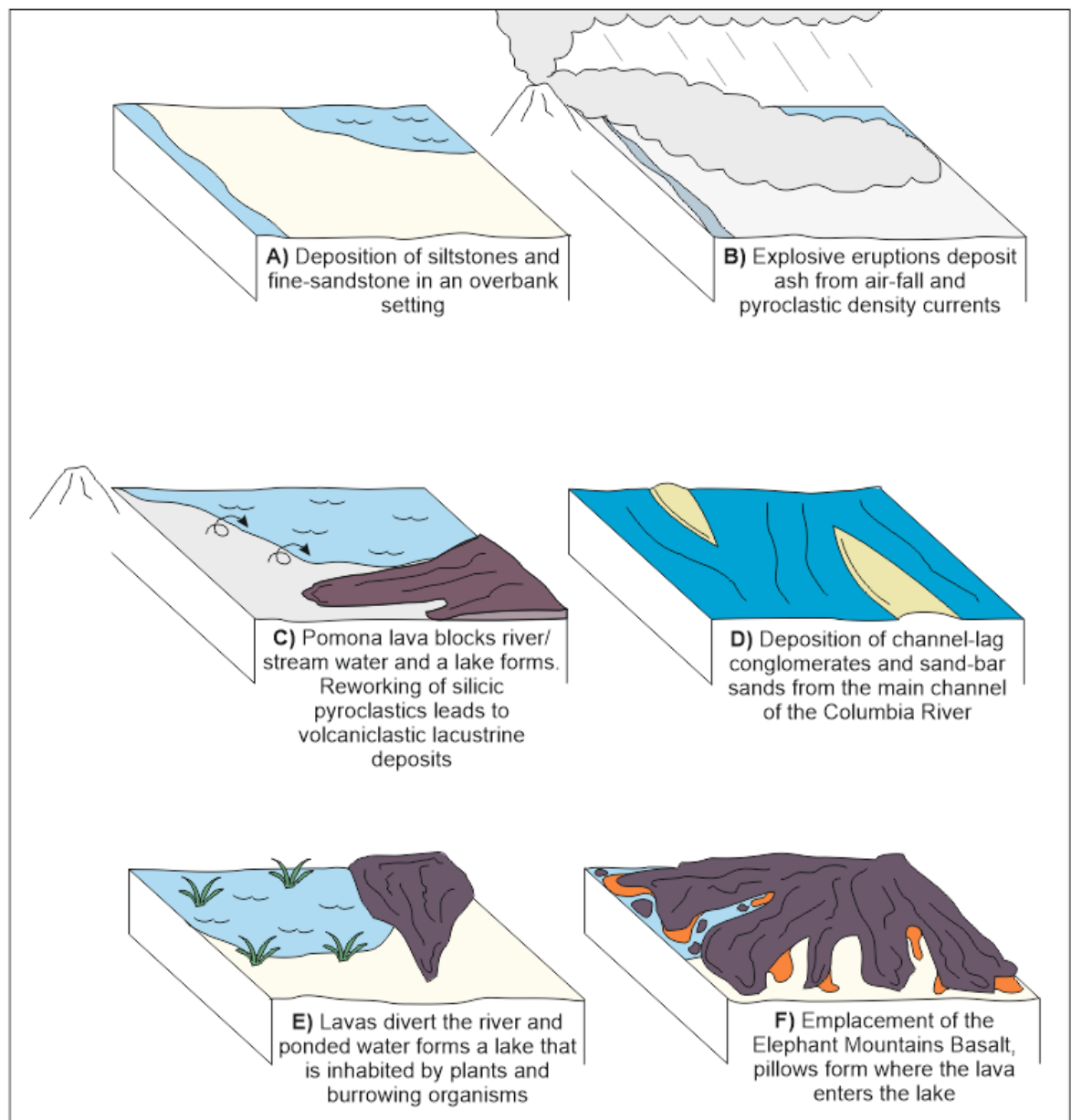


Figure 6-87 Summary of interpretations for the depositional history of the Ellensburg Formation exposed at Beverly Quarry (L4). A) Firstly, deposition occurred within a low energy, possibly fluvial overbank setting; this was later influenced by ash-fall and deposition from PDCs associated with large-scale silicic eruptions up to 150 km distant (B). C) Emplacement of the Pomona Basalt may have caused the damming of streams or a river, which allowed a thick unit (ca. 12 m) of volcanoclastic siltstones and sandstones to be deposited. D) Channel-lag conglomerates and cross-stratified sandstones and granule-/pebble-conglomerates were deposited in the main channel of the ancestral Columbia River. E) Emplacement of the Elephant Mountains Basalt diverted the ancestral Columbia River and most likely caused ponding of water behind a lava-dam, in which organisms and plants became established. F) Emplacement of the Elephant Mountains Basalt proper, with a pillow facies at the base of the lava suggesting that emplacement initially occurred into shallow water.

6.6.1.5 Yellpit (L5)

Silicic tuffs containing rare whole and fragmented ash aggregates similar those identified at L4 (Figure 6-22), represent the entire EF exposed at L5 (Figure

6-88). The overlying Pomona Basalt has caused welding of the underlying tuffs, creating a zone of glassy 'obsidian-like' material at the lava-tuff contact that grades into non-glassy welded and non-welded tuffs with increasing distance from the contact. It is most likely that emplacement of very high temperature lava formed this assemblage of lithologies, rather than it representing a welded ignimbrite - as the closest source of silicic volcanism at this time lay >100 km away (see section 6.7.3.2), a distance that is, most likely, too great for a PDC to maintain a high enough temperature to cause welding. However, the nature of the non-glassy welded tuff, with its clast alignment (Figure 6-53) and abundance of rod-like pyroclasts (>50%; Figure 6-83 WASH_13), does imply that highly explosive silicic eruptions were the source of the original ashes. Deposition of the ashes likely occurred through a water column, as indicated by the presence of centric freshwater diatom frustules and granular-lithic clasts (Figure 6-53), although these are only a minor component of the deposit (<20%; Figure 6-82 WASH_13).

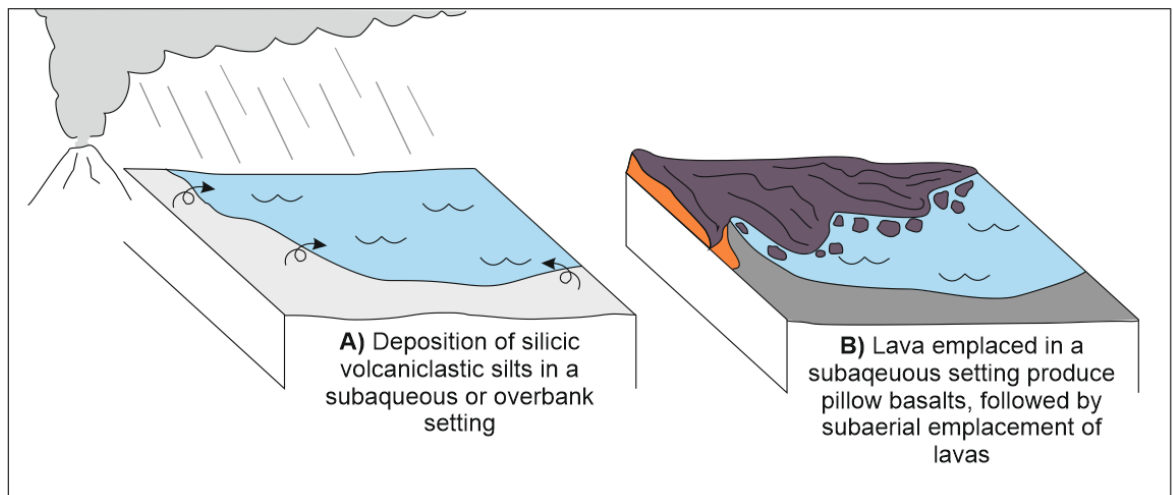


Figure 6-88 Depositional and volcanic history interpreted for the EF of L5. **A)** Deposition of silicic air-fall ash into an overbank or deeper-subaqueous setting, alongside diatoms. **B)** Emplacement of lava into water formed pillow basalts, followed by subaerial emplacement of lavas.

6.6.1.6 Finley Quarry (L6)

Silicic pyroclasts between the Umatilla and Pomona Basalts at L6 (Figure 6-54) may have been deposited as primary fall-out, possibly with some reworking (Figure 6-89c). SEM analysis was inhibited by electron charging across the sample and therefore the nature of the pyroclasts could not be examined in detail to

deduce whether these ashes are of primary or reworked material. The lack of any other clastic deposits could suggest that the ash was deposited from fall-out. However, this deposit lies at the bottom of a palaeo-valley cut into the (underlying) Umatilla Basalts (Figure 6-54). This indicates that substantial rivers were present in this area sometime between emplacement of the Umatilla and the Pomona Basalts (Figure 6-89b). Therefore, it is also possible that these silicic tuffs were deposited as volcanoclastic material, but all other sedimentary deposits have been eroded, or removed by emplacement of the overlying lavas (Figure 6-89d; e.g. Reidel et al. 2013).

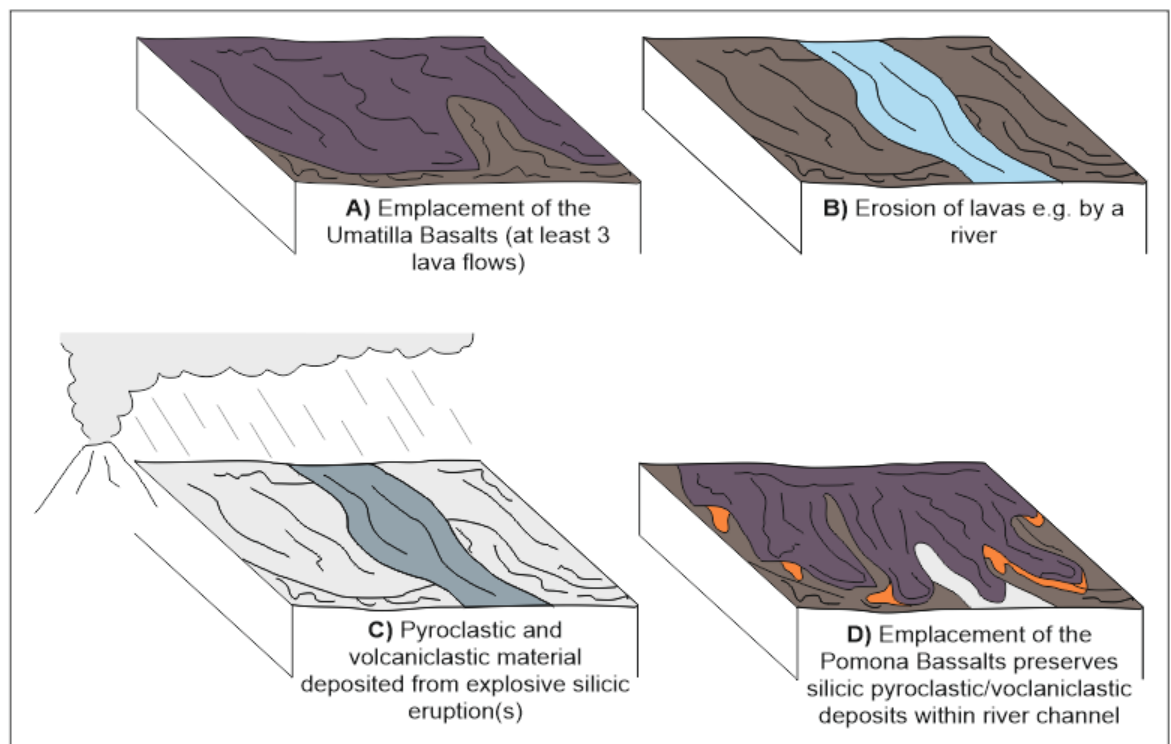


Figure 6-89 Depositional history interpreted for L6. **A)** Emplacement of the Umatilla Basalts occurred by at least three separate flows. Fluvial erosion cut channels into the Umatilla Basalts. **B).** Explosive silicic eruptions deposited ash-fall across the area (**C**), some of which was reworked and preserved in the channel into which the Pomona Basalt was emplaced (**D**).

6.6.1.7 Sellards Road (L7)

The EF at L7 is composed of siliciclastic and volcanoclastic materials that were most likely deposited in an overbank setting (see section 6.5.7; Figure 6-90a,b; Reading 1978; Singh et al. 1999; Bayliss & Pickering 2015; Yamada et al. 2016). Sample WASH_34, from a volcanoclastic cross-laminated sandstone, is comprised of pyroclasts with rough, fractured edges produced by abrasion during

reworking; these are also associated with a very fine-ash matrix and granular lithic clasts composed of pyroclasts and fine-ash (Figure 6-62): features are characteristic of volcanoclastic deposits in which glassy pyroclasts have undergone reworking and re-deposition. Samples WASH_32 and _33 are volcanoclastic siltstones that contain a higher abundance of siliciclastic clast-types (Figure 6-59, Figure 6-60, Figure 6-61).

Image analysis shows that WASH_34 (Figure 6-56) contains almost equal amounts of the different pyroclast morphologies (blocky, bubble-wall, irregular and rod-like; Figure 6-83). This is, in part, due to abrasion and brittle fragmentation of the pyroclasts during reworking and does not represent the original conditions of magmatic processes during their eruption. However, 20% of the pyroclasts are vesicular (Table 6-4); on average these are poorly vesicular (<45% vesicles; Table 6-5) but some are more moderately vesicular (up to 66% vesicles; Table 6-5). These values suggest that the pyroclasts were originally produced in explosive silicic eruptions driven by magmatic processes (e.g. magmatic volatiles; Walker & Croasdale 1971; Heiken 1972, 1974; Wohletz 1983; Wohletz & Sheridan 1983; Cas & Wright 1988; Rose & Durant 2009; Brown et al. 2012; Graettinger et al. 2013).

A period of non-deposition and weathering is represented by a thin (*ca.* 10 cm) palaeosol that formed due to subaerial exposure of the volcanoclastic sandstone (Figure 6-90c). A return to overbank deposition is interpreted by the siltstones that overlie this palaeosol (e.g. Reading 1978; Singh et al. 1999; Bayliss & Pickering 2015; Yamada et al. 2016). Sub-aerial conditions may have occurred during emplacement of the overlying basaltic lava (Figure 6-90e), as indicated by the sharp, sub-horizontal contact and fractures within the sediment directly below the lava-sediment contact (Figure 6-56).

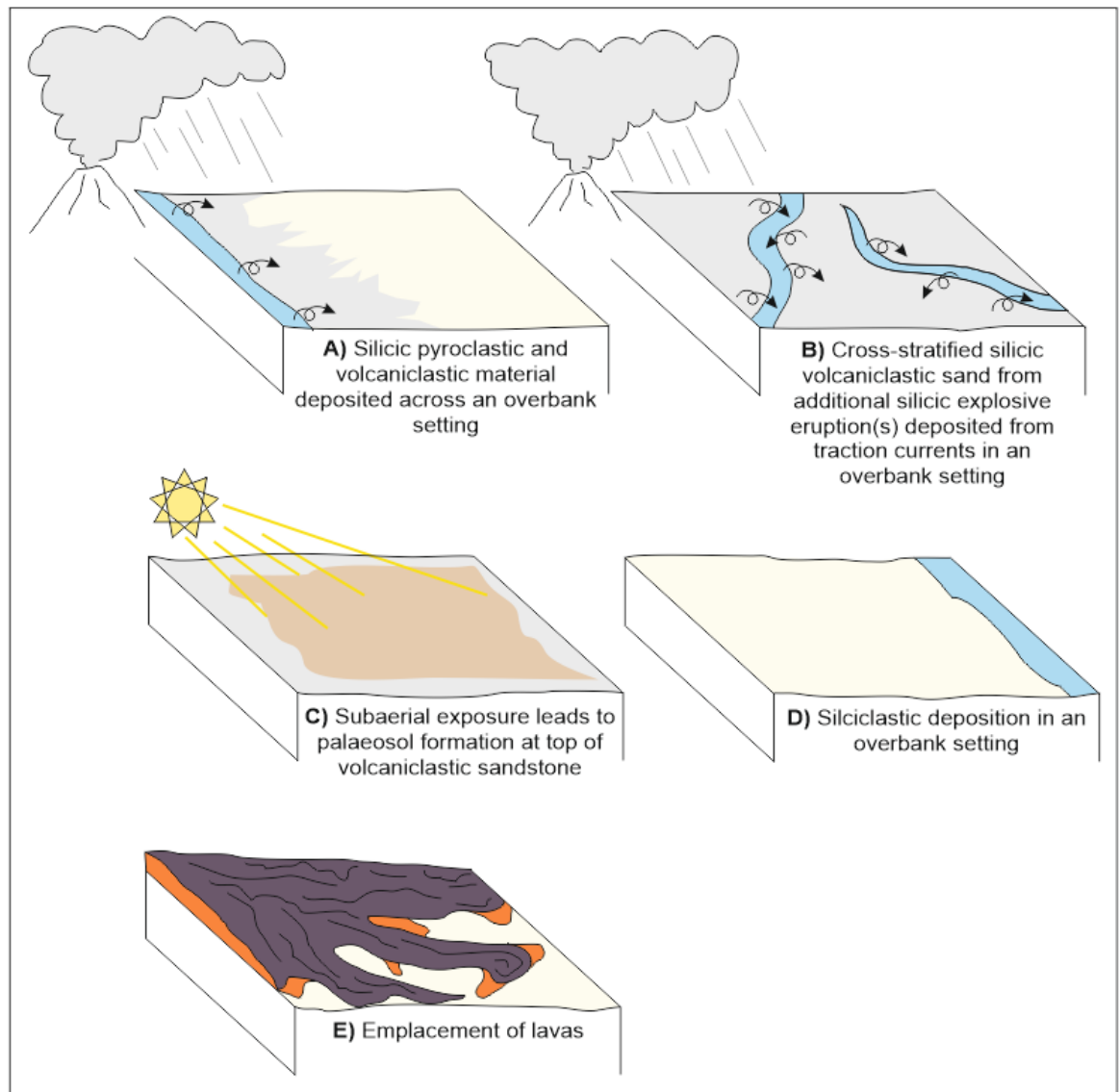


Figure 6-90 Interpretation of the depositional history of the EF of L7. A) Silicic eruptions deposited silicic pyroclastic and subsequent reworking of this material deposited volcaniclastic units within an overbank setting. B) Further silicic eruptions and reworking occurred leading to further overbank deposition of volcaniclastic sand, possibly with a greater influence of traction currents. C) Subaerial exposure and weathering of these deposits led to the formation of a thin (few cm's) palaeosol. D) Deposition in an overbank setting resumed with the accumulation of siliciclastic sediments. E) Emplacement of basalt lavas.

6.6.1.8 Mabton-Bickleton Road (L8)

The EF exposed at L8, is composed of siliciclastic siltstones and sandstones (Figure 6-63). Samples WASH_37 and _40 consists of siliciclastic clast-types with no input of pyroclastic or volcaniclastic materials (Figure 6-65, Figure 6-66). In contract, WASH_44 contains a mixture of siliciclastic and volcaniclastic clast-types (Figure 6-67; Figure 6-82). The delicate, fluidal, fine-scale features of some of the pyroclasts in this sample may have been preserved, even during reworking and re-deposition, due to the presence of a clay-matrix (Figure 6-67b,

c). Removal of this clay matrix by fluid-flow or during transport could allow pyroclasts to be re-deposited whilst still retaining their primary pyroclastic features.

Deposition of siliciclastic siltstones and interbedded sandstones were may have been initially deposited in an overbank setting (Figure 6-91b). A thicker (*ca.* 6 m) unit of cross-stratified volcanoclastic sandstones was then deposited from steams or rivers as they migrated over the area (Figure 6-91d,e). A thin unit of basaltic lava (Figure 6-91f) separates this unit from the overlying quartzite-rich channel-lag conglomerates of the main ancestral Columbia River (Figure 6-91g; Warren 1941; Mackin 1961; Waters 1965; Schmincke 1967a; Smith 1988a, 1988b). The presence of the lava separating these river-derived sandstones and conglomerates possibly suggests that emplacement of the lava displaced the main river channel, and caused channel-lag conglomerate to be deposited directly on top of the lava.

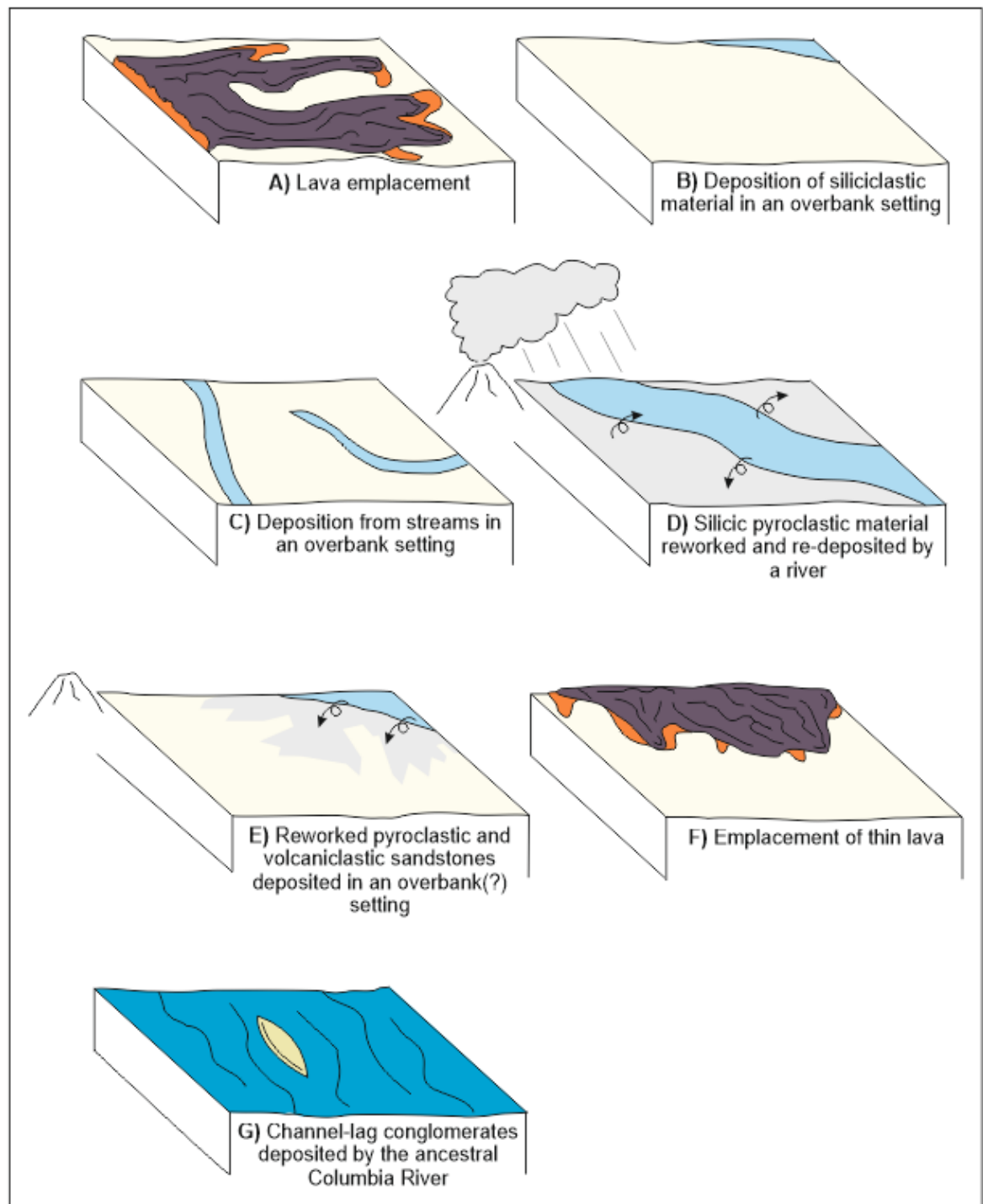


Figure 6-91 Summary of the depositional history of the Ellensburg Formation exposed at L8. A) Lavas are present at the base of this exposure, and are overlain by siliciclastic sediments possibly deposited in an overbank setting (B). Deposition of siliciclastic sediments subsequently occurred from streams or alternatively, from traction currents within the overbank setting (C). Silicic eruptions supplied pyroclastic and volcaniclastic material into the area, with some reworking occurring from streams or adjacent rivers during floods and traction currents. (D) E) Volcaniclastic sands deposited within an overbank setting. F) Emplacement of another basaltic lava. G) The main channel of the ancestral Columbia River migrated across this area, depositing channel-lag gravels, pebbles and sands.

Subsequent growth of the Yakima Fold Belt caused tilting of the rocks at L8, and led to the formation of the Horse Heaven Hills anticline (Waters 1965; Blackely et al. 2011; Pratt 2012).

6.6.2 Deposition of the Ellensburg Formation equivalent of western Idaho (Latah/Payette Member)

6.6.2.1 *Whitebird (Locality 9)*

The various exposures of the Latah/Payette Member along Old Highway 95 eastward from Whitebird consist of claystones and siltstones interbedded with lignite (Figure 6-68), most likely deposited in a lake (e.g. Berry 1934; Camp 1981; Engel 2004). The rocks are thinly laminated with leaf and seed fossils of, for example, *Fagus Pacifica* and *Cercis idahoensis*, preserved within the laminae (Figure 6-69, Figure 6-70; Berry 1934). These fossil deciduous and conifer leaves show that the area experienced a temperate climate, with ample rainfall (Berry 1934). The exceptional preservation of the leaves and seeds suggest that they were deposited in a very low-energy environment, most likely within a lake (Berry 1934; Yang & Huang 2003; Allison et al. 2008). Preservation of leaf-fossil-bearing laminae may indicate seasonal (autumnal) accumulation through lake waters (e.g. Allison et al. 2008). An alternative model could involve rapid deposition of the interbedded silts and clays, still leading to preservation of these delicate flora, by inhibiting decomposition and disturbance by burrowing organisms (e.g. Allison et al. 2008). The lack of any other micro- or macro-fossil fauna, or evidence of burrowing, may indicate that deposition occurred rapidly.

The claystones and siltstones have a very low density and most likely represent clay-/silt-grade diatomites (e.g. Yang & Huang 2003). Diatom blooms often occur in the Spring in temperate climates (Ferris & Lehman 2007; Grami et al. 2011; Ibelings et al. 2011; Zahrer et al. 2013), therefore it is possible that the leaves were deposited through the lake during the autumn and winter (Figure 6-92b) and preserved within diatomite when a diatom-bloom occurred in the following Spring and summer (Figure 6-92a). Varves of annual diatom accumulation can occur in this way, with each varve generally only reaching up to a millimetre in thickness (Zahrer et al. 2013). This suggests that these sedimentary deposits

could record many hundreds, or thousands of years of sediment deposition in this area, during the Miocene.

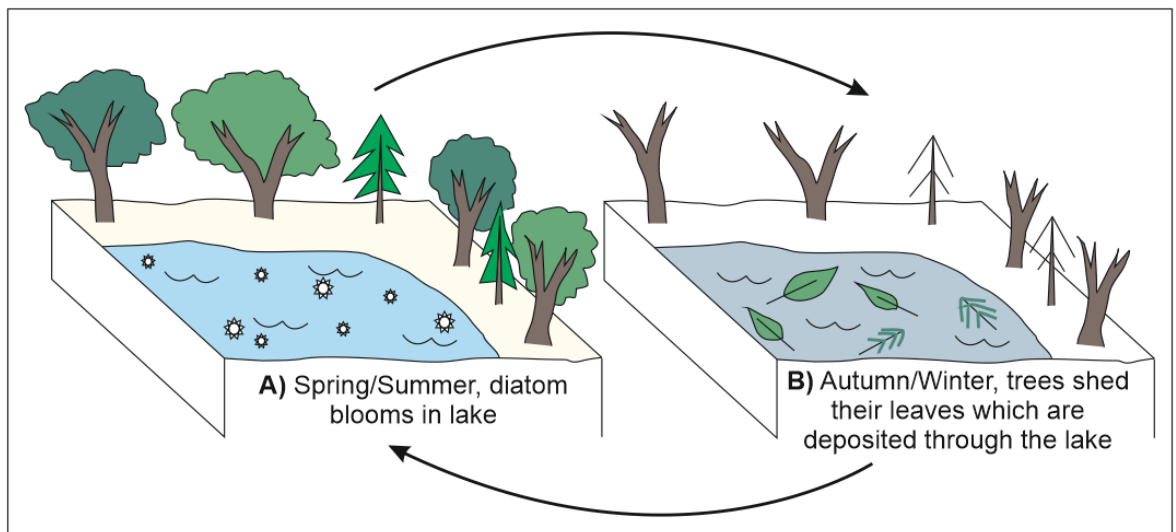


Figure 6-92 Interpretation of the depositional history of Whitebird (L9a-c). Diatom blooms occurred within a lake in the spring/summer (A). In the winter/autumn deciduous trees surrounding the lake shed their leaves and are incorporated into low energy, fine-grained sediments that are accumulating (B) and became preserved in layers of diatomite when the diatom bloom of the following spring/summer came to an end. This process repeated for several hundreds or thousands of years.

6.6.2.2 Idaho, State Road 95 (L10)

In the east of the CRFBP the source of the Saddle Mountains lavas lies relatively proximal to L10 (Figure 6-3). The presence of basaltic pyroclasts within these deposits (sample ID_13; Figure 6-77, Figure 6-79), suggests that eruptions involved episodes of more explosive activity, between or during periods of flood lava effusion (e.g. Head & Wilson 1989; Brown et al. 2015). Alternatively, the deposits may represent material produced by rootless explosions, due to lava-water interactions (Figure 6-93a; e.g. Branney et al. 2008; Hamilton et al. 2010; Reynolds et al. 2015; Fitch et al. 2015). The presence of localised lakes, rivers, and waterlogged ground, as suggested by the lacustrine deposits at nearby Whitebird, L9, and across other areas of the CRFBP (e.g. L1 - L8), could have enabled explosive interactions between lava and water in rootless eruptions.

Rootless eruptions could produce abundant fine-ash of blocky and bubble-wall morphologies (Reynolds et al. 2015), that resemble those of hydrovolcanic eruptions that occur at a vent. Comparison of the shapes of these ash particles

with the ash from silicic tuffs at other locations (e.g. Figure 6-17, Figure 6-53a), shows that the basaltic ash contains a higher abundance of blocky pyroclast-types and few irregular/fluidal or rod-like pyroclasts (ID_13 Figure 6-83), in contrast to the silicic deposits from highly explosive Plinian eruptions which predominantly display rod-like morphologies (WASH_13 and_22 Figure 6-83). The dominantly blocky (Figure 6-83), non- to poorly-vesicular (Table 6-4, Table 6-5), very fine-grained (Figure 6-81) nature of the ID_13 basaltic ash suggests that the ash of this pyroclastic deposit was produced either by an hydrovolcanic eruption (Heiken 1972, 1974; Wohletz & Sheridan 1983; Cas & Wright 1988; Ross & White 2012; Graettinger et al. 2013), alternatively it is possible that rootless explosions produced tephra via explosive lava-water interactions (e.g. Branney et al. 2008; Reynolds et al. 2015).

The siliciclastic and pyroclastic deposits may have been deposited in an overbank setting (Figure 6-93b; Reading 1978). Pillow basalts are not present at the base of the overlying lava, suggesting that there was no significant water-body present at this location when the lava was emplaced. However, unlike the sharp, sub-horizontal contact at Sellards Road (L7; Figure 6-56), the lava here has intruded into the sediments (Figure 6-76; Figure 6-93c). The sediment between these lava injections has retained some of its original bedding features, such as parallel lamination, suggesting that the sediment was relatively coherent at the time of emplacement (e.g. Reidel et al. 2013).

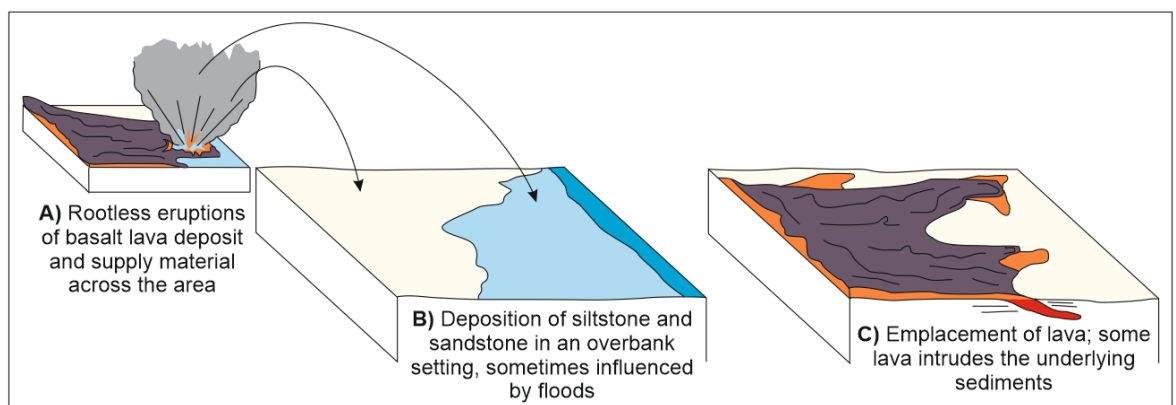


Figure 6-93 Interpreted depositional history for State Road 95 (L10). Deposition of siliclastic silts and sands was occasionally influenced by the input of basaltic ash from rootless eruptions caused by explosive lava-water interactions (A-B). C) Lava flowed over the area and intruded down into the sediments, below.

6.7 Conclusions

6.7.1 Comparison of lithologies across the CRFBP

All the clastic units described in this chapter occur between lavas of the Saddle Mountains Basalt, which were emplaced *ca.* 15 to 6 Ma (Reidel et al. 2013). The localities in western Idaho (L9 and L10) are from older sections within the Saddle Mountains Basalts, compared to those of Washington (L1-8) that are found between the Umatilla, Pomona and Elephant Mountains Basalts (Figure 6-4). More generally these deposits are associated with the Pomona and Elephant Mountains Basalts and were likely deposited between *ca.* 11.5 and 10.5 Ma (Barry et al. 2013).

The Ellensburg Formation contains a variety of pyroclastic, siliciclastic and volcanoclastic rock-types, in addition to basaltic lavas. The emplacement of lavas does not appear to have influenced the clast-types deposited in any of the locations studied. However, lavas do appear to have influenced the position of major water bodies, for example, the ancestral Columbia River, which deposited thick units of quartzite-rich channel conglomerates and sand-bar cross-stratified sandstones. These conglomerates are clearly visible in the exposure at Snipes Mountains, leading previous authors to refer to these conglomerates at the 'Snipes Mountain Conglomerate' (Warren 1941; Waters 1965; Schmincke 1964; Smith 1988a, 1988b). In Idaho, the ancestral Clearwater River was most likely responsible for the transport and deposition of much of the sediment found between lavas in the Lewiston Basin. However, smaller streams and rivers most likely deposited sediments at State Road 95 (L10). Generally, siliciclastic material was eroded and transported from the north of the CRFBP, by rivers, such as, the ancestral Columbia, Naches, Yakima and Clearwater rivers (Mackin 1961; Waters 1965; Schmincke 1967a, b; Swanson et al. 1979; Smith 1988b).

Lavas frequently dammed and displaced fluvial systems, allowing the formation of lakes within the CRFBP. For example, a lake was present at Whitebird (L9; e.g. Nash & Perkins), where annual deposition of leaves and diatomite accumulated, undisturbed, for hundreds to thousands of years.

Deposition of clastic material within a fluvial system (including rivers, lakes and overbank settings) dominate the Ellensburg Formation, with occasional deposition from lahars and silicic pyroclastic eruptions, which could be considered as ‘catastrophic’ depositional events. Silicic volcanism was therefore a source of pyroclastic material, which was commonly reworked and re-deposited by streams and rivers.

No definitive time-markers can be identified within the siliciclastic deposits of the Ellensburg Formation, as lavas continually displaced fluvial systems and were not synchronous in their development across the entire CRFBP. However, marker units may be located from the eruption record of silicic pyroclastic and volcanoclastic deposits (e.g. Schmincke 1967). For example, Schmincke (1967b) suggested that the presence of ash aggregates, accretionary lapilli in particular, can act as a chronostratigraphic marker within the Ellensburg Formation, allowing correlation of deposits across the CRFBP. However, the preservation of pyroclastic material within the Ellensburg Formation gives an incomplete record of the explosive volcanism that occurred during emplacement of the CRFBP (e.g. Smith et al. 1988). Erosion of sedimentary units may have removed part of this record, and it is also possible that some regions did not experience deposition of grains all of the time, leading to a hiatus in the sedimentary record and an absence of volcanic deposits for that interval of time (e.g. Smith et al. 1988).

6.7.2 Lava-sediment interactions

The nature of the lava-sediment contacts varies between the different localities. In some places (e.g. L7) contacts are sharp, indicating that the lava was emplaced subaerially, whereas in other areas (e.g. L4 and L5) pillow lavas can be found, indicating that the lava was emplaced into water (Table 6-6; e.g. Schmincke 1967b). At State Road 95 (L10) the lava appears to have invasively intruded the underlying sediments, with little or no interaction, other than to displace blocks of partly consolidated sediment (Figure 6-76; Table 6-6; e.g. Reidel et al. 2013).

Lava			
Sediment			
Palaeo-environment			
Lava-sediment interaction	Lava flows over-top the well-consolidated sediments in a sub-aerial environment with no interaction	Lava reaches a region of moderately consolidated sediments. The first lava lobes invade the sediment forming irregular blobs of lava that are detached from the main body of the lava in cross-section.	Lava enters a shallow sub-aqueous environment where the surface sediments are poorly consolidated
Resulting deposit	Sharp sub-horizontal contact between the sediment and the overlying lava	Irregularly shaped blobs of lava surrounded by sediments which maintain any original sedimentary structures. The main body of lava over-rides the surface of the sediment above forming a slightly undulating contact	A thin unit of pillow lava forms with a fluidal undulating contact with the underlying sediment. The main body of the lava flow develops above the pillow lavas

Table 6-6 Types of lava-sediment interaction identified in the CRFBP during the present investigation. Three types of lava-sediment interaction have been identified from exposures within the CRFBP; 1) No interaction, where the lava flowed passively on top of the sediment. 2) Invasive sub-aerial interaction with moderately consolidated sediment. And, 3) Passive flow of lava into a sub-aqueous environment on top of a poorly to moderately consolidated sediment, where the lava formed pillows at its base and forms an irregular contact with the underlying sediment.

A glassy welded tuff is present directly below pillow lavas of the Pomona Basalt at Yellpit (L5; Figure 6-50). This lava had to have been emplaced at high enough temperatures ($>600^{\circ}\text{C}$), for a period of several days to fully weld the underlying clastic material to a depth of 10 cm below the lava (Schmincke 1967b). Lavas cool rapidly when emplaced into water (Reidel et al. 2013), with lobes of pahoehoe, like those responsible for the formation of the pillow lava, more likely to cool faster, regardless of subaqueous emplacement (Katternhorn & Schaefer 2008). Schmincke (1967b) suggests that the Pomona Basalt reached this locality (Schmincke's Selah Member of Ninemile Canyon), with a temperature of $1000 - 1200^{\circ}\text{C}$. In addition to high temperature, loading of the lava, and subsequent compaction of the underlying ash deposits helped to weld this material, along with a period of heating that lasted several hours (Figure 6-94; Schmincke 1967b).

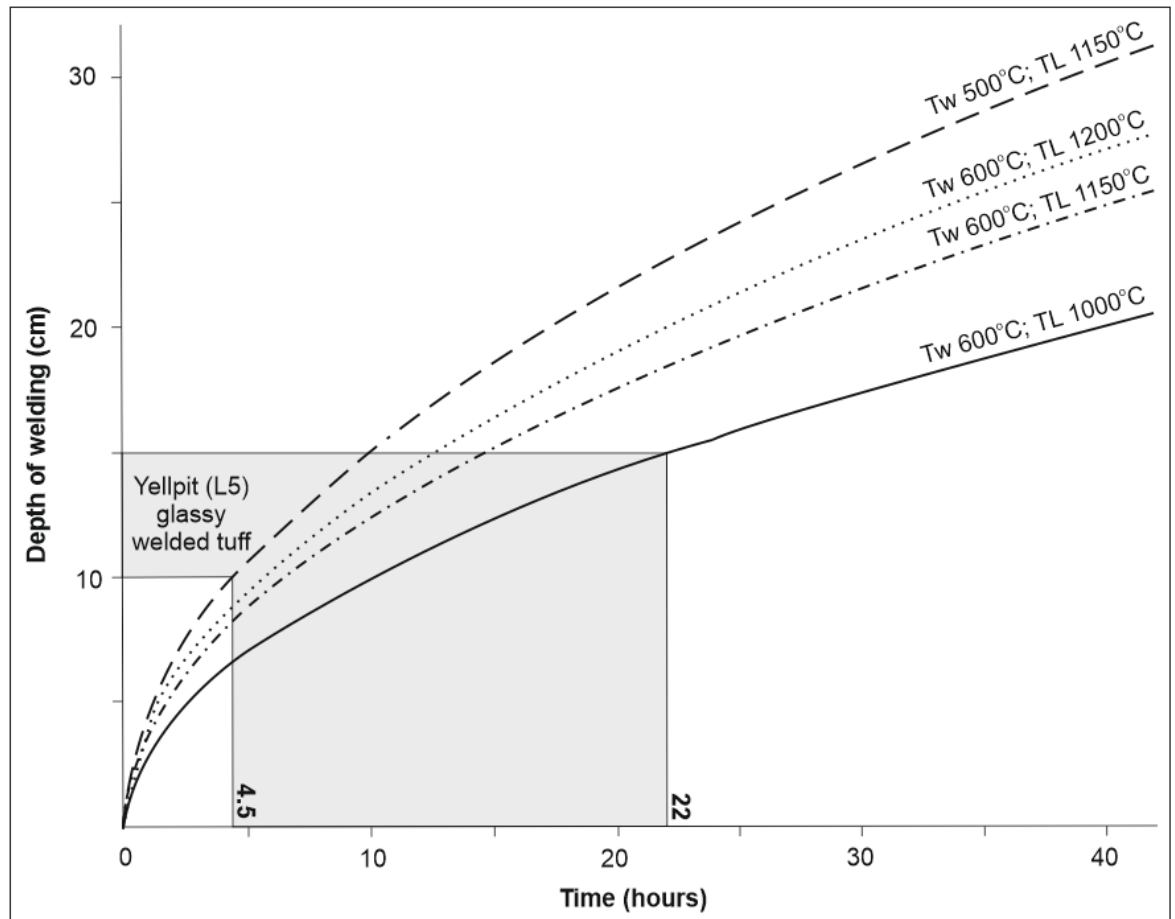


Figure 6-94 Temperature and duration of heating required for lava to weld an underlying tuff of X thickness. Welding of 10-15 cm is observed beneath the Pomona Basalt at Yellpit (L5; grey shaded region), using the calculations by Schmincke (1967b) this would require heating for 4.5 to 22 hours for a 1150°C and 1000°C lava respectively. Tw: welding temperature, the temperature required to weld silicic ash. TL: temperature of the lava.

This locality is likely >100 km away from the source fissures to the east (Figure 6-3), which suggests that the Pomona Basalt must have been erupted at high temperatures (>1100°C), and travelled rapidly with little loss of heat, to enable the lava to maintain high temperatures to allow welding of underlying deposits. Although the temperature of a lava naturally decreases with distance from source (e.g. Soule et al. 2004), lavas of pahoehoe type can rapidly form an insulating crust that allows them to maintain higher temperatures for greater distances and durations (Glaze & Baloga 2016).

Welding of the sediments below lava has not been identified below the lavas at any other location during this study. This suggests that the lavas at other localities had lower emplacement temperatures, below that required to weld the underlying materials.

6.7.3 Large-scale silicic volcanism recorded in the Ellensburg Formation, Washington

The basaltic lavas of the CRFBP can be used as marker units and allow for correlation of the clastic units of the Ellensburg Formation (Figure 6-95). Comparison of the depositional history of each locality (Figure 6-95), suggests that there were two periods of large-scale (Plinian or caldera-forming) silicic eruption(s), which deposited tephra across, or, supplied silicic tephra to be deposited within, the Ellensburg Formation. One of these periods occurred prior to emplacement of the Pomona Basalts, and involved tephra deposition directly from pyroclastic density currents (PDCs).

The second period of large-scale explosive silicic volcanism occurred after emplacement of the Pomona Basalts, and may be a continuation of the silicic volcanism from pre-Pomona Basalt times (Figure 6-95). Regardless, of this, the second period is characterised by reworked pyroclastic material, sourced from the products of large-scale silicic pyroclastic deposits from pre-Pomona Basalt times, and possibly from smaller-scale explosive eruptions outside of the CRFBP. Ancestral rivers flowed across the CRFBP from the north and NW (Waters 1965; Swanson et al. 1979; Smith 1988a, b), suggesting that volcanoclastic material from smaller-scale eruptions most likely came from eruptions in the Cascade Range to the north and NW.

Eruption of the Pomona and Elephant Mountains Basalts took place from *ca.* 11.5 to 10.5 Ma (Figure 6-4; Barry et al. 2013). These ages allow a rough estimation of the timing of the silicic volcanism, occurring sometime between 12- 10.5 Ma, prior to emplacement of the Pomona Basalts, and before eruption of the Elephant Mountains Basalts.

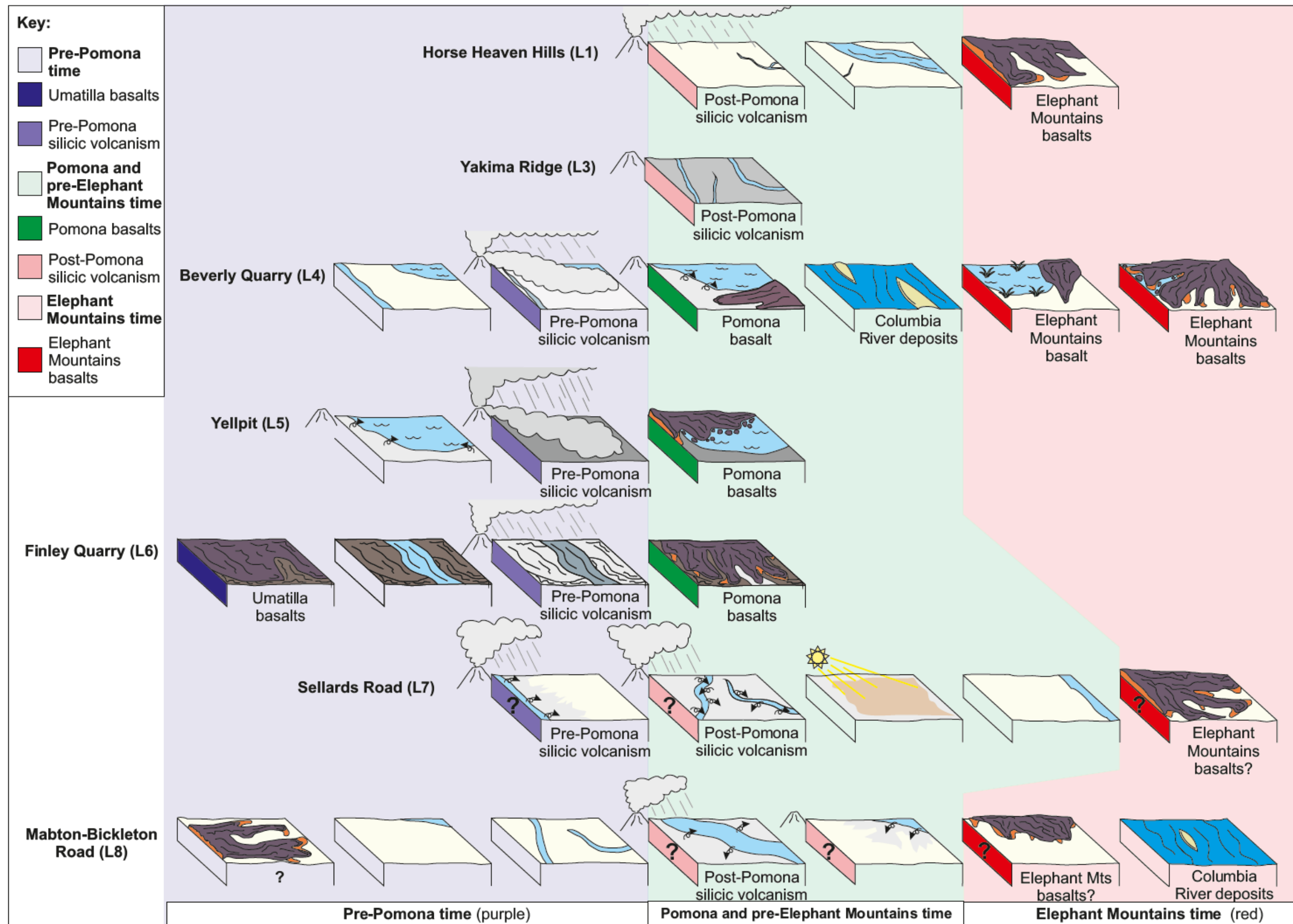


Figure 6-95 Correlation of lavas and clastic deposits across the field localities

6.7.3.1 *Diatoms in silicic pyroclastic deposits*

Rare centric, freshwater diatoms can be found within the volcanoclastic siltstone of Yellpit (L5), along with minor amounts of granular lithic clasts (Figure 6-53). Here, the diatoms were most likely incorporated into this deposit due to deposition within a lake. Pyroclastic and volcanoclastic material was also deposited in the lake, therefore the diatoms are an indication of the depositional environment.

Diatoms are also found in the sequence at Beverly Quarry (L4), where they occur within the fine-grained rims of ash aggregates (accretionary lapilli and coated ash pellets). Here, the diatoms are not found within deposits formed in their natural habitat, but instead, suggest that silicic eruptions interacted with diatom-bearing freshwater prior to deposition of these silicic ashes with their associated ash aggregates.

A high production of fine ash is needed for the formation of accretionary lapilli (Carey & Sigurdsson 1982; Gilbert & Lane 1994; Brown et al. 2012). This suggests that they are more likely to form during highly explosive eruptions (e.g. hydrovolcanic or highly silicic), which involve sufficiently high levels of fragmentation to produce large volumes of fine ash (e.g. Carey & Sigurdsson 1982; Gilbert & Lane 1994; Brown et al. 2010, 2012). Accretionary lapilli are commonly associated with air-fall deposits, although increasing evidence suggests that they can form in a range of different ways (Schumacher & Schmincke 1991; Lane et al. 1993; Scolamacchia et al. 2005; Brown et al. 2010, 2012). These are summarised in Figure 6-96, as:

1) Magma-water interactions at the vent, for example, an eruption through a crater lake or glacier, increases the moisture content within, or close to, the vent; hydrovolcanic eruptions can lead to the formation of accretionary lapilli and other ash aggregates. Ash-aggregates can form in the slurry of ash and water (Brown et al. 2012).

- 2) Turbulence within an ash cloud, particularly one with a high moisture content, can lead to aggregation of ash by the binding of 'sticky' particles. Layering of different grain-sizes can occur as the aggregate is transported through areas of different grain-size through the cloud during turbulence (Brown et al. 2010, 2012).
- 3) Air-fall of aggregates through different regions of the eruption cloud can lead to concentric grain-size layering and the formation of accretionary lapilli. This can also happen during fall-out from a co-PDC cloud or lofted ash plume (Scolamacchia et al. 2005; Brown et al. 2010).
- 4) The moisture content of the ash-cloud and the atmosphere can influence the formation of aggregates, for example those with a higher moisture content enhances aggregation of fine ash (Moore & Peck 1962; Carey & Sigurdsson 1982; Bohor & Triplehorn 1984; Cas & Wright 1988; Schumacher & Schmincke 1991; Gilbert & Lane 1994; Schumacher & Schmincke 1995; Sparks et al. 1997; James et al. 2003; Brown et al. 2012; Van Eaton et al. 2012).
- 5) The processes described in 4 can be achieved by the formation of hydrometeors or ice-rimming of the ash at higher altitudes (Carey & Sigurdsson 1982; Gilbert & Lane 1994; Schumacher & Schmincke 1991; Veitch & Woods 2001; Textor et al. 2006; Brown et al. 2010, 2012).
- 6) Electrostatic forces can build up in ash within a turbulent ash cloud, which can lead to static attraction between particles and the formation of aggregates (Carey & Sigurdsson 1982; Sorem 1982; Reimer 1983; Gilbert & Lane 1994; Schumacher & Schmincke 1991, 1995; James et al. 2003; Brown et al. 2010, 2012).
- 7) Turbulence in a PDC can lead to concentric layering of aggregates and the formation of accretionary lapilli in the same way as turbulence within the ash cloud itself (Cas & Wright 1988; Schumacher & Schmincke 1991, 1995; Brown et al. 2010).

8) Turbulence as described in 7 is also applicable to the formation of accretionary lapilli within a co-PDC cloud or lofted ash plume (Kato 1986; Schumacher & Schmincke 1991, 1995; Durant & Ernst 2001; Scolamacchia et al. 2005; Textor et al. 2006; Brown et al. 2010; Mueller et al. 2016).

9) Meteorological conditions may affect aggregate formation, for example, ash-fall interactions with rain, can allow for fine ash to be scavenged by rain-drops and lead to the formation of aggregates (Cas & Wright 1988; Brown et al. 2012).

10). Post-depositional processes imply that aggregation does not have to occur during an eruption but may happen after deposition has taken place (e.g. Cas & Wright 1988), for example, clumps of ash which may be linked by the interaction of jagged surfaces as loose interlocking clumps can roll around an ash-mud substrate and aggregate layers (E.g. Moore & Peck 1962). Rainfall on fresh ash deposits has also been suggested for a mode of aggregate formation in this way (Moore & Peck 1962). Ash-aggregates may also form by the oscillation of ash within a water body or on a shore face. Thus, their formation may be syn-depositional or post-depositional, and may involve multiple processes

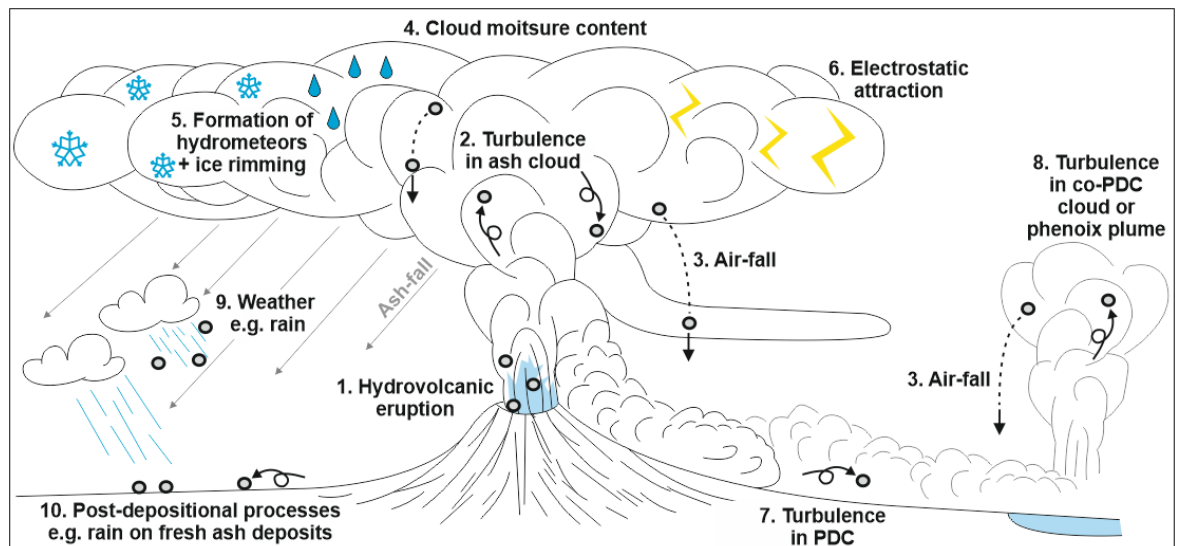


Figure 6-96 Various controls on the formation of accretionary lapilli and other ash aggregates. Descriptions and references in text.

Diatoms could become incorporated into pyroclastic deposits, and within ash aggregates, in a variety of ways, as summarised in Figure 6-97:

- 1) Freshwater diatoms present within a lake may become incorporated into the ash cloud if the eruption occurs through the lake, for example, an eruption through a crater lake that contains diatoms.
- 2) Extreme weather events may loft diatoms up with water particles, for example, during strong evaporation or atmospheric currents across a lake, they might then interact with ash if the weather system and eruption plume combine, or when rain scavenges the diatoms and ash out of the atmosphere.
- 3) Movement of turbulent and erosive PDCs may pick up diatoms or diatom-bearing sediments from the ground over which it travels (e.g. Fauria, et al. 2016).
- 4) When a PDC intersects a lake, ash and lake water, with diatoms, may be explosively ejected into the air.
- 5) Alternatively, deposition of ash from a PDC into a lake, or from ash-fall into the lake could allow diatoms within the lake water to be deposited with ash .
- 6) Post-depositional reworking of ash may lead to the incorporation of diatoms from loose diatom-bearing sediments, this interaction could also occur on the shore of a lake.

The accretionary lapilli and ash pellets in this study have hard outer shells that are preserved as fragments as well as whole aggregates. The presence of this 'shell' has allowed these aggregates to be preserved in the rock-record, which otherwise would be unlikely (Carey & Sigurdsson 1982; Rosi 1992; Taddeucci et al. 2011; Brown et al. 2012). The 'shell' most likely formed prior to deposition, to prevent the aggregate from falling apart upon deposition (Gilbert & Lane 1994; Sparks et al. 1997; James et al. 2003).

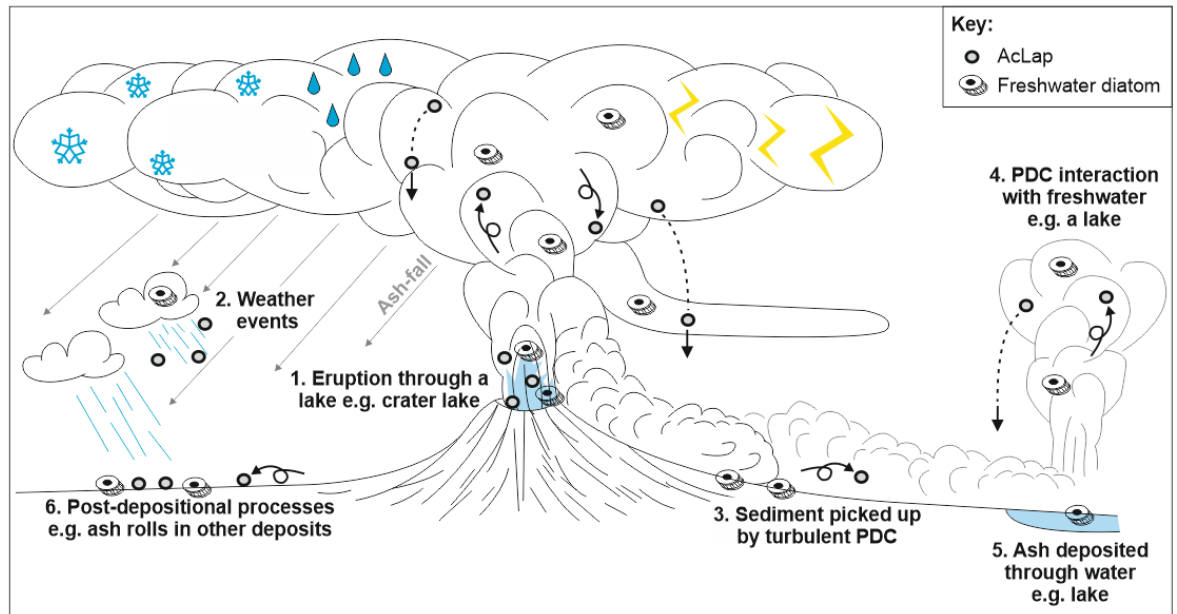


Figure 6-97 Processes responsible for the incorporation of freshwater diatoms into eruption settings and ash aggregates. Descriptions and references in the text.

At Beverly Quarry there are at least three beds containing ash aggregates, and which are found in continuous sub-horizontal intervals within a silicic tuff, in the quarry face (Figure 6-23), and in deformed beds (Figure 6-24). The deposits are associated with rapid lateral and vertical changes in the deposit's characteristics. The sequence of at least three intervals of aggregate-bearing material implies that deposition of ash aggregates was not continuous throughout the eruption and material was deposited during at least three separate periods. These aggregates may have formed when pyroclastic density currents (PDCs) travelled over this area and interacted with the fluvial system that was present, as implied by the overbank, lacustrine and river-channel deposits below and above this unit (see section 6.5.4.2). Each time a PDC arrived and interacted with the water of this fluvial system, lofted ash-plumes of steam and ash may have risen into the atmosphere (Figure 6-98; Brown et al. 2007). Within such a plume, moisture could have acted as a hydrophobe, binding ash together, forming an ash aggregate. Stratification of ash within the cloud may have allowed for different grain-sizes to be scavenged at different times, as the growing aggregate became denser and settled out of the air, forming concentric laminae (Choux et al. 2004; Brown et al. 2010, 2012). Diatoms present within the fluvial system could have been incorporated into the lofted

ash-plume along with water (Figure 6-98). The diatoms would most likely be scavenged with very fine ash by the growing aggregate.

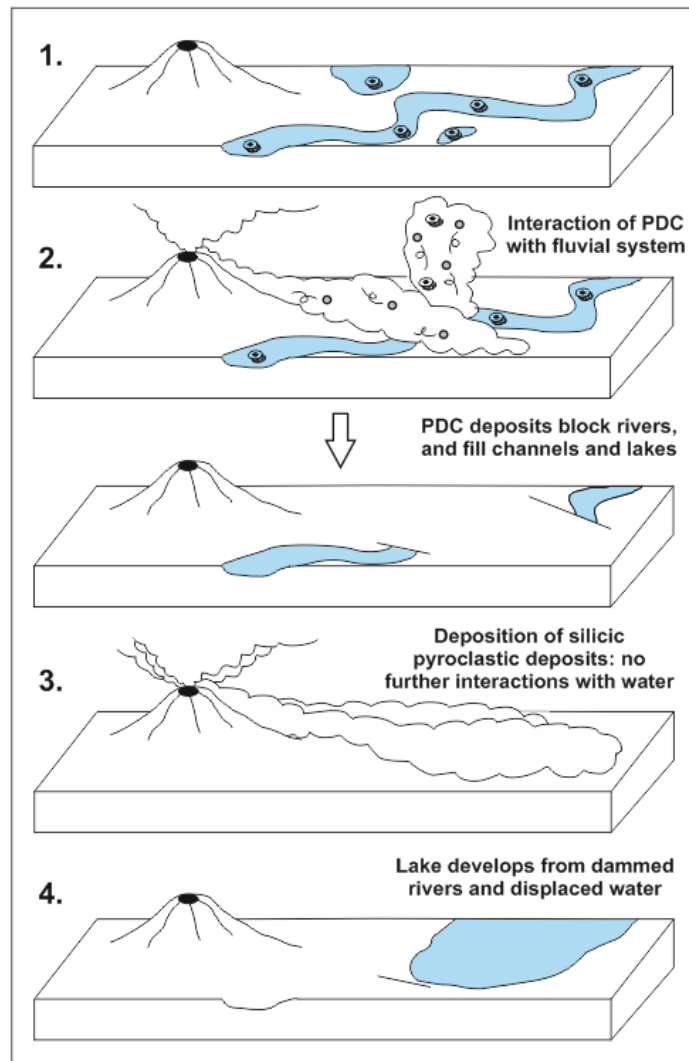


Figure 6-98 Interpreted scenario for the formation of diatom-bearing ash aggregates at Beverly Quarry (L4). PDCs travel across the area and interact with a fluvial system. The interaction causes lofting of the PDC ash plume, which incorporates diatom-bearing water. The turbulence and increased moisture content of the plume allows ash aggregates to form due to the presence of hydrophobes. Diatoms are scavenged with very fine-ash into the outer rims of the aggregates and subsequently fall out. This scenario is repeated at least three times until water is no longer present in sufficient quantity for PDC-water interactions to occur. The PDC deposits block rivers and fill channels and lakes leading to the deposition of PDC material with no ash aggregates. Damming of rivers by the PDC deposits leads to the development of a lake, in which, reworked pyroclastic material is deposited in the lake as parallel laminated pumicite.

All the time that water remained present in the fluvial system, any subsequent PDCs would react with it in the same way. Over time, the river channel would become blocked with pyroclastic deposits that could either displace, dam, or, divert the flow of water (Figure 6-98; e.g. Gihm & Hwang 2014). Damming by

PDC deposits most likely led to the growth of a lake, which subsequently allowed the deposition of parallel-laminated pumicite, comprising reworked pyroclasts and granular lithic clasts (Figure 6-98). Migration of the main Columbia River channel over this area later introduced the quartzite-rich conglomerates and thick cross-stratified sandstones present above the pyroclastic deposits of the main quarry-face.

6.7.3.2 Source areas for the silicic pyroclastic material of the Ellensburg Formation around Pomona Basalt time

Chemical fingerprinting of the pyroclastic and volcanoclastic tuffs of this study was not a primary objective and has not been carried out. However, future studies of this material could allow a more definitive interpretation for the source of these deposits. Regardless of this, the stratigraphy of each locality and comparison to the published literature provide information to help assess the possible source(s) of this material.

The pyroclastic and volcanoclastic units studied here are all silicic, except for one basaltic ash (ID_13) that may have been produced by explosive fissure eruptions (see section 6.6.2.2; Head & Wilson 1989; Brown et al. 2015), or, produced by explosive lava-water interactions (see section 6.6.2.2; Branney et al. 2008; Hamilton et al. 2010; Reynolds et al. 2015; Fitch et al. 2015). The silicic tuffs had a different source, most likely outside of the CRFBP (Waters 1965; Smith 1988a, b; Smith et al. 1988; Perkins et al. 1995, 1998; Retallack et al. 2002; Cathey & Nash 2004; Branney et al. 2008; Streck & Grunder 2008; Ellis et al. 2012; Nash & Perkins 2012; Ellis et al. 2013; Kent-Corson et al. 2013; Knott et al. 2016).

Highly explosive eruptions have been interpreted for all of the tuffs, based on pyroclast morphology. Rod-like, and blocky morphologies are the most abundant (Figure 6-83), indicating that magmatic fragmentation, for example, by the expansion of gases, occurred with little or no hydrovolcanic influence. Vesicularity could not be used to assess the explosivity of the eruption, due to the large amount of fine-grained clasts (Figure 6-80, Figure 6-81), representative of the most efficient levels of magma fragmentation, which produces more non-vesicular pyroclast types as the fine-scale bubble-walls are more likely to

fragment during eruption, transport and deposition (Table 6-4; e.g. Graettinger et al. 2013; See Chapter 7). This leads to the preservation of fine-ash as non-vesicular and poorly vesicular types (Table 6-4, Table 6-5). The abundance of fine-ash (<1mm) in these samples is indicative of distal ash-fall, although reworking and re-deposition within the sedimentary environment may have caused secondary grain-size sorting of these deposits.

Several areas within continental USA may be the source of the pyroclastic and volcanoclastic material of the Ellensburg Formation. It is known, from ^{40}Ar - ^{39}Ar dating that large-scale, highly explosive eruptions occurred to the west of the CRFBP within the Cascade Range between 16.7 and 8 Ma (Camp et al. 2017), and to the SE within the Snake River Plain/Yellowstone (SRP) hotspot track (Perkins et al. 1995; Cathey & Nash 2004; Bonnicksen et al. 2008; Branney et al. 2008; Nash & Perkins 2012; Ellis et al. 2013; Knott et al. 2016; Camp et al. 2017). It is likely that many of the eruptions from both the Cascade Range and SRP-hotspot deposited air-fall ash across the CRFBP. For example, large Plinian eruptions occurring within the Bruneau-Jarbridge volcanic region of the SRP between 12.8 and 8 Ma deposited ash up to 1600 km distant (Nash & Perkins 2012), and therefore could have caused ash-fall across the entire CRFBP (Figure 6-99). These eruptions could not have been the source of PDCs interpreted within the deposits at Beverly Quarry (L4; see section 6.7.3.1), as this volcanic region lies >200 km away, and the largest documented PDCs only travel 150 km from source (Figure 6-99; Wilson et al. 1995; Streck & Grunder 2008). Instead, it is more likely that PDCs from eruptions in the Cascade Range are the source of this material.

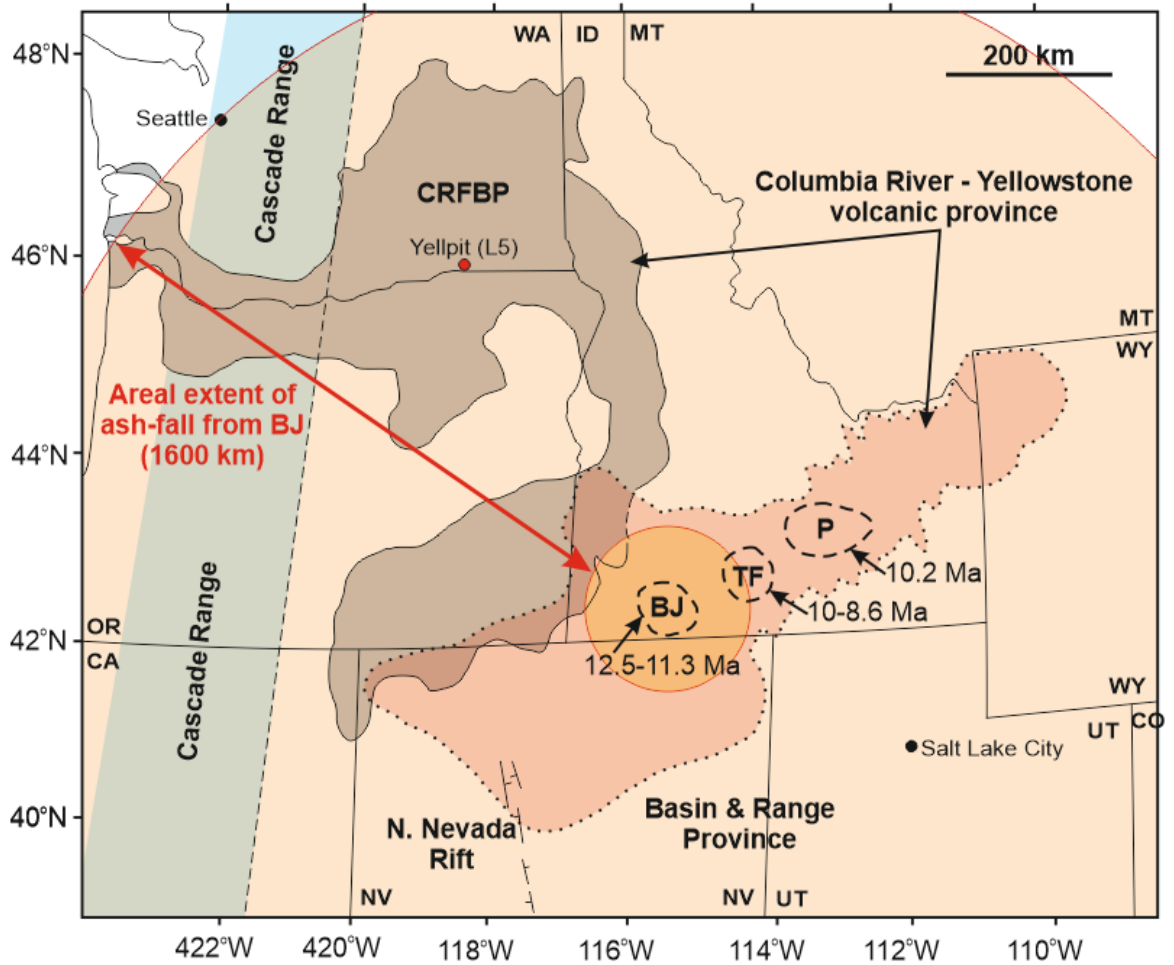


Figure 6-99 Location of various volcanic centres that were active 12-10 Ma around the CRFBP. (Branney et al. 2008). Bruneau-Jarbridge (BJ), Twine Falls (TF) and Picabo (P) are all volcanic centres within the Snake River Plain/Yellowstone volcanic province that experienced large-scale silicic eruptions at 12.5-11.3 Ma, 10-8.6 Ma, and 10.2 Ma, respectively. Orange shading represents the area over which fall-out may have occurred from rhyolitic Plinian eruptions that cover an area up to 1600 km from BJ (Nash & Perkins 2012). The inner orange circle indicates where deposits from pyroclastic density currents might be found based on previous studies of PDC run-out distances (within 200 km; e.g. Wilson et al. 1995; Streck & Grunder 2008).

If the ash aggregates of Beverly Quarry (L4), and Yellpit (L5) are reconsidered as ash-fall deposits, then a source within the Cascade Range is still the most likely source based on the distribution of ash aggregates produced by the 1980 sub-Plinian eruption of Mount St. Helens within the Cascade Range. This eruption involved a weak hydrovolcanic component, which led to ash aggregation: the aggregates fell out within 150 km of the volcano, with secondary thickening of the ash deposits, and further aggregate deposition, up to 350 km away, spanning the majority of the CFRBP of Washington from west to east (Figure 6-100).

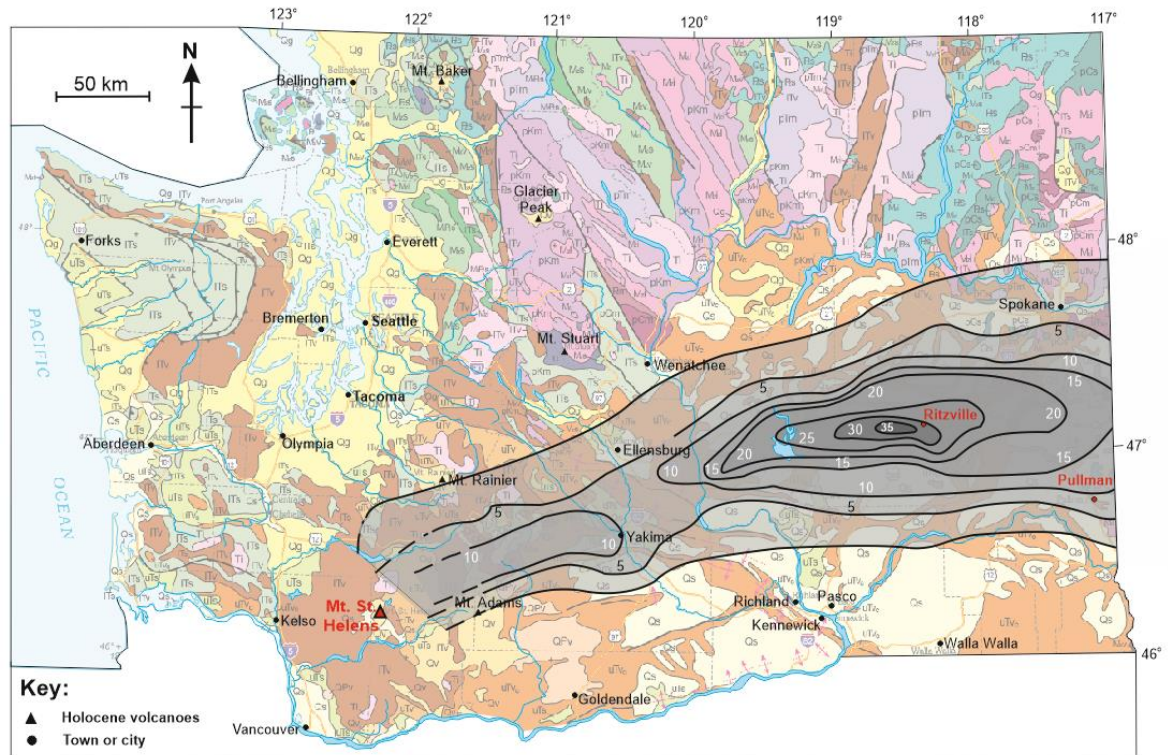


Figure 6-100 Isopach map showing the extent of silicic air-fall ash deposition from the eruption of Mount St Helens 1980. Ash-aggregates fell in Pullman (Carey & Sigurdsson 1982). Thicknesses are given for 10 mm contours are rain-compacted thicknesses (Carey & Sigurdsson 1982); the thickest deposits are found near Ritzville, representing a secondary thickening distally from the source. The secondary thickening was likely caused by aggregation scavenging fine ash closer to the source (Carey & Sigurdsson 1982). Shown on the geological map of Washington (from the Washington Division of Geology and Earth Resources 2013).

The presence of lahar deposits at Snipes Mountain (L2) indicate that volcanic activity in the Cascade Range was a source for volcaniclastic material within the CRFBP. Lahars often accompany explosive eruptions and are known from historic eruptions within the Cascade Range (e.g. Mount St Helens). It is therefore likely that pyroclastic and volcaniclastic deposits within the Ellensburg Formation were produced by eruptions occurring in both the Cascade Range and the SRP. Rivers draining the eastern margin of the Cascade Range during the Miocene may have supplied additional silicic volcaniclastic material to the basins of the CRFBP from smaller eruptions that would not have necessarily deposited distal ash fall across the CRFBP.

Chapter 7: Discussion and conclusions

7.1 Summary

Large-scale explosive eruptions produce ash that can be deposited and preserved as tuffs in both proximal and distal settings, up to hundreds of kilometres away from their source vent(s). These Plinian-scale eruptions are commonly associated with ‘dry’ magmatic eruptions of silicic magmas; however, an increasing record of basaltic Plinian-scale eruption deposits is being recognised in the literature (Walker et al. 1984; Hanson & Elliot 1996; Houghton et al. 2004; White et al. 2004; Gurenko et al. 2005; Sable et al. 2006; Carey et al. 2007; Kutterolf et al. 2007; Houghton & Gonnermann 2008; Costantini et al. 2009; Pérez et al. 2009; Costantini et al. 2010; Goepfert & Gardner 2010; Freda et al. 2011; Brand & Clarke 2012; Oddsson et al. 2012; Szramek 2016).

One way that a basaltic magma can erupt more explosively is via magma-water interactions, particularly where eruptions occur in shallow marine settings (Wohletz 1983; Clarke et al. 2009; Dellino et al. 2012). The characteristics of the resultant deposits, together with grain-scale features of the component tephra, can provide information on the eruption and depositional processes (Heiken 1972, 1974; Walker 1981; Wohletz 1983; Wohletz & Sheridan 1983; Carey & Sparks 1986; Cas & Wright 1988; Barberi et al. 1989; Houghton & Wilson 1989; Cioni et al. 1992; Blower et al. 2001; Riley et al. 2003; Gaonac’h et al. 2005; Houghton & Gonnermann 2008; Polacci et al. 2008; Clarke et al. 2009; Rose & Durant 2009; Mattsson 2010; Shea et al. 2010; Bonadonna et al. 2011; Brown et al. 2012; Ross & White 2012; Graettinger et al. 2013; Moitra et al. 2013; Cioni et al. 2014; D’Orlando et al. 2014; Heap et al. 2014). The research presented here provides details of the differences between the pyroclast morphologies of highly explosive basaltic and silicic eruptions, in addition to evaluating the characteristics of fine-ash to distinguish eruption processes in distal deposits. Additionally, evidence is presented for the discrimination of pyroclastic and volcaniclastic material in various onshore and offshore depositional settings.

In Chapter 2 the nature and origin of the Saksunarvatn Ash from the *ca.* 10.3 ka highly-explosive basaltic eruptions of the Grímsvötn Volcano are presented for

three field localities in Iceland. This analysis provides an introduction to relatively unaltered and non-lithified ash deposits, and the grain-morphologies used to interpret eruption style and post-eruption reworking and re-deposition. The main findings of this chapter are:

- Multiple explosive eruptions involving magma-water interactions (hydrovolcanic processes) deposited ash and fine-ash to the west and northwest of Grímsvötn Volcano. In this example, glacial ice and meltwater are a likely source for the water in these magma-water interactions, as the volcano is located beneath Iceland's largest glacier: Vatnajökull.
- The Saksunarvtn Ash is homogenously basaltic (e.g. Andrews et al. 2002; Jennings et al. 2002; Gudmundsdóttir et al. 2011; Thornalley et al. 2011; Bramham-Law et al. 2013; Lind et al. 2013; Lohne et al. 2013; Jennings et al. 2014; Neave et al. 2015) but the deposits locally include ash from a more silicic magma, suggesting that at times multiple explosive eruptions occurred simultaneously from different sources *ca.* 10.3 ka in Iceland.
- The Saksunarvtn Ash comprises several hydrovolcanic ash deposits that are dominated by blocky non- to poorly-vesicular pyroclast morphologies, which are indicative of brittle fragmentation caused by rapid quenching of hot pyroclasts in contact with water (e.g. Heiken 1972, 1974; Wohletz 1983; Wohletz & Sheridan 1983; Cas & Wright 1988; Zimanowski et al. 1997; Mattsson 2010; Dellino et al. 2012; Ross & White 2012; Graettinger et al. 2013; LaRue et al. 2013). Crystalline igneous clasts/accidental lithic clasts are abundant in these deposits and indicate that explosive interactions between the erupting magma and water most likely took place within the vent or conduit (e.g. Graettinger et al. 2013), leading to fragmentation and incorporation of pre-existing rocks.
- 'Fresh' pyroclasts that have undergone little to no reworking tend to have smooth edges and empty vesicles, with a limited amount of alteration of the original glass. If the deposit in general is devoid of siliciclastic or volcanoclastic clast-types or sedimentary structures, such as, cross-

stratification or ripple-laminations, then the deposit may be considered as pyroclastic, or having undergone little additional transport prior to final deposition (discussed in detail below 7.3).

- Reworked pyroclasts have jagged/rough edges as a result of abrasion, and their original glass has commonly begun to alter. Vesicles are typically infilled with fine-grained matrix material and the pyroclasts are found alongside an array of other clast-types, including granular lithic clasts and fine-grained matrix material.

In Chapter 3 the characteristics of basaltic ash are assessed further by analysis of marine tuffs in cores of the Early Eocene North Sea Balder Formation. These tuffs are interbedded with marine claystones, siltstones and sandstones and the deposits of submarine fans. The tuffs are almost entirely basaltic and were associated with explosive volcanism in the North Atlantic Igneous Province *ca.* 54 - 54.5 Ma (Jacqué & Thouvenin 1975; Deegan & Scull 1977; Knox & Harland 1979; Knox & Morton 1983; Lott et al. 1983; Mudge & Bliss 1983; Malm et al. 1984; Roberts et al. 1984; Knox & Morton 1988; Vierick et al. 1988; Morton & Knox 1990; Jolley & Morton 1992; Knox & Holloway 1992; Mudge & Copestake 1992a; Hitchen & Ritchie 1993; Ebdon et al. 1995; Waagstein & Heilmann-Clausen 1995; Ali & Jolley 1996; Knox 1996; Mudge & Bujak 1994, 1996; Ritchie & Hitchin 1996; Nadin et al. 1997; Haaland et al. 2000; Smallwood & Gill 2002; Jolley & Bell 2002; Mudge & Jones 2004; Jolley & Widdowson 2005; Ross et al. 2005; Dmitrieva et al. 2012; Aldiss 2014; King 2016). The main findings of this chapter are:

- Deposition of sediments and ash in the North Sea Basin most likely occurred in a restricted lake-like marine basin with a stratified water column. Anoxic conditions within or above the water-sediment interface are implied by an abundance of pyrite framboids, pyrite cement and rare pyritised micro-fossils throughout the Balder Formation, as well as an absence of bioturbation/trace-fossils or micro-fauna and -flora (e.g. Knox & Harland 1979; Morton & Knox 1990; Mudge & Bujak 1994, 1996; Knox 1996).

- Pelagic settling was the dominant mode of deposition for the majority of the Balder Formation sediments and ashes throughout the North Sea Basin, as indicated by an abundance of laterally-extensive, fine-grained siltstones and claystones and normal-graded tuffs.
- Originally glassy pyroclasts have undergone palagonitisation and subsequent replacement by clay and/or calcite. However, in many cases the original features of these pyroclasts have been preserved, allowing the identification and classification of their features.
- The originally glassy pyroclasts of the Balder Formation tuffs are predominantly blocky and non- to poorly-vesicular. The low vesicularity of the pyroclasts suggests that the parent magma was not significantly volatile-rich. Therefore, it is unlikely that the volatile content of the magma(s) was responsible for these highly-explosive eruptions of basaltic magma. The morphologies of the pyroclasts indicate that hydrovolcanism could be a likely cause of the explosivity and production of fine-ash.
- The dominant clast-type in the tuffs is not pyroclasts, but microcrystalline lava-like clasts with irregular or fluidal morphologies. These clast-types and the blocky non-vesicular pyroclasts are similar to features identified in ash from Surtseyan eruptions (Walker 1973; Pedersen & Jørgensen 1981; Kokelaar & Durant 1983; Cas & Wright 1987; Pyle 1989; Haaland et al. 2000; Dellino et al. 2001; Mattsson et al. 2010; Gjerløw et al. 2015). However, Surtseyan eruptions deposit ash on a relatively small scale (within 50 km; Machado et al. 1962; Corcoran & Moore 2008; Mattsson 2010; Vaughan & Webley 2010; Gjerløw et al. 2015) that would not distribute ash on the scale observed by the Balder Formation tuffs (≥ 1000 km). Surtseyan eruptions are also associated with monogenetic volcanism and would require the presence of hundreds of proximal volcanic edifices within the North Sea Basin, for which there is no evidence (Pedersen & Jørgensen 1981; Kokelaar & Durant 1983; Morton & Knox 1990; Walker 1993; Solgevik et al. 2007; Corcoran & Moore 2008; Gjerløw et al. 2015; Moorehouse et al. 2015).

- Multiple Plinian-scale explosive hydrovolcanic eruptions are a likely source for the production, distribution and deposition of basaltic ash within the North Sea Basin in the Early Eocene. With magma-water interactions likely associated with eruptions occurring within a shallow marine setting. It is possible that these eruptions may have been associated with initial sea-floor spreading and the presence of the proto-Icelandic mantle plume that may have led to the production of large volumes of basaltic magma during separation of Greenland from NW Europe, and formation of the North Atlantic Igneous Province (Pedersen et al. 1975; Pedersen & Jørgensen 1981; Knox & Morton 1983; Roberts et al. 1984; Knox & Morton 1988, 1990; Kanaris-Sotiriou et al. 1993; Mudge & Bujak 1994; Knox 1996; Ritchie & Hitchen 1996; Nadin et al. 1997; Saunders et al. 1997; Larsen et al. 1999, 1999a; Kent & Fitton 2000; Skogseid et al. 2000; Jolley & Bell 2002; Larsen et al. 2003; Thomas & Bralower 2005; Breivik et al. 2006; Brooks 2006; Breivik et al. 2009; Passey & Jolley 2009; Stoker et al. 2012; Obst et al. 2015).
- Many of the Balder Formation 'tuffs' are the result of reworking and re-deposition of ash that was originally deposited onshore and offshore. Therefore, many of the tuffs are actually volcanoclastic siltstones and sandstones.
- An adaptation to the nomenclature for primary pyroclastic and volcanoclastic deposits is recognised as being needed for the description of water-lain tuffs and ashes; this is discussed in detail below (see section 7.4)

In Chapter 4 the nature of the Balder Formation is assessed for the Faroe-Shetland Basin from the interpretation of seismic and wire-line data from UK Continental Shelf Quad 204. Variation in the wire-line response, particularly for gamma-ray and sonic response, shows that the Balder Formation is comprised of a range of lithologies, including claystone, sandstone, limestone, coal and tuffs. Sandstone and coals are common in the south of Quad 204 and are interpreted as a prograding delta facies, the units become more dominated by marine claystones towards the north. An anomalous reflector was observed in 3D seismic

lines in the northern section of Quad 204, this corresponds to a high-gamma ray anomaly in the wire-line that has been interpreted as indicating the presence of basaltic volcanic material. This anomaly is localised and correlates with the presence of a palaeo-shoreline in 3D seismic models. The RGB blended spectral decomposition for this area shows that lavas underlie the Balder Formation at this locality and that a meandering river channel cuts through these to supply material to the Balder Formation. It is therefore likely that the seismic and high-gamma ray anomalies are associated with the presence of basaltic-clast-rich sediments produced by erosion of the underlying basalt lavas that were deposited by rivers into a shallow marine setting that became preserved within the Balder Formation.

In Chapter 5 the lithologies of the Early Eocene Wrabness Member of the Harwich Formation of SE England are critically analysed for the presence of basaltic tuffs. This Member is exposed onshore but is laterally and chronostratigraphically equivalent to the Balder Formation of the North Sea Basin (Knox & Ellison 1979; Knox & Morton 1983; Mudge & Bliss 1983; Malm et al. 1984; Roberts et al. 1984; Knox & Morton 1988; Morton & Knox 1990; Ellison et al. 1994; Jolley 1996; Knox 1996; King 2016). The non-volcanic sediments and ashes of this Member were originally deposited within a shallow marine environment that was an extension of the southern North Sea Basin during the Early Eocene. The main findings of this chapter are:

- The Wrabness Member is predominantly composed of clay-rich siltstones that were deposited in an oxygenated shallow-marine setting, as indicated by high levels of bioturbation.
- Lithological logging of the Shotley Borehole core allows sub-division of the Wrabness Member into three parasequences. These may be attributed to at least three phases of marine transgression.
- Stratification of the sequence, observed in the field, is not seen in the core of the Shotley Borehole and does not appear to correspond to the presence of tuffs interbedded with siliciclastic material as suggested in

the literature (Elliott 1971; Knox & Ellison 1979; Ali & Jolley 1996; Jolley 1996).

- Systematic sampling of pale-grey and brown/grey layers in the field and detailed thin-section analysis shows that the Wrabness Member does not contain 44 (Knox & Ellison 1979) or 32 (Jolley 1996) basaltic tuffs. Instead, only two basaltic tuffs were positively identified.
- The two tuffs were most likely deposited as water-lain ash, produced by hydrovolcanic eruptions, as indicated by the dominance of blocky, non- to poorly-vesicular pyroclasts, with >50 % crystalline igneous/accidental lithic clasts, and normal-grading of the deposit.
- One tuff is preserved in the calcite-cemented Harwich Stone Band located within the Wrabness Member. Cementation of this unit appears to have occurred early during diagenesis as suggested by the relatively 'fresh' appearance of glassy pyroclasts that have only undergone limited palagonitisation or additional alteration. The relatively fresh nature of these pyroclasts and their angular and smooth edges, suggest that little to no reworking of this material has occurred.
- The Wrabness Blue Band is a blue clay layer above the Harwich Stone Band and contains rare altered pyroclasts. These pyroclasts represent significantly <50 % of the deposit. Consequently, this deposit is a siliciclastic claystone with only a minor component of volcanoclastic clast-types (see terminology of section 7.4).

Chapters 3 and 4 review tuffs that were likely deposited from the same period of explosive basaltic volcanism in the North Atlantic Igneous Province during the Early Eocene. The two tuffs of the Harwich Formation of E. Anglia correlate to >200 tuffs of the North Sea Balder Formation (Knox & Ellison 1979; Knox & Morton 1983; Mudge & Bliss 1983; Malm et al. 1984; Roberts et al. 1984; Knox & Morton 1988; Morton & Knox 1990; Ellison et al. 1994; Jolley 1996; Knox 1996; King 2016). The deposits in E. Anglia therefore provide data for more southerly and distal localities. It could therefore be expected that the grain-size of the

pyroclasts within the Harwich Formation would be less than those of the Balder Formation further north, if the source lay within the opening NE Atlantic rift; due to the concept of grain-size decreasing with increasing distance from source. However, comparison of the grain-size distribution of all samples shows that the Harwich Formation (E.Anglia) tuffs have a grain-size similar, or coarser than those of the Balder Formation (Figure 7-1). This could suggest that the sampled tuffs between each locality are not directly comparable, for example, due to a larger number of samples from the Balder Formation. Alternatively, the aggregation of ash closer to the vent, may allow an increase in the deposition of fine-ash closer to source with coarser-grade material being deposited in more distal localities (Carey & Sigurdsson 1982; Gilbert & Lane 1994; Brown et al. 2010, 2012). Ash aggregates are more likely to form from hydrovolcanic eruptions where there is a large amount of fine-ash that can be scavenged by water droplets or be bound by the formation of hydrometeors (see section 6.7.3.1; Carey & Sigurdsson 1982; Gilbert & Lane 1994; Brown et al. 2010, 2012). Comparison of the grain-size distribution for all of these Early Eocene samples could therefore be further evidence to support the interpretation of hydrovolcanic eruption processes for the basaltic tuffs of the Harwich Formation, and at least some of the tuffs of the Balder Formation.

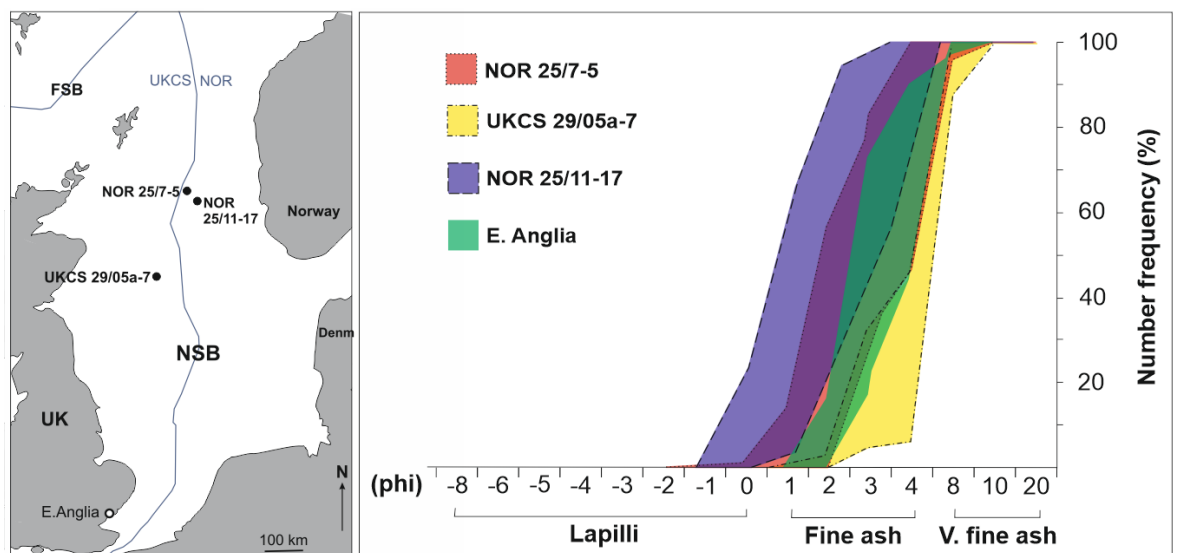


Figure 7-1 Comparison of the grain-size distribution of basaltic tuffs from the Balder and Harwich formations. Balder Formation, North Sea Basin data from wells NOR 25/7-5 (red), 25/11-17 (blue) and UKCS 29/05a-7 (yellow). Harwich Formation, E.Anglia (green). Map to the left shows the location of each well/locality.

In Chapter 6 the non-lava lithologies of the Miocene Ellensburg Formation of the Columbia River Flood Basalt Province, USA are investigated to provide an understanding of sedimentary and pyroclastic processes within a terrestrial flood basalt province. This investigation was carried out to contribute new data and insights into pyroclastic and volcanoclastic processes that contrast with the results from the North Atlantic Igneous Province and distal deposits associated with rifting and sea-floor spreading (chapters 3-5). This analysis also provided a comparison of silicic pyroclastic and volcanoclastic deposits from large-scale explosive silicic eruptions that could be compared to the basaltic tuffs and ashes of the Balder Formation and the Saksunarvatn Ash, respectively. Further definitions of the characteristics of primary pyroclastic and volcanoclastic material, based upon the morphologies of fine-ash in distal localities, and the presence of ash aggregates, including accretionary lapilli, are also discussed. The main findings of this chapter are:

- The non-lava lithologies of the Columbia River Flood Basalt Province include pyroclastic, volcanoclastic and siliciclastic rocks. Some intervals of the Ellensburg Formation contain limited or no basaltic clasts. The distribution and preservation of many of the deposits are controlled by the emplacement of lavas, together with the disruption and relocation of water-bodies during active flood basalt volcanism.
- Pyroclastic and volcanoclastic rock-types are predominantly silicic, with rare basaltic tuffs occurring in western Idaho. The silicic tuffs are dominated by non- to moderately-vesicular rod-like and bubble-wall pyroclasts that are found in distal locations from their possible source in the Cascade Range Volcanic Arc or the Yellowstone and Snake River Plain hotspot (Waters 1965; Smith 1988a, b; Smith et al. 1988; Perkins et al. 1995, 1998; Cathey & Nash 2004; Branney et al. 2008; Ellis et al. 2012; Nash & Perkins 2012; Ellis et al. 2013; Kent-Corson et al. 2013; Knott et al. 2016). The pyroclast morphologies suggest that these eruptions were highly explosive ‘dry’ magmatic eruptions, driven by the expansion of magmatic volatiles.

- The presence of ash aggregates, including accretionary lapilli and coated ash pellets, may be interpreted as forming due to interactions with water (Moore & Peck 1962; Carey & Sigurdsson 1982; Bohor & Triplehorn 1984; Cas & Wright 1988; Schumacher & Schmincke 1991; Gilbert & Lane 1994; Schumacher & Schmincke 1995; Sparks et al. 1997; James et al. 2003; Scolamacchia et al. 2005; Brown et al. 2010, 2012; Van Eaton et al. 2012;). These interactions could occur at the vent, or they may be associated with pyroclastic density currents disrupting local water bodies (e.g. Kato 1986; Schumacher & Schmincke 1991, 1995; Durant & Ernst 2001; Scolamacchia et al. 2005; Textor et al. 2006; Brown et al. 2010, 2012; Mueller et al. 2016). The disruption of water bodies is implied by the presence of freshwater diatoms within the fine-grained rims of the ash aggregates, although a range of processes that could be responsible for creating diatom-bearing ash aggregates are also considered (see section Chapter 6).
- Results and descriptions of thin-sections and grain-mounts of the silicic tuffs support the conclusions given by the Saksunarvatn Ash (Chapter 2) for the discrimination of pyroclastic and volcanoclastic deposits. In both localities, the pyroclasts of the volcanoclastic deposits have rough/jagged and fractured edges that are indicative of abrasion, are variably altered, and are associated with other clast-types such as granular lithic clasts and finer-grained matrix material.
- The presence of significant amounts of silicic, and rare basaltic, material in the Columbia River Flood Basalt Province shows that a range of magma-types can be erupted during development of a flood basalt/large igneous province. This also highlights how unusual the large number of basaltic tuffs are within the Early Eocene Balder Formation associated with formation of the North Atlantic Igneous Province (Chapter 3).

7.2 The use of distal ash in the interpretation of eruption processes

Ash includes the finest-grained tephra that is produced by any style of eruption and is representative of the highest levels of magma fragmentation. High volumes of ash are characteristically produced by highly-explosive ‘dry’ magmatic eruptions and hydrovolcanic (‘wet’) eruptions. The fine-scale of ash and its relatively low density, in comparison to other tephra, allows it to be dispersed and deposited hundreds to thousands of kilometres distant from a vent. The morphology and vesicularity of tephra can record the conditions of the parent magma and the eruption processes in which they formed; therefore, the ash in distal locations may record important information regarding eruptions, particularly where more proximal deposits are not preserved or exposed.

In this study four main pyroclast morphologies have been recognised (Table 7-1):

- *Blocky* - Equant, angular pyroclasts with planar edges and few bubble-wall features. These are interpreted as being formed by brittle fragmentation, either due to rapid quenching of the magma, for example due to interactions with water, or by abrasion of pyroclasts within the vent or eruption column. This morphology may be the dominant morphology in deposits of ash and fine-ash, regardless of eruption processes.
- *Bubble-wall* - Pyroclasts dominated by concave or irregular bubble-walls, where the magma fragmented between expanding bubbles prior to quenching. Where such pyroclasts have pointed edges that taper-off, this implies that volatile-expansion was responsible for fragmentation of the magma; therefore, indicating ‘dry’ magmatic processes. Where the bubble edges do not taper, this may represent brittle fragmentation and shows a combination of magmatic and brittle fragmentation, that may be caused by water-interactions, or subsequent abrasion of the pyroclast, for example, within an eruption column.
- *Irregular* - Fluidal-shaped pyroclasts indicative of the ductile deformation of the magma prior to its complete quenching. This morphology is

interpreted as representing pieces of magma that were not immediately quenched following their initial eruption, therefore suggesting that magma-water interactions were not responsible for their formation, as the presence of water or water vapour would more likely lead to rapid quenching that would inhibit further deformation of a pyroclast once it formed.

- *Rod-like* - Elongate pyroclasts that are commonly non-vesicular or associated with tube-vesicles. These are interpreted to be created in highly explosive ‘dry’ magmatic eruptions driven by rapid magma ascent rates in which bubbles get drawn out (forming tubes) and the magma fragments due to high levels of strain (e.g. Gaonac’h et al. 2005). This pyroclast morphology is most common in ash produced by ‘dry’ silicic Plinian eruptions. It is also suggested that these pyroclasts may represent Limu-o-Pele in basaltic deposits and could be formed by the incorporation of water droplets at an erupting vent (Graettinger et al. 2013).






	Blocky	Bubble-wall		Irregular	Rod-like
Examples					
Fragmentation mechanism	Brittle fragmentation, can be an indicator of rapid quenching of the erupted magma.	Bubble-walls with horizontal edges formed by brittle fragmentation (red) and magmatic fragmentation via the expansion of bubbles	Bubble-walls with edges that taper-off forming delicate sharp points, and circular segments of bubble films (blue), formed by magmatic fragmentation due to bubble growth	Fluidal shapes forming irregular pyroclast morphology, formed during slower cooling of the erupted magma which allows the pyroclasts to deform in a ductile-manner prior to solidifying	Elongate rod-like pyroclasts formed by stretching of silicic magma during rapid ascent, with brittle fragmentation of the magma caused by high strain. Or, water droplets interacting with an erupting basaltic magma creating Limu-o-Pele
Eruption type	Magmatic and/or Hydrovolcanic	Magmatic and/or Hydrovolcanic	Magmatic	Magmatic	Magmatic (silicic) or Hydrovolcanic (basaltic)

Table 7-1 Examples of pyroclast morphologies and their inferred mode of formation.

Ash and fine-ash are commonly non- to poorly-vesicular; within this grain-size fraction it is unlikely that highly-vesicular pyroclasts will be present unless

vesicles are smaller than the size of the pyroclast. Therefore, any record of macro-vesicles is likely to be lost in deposits of ash. This may inhibit the interpretation of the original conditions of the parent magma, for example, regarding volatile content and the degree of magma vesiculation (e.g. Gaonac'h et al. 2005), particularly in magmas that evolve multiple vesicle-size populations (e.g. Blower et al. 2001; Sable et al. 2006; Polacci et al. 2008; Shea et al. 2010; Ross & White 2012; LaRue et al. 2013; Moitra et al. 2013; Heap et al. 2014). The morphologies of the pyroclasts are more useful for the interpretation of eruption processes than vesicularity, which cannot be used reliably for such fine-grain sizes, without the addition of other data. For example, a large number of bubble-wall pyroclasts could indicate that there was a macro-vesicle population and that magma vesiculation and the expansion of gases were, at least partly, responsible for fragmentation of the erupting magma.

The interpretation of eruption processes from the features of pyroclasts may be complicated by subsequent reworking of the material. It is therefore important to consider the deposit as a whole and to be able to distinguish between pyroclastic and volcanoclastic features.

7.3 Pyroclastic versus volcanoclastic deposits

Reworking can lead to the erosion and ultimate removal of the (original) pyroclastic material that is deposited in many environments, particularly on-land. Consequently, the preservation of primary pyroclastic deposits can be relatively poor, particularly on an extended time scale of thousands to millions of years. The reworking of primary pyroclastic material may lead to the deposition of ash in significant thicknesses in some settings (e.g. valleys or river channels); if these deposits are not correctly identified as being volcanoclastic then it is possible for an overestimation of the thickness and distribution of eruption deposits to be made. Thus, this could lead to an overestimation of eruption volumes and a misinterpretation of eruption-style and processes. However, it is also possible that without correct identification, pyroclastic deposits may be misinterpreted as volcanoclastic therefore giving the opposite effect, leading to underestimations of eruption volumes and tephra dispersal. In modern settings, this could have consequences for the understanding of hazards

in areas surrounding volcanoes. The ability to distinguish primary pyroclastic deposits from volcanoclastic deposits is particularly important in ancient distal tuffs, whereby the proximal deposits may be absent from the rock record due to erosion.

Descriptions and lithological logs of unconsolidated and consolidated ash/tuff in the field or from core can provide the first essential data needed to interpret the nature of these deposits (Figure 7-2). Lithological logging and identification of rock/deposit types can aid the interpretation of the environment of deposition. This is important as primary pyroclastic deposits are unlikely to be found in some settings, for example, where deposition has occurred within a river channel: where volcanoclastic material is more likely to be preserved (Figure 7-2). Deposition in a lake or marine setting may include air-fall water-lain tephra, and/or volcanoclastic deposits (Figure 7-2). Where the structures of the deposit do not give a definite identification of the deposit/rock-type, the clast-types and grain-size features should be analysed (Figure 7-2). The features associated with each type of distal ash-grade deposit can be summarised as follows:

- *Pyroclastic* - A deposit that contains up to 100 % igneous clast-types, including glassy pyroclasts (or their altered equivalents), where the grains are predominantly angular. The glassy pyroclasts will predominantly display smooth edges with minimal fractures and commonly have empty vesicles. Delicate pyroclast features, such as very thin bubble-walls, may be preserved. *Primary pyroclastic* deposits are those deposited directly from an eruption and include air-fall ash/tuff and deposits from pyroclastic density currents. *Secondary pyroclastic* deposits are pyroclastic deposits that may have been influenced by some secondary processes, such as settling of air-fall ash through water.
- *Volcanoclastic* - A deposit that contains >50 % pyroclastic igneous clast-types, along with lesser amounts of other non-igneous clast-types. The grains may remain angular, but some may have undergone rounding due to abrasion during transport. Pyroclasts will have jagged/rough edges and fractures may be more common. The pyroclasts may be variably altered

and associated with matrix material that may infill vesicles. Delicate pyroclast features, such as very thin bubble-walls, are unlikely to be preserved in these deposits.

- *Sedimentary* - A deposit containing <50 % pyroclastic igneous clast-types. These deposits can be comprised of fragments of pre-existing igneous, pyroclastic or volcanoclastic rocks, in addition to non-igneous clast-types.

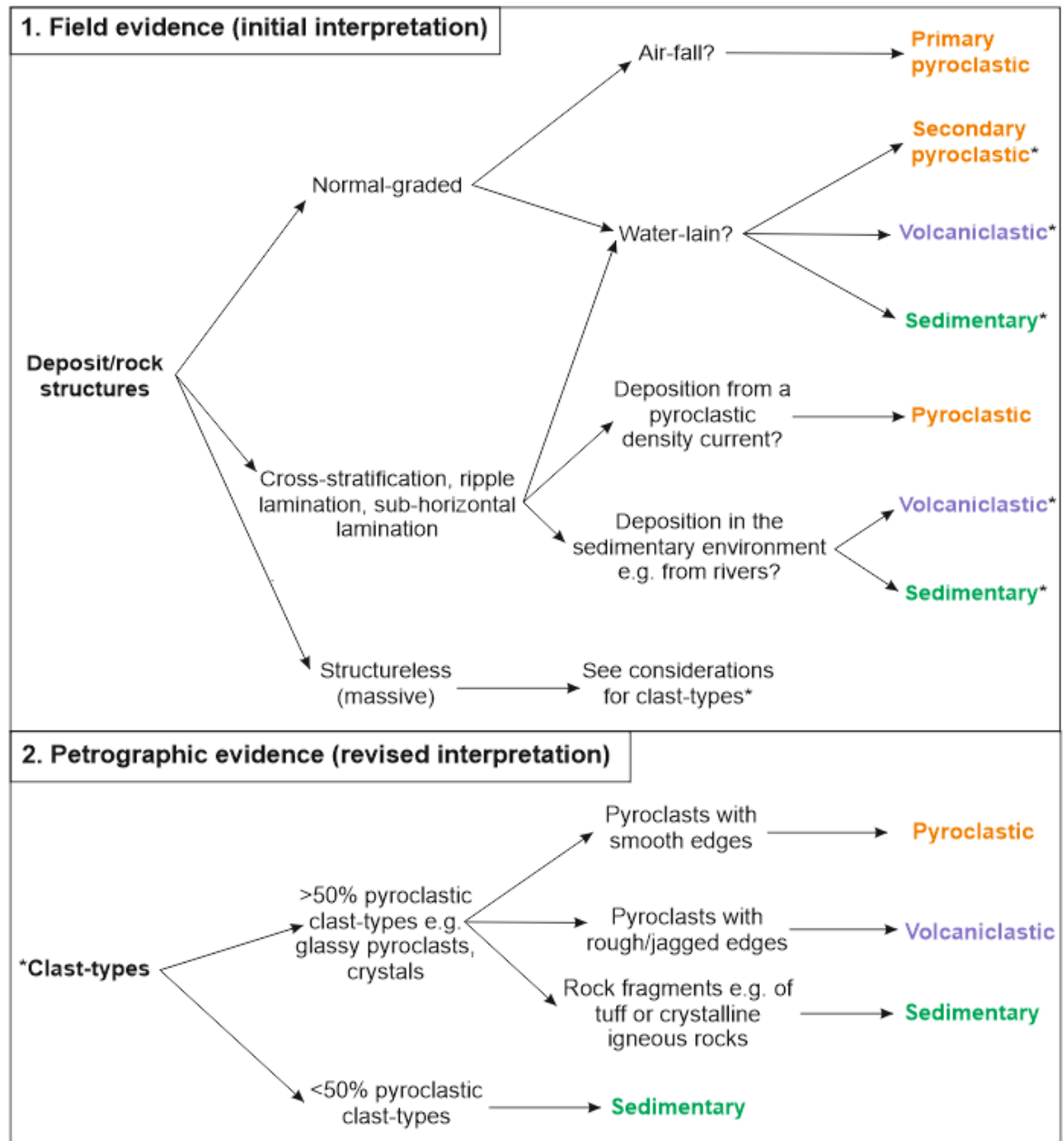


Figure 7-2 Flow diagrams showing the use of sedimentary structures and grain-scale features required to distinguish between deposits of pyroclastic, volcanoclastic and sedimentary material. 1) Field evidence that is required to give an initial interpretation of the deposit type, stars (*) show where further evidence is required to confirm the interpretation via the study of clast-types (2).

Complications and mis-identification of ash/tuff may arise in volcanoclastic or sedimentary deposits where delicate pyroclast features have been preserved. For example, when surrounded by a fine-grained matrix, where the matrix material has been removed by subsequent transportation and re-deposition, or where subsequent transport and re-deposition has occurred from ice, as ice transport may preserve the original air-fall features of tephra, even during transport. Alternatively, reworking of unconsolidated pyroclastic material in low concentrations may inhibit abrasion and the formation of features associated with volcanoclastic material. Additional abrasion and reworking of pyroclasts may also occur by the recycling of material at the vent, or within a pyroclastic density current. Therefore, recycled pyroclasts may be incorporated into eruption deposits alongside primary pyroclastic ash (e.g. D'Oriano et al. 2014). Thus, it is important to first identify the environment of deposition and to analyse the deposits above and below to assess the most appropriate depositional processes (Figure 7-3).

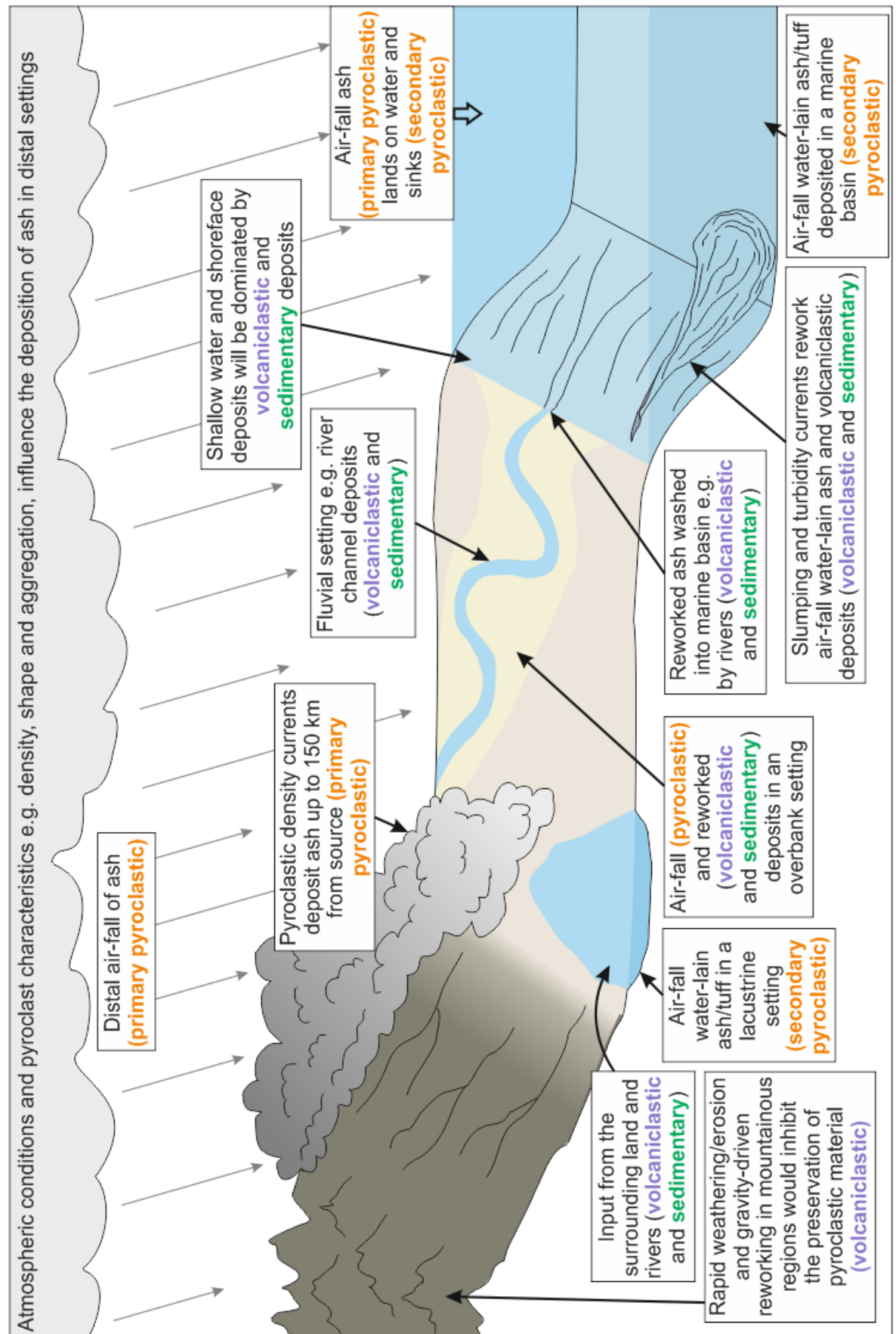


Figure 7-3 Environments of deposition for pyroclastic, volcanoclastic and sedimentary deposits.

7.4 Revised nomenclature

The naming and definition of pyroclastic and volcanoclastic deposits has been widely debated in the literature, with authors opting for naming based on the origin of grains (Fisher 1961) or depositional mechanisms (Cas & Wright 1987; White & Houghton 2006). A comparison of the naming schemes applied by different authors is summarised in Table 7-2.

Reference	Naming scheme		
Fisher (1961)	Primary volcanoclastic	Secondary volcanoclastic	Epiclastic
Cas & Wright (1987)	Pyroclastic (excludes water-lain tephra)	Volcanoclastic (includes all water-lain tephra) (includes all tephra that has undergone any amount of subsequent transport from where it originally intersected the Earth's surface)	Sedimentary
White & Houghton (2006)	Primary volcanoclastic (the term volcanoclastic is used to describe ALL material deposited by volcanic eruptions) (includes water-lain tephra)	Sedimentary (supported by Manville et al. 2009)	
(This study)	Pyroclastic (primary or secondary) (includes all water-lain tephra, e.g. deposits of subaqueous eruptions)	Volcanoclastic (includes all reworked, unconsolidated material) (deposition influenced by sedimentary processes)	Sedimentary (includes all eroded, fragments of pre-existing igneous, pyroclastic and volcanoclastic rocks in addition to non-igneous clasts e.g. fossils and siliciclastic material)

Table 7-2 Comparison of the naming schemes used for pyroclastic and volcanoclastic deposits in the literature, and the naming schemes proposed by the current study.

The naming schemes proposed in the current study combine some of the views from the published literature. For example, the term ‘pyroclastic’ is proposed to include all material that is deposited directly by volcanic eruptions, in support of Fisher (1961), Cas & Wright (1987) and White and Houghton (2006). The proposed scheme uses the terminology of Cas & Wright (1987) but its definition includes water-lain tephra such as air-fall water-lain ash and the deposits of subaqueous eruptions, in support of White & Houghton (2006). However, in this study the deposits of air-fall ash and subaqueous eruptions or air-fall water-lain tephra can be defined further by dividing these into primary and secondary pyroclastic (Table 7-3). Primary pyroclastic deposits would be those that are deposited directly onto the Earth's surface from eruptions, such as, all air-fall tephra, deposits from pyroclastic density currents, and tephra from subaqueous eruptions (Figure 7-4). Secondary pyroclastic deposits would be those where some secondary conditions may have affected the original (pyroclastic) features of a deposit, for example, the settling of air-fall tephra through water, where the greater density of the water may alter the features of the deposit compared to those not deposited through water (Figure 7-4). Secondary pyroclastic deposits are those deposited through more than one fluid medium, for example air *and* water, whereas primary pyroclastic deposits are associated with deposition within one medium, for example air *or* water (Figure 7-4). Further description of pyroclastic deposits should be given when they are named, for example air-fall ash/tuff or air-fall water-lain ash/tuff (Table 7-3). Where the mode of deposition is not known then the term ash/tuff should be applied; however, this will also indicate that it is not known whether the deposit is of pyroclastic or volcanoclastic nature.

The term ‘volcanoclastic’ is used following the definitions of Cas & Wright (1987), whereby an aspect of transport is required for a pyroclastic deposit to become volcanoclastic. However, transport needs to affect the overall character of the deposit from that produced by original deposition of the pyroclastic material (Figure 7-4), and therefore requires transport to occur over larger distances than a few millimetres, and likely over greater time-scales than those proposed by Cas & Wright (1987). The transport and deposition of volcanoclastic material will be controlled by sedimentary processes and the reworked pyroclastic clasts could be considered as sedimentary grains, therefore

nomenclature should refer to grain-size using the sedimentary naming scheme of Wentworth (1922) (Table 7-3). However, the presence of >50 % pyroclastic igneous clast-types in volcanoclastic deposits represents abnormal deposition, likely effected by the relatively instantaneous influx of pyroclastic material from volcanic eruptions. Additionally, volcanoclastic clast-types may behave differently within a sedimentary environment, for example vesicular clasts may have different hydrodynamic properties, compared to siliciclastic clasts (e.g. Suthren 1985). Therefore, these deposits cannot be named using only sedimentary naming schemes without reference to their volcanic content, hence the need for the prefix ‘volcanoclastic’, for example volcanoclastic siltstone (Table 7-3).

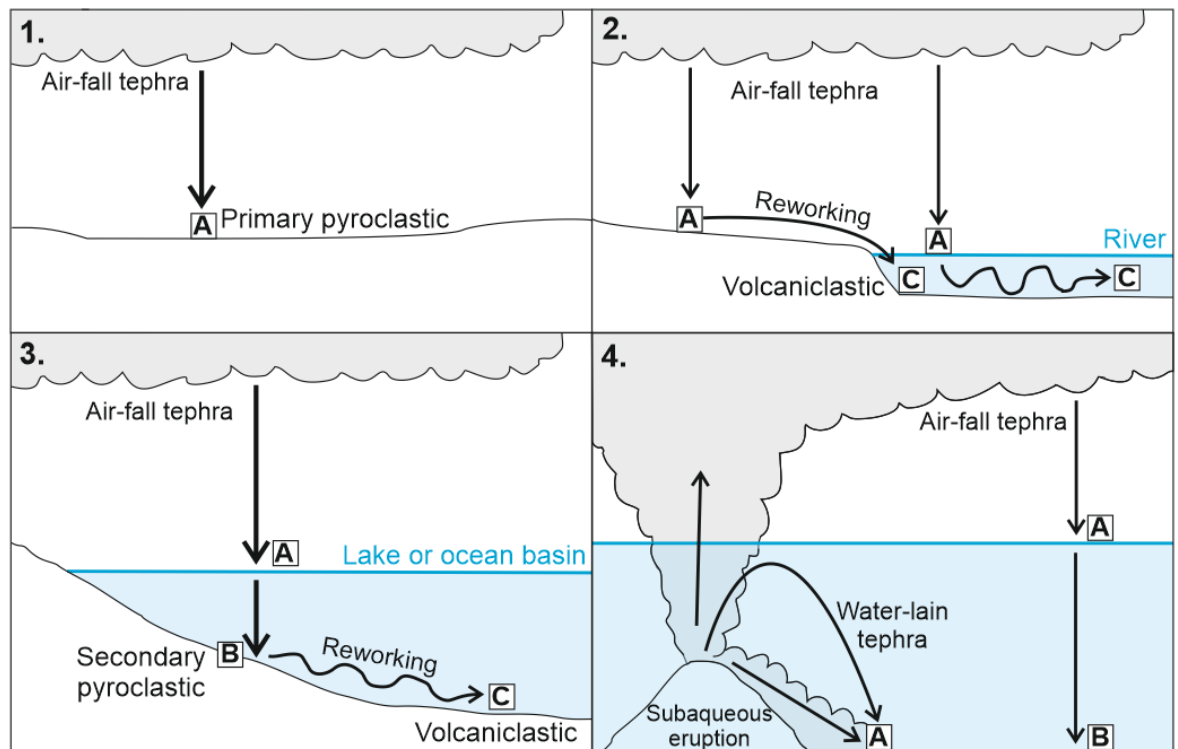


Figure 7-4 Examples of the naming for primary (A) and secondary pyroclastic (B) and volcanoclastic (C) deposits using the terminology proposed in the current study. 1) Primary pyroclastic tephra deposited from air-fall onto the ground. 2) Primary pyroclastic tephra deposited from air-fall onto the ground (A) may be reworked and re-deposited as volcanoclastic material within a river channel (C). Alternatively, air-fall tephra may be deposited directly into a river as primary pyroclastic tephra (A), subsequent reworking by river currents will lead to deposition of this tephra as volcanoclastic material (C). 3) Air-fall tephra is deposited as primary pyroclastic material onto the water surface (A). Sinking of the tephra through the water column results in a secondary pyroclastic deposit (B). Any additional reworking (transport and deposition) will cause this material to become volcanoclastic (C). 4) Subaqueous eruptions will deposit primary pyroclastic material as water-lain tephra either from a subaqueous eruption column or subaqueous pyroclastic density currents (A). Any tephra that is erupted above the water will behave like tephra in subaerial eruptions – it will be deposited on the Earth’s surface as primary pyroclastic

material (A), if this subsequently settles through water it will form a secondary pyroclastic deposit (B).

The influx of pyroclastic material on land, or within a marine basin can disrupt background sedimentary processes, for example by inundating fluvial systems, blocking river channels and forming ephemeral lakes that may then cause lake-burst floods (e.g. case-studies from Mount St. Helens 1980 to present). These deposits can therefore have a major effect on the sedimentary depositional environment that may last for many years, until the environment stabilises and normal sedimentation resumes. In distal localities the sedimentary environment is likely to recover and resume normal sedimentation relatively rapidly, due to the lower volumes of tephra and their finer grain-size, compared to deposition in proximal locations. However, the presence of both pyroclastic and volcaniclastic deposits would still represent a unique sequence of depositional events, associated with a period of active volcanism.

In contrast, the traditional sedimentary nomenclature of Wentworth (1922) should be used to describe all material predominantly comprised of fragments of pre-existing igneous, pyroclastic and volcaniclastic rocks (including fragments of lava) (Table 7-3). These clast-types represent the normal erosional and depositional processes of the sedimentary environment.

Some authors have also presented the terms autoclastic and hyaloclastic, where various deposits have been created from lava flows and their interactions with the environment (Fisher 1961, 1984; Cas & Wright 1987, 1988; White & Houghton 2006). These terms are not discussed here as they are directly associated with lava flows and are unlikely to be found in distal ash deposits. However, it is worth noting that other volcanic materials may be named differently to the scheme proposed here for distal ash and tuff.

PYROCLASTIC		VOLCANICLASTIC	SEDIMENTARY
PRIMARY	SECONDARY		
Controls on deposition: Eruption processes, atmospheric or water conditions		Controls on deposition: Sedimentary processes e.g. erosion, transport and re-deposition	
<p>Air-fall: denotes deposition of tephra from a subaerial eruption onto the surface of the Earth only</p>	<p>Air-fall water-lain: denotes deposition of tephra from a subaerial source through the air and subsequently through a water column. Whereby features of the deposit may have been influenced by secondary conditions within the water column</p>	<p>Deposits formed from the reworking or non-lithified pyroclastic material, comprised of >50% pyroclastic clast-types</p> <p>Named by reference to a sedimentary grain-size descriptor e.g. volcaniclastic siltstone</p> <p>Some comment on the environment of deposition could also support the interpretation of volcaniclastic deposits e.g. volcaniclastic siltstone deposited from traction currents within a river</p>	<p>Deposits comprising fragments of pre-existing pyroclastic and/or volcaniclastic rocks; these may be present in addition to non-igneous clast-types</p> <p>Named using sedimentary terminology e.g. fine-sand(stone)</p> <p>These deposits may be described further by commenting on the clast-types e.g. fine-sand(stone) containing fragments of volcaniclastic rocks, or, tuff</p>
Example: Air-fall ash/tuff		Example: Volcaniclastic silt(stone)	Example: Silt(stone)

Table 7-3 Summary of the revisions to the nomenclature of pyroclastic, volcaniclastic and sedimentary deposits/rocks proposed in the current study for ash-grade distal deposits and rocks.

The term ‘tuffaceous’ has previously been used throughout the literature to describe both pyroclastic and volcaniclastic deposits of unconsolidated and consolidated types (e.g. Manville et al. 2009). Its use refers to the presence of igneous clast-types within a deposit or rock. The terminology proposed here removes this term and replaces it with more useful descriptive terms referring to the origin of clasts and their mode of deposition using pyroclastic, volcaniclastic or sedimentary terminology, along with further interpretation/definition of the depositional processes. For example, a fluvial ash-rich deposit is referred to as a tuffaceous siltstone by Cas & Wright (1987) and McPhie et al. (1993), but in the current study this would be referred to as a volcaniclastic siltstone deposited in a fluvial environment. Schmid (1981) uses the term ‘tuffaceous’ to describe deposits that contain a mixture of pyroclastic and sedimentary clasts, although there is no reference as to the environment in which these kinds of deposits could be found. However, the term tuff can be used as a general name for lithified fine-grained tephra (particularly ash) and therefore, it would seem that

the term tuffaceous may be more applicable where sediments are comprised of fragments of tuffs.

7.5 Use of ash and fine-ash for the identification of eruption processes and the recognition of pyroclastic and volcanoclastic deposits in distal settings

Several data have been created and used in this study for the characterisation of pyroclastic and volcanoclastic deposits. Overall, deposit characteristics and lithological logging were used for the assessment of the environment of deposition. Grain-type analysis, grain-size distributions, degree of grain-size sorting and clast morphologies were used for the assessment of pyroclastic and volcanoclastic features and original eruption processes. Additional data on the % vesicularity and morphology of pyroclasts were obtained for use in the interpretation of eruption processes and the original formation of pyroclasts now present in ash and tuffs. These data have previously been used in proximal settings but limited information is available in the published literature for the use of these data in distal deposits of ash and fine-ash (>100 km away) for distinguishing between pyroclastic and volcanoclastic materials (Kandlbauer et al. 2013; Breitzkreuz et al. 2014) and original eruption processes, including eruption-style and magma conditions prior to or during eruption (Watson et al. 2016). The applicability of each type of data is provided based on the results of the current study in Table 7-4.

Method	Applicability for the characterisation of distal deposits of ash and fine-ash	Reason
Overall deposit characteristics	Essential	Assessment of the characteristics of a deposit in the field or in core is essential in determining if material is pyroclastic or volcaniclastic. If the deposit is interpreted to be pyroclastic then the features may also provide evidence of eruption processes e.g. pyroclastic density currents, or, aggregation of ash
Assessment of the environment of deposition	Essential	Interpretation of the environment of deposition is essential for distinguishing pyroclastic and volcaniclastic deposits; and for the interpretation of subaqueous eruptions and depositional processes. Environmental interpretations may also provide information on the likely causes of hydrovolcanism, allowing an interpretation of the water-source e.g. eruption through a lake
Grain-type analysis	Essential	Analysis of grain-types is essential for characterising pyroclastic and volcaniclastic or sedimentary deposits based on the abundance of igneous and non-igneous clast types. The assessment of juvenile and accidental clast-types may also assist in interpretation of eruption style and eruption processes within the conduit or vent
Grain-size and degree of sorting	Not essential	The grain-size and degree of sorting can vary for deposits of ash due to atmospheric conditions or the mode of deposition, or subsequent reworking. Grain-size and sorting analysis will not provide significant information for the determination of eruption processes or pyroclastic versus volcaniclastic classification of deposits, particularly in distal settings.
Pyroclast morphology	Essential, but may be biased	Fine-ash is representative of the highest levels of fragmentation, and will produce a greater abundance of blocky pyroclast morphologies, regardless of eruption style. Non-blocky morphologies (e.g. bubble-wall, irregular or rod-like) may provide more detailed information regarding eruption processes than the presence and abundance of blocky pyroclasts.
% vesicularity/ vesicle number/ vesicle density and morphology	Not essential	High levels of fragmentation would lead to the loss of vesicles, particularly macro-vesicles, leading to predominantly non- to poorly-vesicular pyroclasts; irrespective of the original volatile content/vesicularity of the magma

Table 7-4 The applicability of different sources of data used in the characterisation of distal deposits of ash and fine-ash.

7.6 Volcanism associated with flood basalt and large igneous provinces

Field evidence shows that significant silicic volcanism occurred simultaneously with the emplacement of large volumes of basaltic lava during formation of the Miocene Columbia River Flood Basalt Province, USA. However, most, if not all, of this silicic volcanism occurred outside of the flood basalt province, itself. The presence of a few silicic pyroclastic tuffs within the North Sea Balder Formation, and abundant silicic pyroclastic tuffs in the underlying Sele Formation, also supports the concept that silicic volcanism was significant during the formation of the Palaeocene-Eocene North Atlantic Igneous Province.

Basaltic tuffs are generally absent from the non-lava lithologies of the Columbia River Flood Basalt Province, but are abundant within the distal deposits of the North Atlantic Igneous Province. These differences show a variation in eruption dynamics, likely caused by differences in the overall environment(s) where volcanism occurred. For example, the basaltic volcanism of the Columbia River Flood Basalt Province likely occurred on land, with little or no interaction with water. In contrast, the basaltic volcanism of the North Atlantic Igneous Province was commonly associated with eruptions within shallow water, which resulted in highly explosive magma-water interactions. This different style of eruption is represented by the >200 basaltic tuffs of the Balder Formation, with pyroclasts that contain features typical of hydrovolcanic fragmentation. Therefore, eruptions within shallow oceans or at opening oceanic rifts are more likely to be associated with large-scale explosive basaltic volcanism than those on-land.

7.7 Further work

Future research following the results and interpretations of this thesis could include:

- Further characterisation of pyroclasts from each of the localities via chemical analysis, where feasible/possible. Electron probe and/or laser ablation techniques would be required to produce quantifiable data for comparison and further detailed analysis of glassy and altered pyroclasts.

- Chemical fingerprinting of glassy pyroclasts in the Ellensburg Formation, USA, could lead to a better understanding of Miocene volcanism associated with the growing Cascade Range Volcanic Arc, and/or the Yellowstone and Snake River hotspot.
 - Chemical analysis of the North Sea Balder Formation tuffs in addition to those of the E. Anglia Wrabness Member, may allow correlation of tuffs between the North Sea Basin, NE Atlantic and NW Europe, eventually leading to better estimations of the volume of tephra deposited, hydrovolcanic processes and the likely source area of these Early Eocene large-scale basaltic eruptions.
 - Chemical fingerprinting of glassy pyroclasts from the Saksunarvatn Ash could allow identification of eruption sources to be made, confirming or disproving the conclusion made here that multiple vents were erupting in Iceland ~10.3 Ka.
- Detailed mapping and lithological logging of exposures of the Ellensburg Formation throughout the Columbia River Flood Basalt Province could allow correlation of pyroclastic and sedimentary units. This could lead to more appropriate sub-divisions of the non-lava stratigraphy.
 - Comparison of recent and ancient ashes/tuffs for the interpretation of eruption and depositional processes in both distal and proximal settings. In addition, there should be comparison of pyroclastic and volcanoclastic deposits on an exposure and grain-scale to further define the characteristics of tephra and the definitions used to identify and name these deposits.
 - Further analysis of the mechanisms for explosive basaltic volcanism is required, particularly for its application in hazard management in areas surrounding modern-day basaltic volcanoes.

List of references

- ACKERS, M.A. & BRYN, B.K.L. 2015. Common characteristics of remobilised sand mounds from seismic attributes. *EAGE First Break*, **33**, 39-49.
- ALDISS, D.T. 2014. The stratigraphical framework for the Palaeogene successions of the London Basin, UK. Version 2. *British Geological Survey Open Report OR/14/008*, 95.
- ALEKSANDROVA, G.N., ORESHKINA, T.V., LAKOVLEVA, A.I. & RADIONOVA, E.P. 2012. Late Paleocene-Early Eocene Diatoms and Dinocysts from Biosiliceous Facies of the Middle Trans-Urals Region. *Stratigraphy and Geological Correlation*, **20** (4), 380-404.
- ALI, J.R., HAILWOOD, E.A. & KING, C. 1996. The 'Oldhaven magnetozone' in East Anglia: a revised interpretation. *Geological Society, London, Special Publications*, **101**, 195-203.
- ALI, J.R. & JOLLEY, D.W. 1996. Chronostratigraphic framework for the Thanetian and lower Ypresian deposits of southern England. *Geological Society, London, Special Publications*, **101**, 129-144.
- ALLISON, P.A., MAEDA, H., TUZINO, T. & MAEDA, Y. 2008. Exceptional preservation within Pleistocene lacustrine sediments of Shiobara, Japan. *PALAIOS*, **23**, 260-266.
- ANDREWS, J.T., GEIRSDÓTTIR, A., HARDARDÓTTIR, J., PRINCIPATO, S., GRÖNVOLD, K., KRISTJANDÓTTIR, G. B., HELGADÓTTIR, G., DREXLER, J. & SVEINBJÖRNSDÓTTIR, A. 2002. Distribution, sediment magnetism and geochemistry of the Saksunarvatn ($10\,180 \pm 60$ cal. yr BP) tephra in marine, lake, and terrestrial sediments, northwest Iceland. *Journal of Quaternary Science*, **17** (8), 731-745.
- ANELL, I., THYBO, H. & SRATFORD, W. 2010. Relating Cenozoic North Sea sediments to topography in southern Norway: The interplay between tectonics and climate. *Earth and Planetary Science Letters*, **300**, 19-32.
- AUGUSTÍN-FLORES, J., NÉMETH, K., CRONIN, S.J., LINDSAY, J.M. & KERESZTURI, G. 2015. Shallow-seated explosions in the construction of the Motukorea tuff ring (Auckland, New Zealand): Evidence from lithic and sedimentary characteristics. *Journal of Volcanology and Geothermal Research*, **304**, 272-286.
- BAAS, J.H. 1994. A flume study on the development and equilibrium morphology of current ripples in very fine sand. *Sedimentology*, **41**, 185-209.
- BAILEY, I., HOLE, G.M., FOSTER, G.L., WILSON, P.A., STOREY, C.D., TRUEMAN, C.N. & RAYMO, M.E. 2013. An alternative suggestion for the Pliocene onset of major northern hemisphere glaciation based on the geochemical provenance of North Atlantic Ocean ice-rafted debris. *Quaternary Science Reviews*, **75**, 181-194.
- BARBERI, F., CIONI, R., ROSI, M., SANTACROCE, R., SBRANA, A & VECC, R. 1989. Magmatic and phreatomagmatic phases in explosive eruptions of Vesuvius as

deduced by grain-size and component analysis of the pyroclastic deposits. *Journal of Volcanology and Geothermal Research*, **38**, 287-307.

BARRY, T.L., KELLEY, S.P., REIDEL, S.P., CAMP, V.E., SELF, S., JARBOE, N.A., DUNCAN, R.A. & RENNE, P.R. 2013. Eruption chronology of the Columbia River Basalt Group. *Geological Society of America, Special Paper*, **497**, 45-66.

BARTHOLDY, J., ERNSTEN, V.B., FLEMMING, B.W., WINTER, C., BARTHOLOMÄ, A. & KROON, A. 2015. On the formation of current ripples. *Scientific Reports*, **5**, 11390, DOI: 10.1038/srep11390.

BAYLISS, N. & PICKERING, K.T. 2015. Transition from deep-marine lower-slope erosion channels to proximal basin-floor stacked channel-levée-overbank deposits, and syn-sedimentary growth structures, Middle Eocene Banastón System, Ainsa Basin, Spanish Pyrenees. *Earth-Science Reviews*, **144**, 23-46.

BENNETT, M.R., DOYLE, P. & MATHER, A.E. 1996. Dropstones: their origin and significance. *Palaeogeography, Palaeoclimatology, Palaeoecology*, **121**, 331-339.

BERGOMI, M.A., ZANCHETTA, S. & TUNESI, A. 2015. The Tertiary dike magmatism in the Southern Alps: geochronological data and geodynamic significance. *International Journal of Earth Sciences*, **104** (2), 449-473.

BERRY, E.B. 1934. Miocene Plants from Idaho. United States Department of the Interior, Geological Survey, Professional Paper, **185-E**, 1-36.

BIRKS, H., GULLIKSEN, S., HAFLIDASON, H., MANGERUD, J. & POSSNERT, G. 1996. New radiocarbon dates for the Vedde Ash and the Saksunarvatn Ash from western Norway. *Quaternary Research*, **45**, 119-127.

BISHOP, A.C., WOOLLEY, A.R. & HAMILTON, W.R. 2007. Guide to minerals, rocks and fossils. Phillip's; in association with the Natural History Museum, 336.

BLAKELY, R.J., SHERROD, B.L., WEAVER, C.S., WELLS, C.S., ROHAY, A.C., BARNETT, E.A. & KNEPPRATH, N.E. 2011. Connecting the Yakima fold and thrust belt to active faults in the Puget Lowland, Washington. *Journal of Geophysical Research*, **116**, B07105.

BLOWER, J.D., KEATING, J.P., MADER, H.M., & PHILLIPS, J.C. 2001. Inferring volcanic degassing processes from vesicle size distributions. *Geophysical Research Letters*, **28** (2), 347-350.

BØGGILD, O.B. 1918. Den vulkanske aske i Moleret samt en oversigt over Danmarks ældre Tertiærbjergarter. *Dan. Geol. Unders., række 2*, **33**, 159.

BONADONNA, C. & COSTA, A. 2013. Plume height, volume, and classification of explosive volcanic eruptions based on the Weibull function. *Bulletin of Volcanology*, **75**, 742.

BONADONNA, C., GENCO, R., GOUHIER, M., PISTOLESI, M., CIONI, R., ALFANO, F., HOSKULDSSON, A. & RIPEPE, M. 2011. Tephra sedimentation during the 2010 Eyjafallajökull eruption (Iceland) from deposit, radar, and satellite observations. *Journal of Geophysical Research*, **116**, B12202.

- BONNICHSEN, B., LEEMAN, w.p., HONJO, N., McINTOSH, W.C. & GODCHAUX, M.M. 2008. Miocene silicic volcanism in southwestern Idaho: geochronology, geochemistry, and evolution of the central Snake River Plain. *Bulletin of Volcanology*, **70**, 315-342.
- BOWMAN, V.C., FRANCIS, J.E., RIDING, J.B., HUNTER, S.J. & HAYWOOD, A.M. 2012. A latest Cretaceous to earliest Paleogene dinoflagellate cyst zonation from Antarctica, and implications for phytoprovincialism in the high southern latitudes. *Review of Palaeobotany and Palynology*, **171**, 40-56.
- BOYGLE, J. 2004. Towards a Holocene tephrochronology for Sweden: geochemistry and correlation with the North Atlantic tephra stratigraphy. *Journal of Quaternary Science*, **19** (2), 103-109.
- BRAMHAM-LAW, C.W.F., THEUERKAUF, M., LANE, C.S. & MANGERUD, J. 2013. New findings regarding the Saksunarvatn Ash in Germany. *Journal of Quaternary Science*, **28** (3), 248-257.
- BRAND, B.D. & CLARKE, A.B. 2012. An unusually energetic basaltic phreatomagmatic eruption: Using deposit characteristics to constrain dilute pyroclastic density current dynamics. *Journal of Volcanology and Geothermal Research*, **243-244**, 81-90.
- BRANNEY, M.J., BONNICHSEN, B., ANDREWS, G.D.M., ELLIS, B., BARRY, T.L. & McCURRY, M. 2008. 'Snake River (SR)-type' volcanism at the Yellowstone hotspot track: distinctive products from unusual high-temperature silicic super-eruptions. *Bulletin of Volcanology*, **70**, 293-314.
- BREITKREUZ, C., DE SILVA, S.L., WILKE, H.G., PFANDER, J.A. & RENNO, A.D. 2014. Neogene to Quaternary ash deposits in the Coastal Cordillera in northern Chile: Distal ashes from supereruptions in the Central Andes. *Journal of Volcanology and Geothermal Research*, **269**, 68-82.
- BREIVIK, A.J., FALEIDE, J.I., MJELDE, R. & FLUEH, E.R. 2009. Magma productivity and early seafloor spreading rate correlation on the northern Vøring Margin, Norway - Constraints on mantle melting. *Tectonophysics*, **468**, 206-223.
- BREIVIK, A.J., MJELDE, R., FALEIDE, J.I. & MURAI, Y. 2006. Rates of continental breakup magmatism and seafloor spreading in the Norway Basin-Iceland plume interaction. *Journal of Geophysical Research*, **111**, B07102. DOI 10.1029/2005JB004004.
- BRENDRYEN, J., HAFLIDASON, H. & SEJRUP, H.P. 2010. Norwegian Sea tephrostratigraphy of marine isotope stages 4 and 5: Prospects and problems for tephrochronology in the North Atlantic region. *Quaternary Science Reviews*, **29**, 847-864.
- BROOKFIELD, M.E. 2004. Principles of Stratigraphy. *Blackwell Publishing*, 340.
- BROOKS, K., 1980. Episodic volcanism, epeirogenesis and the formation of the North Atlantic Ocean. *Palaeogeography, Palaeoclimatology, Palaeoecology*, **30**, 229-242.

- BROOKS, K. 2006. When the Sun dies over northern Europe: the unique geology of Denmark's inland islands. *Geology Today*, **22** (5), 180-186.
- BROWN, R.J., BONADONNA, C. & DURANT, A.J. 2012. A review of volcanic ash aggregation. *Physics and Chemistry of the Earth*, **45-46**, 65-78.
- BROWN, R.J., KOKELAAR, B.P. & BRANNEY, M.J. 2007. Widespread transport of pyroclastic density currents from a large silicic tuff ring: the Glaramara tuff, Scafell caldera, English Lake District, UK. *Sedimentology*, **54**, 1163-1189.
- BROWN, R.J., THORDARSON, T., SELF, S. & BLAKE, S. 2015. Disruption of tephra fall deposits caused by lava flows during basaltic eruptions. *Bulletin of Volcanology*, **77**, 90. DOI 10.1007/s00445-015-0974-3
- BRUESEKE, M.E., HEIZLER, M.T., HART, W.K. & MERTZMAN, S.A. 2007. Distribution and geochronology of Oregon Plateau (U.S.A.) flood basalt volcanism: The Steens Basalt revisited. *Journal of Volcanology and Geothermal Research*, **161**, 187-214.
- BRUNSTAD, H., GRADSTEIN, F.M., VERGARA, L., LIE, J.E. & HAMMER, O. 2009. A Revision of the Rogaland Group, Norwegian North Sea. *Norwegian Stratigraphic Lexicon*, 157.
- BUCKLAND, H.M., CASHMAN, K.V., RUST, A.C., CARSON, R.J. & NICOLAYSEN, K.P. 2018. The deposition and remobilisation of distal Mazama ash (~7ka) in eastern Oregon and Washington. In: Manville, V (ed) Programme and Abstracts, VMSG 54th Annual Conference, Leeds, UK, January 2018, 27.
- BURSIK, M. 1998. Tephra dispersal. In: Gilbert, J.S. & Sparks, R.S.J. (eds) The physics of explosive volcanic eruptions. *Geological Society, London. Special Publications*, **145**, 115-144.
- BUTLER, I.B. & RICKARD, D. 2000. Framboidal pyrite formation via the oxidation of iron (II) monosulfide by hydrogen sulphide. *Geochimica et Cosmochimica Acta*, **64** (15), 2665-2672.
- CAMP, V.E. 1981. Geologic studies of the Columbia Plateau: Part II. Upper Miocene basalt distribution, reflecting source locations, tectonism, and drainage history in the Clearwater embayment, Idaho. *Geological Society of America Bulletin*, **92** (1), 669-678.
- CAMP, V.E. 1995. Mid-Miocene propagation of the Yellowstone mantle plume head beneath the Columbia River basalt source region. *Geology*, **23** (5), 435-438.
- CAMP, V.E., 2013. Origin of Columbia River Basal: Passive rise of shallow mantle, or active upwelling of a deep-mantle plume? In: Reidel, S.P., Camp, V.E., Ross, M.E., Wolff, J.A., Martin, B.S., Tolan, T.L. & Wells, R.E. (edS). The Columbia River Flood Basalt Province. *Geological Society of America Special Paper*, **497**, 181-199.
- CAMP, V.E., ROSS, M.E., DUNCAN, R.A. & KIMBROUGH, D.L. 2017. Uplift, rupture, and rollback of the Farallon slap reflected in volcanic perturbations along the Yellowstone adakite hot spot track. *Journal of Geophysical Research: Solid Earth*, **122**, 7009-7041.

- CAREY, R.J., HOUGHTON, B.F., SABLE, J.E. & WILSON, C.J.N. 2007. Contrasting grain size and componentary in complex proximal deposits of the 1886 Tarawera basaltic Plinian eruption. *Bulletin of Volcanology*, **69**, 903-926.
- CAREY, S.N. & SIGURDSSON, H. 1982. Influence of particle aggregation on deposition of distal tephra from the May 18, 1980, eruption of Mount St. Helens volcano. *Journal of Geophysical Research*, **87** (B8), 7061-7072.
- CAREY, S. & SPARKS, R.S.J. 1986. Quantitative models of the fallout and dispersal of tephra from volcanic eruption columns. *Bulletin of Volcanology*, **48**, 109-125.
- CARRIOL, R-P., BONDE, N., JAKOBSEN, S.L. & HØEG, J.T. 2016. New stalked and sessile cirripedes from the Eocene Mo Clay, northwest Jutland (Denmark). *Geodiversitas*, **38** (1), 21-32.
- CARTER, S.R., EVENSEN, N.M., HAMILTON, P.J. & O'NIONS, R.K. 1979. Basalt magma sources during the opening of the North Atlantic. *Nature*, **281**, 28-30.
- CAS, R. & BUSBY-SPER, C. 1991. Volcaniclastic sedimentation. *Sedimentary Geology*, **74**, 1.
- CAS, R.A.F. & WRIGHT, J.V. 1987. Volcanic successions modern and ancient - a geological approach to processes, products and successions. *Allen & Unwin, London*, 487.
- CATHEY, H.E. & NASH, B.P. 2004. The Cougar Point Tuff: Implications for Thermochemical Zonation and Longevity of High-Temperature, Large-Volume Silicic Magmas of the Miocene Yellowstone Hotspot. *Journal of Petrology*, **45** (1), 27-58.
- CHAROLA, A.E., PÜHRINGER, J. & STEINGER, M. 2007. Gypsum: a review of its role in the deterioration of building materials. *Environmental Geology*, **52**, 339-352.
- CHEN, Y-C. & LEE, C-G. 2011. Evaluation of liquefaction resistance of sand by maximum shear modulus. *Journal of the Chinese Institute of Engineers*, **17** (5), 689-699.
- CHOUX, C., DRUITT, T. & THOMAS, N. 2004. Stratification and particle segregation in flowing polydisperse suspensions, with applications to the transport and sedimentation of pyroclastic density currents. *Journal of Volcanology and Geothermal Research*, **138** (3-4), 223-241.
- CIONI, R., SBRANA, A. & VECCHI, R. 1992. Morphologic features of juvenile pyroclasts from magmatic and phreatomagmatic deposits of Vesuvius. *Journal of Volcanology and Geothermal Research*, **51**, 61-78.
- CIONI, R., PISTOLESI, M., BERTAGNINI, A., BONADONNA, C., HOSKILDSSON, A. & SCATENI, B. 2014. Insights into the dynamics and evolution of the 2010 Eyjafjallajökull summit eruption (Iceland) provided by volcanic ash textures. *Earth and Planetary Science Letters*, **394**, 111-123.

CLARKE, H., TROLL, V.R. & CARRECEDO, J.C. 2009. Phreatomagmatic to strombolian eruptive activity of basaltic cinder cones: Montaña Los Erales, Tenerife, Canary Islands. *Journal of Volcanology and Geothermal Research*, **180**, 225-245.

COLE, P.D., GUEST, J.E., DUNCAN, A.M. & PACHECO, J-M. 2001. Capelinhos 1957-1958, Faial, Azores: deposits formed by an emergent Surtseyan eruption. *Bulletin of Volcanology*, **63**, 204-220.

Collins English Dictionary. 2014. 12th Edition. HarperCollins Publishers.

COLLINSON, J.D. 1978. Lakes, Chapter 4. In: Reading, H.G. (ed). *Sedimentary Environments and Facies. Blackwell Scientific Publications*, 569.

COLLINSON, J.D. 1981. Alluvial Sediments. In: Reading, H.G. (ed). *Sedimentary Environments and Facies. Blackwell Scientific Publications*, 569.

COLLINSON, J.D., MOUNTNEY, N.P. & THOMPSON, D.B. 2006. *Sedimentary Structures*, Third edition. 292.

COLTELLI, M., DEL CARLO, P. & VEZZOLI, L. 2000. Stratigraphic constraints for the explosive activity in the past 100 ka at Etna Volcano, Italy. *International Journal of Earth Sciences*, **89** (3), 665-677.

CONSTANTINI, L., BONADONNA, C., HOUGHTON, B.F. & WEHRMANN, H. 2009. New physical characterization of the Fontana Lapilli basaltic Plinian eruption, Nicaragua. *Bulletin of Volcanology*, **71**, 337-355.

CONSTANTINI, L., HOUGHTON, B.F. & BONADONNA, C. 2010. Constraints on eruption dynamics of basaltic explosive activity derived from chemical and microtextural study: The example of the Fontana Lapilli Plinian eruption, Nicaragua. *Journal of Volcanology and Geothermal Research*, **189**, 207-224.

COOKE, N., SZAFIAN, P., GRUENWALD, R. & SCHULER, L. 2014. Forward modelling to understand colour responses in an HDFD RGB blend around a gas discovery. *First break*, **32**, 1-7.

CORCORAN, P.L. & MOORE, L.N. 2008. Subaqueous eruption and shallow-water reworking of a small-volume Surtseyan edifice at Kakanui, New Zealand. *Canada Journal of Earth Science*, **45**, 1469-1485.

CORS, J., HEIMHOFER, U., ADATTE, T., HOCHULIS, P.A., HUCK, S. & BOVER-ARNAL, T. 2014. Climatic evolution across oceanic anoxic event 1a derived from terrestrial palynology and clay minerals (Maestrat Basin, Spain). *Geology Magazine, Cambridge University Press*, **152** (4), 632-647.

COSTA, L. I. 2012. High resolution biostratigraphy, 204/10a-4 & -4z Wells, Cambo Field, Faroe-Shetland Basin. 204/10a-4 Well: Interval 5800'-9000'. 204/10a-4z: Interval 8780'-8860'. Report No. 7170/1a. Project No. 1a/GC469. 41.

COUVES, C., ROBERTS, S., RACEY, A., TROTH, I. & BEST, A. 2016. Use of X-Ray computed tomography to quantify the petrophysical properties of volcanic rocks: a case study from Tenerife, Canary Islands. *Journal of Petroleum Geology*, **39** (1), 79-94.

- CUTTLE, M.V.W., LOWE, R.J., FALTER, J.L. & BUSCOMBE, D. 2017. Estimating the settling velocity of bioclastic sediment using common grain-size analysis techniques. *Sedimentology*, **64**, 987-1004.
- DAVIES, J.F., GRANT, R.W.E. & WHITEHEAD, R.E.S. 1979. Immobile trace elements and Archean volcanic stratigraphy in the Timmins mining area, Ontario. *Canadian Journal of Earth Sciences*, **16** (2), 305-311.
- DAWSON, F., HARRIS, C. & STEAD, D. 2013. West of Shetland Well 204/5a-1 (Cambo-5). Biostratigraphy of the Interval 6240'-9144'(TD). Project No. SPA6649. 24.
- DEAN, K., McLACHLAN, K. & CHAMBERS, A. 1999. Rifting and the development of the Faeroe-Shetland Basin. *Petroleum Geology of Northwest Europe: Proceedings of the 5th Conference*, 533-544.
- DEEGAN, C.E. & SCULL, B.J. 1977. A standard lithostratigraphic nomenclature for the Central and northern North Sea. *Institute of Geological Sciences Report*, **77** (25), 1-36.
- DEEV, E.V., ZOLNIKOV, I.D. & LOBOVA, E.Y. 2015. Late Pleistocene-Holocene coseismic deformations in the Malyi Yaloman River Valley (Gorny Altai). *Russian Geology and Geophysics*, **56**, 1256-1272.
- DELLINO, P., GUDMUNDSSON, M.T., LARSEN, G., MELE, D., STEVENSON, J.A., THORDARSON, T. & ZIMANOWSKI, B. 2012. Ash from the Eyjafjallajökull eruption (Iceland): Fragmentation processes and aerodynamic behaviour. *Journal of Geophysical Research*, **117**, B00C04. DOI: 10.1029/2011JB008726
- DMITRIEVA, E., JACKSON, C.A-L., HUUSE, M. & MCCARTHY, A. 2012. Paleocene deep-water depositional systems in the North Sea Basin: a 3D seismic and well data case study, offshore Norway. *Petroleum Geoscience*, **18**, 97-114.
- D'ORIANO, C., BERTAGNINI, A., CIONI, R. & POMPILIO, M. 2014. Identifying recycled ash in basaltic eruptions. *Scientific Reports*, **4**, 5851. DOI: 10.1038/srep05851
- DORONZO, D.M. & DELLINO, P. 2013. Hydraulics of subaqueous ash flows as deduced from their deposits: 2. Water entrainment, sedimentation, and deposition, with implications on pyroclastic density current deposit emplacement. *Journal of Volcanology and Geothermal Research*, **258**, 176-186.
- DOUBLET, S. & GARCIA, J-P. 2004. The significance of dropstones in a tropical lacustrine setting, eastern Cameros Basin (Late Jurassic-Early Cretaceous, Spain). *Sedimentary Geology*, **163** (3-4), 293-309.
- DUGUID, S.M.A., KYSER, T.K., JAMES, N.P. & RANKEY, E.C. 2010. Microbes and Ooids. *Journal of Sedimentary Research*, **80**, 236-251.
- DURANT, A.J., ROSE, W.I., SARNA-WOJCICKI, A.M., CAREY, S., & VOLENTICK, A.C.M. 2009. Hydrometeor-enhanced tephra sedimentation: Constraints from the 18 May 1980 eruption of Mount St. Helens. *Journal of Geophysical Research*, **114**, B03204, 21.

EBDON, C.C., GRANGER, P.J., JOHNSON, H.D. & EVANS, A.M. 1995. Early Tertiary evolution and sequence stratigraphy of the Faeroe-Shetland Basin: implications for hydrocarbon prospectivity. *In*: Scrutton, R.A., Stoker, M.S., Shimmield, G.B. & Tudhope, A.W. (eds). The Tectonics, Sedimentation and Palaeoceanography of the North Atlantic Region. *Geological Society Special Publications*, No. 90, 51-69.

EBINGHAUS, A., HARTLEY, A.J., JOLLEY, D.W., HOLE, M. & MILLETT, J. 2014. Lava-sediment interaction and drainage-system development in a large igneous province: Columbia River flood basalt province, Washington State, U.S.A. *Journal of Sedimentary Research*, **84**, 1041-1063.

ELLIOT, W.C., ARONSON, J.L. & MILLARD Jr, H.T. 1992. Iridium content of basaltic tuffs and enclosing black shales of the Balder Formation, North Sea. *Geochimica et Cosmochimica Acta*, **56**, 2955-2961.

ELLIOTT, G.F. 1971. Eocene volcanics in south-east England. *Nature, Physical Sciences*, **230**, 9.

ELLIOTT, C.G. & WILLIAMS, P.F. 1988. Sediment slump structures: a review of diagnostic criteria and application to an example from Newfoundland. *Journal of Structural Geology*, **10** (2), 171-182.

ELLIS, B.S., BRANNEY, M.J., BARRY, T.L., BRIFORD, D., BINDEMAN, I., WOLFF, J.A. & BONNICHSEN, B. 2012. Geochemical correction of three large-volume ignimbrites from the Yellowstone hotspot track, Idaho, USA. *Bulletin of Volcanology*, **74**, 261-277.

ELLIS, D. & STOKER, M.S. 2014. The Faroe-Shetland Basin: a regional perspective from the Paleocene to the present day and its relationship to the opening of the North Atlantic Ocean. *Geological Society, London, Special Publications*, **397**, 11-31.

ELLIS, B.S., WOLFF, J.A., BOROUGHS, S., MARK, D.F., STARKEL, W.A. & BONNICHSEN, B. 2013. Rhyolitic volcanism of the central Snake River Plain: a review. *Bulletin of Volcanology*, **75**, 745. DOI 10.1007/s00445-013-0745-y

ELLISON, R.A., KNOX, R.W.O'B., JOLLEY, D.W. & KING, C. 1994. A revision of the lithostratigraphical classification of the early Palaeogene strata of the London Basin and East Anglia. *Proceedings of the Geologists' Association*, **105**, 187-197.

ELSIK, W.C. 1977 (1975). *Paralecaniella indentata* (Defl. & Cookson 1955) Cookson Eisenack 1970 and allied dinocysts. *Palynology*, **1**, Proceedings of the Eighth Annual Meeting, October 1975 (1977), 95-102.

ENGEL, M.S. 2004. Notes on a Megachiline Bee (Hymenoptera: Megachilidae) from the Miocene of Idaho. *Transactions of the Kansas Academy of Science*, **107** (1), 97-100.

ERTAN, I.E. & LEEMAN, W.P. 1999. Fluid inclusions in mantle and lower crustal xenoliths from the Simcoe volcanic field, Washington. *Chemical Geology*, **154** (1-4), 83-95.

- FAURIA, K.E., MANGA, M. & CHAMBERLAIN, M. 2016. Effect of particle entrainment on the runout of pyroclastic density currents. *Journal of Geophysical Research: Solid Earth*, **121** (9), 6445-6461.
- FERGUSON, D.J., GONNERMAN, H.M., RUPRECHT, P., PLANK, T., HAURI, E.H. & HOUGHTON, B.F. 2016. Magma decompression rates during explosive eruptions of Kilauea volcano, Hawaii, recorded by melt embayments. *Bulletin of Volcanology*, **78**, 71.
- FERGUSON, R.I. & CHURCH, M. 2004. A simple universal equation for grain settling velocity. *Journal of Sedimentary Research*, **74** (6), 933-937.
- FERREIRA, T. & RASBAND, W. 2012. ImageJ User Guide. *IJ 1.46r Revised Edition*, 198.
- FERRIS, J.A. & LEHMAN, J.T. 2007. Interannual variation in diatom bloom dynamics: Roles of hydrology, nutrient limitation, sinking, and whole lake manipulation. *Water Research*, **41**, 2551-2562.
- FISHER, R.V. 1961. Proposed classification of volcanoclastic sediments and rocks. *Geological Society of America Bulletin*, **72**, 1409-1414.
- FISHER, R.V. 1984. Submarine volcanoclastic rocks. *Geological Society of London Special Publications*, **16**, 5-27.
- FITCH, E.P., FAGENTS, S.A., THORDARSON, T. & HAMILTON, C.W. 2017. Fragmentation mechanisms associated with explosive lava-water interactions in a lacustrine environment. *Bulletin of Volcanology*, **79**, 12. DOI 10.1007/s00445-016-1087-3
- FLÜGEL, E. 2010. Microfacies of Carbonate Rocks. Analysis, Interpretation and Application. Second Edition. *Springer*, 1006.
- FOLK, R.E. 1968. Petrology of Sedimentary Rocks. *Hamphill, Austin, Texas*, 170.
- FOLK, R.L. & WARD, W. 1957. Brazos River bar: a study in the significance of grain size parameters. *Journal of Sedimentary Petrology*, **27**, 3-26.
- FRASER, C., HILL, P.R. & ALLARD, M. 2005. Morphology and facies architecture of a falling sea level strandplain, Umiujaq, Hudson Bay, Canada. *Sedimentology*, **52**, 141-160.
- FREEMAN, P., KELLY, S., MacDONALD, C., MILLINGTON, J. & TOTHILL, M. 2008. The Schiehallion Field: lessons learned modelling a complex deepwater turbidite. From: Robinson, A., Griffiths, P., Price, S., Hegre, J. & Muggeridge, A. (eds). The future of geological modelling in hydrocarbon development. *The Geological Society of London, Special Publications*, **309**, 205-219.
- FREDA, C., GAETA, M., GIACCIO, B., MARRA, F., PALLADINO, D.M., SCARLATO, P. & SOTTILI, G. 2011. CO₂-driven large mafic explosive eruptions: the Pozzolane Rosse case study from the Colli Albani Volcanic District (Italy). *Bulletin of Volcanology*, **73**, 241-256.

- FROLOVA, Y.V. 2008. Specific Features in the Composition, Structure, and Properties of Volcaniclastic Rocks. *Moscow University Geology Bulletin*, **63** (1), 28-37.
- GAMI, B., RASCONI, S., NIQUIL, N., JOBARD, M., SAINT-BÉAT, & SIME-NGANDO, T. 2011. Functional Effects of Parasites on Food Web Properties during the Spring Diatom Bloom in Lake Pavin: A Linear Inverse Modeling Analysis. *PLoS ONE*, **6** (8), e23273. DOI 10.1371/journal.pone.0023273
- GAO, S. & COLLINS, M. 1992. Net sediment transport patterns inferred from grain-size trends, based upon definition of 'transport vectors'. *Sedimentary Geology*, **80**, 47-60.
- GAONAC'H, H., LOVEJOY, S. & SCHERTZER, D. 2005. Scaling vesicle distributions and volcanic eruptions. *Bulletin of Volcanology*, **67**, 350-357.
- GERNIGON, L., GAINA, C., OLESEN, O., BALL, P.J., Péron-Pinvidic, G. & Yamasaki, T. 2012. The Norway Basin revisited: From continental breakup to spreading ridge extinction. *Marine and Petroleum Geology*, **35**, 1-19.
- GIHM, Y.S. & HWANG, I.G. 2014. Syneruptive and intereruptive lithofacies in lacustrine environments: The Cretaceous Beolkeum Member, Wido Island, Korea. *Journal of Volcanology and Geothermal Research*, **273**, 15-32.
- GIRESE, P., WIEWIÓRA, A. 1999. Origin and diagenesis of blue-green clays and volcanic glass in the Pleistocene of the Côte d'Ivoire-Ghana Marginal Ridge (ODP Leg 159, Site 959). *Sedimentary Geology*, **127**, 247-269.
- GJERLØW, E., HÖSKULDSSON, A. & PEDERSEN, R-B. 2015. The 1732 Surtseyan eruption of Eggøya, Jan Mayen, North Atlantic: deposits, distribution, chemistry and chronology. *Bulletin of Volcanology*, **77** (14), DOI 10.1007/s00445-014-0895-6.
- GLAZE, L.S. & BALOGA, S.M. 2016. Simulation of cooling and pressure effects on inflated pahoehoe lava flows. *Journal of Geophysical Research: Solid Earth*, **121**, 38-47.
- GLENN, C.R. & KELTS, K. 1991. Sedimentary Rhythms in Lake Deposits. In: Einsele, G., Ricken, W. & Seilacher, A. 1991. *Cycles and Events in Stratigraphy*. Springer-Verlag, 955.
- GLUYAS, J.G. & SWARBRICK, R.E. 2004. Petroleum Geoscience. *Blackwell Science Ltd*, 359.
- GOEPFERT, K. & GARDNER, J.E. 2010. Influence of pre-eruptive storage conditions and volatile contents on explosive Plinian style eruptions of basic magma. *Bulletin of Volcanology*, **72**, 511-521
- GRADSTEIN, F.M., KRISTIANSEN, I.L., LOEMO, L. & KAMINSKI, M.A. 1992. Cenozoic foraminiferal and dinoflagellate cyst biostratigraphy of the central North Sea. *Micropaleontology*, **38** (2), 101-137.
- GRADSTEIN, F.M., OGG, J.G., SCHMITZ, M.D. & OGG, G.M. (eds). 2012. *The Geologic Time Scale*. ISBN: 978-0-444-59425-9.

- GRAETTINGER, A.H., SKILLING, I., MCGARVIE, D. & HÖSKULDSSON, Á. 2013. Subaqueous basaltic magmatic explosions trigger phreatomagmatism: A case study from Askja, Iceland. *Journal of Volcanology and Geothermal Research*, **264**, 17-35.
- GRÖNVOLD, K., ÓSKARSSON, N., JOHNSEN, S.J., CLAUSEN, H.B., HAMMER, C.U., BOND, G. & BARD, E. 1995. Express Letter. Ash layers from Iceland in the Greenland GRIP ice core correlated with oceanic and land sediments. *Earth and Planetary Science Letters*, **135**, 149-155.
- GROVE, C. & JERRAM, D.A. 2011. jPOR: An ImageJ macro to quantify total optical porosity from blue-stained thin sections. *Computers and Geosciences*, **37**, 1850-1859.
- GUASTI, E., KOUWENHOVEN, T.J., BRINKUIS, H. & SPEIJER, R.P. 2005. Paleocene sea-level and productivity changes at the southern Tethyan margin (El Kef, Tunisia). *Marine Micropaleontology*, **55**, 1-17
- GUDMUNDSDÓTTIR, E.R., EIRÍKSSON, J. & LARSEN, G. 2011. Identification and definition of primary and reworked tephra in Late Glacial and Holocene marine shelf sediments off North Iceland. *Journal of Quaternary Science*, **26** (6), 589-602.
- GURENKO, A.A., BELOUSOV, A.B., TRUMBULL, R.B. & SOBOLEV, A.V. 2005. Explosive basaltic volcanism of the Chikurachki Volcano (Kurile arc, Russia): Insights on pre-eruptive magmatic conditions and volatile budget revealed from phenocryst-hosted melt inclusions and groundmass glasses. *Journal of Volcanology and Geothermal Research*, **147**, 203-232.
- GUTJAHR, M., RIDGWELL, A., SEXTON, P.F., ANAGNOSTOU, E., PEARSON, P.N., PÄLIKE, H., NORRIS, R.D., THOMAS, E. & FOSTER, G.L. 2017. Very large release of mostly volcanic carbon during the Palaeocene-Eocene Thermal Maximum. *Nature*, **548**, 573-577.
- HAALAND, H.J., FURNES, H. & MARTINSEN, O.J. 2000. Paleogene tuffaceous intervals, Grain Field (Block 25/11), Norwegian North Sea: their depositional, petrographical, geochemical character and regional implications. *Marine and Petroleum Geology*, **17**, 101-118.
- HALLAM, A. 1972. Relation of Palaeogene ridge and basin structures and vulcanicity in the Hebrides and Irish Sea regions of the British Isles to the opening of the North Atlantic. *Earth and Planetary Science Letters*, **16**, 171-177.
- HAMBLIN, W.K. 1994. Late Cenozoic Lava Dams in the Western Grand Canyon. *Geological Society of America Memoir*, **13**, 139.
- HAMILTON, C.W., THORDARSON, T. & FAGENTS, S.A. 2010. Explosive lava-water interactions I: architecture and emplacement chronology of volcanic rootless cone groups in the 1783-1784 Laki lava flow, Iceland. *Bulletin of Volcanology*, **72**, 449-467.
- HANSEN, J., JERRAM, D.A., MCCAFFREY, K. & PASSEY, S.R. 2009. The onset of the North Atlantic Igneous Province in a rifting perspective. *Geological Magazine*, **146** (3), 309-325.

- HANSON, R.E. & ELLIOT, D.H. 1996. Rift-related Jurassic basaltic phreatomagmatic volcanism in the central Transantarctic Mountains: precursory stage of flood-basalt effusion. *Bulletin of Volcanology*, **58**, 327-347.
- HARDING, I.C., CHARLES, A.J., MARSHALL, J.E.A., PÄLIKE, H., ROBERTS, A.P., WILSON, P.A., JARVIS, E., THORNE, R., MORRIS, E., MOREMON, R., PEARCE, R.B. & AKBARI, S. 2011. Sea-level and salinity fluctuations during the Paleocene-Eocene thermal maximum in Arctic Spitsbergen. *Earth and Planetary Science Letters*, **303**, 97-107.
- HASS, H.C. 2002. A method to reduce the influence of ice-rafter debris on a grain size record from northern Fram Strait, Arctic Ocean. *Polar Research*, **21** (2), 299-306.
- HASTIE, A.R., KERR, A.C., PEARCE, J.A. & MITCHELL, S.F. 2007. Classification of Altered Volcanic Island Arc Rocks using Immobile Trace Elements: Development of the Th-Co Discrimination Diagram. *Journal of Petrology*, **48** (12), 2341-2357.
- HASZELDINE, R.S., RITCHIE, J.D. & HITCHEN, K. 1987. Seismic and well evidence for the early development of the Faeroe-Shetland Basin. *Scottish Journal of Geology*, **23** (3), 283-300.
- HEAD, J.W. & WILSON, L. 1989. Basaltic pyroclastic eruptions: Influence of gas-release patterns and volume fluxes on fountain structure, and the formation of cinder cones, spatter cones, rootless flows, lava ponds and lava flows. *Journal of Volcanology and Geothermal Research*, **37**, 261-271.
- HEAP, M.J., XU, T. & CHEN, C-f. 2014. The influence of porosity and vesicle size on the brittle strength of volcanic rocks and magma. *Bulletin of Volcanology*, **76**, 856, 15.
- HEIKEN, G.H. 1972. Morphology and petrology of volcanic ashes. *Geological Society of America Bulletin*, **83**, 1961-1988.
- HEIKEN, G.H. 1974. An atlas of volcanic ash. *Smithsonian Contributions to Earth Science*, **12**.
- HEILBRONNER, R. & BARRETT, S. 2014. Image Analysis in Earth Sciences. Microstructures and Textures of Earth Materials. *Springer Heidelberg*, 520.
- HEISTER, L.E., O'DAY, P.A., BROOKS, C.K., NEUHOFF, P.S. & BIRD, D.K. 2001. Pyroclastic deposits within the East Greenland Tertiary flood basalts. *Journal of the Geological Society, London*, **158**, 269-284.
- HENDRY, J.P., WILKINSON, M., FALLICK, A.E. & HASZELDINE, R.S. 2000. Ankerite cementation in deeply buried Jurassic sandstone reservoirs of the Central North Sea. *Journal of Sedimentary Research*, **70** (1), 227-239.
- HETÉNYI, G., TAIŠNE, B., GAREL, F., MÉDARD, É., BOSSHARD, S. & MATTSSON, H.B. 2012. Scales of columnar jointing in igneous rocks: field measurements and controlling factors. *Bulletin of Volcanology*, **74**, 457-482.

- HITCHEN, K. & RITCHIE, J.D. 1993. New K-Ar ages, and a provisional chronology, for the offshore part of the British Tertiary Igneous Province. *Scottish Journal of Geology*, **29**, 73-85.
- HOLMES, N. A., AYRESS, M. & ALDERSON, A. 1999a. A biostratigraphical Evaluation of the Conoco Well 204/14-1, West of Shetland. Prepared for Conoco (UK) Ltd by Ichron Limited. Ref no. 98/195/B. 28.
- HOLMES, N. A., AYRESS, M. & ALDERSON, A. 1999b. A biostratigraphical Evaluation of the Conoco Well 204/14-2, West of Shetland. Prepared for Conoco (UK) Ltd by Ichron Limited. Ref no. 98/225/B. 28.
- HOMUTH, S., PALSSON, B., HOLGEIRSSON, S. & SASS, I. 2010. Risk Management and Contingency Planning for the First Icelandic Deep Drilling Project Well in Krafla, Iceland. *Proceedings World Geothermal Congress*, 1-12.
- HOOKE, J.J. 1996. Mammalian biostratigraphy across the Paleocene-Eocene boundary in the Paris, London and Belgian basins. *From: Knox, R.W.O'B., Corfield, R.M. & Dunay, R.E. (eds). Correlation of the Early Paleogene in Northwest Europe. Geological Society Special Publication*, **101**, 205-218.
- HOOPER, P.R. 1982. The Columbia River Basalts. *Science*, **215**, 1463-1468.
- HOOPER, P.R. 1985. A case of simple magma mixing in the Columbia River Basalt Group: The Wilbur Creek, Lapwai, and Asotin Flows, Saddle Mountains Formation. *Contributions to Mineralogy and Petrology*, **91**, 66-73.
- HOPKINS, J.L., WILSON, C.J.N., MILLET, M-A., LEONARD, G.S., TIMM, C., MCGEE, L.E., SMITH, I.E. & SMITH, E.G.C. 2017. Multi-criteria correlation of tephra deposits to source centres applied in the Auckland Volcanic Field, New Zealand. *Bulletin of Volcanology*, **79**, 55.
- HÖSKULDSSON, Á., ÓSKARSSON, N., PEDERSEN, R., GRÖNVOLD, K., VOGFJÖRD, K. & ÓLAFSDÓTTIR, R. 2007. The millennium eruption of Hekla in February 2000. *Bulletin of Volcanology*, **70** (2), 169-182.
- HOUGHTON, B.F. & GONNERMANN, H.M. 2008. Basaltic explosive volcanism: Constraints from deposits and models. *Chemie der Erde*, **68**, 117-140.
- HOUGHTON, B.F., SWANSON, D.A., CAREY, R.J., RAUSCH, J., & SUTTON, A.J. 2011. Pigeonholing pyroclasts: Insights from the 19 March 2008 explosive eruption of Kilauea volcano. *Geology*, **39**, 263-266.
- HOUGHTON, B.F. & WILSON, C.J.N. 1989. A vesicularity index for pyroclastic deposits. *Bulletin of Volcanology*, **51**, 451-462.
- HOUGHTON, B.F., WILSON, C.J.N. & SMITH, I.E.M. 1999. Shallow-seated controls on styles of explosive basaltic volcanism: a case study from New Zealand. *Journal of Volcanology and Geothermal Research*, **91**, 97-120.
- HOUGHTON, B.F., WILSON, C.J.N., DEL CARLO, P., COLTELLI, M., SABLE, J.E. & CAREY, R. 2004. The influence of conduit processes on changes in style of basaltic Plinian eruptions: Tarawera 1886 and Etna 122 BC. *Journal of Volcanology and Geothermal Research*, **137**, 1-14.

- HURST, A., SCOTT, A. & VIGORITO, M. 2011. Physical characteristics of sand injectites. *Earth-Science Reviews*, **106**, 215-246.
- IBELINGS, B.W., GSELL, A.S., MOOIJ, W.M., VAN DONK, E., VAN DEN WYNGAERT, S. & DE SENERPONT DOMIS, L.N. 2011. Chytrid infections and diatom spring blooms: paradoxical effects of climate warming on fungal epidemics in lakes. *Freshwater Biology*, **56** (4), 754-766.
- INMAN, D.L. 1952. Measures for describing the size distribution of sediments. *Journal of Sedimentary Petrology*, **22**, 125-145.
- JACQUÉ, M. & THOUVENIN, J. 1975. Lower Tertiary tuffs and volcanic activity in the North Sea. *Petroleum and the continental shelf of north-west Europe*, **1**, 455-465.
- JAMES, M.R., LANE, S.J. & GILBERT, J.S. 2003. Density, construction, and drag coefficient of electrostatic volcanic ash aggregates. *Journal of Geophysical Research*, **108** (B9), 2435-2447.
- JANEBO, M.H., THORDARSON, T., HOUGHTON, B.F., BONADONNA, C., LARSEN, G. & CAREY, R.J. 2016. Dispersal of key subplinian-Plinian tephra from Hekla volcano Iceland: implications for eruption source parameters. *Bulletin of Volcanology*, **78**, 66. DOI 10.1007/s00445-016-1059-7
- JEANS, C.V., WRAY, D.S., MERRIMAN, R.J. & FISHER, M.J. 2000. Volcanogenic clays in Jurassic and Cretaceous strata of England and the North Sea Basin. *Clay Minerals*, **35**, 25-55.
- JENNINGS, A.E., GRÖNVOLD, K., HILBERMAN, R., SMITH, M. & HALD, M. 2002. High-resolution study of Icelandic tephra in the Kangerlussuaq Trough, southeast Greenland, during the last deglaciation. *Journal of Quaternary Science*, **17** (8), 747-757.
- JENNINGS, A., THORDARSON, T., ZALZAL, K., STONER, J., HAYWARD, C., GEIRSDÓTTIR, Á. 2014. Holocene tephra from Iceland and Alaska in SE Greenland Shelf Sediments. *From: Austin, W.E., Abbott, P.M., Davies, S.M., Pearce, N.J.G. & Wastegård, S. (eds). Marine Tephrochronology. Geological Society, London, Special Publications*, **398**, 157-193.
- JERRAM, D.A., GOODENOUGH, K.M. & TROLL, V.R. 2009. Introduction: from the British Tertiary into the future - modern perspectives on the British Palaeogene and North Atlantic Igneous provinces. *Geological Magazine*, **146** (3), 305-308.
- JOHANNSDÓTTIR, G.E., THORDARSON, T. & LARSEN, G. 2004. The widespread ~10ka Saksunarvatn tephra: a product of large-scale basaltic phreatoplinian eruption? *IAVCIE Chile Gen Assembly, Puco, 2004, abstract S12_o_03*.
- JOLLEY, D.W. 1996. The earliest Eocene sediments of eastern England: an ultra-high resolution palynological correlation. *From: Knox, R.W., O'B., Corfield, R.M. & Dunay, R.E. (eds). 1996. Correlation of the Early Paleogene in Northwest Europe. Geological Society Special Publications*, **101**, 219-254.

JOLLEY, D. W. 2011. Biostratigraphy and ecology of the earliest Eocene and Late Palaeocene in Well 204/10a-3 Faroe-Shetland Basin. Prepared on behalf of Hess UK. 32.

JOLLEY, D. W. 2014. Biostratigraphy and ecology of Late Paleocene to Early Eocene Lamba, Flett and BF's in Well 204/5a-1, Cambo Prospect, Corona Ridge, Faroe-Shetland Basin. Prepared on behalf of Hess UK. 41.

JOLLEY, D.W. & BELL, B.R. 2002. The evolution of the North Atlantic Igneous Province and the opening of the NE Atlantic rift. *Geological Society, London, Special Publications*, **197**, 1-23.

JOLLEY, D.W. & MORTON, A.C. 1992. Palynological and petrological characterization of a North Sea Palaeocene volcanoclastic sequence. *Proceedings of the Geologists' Association*, **103** (2), 119-127.

JOLLEY, D.W. & MORTON, A.C. 2007. Understanding basin sedimentary provenance: evidence from allied phytogeographic and heavy mineral analysis of the Palaeocene of the North East Atlantic. *Journal of the Geological Society, London*, **164**, 553-563.

JOLLEY, D.W., MORTON, A.C. & PRINCE, I. 2005. Volcanogenic impact on phytogeography and sediment dispersal patterns in the North East Atlantic. *From: Doré, A.G. & Vining, B.A. (eds). Petroleum Geology: North-West Europe and Global perspectives - Proceedings of the 6th Petroleum Conference*, 969-975.

JOLLEY, D.W. & WIDDOWSON, M. 2005. Did Paleogene North Atlantic rift-related eruptions drive early Eocene climate cooling? *Lithos*, **79**, 355-366.

JONK, R. 2010. Sand-rich injectites in the context of short-lived and long-lived fluid flow. *Basin Research*, **22** (4), 603-621.

JONKERS, L., BARKER, S., HALL, I.R. & PRINS, M.A. 2015. Correcting for the influence of ice-rafted detritus on grain size-based paleocurrent speed estimates. *Paleoceanography*, **30** (10), 1347-1357.

JORDT, H., FALEIDE, J.I., BJØRLYKKE, K. & IBRAHIM, M.T. 1995. Cenozoic sequence stratigraphy of the central and northern North Sea Basin: tectonic development, sediment distribution and provenance areas. *Marine and Petroleum Geology*, **12** (8), 845-879.

JOY, A.M. 1996. Controls on Eocene sedimentation in the central North Sea Basin: results of a basinwide correlation study.

JUNG, C., JUNG, S., HOFFER, E. & BERNDT, J. 2006. Petrogenesis of Tertiary Mafic Alkaline Magmas in the Hoheifel, Germany. *Journal of Petrology*, **47** (8), 1637-1671.

JUTZELER, M., PROUSSEVITCH, A.A. & ALLEN, S.R. 2012. Grain-size distribution of volcanoclastic rocks 1: A new technique based on functional stereology. *Journal of Volcanology and Geothermal Research*, **239-240**, 1-11.

KALE, M.G., PUNDALIK, A.S., DURAI SWAMI, R.A. & KARMALKAR, N.R. 2016. Soft Sediment Deformation Structures from Khari River Section of Rudramata Member, Jhuran Formation, Kutch: A Testimony of Jurassic Seismites. *Journal Geological Society of India*, **87**, 194-204.

KANARIS-SOTIRIOU, R., MORTON, A.C. & TAYLOR, P.N. 1993. Paleogene peraluminous magmatism, crustal melting and continental break-up: the Erland Complex, Faroe-Shetland Basin, NE Atlantic. *Journal of the Geological Society, London*, **150**, 903-914.

KANDLBAUER, J., CAREY, S.N. & SPARKS, S.J. 2013. The 1815 Tambora ash fall: implications for transport and deposition of distal ash on land and in the deep sea. *Bulletin of Volcanology*, **75**, 708 DOI: 10/1007/s00445-01300708-3

KANE, I.A. 2010. Development and flow structures of sand injectites: The Hind Sandstone Member injectite complex, Carboniferous, UK. *Marine and Petroleum Geology*, **27**, 1200-1215.

KATTENHORN, S.A. & SCHAEFER, C.J. 2008. Thermal-mechanical modelling of cooling history and fracture development in inflationary basalt lava flows. *Journal of Volcanology and Geothermal Research*, **170**, 181-197.

KENDER, S., STEPHENSON, M.H., RIDING, J.B., LENG, M.L., KNOX, R.W.O'B. PECK, V.L., KENDRICK, C.P., ELLIS, M.A., VANE, C.H. & JAMIESON, R. 2012. Marine and terrestrial environmental changes in NW Europe preceding carbon release at the Paleocene-Eocene transition. *Earth and Planetary Science Letters*, **353-354**, 108-120.

KENT-CORSON, M.L., BARNOCKY, A.D., MULCH, A., CARRASCO, M.A. & CHAMBERLAIN, C.P. 2013. Possible regional tectonic controls on mammalian evolution in western North America. *Palaeogeography, Palaeoclimatology, Palaeoecology*, **387**, 17-26.

KENT, R.W. & FITTON, J.G. 2000. Mantle sources and melting dynamics in the British Palaeogene Igneous Province. *Journal of Petrology*, **41** (7), 1023-1040.

KIIPLI, T., ORLOVA, K., KIIPLI, E. & KALLASTE, T. 2008. Use of immobile trace elements for the correlation of Telychian bentonites on Saaremaa Island, Estonia, and mapping of volcanic ash clouds. *Estonian Journal of Earth Sciences*, **57**, 1, 39-52.

KING, C. 1981. The stratigraphy of the London Clay and Associated deposits. *Tertiary Research Special Paper*, **6**. Backhuys, Rotterdam.

KING, C. (Gale, A.S. & Barry, T.L. eds). 2016. A Revised Correlation of Tertiary Rocks in the British Isles and adjacent areas of NW Europe. *The Geological Society, Special Report*, **27**, 719.

KINSELA, M.A., DALEY, M.J.A. & COWELL, P.J. 2016. Origins of Holocene coastal strandplains in Southeast Australia: Shoreface sand supply driven by disequilibrium morphology. *Marine Geology*, **374** (1), 24-43.

KNOTT, T.R., REICHOW, M.K., BRANNEY, M.J., FINN, D.R., COE, R.S., STOREY, M. & BONNICHSEN, B. 2016. Rheomorphic ignimbrites of the Rogerson Formation,

central Snake River Plain, USA: record of mid-Miocene rhyolitic explosive eruptions and associated crustal subsidence along the Yellowstone hotspot track. *Bulletin of Volcanology*, **78**, 23. DOI 10.1007/s00445-016-1003-x

KNOX, R.W.O'B. 1984. Nannoplankton zonation and the Palaeocene/Eocene boundary beds of NW Europe: in an indirect correlation by means of volcanic ash layers. *Journal of the Geological Society*, **141**, 993-999.

KNOX, R.W.O'B. 1996. Tectonic controls on sequence development in the Palaeocene and earliest Eocene of southeast England: implications for the North Sea stratigraphy. *Geological Society Special Publication*, **103**, 209-230.

KNOX, R.W.O'B. 1997. The late Paleocene to early Eocene ash layers of the Danish Mo-clay (Fur Formation): stratigraphic and tectonic significance. In: Thomsen, E., Pedersen, S.A.S. (eds) *Geology and palaeontology of the mo-clay. Aarhus Geoscience*, **6**, 7-11.

KNOX, R.W.O'B. & ELLISON, R.A. 1979. A Lower Eocene ash sequence in SE England. *Journal of the Geological Society*, **136**, 251-253.

KNOX, R.W.O'B. & HARLAND, R. 1979. Stratigraphical relationships of the early Palaeogene ash-series of NW Europe. *Journal of the Geological Society*, **136**, 463-470.

KNOX, R.W.O'B. & MORTON, A.C. 1983. Stratigraphical distribution of early Palaeogene pyroclastic deposits in the North Sea Basin. *Proceedings of the Yorkshire Geological Society*, **44** (3), 993-999.

KNOX, R.W.O'B. & MORTON, A.C. 1988. The record of early Tertiary N Atlantic volcanic in sediments of the North Sea Basin. *Geological Society Special Publication*, **39**, 407-419.

KNOX, R.W.O'B. & HOLLOWAY, S. 1992. 1. Paleogene of the Central and Northern North Sea. In: Knox, R.W.O'B. & Cordey, W.G. (eds). *Lithostratigraphic nomenclature of the UK North Sea. British Geological Survey, Nottingham*, 160.

KOKELAAR, B.P. 1983. The mechanisms of Surtseyan volcanism. *Journal of Geological Society, London*, **140**, 939-944.

KOKELAAR, P.B. & DURANT, G.P. 1983. The submarine eruption and erosion of Surtla (Surtsey), Iceland. *Journal of Volcanology and Geothermal Research*, **19**, 239-246.

KOUFOS, G.D. 2016. *Hipparion macedonicum* revisited: New data on evolution of hipparionine horses from the Late Miocene of Greece. *Acta Palaeontologica Polonica*, **61** (3), 519-536.

KURIBAYASHI, E. & TATSUOKA, F. 1975. Brief review of liquefaction during earthquakes in Japan. *Soils*, **15** (4), 81-92.

KUTTEROLF, S., FREUNDT, A., PÉREZ, W., WEHRMANN, H. & SCHMINCKE, H.-U. 2007. Late Pleistocene to Holocene temporal succession and magnitudes of highly-explosive volcanic eruptions in west-central Nicaragua. *Journal of Volcanology and Geothermal Research*, **163**, 55-82.

- KUTTEROLF, S., FREUDT, A. & PERÉZ, W. 2008. Pacific offshore record of Plinian arc volcanism in Central America: 2. Tephra volumes and erupted masses. *Geochemistry, Geophysics, Geosystems*, **9** (2), Q02S02. DOI: 10.1029/2007GC001791
- LARSEN, G. & EIRÍKSSON, J. 2008. Late Quaternary terrestrial tephrochronology of Iceland - frequency of explosive eruptions, type and volume of tephra deposits. *Journal of Quaternary Science*, **23** (2), 109-120.
- LARSEN, L.M., FITTON, J.G. & PEDERSEN, A.K. 2003. Paleogene volcanic ash layers in the Danish Basin: compositions and source areas in the North Atlantic Igneous Province. *Lithos*, **71**, 47-80.
- LARSEN, L.M., WAAGSTEIN, R., PEDERSEN, A.K. & STOREY, M. 1999a. Trans-Atlantic correlation of the Palaeogene volcanic successions in the Faroe Islands and East Greenland. *Journal of the Geological Society, London*, **156**, 1081-1095.
- LARSEN, M., HAMBERG, L., OLAUSSEN, S., PREUSS, T. & STEMMERIK, L. 1999. Sandstone wedges of the Cretaceous-Lower Tertiary Kangerlussaq Basin, East Greenland - outcrop analogues to the offshore North Atlantic. In: Fleet, A.J. & Boldy, S.A.R. (eds). *Petroleum Geology of Northwest Europe: Proceedings of the 5th Conference*, 337-348.
- LaRUE, A., BAKER, D.R., POLACCI, M., ALLARD, P. & SODINI, N. 2013. Can vesicle size distributions assess eruption intensity during volcanic activity? *Solid Earth*, **4**, 373-380.
- LAUTZE, N. & HOUGHTON, B.F. 2007. Linking variable explosion style and magma textures during 2002 at Stromboli volcano, Italy. *Bulletin of Volcanology*, **69**, 445-460.
- LAWTON, T.F. & BUCK, B.J. 2006. Implications of diapir-derived detritus and gypsic paleosols in Lower Triassic strata near the Castle Valley salt wall, Paradox Basin, Utah. *Geology*, **34** (10), 885-888.
- LENHARDT, N., HORNING, J., HINDERER, M., BÖHNEL, H., TORRES-ALVARADO, I.S. & TRAUTH, N. 2011. Build-up and depositional dynamics of an arc front volcanoclastic complex: the Miocene Tepoztlán Formation (Transmexican Volcanic Belt, Central Mexico). *Sedimentology*, **58**, 785-823.
- LERBEKMO, J.F. 2008. The White River Ash: largest Holocene Plinian tephra. *Canadian Journal of Earth Sciences*, **45**, 693-700.
- LEWIS, T., FRANCUS, P., BRADLEY, R.S. & KANAMARU, K. 2010. An automated system for the statistical analysis of sediment texture and structure at the micro scale. *Computers and Geosciences*, DOI: 10.1016/j.cageo.2010.03.018
- LIND, E.M., WASTEGÅRD, S. & LARSEN, J.J. 2013. A Late Younger Dryas-Early Holocene tephrostratigraphy for Fosen, Central Norway. *Journal of Quaternary Science*, **28** (8), 803-811.
- LOCKHEART, M.J., VAN BERGEN, P.F. & EVERSLED, R.P. 2000. Chemotaxonomic classification of fossil leaves from the Miocene Clarkia lake deposit, Idaho, USA

based on *n*-alkyl lipid distributions and principal component analyses. *Organic Geochemistry*, **31**, 1223-1246.

LOHNE, Ø, S., MANGERUD, J. & BIRKS, H.H. 2013. Precise ¹⁴C ages of the Vedde and Saksunarvatn ashes and the Younger Dryas boundaries from western Norway and their comparison with the Greenland Ice Core (GICC05) chronology. *Journal of Quaternary Science*, **28** (5), 490-500.

LOHNE, Ø.S., MANGERUD, J. & BIRKS, H.H. 2014. IntCal13 calibrated ages of the Vedde and Saksunarvatn ashes and the Younger Dryas boundaries from Kråkenes, western Norway. *Journal of Quaternary Science*, **29** (5), 506-507.

LOTT, G.K., KNOX, R.W., O'B, HARLAND, R. & HUGHES, M.J. 1983. The stratigraphy of Palaeogene sediments in a cored borehole off the coast of north-east Yorkshire. *Institute of Geological Sciences Report*, **89**(3), 1-8.

LOURENS, L.J., SLUIJS, A., KROON, D., ZACHOS, J.C., THOMAS, E. & ROHL, U. 2005. Astronomical pacing of late Palaeocene to early Eocene global warming events. *Nature*, **435**, 1083-1087.

LOWE, D.J. 2011. Tephrochronology and its application: A review. *Quaternary Geochronology*, **6** (2), 107-153.

MACFADDEN, B.J. 1985. Patterns of Phylogeny and Rates of Evolution in Fossil Horses: Hipparions from the Miocene and Pliocene of North America. *Paleobiology*, **11** (3), 245-257.

MACHADO, F., PARSONS, W.H., RICHARDS, A.F. & MULFORD, J.W. 1962. Capelinhos eruption of Fayal Volcano, Azores, 1957-1958. *Journal of Geophysical Research*, **67** (9), 3519-3569.

MAHDI, S. 2004. Well 204/10-2 West of Shetland Basin. Biostratigraphy of the Interval 1580m-3539mTD. Report No. B-759. Project No. AB596.

MAHDI, S. A. 2003. Well 204/10-1 (Cambo) Faeroe-Shetland Basin. Biostratigraphy of the Interval 1662m-2523mTD. Report no. B-707. Project No. AB538.

MAKIN, J.H. 1947. Diatomite deposits in eastern Washington (Abstract). *Northwest Science*, **21**, 33.

MALM, O.A., CHRISTENSEN, O.B., FURNES, H., LØVLIE, R., RUSELÅTTEN, H. & ØSTBY, K.L. 1984. The Lower Tertiary Balder Formation: An organogenic and tuffaceous deposit in the North Sea region. *Petroleum geology of the North European margin, Norwegian Petroleum Society*, 149-170.

MANDEVILLE, C., CAREY, S., SIGURDSSON, H. 1996. Sedimentology of the Krakatau 1883 submarine pyroclastic deposits. *Bulletin of Volcanology*, **57** (7), 512-529.

MANGER, G.E. 1963. Porosity and Bulk Density of Sedimentary Rocks. *Contributions to Geochemistry, Geological Survey Bulletin*, **1144-E**, 55.

- MANGERUD, J., FURNES, H. & JÓHANSEN, J. 1986. A 9000-Year-Old Ash Bed on the Faroe Islands. *Quaternary Research, Short Papers*, **26**, 262-265.
- MANNEN, K. 2006. Total grain size distribution of a mafic subplinian tephra, TB-2, from the 1986 Izu-Oshima eruption, Japan: An estimation based on a theoretical model of tephra dispersal. *Journal of Volcanology and Geothermal Research*, **155** (1-2), 1-17.
- MANTAS, V.M., PEREIRA, A.J.S.C. & MORAIS, P.V. 2011. Plumes of discoloured water of volcanic origin and possible implications for algal communities. The case of Home Reef eruption of 2006 (Tong, Southwest Pacific Ocean). *Remote Sensing of Environment*, **115**, 1341-1352.
- MANVILLE, V. & WILSON, C.J.N. 2004. Vertical density currents: a review of their potential role in the deposition and interpretation of deep-sea ash layers. *Journal of the Geological Society, London*, **161**, 947-958.
- MANVILLE, V., NÉMETH, K. & KANO, K. 2009. Source to sink: A review of three decades of progress in the understanding of volcanoclastic processes, deposits, and hazards. *Sedimentary Geology*, **220**, 136-161.
- MARTÍN-GONZÁLEZ, A., WIERZCHOS, J., GUTIÉRREZ, J-C., ALONSO, J. & ASCASO, C. 2009. Double fossilization in eukaryotic microorganisms from Lower Cretaceous amber. *BMC Biology*, **7** (9).
- MARUYAMA, S., HATTORI, K., HIRATA, T., SUZUKI, T. & DANHARA, T. 2016. Simultaneous determination of 58 major and trace elements in volcanic glass shards from the INTAV sample mount using femtosecond laser ablation-inductively coupled plasma-mass spectrometry. *Geochemical Journal*, **50** (5), 403-422.
- MASCARENHAS-PEREIRA, M.B.L., NAGENDER NATH, B., BOROLE, D.V. & GUPTA, S.M. 2006. Nature, source and composition of volcanic ash in sediments from a fracture zone trace of Rodriguez Triple Junction in the Central Indian Basin. *Marine Geology*, **229**, 79-90.
- MATTSSON, H.B. 2010. Textural variation in juvenile pyroclasts from an emergent, Sutseyan-type, volcanic eruption: the Capelas tuff cone, Sao Miguel (Azores). *Journal of Volcanology and Geothermal Research*, **189**, 81-91.
- MAZUMDER, R. 2000. Turbulence-particle interactions and their implications for sediment transport and bedform mechanics under unidirectional current: some recent developments. *Earth-Science Reviews*, **50**, 113-124.
- McLEAN, D.M. 1976. *Eocladopyxis peniculatum* Morgenroth, 1966, Early Tertiary ancestor of the modern dinoflagellate *Pyrodinium bahamense* Plate, 1906. *Micropaleontology*, **22** (3), 347-351.
- MERKT, J., MÜLLER, H., KNABE, W., MÜLLER, P., & WEISER, T. 1993. The early Holocene Saksunarvatn tephra found in lake sediments in NW Germany. *Boreas*, **22**, 93-100.
- MERRISON, J.P. 2012. Sand transport, erosion and granular electrification. *Aeolian Research*, **4**, 1-16.

- MIALL, A. 2014. Fluvial Depositional Systems. *Springer*, 322.
- MILLER, M.B. 2014. Roadside Geology of Oregon, Second Edition. *Mountain Press Publishing Company*, 386.
- MILTON, N.J., BERTRAM, G.T. & VANN, I.R. 1990. Early Palaeogene tectonics and sedimentation in the Central North Sea. *In*: Hardman, R.P.F & Brooks, J. (eds). Tectonic Events Responsible for Britain's Oil and Gas Reserves. *Geological Society of London, Special Publication*, **55**, 339-351.
- MITLEHNER, A.G. 1996. Paleoenvironments in the North Sea Basin around the Paleocene-Eocene boundary: evidence from diatoms and other siliceous microfossils. *From*: Knox, R.W.O'B., Corfield, R.M. & Dunay, R.E. (eds), 1996. Correlation of the Early Paleogene in Northwest Europe, *Geological Society Special Publication*, **101**, 255-273.
- MOITRA, P., GONNERMANN, H.M., HOUGHTON, B.F. & GIACHETTI, T. 2013. Relating vesicle shapes in pyroclasts to eruption styles. *Bulletin of Volcanology*, **75**, 691.
- MOOREHOUSE, B.L., WHITE, J.D.L. & SCOTT, J.M. 2015. Cape Wanbrow: A stack of Surtseyan-style volcanoes built over millions of years in the Waiareka-Deborah volcanic field, New Zealand. *Journal of Volcanology and Geothermal Research*, **298**, 27-46.
- MORGENSTERN, D.P., 1967. Submarine slumping and the initiation of turbidity currents. *In*: Richards, A.F. (editor). Marine Geotechnique. *University of Illinois Press, Urbana Ill*, 189-219.
- MORTENSEN, A.K., BIGLER, M., GRÖNVOLD, K., STEFFENSEN, J.P. & JOHNSEN, S.J. 2005. Volcanic ash layers from the Last Glacial Termination in the NGRIP ice core. *Journal of Quaternary Science*, **20** (3), 209-219.
- MORTON, A.C. & KNOX, R. W. O'B. 1990. Geochemistry of late Palaeocene and early Eocene tephra from the North Sea Basin. *Journal of the Geological Society*, **147**, 425-437.
- MORTON, A.C., BOYD, J.D. & EWEN, D.F. 2002. Evolution of Paleocene sediment dispersal systems in the Foinaven Sub-basin, West of Shetland. *From*: Jolley, D.W. & Bell, B.R. (eds). The North Atlantic Igneous Province: Stratigraphy, tectonic, volcanic and magmatic processes. Geological Society, London, Special Publications, **197**, 69-93.
- MUDGE, D.C. 2014. Regional controls on Lower Tertiary sandstone distribution in the North Sea and NE Atlantic margin basins. *From*: McKie, T., Rose, P.T.S., Hartley, A.J., Jones, D.W. & Armstrong, T.L. (eds). Tertiary Deep-Marine Reservoirs of the North Sea Region. *Geological Society, London, Special Publications*, **403**, pp 26.
- MUDGE, D.C. & BLISS, G.M. 1983. Stratigraphy and sedimentation of the Palaeocene sands in the Northern North Sea. *Geological Society, London, Special Publications*, **12**, 95-111.

- MUDGE, D.C. & BUJAK, J.P. 1994. Eocene stratigraphy of the North Sea basin. *Marine and Petroleum Geology*, **11** (2), 166-181.
- MUDGE, D.C. & BUJAK, J.P. 1996. An integrated stratigraphy for the Paleocene and Eocene of the North Sea. *Geological Society, London, Special Publications*, **101**, 91-113.
- MUDGE, D.C. & COPESTAKE, P. 1992a. Lower Palaeogene stratigraphy of the northern North Sea. *Marine and Petroleum Geology*, **9**, 287-301.
- MUDGE, D.C. & JONES, S.M. 2004. Palaeocene uplift and subsidence events in the Scotland-Shetland and North Sea region and their relationship to the Iceland Plume. *Journal of the Geological Society, London*, **161**, 381-386.
- MUELLER, W.U., GARDE, A.A. & STENDAL, H. 2000. Shallow-water, eruption-fed, mafic pyroclastic deposits along a Paleoproterozoic coastline: Kangerluluk volcano-sedimentary sequence, southeast Greenland. *Precambrian Research*, **101**, 163-192.
- MUELLER, S.B., Kueppers, U., Ayris, P.M., Jacob, M. & Dingwell, D.B. 2016. Experimental volcanic ash aggregation: Internal structuring of accretionary lapilli and the role of liquid bonding. *Earth and Planetary Science Letters*, **433**, 232-240.
- MURTAGH, R.M., WHITE, J.D.L. & SOHN, Y.K. 2011. Pyroclast textures of the Ilchulbong 'wet' tuff cone, Jeju Island, South Korea. *Journal of Volcanology and Geothermal Research*, **201**, 385-396.
- MUSSETT, A.E., DAGLEY, P. & SKELHORN, R.R. 1988. Time and duration of activity in the British Tertiary Igneous Province. In: Morton, A.C. & Parseon, L.M. (eds) Early Tertiary Volcanism and the Opening of the NE Atlantic. *Geological Society Special Publication*, **39**, 337-348.
- NADIN, P.A., KUSZNIR, N.J. & CHEADLE, M.J. 1997. Early Tertiary plume uplift of the North Sea and Faeroe-Shetland Basins. *Earth and Planetary Science Letters*, **148**, 109-127.
- NASH, B.P. & PERKINS, M.E. 2012. Neogene Fallout Tuffs from the Yellowstone Hotspot in the Columbia Plateau Region, Oregon, Washington and Idaho, USA. *PLOS ONE*, **7** (10), e44205.
- NAYLOR, P.H., BELL, B.R., JOLLEY, D.W., DURNALL, P. & FREDSTED, R. 1999. Palaeogene magmatism in the Faeroe-Shetland Basin: influences on uplift history and sedimentation. *Petroleum Geology of Northwest Europe: Proceedings of the 5th Conference*, 545-558.
- NEAL, J.E. 1996. A summary of Paleogene sequence stratigraphy in northwest Europe and the North Sea. In: Knox, R.W.O'B., Corfield, R.M. & Dunay, R.E. (eds). Correlation of the Early Paleogene in Norwest Europe. *Geological Society Special Publication*, **101**, 15-42.
- NEAVE, D.A., MACLENNAN, J., THORDARSON, T. & HARTLEY, M.E. 2015. The evolution and storage of primitive melts in the Eastern Volcanic Zone of Iceland:

- the 10 ka Grímsvötn tephra series (i.e. the Saksunarvatn ash). *Contributions to Mineralogy and Petrology*, **170** (2), 1-23.
- NÉMETH, K. & CRONIN, S.J. 2009. Phreatomagmatic volcanic hazards where rift-systems meet the sea, a study from Ambae Island, Vanuatu. *Journal of Volcanology and Geothermal Research*, **180**, 246-258.
- NEWELL, A.J. 2014. Paleogene rivers of southern Britain: climatic extremes, marine influence and compressional tectonics on the southern margin of the North Sea Basin. *Proceedings of the Geologists' Association*, **125**, 578-590.
- NIELSEN, O.B. 1974. Sedimentation and diagenesis of Lower Eocene sediments at Ölst, Denmark. *Sedimentary Geology*, **12**, 25-44.
- NORIN, R. 1940. Problems concerning the volcanic ash layers of the Lower Tertiary of Denmark. *Geologiska Föreningen I Stockholm Förhandlingar*, **62** (1), 31-44.
- NORMANDEAU, A., LAJEUNESSE, P. & St-ONGE, G. 2013. Shallow-water onshore drift-fed submarine fan deposition (Mosisie River Delta, Eastern Canada). *Geo-Marine Letters*, **33**, 391-403.
- Norsk Hydro a.s. 1993. Final Well Report, Well 25/11-17, Licence 169. 127.
- OBST, K. ANSORGE, J., MATTING, S. & HÜNEKE. 2015. Early Eocene volcanic ashes on Greifswalder Oie and their depositional environment, with an overview of coeval ash-bearing deposits in northern Germany and Denmark. *International Journal of Earth Science*, **104**, 2179-2212.
- ODDSSON, B., GUDMUNDSSON, M.T., LARSEN, G. & KARLSDÓTTIR, S. 2012. Monitoring of the plume from the basaltic phreatomagmatic 2004 Grímsvötn eruption - applications of weather radar and comparison with plume models.
- OHFUJI, H. & RICKARD, D. 2005. Experimental syntheses of frambooids - a review. *Earth-Science Reviews*, **71**, 147-170.
- ORTÍ, F., GÜNDÖGAN, I. & HELVACI, C. 2002. Sodium sulphate deposits of Neogene age: the Kirmir Formation, Beypazari Basin, Turkey. *Sedimentary Geology*, **146**, (3-4), 305-333.
- OWEN, G., MORETTI, M. & ALFARO, P. 2011. Recognising triggers for soft-sediment deformation: Current understanding and future directions. *Sedimentary Geology*, **235**, 133-140.
- PARFITT, E.A. 2004. A discussion of the mechanisms of explosive basaltic eruptions. *Journal of Volcanology and Geothermal Research*, **134**, 77-107.
- PARTYKA, G.A., BUSH, M.D., GAROSSINO, P.G.A. & GUTOWSKI, P.R. 2011. Spectral Decomposition. *From: Brown, A.R. (ed). AAPG Memoir 42*, 7th edition, 646.
- PASSEY, S.R. & BELL, B.R. 2007. Morphologies and emplacement mechanisms of the lava flows of the Faroe Islands Basalt Group, Faroe Islands, NE Atlantic Ocean. *Bulletin of Volcanology*, **70**, 139-156.

PASSEY, S.R. & JOLLEY, D.W. 2009. A revised lithostratigraphic nomenclature for the Palaeogene Faroe Islands Basalt Group, NE Atlantic Ocean. *Earth and Environmental Science Transactions of the Royal Society of Edinburgh*, 99, 127-158.

PEDERSEN, A.K., ENGELL, J. & RØNSBO, J.G. 1975. Early Tertiary volcanism in the Skagerrak: New chemical evidence from ash-layers in the mo-clay of northern Denmark. *Lithos*, 8, 255-268.

PEDERSEN, A.K. & JØRGENSEN, K.A. 1981. A textural study of basaltic tephras from lower Tertiary diatomites in Northern Denmark. In: Self, S. & Sparks (eds). *Tephra Studies. Proceedings of the NATO Advanced Study Institute 'Tephra Studies as a Tool in Quaternary Research.'* 213-218.

PEDERSEN, G.K. & SURLYK, F. 1983. The Fur Formation, a late Paleocene ash-bearing diatomite from northern Denmark. *Bulletin of the Geological Society of Denmark*, 32, 43-65.

PEMBERTON, G.S., MacEACHERN, J.A., DASHTGARD, S.E., BANN, K.L., GINGRAS, M.K. & ZONNEVELD, J-P. Shorefaces. In: Knaust, D. & Bromley, R.G. (eds) *Trace Fossils as Indicators of Sedimentary Environments. Developments in Sedimentology*, 64, 563-603.

PÉREZ, W., FREUNDT, A., KUTTEROLF, S. & SCHMINCKE, H.-U. 2009. The Masaya Triple Layer: A 2100 year old basaltic multi-episodic Plinian eruption from the Masaya Caldera Complex (Nicaragua). *Journal of Volcanology and Geothermal Research*, 179 (3-4), 191-205.

Perillo, M.M., Best, J.L., Yokokawa, M., Sekiguchi, T., Takagawa, T. & Garcia, M.H. 2014. A unified model for bedform development and equilibrium under unidirectional, oscillatory and combined-flows. *Sedimentology*, 61 (7), 2063-2085.

PERKINS, M.E., NASH, W.P., BROWN, F.H., FLECK, R.J. 1995. Fallout tuffs of Trapper Creek, Idaho - A record of Miocene explosive volcanism in the Snake River Plain volcanic province. *Geological Society of America Bulletin*, 107 (12), 1484-1506.

PERKINS, M.E., BROWN, F.H., NASH, W.P., McINTOSH, W., WILLIAMS, S.K. 1998. Sequence, age, and source of silicic fallout tuffs in middle to late Miocene basins of the northern Basin and Range province. *Geological Society of America Bulletin*, 110 (3), 344-360.

PERUCCA, L.P., GODOY, E. & PANTANO, A. 2014. Late Pleistocene-Holocene earthquake-induced slumps and soft-sediment deformation structures in the Acequion River valley, Central Precordillera, Argentina. *Geologos*, 20 (2), 147-156.

PETZING, J. & CHESTER, R. 1979. Authigenic marine zeolites and their relationship to global volcanism. *Marine Geology*, 29, 253-271.

PHILLIPS, J.C., HUMPHREYS, M.C.S., DANIELS, K.A., BROWN, R.J. & WITHAM, F. 2013. The formation of columnar joints produced by cooling in basalt at Staffa, Scotland. *Bulletin of Volcanology*, 75:715, DOI: 10.1007/s00445-013-0715-4

- PISARSKA-JAMROŻY, M. & WECKWERTH, P. 2012. Soft-sediment deformation structures in a Pleistocene glaciolacustrine delta and their implications for the recognition of subenvironments in delta deposits. *Sedimentology*, **60** (3), 637-665.
- POLACCI, M., BAKER, D.R., BAI, L. & MANCINI, L. 2008. Large vesicles record pathways of degassing at basaltic volcanoes. *Bulletin of Volcanology*, **70**, 1023-1029.
- POMPILIO, M., BERTAGNINI, A., DEL CARLO, P. & DI ROBERTO, A. 2017. Magma dynamics within a basaltic conduit revealed by textural and compositional features of erupted ash: the December 2015 Mt. Etna paroxysms. *Scientific Reports*, **7**, 4805. DOI: 10.1038/s41598-017-05065-x
- POPESCUOP, R. 2002. Finite element assessment of the effects of seismic loading rate on soil liquefaction. *Canadian Geotechnical Journal*, **39** (2), 331.
- PRATT, T.L. 2012. Large-scale splay faults on a strike-slip fault system: The Yakima Folds, Washington State. *Geochemistry, Geophysics, Geosystems*, **13** (11), Q11004.
- PROTHERO, D.R. 1990. Interpreting the stratigraphic record. *Freeman & Company*, 410.
- PSZONKA, J. & WENDORFF, M. 2017. Carbonate cements and grains in submarine fan sandstones - the Cergowa Beds (Oligocene, Carpathians of Poland) recorded by cathodoluminescence. *International Journal of Earth Sciences*, **106**, 269-282.
- PUEYO, E.L., MUÑOZ, A., LAPLANA, C. & PARÉS, J.M. 2016. The Last Appearance Datum of *Hipparion* in Western Europe: magnetostratigraphy along the Pliocene-Pleistocene boundary in the Villarroja Basin (Northern Spain). *International Journal of Earth Science*, **105**, 2203-2220.
- PYLE, D. 1989. The thickness, volume and grainsize of tephra fall deposits. *Bulletin of Volcanology*, **51**, 1-15.
- QUINN, M., VARMING, T. & ÓLAVSDOTTIR, J. 2011. 12 Petroleum geology. *From: Ritchie, J.D., Ziska, H., Johnson, H. & Evans, D. (eds). Geology of the Faroe-Shetland Basin and adjacent areas. British Geological Survey Research Report, RR/11/01; Jarðfeingi Research Report, RR/11/01.*
- RAILSBACK, L.B. 2011. Petroleum Geoscience and Subsurface Geology
- RAO, V.P. & MILLIMAN, J.D. 2017. Relict ooids off northwestern India: Inferences on their genesis and late Quaternary sea level. *Sedimentary Geology*, **358**, 44-50.
- RASMUSSEN, T.L., THOMSEN, E., NIELSEN, T. & WASTEGÅRD, S. 2011. Atlantic surface water inflow to the Nordic seas during the Pleistocene-Holocene transition (mid-late Younger Dryas and Pre-Boreal periods, 12 450-10 000 a BP). *Journal of Quaternary Science*, **26** (7), 723-733.
- READING, H.G. 1996. Sedimentary Environments: Processes, Facies and Stratigraphy. *Blackwell Science*, Third edition, 688.

- READING, H.G. 2009. Sedimentary environments: processes, facies, and stratigraphy. Third edition. *Wiley-Blackwell*, 669.
- REIDEL, S.P., CAMP, V.E., TOLAN, T.L. & MARTON, B.S. 2013. The Columbia River flood basalt province: Stratigraphy, areal extent, volume, and physical volcanology. *The Geological Society of America, Special Paper*, **497**, 1-43.
- RIEGEL, W., LENZ, O.K. & WILDE, V. 2015. From open estuary to meandering river in a greenhouse world: An ecological case study from the middle Eocene of Helmstedt, Northern Germany. *Palaios*, **30**, 304-326.
- RETALLACK, G.J., TANAKA, S. & TATE, T. 2002. Late Miocene advent of tall grassland paleosols in Oregon. *Palaeogeography, Palaeoclimatology, Palaeoecology*, **183**, 329-354.
- REYNOLDS, P., BROWN, R.J., THORDARSON, T., LLEWELLIN, E.W. & FIELDING, K. 2015. Rootless cone eruption processes informed by dissected tephra deposits and conduits. *Bulletin of Volcanology*, **77** (72), 1-17.
- RICHEY, J.E., MACGREGOR, A.G. & ANDERSON, F.W. 1961. British Regional Geology. Scotland: The Tertiary Volcanic Districts (third editions). *Natural Environment Research Council, Institute of Geological Sciences, Geological Survey and Museum, Edinburgh, Her Majesty's stationary office*, 121.
- RICKARD, D.T. 1970. The origin of framboids. *Lithos*, **3**, 269-293.
- RIGGS, N.R., ORT, M.H., WHITE, J.D.L., WILSON, C.J.N., HOUGHTON, B.F. & CLARKSON, R. 2001. Post-1.8-ka marginal sedimentation in Lake Taupo, New Zealand: effects of wave energy and sediment supply in a rapidly rising lake. In: White, J.D.L. & Riggs, N.R. (editors). Volcaniclastic sedimentation in Lacustrine Settings. *Special Publication number 30 of the International Association of Sedimentologists*, 151-177.
- RILEY, C.M., ROSE, W.I. & BLUTH, G.J. 2003. Quantitative shape measurements of distal volcanic ash. *Journal of Geophysical Research*, **108** (B10), 2504.
- RINDSBERG, A.K. 2012. Inchnotaxonomy: Finding Patterns in a Welter of Information. In: Knaust, D. & Bromley, R.G. (eds) Trace Fossils as Indicators of Sedimentary Environments. *Developments in Sedimentology*, **64**, 45-78.
- RITCHIE, D., ZISKA, H., KIMBELL, G., QUINN, M. & CHADWICK, A. 2011. 2 Structure. From: Ritchie, J.D., Ziska, H., Johnson, H. & Evans, D. (eds). Geology of the Faroe-Shetland Basin and adjacent areas. *British Geological Survey Research Report*, RR/11/01; *Jardfeingi Research Report*, RR/11/01.
- RITCHIE, J.D. & HITCHEN, K. 1996. Early Paleogene offshore igneous activity to the northwest of the UK and its relationship to the North Atlantic Igneous Province. *Geological Society, London, Special Publications*, **101**, 63-78.
- ROBERTS, D.G., MORTON, A.C. & BACKMAN, J. 1984. Late Paleocene-Eocene volcanic events in the northern North Atlantic Ocean. *Initial Reports of the DSDP*, **81**, 913 - 923.

- ROSE, W.I., SELF, S., MURROW, P.J., BONADONNA, C., DURANT, A.J. & ERNST, G.G.J. 2008. Nature and significance of small volume fall deposits at composite volcanoes: Insights from the October 14, 1974 Fuego eruption, Guatemala. *Bulletin of Volcanology*, **70** (9), 1043-1067.
- ROSE, W.I. & DURANT, A.J. 2009. Fine ash content of explosive eruptions. *Journal of Volcanology and Geothermal Research*, Article in Press, VOLGEO-04233.
- ROSS, P-S. & BÉDARD, J.H. 2009. Magmatic affinity of modern and ancient subalkaline volcanic rocks determined from trace-element discrimination diagrams. *Canadian Journal of Earth Science*, **46**, 823-839.
- ROSS, P-S., PEATE, I.U., McCLINTOCK, M.K., XU, Y.G., SKILLING, I.P., WHITE, J.D.L. & HOUGHTON, B.F. 2005. Mafic volcanoclastic deposits in flood basalt provinces: A review. *Journal of Volcanology and Geothermal Research*, **145**, 281-314.
- ROSS, P-S. & WHITE, J.D.L. 2012. Quantification of vesicle characteristics in some diatreme-filling deposits and the explosivity levels of magma-water interactions within diatremes. *Journal of Volcanology and Geothermal Research*, **245-246**, 55-67.
- ROUND, F.E., CRAWFORD, R.M. & MANN, D.G. 1990. The Diatoms: biology & morphology of the genera. *Cambridge University Press*, 747.
- ROYSE, K.R., DE FREITAS, M., BURGESS, W.G., COSGROVE, J., GHAIL, R.C., GIBBARD, P., KING, C., LAWRENCE, U., MORTIMORE, R.N., OWEN, H. & SKIPPER, J. 2012. Geology of London, UK. *Proceedings of the Geologists' Association*, **13**, 22-45.
- SABLE, J., HOUGHTON, B.F., DEL CARLO, P. & COLTELLI, M. 2006. Changing conditions of magma ascent and fragmentation during the Etna 122 BC basaltic Plinian eruption: evidence from clast microtextures. *Journal of Volcanology and Geothermal Research*, **158**, 333-354.
- SAMSON, S.D., MATTHEWS, S., MITCHELL, C.E. & GOLDMAN, D. 1995. Tephrochronology of highly altered ash beds: The use of trace element and strontium isotope geochemistry of apatite phenocrysts to correlate K-bentonites. *Geochimica et Cosmochimica Acta*, **59** (12), 2527-2536.
- SAUNDERS, A.D., FITTON, J.G., KERR, A.C., NORRY, M.J. & KENT, R.W. 1997. The North Atlantic Igneous Province. In: Mahoney, J.J., Coffin, M.L. (eds). Large Igneous Provinces: Continental, Oceanic, and Planetary Flood Volcanism. *American Geophysical Union, Geophysical Monographs*, **100**, 45-93.
- SCHINLBECK, J.C., KUTTEROLF, S., FREUNDT, A., SCUDDER, R.P., PICKERING, K.T. & MURRAY, R.W. 2013. Emplacement processes of submarine volcanoclastic deposits (IODP Site C0011, Nankai Trough). *Marine Geology*, **343**, 115-124.
- SCHOFIELD, N. & JOLLEY, D.W. 2013. Development of intra-basaltic lava-field drainage systems within the Faroe-Shetland Basin. *Petroleum Geoscience*, **19**, 273-288.

- SCHMINCKE, H.-U. 1964. Petrology, paleocurrents, and stratigraphy of the Ellensburg Formation and interbedded Yakima Basalt flows, south-central Washington [PhD thesis]: Baltimore, Maryland, Johns Hopkins University, 426.
- SCHMINCKE, H.-U. 1967a. Graded lahars in the type sections of the Ellensburg Formation, South-Central Washington. *Journal of Sedimentary Petrology*, **37** (2), 438-448.
- SCHMINCKE, H.-U. 1967b. Fused tuff and peperites in South-Central Washington. *Geological Society of America, Bulletin*, **78**, 319-330.
- SCHMID, R. 1981. Descriptive nomenclature and classification of pyroclastic deposits and fragments: Recommendations of the IUGS Subcommission on the Systematics of Igneous Rocks. *Geology*, **9**, 41-43.
- SCOLAMACCHIA, T., MACÍAS, J.L., SHERIDAN, M.F. & HUGHES, S.R. 2005. Morphology of ash aggregates from wet pyroclastic surges of the 1982 eruption of El Chichón Volcano, Mexico. *Bulletin of Volcanology*, **68**, 171-200.
- SCOTT, B. & PRICE, S. 1988. Earthquake-induced structures in young sediments. *Tectonophysics*, **147**, 165-170.
- SCOTT, J.J. BUATOIS, L.A. & MÁNGANO, G.M. 2012. Lacustrine Environments. In: Knaust, D. & Bromley, R.G. (eds) Trace Fossils as Indicators of Sedimentary Environments. *Developments in Sedimentology*, **64**, 379-417.
- SEED, H.B. & LEE, K.L. 1966. Liquefaction of saturated sands during cyclic loading. *Journal of Soil Mechanics*, **93**, 83-108.
- SELLEY, R.C. 1976. An Introduction to Sedimentology. *Academic Press*, 408.
- SHAW, G.H. 2003. Trace element chemistry of individual apatite phenocrysts as a tool for fingerprinting altered volcanic ash beds: Assessing interbed and intrabed variation at local and regional scales. *Geological Society of America Bulletin*, **115** (8), 933-942.
- SHEA, T., HOUGHTON, B.F., GURIOLI, L., CASHMAN, K.V., HAMMER, J.E. & HOB DEN, B.J. 2010. Textural studies of vesicles in volcanic rocks: An integrated methodology. *Journal of Volcanology and Geothermal Research*, **190**, 271-289.
- SHERIDAN, M.F. & WOHL ETZ, K.H. 1983. Hydrovolcanism: Basic considerations and review. *Journal of Volcanology and Geothermal Research*, **17**, 1-29.
- SHIFA, Z., XIAOMIN, Z., XIN, L., DONG, W., DONGNA, Z. 2016. Authigenic minerals and diagenetic evolution in altered volcanic materials and their impacts on hydrocarbon reservoirs: evidence from the lower Permian in the northwestern margin of Junggar Basin, China. *Arabian Journal of Geoscience*, **9**, 97.
- SIMONSEN, L. & TOFT, J. 2006. Texture, composition and stratigraphy of volcanic ash beds in lower Palaeocene chalk from the North Sea Central Graben area. *Marine and Petroleum Geology*, **23**, 767-776.

SINGH, I.B., SRIVASTAVA, P., SHARMA, S., SHARMA, M., SIGNH, D.S., RAJAGOPALAN, G. & SHUKLA, U.K. 1999. Upland interfluvial (Doab) deposition: Alternative model to muddy overbank deposits. *Facies*, **40**, 197-210.

SJØHOLM, J., SEJRUP, H.P., & FURNES, H. 1991. Quaternary volcanic ash zones on the Iceland Plateau, southern Norwegian Sea. *Journal of Quaternary Science*, **6** (2), 159-173.

SKOGSEID, J., PLANKE, S., FALEIDE, J.I., PEDERSEN, T., ELDHOLM, O. & NEVERDAL, F. 2000. NE Atlantic continental rifting and volcanic margin formation. In: Nøttvedt et al. (eds) Dynamics of the Norwegian Margin. *Geological Society, London, Special Publications*, **167**, 295-326.

SLUIJS, A., BRINKHUIS, H., CROUCH, E.M., JOHN, C.M., HANDLEY, L., MUNSTERMAN, D., BOHATY, S.M., ZACHOS, J.C., REICHAERT, G.-J., SCHOUTEN, S., PANCOST, R.D., SINNINGHE DAMASTE, J.S., WELTERS, N.L.D., LOTTER, A.F. & DICKENS, G.R. 2008. Eustatic variations during the Paleocene-Eocene greenhouse world. *Paleoceanography*, **23**, 1-18.

SMALLWOOD, J.R. 2008. Uplift, compression and the Cenozoic Faroe-Shetland sediment budget. From: Johnson, H., Doré, A.G., Gatliff, R.W., Holdsworth, R., Lundin, E.R. & Ritchie, J.D. (eds). The nature and origin of compression in passive margins. *Geological Society, London, Special Publications*, **306**, 137-152.

SMALLWOOD, J.R. & GILL, C. 2002. The rise and fall of the Faroe-Shetland Basin: evidence from seismic mapping of the Balder Formation. *Journal of the Geological Society, London*, **159**, 627-630.

SMALLWOOD, J.R. & KIRK, W.J. 2005. Paleocene exploration in the Faroe-Shetland Channel: disappointments and discoveries. In: Doré, A.G. & Vining, B.A. (eds) *Petroleum Geology: North-West Europe and Global Perspectives - Proceedings of the 6th Petroleum Geology Conference*, 977-991.

SMITH, G.A. 1986. Coarse-grained nonmarine volcanoclastic sediment: Terminology and depositional process. *Geological Society of America Bulletin*, **97** (1), 1-10.

SMITH, G.A. 1988a. Sedimentology of proximal to distal volcanoclastics dispersed across an active foldbelt: Ellensburg Formation (late Miocene), central Washington. *Sedimentology*, **35**, 953-977.

SMITH, G.A. 1988b. Neogene synvolcanic and syntectonic sedimentation in central Washington. *Geological Society of America Bulletin*, **100**, 1479-1492.

SMITH, G.A., CAMPBELL, N.P., DEACON, M.W. & SHAFIQUILLAH, M. 1988. Eruptive style and location of volcanic centers in the Miocene Washington Cascade Range: Reconstruction from the sedimentary record. *Geology*, **16**, 337-340.

SMITH, T., QUESNEL, F., De Plöeg, G., De Franceschi, D., Métails, G., De Bast, E., Solé, F., Folie, A., Boura, A., Claude, J., Dupuis, C., Gagnaison, C., Iakovleva, A., Martin, J., Maubert, F., Prieur, J., Roche, E., Storme, J.-Y., Thomas, R., Tong, H., Yans, J. & Buffetaut, E. 2014. First Clarkforkian Equivalent Land Mammal Age in the Latest Paleocene Basal Sparnacian Facies of Europe: Fauna, Flora, Paleoenvironment and (Bio)stratigraphy. *PLoS ONE*, **9** (1), 1-20.

SMYTHE, D.K., CHALMERS, J.A., SKUCE, A.G., DOBBINSON, A. & MOULD, A.S. 1983. Early opening history of the North Atlantic - I. Structure and origin of the Faeroe-Shetland Escarpment. *Geophys. J. R. astr. Soc.* **72**, 373-398.

SNAVELY, P.D., MACLEOD, N.S. & WAGNER, H.C. 1973. Miocene Tholeiitic Basalts of Coastal Oregon and Washington and Their Relations to Coeval Basalts of the Columbia Plateau. *Geological Society of America Bulletin*, **84** (2), 387-424.

SOHN, Y.K., PARK, K, H. & YOON, S-H. 2008. Primary versus secondary and subaerial versus submarine hydrovolcanic deposits in the subsurface of Jeju Island, Korea. *Sedimentology*, **55**, 899-924.

SOLIMAN, A. 2012. Oligocene dinoflagellate cysts from the North Alpine Foreland Basin: new data from the Eggerding Formation (Austria). *Geologica Carpathica*, **63** (1), 49-70.

SOLGEVIK, H., MATTSSON, H.B. & HERMELIN, O. 2007. Growth of an emergent tuff cone: Fragmentation and depositional processes recorded in the Capelas tuff cone, São Miguel, Azores. *Journal of Volcanology and Geothermal Research*, **159**, 246-266.

SOMOZA, L., BARNOLAS, A., ARASA, A., MAESTRO, A., REES, J.G. & HERNANDES-MOLINA, F.J. 1998. Architectural stacking patterns of the Ebro delta controlled by Holocene high-frequency eustatic fluctuations, delta-lobe switching and subsidence processes. *Sedimentary Geology*, **117**, 11-32.

SORRENTINO, L., CAS, R.A.F. & STILLWELL, J.D. 2010. Evolution and facies architecture of Paleogene Surtseyan volcanoes on Chatham Islands, New Zealand, Southwest Pacific Ocean. *Journal of Volcanology and Geothermal Research*, **202**, 1-21.

SORRENTINO, L., STILLWELL, J.D. & MAYS, C. 2013. A model of tephra dispersal from an early Palaeogene shallow submarine Surtseyan-style eruption(s), the Red Bluff Tuff Formation, Chatham Island, New Zealand. *Sedimentary Geology*, **300**, 86-102.

SOULE, S.A., CASHMAN, K.V. & KAUAHIKAUA, J.P. 2004. Examining flow emplacement through the surface morphology of three rapidly emplaced, solidified lava flows, Kilauea Volcano, Hawai'i. *Bulletin of Volcanology*, **66**, 1-14.

ST JOHN, K., PASSCHIER, S., TANTILLO, B., DARBY, D. & KEARNS, L. 2015. Microfeatures of modern sea-ice-rafted sediment and implications for paleo-sea-ice reconstructions. *Annals of Glaciology*, **56** (69), 83-93.

STAROSTIN, A.B., BARMIN, A.A. & MELNIK, O.E. 2005. A transient model for explosive and phreatomagmatic eruptions. *Journal of Volcanology and Geothermal Research*, **143**, 133-151.

Statoil/Union/Tenneco. 1984. Completion Report, Well 30/2-1. Accessed through the Norwegian Petroleum Directorate 2016.

STEURBAUT, E., DE CONINCK, J., DUPUIS, C. & KING, C. 2009. Dinoflagellate cyst events and depositional history of the Paleocene/Eocene boundary interval in the southern North Sea Basin. *GFF*, **122**, 154-157.

STOKER, M.S., KIMBELL, G.S., McINROY, D.B. & MORTON, A.C. 2012. Eocene post-rift tectonostratigraphy of the Rockall Plateau, Atlantic margin of NW Britain: Linking early spreading tectonics and passive margin response. *Marine and Petroleum Geology*, **30**, 98-125.

STOKER, M. & VARMING, T. 2011. 8. Cenozoic (sedimentary). 151-208. In: *Geology of the Faroe-Shetland Basin and adjacent areas*. Ritchie, J. D., Ziska, H., Johnson, H. & Evans, D (editors). *British Geological Survey Research Report*, RR/11/01, *Jardfeingi Research Report*, RR/11/01.

STOREY, M., DUNCAN, R.A., TEGNER, C. 2007. Timing and duration of volcanism in the North Atlantic Igneous Province: Implications for geodynamics and links to the Iceland hotspot. *Chemical Geology*, **241**, 264-281.

STOVAL, W., HOUGHTON, B.F., GONNERMANN, H., FAGENTS, S. & SWANSON, D. 2011. Eruption dynamics of Hawaiian-style fountains: the case study of episode 1 of the Kilauea Iki 1959 eruption. *Bulletin of Volcanology*, **73**, 511-529.

STRAND, K. 2005. Sequence stratigraphy of the siliciclastic East Puolanka Group, the Palaeoproterozoic Kainuu Belt, Finland. *Sedimentary Geology*, **176**, 149-166.

STRECK, M.j., JOHNSON, J.A. & GRUNDNER, A. 1999. Field guide to the Rattlesnake Tuff and High Lava Plains near Burns, Oregon. *Or. Geol*, **61**, 64-76.

STRECK, M.J. & GRUNDER, A.L. 2008. Phenocryst-poor rhyolites of bimodal, tholeiitic provinces: the Rattlesnake Tuff and implications for mush extraction. *Bulletin of Volcanology*, **70**, 385-401.

SUAN, G., POPESCU, S-M., SUC, J-P., SCHNYDER, J., FAUQUETTE, S., BAUDIN, F., YOON, D., PIEPJOHN, K., SOBOLEV, N.N. & LABROUSSE, L. 2017. Subtropical climate conditions and mangrove growth in Arctic Siberia during the early Eocene. *Geology*, **45** (6), 539-542.

SUTHREN, R.J. 1985. Facies analysis of volcanoclastic sediments: a review. *Geological Society of London, Special Publications*, **18**, 123-146.

SVENSEN, H., PLANKE, S., MALTHE-SORENSEN, A., JAMTVEIT, B. & EIDEM, T.R. 2004. Release of methane from a volcanic basin as a mechanism for initial Eocene global warming.

SWANSON, D.A., WRIGHT, T.L., HOOPER, P.R. & BENTLEY, R.D. 1979. Revisions in Stratigraphic Nomenclature of the Columbia River Basalt Group. *Contributions to Stratigraphy. Geological Survey Bulletin*, **1457**, G1-G59.

SZramek, L.A. 2016. Mafic Plinian eruptions: Is fast ascent required? *Journal of Geophysical Research: Solid Earth*, **121** (10), 7119-7136.

TA, T.K.O., NGUYEN, V.L., TATEISHI, M., KOBAYASHI, I., SAITO, Y. & NAKAMURA, T. 2002. Sediment facies and Late Holocene progradation of the Mekong River Delta in Bentre Province, Southern Vietnam: an example of evolution from a

- tide-dominated to a tide-and wave-dominated delta. *Sedimentary Geology*, **152**, 313-325.
- TADDEUCCI, J., SCARLATO, P., MONTANARO, C., CIMARELLI, C., DEL BELLO, E., FREDA, C., ANDRONICO, D., GUDMUNDSSON, M.T. & DINGWELL, D.B. 2011. Aggregation-dominated ash settling from the Eyjafjallajökull volcanic cloud illuminated by field and laboratory high-speed imaging. *Geology*, **39** (9), 891-894.
- TANG, D., SHI, X., SHI, Q., WU, J., SONG, G. & JIANG, G. 2015. Organomineralization in Mesoproterozoic giant ooids. *Journal of Asian Earth Sciences*, **107**, 195-211.
- TAPPE, S. 2004. Mesozoic mafic alkaline magmatism of southern Scandinavia. *Contributions to Mineral Petrology*, **148**, 312-334.
- TAYLOR, B., GOODLIFFE, A., MARTINEZ, F. & HEY, R. 1995. Continental rifting and initial sea-floor spreading in the Woodlark basin. *Nature*, **374**, 534-537.
- THOMAS, D.J., BRALOWER, T.J. & JONES, C.E. 2003. Neodymium isotopic reconstruction of late Paleocene-early Eocene thermohaline circulation. *Earth and Planetary Science Letters*, **209**, 309-322.
- THOMAS, D.J. & BRALOWER, T.J. 2005. Sedimentary trace element constraints on the role of North Atlantic Igneous Province volcanism in late Paleocene-early Eocene environmental change. *Marine Geology*, **217**, 233-254.
- THORDARSON, T. 2014. The widespread ~10ka Saksunarvatn tephra is not a product of single eruption. *American Geophysical Union, Fall Meeting 2014*, abstract #V24B-04.
- THORDARSON, T. & HÖSKULDSSON, Á. 2008. Postglacial volcanism in Iceland. *Jökull*, No. **58**, 197-228.
- THORNALLEY, D.J.R., McCABE, I.N. & ELDERFIELD, H. 2011. Tephra in deglacial ocean sediments south of Iceland: Stratigraphy, geochemistry and oceanic reservoir ages. *Journal of Quaternary Science*, **26** (2), 190-198.
- TORSVIK, T.H., MOSAR, J. & EIDE, E.A. 2001. Cretaceous-Tertiary geodynamics: a North Atlantic exercise. *International Journal of Geophysics*, **146**, 850-866.
- TRIGILA, R., BATTAGLIA, M. & MANGA, M. 2007. An experimental facility for investigating hydromagmatic eruptions at high-pressure with application to the importance of magma porosity for magma-water interaction. *Bulletin of Volcanology*, **69**, 365-372.
- UEE/33. 1985. Sedimentological Note No. 118. Sedimentology of Eocene cores 1 to 3, Paleocene core 4 and Upper Jurassic core 5 from Shell/Esso Well 22/30a-1. 22.
- URAI, M. & MACHIDA, S. 2005. Discolored seawater detection using ASTER reflectance products: A case study of Satsuma-Iwojima, Japan. *Remote Sensing of Environment*, **99**, 95-104.

- VAN EATON, A.R., MUIRHEAD, J.D., WILSON, C.J.N. & CIMARELI, C. 2012. Growth of volcanic ash aggregates in the presence of liquid water and ice: an experimental approach. *Bulletin of Volcanology*, **74**, 1963-1984.
- VALENTINE, G.A. & WHITE, D.L. 2012. Revised conceptual model for maar-diatremes: Subsurface processes, energetics, and eruptive products. *Geology*, **40** (12), 1111-1114.
- VALENTINE, G.A., GRAETTINGER, A.H. & SONDER, I. 2014. Explosion depths for phreatomagmatic eruptions. *Geophysical Research Letters*, **41**, 3045-3051.
- VAUGHAN, R.G. & WEBLEY, P.W. 2010. Satellite observations of a Surtseyan eruption: Hunga Ha'apai, Tonga. *Journal of Volcanology and Geothermal Research*, **198**, 177-186.
- VERGNIOLE, S. & CAPLAN-AUERBACH, J. 2004. Acoustic measurements of the 1999 basaltic eruption of Shishaldin volcano, Alaska: 2. Precursor to the Subplinian phase. *Journal of Volcanology and Geothermal Research*, **137** (1-3), 135-151.
- VERGNIOLE, S. & CAPLAN-AUERBACH, J. 2006. Basaltic thermals and Subplinian plumes: Constraints from acoustic measurements at Shishaldin volcano, Alaska. *Bulletin of Volcanology*, **68** (7-8), 611-630.
- VIERA, M. & AYRESS, M. 2010. A Biostratigraphic Evaluation of Wells 204/13-1 and Sidetrack 204/13-1Z, Tornado Field, West of Shetlands. Prepared for OMV (UK) Limited By Ichron Limited. Ref no. 09/1565/B. 28.
- VIERICK, L.G., TAYLOR, P.N., PARSON, L.M., MORTON, A.C., HERTOGEN, J., GIBSON, I.L. & the ODP Leg 104 Scientific Party. 1988. Origin of the Palaeogene Vøring Plateau volcanic sequence. In: Morton, A.C. & Parson, L.M. (eds). Early Tertiary Volcanism and the Opening of the NE Atlantic. *Geological Society Special Publication*, **39**, 69-83.
- WAAGSTEIN, R. 1988. Structure, composition and age of the Faeroe basalt plateau. In: Morton, A.C. & Parson, L.M. (eds). Early Tertiary Volcanism and the Opening of the NE Atlantic. *Geographical Society Special Publication*, **39**, 225-238.
- WAAGSTEIN, R. & HEILMANN-CLAUSEN, C. 1995. Petrography and biostratigraphy of Palaeogene volcanoclastic sediments dredged from the Faeroes shelf. *Geological Society, London, Special Publications*, **90**, 179-197.
- WAITT, R.B. 2007. Primary volcanoclastic rocks: COMMENT and REPLY. *Geology*, **35**, e141. DOI: 10.1130/G23685C.1
- WALKER, G.P.L. 1973. Explosive volcanic eruptions - a new classification scheme. *Geol Rundsch*, **62**, 431-446.
- WALKER, G.P.L. 1981. Characteristics of two phreatoplinian ashes and their water-flushed origin. *Journal of Volcanology and Geothermal Research*, **9**, 395-407.

- WALKER, G.P.L. 1981a. Generation and dispersal of fine ash and dust by volcanic eruptions. *Journal of Volcanology and Geothermal Research*, **11**, 81-92.
- WALKER, G.P.L. & CROASDALE, R. 1971. Characterisation of Some Basaltic Pyroclastics. *Bulletin Volcanologique*, **35** (2), 303-317.
- WALKER, G.P.L., SELF, S. & WILSON, L. 1984. Tarawera 1886, New Zealand - A basaltic Plinian Fissure Eruption. *Journal of Volcanology and Geothermal Research*, **21**, 61-78.
- WALKER, J.A., WILLIAMS, S.N., KALAMARIDES, R.I. & FEIGENSON, M.D. 1993. Shallow open-system evolution of basaltic magma beneath a subduction zone volcano: the Masaya Caldera Complex, Nicaragua. *Journal of Volcanology and Geothermal Research*, **56**, 379-400.
- WALLRABE-ADAMS, H-J. & LACKSCHEWITZ, K.S. 2003. Chemical composition, distribution, and origin of silicic volcanic ash layers in the Greenland-Iceland-Norwegian Sea: explosive volcanism from 10 to 2000 ka as recorded in deep-sea sediments. *Marine Geology*, **193**, 273-293
- WANMER, S.R. 2013. BSc Dissertation: A study into the Formation of Oscillatory Zoning in Plagioclase, and Related Magma Chamber Processes. *University of Leicester*, Unpublished.
- WANMER, S.R. 2014. Master's thesis: Geochemistry of Kumseongsan, Sonamsan and Hwasan: The tectono-magmatic history of three Late Cretaceous to Early Cenozoic caldera volcanoes in the Gyeongsang Basin, SE Korea. *University of Leicester*, Unpublished.
- WARREN, C.R. 1941. Course of Columbia River in southern central Washington. *American Journal of Science*, **239**, 209-232.
- WASTL, M., STOTTER, J. & CASELDINE, C. 1999. Tephrochronology - a tool for correlating records of Holocene environmental and climatic change in the North Atlantic region. *Geological Society of America, Abstract Volume*, **31**, A315.
- WATERS, A.C. 1965. Geomorphology of South-Central Washington, Illustrated by the Yakima East Quadrangle. *Bulletin of the Geological Society of America*, **66**, 663-684.
- WATSON, D., SCHOFIELD, N., JOLLEY, D., ARCHER, S., FINLAY, A.J., MARK, N., HARDMAN, J. & WATTON, T. 2017. Stratigraphic overview of Palaeogene tuffs in the Faroe-Shetland Basin, NE Atlantic Margin. *Journal of the Geological Society of London*, **174**, 627-645.
- WATSTON, E.J., SWINDLES, G.T., STEVENSON, J.A., SAVOV, I. & LAWSON, I.T. 2016. The transport of Icelandic volcanic ash: Insights from northern European cryptotephra records. *Journal of Geophysical Research: Solid Earth*, **121**, 7177-7192.
- WEBSTER, J.D., CONGDON, R.D. & LYONS, P.C. 1995. Determining pre-eruptive compositions of late Paleozoic magma from kaolinized volcanic ashes: Analysis of glass inclusions in quartz microphenocrysts from tonsteins. *Geochimica et Cosmochimica Acta*, **59** (4), 711-720.

WEHRMANN, H., HOERNLE, K., JACQUES, G., GARBE-SCHÖNBERG, D., SCHMANN, K., MAHLKE, J., LARA, L.E. 2014. Volatile (sulphur and chlorine), major, and trace element geochemistry of mafic to intermediate tephras from the Chilean Southern Volcanic Zone (33-43° S). *International Journal of Earth Sciences*, **103** (7), 1945-1962.

WENTWORTH, C.K. 1922. A scale of grade and class terms for clastic sediments. *The Journal of Geology*, 377-392.

WETZEL, A. & UCHMAN, A. 2012. Hemipelagic and Pelagic Basin Plains. In: Knaust, D. & Bromley, R.G. (eds) Trace Fossils as Indicators of Sedimentary Environments. *Developments in Sedimentology*, **64**, 673-701.

WHITE, J.D.L. 1996. Impure coolants and interaction dynamics of phreatomagmatic eruptions. *Journal of Volcanology and Geothermal Research*, **74**, 155-170.

WHITE, J.D.L. 2000. Subaqueous eruption-fed density currents and their deposits. *Precambrian Research*, **101**, 87-109.

WHITE, J.D.L. & HOUGHTON, B.F. 2006. Primary volcanoclastic rocks. *Geology*, **34**, 677-680.

WHITE, J.D.L. & HOUGHTON, B.F. 2007. Primary volcanoclastic rocks: comment and reply: reply. *Geology*, **35**, e142.

WHITE, R.V., CASTILLO, P.R., NEAL, C.R., FITTON, J.G. & GODARD, M. 2004. Phreatomagmatic eruptions on the Ontong Java Plateau: chemical and isotopic relationship to Ontong Java Plateau basalts. *Geological Society, London, Special Publications*, **229**, 307-323.

WILKIN, R.T., BARNES, H.L. & BRANTLEY, S.L. 1996. The size distribution of framboidal pyrite in modern sediments: An indicator of redox conditions. *Geochimica et Cosmochimica Acta*, **60** (20), 3897-3912.

WILLIAMS, S.N. 1983. Plinian airfall deposits of basaltic composition. *Geology*, **11**, 211-214.

WILSON, L. & HEAD, J.W. 1981. Ascent and Eruption of Basaltic Magma on the Earth and Moon. *Journal of Geophysical Research*, **86** (B4), 2971-3001.

WILSON, C.J.N., HOUGHTON, B.F., KAMP, P.J.J. & McWILLIAMS, M.O. 1995. An exceptionally widespread ignimbrite with implications for pyroclastic flow emplacement. *Nature*, **378**, 605-607.

WINCHESTER, J.A. & FLOYD, P.A. 1977. Geochemical discrimination of different magma series and their differentiation products using immobile elements. *Chemical Geology*, **20**, 325-343.

WINNICK, M.J., CAVES, J.K. & CCHAMBERLAIN, C.P. 2015. A mechanistic analysis of early Eocene latitudinal gradients of isotopes in precipitation. *Geophysical Research Letters*, **42** (19), 8216-8224.

- WINTERWERP, J.C. 2002. On the flocculation and settling velocity of estuarine mud. *Continental Shelf Research*, **22**, 1339-1360.
- WOHLETZ, K.H. 1983. Mechanisms of hydrovolcanic pyroclast formation: Grain-size, Scanning Electron Microscopy, and Experimental studies. *Journal of Volcanology and Geothermal Research*, **17**, 31-63.
- WOHLETZ, K. & HEIKEN, G. 1992. Volcanology and Geothermal Energy. *Berkeley: University of California Press*. <https://cdlib.org/ucpressebooks> - Accessed 31/01/2018.
- WOHLETZ, K., ORS, G. & DE VITA, S. 1995. Eruptive mechanisms of the Neapolitan Yellow Tuff interpreted from stratigraphic, chemical, and granulometric data. *Journal of Volcanology and Geothermal Research*, **67**, 263-290.
- WOHLETZ, K.H. & SHERIDAN. 1983. Hydrovolcanic explosions II. Evolution of basaltic tuff rings and tuff cones *American Journal of Science*, **283**, 385-413.
- WOLDE-GABRIEL, G., BROXTON, D.E. & BYRES Jr, F.M. 1996. Mineralogy and temporal relations of coexisting authigenic minerals in altered silicic tuffs and their utility as potential low-temperature dateable minerals. *Journal of Volcanology and Geothermal Research*, **71**, 155-165.
- WOLFF, J.A. & RAMOS, F.C. 2013. Source materials for the main phase of the Columbia River Basalt Group: Geochemical evidence and implications for magma storage and transport. In: Reidel, S.P., Camp, V.E., Ross, M.E., Wolff, J.A., Martin, B.S., Tolan, T.L. & Wells, R.E. (edS). The Columbia River Flood Basalt Province. *Geological Society of America Special Paper*, **497**, 273-291.
- WOODBURNE, M.O., MACFADDEN, B.J. & SKINNER, M.F. 1981. The North American *Hipparion* Datum and implications for the Neogene of the Old World. *Geobios*, **14** (4), 493-524.
- WOODS, A.W. 1993. Moist convection and the injection of volcanic ash into the atmosphere. *Journal of Geophysical Research*, **98** (B10), 17627-17636.
- WU, W. & WANG, S.Y. 2006. Formulas for Sediment Porosity and Settling Velocity. *Journal of Hydraulic Engineering*, **132** (8), 858-862.
- YAMADA, M., FUJINO, S., GOFF, J. & CHAGUÉ-GOFF, C. 2016. Large-scale erosion and overbank deposition caused by the July 2013 flood of the Abu River, Yamaguchi City, Japan. *Island Arc*, **25** (5), 386-399.
- YAMAMOTO, Y., HISATAKA, F. & HARADA, S. 2015. Numerical simulation of concentration interface in stratified suspension: Continuum-particle transition. *International Journal of Multiphase Flow*, **73**, 71-79.
- YANG, H. & HUANG, Y. 2003. Preservation of lipid hydrogen isotope ratios in Miocene lacustrine sediments and plant fossils at Clarkia, northern Idaho, USA. *Organic Geochemistry*, **34** (3), 413-423.
- YANG, R. & VAN LOON, A.J. 2016. Early Cretaceous slumps and turbidites with peculiar soft-sediment deformation structures on Lingshan Island (Quingdao,

China) indicating a tensional tectonic regime. *Journal of Asian Earth Sciences*, **129**, 206-2019.

YOUNG, T.L. 1977. Discussion of 'Brief Review of liquefaction during earthquakes in Japan' by Kuribayashi & Tatsuoka. *Soils*, **17** (1), 82-85.

ZACHOS, J., PAGANI, M., SLOAN, L., THOMAS, E. & BILLUPS, K. 2001. Trends, Rhythms, and Aberrations in Global Climate 65 Ma to Present. *Science*, **292**, 686-693.

ZACHOS, J.C., DICKENS, G.R. & ZEEBEE, R.E. 2008. An early Cenozoic perspective on greenhouse warming and carbon-cycle dynamics. *Nature*, **451**, 279-283.

ZÄHRER, J., DREIBRODT, S. & BRAUER, A. 2013. Evidence of the North Atlantic Oscillation in varve composition and diatom assemblages from recent, annually laminated sediments of Lake Belau, northern Germany. *Journal of Palaeolimnology*, **50**, 231-244.

ZAPOROZHETS, N.I., SINEL'NIKOVA, V.N. & AKHMET'EV, M.A. 2006. Organic-walled Phytoplankton from Paleogene Sections of Kamchatka. *Stratigraphy and Geological Correlation*, **14** (6), 668-689.

ZIMANOWSKI, B., BÜTTNER, R., LORENZ, V. & HÄFELE, H-G. 1997. Fragmentation of basaltic melt in the source of explosive volcanism. *Journal of Geophysical Research*, **102** (B1), 803-814.

ZHOU, Y., BOHOR, B.F. & REN, Y. 2000. Trace element geochemistry of altered volcanic ash layers (tonsteins) in Late Permian coal-bearing formations of eastern Yunnan and western Guizhou Provinces, China. *International Journal of Coal Geology*, **44** (3-4), 305-324.

List of wells for which the well completion report was used in this study. The completion reports and information on the upper and basal depths of the BF in each well of the Norwegian NSB are publicly available on the Norwegian Petroleum Directorate fact pages website: <http://factpages.npd.no/factpages/Default.aspx>

Index of digital appendices

All image analysis data are presented in these appendices as labelled Microsoft Excel spreadsheet files available on a disk (2x copies) in the back of the hard copy of this thesis available at the University of Glasgow. Each appendix represents a separate Excel file with subdivisions of the appendix (e.g. 1a, 1b, 1c, 1d) representing data found in the tabs of these spreadsheets. These data are additionally available upon request to the author.

Data from UKCS wells 29/05a-7 and 22/30a-1 are also held by the British Geological Survey Data Repository in addition to core samples and thin-sections held at the British Geological Survey Core Store.

1. Vesicularity data

Appendix 1 contains raw data used in the calculation of vesicurity of vesicular grains. The area of the grain (either measured as pixels or μm) and the area of the grain minus vesicles were calculated for each vesicular grain, these values were then used to calculate the percentage of vesicles (% vesicularity) in each grain (see Methods 1.3.3). The resultant percentage vesicularity of each grain is also presented.

1a: Vesicularity data for samples of the Saksunarvtn Ash (Iceland) associated with Chapter 2.

1b: Vesicularity data for samples of the Balder Formation from North Sea Basin wells UKCS 29/05a-7, NOR 25/7-5, NOR 25/11-17, NOR 30/2-1 and Faroe-Shetland Basin Well FSB 6104/25-1, associated with Chapter 3.

1c: Vesicularity data for samples of the Wrabness Member (E.Anglia, UK) that were shown to contain vesicular pyroclasts: samples from the Harwich Stone Band and LEVNAC-14A, associated with Chapter 5.

1d: Vesicularity data used for samples from the Ellensburg Formation (Wahsington and Idaho, USA) associated with Chapter 6.

2. Image analysis grain data

Appendix 2 contains the raw data generated from the image analysis of 8-bit backscatter scanning electron microscope images. A range of data are generated using ImageJ software and are presented. The 'Feret' values were used to indicate the grain-size of individual grains and were sorted and used to calculate the grain-size distribution of each sample.

2a: Image analysis grain data for samples of the Saksunarvatn Ash (Iceland), associated with Chapter 2. Values for the circularity (Circ.) of grains were used to identify elongate grains when calculating the preferred orientation of elongate grains in lacustrine samples (ICE_02A, ICE_04A, ICE_09A). These samples were orientated the correct way up (up is up) and the Angle of elongate grains were calculated by ImageJ, giving the orientation of the grains relative to a horizontal plane (see Methods 1.3.3)

2b: Image analysis grain data produced for samples of the Balder Formation from North Sea Basin wells UKCS 29/05a-7, NOR 25/7-5, NOR 25/11-17, NOR 30/2-1 and Faroe-Shetland Basin Well FSB 6104/25-1, associated with Chapter 3.

2c: Image analysis grain data produced for samples of the Wrabness Member (E.Anglia, UK) associated with Chapter 5.

2d: Image analysis grain data produced for samples of the Ellensburg Formation (Washington and Idaho, USA) associated with Chapter 6.

3. Manual point-count data

Appendix 3 contains the results of manual point-count analysis on samples that was used to determine the percentage of different clast-types and pyroclast morphologies in pyroclastic and volcanoclastic samples. This data was produced by placing a 10 by 10 grid across backscatter scanning electron microscope images from samples and recording the grain information from clasts found at the grid intersections (see Methods 1.3.3).

3a: Manual point-count data produced for samples of the Saksunarvatn Ash (Iceland) associated with Chapter 2.

3b: Manual point-count data produced for samples of the Balder Formation from North Sea Basin wells UKCS 29/05a-7, NOR 25/7-5, NOR 25/11-17, NOR 30/2-1 and Faroe-Sheltand Basin Well FSB 6104/25-1, associated with Chapter 3.

3c: Manual point-count data produced for samples of the Wrabness Member (E.Anglia, UK) associated with Chapter 5.

3d: Manual point-count data produced for samples of the Ellensburg Formation (Washington and Idaho, USA) associated with Chapter 6.